

Springer Series in Optical Sciences 161

Herbert Venghaus  
Norbert Grote *Editors*

# Fibre Optic Communication

Key Devices



Springer

*founded by H.K.V. Lorsch*

Editor-in-Chief: W. T. Rhodes, Atlanta

Editorial Board: A. Adibi, Atlanta

T. Asakura, Sapporo

T. W. Hänsch, Garching

T. Kamiya, Tokyo

F. Krausz, Garching

B. Monemar, Linköping

H. Venghaus, Berlin

H. Weber, Berlin

H. Weinfurter, München

# Springer Series in OPTICAL SCIENCES

---

The Springer Series in Optical Sciences, under the leadership of Editor-in-Chief William T. Rhodes, Georgia Institute of Technology, USA, provides an expanding selection of research monographs in all major areas of optics: lasers and quantum optics, ultrafast phenomena, optical spectroscopy techniques, optoelectronics, quantum information, information optics, applied laser technology, industrial applications, and other topics of contemporary interest.

With this broad coverage of topics, the series is of use to all research scientists and engineers who need up-to-date reference books.

The editors encourage prospective authors to correspond with them in advance of submitting a manuscript. Submission of manuscripts should be made to the Editor-in-Chief or one of the Editors. See also [www.springer.com/series/624](http://www.springer.com/series/624)

## *Editor-in-Chief*

William T. Rhodes

Georgia Institute of Technology  
School of Electrical and Computer Engineering  
Atlanta, GA 30332-0250, USA  
E-mail: [bill.rhodes@ece.gatech.edu](mailto:bill.rhodes@ece.gatech.edu)

## *Editorial Board*

Ali Adibi

Georgia Institute of Technology  
School of Electrical and Computer Engineering  
Atlanta, GA 30332-0250, USA  
E-mail: [adibi@ee.gatech.edu](mailto:adibi@ee.gatech.edu)

Toshimitsu Asakura

Hokkai-Gakuen University  
Faculty of Engineering  
1-1, Minami-26, Nishi 11, Chuo-ku  
Sapporo, Hokkaido 064-0926, Japan  
E-mail: [asakura@eli.hokkai-s-u.ac.jp](mailto:asakura@eli.hokkai-s-u.ac.jp)

Theodor W. Hänsch

Max-Planck-Institut für Quantenoptik  
Hans-Kopfermann-Straße 1  
85748 Garching, Germany  
E-mail: [t.w.haensch@physik.uni-muenchen.de](mailto:t.w.haensch@physik.uni-muenchen.de)

Takeshi Kamiya

Ministry of Education, Culture, Sports,  
Science and Technology  
National Institution for Academic Degrees  
3-29-1 Otsuka, Bunkyo-ku  
Tokyo 112-0012, Japan  
E-mail: [kamiyatk@niad.ac.jp](mailto:kamiyatk@niad.ac.jp)

Ferenc Krausz

Ludwig-Maximilians-Universität München  
Lehrstuhl für Experimentelle Physik  
Am Coulombwall 1  
85748 Garching, Germany *and*  
Max-Planck-Institut für Quantenoptik  
Hans-Kopfermann-Straße 1  
85748 Garching, Germany  
E-mail: [ferenc.krausz@mpq.mpg.de](mailto:ferenc.krausz@mpq.mpg.de)

Bo Monemar

Department of Physics  
and Measurement Technology  
Materials Science Division  
Linköping University  
58183 Linköping, Sweden  
E-mail: [bom@ifm.liu.se](mailto:bom@ifm.liu.se)

Herbert Venghaus

c/o Fraunhofer Institut für Nachrichtentechnik  
Heinrich-Hertz-Institut  
Einsteinufer 37  
10587 Berlin, Germany  
E-mail: [herbert.venghaus@hhi-extern.fraunhofer.de](mailto:herbert.venghaus@hhi-extern.fraunhofer.de)

Horst Weber

Technische Universität Berlin  
Optisches Institut  
Straße des 17. Juni 135  
10623 Berlin, Germany  
E-mail: [weber@physik.tu-berlin.de](mailto:weber@physik.tu-berlin.de)

Harald Weinfurter

Ludwig-Maximilians-Universität München  
Sektion Physik  
Schellingstraße 4/III  
80799 München, Germany  
E-mail: [harald.weinfurter@physik.uni-muenchen.de](mailto:harald.weinfurter@physik.uni-muenchen.de)

Please view available titles in *Springer Series in Optical Sciences*  
on series homepage <http://www.springer.com/series/624>

Herbert Venghaus  
Norbert Grote

Editors

# Fibre Optic Communication

Key Devices

 Springer

*Editors*

Dr. Herbert Venghaus

Dr. Norbert Grote

Fraunhofer Institute for Telecommunications

Heinrich Hertz Institute

Berlin, Germany

ISSN 0342-4111

ISSN 1556-1534 (electronic)

ISBN 978-3-642-20516-3

ISBN 978-3-642-20517-0 (eBook)

DOI 10.1007/978-3-642-20517-0

Springer Heidelberg Dordrecht London New York

Library of Congress Control Number: 2012943621

© Springer-Verlag Berlin Heidelberg 2012

This work is subject to copyright. All rights are reserved, whether the whole or part of the material is concerned, specifically the rights of translation, reprinting, reuse of illustrations, recitation, broadcasting, reproduction on microfilm or in any other way, and storage in data banks. Duplication of this publication or parts thereof is permitted only under the provisions of the German Copyright Law of September 9, 1965, in its current version, and permission for use must always be obtained from Springer-Verlag. Violations are liable to prosecution under the German Copyright Law.

The use of general descriptive names, registered names, trademarks, etc. in this publication does not imply, even in the absence of a specific statement, that such names are exempt from the relevant protective laws and regulations and therefore free for general use.

*Cover concept:* eStudio Calamar Steinen

Printed on acid-free paper

Springer is a part of Springer Science+Business Media ([www.springer.com](http://www.springer.com)).

# Preface

Fibre optic communication networks have become one of the foundations of modern society and economic progress. They have revolutionised the concept of individual communication, enabled easy and cheap access to vast sources of data, and have had a radical impact on industrial development.

The nature of economic and social co-operation has been transformed from localised activities to global action with fibre optic communication networks as the backbone, assuring the information flow needed for working on common projects and tasks. Other enabling applications include ubiquitous surveillance and monitoring networks, distributed sensing and remote healthcare to name just a few.

The fundamental building block for such networks is the optical fibre and the concept for the transmission of information via such fibres as proposed by Charles K. Kao in his seminal paper in 1966.

Only very recently (2009) has this achievement been honoured by the Nobel prize in physics. Another key prerequisite for fibre optic communication is heterostructure semiconductor lasers as proposed independently by Z. Alferov and H. Kroemer in the early 1960s and also honoured by the Nobel prize in physics (2000).

However, today's fibre optic communication networks rely on a number of other key components, and these will be covered in more detail in this work. This text, written by internationally renowned experts in the field, will start with the basic physics behind a particular device, illustrate typical implementations, describe current research topics and discuss commercially available solutions.

After the stage has been set by a chapter on the fundamentals of digital transmission and on optical networks, the next chapter focuses on optical fibres. This will be followed by three laser-related chapters devoted to different types of lasers developed for distinctly different applications in optical networks.

Photodetectors, needed for the conversion of the optical data into the electrical domain again, are covered in a separate chapter.

Single channel bit rates have been raised from the 100 kbit/s range by about two orders of magnitude in the last three decades, and for corresponding systems simple on-off laser modulation is no longer sufficient, but external modulators have to be used. The strategy of steadily raising single channel bit rates, which has proven to

be successful until fairly recently, no longer seems to be a viable approach for raising the channel transmission capacity, however, higher-order modulation schemes look much more promising in this respect. The fundamentals of modulators and the concepts for higher order modulation formats including enabling components are treated in two corresponding chapters.

The total transmission capacity per optical fibre has experienced a tremendous, almost step-like, increase in the 1990s by the introduction of wavelength division multiplexing. The key ingredients for this approach have been, on the one hand and primarily, the Erbium-doped fibre amplifier which allowed the simultaneous optical amplification of many channels within the so-called C-band (1525–1560 nm) or the L-band (1560–1625 nm) as well but additionally dedicated wavelength filters and sufficiently wavelength-tunable lasers. As a consequence, not only widely tunable lasers, but fibre amplifiers and wavelength filters are covered in dedicated chapters as well. For particularly compact solutions, semiconductor optical amplifiers (SOAs) are the preferred choice, which is particularly rewarding if the SOA can be monolithically integrated with other optoelectronic devices on a single chip. On the other hand, SOAs can also be operated beyond the linear regime and under these conditions, they enable all-optical processing. This has been an attractive topic for quite a while and, as outlined in the corresponding chapter, all-optical signal processing still has a lot of promise, but it has not yet reached the status of commercial products.

As fibre optic communication systems become more and more complex (in contrast to the earlier long-haul point-to-point links), the technical implementation of complex structures gets more and more important, and the fundamentals and key issues of passive enabling components are therefore treated in another chapter.

Finally, it has been a vision for many years to combine the potential of silicon-based electronics with photonic functionality on a single chip, and a lot of work is going on towards this goal. The key challenge is getting an electrically pumped optical source onto a silicon chip, and the current state-of-the-art in this field, including the most promising concepts and the results achieved so far, are the topic of the final chapter of this book.

In 2001, Springer published the book “Fibre Optic Communication Devices,” of which we had the pleasure to act as the editors. This book sold successfully, and was even translated into Chinese. This encouraged us to build on this success, and as a result, we have the pleasure of presenting this new text.

It became clear when we started the editing process that this book shouldn't simply be a revised edition, considering the tremendous technical progress achieved in optical communications within the past decade. Instead, the new book represents a radical update, with a number of highly renowned new authors and exciting, novel subject matter.

We are grateful to all contributors for sacrificing valuable time and effort in writing the text, acknowledging that they are already fully absorbed by their professional engagements and daily duties.

Though this book was designed to cover a broad range of the most relevant device topics, nonetheless, it should be appreciated that it only covers a selection, and

we acknowledge that many other important achievements will be omitted. This is particularly true for the references to external sources, which should be considered as exemplary and a good starting point for further research.

Berlin, August 2012

Herbert Venghaus  
Norbert Grote



# Contents

<b>1</b>	<b>Optical Networks</b> .....	1
	D.B. Payne	
1.1	Introduction .....	1
1.2	Background to Optical Communications Networks .....	4
1.2.1	Optical Fibre Transmission Systems .....	4
1.2.2	Fibre Attenuation .....	5
1.2.3	Fibre Dispersion .....	6
1.2.4	Non-linear Effects in Optical Fibre .....	8
1.2.5	A Simple Point-to-point Fibre Link .....	12
1.2.6	Receiver Sensitivity .....	13
1.2.7	Coherent Optical Systems .....	15
1.3	Why Optical Networks? .....	19
1.3.1	Physical Limits .....	19
1.3.2	Commercial Considerations .....	21
1.3.3	Service and Bandwidth Growth .....	24
1.4	Financial Barriers to All-optical Networking .....	27
1.4.1	Network Bandwidth Growth .....	27
1.4.2	Bandwidth Growth vs. Revenue Growth .....	29
1.4.3	Implications for Bandwidth Price Decline .....	30
1.5	Impact on Network Architecture .....	32
1.5.1	Options for Optical Networks .....	33
1.5.2	Long-reach Access .....	41
1.5.3	Metro Network .....	44
1.5.4	Core Networks .....	46
1.6	Summary – Future Evolution of Optical Networking .....	50
	References .....	52
<b>2</b>	<b>Optical Fibers</b> .....	55
	P. Nouchi, P. Sillard and D. Molin	
2.1	Introduction .....	55
2.2	Fiber Basics .....	56

2.2.1	Principle of Light Propagation in Optical Fibers . . . . .	56
2.2.2	Modal Theory of Light Propagation in Optical Fibers . . .	57
2.2.3	Fiber Fabrication . . . . .	60
2.2.4	Fiber Loss . . . . .	61
2.2.5	Fiber Dispersion . . . . .	62
2.3	Multimode Fibers . . . . .	63
2.3.1	Key Characteristics . . . . .	64
2.3.2	Different Types of Multimode Fibers . . . . .	67
2.3.3	Standardization . . . . .	70
2.4	Single-mode Fibers . . . . .	71
2.4.1	Key Characteristics . . . . .	71
2.4.2	Standardization . . . . .	73
2.4.3	Fiber Types . . . . .	77
2.5	Optical Fiber Cables . . . . .	83
2.5.1	Basic Elements of a Cable . . . . .	83
2.5.2	Cable Environment and Cable Types . . . . .	86
2.6	New Developments . . . . .	87
2.6.1	Microstructured Optical Fibers . . . . .	87
2.6.2	Bragg Fibers . . . . .	89
2.6.3	Fibers Mixing Glass and Semiconductors . . . . .	89
2.6.4	Multicore and Multimode Fibers . . . . .	90
	References . . . . .	91
<b>3</b>	<b>Laser Components . . . . .</b>	<b>99</b>
	M. Moehrle, W. Hofmann and N. Grote	
3.1	Introduction . . . . .	99
3.2	Materials for “Long-wavelength” Laser Diodes . . . . .	100
3.3	Laser Diode Structures . . . . .	102
3.3.1	Layer Structure . . . . .	102
3.3.2	Lateral Structure . . . . .	103
3.4	Active Medium . . . . .	105
3.4.1	Quantum-well Layers . . . . .	105
3.4.2	Strained QWs . . . . .	107
3.4.3	Quantum Dots . . . . .	109
3.5	Fabry–Pérot Lasers . . . . .	110
3.6	Single-mode Laser Diodes . . . . .	113
3.6.1	Distributed Feedback Lasers . . . . .	114
3.6.2	Advanced Single-mode Laser Structures . . . . .	121
3.7	Surface-emitting Laser Diodes . . . . .	125
3.7.1	Vertical-cavity Surface-emitting Laser . . . . .	125
3.7.2	Horizontal Cavity Surface-emitting Laser Concepts . . . . .	132
3.8	Concluding Remarks . . . . .	134
	References . . . . .	134

<b>4</b>	<b>Ultrafast Semiconductor Laser Sources</b> .....	139
	M. Aoki	
4.1	Introduction .....	139
4.2	Ultrafast Directly Modulated Laser Sources .....	141
4.2.1	High-speed Characteristics of Directly Modulated Lasers	141
4.2.2	Large-signal Dynamic Analysis of Rate Equations .....	144
4.2.3	Chirp Characteristics of Directly Modulated Lasers .....	145
4.2.4	High-gain Active Materials for Ultrafast Uncooled Lasers	146
4.2.5	Short-cavity Ultrafast Lasers .....	151
4.3	Ultrafast, Low-chirp Externally Modulated Laser Sources .....	157
4.3.1	High-speed Characteristics of Externally Modulated Lasers .....	158
4.3.2	Chirp Characteristics of Externally Modulated Lasers ...	160
4.3.3	Facet-reflection Induced Chirp in Externally Modulated Lasers .....	161
4.3.4	Transmission Simulation of Externally Modulated Lasers Considering Facet-reflection Induced Chirp .....	163
4.3.5	Effect of Photogenerated Current on Modulation Characteristics .....	168
4.3.6	Packaged High-speed Externally Modulated Lasers .....	171
4.3.7	Uncooled, High-speed, Low-chirp Externally Modulated Lasers .....	172
4.4	New Challenges for Ultrafast Semiconductor Light Sources .....	175
4.4.1	High-speed Active/Passive Feedback Diode Lasers .....	175
4.4.2	EA/DFB Laser Devices with Traveling-wave Modulator .	177
4.4.3	Directly IC-driven High-speed Modulators .....	180
	References .....	181
<b>5</b>	<b>Widely Tunable Laser Diodes</b> .....	189
	H. Debrégeas-Sillard	
5.1	Basics of Current Injection Tuning, DBR Lasers .....	191
5.1.1	Current Injection Tuning Mechanisms .....	191
5.1.2	DBR Lasers: Principle of Operation .....	195
5.2	Widely Tunable Lasers by Current Injection .....	200
5.2.1	Sampled Gratings .....	200
5.2.2	SG-DBR Lasers .....	202
5.2.3	SSG-DBR Lasers .....	204
5.2.4	Y-Lasers .....	205
5.2.5	Multiple Peak Grating and Tunable Wide Filter Lasers (GCSR, DS-DBR) .....	205
5.2.6	DBR-MMI .....	207
5.3	Control Issues .....	208
5.3.1	Control Algorithms .....	208
5.3.2	Influence of Cavity Length and Nonlinear Effects .....	210
5.3.3	Fast Tuning .....	213

5.4	Other Wavelength Tunable/Selectable Lasers . . . . .	213
5.4.1	Thermally Tuned DFB Array . . . . .	214
5.4.2	Tunable Vertical Cavity Surface Emitting Lasers . . . . .	214
5.4.3	External Cavity Tunable Lasers . . . . .	216
5.4.4	Tunable Lasers with Ring Resonators . . . . .	218
5.5	Subsystems and Tunable Photonic Integrated Circuits . . . . .	219
5.5.1	Tunable Laser Integrated with Modulator . . . . .	220
5.5.2	Tunable Subsystems . . . . .	221
5.6	Conclusion . . . . .	222
	References . . . . .	224
<b>6</b>	<b>Semiconductor-based Modulators . . . . .</b>	<b>227</b>
	H. Yasaka and Y. Shibata	
6.1	Overview of the Methods to Generate a Digital Optical Signal . . . . .	228
6.1.1	Direct Modulation of Semiconductor Lasers . . . . .	229
6.1.2	Electroabsorption Modulators (EAMs) . . . . .	231
6.1.3	Mach–Zehnder Interferometer (MZI) Modulators . . . . .	233
6.2	Semiconductor-based MZI Modulators . . . . .	239
6.2.1	Fundamentals/Refractive Index Control of Semiconductor Materials . . . . .	239
6.2.2	GaAs- and InP-based MZI Modulators . . . . .	245
6.3	High-speed Modulator Design . . . . .	246
6.4	Performance of Current MZI Modulators . . . . .	251
6.4.1	n-i-n Structure MZI Modulators . . . . .	251
6.4.2	Advanced MZI Modulator Modules . . . . .	258
6.5	High Performance Modulators for Advanced Modulation Formats . . . . .	262
6.5.1	Optical Duobinary (ODB) Modulation . . . . .	263
6.5.2	Optical DPSK Modulation . . . . .	266
6.5.3	Semiconductor Optical DQPSK Modulators . . . . .	269
6.5.4	Semiconductor Multilevel Modulators . . . . .	273
6.6	Summary and Future Issues . . . . .	273
	References . . . . .	273
<b>7</b>	<b>Photodetectors . . . . .</b>	<b>281</b>
	A. Beling and J.C. Campbell	
7.1	Introduction . . . . .	281
7.1.1	Fundamentals . . . . .	281
7.1.2	Material Systems . . . . .	286
7.2	Photodiode Types . . . . .	287
7.2.1	p-i-n Photodiode . . . . .	287
7.2.2	Metal–semiconductor–metal Photodetector . . . . .	289
7.2.3	Avalanche Photodiodes . . . . .	291
7.3	High-speed Photodetectors . . . . .	296
7.3.1	Advanced Photodiode Structures . . . . .	296
7.3.2	High-speed Side-illuminated Photodiodes . . . . .	300

7.3.3	Traveling Wave Photodetectors .....	307
7.3.4	Photoreceivers .....	312
7.4	Summary .....	314
	References .....	314
<b>8</b>	<b>Systems with Higher-order Modulation .....</b>	<b>325</b>
	Y. Achiam, A. Kaplan and M. Seimetz	
8.1	Introduction .....	325
8.1.1	Coherent Detection .....	327
8.1.2	Higher-order Optical Modulation .....	328
8.1.3	Coherent Optical Orthogonal Frequency-division Multiplexing .....	330
8.2	System Configurations .....	331
8.2.1	Transmitter Structures .....	331
8.2.2	Receiver Concepts .....	336
8.3	Key Components for Higher-order Modulation .....	342
8.3.1	Quadrature Modulators .....	342
8.3.2	Integrated Coherent Receivers .....	349
8.3.3	Integrated Balanced Four-branch Receivers .....	356
8.4	Trends in System Performance .....	362
8.5	Issues of Future Research .....	367
	References .....	368
<b>9</b>	<b>Wavelength Filters .....</b>	<b>375</b>
	H. Venghaus	
9.1	Introduction .....	375
9.2	Phase Effects .....	377
9.2.1	General Considerations .....	377
9.2.2	Phase Characterization Techniques .....	379
9.2.3	Typical Group Delay Characteristics .....	379
9.2.4	Group Delay Ripple .....	381
9.2.5	System Implications of Non-ideal Filter Characteristics ..	382
9.3	Fibre Couplers .....	383
9.3.1	Basics of Coupled Mode Theory .....	383
9.3.2	Fabrication of Fibre Couplers .....	385
9.3.3	Characteristics of Fibre Coupler-based Wavelength Filters	386
9.3.4	Applications Beyond Wavelength Channel Filters .....	386
9.4	Diffraction Gratings .....	387
9.4.1	Planar Diffraction Gratings .....	387
9.4.2	Relevant Parameters of Diffraction Gratings .....	388
9.4.3	Diffraction Gratings Used in Fibre Optic Communication	390
9.4.4	InP- and Si-based Planar Gratings .....	391
9.5	Arrayed Waveguide Gratings .....	392
9.5.1	Basics of AWGs .....	392
9.5.2	AWGs in Silica-on-Silicon .....	395

9.5.3	AWGs in InP .....	398
9.5.4	AWGs in Other Material Systems .....	399
9.6	Fibre Bragg Gratings .....	399
9.6.1	Generic Properties .....	399
9.6.2	Types of Gratings .....	401
9.6.3	Apodization .....	402
9.6.4	Temperature and Strain Dependence .....	402
9.6.5	Chirped Gratings .....	403
9.6.6	Long-period Fibre Bragg Gratings .....	403
9.6.7	Commercially Available Devices .....	404
9.7	Fabry–Pérot Interferometers .....	405
9.7.1	Multiple-reflection Cavities .....	405
9.7.2	Wavelength/Frequency Characteristics .....	407
9.7.3	Implementations .....	408
9.7.4	Typical Performance Characteristics .....	409
9.7.5	Applications .....	409
9.8	Thin-film Filters .....	410
9.8.1	Generic Functionalities of TFFs .....	410
9.8.2	Fabrication of TFFs .....	412
9.8.3	Filters for Telecom Applications .....	413
9.8.4	Filter Modules .....	415
9.9	Microrings .....	417
9.9.1	Key Features of Microring Resonators .....	418
9.9.2	Polarization-dependent Effects .....	420
9.9.3	Higher Order Filters .....	420
9.9.4	Experimental Results .....	421
9.9.5	Microring-based Filters with Extended FSR .....	422
9.9.6	Prospects and Further Developments of MR-based Filters .....	422
9.10	Interleavers .....	422
9.10.1	Operation Principle .....	422
9.10.2	Interleaver Types .....	423
9.10.3	Characteristics of Commercially Available Interleavers .....	424
9.11	Acousto-optic Tunable Filters .....	425
9.12	Filters for Silicon Photonics .....	426
9.12.1	General and Technological Aspects .....	426
9.12.2	Examples of CMOS-based Filters .....	427
9.13	Conclusions .....	428
	References .....	430
<b>10</b>	<b>Passive Devices .....</b>	<b>441</b>
	W. Coenning and F. Caloz	
10.1	Optical Connectors .....	442
10.1.1	Introduction .....	442
10.1.2	Connecting Different Types of Fibres .....	442
10.1.3	Basics of FO-Connectors .....	444

10.1.4	Relevant Standards for Optical Connectors	445
10.1.5	Optical Requirements for Single-mode FO-Connectors	446
10.1.6	Mechanical and Climatic Requirements for FO-Connectors	449
10.1.7	Available Standard Connector Types	449
10.1.8	FO-cables for Patch Cords	449
10.1.9	Connectors for Special Fibres or Special Use	451
10.1.10	Cleaning and Inspection	456
10.2	Fibre-optical Couplers	457
10.2.1	Introduction	457
10.2.2	Modelling of Optical Directional Couplers/Power Splitters	457
10.2.3	Fibre Coupler Technologies	461
10.2.4	Classification	461
10.2.5	Star Couplers	463
10.3	Optical Circulators	464
10.4	Optical Isolators	466
10.4.1	General Characteristics	466
10.4.2	Polarisation-independent Optical Isolators	468
10.4.3	Planar Integrated Waveguide-based Optical Isolators	470
	References	471
<b>11</b>	<b>Fiber Amplifiers</b>	<b>473</b>
	K. Rottwitt	
11.1	The EDFA	474
11.1.1	Energy Levels	475
11.1.2	Rate Equations	476
11.1.3	Signal Propagation	476
11.1.4	Emission and Absorption Cross Sections	478
11.1.5	Characteristics	479
11.1.6	Amplifier Performance	480
11.1.7	Recent Applications	483
11.2	Raman Amplifiers	485
11.2.1	Propagation Equations	486
11.2.2	The Raman Gain Coefficient	488
11.2.3	Characteristics	489
11.2.4	Amplifier Performance	491
11.2.5	System Considerations	494
11.2.6	Recent Applications	496
11.3	Parametric Amplifiers	498
11.3.1	Propagation Equations	498
11.3.2	Amplifier Gain Spectrum	500
11.3.3	Characteristics	501
11.3.4	Amplifier Performance	501
11.3.5	Application Issues	503

11.3.6	Recent Applications .....	504
11.4	Conclusion .....	506
	References .....	507
<b>12</b>	<b>Linear Semiconductor Optical Amplifiers</b> .....	<b>511</b>
	R. Bonk, T. Vallaitis, W. Freude, J. Leuthold, R.V. Penty, A. Borghesani and I.F. Lealman	
12.1	Introduction .....	512
12.2	SOA Basics .....	513
12.2.1	Absorption and Emission of Light .....	513
12.2.2	Compound Semiconductors and Heterostructures .....	516
12.2.3	Properties of the Active Region .....	519
12.2.4	SOA Structures and Devices .....	523
12.2.5	Packaging and Photonic Integrated Circuits .....	525
12.2.6	Applications as Booster, Inline and Preamplifiers .....	526
12.3	Parameters of Semiconductor Optical Amplifiers .....	527
12.3.1	Physics of Media with Gain .....	527
12.3.2	Gain and Phase .....	530
12.3.3	Noise Figure .....	532
12.3.4	Gain Saturation .....	536
12.3.5	SOA Dynamics .....	539
12.3.6	Alpha-factor .....	545
12.4	Linear SOAs in Optical Networks .....	549
12.4.1	Parameters of SOAs for Network Applications .....	549
12.4.2	Linear Amplification Range .....	552
12.4.3	SOA Dynamic Range for Different Modulation Formats .....	554
12.5	Commercial SOAs .....	559
12.5.1	SOAs for High Data Rate Signal Amplification .....	560
12.5.2	Extended Wavelength Range and Multi-wavelength Operation .....	563
12.5.3	Reflective SOAs for WDM-PON Applications .....	564
12.6	Conclusion .....	566
	References .....	566
<b>13</b>	<b>Optical Signal Processing for High-speed Data Transmission</b> .....	<b>573</b>
	H.G. Weber and R. Ludwig	
13.1	Introduction .....	573
13.2	OTDM Transmission Systems .....	576
13.2.1	OTDM Transmission System Using OOK Modulation .....	576
13.2.2	1.28 Tbit/s OTDM Transmission System with Conventional Receiver .....	577
13.2.3	1.28 Tbit/s OTDM Transmission System with Coherent Receiver .....	578
13.3	Introduction to Optical Signal Processing for OTDM Systems .....	579



13.3.1	Self-phase Modulation (SPM) and Cross-phase Modulation (XPM) .....	580
13.3.2	Four-Wave Mixing (FWM) .....	582
13.4	OTDM Transmitter .....	583
13.4.1	Optical Pulse Generator .....	583
13.4.2	Optical Pulse Compressor and Pulse Cleaner .....	585
13.4.3	Characterization of Optical Pulses .....	587
13.4.4	Modulation of an Optical Pulse Train .....	588
13.4.5	OTDM-multiplexer .....	592
13.5	Conventional OTDM Receiver .....	594
13.5.1	NOLM as the Optical Gate .....	595
13.5.2	SOA- and EAM-based Optical Gates .....	597
13.5.3	Timing Extraction Devices .....	601
13.5.4	Optoelectronic Base Rate Receiver .....	602
13.6	Coherent OTDM Receiver .....	604
13.6.1	Principle of the Phase-diversity Homodyne Receiver ...	604
13.6.2	Coherent Receiver as an OTDM Demultiplexer .....	607
13.6.3	Postdetection Electrical Signal Processing .....	608
13.7	Optical Signal Processing for Combating Impairments in the Fiber Link .....	609
13.7.1	Fiber Nonlinearity and Choice of Appropriate Transmission Fiber .....	609
13.7.2	Compensation of Chromatic Dispersion by DCF .....	610
13.7.3	Compensation of Higher Order Chromatic Dispersion ...	612
13.7.4	Compensation of Polarization-mode Dispersion .....	613
13.8	Concluding Remarks .....	616
	References .....	617
<b>14</b>	<b>Silicon Lasers and Photonic Integrated Circuits .....</b>	<b>625</b>
	Di Liang, A.W. Fang and J.E. Bowers	
14.1	Silicon as a Platform for PICs .....	626
14.2	Lasers (Emitters) and Amplifiers on Silicon .....	628
14.2.1	Low-dimensional Silicon Approaches .....	630
14.2.2	Raman Effect .....	636
14.2.3	Monolithic Integration Approaches .....	638
14.2.4	Hybrid Integration Approach .....	642
14.3	High-speed Signal Processing in Silicon .....	651
14.3.1	Silicon Optical Modulators .....	652
14.3.2	Hybrid Silicon Modulators .....	654
14.4	Summary .....	657
	References .....	658
	<b>About the Authors .....</b>	<b>665</b>
	<b>Index .....</b>	<b>677</b>

# List of Contributors

**Yaakov Achiam, Ph.D.** 4 Tseelas St., Omer 8496500, Israel,  
email: Yachiam@gmail.com

**Masahiro Aoki, Ph.D.** Hitachi, Ltd., Research & Development Group, 1-6-1,  
Marunouchi, Chiyoda-ku, Tokyo 100-8220, Japan,  
email: masahiro.aoki.ev@hitachi.com

**Andreas Beling, Ph.D.** Department of Electrical & Computer Engineering, Uni-  
versity of Virginia, 351 McCormick Rd., P.O. Box 400743, Charlottesville, VA  
22904, USA,  
email: ab3pj@virginia.edu

**Dr. René Bonk** Alcatel-Lucent Deutschland AG, Bell Labs/Optical Access, Lo-  
renzstr. 10, 70435 Stuttgart, Germany,  
email: Rene.Bonk@alcatel-lucent.com

**Dr. Anna Borghesani** CIP Technologies, Phoenix House, Adastral Park, Martles-  
ham Heath, Ipswich, IP5 3RE, UK,  
email: anna.borghesani@huawei.com

**Prof. Dr. John E. Bowers** Electrical and Computer Engineering Department, Uni-  
versity of California, Santa Barbara, CA 93106-9560, USA,  
email: bowers@ece.ucsb.edu

**Dr. François Caloz** Diamond SA, via dei Patrizi 5, 6616 Losone, Switzerland,  
email: francois.caloz@diamond-fo.com

**Prof. Dr. Joe C. Campbell** Department of Electrical & Computer Engineering,  
University of Virginia, 351 McCormick Road, P.O. Box 400743, Charlottesville,  
VA 22904, USA,  
email: jccuva@virginia.edu

**Prof. Dr. Ing. Wolfgang Coenning** Hochschule Esslingen, Flandernstraße 101,  
03732 Esslingen, Germany,  
email: wolfgang.coenning@hs-esslingen.de

**Dr. Hélène Debrégeas** III–V Lab, Route de Nozay, 91460 Marcoussis, France,  
email: helene.debregeas@3-5lab.fr

**Alexander W. Fang, Ph.D.** Aurion, 130 Robin Hill Rd, Suite 300, Goleta, CA  
93117, USA  
email: alexander.fang@aurion.com

**Prof. Dr. Wolfgang Freude** Karlsruhe Institute of Technology (KIT), Institute of  
Photonics & Quantum Electronics (IPQ), Engesserstr. 5, 76131 Karlsruhe, Ger-  
many,  
email: W.Freude@kit.edu

**Dr. Norbert Grote** Fraunhofer Institute for Telecommunications, Heinrich Hertz  
Institute, Einsteinufer 37, 10587 Berlin, Germany,  
email: norbert.grote@hhi.fraunhofer.de

**Dr. Werner Hofmann** Technische Universität Berlin, Institute of Solid State  
Physics and Center of Nanophotonics, Hardenbergstr. 36, 10623 Berlin, Germany,  
email: Werner.Hofmann@tu-berlin.de

**Dr. Arkady Morris Kaplan** CeLight Inc., 12200 Tech Rd., Silver Spring, 20904  
MD, USA,  
email: arkady0@yahoo.com

**Dr. Ian F. Lealman** CIP Technologies, Phoenix House, Adastral Park, Martlesham  
Heath, Ipswich, IP5 3RE, UK,  
email: Ian.Lealman@huawei.com

**Prof. Dr. Juerg Leuthold** Institut für Photonik und Quantenelektronik, Universität  
Karlsruhe (TH), Engesserstr. 5, 76131 Karlsruhe, Germany,  
email: j.leuthold@ihq.uni-karlsruhe.de

**Di Liang, Ph.D.** Electrical and Computer Engineering Department, University of  
California (UCSB), Santa Barbara, CA 93106, USA,  
email: dliang@ece.ucsb.edu

**Dr. Reinhold Ludwig** Picowave Microelectronics GmbH, Möwenweg 17, 12359  
Berlin, Germany,  
email: reinhold.ludwig@hhi.fraunhofer.de

**Dr. Martin Möhrle** Fraunhofer Institute for Telecommunications, Heinrich Hertz  
Institute, Einsteinufer 37, 10587 Berlin, Germany,  
email: martin.moehrle@hhi.fraunhofer.de

**Denis Molin** Prysmian Group, Site Data 4, Route de Nozay, 91460 Marcoussis,  
France, email: denis.molin@prysmiangroup.com

**Dr. Pascale Nouchi** THALES Research & Technology France, Campus Polytech-  
nique, 1 avenue Augustin Fresnel, 91767 Palaiseau cedex, France,  
email: pascale.nouchi@thalesgroup.com

**Dr. David B. Payne** Optical Network Architectures in the CTVR center, Trinity College, Dublin, Ireland,  
email: david.b.payne@btinternet.com

**Prof. Richard Penty** Cambridge University Engineering Department, Electrical Engineering Building, 9 JJ, Thomson Ave, Cambridge, CB3 0FA, UK,  
email: rvp11@cam.ac.uk

**Prof. Dr. Karsten Rottwitt** DTU Fotonik, Department of Photonics Engineering, Technical University of Denmark, DTU, 2800 Kgs. Lyngby, Denmark,  
email: karo@fotonik.dtu.dk

**Prof. Dr.-Ing. Matthias Seimetz** Beuth Hochschule für Technik Berlin, FB VII: Elektrotechnik – Mechatronik – Optometrie, Luxemburger Str. 10, 13353 Berlin, Germany,  
email: matthias.seimetz@beuth-hochschule.de

**Yasuo Shibata, Ph.D.** NTT Photonics Laboratories, 3-1 Morinosato Wakamiya, Atsugi-shi, Kanagawa Pref., 243-0198, Japan,  
email: shibata.yasuo@lab.ntt.co.jp

**Dr. Pierre Sillard** Prysmian Group, Site Data 4, Route de Nozay, 91460 Marcoussis, France,  
email: pierre.sillard@prysmiangroup.com

**Dr. Thomas Vallaitis** Infinera, 1322 Bordeaux Drive, Sunnyvale, CA 94089,  
email: tvallaitis@infinera.com

**Dr. Herbert Venghaus** c/o Fraunhofer Institute for Telecommunications, Heinrich Hertz Institute, Einsteinufer 37, 10587 Berlin, Germany,  
email: herbert.venghaus@hhi-extern.fraunhofer.de

**Prof. Dr. Hans-Georg Weber** Sudetenstrasse 16, 63916 Amorbach, Germany,  
email: hans-georg.weber@gmx.de

**Prof. Hiroshi Yasaka, Ph.D.** Research Institute of Electrical Communication, Tohoku University, 2-1-1 Katahira, Aoba-ku, Sendai-shi, Miyagi Pref., 980-8577, Japan,  
email: yasaka@riec.tohoku.ac.jp

# Acronyms

AC	as cleaved
ADM	add-drop multiplexer
ADSL	asymmetric digital subscriber line
AOC	active optical cable
AOM	acousto-optic modulator
AOTF	acousto-optic tunable filter
APC	angled physical-contact
APD	avalanche photodiode
APON	ATM passive optical network
AR	anti-reflection
ASE	amplified spontaneous emission
ASK	amplitude shift keying
ATM	asynchronous transfer mode
AWG	arrayed waveguide grating
BCB	benzocyclobutene
BER	bit error rate (or $\sim$ ratio)
BERT	bit error rate tester
BH	buried heterostructure
BM	Bragg mirror
BPON	broadband passive optical network
BPSK	binary phase shift keying
BR	buried ridge
BRS	buried ridge stripe
CAGR	compound annual growth rate
CB	conduction band
CC	carrier cooling
CD	chromatic dispersion
CDP	carrier density pulsation
CDWM	coarse wavelength division multiplexing
CH	carrier heating
CI	carrier injection

CMOS	complementary metal oxide semiconductor
CO	central office
CO-OFDM	coherent optical OFDM
CR	coupling ratio
CSDFB	curved stripe DFB (laser)
CS-RZ	carrier-suppressed return-to-zero
CTE	coefficient of thermal expansion
CVD	chemical vapour deposition
CW	continuous wave
D	directivity
DBA	dynamic bandwidth assignment
DBPSK	differential binary phase shift keying
DBR	distributed Bragg reflector
DC	direct current
DCA	digital communications analyzer
DCG	dispersion compensating (fibre Bragg) grating
DCF	dispersion-compensating fibre
DDF	dispersion decreasing fibre
DDR	dual-depletion region (photodiode)
DEMUX	demultiplexer
DER	dynamic extinction ratio
DFB	distributed feedback
DGTE	distributed Gires-Tournois etalon
DI	delay interferometer
DILM	dispersion-imbalanced loop mirror
DLI	delay line interferometer
DMA	differential mode attenuation
DMD	differential mode delay
DOS	density of states
DP-QPSK	dual-polarization QPSK
DPSK	differential phase-shift keying
DQPSK	differential quadrature phase shift keying
DS-DBR	digital supermode DBR (laser)
DSF	dispersion-shifted fibre
DSL	digital subscriber line
DSP	digital signal processing
DUT	device under test
DWDM	dense wavelength division multiplexing
E/E	electrical/electrical
E/O	electrical/optical
EA	electroabsorption
EA/DFB	electroabsorption modulator with monolithic integrated DFB laser
EAM	electroabsorption modulator
EDFA	erbium doped fibre amplifier
EL	excess loss

EL	electroluminescence
ELO	epitaxial layer overgrowth
EMB	effective modal bandwidth
EMBc	effective modal bandwidth (computed)
EML	externally modulated laser
ER	extinction ratio
ER-GPON	extended reach GPON
EVM	error-vector magnitude
FBC	fused biconical coupler
FBG	fibre Bragg grating
FCA	free carrier absorption
FDM	frequency-division multiplexing
FEC	forward error correction
FFT	fast Fourier transform
FIC	full range wavelength independent coupler
FIN	finesse
FOM	figure of merit
FOPA	fibre optic parametric amplifier
FPI	Fabry–Pérot interferometer
FROG	frequency resolved optical gating
FRP	fibre glass reinforced plastic
FSAN	Full Service Access Network (Group)
FSR	free spectral range
FTTCab	fibre-to-the-cabinet
FTTH	fibre-to-the-home
FTTP	fibre-to-the-premises
FTTx	fibre-to-the- <i>x</i>
FWHM	full-width half maximum
FWM	four-wave mixing
GCSR	grating-assisted codirectional coupled sampled grating reflector (laser) grating-assisted codirectional coupler with sampled reflector (laser) grating coupler sampled reflector (laser)
GDP	gross domestic product
GDR	group delay ripple
GE	gigabit Ethernet
GEM	GPON encapsulation method
GFF	gain flattening filter
GFP	general framing protocol
GI-POF	graded-index POF
GPON	gigabit PON
GRIN	graded-index (lens)
GTI	Gires-Tournois interferometer
GVD	group velocity dispersion
HCSEL	horizontal cavity surface emitting laser
HEMT	high electron mobility transistor

HFFR	halogen free fire retardant
HH	heavy hole
HOM	higher order mode (fibre)
HPLD	high power laser diodes
HR	high reflectivity, high reflection
HSEP	hybrid silicon evanescent platform
I <sup>2</sup> E	impact ionization engineering
IAD	ion-assisted deposition
IBS	ion beam sputtering
IC	integrated circuit
IETF	Internet Engineering Task Force
IFB	integrated feedback
IFFT	inverse FFT
IL	insertion loss
IPDR	input power dynamic range
ISI	inter-symbol interference
ISO	International Standards Organisation
IT	information technology
ITRS	international technology roadmap for semiconductors
ITU	International Telecommunication Union
LC	liquid crystal
LH	light hole
LIDAR	light detection and ranging
LLU	local loop unbundling
LMS	least mean square
LO	local oscillator
LO-MMF	laser optimized MMF
LPCVD	low pressure CVD
LPF	long-pass filter
LPG	long period (fibre Bragg) grating
LR	low reflectivity
LR-PON	long reach PON
LSZH	low smoke zero halogen
LTOPA	low-temperature oxygen plasma-assisted (wafer bonding)
<i>M</i> ASK	<i>M</i> -ary amplitude shift keying
MBE	molecular beam epitaxy
MCVD	modified chemical vapour deposition
MEMS	microelectromechanical system
MESFET	metal semiconductor field effect transistor
MFD	mode field diameter
MI	Michelson interferometer
MLFL	mode-locked fibre laser
MLLD	mode-locked laser diode
MLSL	mode-locked solid state laser
MM	multimode



MMF	multimode fibre
MMI	multimode interference
MOCVD	metal-organic vapour phase epitaxy
MOF	micro-structured optical fiber
MQW	multi-quantum well
MSAN	multi-service access nodes
MSL	micro strip line
MSM	metal-semiconductor-metal
MUTC	modified UTC
MUX	multiplexer
MZ	Mach-Zehnder
MZDI	Mach-Zehnder delay interferometer
MZI	Mach-Zehnder interferometer
MZM	Mach-Zehnder modulator
NA	numerical aperture
NF	noise figure
NOLM	nonlinear optical loop mirror
NLSE	nonlinear Schrödinger equation
NRZ	non-return-to-zero
NZDSF	nonzero dispersion shifted fibre
OA&M	operations, administration, and maintenance
OADM	optical add-drop multiplexer
ODB	optical duo-binary
OEIC	optoelectronic integrated circuit
OEO	optical-electrical-optical
OFDM	orthogonal frequency division multiplexing
OFL	over-filled launch (condition)
OLT	optical line termination
ONT	optical network termination
ONU	optical network unit
OOK	on off keying
OPGW	optical ground wire (cable)
OPLL	optical phase locked loop
OPO	optical parametric oscillator
OSA	optical spectrum analyzer
OSNR	optical signal to noise ratio
OTDM	optical time division multiplexing
OVD	outside vapour deposition
PBG	photonic band gap
PBS	polarization beam splitter
PC	physical-contact
PCG	planar concave grating
PCP	primary cross-connect point
PCVD	plasma chemical vapour deposition
PD	photodiode

PDA	partially-depleted-absorber (photodiode)
PDG	polarization dependent gain
PDH	plesiochronous digital hierarchy
PDL	polarization-dependent loss
PECVD	plasma enhanced chemical vapour deposition
PER	polarization extinction ratio
PIC	photonic integrated circuit
PLC	planar lightwave circuit
PLL	phase-locked loop
PM	polarization maintaining
PMD	polarization mode dispersion
PMMA	polymethylmethacrylate
POF	plastic optical fibre
PON	passive optical network
POTS	plain old telephone service
PRBS	pseudo random binary sequence
PRBS	pseudo-random bit stream
PSK	phase shift keying
PSTN	public switched telephone network
PVD	physical vapour deposition
QAM	quadrature amplitude modulation
QCSE	quantum-confined Stark effect
QD	quantum dot
QPSK	quadrature phase shift keying
QSPF	quad small form factor pluggable
QW	quantum well
QWI	quantum well intermixing
RCE	resonant cavity enhanced
RDF	reverse dispersion fibre
RF	radio frequency
RFPD	refracting facet photodiode
RL	return loss
ROADM	reconfigurable OADM
ROCE	return on capital expenditure
RSOA	reflective SOA
RW	ridge waveguide
RWG	ridge waveguide
RZ	return-to-zero
SACM	SAM with additional charge layer
SAM	separate amplification and multiplication
SBS	stimulated Brillouin scattering
SC	super continuum
SCEEL	short cavity edge emitting laser
SCH	separate confinement heterostructure
SDH	synchronous digital hierarchy

SEM	scanning electron microscope
SFP	small form-factor pluggable
SG	sampled grating
SHB	spectral hole burning
SHG	second harmonic generation
SI	semi-insulating
SI-POF	step-index POF
SK	Stranski–Krastanov (growth regime)
SLA	service level agreement
SLA	super large area (fibre)
SM	single-mode
SMF	single mode fibre
SMSR	side-mode suppression ratio
SNR	signal to noise ratio
SO	split-off
SOA	semiconductor optical amplifier
SOI	silicon-on-insulator
SOP	state of polarization
SoS	silica-on-silicon
SPF	short-pass filter
SPM	self phase modulation
SRS	stimulated Raman scattering
SSC	standard single-mode coupler
SSFM	split step Fourier method
SSG	super-structure grating
SSMF	standard single-mode fibre
STM	synchronous transport module
SWP	spatial walk-off polarizer
TDM	time division multiplexing
TE	transverse-electric (mode polarization)
TEC	thermal expanded core (fibre)
TEC	thermal expansion coefficient
TEC	thermo-electric cooler
TFF	thin-film filter
TIA	transimpedance amplifier
TIR	total internal reflection
TJ	tunnel junction
TLA	tunable DFB laser array
TLS	tunable laser source
TM	transverse-magnetic (mode polarization)
TOSA	transmitter optical sub-assembly
TPA	two photon absorption
TTG	tunable twin guide (laser)
TWPD	travelling wave photodetector
TWRS	TrueWave reduced slope (fibre)

UTC	uni-travelling carrier (photodiode)
VAD	vapour (phase) axial deposition
VB	valence band
VCSEL	vertical cavity surface emitting laser
VDSL	very high speed digital subscriber line
VOA	variable optical attenuator
VPH	volume-phase holographic (grating)
VSL	variable stripe length (method)
WDL	wavelength-dependent loss
WDM	wavelength division multiplexing
WFC	wavelength flattened coupler
WG	waveguide
WGPD	waveguide photodiode
WIC	wavelength independent coupler
WSS	wavelength selective switch
XENPAK	multi-source agreement defining transceiver modules which conform to the 10 Gigabit Ethernet standard
XFP	10-Gbps small form factor pluggable module
XGM	cross gain modulation
XPM	cross phase modulation
XRD	X-ray diffraction

# Chapter 1

## Optical Networks

David B. Payne

**Abstract** After a compilation of the fundamentals of optical communication networks the chapter continues with technical arguments in favour of optical networks. Specific attention is given to financial barriers, which have to be overcome for the introduction of all-optical networks, in particular in the access area. Different options for optical access networks are explained, including the pros and cons for their implementation. Examples are point-to-point fibre solutions and various kinds of passive optical networks (PONs). The rest of the chapter covers metro and core networks and ends with an outlook on expected future developments.

### 1.1 Introduction

Using visible light for communications purposes fades into pre-history. It is known that early systems such as fire beacons were used by the ancient Greeks and more sophisticated systems using torches to convey letters of the alphabet are described by Polybius in his book “The Histories” in the 2nd century BC. Smoke signals were used by the North American Indians since ancient times and more recently semaphore was developed by the French in the 18th century. In 1880 Alexander Graham Bell transmitted speech via his “Photophone” which used sunlight reflected off a mirror caused to vibrate by the incident sound pressure waves. This vibration modulated the light intensity falling on a parabolic mirror and a selenium optical detector some distance away. The electrical resistance of the selenium detector varies with incident light and therefore was used to modulate the current flowing in an electrical circuit containing an electro-magnetic telephone earpiece thus converting the original vibration back to sound. All these systems were using “free space” op-

---

David B. Payne (✉)  
Optical Network Architectures in the CTVR center, Trinity College, Dublin, Ireland  
e-mail: david.b.payne@btinternet.com

tical communications and as such were dependent on environmental factors such as weather conditions and local visibility.

The first practical proposal to use light, guided by glass optical fibres for long-distance, high-capacity, communications purposes was by Kao & Hockham of Standard Telecommunications Laboratories in their now seminal 1966 paper [1]. In this paper they proposed a fibre with a glass core 3 to 4 microns in diameter clad with another glass of refractive index about one percent smaller than the core. At that time optical fibre had losses of  $\sim 1000$  dB/km but Kao and his team were proposing that these losses could be reduced to only tens of decibels per kilometre. Kao's target loss was 20 dB/km which would, at that time, enable optical transmission to be economically competitive with co-axial cable.

It would take four years for Kao's prediction for fibre loss to be realised but his 1966 paper did trigger considerable interest in the possibility and potential for optical fibre communications. At the British Post Office Research Laboratory at Dollis Hill in London, F.F. Roberts got support to set up an optical communications research project. With Kao's paper and the Post Office interested in the potential for optical communications, research into optical fibre and optical fibre communications began to spring up around the world.

In 1970 Corning Glass Works using pure fused silica and a vapour phase deposition process produced a fibre with the target 20 dB/km loss at 633 nm [2]; this result was confirmed at the British Post Office Research Labs. Also in 1970 teams working in Russia (led by Zhores I. Alferov at Ioffe Physico-Technical Institute of the USSR Academy of Sciences) and in the USA Bell Labs (Izuo Hayashi, Morton Panish) [3, 4] reported continuous wave operation of semiconductor lasers at room temperature; the main ingredients for optical communications were in place!

This early work was focused on single-mode optical fibres or mono-mode as they were then called. In these fibres the guiding region or core of the fibre has a small diameter of a few microns. This made alignment of lasers to the fibre and splicing and connectors difficult and in 1971 to 1972 the emphasis moved to larger core fibres with multi-mode propagation characteristics. Over the next few years fibre losses continued to decline and laser lifetimes continued to increase, in 1977 after a number of field trials in the intervening years, live traffic was carried over fibre systems in the USA by the General Telephone and Electronics Corporation and in the UK by the British Post Office. These systems and the first generation of commercial systems used multi-mode fibre and semiconductor lasers operating in the 850 nm region. Operating fibres in a multi-mode region causes a number of problems that limit the performance of the optical system (see Sect. 1.2) and research continued with single-mode fibre which offered both lower potential fibre loss and much higher bandwidths. In 1982 after successful field trials the British Post Office changed its optical fibre strategy from multi-mode fibre to single-mode fibre. Single-mode fibre is now the dominant fibre in telecommunications networks world wide, although multi-mode fibre is still extensively used in the shorter distance data networks.

Loss in optical fibre is always going to be a fundamental limitation and in these early systems the only way of overcoming the problem of attenuation was to regen-

erate the signal by first detecting the optical signal, converting it to an electronic signal and then regenerating this signal with electronic amplification and signal processing. These regenerators were expensive and power consuming requiring buildings or other physical infrastructure to house them, often remote from switching centres. What was needed was a device that could amplify the optical signal without conversion to the electrical domain. The concept of optical amplification was not new: the laser that was at the heart of the optical transmitter has inherent optical gain with feedback to make it oscillate. The problem was making a practical optical amplifier that could be low cost and exhibit low power consumption and could extend the reach of optical systems such that remote regenerators would not be needed. Any regeneration equipment required could then be located at switching centres. The answer was the erbium-doped fibre amplifier (EDFA) concept first published and demonstrated by David N. Payne and others at Southampton University in 1987 [5]. These components: low-loss optical fibre, semiconductor laser transmitters and erbium-doped fibre optical amplifiers paved the way for modern optical communications systems and the dominant role that they now play in the transmission networks of the world.

This chapter will give an overview of optical networking and its potential evolution. The direction in which networks might evolve is driven by a complex mix of: demand for new services, economic viability, regulatory/political intervention and then finally technological developments. Optical network evolution and the components required to service them into the future could go down a number of different paths which would put different emphasis on the type of components required, their functionality and their performance. To understand these options it is necessary to consider future service scenarios, network architectural options and the economics of end-to-end network structures.

There are some major challenges facing future network architectures, and current approaches may not be sustainable into the future. One challenge is the unprecedented growth in user bandwidth that could arise if fibre-to-the-home (FTTH) is deployed on a major scale. A second problem is the energy consumption of always-on high speed networks. Although communication devices are low power compared to machinery in other industries, the sheer volume and always-on nature of the technology now makes the communications industry one of the largest users of electrical energy. As broadband usage increases, as it inevitably will, reducing energy requirements is going to be a very important consideration for future network design.

The major issue for future communications networks is however going to be economic viability. During the transition from networks being telephony (voice) services dominated to becoming data services dominated, there has been a massive shift in the revenue structure of the industry. This shift in its simplest form has been a shift from usage charging to flat rate charging. The upshot of which is that there is now little relationship between the revenue earned and the bandwidth consumed. When this is coupled with the growth of bandwidth and the required price decline per unit of network bandwidth as networks grow, it becomes apparent that current network architectures will not scale economically to meet the potential future demand; this will be discussed in more detail later. New approaches are required that

could challenge the conventional evolutionary direction for networks and will determine the direction for optical component evolution and market sizing.

Before we examine some of these implications in more detail the next section will give a brief background to optical communications systems and an overview of the development of today's network architectures.

## **1.2 Background to Optical Communications Networks**

Communications networks that we see around the world today have evolved from telephone networks that were originally designed to interconnect voice circuits with channel bandwidths of  $\sim 4$  kHz. The technology used in these early networks has left a lasting legacy on the layout of the physical infrastructure of today's networks, particularly the building locations and the physical routing of cables and duct.

Telephone networks used a copper pair from the customer to a local interconnection point which was usually in a building owned by the network operator. The physical limitations of the transmission characteristics of the copper pair to carry the analogue speech signals, and also the DC current required to power the early telephones, meant that the local switch needed to be relatively close to the end customer's telephone equipment and therefore the distance from exchange to customer is typically less than 2 km and rarely exceeds 7 km. These local switches, known as local exchanges or central offices (COs), collect traffic from the customers they service, concentrate and multiplex the traffic and send it over higher capacity links to a hierarchy of other switches. Before digital transmission systems the multiplexing technique was analogue frequency-division multiplexing (FDM) which limited the number of channels to a few hundreds on even the highest capacity transmission systems. Today transmission and switching is carried out digitally and modern high-capacity transmission links can carry the equivalent of tens to hundreds of thousands of telephony channels.

### ***1.2.1 Optical Fibre Transmission Systems***

Optical fibre is the latest in a long line of communications transmission technology stretching back to parallel copper wires strung along wooden poles which in turn evolved to twisted pairs of copper wires assembled into cables, higher bandwidth systems using coaxial cables and even microwave waveguides as long-distance transmission media. Optical fibre is currently the most advanced transmission technology we have and there is currently no better technology on the horizon.

As outlined in more detail in Chap. 2, there is a wide range of types of optical fibre targeted at different applications and industries. In communication networks the two dominant types of fibre are made from ultra pure silica pulled into a thin strand of glass (125  $\mu\text{m}$  in diameter). To provide a light guiding region there is a central



core where the pure silica is doped with very low absorption materials to raise the refractive index. This produces a coaxial glass fibre which guides light by confining the electromagnetic field to the doped core region. The difference between the main two fibre types is the size of the core doped region and the level of doping. The most common fibre in wide-area telecommunications networks is fibre with a small core  $\sim 10\ \mu\text{m}$  and a doping level such that only the simplest electromagnetic field pattern or mode can propagate at the wavelengths of interest. This fibre is known as single-mode fibre and totally dominates the wide-area telecommunications networks around the world.

The other type of fibre, which is predominant in high-performance, short-distance, data networks, has a larger core  $\sim 50\ \mu\text{m}$  with more dopant producing a larger refractive index in the core region. This means the fibre can propagate a large number of modes and as such is known as multi-mode fibre. The larger core of multi-mode fibre enables easier splicing and connectors compared with single-mode fibre, it also enables easier coupling of light sources to the fibre including LED devices. This easier coupling leads to simpler and cheaper production processes for the transmitter and receiver devices leading to lower component costs and also simpler cable installation practices requiring less expensive equipment. This easier coupling is the only advantage of multi-mode fibre over single-mode fibre, in terms of sheer performance single-mode fibre massively outperforms multi-mode fibre.

The two main impairments introduced into a transmission link by the optical fibre are attenuation of the propagating light and dispersion which broadens the pulses being transmitted with the distance propagated. Both attenuation and dispersion increase the probability that the signal is detected in error at the receiver and therefore increase the error rate in the received data. To ensure adequate system performance both attenuation and dispersion penalties need to be kept within carefully controlled limits.

### ***1.2.2 Fibre Attenuation***

Attenuation in optical fibre arises from a number of mechanisms. The fundamental mechanism is Rayleigh scattering whereby photons are scattered out of the guiding region by the fine grain structure of the silica material making up the bulk of the fibre. This scattering is wavelength dependent and reduces in proportion to the fourth power of the wavelength. This loss mechanism is the same for both single-mode and multi-mode fibre.

Pure silica, which forms the bulk of the fibre, has a window of low absorption lying between two intrinsic absorption regions, at short wavelengths (the ultra violet region) absorption occurs via electron transitions. At long wavelengths (the infra-red region) absorption occurs by photon interaction with silicon–oxygen (Si–O) bonds. The dopant materials, used to increase the refractive index of the guiding core region, produce additional attenuation and because dopant levels are greater in multi-mode fibre, these absorption losses are higher than those in single-mode fibre. Water introduced into the fibre during manufacture produces Si–OH bonds which have ab-

sorption processes operating between 2700 nm and 4200 nm and overtones that fall into the operating region of the fibre at 1383 nm and 950 nm. Modern manufacturing processes can virtually eliminate water and produce so-called 'dry fibre' that does not exhibit the OH absorption peaks. This will be particularly valuable for opening up the full fibre operating spectrum for dense wavelength-division multiplexing (DWDM) in the future.

The third major loss mechanism in optical fibre is leakage of photons from the guiding region due to bends in the fibre. Bends in fibre arise from the large-scale bends introduced by the installation of the cable containing the fibre into a real physical environment, small-scale bends arise from the structure of the cables the fibres are put into and the surfaces of the protective coatings and sheaths etc. that go into the make-up of the cable. The fibre will also experience different contact pressures with these materials and components dependent on environmental parameters such as temperature and pressure.

The loss produced by large-scale bends is called macro-bend loss and the loss produced by the small-scale bends is called micro-bend loss. Bend losses arise because the propagating mode of a curved fibre is slightly different from the propagating mode of a straight fibre. As the mode enters a bend, the mode can be thought of as being composed of two components, the larger component corresponds to the mode of the curved fibre, the second component is the difference between this mode and the mode of the straight fibre that entered the bend. This small component is the loss due to the transition from straight to curved fibre propagation modes and is sometimes called transition loss and is the main mechanism in micro-bend loss.

The propagation mode of a curved fibre is displaced from the centre of the core and moves to a slightly larger radius of curvature. More of the mode field is outside the core region and the outer edge of this mode is travelling a longer distance than the inner edge due to the curvature and therefore needs to travel faster than the inner edge. A portion of the mode field would be required to travel faster than the speed of light for the medium and is therefore lost. This loss is continuous around the bend and therefore is proportional to the length of the bend. Higher order modes with complex field patterns are less well guided than lower order modes and suffer greater losses from bends. In multi-mode fibre the effects of bends and the subsequent loss is twofold: the fibre suffers greater losses for a given bend due to the weaker guiding properties of the higher order modes but also the distribution of power across the mode volume is changed with higher order modes effectively being stripped of power relative to the lower order modes. Macro- and micro-bend losses increase with wavelength and become dominant at long wavelengths beyond  $\sim 1600$  nm.

### ***1.2.3 Fibre Dispersion***

Dispersion in optical fibre produces pulse broadening which increases the overlapping or interference between adjacent transmitted symbols (inter-symbol interference, ISI). The effect of this is to increase the probability at the optical receiver that

a '1' state is received in error as a '0' state and a '0' state is received in error as a '1' state and therefore increase the bit error rate of the system. Dispersion in optical fibre arises through several mechanisms. For multi-mode fibre the dominant mechanism is inter-modal dispersion which is caused by the different group velocities of the propagating modes of the fibre.

Single-mode fibre has one propagating mode only so inter-modal dispersion is eliminated. In single-mode fibre there are three main dispersion mechanisms: material dispersion, waveguide dispersion and polarisation-mode dispersion (PMD). Material dispersion arises because the refractive index  $n(\lambda)$  of the fibre material is wavelength dependent and the phase velocity of light in the medium  $v(\lambda) = \frac{c}{n(\lambda)}$  is therefore also dependent on wavelength ( $\lambda$ : vacuum wavelength of the propagating light,  $c$ : vacuum speed of light). In communications systems a message has a band or group of frequencies, and it is the velocity of this group of frequencies, known as the group velocity, which is of interest. The variation of group velocity as a function of wavelength produces group velocity dispersion (GVD) and produces the pulse spreading that leads to ISI and an increase in bit error rate. The GVD due to material dispersion is proportional to the second derivative of  $n(\lambda)$ . Silica fibre has zero material dispersion near a wavelength of 1280 nm, below this wavelength the material dispersion is negative and above it is positive.

In an optical fibre the field distribution across the light-guiding core region of the fibre varies with wavelength, for standard fibre the mode field expands with wavelength and a larger portion of the field travels through the lower index cladding material. This has the effect of reducing the average refractive index that the mode experiences and increases the phase velocity. This effect produces waveguide dispersion and the GVD produced over the wavelength range of optical fibre is always negative. The effect of the waveguide dispersion for standard fibre is to shift the zero dispersion point from  $\sim 1280$  nm to  $\sim 1310$  nm. By suitable design of the refractive index profile of special fibres the waveguide dispersion can be used to offset the material dispersion to produce zero dispersion in the 1500 nm region or even dispersion-flattened fibre. A special dispersion-compensating fibre (DCF) can be designed to have large negative dispersion in the 1500 nm region to compensate for the positive dispersion of standard fibre. DCF is used in long-haul high bit rate systems to ensure the end-to-end dispersion of a fibre link is within carefully managed limits.

The third dispersion mechanism mentioned above is polarisation-mode dispersion, which is a form of mode dispersion even though the fibre is designed to be single mode. It arises because of residual birefringence in the fibre due to imperfect geometry and the effect of stresses on the fibre produced at bends et cetera. The orthogonal polarisations of the fundamental mode will therefore experience different propagation delays over a fibre link and produce pulse broadening.

Polarisation-mode dispersion is small compared to material and waveguide dispersion. In early systems, before the year 2000, it was generally ignored for practical transmission systems and most of the fibre installed before this year did not have a PMD specification. However, unlike material and waveguide dispersion, which are static properties of the fibre and can be compensated by using dispersion-

compensation elements (such as DCF), PMD is time varying because it depends on the physical environment the fibre is experiencing and this changes due to environmental parameters such as temperature and pressure. These changes in environmental parameters affect both the degree of birefringence in the fibre link and the state of polarisation of the propagating light, both these effects affect the differential group delay and therefore the overall pulse broadening at the receiving end of the system.

PMD therefore has to be treated statistically and – although small – can become the limiting dispersion parameter in very high bit rate systems from 10 Gbit/s and upwards. After the year 2000 most fibre installed had a PMD tolerance specified and PMD is not generally a major issue for 10 Gbit/s systems if a fibre link is installed with all new fibre. In practice this is not always possible and sections of a link may have to operate with pre PMD specified fibre. PMD is still a major concern for operators today, active PMD compensation is expensive and upgrading 10 Gbit/s systems to higher bit rates such as 40 Gbit/s or 100 Gbit/s can be problematic and potentially expensive. To help overcome this problem complex modulation schemes (see Chap. 8) and line coding that limit the optical bandwidth of 40 to 100 Gbit/s systems to the order of a 10 Gbit/s binary channel are receiving much attention. These schemes are all effectively trading channel bandwidth for signal-to-noise ratio but the benefit from the reduction in channel bandwidth required for the higher bit rates can mean that the dispersion management for 10 Gbit/s systems can be used with little or no modification for 40 Gbit/s and possibly even for 100 Gbit/s. This approach provides an upgrade path for operators without needing to change the location of repeaters and regenerators and can enable mixed use of wavelengths in WDM systems.

#### ***1.2.4 Non-linear Effects in Optical Fibre***

When light propagates through a physical medium such as the silica of optical fibre, the electric field of the propagating light can locally modify the physical properties of the medium. These effects give rise to non-linear interactions with the propagating light producing non-linear behaviour. Silica is actually a very linear material with very small non-linear characteristics and requires very high optical intensities to generate noticeable non-linear phenomena. However, the very small core region that guides the light in a single-mode fibre can produce very high optical intensities with relatively small input optical power levels. Also optical fibres provide very long interaction lengths so that even small effects can become very significant over the distances of optical transmission systems.

There are two fundamental mechanisms giving rise to non-linear effects in optical fibres: one is where the light intensity in the fibre locally affects the refractive index. This effect is known as the Kerr effect and gives rise to three processes that can affect the communications channel, these are self-phase modulation (SPM), cross-phase modulation (XPM) and four-wave mixing (FWM). The other process is inelastic scattering which produces two major phenomena: stimulated Brillouin scattering (SBS) and stimulated Raman scattering (SRS).

In this section we will briefly describe these effects and the implications for optical communications systems. It should be noted upfront that ideally the transmission media would be perfectly linear and non-linear effects generally reduce the performance of optical transmission systems. However, given that fibre is also a dispersive transmission medium well-controlled non-linear effects can also be used to enhance transmission capability in certain circumstances. Non-linear effects can also be exploited in devices for functions such as fast optical switching and optical signal processing, for example in 2R and 3R optical signal regenerators. For a more thorough grounding in non-linearities in optical fibre see [6].

### 1.2.4.1 Stimulated Brillouin Scattering (SBS)

When an incident light wave reaches sufficient intensity, electrostriction effects can be sufficiently large to generate acoustic waves in the material. The incident light and the scattered light (Stokes light) interfere to produce a travelling acoustic wave which produces a periodic refractive index variation that acts as a Bragg grating. This travelling acoustic wave Bragg grating Doppler shifts the scattered light so that, when it interferes with the incident light, the frequency difference reinforces the initial travelling acoustic wave producing a positive feed-back effect. In SBS the dominant scattered light is back scatter from a forward travelling acoustic wave. The greater the incident light intensity the greater the magnitude of the acoustic wave generated and the greater the backscattered light wave. This effectively limits the amount of optical power that can be transmitted through an optical fibre. SBS becomes a problem at quite low optical power (a few mW) in standard fibre and is therefore a major problem for optical communications transmission systems.

Mitigation of SBS to increase the threshold power is therefore very important in communication systems if higher power laser sources for long-distance transmission systems are to be used.

The optical power threshold for SBS in optical fibre is approximately [7]:

$$P_{\text{th}} \approx \frac{21bA_e}{g_B L_e} \left[ 1 + \frac{\Delta f_s}{\Delta f_B} \right], \quad (1.1)$$

where:  $1 \leq b \leq 2$  is dependent on the polarisation state [8],  $A_e$ : effective area of the fibre core ( $\sim 50 \mu\text{m}^2$ ) for standard single-mode fibre,  $g_B$ : SBS gain coefficient which for silica fibre is  $4.5 \times 10^{-11} \text{ m/W}$ ,  $L_e$ : effective fibre length,  $\Delta f_s$ : line width of the incident light (Hz),  $\Delta f_B$ : SBS interaction bandwidth ( $\sim 20 \text{ MHz}$  at  $1.55 \mu\text{m}$ ).

For standard single-mode fibre systems the only parameter available to increase the SBS threshold is the source line width. The system length is predetermined by the physical system topology and adding regenerators to reduce system lengths is not usually an economic option. High bit rate systems have inherently greater line width than lower bit rate systems and will therefore have higher thresholds but there can still be a significant component of the narrow line width optical carrier present, depending on the modulation scheme used. Some modulation schemes such as phase

modulation can be used to increase the line width of the transmission system, however with pressure to increase fibre utilisation and spectral efficiency, advanced modulation techniques are more often used to reduce the modulation bandwidth not increase it (see Chap. 8), as increasing line width also increases dispersion penalties. A technique to increase the SBS threshold often used in direct detection systems is to dither the laser source wavelength at a dither frequency below the low frequency cut-off of the system receiver (the low frequency bound of the transmitted signal can be increased by use of suitable line codes). In this way relatively large laser output frequency deviations can be achieved, to suppress SBS, without increasing the dispersion penalty of the system (the deviation frequency is much greater than the dither frequency).

#### **1.2.4.2 Stimulated Raman Scattering (SRS)**

Raman scattering is an inelastic scattering process produced when the input source photons interact with the molecules of the transmission media and are either re-emitted with higher energy (anti-Stokes wave) or, more usually in a silica fibre, with lower energy (Stokes wave) and therefore longer wavelength than the incident wavelength. The wavelength shift of the Stokes wave in SBS is around 11 GHz whereas for SRS the wavelength shift is  $-15.6$  THz ( $\sim +120$  nm). The other main difference is that SBS produces back-scattered light whereas SRS produces co-propagating light. However, the optical intensity threshold for SRS is much higher ( $\sim 1$  W for standard single-mode fibre) than for SBS (assuming SBS mitigation techniques have not been employed).

SRS can be a problem for a widely spaced WDM system because the short wavelength channels can act as pump sources for longer wavelength channels; this has two detrimental effects. Power is lost from the short wavelength channels, effectively increasing the attenuation of these channels and also light coupled from these channels into longer wavelength channels can produce crosstalk which can increase the error rate of the system.

However, SRS can also be used to amplify optical signals by coupling power from non-modulated pump wavelengths into longer information carrying wavelengths. This can produce optical amplification at wavelengths outside the relatively narrow wavelength range of erbium-doped fibre amplifiers (see Chap. 11, Sect. 11.2).

#### **1.2.4.3 Self-Phase Modulation (SPM)**

Self-phase modulation is caused by the Kerr effect and produces chirp across the optical pulse with lower frequencies at the leading edge of the pulse and higher frequencies at the trailing edge. This induced chirp increases the spectral width of the pulse and the normal positive dispersion of the fibre will act on this chirp to broaden the pulse as it propagates down the fibre. This causes increased ISI at the receiver which increases the system error rate. However, if the fibre exhibits nega-

tive (anomalous) dispersion, then the pulse can be compressed by SPM. Standard single-mode fibre exhibits positive dispersion over most of the operating wavelength range and SPM is therefore undesirable and needs to be taken into account in the dispersion management of the fibre link.

However, in specially designed dispersion-managed fibre links, for long-haul, high bit rate systems, the pulse compression possibilities of SPM can be utilised to generate very short intense pulses that can propagate as solitons along the fibre where the normal dispersion is exactly cancelled by the SPM pulse compression in anomalous dispersion components or DCF thus maintaining the pulse width over very long distances. These techniques can be used in ultra-long-haul transmission systems.

#### 1.2.4.4 Cross-Phase Modulation (XPM)

Cross-phase modulation is generated by the same physical mechanism as self-phase modulation but is produced by a second wave which co-propagates with the first wave. If the pulses in each optical wave overlap, the two waves each locally modify the refractive index for the other wave and introduce phase changes in the pulses of the other wave. Although in direct detection systems phase distortion in pulses is not important, when the pulses are propagated through a dispersive fibre then phase-to-amplitude conversion occurs and amplitude crosstalk can be produced which causes an increase in system error rate. XPM-induced crosstalk can be significant in high-bit rate WDM systems with close channel spacing.

#### 1.2.4.5 Four-Wave Mixing (FWM)

Four-wave mixing is a non-linear phenomenon also produced by the Kerr effect. In this case the interaction of two or more incident light waves produces additional wavelengths which in turn can mix with the incident wavelengths to create more waves. The general relationship for the FWM products is given by

$$f_{ijk} = f_i + f_j - f_k, \quad (1.2)$$

where  $f_i$ ,  $f_j$ , and  $f_k$  are the frequencies of incident light waves (which in turn can be FWM generated waves) while  $f_{ijk}$  is the frequency of the light wave resulting from the non-linear interaction. The four waves involved in the process give FWM its name.

The total number of frequency products  $M$  produced by FWM for a DWDM system with  $N$  wavelength channels is given by:

$$M = \frac{1}{2} (N^3 - N^2). \quad (1.3)$$

If these products fall onto the DWDM system wavelength channels, then there is potential for significant levels of crosstalk-induced noise that will increase the error

rate in the optical channels. If the frequency spacing of the channels is uniform, then the products that fall inside the spectral range of the DWDM band will fall onto wavelength channels with the majority falling on the centre channels of the DWDM band. Assuming that all WDM systems will utilise the wavelengths defined by the ITU G694.1 standard grids for DWDM systems (which have equal frequency spacing of 100, 50, 25, and 12.5 GHz with a reference channel at 1552.52 nm), then the FWM products will fall on the DWDM channel wavelengths. However the efficiency of the FWM product generation process is crucially dependent on the phase matching of the frequency components in the FWM mixing process and also the interaction length. It is also much greater for closely spaced wavelength channels.

The dispersion of the fibre has a major effect on this phase-matching constraint and fibres with higher dispersion such as standard G652 single-mode fibre do not have a significant problem with FWM even with 12.5 GHz spacing [9]. However, operators that have installed dispersion-shifted fibre (DSF) for long-haul transmission networks have a major problem as they operate in a low dispersion region around the dispersion zero position. Advanced modulation techniques exploiting phase modulation can help to reduce FWM susceptibility but ideally DSF would be used with non-uniform frequency grids, unfortunately there are no standards for such grids.

Outside of the requirements for transmission systems four-wave mixing can be a useful process for other functions such as optical wavelength conversion, parametric amplification and optical time-division multiplexing for very high bit rate systems (see also Chap. 13, Sects. 13.3.2 and 13.5.2.2). For a review of four-wave mixing see [10].

### ***1.2.5 A Simple Point-to-point Fibre Link***

A point-to-point single-mode fibre transmission link will be power budget limited; the penalty due to dispersion will be designed to be small compared to losses in the transmission path. The power budget available for the link will be the difference between the optical transmitter power and the receiver sensitivity. This power budget has to be spread over all the losses in the transmission path, fibre loss, splice loss, connector loss etc., and also allow for a system margin that is provided as a contingency against changes to the power budget and link losses over the lifetime of the system. The receiver sensitivity will take into account the bit rate and modulation scheme used over the transmission link. A simple point-to-point optical transmission link is shown in Fig. 1.1.

The ratio (transmitter power)/(minimum required receiver power) is normally designated as the optical power budget expressed in decibels or given by the difference  $T_x$  (dBm) –  $R_x$  (dBm):

$$T_x - R_x = Ll_f + \left( \frac{L}{d} + 2N_s \right) l_s + 2l_c + M, \quad (1.4)$$

where  $T_x$ : transmitter power (dBm),  $R_x$ : receiver sensitivity (dBm),  $L$ : fibre length,  $l_f$ : cabled fibre loss per unit length,  $d$ : mean splice spacing,  $N_s$ : the number of splices



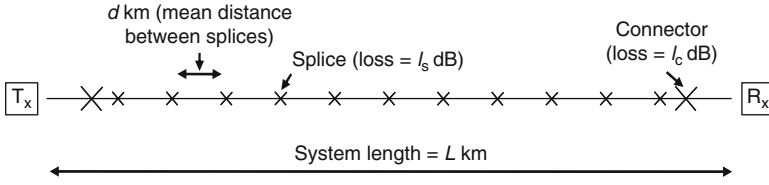


**Fig. 1.1** Simple point-to-point optical system

in the exchange building (depends on working practices), note the factor 2 is to account for the two terminating exchange buildings,  $l_s$ : splice loss,  $l_c$ : connector loss, and  $M$ : system margin.

The system margin includes: Transmitter power and receiver sensitivity variations – environmental and ageing; cabled fibre loss variations – environmental and ageing; maintenance splices, imperfect equalisation, dispersion penalty and PMD margin (for high bit rate systems), and jitter and timing errors.

The power budget is a simple addition of all the loss parameters in the system plus the system margin, the loss parameters are in practice random variables and statistical methods can be employed to give a probability distribution of total system loss. Operators could use such a distribution as part of the calculation of the margin required against a probability of the margin being used up and excessive error rates being produced. However, many operators and designers of optical transmission systems use worst-case design rules which result in conservative designs with large system margins for the majority of links.

### 1.2.6 Receiver Sensitivity

A key parameter in system power budget calculations and hence system design is the receiver sensitivity which is the minimum optical power needed at the receiver to achieve a desired bit error rate. The optical power at the receiver is

$$P_s = Nhf, \quad (1.5)$$

where  $N$  is the photon arrival rate,  $hf$  the photon energy,  $h$  is Planck's constant, and  $f$  is the optical frequency. The receiver photodiode current produced by  $P_s$  is

$$I_s = \eta Ne = \eta \frac{P_s e}{hf}, \quad (1.6)$$

where  $\eta$  is the quantum efficiency and  $e$  the electron charge. The photon arrival rate at the receiver will have fluctuations which are described by Poisson statistics and appear as noise on the received photo-current. The mean square value of the noise current is proportional to the signal current  $I_s$  and the receiver post-detection bandwidth  $B$  and is given by

$$\overline{i_s^2} = 2eI_sB. \quad (1.7)$$

The resulting signal-to-noise ratio (SNR) is

$$\text{SNR} = \frac{I_s^2}{i_s^2} = \frac{I_s^2}{2eI_sB} = \frac{I_s}{2eB} \quad (1.8)$$

and combining (1.6) and (1.8) yields

$$\text{SNR} = \frac{\eta N}{2hfB}. \quad (1.9)$$

Equation (1.9) is the ‘quantum-limited’ signal-to-noise ratio.

For an ideal receiver the quantum efficiency  $\eta = 1$ , also the receiver would be noiseless, therefore there would be no noise when zeros are received and the decision threshold can be set at ‘0’. The only noise present is in the ‘1’ state when light is present at the receiver. The number of photons per ‘1’ bit exhibits a Poisson distribution.

For any bit containing a ‘1’ symbol the probability of the number of photons arriving  $P[n]$  is given by the Poisson distribution

$$P[n] = \frac{\mu^n \exp(-\mu)}{n!}, \quad (1.10)$$

where  $\mu =$  mean number of photons per bit. Because the decision threshold is set at zero, the probability of an error is the probability of a ‘1’ being received with zero photons. For equal ‘1’s and ‘0’s the probability of a ‘1’ equals 1/2 and the probability of that ‘1’ being an error is  $P[n = 0]$ , therefore

$$P_e = P[n = 0] = \frac{1 \mu^0 \exp(-\mu)}{0!} = \frac{1}{2} \exp(-\mu). \quad (1.11)$$

From this equation we can derive the average number of photons per ‘1’ bit for a given target error rate  $P_e$ :

$$\mu(P_e) = \ln\left(\frac{1}{2P_e}\right) \text{ photons per bit} \quad (1.12)$$

and an average received power

$$P_s = \frac{\mu hf}{\tau} = \frac{hfB_r}{2} \ln\left(\frac{1}{2P_e}\right), \quad (1.13)$$

where  $\tau$  is the bit period,  $B_r = 1/\tau$  is the bit rate, and  $P_s$  is the quantum-limited receiver sensitivity.

The quantum-limited error probability is shown against photons per bit in Fig. 1.2 and the corresponding quantum-limited sensitivity for a 1550 nm receiver operating at a range of system bit rates is shown in Fig. 1.3.

Nearly all optical receivers used in communications systems are square law detectors that produce an output signal proportional to the received optical power or field intensity squared. A square law detector acts as a low pass filter and the detection process removes any information associated with the optical carrier frequency

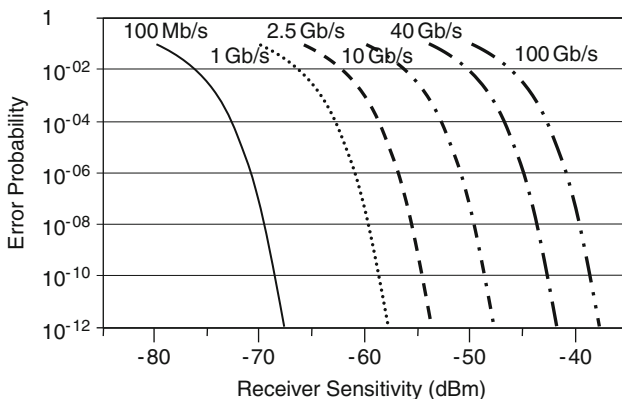


**Fig. 1.2** Quantum-limited error probability vs. photons/bit

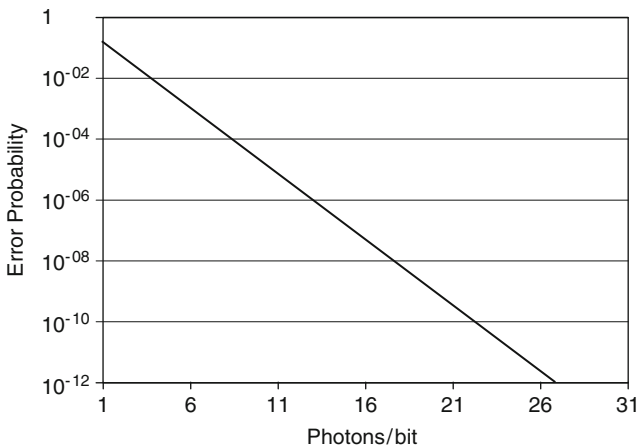


**Fig. 1.3** 1550 nm quantum-limited receiver sensitivity

or phase. A practical receiver has additional noise processes, the dominant one being thermal noise, which results in the receiver sensitivity, even for “good” receivers, being 30 dB and more from the quantum limit. Photodetectors are covered in more detail in Chap. 7 and will therefore not be treated in more detail here.

### 1.2.7 Coherent Optical Systems

The vast majority of commercially deployed optical systems use direct detection receivers where the power of the received optical signal is converted directly to an electrical current. In these systems a message signal  $m(t)$  directly modulates the intensity ( $E_s^2$ ) of the electric field ( $E_s$ ) of the optical carrier. The photodiode at the

receiver is a square law detector the output of which is proportional to the electric field amplitude squared ( $E_s^2$ ) and therefore directly recovers the intensity-modulated message signal. Consider the optical carrier

$$e_s = E_s \cos(\omega_s t). \quad (1.14)$$

The average power in the optical carrier  $P_r$  is

$$P_r = \frac{1}{T} \int_0^T e_s^2 dt = \frac{E_s^2}{T} \int_0^T \cos^2(\omega_s t) dt = \frac{E_s^2}{2}. \quad (1.15)$$

The modulated optical carrier intensity is

$$[1 + m(t)] e_s^2 = (1 + m(t)) E_s^2 \cos^2(\omega_s t) = (1 + m(t)) \frac{1}{2} E_s^2 (\cos(2\omega_s t) + 1) \quad (1.16)$$

and

$$[1 + m(t)] e_s^2 = \frac{E_s^2}{2} \cos(2\omega_s t) + \frac{E_s^2}{2} m(t) \cos(2\omega_s t) + \frac{E_s^2}{2} + \frac{E_s^2}{2} m(t). \quad (1.17)$$

The high-frequency terms containing  $\cos(2\omega_s t)$  are removed by the optical receiver so that we get for the detector output  $P_{\text{dect}}$

$$P_{\text{dect}} = \frac{E_s}{2} + \frac{E_s}{2} m(t) = P_r (1 + m(t)), \quad (1.18)$$

where  $P_r$  is the average received power of the unmodulated optical carrier, and (1.18) is simply the power in the optical carrier (not the field), amplitude modulated by the message signal  $m(t)$ .

It should be noted that the output direct detection signal is not dependent on the optical frequency or the optical source line width.

In coherent systems the optical frequency and phase of the signal are used in the detection process which enables modulation schemes used in traditional electrical communications systems to be used in optical systems. The main advantages of coherent detection systems are more efficient use of the optical spectrum and greater receiver sensitivities. The latter advantage was the main driver of the coherent optical research carried out during the 1980s, the advent of the erbium fibre optical amplifiers in the late 1980s offset this advantage and the technological difficulties associated with coherent optical systems led to an almost complete decline in optical coherent systems research. In recent years the growing pressure to increase fibre utilisation and the advancement of optical component technologies has seen a resurgence of interest in coherent systems and they could become very important in future optical networks.

To compare coherent transmission systems with direct detection we will consider amplitude modulation systems although advanced modulation techniques are now

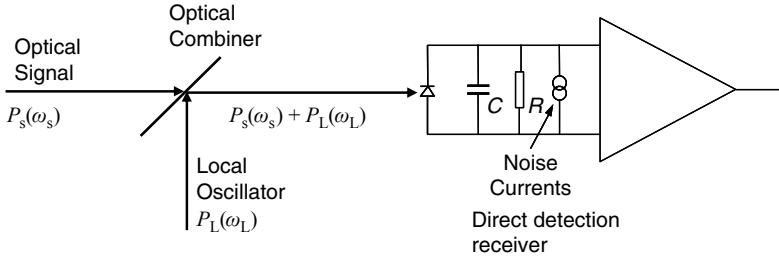


**Fig. 1.4** Schematic of simple coherent detection receiver

being considered that use phase-, frequency- and amplitude-modulation schemes (see Chap. 8 of this book for more details).

In a simple coherent detection system the modulated optical signal is compared with a reference source or local oscillator. Both the local oscillator source and the modulated optical source require narrow optical line width or “coherent” sources. The arrangement is shown schematically in Fig. 1.4.

The optical input signal is mixed with the local oscillator signal before entering the square law detector photodiode.

The electric field of the input optical signal and local oscillator are given by:

$$e_s(t) = E_s (1 + m(t)) \cos(\omega_s t) \quad \text{and} \quad e_L(t) = E_L \cos(\omega_L t + \phi), \quad (1.19)$$

where  $E_s$  is the field amplitude of the optical signal carrier angular frequency  $\omega_s$ , and  $E_L$  is the field amplitude of the optical local oscillator angular frequency  $\omega_L$ . Note the message signal  $m(t)$  is now modulating the amplitude of the optical field, not the intensity as in the direct detection system.

The field on the photodiode of the receiver is the sum of these two fields

$$e_s(t) + e_L(t) = E_s (1 + m(t)) \cos(\omega_s t) + E_L \cos(\omega_L t + \phi). \quad (1.20)$$

The photodiode responds to the square of this incident field:

$$(e_s(t) + e_L(t))^2 = e_s^2(t) + 2e_s(t)e_L(t) + e_L^2(t) = e_{ph}^2, \quad (1.21)$$

where

$$e_s^2 = \frac{E_s^2}{2} \left[ (1 + m(t))^2 (\cos(2\omega_s t) + 1) \right], \quad e_L^2 = \frac{E_L^2}{2} [\cos(2(\omega_L t + \phi)) + 1] \quad (1.22)$$

and

$$\begin{aligned} 2e_s e_L &= 2E_s (1 + m(t)) \cos(\omega_s t) E_L \cos(\omega_L t + \phi) \\ &= 2E_s E_L (1 + m(t)) \left( \frac{1}{2} (\cos(\omega_s t + \omega_L t + \phi) + \cos(\omega_s t - \omega_L t - \phi)) \right) \\ &= E_s E_L (1 + m(t)) [\cos(\omega_s t + \omega_L t + \phi) + \cos(\omega_s t - \omega_L t - \phi)]. \end{aligned} \quad (1.23)$$

All the terms at optical frequencies or higher are lost in the square law receiver and the resulting photo current is

$$I_{\text{ph}} = \frac{E_s^2}{2} (1 + m(t))^2 + E_s E_L (1 + m(t)) \cos(\omega_s t - \omega_L t - \phi) + \frac{E_L^2}{2}. \quad (1.24)$$

Let us next consider the components of the photo current. The currents from the optical signal carrier and the local oscillator are

$$I_s = \frac{E_s^2}{2} \quad \text{and} \quad I_L = \frac{E_L^2}{2}, \quad (1.25)$$

respectively, and therefore

$$E_s = \sqrt{2I_s}, \quad E_L = \sqrt{2I_L} \quad \text{and} \quad E_s E_L = 2\sqrt{I_s I_L} \quad (1.26)$$

so that the photo current becomes

$$I_{\text{ph}} = I_s (1 + m(t))^2 + 2\sqrt{I_s I_L} (1 + m(t)) \cos(\omega_s t - \omega_L t - \phi) + I_L. \quad (1.27)$$

The local oscillator power can be arranged to be very large compared to the received signal power i.e.  $I_L \gg I_s$ , and the photo current then approximates to

$$I_{\text{ph}} \approx 2\sqrt{I_s I_L} (1 + m(t)) \cos(\omega_{\text{if}} t - \phi) + I_L, \quad (1.28)$$

where  $\omega_{\text{if}} = \omega_s - \omega_L$  represents an intermediate frequency with a phase  $\phi$  modulated by the message signal. The local oscillator term does not contain message information but does contribute to the quantum noise.

We now have two options: a Heterodyne system where  $\omega_{\text{if}}$  is non zero, i.e. the local oscillator frequency is deliberately tuned away from the message signal optical carrier frequency. This allows the modulated intermediate frequency to be processed by conventional radio frequency electronic techniques. The intermediate frequency must be high enough to accommodate the *modulated* signal bandwidth which for amplitude modulation is twice the message signal bandwidth, i.e.  $\omega_{\text{if}} \geq 2B$ , where  $B$  is the message bandwidth.

The other option is a Homodyne system where the local oscillator is locked to the message signal optical carrier frequency and  $\omega_{\text{if}} = 0$ , in this case the message signal photo current is produced directly from the photo detector but is now dependent on the phase  $\phi$ :

$$I_{\text{ph}} \approx 2\sqrt{I_s I_L} (1 + m(t)) \cos \phi. \quad (1.29)$$

This requires the local oscillator to be optically frequency and phase locked to the incoming optical signal which is a difficult process and generally heterodyne systems have been preferred because of the electronic processing enabled by the use of an intermediate frequency and also because the frequency stability of the local oscillator is easier to achieve than phase locking. An additional advantage of heterodyne

systems is that the optical local oscillator can also be used to tune closely spaced frequency/wavelength-multiplexed optical channels.

As previously mentioned one of the advantages of coherent detection is the potential for much improved receiver sensitivities compared to direct detection systems: The mean square signal photo current is proportional to the signal power  $P_s$ :

$$P_s = \frac{4I_s I_L \overline{m^2(t)}}{2} = 2I_s I_L \overline{m^2(t)} \quad (1.30)$$

while the noise power  $P_N$  is given by

$$P_N = 2e(2B)(I_s + I_L + 2\sqrt{I_s I_L} + I_d) + 8\pi CkT(2B)^2. \quad (1.31)$$

Note that  $2B$  is the minimum receiver bandwidth to accommodate both sidebands of the modulated message signal. The first term in the noise equation is the quantum noise from the photo current components, the second term is the thermal noise assuming a simple receiver as discussed in Sect. 1.2.6.

The signal-to-noise ratio SNR is

$$\text{SNR} = \frac{2I_s I_L \overline{m^2(t)}}{2e(2B)(I_s + I_L + 2\sqrt{I_s I_L} + I_d) + 8\pi CkT(2B)^2} \quad (1.32)$$

and when  $I_L \gg I_s$  this simplifies to

$$\text{SNR} = \frac{I_s \overline{m^2(t)}}{2eB}. \quad (1.33)$$

This is equivalent to the quantum-limit receiver sensitivity for the direct detection case discussed in Sect. 1.2.6.

Coherent detection opens the way for optical systems to exploit the advanced modulation techniques used in electrical and radio communications systems. These modulation schemes have relative advantages and disadvantages that can help in the design of optical transmission systems for different environments and system characteristics; for example, enabling higher bit rate systems at say 40 Gbit/s or 100 Gbit/s to operate over channels originally designed for 10 Gbit/s transmission rates. For more details of these advanced modulation systems see Chap. 8.

## 1.3 Why Optical Networks?

### 1.3.1 Physical Limits

During the history of the development of communications systems there has always been an increasing demand for more capacity or bandwidth. To satisfy this demand communications technology has developed to exploit higher and higher “carrier”

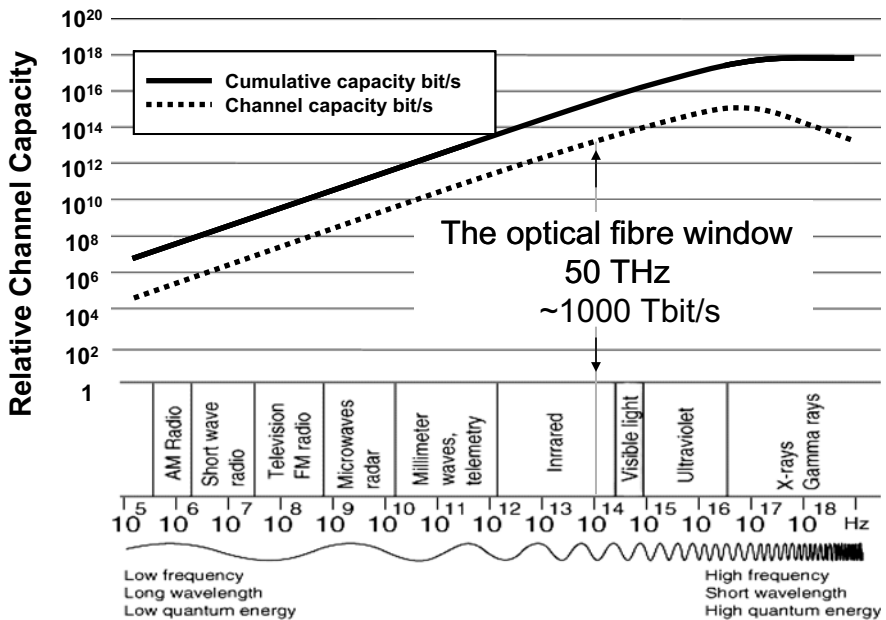


Fig. 1.5 Physical channel capacity limits as a function of “carrier” frequency

frequencies enabling higher bandwidth modulation of the communication channels. The current generation of optical communications technology uses optical fibre operating in the  $\sim 1600$  nm to 1260 nm wavelength range, and a “carrier” frequency range from 187 THz to 238 THz. It might be supposed that as technology progresses we could continue to exploit higher and higher “carrier” frequencies indefinitely. However, the photonic nature of electromagnetic radiation means that the photon energy is also increasing in proportion to the carrier frequency. Higher photon energies coupled with the uncertainty in the arrival time at a detector produces quantum noise and this fundamental noise becomes the limiting factor to the information-carrying capacity of a channel at very high carrier frequencies.

At low frequencies thermal noise dominates communication systems and is the fundamental limit to channel capacity. As frequencies approach optical frequencies quantum noise becomes more significant and at ultra violet and beyond, quantum noise begins to severely limit channel capacity. The effect of quantum noise on channel capacity is illustrated in Fig. 1.5.

The channel capacity curve was derived by assuming that a constant percentage of the carrier frequency can be used for the information bandwidth modulated onto the carrier. Using this assumption it can be seen that the channel capacity peaks around  $5 \times 10^{16}$  Hz ( $\sim 3$  nm wavelength). The roll-off in information capacity beyond 3 nm wavelength is due to the dominance of quantum noise and is sufficient to produce a ceiling to the total information capacity as illustrated by the cumulative capacity curve.



It is interesting to note that today's optical fibre technology is only  $\sim$  two orders of magnitude from this ceiling, so in the future we can not expect the enormous capacity gains achieved when technology moved from radio frequency communications to optical frequency communications. Although it is possible that higher frequency technologies beyond today's optical technology may emerge, there is currently no sign of these technologies and optical technology exploits the highest frequencies used for communications purposes.

There is a subtle consequence of this that does affect the design and choice of future network architectures: as fibre penetrates into all parts of the network (access, metro and core or backbone networks), the same intrinsic technology is being used and the same fundamental capacity is available in the access network as in the core network. This is the first time in the history of communications networks that this has happened. In the past there has always been a higher capacity transmission technology for use in the core network that traffic from the access transmission media could be multiplexed into.

Multiplexing of traffic from the access network into core transmission systems will have to continue if optical communications networks are to remain practicable and economically viable. Therefore, if the core technology is optical fibre and the access technology is also optical fibre, it is implicit that the end users connected to the access network via fibre cannot have all the capacity of the optical fibre dedicated to them. They must be sharing the total capacity of the fibre with other users at least in the core of the network, and because the fibre capacity must be shared, it makes eminent economic sense to enable that sharing at the earliest possible point in the network architecture, that is, the access network.

Multiplexing at the optical layer in the access network also means that capacity can be shared on a statistical basis. This gives users capacity when they need it without locking that capacity up and therefore allowing it to be available for other users as required.

### ***1.3.2 Commercial Considerations***

The major growth of national communications networks during the last century was carried out either via large monopolistic companies or state-owned utilities. In the latter part of the 20th century governments around the world encouraged much greater competition in the provision of telecommunications services by selling off state-owned utilities and breaking up very large monopolies. The access technology in place during this era was mainly copper twisted pair and one of the mechanisms introduced to encourage competitive service provision was copper pair unbundling or local loop unbundling (LLU) as it became known. Local loop unbundling enables new competitive operators to have physical access to the copper pairs that connect customers to the local exchange. This was done either by placing competitor's equipment directly into the local exchange or diverting pairs to a short cable that connected to nearby competitor's equipment.

Copper pair technology is very limited in bandwidth and even with very sophisticated modulation schemes as utilised in digital subscriber line (DSL) technology, bandwidths to customers are limited to a few megabits per second. To increase bandwidths further, network providers need to reduce the length of the copper access pair. This has led to technologies such as very high speed DSL (VDSL) with optical fibre extended from local exchanges to the street cabinet, in this scheme the copper pair only exists between the cabinet and the customer, and copper transmission lengths are reduced from a few kilometres to a kilometre or less. This technology enables bandwidths to be increased to a few tens of megabits per second under favourable conditions.

The next obvious extension is to move fibre all the way to the customer premises and completely eliminate the copper pair. When a fibre to the premises network (FTTP) is installed and optical networking is also available in the higher layers of the network, then, as discussed above, there is no competing network technology that can outperform it in terms of technical capability. There may be performance differences, due to the choice of equipment and architecture, in terms of service quality and economic viability but the physical fibre infrastructure cannot be bettered by any currently known technology.

This begs the question whether competition at the physical infrastructure layer has any real meaning or advantage in an all fibre network future, the economic pay-back is difficult with only one network to finance, more than one physical network is probably just not viable. There may therefore be a need to shift from competition at the physical layer to competition at higher layers (see Table 1.3, below), maybe just the service and application layers, with competitors sharing the capacity of the underlying physical infrastructure.

Sharing capacity on a statistical basis rather than being rigidly divided between service providers can improve the user experience by enabling users to gain flexible access to very high peak bandwidths when required and releasing it when it is not. Statistical assignment of user bandwidth can also enable network capacity assignment to service providers to be determined by end user demand on a dynamic basis rather than pre-allocation via SLAs (service level agreements) with the network provider. This would ensure much greater levels of competition at the service layers with service quality and customer care becoming much more important and lock-in via fixed term contracts could be eliminated. Customers could simply purchase services on demand from service providers and indeed be using multiple services from different service providers simultaneously.

This service provision model is perfectly possible with optical access and all-optical networking because the access capacity and network throughput is more than sufficient to enable such capability. With copper access it is more difficult because of the bandwidth constrictions of the copper feed into the customer premises which limits the number of simultaneous services and the statistical multiplexing capability for both customers and service providers.

As new high bandwidth requirements emerge, particularly high definition video and high-resolution imaging, customers will demand much faster access speeds and will become increasingly impatient and dissatisfied with slow networks. This in

turn will put pressure on operators and administrations to put high bandwidth FTTP networks in place. This may be especially so if there are neighbouring and competing regions offering FTTP and by doing so having an inward investment advantage boosting local economies, employment, house prices et cetera. This certainly appears to be one of the drivers for municipalities who are willing to invest in basic fibre infrastructure for the benefit of their local communities, and indeed there does seem to be some evidence that higher bandwidth access networks can provide these local economic advantages, see [11].

The concept of staying internationally competitive through deployment of the best telecommunications infrastructure is a major driver for Japan and Korea and there is growing concern in the US that America is falling behind and is not the technology leader it once was [12]. Communications is seen as one of the key areas where America has fallen well behind the Far East and even Europe in terms of mobile and broadband penetration and capability. When it comes to FTTP Europe may well fall behind both the Far Eastern economies and the US if it fails to grasp the opportunities over the next few years.

Operational cost associated with the day to day running of communications networks are generally increasing for operators with large copper access networks. One of the reasons is that the higher bandwidth required by DSL technologies stresses the copper network and reveals additional faults that would not significantly impair basic telephony services. As bandwidths increase further and if equipment is placed in the field with technologies such as FTTCab – fibre to the cabinet – using VDSL, then there are further operational cost increases due to the amount of electrical equipment being placed in a relatively harsh physical environment and the cost of providing and maintaining power, including battery backup of street-based equipment. The increasing incidence of flash flooding is also a problem which will only grow in the future if street-based electronics systems become widespread. This suggests that operators and network providers with copper technology and/or remote electronic nodes are likely to see increasing operational costs in the future.

There is however good evidence that fibre networks are intrinsically more reliable than copper pair networks leading to much lower fault rates and reduced network visits (one of the major operational costs for operators) which in turn leads to fewer intervention induced faults. Also because fibre can support all services, service provision and service churn can be automated processes only rarely requiring an end user or network visit. With properly engineered end user and service management systems the vast majority of service changes and provisions could be configured remotely. It has been argued that operational savings alone could justify FTTP being installed [13].

One driver for FTTP is of course the promise of new revenues from all the new services that could be provided, however new revenue generation is an area of major uncertainty. Although FTTP will certainly enable new high-capacity services it is unclear whether there will be any significant net revenue growth over and above traditional trends. The problem is that revenue generation derived directly from new IT and bit transport services are often substitutional that is, new service revenue simply

displaces legacy service revenue and net revenue growth remains relatively static. To exacerbate this problem the advent of flat rate charging, which has displaced usage charging, has removed the linkage between bandwidth usage and revenue. This has caused a fundamental problem for operators as investment in core network capacity can be seen as capital investment without any clear path to a return on that investment. In a commercial market this makes little financial sense and there is little incentive for network investment to increase capacity for future bandwidth hungry services [14].

Historical analyses of revenue growth and bandwidth price decline suggest that there may not be sufficient revenue growth to sustain traditional network builds and that radically new architectures will be necessary to change the end-to-end cost structure of networks to massively reduce the cost of bandwidth provision [15], this will be considered in Sect. 1.4.

### ***1.3.3 Service and Bandwidth Growth***

Bandwidth growth driven by new services is obviously the ultimate driver for end-to-end optical networking and some idea of how bandwidth might grow in the future is extremely useful as an aid to strategic network design and investment planning. The approach outlined in this section is based on user service scenarios coupled with usage behaviour. Take-up and actual usage of new services are random processes and should be treated statistically, often however access bandwidths are simply calculated from basic assumptions of simultaneous usage of services and average bandwidth for the services. This approach can grossly overestimate the average bandwidth required but at the same time grossly underestimate the instantaneous peak bandwidth required for good user experience. To illustrate potential future bandwidth demand and usage this section will give some service scenarios and examine the implications for bandwidth growth for the end-to-end network.

Table 1.1 shows an example service scenario for an FTTP termination serving a small number of users, for example a family home, probabilities of service take up and usage in a hypothetical busy hour are indicated.

The multiple entries in the table represent simultaneous use of a particular service by more than one user at a customer premises site. Using such an example a simple statistical Monte Carlo analysis can be used to generate user bandwidth in a hypothetical busy period.

Results for such an analysis are shown in Figs. 1.6, 1.7, 1.8 and 1.9.

The distribution of mean downstream bandwidths for FTTP premises for the first year in the model (nominally 2010) is shown in Fig. 1.6. It shows an ensemble mean bandwidth of 3.4 Mbit/s with some premises requiring average bandwidths beyond 7.0 Mbit/s. It also shows a significant number of premises that required no services in this particular busy period. Figure 1.7 shows the results (for the same run of the model) of the distribution of the sum of the bandwidths for all the services the customers had signed up for. This is the simplistic sum of service bandwidth that sometimes gets used to determine access pipe bandwidth. The mean of this

**Table 1.1** Example service scenario

Streaming Services	Probability of take-up		Probability of using service in busy hour	
	2010	2020	2010	2020
Internet Surfing	69 %	99 %	46 %	69 %
IP HDTV HR (High Resolution, 1080 p)	44 %	99 %	75 %	80 %
IP HDTV HR	19 %	69 %	53 %	60 %
IP HDTV LR (Low Resolution, 720 p)	15 %	30 %	33 %	40 %
IP HDTV LR	10 %	12 %	11 %	20 %
IP SDTV (Standard-Definition Television)	75 %	2 %	72 %	80 %
IP SDTV	67 %	1 %	52 %	60 %
IP SDTV	35 %	1 %	31 %	40 %
IP SDTV	18 %	0 %	11 %	20 %
Video comms Cam-corder	8 %	49 %	21 %	30 %
Web Cam comms	12 %	25 %	21 %	30 %
Voice	100 %	100 %	20 %	20 %
Voice	81 %	100 %	15 %	15 %
Voice	50 %	50 %	10 %	10 %
Thin-client computing	8 %	59 %	15 %	49 %
Thin-client computing	3 %	29 %	15 %	49 %
<b>File Transfers:</b>				
e-mail	85 %	100 %	11 %	20 %
e-mail	8 %	59 %	10 %	15 %
Photos	37 %	69 %	5 %	10 %
Photos	21 %	30 %	5 %	10 %
Video clips	26 %	59 %	16 %	25 %
Video clips	23 %	40 %	16 %	25 %
Music	31 %	40 %	6 %	15 %
Music	21 %	30 %	6 %	15 %
Documents	14 %	39 %	5 %	10 %
Documents	6 %	20 %	5 %	10 %
Software	5 %	10 %	3 %	8 %
Software	2 %	5 %	2 %	5 %
Web site uploads	4 %	10 %	1 %	5 %
Web site uploads	0 %	2 %	1 %	5 %
Peer-to-peer file sharing	9 %	39 %	42 %	50 %
Peer-to-peer file sharing	5 %	20 %	31 %	40 %
Storage services	13 %	59 %	1 %	5 %
Storage services	7 %	39 %	1 %	2 %

distribution is 42.3 Mbit/s which is  $\sim 12$  times the bandwidth determined by busy period usage statistics.

As services evolve and usage increases, average bandwidths will increase over time, the  $\sim 2020$  results for the example scenario are shown in Figs. 1.8 and 1.9.

The average of the distribution of site bandwidths with statistical multiplexing increases to  $\sim 13$  Mbit/s from 3.4 Mbit/s. The probability of sites taking no services in the busy period is very much reduced but is still significant enough to be the point of greatest probability within the distribution. The distribution of the maximum site bandwidth based on simultaneous use of all services taken is shown in Fig. 1.9

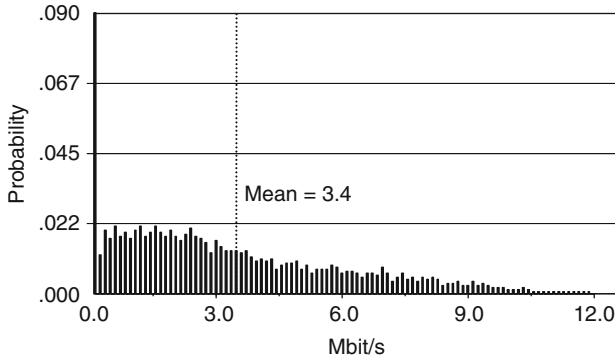


**Fig. 1.6** Distribution of mean FTTP site bandwidth for  $\sim 2010$

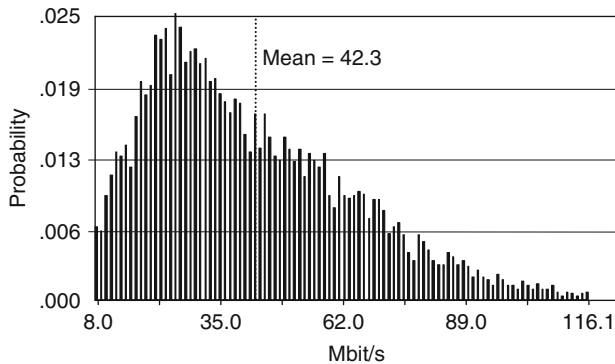


**Fig. 1.7** Distribution of sum of take-up bandwidths for  $\sim 2010$

and has a mean of  $\sim 120$  Mbit/s, still  $\sim 10$  times the required mean bandwidth if statistical multiplexing is used. By using mean values for busy hour bandwidth, models can be built to estimate the ingress bandwidth into the core network. In such a model it is also necessary to take into account technology evolution and adoption as service take up and usage will be affected by the access technology available to the end users.

By extrapolating broadband take up and usage and making assumptions about VDSL and FTTP penetration, estimates for the evolution of technology penetration can be made for a range of scenarios. Combining this with service scenarios similar to those described above but also linked to the technology take up, enables bandwidth growth estimates to be made for a country-wide network. Applying the models to other countries, taking into account relative adoption rates of technology, population growth etc., country and world bandwidth growth can be estimated. Such country and world bandwidth growth scenarios can then be used for such things as network architecture strategy and market sizing analyses for communications systems and component volumes.

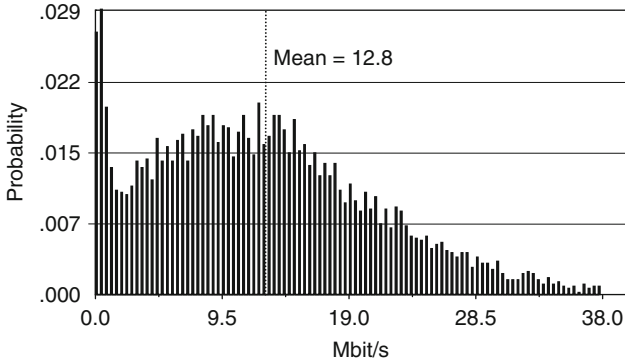


**Fig. 1.8** Distribution of mean FTTP site bandwidth for ~2020

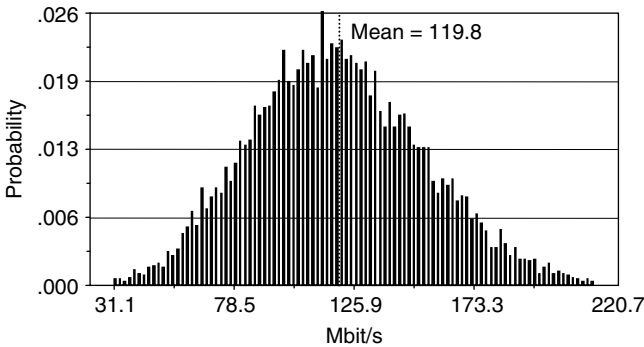


**Fig. 1.9** Distribution of sum of take-up bandwidths for ~2020

## 1.4 Financial Barriers to All-optical Networking

### 1.4.1 Network Bandwidth Growth

The major problem arising from an FTTP future will be the huge level of bandwidth growth that can be delivered into the metro and core networks. By using service scenarios and traffic scenario models as discussed in Sect. 1.3.3 it is possible to get a feel for the level of bandwidth growth that may arise in the future.

Bandwidth growth is dependent on technology adoption as well as new high-bandwidth services becoming available. The adoption of FTTP will have the greatest impact on bandwidth growth and the consequential deployment of optical networking equipment within the network infrastructure. The main effect of FTTP deployment is substitution of other broadband technologies with only a modest impact on overall broadband Internet connections. This is illustrated in Fig. 1.10 which shows estimates of world communications technology volumes, for an optimistic FTTP deployment scenario [16] to the year 2020.

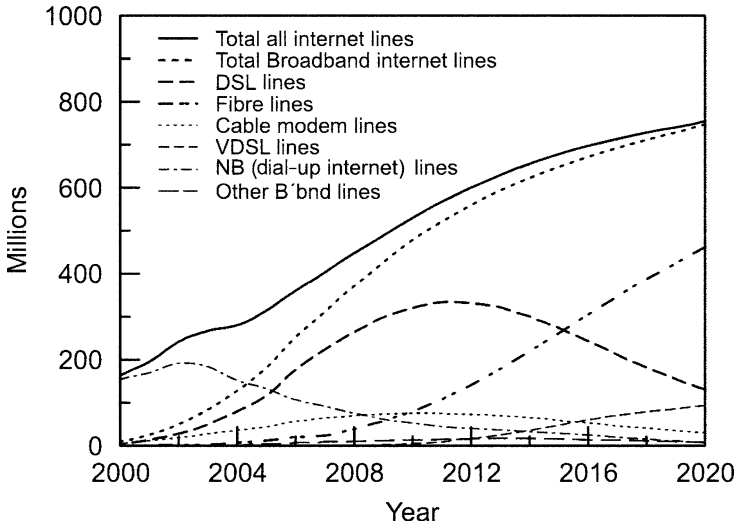


**Fig. 1.10** World technology evolution – optimistic scenario

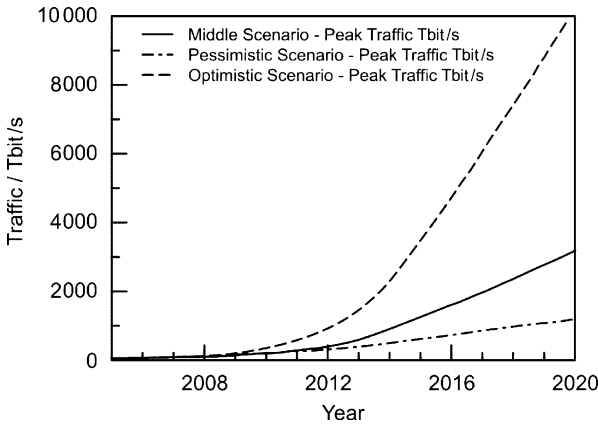


**Fig. 1.11** World bandwidth growth

In this optimistic scenario DSL technology deployment peaks around 2012 and then declines due to substitution from FTTP. It is also assumed that if FTTP is deployed at a reasonable rate the greater performance and lower operational cost of FTTP will curtail VDSL deployment.

Figure 1.11 illustrates the range of estimates for world total traffic growth using different rates for FTTP deployment.

The results for Fig. 1.11 are produced by using data for the OECD countries plus China and Russia, and extrapolating to the rest of the world. Network bandwidth growth is calculated from service adoption and usage scenarios tailored to the different technologies and technology adoption rates of the individual countries.



Bandwidth can then be accumulated on an area basis for each country to yield country bandwidth growth results. These country results can then be summed and scaled to produce the world bandwidth growth results as shown in Fig. 1.11.

### ***1.4.2 Bandwidth Growth vs. Revenue Growth***

A barrier to mass deployment of fibre in the access network is the high capital investment required. In a commercial and competitive environment network providers need to get a return on capital expenditure in line with market rates. Indeed regulators will insist on sensible returns on capital expenditure to avoid cross subsidising of products and services which could distort the competitive environment.

Early FTTP systems targeted specific or niche markets, for example many of the first generation of commercially available APON (ATM passive optical network, see [17] for an overview of ATM) and BPON (broadband passive optical network) systems were aimed at data services for the medium and small enterprises market and did not support POTS (plain old telephony services). The problem with this approach is that they cause a fragmentation of revenue streams with revenues from different service portfolios being required to support different network platforms. For mass-market deployment this is not viable and all revenue streams will be needed to support the deployment and operation of a single platform. An FTTP solution needs to deliver all services: voice (including the regulated PSTN (public switched telephone network) – unless regulation changes), video and data to have any chance of being financially viable.

The other issue for broadband access is that historically overall revenues from the customer base grow relatively slowly. Although revenues from a particular service can grow much faster than the overall rate, it is usually via revenue substitution from other services within the totality of the telecommunications business.

From a macro-economic perspective this is perfectly reasonable and a large sector of the economy such as telecommunications can be expected to grow in line with GDP (gross domestic product) of the country (typically  $\sim 1-3\%$ ). To have telecommunications growing at rates much faster than GDP growth, particularly over an extended period of time, would imply significant underlying economic change with spending in telecommunications substituting spending in other parts of the economy resulting in a down turn in those economic sectors. Growth in telecommunications spend has indeed exceeded growth in GDP for several years implying underlying changes in spending patterns have been occurring, however expecting significantly greater and sustainable increases in telecommunications spend in the future is unrealistic.

It can be seen from the results in Fig. 1.11 that there could be big differences in the bandwidth demands that future network architectures may need to deliver. A higher bandwidth growth rate implies greater levels of investment but from the discussion above it is unlikely that revenues will grow fast enough to fund the investment required. If costs grow faster than revenues, margins are shrinking and this

is not a good business to be in, and such an economic situation would not encourage investment in the network infrastructure required to provide the capacity for the new broadband services and there is a danger that growth could stagnate.

### ***1.4.3 Implications for Bandwidth Price Decline***

Ideally the telecommunications industry would like to maintain the return on capital expenditure (ROCE) during a sustained period of growth, otherwise there is a risk of profitability suffering or even companies going out of business. A question that arises as a result of the bandwidth growth in Fig. 1.11 is: what price decline or learning curve for bandwidth is going to be required to enable the business to remain viable and maintain ROCE?

If growths are expressed as a compound annual growth rate (CAGR), a macro-economic analysis produces an analytic relationship which relates revenue growth, bandwidth growth and the learning curve for the price decline per unit of bandwidth required to maintain ROCE:

$$1 + G_R \geq (1 + G_B)^{1+L}, \quad (1.34)$$

where  $G_R$ : CAGR for revenues,  $G_B$ : CAGR for bandwidth,

$$L = \log(L\%/100)/\log(2),$$

and  $L\%$  is the learning curve (expressed traditionally as a percentage)<sup>1</sup>.

This is the macro-economic condition that needs to be met for a sustainable business as bandwidth grows in the broadband future. This relationship is plotted in Fig. 1.12 with contours of constant revenue growth. It is reasonable to expect time-averaged revenue growths to be within a few percent of GDP growth around 2% to 6% CAGR. The price decline of communications systems transmission equipment has typically followed an 80% learning curve, in recent years. This is in line with the general electronics industry which follows an 80% learning curve although Ethernet-based equipment has followed a faster learning curve at ~70%. Using this range of values with Fig. 1.12 would suggest that overall network bandwidth growths of ~10% would be economically sustainable. Before the advent of broadband, bandwidth growth of networks were of this order or less, and the whole economic system for communications networks was internally consistent with price declines, revenue growth and bandwidth growth.

An approximate CAGR can be fitted to the regions in Fig. 1.11 where bandwidth from broadband begins to become significant. Using these fitted bandwidth growth rates and assuming an optimistic 5% per annum revenue growth, the relationships

---

<sup>1</sup> A learning curve is defined as the percentage decline in price of a product as the product volume doubles, an 80% learning curve will mean that the price of a product at a volume  $V$  will decline to 80% of that price at volume  $2V$ . In this case the product is bandwidth.

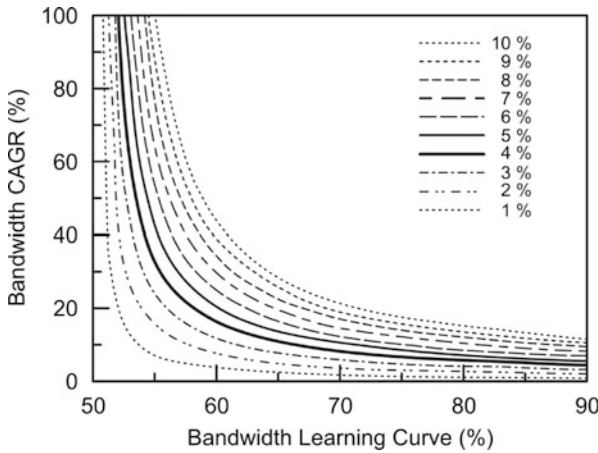


**Fig. 1.12** Relationship between bandwidth growth, revenue growth, and bandwidth price decline for economic stability, the curves are contours of constant revenue growth

**Table 1.2** Learning curves required for given network bandwidth growths

Scenario	Bandwidth CAGR fit	Bandwidth learning curve
Pessimistic	~ 20 %	~ 60 %
Middle	~ 34 %	~ 56 %
Optimistic	~ 55 %	~ 54 %

shown in Fig. 1.12 produce estimates of the required learning curves for bandwidth price decline as shown in Table 1.2.

Even the pessimistic scenario has 20 % growth and is unlikely to remain economically viable with the electronic centric network architectures of today even if some additional new revenues can be obtained from new service offerings. This would suggest that the current strategies of operators predominantly deploying asymmetric DSL (ADSL) or Cable Modem for Internet surfing, e-mail etc. and assuming little take up and provisioning of high-quality video services, will still struggle to remain viable as usage and bandwidth continue to grow leading to increasing use of bandwidth capping policies and degradation of service performance.

The middle and optimistic scenarios require even faster bandwidth price declines which are much faster than the typical 80 % learning curves found in the electronics industry. A bandwidth learning curve of ~ 55 % is so fast that it can be safely assumed it will not be met via electronic equipment price decline. Therefore, future network architectures that continue to use traditional electronic solutions will not produce sufficient bandwidth price decline when FTTP is deployed on a large scale.

Operators and network providers can control bandwidth growth to some extent by allowing contention for backhaul and core bandwidth to increase. From a user perspective this will appear as increased delay for upload and download as the network

gets congested in busy periods, effectively reducing the average session bandwidth per user. Operators can also use bandwidth capping to limit usage by imposing financial disincentives if users exceed predetermined bandwidth limits. This strategy can limit average bandwidth demand but will still often lead to poor network performance in peak periods and of course does not satisfy the latent demand for new services. The other approach is to consider alternative network architectures that require significantly less electronic equipment.

## 1.5 Impact on Network Architecture

The price decline of bandwidth in current networks is in line with the price decline of electronics. Once this observation was noted, it was fairly obvious that this should be the case. Today's networks are heavily dependent on the electronics embedded throughout the infrastructure. Although optical transmission is the dominant technology for transport within the networks, they are mainly used as point-to-point links terminating in electronic equipment and interconnected by electronic nodes. The cost of this electronic equipment dominates network costs (once the trenching for cables has been absorbed as a sunk cost – which is the case for established networks in the developed world). As network capacity increases, the amount of electronics and the speed of the electronic terminations also increases often super linearly. It is the price decline of the electronic technology that limits the price decline of bandwidth provision.

To break this relationship and provide much larger price decline per unit of bandwidth provision it is necessary to reduce the relative amount of electronics in the network. To do this it will become necessary to reduce the number of port cards and electronic nodes. This means using optical technology for far more than just point-to-point transmission and to move to greater use of all-optical networking together with a massive reduction in the number of interconnecting routing/switching centres.

For this chapter “all-optical networking” means that optical technology is used for routing as well as transmission purposes. This does not necessarily mean that the routing function is optical packet routing or switching (although this is not excluded) but it does at least include circuit switching of optical channels using optical space switches and also optical wavelength-selective switches if appropriate. Whether or not optical packet switching is required is a further debate. The author's view is that optical packet switching is not required over the time scales covered by the analyses in this chapter, i.e. up to the year 2020. The bandwidth growths, although unprecedented in the higher bandwidth growth scenarios, can be accommodated by architectural changes that use optical circuit switching coupled with electronic packet switching. What is required is the reduction of opto-electronic ports, equipment and nodes. This will need optical circuit bypass of the nodes in the electronic centric architectures of today's networks.

Before we examine possible new architectures that could bring this about, Sect. 1.5.1 will briefly review the network options available today. This is important because any future network must evolve from today's architectures and will largely still exploit much of the technology available today.

### ***1.5.1 Options for Optical Networks***

Networks are conveniently thought of in terms of layers, the standard model is the seven layer ISO (International Standards Organisation) model shown in Table 1.3. It was developed for data communications networks in the late 1970s and is an abstraction of the processes necessary for reliable and secure communications, the layering is only a model and is to a large extent arbitrary. This is illustrated by the third column in Table 1.3 which shows the layering used by the Internet Engineering Task Force (IETF) for TCP/IP.

The functionality in real networks does not get conveniently assigned to the layers but will often straddle multiple layers of the ISO model, for example ATM [17] straddles layers 1 and 2 and even goes into layer 3.

The model also lumps the bulk of the network into layer 1, the physical layer, and in this chapter we are concerned predominantly with this layer. Most of the capital investment in a communications network goes into the physical layer and it is also the layer where the operation, capability and functionality are determined by physical processes. The upper layers are arbitrary in comparison and are in the form they are because of agreements in standards bodies and adoption by the community at large.

The physical layer can also be subdivided into layers and a hierarchy. The basic cables, duct, manholes, footway boxes and buildings for switching and transmission equipment is often called layer 0, to fit into the ISO model structure. It is the most expensive part of a network build, or conversely the most valuable asset of an existing network, easily representing 80 % or more of the capital expenditure on network infrastructure. Much of the layer 0 investment is in the access network and the huge level of investment required has been the major barrier to wide-scale deployment of FTTP. It is also what has shaped regulatory policy in many parts of the world where governments have introduced competition into communications services provision.

These local loop unbundling policies were aimed at introducing competition into the incumbent operators' copper pair access network. LLU has been the key to stimulating effective competition with incumbent operators, the investment required by start-up service providers to install access network infrastructure would have been prohibitive and the businesses would not have been viable. LLU provided a means of enabling new service providers access to their customers without the need to invest in an access network. It did this by forcing incumbent operators to provide access to the local copper pairs terminated in the local exchange. The competitive operators could install their own equipment in the local exchange to terminate the lines of the customers they had recruited for new broadband services or indeed for both broadband and telephony services.

**Table 1.3** The ISO seven layer network model

ISO Layer	Function	TCP/IP Model
7 Application	Supports actual applications such as e-mail and allows access to the network services that support the applications	Application
6 Presentation	Formats the data for transmission over the network, handles data encryption, compression, protocol conversion etc.	
5 Session	This layer sets up the actual session between two terminals (usually computers) e.g. login and file transfer processes. It manages and maintains the session for the required time	
4 Transport	Provides the processes and protocols for actual transfer of data for example Transmission Control Protocol (TCP), User Datagram Protocol (UDP)	Transport
3 Network	Provides routing through the network, addressing and address translation, congestion control etc.	Network
2 Data Link	Responsible for the processes that transfer data between network elements. It has two sub layers Media Access Control (MAC) for controlling access on multi-point networks and Logical Link Control (LLC) which controls framing, synchronisation and data bit error checking	Link
1 Physical	This layer conveys the physical signals over the hardware platform of the network, i.e. cables line/port cards, switches, routers etc. It also contains the transmission protocols such as SDH, ATM that convey the data bits through the network	

This enabled customers to choose to keep their telephony service with the incumbent operator and have a broadband service with a competing operator or move all their services to a competing operator or keep them all with the incumbent operator. The regulator controls the price at which the incumbent operator can lease the line to the LLU operator, usually at a fixed annual rental.

Unfortunately LLU is now becoming a barrier to FTTP as incumbent operators are required to keep copper cables maintained in a fit state for LLU operators. While the incumbent operators and the LLU operators are both using the copper network, the operational costs are manageable (although they are increasing as DSL technologies keep stressing the copper technology). However, if the incumbent starts to move customers onto FTTP, the average operational cost per working copper pair increases almost in proportion to the ratio of total connections to remaining copper connections, so that if half the customers moved onto fibre, the operational cost per pair of the working copper pairs will almost double. If these costs are not passed on to the operators using the copper network, the incumbent operator faces a severe financial penalty which itself is a major barrier to FTTP investment. Of course the problem for the regulator is that passing the increased cost on to the LLU operator could drive them out of business which defeats the original objective of LLU!

There is a further problem with LLU policy which is a consequence of the bandwidth growth issue discussed earlier. As we will see in discussions later in this sec-

tion, one of the ways of changing the network architecture to significantly reduce network costs will be to bypass local exchanges and reduce the number of network nodes dramatically. Most of the nodes that will be bypassed are local exchanges that terminate the copper pairs. However, current LLU policies can place a requirement on operators to maintain local exchanges indefinitely because that is where the copper access network terminates and handover to LLU operators occurs. This may mean that a future FTTP network that depends on node bypass for economic viability will have additional barriers to overcome arising from regulatory policy. At present regulators have not found a suitable evolutionary policy that gets around the LLU legacy problem, lack of a policy could therefore inadvertently delay large-scale deployment of FTTP.

### **1.5.1.1 Access Network Options**

If operators and service providers want to meet the customer requirements arising from the service scenarios discussed in Sect. 1.3.3, they will need to deploy FTTP solutions to the mass market. In the following Sects. 1.5.1.2–1.5.1.7 the main options for optical access are discussed. Not all the options are available as standardised, commercial products today but all are being worked on in some form or another in R&D laboratories around the world and can be options for consideration as part of future optical network architectures. The options which are targeted at the problem of the cost of equipment required for bandwidth growth (driven by FTTP), exceeding growth in revenues, are discussed in Sect. 1.5.2, including a description of an intermediate option based on GPON that could be a bridge between the longer term vision and the commercial solutions available today.

### **1.5.1.2 Point-to-point Fibre Solutions**

A point-to-point fibre solution is the “obvious” architecture for FTTP, it has a dedicated fibre (or fibre pair) from the local exchange or central office to each FTTP customer and is therefore a direct analogue of the copper pair telephony network that is ubiquitous today (see Fig. 1.13).

This is conceptually a very simple architecture that has a number of advantages: in principle each optical path between exchange and customer is independent of the other paths and therefore customers can be upgraded as required, each customer has access to all the fibre bandwidth, the system is relatively secure as no traffic is available to all customers, the point-to-point nature and short distance does not demand high-performance opto-electronic devices, simple protocols can be used, and an access line termination equipment fault at the exchange should only affect one customer.

Unfortunately many of these advantages also lead to disadvantages: The point-to-point nature leads to high fibre-count cable, several thousand fibres per cable will be required as the cables converge onto the local exchange and fibre cost is

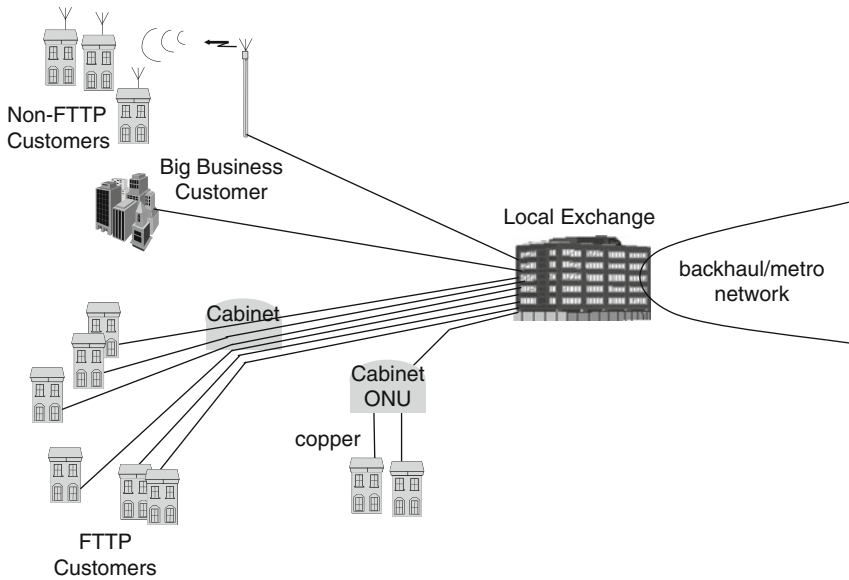


**Fig. 1.13** Point-to-point fibre from local exchange site

a significant proportion of the installation cost. Also large cables can lead to greater duct congestion and significantly increased cost if this leads to additional trenching and duct build. In the event of cable damage high fibre-count cables are expensive to maintain in both time and materials. The huge fibre bandwidth cannot be shared or flexibly assigned as it is nailed up to each customer and upgrades require a change to be made at both the exchange and the customer simultaneously. Also upgrades to one customer may affect customers connected to the same common interface cards in the exchange. Routine testing requires access to each individual fibre at the optical level and is complex and potentially expensive (because of the high fibre count) and may need to be built into every fibre termination at the exchange. There needs to be two optical transceivers and optical line terminations per customer (one at the exchange and one at the customer).

Point-to-point systems that are point-to-point all the way to the local exchange have to remain short range because of the very high cost of high fibre-count cable installed over any significant distance. At the local exchange there must be electronic multiplexing equipment that aggregates the traffic from the access fibre systems onto a separate transport network for transmission to the first core node. This keeps the basic architecture and cost structure the same as today's copper network and the opportunity for cost reduction is limited to equipment price declines which, as discussed above in Sect. 1.4.3, is not sufficient to support the high bandwidth growths that could be generated by FTTP.

Fibre installed from the customer to the exchange is only one of the options for point-to-point fibre architectures. Another alternative is to use point-to-point fibre



to a street node which is much closer to the customer. A convenient place for this node would be the primary cross-connect point (PCP) or cabinet location, which typically serves a few hundred customers and is usually less than 1 km from the premises.

At the cabinet multiplexing equipment aggregates traffic onto a feeder fibre (or fibre pair) which backhauls the traffic to the local exchange site. Because the feeder fibre count is much smaller, the cables sizes to the local exchange are correspondingly smaller and it should be possible to economically take them deeper into the network before further multiplexing or switching is required. This could enable bypass and eventual closure of many of the local exchange sites, therefore reducing costs.

The major disadvantage of this solution is of course the large number of powered and equipped cabinets, which could push the number of active nodes for a moderately sized network with  $\sim 6000$  local exchanges to about  $\sim 80\,000$  active cabinets. These active cabinets are in a relatively harsh physical environment and of course require mains electrical power and battery backup in case of failure of the mains power source. The use of active cabinets will increase operational costs, although it is unclear by how much, but of course it is no worse than fibre-to-the-cabinet (FTTCab) proposals which have active street cabinets to house VDSL equipment or street MSANs (multi-service access nodes), with reuse of the existing copper connections from the cabinet to the customer premises.

### 1.5.1.3 Passive Optical Networks

Passive optical networks (PONs) were developed as a lower cost solution for fibre to the premises by tackling the problem of high fibre-count cable (particularly the point-to-point fibre to the exchange solution) and the large number of opto-electronic devices required for the point-to-point solutions. It does this by using passive optical splitters placed in the fibre distribution network connecting the customer to the exchange. These are mounted in fibre splice housings in footway boxes or manholes.

The passive splitters enable a feeder fibre from the exchange to be shared over a number of customers; it also shares the exchange termination and the associated opto-electronic devices (see Fig. 1.14).

The advantages of the PON solution are the smaller cable sizes required and the reduced number of opto-electronic components. The protocol, that is used to direct and marshal the customer traffic and avoid collisions, also assigns the capacity of the PON across the customers connected. This bandwidth assignment can be done dynamically and on demand with a process called dynamic bandwidth assignment (DBA) and enables high utilisation of the PON capacity. The optical splitters also enable broadcast services to be provided very simply with only one copy of the broadcast channels needed on each PON; the appropriate service being selected at the customer equipment (the ONT – optical network termination).

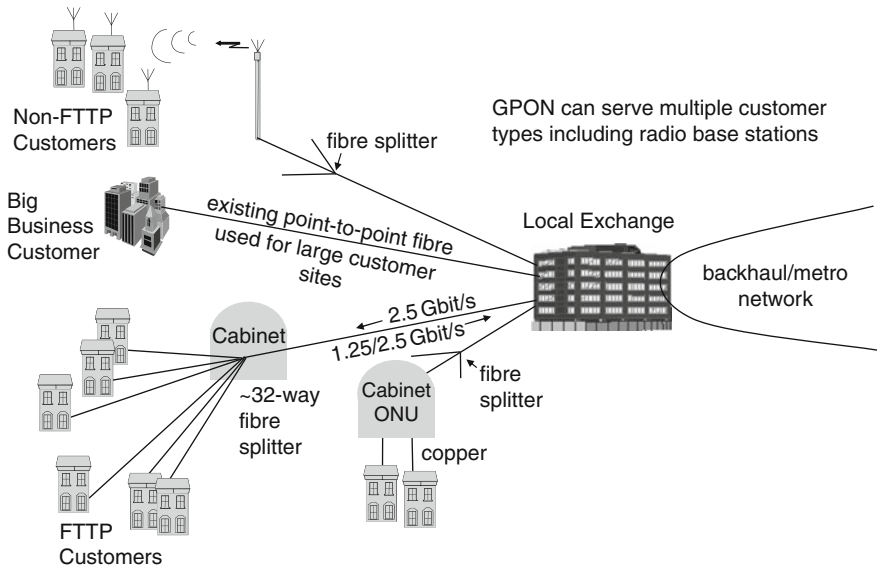


**Fig. 1.14** Passive Optical Network (PON) – GPON bit rates illustrated

#### 1.5.1.4 BPON (Broadband PON)

BPON was the first fully standardised solution for a PON system although proprietary solutions had previously been available for many years. The disadvantage of the BPON solution is the relatively low bandwidth, typically 622 Mbit/s upstream and downstream (although early systems where only 155 Mbit/s upstream). Also the limited power budget provided by standard optical components limit the split to about 32 ways and the distance or reach to a few kilometres. This limited reach means that the physical topology of BPON networks doesn't fundamentally change, for example there is little opportunity for exchange bypass and therefore termination equipment is placed in existing local exchange buildings together with routing, switching and traffic aggregation (multiplexing) equipment. The exchange therefore still needs traffic aggregation and grooming equipment with a separate transmission system for backhaul of the aggregated traffic to the core nodes and, as with the point-to-point architectures, the cost structure of the network is largely unchanged with little scope for the radical cost reductions needed.

#### 1.5.1.5 GPON (Gigabit PON)

The limited bandwidth of BPON and some protocol limitations on range and split were improved considerably with the later GPON standard from the FSAN (Full Service Access Network) forum and the ITU (G984). Although GPON specifications cover a wide range of bandwidth possibilities, the version of interest to

most operators is 2.4 Gbit/s downstream and 1.2 Gbit/s or 2.4 Gbit/s upstream. The GPON protocol is also very versatile and efficient, capable of native TDM services, ATM transport and efficient packet transport, including Ethernet, using the GPON encapsulation method (GEM) which is based on the SDH generic framing protocol (GFP). The latest versions of the GPON standards have deprecated the native ATM mode so this will no longer be supported in future versions of GPON. GPON also has DBA and a comprehensive operations, administration, and maintenance (OA&M) capability including network protection mechanisms.

The protocol extends the split up to 128 ways with 60 km total range and 20 km differential range. However, as with BPON the standard optical components specified do not allow the full range and split offered by the protocol to be achieved simultaneously, and generally the combined range and split capability is in practice no better than BPON, although the higher bandwidths are available.

#### **1.5.1.6 EPON (Ethernet PON)**

EPON (Ethernet PON) also called GEAPON is the Ethernet only version of PON systems. This is an important option because it has been widely deployed in Japan as a broadband overlay solution offering high-speed data services. The widely deployed standard is a 1 Gbit/s system (a Gigabit Ethernet (GE) payload). It has similar performance to BPON and GPON with standard optical components, although GPON has a greater payload with current generation equipment. The more important limitation of EPON is the limited standardised OA&M capability, the fact that it is Ethernet only, and it is still unclear how well legacy services can be transported over such a system, particularly POTS and TDM services (particularly those that extract timing from the network clock).

In Japan EPON has been used as an overlay network delivering new broadband services so the legacy issues have initially been avoided. However, it is more likely in Europe that an FTTP solution must deliver all services in order to displace legacy networks and reduce operational costs where deployed. Therefore, at present the GPON solution is favoured over the EPON solution. However, developments are still occurring to both systems (a 10 Gbit/s IEEE standard version is becoming available) and the two solutions need to be continuously monitored and compared.

#### **1.5.1.7 WDM PON**

WDM PON is a relatively new development for PON systems, which tries to exploit the fibre-sharing advantage of the PON system while logically being a point-to-point solution (see Fig. 1.15).

As the name suggests it does this by exploiting the wavelength domain by setting up a dedicated wavelength channel over a common feeder fibre to a wavelength demultiplexing device at a location near to the customers being served (the same

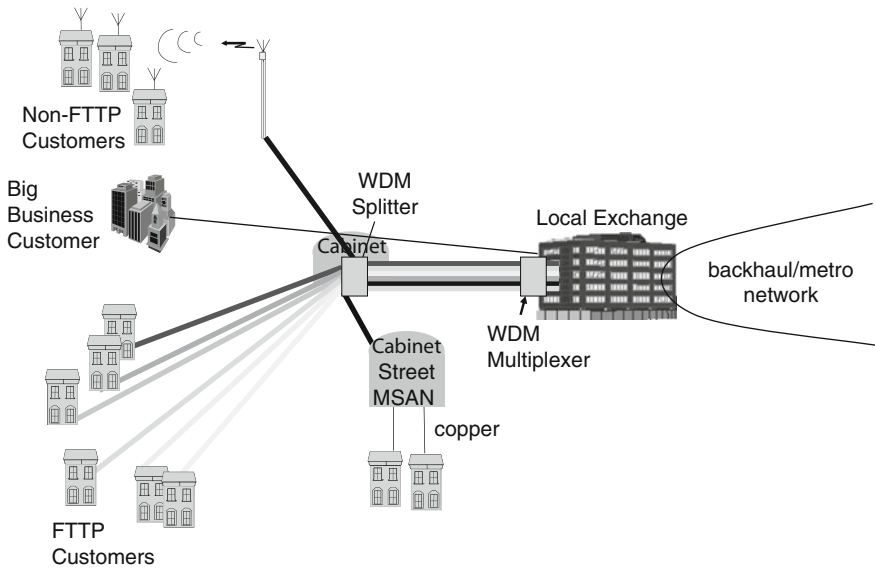


**Fig. 1.15** WDM PON, logically a point-to-point system with one wavelength to each terminal

device can act as a multiplexing device for the upstream direction). From this device individual fibres are fed to the optical terminations such that the fibre architecture is similar to BPON or GPON but the splitting device is a WDM device rather than a power splitter.

The use of a WDM device relaxes the power budget by avoiding the inherent  $10 \log(N)$  dB loss of the passive power splitter used in BPON, EPON or GPON. However the broadcast capability has now been lost, as has the DBA capability that can share unused bandwidth across customers on demand. The WDM device also locks the network spectrally and means that upgrades can only be achieved by changing the exchange and customer terminal equipment simultaneously (the same as point-to-point systems) and the ability to have wavelength agility in the future has been lost. WDM PON also requires a pair of opto-electronic devices per customer and to simplify the logistics of stores holding, installation practice and repair processes the ONT needs to be “colourless”. That is any ONT connected to the WDM PON must be able to work on any of the wavelengths operating on the system. One way of doing this is to lock the ONT optical transmitter to a seed wavelength transmitted from the exchange. To keep these devices low cost and simple is a technical challenge for device manufacturers and the solution chosen could have a major impact on system performance and is still a topic being researched. Currently there are no standards and the economics of such a system are very unclear.

The lower power budget requirements could mean that longer reaches would be technically possible, however the WDM splitter has a similar total split to a 32-way split BPON which means there will only be of the order of 32 customers per feeder fibre. This is a useful level of fibre sharing to reduce the size of the very high

fibre-count cables that are required for point-to-point solutions but the economics of long lengths of the moderately high fibre-count cables required with WDM PON will limit the scope for major exchange bypass. Generally WDM PON systems will be terminated on to local exchanges and, as with BPON, separate backhaul and aggregation equipment will be required at the local exchange. Therefore as for all the systems described above there is little fundamental change to the structure of the end-to-end network economics and little potential for any radical cost reduction.

### ***1.5.2 Long-reach Access***

The common issue with all the above systems is the economic viability of FTTP for mass market deployment. All the architectures above rely on equipment price decline to reduce the cost of bandwidth in order to remain economically viable. None of the above architectures produce any fundamental change to network economics, in particular they keep the backhaul and access networks separate and require multiplexing and aggregation electronics at the local exchange site. The cost of the local exchange and the corresponding backhaul networks can be as large as the access network, particularly when the high bandwidth and low contention required for high-quality personalised video services is to be provided. To solve this problem full end-to-end network economics must be taken into account as consideration and design of access, metro/backhaul and core networks separately is generally not going to lead to economically viable solutions.

The need to reduce electronic nodes in the end-to-end network led to the long-reach access solution as a means to eliminate the separate backhaul/metro network and also the electronic aggregation node at the local exchange or central office. The basic architecture (shown in Fig. 1.16) is a single wavelength amplified PON system with 100 km reach, a line speed of 10 Gbit/s and up to 1000 way split (to share the backhaul fibre as much as possible and also to get maximum statistical gain from traffic carried). The 10 Gbit/s line rate provides a sustained or average rate of 10 Mbit/s per customer (if the full 1000 way split is deployed) but more importantly enables customers to burst for short durations up to Gbit/s speeds, depending on the ONT capability and customer interface port speeds. This allows large files to be transferred very quickly and even high-definition feature length films could be transferred in a few 10s of seconds. In Fig. 1.17 a further stage of evolution is shown where WDM has been added to increase the capacity and provide flexibility in the wavelength domain for customer and bandwidth management. Also shown for completeness is the optically switched inner core, which together with the long-reach access could reduce a UK-sized network from currently  $\sim 5600$  exchange locations to only  $\sim 100$  large nodes.

Work at BT Martlesham and the Tyndall Institute in Cork, Ireland, has experimentally verified that from an optical power budget and transmission perspective such a long-reach access system is technically viable [18] and WDM options have been investigated in the EU collaborative project PIEMAN [19–21] with initial sys-

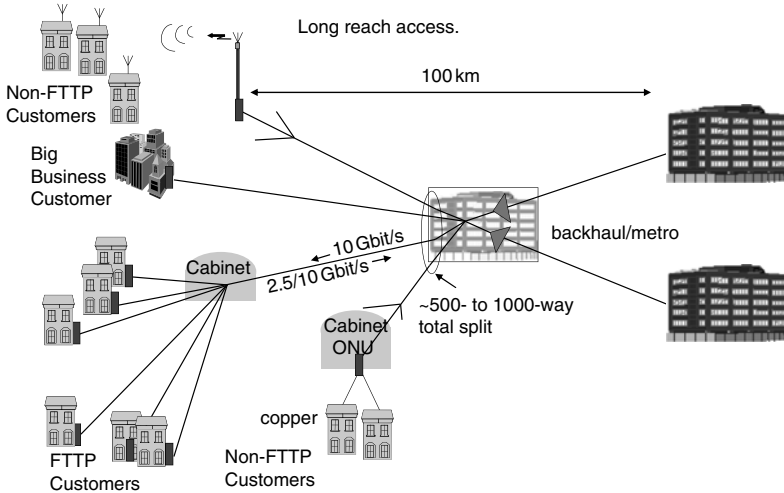


**Fig. 1.16** Basic long-reach access network bypasses local exchange and metro network. All ONUs have fixed band-pass “blocking filters” which only select the initial operating wavelength and block all others. When WDM is added at a later stage, the “new” ONUs will have a band pass filter at one of the additional wavelengths. EDFA technology constrains operation to C-band wavelength range

tems and protocol issues investigated within the EU MUSE project [22]. An early LR-PON solution has also been demonstrated by Siemens [23].

### 1.5.2.1 Extended-Reach GPON

There are a number of technical and design issues still to be resolved for a viable long-reach access solution to be developed into a standard product ready for deployment. However, an interim solution that paves the way for this architectural approach is “Extended-Reach GPON” [24]. As mentioned in Sect. 1.5.1.5 the GPON protocol can support up to 128 way split and 60 km range but the standard optical components cannot realise this capability in a practical system. By adopting the ideas from the long-reach access vision, an amplifier module can be added to GPON to enable the full protocol capability while still keeping the standard GPON optical component specification. This means that a standards-compliant GPON system can be easily upgraded to a longer reach version simply by incorporating the in-line amplifier module. The architecture is schematically shown in Fig. 1.18 and uses commercially available semiconductor optical amplifiers (SOAs) capable of operating at the wavelengths of standard GPON.

A  $4 \times 4$  optical star coupler is added at the local exchange site where the OLT for standard GPON would be placed. The  $4 \times 4$  coupler increases the split of standard GPON from 32 ways to 128 ways by combining together four, 32-way GPON access networks. The four ports on the metro-node side of the star coupler have the

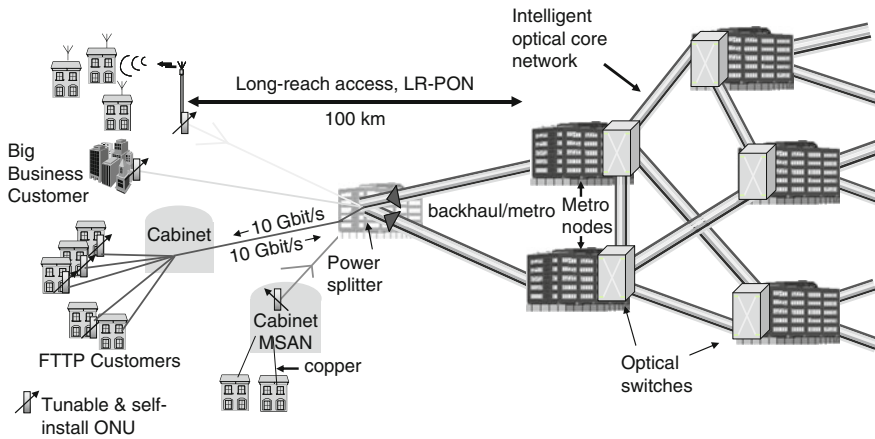


**Fig. 1.17** Long-reach PON with flexible wavelength assignment and all-optical circuit-switched core network. Power splitters (not WDM splitters) enable any  $\lambda$  or combination of  $\lambda$ 's to any customer. New optical amplifier technology assumed (e.g. quantum dot) to enable operation across fibre spectrum

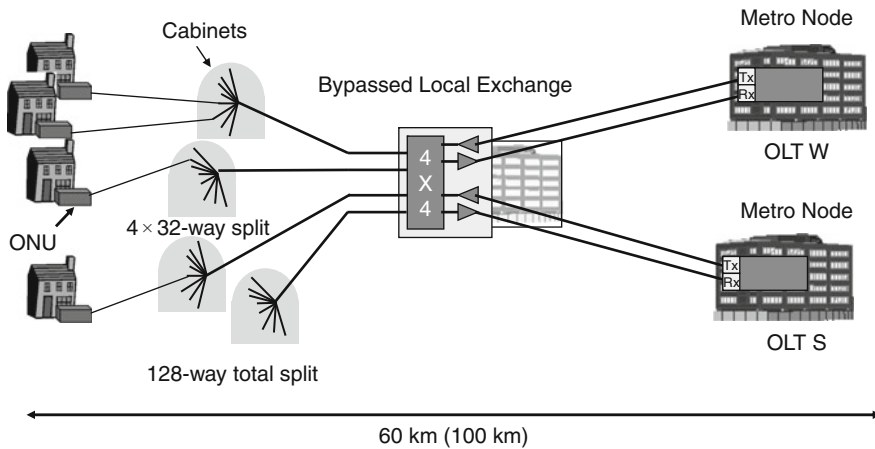


**Fig. 1.18** Extended-reach GPON – an interim solution to long-reach PON

semiconductor amplifiers attached, the use of four ports enables two fibres working over two fibre paths to two separate metro-nodes enabling dual parenting protection switching. One of the metro-nodes is the protection site and the other is the primary site. The protection metro-node sites will house a standby OLT (OLT S in Fig. 1.18) which can be switched to an operational state in the event of a fault in the equipment or connection to the primary metro-node.

Amplified extended-reach GPON (ER-GPON) can offer a short-term expedient to long-reach access, enabling bypass of a large proportion of the local exchanges and elimination of the backhaul transport network where it is deployed. The fibre

architecture is compatible with long-reach access and could be upgraded at a later date when the long-reach access system becomes available for deployment and the service demands and business environment make it viable. Recently a new XGPON standard G987 has been published which is an interim between a full long-reach PON and extended-reach GPON. It provides for greater split and higher bit rates compared to GPON and will probably be the standard that will evolve to a full wavelength-flexible 10 Gbit/s symmetrical bandwidth long-reach PON in the future.

### ***1.5.3 Metro Network***

The metro network provides the interconnectivity between the access network and the core network and is sometimes also known as the backhaul network. In countries with relatively small geographical coverage this interconnectivity largely consists of transmission systems that collect the aggregated traffic from the access nodes or exchanges and transports that traffic to the nodes of the outer core network also called metro nodes. In countries with large geographical coverage the metro network is sometimes subdivided into a metro access network and a metro core network.

#### **1.5.3.1 Metro Network Architectures**

Architecturally, small country and large country networks are not too dissimilar, the main differences being of scale/geographical range and nomenclature. The metro access region is similar to the network connecting access nodes to outer core nodes in small country networks and can also be called the backhaul network. The metro core network is then similar to the outer core network which connects the outer core nodes sitting on the edge of the core network to the inner core nodes that are interconnected via the long-distance transmission links. There are a wide range of technologies used for the transmission systems for metro networks which are usually implemented in either point-to-point or ring topologies.

When networks carried predominantly telephony traffic, the backhaul or metro access networks were often implemented using point-to-point transmission systems based on PDH technology (plesiochronous digital hierarchy) at rates between 1.5 Mbit/s and 565 Mbit/s, although the higher rates were usually found in the core network rather than the backhaul network (prior to the digital era this transmission was analogue and used FDM over copper transmission technology, e.g. coaxial cable). PDH was not a synchronous system and required a complex multiplexing procedure to multiplex data streams from multiple sources having slightly different clock rates. This meant that adding and dropping traffic at intermediate nodes along a transmission path was complex and costly requiring full demultiplexing and re-multiplexing of the data stream. When SDH technology emerged in the late 1980s, it was designed as a synchronous system and had a frame structure that was very flexible both for mapping all types of digital traffic into it and also for



adding and dropping traffic efficiently at intermediate points along the transmission path. The add-drop multiplexers (ADMs) used to remove or insert traffic at the intermediate node could also be connected in closed rings which gave a protection mechanism whereby traffic could be switched at an ADM to go round the ring in the other direction enabling circumvention of a fault or cable cut in a section of the ring. In the metro network SDH is used in both point-to-point and ring configurations.

Ring networks are particularly useful at low to moderate traffic levels where the traffic inserted and dropped at each node in the ring is a small fraction of the ring capacity. Rings become more problematic at high traffic levels where the total traffic exceeds the capacity of the ring. In these cases rings need to be stacked and a cross-connect is required to move traffic from one ring to another which increases the cost associated with the transmission systems.

To increase the capacity of the fibre links, WDM can be used, and in these systems capacity can be added incrementally by additional wavelengths as traffic growth demands. The basic optical WDM devices need to be installed at day one but the additional transponders/line cards needed for each wavelength are only added when required. At each node interconnected via the WDM system an optical add-drop multiplexer (OADM) is installed. In simple systems the wavelengths added and dropped at the OADM are configured manually often as part of the initial system design and installation. Subsequent changes to the configuration require manual intervention which is perfectly viable if changes are relatively infrequent. However, if network operators need more dynamic and frequent reconfigurability, then reconfigurable OADMs (ROADMs) can be used. These are more complex and consequently more expensive than simple OADMs but have the advantage that they can be remotely configured and therefore save operational costs in a more dynamic traffic environment. The number of fibre routes connecting an ROADM to other nodes is called the degree of the node; a ring has two routes at each ROADM and therefore has degree 2. However, in recent years ROADMs with degree greater than 2 have emerged. These ROADMs can be used for ring interconnections enabling wavelengths to traverse from one ring to another. They also enable metro networks to migrate from ring topologies to mesh topologies as bandwidths grow in the future making ring topologies less viable. With these higher degree ROADMs the distinction between a full optical cross-connect (that would more usually be considered for mesh networking) and an ROADM is blurring.

### 1.5.3.2 Elimination of Metro Networks

In Sect. 1.5.2 the concept of long-reach access (namely LR-PON) was discussed, long-reach access takes the access network deep into the network to the outer core switches/routers or metro nodes which effectively eliminates the separate metro access transmission network. The LR-PON performs the aggregation, multiplexing and routing function normally performed by the local exchange equipment, the PON protocol can also assign bandwidth as required to customers using a DBA protocol.

It can therefore also perform the functions of the access aggregation switches/routers at the local exchanges and therefore eliminate this equipment and the buildings required to house it, which in time could be closed down and sold off to be re-used for other purposes. The additional cost for the long-reach access network is the amplifier module at the old local exchange site, this is required to extend the PON reach, split and capacity. The cost of this optical amplifier equipment and infrastructure is significantly less than the cost of the local exchange equipment, buildings and the metro transmission systems the LR-PON replaces. Furthermore, it also consumes significantly less power and therefore paves the way for a much “greener” network solution.

The large split of the long-reach PON enables a very fibre-lean network with a high degree of fibre sharing and utilisation of the long-distance “metro fibre” between the old local exchange site and the outer core or metro nodes.

When the economics of these networks are compared via a cash flow analysis, the long-reach PON solution produces the shortest time to positive cash flow and also the lowest investment of risk capital.

### ***1.5.4 Core Networks***

In the previous sections the options for the access and metro networks have been discussed and from the perspective of bandwidth growth and economic considerations the most favourable solution for a future generation FTTP network will be long-reach access networks connecting directly into the core network nodes. This solution enables bypass of the local exchange sites and the elimination of the metro access transmission systems which reduces the combined access and metro network costs significantly and gives the lowest risk and shortest time to positive cash flow. The high bandwidths enabled by FTTP will also drive significant bandwidth growth into the core network and will also put pressure on the economic viability of the core network architecture and technology.

From the simple service scenario discussed earlier it can be expected that FTTP customers could easily drive sustained bandwidths to  $\sim 10$  Mbit/s or more. This level of bandwidth growth is unprecedented and is a real paradigm shift in the levels of traffic networks will be required to cope with. To get some feel for the impact of such growth consider some very simple order of magnitude calculations for a network with  $\sim 20$  million premises. Assuming 50% of end user premises will take up and use an FTTP offering then it would mean:

- 10 million end users at 10 Mbit/s per end user
- 100 Tbit/s total sustained busy period traffic
- $\sim 100$  core nodes (assuming an LR-PON access network architecture with 100 km reach)
- 1 Tbit/s average traffic per node
- $\sim 10$  Gbit/s average traffic between each node pair (assuming little turn-around traffic at the traffic ingress node).

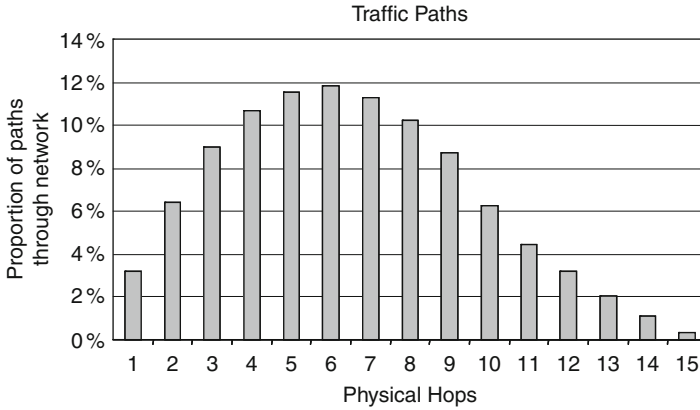


**Fig. 1.19** Number of nodes traversed by an optical path through a 100-node network

It should be noted that statistically the probability of all users using a sustained rate of 10 Mbit/s simultaneously would be vanishingly small and that practical network bandwidths even for this scenario would be significantly lower. If traffic levels are of the order of 10 Gbit/s between all node pairs, then this is equivalent to assigning one optical wavelength between all node pairs. With direct optical wavelength connections between all node pairs there is no need for grooming or add-drop electronics at intermediate nodes. If there is no intermediate grooming, then the network could be a flat, single layer all-optical network, and such an architecture reduces a network of UK size from one with  $\sim 5600$  exchange locations containing electronic equipment to  $\sim 100$  electronic switching/routing nodes.

The use of an all-optical core network will considerably reduce the amount of electronics required in each of the core nodes. The reduction in traffic that needs to pass through the core node router can be seen by considering the traffic paths required across a 100-node core network.

All nodes will need at least one wavelength to all other nodes. These optical paths will traverse the network and in doing so will pass through intermediate nodes.

The distribution in Fig. 1.19 shows the number of nodes traversed by these optical paths for a 100-node network. In today's electronics centric networks each optical path would be terminated at each node it passes through, requiring opto-electronic conversion on the ingress and egress ports for every wavelength. The traffic carried on each wavelength would then be switched/routed through each intermediate node from the ingress port to the egress port; this requires the switch/router capacity to cope with all the through traffic as well as the traffic destined for that particular node. Studies of the UK network show that as much as 70–80% of the traffic entering a node can be through traffic. If this traffic can be made to bypass the node router by remaining in the optical domain, then there are enormous savings in opto-electronic interfaces and significant reduction in switch/router capacity required. To provide

optical bypass in the wavelength domain will require cost-effective optical switches to be added as an optical layer at each metro/core node in the network.

This optical layer effectively creates a flat rather than hierarchical core network. The flat architecture avoids the need for the opto-electronic conversions at layer boundaries as transmission paths traverse the network, and as mentioned above it also reduces the size of the routers required by not electronically handling the through traffic. The hierarchical architecture however allows for sub-wavelength grooming whereby traffic from several nodes could be multiplexed on to a shared wavelength for onward transmission to a destination node and also allows traffic to be added and dropped at any of the intermediate nodes on the route.

From this simple qualitative discussion, it can be seen that for low traffic levels a hierarchical core would use optical transmission capacity more efficiently but requires greater router capacity, while for higher traffic levels the flat architecture makes more efficient use of core node resources but could under utilise wavelengths if the traffic levels are too low. It can be expected therefore that as traffic levels rise a transition will occur whereby, to minimise cost, networks will need to evolve from a hierarchical architecture to a flat all-optical architecture.

The flat architecture is expensive for low traffic levels because the flat core requires large numbers of wavelengths at each node to simply provide the wavelength mesh connectivity required and therefore has high up-front expenditure. At low traffic levels the wavelengths are inefficiently filled but traffic can grow to high levels without further expenditure. The hierarchical network however can efficiently fill the wavelengths by use of sub-wavelength grooming and therefore requires significantly fewer optical wavelengths in the core to provide the required connectivity. However, as traffic grows the equipment required grows and eventually crosses the flat optical core curve at some traffic level in the future. Estimates suggest that this could occur by 2015 but planning and early implementation of the optical layer to enable the transition would need to start much earlier than this date. It should be noted at this point that the size of the all-optical flat core will need to be limited as the number of wavelengths required for full interconnectivity grows as  $N^2$ . Networks for very large countries will therefore probably need optical islands with a limited number of nodes which in turn will be interconnected by another very long-haul flat optical layer. At the boundary of this layer and the interconnecting nodes of the optical islands there would be optical-electrical-optical (OEO) conversions and regeneration of the optical signals as well as routing capacity to groom traffic onto the inter-island transmission paths. The optimum size of the optical islands will be a trade-off between optical and electrical switching costs and transmission costs.

The simple analysis used at the beginning of Sect. 1.5.4 assumed that all the metro/core nodes are equal in size, in practice there will be a considerable range of core node sizes. The larger core nodes will have several 10s of fibre links connected to them even with 80-channel DWDM systems. Many of these fibres will have all the wavelengths carried as through wavelengths to other nodes. The architecture of the metro/core node may therefore need two layers of optical switching – a low-

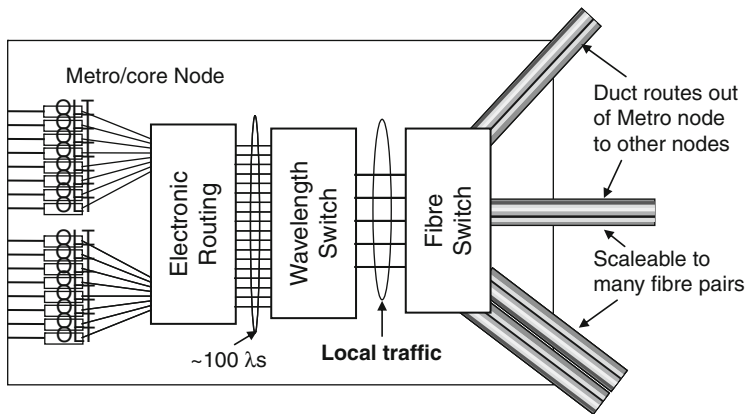


**Fig. 1.20** Future optical metro/core node architecture. Fibre switch enables fibre bypass of node, cascading nodes leads to requirement for ultra-low-loss optical switches. Electronic switch/router only needs to process destination traffic. Therefore size, power consumption and OEO port count are minimised. Some fibres from the optical space switch are diverted to the wavelength switch for local node wavelength add/drop

loss fibre space switch switching at the fibre level and a wavelength-selective switch (WSS) switching at the wavelength level. The architecture of the node would then look something like that shown in Fig. 1.20 [25].

The optimisation of such an architecture, getting the right balance between fibre switching, wavelength switching/multiplexing and electronic switching/routing/multiplexing functions is still an area of research as are methods and technologies that can enable graceful growth at any of the layers to meet the conditions at any particular node.

Of particular relevance to this all-optical architecture is the balance between wavelength multiplexing versus higher transmission speeds. High transmission speeds can mean lower wavelength counts and fewer transponders at terminating nodes. However, getting efficient fill on higher granularity wavelengths may require sub-wavelength grooming which gets away from the advantages of the flat optical core network. More wavelengths give more optical switching flexibility with possibly more graceful growth and simpler transmission systems but at the expense of more line equipment. However, an additional advantage may be greater resilience and therefore networks with greater overall availability. It may be that higher speed systems (40 Gbit/s or 100 Gbit/s) are used selectively on the highest capacity links where there is sufficient traffic between nodes that sub-wavelength grooming will not be required while 10 Gbit/s may be used more ubiquitously on the larger number of lower capacity routes. The actual choice will depend as much on economic and resilience analyses as technical capability of the transmission equipment and is a continuing research topic.

## 1.6 Summary – Future Evolution of Optical Networking

The aim of this chapter was to give an overview of the principles of optical networking and the issues to be addressed as the true broadband network of the future evolves. Section 1.1 was a very brief historical introduction. Section 1.2 was a brief overview of optical networking. The reasons and drivers for moving to optical networking including fibre to the premises (FTTP) was discussed in Sect. 1.3, Sect. 1.4 examined the economic challenges introduced by FTTP and Sect. 1.5 reviewed the network architectural issues and options.

Optical networking with fibre to customer premises will provide a network with the best capability possible with known technology but it is going to bring some major economic and operational challenges for operators and network providers. All-optical networking in the access, metro, and core networks means that the same basic transmission technology and capability is present in all layers of the network hierarchy. That being the case and given the economic necessity to share the capacity of metro and core fibre across many customers, it is apparent that customers cannot have all the capacity of the access fibres connected to them. This implies sharing of the access fibre capacity and that multiplexing, traffic grooming and consolidation must either occur at the access-metro network boundary or preferably, from an economic perspective, in the access network itself. When reviewing the possible access network options it was shown that the lowest cost FTTP solution is based on the passive optical network architecture with passive splitting close to the customer. This enables maximum fibre and network resource sharing by the customers connected to the network.

In Sect. 1.4 the economic challenges arising from the bandwidth growth enabled by FTTP were discussed. It was shown that there is a fundamental problem with current electronic centric architectures because the price decline of the network equipment required to service the potential bandwidth growth is insufficient to enable the network provisioning cost to grow at rates less or equal to the revenue growth that can realistically be anticipated. It was concluded that the only way of resolving this challenge would be to reduce the amount of the expensive electronic equipment in the network by eliminating access nodes (central office/local exchanges) and also elimination of the metro access transmission systems. The architecture proposed to achieve this was based on a long-reach PON with enhanced capacity, reach and split enabled by using optical amplifiers at the site of the old COs/local exchanges.

The huge growth in bandwidth also has major implications for the core network where minimisation of electronics for OEO conversions, transponders, routers etc., is also very important if an economically viable network is to be achieved. The solution discussed was migration of the core network to include an all-optical, circuit-switched layer, above the electronic router layer. In this way traffic paths traversing the core network from ingress nodes to egress nodes can bypass the electronic routers in the traversed core nodes and stay in the optical domain. For high-capacity networks this results in a large reduction in OEO conversions required for transponders and router I/O cards (router blades). This also reduces the required capacity, size and power consumption of the core node routers leading to much lower costs

and a much “greener” solution for the future network. However, it was also pointed out that for the traffic levels in today’s network the electronic centric core is eminently sensible because there is generally insufficient traffic to efficiently fill the majority of the optical circuit-switched channels that would be required to fully interconnect all the core nodes of a country-wide (or large region) network. However, at some point in the future as network bandwidth grows the all-optical core network layer will be necessary to keep core network costs under control. There is therefore the outstanding problem of how best to transition from the electronic centric core networks of today to the all-optical network required for the future.

Although not discussed in this chapter there is also much work to be done on core bandwidth mitigation techniques where the architecture and operation of the network minimises the amount of traffic that needs to enter and transit the core network and could instead be kept or turned round in the access network (this is particularly relevant to the long-reach access network architecture).

In conclusion the most significant features of future networks compared with today’s networks will be the growth in bandwidth they will need to cope with and that optical networking will be required in all parts of the hierarchy. This has an impact on the requirements for future optical components and technology.

The greatest challenge for the photonics industry is to move much of the high-performance technology used in core networks into high volume and low price components for the access network. The access network will require stable high-performance components at consumer electronic prices (10 Gbit/s and possibly even coherent technology in the future). Customer premises transmitter and receiver modules will need to become wavelength-tuneable devices to be both “colourless” and provide the ultimate flexibility in bandwidth management in the network. Low-cost, optical amplifiers with low noise figure (and ideally wide spectral width covering much if not all of the optical fibre windows) will be needed and they ideally should be capable of multi-wavelength operation without introducing crosstalk (quantum dot amplifier technology may be a solution for this). Low-loss optical circuit switching including wavelength-selective switches will be required for the core network and long-distance high-capacity transmission systems including coherent solutions will also be required for the higher capacity routes across the core.

Whether or not optical signal processing and also optical packet switching will be required is a further debate not discussed in this chapter. If it is required, it is probably a long time in the future. Optical circuit switching enabling optical layer bypass of through traffic in the core network significantly reduces the capacity requirements of the core nodes enabling electronic routers a much longer life. Also there has been negligible work on core bandwidth mitigation techniques which may further reduce the growth in core network bandwidth and enable electronic routers to cope with traffic demands for many years to come.

Whatever the final evolution and direction of network technology development and deployment the selection process is ultimately going to become one of lowest cost and, end-to-end network, economic viability for all the players in the communications business.

## References

1. K.C. Kao, G.A. Hockham, Dielectric surface waveguides for optical frequencies. *Proc. IEE* **113**, 1151–1158 (1966)
2. F.P. Kapron, D.B. Keck, R.D. Maurer, Radiation losses in glass optical waveguides. *Appl. Phys. Lett.* **17**, 423–425 (1970)
3. Zh.I. Alferov, V.M. Andreev, D.Z. Garbuzov, Yu.V. Zhilyaev, E.P. Morozov, E.L. Portnoi, V.G. Trofim, Investigation of the influence of the AlAs-GaAs heterostructure parameters on the laser threshold current and realization of the continuous emission at room temperature. *Sov. Phys. Semicond.* **4**, 1573–1575 (1970)
4. I. Hayashi, M.B. Panish, P.W. Foy, S. Sumski, Junction lasers which operate continuously at room temperature. *Appl. Phys. Lett.* **17**, 109–111 (1970)
5. R.J. Mears, L. Reekie, I.M. Jauncey, D.N. Payne, Low-noise erbium-doped fibre amplifier operating at 1.54  $\mu\text{m}$ . *Electron. Lett.* **23**, 1026–1028 (1987)
6. G.P. Agrawal, *Nonlinear Fibre Optics*, 4th edn. (Academic Press, Burlington, USA, 2007)
7. S.P. Singh, R. Gangwar, N. Singh, Nonlinear scattering effects in optical fibers. *Prog. Electromagn. Res.* **74**, 379–405 (2007)
8. R.J. Stolen, Polarization effects in Raman and Brillouin lasers. *IEEE J. Quantum Electron.* **QE-15**, 1157–1160 (1979)
9. P.B. Harboe, E. da Silva, J.R. Souza, Analysis of FWM penalties in DWDM systems based on G.652, G.653, and G.655 optical fibers, World Academy of Science. Engineering and Technology Issue **48**, Article 13, 77–83 (2008)
10. R. Billington, A report on four-wave mixing in optical fibre and its metrological applications, National Physical Laboratory, NPL Report COEM 24, January 1999
11. W. Lehr, S. Gillett, A. Sirbu, Measuring broadband's economic impact, Broadband properties (December 2005), <http://www.broadbandproperties.com>
12. America's technology future at risk: Broadband and investment strategies to refire innovation (Economic Strategy Institute, March 2006), [http://www.econstrat.org/index.php?option=com\\_content&task=view&id=230&Itemid=5](http://www.econstrat.org/index.php?option=com_content&task=view&id=230&Itemid=5)
13. J. Halpern, G. Garceau, S. Thomas, Fibre: Revolutionizing the Bell's telecoms networks (2004) [http://www.telcordia.com/products/fttp/bernstein\\_report.html](http://www.telcordia.com/products/fttp/bernstein_report.html)
14. The broadband incentive problem, <http://cfp.mit.edu/docs/incentive-wp-sept2005.pdf>
15. D.B. Payne, R.P. Davey, The future of fibre access systems?. *BT Technol. J.* **20**, 104–114 (2002)
16. D.B. Payne, World bandwidth growth over the next decade – is it viable?, [http://www.ciphotonics.com/Technical\\_papers/BandwidthGrowthInterWhiteP.doc.pdf](http://www.ciphotonics.com/Technical_papers/BandwidthGrowthInterWhiteP.doc.pdf)
17. L.G. Cuthbert, J.-C. Sapanel, *ATM The Broadband Telecommunications Solution*. IEE Telecommunications Series, vol. 29 (IEE, London, 1993). ISBN: 0-85296-815-9
18. D. Nettet, R. Davey, D. Shea, P. Kirkpatrick, S. Shang, M. Lobel, B. Christensen, 10 Gbit/s bidirectional transmission in 1024-way split, 110 km reach, PON system using commercial transceiver modules, super FEC and EDC, *Proc. 31st Europ. Conf. Opt. Commun.* (ECOC'05), Glasgow, UK (2005), paper Tu1.3.1
19. The Photonic Integrated Extended Metro and Access Network (PIEMAN) EU FP6 Project, <http://www.ist-pieman.org/>
20. C. Antony, P. Ossieur, A.M. Clarke, A. Naughton, H.-G. Krimmel, Y.F. Chang, A. Borghesani, D. Moodie, A. Poustie, R. Wyatt, B. Harmon, I. Lealman, G. Maxwell, D. Rogers, D.W. Smith, D. Nettet, R.P. Davey, P.D. Townsend, Demonstration of a carrier distributed, 8192-split hybrid DWDM-TDMA PON over 124 km field-installed fibers, *Opt. Fiber Commun. Conf. and Nat. Fiber Opt. Eng. Conf.* (OFC/NFOEC'10), Techn. Digest (San Diego, CA, USA, 2010), post-deadline paper PDPD8
21. P. Ossieur, C. Antony, A. Naughton, A. Clarke, P.D. Townsend, H.G. Krimmel, T. De Ridder, X.Z. Qiu, C. Melange, A. Borghesani, D. Moodie, A. Poustie, R. Wyatt, B. Harmon, I. Lealman, G. Maxwell, D. Rogers, D.W. Smith, A symmetric 320 Gbit/s capable, 100 km extended reach hybrid DWDM-TDMA PON, *Opt. Fiber Commun. Conf. and Nat. Fiber Opt. Eng. Conf.* (OFC/NFOEC'10), Techn. Digest (San Diego, CA, USA, 2010), paper NWB1



22. Multi Service Access Everywhere (MUSE) EU FP6 Project, <http://www.ist-muse.org/>
23. M. Rasztoivts-Wiech, A. Stadler, S. Gianordoli, K. Kloppe, Is a 10/2.5 Gbit/s extra-large PON far from reality?, *Proc. 9th Int. Conf. Transparent Opt. Netw. (ICTON 2007)*, Rome, 1–5 July, pp. 283–286, paper Th.B1.4
24. D. Nettet, D. Payne, R. Davey, T. Gilfedder, Demonstration of enhanced reach and split of a GPON system using semiconductor optical amplifiers, *Proc. 32nd Europ. Conf. Opt. Commun. (ECOC'06)*, Cannes, France (2006), paper Mo4.5.1
25. A. Lord, M. Wade, Techno-economic issues in future telecom networks, *Opt. Fiber Commun. Conf. and Nat. Fiber Opt. Eng. Conf. (OFC/NFOEC'07)*, Techn. Digest (Anaheim, CA, USA, 2007), paper OWK1

# Chapter 2

## Optical Fibers

Pascale Nouchi, Pierre Sillard, and Denis Molin

**Abstract** The chapter starts with the fundamentals of light propagation in optical fibers, followed by the essentials of fiber fabrication. Subsequent sections focus on typical loss and dispersion characteristics of single- and multimode fibers including relevant information on standardization. The basic elements of fiber cables for various applications constitute another topic followed by new developments such as microstructured and Bragg fibers, hybrid devices combining glass fibers and semiconductors, and multicore and multimode fibers as well.

### 2.1 Introduction

Within the past 40 years, optical fibers have evolved from a not-so-transparent glass tube to an extraordinarily efficient transmission medium, now acknowledged as a central element of modern telecommunication networks. Who could have imagined then, that by now several hundred million kilometers of fibers would have been installed worldwide, allowing today's highly sophisticated World Wide Web (WWW) to link the whole planet in real time? Since the first proposition of using glass fibers as a data transmission medium in 1966 [1], optical fibers have had an extremely dynamic development, always sustaining the evolution of transmission systems and the growing needs for bandwidth.

It is the purpose of this chapter to give the reader some basic knowledge about optical fibers: How are they fabricated? What are the key characteristics and what

---

P. Nouchi (✉)

THALES Research and Technology France, Campus Polytechnique, 1 Avenue Augustin Fresnel,  
91767 Palaiseau Cedex, France  
e-mail: pascale.nouchi@thalesgroup.com

P. Sillard · D. Molin

Prysmian Group, Site Data 4, Route de Nozay, 91460 Marcoussis, France  
e-mail: pierre.sillard@prysmiangroup.com, denis.molin@prysmiangroup.com

are the different optical fibers? What are the latest innovations? This chapter is thus organized as follows: The first section includes some fiber basics to give the reader a very first insight into fiber propagation and to introduce the two main categories of optical fibers, that is, single-mode and multimode. The following two sections are dedicated specifically to multimode and single-mode telecom fibers, respectively. In each of those two sections, we describe in detail key fiber characteristics, the different types of fibers that have been developed over the past few years, and some standardization basics. The subsequent section will shortly present fiber cables for telecom applications, and we will finish with the latest developments on novel optical fibers.

## 2.2 Fiber Basics

### 2.2.1 Principle of Light Propagation in Optical Fibers

An optical fiber is a thin cylindrical strand of silica glass, consisting of a central core surrounded by a cladding: the core has higher refractive index  $n_{co}$  than the surrounding cladding  $n_{cl}$  ( $n_{co} > n_{cl}$ ), thus allowing light to be guided through internal reflection. Typical dimensions are from 10 to a few 10s of  $\mu\text{m}$  for the core diameter, depending on fiber type, and 125  $\mu\text{m}$  for the cladding. The index difference between the core and the cladding is very small, ranging from  $\sim 5 \times 10^{-3}$  to  $\sim 30 \times 10^{-3}$ , again depending on fiber type.

Geometrical optics is often used to get a first physical insight into light propagation. Indeed, light guidance can be simply described by a succession of total internal reflections (TIR) at the core–cladding interface, with each optical path within the fiber corresponding to one “mode” of propagation. This is illustrated in Fig. 2.1. Fibers allowing several modes to propagate are called multimode fibers (MMF), while fibers allowing only one mode to propagate are called single-mode (SMF).

Snell–Descartes law can be used in a straightforward way to derive the angle of acceptance, or critical angle  $\theta_0$ , which defines how much light is captured and guided through a multimode fiber. Any light coming into the fiber at an incident angle larger than  $\theta_0$  will not experience TIR and will thus not be guided through the fiber. The following relation relates  $\theta_0$  to the fiber characteristics:

$$\sin \theta_0 = \sqrt{n_{co}^2 - n_{cl}^2} = \text{NA}, \quad (2.1)$$

where NA is the numerical aperture. The larger the NA, the larger the number of modes. Classical silica-based multimode fibers have NA ranging from 0.2 to 0.3. Again, geometrical optics cannot replace a full description based on electromagnetic theory and Maxwell’s equation. Basic principles will be given in the next section. It should also be emphasized that TIR is not the only mechanism that allows light to be guided. Over the past 10 years, much research has been devoted to new fiber types

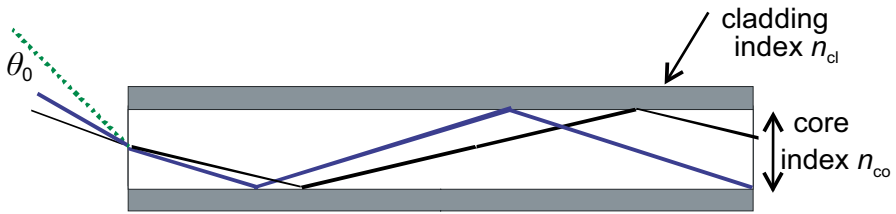


**Fig. 2.1** Schematic of light propagation, based on geometrical optics

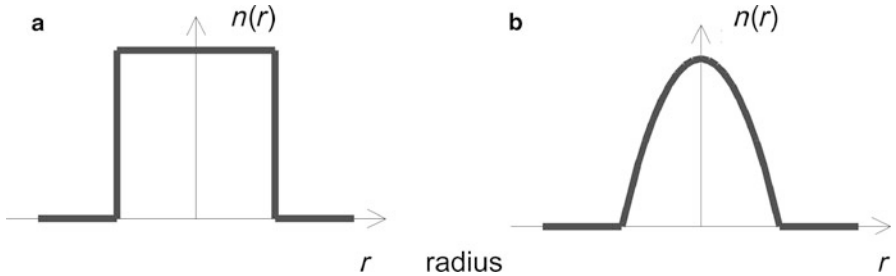


**Fig. 2.2** Step index profile (a) and parabolic index profile (b)

that rely on different physical mechanisms to guide light. This will be described in the last Sect. 2.6 of this chapter.

We conclude this section with a few words about the refractive index profile  $n(r)$  that describes the change of index over the fiber cross-section. The index profile fully defines the properties of light propagating through the fiber. The most simple index profile consists of a step, i.e., a core with a constant index of refraction, but we will see in Sect. 2.4 that profile shapes have become increasingly complicated as fiber requirements have become more stringent. Figure 2.2 illustrates the two most common index profiles, that is the step and parabolic profiles. The parabolic shape, also called graded-index, is essentially used for multimode fibers, while a large variety of shapes can be used for single-mode fibers (SMF), ranging from the simple step to more complex segmented structures.

## 2.2.2 Modal Theory of Light Propagation in Optical Fibers

Light propagation in optical fibers is governed by Maxwell's equations, like all electromagnetic phenomena. For a detailed theory, the reader can refer to well-established textbooks about optical fibers [2, 3]. In this section, we intend to give a short overview of the most important equations and to introduce the concept of modes from an electromagnetic perspective.

Recall that for an isotropic, nonconducting, nonmagnetic medium, Maxwell's equations can be written as:

$$\nabla \times \mathbf{E} = -\partial \mathbf{B} / \partial t, \quad (2.2)$$

$$\nabla \times \mathbf{H} = \partial \mathbf{D} / \partial t, \quad (2.3)$$

$$\nabla \cdot \mathbf{D} = 0, \quad (2.4)$$

$$\nabla \cdot \mathbf{B} = 0, \quad (2.5)$$

where  $\mathbf{E}$  and  $\mathbf{H}$  are the electric and magnetic vectors, respectively, and  $\mathbf{D}$  and  $\mathbf{B}$  the corresponding flux densities. In a dielectric medium, they are related to field vectors by:

$$\mathbf{D} = \varepsilon \mathbf{E}, \quad (2.6)$$

$$\mathbf{B} = \mu_0 \mathbf{H}, \quad (2.7)$$

where  $\varepsilon$  is the dielectric permittivity and  $\mu_0$  is the vacuum permeability.

The wave equation is obtained by combining the above equations to isolate the electric vector  $\mathbf{E}$ . Assuming that loss is low enough so that permittivity  $\varepsilon$  is real and replacing  $\varepsilon$  by  $\varepsilon_0 n^2$  – where  $n$  is the refractive index profile – leads to the following wave equation:

$$\nabla^2 \mathbf{E} - \frac{n^2}{c^2} \frac{\partial^2 \mathbf{E}}{\partial t^2} = \nabla(\nabla \cdot \mathbf{E}) = -\nabla(\nabla(\ln(n^2)) \cdot \mathbf{E}). \quad (2.8)$$

We saw in the preceding section, that in optical fibers the index difference between the core and the cladding is small, of the order of  $\sim 10^{-2}$ . This feature allows one to fully neglect the term on the right side of (2.8). This is called the “weakly guiding approximation” [4], which allows for a simpler description of guided wave propagation.

Cylindrical symmetry of the guiding structure is another important feature that allows writing any of the field components in cylindrical coordinates  $(r, \theta)$  as:

$$\mathbf{E} = F(r)G(\theta)e^{i(\omega t - \beta z)}, \quad (2.9)$$

where  $\omega$  is the angular frequency and  $\beta$  the propagation constant of the field propagating along the  $z$ -axis.

Inserting (2.9) into the wave equation (2.8) within the weakly guiding approximation yields the following important equations:

$$\begin{cases} \frac{d^2 F}{dr^2} + \frac{1}{r} \frac{dF}{dr} + \left( k^2 n^2 - \beta^2 - \frac{\nu^2}{r^2} \right) F = 0, \\ \frac{d^2 G}{d\theta^2} + \nu^2 G = 0. \end{cases} \quad (2.10)$$

Here,  $k$  is the wavenumber, equal to  $\omega/c$  or  $2\pi/\lambda$ , and  $\nu$  is the azimuthal number, that can only take integer values due to the  $2\pi$  field periodicity.

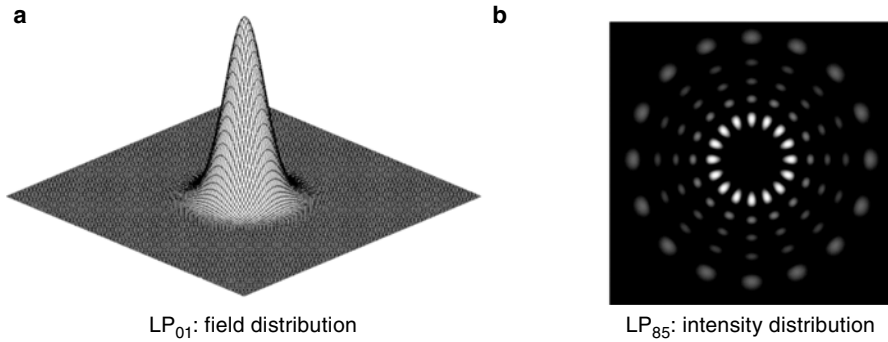


**Fig. 2.3** Schematic of radial distribution of LP<sub>01</sub> mode (a) showing a 3D computed plot, and LP<sub>85</sub> mode (b) showing a computed cross-section of the intensity

In the case of a simple step-index profile, with constant index values in the core with radius  $a$  and in the cladding, the solution of (2.10) is well known and takes the form of Bessel functions. In the case of more complicated index-profile shapes within the core, even though many strategies have been developed in the past to solve this scalar wave equation, numerical methods are applied.

There are many solutions to (2.10), each solution being called a mode and being defined by its propagation constant and field distribution. However, we are only interested in the guided modes, whose radial distributions should be finite at  $r = 0$  and decay to 0 at infinity. It is then possible to show that all the guided modes have a propagation constant that follows:

$$n_{\text{cl}} < \frac{\beta}{k} < n_{\text{co}}, \quad (2.11)$$

where  $\beta/k$  is the effective refractive index  $n_{\text{eff}}$ ,  $n_{\text{co}}$  is the maximum index within the core, and  $n_{\text{cl}}$  is the cladding index.

Whatever the index profile is, it is necessary to apply the boundary conditions, that is the electric field and its derivative are continuous at the core–cladding interface, leading to the well-known eigenvalue equation which only depends on the index profile, the wavelength, and the azimuthal number and whose solution is the propagation constant  $\beta$ . Depending on the profile parameters and wavelength, this equation will have one or more solutions for each integer value  $\nu$ . Each solution is labeled  $\beta_{\nu\mu}$ , (where  $\mu = 1, 2, \dots$ ) and corresponds to a mode of propagation labeled LP <sub>$\nu\mu$</sub>  whose optical field distribution is obtained from (2.10), knowing  $\beta_{\nu\mu}$ . LP stands for linearly polarized. Indeed, it is possible to show that modes are nearly transverse. Figure 2.3 shows examples of radial distributions of different modes.

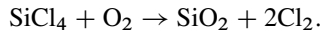
In an SMF profile parameters are chosen so that the only mode that propagates is the LP<sub>01</sub> mode. As can be seen on Fig. 2.3, this mode is nearly Gaussian.

### 2.2.3 Fiber Fabrication

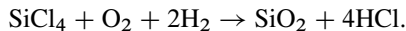
Over the past 40 years, silica glass has proven to be the material of choice for optical fibers, combining both low loss and good reliability and being easy to process. Research is still going on to find alternative materials, but current interest is directed toward very specific applications in the field of nonlinear optics. In the case of silica glass, the index profile can be tailored by the addition of a small quantity of dopants: Ge (P in some cases) to increase the index of refraction, and F (B in some cases) to lower it. For example, changing the index of refraction by  $1 \times 10^{-3}$  with respect to silica requires about 1 wt% of Ge only.

Fiber manufacturing has become an extremely well-mastered process. Geometry is controlled to the micron level, while material purity is controlled to well below parts per billion levels.

Fiber manufacturing is a two-step process. The first step is the fabrication of a high-purity rod called preform. This rod has exactly the same composition and cross-sectional profile as the fiber but its diameter is a few centimeters. Because of its larger size, it is possible to achieve a very good control of the index profile. Different techniques are currently used by fiber manufacturers to make preforms [5]: modified chemical vapor deposition (MCVD), plasma chemical vapor deposition (PCVD), vapor axial deposition (VAD), and outside vapor deposition (OVD). For all these methods, glass is created from a high-temperature reaction between gases. In the case of MCVD, glass is formed layer after layer on the inner surface of a tube through the oxidation of  $\text{SiCl}_4$  gas (1400 °C to 1600 °C):



The high temperature is usually obtained by a burner or a furnace. PCVD, as MCVD, is an inside deposition process but reactions occur within a microwave-generated plasma. For OVD and VAD, as opposed to MCVD and PCVD, soot is formed through hydrolysis:



Thus, both methods require an extra step consisting of dehydration and vitrification in a heating furnace ( $\sim 1500$  °C) to eventually obtain glass. OVD is an external-deposition process, where soot layers are deposited one after another onto a starting rod. In the case of VAD, the rod is built vertically with core and cladding made at the same time.

The second step consists in drawing the preform rod into the 125  $\mu\text{m}$  fiber, which becomes an exact smaller size replica of the rod. This is usually done in a drawing tower, over 10 m high that includes a high-temperature furnace at the top to melt down the preform and a spooling device at the bottom to wind the fiber. The end of the preform rod is thus heated in the furnace ( $\sim 2000$  °C) above the melting point to allow the fiber to be drawn by the winding device with a controlled bare-fiber tension. Fiber is also coated with polymer during the drawing process to ensure

mechanical protection. Two polymer coatings are generally applied onto the glass fiber: a first soft material to protect the fiber from lateral pressure when cabled and a more rigid layer to provide mechanical protection. Coating is usually transparent, but color components can be directly added to the secondary layer, thus eliminating the need for an extra inking-process step before cabling. The final diameter of coated fiber is typically 250  $\mu\text{m}$ .

### 2.2.4 Fiber Loss

Fiber loss is a fundamental limiting factor, as it reduces signal power propagating through the fiber. It is described by an attenuation coefficient  $\alpha$  in dB/km. As for any material, loss is linked to either absorption or scattering mechanisms.

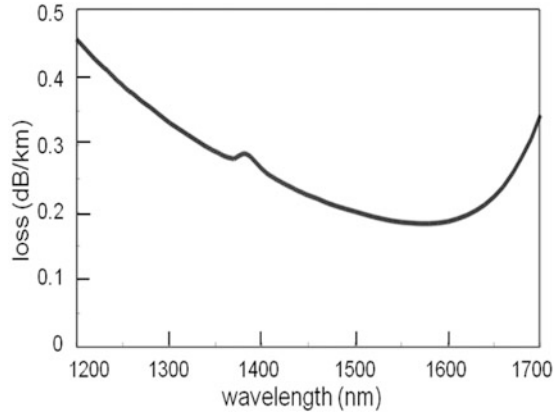
Pure silica absorbs in the ultraviolet (electronic transitions) and in the far-infrared region (molecular vibrations of  $\text{SiO}_2$ ). Metallic impurities could give rise to additional absorption peaks [6], but fiber fabrication process has improved to a point where impurities are no longer a significant concern, with much less than ppb levels and no impact on loss. Hydrogen is also one of the well-known impurities, which has to be avoided during fiber fabrication and once the fiber is installed. Hydrogen diffuses easily and can undergo chemical reactions with the network of silica glass, leading to the formation of numerous defects, the most detrimental one being SiOH. The SiOH vibration has a fundamental absorption peak at 2.73  $\mu\text{m}$  and overtones at 1.38  $\mu\text{m}$  and 0.95  $\mu\text{m}$ , and a concentration of 1 ppm<sub>w</sub> only leads to a few tens of dB/km attenuation at 1.38  $\mu\text{m}$  [7]. From the early days of fiber fabrication, much work has been devoted to the reduction of the so-called OH peak. Latest advances at the end of the 1990s have allowed manufacturers to produce virtually OH-free fibers with additional loss of less than 0.1 dB/km at 1.38  $\mu\text{m}$ . These fiber types are now very well described by standardization bodies and referred to as G.652.D for SMFs.

Rayleigh scattering is the dominant scattering mechanism in silica fibers. It varies as  $\lambda^{-4}$  and is also dependent on fiber composition. In most cases, the higher the dopant concentration, the higher the corresponding scattering. In pure silica, the Rayleigh scattering coefficient is of the order of 0.6–0.8 dB  $\mu\text{m}^4/\text{km}$  and depends on fabrication process and thermal history of the glass measured through its fictive temperature [8]. The influence of Ge doping on Rayleigh scattering has been extensively studied in the past and it can be considered to grow linearly with composition: Rayleigh scattering is doubled compared to pure silica at a germanium incorporation equivalent to a refractive index increase of about  $25 \times 10^{-3}$  [8]. Additional scattering can also be generated by any defects or small fluctuations at the core–cladding interface, also referred to as “waveguide imperfection” [9]. This component is negligible for standard SMFs, but can be significant for higher dopant contents [10].

When summing up all these contributions, minimum loss is found around 1.55  $\mu\text{m}$  where most of today’s telecommunication systems operate. Figure 2.4 shows a typical loss spectrum for commercially available SMFs with typical values of 0.2 dB/km



**Fig. 2.4** Spectral loss of a commercial single-mode fiber



at 1.55  $\mu\text{m}$ . In this wavelength range, Rayleigh scattering is the main contribution. Even though these values are very close to the fundamental limit for silica, there is still some research to further reduce fiber loss, with a record loss of 0.152 dB/km recently reported and achieved through careful profile design and fiber fabrication [11].

One important feature of optical fibers is that they can be bent. However, light is not guided as well in a bent fiber as it is in a straight fiber, it scatters away and loss occurs. The smaller the bending radius, the higher is the loss. In addition, when fibers are in cable form, they are pressed against a surface that is never perfectly smooth, thus generating random axial oscillations for the fibers, referred to as microbending. Both, bending and microbending loss, will be further discussed in Sect. 2.4, as their control is important when designing fibers.

### 2.2.5 Fiber Dispersion

Dispersion is the other important limiting factor when considering data transmission. It causes a light pulse to broaden as it propagates through the fiber and limits transmission capacity, whether the system is digital or analog. Dispersion is very different in multimode and SMFs.

In a multimode fiber, it can be very well understood using geometrical optics. Injected light is coupled to the different modes that the fiber can sustain (or part of them, depending on how injection is made). Modes have different paths, thus leading to different time-of-flight at the output of the fiber. This is called intermodal dispersion. Very simple geometrical-optics computations show that, in a multimode step-index fiber, it is of the order of tens of ns/km. This is exactly why graded-index profiles have been developed: to decrease the intermodal dispersion and allow higher data rates to be transmitted. This will be further discussed in the next section dedicated to multimode fibers.

In an SMF, intermodal dispersion does not occur because all the light is carried within one mode. However, pulse broadening is still present because any given source emits over a certain wavelength band, even single-mode lasers, and different wavelengths travel at a different speed. This is called intramodal dispersion or chromatic dispersion. The chromatic dispersion coefficient is given in ps/(nm km). Chromatic dispersion exists in all dielectric materials and is intrinsically related to the wavelength dependence of the refractive index. In fibers, dispersion can be computed easily, when knowing the wavelength dependence of effective index  $n_{\text{eff}}$ , through:

$$D = \frac{d\tau_g}{d\lambda} = -\frac{\lambda}{c} \frac{d^2 n_{\text{eff}}}{d\lambda^2}, \quad (2.12)$$

where  $\tau_g$  is the group delay. It can be shown that dispersion can be very well approximated by the sum of two contributions: that of silica itself, called “material dispersion” and that of the guiding structure, called “waveguide dispersion.”

In the telecom wavelength range, silica dispersion increases with wavelength. It zeroes near 1.28  $\mu\text{m}$  and is  $\sim 20$  ps/(nm km) at 1.55  $\mu\text{m}$  [12]. Conversely, waveguide dispersion is negative over a broad spectral range. Waveguide dispersion depends on profile shape and can thus strongly modify material dispersion. Chromatic dispersion is a very important characteristic, and many fiber types have been developed with different dispersion properties. This will be further discussed in Sect. 2.4 devoted to SMFs.

## 2.3 Multimode Fibers

MMF were the first fibers to be commercialized in the 1970s, being used for both short- and long-distance telecommunications, operating mainly at 850 nm with Light-Emitting Diode (LED) sources. SMFs were of course recognized for their higher bandwidth, but there were no sources to couple light efficiently into the narrower core of SMFs. At the beginning of the 1980s, research on sources resulted in reliable semiconductor lasers suited for smaller core SMFs, which narrowed down the application of multimode fibers to short-distance systems.

Multimode fiber development has continued from the 1980s up to now, mainly in the framework of Ethernet dedicated to data communications, that successively promoted bit rates from 10 Mbit/s at the beginning up to 10 Gbit/s since 2002 and 100 Gbit/s expected to come soon. Multimode fibers could follow this increase in bit rate, thanks to process improvements and technological breakthroughs in sources that provided low-cost 10 Gbit/s sources at the end of the 1990s, in particular the vertical cavity surface-emitting laser (VCSEL) operating at 850 nm (see also Chap. 3).

Compared to SMFs, multimode fibers offer much more relaxed tolerances in the connectorization between fibers and to sources.

### 2.3.1 Key Characteristics

#### 2.3.1.1 Modal Bandwidth

Bandwidth is one of the main characteristics of multimode fibers: it quantifies the light-carrying capacity, the higher, the better. It is generally normalized by the fiber length and thus expressed in MHz km, referring to the analog world, but a relation between maximum bit rate and modal bandwidth can be derived.

A fiber can be seen as a passive low-pass filter. Its bandwidth is then defined as the modulation frequency that is reduced by 3 dB as compared to the zero frequency (DC) response. This is illustrated in Fig. 2.5. Bandwidth can be measured either in the time or the frequency domain [13]. In the time domain, it consists in measuring the temporal response of the fiber by injecting a short pulse. The transfer function  $TF(f)$  can then be computed from the recorded input  $s_{in}(t)$  and output  $s_{out}(t)$  signals as the ratio of their respective fast Fourier transform  $\tilde{s}_{in}(f)$  and  $\tilde{s}_{out}(f)$ :

$$TF(f) = 10 \cdot \log_{10} \left( \frac{\tilde{s}_{out}(f)}{\tilde{s}_{in}(f)} \right). \quad (2.13)$$

One of the main features of multimode fibers is that many of their characteristics depend on the way light is coupled, more commonly called the launching conditions. The launching condition defines which modes are excited or not, and what the corresponding power distribution is. However, the launching conditions provided by LEDs and VCSELs are very different, and very different even within the VCSELs family. LEDs usually excite all the guided modes, while VCSELs excite a smaller number of modes, which varies widely from one VCSEL to another.

Therefore, in order to ensure consistent bandwidth measurements and enable a comparison of fibers on the same basis, bandwidth is measured under what is called the over-filled launch condition (OFL), which corresponds to a uniform excitation of all guided modes in the fiber. In practice, a mode scrambler is inserted between the laser and the fiber to provide a spatially, angularly, and uniformly over-filled launch. Typical values for OFL modal bandwidth are several hundreds of MHz km, with the best modern fibers exhibiting values over 10 GHz km at 850 nm. The OFL modal bandwidth renders fiber properties very well when a fiber is coupled to an LED.

Modal bandwidth under VCSEL launch is called effective modal bandwidth (EMB). Because of the plurality of VCSEL patterns, no standardized launching conditions have been defined, but dedicated measurement strategies have been developed to best characterize fiber performance. It mainly relies on differential mode delay (DMD) measurements, as explained in the next paragraph.

#### 2.3.1.2 Differential Mode Delay

DMD measurement is another way of characterizing the modal properties of multimode fibers. It is now widely used by fiber manufacturers to assess performance

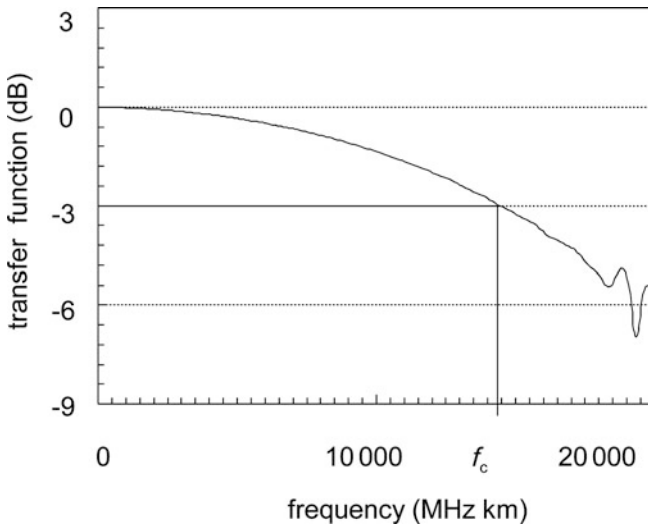


**Fig. 2.5** Computed transfer function of a multimode fiber ( $f_c$ : modal bandwidth)

of fibers dedicated to high-speed networks operating at 10 Gbit/s and using VCSEL sources. Because VCSELs excite only a limited number of modes, OFL bandwidth is thus less relevant for such applications.

Examples of DMD measurements at 850 nm are shown in Fig. 2.6 for two different multimode fibers with a core radius of 50  $\mu\text{m}$ . DMD provides a cartography of the modal dispersion across the fiber radius. Indeed, each line of this plot corresponds to the power evolution as a function of time when a short laser pulse (20 ps to 1 ns) is launched – through an SMF – at one specific position across the multimode fiber radius, called the “offset launch” on the graph. The mode field diameter of the SMF is of the order of several microns – below the diameter of typical multimode fibers – so that it can only excite a subset of modes. A centered launch (offset launch equal to 0  $\mu\text{m}$ ) excites mainly the lowest order modes, while large offset launches excite the highest order modes. Here, the fiber is scanned from its center to the edge of its core with 1  $\mu\text{m}$  steps. The DMD plot depends on several settings such as the spot size used at the launching stage, the pulse duration, the fiber length, and so on. In order to ensure consistent measurements, DMD measurements were standardized in 2003 [14] for 50  $\mu\text{m}$ -core multimode fibers.

The DMD plot shown in Fig. 2.6a reveals that the highest order modes, those excited by the largest offset launches, travel faster than the lower order modes, excited by the lowest offset launches. This fiber thus exhibits a large modal dispersion, especially when compared to the fiber whose plot is shown in Fig. 2.6b. For this last fiber group delays are well equalized.

In addition, the standards provide a set of tools dedicated to the analysis of the DMD plot: the DMD values, expressed in ps/m [14]. They roughly correspond to the delay between the fastest and the slowest pulses within a given subgroup of offset

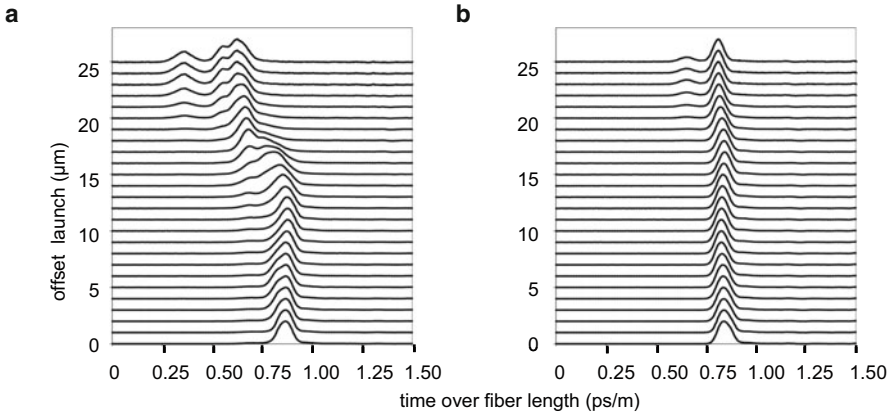


**Fig. 2.6 a, b** Measured DMD plot for two different multimode fibers

launches, also called templates. The standards define three DMD values with their respective templates and named inner, outer, and an unofficially called “sliding” value. For instance, the inner DMD value corresponds to offset launches between 5  $\mu\text{m}$  and 18  $\mu\text{m}$  only. The fibers of Fig. 2.6 have an inner DMD value of 0.141 ps/m (a) and 0.025 ps/m (b). As further developed in Sect. 2.3.3 (Standardization), specifications have been defined for those DMD values, to allow for a minimum EMB value.

The same standards also propose an alternative to the DMD values: the EMB<sub>c</sub> (effective modal bandwidth, where “c” stands for computed), which has been defined to evaluate the worst EMB the fiber may exhibit when coupled to VCSELs [14]. Indeed, DMD plots also allow to simulate fiber response – that is the output pulse shape – from a linear combination of each individual trace. Standards define ten different sets of weights to compute this linear combination and to render the variety of VCSEL launches. EMB can then be computed from those ten output pulses, and the worst value is called EMB<sub>c</sub>. The fibers of Fig. 2.6 have EMB<sub>c</sub> values of 4140 MHz km (a) and greater than 15 000 MHz km (b), with respective OFL modal bandwidth of 3300 MHz km and greater than 14 000 MHz km.

### 2.3.1.3 Loss

Loss in a multimode fiber may be more complex than in an SMF because each mode may experience different attenuation levels. This effect is called differential mode attenuation (DMA). In practice, DMA is negligible in modern silica multimode fibers, and loss does not depend on the launching condition and linearly increases with fiber length. As for SMFs, it is expressed in dB/km. Typical loss values of a 50  $\mu\text{m}$  multimode fiber are about 2.2 dB/km at 850 nm and 0.5 dB/km at 1300 nm.

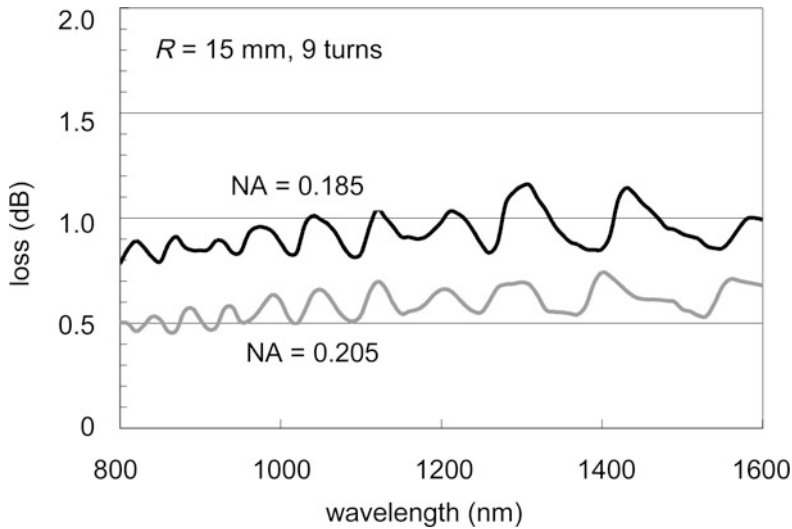


**Fig. 2.7** Bending loss as a function of wavelength for two 50  $\mu\text{m}$ -core multimode fibers with respective NA of 0.205 and 0.185 after nine turns around a 15 mm radius mandrel

#### 2.3.1.4 Bending Loss

Multimode fibers generally do not behave like SMFs under bending. Each mode exhibits significantly different bend sensitivities: the highest order modes are weakly guided compared to the lowest order modes and thus far more sensitive to bending than the lowest order ones. As a consequence, bending loss level strongly depends on launching conditions: a launching condition that mainly excites the highest order modes yields higher bend loss, whereas injection that confines the light in the lowest order mode may exhibit a very good bend resistance. Another consequence is that bend loss of a multimode fiber cannot be expressed in dB/turn or dB/m, as in SMFs. It is recommended to express them in dB for a given number of turns and a given launching condition [15].

Another very different feature of bending loss of multimode fibers compared to SMFs is their spectral dependence. Indeed, bend loss does not exponentially increase with wavelength as is the case with SMFs, but, under the OFL condition, it oscillates around a fairly constant value over the whole spectrum, as shown in Fig. 2.7. The oscillations come from the cutoff of the highest order modes [16].

### 2.3.2 Different Types of Multimode Fibers

#### 2.3.2.1 Silica Step-index Multimode Fiber

Step-index multimode fibers were the first ones to be developed in the early days of optical communication. As briefly explained in Sect. 2.2.4, the difference of arrival

times between the slowest mode and the fastest one can be written as:

$$\Delta t = \frac{L \times \text{NA}^2}{2cn_{\text{cl}}}, \quad (2.14)$$

where  $n_{\text{cl}}$  is the refractive index of the cladding, NA is the numerical aperture,  $L$  the fiber length, and  $c$  the speed of light. Modal dispersion in such fibers depends on the square of the numerical aperture. OFL bandwidth of step-index multimode fibers usually does not exceed a few tens of MHz km, making these fibers definitively not suited for high-speed transmissions.

### 2.3.2.2 Silica Graded-index Multimode Fiber

Graded-index multimode fibers were soon introduced to improve and reduce modal dispersion of step-index fibers [17]. The idea consists in equalizing the various optical paths followed by all rays of light by lowering the refractive index experienced by the longest paths. The core profile follows a power law parameterized by the  $\alpha$  parameter:

$$n(r) = \begin{cases} n_{\text{co}} \sqrt{1 - 2\Delta \left(\frac{r}{a}\right)^\alpha}, & r \leq a, \\ n_{\text{cl}}, & r \geq a, \end{cases} \quad (2.15)$$

where  $n_{\text{co}}$  is the core maximum refractive index,  $n_{\text{cl}}$  is the cladding index, and  $\Delta$  is defined as

$$\Delta = \frac{n_{\text{co}}^2 - n_{\text{cl}}^2}{2n_{\text{co}}^2}. \quad (2.16)$$

With such an  $\alpha$ -parameterized profile and by a proper choice of the  $\alpha$  parameter, it is possible to maximize the OFL bandwidth at a given wavelength [18, 19]. Indeed, multimode fibers can be used either around 850 nm (LEDs or VCSELs) or around 1300 nm (LEDs). The  $\alpha$  values typically used for maximizing the OFL bandwidth at wavelengths of 850 and 1300 nm are  $\sim 2.07$  and  $\sim 1.98$ , respectively, as shown in Fig. 2.8.

One can see from Fig. 2.8 that, in practice, it is not easy to achieve very high bandwidths in a reproducible way because bandwidth strongly depends on the  $\alpha$  value: a slight variation of less than 0.01 for  $\alpha$  shifts the optimal wavelength by tens of nanometers. In addition, any defects in the index profile will lower the bandwidth. This indicates that the achievement of very high bandwidth requires an extremely precise process control, while a slight error on the refractive index profile leads to a dramatic decrease of fiber performance.

Nowadays, two classes of graded-index multimode fibers dominate: the 50  $\mu\text{m}$  and the 62.5  $\mu\text{m}$  multimode fibers that exhibit a 50  $\mu\text{m}$  and 62.5  $\mu\text{m}$  core diameter, respectively, and a numerical aperture of 0.200 and 0.275. The 50  $\mu\text{m}$  multimode fiber is historically the first fiber that was developed, followed very rapidly

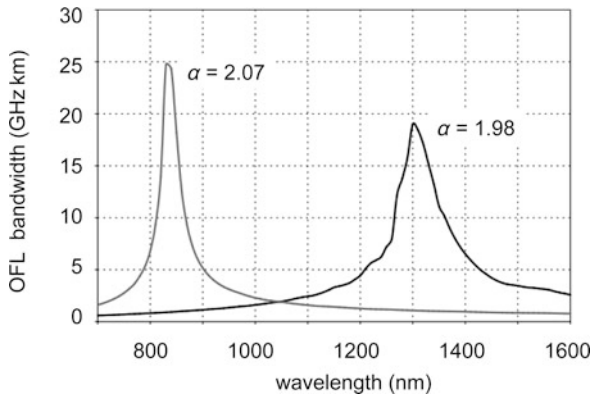


**Fig. 2.8** Computed OFL modal bandwidth vs. wavelength for  $\alpha = 2.07$  and  $\alpha = 1.98$  for a 50  $\mu\text{m}$ -core multimode fiber

by the 62.5  $\mu\text{m}$  one that is still the most widely installed multimode fiber all over the world. This trend is about to reverse due to the advent of the VCSEL sources at the end of the 1990s, which are able to sustain the high modulation speeds required for multigigabit-per-second transmission. This breakthrough pushed the fiber manufacturers to improve their process control in order to allow today's mass production of the new class of 50  $\mu\text{m}$  multimode fibers (also known as OM3 fibers and further explained in Sect. 2.3.3), which exhibits the high bandwidths required for 10 Gbit/s transmission. Their OFL modal bandwidth at 850 nm is typically greater than 1500 MHz km for OM3 and greater than 3500 MHz km for OM4.

Another aspect that has recently been in the focus of attention is the bending sensitivity of MMFs. The important rise of traffic in data centers, subject to harsh environments (massive cabling, plurality of connectors, and reduced footprint), has spurred the development of a new type of MMFs: bend-resistant OM3 and OM4 fibers. These fibers typically exhibit macrobending sensitivities that are 10 times lower than those of legacy OM3 and OM4 fibers, with macrobend losses below 0.2 dB for two turns at 7.5 mm bend radius. They all have a depressed-index area in the cladding, i.e., a trench near the graded-index core that allows for better light confinement. These new trench-assisted graded-index MMFs are paving the way to more reliable cable management in data centers and to innovative and more compact cable designs [20, 21].

### 2.3.2.3 Plastic Optical Fibers

Plastic optical fibers (POF) are multimode fibers whose core and cladding are made of plastic material. They usually have a larger core than silica fibers, up to the millimeter range, and can be operated down to the visible. POF are easy to connectorize and easy to bend. They offer a cheap alternative to silica multimode fibers, but are limited to very short transmission distances due to their inherent higher loss and



lower bandwidth. POFs were first used in automation, mainly in the visible, but the past few years have witnessed a shift to the Ethernet world with operating wavelength of 850 and 1300 nm.

The original POF design consists of a step-index profile (SI-POF), also known as the standard POF, with a large core of 980  $\mu\text{m}$  made of poly-methylmetacrylate (PMMA) surrounded by a thin 10  $\mu\text{m}$  cladding of fluorinated polymer. The typical numerical aperture is about 0.5. This material exhibits high absorption of about 100 dB/km at 520 nm, 560 nm, and 650 nm.

A graded-index profile is mandatory for higher transmission speed and/or distance. The early trials did not yield satisfactory loss results, but in the early 1990s, thanks to the use of perfluorinated polymer, feasibility of low-loss graded-index plastic optical fibers (GI-POFs) was demonstrated [22] and first fibers were commercialized in 2000. Nowadays, losses of GI-POF are kept below 20 dB/km over the 800–1300 nm range [23], and fibers with core sizes as small as 50  $\mu\text{m}$  are available. They show good transmission capabilities and can provide OFL-bandwidth larger than 400 MHz km [24, 25].

### 2.3.3 Standardization

The concern for standardization has started at an early stage of fiber development. Several bodies are active: the Telecommunication Standardization Sector of the International Telecommunication Union (ITU-T), the International Electrotechnical Commission (IEC), the ISO/IEC jointly operated by the International Organization for Standardization and the IEC, and the Telecommunications Industry Association (TIA). The first ITU-T recommendation on multimode fibers was published in 1984 (G.651).

One of the most common classifications is that of ISO/IEC, which defines four main multimode fiber classes known as OM1, OM2, OM3 and OM4 [26]. OM1 and OM2 define specifications for both 50  $\mu\text{m}$  and 62.5  $\mu\text{m}$  multimode fibers, while OM3 and OM4 deal with 50  $\mu\text{m}$  multimode fibers only, as shown in Table 2.1. OM3 was published in 2002 and is closely linked to the IEEE 802.3 10GbE Ethernet Standard released in 2002. An OM3-type fiber, when operated at 850 nm in combination with VCSEL sources, is able to bridge 300 m at 10 Gbit/s.

In the early 2000s, in the framework of the IEEE 802.3 standards, it was shown through extensive modeling that an error-free 10GbE transmission over 300 m requires an EMB larger than 2000 MHz km. The OM3 standards translate this system requirement into specifications on the DMD values computed from the DMD plots, whose definition has been explained in Sect. 2.3.1 [27]. These specifications are summarized in Table 2.2, which includes six different sets of DMD values. To be compliant, a fiber needs to fulfill one of the six sets only.

Since the introduction of the OM3-type fiber, fiber manufacturers have developed a higher grade of Laser Optimized MMF (LO-MMF), with tighter DMD specifications intended to ensure EMB greater than 4700 MHz km. In November 2009, such

**Table 2.1** OFL modal bandwidth specifications for OM1, 2, 3 and 4 fibers

Fiber class	Core diameter ( $\mu\text{m}$ )	OFL-BW at 850 nm (MHz km)	OFL-BW at 1300 nm (MHz km)
OM1	50 and 62.5	> 200	> 500
OM2	50 and 62.5	> 500	> 500
OM3	50 only	> 1500	> 500
OM4	50 only	> 3500	> 500

**Table 2.2** DMD specifications ensuring an EMB greater than 2000 MHz km

Specifications	Outer DMD (ps/m)	Inner DMD (ps/m)	Sliding DMD (ps/m)
1	$\leq 0.33$	$\leq 0.33$	$\leq 0.25$
2	$\leq 0.27$	$\leq 0.35$	$\leq 0.25$
3	$\leq 0.26$	$\leq 0.40$	$\leq 0.25$
4	$\leq 0.25$	$\leq 0.50$	$\leq 0.25$
5	$\leq 0.24$	$\leq 0.60$	$\leq 0.25$
6	$\leq 0.23$	$\leq 0.70$	$\leq 0.25$

fibers, labeled OM4, were added to the TIA 492AAAD. They provide point-to-point 40 & 100 Gbit/s Ethernet links over 4 or 10 pairs of fibers, up to 150 m (cf. IEEE 802.3ba-2010 standard). Discussions are still ongoing to standardize 400 m-long 10 GbE links implementing OM4 fibers, to extend the 300 m reach provided by OM3.

## 2.4 Single-mode Fibers

SMFs have replaced MMFs for long-distance transmission in the early 1980s, when semiconductor laser sources became available. Since then, steady progress in transmission capacity has been made, with bit rates as high as several Tbit/s being now transmitted over several thousands of kilometers [28]. SMFs have continually evolved to meet the permanently increasing system and capacity requirements, yielding several fiber types, as we will see in this section.

### 2.4.1 Key Characteristics

We discuss here the main characteristics of SMFs, that are of importance to assess fiber performance with respect to given applications, that is, loss, dispersion, cutoff wavelength, mode field diameter, and effective area. Loss and dispersion were described above in the fiber basics Sects. 2.2.4 and 2.2.5. Recall that loss is in the range of 0.20 dB/km at 1550 nm for straight fibers. When a fiber is bent on a macroscale or subject to microdeformations causing microbends, light scatters away, and loss

occurs. Macrobending loss mainly depends on the optical properties of the fiber, and proper profile design allows making it negligible for bend radii around 15 mm or down to 7.5 mm for some applications (see sections below). Microbending loss depends on both optical and material properties of the fiber, and careful choice of both profile and coating renders it negligible when fiber is put into a cable or under compression or lateral stress. Extensive literature exists on both topics, starting from the early days of fiber optics history. The reader is referred to [2, 3] for a theoretical treatment.

Chromatic dispersion is especially important in SMFs, because of its double impact on light-pulse broadening and pulse distortions due to nonlinear effects. We saw in Sect. 2.2.5 that fiber chromatic dispersion can be made very different from that of silica, thanks to profile design. Indeed, all along fiber history, much research work has been done to tailor fiber dispersion through proper design to best fit telecommunication systems requirements. Usually, dispersion characteristics are given in terms of zero-chromatic dispersion wavelength  $\lambda_0$ , chromatic dispersion, and dispersion slope (first derivative of chromatic dispersion with respect to wavelength) at the operating wavelength. Fibers with dispersion values ranging from 17 ps/(nm km) to well below  $-100$  ps/(nm km) at 1550 nm are now commercially available.

Another source of dispersion arises in SMF when circular symmetry is broken, yielding a slight birefringence and different group velocity for orthogonal modes of polarization. It is referred to as polarization-mode dispersion (PMD) [29]. Because fiber birefringence is small and varies in a random fashion along the fiber, PMD is not linear with length, but is given in ps/ $\sqrt{\text{km}}$ . PMD of recent SMFs is well mastered and below 0.10 ps/ $\sqrt{\text{km}}$ .

The cutoff wavelength characterizes the wavelength range over which a fiber is single-moded and carries only the LP<sub>01</sub> mode, as seen in Sect. 2.2.2. In theory, each higher order mode is allowed to propagate for wavelengths below its cutoff wavelength, so that the term “cutoff wavelength” refers to the largest cutoff wavelength of all higher order modes, being in most cases that of the LP<sub>11</sub> mode. In practice, one speaks of fiber and cable cutoff wavelengths ( $\lambda_{cf}$  and  $\lambda_{cc}$ , respectively), which are measured by standardized methods (FOF-80 EIA-TIA-455-80) and correspond to the wavelength above which higher order modes can be neglected due to their high losses. Most transmission fibers are specified with  $\lambda_{cc} < 1260$  nm, or  $< 1450$  nm, or even  $< 1530$  nm.

Two quantities are used to characterize the mode spatial extension: the mode field diameter (MFD) in units of  $\mu\text{m}$  and the effective area  $A_{\text{eff}}$  in  $\mu\text{m}^2$ :

$$\text{MFD} = \frac{2\sqrt{\int_0^\infty F(r)^2 r dr}}{\int_0^\infty \frac{dF(r)}{dr}^2 r dr}, \quad (2.17)$$

$$A_{\text{eff}} = \frac{2\pi\left(\int_0^\infty |F(r)|^2 r dr\right)^2}{\int_0^\infty |F(r)|^4 r dr}, \quad (2.18)$$

where  $F$  is the electric field as seen in Sect. 2.2.2.

The MFD definition was first proposed in 1983 [30] and is related to the r.m.s. width of the far-field intensity. It is commonly used to evaluate splice losses. On the other hand, the effective area is used as a measure of nonlinear effects that might occur in fibers. The larger the effective area, the more effectively can nonlinear effects be avoided, since they are proportional to the signal intensity through the nonlinear index  $n_2$  [31, 32]. Transmission fibers have  $A_{\text{eff}}$  ranging from  $\sim 50$  to  $\sim 100 \mu\text{m}^2$  and  $n_2$  ranging from  $2.5$  to  $2.7 \times 10^{-20} \text{ m}^2/\text{W}$ .

## 2.4.2 Standardization

As is the case with MMFs, standardization bodies have always been very active in following closely or even anticipating fiber developments. The most common classification is that of the Telecommunication Standardization Sector of the ITU-T, defining a range of fiber values for each recommendation or fiber type. They are named G.652, G.653, and so on.

### 2.4.2.1 ITU-T Recommendation for Standard Single-mode Fibers (G.652)

This recommendation describes what is also called the “standard” single-mode fiber (SSMF), whose main feature is a zero chromatic dispersion wavelength around 1310 nm. This recommendation was released in 1984, and at that time, fiber was optimized for 1310 nm operation. The recommendation has been updated several times, again to follow the latest advances in fiber development, essentially regarding loss and PMD.

By now, this fiber is mostly operated at 1550 nm and it is the most widely installed fiber in the world. Overall, these fibers have chromatic dispersion curves very close to that of silica, with values around  $17 \text{ ps}/(\text{nm km})$  at 1550 nm. There is no need for complicated fiber design in that case, and a simple step-index profile is used, with typical core–cladding index difference of  $\sim 5 \times 10^{-3}$  and core diameter of  $\sim 9 \mu\text{m}$ .

### 2.4.2.2 ITU-T Recommendations for Dispersion-tailored Fibers (G.653, G.655, and G.656)

Recommendation G.652 was soon followed by G.653 in 1988, describing dispersion-shifted fibers (DSFs) with the zero-dispersion wavelength  $\lambda_0$  shifted to 1550 nm instead of the previous 1310 nm, intended to be used for single-channel operation at 1550 nm and thus to the benefit of the lowest-loss window of silica fibers.

At the same time, however, the discovery of erbium-doped fiber amplifiers (EDFA) made possible the amplification of signals within a whole band around

1550 nm (the C-band from 1530 to 1565 nm) and paved the way for multiple wavelength channel transmission, well known as wavelength-division multiplexing (WDM) systems. It was soon recognized that DSFs favored deleterious inter-channel nonlinear effects and were thus not suited for WDM transmission. As a consequence, nonzero-dispersion-shifted fibers (NZDSFs) have been developed featuring a zero-dispersion wavelength  $\lambda_0$  between  $\sim 1400$  and  $\sim 1600$  nm and a small but nonzero chromatic dispersion value at 1550 nm.

The ITU-T recommendation G.655 was first released in 1996 to cover NZDSFs. G.655 fibers have an absolute value of chromatic dispersion between 0.1 and 6 ps/(nm km) over the C-band. Over the past few years it was amended twice, and now includes five different subtypes: G.655.A (the original description); G.655.B and G.655.C to allow the maximum absolute value of dispersion to reach 10 ps/(nm km) over the C-band, further handling parasitic interchannel nonlinear effects for dense WDM (DWDM); and G.655.D and G.655.E to better account for the wavelength dependence of dispersion over the S-, C-, and L-bands, ranging from 1460 to 1625 nm, as depicted in Fig. 2.9.

The last recommendation, G.656, was introduced in 2004 and covers NZDSFs optimized for wideband operation in the S-, C-, and L-band. The zero-chromatic dispersion wavelength  $\lambda_0$  is below 1460 nm, thus reducing interchannel nonlinear effects compared to G.655-only compliant NZDSFs and allowing for efficient multiple-wavelength Raman pumping. This recommendation was also updated in 2006 by expressing the chromatic dispersion requirements as a pair of bounding curves versus wavelength from 1460 nm to 1625 nm. Note that G.655.E fibers are also G.656 compliant, which is not the case for G.655.D fibers (see Fig. 2.9).

All these categories allow for longer  $\lambda_{cc}$  (up to 1450 nm) than those specified in G.652. This can offer higher margins in profile designs (see Sect. 2.4.3) but at the expense of losing 1310 nm applicability.

### 2.4.2.3 ITU-T Recommendation for Bend-Optimized Fibers (G.657)

Over the past few years, fiber penetration deeper into the network – that is for Fiber-to-the- $x$  (FTTx,  $x$  = curb, building, home, ...) applications – has spurred the development of fibers with reduced bending sensitivity compared to that of G.652 fibers. Increased resistance against bending is needed for such applications because of a greater risk of encountering incidental bends, sharp bends when installed in corners, or when stapling the cable along a wall.

These bend-insensitive fibers are described in recommendation G.657, released in 2006. The first version included two classes: G.657.A, which is G.652 compliant and exhibits a reduced bending sensitivity; G.657.B, which shows further reduced bending sensitivity, but it is not G.652 compliant because it contains a wider range of characteristics, especially concerning MFD and chromatic dispersion parameters (see Table 2.3). For both categories, the cable cutoff wavelength is specified to be below 1260 nm to ensure single-mode operation in the O-band, ranging from

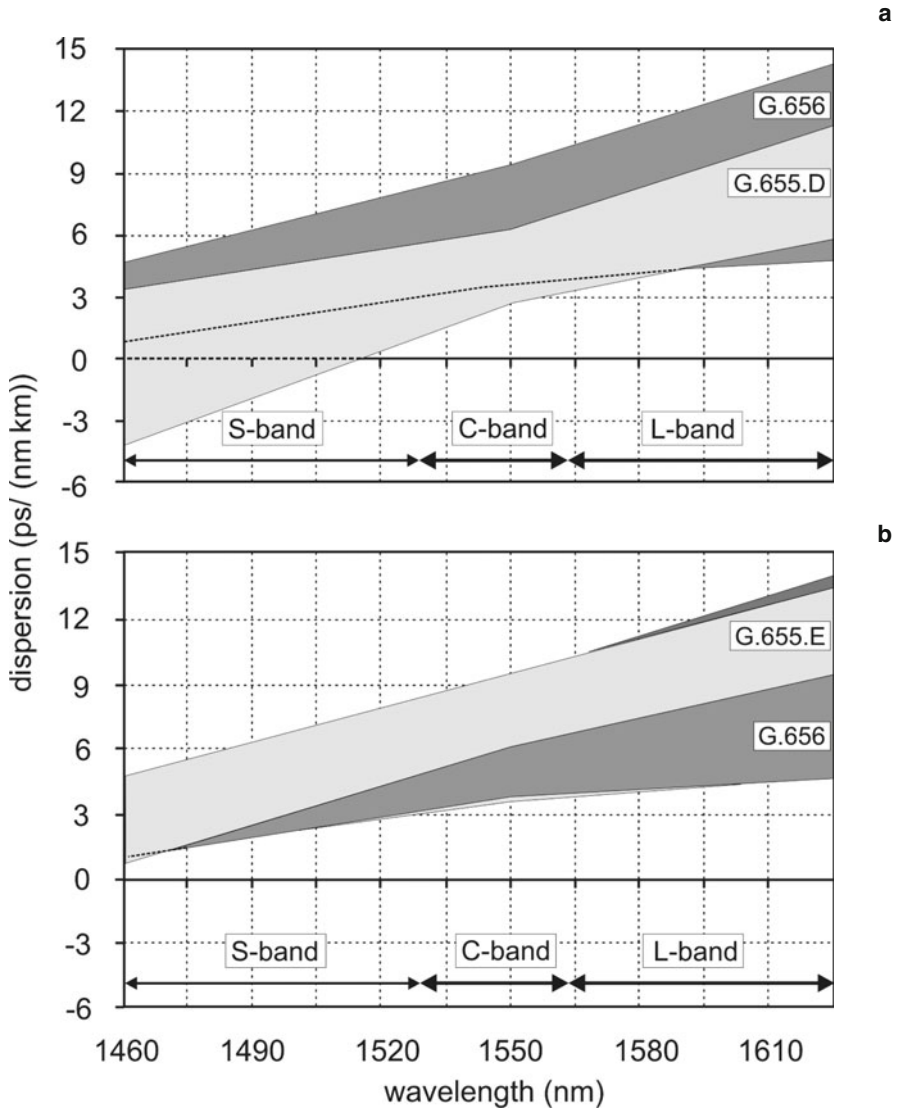


**Fig. 2.9** Ranges of dispersion values that are allowed across the S-, C-, and L-bands for: **a** G.656 dark-gray shaded area and G.655.D, light-gray shaded area; **b** G.656 dark-gray shaded area and G.655.E, light-gray shaded area

1260 nm to 1360 nm. In 2009, this recommendation was updated to include two new subclasses G.657.A1 (former G.657.A) and G.657.A2, and G.657.B2 (former G.657.B) and G.657.B3 with bend-loss specifications at bend radii down to 5 mm (see Table 2.3).

Table 2.3 G.652, G.657.A, and G.657.B attributes

Cable cutoff wavelength		G.652		G.657									
		G.652.B	G.652.D	G.657.A1	G.657.A2	G.657.B2	G.657.B3						
		< 1260 nm		< 1260 nm									
MFD	Nominal value at 1310 nm	8.6–9.5 $\mu\text{m}$		8.6–9.5 $\mu\text{m}$									
	Tolerance	$\pm 0.6 \mu\text{m}$		$\pm 0.4 \mu\text{m}$									
	Radius (mm)	30		15	10	15	10	7.5	10	7.5	10	7.5	5
Macrobend loss	Number of turns	100		10	1	10	1	10	1	10	1	10	1
	Max. at 1550 nm (dB)	0.1		0.25	0.75	0.03	0.1	0.5	0.03	0.1	0.5	0.03	0.08
	Max. at 1625 nm (dB)	0.1		1	1.5	0.1	0.2	1	0.1	0.2	1	0.1	0.25
Dispersion	$\lambda_0$	1300–1324 nm		1300–1324 nm									
	Slope	< 0.092 ps/nm <sup>2</sup> ·km at $\lambda_0$		< 0.092 ps/nm <sup>2</sup> ·km at $\lambda_0$									
Proof test	Minimum	0.69 GPa		0.69 GPa									
	Nominal	125		125									
Cladding diameter	Tolerance	$\pm 1 \mu\text{m}$		$\pm 0.7 \mu\text{m}$									
	Maximum	0.6 $\mu\text{m}$		0.5 $\mu\text{m}$									
Core concentricity error	Minimum	1%		1%									
	Maximum	1%		1%									
Attenuation (cable)	Max. at 1310 nm	0.4 dB/km		0.4 dB/km									
	Max. at 1550 nm	0.35 dB/km		0.3 dB/km									
	Max. at 1625 nm	0.4 dB/km		0.3 dB/km									
	Max. 1310–1625 nm	0.4 dB/km		0.4 dB/km									
	Max. at 1383 nm	< Max. 1310–1625 nm		< Max. 1310–1625 nm									
PMD (cable)	M	20 cables		20 cables									
	Q	0.01%		0.01%									
	Max. PMD <sub>Q</sub>	0.2 ps/km <sup>0.5</sup>		0.2 ps/km <sup>0.5</sup>									

### 2.4.3 Fiber Types

#### 2.4.3.1 Dispersion-tailored Transmission Fibers

As outlined earlier, the shift to the 1550 nm transmission wavelength region in order to benefit from the lowest-loss window of silica fibers and the subsequent advent of WDM systems have both triggered much research to design dispersion-optimized fibers. However, other parameters such as the MFD or effective area (the larger the better) and the dispersion slope (the smaller the better) are also important, and depending on system constraints, an optimum compromise has to be found.

For those fiber types, step-index profiles offer limited possibilities only: a higher index difference (from  $\sim 6 \times 10^{-3}$  to  $\sim 10 \times 10^{-3}$ ) and a smaller diameter (from  $\sim 8 \mu\text{m}$  to  $\sim 5 \mu\text{m}$ ) are required to lower chromatic dispersion, yielding small  $A_{\text{eff}}$  ( $\leq 50 \mu\text{m}^2$  at 1550 nm) for standard dispersion slopes ( $\sim 0.055 \text{ ps}/(\text{nm}^2 \text{ km})$ ) at 1550 nm, as illustrated in Fig. 2.10a.

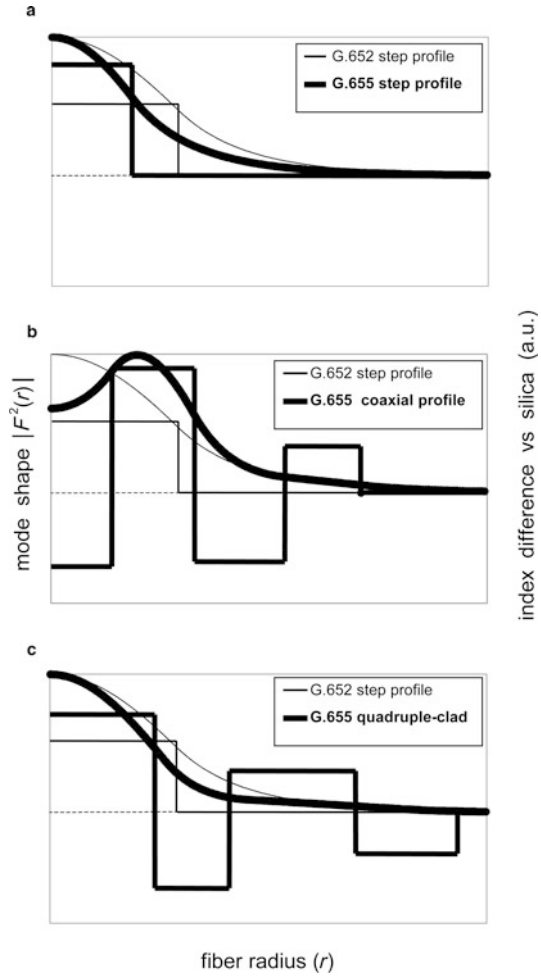
To overcome such a problem, multilayered core index structures were proposed quite early in the history of optical fibers [33]. Larger  $A_{\text{eff}}$  are then obtained at the expense of more complicated profile structures and, sometimes, longer  $\lambda_{\text{cc}}$ . For a given profile family,  $A_{\text{eff}}$  is unfortunately proportional to the dispersion slope, thus leading to trade-offs: a large  $A_{\text{eff}}$  with a relatively high dispersion slope or a small dispersion slope with a small  $A_{\text{eff}}$  [34, 35]. Two profile families are of particular interest: the coaxial family, which includes a depressed center (negative index difference with respect to cladding) surrounded by one or several rings; and the multiple-clad family, which includes a central step surrounded by rings with alternate negative and positive index differences, as illustrated in Fig. 2.10b, c, respectively. Figure 2.10c shows a quadruple-clad design. Coaxial profiles offer very large  $A_{\text{eff}}$  for acceptable dispersion slopes ( $> 95 \mu\text{m}^2$  for  $\sim 0.060\text{--}0.070 \text{ ps}/(\text{nm}^2 \text{ km})$ ) at 1550 nm [36, 37]) but exhibit relatively large loss ( $> 0.21 \text{ dB km}$ ) because of their unusual shape. Multiple-clad profiles offer low dispersion slopes for acceptable  $A_{\text{eff}}$  ( $\sim 45\text{--}55 \mu\text{m}^2$  ( $< 0.030 \text{ ps}/(\text{nm}^2 \text{ km})$ ) for  $\sim 45\text{--}55 \mu\text{m}^2$  at 1550 nm [38–40]) and loss around 0.20 dB/km.

#### 2.4.3.2 Ultra-long-haul Transmission Fibers

For ultra-long-haul WDM terrestrial or submarine networks, the picture is somewhat different. Research has focused on the two factors that directly limit optical transmission: loss with the early demonstration of record loss values [41], and, more recently in the early 2000s, nonlinear effects. In this context, fibers with low loss (from 0.17 to 0.18 dB/km at 1550 nm) and large  $A_{\text{eff}}$  ( $> 100 \mu\text{m}^2$  at 1550 nm) have been developed [42–49], and dispersion is dealt with using newly developed and high-performance dispersion-compensating fibers, either in modules or in cables (see Sect. 2.4.3.4), or using advanced coherent detection and digital signal processing techniques.



**Fig. 2.10** G.655 fibers, 1550 nm values. **a** Step profile with  $A_{\text{eff}} \sim 45 \mu\text{m}^2$  and slope  $\sim 0.050 \text{ ps}/(\text{nm}^2 \text{ km})$  and  $\lambda_{\text{cc}} < 1100 \text{ nm}$ ; **b** coaxial profile with  $A_{\text{eff}} \sim 105 \mu\text{m}^2$  and slope  $\sim 0.060 \text{ ps}/(\text{nm}^2 \text{ km})$  and  $\lambda_{\text{cc}} \sim 1375 \text{ nm}$  [37]; and **c** quadruple-clad profile  $A_{\text{eff}} \sim 50 \mu\text{m}^2$  and slope  $\sim 0.010 \text{ ps}/(\text{nm}^2 \text{ km})$  and  $\lambda_{\text{cc}} \sim 1395 \text{ nm}$  [39]; all compared to G.652 step profile with  $A_{\text{eff}} \sim 80 \mu\text{m}^2$  and slope  $\sim 0.058 \text{ ps}/(\text{nm}^2 \text{ km})$  and  $\lambda_{\text{cc}} \sim 1180 \text{ nm}$ ; and mode shapes



Complicated index profiles are not needed and simple step-index profiles with small index difference (around  $4 \times 10^{-3}$ ) and a large diameter (around  $12 \mu\text{m}$ ) can be used, contrary to NZDSFs. The drawback of this option, however, is that smaller fractions of the modes propagate in the cladding, yielding larger chromatic dispersion ( $\sim 20 \text{ ps}/(\text{nm km})$ ) at 1550 nm and longer  $\lambda_{\text{cc}}$  compared to those of standard G.652 step-index fibers. These fibers are called cutoff-shifted and are described in the ITU-T recommendation G.654 that specifies  $\lambda_{\text{cc}} < 1530 \text{ nm}$ .

To limit this  $\lambda_{\text{cc}}$  increase without jeopardizing the bending and microbending performances, a slightly depressed cladding can be added next to the step core. In this way,  $A_{\text{eff}}$  around  $105 \mu\text{m}^2$  at 1550 nm was demonstrated in the beginning of the previous decade [42–44] and more recently  $A_{\text{eff}}$  of  $134 \mu\text{m}^2$  [47]. An alternative to these depressed-cladding structures has been presented [45]. It consists in using

a trench in the cladding. As will be seen in the next section, the trench can be used to reduce the bending sensitivity of fibers while keeping the same MFD (or  $A_{\text{eff}}$ ) and the same  $\lambda_{\text{cc}}$  as those of G.652 step-index fibers. Here, the trench is used to enlarge  $A_{\text{eff}}$  and to control  $\lambda_{\text{cc}}$  while slightly improving bending and microbending performance compared to those of G.652 step-index fibers. With such a profile,  $A_{\text{eff}}$  of around  $155 \mu\text{m}^2$  at 1550 nm has recently been demonstrated [49].

### 2.4.3.3 Bend-optimized Fibers

As mentioned in Sect. 2.4.2.3, the reduction of bending losses is mandatory for FTTx networks. For a given bend radius, bending losses are proportional to the power fraction of the mode propagating after the radiation caustic. As explained in [50], the radiation caustic is the radius for which the effective index of the mode (see Sect. 2.2.2) intersects the index of the cladding of a tilted index profile representing the bent fiber.

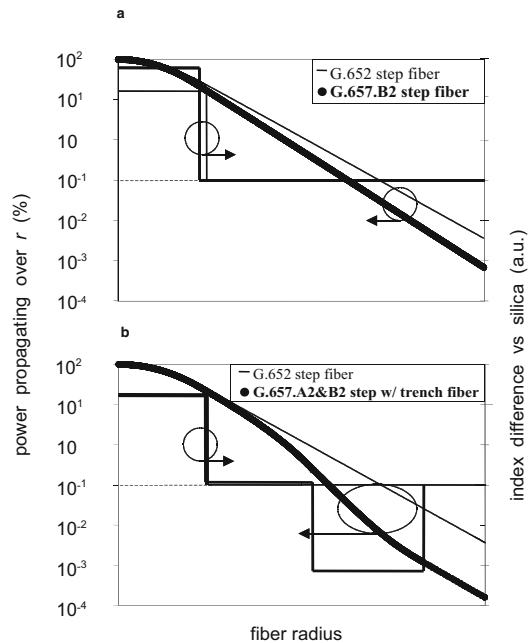
One way to reduce the bending sensitivity is to decrease this power fraction without changing the shape of the power profile. For step-index profiles, this means to use a higher index difference and/or a larger diameter than those of G.652 fibers. This results in smaller MFDs and/or larger  $\lambda_{\text{cc}}$ , which might be a problem when splicing to G.652 fibers. This is illustrated in Fig. 2.11a, which shows a step-index G.657.B2 fiber exhibiting a small MFD of  $8.0 \mu\text{m}$  at 1310 nm, compared to typical  $9.1 \mu\text{m}$  for SSMFs. Also, the bend loss levels remain significantly high when applying incidental kinks with radii of the order of 1 mm to 10 mm.

The alternative and much more efficient way to reduce the bending sensitivity is to change the shape of the power profile for a given set of MFD and  $\lambda_{\text{cc}}$ . For this purpose, new index profile types have to be used. The common feature of these profiles is a trench (either made with solid down-doped silica or with random voids or holes) that is added in the cladding close to the core [51–55]. The trench confines the tail of the mode without modifying its intrinsic nature, as illustrated in Fig. 2.11b. MFD,  $\lambda_{\text{cc}}$ , and chromatic dispersion characteristics are kept unchanged. As a consequence, bend loss can be significantly reduced by a factor of  $\sim 100$  compared to SSMFs, while ensuring full compliance with G.652 attributes.

### 2.4.3.4 Dispersion-compensating Fibers

The demonstration that fibers can exhibit very negative dispersion at 1550 nm was soon recognized in the development of optical fibers [56]. Its application to compensate the dispersion accumulated over already installed SSMFs started in the early 1990s [57, 58] and allowed upgrades of existing infrastructure to 10 Gbit/s. Currently, there are two different kinds of dispersion-compensating fibers (DCFs), whether the fiber is put inside a module at the amplifier location or into a cable as part of the transmission link. Because of the increase in data rates, compensating dispersion for all fiber types (SSMF or NZDSF) has become mandatory.

**Fig. 2.11 a** G.657.B2 fiber: step profile with MFD  $\sim 8.0 \mu\text{m}$  at 1310 nm and  $\lambda_{\text{cc}} < 1260 \text{ nm}$ ; **b** G.657.A2 and G.657.B2 fiber: step with trench profile with MFD  $\sim 8.9 \mu\text{m}$  at 1310 nm and  $\lambda_{\text{cc}} \sim 1210 \text{ nm}$  [8], both compared to G.652 step profile with MFD  $\sim 9.0 \mu\text{m}$  at 1310 nm and  $\lambda_{\text{cc}} \sim 1180 \text{ nm}$ , power shape also shown



DCF design is similar to NZDSF design (a triple-clad index profile is most commonly used) only more extreme: the fraction of the mode that propagates in the cladding becomes so large in order to get very large waveguide dispersion and negative chromatic dispersion, that the mode is only weakly guided. This is achieved with cores with very high index differences ( $> 15 \times 10^{-3}$ ) and small diameters ( $< 5 \mu\text{m}$ ). As a result, DCFs suffer from small  $A_{\text{eff}}$  ( $< 30 \mu\text{m}^2$  at 1550 nm), high loss ( $> 0.25 \text{ dB/km}$  at 1550 nm), and high bending sensitivities. The characteristics of DCFs are also more sensitive to small core index variations and to core ovalities than SSMFs or NZDSFs. Fiber manufacturing has to be done extremely carefully to tightly control longitudinal and radial core homogeneities and thus chromatic dispersion and PMD of the DCF [59].

When used in modules that are not part of the transmission distance, the extra loss introduced by DCFs depends on fiber loss and also on length. A commonly used figure of merit (FOM) for such DCFs is the ratio of the absolute value of chromatic dispersion to fiber loss, measured in  $\text{ps}/(\text{nm dB})$ . Considerable work has been performed to improve this parameter, and DCFs with values ranging from  $200 \text{ ps}/(\text{nm dB})$  to more than  $300 \text{ ps}/(\text{nm dB})$  for chromatic dispersions between  $-100 \text{ ps}/(\text{nm km})$  and  $-200 \text{ ps}/(\text{nm km})$  at 1550 nm are now available [45, 60–62].  $A_{\text{eff}} \sim 20 \mu\text{m}^2$  and  $\text{PMD} \sim 0.10 \text{ ps}/\sqrt{\text{km}}$  at 1550 nm are generally associated with such features. When used in cables that are part of the transmission distance, the situation is different [63]. Loss of spans consisting of transmission fibers and DCFs should be minimized and high FOM DCFs are no longer the optimum. Chromatic dispersion around  $-40 \text{ ps}/(\text{nm km})$  with loss around  $0.25 \text{ dB/km}$  at 1550 nm proves

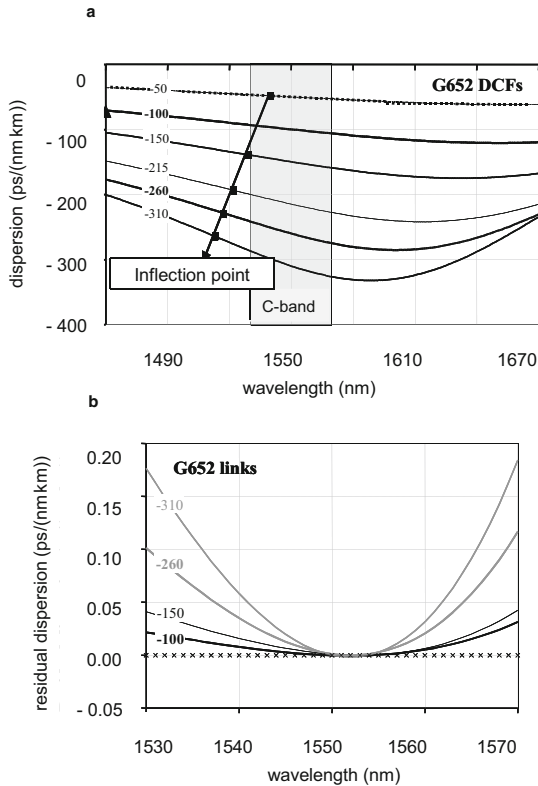


**Fig. 2.12** **a** G.652: chromatic dispersion spectra of DCFs for different dispersion values at 1550 nm detailed on each curve; **b** residual dispersion of the compensated links; indicated dispersion values given in ps/(nm km)

to be better suited for such applications [42–44]. In addition, larger  $A_{\text{eff}}$  ( $\sim 30 \mu\text{m}^2$ ) and smaller PMD ( $\sim 0.06 \text{ ps}/\sqrt{\text{km}}$ ) can be obtained.

To achieve optimum WDM performance, DCFs must not only compensate for chromatic dispersion at a given wavelength but also over the whole range of wavelengths used. This implies that both chromatic dispersion and dispersion slope should be negative. Simple step-index profiles are again insufficient for such a purpose. Adding a depressed cladding next to the core provides a better control of the wavelength dependence of the waveguide dispersion, and negative dispersion slope can be obtained [58]. A ring surrounding the depressed region can also be included to improve bending sensitivities. In the past few years, DCFs with negative chromatic dispersions and negative dispersion slopes that match those of all types of transmission fibers have been introduced [35, 60, 61].

Chromatic dispersion, however, does not vary linearly as a function of wavelength, and chromatic dispersion and dispersion slope are insufficient to describe how well a DCF matches a transmission fiber within a wide bandwidth ( $> 30 \text{ nm}$ ).

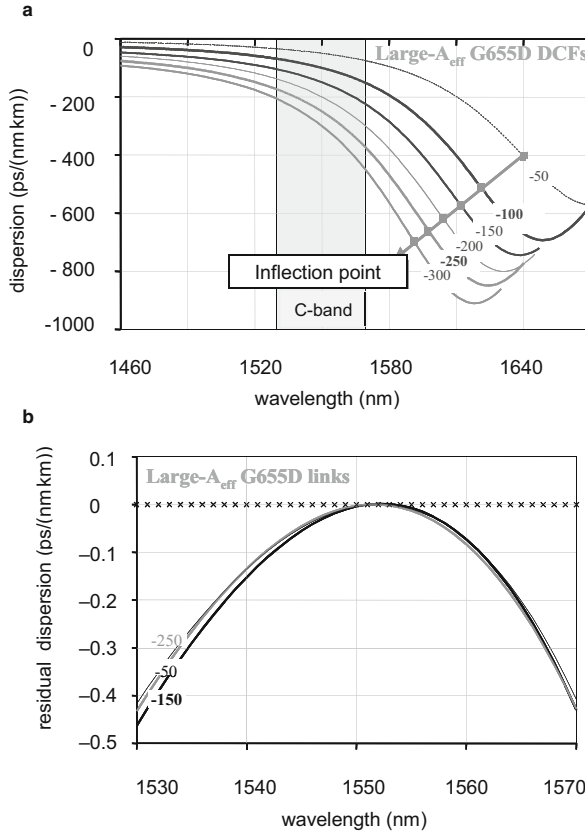


**Fig. 2.13** Large- $A_{\text{eff}}$  G.655.D: **a** chromatic dispersion spectra of DCFs for different dispersion values at 1550 nm detailed on each curve; **b** residual dispersion of the compensated link; indicated dispersion values given in ps/(nm km)

Variations of the dispersion slope have to be considered. These variations are responsible for the chromatic dispersion excursion, or residual dispersion, that remains in the waveband after the compensation. This residual dispersion has a direct impact on WDM performance and depends on the transmission fiber type that is used [64].

Figures 2.12 and 2.13 show the two extreme cases of DCFs adapted to compensate for G.652 fibers and for large- $A_{\text{eff}}$  G.655.D fibers (with chromatic dispersion of 4 ps/(nm km): dispersion slope of 0.080 ps/(nm<sup>2</sup> km) and  $A_{\text{eff}} \sim 70 \mu\text{m}^2$  at 1550 nm) [65]. The typical chromatic dispersion spectrum of a DCF can be described as follows [60]: first, the chromatic dispersion starts to decrease with wavelength and passes through an inflection point where the dispersion slope can be made approximately constant over a certain waveband; then it reaches its minimum (where the dispersion slope is null), and finally, it increases. What is noticeable is

that the inflection point of G.652 DCFs is inside, or below, the C-band and that it moves away from this band when the chromatic dispersion value at 1550 nm decreases (see Fig. 2.12a). On the contrary, the inflection point of large- $A_{\text{eff}}$  G.655.D DCFs is always above the C-band, which imposes high variations of the dispersion slope in this band, whatever the chromatic dispersion value might be at 1550 nm (see Fig. 2.13a). As a consequence, for G.652 DCFs the residual dispersion in the C-band is relatively small and it increases when the chromatic dispersion value at 1550 nm decreases (see Fig. 2.12b), whereas for large- $A_{\text{eff}}$  G.655.D DCFs the residual dispersion is intrinsically high and almost independent of the chromatic dispersion value at 1550 nm (see Fig. 2.13b). For G.655.E and G.656 DCFs, the situation is in-between these two cases: the residual dispersion is slightly larger than that of G.652 DCFs but the impact of the chromatic dispersion value at 1550 nm is smaller.

These considerations help to choose the appropriate DCF for a dedicated application. Note that within a given residual dispersion limit, DCFs with high negative chromatic dispersion are often preferable because they limit the impact of loss and nonlinearity [60, 62, 65], thereby improving the performance of optical networks [65, 66].

## 2.5 Optical Fiber Cables

We have discussed in the previous sections the different kinds of optical fibers for telecommunication. For this application, fibers will eventually be installed and operated in many different environments: they can be buried underground or undersea, strung aerially between poles, or run through intricate paths within buildings, and so on. Cabling is then the packaging of optical fibers that will protect them from anything that may damage them. The list is long and diverse: rodent attacks, lightning, more gradual degradation mechanisms like long-term exposure to moisture, heat and extreme temperatures, crush, and of course tensile strength when cables are installed. Cables also allow for easier handling and grouping of optical fibers.

There is a large variety of cables due to the differing environments and requirements they must fulfill. The simplest cable includes one fiber at its center and has a diameter of a few millimeters, while the most complex cables can include up to several hundreds of fibers, and their diameter can be as large as several centimeters. In this section, we will briefly review some cable basics, that is, the key elements of an optical cable and the different types of environments and associated cables. Interested readers can refer to some textbooks dedicated to cables [5, 67].

### 2.5.1 Basic Elements of a Cable

As stated above, cables can be very different to fit the diverse environments they encounter. However, their design always comes down to the same few basic elements.

There are four basic cable constructions: loose tube, micromodule, tight-buffered, and ribbon. Cables that include a large number of fibers are built up in a modular structure, starting from those basic elements. For example, a 96-fiber cable can be made from eight loose tube modules containing 12 fibers each.

A loose tube simply consists of a larger tube, containing several  $\sim 250\ \mu\text{m}$  coated optical fibers. Fiber length is slightly longer than that of the tube, so that the fiber can adjust itself within the tube, thus nearly eliminating microbending losses. The loose-tube construction is widely used for outdoor applications, but can also be found for indoor applications. Figure 2.14a shows an example of a cable based on a loose-tube construction.

The micromodule structure consists of several fibers, typically 12, which are put together and covered by a thin and flexible plastic layer. This structure allows one to build high-count fiber cables in a very compact and flexible way. They are also easy to handle within splice boxes.

Tight-buffered cables, as the name implies, only contain tight-buffered fibers, and are mainly used for indoor applications. A tight-buffered fiber consists of a  $250\ \mu\text{m}$  fiber with an additional layer of plastic extruded on top of it. The resulting element is typically  $900\ \mu\text{m}$  in diameter and can be easily terminated with connectors. This forms also the basic element of patchcords, which only include one or two additional protective layers. Figure 2.14b depicts a tight-buffered cable.

At last, ribbon is manufactured by aligning several fibers (from 4 to 24) side by side and binding them together using a UV-curable matrix. This structure is quite popular in the USA. Ribbons ensure that fibers are precisely located so that splicing can be automated easily with dedicated splicers. Mass splicing is seen as one of the key advantages of ribbons.

A key role of cables is to protect fibers from longitudinal stress, for example, when the cable is pulled during installation. A strength member, made out of metal or hard plastic like fiber glass reinforced plastic (FRP) and located at the center of the cable, is then used to isolate the fibers from stress and cable is built by stranding the fiber-containing tubes around the strength member. For further protection, one or more layers can be added. For smaller count and smaller size cables, glass-yarns or aramid-yarns protective layers insure a good tensile strength. Finally, crush resistance is accomplished by adding protective layers of metal or hard plastic material. Metal is also a good protection against rodents that can chew away cables.

Water protection is another key feature for cables. Water causes microcracking in the glass that can weaken the fiber significantly and eventually break it. Water protection is especially relevant for outdoor cables. The moisture can enter the cable in two ways: radially if the sheath is damaged during installation or longitudinally when moisture can enter through the unprotected ends of the cables. Several strategies have been deployed all along, mainly including hydrophobic gel-filling of tubes or using water-swelling tape.

Layers of metal conductors can also be included in fiber-optic cables when electrical power is needed. This is especially true for submarine applications, in order to supply power to the repeaters.

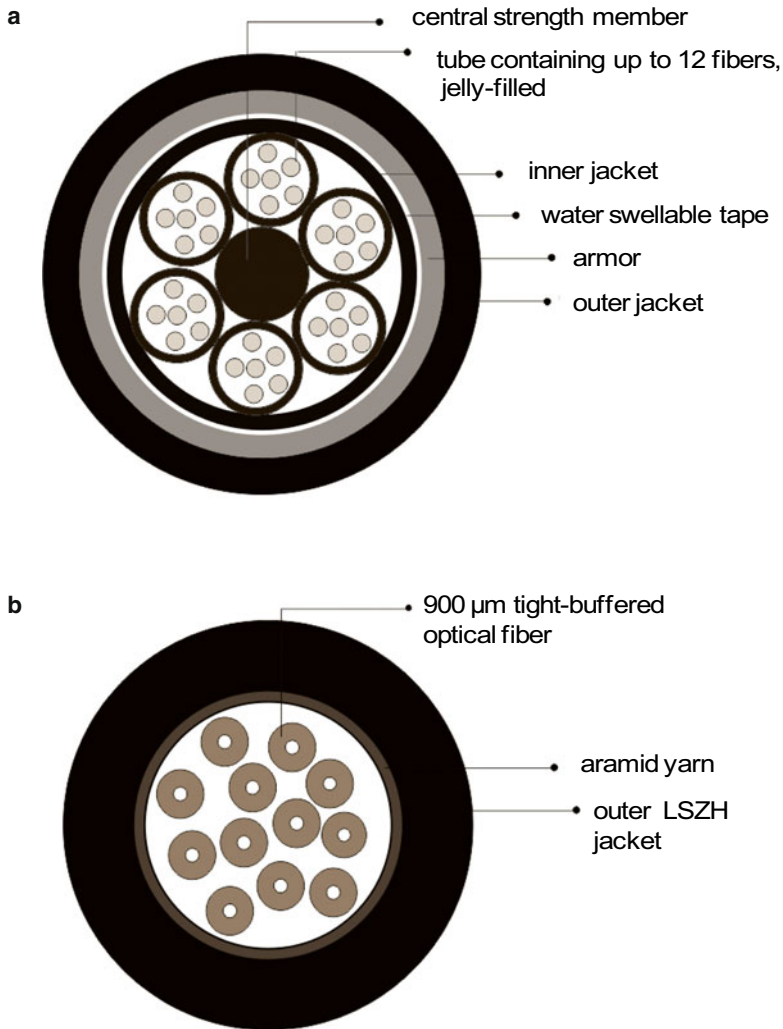


**Fig. 2.14** Schematic of cables: **a** shows a loose-tube construction consisting of  $6 \times 12$ -fiber tubes stranded around the central strength member, **b** shows a tight-buffered construction including 12 tight-buffered optical fibers

As described above, cables can include one or more of the basic structures containing the fibers, which, for large-count cables, are stranded around a strength member or loosely stranded in a bigger tube. Then, one or more layers are added to ensure protection against crush, water, rodents, etc., until the last outer jacket or sheath. Several materials can be used for outer jacketing: polyethylene, which is most widely used and which offers a good durability, and also Poly Vinyl Chloride (PVC), polypropylene, and others. For some applications, essentially indoor, special



fire-code requirements have to be fulfilled and specific classes of materials have to be used: low smoke zero halogen (LSZH) or halogen-free fire retardant (HFFR) that retard fire and avoid toxic fumes to be released.

### ***2.5.2 Cable Environment and Cable Types***

Cables are specially designed to withstand particular conditions in each environment. As is the case with fibers, cable specifications and characterization are standardized (CENELEC EN 187000 and IEC 60794). The range of cable characteristics is very broad and diverse, including tensile performance, kinking, cable crush, and also temperature cycling, water penetration, flame propagation, and so on.

It is customary to classify the cables between outdoor and indoor applications. For outdoor cables, there is a further subclassification mainly depending on their final implementation: outdoor direct-burial cables, outdoor ducted cables, outdoor aerial, and undersea cables.

Outdoor direct-burial cables usually contain a large number of SMFs. They are designed with very extensive waterproofing, strength members, and often armoring to protect against gnawing by all kinds of rodents. This is illustrated schematically in Fig. 2.14a.

Outdoor ducted cables are installed in plastic ducts buried underground. Very often, it is a large main duct that includes smaller subducts (called microducts) for progressive installation. Those cables are installed by pulling or blowing. Corresponding cables are usually lighter and smaller and they need to combine good flexibility, high tensile strength, and a good friction factor.

Outdoor aerial cables have been developed to benefit from the existing pole infrastructure, thus avoiding the need to dig roads to bury cables in new ducts. They can be either directly suspended between the poles or lashed to a messenger wire that runs between poles and takes the stress outside the fiber cable. Aerial cables have to sustain environmental extremes (ice and wind loadings, solar radiation, lightning, ...) and need heavy strength membering, both central and radial. When lightning is a hazard, they do not include any metal. There is a special subset of aerial cables, called optical ground wire (OPGW), which is included in the earth wire of a high-voltage electrical system.

The most sophisticated cables are the transoceanic undersea ones that run thousands of kilometers between continents. Long-distance cables have to protect fibers from strain during cable laying and repair, from pressure in the ocean depth, and from water. They do not include such a large number of fibers, from 12 to 24 generally, but include a large number of protective layers of all kinds and as mentioned earlier, a conductor to carry power for repeaters that lie undersea. Cables that are intended to operate over short distances are essentially rugged and waterproof versions of direct burial cables. Those cables can either be buried in the sea floor or just laid, but with extra armoring to account for any damages due to shipping or fishing activities.

There is a large variety of indoor cables as well, and with the advent of FTTH, much activity has been devoted to develop optimized cable structures over the past few years. One of the main requirements for indoor cables is flexibility and compactness. Indoor cables usually include a smaller number of fibers and there is less need for waterproofing and armoring, but some protection from rats is still needed. In addition, cable materials have to be chosen following fire-code requirements. A typical indoor cable structure would then consist of a number of 900  $\mu\text{m}$  tight-buffered elements wrapped either around a central strength member or within a yarn-based layer surrounded by an outer jacket made out of HFFR or LSZH material, as depicted in Fig. 2.14b.

## 2.6 New Developments

Research in the area of silica-based optical fiber is very active. In this section, we give a brief overview of innovative research works on microstructured optical fibers (MOF) (Sect. 2.6.1), Bragg fibers (Sect. 2.6.2), fibers mixing glass and semiconductors (Sect. 2.6.3) and multicore and slightly multimode fibers (Sect. 2.6.4).

### 2.6.1 *Microstructured Optical Fibers*

A MOF contains an arrangement of air holes that run along its length. Light is guided using modified TIR or the photonic-band-gap (PBG) effect. In TIR-MOFs, holes act to lower the index in the cladding so that light is confined in the solid core that has a higher index, similarly to conventional solid fibers [68]. In PBG-MOFs, the holes that define the cladding are arranged on a periodic lattice and a hole that breaks the periodicity of the cladding acts as the core. As a result, certain ranges of propagation constants are forbidden in the cladding and allowed in the core [69]. These fibers are usually made by stacking an array of hollow silica rods to form the preform, which is then drawn into a fiber. Figure 2.15 shows a schematic of both fiber types.

TIR-MOFs exhibit novel optical properties. Broadband single-mode guidance was the first one to be experimentally demonstrated in 1997 [70]. At long wavelengths, TIR-MOFs act as solid fibers, i.e., higher order modes are cut off because they are less confined in the solid core and their propagation constants decrease and become equal to that of the cladding (see Sect. 2.4.1). At short wavelengths, unlike solid fibers, higher order modes are cut off because they are more confined in the silica regions and avoid the holes, thus raising the effective propagation constant of the cladding that becomes equal to theirs. Eventually, the single-mode range is extended. These “endlessly single-mode” TIR-MOFs have been used to transmit WDM signals in the 1000 nm region [71]. Such transmissions have also been possi-

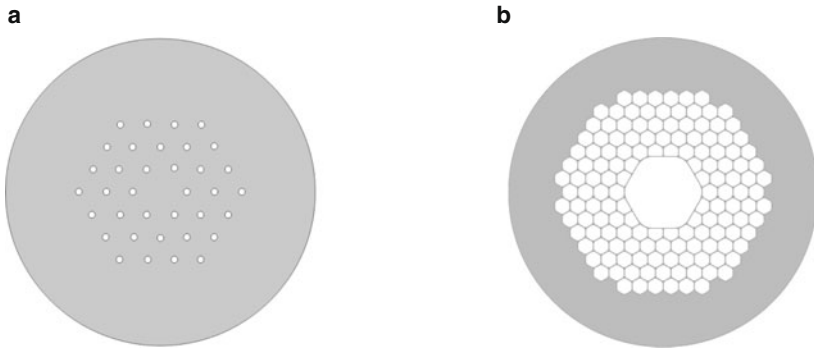


**Fig. 2.15** Schematic of microstructured optical fiber, **a**: TIR-MOF, **b**: PGF-MOF

ble thanks to impressive work on loss reduction [72, 73]: from a few 100 dB/km in the late 1990s down to 0.18 dB/km in 2007 [73].

TIR-MOFs are also attractive because of the high index difference between silica and air that cannot be achieved with solid fibers. This specific feature can be used to design bend-optimized fibers (also called hole-assisted fibers) for which air holes in the cladding act as a trench that confines light at bends (see Sect. 2.4.3.3). It also offers more degrees of freedom when tailoring the waveguide dispersion that can become very negative (similarly to solid DCFs but in a more extreme way) with values below  $-1000$  ps/(nm km) at 1550 nm [74] or very positive, thus shifting  $\lambda_0$  below 1000 nm [75]. Unlike solid fibers, anomalous dispersion arises because a large fraction of the mode propagates in the holes. This latter feature is used to extend generations of supercontinua or soliton techniques to shorter wavelengths [76, 77]. Tailoring the mode area to reach extremely small or large  $A_{\text{eff}}$  (ranging from a few  $\mu\text{m}^2$  to more than  $500 \mu\text{m}^2$ ) is also possible. This leads to highly nonlinear fibers [78, 79] used for all-optical signal processing, Raman amplification and broadband sources, or to large mode area fibers [80, 81] used for high-power applications (delivery, amplifier, or laser).

PBG-MOFs offer even more unusual features because light propagates in a “hollow core.” This opens the door to ultra low nonlinearity and thus to high-power deliveries [82], and also to new spectral regions both in terms of dispersion and loss characteristics [83]. Concerning loss, some mechanisms are common to solid fibers (see Sect. 2.2.4), but roughness of the hole surfaces also causes scattering loss. This can be of importance for some TIR-MOFs for which modes overlap with the holes; however, it is a fundamental limit for PBG-MOFs for which 1.2 dB/km obtained at 1620 nm [84] might be close to the ultimate lower limit [85]. Finally, filling the core with gas leads to sustainable light interactions with gas over long lengths and enables applications such as gas sensing [86].

All these new features make possible a wide array of applications. Practical realizations, however, remain critical. Issues such as loss, bending sensitivities, polarization effects, splices, and mechanical strength are still subject to intense research.

### 2.6.2 Bragg Fibers

There are three types of PBG fibers: hollow-core PBG-MOFs, described in the previous section, where the cladding is composed of two-dimensional arrays of holes; solid versions of these structures, where the core is made of doped or non-doped silica and the cladding holes are replaced with high-index rods [87–89]; and one-dimensional PBG fibers, where a low-index core is surrounded by a cladding made of cylindrical layers with alternating high and low indices, also called Bragg fibers [90]. Bragg fibers were first demonstrated using all-dielectric structures (for CO<sub>2</sub> laser transmission) in 1999 [91], closely followed by all-silica [92] and air-silica [93] realizations.

All-silica Bragg fibers are of particular interest because they offer the unique properties of PBG fibers with the advantage of solid cores that can be used to write Bragg gratings or can be doped to realize fiber amplifiers or lasers. In addition, Bragg fibers have one-dimensional structures that allow for low index differences [89] that can easily be made with standard CVD techniques [92, 94, 95] (see Sect. 2.2.3), thus avoiding the inherent drawbacks of holey structures.

Such Bragg fibers can be designed to exhibit large mode areas together with good bending sensitivities, making them suitable for high-power applications [95].

Many theoretical studies have also investigated the potential of Bragg fibers for chromatic dispersion tailoring, but most examples concern air-core structures that are difficult to realize [96, 97]. Few examples of all-silica structures have been reported [98–100], among which was one experimental demonstration of a large- $A_{\text{eff}}$  Bragg fiber with chromatic dispersion below  $-1000$  ps/(nm km) at 1480 nm, obtained at the expense of high loss ( $> 100$  dB/km) [100].

Bragg fibers were first proposed in the 1970s [90], but it is only recently that they have received more attention. Experimental demonstrations and applications are in their early stages and a lot of research work needs to be conducted yet to exploit the full potential of such fibers.

### 2.6.3 Fibers Mixing Glass and Semiconductors

Modern telecommunications do not only use 100s of millions of optical fiber km to transmit light but also 100s of millions of semiconductor devices to generate, control, and detect the light. Nowadays, these two technologies are heterogeneously interfaced using costly and complex optical–electronic conversion techniques.

Recently, efforts have been made to combine these two technologies [101–104], the ultimate goal being the realization of fiber-integrated optical–electronic devices that bring together capabilities to manipulate photons and electrons. Silica glass and crystalline semiconductors, however, have different properties at high temperature and cannot be drawn together into a fiber. To overcome this difficulty, research has focused on MOFs (see Sect. 2.6.1) that offer the possibility to embed semiconduc-

tors into their capillary holes. Traditional chemical vapor deposition methods for the formation of semiconductors cannot efficiently be applied to such a confined space; as a consequence, new techniques such as high-pressure microfluidic chemical deposition have been developed [103].

With these processes, realizations of hybrid devices have been reported. In-fiber silicon wires have proved to function as field-effect transistors and light waveguides [103], and all-optical modulation of light has been demonstrated in amorphous silicon-filled MOFs [104].

This new field of research exploits the design capabilities of both technologies but fundamental materials science has still to be developed to fully realize its promises.

### ***2.6.4 Multicore and Multimode Fibers***

The concept of space division multiplexing, introduced more than three decades ago, is currently the subject of intense research in order to increase by more than tenfold the present 10 Tbit/s capacity of single-core, single-mode transmission systems and thus avoid the anticipated capacity crunch [105, 106]. Recent studies have exploited multiple-core or multiple-mode techniques that can be used on top of conventional wavelength- and polarization-division multiplexing operations.

Studies on multicore fibers [107, 108] have recently focused on a 7-core configuration [109–115]. One important issue in such structures is the crosstalk experienced by the different cores [109]. Heterogeneous or quasi-homogeneous core structures are well-known techniques to reduce the crosstalk [110]. Another promising technique consists of reducing the expansion of the fundamental modes of the different cores in the cladding. The use of trench assistance, which allows for better light confinement, has very recently been reported. This has enabled us to go from  $\sim -20$  dB to  $\sim -35$  dB crosstalk values after  $\sim 100$  km at 1550 nm for  $A_{\text{eff}}$  of  $\sim 80 \mu\text{m}^2$  and standard cutoff and bending behavior (135–150  $\mu\text{m}$  glass diameters) [111, 112]. Another important issue is how to enlarge  $A_{\text{eff}}$  above 100  $\mu\text{m}^2$  at 1550 nm without degrading the crosstalk and the attenuation levels, especially those of the outer cores that suffer from high microbending sensitivities and for which standard values below 0.19 dB/km are difficult to achieve. One straightforward way to solve this issue is to increase the glass diameter to values larger than the standard 125  $\mu\text{m}$  [113]. Despite these challenges, 97 channels/core at 160 Gbit/s over 16.8 km of a 7-core fiber (150  $\mu\text{m}$  glass diameter) [114] and 80 channels/core at 100 Gbit/s over 76.8 km of a 7-core fiber (186.5  $\mu\text{m}$  glass diameter) [115] have recently been transmitted.

Mode division multiplexing [116] has recently been reformulated to increase the bandwidths of standard multimode fibers using multiple-input multiple-output (MIMO) processing [117]: different modes or groups of modes carrying independent signals are excited and detected after transmission [118–120]. This way, transmission of two signals at 4 Gbit/s over 5 km of a standard 50  $\mu\text{m}$  graded-index multimode fiber [121] and of three modes at 25 Gbit/s over 10 km of a few-mode

fiber [122] has recently been demonstrated. One important issue in such transmissions is the mode-coupling phenomenon. Elaborate MIMO techniques do help to mitigate this deleterious effect. Another approach consists of reducing it by design, i.e., by reducing the number of modes in the fiber and by ensuring that their propagation constants are as different as possible [116]. A theoretical study of the transmission performance of such few-mode fiber has recently been presented [123], and first experimental demonstrations proving the concept (two modes at 10 Gbit/s at 1080 nm over 10 km [124], two modes at 50 Gbit/s at 1550 nm over 4.5 km [125], and two modes at 100 Gbit/s at 1550 nm over 40 km [126]) have been reported.

As a final note, although this field of research is currently very active, important challenges are still ahead before space division multiplexing can be used in long-haul transmissions, namely connectivity (multiplexing/demultiplexing devices, splices, and connectors) and amplification.

## References

1. C.K. Kao, G.A. Hockham, Dielectric fiber surface waveguides for optical frequencies. *Proc. IEE* **113**, 1151–1158 (1966)
2. D. Marcuse, *Theory of Dielectric Optical Waveguides*, 2nd edn. (Academic Press, San Diego, 1991)
3. A.W. Snyder, J.D. Love, *Optical Waveguide Theory* (Chapman and Hall, New York, 1983)
4. D. Gloge, Weakly guiding fibers. *Appl. Opt.* **10**, 2252–2258 (1971)
5. H. Murata, *Handbook of Optical Fibers and Cables*, 2nd edn. (Marcel Dekker, New York, 1996)
6. P.C. Schultz, Optical absorption of the transition elements in vitreous silica. *J. Am. Ceram. Soc.* **57**, 309–313 (1974)
7. O. Humbach, H. Fabian, U. Grzesik, U. Haken, W. Heitmann, Analysis of OH absorption bands in synthetic silica. *J. Non-Cryst. Solids* **203**, 19–26 (1996)
8. K. Tsujikawa, K. Tajima, K. Shiraki, I. Sankawa, Method for predicting Rayleigh scattering loss of silica-based optical fibers. *J. Lightw. Technol.* **25**, 2122–2128 (2007)
9. M.E. Lines, W.A. Reed, D.J. Di Giovanni, J.R. Hamblin, Explanation of anomalous loss in high delta singlemode fibres. *Electron. Lett.* **35**, 1009–1010 (1999)
10. P. Guenot, P. Nouchi, B. Poumellec, Influence of drawing temperature on light scattering properties of single-mode fibers, *Opt. Fiber Commun. Conf. (OFC'99)*, Techn. Digest (San Diego, CA, USA, 1999), paper ThG2, pp. 84–86
11. K. Nagayama, M. Kakui, M. Matsui, I. Saitoh, Y. Chigusa, Ultra-low-loss (0.1484 dB/km) pure silica core fibre and extension of transmission distance. *Electron. Lett.* **38**, 1168–1169 (2002)
12. J.W. Fleming, Dispersion in GeO<sub>2</sub>-SiO<sub>2</sub> glasses. *Appl. Opt.* **23**, 4486–4493 (1984)
13. CEI/IEC Recommendation 60793–1–41 (2003)
14. TIA Recommendation TIA-455–220-A (2003)
15. ITU-T Recommendation G.651.1 (2007)
16. D. Molin, P. Matthijsse, G. Kuyt, P. Sillard, Reduced bend sensitivity of multimode fibers in FttX applications, *Proc. 56th Intern. Wire & Cable Symposium (IWCS'07)*, Lake Buena Vista, Florida, USA, 10–1 (2007)
17. D. Gloge, A.J. Marcattili, Multimode theory of graded-core fibers. *Bell Syst. Tech. J.* **52**, 1563–1579 (1973)
18. R. Olshansky, D.B. Keck, Pulse broadening in graded-index multimode fibers. *Appl. Opt.* **15**, 483–491 (1976)

19. M. Horiguchi, Y. Ohmori, H. Takata, Profile dispersion characteristics in high-bandwidth graded-index multimode fibers. *Appl. Opt.* **19**, 3159–3167 (1980)
20. D. Molin, M. Bigot-Astruc, K. de Jongh, P. Sillard, Trench-assisted bend-resistant OM4 multi-mode fibers, *Proc. 36th Europ. Conf. Opt. Commun.* (ECOC'10), Torino, Italy (2010), paper P1.11
21. M.-J. Li, P. Tandon, D.C. Bookbinder, S.R. Bickham, K.A. Wilbert, J.S. Abbott, D.A. Nolan, Designs of bend-insensitive multimode fibers, *Opt. Fiber Commun. Conf. and Nat. Fiber Opt. Eng. Conf.* (OFC/NFOEC'11), Techn. Digest (Los Angeles, CA, USA, 2011), paper JThA3
22. T. Ishigure, E. Nihei, Y. Koiye, Graded-index polymer optical fiber for high speed data communication. *Appl. Opt.* **33**, 4261–4266 (1994)
23. Y. Koiike, T. Ishigure, High-bandwidth plastic optical fiber for fiber to the display. *J. Lightw. Technol.* **24**, 4541–4553 (2006)
24. N. Yoshihara, Y. Watanabe, T. Onishi, T. Tsukamoto, Transmission trials of perfluorinated GI-POF, *Opt. Fiber Commun. Conf.* (OFC'2000), Techn. Digest (Baltimore, MD, USA, 2000), paper ThR2–1
25. W.R. White, L.L. Blyler, Jr., R. Ratnagiri, M. Park, Manufacture of perfluorinated plastic optical fibers, *Opt. Fiber Commun. Conf.* (OFC'04), Techn. Digest (Los Angeles, CA, USA, 2004), paper ThC3
26. ISO/IEC Recommendation 11801 (2002)
27. P. Pepeljugoski, M.J. Hackert, J.S. Abbott, S.E. Swanson, S.E. Golowich, A.J. Ritger, P. Kolesar, Y.C. Chen, P. Pleunis, Development of system specification for laser-optimized 50  $\mu\text{m}$  multimode fiber for multigigabit short-wavelength LANs. *J. Lightw. Technol.* **21**, 1256–1275 (2003)
28. G. Charlet, M. Salsi, H. Mardoyan, P. Tran, J. Renaudier, S. Bigo, M. Astruc, P. Sillard, L. Provost, F. C  rou, Transmission of 81 channels at 40 Gbit/s over a transpacific-distance, erbium-only link, using PDM-BPSK modulation, coherent detection, and a new large effective area fibre, *Proc. 34th Europ. Conf. Opt. Commun.* (ECOC'08), Brussels, Belgium (2008), paper Th3.E.3
29. G.J. Forschini, C.D. Poole, Statistical theory of polarization dispersion in single mode fibers. *J. Lightw. Technol.* **9**, 1439–1456 (1991)
30. K. Petermann, Constraints for fundamental-mode spot size for broadband dispersion-compensated single-mode fibres. *Electron. Lett.* **19**, 712–714 (1983)
31. G.P. Agrawal, *Nonlinear Fiber Optics*, 3rd edn. (Academic Press, San Diego, 2001)
32. P. Sillard, P. Nouchi, J.-C. Antona, S. Bigo, Modeling the non-linear index of optical fibers, *Opt. Fiber Commun. Conf.* (OFC'05), Techn. Digest (Anaheim, CA, USA, 2005), paper OFH4
33. V.A. Bhagavatula, M.S. Spatz, D.E. Quinn, Uniform waveguide dispersion segmented-core designs for dispersion-shifted single mode fibers, *9th Opt. Fiber Commun. Conf.* (OFC'84), Techn. Digest (New Orleans, LA, USA, 1984), paper MG2
34. P. Nouchi, Maximum effective area for non-zero dispersion-shifted fiber, *Opt. Fiber Commun. Conf.* (OFC'98), Techn. Digest (San Jose, CA, USA, 1998), paper ThK3
35. P. Nouchi, L.-A. de Montmorillon, P. Sillard, New transmission fibers for future networks, *Proc. 30th Europ. Conf. Opt. Commun.* (ECOC'04), Stockholm, Sweden (2004), paper Th3.3.1
36. S. Matsuo, K. Aikawa, N. Shimida, S. Tanigawa, K. Himeno, K. Harada, Non-linearity suppressed fiber link of large-effective area medium dispersion fiber and dispersion compensation, *Proc. 28th Europ. Conf. Opt. Commun.* (ECOC'02), Copenhagen, Denmark (2002), paper 3.2.4
37. L. Expert, L.-A. de Montmorillon, P. Gu  not, M. Gorlier, L. Fleury, D. Molin, P. Sillard, V. Salles, P. Nouchi, Low nonlinearity medium-dispersion fiber-based link, *Proc. 29th Europ. Conf. Opt. Commun.* (ECOC'03), Rimini, Italy (2003), paper Th2.3.6
38. N. Kumano, K. Mukasa, S. Matsushita, T. Yagi, Zero-dispersion slope NZDSF with ultra wide bandwidth over 300 nm, *Proc. 28th Europ. Conf. Opt. Commun.* (ECOC'02), Copenhagen, Denmark (2002), paper PD1.4

39. D. Molin, L. Fleury, M. Gorlier, F. Beaumont, L. Expert, L.-A. de Montmorillon, P. Sillard, P. Nouchi, Ultra-low slope medium-dispersion fiber for wide-band terrestrial transmissions, *Opt. Fiber Commun. Conf. (OFC'03)*, Techn. Digest (Atlanta, GA, USA, 2003), paper TuB2
40. L.A. de Montmorillon, P. Sillard, M. Astruc-Bigot, B. Dany, P. Nouchi, B. Lavigne, E. Balmeffre, J.-C. Antona, O. Leclerc, Transmission fiber optimized for metro optical network, *Opt. Fiber Commun. Conf. (OFC'05)*, Techn. Digest (Anaheim, CA, USA, 2005), paper OFH1
41. H. Yokota, H. Kanamori, Y. Ishiguro, G. Tanaka, S. Tanaka, H. Takada, M. Watanabe, S. Suzuki, K. Yano, M. Hoshikawa, H. Shimba, Ultra-low-loss pure-silica-core single-mode fiber and transmission experiment, *11th Opt. Fiber Commun. Conf. (OFC'86)*, Techn. Digest (Atlanta, GA, USA, 1986), paper PD3-1
42. M. Tsukitani, T. Kato, E. Yanada, M. Hirano, M. Nakamura, Y. Ohga, M. Onishi, E. Sasoaka, Y. Makio, M. Nishimura, Low-loss dispersion-flattened hybrid transmission lines consisting of low-nonlinearity pure silica core fibers and dispersion compensating fibers. *Electron. Lett.* **36**, 64-66 (2000)
43. W.D. Cornwell, O.E. Edwards, N.H. Taylor, D.S. Lotay, S.A. Smith, S. Hamidi, Comparison of  $64 \times 10$  Gbit/s NRZ and RZ transmission over 6,000 km using a dispersion-managed fiber solution, *Opt. Fiber Commun. Conf. (OFC/IOOC'02)*, Techn. Digest (Anaheim, CA, USA, 2002), paper WP4
44. S.N. Knudsen, B. Zhu, L.E. Nelson, M.O. Pederson, D.W. Peckham, S. Stultz, 420 Gbit/s ( $42 \times 10$  Gbit/s) WDM transmission over 4000 km of UltraWave fiber with 100 km dispersion-managed spans and distributed Raman amplification. *Electron. Lett.* **37**, 965-967 (2001)
45. M. Bigot-Astruc, F. Gooijer, N. Montaigne, P. Sillard, Trench-assisted profiles for large-effective-area single-mode fibers, *Proc. 34th Europ. Conf. Opt. Commun. (ECOC'08)*, Brussels, Belgium (2008), paper Mo.4.B.1
46. S. Chandrasekhar, Xiang Liu, B. Zhu, D.W. Peckham, Transmission of a 1.2 Tbps 24-carrier no-guard-interval coherent OFDM superchannel over 7200 km of ultra-large-area fiber, *Proc. 34th Europ. Conf. Opt. Commun. (ECOC'09)*, Vienna, Austria (2009), paper PD2.6
47. Y. Yamamoto, M. Hirano, K. Kuwahara, T. Sasaki, OSNR-enhancing pure-silica-core fiber with large effective area and low attenuation, *Opt. Fiber Commun. Conf. and Nat. Fiber Opt. Eng. Conf. (OFC/NFOEC'11)*, Techn. Digest (Los Angeles, CA, USA, 2011), paper OTuI2
48. J.D. Downie, J. Hurley, J. Cartledge, S. Ten, S. Bickham, S. Mishra, Xianming Zhu, A. Kobayakov,  $40 \times 112$  Gbps transmission over an unrepeated 365 km effective area-managed span comprised of ultra-low loss optical fiber, *Proc. 36th Europ. Conf. Opt. Commun. (ECOC'10)*, Torino, Italy (2010), paper We.7.C.5
49. M. Bigot-Astruc, L. Provost, G. Krabshuis, P. Dhenry, P. Sillard, 125  $\mu\text{m}$  glass diameter single-mode fiber with Aeff of 155  $\mu\text{m}^2$ , *Opt. Fiber Commun. Conf. and Nat. Fiber Opt. Eng. Conf. (OFC/NFOEC'11)*, Techn. Digest (Los Angeles, CA, USA, 2011), paper OTuJ2
50. D. Marcuse, Influence of curvature on the losses of doubly clad fibers. *Appl. Opt.* **21**, 4208-4213 (1982)
51. K. Himeno, S. Matsuo, N. Guan, A. Wada, Low-bending-loss single-mode fibers for fiber-to-the-home. *J. Lightw. Technol.* **23**, 3494-3499 (2005)
52. L.-A. de Montmorillon, P. Matthijsse, F. Gooijer, D. Molin, F. Achten, X. Meerssemann, C. Legrand, Next generation SMF with reduced bend sensitivity for FTTH networks, *Proc. 32nd Europ. Conf. Opt. Commun. (ECOC'06)*, Cannes, France (2006), paper Mo3.3.2
53. T. Hasegawa, T. Saitoh, D. Nishika, E. Sasoaka, T. Hosoya, Bend-insensitive singlemode holey fiber with SMF-compatibility for optical wiring applications, *Proc. 29th Europ. Conf. Opt. Commun. (ECOC'03)*, Rimini, Italy (2003), paper We2.7.3
54. Y. Tsuchida, K. Saitoh, M. Koshiha, Design and characterization of single-mode holey fibers with low bending losses. *Opt. Express* **13**, 4770-4779 (2005)
55. M.-J. Li, P. Tandon, D.C. Bookbinder, S.R. Bickham, M.A. McDermott, R.B. Desorcie, D.A. Nolan, J.J. Johnson, K.A. Lewis, J.J. Englebert, Ultra-low bending loss single-mode fiber for FTTH, *Opt. Fiber Commun. Conf. and Nat. Fiber Opt. Eng. Conf. (OFC/NFOEC'08)*, Techn. Digest (San Diego, CA, USA, 2008), paper PDP10



56. S. Sudo, H. Itoh, Efficient non-linear optical fibres and their applications. *Opt. Quantum Electron.* **22**, 187–212 (1990)
57. J.M. Dugan, A.J. Price, M. Ramadan, D.L. Wolf, E.F. Murphy, A.J. Antos, D.K. Smith, D.W. Hall, All optical, fiber-based 1550 nm dispersion compensation in a 10 Gbit/s, 150 km transmission experiment over 1310 nm optimized fiber, *17th Opt. Fiber Commun. Conf. (OFC'92)* Techn. Digest (San Jose, CA, USA, 1992), paper PDP14
58. A.M. Vengsarkar, A.E. Miller, W.A. Reed, Highly efficient single-mode fiber for broadband dispersion compensation, *18th Opt. Fiber Commun. Conf. (OFC'93)* Techn. Digest (San Jose, CA, USA, 1993), paper PD13
59. P. Nouchi, H. Laklalech, P. Sansonetti, J. von Wirth, J. Ramos, F. Bruyère, C. Brehm, J.-Y. Boniort, B. Perrin, Low-PMD dispersion-compensating fibers, *Proc. 21st Europ. Conf. Opt. Commun. (ECOC'95)*, Brussels, Belgium (1995), paper TuP04
60. L. Grüner-Nielsen, M. Wandel, P. Kristensen, C. Jorgensen, L. Vilbrad Jorgensen, B. Edvold, B. Palsdottir, D. Jakobsen, Dispersion-compensating fibers. *J. Lightw. Technol.* **23**, 3566–3579 (2005)
61. M.J. Li, Recent progress in fiber dispersion compensators, *Proc. 27th Europ. Conf. Opt. Commun. (ECOC'01)*, Amsterdam, The Netherlands (2001), paper ThM1.1
62. T. Sasaki, K. Makihara, M. Hirano, T. Haruna, T. Kashiwada, S. Hagihara, M. Onishi, Novel dispersion compensating fiber with fluorine-doped cladding for simultaneous realization of high dispersion compensation efficiency and low attenuation, *Opt. Fiber Commun. Conf. (OFC'06)*, Techn. Digest (Anaheim, CA, USA, 2006), paper OThA2
63. K. Mukasa, Y. Akasaka, Y. Suzuki, T. Kamiya, Novel network fiber to manage dispersion at 1.55  $\mu\text{m}$  with combination of 1.3  $\mu\text{m}$  zero dispersion single-mode fiber, *Proc. 23rd Europ. Conf. Opt. Commun. (ECOC'97)*, Edinburgh, UK (1997), vol. 1, pp. 127–130
64. J.-C. Antona, P. Sillard, S. Bigo, Impact of imperfect wideband dispersion compensation on the performance of WDM transmission systems at 40 Gbps, *Proc. 32nd Europ. Conf. Opt. Commun. (ECOC'06)*, Cannes, France (2006), paper Th1.6.4
65. J.-C. Antona, P. Sillard, Relationship between the achievable distance of WDM transmission systems and criterion of quality for DCM, *Opt. Fiber Commun. Conf. (OFC'06)*, Techn. Digest (Anaheim, CA, USA, 2006), paper OWJ2
66. P. Sillard, J.-C. Antona, S. Bigo, Optimized chromatic dispersion of DCMs in WDM transmission systems at 40 Gbps, *Opt. Fiber Commun. Conf. and Nat. Fiber Opt. Eng. Conf. (OFC/NFOEC'08)*, Techn. Digest (San Diego, CA, USA, 2008), paper JWA13
67. B. Elliott, M. Gilmore, *Fiber Optic Cabling*, 2nd edn. (Oxford, Great Britain, 2002)
68. J.C. Knight, T.A. Birks, P.St.J. Russell, D.M. Atkin, Pure silica single-mode fiber with hexagonal photonic crystal cladding, *Opt. Fiber Commun. Conf. (OFC'96)* Techn. Digest (San Jose, CA, USA, 1996), paper PD3
69. J.C. Knight, J. Broeng, T.A. Birks, P.St.J. Russell, Photonic band gap guidance in optical fibers. *Science* **282**, 1476–1478 (1998)
70. T.A. Birks, J.C. Knight, P.St.J. Russell, Endlessly single-mode photonic crystal fibers. *Opt. Lett.* **22**, 961–963 (1997)
71. K. Kurukawa, T. Yamamoto, K. Tajima, A. Aratake, K. Suzuki, T. Kurashima, High capacity WDM transmission in 1.0  $\mu\text{m}$  band over low low PCF using supercontinuum source, *Opt. Fiber Commun. Conf. and Nat. Fiber Opt. Eng. Conf. (OFC/NFOEC'08)*, Techn. Digest (San Diego, CA, USA, 2008), paper OMH5
72. L. Farr, J.C. Knight, B.J. Mangan, P.J. Roberts, Low loss photonic crystal fibre, *Proc. 28th Europ. Conf. Opt. Commun. (ECOC'02)*, Copenhagen, Denmark (2002), paper PD1.3
73. K. Tajima, Low loss PCF by reduction of hole surface imperfection, *Proc. 33rd Europ. Conf. Opt. Commun. (ECOC'07)*, Berlin, Germany (2007), paper PDP 2.1
74. B.J. Mangan, F. Couny, L. Farr, A. Langford, P.J. Roberts, D.P. Williams, M. Banham, M.W. Mason, D.F. Murphy, E.A.M. Brown, H. Sabert, T.A. Birks, J.C. Knight, P.St.J. Russell, Slope-matched dispersion-compensating photonic crystal fiber, *Conf. Lasers Electro-Opt. (CLEO'04)*, Baltimore, MD, USA (2004), paper CPDD3

75. P.J. Bennett, T.M. Monro, N.G.R. Broderick, D.J. Richardson, Towards practical holey fiber technology: fabrication, splicing and characterization, *Proc. 25th Europ. Conf. Opt. Commun.* (ECOC'99), Nice, France (1999), vol. I, pp. 20–23
76. K.J. Ranka, S.R. Windeler, A.J. Stentz, Visible continuum generation in air-silica microstructure optical fibers with anomalous dispersion at 800 nm. *Opt. Lett.* **25**, 25–27 (2000)
77. K. Kurukowa, K. Tajima, K. Nakajima, 10 GHz 0.5 ps pulse generation in 1000 nm band in PCF for high speed optical communication, *Proc. 32nd Europ. Conf. Opt. Commun.* (ECOC'06), Cannes, France (2006), paper PDP5
78. P. Petropoulos, T.M. Monro, W. Belardi, K. Furusawa, J.H. Lee, D.J. Richardson, 2R regenerative all-optical switch based on a highly nonlinear holey fiber. *Opt. Lett.* **26**, 1233–1235 (2001)
79. G. Mélin, L. Provost, A. Fleureau, S. Lempereur, X. Rejeaunier, A. Bourova, L. Gasca, Innovative design for highly non-linear microstructured fibers, *Proc. 30th Europ. Conf. Opt. Commun.* (ECOC'04), Stockholm, Sweden (2004), paper Th4.3.2
80. W.S. Wong, X. Peng, J.M. McLaughlin, L. Dong, Breaking the limit of maximum effective area for robust single-mode operation in optical fibers. *Opt. Lett.* **30**, 2855–2857 (2005)
81. J.M. Fini, Bend-resistant design of conventional and micro-structure fibers with very large mode area. *Opt. Express* **14**, 69–81 (2006)
82. J.D. Shephard, J.D.C. Jones, D.P. Hand, G. Bouwmans, J.C. Knight, P.St.J. Russell, B.J. Mangan, High energy nanosecond laser pulses delivered single-mode through hollow-core PBG fibers. *Opt. Express* **12**, 717–723 (2004)
83. C.J.S de Matos, J.R. Taylor, T.P. Hansen, K.P. Hansen, J. Broeng, All-fiber chirped pulse amplification using highly-dispersive air-core photonic bandgap fiber. *Opt. Express* **11**, 2832–2835 (2003)
84. P.J. Roberts, F. Couny, H. Sabert, B.J. Mangan, D.P. Williams, L. Farr, M.W. Mason, A. Tomlinson, T.A. Birks, J.C. Knight, P.St.J. Russell, Ultimate low loss of hollow-core photonic crystal fibres. *Opt. Express* **13**, 236–244 (2005)
85. T.A. Birks, Reducing losses in photonic crystal fibers, *Opt. Fiber Commun. Conf.* (OFC'06), Techn. Digest (Anaheim, CA, USA, 2006), paper OFC7
86. T. Ritari, J. Tuominen, H. Ludvigsen, J. Petersen, T. Sørensen, T.P. Hansen, H. R. Simonsen, Gas sensing using air-guiding photonic bandgap fibers. *Opt. Express* **12**, 4080–4087 (2004)
87. N.M. Litchinitser, S.C. Dunn, B. Usner, B.J. Eggleton, T.P. White, R.C. McPhedran, C. Martijn de Sterke, Resonances in microstructured optical waveguides. *Opt. Express* **11**, 1243–1251 (2003)
88. A. Agyros, T.A. Birks, S.G. Leon-Saval, C.M.B. Cordeiro, F. Luan, P.St.J. Russell, Photonic bandgap with an index step of one percent. *Opt. Express* **13**, 309–314 (2005)
89. G. Bouwmans, L. Bigot, Y. Quiquempois, F. Lopez, L. Provino, M. Douay, Fabrication and characterization of an all-solid 2D photonic bandgap fiber with a low-loss region (< 20 dB/km) around 1550 nm. *Opt. Express* **13**, 8452–8459 (2005)
90. P. Yeh, A. Yariv, E. Marom, Theory of Bragg fiber. *J. Opt. Soc. Am.* **68**, 1196–1201 (1978)
91. Y. Fink, D.J. Ripin, S. Fan, C. Chen, J.D. Joannopoulos, E.L. Thomas, Guiding optical light in air using an all-dielectric structure. *J. Lightw. Technol.* **17**, 2039–2041 (1999)
92. F. Brechet, P. Roy, J. Marcou, D. Pagnoux, Single-mode propagation into depressed core-index photonic bandgap fiber designed for zero-dispersion propagation at short wavelengths. *Electron. Lett.* **36**, 514–515 (2000)
93. G. Vienne, Y. Xu, C. Jakobsen, H.J. Deyerl, T.P. Hansen, B.H. Larsen, J. B. Jensen, T. Sørensen, M. Terrel, Y. Huang, M. R. K. Lee, N. A. Mortensen, H. Simonsen, A. Bjarklev, A. Yariv, First demonstration of air-silica Bragg fiber, *Opt. Fiber Commun. Conf.* (OFC'03), Techn. Digest (Atlanta, GA, USA, 2003), paper PDP25
94. C. Baskiotis, D. Molin, G. Bouwmans, F. Gooijer, P. Sillard, Y. Quiquempois, M. Douay, Bend-induced transformation of the transmission window of a large-mode-area Bragg fiber, *Proc. 34th Europ. Conf. Opt. Commun.* (ECOC'08), Brussels, Belgium (2008), paper Mo.4.B.2

95. D. Gapanov, P. Roy, S. Février, M.E. Likhachev, S.L. Semjonov, M.M. Bubnov, E.M. Dianov, M. Yu. Yashkov, V.F. Khopin, M.Yu. Salganskii, A.N. Guryanov, High-power photonic bandgap fiber laser, *Proc. 33rd Europ. Conf. Opt. Commun. (ECOC'07)*, Berlin, Germany (2007), paper PD 3.9
96. G. Ouyang, Y. Xu, A. Yariv, Theoretical study on dispersion compensation in air-core Bragg fibers. *Opt. Express* **10**, 889–908 (2002)
97. T. Engeness, M. Ibanescu, S. Johnson, O. Weisberg, M. Skorobogatiy, S. Jacobs, Y. Fink, Dispersion tailoring and compensation by modal interactions in OmniGuide fibers. *Opt. Express* **11**, 1175–1196 (2003)
98. J. Marcou, F. Brechet, Ph. Roy, Design of weakly guiding Bragg fibers for chromatic dispersion shifting towards short wavelengths. *J. Opt. A: Pure Appl. Opt.* **3**, 144–153 (2001)
99. N. Yi, Z. Lei, G. Chong, J. Shu, P. Jiangde, A novel design for all-solid silica Bragg fiber with zero-dispersion wavelength at 1550 nm. *Opt. Express* **12**, 4602–4607 (2004)
100. F. Gérôme, S. Février, A.D. Pryamikov, J.L. Auguste, R. Jamier, J.M. Blondy, M.E. Likhachev, M.M. Bubnov, S.L. Semjonov, E.M. Dianov, Highly dispersive large mode area photonic bandgap fiber. *Opt. Lett.* **32**, 1208–1210 (2007)
101. M. Fokine, L.E. Nilsson, A. Claesson, D. Berlemont, L. Kjellberg, L. Krummenacher, W. Margulis, Integrated fiber Mach–Zehnder interferometer for electro-optic switching. *Opt. Lett.* **27**, 1643–1645 (2002)
102. M. Bayindir, F. Sorin, A.F. Abouraddy, J. Viens, S.D. Hart, J.D. Joannopoulos, Y. Fink, Metal-insulator-semiconductor optoelectronic fibers. *Nature* **431**, 826–829 (2004)
103. P.J.A. Sazio, A. Amezcua-Correa, C.E. Finlayson, J.R. Hayes, T.J. Scheidemantel, N.F. Baril, B.R. Jackson, D.-J. Won, F. Zhang, E.R. Margine, V. Gopalan, V.H. Crespi, J.V. Badding, Microstructured optical fibers as high-pressure microfluidic reactors. *Science* **311**, 1583–1586 (2006)
104. D.J. Won, M.O. Ramirez, H. Kang, V. Gopalan, N.F. Baril, J. Calkins, J.V. Badding, P.J.A. Sazio, All-optical modulation of laser light in amorphous silicon filled microstructured optical fibers. *Appl. Phys. Lett.* **91**, 161112 (2007)
105. R.-J. Essiambre, G.J. Foschini, P.J. Winzer, G. Kramer, Capacity limits of fiber-optic telecommunication systems, *Opt. Fiber Commun. Conf. and Nat. Fiber Opt. Eng. Conf. (OFC/NFOEC'09)*, Techn. Digest (San Diego, CA, USA, 2009), paper OThL1
106. R.W. Tkach, Network Traffic and System Capacity: Scaling for the Future, *Proc. 36th Europ. Conf. Opt. Commun. (ECOC'10)*, Torino, Italy (2010), paper We.7.D.1
107. S. Inao, T. Sato, S. Senstsu, T. Kuroha, Y. Nishimura, Multicore optical fiber, *4th Opt. Fiber Commun. Conf. (OFC'79)* Techn. Digest (Washington, DC, USA, 1979), paper WB1
108. J.-F. Bourhis, R. Meilleur, P. Nouchi, A. Tardy, G. Orcel, Manufacturing and characterization of multicore fibers, *Proc. 46th Intern. Wire & Cable Symposium (IWCS'97)*, Eatontown, NJ, USA (1997), pp. 584–589
109. T. Hayashi, T. Nagashima, O. Shimakawa, T. Sasaki, E. Sasaoka, Crosstalk variation of multicore fibre due to fibre bend, *Proc. 36th Europ. Conf. Opt. Commun. (ECOC'10)*, Torino, Italy (2010), paper We.8.F.6
110. M. Koshiba, Recent progress in multi-core fibers for ultralarge-capacity transmission, *Proc. OptoElectron. Comm. Conf. (OECC'10)* Sapporo, Japan (2010), paper 6B1–3
111. K. Takenaga, Y. Arakawa, S. Tanigawa, N. Guan, S. Matsuo, K. Saitoh, M. Koshiba, Reduction of crosstalk by trench-assisted multi-core fiber, *Opt. Fiber Commun. Conf. and Nat. Fiber Opt. Eng. Conf. (OFC/NFOEC'11)*, Techn. Digest (Los Angeles, CA, USA, 2011), paper OWJ4
112. T. Hayashi, T. Taru, O. Shimakawa, T. Sasaki, E. Sasaoka, Low-crosstalk and low-loss multicore fiber utilizing fiber bend, *Opt. Fiber Commun. Conf. and Nat. Fiber Opt. Eng. Conf. (OFC/NFOEC'11)*, Techn. Digest (Los Angeles, CA, USA, 2011), paper OWJ3
113. K. Imamura, K. Mukasa, T. Yagi, Investigation of multi-core fibers with large Aeff and low micro-bending loss, *Opt. Fiber Commun. Conf. and Nat. Fiber Opt. Eng. Conf. (OFC/NFOEC'10)*, Techn. Digest (San Diego, CA, USA, 2010), paper OWK6

114. J. Sakaguchi, Y. Awaji, N. Wada, A. Kanno, T. Kawanishi, T. Hayashi, T. Taru, T. Kobayashi, M. Watanabe, 109 Tbps ( $7 \times 97 \times 172$  Gbps SMD/WDM/PDM) QPSK transmission through 16.8 km homogeneous multi-core fiber, *Opt. Fiber Commun. Conf. and Nat. Fiber Opt. Eng. Conf. (OFC/NFOEC'11)*, Techn. Digest (Los Angeles, CA, USA, 2011), paper PDPB6
115. B. Zhu, T.F. Taunay, M. Fishteyn, X. Liu, S. Chandrasekhar, M.F. Yan, J.M. Fini, E.M. Monberg, F.V. Dimarcello, Space-, wavelength-, polarization-division multiplexed transmission of 56 Tbps over 76.8 km seven-core fiber, *Opt. Fiber Commun. Conf. and Nat. Fiber Opt. Eng. Conf. (OFC/NFOEC'11)*, Techn. Digest (Los Angeles, CA, USA, 2011), paper PDPB7
116. S. Berdagué, P. Facq, Mode division multiplexing in optical fibers. *Appl. Opt.* **21**, 1950–1955 (1982)
117. H.R. Stuart, Dispersive multiplexing in multimode optical fiber. *Science* **289**, 281–283 (2000)
118. C.P. Tsekrekos, A. Martinez, F.M. Huijskens, A.M.J. Koonen, Design consideration for a transparent mode group diversity multiplexing link. *IEEE Photon. Technol. Lett.* **18**, 2359–2361 (2006)
119. S. Schöllmann, W. Rosenkranz, Experimental equalization of crosstalk in  $2 \times 2$  MIMO system based on mode group diversity multiplexing in MMF systems @ 10.7 Gbps, *Proc. 33rd Europ. Conf. Opt. Commun. (ECOC'07)*, Berlin, Germany (2007), paper 7.4.2
120. B.C. Thomsen, MIMO enabled 40 Gb/s transmission using mode division multiplexing in multimode fiber, *Opt. Fiber Commun. Conf. and Nat. Fiber Opt. Eng. Conf. (OFC/NFOEC'10)*, Techn. Digest (San Diego, CA, USA, 2010), paper OThM6
121. B. Franz, D. Suikat, R. Dischler, F. Buchali, H. Buelow, High speed OFDM transmission over 5 km of GI-multimode fiber using spatial multiplexing with  $2 \times 2$  MIMO, *Proc. 36th Europ. Conf. Opt. Commun. (ECOC'10)*, Torino, Italy (2010), paper Tu.3.C.4
122. R. Ryf, S. Randel, A.H. Gnauck, C. Bolle, R.-J. Essiambre, P. Winzer, D.W. Peckham, A. McCurdy, R. Lingle, Space-division multiplexing over 10 km of three-mode fiber using coherent  $6 \times 6$  MIMO processing, *Opt. Fiber Commun. Conf. and Nat. Fiber Opt. Eng. Conf. (OFC/NFOEC'11)*, Techn. Digest (Los Angeles, CA, USA, 2011), paper PDPB10
123. C. Koebele, M. Salsi, G. Charlet, S. Bigo, Nonlinear effects in long-haul transmission over bimodal optical fibre, *Proc. 36th Europ. Conf. Opt. Commun. (ECOC'10)*, Torino, Italy (2010), paper Mo.2.C.6
124. N. Hanzawa, K. Saitoh, T. Sakamoto, T. Matsui, S. Tomita, M. Koshihara, Demonstration of mode-division multiplexing transmission over 10 km two-mode fiber with mode coupler, *Opt. Fiber Commun. Conf. and Nat. Fiber Opt. Eng. Conf. (OFC/NFOEC'11)*, Techn. Digest (Los Angeles, CA, USA, 2011), paper OWA4
125. A. Li, A.A. Amin, X. Chen, W. Shieh, Reception of mode and polarization multiplexed 107 Gbps CO-OFDM signal over a two-mode fiber, *Opt. Fiber Commun. Conf. and Nat. Fiber Opt. Eng. Conf. (OFC/NFOEC'11)*, Techn. Digest (Los Angeles, CA, USA, 2011), paper PDPB8
126. M. Salsi, C. Koebele, D. Sperti, P. Tran, P. Brindel, H. Mardoyan, S. Bigo, A. Boutin, F. Verluise, P. Sillard, M. Bigot-Astruc, L. Provost, F. Cerrou, G. Charlet, Transmission at  $2 \times 100$  Gbps, over two-modes of 40 km-long prototype few-mode fiber, using LCOS-based mode multiplexer and demultiplexer, *Opt. Fiber Commun. Conf. and Nat. Fiber Opt. Eng. Conf. (OFC/NFOEC'11)*, Techn. Digest (Los Angeles, CA, USA, 2011), paper PDPB9

# Chapter 3

## Laser Components

Martin Moehrle, Werner Hofmann, and Norbert Grote

**Abstract** The chapter covers InP-based laser diodes (1300–1650 nm wavelength range) deployed as transmitter devices in today’s optical communication systems. Only discrete directly modulated devices are considered in this chapter which is followed by two other laser-related articles dealing specifically with ultra-fast and wavelength-tunable devices. In the first part, a description of basic laser structures and technology, of relevant gain materials and their impact on lasing properties, and of fundamental characteristics of Fabry–Pérot devices will be presented. The second part is devoted to single-wavelength lasers focusing on design rules and various implementations. Essentially, distributed feedback (DFB) devices are treated but other options such as the so-called “discrete mode” laser diodes will also be outlined. In the third part, surface-emitting laser diodes are addressed including vertical cavity surface-emitting lasers (VCSEL) and horizontal cavity DFB structures designed for surface emission.

### 3.1 Introduction

Semiconductor laser diodes used as optical transmitters represent one of the principal components in any fiber-based communication system. Laser diodes are used because these devices can be directly current modulated with modulation rates of up to several tens of Gbit/s being achievable today, they are extremely small in size

---

M. Moehrle (✉) · N. Grote

Fraunhofer Institute for Telecommunications, Heinrich Hertz Institute, Einsteinufer 37, 10587 Berlin, Germany  
e-mail: martin.moehrle@hhi.fraunhofer.de, norbert.grote@hhi.fraunhofer.de

W. Hofmann

Institute of Solid State Physics and Center of Nanophotonics, Technische Universität Berlin, Hardenbergstr. 36, 10623 Berlin, Germany  
e-mail: Werner.Hofmann@tu-berlin.de

and power efficient, and can be made at very low cost due to the use of semiconductor wafer batch fabrication. Nowadays, market prices of state-of-the-art single-wavelength laser chips have reached even the lower single-digit US\$ range, depending on performance demands and volumes.

The first functioning semiconductor laser devices came into existence as early as 1962 [1, 2], and a major breakthrough was achieved in 1969 [3, 4] by demonstrating a heterojunction design which was honored recently with the year 2000 Nobel prize. Those laser diodes were based on Ga(Al)As generating laser emission in the wavelength window around 850 nm. This spectral range is still prevailing for short-reach (< 300 m) data communications (data centers, local area and storage area networks, office communication, etc.) using multimode fibers (MMF) and GaAs-based laser diodes in the form of vertical cavity surface-emitting lasers (VCSELs). In the telecommunications arena and for longer datacom transmission distances, however, the 1.3–1.6  $\mu\text{m}$  infrared wavelength range is dominating due to optimal transmission properties (attenuation, dispersion) of the optical fiber, as outlined in the previous chapter. Laser diodes covering this spectral range are made on InP, rather than on GaAs, using the compounds InGaAsP and InGaAlAs. Development of InGaAsP/InP lasers had already commenced in the mid-1970s, for example [5, 6]. Although more than 30 years have passed since then, development efforts are continuously strong worldwide targeting the optimization of specific laser parameters to meet enhanced and new systems requirements without compromising the wide range of other relevant properties. Wavelength tunability, enhancement of modulation capability, uncooled operation up to 85 °C and above, and lower power consumption are in the focus of current developments, not to forget the never-ending call for cost reduction.

In this article, we focus on laser diodes for the “long-wavelength” range (1.3–1.6  $\mu\text{m}$ ). In the first part some basics including material aspects and device structures will be addressed. A more in-depth description of the fundamentals of laser diodes may be found in distinct text books, for example [7]. In the second part of this chapter, a review of single-mode laser diodes will be presented. Finally, we will deal with surface-emitting lasers, mainly VCSELs but also variants building on horizontal cavity structures. Two special topics of high relevance, namely wavelength-tunable and very high bit-rate laser devices, will be treated in the subsequent Chaps. 4 and 5.

### 3.2 Materials for “Long-wavelength” Laser Diodes

To create semiconductor laser diodes two basic requirements have to be fulfilled: The semiconductor needs to possess a *direct* band structure to efficiently generate laser light, and allow a band-gap energy to be adjusted that corresponds to the desired emission wavelength. For the wavelength range of interest here, the materials of choice are the III–V semiconductor InP and the related quaternary compounds InGaAsP and InGaAlAs illustrated in the “band gap vs. lattice constant” diagram in Fig. 3.1. The binary semiconductors, such as GaAs and InP, are characterized by a naturally given band gap and a fixed lattice constant. By mixing binaries, i.e.,

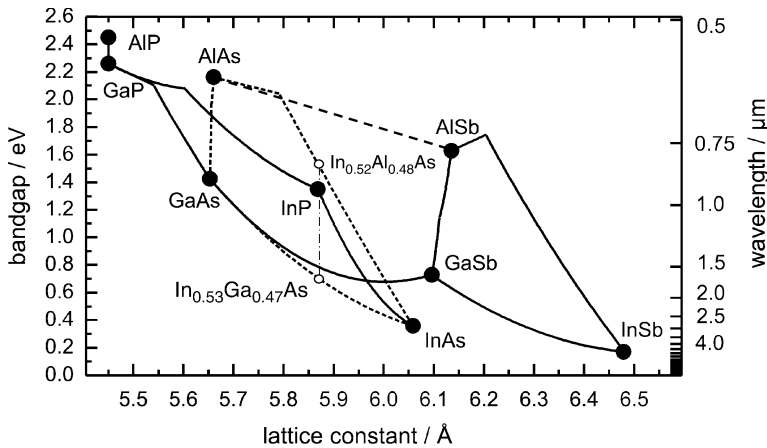


**Fig. 3.1** Band gap vs. lattice constant diagram for “long-wavelength” III–V compound semiconductors (*solid line*: direct band gap; *broken line*: indirect band gap; *dotted vertical line* between InGaAs and InP/InAlAs: lattice-matched quaternary compositions)

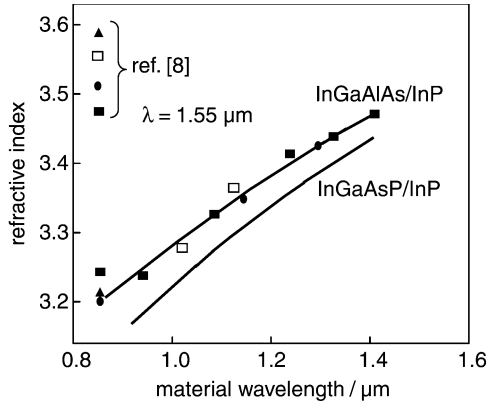
by replacing a fraction of the group (III) and/or group (V) elements, generally any ternary and quaternary composition can be adjusted within the area spanned between the binaries concerned. In practice, such composites are deposited as crystalline layers onto a binary substrate wafer utilizing well-established epitaxial techniques, and to achieve layers of high crystal quality virtually perfect lattice matching ( $< 0.1\%$  deviation) is required.

Hence, starting from InP, only layers can be stacked that have a composition which is defined by a vertical line through the InP point. Thus restricted, only selected InGaAsP materials can be used that cover the compositional range between InP and the ternary end constituent  $\text{In}_{0.53}\text{Ga}_{0.47}\text{As}$ , associated with a band-gap span from 1.35 to 0.75 eV, or in terms of wavelengths from 920 to 1650 nm. Another InP-related material family is InGaAlAs covering the range from  $\text{In}_{0.52}\text{Al}_{0.48}\text{As}$  (1.48 eV, 840 nm) to again  $\text{In}_{0.53}\text{Ga}_{0.47}\text{As}$ . The optical index of refraction, which is a crucial parameter for optical waveguiding properties (Fig. 3.2), varies along with the band gap.

The indicated band-gap values refer to room temperature but change with temperature, roughly by – in terms of wavelengths – 0.5 nm/K. This means a variation of the order of 60 nm over the full temperature range of practical interest for fiber optics components, i.e., from  $-40$  to  $+85$  °C in the extreme case. This behavior has substantial implications for the design and operation of laser diodes, in particular regarding wavelength stability and adjustment.

There is one important exception to the stringent lattice-match requirement: Below a certain layer thickness, which is dependent on the mismatch in lattice constant and referred to as the critical thickness, the layer may be elastically strained by purposely introducing lattice mismatch without affecting crystalline integrity. The figure-of-merit here is the “thickness  $\times$  strain” product which as a rule of thumb

**Fig. 3.2** Dependence of optical refraction index on material composition of InGaAsP and InGaAlAs lattice matched to InP at 1.55  $\mu\text{m}$  wavelength (taken from [8] and references therein; relationship for InGaAsP after [9])



should not exceed the critical value of around 20 nm%, with the strain,  $\varepsilon$ , represented by the percentage of relative lattice mismatch of the unstrained materials. The lattice deformation is associated with a modification of the band structure that is beneficially exploited in strained multiquantum well (MQW) layer structures widely employed as the active medium in laser diodes today.

### 3.3 Laser Diode Structures

#### 3.3.1 Layer Structure

To build a real laser diode, the lasing layer is embedded between layers of higher band gap and thus lower refractive index. In this way, an optical waveguide is formed in which the light traveling forth and back within the laser cavity is vertically confined. Concurrently, the injected carriers interact with the optical wave to generate stimulated light emission. This layer stack is designed as a so-called double-heterostructure comprised of inner quaternary layers and n- and p-doped InP cladding layers to create a pn-diode. The quaternary layers may also be lightly doped. By applying an electrical forward current to the diode hole and electron carriers are injected from the doped InP layers into the active layer where they are electrically confined and converted into photons by recombination. Once the carrier densities have reached critical levels to yield population inversion in the conduction and valence band light amplification can occur by stimulated emission. A basic layer structure is sketched in Fig. 3.3.

The highly doped InGaAs cap layer facilitates formation of ohmic p-contacts of very-low resistivity ( $\sim 10^{-6} \Omega \text{ cm}^2$ ) which is essential for achieving high modulation bandwidth and for minimizing heat dissipation. Additional layers may be inserted for performance or fabrication reasons (e.g., etch stop layer). Altogether, advanced lasers may contain even more than 20 different layers yielding a total



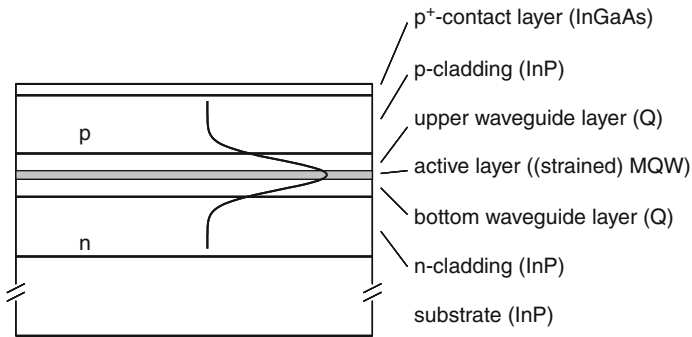


**Fig. 3.3** Basic layer structure of an InP-based double-heterostructure laser diode; inserted profile schematically indicating vertical intensity distribution of laser light propagating along the laser cavity (*MQW* multiquantum well (refer to Sect. 3.4); *Q* quaternary composition)

thickness of about 3 to  $> 5 \mu\text{m}$ . Mainly n-type InP substrates are used but inverted designs building on a p-doped substrate (Zn doped) are being employed as well [10]. Substrate wafers of 2- and 3-inch diameter are common.

### 3.3.2 Lateral Structure

Whereas in the vertical direction the laser waveguide is defined by the layer stack, structural measures have to be taken that define the waveguide in the lateral direction too. Simultaneously carrier injection needs to be efficiently restricted to this active region which is typically nearly  $2 \mu\text{m}$  wide to guarantee monomode waveguiding. In actual lasers two fundamentally different designs are used (Fig. 3.4a–d): (a) ridge waveguide (RW) and (b) buried-heterostructure (BH). In the former, a mesa ridge is etched into the upper layers along the laser cavity resulting in a lower effective refractive index outside the ridge and thus lateral optical confinement. The p-contact is applied to the ridge area, thereby confining the current flow. Because of lateral current spreading and unavoidable lateral diffusion of carriers inside the active layer, current-dependent broadening of the lasing region occurs, and this outdiffusion effect causes a certain portion of carriers to no longer contribute to lasing.

In BH-type laser diodes the active region is fully surrounded by InP, thus creating a well-defined buried waveguide. This is achieved by a special selective regrowth process of InP layers at both sides of the previously etched active stripe. Because these layers are n–p doped to provide a built-in reverse-biased junction, current flow is effectively blocked such that it is completely funneled into the active stripe. Outdiffusion of carriers is suppressed by the energetic barrier between the lower band gap of the active material and the adjacent InP. As opposed to the RW design, the upper InP cladding layer extends over the full structure. Therefore, the p-contact can be made significantly wider implying lower series resistance.

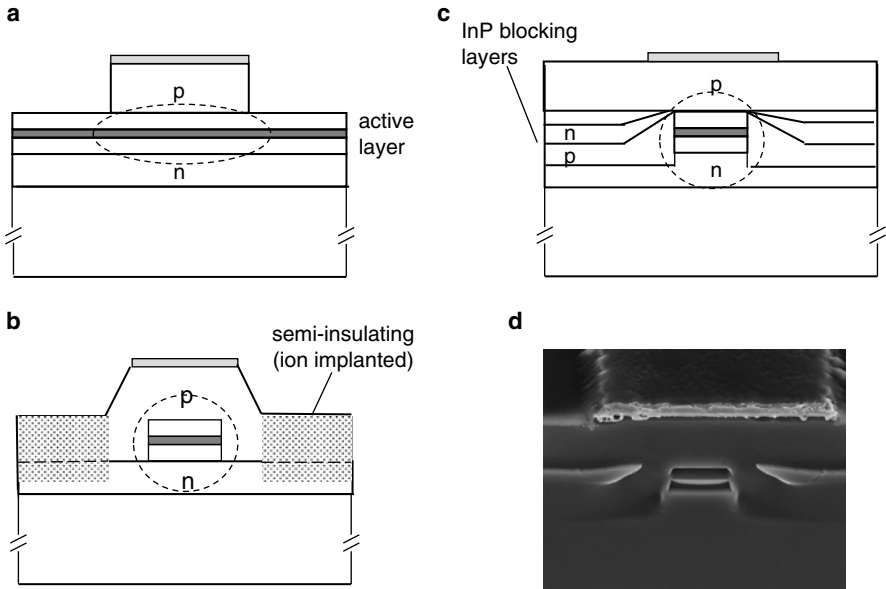


**Fig. 3.4** Schematic cross sections of basic structures used with InP laser diodes: **a** ridge waveguide (RW); **b** buried ridge stripe (BRS); **c** buried heterostructure (BH) with pn current-blocking layers; **d** REM image of real BH cross section; *dotted ellipse* and *circle* illustrate near-field profiles (not drawn to scale)

While BH lasers with pn current-blocking layers are the most common, there are other variants that are being successfully used. Instead of pn blocking layers semi-insulating InP has been employed, the high resistivity ( $\sim 10^8 \Omega \text{ cm}$  at room temperature) of which is achieved through doping with Fe (conc.  $\sim 10^{17} \text{ cm}^{-3}$ ). Such semi-insulating layers are advantageous regarding lower parasitic capacitance and therefore for high-speed laser devices. However, the specific resistivity decreases by almost three orders of magnitude between  $20^\circ\text{C}$  and  $85^\circ\text{C}$ , and Fe diffusion effects may raise reliability concerns. Another version is the so-called buried ridge stripe laser (BRS) which may be considered a hybrid of the RW and BH structure. Here, the etched laser ridge is conformally overgrown with the p-InP cladding layer. Whereas most of this layer is rendered electrically insulating by means of ion implantation, parasitic current flow through the small remaining conductive InP regions adjacent to the active part is suppressed due to the higher built-in voltage at the InP pn junction.

Generally, the overall performance of BH-type lasers is superior to their RW counterparts: lower threshold current, better high-temperature output power and high-frequency characteristics, and almost circular rather than elliptical beam profile. Conversely, fabrication of RW lasers is less complex and hence more cost-efficient, thanks to fewer epitaxial steps. Nonetheless, due to performance requirements, a great deal of the long-wavelength lasers marketed today are BH devices.

The RW design is, however, the structure of choice when any Al-containing layers are involved. This is especially true for 1300 nm uncooled 10 Gbit/s lasers widely used for datacom applications as well as for externally modulated lasers (EML, see Chap. 4), the latter benefiting from the better electroabsorption behavior of InGaAlAs structures. The issue encountered with BH lasers is that InGaAlAs materials are prone to surface oxidation when exposed to air. This effect is difficult to avoid during processing. There have been several reports on BH laser diodes containing InGaAlAs layers; however, a real breakthrough of this technology is still missing. Any residual oxide remaining on the regrown BH interface may introduce nonradiative recombination centers and may be regarded as a potential source for lifetime issues with these lasers. Removing the oxidized surface by etching with a suitable cleaning gas inside the epitaxy reactor has been primarily investigated to tackle this issue, and achievement of highly reliable 1300 nm devices was claimed [11]. Exploiting narrow stripe selective area growth has been another approach in which case the InGaAlAs MQW layers are covered in situ with an InP layer [12].

### 3.4 Active Medium

In its simplest form the active medium of the laser diode consists of a bulk layer made of InGaAsP. Basically, the lasing transitions occur between the conduction and the valence band edges to yield laser wavelengths corresponding to the composition-dependent band gap,  $E_g$ . However, such “bulk” lasers exhibit comparably high threshold currents because of lower material gain, resulting in low output power and poor high-temperature performance.

#### 3.4.1 *Quantum-well Layers*

More advantageous are the so-called quantum-well (QW) structures. In such a structure a thin well layer is sandwiched between two barrier layers of higher band gap. If the thickness of the embedded well layer is smaller than the De Broglie wavelength of the electrons and holes in this material, quantization of the electron and hole energy levels occurs. The optical transitions then take place between the quantized electron and hole levels in the QW rather than between the virtual conduction and valence band (Fig. 3.5). The well/barrier (QW) layer stack is made of either InGaAsP or InGaAlAs but mixed InGaAsP/InGaAlAs QWs have also been employed and have shown distinct benefits for enhancing the modulation bandwidth (30 GHz [13]). Typical thicknesses range from 4 to 8 nm and from 7 to 15 nm for the well and barrier layer, respectively. The former thickness has a substantial effect on the emission wavelength which increases with decreasing well width. Commonly, a series of QW layers is vertically stacked to result in MQW structures.

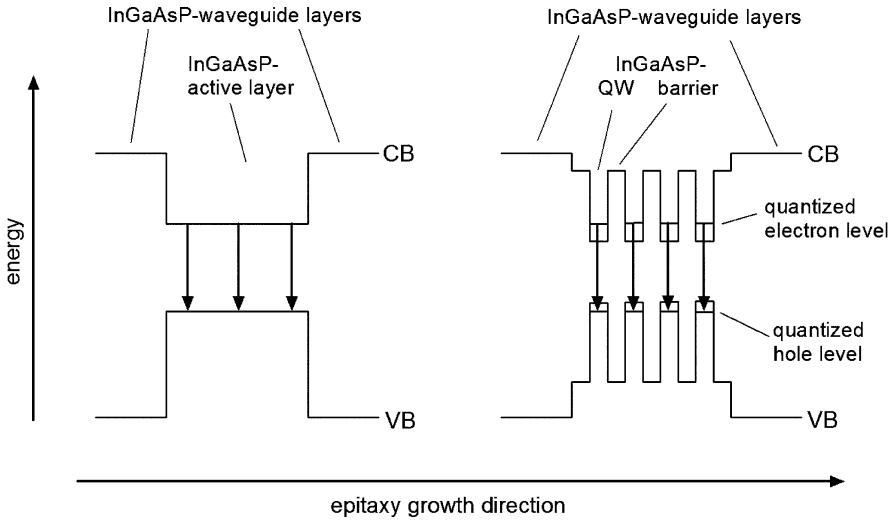


**Fig. 3.5** Schematic energy band structure and corresponding optical transitions in a bulk (*left*) and a multiquantum well structure (*right*); *CB* conduction band; *VB* valence band

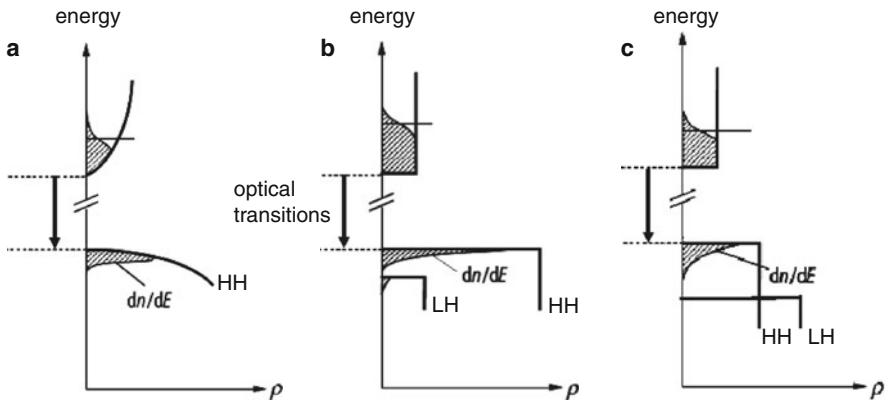


**Fig. 3.6** Schematic representation of density of states and corresponding spectral carrier density  $dn/dE$  at transparency condition for **a** bulk, **b** lattice-matched quantum-well structure, and **c** compressively strained quantum-well structure (*LH* light hole; *HH* heavy hole; *n* carrier density; *E* energy)

Physically, the advantage of QWs originates from the density of states. As a consequence of the quantized electron and hole states, the respective energy dependence of the density of states in the conduction (CB) and valence band (VB) changes from parabolic curves in the case of a bulk layer to step-like functions in the case of QW layers. If electrically pumped, these carrier states are filled according to Boltz-

mann's thermal occupation statistics resulting in spectral carrier densities,  $dn/dE$ , as depicted in Fig. 3.6a, b. Because of the fact that, as a first approximation, the optical gain of a semiconductor material for a specific optical transition is proportional to the product of the respective spectral carrier densities in the conduction and the valence band, it is obvious that QW structures exhibit higher optical gain than their bulk counterparts (Fig. 3.6b). MQW structures therefore show lower threshold current densities and accordingly superior temperature behavior and high-frequency characteristics.

### 3.4.2 Strained QWs

By incorporating strain into the quantum wells, the gain characteristics can be further improved considerably. Typical strain values used here range from  $-1.5\%$  (tensile strain) to  $+1.5\%$  (compressive strain). The main physical effect of strain in the quantum wells is the breakup of the energy degeneration of the heavy hole (HH) and light hole (LH) valence bands at  $k = 0$  and corresponding significant changes in the shape of the respective in-plane energy dependence (Fig. 3.7). By applying compressive strain in the quantum well, the in-plane HH mass is reduced and the density of states in the HH valence band decreased. Accordingly, band filling at the same electrical pumping level increases to yield lower threshold current densities and also higher differential gain values. Furthermore, the effect of optical intraband losses due to absorption between the HH- and the split-off- (SO) valence band at the optical transition energy is substantially reduced. The benefit of the strained layer MQW laser had already been recognized by the end of the 1980s [14], and nowadays commercial laser diodes are commonly designed this way using compressively strained wells in the MQW structures. One percent of compressive strain was discovered to be optimal [15]. The barrier layers may be tensile-strained for (partial) strain compensation to allow for implementation of higher-period MQW structures without exceeding the critical thickness. It should be noted that unstrained and compressively strained QWs strongly support TE-polarized laser emission, whereas tensile strain results in TM polarization. This behavior is exploited, for example in semiconductor optical amplifiers (SOA, see also Chap. 12) to balance TE/TM gain [16].

For many applications, the high-temperature performance of laser diodes is of crucial importance. Optical datacom links and fiber-to-the-home (FTTH) networks demand uncooled operation up to ambient temperatures of  $+85^\circ\text{C}$ . At higher temperatures, the optical gain reduces due to thermal broadening of the energetic band filling distribution of the carriers resulting in smaller  $dn/dE$  values at a specific energy. Material inherent optical losses such as Auger absorption also increase with increasing temperature. Both effects lead to an increase of laser threshold current and a decrease of external power vs. current efficiency (slope efficiency) with increasing temperature. This is also true for the electrical pumping efficiency of an MQW structure which tends to get lower at higher temperatures. This is

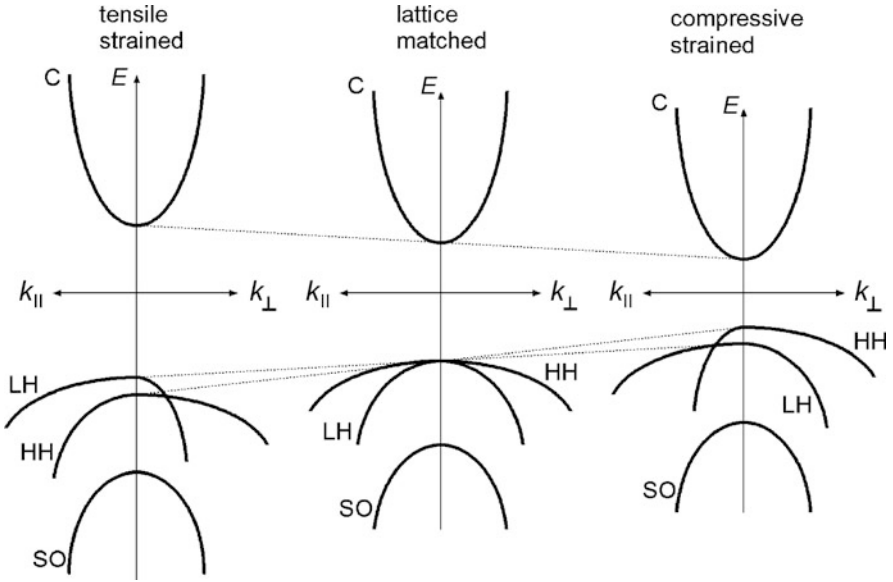


**Fig. 3.7** Schematic energy band structure of strained InGaAsP material on InP for the cases: tensile strained (*left*), lattice matched (*middle*), and compressively strained (*right*)

because carriers may be thermally released from the well into the adjacent barrier and waveguide layers (referred to as carrier leakage). Because of their lower mass, this mechanism mainly affects electron injection and is largely dependent on the conduction band discontinuity between well and barrier layer (Fig. 3.8). In InGaAsP/InGaAsP structures, the conduction band discontinuity makes up only some 40 % of the band-gap difference,  $\Delta E_g$ , of the layers involved. More advantageous with respect to this carrier overflow issue are InGaAlAs/InGaAlAs structures and also the combination InGaAsP/InGaAlAs. Here, the conduction band discontinuity amounts to 72 % and 80 % of  $\Delta E_g$ , respectively. To further avoid electron leakage into the surrounding optical waveguide regions, an additional very thin InAlAs layer is often inserted into the laser layer stack to serve as an electron stopper.

Another advantage of the Al-containing QW option is related to the modulation capability. The lower valence band discontinuity, in accordance with the higher conduction band discontinuity, of InGaAlAs/InGaAlAs MQW structures favors the hole transport in and out of the quantum wells, allowing for significantly faster high-frequency response and thus larger modulation bandwidth compared to InGaAsP/InGaAsP. In accordance with this, a higher number of QWs can be uniformly pumped with holes. Uncooled 1300 nm lasers with 10 Gbit/s modulation capability which have been receiving great attention recently for 10 Gbit/s datacom links commonly rely on InGaAlAs technology (refer to Chap. 4).

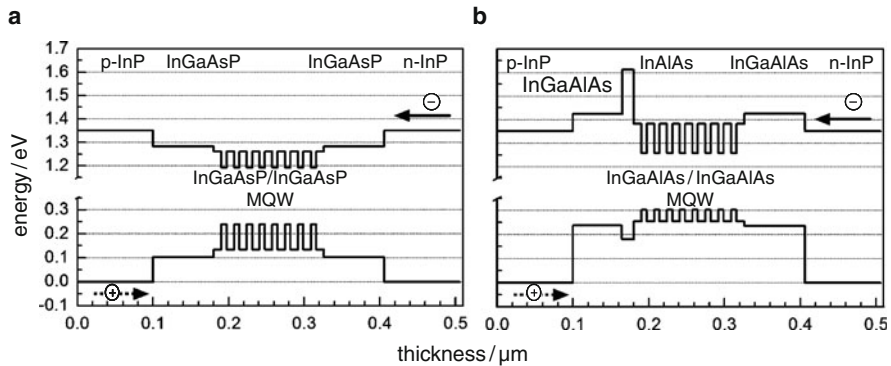


**Fig. 3.8** Schematic energy band structure of a typical InGaAsP/InGaAsP (a) and InGaAlAs/InGaAlAs MQW structure (b); quantization effects are not regarded for the sake of clarity. Note the “inverted” MQW band structure of the two material systems

### 3.4.3 Quantum Dots

Quantum-dot (QD) materials have attracted a great deal of attention in recent years as a novel active laser medium. QDs are tiny pyramidal nanocrystals of about 10–20 nm footprint that are embedded in host layers. The formation of such QD structures is accomplished using highly lattice-mismatched material (e.g., InAs) deposited under dedicated epitaxial growth conditions. QDs feature  $\delta$ -function-like density-of-state functions and thus much higher maximum gain values than QW structures. Theoretically, they offer unique lasing properties, such as ultra-low threshold current density, high-temperature stability, zero chirping, low noise, and ultrahigh-frequency capability. In reality, however, the hitherto unavoidable size dispersion of the QD particles and their low total active volume inhibit the exploitation of these properties.

The bulk of QD research has been devoted to GaAs-based lasers and has yielded a range of impressive laser results, for instance, threshold densities of  $< 10 \text{ A cm}^2$  and very high and even negative  $T_0$  values [17]. However, it appears that such unprecedented values are difficult to accomplish without compromising other specifications that need to be simultaneously met for practical applications. With InP, quantum-dot structures appear to be more challenging to grow, and quantum dashes rather than dots may be generated depending on growth conditions. The basic laser properties achieved to date generally do not outperform those of QW lasers. Among the apparent advantages of QD lasers is their improved noise behavior, which is beneficially exploited in superior mode-locked lasers and all-optical clock recovery devices [18]. The QD size distribution resulting in an excessively broad gain spectrum has been exploited to create so-called comb lasers [19]. Superior performance of QD-based optical amplifiers (SOA, see Chap. 12) has been well recognized. A unique future application may be as an active medium for single photon sources for quantum cryptography applications. Despite these achievements, one

can state that although QD technology is useful for enhancing specific laser parameters, it has to date not led to a revolution in semiconductor laser technology.

### 3.5 Fabry–Pérot Lasers

The simplest form of a laser diode is the Fabry–Pérot (FP) type. The laser cavity length is defined by cleaving, and the resonator mirrors are simply provided by the resulting crystal facets. Assuming an effective refraction index of the laser material of  $n_1 = 3.5$ , the resulting mirror reflectivity against air ( $n = 1$ ) amounts to some 30 %. By applying optical reflection coatings to the facets, other values can be easily adjusted. In particular, using a high-reflectivity (HR) coating at the back facet and a low-reflectivity (LR) one at the front facet, the optical output power from either facet can be made highly asymmetric. In this way, compared to symmetrical mirror conditions, the optical power from the front side may be almost doubled at the expense of the power from the backside. The latter is commonly exploited for optical power control by means of a monitor photodiode for which an only moderate intensity is sufficient.

For the reflection coating, the wafer needs to be cleaved into bars several tens of which can be simultaneously coated by evaporation or (ion beam) sputtering, one run for either facet. Because of the large handling effort involved, this process is rather costly. The coating films consist of periodic pairs of quarter-wavelength dielectric layers of different refractive index, for example  $\text{SiO}_2$  and  $\text{TiO}_2$ . Care has to be taken to minimize undesirable spillage on the surface and backside of the laser chips. Besides their optical function, the coatings also serve to protect the facets against detrimental environmental effects. Following the coating process, individual laser chips are singulated by a scribe-and-break process. To ease this process and the previous bar cleaving, the full processed wafer is thinned to a thickness of only some 100  $\mu\text{m}$ . The dimensions of a representative laser chip used for optical data transmission are given by a cavity length of 200–400  $\mu\text{m}$  and a width of 250–400  $\mu\text{m}$ , to some extent depending on the targeted application.

A typical emission spectrum of an InP-based FP laser diode is represented in Fig. 3.9. Since the gain spectrum of the laser material is fairly broad ( $\gtrsim 30$  nm full width at half maximum) and the reflectivity of the facet mirrors is practically wavelength independent, multiple emission wavelengths appear manifesting the longitudinal Eigen modes of the cavity.

Taking into account the chromatic dispersion of optical fibers, the width of the emission spectrum is crucial for the maximum achievable transmission length at a given bit rate. A measure for the spectral width is the RMS value which is a weighted quantity according to (3.1) considering all modes ( $i$ ) with intensities  $p_i$  within the  $-20$  dB range relative to the prevailing one:

$$\Delta\lambda_{\text{RMS}} = \sqrt{\frac{M}{I}} = \sqrt{\frac{\sum p_i (\lambda_i - \lambda_c)^2}{\sum p_i}}; \quad \lambda_c = \frac{\sum p_i \lambda_i}{\sum p_i}. \quad (3.1)$$



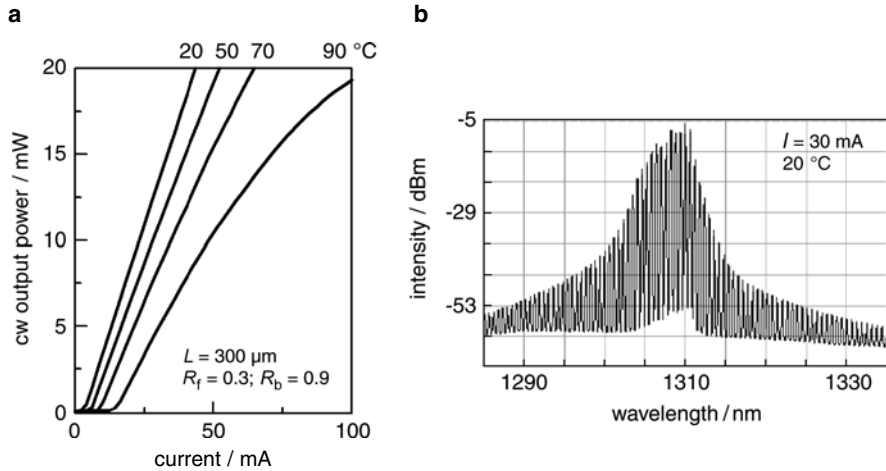


**Fig. 3.9** Representative  $P$ – $I$  curves (a) and emission spectrum (b) of an InGaAsP/InP MQW BH–FP laser. These characteristics are basically similar for any other emission wavelengths in the accessible wavelength range ( $R_f$ ,  $R_b$  = reflectivity at front and back facet, resp.)

Typical RMS values are in the 1–2 nm range, with 3 nm representing a specified upper limit for, e.g., 10 Gbit/s 1300 nm FP lasers at any operational condition.

Also shown in Fig. 3.9 are optical power vs. current characteristics of a BH–FP transmitter laser diode at various temperatures. Threshold currents in the < 5–10 mA region and optical output power well exceeding 40 mW are representative for those lasers at room temperature. Because of the physical effects outlined in the previous section, the output power tends to significantly decrease with increasing temperature ( $T$ ), whereas the threshold current ( $I_{\text{th}}$ ) increases exponentially according to the empirical equation (3.2) ( $T_r$  = reference temperature, e.g., 20 °C):

$$I_{\text{th}}(T) = I_{\text{th}}(T_r) \exp[(T - T_r)/T_0]. \quad (3.2)$$

Here,  $T_0$  denotes the so-called characteristic temperature which for InP laser diodes comprising an active InGaAsP MQW region ranges from  $\sim 40$  to  $\sim 60$  K, depending on active volume, cavity length, and facet reflectivity. Using InGaAlAs instead higher values up to some 80 K are achievable. These values hold for operation up to some 60 °C but tend to be lower beyond that point. Altogether, compared to their Ga(Al)As counterparts the temperature behavior of InP-based laser diodes proves to be substantially worse which largely impacts practical applications and has demanded large R&D efforts in recent years to accomplish uncooled laser operation.

As opposed to other laser systems, the output beam of semiconductor lasers is highly divergent due to optical diffraction. The far-field of the laser beam is essentially determined by the design of the laser waveguide. RW lasers exhibit a pronounced elliptical intensity profile, whereas the one of BH structures is fairly circular. The circular shape is highly desirable because it matches well to single-mode fibers for the benefit of efficient optical coupling. The far-field pattern is often char-

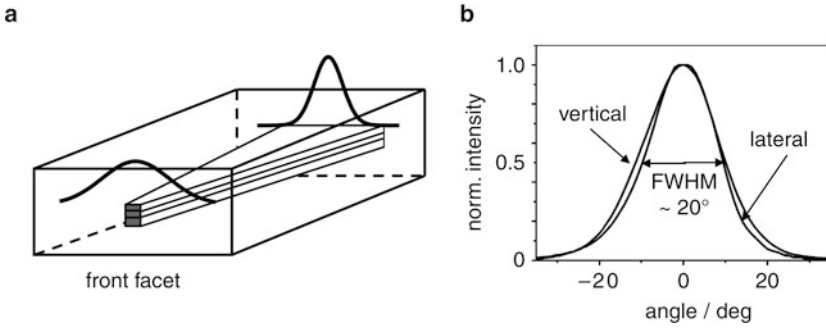


**Fig. 3.10** Schematic representation of a tapered laser diode exploiting the concept of a laterally tapered active stripe leading to mode expansion due to weaker optical guidance (a); optical far-field pattern of a tapered BH laser in vertical and lateral direction (b); the value of  $20^\circ$  has to be compared to  $> 30^\circ$  for nontapered structures

acterized by the divergence angle, taken as the full angle at half intensity maximum (FWHM angle). The following values (vertical  $\times$  lateral) may be considered representative for transmitter laser diodes:  $45^\circ \times 20^\circ$  for RW and  $> 30^\circ \times 30^\circ$  for BH structures.

To accomplish lower values, so-called tapered lasers have been developed. A simple yet efficient method is to gradually narrow the active stripe in the lateral direction toward the front facet, as illustrated in Fig. 3.10a. As optical guiding becomes weaker the more the waveguide narrows, the optical mode broadens accordingly to result in lower beam divergence. This design does not require any extra process steps but is applicable to BH structures only. Depending on the taper design, the far-field angle can be nearly halved to angles down to as small as  $15^\circ$  in this way. An example is depicted in Fig. 3.10b, with the FWHM angle amounting to some  $20^\circ$  in this case. In [20] it is shown that such a reduction leads to an improvement in coupling efficiency by 6 dB when directly butt-coupled to a flat SMF, comparing tapered and nontapered laser diodes of otherwise the same design. Other taper techniques that provide even smaller far-fields have been published but these involve a much higher fabrication complexity [21], including selective area growth [22]. It should be noted that VCSELs (see Sect. 3.7.1) inherently provide a circular-shaped far-field of low divergence angles, which is one of their great advantages.

For efficient laser–fiber coupling, tapered lasers are advantageous but not really mandatory because low-cost lenses can be used. They are, however, extremely helpful in hybrid integration technology where such diodes are to be directly coupled to optical waveguides without any beam-shaping optics. In addition to the enhanced coupling efficiency, they also provide larger alignment tolerances.

The main application of FP lasers in optical communications has been for uplink transmission (1310 nm) in FTTH passive optical networks. Generally, the importance of FP lasers has been decreasing in recent years, mainly because of the spectral bandwidth-related restrictions in transmission bit rate and distance, and also because of the drastic price decline of their superior DFB counterparts (refer to Sect. 3.6.1).

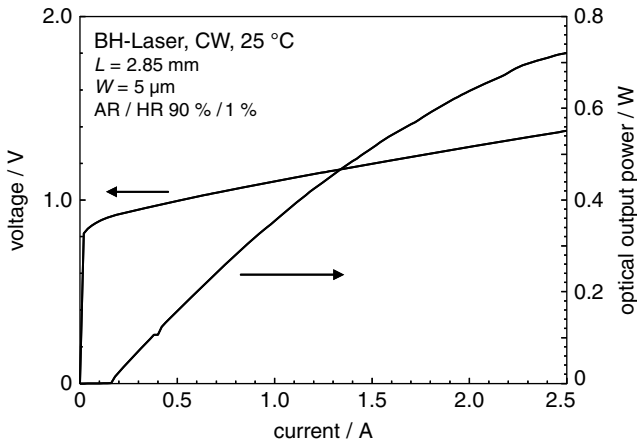


**Fig. 3.11** Optical output power characteristic of a BH-HPLD emitting at 1480 nm (source: FhG-HHI)

One remaining prominent application area, however, is high-power laser diodes (HPLD), in the form of either (spatially) single-mode or broad area devices. The design of such laser diodes, which are normally operated in CW (continuous wave) or pulsed mode, is substantially different from transmitter lasers. Key to achieving high output power is to minimize series resistance and internal optical losses. The former issue mainly requires optimizing doping profiles and layer transitions, whereas the latter aspect relates to the waveguide design. One has to bestow great care on keeping the portion of the optical intensity profile penetrating into the lossy p-doped waveguide region low. This leads to an asymmetric waveguide design associated with a relatively small confinement factor of the active region. To compensate for this, the HPLDs are built excessively long ( $\sim 2\text{--}3$  mm). Reported optical output power of 1480 nm HPLD lasers emitting in the fundamental mode have reached the 1 W level at room temperature [23].

Figure 3.11 shows the optical power/current curve of a BH-type HPLD delivering about 700 mW at 1480 nm of ex-facet output power which may be regarded more state-of-the-art. Such lasers are mainly used as pump sources for Er-doped fiber amplifiers (pump wavelength: 1480 nm) and for Raman fiber amplification (14xx nm wavelengths) [24]. Besides that there are diverse applications outside the telecom field, for example for LIDAR.

### 3.6 Single-mode Laser Diodes

To cope with the effect of optical fiber dispersion, which restricts achievable bit rate and transmission distance, transmitter lasers are demanded that emit a single rather than multiple wavelengths. Typically, residual side wavelengths need to be suppressed by at least 35 dB, commonly referred to as side-mode suppression ra-

tio (SMSR). Various types of single-mode laser diode devices are well known, including distributed feedback (DFB) lasers, distributed Bragg reflector (DBR) lasers (see also Chap. 5), external cavity lasers, coupled cavity lasers, discrete-mode lasers (Sect. 3.6.2), and VCSEL (Sect. 3.7.1).

### 3.6.1 Distributed Feedback Lasers

DFB lasers, the concept of which was introduced more than 35 years ago [25], have become the most established single-wavelength laser type. The key structural element of such laser diodes is the so-called DFB grating providing a periodic change of the effective optical index of refraction along the laser cavity. Thereby partial reflection occurs at each index step (real or complex) to generate distributed optical feedback by constructive interference. This mechanism is wavelength-selective, thus enabling longitudinal single-mode operation. The DFB grating is realized by etching a “washboard”-like structure into the optical waveguide stack of the laser heterostructure (Fig. 3.12) which is subsequently overgrown with the p-cladding/contact layers. In this way, the DFB coupling relies on the periodic variation of the *real* part of the refractive index, which represents the commonly used solution. Alternatives, though less often applied, are gratings that are formed in the substrate, i.e., below the active region, and metal gratings placed beside the ridge of RW laser structures [26].

In order to obtain longitudinal mode selection, the grating period  $\Lambda$  has to fulfill the so-called Bragg condition:

$$\Lambda = \frac{\lambda m}{(2n_{\text{eff}})}, \quad (3.3)$$

where  $\Lambda$  denotes the grating period,  $\lambda$  the emission wavelength,  $n_{\text{eff}}$  the effective refractive index of the laser structure, and  $m$  the grating order ( $m = 1, 2, \dots$ ). First-order gratings ( $m = 1$ ) have the advantage that virtually all the light is reflected back and forth only in the direction of the waveguide, thus resulting in very efficient optical feedback. In the case of higher order gratings, part of the light is vertically coupled out of the waveguide, causing excess optical loss for the laser. Therefore, first-order gratings are predominantly utilized, whereas second-order gratings have been exploited in special surface-emitting DFB laser designs (see Sect. 3.7.2.2), and higher order gratings in high-power DFB devices because of their particularly long cavity. Mathematically, DFB lasers can be described and simulated by the well-proven coupled mode and transmission line models, respectively. Both theoretical models are thoroughly described, for example in [27].

#### 3.6.1.1 Basic DFB Design

In order to fully exploit the longitudinal mode selection mechanism of the DFB grating, any back-reflections from the facets have to be avoided. This is commonly

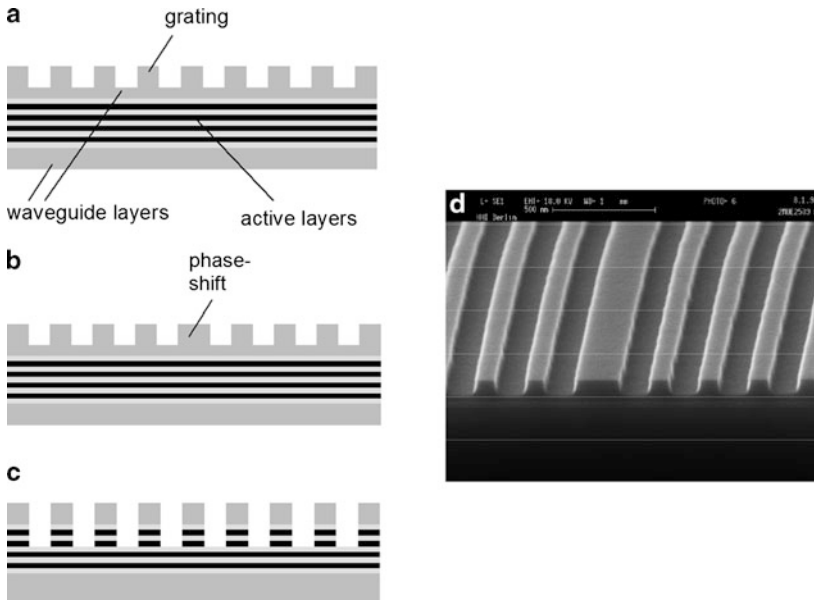


**Fig. 3.12** Schematic views of DFB gratings: **a** uniform real-index coupling, **b** index-coupled grating with integrated  $\lambda/4$  phase shift, and **c** complex coupling. Not shown are the upper cladding layers which are grown on top to complete the laser structure. In **d** an SEM image of a real  $\lambda/4$  phase-shifted DFB grating is depicted made by electron beam lithography and subsequent reactive ion etching. The grating period (1st order) for a 1550 nm DFB laser amounts to some 220 nm only

achieved by applying antireflection (AR) coating layers to either end facet. Index-coupled DFB lasers (Fig. 3.12a) with AR-coated facets, however, show a two-mode spectrum corresponding to the Bragg grating stop band modes, as depicted in Fig. 3.13a. To achieve single-mode operation, an additional  $\lambda/4$  phase shift in the center part of the grating can be implemented (Fig. 3.12b). In that case, single-mode operation at the Bragg wavelength (3.3) is obtained (Fig. 3.13b). Alternatively, also multiple phase shifts distributed along the DFB grating can be used here [28]. Another means to obtain single-mode operation is to use the so-called *complex* coupling, in which case an additional imaginary index (gain or absorption) coupling component adds to the real-index coupling. As a result, single-wavelength emission is obtained that corresponds to the “red” (gain) or “blue” (absorption) side stop band mode (Fig. 3.13c). In reality, as one approach, such complex coupling is accomplished by etching the DFB grating further into the active layer (Fig. 3.12c). Although there have been concerns about the reliability of such DFB structures, it could be demonstrated that appreciably good lifetime behavior is achievable if the fabrication is done properly. Because of the oxidation issue (see Sect. 3.3) this “active layer etching” approach is not readily applicable to Al-containing layer structures.

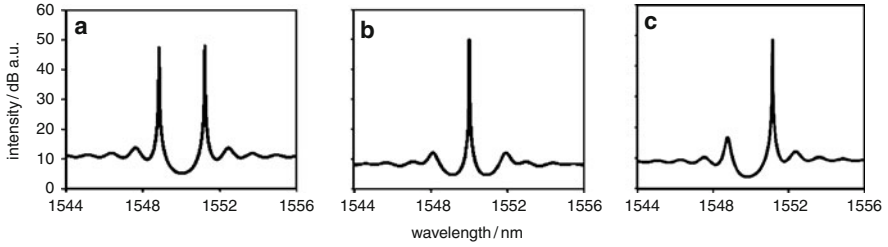
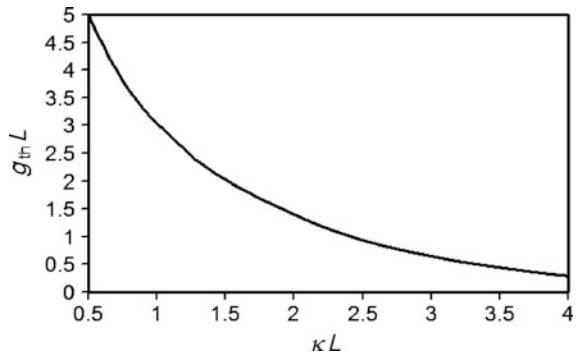


**Fig. 3.13** Typical spectra at laser threshold (simulation) of **a** uniformly index-coupled, **b**  $\lambda/4$ -phase-shifted index-coupled, and **c** complex-coupled DFB structure with both facets AR coated ( $L = 300 \mu\text{m}$ ,  $\kappa = 50 \text{ cm}^{-1}$ )

**Fig. 3.14** Dependence of threshold gain  $\times$  length product,  $g_{\text{th}}L$ , on the coupling coefficient  $\kappa L$  product for  $\lambda/4$ -phase-shifted DFB lasers with AR-coated facets (optical losses neglected).  $L$  denotes the length of the DFB grating

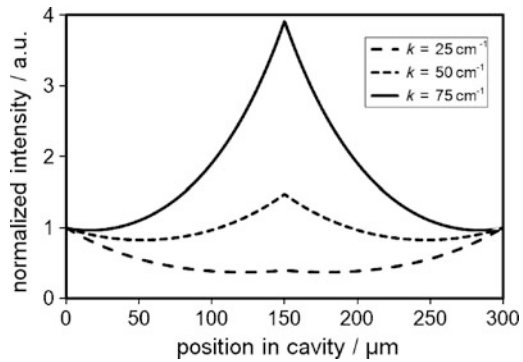


A key parameter in the design of DFB lasers is the coupling strength of the DFB grating, denoted by the coupling coefficient  $\kappa$  and defined as the fraction of light intensity reflected back at each periodical index step.  $\kappa$  depends on the amount of light confined in the grating layer, i.e., on the grating depth and on the effective refractive index difference between the materials that compose the grating. The value of  $\kappa$  largely impacts, among others, the threshold current of a DFB laser. Figure 3.14 exemplarily shows the dependency of the threshold gain,  $g_{\text{th}}$ , on the coupling strength  $\kappa$  for a  $\lambda/4$  phase-shifted DFB laser.

Another effect governed by the  $\kappa$ -coefficient is the intensity distribution inside the DFB laser structure. This is illustrated in Fig. 3.15 where the resulting optical intensity profile along the cavity is drawn for different  $\kappa$ -values in case of a  $300 \mu\text{m}$ -long phase-shifted DFB device. Strong coupling leads to pronounced intensity peaking at the phase-shift position causing local depletion of the optical gain in that region of the cavity, also known as spatial hole burning [29]. As a consequence, the side mode suppression is reduced and the lasers tend to become spectrally multimode. For this reason, such a strong index coupling is generally avoided, and  $\kappa L$  product values between 1 and 2 are mostly used.

DFB laser devices with AR-coated facets generate equal optical output power from both cavity sides (Fig. 3.15). In most practical applications, however, asymmetrical output power distribution is desired to increase the usable power from the

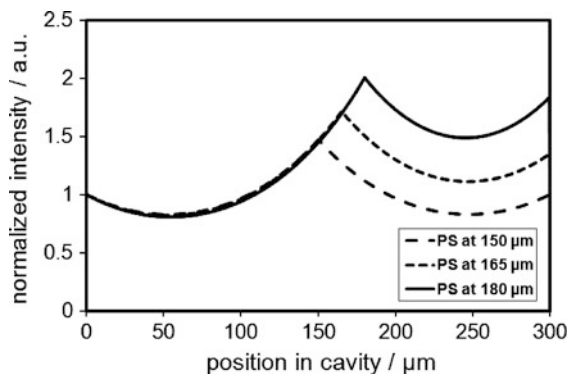
**Fig. 3.15** Normalized intensity distribution along the DFB cavity at laser threshold for different coupling coefficients  $\kappa$  ( $L = 300 \mu\text{m}$ , both facets AR coated)



front facet at the expense of the light emission from the rear facet, with the latter commonly utilized to feed a monitor photodiode. This can be accomplished in two alternative ways. The first one is to implement gratings with an off-center phase shift (Fig. 3.16). By this means the optical intensity can be lifted such as to yield higher values at the front facet, and accordingly increased output power. However, as a trade-off, side-mode suppression tends to decrease with increasing phase-shift displacement from the center position of the DFB grating. Typically, a front/back optical power ratio up to 2–3 can be achieved using this method.

The second solution is to employ a cleaved ( $R = 30\%$ ) or high reflection (HR,  $R \sim 60\text{--}90\%$ ) coated back facet. Depending on the chosen HR value, the optical output, or in other terms the external slope efficiency ( $\text{SLE} = \Delta P / \Delta I$ ), at the front facet can almost be doubled, associated with a high front-to-back asymmetry factor. However, this cavity design again largely affects the statistical single-mode yield which tends to drop significantly as a consequence of the random phase value of the reflective back facet relative to the DFB grating. Laser facets are created by a cleaving process, the positional precision of which is limited to values between  $\pm 5 \mu\text{m}$  and  $\pm 10 \mu\text{m}$ , unless special demanding technological measures are taken. In any case, it is impossible to perform the cleaving so as to result in a facet with a well-

**Fig. 3.16** Normalized intensity distribution at laser threshold along the DFB cavity for different positions of the  $\lambda/4$  phase shift ( $L = 300 \mu\text{m}$ ,  $\kappa = 50 \text{cm}^{-1}$ , both facets AR coated)



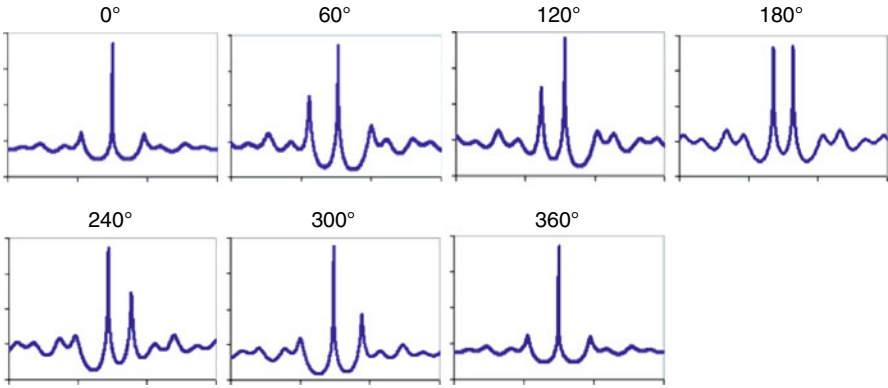


**Fig. 3.17** Normalized calculated optical output spectra at laser threshold of a  $\lambda/4$  phase-shifted DFB laser ( $L = 300 \mu\text{m}$ ,  $\kappa = 50 \text{ cm}^{-1}$ , AR/60 % facet coating) for different phase values at the back facet

defined phase value relative to the DFB grating. This would require nanometer-scale accuracy.

The strong influence of the back facet phase condition on the single-mode behavior is illustrated in Fig. 3.17. Here, the optical output spectra at the laser threshold of a  $\lambda/4$  phase-shifted DFB laser are depicted for different phase values. Their strong effect on the onset of the competing DFB modes is clearly visible. At phase  $0^\circ$ , the lasers behave purely single-moded, whereas at  $180^\circ$  they emit at the Bragg grating stop band modes (see Fig. 3.13). As a consequence, assuming an even phase distribution such lasers typically exhibit a single-mode yield of around 50 % only, depending on the specified SMSR limit. Along with this, a statistical fluctuation of the output power occurs.

To conclude, with traditional DFB laser designs there is a distinct trade-off between SM yield and achievable optical output power/slope efficiency: Two-sided AR-coated devices give high SM yields (virtually 100 %) but limited SLE values (typically  $\sim 0.25 \text{ mW/mA}$ ). Conversely, with AR/HR-coated DFB lasers the SM yield is significantly reduced to the 50 % range but high SLE values are achievable ( $> 0.4 \text{ mW/mA}$ ). For commercial applications, actually the best of both variants, i.e., high SM yield and high slope efficiency, is desired for obvious reasons.

DFB lasers are widely deployed in wavelength-division-multiplex (WDM) networks. To this end, special demands are posed on the accuracy of emission wavelength. With dense WDM (DWDM), a spacing of the transmission wavelength channels down to 50 GHz of optical frequency (equivalent to 0.4 nm at 1550 nm) is used, and respective DFB devices have to be assigned by selection. Because of the temperature dependence of the material refractive index, the wavelength of a DFB laser rises with temperature at a rate of about 0.1 nm/K, i.e., by a factor of 5 smaller than the gain spectrum ( $\sim 0.5 \text{ nm/K}$ ). For DWDM lasers, precise temperature adjustment and stabilization using a Peltier cooler is therefore mandatory to match the exactly specified DWDM wavelengths (“ITU grid”). Under such temperature-



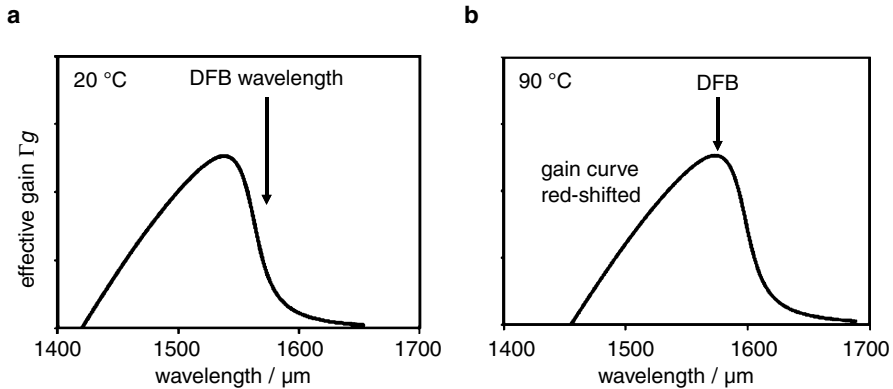


**Fig. 3.18** Schematic illustration of wavelength detuning of DFB lasers to optimize laser characteristics at high operation temperatures. The *drawn curve* represents the gain profile, and the *arrow* the position of the emission wavelength as defined by the DFB grating. **a** shows the normalized profiles' wavelength position at 20 °C and **b** at 90 °C

controlled conditions, modulation rates up to 10 Gbit/s are state of the art. Nowadays, there is a strong trend to deploy wavelength tunable transmitter devices (see Chap. 5) rather than fixed wavelength devices to both avoid selection and reduce inventory costs.

For single-channel (e.g., FTTH PON applications) and coarse WDM (CWDM) transmission systems, uncooled operation is required to eliminate cooling power and cooler costs. In the extreme case, the lasers need to be operated in the range from  $-40$  to  $+85$  °C. With CWDM applications ( $\Delta\lambda = 20$  nm channel spacing), quite a challenging fabrication tolerance of the lasing wavelength of only  $\pm 2.5$  nm has to be met to stay within a specified transmission window of 12.5 nm over the temperature range from 0 to 75 °C. To compensate for the lower gain at higher temperature – at least to a certain degree – the different temperature shift of the spectral gain and the DFB wavelength is exploited to optimize DFB laser diodes for high-temperature operation, as illustrated in Fig. 3.18.

At room temperature, the DFB wavelength is intentionally positioned on the long-wavelength side of the optical gain spectrum by adjusting the DFB grating accordingly. This design measure is referred to as “wavelength detuning.” With increasing temperature, differently from FP lasers, the emission wavelength shifts to the gain peak region to benefit from the higher gain and hence to assure fairly low threshold currents even at high operation temperatures. In this case, the resulting effective  $T_0$ -value is no longer related to material properties alone but is also detuning dependent.

In applications where cooled operation is applicable, wavelength detuning can also be used to optimize modulation parameters. If the DFB wavelength is detuned to the short-wavelength side of the gain peak, an increase in differential gain and thus a higher modulation bandwidth can be achieved (for further reading see

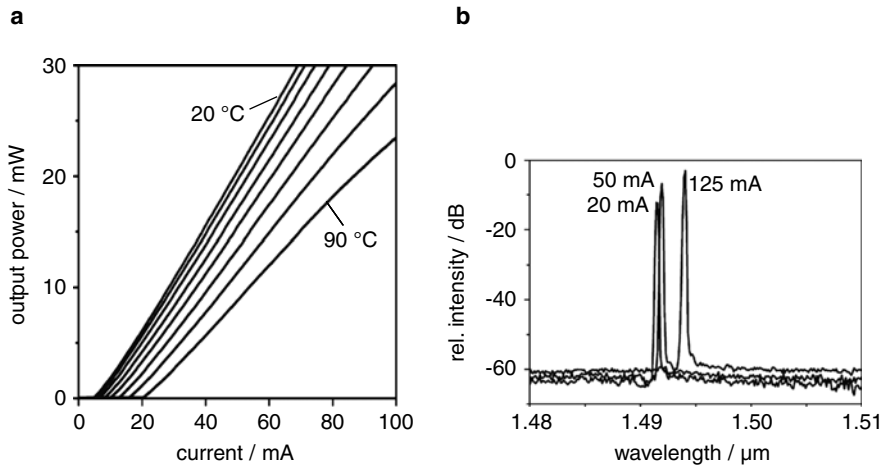


**Fig. 3.19** Representative  $P$ – $I$  curves of a 1490 nm BH–DFB laser diode designed for uncooled operation, 10 K temperature steps (a), and current-dependent emission spectra taken at 20 °C (b)

Chap. 4). This design measure is however limited by the associated increase of the threshold current with increasing deviation from the gain peak. To some extent this behavior may be compensated for by adjustment of the grating coupling strength or the use of a suitable HR back facet coating though this results in high-modulation bandwidth [30]. Along with the increase of the differential gain the Henry (or  $\alpha$ -) factor tends to decrease which has a crucial effect on the static and dynamic spectral linewidth of the emission wavelength. The former characteristic is essential with narrow-linewidth lasers required for, e.g., local oscillator lasers in coherent detection schemes, whereas the latter one describing linewidth broadening under modulation (“chirp effect”) largely affects dispersion-related transmission properties.

### 3.6.1.2 Performance of DFB Lasers

Representative output power characteristics are shown in Fig. 3.19 for an AR/HR-coated BH–DFB transmitter laser based on InGaAsP/InP and designed for uncooled operation. Room-temperature threshold currents around 5 mA and optical output power levels even exceeding 50 mW are obtainable with elaborated designs and today’s highly developed fabrication technology. Inherent to InP laser diodes is the relatively large material-related degradation of maximum output power and slope efficiency with increasing temperature. SMSR values  $> 50$  dB are readily achievable. It may not be taken for granted, however, that such values are maintained over the full operational current and temperature range. Instead, the single-mode behavior may get worse and even out-of-specification, which is of particular concern in the low-temperature region.

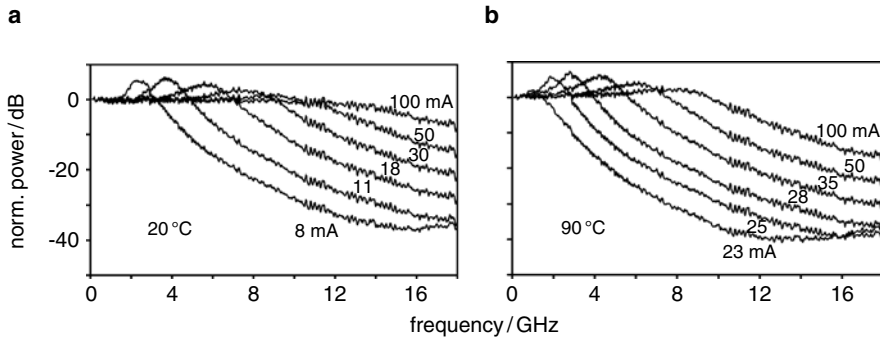


**Fig. 3.20** Small-signal modulation curves of an InGaAsP/InP BH-DFB-laser diode at 20°C (a) and 90°C (b); indicated bias currents including threshold currents

The frequency performance can be characterized by small-signal modulation curves, as shown in Fig. 3.20 for a device similar to the one demonstrated in Fig. 3.19. The characteristic  $-3$ -dB cut-off frequency is well known to increase with increasing bias current until a saturation limit is reached. At high operation temperature, the maximum modulation bandwidth tends to diminish rendering it difficult to modulate uncooled InGaAsP/InP DFB devices at 10 Gbit/s, at least at practical current conditions. InGaAlAs/InP-based lasers provide superior performance in this respect, thanks to their “inverse” QW band structure (Sect. 3.4), and are therefore prevailing for uncooled 10 Gbit/s applications to date (see also Chap. 4).

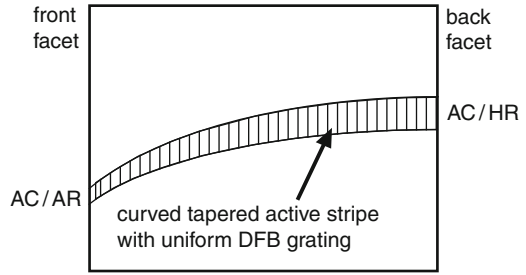
### 3.6.2 Advanced Single-mode Laser Structures

From the previous section it becomes apparent that ordinary DFB lasers do not meet all the requirements that the fiber optics industry desires. Hence, much effort has been made recently on achieving improved performance.

#### 3.6.2.1 Complex-coupled DFB Lasers

One approach has been the introduction of complex-coupled DFB lasers [31], already introduced above (see Fig. 3.12). Using this concept in conjunction with a reflective back facet, the single-mode yield indeed tends to substantially increase, compared to the conventional purely real-index-coupled DFB devices. Another motivation is their reduced optical feedback sensitivity [32]. Optical feedback in fact represents a major issue with DFB lasers: When laser light is reflected back from any external reflection site, this light, depending on the phase conditions, may render the laser to become multimode and even chaotic. A feedback sensitivity – described by the threshold ratio of reflected-to-emitted intensity at which multimode behavior starts to occur – as high as possible is desired to avoid an optical isolator. Mostly, an

**Fig. 3.21** Schematic top view of a curved stripe DFB laser indicating the basic architecture (*AC* as-cleaved, *AR* antireflection, *HR* high reflection, as-cleaved (30%) or coated)



optical isolator is needed to sufficiently eliminate this detrimental feedback effect. In spite of these advantages, complex-coupled DFB variants to date still appear to play only a minor role in commercial applications because of the more challenging fabrication technology and potentially larger reliability risks, although good lifetime results have been demonstrated [33].

### 3.6.2.2 Curved Stripe DFB Laser

An alternative innovative concept relying on conventional index coupling has been introduced recently, named curved stripe DFB (CSDFB) [34]. Initially designed to realize a tapered DFB diode by pursuing an implementation similar to the one sketched in Fig. 3.10, it turned out that the CSDFB structure offers additional features overcoming drawbacks of traditional DFB lasers. A schematic view of such a device is shown in Fig. 3.21. Inherent to the design is a curved active BH stripe tapered toward the front side. The resulting angled front facet provides an effective AR behavior, thus enabling these lasers to emit single mode even without any antireflection coating on the front facet. The purpose of the curved active stripe is as follows: Because of the tapered design, the effective index  $n_{\text{eff}}$  of the laser structure decreases in the longitudinal direction toward the front facet, and the Bragg condition (3.3) varies accordingly along the cavity. Rather than using a DFB grating with a gradually varying period, which would be quite expensive to define, the required spatial effective index variation is created by a properly designed curvature in conjunction with a constant period grating. In this way, established techniques for grating formation can be utilized, such as the inexpensive UV interference exposure technique.

The combined effect of decreasing optical gain and index coupling strength toward the front facet and the bending of the active stripe was consistently found to lead to efficient suppression of the short-wavelength Bragg mode. This feature is of special advantage if tight wavelength tolerances are required. Calculations similar to those depicted in Fig. 3.13 clearly indicate that the adverse effect of the phase variation at the as-cleaved (or HR) back facet on the single-mode yield is significantly reduced in CSDFB structures. As a consequence, these lasers were found to exhibit a single-mode yield in the higher 90% range even in the absence of any facet coating [34].

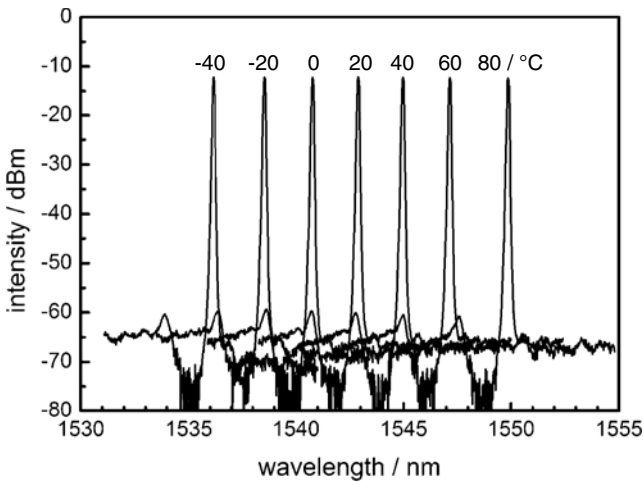


**Fig. 3.22** Emission spectra of a CSDFB laser diode in the temperature range from  $-40$  to  $+80$  °C

The apparently superior mode stability becomes manifest also when regarding the single-mode behavior over the operating temperature range. It has been verified that stable single-mode emission is well maintained particularly in the lower range ( $< 0$  °C). An example is given in Fig. 3.22.

Another evidence is the fact that CSDFB lasers prove to be less sensitive to optical feedback effects. Comparative measurements on index-coupled CSDFB and straight structures of otherwise comparable design indicated enhanced immunity against optical feedback by a factor of more than 3 dB [35]. By combining the CSDFB laser concept with complex coupling, further improvement by 3–4 dB could be achieved [36], as illustrated in Fig. 3.23.

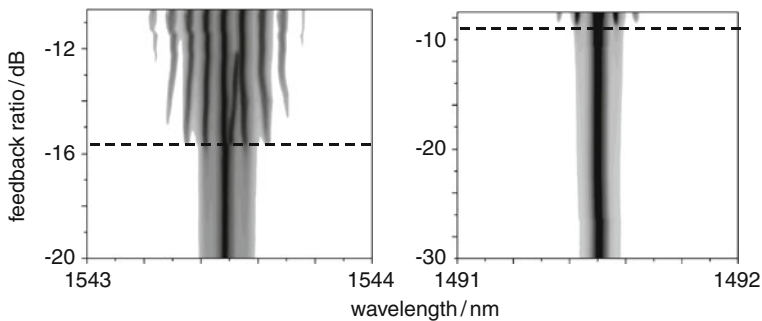
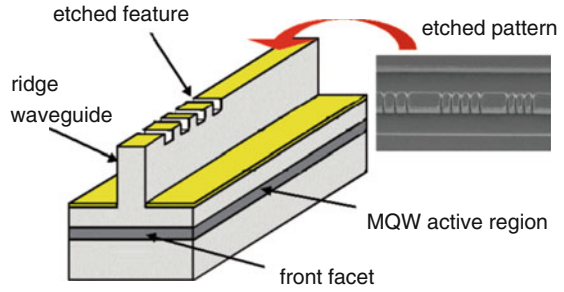


**Fig. 3.23** Comparative optical feedback measurements on a conventional (*straight stripe*) index-coupled and a complex-coupled curved stripe DFB laser of otherwise comparable design but slightly different wavelengths (measurements according to IEEE Standard 802.3ae™-2002, 1 mW in fiber); *dashed lines* indicate onset of multimode emission depicted by the lobes; note the different scale of the feedback ratio (= reflected/launched optical power)

**Fig. 3.24** Schematic view of a discrete-mode laser diode: the etched patterns in the laser ridge locally perturb the effective refractive index of the guided mode along very small sections of the laser cavity (after [37])



### 3.6.2.3 Discrete-mode Laser Diode

This variant relies on a new photonic crystal laser diode technology [37]. Basically, the discrete-mode laser is an RW Fabry–Pérot device which is converted into a single-mode laser by perturbing the effective refractive index along the cavity. This is accomplished by partially etching features into the ridge waveguide, which have a small overlap with the transverse field profile of the unperturbed mode. Suitable positioning of these interfaces allows the mirror loss spectrum to enhance one FP mode while suppressing the others resulting in single-mode operation. The detail of the modified reflectivity spectrum will depend on the number of perturbations, their topology, and configuration. The mechanism used to achieve the single-mode emission is clearly different from that in a DFB laser as the FP facets play a significant role in determining the emission spectrum of a discrete-mode laser device. In fact, the structure will not lase in the absence of feedback from the cleaved laser facets, opposite to DFB laser structures. The basic structure of a discrete-mode laser diode and spectral features are depicted in Figs. 3.24 and 3.25, respectively (after [37]).

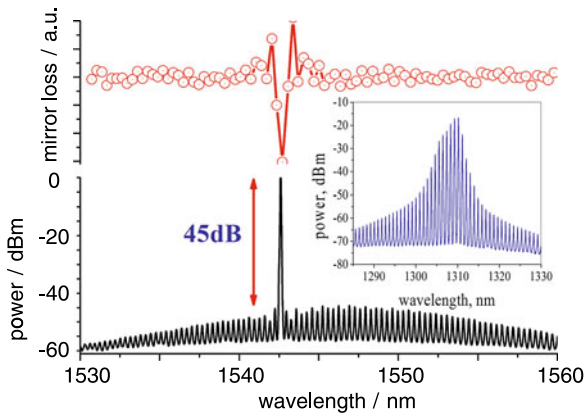


**Fig. 3.25** Spectral behavior of a discrete-mode laser: resulting single-mode spectrum (*bottom*); FP spectrum of the unperturbed RW structure (InGaAlAs MQW, 40 mA) (*inset*); and calculated mirror loss as a function of wavelength (*top*)

SMSR values of 45 dB and higher are readily achievable. Mode-hop free operation over the full-temperature range from  $-40$  to  $+95$  °C was demonstrated [38]. Very narrow spectral emission, characterized by a linewidth of as low as 200 kHz, has been demonstrated at reasonably low power levels ( $< 10$  mW) [39]. This feature renders discrete-mode lasers particularly useful as local oscillator lasers in coherent detection schemes. Furthermore, these lasers also show enhanced immunity against optical feedback. From the technological point of view, a noteworthy advantage is the fact that only a single epitaxial growth for the base wafer, without any regrowth, is required.

## 3.7 Surface-emitting Laser Diodes

### 3.7.1 Vertical-cavity Surface-emitting Laser

The vertical-cavity surface-emitting laser (VCSEL) is a modern laser concept which was proposed as early as in 1977 [40]. Devices emitting continuous waves at room temperature were reported in [41]. Since the mid-1990s, VCSELs based on GaAs have been intensely studied, and 850 nm devices are now widely used in optical systems ranging from the laser mouse to optical Ethernet modules. In fact, some 75 % of laser diodes commercially employed today are of the VCSEL type.

Different from edge-emitting laser-diodes, the optical beam of a VCSEL is coupled out perpendicularly to the wafer plane. Because of this design, the devices can be fully processed and characterized on-wafer without prior cleaving, resulting in a significant reduction of production costs. Owing to the very short optical cavity, VCSELs are always longitudinal and, for sufficiently small apertures, also transverse single mode. Additionally, VCSELs can be operated at very low power consumption levels of only a few tens of mW, rendering these devices extremely attractive for mobile applications, and “green” IT solutions in general. To mention a popular example, laser mice for personal computers are actually VCSEL-based ones representing an energy-efficient, coherent single-mode light source that is available for a few dollar cents only. Another emerging application field for VCSELs is optical interconnects for computers, for instance, in the form of active optical cables (AOCs). Low power consumption associated with low heat dissipation is a particular requirement for those “parallel optics” applications, regarding the extremely compact transceiver assemblies. The VCSEL devices employed for those applications are based on GaAs (emission wavelength  $< 1000$  nm) which have reached a high degree of maturity. This is true to a lesser degree for long-wavelength (1300–1600 nm) VCSELs which will be addressed here only. Different sophisticated designs and alternative material options have been studied to cope with their generally inferior physical properties.

### 3.7.1.1 Challenges of Long-wavelength VCSELs

With VCSELs, there are two principal issues that are mostly material related: (a) how to realize a low-loss laser cavity and (b) how to efficiently confine the laser current to the active area whilst concurrently avoiding excessive heating? To reach the lasing threshold mirror and cavity losses have to be compensated by the gain of the active laser section as given by the well-known equation

$$\Gamma g_{\text{th}} = \alpha_i + \alpha_m = \alpha_i - \frac{1}{2L_{\text{eff}}} \ln(R_t R_b) \quad (3.4)$$

with  $\Gamma$  denoting the optical confinement factor,  $g_{\text{th}}$  the threshold gain,  $\alpha_i$  and  $\alpha_m$  the internal and mirror losses,  $L_{\text{eff}}$  the effective resonator length, and  $R_t$  and  $R_b$  the top- and bottom-mirror power reflectivity, respectively.

Compared to edge-emitting lasers, VCSELs feature a much shorter gain section given by the thickness of the active region which amounts to a few tens of nanometers only. Whereas in the former case the optical reflectivity of around 30% of a cleaved FP laser facet is sufficiently high to reach laser threshold, much higher mirror reflectivities in excess of 99.5% are needed with VCSELs to keep mirror losses low. This kind of reflectors is typically realized by a thick stack of quarter-wave layers with alternating refractive index, the so-called Bragg mirrors (BM). The peak reflectivity of a BM can be calculated using (3.5) and (3.6), with  $\rho$  as amplitude and  $R$  as power reflectivity:

$$\rho = \pm \frac{r(n_m + n_2) - (n_m - n_2)}{(n_m + n_2) - r(n_m - n_2)} \quad \text{with } r = \pm \frac{\left(\frac{n_2}{n_1}\right)^{2N} - \frac{n_2}{n_s}}{\left(\frac{n_2}{n_1}\right)^{2N} + \frac{n_2}{n_s}}. \quad (3.5)$$

In (3.5) we choose “+” if the Bragg starts with the substrate  $n_s$ , followed by  $N$  times two layers of a quarter-wavelength, each with refractive indexes  $n_1$  and  $n_2$ , finally terminated by an infinite media  $n_m$ . In case the last layer next to the medium (of refractive index  $n_2$ ) is missing, i.e., for  $N - 1/2$  pairs, we choose “-”. For  $n_s = n_1$  and allowing whole mirror pairs only, (3.5) simplifies to:

$$R = \left| \frac{\frac{n_1}{n_m} - \left(\frac{n_1}{n_2}\right)^{2N}}{\frac{n_1}{n_m} + \left(\frac{n_1}{n_2}\right)^{2N}} \right|^2. \quad (3.6)$$

Assuming lossless materials and neglecting beam scattering, arbitrary BM reflectivity values can be achieved increasing with the number of mirror pairs and the refractive index contrast. Commonly, VCSEL mirrors have been implemented as epitaxially grown Bragg layer stacks utilizing lattice-matched semiconductor materials. Infrared GaAs VCSELs largely benefit from the comparably high index contrast obtainable with the naturally utilized GaAlAs compound system ( $\Delta n_{\text{GaAs-AlAs}} \sim 0.6$ ). With InP, different material choices are available: InP/InGaAsP, InP/InGaAlAs, and InAlAs/InGaAlAs. With any of these combinations, however, adjustable val-



ues are restricted to below nearly 0.3 (see Fig. 3.2), depending on the targeted laser wavelength. This implies not only lower spectral reflection bandwidth but also larger total BM thickness to achieve a given reflectivity, which again is associated with increased optical cavity loss. Another option is utilizing lattice-matched AlAsSb/GaAlAsSb (see Fig. 3.1) which offers similar  $\Delta n$ -values as the GaAlAs system but was nonetheless only rarely used [42], one reason being the poor thermal properties. Heat generation and extraction are of particular concern in any VCSEL device. In long-wavelength VCSELs ( $1300 \text{ nm} < \lambda < 1600 \text{ nm}$ ) made on the InP-based material platform, the BM inevitably contains quaternary compounds, at least for the “high-index” layer. These materials, however, are well known to exhibit very low thermal conductivity. Regarding optical losses, it should be kept in mind that free-carrier absorption in p-conducting materials scales with wavelength squared which principally tends to worsen the conditions in the case of long-wavelength VCSEL devices. Furthermore, the series resistance of p-doped BM stacks is substantially increased, causing excess heat generation. Because of these effects, long-wavelength VCSELs with a p-doped BM never showed satisfactory performance.

To mitigate these issues, advanced mirror concepts have been introduced recently, such as hybrid mirrors [43] and subwavelength high-contrast gratings [44, 45].

The second major issue relates to the optical mode and the current flow, which have to be confined in a vertical direction. With an out-coupling mirror on top, the current has to be injected laterally in a suitable way and then funneled to the center of the device via an aperture. With GaAs-based devices, this aperture is nowadays commonly formed by incorporating an insulating layer created by wet oxidation of a dedicated Al(Ga)As layer. This aperture formation technology is however practically not transferable to InP-related materials, even when using InGaAlAs of high Al content, because of the extremely low achievable oxidation rate. Therefore, other techniques such as buried tunnel junctions (BTJ) [46] or proton implants [45, 47] have been used to confine the current flow. Figure 3.26 shows a schematic VCSEL layout using BMs as the front and bottom mirror. The standing cavity wave is also depicted. It should be noted that for real devices sometimes several tens of semiconductor mirror pairs – each having a thickness equal to half the laser wavelength in the material – are needed due to the unfavorably low refractive-index contrast of the InP-based materials used.

### 3.7.1.2 Realization of Long-wavelength VCSELs

Because of the severe challenges originating from distinctly disadvantageous material properties of the InP materials, until the late 1990s the scientific community strongly doubted whether long-wavelength VCSELs could ever show reasonable performance allowing industrial application. In the last decade, however, strong efforts have been made in realizing such devices to result in remarkable results. Single-mode output powers in excess of 2 mW at 85 °C [48] and modulation speed in excess of 20 Gbit/s [49] have been demonstrated. This makes these devices strong

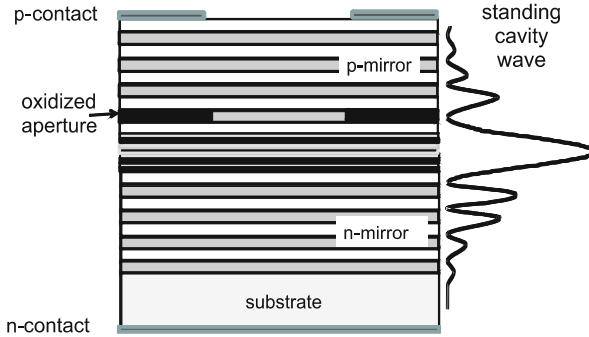


**Fig. 3.26** Schematic structure of a “classical” GaAs-based VCSEL with aperture formed by wet oxidation of an Al(Ga)As layer yielding electrically insulating material; note that in real devices the number of layer pairs constituting the Bragg mirrors may be as large as 30 each

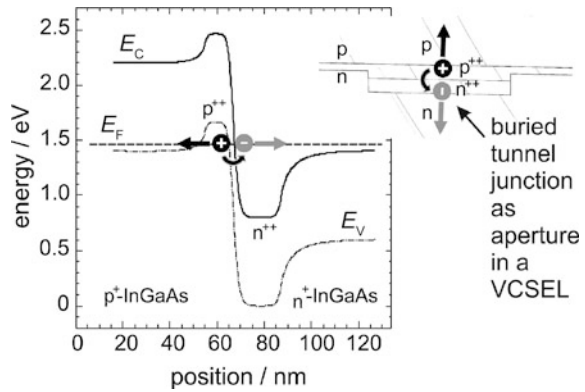
candidates as light sources in future optical access networks addressing high bandwidth, low cost, and energy efficiency.

Nowadays, three quite different design concepts have been pursued and have reached a fairly mature development stage. Respective VCSEL devices are commercially available. Besides utilizing structures that rely solely on InP materials, alternative GaAs-based structures have been developed, essentially to make use of the superior GaAs/Al(Ga)As mirror layers.

### 3.7.1.3 InP-based Buried Tunnel Junction VCSELs

This VCSEL design comprises a semiconductor top mirror made of InP materials (namely InGaAlAs), an MQW gain region, and an InGaAs  $n^+/p^+$  tunnel junction diode buried by an overgrown n-InP layer. The resulting BTJ forms the current aperture and thus defines the active area of the VCSEL. The purpose of the BTJ structure is to avoid lossy p-conducting layers in the VCSEL structure (except for the extremely thin  $p^+$  BTJ layer) [50, 51]. Basically, a tunnel junction is a very highly doped reversed biased pn junction, with the space-charge region so narrow that carriers are tunneling. Utilizing low-band gap material such as InGaAs drastically raises the tunneling rates and enables ohmic behavior. Figure 3.27 shows the band structure of a tunnel junction and a schematic illustrating its incorporation into a VCSEL structure. In that case, the highly doped tunnel junction has to be placed into an antinode of the optical standing cavity wave to avoid excessive loss. Such a tunnel structure is concurrently used to implement the current aperture simply by means of lithography. To this end, the epitaxial growth is stopped at the tunnel junction and the aperture defined by etching away the TJ layers where no current flow should occur in the device. After regrowth, a reverse-biased blocking diode is created in these outer parts of the VCSEL, whereas the current is guided through the aperture formed by the BTJ. Using this approach, both the current and the optical wave are confined in a self-aligned way.

**Fig. 3.27** Schematic band diagram and structure of a buried tunnel junction consisting of two  $n^+$ - and  $p^+$ -doped InGaAs layers. Because of the high doping levels, high current flow is generated under reverse bias conditions due to carrier tunneling converting the holes into electrons



After fabricating the VCSEL wafer composed of the above-mentioned layers, it is mounted upside down onto a gold heat sink, and the InP substrate is subsequently removed. The Au layer simultaneously serves as back-reflector, thus eliminating a second semiconductor BM. To achieve the very high levels of reflectivity needed, a few layers of dielectrics are incorporated on top of the plated gold to form a hybrid mirror. Figure 3.28 schematically depicts a complete BTJ-VCSEL chip.

BTJ-VCSELs, the fabrication of which appears to be rather sophisticated, have been realized with emission wavelengths ranging from  $< 1300$  nm up to even  $2300$  nm. Figure 3.29 shows representative  $P-I-V$  characteristics in dependence of the active area as given by the aperture. In Fig. 3.30, single-mode VCSEL output power of  $4$  mW recently achieved on  $1550$  nm devices (C. Neumeyr, private communication) is demonstrated along with an output curve at  $+85^\circ\text{C}$ . Record-high modulation speeds could be demonstrated with this design concept [49]. In

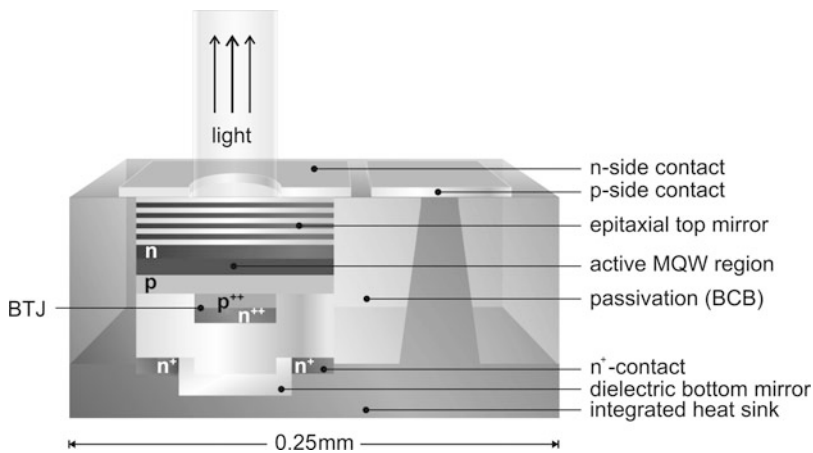


**Fig. 3.28** Structure of an InP-based BTJ-VCSEL (courtesy: VERTILAS GmbH)

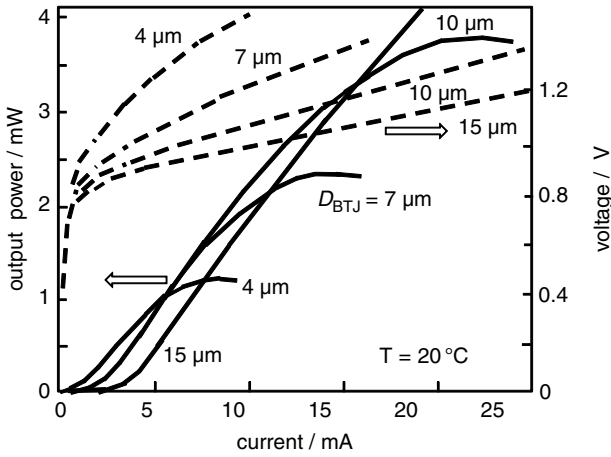


**Fig. 3.29** Output characteristics of a BTJ-VCSEL: influence of size of active area

**Fig. 3.30**  $P-I-V$  curve of a 1550 nm BTJ-VCSEL at  $20^\circ\text{C}$  and  $85^\circ\text{C}$

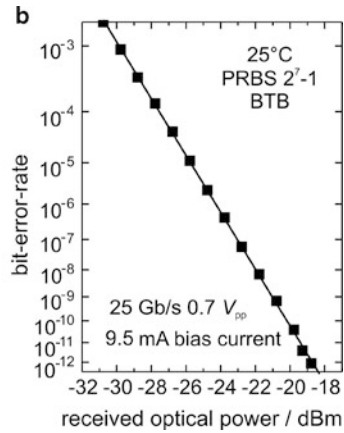
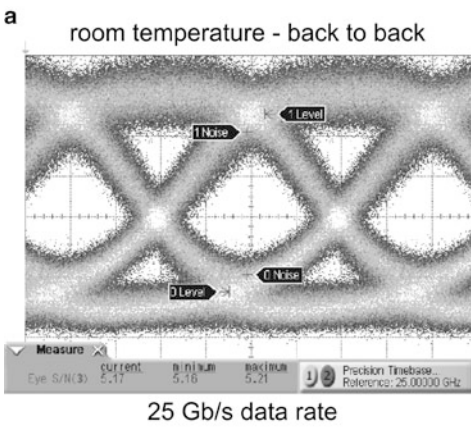
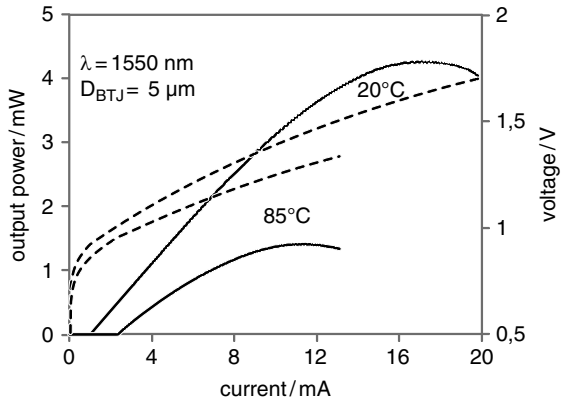


**Fig. 3.31** **a** 25 Gbit/s data eye diagram measured on a 1550 nm BTJ-VCSEL and **b** the corresponding bit-error-rate plot

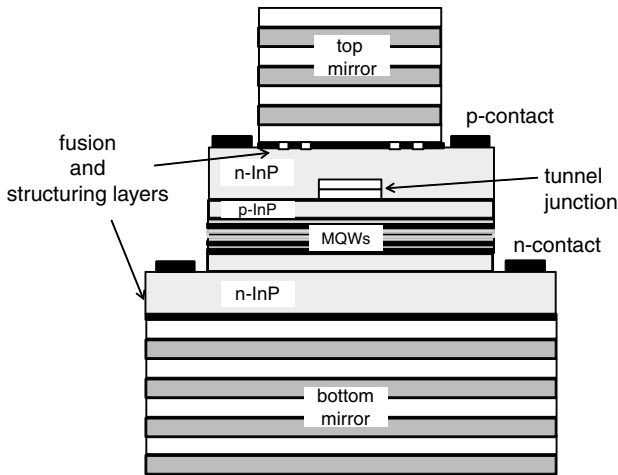


**Fig. 3.32** Cross section of a wafer-fused longer-wavelength VCSEL combining undoped GaAs-based reflectors and InP-based active material (after [52]). Two fusion steps are involved in the fabrication

Fig. 3.31a,b an eye diagram and a corresponding bit-error-rate plot at 25 Gbit/s data rate are presented. The transmission experiment was carried out at room temperature in back-to-back configuration.

#### 3.7.1.4 Wafer-fused Long-wavelength VCSELs

Another approach relies on growing GaAs/Al(Ga)As Bragg mirrors on GaAs substrate, and the active region on InP to combine specific advantages of these different material systems: high “long-wavelength” optical gain and reliable InP-based quantum wells, and the superior optical and thermal properties of the GaAs/Al(Ga)As reflectors. Starting from three different wafers, the final layer stack is created by applying two wafer-bonding steps. A respective structure is shown in Fig. 3.32 (after [52]). Again, a BTJ current aperture is incorporated. Undoped and thus low-loss BMs are employed requiring lateral intracavity contacts to be applied. This contacting scheme also avoids the situation where the VCSEL current flows across the bonded interfaces, which may exhibit rather poor electrical properties. Record-high single-mode optical powers (CW) of 6 mW at 20 °C and 2.5 mW at 80 °C were achieved at 1320 nm, and of 4 mW and 1.5 mW, respectively in the 1550 nm band [53], using this wafer-fusion-based technology. A value of 0.5 mW was reached at 2000 nm [52], a wavelength range of interest for spectroscopical applications. In the former cases, 10 Gbit/s modulation was demonstrated at 70 °C [53, 54]. The electrical parasitics associated with the intracavity contacts, however, tend to limit modulation speed and may severely impede the achievement of bit rates  $\gg$  10 Gbit/s.

### 3.7.1.5 Extending the Active Region on GaAs

A third route to accomplishing high-performance long-wavelength VCSELs utilizes fully GaAs-based structures. This allows using the well-established and mature GaAs-based VCSEL technology, employing common GaAs/Al(Ga)As mirrors and oxidized apertures (refer to Fig. 3.26). As the gain medium, different material options have been investigated, including GaInNAs material [55] where the addition of small amounts of nitrogen to strained InGaAs on GaAs (“diluted nitrides”) shifts the emission wavelength toward longer wavelengths (see also Sect. 4.2.4); In(Ga)As quantum-dot material [56]; and GaAsSb MQW layers [57]. All of these approaches were focused on VCSELs emitting in the 1300 nm range for data links. To extend the wavelength range significantly further proves to be more and more complicated, however. Active InGaSb-based QD gain medium was tried to achieve 1550 nm VCSEL emission [58].

Nitrogen-containing materials are not fully understood yet. They tend to decompose under certain conditions such as extreme temperatures or high current densities. These parameters appear to be particularly critical with VCSELs, which are typically driven at rather high current densities and whose active region suffers from self-heating. Indeed, lifetime issues have been encountered with GaInAsN-based VCSELs when operated at higher temperatures ( $\gtrsim 60^\circ\text{C}$ ). When aiming at high modulation speeds, high carrier and photon densities are needed to boost the relaxation oscillation frequency, i.e., the intrinsic bandwidth of the laser. Therefore, top performance and reliability are somehow contradictory in this approach but the success will depend on the quality of the nitrogen-containing layers. Nevertheless, reliable devices could be demonstrated using molecular beam epitaxial (MBE) growth [59], but wider commercialization is missing to date, despite the apparent advantages regarding device fabrication cost.

As an alternative to diluted nitrides, QD active material has also been investigated. Generally, however, QD-based VCSEL devices suffer from the small active volume limiting the total achievable gain. Because of this restriction, very high modulation speeds requiring high gain conditions could not be demonstrated yet [60]. It remains rather questionable whether QD technology may eventually represent the technology of choice for the realization of long-wavelength VCSEL devices.

### 3.7.2 Horizontal Cavity Surface-emitting Laser Concepts

There have been several approaches recently to combine surface emission with “normal” laser structures, that is, lasers with horizontal cavities. The aim of these developments is to benefit from the laser performance of those lasers while simultaneously retaining the economical advantages (e.g., on-wafer testing) of VCSEL devices. Like VCSELs, horizontal cavity surface-emitting lasers are also attractive light sources for hybrid integration technology as surface-mount devices on optical waveguide boards.

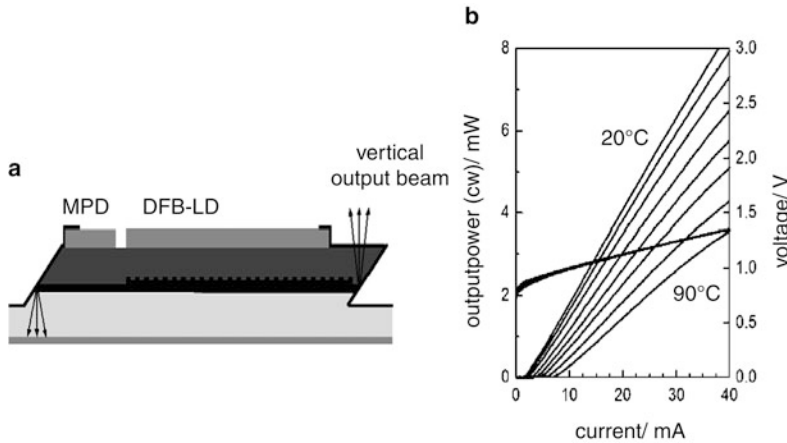


**Fig. 3.33** Schematic structure of a single-mode (DFB) HCSEL integrated with a monitor photodiode (MPD, **a**) and optical output characteristics (**b**)

### 3.7.2.1 Surface-emitting Lasers with Turning Mirrors

This laser type, known under the acronym HCSEL, is basically an edge-emitting laser comprising a  $45^\circ$  mirror facet for vertical out-coupling of the laser beam, as represented in Fig. 3.33. Both FP and DFB embodiments are feasible. The characteristics of HCSELs, including output power, beam shape, polarization stability, and wavelength precision, are basically the same as with their edge-emitting counterparts, whereas full on-wafer processing and on-wafer testability, packaging cost, and monolithic 2D-array fabrication are advantages that are shared with VCSELs. Further, epitaxial growth and manufacturing processes are identical to those utilized in the mature edge-emitter technology, apart from the additional etching process needed to form the  $45^\circ$  turning mirror. HCSELs can outperform VCSELs regarding specific advantages of edge emitters, such as higher output power and the possibility of monolithically integrating further devices in the horizontal plane, namely a monitor photodiode as indicated in Fig. 3.33. Conversely, HCSELs exhibit higher power consumption and larger beam divergence than VCSELs. Nonetheless, recent HCSEL developments have led to achieving appreciably low laser currents [61] which eventually have enabled employing low-power laser driver integrated circuits developed for VCSELs [62].

Recently, a concept similar to HCSELs was realized but with the  $45^\circ$  turning mirror formed so as to direct the output beam through the substrate. At the backside of the substrate, a collimating lens was monolithically integrated that yields a very low beam divergence of  $2.5^\circ$  only [63]. Using a  $1.3\ \mu\text{m}$  InGaAlAs/InP RW laser structure, 25 Gbit/s direct modulation up to  $100^\circ\text{C}$  was demonstrated on such lasers [64], called LISEL (lens integrated surface-emitting laser). Thanks to the substrate-side emission, they could be flip-chip mounted directly on high-frequency coplanar lines.

### 3.7.2.2 Surface-emitting Lasers with Second-order Grating

Another approach for surface-emitting lasers relies on exploiting second-order DFB gratings to direct the laser beam to vertical emission. In contrast to first-order gratings providing optical feedback in the longitudinal direction only, with second-order designs a substantial portion of the light is reflected into a vertical direction. Both second-order DBR [65, 66] and DFB structures [67] have been demonstrated. In the former case, one laser facet is replaced by a DBR grating, enabling longitudinal mode selection, optical feedback into the laser resonator as well as vertical deflection of the out-coupled optical light. In SE-DFB lasers the second-order grating can provide surface emission in the center of the DFB resonator [67] and can be designed to shape the optical output beam of the laser. It is, for instance, possible to focus the output beam into one or more spots or to optimize the beam quality [66]. Compared to HCSELs the challenge in manufacturing is shifted from the formation of a smooth  $45^\circ$  plane to lithographically defining complex high-precision gratings with nanoscale accuracy. Despite the existent advantages, to our knowledge such second-order grating deflection devices have not been commercialized so far.

## 3.8 Concluding Remarks

In this chapter we have covered the basics of InP-based long-wavelength semiconductor laser diodes, including material options, laser structures and related technologies, multi- and single-mode emitting lasers, and different variants of surface-emitting laser devices. Many of these components are commercially available today; nonetheless, continuous efforts are made to improve on their overall performance and on specific parameters, and to reduce fabrication costs. Reliability issues have been largely overcome but need to be revalidated whenever structural and technology changes are introduced. The different laser diodes addressed essentially exhibit modulation capability of up to 10 Gbit/s, at least at room-temperature conditions. However, there is a strong trend these days to push this limit to much higher values, namely  $>25$  Gbit/s and 40 Gbit/s and even more. Those developments are dealt with in the next chapter. A second major focus is on wavelength tunability which will be the subject of a third laser-related article, Chap. 5.

## References

1. R.N. Hall, G.E. Fenner, J.D. Kingsley, T.J. Soltys, R.O. Carlson, Coherent light emission from GaAs p-n junctions. *Phys. Rev. Lett.* **9**, 366–368 (1962)
2. M.I. Nathan, W.P. Dumke, G. Burns, F.H. Dill, G.J. Lasher, Stimulated emission of radiation from GaAs p-n junction. *Appl. Phys. Lett.* **1**, 62–64 (1962)
3. Z.I. Alferov, V.M. Andreev, V.I. Korolkov, E.L. Portnoi, D.N. Tretyakov, Injection properties of n-Al<sub>x</sub>Ga<sub>1-x</sub>As p-GaAs heterojunctions. *Sov. Phys. Semicond.* **2**, 843 (1969)



4. I. Hayashi, M.B. Panish, P.W. Foy, A low threshold room temperature injection laser. *IEEE J. Quantum Electron.* **QE-5**, 210–211 (1969)
5. J.J. Hsieh, Room temperature operation of GaInAsP/InP double heterostructure diode lasers emitting at 1.1  $\mu\text{m}$ . *Appl. Phys. Lett.* **28**, 283–285 (1976)
6. T. Yamamoto, K. Sakai, S. Akiba, Y. Suematsu, In<sub>1-x</sub>Ga<sub>x</sub>As<sub>y</sub>P<sub>1-y</sub>/InP DH lasers fabricated on InP(100) substrates. *IEEE J. Quantum Electron.* **QE-14**, 95–98 (1978)
7. G.H.B. Thompson, *Physics of Semiconductor Laser Devices* (Wiley, New York, 1980). ISBN: 0-471-27685-5
8. N. Grote, The III–V materials for Infra-red devices, in *Materials for Optoelectronics*, ed. by M. Quillec (Kluwer Academic, Amsterdam, 1996), pp. 153–183
9. K. Utaka, K. Kobayashi, Y. Suematsu, Lasing characteristics of 1.5–1.6  $\mu\text{m}$  GaInAsP/InP integrated twin-guide lasers with first-order distributed Bragg reflectors. *IEEE J. Quantum Electron.* **QE-17**, 651–658 (1981)
10. K. Kadoiwa, K. Ono, H. Nishiguchi, K. Matsumoto, Y. Ohkura, T. Yagi, p-substrate partially inverted buried heterostructure distributed feedback laser diode performance improvement by inserting Zn diffusion-stopping layer. *Jpn. J. Appl. Phys.* **45**, 7704–7708 (2006)
11. H. Sato, T. Tsuchuya, T. Kitatani, N. Takahashi, K. Oouchi, K. Nakahara, M. Aoki, Highly reliable 1.3  $\mu\text{m}$  InGaAlAs buried heterostructure laser diode for 10GbE, *Proc. 16th Internat. Conf. Indium Phosphide Relat. Mater.* (IPRM 2004) Kagashima, Japan, 2004, pp. 731–733.
12. W. Feng, J.Q. Pan, L.F. Wang, J. Bian, B.J. Wang, F. Zhou, X. An, L.J. Zhao, H.L. Zhu, W. Wang, Fabrication of InGaAlAs MQW buried heterostructure lasers by narrow stripe selective MOVPE. *J. Phys. D Appl. Phys.* **40**, 361–365 (2007)
13. Y. Matsui, H. Murai, S. Arahira, Y. Ogawa, A. Suzuki, Enhanced modulation bandwidth for strain-compensated InGaAlAs-InGaAsP MQW lasers. *IEEE J. Quantum Electron.* **34**, 1970–1978 (1998)
14. P.J.A. Thijs, E.A. Montie, T. van Dongen, Structures for improved 1.5  $\mu\text{m}$  wavelength lasers grown by LP-OMVPE; InGaAs-InP strained-layer quantum wells a good candidate. *J. Cryst. Growth* **107**, 731–740 (1991)
15. P.J.A. Thijs, J.J.M. Binsma, L.F. Tiemeijer, T. van Dongen, Improved performance 1.5  $\mu\text{m}$  wavelength tensile and compressively strained InGaAs-InGaAsP quantum well lasers, *Proc. 17th Europ. Conf. Opt. Commun.* (ECOC'91), Paris, France (1991), pp. 31–38
16. M.A. Newkirk, B.I. Miller, U. Koren, M.G. Young, M. Chien, R.M. Jopson, C.A. Burrus, 1.5  $\mu\text{m}$  multi quantum-well semiconductor optical amplifier with tensile and compressively strained wells for polarization-independent gain. *IEEE Photon. Technol. Lett.* **5**, 406–408 (1993)
17. T.J. Badcock, H.Y. Liu, K.M. Groom, C.Y. Jin, M. Gutierrez, M. Hopkinson, D.J. Mowbray, M.S. Skolnick, 1.3  $\mu\text{m}$  InAs/GaAs quantum-dot laser with low-threshold current density and negative characteristic temperature above room temperature. *Electron. Lett.* **42**, 922–923 (2006)
18. G.H. Duan, A. Shen, A. Akrouf, F. van Dijk, F. Lelarge, F. Pommereau, O. Le-Gouezigou, J.G. Provost, H. Gariah, High performance InP-based quantum dash semiconductor mode-locked lasers for optical communications. *Bell Labs Tech. J.* **14**, 63–84 (2009)
19. C.S. Lee, W. Guo, D. Basu, P. Bhattacharya, High performance tunnel injection quantum dot comb laser. *Appl. Phys. Lett.* **96**, 101107 (2010)
20. M. Moehrle, H. Roehle, A. Sigmund, A. Suna, F. Reier, High-performance all-active tapered 1550 nm InGaAsP BH-FP lasers, *Proc. 14th Internat. Conf. Indium Phosphide Relat. Mater.* (IPRM 2002), Stockholm, 2002, pp. 27–30
21. S.W. Park, J.H. Han, Y.T. Han, S.S. Park, B.Y. Yoon, B.K. Kim, H.K. Sung, J.I. Song, Two-step laterally tapered spot-size convertor 1.55  $\mu\text{m}$  laser diode having a high slope efficiency. *IEEE Photon. Technol. Lett.* **18**, 2138–2140 (2006)
22. H. Kobayashi, M. Ekawa, N. Okazaki, O. Aoki, S. Ogita, H. Soda, Tapered thickness MQW waveguide BH MQW lasers. *IEEE Photon. Technol. Lett.* **6**, 1080–1081 (1994)
23. A. Guermache, V. Voiriot, N. Bouche, F. Lelarge, D. Locatelli, R.M. Capella, J. Jacquet, 1 W fiber coupled power InGaAsP/InP 14xx pump laser for Raman amplification. *Electron. Lett.* **40**, 1535–1536 (2004)

24. M. Haverkamp, G. Kochem, K. Boucke, E. Schulze, H. Roehle, 1.1 W four-wavelength Raman pump using BH lasers, *Opt. Fiber Commun. Conf. and Nat. Fiber Opt. Eng. Conf. (OFC/NFOEC'07)*, Techn. Digest (Anaheim, CA, USA, 2007), paper OMK7
25. H. Kogelnik, C.V. Shank, Coupled-wave theory of distributed feedback lasers. *J. Appl. Phys.* **43**, 2327–2335 (1972)
26. M. Kamp, J. Hofmann, F. Schaefer, M. Reinhard, M. Fischer, T. Bleuel, J.P. Reithmaier, A. Forchel, Lateral coupling – a material independent way to complex coupled DFB lasers. *Opt. Mater.* **17**, 19–25 (2001)
27. H. Burkhard, S. Hansmann, Transmitters, in *Fiber Optic Communication Devices*, ed. by N. Grote, H. Venghaus (Springer, Berlin, 2001), pp. 71–116
28. G.P. Agrawal, A.H. Bobeck, Modeling of distributed-feedback semiconductor lasers with axially-varying parameters. *IEEE J. Quantum Electron.* **24**, 2407–2414 (1988)
29. A.J. Lowery, A. Keating, C.N. Murtonen, Modeling the static and dynamic behavior of quarter-wave-shifted DFB lasers. *IEEE J. Quantum Electron.* **28**, 1874–1883 (1992)
30. A.K. Verma, M. Steib, Y.L. Ha, T. Sudo, 25 Gbps 1.3  $\mu\text{m}$  DFB laser for 10–25 km transmission in 100 GbE systems, *Opt. Fiber Commun. Conf. and Nat. Fiber Opt. Eng. Conf. (OFC/NFOEC'09)*, Techn. Digest (San Diego, CA, USA, 2009), paper OThT2
31. G.P. Li, T. Makino, R. Moore, N. Puetz, K.-W. Leong, H. Lu, Partly gain-coupled 1.55  $\mu\text{m}$  strained-layer multiquantum-well DFB laser. *IEEE J. Quantum Electron.* **29**, 1736–1742 (1993)
32. J. Kreissl, W. Brinker, E. Lenz, T. Gaertner, W. Rehbein, S. Bauer, B. Sartorius, Isolator-free directly modulated complex-coupled DFB lasers for low cost applications, *Opt. Fiber Commun. Conf. (OFC'05)*, Techn. Digest (Anaheim, CA, USA, 2005), vol. 4, pp. 3–4
33. J. Kreissl, U. Troppenz, W. Rehbein, T. Gaertner, P. Harde, M. Radziunas, 40 Gbit/s directly modulated passive feedback laser with complex-coupled DFB section, *Proc. 33rd Europ. Conf. Opt. Commun. (ECOC'07)*, Berlin, Germany (2007), paper We.8.1.4
34. M. Moehrle, A. Sigmund, A. Suna, L. Moerl, W. Fuerst, A. Dounia, W.D. Molzow, High single-mode yield, tapered 1.55  $\mu\text{m}$  DFB lasers for CWDM applications, *Proc. 31st Europ. Conf. Opt. Commun. (ECOC'05)*, Glasgow, UK (2005), paper Tu 4.5.4
35. L. Moerl, M. Moehrle, W. Brinker, A. Sigmund, N. Grote, Tapered 1550 nm DFB lasers with low feedback sensitivity, *Proc. 32th Europ. Conf. Opt. Commun. (ECOC'06)*, Cannes, France (2006), paper Mo3.4.3
36. M. Moehrle, W. Brinker, C. Wagner, G. Przyrembel, A. Sigmund, W.D. Molzow, First complex coupled 1490 nm CSDFB lasers: High yield, low feedback sensitivity, and uncooled 10 Gbit/s modulation, *Proc. 35th Europ. Conf. Opt. Commun. (ECOC'09)*, Vienna, Austria (2009), paper We 8.1.2
37. C. Herbert, D. Jones, A. Kaszubowska, B. Kelly, M. Rensing, J. O'Carroll, P.M. Anandarajah, P. Perry, L.P. Barry, J. O'Gorman, Discrete mode lasers for communication applications. *IET J. Optoelectron.* **3**, 1–17 (2009)
38. R. Phelan, B. Kelly, J. O'Carroll, C. Herbert, A. Duke, J. O'Gorman,  $-40^\circ\text{C} < T < 95^\circ\text{C}$  mode-hop-free operation of uncooled AlGaInAs-MQW discrete-mode laser diode with emission at  $\lambda = 1.3 \mu\text{m}$ . *Electron. Lett.* **45**, 43–45 (2009)
39. B. Kelly, R. Phelan, D. Jones, C. Herbert, J. O'Carroll, M. Rensing, J. Wendelboe, C.B. Watts, A. Kaszubowska-Anandarajah, P. Perry, C. Guignard, L.P. Barry, J. O'Gorman, Discrete mode laser diodes with very narrow linewidth emission. *Electron. Lett.* **43**, 1282–1283 (2007)
40. K. Iga, Surface-emitting laser – its birth and generation of new optoelectronics field. *IEEE J. Sel. Top. Quantum Electron.* **6**, 1201–1215 (2000)
41. F. Koyama, S. Kinoshita, K. Iga, Room-temperature continuous wave lasing characteristics of GaAs vertical cavity surface-emitting laser. *Appl. Phys. Lett.* **55**, 221–222 (1989)
42. S. Nakagawa, E. Hall, G. Almuneau, J.K. Kim, D.A. Buell, H. Kroemer, L.A. Coldren, 1.55  $\mu\text{m}$  InP-lattice-matched VCSELs with AlGaAsSb-AlAsSb DBR. *IEEE J. Sel. Top. Quantum Electron.* **7**, 224–230 (2001)
43. M. Müller, W. Hofmann, G. Böhm, M.-C. Amann, Short-cavity long-wavelength VCSELs with modulation-bandwidth in excess of 15 GHz. *IEEE Photon. Technol. Lett.* **21**, 1615–1617 (2009)

44. W. Hofmann, C. Chase, M. Müller, Y. Rao, C. Grasse, G. Böhm, M.-C. Amann, C. Chang-Hasnain, Long-wavelength high-contrast grating vertical-cavity surface-emitting laser. *IEEE Photon. Technol. Lett.* **22**, 415–422 (2010)
45. C. Chase, Y. Rao, W. Hofmann, C. Chang-Hasnain, 1550-nm high contrast grating VCSEL. *Opt. Express* **18**, 9358–9365 (2010)
46. M. Ortsiefer, R. Shau, G. Böhm, F. Köhler, G. Abstreiter, M.-C. Amann, Low-resistance InGa(Al)As tunnel junctions for long-wavelength vertical-cavity surface-emitting lasers. *Jpn. J. Appl. Phys.* **39**, 1727–1729 (2000)
47. K. Yashiki, N. Suzuki, K. Fukatsu, T. Anan, H. Hatakeyama, M. Tsuji, 1.1  $\mu\text{m}$ -range high-speed tunnel junction vertical-cavity surface-emitting lasers. *IEEE Photon. Technol. Lett.* **19**, 1883–1885 (2007)
48. E. Kapon, A. Sirbu, Long-wavelength VCSELs: Power – efficient answer. *Nat. Photon.* **3**, 27–29 (2009)
49. W. Hofmann, M. Müller, A. Nadtochiy, C. Meltzer, A. Mutig, G. Böhm, J. Roskopf, D. Bimberg, M.-C. Amann, C. Chang-Hasnain, 22-Gbit/s long wavelength VCSELs. *Opt. Express* **17**, 17547–17554 (2009)
50. M. Ortsiefer, R. Shau, G. Böhm, F. Köhler, M.-C. Amann, Room-temperature operation of index-guided 1.55  $\mu\text{m}$  InP-based vertical-cavity surface-emitting laser. *Electron. Lett.* **36**, 437–438 (2000)
51. N. Nishiyama, C. Caneau, B. Hall, G. Guryanov, M.H Hu, X.S. Liu, M.J. Li, R. Bhat, C.E. Zah, Long-wavelength vertical-cavity surface-emitting lasers on InP with lattice matched AlGaInAs–InP DBR grown by MOCVD. *IEEE J. Sel. Top. Quantum Electron.* **11**, 990–998 (2005)
52. A. Mereuta, V. Iakovlev, A. Caliman, A. Syrbu, P. Royo, A. Rudra, E. Kapon, InAlGaAs – AlGaAs wafer fused VCSELs emitting at 2  $\mu\text{m}$  wavelength. *IEEE Photon. Technol. Lett.* **20**, 24–26 (2008)
53. A. Syrbu, A. Mereuta, V. Iakovlev, A. Caliman, P. Royo, E. Kapon, 10 Gbps VCSELs with high single mode output in 1310 nm and 1550 nm wavelength bands, *Conf. Opt. Fiber Commun. Conf. and Nat. Fiber Opt. Eng. Conf. (OFC/NFOEC'08)*, Techn. Digest (San Diego, CA, USA, 2008), paper OThS2
54. A. Mircea, A. Caliman, V. Iakovlev, A. Mereuta, G. Suruceanu, C.A. Berseth, P. Royo, A. Syrbu, E. Kapon, Cavity mode – gain peak tradeoff for 1320 nm wafer-fused VCSELs with 3-mW single-mode emission power and 10 Gbit/s modulation speed up to 70 °C. *IEEE Photon. Technol. Lett.* **19**, 1221–123 (2007)
55. H. Riechert, A. Ramakrishnan, G. Steinle, Development of InGaAsN-based 1.3  $\mu\text{m}$  VCSELs. *Semicond. Sci. Technol.* **17**, 892–897 (2002)
56. J.A. Lott, N.N. Ledentsov, V.M. Ustinov, N.A. Maleev, A.E. Shukov, A.R. Kovsh, M.V. Maximov, B.V. Volovik, Z.I. Alferov, D. Bimberg, InAs-InGaAs quantum dot VCSEL's. *Electron. Lett.* **36**, 1384–1385 (2000)
57. P. Dowd, S.R. Johnson, S.A. Field, M. Adamczyk, S.A. Chaparro, J. Joseph, K. Hilgers, M.P. Horning, K. Shiralagi, Y.H. Zhang, Long wavelength GaAsP/GaAs/GaAsSb VCSELs on GaAs substrates for communication applications. *Electron. Lett.* **39**, 978–988 (2003)
58. N. Yamamoto, K. Akahane, S. Gozu, A. Ueta, N. Ohtani, 1.55  $\mu\text{m}$ -waveband emissions from Sb-based quantum-dot vertical-cavity surface-emitting laser structures fabricated on GaAs substrate. *Jpn. J. Appl. Phys.* **45**, 3423–3426 (2006)
59. J. Jewell, L. Graham, M. Crom, K. Maranowski, J. Smith, T. Fanning, M. Schnoes, Commercial GaInNAs VCSELs grown by MBE. *phys. stat. sol. (c)* **5**, 2951–2956 (2008)
60. M. Laemmlin, G. Fiol, M. Kuntz, F. Hopfer, A. Mutig, N.N. Ledentsov, A.R. Kovsh, C. Schubert, A. Jacob, A. Umbach, D. Bimberg, Quantum dot based photonic devices at 1.3  $\mu\text{m}$ : Direct modulation, mode-locking, SOAs and VCSELs. *phys. stat. sol. (c)* **3**, 391–394 (2006)
61. M. Moehrle, J. Kreissl, W.D. Molzow, G. Przyrembel, C. Wagner, A. Sigmund, L. Moerl, N. Grote, Ultra-low 1490 nm surface-emitting BH-DFB laser diode with integrated monitor photodiode, *Proc. 22th Internat. Conf. Indium Phosphide Relat. Mater. (IPRM 2010)*, Takamatsu, Japan, 2010, pp. 55–58

62. M. Moehrle, J. Kreissl, A. Sigmund, G. Przyrembel, N. Grote, V. Plickert, I. Schlosser, K. Droegemüller, T. Neuner, 1490 nm surface emitting DFB laser diodes operated by VCSEL driver ICs, *Proc. 17th OptoElectron. Commun. Conf.* (OECC 2012), Busan, Korea, 2012 (in press)
63. K. Adachi, K. Shinoda, T. Fukamachi, T. Shiota, T. Kitatani, K. Hosomi, Y. Matsuoka, T. Sugawara, M. Aoki, A 1.3  $\mu\text{m}$  lens-integrated horizontal-cavity surface-emitting laser with direct and highly efficient coupling to optical fibers, *Opt. Fiber Commun. Conf. and Nat. Fiber Opt. Eng. Conf.* (OFC/NFOEC'09), Techn. Digest (San Diego, CA, USA, 2009), paper JThA31
64. K. Adachi, K. Shinoda, T. Shiota, T. Fukamachi, T. Kitatani, K. Hosomi, Y. Matsuoka, T. Sugawara, M. Aoki, 100 °C, 25 Gbit/s direct modulation of 1.3  $\mu\text{m}$  surface emitting laser, *Conf. Lasers Electro-Opt.* (CLEO/QELS 2010), Techn. Digest (San Jose, USA, 2010), paper CME4
65. L. Vaissie, O.V. Smolski, A. Mehta, E.G. Johnson, High efficiency surface-emission laser with subwavelength antireflection structure. *IEEE Photon. Technol. Lett.* **17**, 732–734 (2005)
66. P. Modh, J. Backlund, J. Bengtsson, A. Larsson, N. Shimada, T. Suhara, Multifunctional gratings for surface-emitting lasers: Design and implementation. *Appl. Opt.* **42**, 4847–4854 (2003)
67. G. Witjaksono, S. Li, J.L. Lee, D. Botez, W.K. Chan, Single-lobe, surface-normal beam surface emission from second-order distributed feedback lasers with half-wave grating phase. *Appl. Phys. Lett.* **83**, 5365–5367 (2003)

# Chapter 4

## Ultrafast Semiconductor Laser Sources

Masahiro Aoki

**Abstract** This chapter reviews recent technological progress in the development of ultrafast light sources for achieving small footprint and low-power consumption optical transceivers. The focus is on various important light sources, for example, directly modulated diode lasers with high optical-gain materials, low-chirp externally modulated diode lasers, and ultrafast diode lasers with new structure and modulation scheme. The coverage of the topics starts with an in-depth theoretical treatment of key characteristics and dependences, illustrates typical realizations of ultrafast diode lasers and integrated laser-modulators, and includes relevant operation and performance characteristics as well.

### 4.1 Introduction

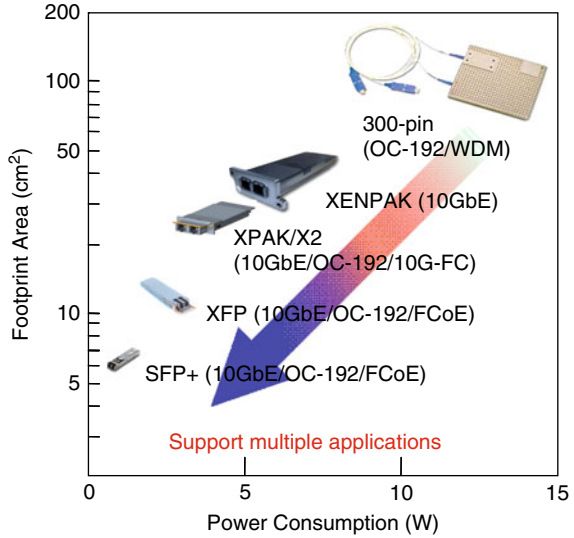
Since the recovery from the “dot-com bubble” (or “information technology bubble”) that occurred at the beginning of this century, the demand for highly efficient transmission of large amounts of data has soared with the explosive growth of broadband/broadgather data networks. Core/edge routers, switches, and data servers are now essential for information and communications technology (ICT), providing the infrastructure for our daily lives and our business activities in today’s ICT-based society. High-end ICT equipment depends heavily on fast optical data transmission technologies. Such technologies are essential not only in communication networks (for both telecommunications and mobile backhaul communication), but also in storage networks (so-called fiber channels) as well as in local area networks.

Common technological keys enable high data throughput, high port densities, and, at the same time, cost effectiveness. The total system performance depends

---

M. Aoki (✉)  
Hitachi, Ltd., Research & Development Group, 1-6-1, Marunouchi, Chiyoda-ku, Tokyo 100-8220,  
Japan  
e-mail: masahiro.aoki.ev@hitachi.com

**Fig. 4.1** Footprint area and power consumption of 10 Gbit/s optical transceivers



heavily both on the data throughput of each channel port and on the integration density determined by the assembly size and power consumption of the components. This is why gigabit-per-second (Gbit/s) class optical transceivers with low power consumption and small footprints are so important. An example of the technology trend of optical transponders used for 10 Gbit/s systems is shown in Fig. 4.1, which plots the relationship between module footprint and total power consumption for several types of standard transceiver modules.

The standard 10 Gbit/s optical transceivers started with 300 pins in 2000 [1], with a large footprint (ca. 100 cm<sup>2</sup>) and high-power consumption (ca. 15–20 W). To meet the demands for reduced size and power consumption, several types of de facto standard 10 Gbit/s transceiver packages – XENPAK [2], XPAK [3], X2 [4], XFP [5], and SFP+ [6] – have been developed and, as a result, the footprint and power consumption have been reduced in rapid succession. Moreover, the optical connector has changed from a pigtail to a receptacle, thus simplifying the assemblies. Currently, multiprotocol data rates are feasible and the cost of the components has decreased. Nowadays, the system requirements for the components exceed 10 Gbit/s, and 40–100 Gbit/s optical transceivers are under development. In fact, in mid 2010, a new standard (IEEE 802.3ba [7]) for 40 G- and 100 G-Ethernet was approved, relying on wavelength-multiplexed 4 × 10 Gbit/s, 10 × 10 Gbit/s, and 4 × 25 Gbit/s transmission schemes. For the latter scheme, laser sources with specified emission wavelengths around 1.3 μm (four wavelengths with 800 GHz spacing, referred to as LAN-CWDM (Local Area Network Coarse Wavelength Division Multiplexing)) are required that are capable of generating 25 Gbit/s bit streams. To achieve 40 Gbit/s transmission, the current 4-lane 10 Gbit/s approach is likely to be replaced by a serial 1 × 40 Gbit/s solution as the next generation, and developments for 400 G-Ethernet are already on the horizon. For implementing respective multi-lane transmitter modules, 40 Gbit/s lasers will be needed as key building blocks.

In order to reduce the size and power consumption of optical modules, lower-current/voltage drivability is crucial, and the elimination of thermoelectric coolers is highly desired. The keys to meeting these requirements are high-speed, uncooled semiconductor laser sources with small drive current/voltage. This chapter reviews the recent technological progress in ultrafast light sources for achieving small footprints and low-power consumption optical transceivers. We address several important light source devices, for example, directly modulated diode lasers with high-optical gain materials, externally modulated diode lasers, and ultrafast diode lasers exploiting new structures and modulation schemes.

## 4.2 Ultrafast Directly Modulated Laser Sources

### 4.2.1 High-speed Characteristics of Directly Modulated Lasers

The small-signal frequency response  $R(f)$  of a diode laser is derived from the rate equations that describe the interaction between the carrier density  $N$  and the photon density  $S$  in the active medium of a laser [8]. Above the threshold condition, these are expressed as

$$\frac{dN}{dt} = \frac{I}{eV} - v_g \frac{dg}{dN} (1 - \varepsilon S)(N - N_T)S - \frac{N}{\tau_N}, \quad (4.1)$$

$$\frac{dS}{dt} = v_g \frac{dg}{dN} \xi (N - N_T)(1 - \varepsilon S)S - \frac{S}{\tau_P} + \xi \beta \frac{N}{\tau_N}, \quad (4.2)$$

where  $I$  is the current injected into the active region of total volume  $V$ ,  $e$  is the electron charge,  $v_g$  is the group velocity of light in the laser medium,  $dg/dN$  is the differential gain,  $\varepsilon$  is the gain saturation coefficient,  $N_T$  is the transparency carrier density,  $\tau_N$  is the carrier lifetime,  $\tau_P$  is the photon lifetime,  $\xi$  is the optical confinement factor, and  $\beta$  is the spontaneous emission fraction for lasing. Assuming small signal current modulation (i.e.,  $I(t) = I_0 + \delta I_1 e^{j\omega t}$ ),  $R(f)$  is expressed as

$$R(f) = \frac{f_r^4}{(f^2 - f_r^2)^2 + f^2 \Gamma^2 / (2\pi)^2} \frac{1}{1 + (2\pi C_{ld} R_{ld} f)^2}, \quad (4.3)$$

where  $f_r$  is the relaxation oscillation frequency,  $\Gamma$  is the damping constant, and  $C_{ld} R_{ld}$  is the laser parasitic constant (the index “ld” denotes laser diode).  $f_r$  and  $\Gamma$  are expressed as

$$f_r = \frac{1}{2\pi} \sqrt{v_g \frac{dg}{dN} (1 - \varepsilon S) \eta_i \frac{\xi}{eV} (I - I_{th})}, \quad (4.4)$$

$$\Gamma = \frac{1}{\tau_N} + v_g \frac{dg}{dN} S + \frac{\varepsilon S}{\tau_P} = \frac{1}{\tau_N} + K f_r^2, \quad (4.5)$$

where  $\eta_i$  is the internal quantum efficiency.  $K$  is called the nonlinear  $K$ -factor and is expressed as

$$K = \frac{4\pi^2}{v_g} \left( \frac{\varepsilon}{dg/dN} + \frac{1}{\alpha_m + 2\alpha_{th}} \right), \quad (4.6)$$

with  $\alpha_m$  and  $\alpha_{th}$  being the mirror loss and lasing threshold gain, respectively.

It is apparent from (4.3), that in order to achieve high-speed lasers, it is important to enhance the relaxation oscillation frequency  $f_r$  or to reduce the laser parasitic constant  $C_{ld}R_{ld}$  and the damping constant  $\Gamma$ . The quantitative effects of these factors on the high-speed performance are discussed below.

**Reduction of laser parasitic constant  $C_{ld}R_{ld}$**  From (4.3), the CR (capacitance–resistance)-limited frequency bandwidth  $f_{3\text{dB}}^{\text{CR}}$ , where  $f_{3\text{dB}}$  is the 3 dB-down bandwidth, is expressed as

$$f_{3\text{dB}}^{\text{CR}} = \frac{1}{2\pi C_{ld}R_{ld}}. \quad (4.7)$$

With today's device/process techniques in III–V semiconductor-based optoelectronics, laser capacitances  $C_{ld}$  can be designed to be less than a few hundred femtofarads (fF). Moreover, the laser series resistance,  $R$ , is in the range from several ohms to several tens of ohms ( $\Omega$ ). If we assume  $C_{ld} = 400$  fF and  $R_{ld} = 10 \Omega$ , then the calculated value of  $f_{3\text{dB}}^{\text{CR}}$  is 40 GHz. This simply means that 40 Gbit/s direct modulation is theoretically feasible in terms of laser parasitics.

**Enhancement of relaxation oscillation frequency  $f_r$**  By solving  $R(f_{3\text{dB}}^{\text{fr}}) = 1/2$  for the condition  $C_{ld}R_{ld} = 0$ ,  $\Gamma = 0$ , we get

$$f_{3\text{dB}}^{\text{fr}} = \sqrt{1 + \sqrt{2}} f_r \cong 1.55 f_r. \quad (4.8)$$

The relaxation oscillation frequency  $f_r$  is governed by the resonant oscillation behavior between carriers and photons that occurs in a laser resonator, and the laser light output can never respond to a rapidly changing electrical input signal any faster than  $f_r$ . In other words,  $f_r$  is the essential parameter that determines the dynamic limit of semiconductor diode lasers.

**Reduction of damping constant  $\Gamma$**  Damping is known to originate from nonlinear gain saturation, and it adversely affects the laser dynamics. It not only lowers the resonant peak in  $R(f)$ , but also reduces the frequency bandwidth, especially in the high-frequency range above 20 GHz.

Again, by solving  $R(f_{3\text{dB}}^K) = 1/2$  for  $C_{ld}R_{ld} = 0$ ,  $f_r = \infty$ , we get

$$f_{3\text{dB}}^K = 2\sqrt{2\pi}/K. \quad (4.9)$$

In fact, the nonlinear  $K$ -factor is typically 0.3 ns for InGaAsP/InP-based quantum well lasers, and the corresponding  $f_{3\text{dB}}^K$  is calculated to be about 30 GHz. This es-



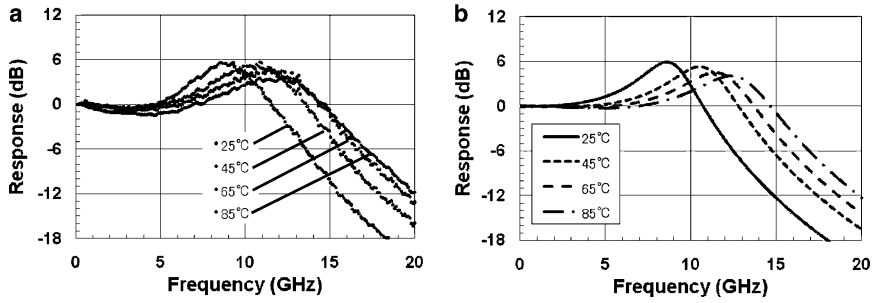


**Fig. 4.2** **a** Example of small-signal frequency responses  $R(f)$  measured on a  $1.3 \mu\text{m}$  wavelength range diode laser [9] compared with **b** fitted responses calculated using (4.3)

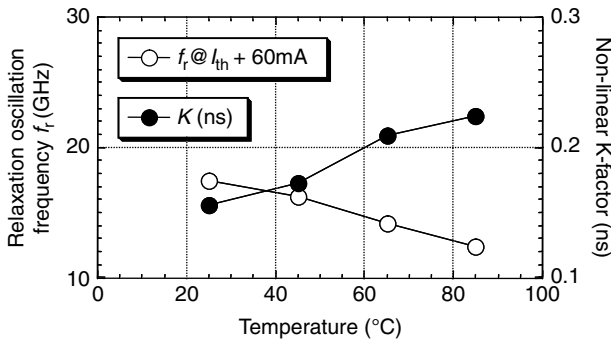


**Fig. 4.3** Temperature dependence of  $f_r$  and nonlinear  $K$ -factor

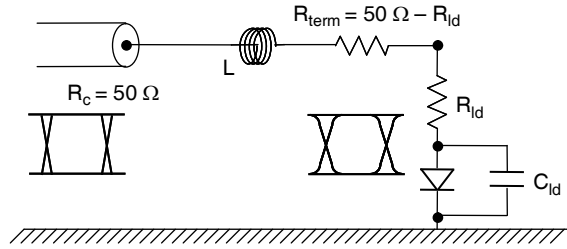
essentially implies that the effect of damping can never be neglected in ultrafast diode lasers modulated in the range of a few tens of GHz.

An example of small-signal frequency responses ( $R(f)$ ) measured on a  $1.3 \mu\text{m}$  wavelength range diode laser [9] is shown in Fig. 4.2a. The laser has an active region composed of InGaAlAs (see Sect. 4.2.4 and also Chap. 3) formed on an InP substrate. It is designed with a  $300 \mu\text{m}$  long cavity and a ridge waveguide (RW) as the striped structure. Data for  $R(f)$  measured at various temperatures ranging from 25 to  $85^\circ\text{C}$  are plotted in Fig. 4.2a. By fitting the measured  $R(f)$  using (4.3), the temperature dependence of  $f_r$  and the nonlinear  $K$ -factor were both extracted; they are plotted in Fig. 4.3.

Fitted responses calculated using these data as parameters are drawn in Fig. 4.2b. The results clearly reveal the good agreement between measured and fitted curves, evidencing the correctness and accuracy of the laser dynamics modeling provided by (4.3).

Lastly, it is important to note here that there could be significant contributions of carrier injection and carrier transport that occur inside or in the vicinity of the active region other than the above limiting factors of the laser dynamics, i.e., the parasitic constant, the relaxation oscillation frequency, and the damping factor. Slow carrier transport or poor carrier injection efficiency into quantum wells easily de-

**Fig. 4.4** Electrical circuit model of laser parasitics.  $C_{ld}$ : laser parasitic capacitance (5.0 pF),  $R_{ld}$ : modulator internal resistance (15  $\Omega$ ),  $R_c$ : characteristic impedance of RF line (50  $\Omega$ ),  $R_{term}$ : termination resistance (50  $\Omega - R_{ld}$ ),  $L$ : wiring inductance (0.4 nH)



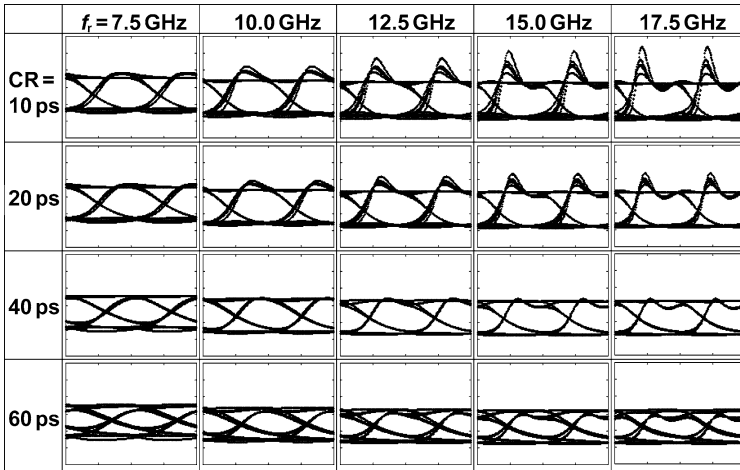
teriorate the high-speed modulation performance, leading to low-frequency roll-off and excess increase of damping. These negative effects can be diminished, and by employing a proper active region design, the inherent high-speed capability can be retained [10, 11].

#### 4.2.2 Large-signal Dynamic Analysis of Rate Equations

Regarding digital modulation of laser sources, large-signal analysis has been performed to understand the dynamic behavior of a laser, which is closely related to fiber transmission performance [12–15]. The large-signal modulation was simulated to obtain the temporal variations in optical intensity  $S(t)$  and carrier density  $N(t)$ . The rate equations (4.1) and (4.2) were solved numerically using the time-developed Runge–Kutta method. A drive-waveform with a maximum 32-bit nonreturn-to-zero (NRZ) pseudorandom pattern was used in this calculation. A bit sequence of “01010111” was used to simulate dynamic changes in  $S(t)$  and  $N(t)$ . The electrical circuit model of the parasitics is shown in Fig. 4.4.

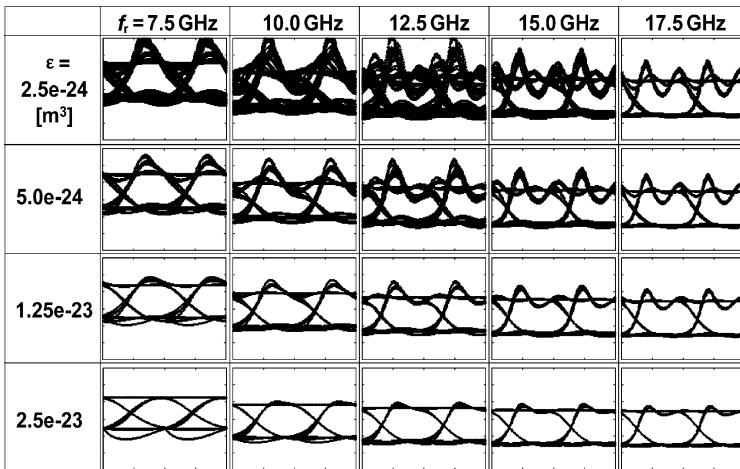
The laser drive current waveform with a trapezoidal pattern (meaning finite rise and fall times) was filtered to account for the parasitics of the laser and assemblies. The model includes laser capacitance  $C_{ld}$ , internal resistance  $R_{ld}$ , wiring inductance  $L$ , and a termination resistor to match the impedance of the radio frequency (RF) signal lines with a standard characteristic impedance of 50  $\Omega$ . In the computation, a signal rate of 10 Gbit/s was used to investigate the feasibility of 10 Gbit/s direct intensity modulation. Most of the parameters used in the computation were extracted from experimental data [9]. As mentioned earlier, the active material was assumed to be comprised of InGaAlAs/InP-based multiple quantum wells (MQW). Calculated eye diagrams for 10 Gbit/s modulation with various values of relaxation oscillation frequency  $f_r$ , CR parasitic, and gain saturation coefficient  $\varepsilon$  are shown in Figs. 4.5 and 4.6.

The results directly indicate the importance of a higher  $f_r$  and a smaller CR constant for obtaining better eye opening. Moreover, a too small value of  $\varepsilon$  results in large peaking in the leading edge of the optical waveform. This implies that the nonlinear gain in high-speed lasers acts to reshape the waveforms through damping effects.



$f_r$ : Relaxation oscillation frequency, CR: CR time constant

**Fig. 4.5** Calculated eye diagrams for 10 Gbit/s modulation with various values of relaxation oscillation frequency  $f_r$  and CR parasitic constant



$f_r$ : Relaxation oscillation frequency,  $\epsilon$ : Gain saturation coefficient

**Fig. 4.6** Calculated eye diagrams for 10 Gbit/s modulation with various values of relaxation oscillation frequency  $f_r$  and gain saturation coefficient  $\epsilon$

### 4.2.3 Chirp Characteristics of Directly Modulated Lasers

In optical fiber transmission systems, the transmission distance and the transmission capacity of a single-channel data stream are mainly limited by the optical loss as well as by the chromatic dispersion of the fiber medium. The latter limiting fac-

tor is linked to the spectral purity of the modulated light source, which is known as dynamic spectrum linewidth or chirp. This chirp is closely related to the broadening that an optical pulse suffers as it propagates over long-distance dispersive fibers. In long-haul transmission systems, fiber-inline amplifiers, such as erbium-doped fiber amplifiers (EDFAs), are commonly used to compensate for the accumulated propagation loss. This makes the chirp-induced pulse broadening severely limit the bit rate and maximum transmission distance [15]. The chirp observed in directly intensity-modulated diode lasers is characterized by the spectral linewidth enhancement factor, also simply known as the  $\alpha$  parameter ( $\alpha_{\text{pld}}$ ), which is described by

$$\alpha_{\text{pld}} = -\frac{4\pi}{\lambda} \frac{\frac{dn}{dN}}{\frac{dg}{dN}}, \quad (4.10)$$

where  $dn/dN$  is the differential index in the laser medium, and  $\lambda$  is the wavelength of the laser light. The numerator in (4.10) denotes the changes in the refractive index in the laser cavity, i.e., the wavelength/frequency fluctuation. On the other hand, the denominator  $dg/dN$ , the differential gain, expresses the degree of intensity modulation. Thus,  $\alpha_{\text{pld}}$  ( $\alpha$ -parameter of a laser diode) can be regarded as the ratio of frequency modulation depth to amplitude modulation depth.

Calculation results showing how the maximum fiber transmission distance ( $L_{\text{max}}$ ) is limited by  $\alpha_{\text{pld}}$  are presented in Fig. 4.7a, b. We assumed a Gaussian-shaped optical signal pulse propagating through a normal single-mode fiber line. Two different signal wavelengths in the 1.3 and 1.55  $\mu\text{m}$  range were used, referring to Fig. 4.7a, b, respectively. We found, as appears reasonable, that  $L_{\text{max}}$  strongly depends on  $\alpha_{\text{pld}}$ . Note that the  $\alpha_{\text{pld}}$  of typical directly modulated lasers operated in a single longitudinal mode is within a range between two and eight, mainly depending on the active material. This limits the maximum transmission distance at 10 Gbit/s, for example, to 10 km in Fig. 4.7b. The figure also shows that the distance is severely restricted by the transmission data rate. These results directly indicate the importance of ultrafast, low-chirp light sources for longer-reach transmission. For achieving maximum transmission distances, it is apparent that reduction of  $\alpha_{\text{pld}}$  is crucial. In general, the use of a laser direct modulation scheme is limited to shorter-reach applications, while external modulation is used to enhance the link distance. Chirp suppression is very important for this purpose, and the use of external modulators is discussed in Sect. 4.3.

#### 4.2.4 High-gain Active Materials for Ultrafast Uncooled Lasers

In present long-reach optical fiber communication systems, different types of light sources are used in the 1.3  $\mu\text{m}$  and 1.55  $\mu\text{m}$  wavelength windows, where the optical loss or effect of fiber chromatic dispersion is minimum. If we focus on the III–V compound materials used for these laser sources, we see that InGaAsP grown on a standard InP substrate has been the most widely used material. This is be-

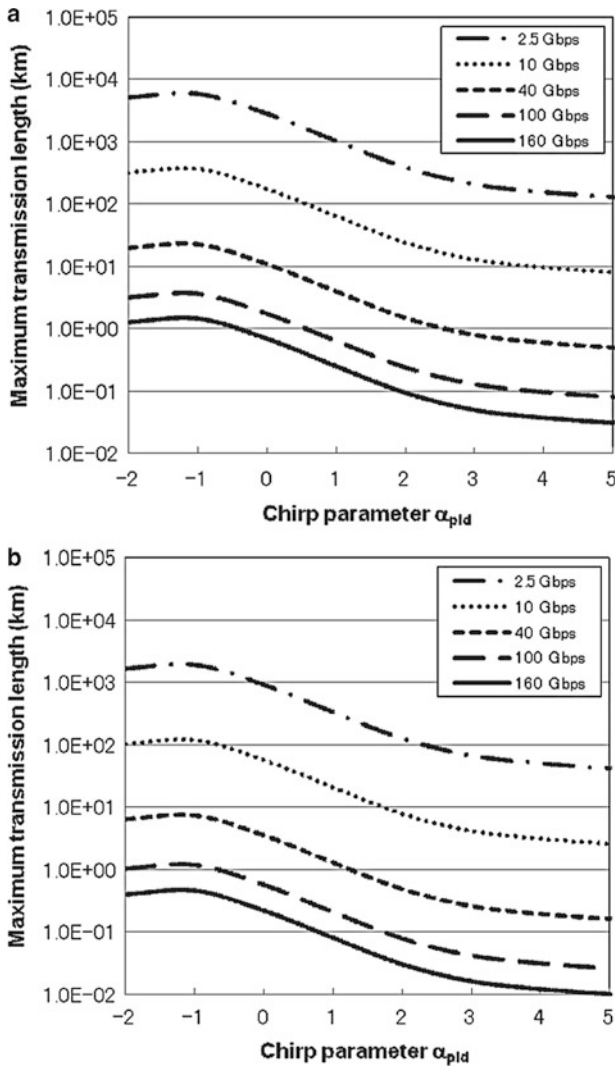


**Fig. 4.7** Calculated results showing how the maximum fiber transmission distance is limited by  $\alpha_{\text{pld}}$ . **a** 1.3  $\mu\text{m}$  range transmission (with chromatic dispersion of 6.5 ps/(nm km)) and **b** 1.55  $\mu\text{m}$  range transmission (with chromatic dispersion of 20 ps/(nm km))

cause it can provide 1.3/1.55  $\mu\text{m}$ -range operation along with superior long-term stability (more than a decade) required for communication infrastructure. Initially, bulk InGaAsP-based laser sources were used, and these were assembled on thermoelectric coolers to compensate for their poor temperature stability. Recently, wide-temperature range or so-called uncooled operation has been demonstrated with this material system through the use of MQWs, which are a new artificial form of material (also refer to Chap. 3). In particular, strained-layer MQWs have been successful

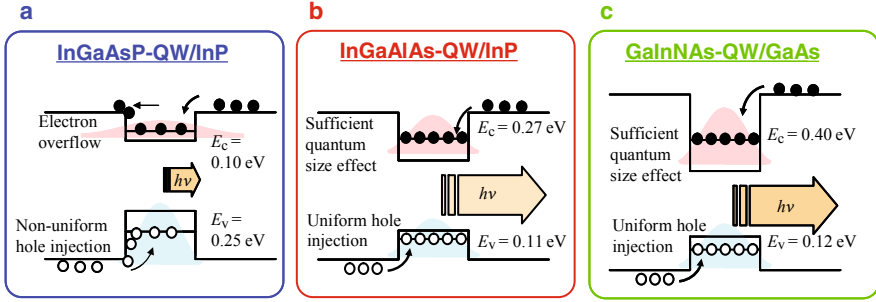


**Fig. 4.8** Band diagrams of the quantum well structures for three types of material systems. **a** InGaAsP/InP, **b** InGaAlAs/InP, and **c** GaInNAs/GaAs.  $\Delta E_c$ ,  $\Delta E_v$  are the typical band-offsets for the respective material

in producing uncooled InGaAsP diode lasers [16–24]. However, with the wide and rapid spread of optical fiber links, operation at 10 Gbit/s or beyond has become essential. Besides, cost effectiveness is naturally important from the commercial perspective. That is why new high-speed, and hopefully uncooled, diode lasers are key devices and have been in the focus of current component developments.

It is apparent from (4.4) that higher differential gain  $dg/dN$  is very effective for faster direct modulation. In general, the optical gain  $g$  of an optically active material is determined by the electric dipole moment  $|M_b|^2$ , the reduced density of states  $\rho_{\text{red}}$ , and the Fermi–Dirac functions of carriers in the conduction and valence bands  $f_c$  and  $f_v$ , respectively. It is written as

$$g(E) = \frac{\pi e^2 \hbar}{nm_0^2 \varepsilon_0 c E} |M_b|^2 \rho_{\text{red}}(E) [f_c(E) - f_v(E)], \quad (4.11)$$

where  $n$  is the refractive index of the laser medium,  $m_0$  is the electron mass,  $\varepsilon_0$  is the permittivity of free space,  $c$  is the velocity of light in vacuum,  $\hbar$  is Planck's constant, and  $E$  is the energy of the light signal. It is important to note that the band structure in active materials has a strong impact on the laser gain  $g$ . The three factors, i.e.,  $|M_b|^2$ ,  $\rho_{\text{red}}$ , and  $[f_c - f_v]$ , in (4.11), are dominated by the quantum size effect in the active materials we use. By introducing the quantum size effect using low-dimensional nanoscale structures, for example, quantum wells, we can greatly enhance  $\rho_{\text{red}}$  due to the step-like density of states. Furthermore, the transition probability between electrons and heavy holes is enhanced since degenerate heavy holes and light holes are split in the quantum wells. This directly increases the dipole moment  $|M_b|^2$ , leading to greater optical gain. Quantitatively, the quantum size effect can be described by the energy depth of the wells in both the conduction and valence bands, which corresponds to the confinement of electrons and holes, respectively. Band diagrams of the quantum well structures for three types of material systems are schematically illustrated in Fig. 4.8 for InGaAsP/InP (a), InGaAlAs/InP (b), and GaInNAs/GaAs (c), all designed for 1.3  $\mu\text{m}$ -range light emission. Note that in the latter one, GaAs is used as substrate material.

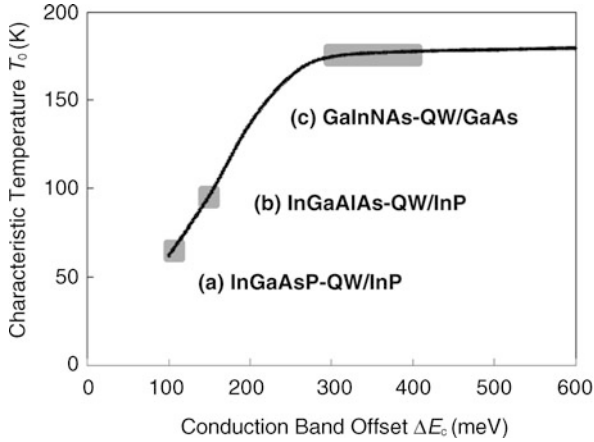


**Fig. 4.9** Calculated characteristic temperature as a function of conduction band offset [25]

The important band offset numbers between quantum wells and barriers are presented for each of the cases in the figures. The conventional InGaAsP/InP system (a) has a small conduction band offset,  $\Delta E_c$ , for electrons of about 100 meV and a large valence band offset,  $\Delta E_v$ , for heavy holes of about 250 meV, meaning an inconvenient band structure. Since electrons are much lighter than holes,  $\Delta E_c$  should be greater than  $\Delta E_v$  in order to achieve strong quantum confinement of electrons. A small  $\Delta E_v$  is desired for simultaneously achieving smooth heavy hole injection.

On the other hand, InGaAlAs/InP (b) and GaInNAs/GaAs (c) both possess distinctly superior band diagrams in these respects. In particular, GaInNAs/GaAs is characterized by  $\Delta E_c$  of as large as 300–500 meV, which should efficiently suppress electron leakage/overflow from the quantum wells. The calculated temperature stability of diode lasers made from these materials is shown in Fig. 4.9 [25].

The diagram indicates how the characteristic temperature  $T_0$  depends on  $\Delta E_c$ . Here,  $T_0$  is employed as a figure-of-merit for high-temperature stability of the threshold current of diode lasers. Using  $T_0$ , the temperature dependence of the threshold current  $I_{th}(T)$  is expressed as  $I_{th}(T) = I_{th}(0) \exp(T/T_0)$ , with  $T$  being the absolute temperature. The calculation is based on the thermionic emission model developed by Suemune [26]. Quasi-Fermi levels for electrons were assumed to be 50 meV and 70 meV at 300 K and 360 K, respectively. For deep quantum wells ( $\Delta E_c > 400$  meV), the calculated  $T_0$  has a very high value of 180 K, meaning that electron leakage from the wells can be largely neglected.

To illustrate the effectiveness of using a high-gain active material, high-temperature/high-speed characteristics of a GaInNAs diode laser operated at 1.3  $\mu\text{m}$  are presented in Fig. 4.10. This GaInNAs laser [25, 27] was grown on a (100)-oriented n-type GaAs substrate by molecular beam epitaxy (MBE) with the nitrogen atoms supplied in the form of radicals. The nitrogen flux was produced by an RF discharge in an appropriate nitrogen radical cell. The laser comprises three GaInNAs quantum wells separated by GaAs barriers. The important quantities  $\Delta E_c$  and  $\Delta E_v$

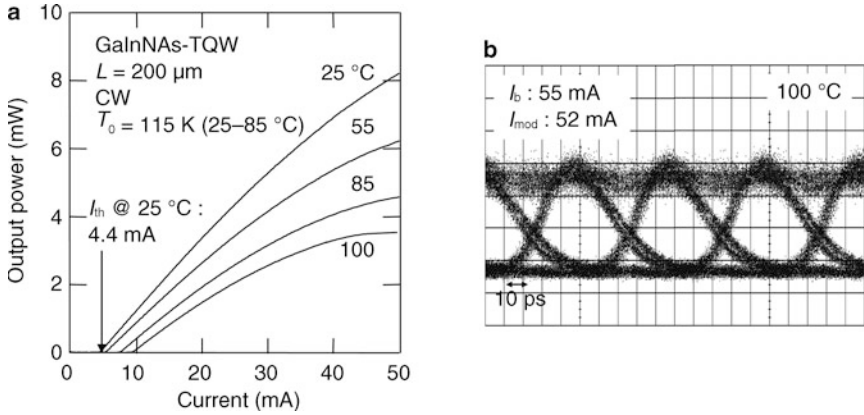


**Fig. 4.10** Light output power versus current characteristics of a GaInNAs RW laser (a) and 10 Gbit/s directly modulated waveform at 100 °C (b)

amount to 400 meV and 150 meV, respectively. To characterize its high temperature stability due to the superior band structure, a high  $T_0$  of over 100 K, uncooled 10 Gbit/s direct modulation at 100 °C, and even 40 Gbit/s direct modulation were obtained [27]. However, with GaInNAs lasers, it proves very difficult to extend the emission wavelength significantly above 1.3  $\mu\text{m}$  while retaining good lasing properties, and lifetime issues still exist.

As discussed earlier, the InGaAlAs MQW structure also possesses fairly large  $\Delta E_c$  and small  $\Delta E_v$  ( $\Delta E_c : \Delta E_v = 7 : 3$ ). Accordingly, sufficient electron confinement in the conduction band and uniform hole injection are expected with this class of material too, again leading to high differential gain and good high-temperature performance.

After the initial demonstration of narrow linewidth InGaAs/InAlAs MQW lasers operating in the 1.55  $\mu\text{m}$  range [28], superior uncooled operation of 1.3  $\mu\text{m}$ -range InGaAlAs MQW RW lasers was demonstrated by Zah et al. [29]. Experimental studies have evidenced that the differential gain of InGaAlAs lasers was distinctly higher than that for InGaAsP lasers. With the explosive growth of Internet traffic, 10 Gbit/s InGaAlAs MQW RW distributed feedback (DFB) lasers have been actively developed and demonstrated by various groups [9, 29–35]. With 10 Gbit/s DFB lasers comprising InGaAlAs active medium, the maximum operating temperature and bit rate have reached 115 °C at 12.5 Gbit/s [24, 32] and 120 °C at 10 Gbit/s [33], while those for InGaAsP appear to be limited to near 100 °C at 10 Gbit/s [22]. These results provide direct evidence that InGaAlAs offers pronounced advantages with respect to high-temperature and high-speed operation. On the basis of these superior material characteristics, 1.3  $\mu\text{m}$  DFB lasers have been successfully demonstrated for use in de facto standard 10 Gbit/s small form factor transceiver modules like SFP+ or XFP. A photograph of an XFP module (10 Gbit/s form factor module pluggable) incorporating a 1.3  $\mu\text{m}$  InGaAlAs-based DFB laser is shown in Fig. 4.11. As a result of the high-gain properties of InGaAlAs, a clear opened eye diagram was ob-



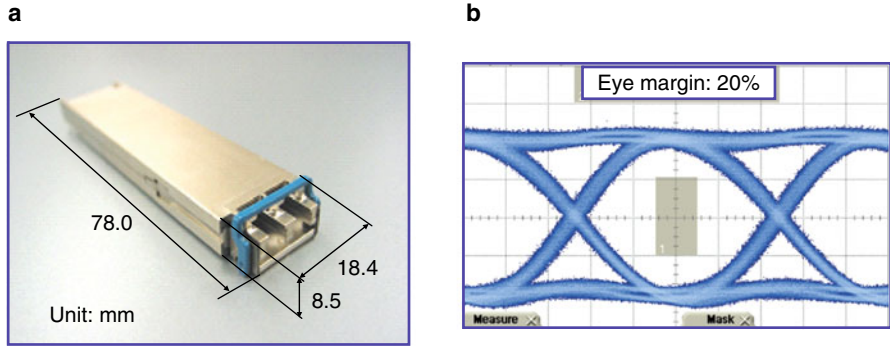


**Fig. 4.11** XFP transponder module incorporating a 1.3 μm InGaAlAs DFB laser (Opnext, TRF5010/TRF5020) (a) and 10 Gbit/s optical waveform (b)

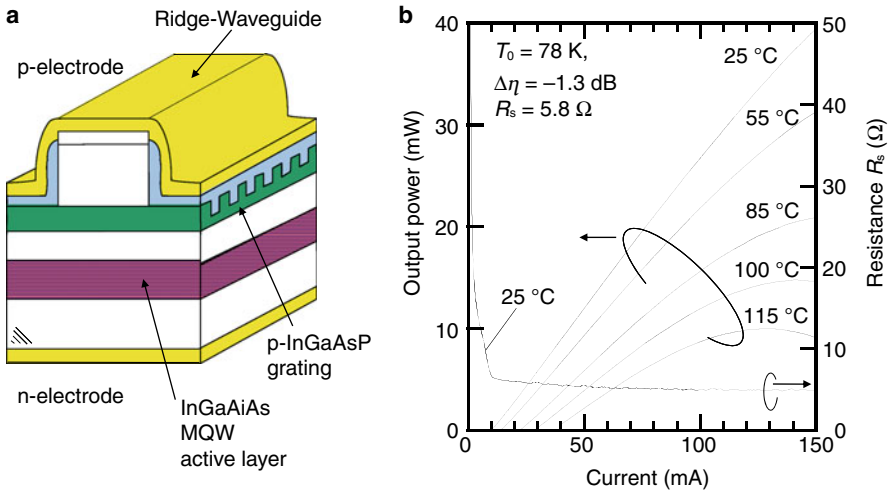


**Fig. 4.12** Device structure (a) and light-current curves (b) of a 1.3 μm InGaAlAs DFB laser [32, 33]

tained at 10 Gbit/s modulation. The structure of the InGaAlAs-based laser chip and light-current characteristics measured at elevated temperatures of up to 115 °C are depicted in Fig. 4.12 [32].

### 4.2.5 Short-cavity Ultrafast Lasers

This section discusses how the downsizing of the laser cavity has a positive effect on laser dynamics. At first glance, (4.4) would suggest that the relaxation oscillation frequency,  $f_r$ , can be raised by minimizing the total volume  $V$  of the active laser region. In reality, however, the gain saturation and strong damping in a small active

region severely limit the high-speed performance. To explore the optimum design of the laser cavity for high-speed characteristics, analytical expressions for optical gain and carrier lifetime are used.

The optical gain generated in an active quantum well laser region can be empirically written using the injection current density  $J$  as [36]

$$g = G_0 \ln \left( \frac{J}{N_w J_0} \right), \quad (4.12)$$

where  $G_0$ ,  $N_w$ , and  $J_0$  denote the gain coefficient, the number of MQWs, and the transparency current density. Here,  $J = I/W_a L_c$ , where  $W_a$  and  $L_c$  are the lateral width and the length of the laser active region, respectively, and  $I$  the applied current. The first term of the rate equation for the carriers, (4.1), denotes the number of injected carriers, and it can be rewritten using the carrier density  $N$  as

$$\frac{I}{eV} = \frac{J W_a L_c}{eV} = AN + BN^2 + CN^3, \quad (4.13)$$

where  $A$ ,  $B$ , and  $C$  are coefficients that describe nonradiative and radiative recombination, and the Auger process. Using (4.12) and (4.13), the differential gain  $dg/dN$  is then calculated as

$$\frac{dg}{dN} = \frac{dg}{dJ} \frac{dJ}{dN} = G_0 \frac{A + 2BN + 3CN^2}{AN + BN^2 + CN^3}. \quad (4.14)$$

Using (4.14) and (4.4), we can derive the current efficiency of  $f_r$ , indicated by  $\eta_{f_r}$ , as

$$\eta_{f_r} = \frac{f_r}{\sqrt{I - I_{th}}} \propto \sqrt{\frac{dg}{dN} \frac{\alpha_i + \alpha_m}{\alpha_m} \frac{1}{L_c}}. \quad (4.15)$$

Here,  $I_{th}$  is the threshold current for lasing,  $\alpha_m$  is the mirror loss at the laser facets, and  $\alpha_i$  is the internal loss of the laser cavity. In the case of Fabry–Pérot-type lasers,  $\alpha_m$  is a function of  $R_f$  and  $R_r$ , which describe the mirror power reflectivities at the end facets, and it is given by

$$\alpha_m = \frac{1}{2L_c} \ln \left( \frac{1}{R_f R_r} \right). \quad (4.16)$$

By solving the lasing condition

$$\Gamma N_w g = \alpha_i + \alpha_m, \quad (4.17)$$

we can calculate  $dg/dN$  at the threshold to determine  $f_r$ .

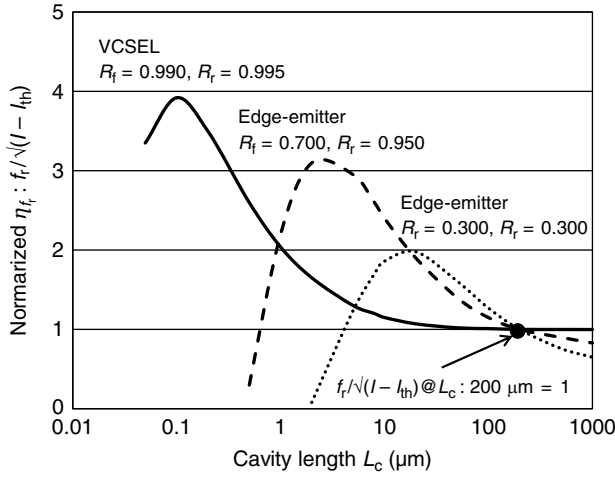
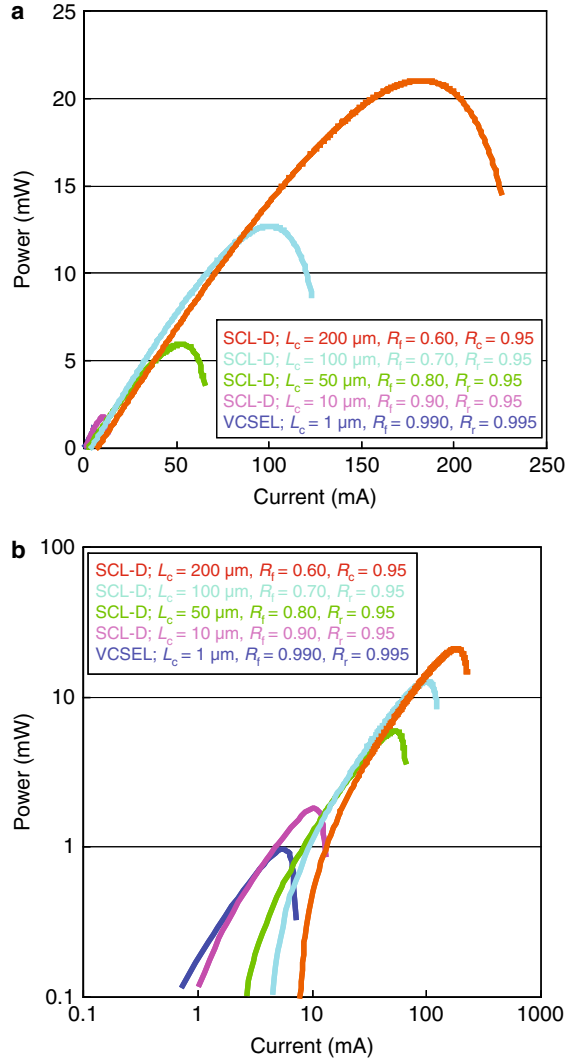


**Fig. 4.13** Calculated  $\eta_{f_r}$  as a function of laser cavity length  $L_c$ . Parameters are  $G_0 = 850 \text{ cm}^{-1}$ ,  $J_0 = 1254 \text{ A/cm}^2$ ,  $\alpha_i = 20 \text{ cm}^{-1}$ ,  $\Gamma = 0.1$ ,  $d = 0.1 \mu\text{m}$ ,  $A = 9.5 \times 10^7 \text{ s}^{-1}$ ,  $B = 7.7 \times 10^{-17} \text{ m}^3/\text{s}$  and  $C = 1.1 \times 10^{-40} \text{ m}^6/\text{s}$

The calculated  $\eta_{f_r}$  is shown in Fig. 4.13 as a function of laser cavity length,  $L_c$ . The parameters used in this simulation, which are indicated in the figure caption, are typical for InGaAlAs-based  $1.3 \mu\text{m}$  diode lasers used in recent 10 Gbit/s systems.  $\eta_{f_r}$  for a  $200 \mu\text{m}$ -long InGaAlAs laser is calculated and used as a reference. The ratio  $\eta_{f_r}(L_c)/\eta_{f_r}(200 \mu\text{m})$  (for  $L_c < 200 \mu\text{m}$ ) illustrates the positive effect of the short-cavity design. The calculation was performed for several sets of  $R_f$  and  $R_r$  to fairly well compare short-cavity edge-emitting lasers (SCEELs) and vertical cavity surface emitting lasers (VCSELs) versus “normal-length” cavity edge-emitting lasers. The results show that  $\eta_{f_r}$  is definitely enhanced by shortening  $L_c$ . We also find that the optimum  $L_c$  strongly depends on facet reflectivity, i.e., stronger facet reflection is essential for shorter  $L_c$  in order to compensate for the increased mirror loss factor of  $1/2L_c \ln(1/R_f R_r)$ . For example, for  $R_f = 70\%$  and  $R_r = 95\%$ , the optimum  $L_c$  was calculated to be  $5 \mu\text{m}$  with a resultant  $\eta_{f_r}(L_c)/\eta_{f_r}(200 \mu\text{m})$  enhancement ratio of about three. It is noteworthy that in the case of a VCSEL ( $R_f = 99.0\%$  and  $R_r = 99.5\%$ ), the optimum  $L_c$  lies naturally within the submicrometer range, and the  $\eta_{f_r}(L_c)/\eta_{f_r}(200 \mu\text{m})$  enhancement turns out to be close to four.

The above findings indicate the potential of achieving faster diode lasers by employing short-cavity designs. However, since thermal effects were neglected in the above model, we then simulated light-current curves of these short-cavity diode lasers, taking into account the electrical resistance  $R_{\text{ld}}$  and thermal resistance  $\Theta_{\text{ld}}$ . When a short-cavity laser is used, both resistances adversely affect the static laser performance. Typical  $I$ - $L$  curves for a range of short-cavity devices are drawn in Fig. 4.14a, b, which have linear and logarithmic vertical scales (light power), respectively.

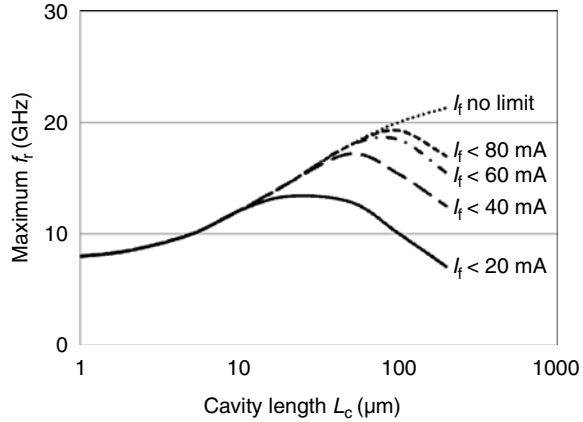
**Fig. 4.14** Typical  $I$ - $L$  curves for a range of short-cavity devices on a linear scale (a) and a log scale (b)



It is obvious that severe power saturation is encountered with short-cavity devices. This suggests that the maximum  $f_r$  should saturate due to this thermal saturation as well. Taking this effect into account, we have calculated the maximum  $f_r$  as a function of  $L_c$ . The results are shown in Fig. 4.15.

It is apparent from this figure that there is an optimum  $L_c$  to suit the drivable laser current swings. For example, if we assume a drive current swing of 20 mA, the best  $f_r$  of 13 GHz would be achieved with a short  $L_c$  of about 40  $\mu\text{m}$ . It is interesting to note that this maximum  $f_r$  for the SCEEL is much higher than those for VCSELs ( $L_c < 1 \mu\text{m}$ ). This simply underlines the promising future potential for very high-speed operation of SCEELs.

**Fig. 4.15** Maximum  $f_r$  calculated as a function of  $L_c$  considering thermal effects



Results calculated using (4.3), (4.4), and (4.5) are shown in Fig. 4.16. They show the requirements for the parameters  $f_r$  and  $K$  essentially governing laser dynamics. The combination of the two parameters was computed using the three equations so that they achieved certain levels of  $f_{3\text{dB}}$ , as indicated in the figure. To highlight the capability of 40 Gbit/s direct modulation, the bold line indicates the criterion for reaching  $f_{3\text{dB}} = 40$  GHz. Moreover, 40 Gbit/s eye diagrams were simulated for several sets of  $L_c$  and  $dg/dN$  using the method described in Sect. 4.2.2. The results directly indicate that a high  $f_r$  value of at least close to 40 GHz is necessary to accomplish 40 Gbit/s opened eyes with a small amount of jitter caused by intersymbol interference. Also evidenced is the effectiveness of a shorter laser cavity via  $f_r$  enhancement. The results of successful 40 Gbit/s direct modulation of an SCEEL [37], designed in accordance with the above rules, are shown in Fig. 4.17.

The respective 1.3  $\mu\text{m}$ -range InGaAlAs laser exhibited a 100  $\mu\text{m}$ -long short cavity realized by using a conventional cleaving technique. The short-cavity length of 100  $\mu\text{m}$  only led  $f_r$  to increase to 28 GHz, and this enhancement successfully resulted in room temperature 40 Gbit/s modulation capability, as demonstrated by the eye-opened optical waveforms represented in Fig. 4.17. Since then, appreciable progress has been achieved with those directly modulated short-cavity laser diodes. The practical fabrication difficulties associated with cleaving and handling such devices were essentially overcome by incorporating passive waveguide sections by butt-joint growth to extend the physical device length. A recently reported DFB laser designed in such a way featured a 3 dB bandwidth of 28 GHz at 60  $^\circ\text{C}$  at a bias current of 45 mA only, enabling 40 Gbit/s operation at that temperature with well opened eyes [38]. In another structure, a waveguide-based Bragg mirror has been formed at either side of the short-cavity DFB laser section to increase feedback to the active region and thus to reduce the threshold gain [39]. A buried heterostructure- (BH-) design using semi-insulating blocking layers was successfully adopted despite the Al-containing active medium. A relaxation oscillation frequency  $f_r$  well beyond 25 GHz was obtained at 25  $^\circ\text{C}$ , and still some 20 GHz even

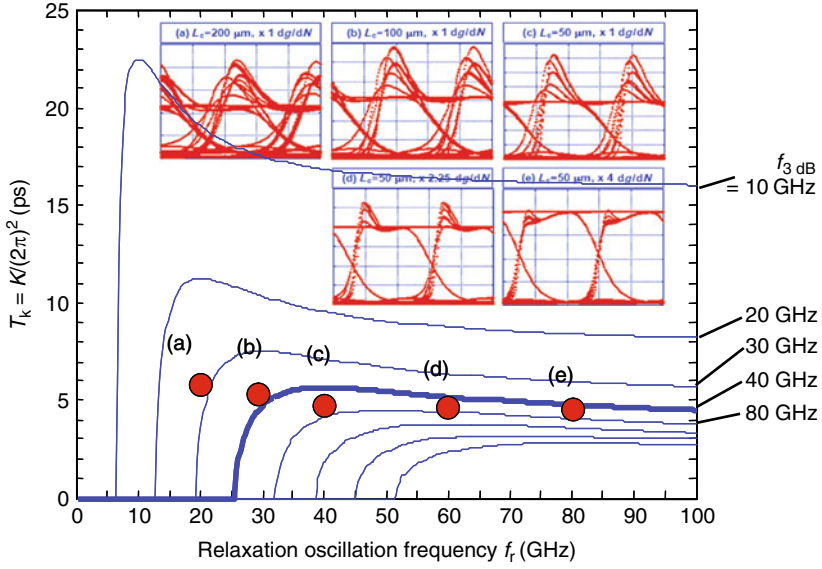
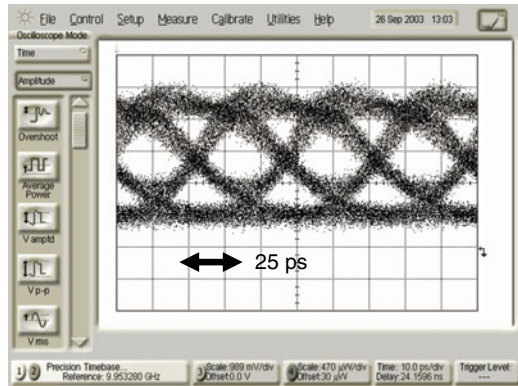


Fig. 4.16 Calculated results indicating the possibility of 40Gbit/s direct modulation

Fig. 4.17 Successful 40 Gbit/s direct modulation waveform using a 100 μm-long SCEEL



at 70 °C. Threshold currents were as low as 4 mA at 25 °C, and below 10 mA at 70 °C. These values enabled error-free 40 Gbit/s transmission over 5 km of SMF even at the higher temperature. The industry’s first 4 × 25 Gbit/s transmitter module employing discrete directly modulated and wavelength-multiplexed DFB lasers to deliver an aggregated 100 Gbit/s bit stream over 20 km of single-mode fiber was recently announced and showcased [40]. These recent developments appear to be quite promising; nonetheless, it needs to be seen how competitive such directly modulated ultrahigh-speed lasers will be with respect to alternative transmitter devices to be discussed in the following.

### 4.3 Ultrafast, Low-chirp Externally Modulated Laser Sources

With the development of high-performance Er-doped fiber amplifiers (EDFA), the loss-limited transmission distance in multigigabit optical-fiber communication systems could be increased dramatically [41]. In high-speed long-haul transmission systems employing such inline fiber amplifiers, the transmission distance is no longer limited by the optical loss in the fiber, but by the chirp of the light source. With chirp-limited transmission, the key components include high-modulation-speed, spectrum-stabilized transmitter light sources operating at a wavelength of 1.55  $\mu\text{m}$ . Therefore, to overcome the problem of chirp-induced pulse broadening, intensive efforts have been made to produce various types of external optical modulators (see Chap. 6). Using these modulators substantially helps to avoid the large wavelength chirping that occurs with conventional laser diodes under direct current modulation. The impact of chirp ( $\alpha_p$ ) reduction on the extended fiber transmission distance was discussed earlier with reference to Fig. 4.7.

Among the various kinds of optical modulators, MQW optical modulators consisting of III/V compound semiconductors are promising candidates. MQW modulators can operate at high frequencies with low chirp and low drive voltage [42–49]. These favorable properties arise from the large field-induced variation in the absorption coefficient (or refractive index), resulting from the quantum-confined Stark effect (QCSE) [50, 51]. In particular, QCSE-based electroabsorption (EA) modulators have a high potential for practical use because of the simplicity of their device physics as well as the good structural feasibility of monolithically integrating them with laser diodes [52–62]. Monolithic laser integration not only reduces size and cost, but also improves performance. The light output, for example, increases substantially because the insertion loss is very low compared with that of discrete modulators, and the long-term reliability is also improved because the packaging is more robust.

Most of the 1.55  $\mu\text{m}$ -band EA modulators developed so far use MQW structures with InGaAsP or InGaAlAs quaternary wells and barriers. Note that in these MQW modulators, barrier materials with optimized well/barrier band discontinuities are chosen to achieve sufficient quantum confinement for enhancing the QCSE as well as for better high-power handling. The latter requirement is related to the sweep-out of photogenerated carriers outside the quantum wells, which is very important, especially when the light source is monolithically integrated with the modulator.

One major difficulty in fabricating photonic integrated circuits has been to reproducibly produce good optical waveguide coupling between functional elements. Although modulators and lasers are fabricated in the same way, it has still been difficult to create a nanometer-sized, smooth, high-quality crystal interface between the components. Nowadays, several monolithic integration methods are available to solve this issue. In-plane bandgap energy control integration techniques based on selective area growth [54, 55, 60, 61] and butt-joint integration [52, 53, 56–58, 62], in which each functional element is implemented separately by selective etching followed by epitaxial regrowth, are now widely used. These methods enable the integration of different MQW structures, and, as a result, the performance of both the

modulator and the laser has been dramatically improved through the exploitation of the quantum size effect in MQW structures.

### 4.3.1 High-speed Characteristics of Externally Modulated Lasers

This section mainly focuses on modulators integrated with a light source rather than on the solitary modulator itself. After describing the basics of EA modulators, the important technical issues associated with laser integration, such as modulator/laser interactions, are discussed. A more general description of external modulators is given in Chap. 6.

The small-signal frequency response  $R(f)$  of an external modulator can be expressed in a much simpler way than that of directly modulated diode lasers. Basically, it is determined by its parasitics and the transport/sweep-out time of photogenerated carriers. Here, we assume a lumped element model in which the modulator is regarded as being much smaller in size than the wavelength of the microwave signal driving the modulator. We also assume that the photogenerated carriers are swept out of the quantum wells so fast that they do not influence the modulator dynamics. A device structure model and an electrical circuit model of an EA modulator integrated with a DFB laser (EA/DFB laser) are depicted in Fig. 4.18.

The EA/DFB device structure is composed of an EA modulator and a DFB laser with an automatically aligned optical axis. The optical coupling efficiency between them is defined as  $C_{\text{out}}$ . As with the standard DFB laser, several crucial optical parameters such as facet reflectivity, along with the optical phase with respect to the DFB grating, have to be considered. The electrical circuit model starts with standard modulator parameters, namely, capacitance  $C_{\text{mod}}$ , internal resistance  $R_{\text{mod}}$ , wiring inductances  $L_1$  and  $L_2$ , and a  $50\ \Omega$  termination resistor  $R_{\text{term}}$  for matching the impedance of RF signal lines with the characteristic impedance of  $50\ \Omega$ . Newly added in this model are the laser capacitance,  $C_{\text{ld}}$ , connected via an isolation resistor,  $R_{\text{iso}}$ , and a constant current source. During operation of the EA/DFB laser, a photogenerated current  $I_{\text{ph}}$  always flows in the modulator section.  $I_{\text{ph}}$  is treated as a constant current source, as indicated in the figure, because it seriously degrades the electric reflection properties. This effect of  $I_{\text{ph}}$  on the modulation characteristics is discussed in the next section.

If we neglect the effects of  $I_{\text{ph}}$  and wiring inductances,  $R(f)$  is simply expressed as

$$R(f) = \frac{1}{1 + \{\pi C_{\text{mod}}(R_{\text{mod}} + R_{\text{term}}/2)f\}^2} = \frac{1}{1 + \{\pi C_{\text{mod}}(R_{\text{mod}} + 25\ \Omega)f\}^2}. \quad (4.18)$$

By solving  $R(f_{3\text{dB}}) = 1/2$ , we get

$$f_{3\text{dB}} = \frac{1}{\pi C_{\text{mod}}(R_{\text{mod}} + 25\ \Omega)}. \quad (4.19)$$



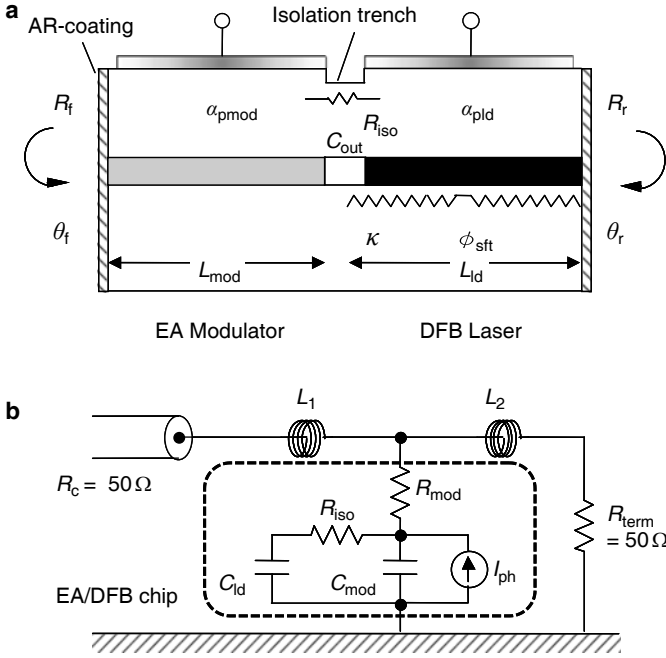


**Fig. 4.18** Physical model of EA/DFB chip (a).  $C_{out}$ : optical coupling efficiency,  $C_{ld}$ : laser parasitic capacitance,  $R_f$ : front facet reflectivity,  $R_r$ : rear facet reflectivity,  $\theta_f$ : front facet phase,  $\theta_r$ : rear facet phase,  $L_{mod}$ : modulator length,  $L_{ld}$ : laser length,  $\kappa$ : coupling efficiency in grating,  $\Phi_{sft}$ : phase shift in grating,  $\alpha_{pmod}$ :  $\alpha$  parameter of the modulator,  $\alpha_{pld}$ :  $\alpha$  parameter of the laser. Electrical circuit model of assembled EA/DFB laser (b).  $C_{mod}$ : modulator parasitic capacitance,  $C_{ld}$ : laser parasitic capacitance,  $R_{mod}$ : modulator internal resistance,  $R_{iso}$ : laser/modulator isolation resistance,  $R_c$ : characteristic impedance of RF line,  $R_{term}$ : termination resistance,  $L_1$ : wiring inductance 1,  $L_2$ : wiring inductance 2,  $I_{ph}$ : photogenerated current

The light extinction ratio (on/off ratio), ER, of the EA modulator is proportional to the modulator length  $L_{mod}$  and the field-induced change in the absorption coefficient  $\Delta\alpha_{abs}$ , and is given by

$$ER(\text{dB}) = 4.34\xi_{MQW}\Delta\alpha_{abs}L_{mod}, \quad (4.20)$$

where  $\xi_{MQW}$  is the optical confinement factor of the MQW absorption layer.

It is apparent from (4.19) that in order to achieve high-speed externally modulated lasers, it is important to reduce the capacitance,  $C_{mod}$ , and the internal resistance,  $R_{mod}$ , of the modulator. As with high-speed diode lasers, shorter modulator lengths are effective in lowering  $C_{mod}$  for this purpose. However, since shortening  $L_{mod}$  has a direct adverse impact on  $R_{mod}$  and the amount of light absorption (and hence light extinction), there is a trade-off between high-speed characteristics and the operating voltage needed to achieve a given extinction ratio. Thus, a simple figure of merit (FOM) of the modulator can be formulated as  $f_{3\text{dB}}/V_m$  (or inversely

$V_m/f_{3\text{ dB}}$ ), where  $V_m$  is the modulation voltage swing. A more accurate FOM is defined in [63]; it considers the amount of modulation drive power  $P = V_m^2/R_{\text{term}}$ . It should be emphasized that a clear trade-off exists between  $f_{3\text{ dB}}$  and  $V_m$  for all kinds of modulators reported so far [63].

Regarding high-speed limitation associated with the mobility of photogenerated carriers, related effects can be expected to be strongly dependent on their density and on the band discontinuities in the quantum wells. Similar to the case of directly modulated lasers, a small valence band offset  $\Delta E_v$  is important for achieving smooth sweep-out of heavy holes under higher light power operation [64–66]. This will be of particular concern when a light-source laser is monolithically integrated.

### 4.3.2 Chirp Characteristics of Externally Modulated Lasers

External modulation techniques can provide high-speed, low-chirp optical signals that are suitable for high-bit-rate long-haul communication. These techniques can avoid the large chirp generated by carrier fluctuation in directly modulated lasers.

As in the case of the latter devices, the chirp observed in external intensity modulators is characterized by an  $\alpha$ -parameter for modulators, which is expressed as

$$\alpha_{\text{pmod}} = \frac{4\pi}{\lambda} \frac{\frac{dn}{dE}}{\frac{d\alpha_{\text{abs}}}{dE}}, \quad (4.21)$$

where the numerator  $dn/dE$  represents the electric-field-induced variation of the refractive index in the modulator medium, which is associated with a phase change in the light signals. The denominator  $d\alpha_{\text{abs}}/dE$  expresses the degree of intensity modulation by light absorption. Like the  $\alpha$ -parameter for diode lasers given in (4.10),  $\alpha_{\text{pmod}}$  corresponds to the ratio of two modulation depths, but in this case to the ratio of phase modulation depth to amplitude modulation depth. More importantly,  $\alpha_{\text{pmod}}$  for EA modulators is typically within the range between  $-0.5$  and  $+1.0$ , which is much smaller than the  $\alpha$ -parameter of directly modulated lasers of typically 2–8 (as noted in Sect. 4.2.3). The simple reason for the smaller EA modulator chirp is that the field-induced change in refractive index ( $(dn/dE)\Delta E$ ) is much smaller than the carrier-induced refractive index change ( $(dn/dN)\Delta N$ ) in (4.10). This is the primary advantage of EA modulators over directly modulated diode lasers. In the case of laser-integrated EA modulators, however, careful attention must be paid to any interactions (or signal crosstalk) between the modulator and the laser which may induce additional chirp. In general, the possible physical origins of those interactions may be electrical, optical, and thermal crosstalk effects. Among these, electrical interaction can be efficiently eliminated by state-of-the-art electrical isolation techniques. For example, isolation (separation) resistance ( $R_{\text{iso}}$ ) between the two device elements can be increased to more than 20 k $\Omega$  by forming a shallow isolation trench in the cladding layer. If the modulator voltage swing  $V_{\text{pp}}$  is assumed to be 2–3 V, this value of  $R_{\text{iso}}$  corresponds to a leakage modulation current  $I_{\text{pp}}$  to the laser section of

less than  $150 \mu\text{A}$ , which is sufficiently small compared to the laser driving current of several tens of milliamperes. Thermal interaction may also be neglected because of the slow response of thermal effects in the order of milliseconds. A normally applied NRZ pseudorandom modulation with a  $2^{31} - 1$  bit sequence corresponds to a lowest modulation frequency of several hundreds of kilohertz.

The remaining interaction effect, optical crosstalk, represents a serious factor in achieving reproducible low-chirp operation. This is why the reduction of modulator facet reflection has been an issue. Any optical reflection at the modulator facet could produce an undesirable fluctuation in the lasing mode, leading to considerable optical feedback-induced excess chirp produced in the laser section. Although, qualitatively, this phenomenon is quite well understood, only few attempts have been made to quantitatively clarify the influence of optical feedback-induced chirp on the performance of high-bit-rate transmission over long-distance dispersive fibers [67–69]. In this section, an outline is given of how fiber transmission can numerically be simulated by taking into account the optical feedback-induced excess chirp. The simulation results allow for designing robust low-chirp EA/DFB lasers. Eye distortion and the resulting transmission penalties are derived as a function of the residual modulator facet reflectivity, and these characteristics are shown to be consistent with experimental results. In getting the required system performance, it is found that not only the modulator facet reflection but also the chirping parameters ( $\alpha$ -parameters) in both the laser ( $\alpha_{\text{pld}}$ ) and the modulator section ( $\alpha_{\text{pmod}}$ ), as well as the optical coupling coefficient in the DFB cavity are critical parameters that need to be well controlled.

Another possible interference is associated with the impact of laser power-induced photogenerated current on modulator performance. Although this effect has been neglected and studied very little, it appears to be of great importance in practical applications. In particular, if the modulator driver circuit and the EA modulator are DC-coupled, a photogenerated current might flow in the driver circuit, which would directly deteriorate the drivability. This type of interference will therefore be quantitatively analyzed and discussed in Sect. 4.3.5.

### ***4.3.3 Facet-reflection Induced Chirp in Externally Modulated Lasers***

The model that accounts for the facet-reflection induced chirp is shown in Fig. 4.18a. It shows an EA/DFB structure with the corrugated Bragg grating and a phase shifter in the middle of the laser cavity. The laser parameters are the cavity length,  $L_{\text{ld}}$ , coupling coefficient of the corrugation,  $\kappa$ , facet reflectivity,  $R_{\text{r}}$  at the laser rear end, relative phase,  $\theta_{\text{r}}$  (with respect to the corrugation phase) at the laser rear end, and the period of the corrugation,  $\Lambda$ . The main parameters of the modulator part are the modulator length,  $L_{\text{mod}}$ , the relative corrugation phase,  $\theta_{\text{f}}$ , and the facet reflectivity ( $R_{\text{f}}$ ) at the modulator front end.

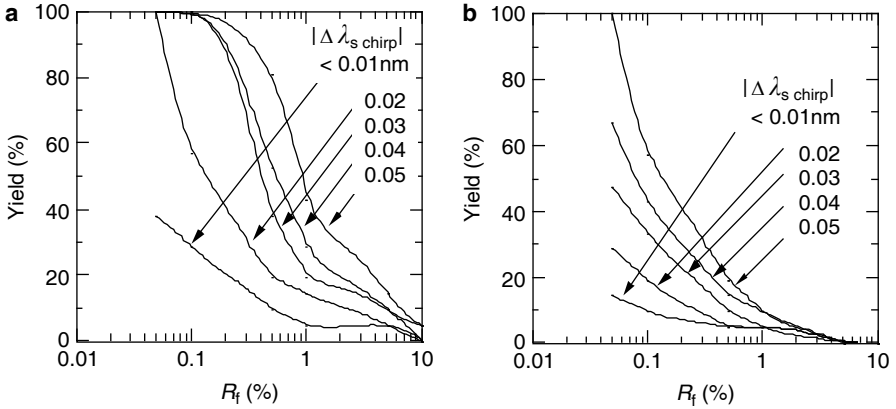


**Fig. 4.19** Comparison of the static chirp yield between bulk- and MQW-based devices. **a**  $\lambda/4$ -shifted DFB structure with an MQW active region ( $\alpha_{\text{pld}} = 3$ ,  $\kappa L_{\text{ld}} = 2$ ,  $\Delta\alpha_{\text{th}} L_{\text{ld}} > 0.3$ ) and **b**  $\lambda/4$ -shifted DFB structure with a bulk active region ( $\alpha_{\text{pld}} = 8$ ,  $\kappa L_{\text{ld}} = 2$ ,  $\Delta\alpha_{\text{th}} L_{\text{ld}} > 0.3$ )

The calculation of the facet-reflection induced chirp is based on coupled-mode and rate equations, respectively. Under DC conditions (static chirp), it is calculated by solving the coupled-mode equations of a modified DFB cavity with a variable front facet [67–69]. The EA modulator section is modeled simply as a piece of waveguide that has variable loss and a propagation constant according to digital modulation. Since the waveguide is directly attached to the front end of the DFB-laser section, it can be regarded as a reflector with variable reflectivity and phase.

The static chirp  $\Delta\lambda_{\text{s chirp}}$  was calculated as follows: The static chirp corresponds to the amount of wavelength variation that occurs between the on- and off-states when the EA modulator is driven by DC signals. To obtain the static chirp, we solve the time-independent rate equation ( $d/dt = 0$ ). The  $16 \times 16$  combinations of phase at the front ( $\theta_f$ ) and rear ( $\theta_r$ ) facet are varied in  $\pi/8$  steps with respect to the grating. The dependence of the calculated  $\Delta\lambda_{\text{s chirp}}$  yield on  $R_f$  when  $\kappa L_{\text{ld}}$  is 2.0 is shown in Fig. 4.19.

Here,  $\kappa L_{\text{ld}}$  expresses the amount of distributed Bragg reflection occurring in the DFB-laser cavity, and it corresponds to the Q-factor in the laser resonator. The calculation was performed for two  $\alpha_{\text{pld}}$  values:  $\alpha_{\text{pld}} = 3$  (Fig. 4.19a), the case for an MQW active region, and  $\alpha_{\text{pld}} = 8$  (Fig. 4.19b), the case for a bulk active region. The figures clearly indicate that for both  $\alpha_{\text{pld}}$  cases, any increase in  $R_f$  leads to a poorer yield in obtaining a certain level of  $\Delta\lambda_{\text{s chirp}}$ . This is reasonably understood from the enhanced perturbation in the lasing mode induced by the fraction of modulated light that is reflected at the modulator front facet back into the laser cavity. The figures also show that the  $\Delta\lambda_{\text{s chirp}}$  yield depends strongly on  $\alpha_{\text{pld}}$ , which is another important parameter that governs the chirp behavior in EA/DFB lasers. It can be clearly seen from the figures that the  $\Delta\lambda_{\text{s chirp}}$  yield for  $\alpha_{\text{pld}} = 3$  is much higher than that for  $\alpha_{\text{pld}} = 8$ . This tendency can be understood more naturally if we consider the fact that facet-reflection induced chirp is produced in the laser medium, and not

in the modulator. The above results directly indicate that not only reduction of the modulator chirp  $\alpha_{\text{pmod}}$ , but also reduction of the laser chirp  $\alpha_{\text{pld}}$  is essential for obtaining low-chirp EA/DFB lasers. The reduction of  $\alpha_{\text{pld}}$  can be achieved in several ways, for instance, by introducing strained MQWs [70–72] combined with negative wavelength detuning [73] of the DFB-laser structure. Indeed, MQW active regions offer a superior robust design for achieving low  $\Delta\lambda_{\text{s chirp}}$  operation of an EA/DFB laser. Furthermore, it can be concluded from the obtained results that a small  $\alpha_{\text{pld}}$  value is essential for suppressing the facet-reflection induced chirp, even though the device is based on an external modulation scheme.

#### 4.3.4 Transmission Simulation of Externally Modulated Lasers Considering Facet-reflection Induced Chirp

The dynamic chirp of EA/DFB lasers was analyzed by combining the coupled-mode and the rate equations [69]. Again, as with directly modulated diode lasers, large-signal analysis was performed using the time-developed Runge–Kutta method to obtain the temporal variations in the optical intensity and phase. A trapezoidal drive waveform with a 32-bit 2.5 Gbit/s NRZ pseudorandom pattern was filtered to account for the parasitics of the modulator and assembly. Most of the parameters for devices and fiber transmission (Table 4.1) were extracted from experimental data.

Assuming InGaAsP/InP-based MQW material, the important chirp parameters for the modulator and laser,  $\alpha_{\text{pmod}}$  and  $\alpha_{\text{pld}}$ , were taken to be 0.4 and 3.0, respectively. The  $8 \times 8$  phase combinations at the front and rear facet with respect to the grating were varied in  $\pi/4$  steps. The transmission behavior over normal-dispersion (17 ps/(nm km)) single-mode fibers was analyzed using the model given in [74, 75], with receiver parameters adjusted to those used in the experiments. The calculation was done for different front facet-reflectivity values ( $R_f$ ) ranging from 0% to 2%, while the rear facet-reflectivity ( $R_r$ ) was kept constant at 90%.

Simulated modulation waveforms and dynamic wavelength shifts (total chirp) occurring in an antireflection–high reflection (AR–HR) coated device are shown in Fig. 4.20. The optical feedback was calculated for (a)  $R_f = 0\%$ , (b)  $R_f = 0.001\%$ , (c)  $R_f = 0.01\%$ , and (d)  $R_f = 0.1\%$ . The rise and fall times used in the computation were 80 ps, and the facet phase combination ( $\theta_f, \theta_r$ ) was  $(0, \pi)$ . This facet phase combination yielded the largest chirp, i.e., corresponds to the worst-case chirp calculation. As is clearly seen in Fig. 4.20d, for  $R_f = 0.1\%$  the time-resolved chirp represents a relaxation oscillation which arises from the dynamic nature of the laser.

It was also found that a reduction in  $R_f$  leads to lower oscillation peaking. Here, the peak-to-peak height of the dynamic chirp is defined as  $\Delta\lambda_{\text{d chirp}}$ . The residual  $\Delta\lambda_{\text{d chirp}}$  that exists even at  $R_f = 0\%$  (Fig. 4.20a) is due to the phase chirp caused by the refractive index modulation in the modulator medium. This modulation is determined by the modulator chirp parameter  $\alpha_{\text{pmod}}$ . It is interesting to note that when  $R_f$  is less than about 0.01%,  $\Delta\lambda_{\text{d chirp}}$  is dominated by  $\alpha_{\text{pmod}}$  rather than  $R_f$ . This might indicate that with this chirp combination of  $\alpha_{\text{pld}}$  and  $\alpha_{\text{pmod}}$ ,  $R_f$  of 0.01%

**Table 4.1** List of device and transmission parameters used to simulate the effect of facet-reflection induced chirp on fiber transmission performance

Parameter	Symbol	Unit	Value
Laser parameters			
Wavelength	$\lambda$	$\mu\text{m}$	1.557
Optical confinement factor	$\xi$	–	0.027
Carrier lifetime	$\tau_N$	ns	0.22
Photon lifetime	$\tau_P$	ns	variable
Differential gain	$dg/dN$	$\text{m}^2$	$5 \times 10^{-12}$
Laser $\alpha$ parameter	$\alpha_{\text{ld}}$	–	3.0
Gain saturation coefficient	$\varepsilon$	$\text{m}^3$	$5 \times 10^{-23}$
Cavity length	$L_{\text{ld}}$	$\mu\text{m}$	400
Active region width	$W_{\text{act}}$	$\mu\text{m}$	1.5
Well number	$N_w$	–	7
Coupling coefficient	$\kappa_L$	–	1.5
Rear facet reflectivity	$R_r$	%	90
Rear facet phase	$\theta_r$	–	variable
Modulator parameters			
Modulator $\alpha$ parameter	$\alpha_{\text{mod}}$	–	0.4
Front facet reflectivity	$R_f$	%	variable
Rear facet phase	$\theta_f$	–	variable
Modulator length	$L_{\text{mod}}$	$\mu\text{m}$	200
Extinction ratio	ER	dB	16
Parasitic capacitance	$C_{\text{mod}}$	pF	1.0
Driver impedance	$R_z$	$\Omega$	50
Transmission parameters			
Bit rate	$B$	Gbit/s	2.5
Fiber dispersion	$D$	ps/(nm km)	17
Fiber loss	$L$	dB/km	0.2
Nonlinear coefficient	$n_2$	$\text{m}^2/\text{W}$	$2.6 \times 10^{-20}$
Fiber input power	$P_{\text{in}}$	dBm	10

is low enough to eliminate the effect of facet reflection on the hybrid chirp behavior. Simulation results showing how the eye diagrams before and after transmission through 125 km, 250 km, 375 km, and 500 km long fibers depend on  $R_f$  are presented in Fig. 4.21.

Facet phase combinations  $(\theta_f, \theta_r)$  of (a)  $(0\pi, 0\pi)$  and (b)  $(\pi/2, \pi/2)$  were chosen as examples. The results clearly indicate serious eye distortion caused by the optical feedback chirp when  $R_f$  is larger than 0.5%. To determine the criterion for  $R_f$ , the simulated transmission power penalty ( $P_d$ ) was plotted against  $R_f$  for all 64 facet phase combinations. The calculation was performed for transmission over normal fibers of 125 km, 250 km, and 500 km length. The results are plotted in Fig. 4.22, which illustrates the  $R_f$  criteria for achieving 2.5 Gbit/s transmission with reproducibly low  $P_d$  values.

From the figure, the  $R_f$  values that reproducibly allow  $P_d$  of less than 1 dB are roughly 0.3%, 0.1%, and 0.04% for the 125 km, 250 km, and 500 km transmission distance, respectively. A linear dispersion limit of  $\alpha_{\text{pld}}$  of 0.4 is also indicated to be

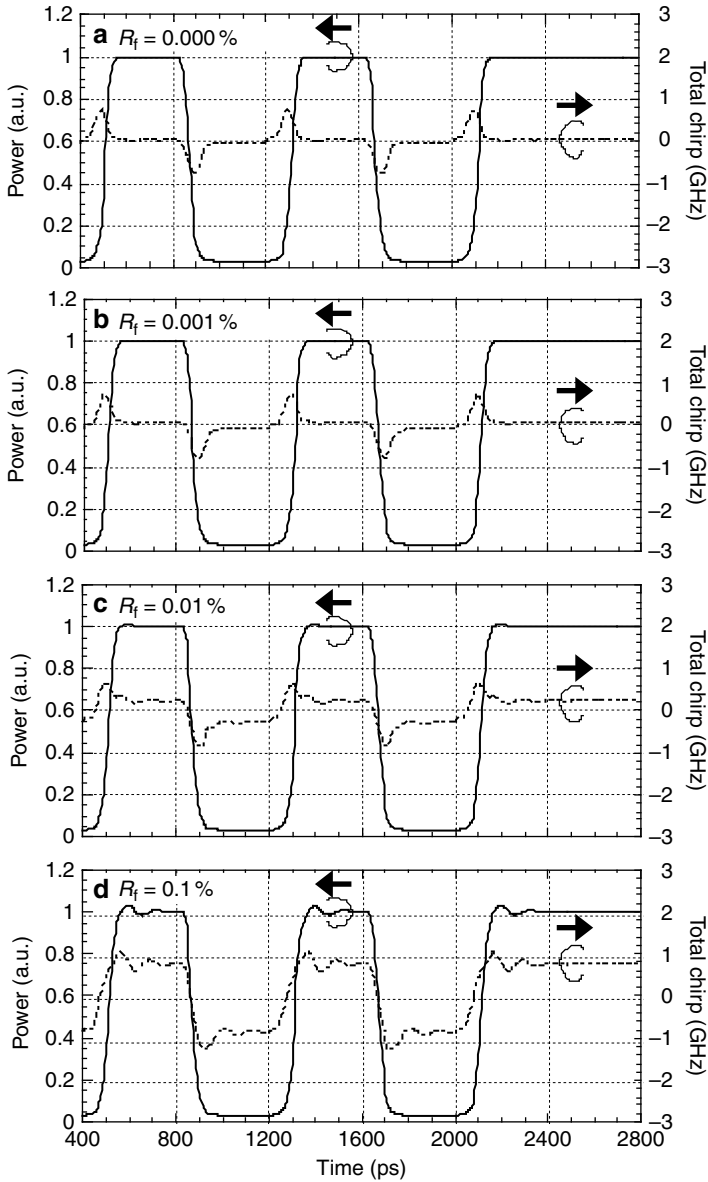


**Fig. 4.20** Calculated modulation waveforms and corresponding dynamic chirp under 2.5 Gbit/s digital modulation with various values of modulator facet reflectivity

effective at about 500 km. This means that the maximum transmission distance is no longer limited by  $R_f$ , but by  $\alpha_{\text{pmod}}$  itself when  $R_f$  is less than 0.04%. This finding is in qualitative agreement with the  $R_f$  dependence of the dynamic chirp shown in Fig. 4.20.

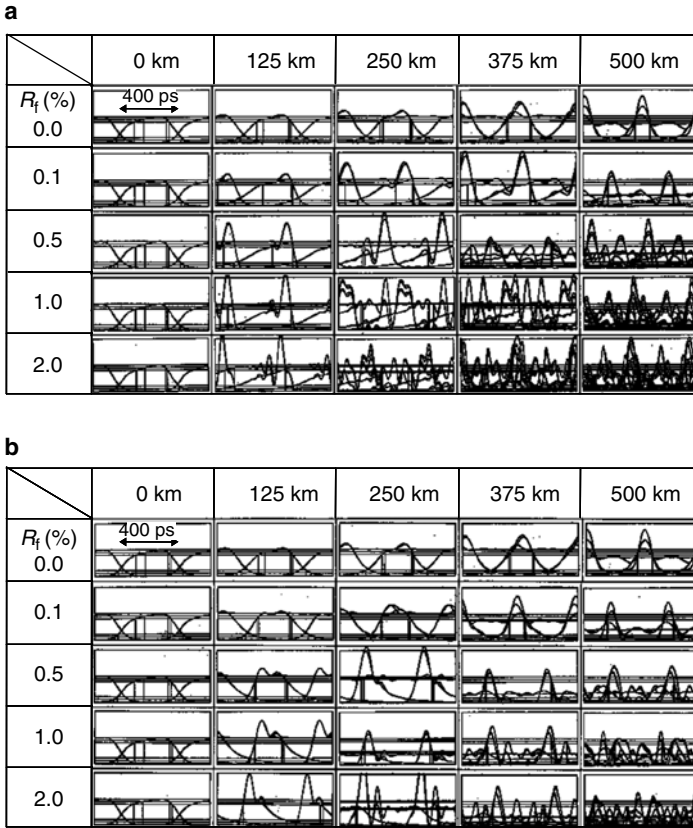


**Fig. 4.21** Calculated transmitted eye diagrams for a signal rate of 2.5 Gbit/s for various values of modulator facet reflectivity: **a**  $\theta_f = 0\pi$ ,  $\theta_r = 0\pi$ ; **b**  $\theta_f = \pi/2$ ,  $\theta_r = \pi/2$ .  $\theta_f$  and  $\theta_r$  denote the relative corrugation phases at the front and rear facet

Next, the measured eye patterns before and after transmission over 120 km and 240 km long fibers are compared with the simulated ones, using the facet phases as fitting parameters. This comparison is shown in Fig. 4.23a for a device with a large  $R_f$  of about 2%. By roughly choosing facet phases with an accuracy of  $\pi/4$ , close correspondences were obtained. This provides a reasonable explanation of the intersymbol interference shown in Fig. 4.23a, where faster propagation of the energy at the leading edge caused by the blue chirp can be seen to occur. This behavior is very similar to directly modulated lasers [75, 76]. It is important to note, however, that the sign of the excess chirp is determined randomly by the facet phase combination, which is difficult to control deliberately. This means that reduction of  $R_f$  is essential to reproducibly attain low-chirp operation independently of the facet phases. Figure 4.23b shows the same results for a device with a lower  $R_f$  of less than 0.02% achieved through the combination of a window structure and/or multilayer antireflection coating techniques. In this case, good agreement was obtained between ex-



**Fig. 4.22** Criteria for modulator facet reflectivity to achieve 2.5 Gbit/s long-distance fiber transmission

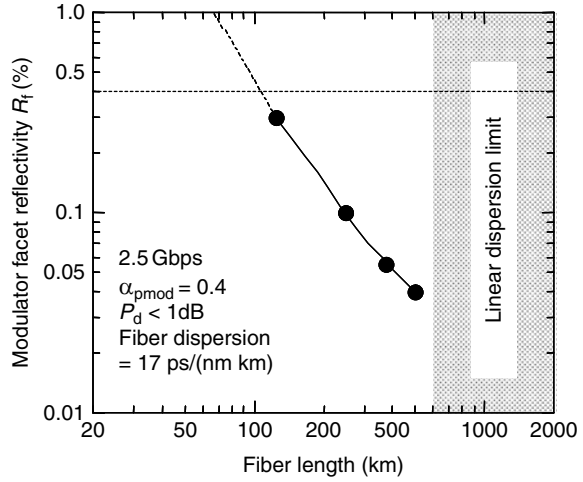


**Fig. 4.23** Comparison of eye diagrams between experiment and simulation for  $R_f = 2\%$  (a) and  $R_f \sim 0.02\%$  (b)

	<b>a</b>			
	exp.	$P_d$	sim.	$P_d$
0 km		-		-
120 km		2.3 dB		2.1 dB
240 km		floor		3.2 dB
	<b>b</b>			
	exp.	$P_d$	sim.	$P_d$
0 km		-		-
120 km		2.3 dB		2.1 dB
240 km		floor		3.2 dB

periment and simulation for all 16 combinations of the facet phases, suggesting that  $R_f$  of 0.02% is small enough for 240 km transmission, in agreement with the above theoretical prediction.

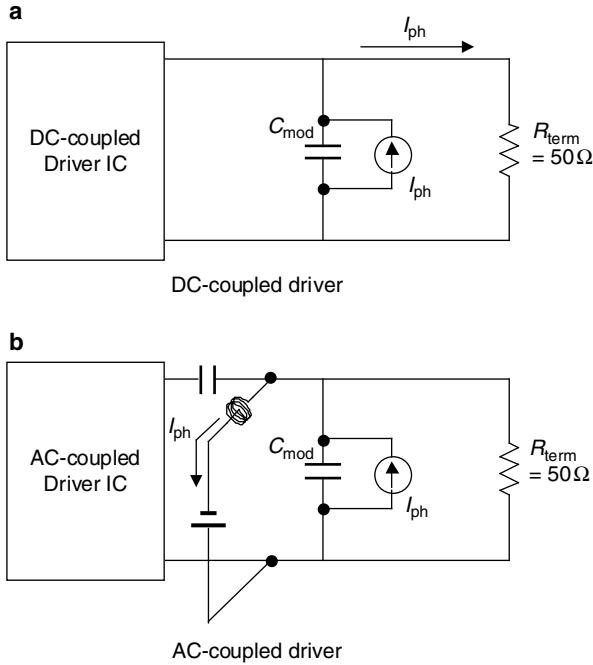


**Fig. 4.24** Electrical circuit model of EA/DFB laser combined with a DC-coupled (a) and an AC-coupled (b) driver IC.  $C_{mod}$ : modulator capacitance,  $R_{term}$ : termination resistance

### 4.3.5 Effect of Photogenerated Current on Modulation Characteristics

When the EA/DFB laser is under operation, photogenerated current  $I_{ph}$  is produced due to light absorption in the EA modulator section. This continuous current may flow in the assembly circuits, which adversely affects the modulator performance. Circuit models of high-speed EA/DFB lasers considering  $I_{ph}$  are shown in Fig. 4.24.

The DC-coupled scheme corresponds to the normal EA/DFB assembly method.  $I_{ph}$  can flow in a  $50\ \Omega$  impedance-matching resistor along with the bias current of  $V_{ca}/50$  because the driver circuit of the modulator is usually designed to have high impedance. This extra  $I_{ph}$  flow into the resistor can severely affect RF reflection. The scattering parameters  $S_{11}$  and  $S_{21}$  of the EA/DFB laser, taking into account the existence of  $I_{ph}$  flow, are modeled in Fig. 4.24 and given by the following equations [76]:

$$S_{21}(\omega) = 10 \log_{10} \left| \frac{H(\omega)}{H(0)} \right|^2 \text{ [dB]}, \tag{4.22}$$

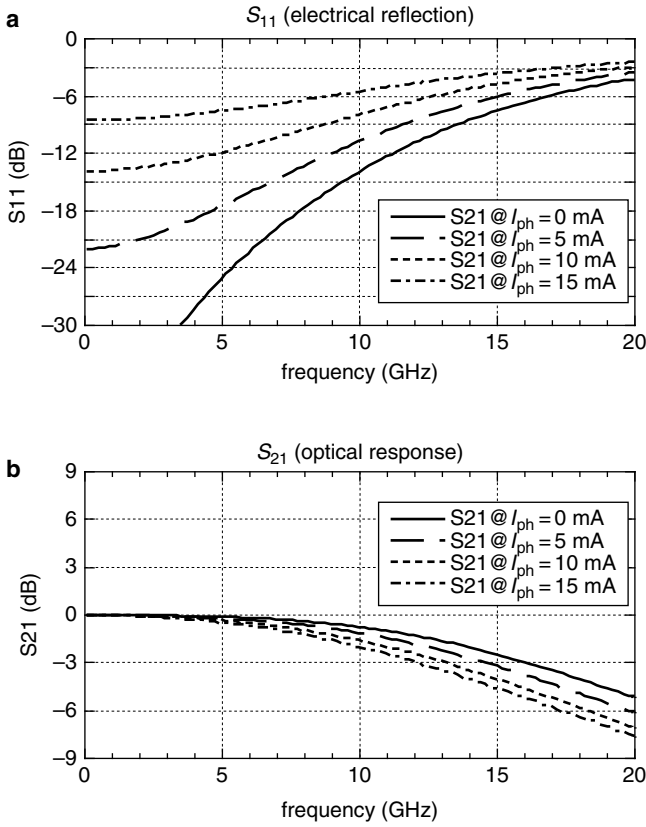


**Fig. 4.25** Calculated frequency responses of  $S_{11}$  (a) and  $S_{21}$  (b) parameters for several photocurrents

where

$$H(\omega) = \frac{\{kR_{\text{mod}} + (1+k)(R_{\text{term}} + j\omega L_2)\}}{j\omega C_{\text{mod}}} \frac{1}{(R_c + j\omega L_1) \left\{ \left( R_{\text{mod}} + \frac{1}{j\omega C_{\text{mod}}} \right) + (R_{\text{term}} + j\omega L_2) \right\} + (R_{\text{term}} + j\omega L_2) \left[ R_{\text{mod}} + \frac{(1+k)}{j\omega C_{\text{mod}}} \right]}, \quad (4.23)$$

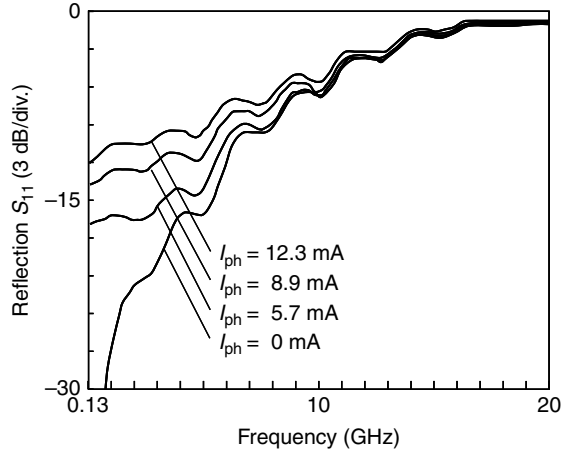
with  $k = R_{\text{term}} I_{\text{ph}} / V_{\text{mod}}$ , and

$$S_{11}(\omega) = 10 \log_{10} \left| \frac{G(\omega)}{G(0)} \right|^2 \quad [\text{dB}], \quad (4.24)$$

with

$$G(\omega) = j\omega L_1 + \frac{(R_{\text{term}} + j\omega L_2) \left\{ \frac{R_{\text{mod}} + (1+k)}{j\omega C_{\text{mod}}} \right\}}{\left( \frac{R_{\text{mod}} + 1}{j\omega C_{\text{mod}}} \right) + (R_{\text{term}} + j\omega L_2)}. \quad (4.25)$$

**Fig. 4.26**  $S_{11}$  parameters measured at several photo-currents



Here, the parameter  $k$  as defined before is a constant that represents  $I_{ph}$ . Calculated frequency responses of the  $S_{11}$  and  $S_{21}$  parameters for several values of  $I_{ph}$  are shown in Fig. 4.25.

The calculated  $S_{11}$  parameter largely decreases with increasing  $I_{ph}$ . The measured frequency dependence of  $S_{11}$  for various values of  $I_{ph}$  is shown in Fig. 4.26, where the response curves can be seen to be similar to those of the theoretical results illustrated in Fig. 4.25a.

It is meaningful to qualitatively explain the  $S_{11}$  dependence. In the circuit model in Fig. 4.24a, any current  $I_{ph}$  that flows into the  $50\ \Omega$  matching resistor reduces the voltage at the input port. This voltage reduction leads to a deviation of the actual terminal resistance  $R_{term}$  from the ideal value of  $50\ \Omega$ . Under DC conditions ( $f = 0\ \text{Hz}$ ),  $R_{term}$  is given by

$$R_{term} [\Omega] = \frac{50}{1 + \frac{50I_{ph}}{V_{mod}}}, \quad (4.26)$$

where  $V_{mod}$  is the bias voltage applied to the modulator. Equation (4.26) indicates that  $R_{term}$  becomes smaller than  $50\ \Omega$  once a photocurrent is generated and that this reduction of  $R_{term}$  can directly deteriorate  $S_{11}$ . Fortunately, as shown in Fig. 4.26, the measured  $|S_{11}|$  at 5 GHz under the worst condition (i.e.,  $I_{ph} > 10\ \text{mA}$ ) is at least 10 dB. Such an  $S_{11}$  value does not cause a critical problem at a data rate of 2.5 Gbit/s. However, it must be improved if higher bit rate transmission, as used in 10 to 40 Gbit/s systems, is envisaged. The curves in Fig. 4.24b reveal the  $I_{ph}$  sensitivity of  $S_{21}$ . When  $I_{ph}$  amounts to 15 mA, the 3 dB-down bandwidth is reduced by about 20%. This reduction should also be taken into account in the design of high-speed EA/DFB lasers.

Another vital issue is the  $I_{ph}$ -induced reduction of the effective modulation voltage swing of EA-driver ICs. A non-negligible amount of  $I_{ph}$  can flow in the driver circuit when this circuit is directly connected to the modulator (DC-coupled scheme,

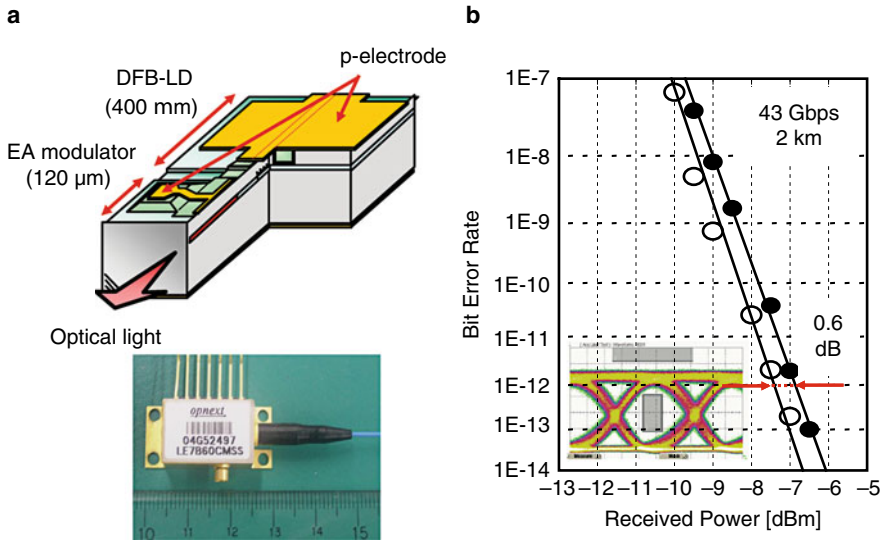


**Fig. 4.27** Example of a 43 Gbit/s low-chirp EA/DFB laser in the 1.55  $\mu\text{m}$  range [77]. Chip schematic and photograph of module (a), and 43 Gbit/s 2 km normal fiber transmission performance (b)

Fig. 4.24a). This leakage current easily produces a voltage drop in the output signal swing of the driver, and this tends to reduce the dynamic extinction ratio. This indicates that careful attention should be paid to this voltage drop when designing RF-signal connections between EA/DFB lasers and driver circuits. One simple solution for this could be to introduce a bypass line for  $I_{\text{ph}}$ , as shown in Fig. 4.24b. If this bypass circuit is integrated into the driver IC, most of the  $I_{\text{ph}}$  flow will take this path to effectively suppress the adverse effects of  $I_{\text{ph}}$  on modulator performance.

### 4.3.6 Packaged High-speed Externally Modulated Lasers

An example of a real high-speed low-chirp EA/DFB laser that operates in the 1.55  $\mu\text{m}$  wavelength range [77, 78] is shown in Fig. 4.27a. 43 Gbit/s operation and 2 km transmission over a standard single-mode fiber has been demonstrated employing those devices. Note that an extended data rate of up to 43 Gbit/s is needed to meet the system demands for forward error correction (FEC). The reported device consists of a short InGaAsP MQW-based EA modulator monolithically integrated with a DFB-laser light source made of the same material. It was bonded onto a chip carrier with a 50  $\Omega$  termination resistor and then packaged in a high-speed module involving lenses, a thermoelectric cooler, a thermistor, and a high-speed standard electrical connector. The module was hermetically sealed for reliability reasons. Evidencing the small parasitics in the EA/DFB chip and the assembly, a 3 dB-down bandwidth of over 40 GHz was measured on this device, and 43 Gbit/s

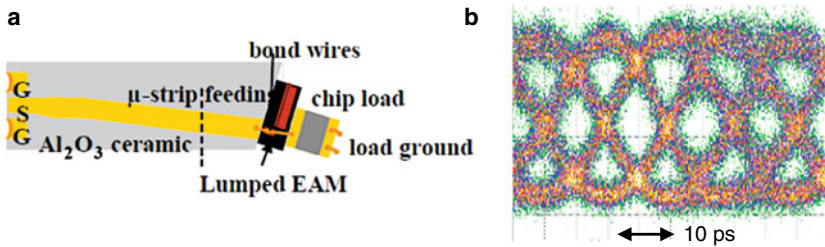


**Fig. 4.28** World's first serial 100 Gbit/s EA/DFB laser [80]. EA/DFB laser assembled on a high-speed carrier (a) and 100 Gbit/s optical waveform (b)

operation was successfully demonstrated at a modulator voltage swing  $V_{pp}$  of 2.5 V (Fig. 4.27b). Currently, 40 Gbit/s EA/DFB lasers are mainly deployed in communications in so-called very-short-reach router-to-router interconnections and/or client interfaces.

Devices capable of even 50 Gbit/s modulation have been developed recently which may be used as building blocks in future >100 Gbit/s multilane transmitters, e.g., for 400 G-Ethernet applications [79], and 50 Gbit/s does by far not yet represent an upper speed limit of EA/DFB devices. In fact, the world's first serial 100 Gbit/s lumped-element EA/DFB laser, shown in Fig. 4.28, was introduced about three years ago [80]. This particular component contained an InGaAlAs-based 10-quantum-well absorption layer structure that was buried by a low-capacitance semi-insulating buried heterostructure. Using a 50  $\mu\text{m}$  short modulator coassembled with a high-speed driver IC, 100 Gbit/s open eye diagrams could be successfully accomplished at such an ultrahigh bit rate for the first time.

#### 4.3.7 Uncooled, High-speed, Low-chirp Externally Modulated Lasers

EA/DFB lasers have been playing an important role in telecommunication networks due to their distinctly advantageous features, namely, ultrahigh speed capability, low chirp, low power consumption, and compactness. With the explosive spread of broadband services, power consumption is becoming more and more critical, and one of the key issues of related photonics/electronics is to find ways to reduce it. Focusing on the environmental temperature of these components, most directly modulated diode lasers have been evolving from temperature-stabilized (cooled) devices to temperature-robust (uncooled) ones. Uncooled operation of directly modulated diode lasers in short-link applications has successfully eliminated the electric power consumed by thermoelectric coolers. Accordingly, cooler-free operation has been strongly desired also for EA/DFB lasers deployed in modules for long-distance transmission. However, this goal proves to be highly challenging, the main reason being that EA/DFB lasers behave very sensitive to changes in operating temperature.

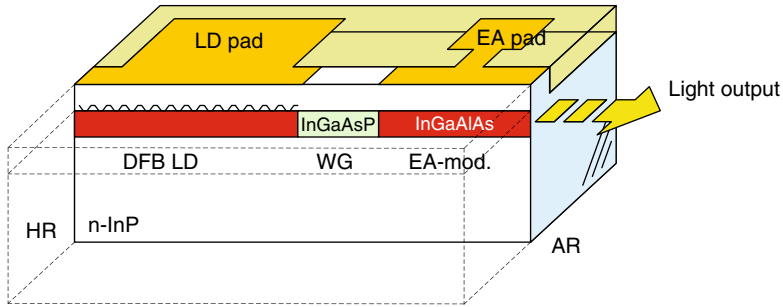


**Fig. 4.29** Schematic chip structure of the first 1.55  $\mu\text{m}$  uncooled EA/DFB laser [84]

This fact essentially arises from the large mismatch in the temperature coefficients of the electroabsorption peak wavelength (typically 0.7 nm/K) and the DFB-lasing wavelength (typically 0.1 nm/K). The phenomenon is widely known, and the mismatch has often been compensated for by controlling the DC bias voltage applied to EA modulators [81, 82]. In most cases, the DC bias has been adapted to the operating temperature set for tuning the DFB wavelength to a targeted wavelength-division-multiplexing (WDM) grid channel [82]. This technique has also been applied to extending the operating temperature range of the device [81]. An uncooled EA/DFB laser for short-reach (10 km) applications has been proposed using this voltage-offset method [83]. When the offset DC-bias applied to the EA modulator was adjusted to suit the temperature variation, the device was able to handle the mismatch in wavelength shift over a wide temperature range. One key issue involved is how to keep the detuning parameter (i.e., the difference between the DFB lasing and the electroabsorption peak wavelength) nearly constant. In addition to this, careful attention must be paid to the increase in optical loss and the change in chirp when applying an offset bias. As to the optical loss, any increment of the applied bias voltage as well as of the temperature is certain to lead to increasing light absorption. Whereas this would be unlikely to occur in case of an ideal step-function-shaped absorption spectrum, in reality it will occur because of the existing tail-shaped absorption spectrum. For these reasons, a properly designed detuning parameter is very important from a practical viewpoint to keep the optical loss within a tolerable range. It should be noted here that the device reported in [83] was designed for short-reach transmission in the 1.3  $\mu\text{m}$  wavelength range, where chirping virtually does not matter so much. For 1.55  $\mu\text{m}$  range long-reach applications, however, there have been serious difficulties in managing the severe trade-off between the extinction ratio and optical loss plus chirp. This renders achieving uncooled operation of 1.55  $\mu\text{m}$  EA/DFB lasers much more difficult, compared to their 1.3  $\mu\text{m}$  counterparts.

The first successfully accomplished uncooled high-speed, low-chirp EA/DFB laser operating in the 1.55  $\mu\text{m}$  range is schematically illustrated in Fig. 4.29 [84]. The device comprised a temperature-robust InGaAlAs EA modulator, an InGaAsP DFB laser, and an InGaAsP bridge waveguide in between, monolithically integrated on an InP substrate. As with directly modulated diode lasers, the InGaAlAs material

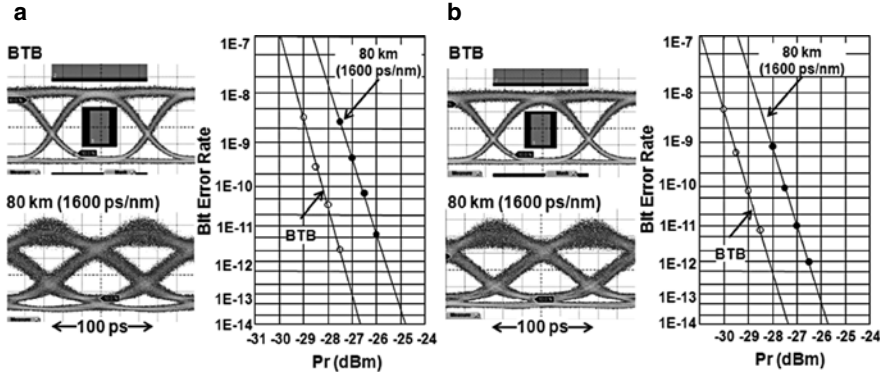


**Fig. 4.30** 10 Gbit/s 80 km (1600 ps/nm) single-mode fiber transmission characteristics. **a** 15 °C: DER = 9.8 dB,  $P_d = 1.7$  dB and **b** 95 °C: DER = 10.9 dB,  $P_d = 1.5$  dB

effectively enhances the temperature tolerance of the EA modulator, owing to its favorable band structure. The large  $\Delta E_c$  associated with InGaAlAs is beneficial for the extinction ratio at low temperatures by effectively maintaining the QCSE under the high electric field applied to quantum wells. On the other hand, a small valence band offset  $\Delta E_v$  supports prompt sweep-out of photogenerated holes over shallow valence band barrier walls, implying high optical power robustness.

Measured eye diagrams obtained under 10 Gbit/s,  $2^{31} - 1$  PRBS modulation are shown in Fig. 4.30 for 15 °C and 95 °C. Clearly opened eye diagrams were obtained at both operating temperatures even after transmission through an 80 km long normal dispersion fiber. The measured error-free bit error rate (BER) performance after 80 km transmission with power penalty ( $P_d$ ) of less than 2 dB and dynamic extinction ratio (DER) of greater than 9 dB are sufficient for practical use in 10 Gbit/s intermediate-reach (40 km) and long-reach (80 km) applications [85–87].

Another emerging application of high-speed EA/DFB lasers is 100-Gigabit Ethernet (100 GE) [88]. As briefly outlined in the beginning of this chapter, 100 GE is becoming the next-generation high-speed network standard to meet the explosive increase in network traffic [7]. The world's first standard-compliant 100 GE transceiver module using EA/DFB light sources operating in the 1.3  $\mu\text{m}$  range is shown in Fig. 4.31.

Four sets of 25 Gbit/s-driven EA/DFB lasers are assembled inside a 100 GE compact form-factor pluggable (CFP) module ( $144 \times 78 \times 13.6 \text{ mm}^3$ ) [89] to form  $4 \times \lambda$ -channels yielding an aggregate data rate of 100 Gbit/s in a wavelength-division-multiplex-manner. Moreover, 25.8 Gbit/s 12 km single-mode-fiber transmission was achieved over a wide temperature range from 0 to 85 °C which is attractive in view of energy efficiency. This module is therefore considered a promising candidate for cost-effective 100 GE client-side technology. A 40 Gbit/s uncooled EA/DFB laser using similar technologies has also been successfully demonstrated [87]. Ideally, the four laser devices and the wavelength multiplexer needed in the above four-lane transmitter configuration would be monolithically integrated on



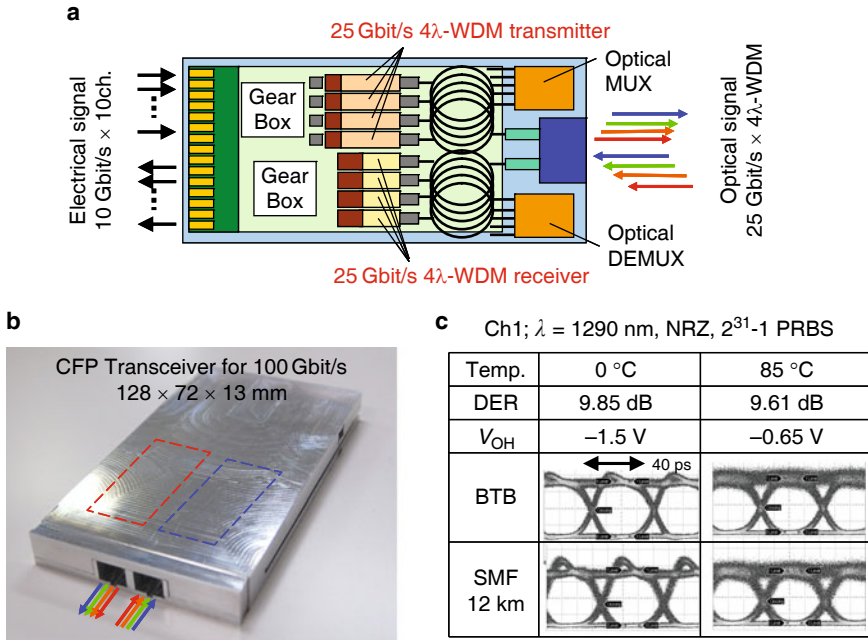


**Fig. 4.31** First parallel 100 Gbit/s transceiver using 25 Gbit/s 4 $\lambda$ -WDM EA/DFB light sources. **a** Schematic structure of 100 GE transponder, **b** 100 Gbit/s CFP transceiver, and **c** 25 Gbit/s optical waveform for uncooled operation

one chip to reduce packaging expenditures and to enable the use of small-size packages. Such a transmitter chip incorporating four monolithic EA/DFB devices, emitting at four different wavelengths ranging from 1.297 to 1.309  $\mu\text{m}$  (LAN-CWDM grid), and a multimode interference (MMI) coupler to form the multiplexer was realized very recently [90] and successfully tested for 100 GE applications at semi-cooled conditions.

## 4.4 New Challenges for Ultrafast Semiconductor Light Sources

### 4.4.1 High-speed Active/Passive Feedback Diode Lasers

The physical limit of the modulation speed of semiconductor diode lasers can be artificially controlled by the modulation scheme employed. In 1985, K. Iga made a clear theoretical prediction for improving laser dynamics [91]. He showed that instead of modulating the injection current into a diode laser, one could alternatively modulate the optical gain, loss, or photon lifetime. He pointed out that the maximum frequency for gain and photon lifetime (cavity  $Q$ -factor) modulation can exceed the relaxation oscillation frequency  $f_r$ . The degree to which the small-signal response

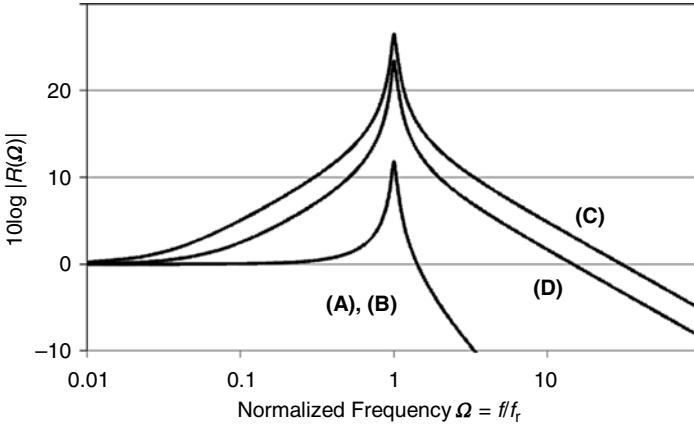


**Fig. 4.32** Calculated modulation responses for various schemes [91]. (A) Injection current modulation, (B) carrier loss modulation, (C) gain modulation, (D) cavity  $Q$  modulation

$R(f)$  may be improved, for example, by  $Q$ -factor modulation (i.e., photon lifetime modulation) or by gain modulation as illustrated in Fig. 4.32 [91]. This figure clearly points out the possibility of achieving faster response in diode lasers by a factor of more than ten using such modulation schemes.

Based on this suggestion, there have been several practical approaches for applying alternative modulation schemes to high-speed diode lasers. These include optical injection locking [92–97], gain switching [98–100], and multisection waveguide lasers, including an active/passive feedback mechanism [101–107].

Here, we focus on active/passive feedback lasers. The high-speed characteristics of diode lasers can be improved by optical feedback to the laser cavity or, in other terms, by modulating the mirror reflectivity [105]. The high-speed operability relies on an enhanced frequency bandwidth achieved by photon lifetime modulation. The relatively slow response associated with carrier–photon interaction that governs relaxation oscillation in diode lasers is replaced by photon–photon interaction. This effect leads to an additional photon–photon resonance peak at frequencies that potentially exceed the usual carrier–photon resonant frequency several times. Using the passive-feedback DFB laser depicted in Fig. 4.33, 40 Gbit/s direct current modulation at an emission wavelength of 1.55  $\mu\text{m}$  could be demonstrated for the first time [107]. The basic laser structure is an active/passive monolithic two-section laser with a standard section length of a few hundred micrometers. AR and HR (>90%) coatings were applied to the DFB and integrated feedback (IFB) facet, respectively.

When the optical modulation response was recorded under different IFB biasing, a strong change in the modulation bandwidth was observed. The feedback effect is shown in more detail in Fig. 4.33. Without any support from the feedback section (absorbing IFB section, dashed line), the behavior was found to be similar to that of a single-section DFB laser, the modulation bandwidth of which is limited by the carrier-photon resonance frequency of typically 8–12 GHz. On the other hand,

**Fig. 4.33** Effect of optical feedback on small-signal response (*inset: laser structure*) [107]

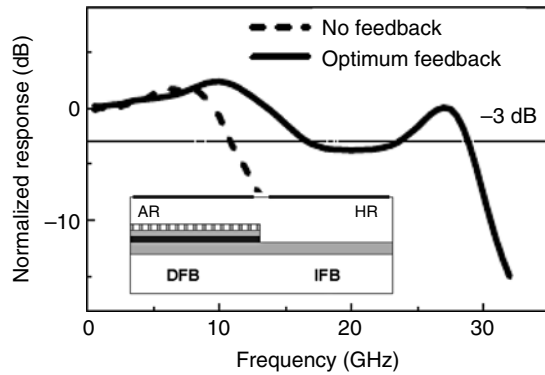
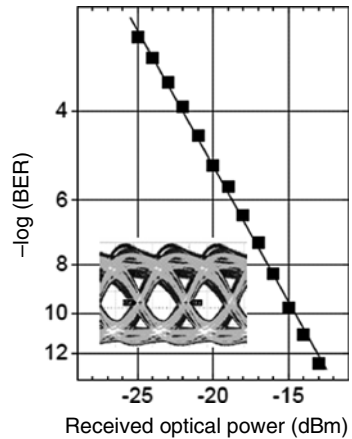


**Fig. 4.34** Results of back-to-back BER measurements at 40 Gbit/s large-signal modulation [107]



a drastically enhanced modulation bandwidth of about 30 GHz was measured under optimum feedback conditions, thus exceeding the normal relaxation oscillation frequency limit by a factor of 3. Figure 4.34 shows successful large-signal modulation at 40 Gbit/s achieved with no bit errors when measured for  $2^7 - 1$  PRBS NRZ data streams [107]. It should be emphasized that the 40 Gbit/s operation was accomplished with low-gain active material, InGaAsP, at a moderate current level of 40 mA.

#### 4.4.2 EA/DFB Laser Devices with Traveling-wave Modulator

As discussed in the previous sections, the EA-modulated laser is currently one of the most promising candidates for high-speed compact light sources for use in long-distance communications. The present EA modulators are based on lumped element designs and models (see Fig. 4.18b), and their high-speed capability is limited by the CR time constant  $C_{\text{mod}}(R_{\text{mod}} + R_{\text{term}}/2)$ , as expressed in (4.20). Here again,  $C_{\text{mod}}$ ,  $R_{\text{mod}}$ , and  $R_{\text{term}}$  denote modulator capacitance, modulator internal resistance,

and a 50- $\Omega$  termination resistor, respectively. With this conventional technology, EA/DFB lasers operating at 40 Gbit/s driven by signals with a voltage swing of 2–3  $V_{pp}$  have been deployed in real subsystems. These values result in a figure of merit (FOM) of roughly 17–20 GHz/V. It will be difficult to further improve this figure significantly in a practical way by simply exploiting conventional schemes because the reduction of  $C_{mod}$  by using even shorter modulator structures leads to poor extinction ratio and, hence, high driving voltage. It should also be mentioned that even if a higher-speed EA modulator, for example, a 100 Gbit/s EA modulator, is realized, we will still face the inherent fiber dispersion limitation. According to the data discussed in Sect. 4.3.2, the maximum transmission distance of 100 Gbit/s, 1.3  $\mu\text{m}$ -range signals produced by the EA modulator will be nearly 1 km. To extend the high-speed limitation of lumped EA modulators, structures featuring “traveling-wave” designs have been demonstrated to overcome the RC-limitation [108–111]. The aim of the traveling wave is to reach very-high-speed intensity modulation by exploiting the electrical/optical velocity matching effect. With traveling-wave EA modulators, the lumped short electrode is replaced by a relatively long transmission-line electrode. This approach was initially developed for Mach–Zehnder interferometer modulators formed on lithium niobate ( $\text{LiNbO}_3$ ) (see Chap. 6), and on III–V compounds (GaAs [112, 113] as well as InP [114–116]). In the traveling wave design, the electrical drive signal propagates in the same direction as the optical modulated signal. Ideally, both signals run at the same speed, permitting the light modulation to accumulate monotonically as they propagate together, which could, in principle, lead to non-RC-limited operation, irrespective of the operating frequency. In reality, however, it is not very easy to perfectly match the velocities of the two waves. This causes a walk-off between the electrical and optical signal waves, which tend to severely degrade the high-speed capability. It can be readily shown that the frequency response  $R(f)$  of an idealized traveling-wave modulator is expressed as [112]

$$R(f) = \left[ \frac{\sin\left(\frac{\pi f |n_{opt} - n_{ele}| L_{mod}}{c}\right)}{\frac{\pi f |n_{opt} - n_{ele}| L_{mod}}{c}} \right]^2, \quad (4.27)$$

where  $n_{opt}$  and  $n_{ele}$  denote the optical and electrical effective refractive indices, and  $L_{mod}$  the modulator length (being equal to the length of the traveling-wave electrodes). From (4.27), the 3 dB-bandwidth can be derived:

$$f_{3\text{ dB}}^{\text{TW}} = \frac{1.39c}{\pi |n_{opt} - n_{ele}| L_{mod}}. \quad (4.28)$$

Because of the negative dependence on  $L_{mod}$ , the bandwidth and drive voltage can be traded for in the same way as with lumped element modulators; thus, the bandwidth-voltage FOM is equally applicable [112]. In the case of traveling-wave EA modulators, however, there is a large mismatch between  $n_{opt}$  and  $n_{ele}$ , which inevitably makes their characteristic impedance small,  $\sim 25\ \Omega$ , about half of the standard 50  $\Omega$  RF connections. This difference is likely to seriously degrade the optical waveforms owing to large electrical reflection. In response, several veloc-

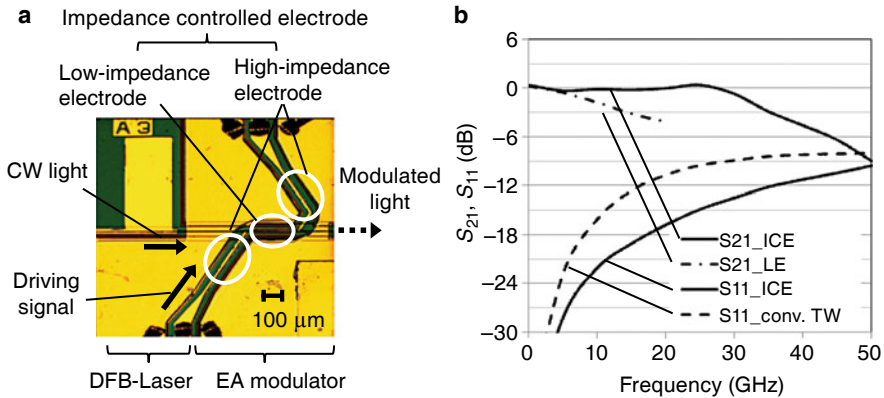


**Fig. 4.35** Improved traveling-wave EA modulator integrated laser [108]. **a** View of an EA/DFB laser with an impedance controlled electrode and **b** improved frequency responses compared with lumped-element (LE) and conventional traveling-wave (TW) designs

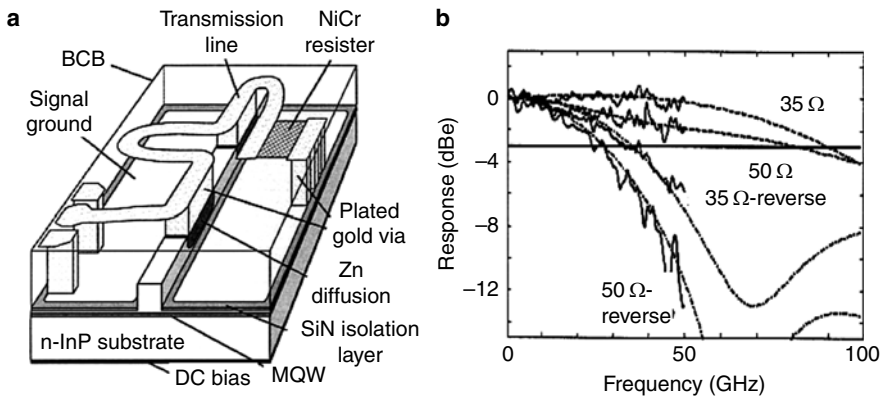


**Fig. 4.36** **a** Device structure and **b** optical small-signal frequency responses of a segmented transmission-line EA modulator [111]

ity/impedance matching techniques have been developed for improving conventional low-impedance traveling-wave EA modulators.

Such a refined traveling-wave EA-integrated laser [108] is shown in Fig. 4.35a. To compensate for the inherently low characteristic impedance of EA modulators, a high-impedance transmission line is integrated with a low-impedance traveling-wave EA modulator. This simple method is quite successful in achieving quasi-impedance matching between the modulator and driver circuit, which greatly enhances the high-frequency performance (Fig. 4.35b), and this kind of artificial impedance control electrode (ICE) was found to be very effective in achieving a compact low-power-consumption 40 Gbit/s EA/DFB laser. A packaged device with an InP/InGaAs hetero-bipolar-transistor (HBT) based IC driver was able to provide 40 Gbit/s, 2 km single-mode-fiber transmission with a 0.3 dB penalty only [108].

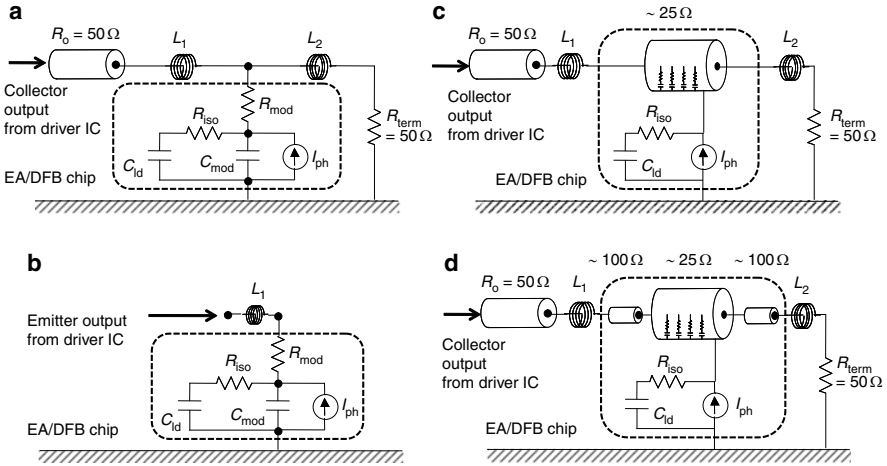


**Fig. 4.37** Circuit models of various high-speed EA-modulator-integrated light sources. **a** Conventional lumped-element EA/DFB, **b** emitter-follower driven EA/DFB, **c** conventional traveling wave EA/DFB, and **d** ICE traveling wave EA/DFB

Another important advanced traveling-wave EA modulator [111] is shown in Fig. 4.36a. Here, a segmented transmission-line electrode was used. This solution enables the design of a traveling-wave EA modulator with a characteristic impedance close to 50 Ω. The device exhibits low electrical reflection (return loss: <15 dB) and excellent frequency response up to 50 GHz. A maximum 3 dB electrical bandwidth of 90 GHz was extrapolated by modeling (Fig. 4.36b).

### 4.4.3 Directly IC-driven High-speed Modulators

To further improve the speed and power consumption, a novel approach for driving the EA modulator, referred to as emitter-follower driving technique, has been proposed [117, 118]. This technique is characterized by the fact that the EA modulator is driven by an emitter-follower rather than by a standard collector-follower. The circuit model for this emitter-follower driving scheme is compared with the conventional driving methods discussed earlier in Fig. 4.37.

The EA modulator is connected directly to the driver output signal port of a low-impedance emitter-follower and does not possess a 50 Ω termination. Mathematically, this means that the term  $C_{\text{mod}}R_{\text{term}}/2$  in (4.20) is eliminated, which causes a significant improvement in the high-speed performance as the intrinsic time constant  $C_{\text{mod}}R_{\text{mod}}$  is reduced to about 1/2 to 1/3 of the previous  $C_{\text{mod}}R_{\text{term}}/2$  value. Physically, this means that the modulator dynamics is determined solely by the charging/discharging time of the modulator capacitance  $C_{\text{mod}}$  via the internal resistor  $R_{\text{mod}}$ . It should be noted that this simple driving method is applicable only to EA modulators whose physical dimensions are much smaller than the wavelength of the millimeter-wave signals.

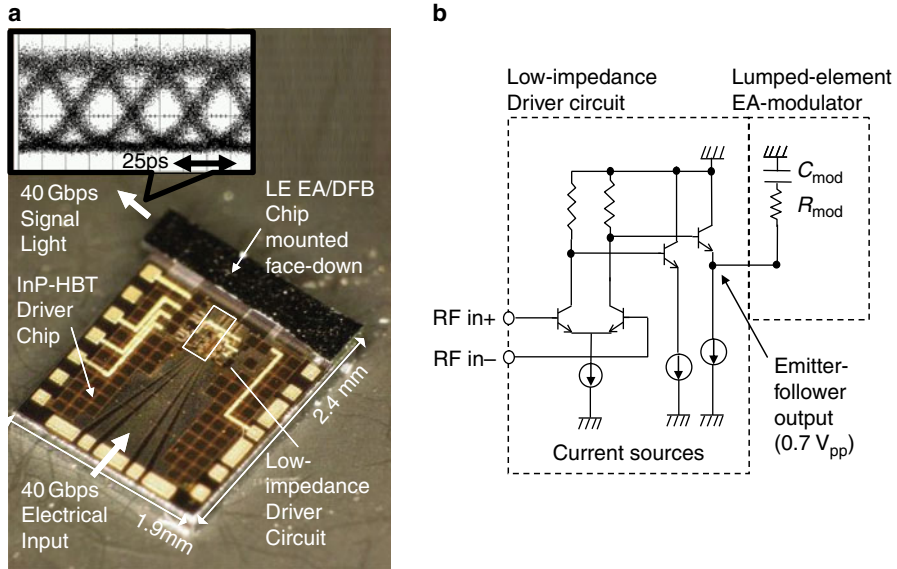


**Fig. 4.38** **a** World's smallest 40 Gbit/s EA/DFB laser based transmitter achieved using the emitter-follower driving technique [117] and **b** the equivalent circuit model

The principle has been experimentally proven using the EA/DFB-on-driver-IC assembly depicted in Fig. 4.38a [117]. As InGaAsP-based MQW EA/DFB laser operating at  $1.55 \mu\text{m}$  was mounted on an InP-based HBT driver IC with the input electrode of the modulator connected directly to the emitter electrode, the output end of the HBT. As shown in Fig. 4.38a, 40 Gbit/s optical eye opening at a low HBT driving voltage of  $0.7 V_{pp}$  was reached, which corresponds to a very high FOM of 57 GHz/V. Due to this low voltage drive along with elimination of the terminal resistor, the transmitter's power consumption amounts to only 0.8 W. Furthermore, its footprint is in the range of a few square millimeters only because the core of the transmitter is determined by the driver IC. This technique will be crucial for low-power consumption dense interconnections in which the signal rate is too high for electrical connections of a few meters encountered on the back planes of terabit-per-second-class high-end servers and routers.

## References

1. <http://www.300pinmsa.org/>
2. <http://www.xenpak.org/>
3. <http://www.xpak.org/>
4. <http://www.x2msa.org/>
5. <http://www.xfpmsa.org/>
6. SFF-8431 Specifications for enhanced 8.5 and 10 Gigabit small form factor pluggable module "SFP+", Revision 2.1, 30 August 2007

7. <http://www.ieee802.org/3/ba/index.html>
8. H. Statz, G. de Mars, *Quantum Electronics*, ed. by C.H. Townes (Columbia University Press, New York, 1960), pp. 530
9. M. Aoki, T.K. Sudo, T. Tsuchiya, D. Takemoto, S. Tsuji, 85 °C 10 Gbit/s operation of 1.3  $\mu\text{m}$  InGaAlAs MQW-DFB laser, *Proc. 26th Europ. Conf. Opt. Commun. (ECOC'00)*, Munich, Germany (2000), vol. 1, pp. 123–124
10. M. Ishikawa, R. Nagarajan, T. Fukushima, J.G. Wasserbauer, J.E. Bowers, Long wavelength high-speed semiconductor lasers with carrier transport effects. *IEEE J. Quantum Electron.* **28**, 2230–2241 (1992)
11. K. Uomi, T. Tsuchiya, H. Nakano, M. Aoki, M. Suzuki, N. Chinone, High-speed and ultralow-chirp 1.55  $\mu\text{m}$  multi-quantum well  $\lambda/4$ -shifted DFB lasers. *IEEE J. Quantum Electron.* **27**, 1705–1713 (1991)
12. D. Marcuse, T.H. Wood, Time-dependent simulation of a laser-modulator combination. *IEEE J. Quantum Electron.* **30**, 2743–2755 (1994)
13. D. Marcuse, T.H. Wood, Simulation of a laser modulator driven by NRZ pulses. *J. Lightw. Technol.* **14**, 860–866 (1996)
14. P.J. Corvini, T.L. Koch, Computer simulation of high-bit-rate optical fiber transmission using single-frequency lasers. *J. Lightw. Technol.* **LT-5**, 1591–1595 (1987)
15. F. Koyama, Y. Suematsu, Analysis of dynamic spectral width of dynamic-single-mode (DSM) lasers and related transmission bandwidth of single-mode fibers. *IEEE J. Quantum Electron.* **QE-21**, 292–297 (1985)
16. H. Temkin, N.K. Dutta, T. Tanbun-Ek, R.A. Logan, A.M. Sergent, InGaAs/InP quantum well lasers with sub-mA threshold current. *Appl. Phys. Lett.* **57**, 1610–1612 (1990)
17. P.J.A. Thijs, L.F. Tiemeijer, P.I. Kuindersma, J.J.M. Binsma, T. van Dongen, High-performance 1.5  $\mu\text{m}$  InGaAs-InGaAsP strained quantum well lasers and amplifiers. *IEEE J. Quantum Electron.* **27**, 1426–1439 (1991)
18. E. Zah, R. Bhat, F.J. Favire, S.G. Menocal, N.C. Andreakis, K.W. Cheung, D.D. Hwang, M.A. Koza, T.P. Lee, Low-threshold 1.5  $\mu\text{m}$  compressive-strained multiple- and single-quantum-well lasers. *IEEE J. Quantum Electron.* **27**, 1440–1450 (1991)
19. T. Namegaya, A. Kasukawa, N. Iwai, T. Kikuta, High temperature operation of 1.3  $\mu\text{m}$  GaInAsP/InP GRINSCH strained-layer quantum well lasers. *Electron. Lett.* **29**, 392–393 (1992)
20. J.S. Osinski, P. Grodzinski, Y. Zou, P.D. Dapkus, Z. Karim, A.R. Tanguay, Low threshold current 1.5  $\mu\text{m}$  buried heterostructure lasers using strained quaternary quantum wells. *IEEE Photon. Technol. Lett.* **4**, 1313–1315 (1992)
21. T. Tsuchiya, M. Komori, K. Uomi, A. Oka, T. Kawano, A. Oishi, Investigation of effect of strain on low-threshold 1.3  $\mu\text{m}$  InGaAsP strained-layer quantum well lasers. *Electron. Lett.* **30**, 788–789 (1994)
22. K. Kojima, O. Mizuhara, L.J.P. Ketelsen, I. Kim, R.B. Bylisma, 1.3  $\mu\text{m}$  uncooled DFB lasers for 10 Gbit/s transmission over 50 km of non-dispersion-shifted fiber, *Opt. Fiber Commun. Conf. (OFC'96)*, Techn. Digest (San Jose, CA, USA, 1996), paper PDP11-2
23. R. Paoletti, M. Agresti, G. Burns, G. Berry, B. Bertone, P. Charles, P. Crump, A. Davies, R.Y. Fang, R. Ghin, P. Gotta, M. Holm, C. Kompocholis, G. Magnetti, J. Massa, G. Meneghini, G. Rossi, P. Ryder, A. Taylor, P. Valenti, M. Meliga, 100 °C 10 Gbit/s directly modulated InGaAsP DFB lasers for uncooled Ethernet applications, *Proc. 27th Europ. Conf. Opt. Commun. (ECOC'01)*, Amsterdam, The Netherlands (2001), PD 84–85
24. G. Sakaino, Y. Hisa, K. Takagi, T. Aoyagi, T. Nishimura, E. Omura, Uncooled and directly modulated 1.3  $\mu\text{m}$  DFB laser diode for serial 10 Gbit/s Ethernet, *Proc. 26th Europ. Conf. Opt. Commun. (ECOC'00)*, Munich, Germany (2000), vol. 1, pp. 125–126
25. M. Kondow, K. Uomi, A. Niwa, T. Kitatani, S. Watahiki, Y. Yazawa, GaInNAs: a novel material for long-wavelength-range laser diodes with excellent high-temperature performance. *Jpn. J. Appl. Phys.* **35**, 1273–1275 (1996)
26. I. Suemune, Theoretical estimation of leakage current in II-VI heterostructure lasers. *Jpn. J. Appl. Phys.* **31**, 95–98 (1992)



27. T. Kitatani, J. Kasai, K. Nakahara, K. Adachi, M. Aoki, High-performance GaInNAs long-wavelength lasers, *Conf. Indium Phosphide Relat. Mater. (IPRM'07)*, Techn. Digest (2007), pp. 354–357
28. Y. Matsushima, K. Utaka, K. Sakai, Narrow spectral linewidth of MBE-grown GaInAs/AlInAs MQW lasers in the 1.55  $\mu\text{m}$  range. *IEEE J. Quantum Electron.* **25**, 1376–1380 (1989)
29. C.E. Zah, R. Bhat, B.N. Pathak, F. Favire, W. Lin, M.C. Wang, N.C. Andreadakis, D.M. Hwang, M.A. Koza, T.P. Lee, Z. Wang, D. Darby, D. Flanders, J.J. Hsieh, High-performance uncooled 1.3  $\mu\text{m}$   $\text{Al}_x\text{Ga}_y\text{In}_{1-x-y}\text{As}/\text{InP}$  strained layer quantum-well lasers for subscriber loop applications. *IEEE J. Quantum Electron.* **30**, 511–522 (1994)
30. T.K. Sudoh, D. Takemoto, T. Tsuchiya, M. Aoki, S. Tsuji, Highly reliable 1.3  $\mu\text{m}$  InGaAlAs MQW DFB lasers, *17th IEEE Internat. Semicond. Laser Conf. (ISLC2000)*, Conf. Digest (Monterey, CA, USA, 2000), paper TuB6, pp. 55–56
31. T. Takiguchi, Y. Hanamaki, T. Kadowaki, T. Tanaka, C. Watatani, M. Takemi, Y. Mihashi, E. Omura, 1.3  $\mu\text{m}$  uncooled AlGaInAs-MQW DFB laser with  $\lambda/4$ -shifted Grating, *Optical Fiber Commun. Conf. (OFC'02)*, Techn. Digest (Anaheim, CA, USA, 2002), paper ThF3, pp. 417–418
32. K. Nakahara, T. Tsuchiya, S. Tanaka, T. Kitatani, K. Shinoda, T. Taniguchi, T. Kikawa, E. Nomoto, S. Fujisaki, M. Kudo, M. Sawada, T. Yuasa, M. Mukaikubo, 115  $^\circ\text{C}$ , 12.5 Gbit/s direct modulation of 1.3  $\mu\text{m}$  InGaAlAs-MQW RWG DFB laser with notch-free grating structure for datacom applications, *Opt. Fiber Commun. Conf. (OFC'03)*, Techn. Digest (Atlanta, GA, USA, 2003), paper PD-40
33. K. Nakahara, T. Tsuchiya, T. Kitatani, K. Shinoda, T. Kikawa, F. Hamano, S. Fujisaki, T. Taniguchi, E. Nomoto, M. Sawada, T. Yuasa, 12.5 Gbit/s direct modulation up to 115  $^\circ\text{C}$  in 1.3  $\mu\text{m}$  InGaAlAs-MQW RWG DFB lasers with notch-free grating structure. *J. Lightw. Technol.* **25**, 159–165 (2004)
34. S. Shirai, Y. Tatsuoka, C. Watatani, T. Ota, K. Takagi, T. Aoyagi, E. Omura, N. Tomita, 120  $^\circ\text{C}$  uncooled operation of direct modulated 1.3  $\mu\text{m}$  AlGaInAs-MQW DFB laser diodes for 10 Gbit/s telecom applications, *Opt. Fiber Commun. Conf. (OFC'04)*, Techn. Digest (Los Angeles, CA, USA, 2004), paper ThD2
35. Y. Muroya, T. Okuda, R. Kobayashi, K. Tsuruoka, Y. Ohsawa, T. Kouji, T. Tsukuda, T. Nakamura, K. Kobayashi, 100  $^\circ\text{C}$ , 10 Gbit/s direct modulation with a low operation current of 1.3  $\mu\text{m}$  AlGaInAs buried heterostructure DFB laser diodes, *Opt. Fiber Commun. Conf. (OFC'03)*, Techn. Digest (Atlanta, GA, USA, 2003), paper FG6, pp. 683–684
36. P.M. Ilroy, A. Kurobe, Y. Uematsu, Analysis and application of theoretical gain curves to the design of multi-quantum-well lasers. *IEEE J. Quantum Electron.* **QE-21**, 1958–1963 (1985)
37. K. Nakahara, T. Tsuchiya, T. Kitatani, K. Shinoda, T. Taniguchi, T. Kikawa, M. Aoki, 40 Gbit/s direct modulation in 1.3  $\mu\text{m}$  InGaAlAs-MQW RWG DFB lasers, *Conf. Lasers Electro-Opt. (CLEO)/Pacific Rim, OSA Techn. Digest (2007)*, pp. 1–2
38. T. Tadokoro, W. Kobayashi, T. Fujisawa, T. Yamanaka, F. Kano, High-speed modulation lasers for 100GbitE applications, *Opt. Fiber Commun. Conf. and Nat. Fiber Opt. Eng. Conf. (OFC/NFOEC'11)*, Techn. Digest (Los Angeles, CA, USA, 2011), paper OWD1
39. T. Simoyama, M. Matsuda, S. Okumura, M. Ekawa, T. Yamamoto, 40-Gbps transmission using direct modulation of 1.3  $\mu\text{m}$  AlGaInAs MQW distributed-reflector lasers up to 70  $^\circ\text{C}$ , *Opt. Fiber Commun. Conf. and Nat. Fiber Opt. Eng. Conf. (OFC/NFOEC'11)*, Techn. Digest (Los Angeles, CA, USA, 2011), paper OWD3
40. <http://www.reuters.com/article/2011/03/08/idUS165345+08-Mar-2011>
41. See for example, Special Issue on Optical Amplifiers, *J. Lightw. Technol.* **9**, 145–296 (1991)
42. T.H. Wood, Multiple quantum well waveguide modulators. *J. Lightw. Technol.* **6**, 743–757 (1988)
43. K. Wakita, I. Kotaka, O. Mitomi, H. Asai, Y. Kawamura, M. Naganuma, High-speed InGaAs/InAlAs multiple quantum well optical modulators with bandwidths in excess of 40 GHz at 1.55  $\mu\text{m}$ , *Conf. Lasers Electro-Opt. (CLEO)*, OSA Techn. Digest (1990), paper CtuC6

44. H. Sano, H. Inoue, H. Nakamura, K. Ishida, J.M. Glinski, Low loss single-mode InGaAs/InAlAs multiquantum well electroabsorption modulator, *Opt. Fiber Commun. Conf. (OFC'90)*, Techn. Digest (San Francisco, CA, USA, 1990), paper WM15
45. U. Koren, B.I. Miller, T.L. Koch, G. Eisenstein, R.S. Tucker, I. Bar-Joseph, D.S. Chemla, Low-loss InGaAs/InP MQW optical electroabsorption waveguide modulator. *Appl. Phys. Lett.* **51**, 1132–1134 (1987)
46. F. Devaux, E. Bigan, B. Rose, M. Mckee, F. Huet, M. Carré, High-speed InGaAsP/InP multiple quantum 1.55  $\mu\text{m}$  single mode modulator. *Electron. Lett.* **27**, 1926–1927 (1991)
47. F. Devaux, E. Bigan, A. Ougazzaden, B. Pierre, F. Huet, M. Carré, A. Carenco, InGaAsP/InGaAsP multiple quantum well modulator with improved saturation intensity and bandwidth over 20-GHz. *IEEE Photon. Technol. Lett.* **4**, 720–722 (1992)
48. H. Sano, H. Inoue, S. Tsuji, K. Ishida, InGaAs/InAlAs MQW Mach-Zehnder optical modulator for 10 Gbit/s long-haul transmission systems, *Opt. Fiber Commun. Conf. (OFC'92)*, Techn. Digest (San Jose, CA, USA, 1992), paper ThG4
49. J.E. Zucker, K.L. Jones, B.I. Miller, M.G. Young, U. Koren, B. Tell, K. Brown-Goebeler, Interferometric quantum well modulators with gain. *J. Lightw. Technol.* **10**, 924–932 (1992)
50. D.A.B. Miller, D.S. Chemla, T.C. Damen, A.C. Gossard, W. Wiegmann, T.H. Wood, C.A. Burrus, Electric field dependence of optical absorption near the band gap of quantum well structures. *Phys. Rev. B* **32**, 1043–1060 (1985)
51. K. Wakita, Y. Kawamura, Y. Yoshikuni, H. Asahi, Electroabsorption on room-temperature excitons in InGaAs/InGaAlAs multiple quantum-well structures. *Electron. Lett.* **21**, 338–340 (1985)
52. Y. Kawamura, K. Wakita, Y. Yoshikuni, Y. Itaya, H. Asahi, Monolithic integration of a DFB laser and an MQW optical modulator in the 1.5  $\mu\text{m}$  wavelength range. *IEEE J. Quantum Electron.* **27**, 915–918 (1991)
53. H. Soda, K. Sato, H. Sudo, S. Takeuchi, H. Ishikawa, Ultralow-chirp characteristics of monolithic electroabsorption modulator/DFB laser light source, *Proc. 17th Europ. Conf. Opt. Commun. (ECOC'91)*, Paris, France (1991), paper WeB7-1
54. T. Kato, T. Sasaki, N. Kida, K. Komatsu, I. Mito, Novel MQW DFB laser diode modulator integrated light source using bandgap energy control epitaxial growth technique, *Proc. 17th Europ. Conf. Opt. Commun. (ECOC'91)*, Paris, France (1991), paper WeB7-2
55. M. Aoki, H. Sano, M. Suzuki, M. Takahashi, K. Uomi, A. Takai, Novel structure MQW electroabsorption-modulator/DFB-laser-integrated device fabricated by selective area MOCVD growth. *Electron. Lett.* **27**, 2138–2140 (1991)
56. M. Suzuki, H. Tanaka, H. Taga, S. Yamamoto, Y. Matsushima,  $\lambda/4$ -shifted DFB laser/electroabsorption modulator integrated light source for multigigabit transmission. *J. Lightw. Technol.* **10**, 90–94 (1992)
57. K. Wakita, I. Kotaka, H. Asai, M. Okamoto, Y. Kondo, M. Naganuma, High-speed and low-drive-voltage monolithic multiple quantum well modulator/DFB laser light source. *IEEE Photon. Technol. Lett.* **4**, 16–18 (1992)
58. U. Koren, B. Glance, B.I. Miller, M.G. Young, M. Chien, T.H. Wood, L.M. Ostar, T.L. Koch, R.M. Jopson, J.D. Evankow, G. Raybon, C.A. Bums, P.D. Magill, K.C. Reichmann, Widely tunable distributed Bragg reflector laser with an integrated electroabsorption modulator, *Opt. Fiber Commun. Conf. (OFC'92)*, Techn. Digest (San Jose, CA, USA, 1992), paper WG5
59. M. Aoki, N. Kikuchi, K. Sekine, S. Sasaki, M. Suzuki, T. Taniwatari, Y. Okuno, T. Kawano, A. Takai, Low-drive-voltage and low-chirp integrated electroabsorption modulator/DFB-laser for 2.5 Gbit/s 200 km normal fiber transmission. *Electron. Lett.* **29**, 1983–1984 (1993)
60. K.C. Reichmann, P.D. Magill, G. Raybon, Y.K. Chen, T. Tanbun-Ek, R.A. Logan, A. Tate, A.M. Sergent, K.W. Wecht, P.F. Sciortino Jr., Long-distance transmission experiment at 2.5 Gbit/s using an integrated laser/modulator grown by selective-area MOVPE, *Opt. Fiber Commun. Conf. (OFC'94)*, Techn. Digest (San Jose, CA, USA, 1994), paper ThM-4
61. K. Komatsu, T. Kato, M. Yamaguchi, T. Sasaki, S. Takano, H. Shimizu, N. Watanabe, M. Kitamura, DFB-LD/modulator integrated light sources fabricated by band-gap-energy-controlled selective MOVPE with stable fiber transmission characteristics, *Opt. Fiber Commun. Conf. (OFC'94)*, Techn. Digest (San Jose, CA, USA, 1994), paper TuC-3

62. B. Clesca, S. Gauchard, V. Rodrigues, D. Lesterlin, E. Kuhn, A. Bodere, H. Haisch, K. Satzke, J.F. Vinchant, 2.5 Gbit/s, 1291 km transmission over nondispersion-shifted fiber using an integrated electroabsorption modulator/DFB laser module, *Proc. 21st Europ. Conf. Opt. Commun.* (ECOC'95), Brussels, Belgium (1995), paper Th.A.3.8
63. K. Wakita, I. Kotaka, O. Mitomi, H. Asai, Y. Kawamura, M. Naganuma, High-speed InGaAlAs/InAlAs multiple quantum well optical modulators. *J. Lightw. Technol.* **8**, 1027–1032 (1990)
64. A.M. Fox, D.A.B. Miller, G. Livescu, J.E. Cunningham, J.E. Henry, W.Y. Jan, Quantum well carrier sweep out: Relation to electroabsorption and exciton saturation. *IEEE J. Quantum Electron.* **27**, 2281–2295 (1991)
65. T.H. Wood, T.Y. Chang, J.Z. Pastalan, C.A. Burrus, Jr., N.J. Sauer, B.C. Johnson, Increased optical saturation intensities in GaInAs multiple quantum wells by the use of AlGaInAs barriers. *Electron. Lett.* **27**, 257–259 (1991)
66. T. Ido, H. Sano, S. Tanaka, H. Inoue, Frequency-domain measurement of carrier escape times in MQW electro-absorption optical modulators. *IEEE Photon. Technol. Lett.* **7**, 1421–1423 (1995)
67. D. Marcuse, DFB laser with attached external intensity modulator. *IEEE J. Quantum Electron.* **26**, 262–269 (1990)
68. Y. Kotaki, H. Soda, Analysis of static and dynamic wavelength shifts in modulator-integrated DFB lasers, *Proc. 19th Europ. Conf. Opt. Commun.* (ECOC'93), Montreux, Switzerland (1993), paper WeP8.6
69. M. Aoki, S. Takashima, Y. Fujiwara, S. Aoki, New transmission simulation of EA-modulator integrated DFB-lasers considering the facet reflection-induced chirp. *IEEE Photon. Technol. Lett.* **9**, 380–382 (1997)
70. R. Adams, Band-structure engineering for low-threshold high-efficiency semiconductor lasers. *Electron. Lett.* **22**, 249–250 (1986)
71. E. Yablonovitch, E.O. Kane, Reduction of lasing threshold current density by the lowering of valence band effective mass. *J. Lightw. Technol.* **LT-4**, 504–506 (1986)
72. T. Ohtoshi, N. Chinone, Linewidth enhancement factor in strained quantum well lasers. *IEEE Photon. Technol. Lett.* **1**, 117–119 (1989)
73. K. Kamite, H. Sudo, M. Yano, H. Ishikawa, H. Imai, Ultra-high-speed InGaAsP/InP DFB lasers emitting at 1.3  $\mu\text{m}$  wavelength. *IEEE J. Quantum Electron.* **QE-23**, 1054–1058 (1987)
74. P.J. Corvini, T.L. Koch, Computer simulation of high-bit-rate optical fiber transmission using single-frequency lasers. *J. Lightw. Technol.* **LT-5**, 1591–1595 (1987)
75. K. Uomi, A. Murata, S. Sano, R. Takeyari, A. Takai, Advantages of 1.55  $\mu\text{m}$  InGaAs/InGaAsP MQW-DFB lasers for 2.5 Gbit/s long-span normal fiber transmission. *IEEE Photon. Technol. Lett.* **4**, 657–660 (1992)
76. M. Aoki, Monolithically-integrated laser diodes for optical telecommunications by selective area growth technologies, Ph.D. Dissertation, Department of Electrical and Electronic Engineering, Tokyo Institute of Technology, Tokyo, Japan, 1999
77. K. Naoe, N. Sasada, Y. Sakuma, K. Motoda, T. Kato, M. Akashi, J. Shimizu, T. Kitatani, M. Aoki, M. Okayasu, K. Uomi, 43 Gbit/s operation of 1.55  $\mu\text{m}$  electro-absorption modulator integrated DFB laser modules for 2 km transmission, *Proc. 31st Europ. Conf. Opt. Commun.* (ECOC'05), Glasgow, UK (2005), vol. 4, pp. 907–908
78. N. Sasada, K. Naoe, Y. Sakuma, K. Motoda, T. Kato, M. Akashi, J. Shimizu, T. Kitatani, M. Aoki, M. Okayasu, K. Uomi, 1.55  $\mu\text{m}$  40 Gbit/s electro-absorption modulator integrated DFB laser modules for very short reach transmission, *10th OptoElectron. Commun. Conf.* (OECC'05), Techn. Digest, Seoul, Korea, 2005, invited paper 6F2–1
79. T. Fujisawa, K. Tahahat, W. Kobayashoi, T. Tadokoro, N. Fujiwara, S. Kanazawa, F. Kano, 1.3  $\mu\text{m}$ , 50 Gbit/s EADFB lasers for 400 GE, *Opt. Fiber Commun. Conf. and Nat. Fiber Opt. Eng. Conf.* (OFC/NFOEC'11), Techn. Digest (Los Angeles, CA, USA, 2011), paper OWD4
80. C. Kazmierski, A. Konczykowska, F. Jorge, F. Blache, M. Riet, C. Jany, A. Scavennec, 100 Gbit/s operation of an AlGaInAs semi-insulating buried heterojunction EML, *Opt. Fiber Commun. Conf. and Nat. Fiber Opt. Eng. Conf.* (OFC/NFOEC'09), Techn. Digest (San Diego, CA, USA, 2009), post-deadline papers, pp. 1–3

81. H. Tanaka, M. Horita, Y. Matsushima, Temperature dependence of InGaAsP electro-absorption modulator module, *Conf. Indium Phosphide Relat. Mater. (IPRM'95)*, Techn. Digest, 1995, paper ThP45, pp. 540–543
82. B. Clesca, S. Gauchard, E. Lantoine, V. Rodrigues, F. Giraud, D. Lesterlin, 3.2 nm wavelength tuning via temperature control for integrated electroabsorption modulator/DFB laser with high tolerance to chromatic dispersion. *Electron. Lett.* **32**, 927–929 (1996)
83. M.R. Gokhale, P.V. Studenkov, J. Ueng-McHale, J. Thomson, J. Yao, J. van Saders, Un-cooled, 10 Gbit/s 1310 nm electroabsorption modulated laser, *Opt. Fiber Commun. Conf. (OFC'03)*, Techn. Digest (Atlanta, GA, USA, 2003), paper PDP-42
84. S. Makino, K. Shinoda, T. Kitatani, T. Tsuchiya, M. Aoki, Wide temperature range (0 to 85 °C), 40 km SMF transmission of a 1.55  $\mu\text{m}$ , 10 Gbit/s InGaAlAs electroabsorption modulator integrated DFB laser, *Opt. Fiber Commun. Conf. and Nat. Fiber Opt. Eng. Conf. (OFC/NFOEC'05)*, Techn. Digest (Anaheim, CA, USA, 2005), paper PDP-14
85. S. Makino, K. Shinoda, T. Shiota, T. Kitatani, T. Fukamachi, M. Aoki, N. Sasada, K. Naoe, K. Uchida, H. Inoue, Wide temperature (15 °C to 95 °C), 80 km SMF transmission of a 1.55  $\mu\text{m}$ , 10 Gbit/s InGaAlAs electroabsorption modulator integrated DFB laser, *Opt. Fiber Commun. Conf. and Nat. Fiber Opt. Eng. Conf. (OFC/NFOEC'07)*, Techn. Digest (Anaheim, CA, USA, 2007), paper OMS-1
86. N. Sasada, K. Naoe, Y. Sakuma, K. Okamoto, R. Washino, D. Nakai, K. Motoda, S. Makino, M. Aoki, Un-cooled operation (10 °C to 85 °C) of a 10.7 Gbit/s 1.55  $\mu\text{m}$  electro-absorption modulator integrated DFB laser for 40 km transmission, *Opt. Fiber Commun. Conf. and Nat. Fiber Opt. Eng. Conf. (OFC/NFOEC'07)*, Techn. Digest (Anaheim, CA, USA, 2007), paper We8.1.5
87. H. Hayashi, S. Makino, T. Kitatani, T. Shiota, K. Shinoda, S. Tanaka, M. Aoki, N. Sasada, K. Naoe, A first uncooled (25 to 85 °C) 43-Gbps light source based on InGaAlAs EA/DFB laser technology, *Proc. 34th Europ. Conf. Opt. Commun. (ECOC'08)*, Brussels, Belgium (2008), paper We.3.C.3
88. S. Makino, K. Shinoda, T. Kitatani, H. Hayashi, T. Shiota, S. Tanaka, M. Aoki, N. Sasada, K. Naoe, High-speed electroabsorption modulator integrated DFB laser for 40 Gbps and 100 Gbps application, *Conf. Indium Phosphide Relat. Mater. (IPRM'09)*, Techn. Digest, 2009, pp. 362–366
89. <http://www.cfp-msa.org/>
90. T. Fujisawa, S. Kanazawa, N. Nunoya, H. Ishii, Y. Kawaguchi, A. Ohki, H. Fujiwara, K. Takahat, R. Iga, F. Kano, H. Oohashi, 4  $\times$  25 Gbit/s, 1.3  $\mu\text{m}$ , monolithically integrated light source for 100 Gbit/s Ethernet, *Proc. 36th Europ. Conf. Opt. Commun. (ECOC'10)*, Turino, Italy (2010), paper Th.9.D.1
91. K. Iga, Modulation limit of semiconductor lasers by some parametric modulation scheme. *Trans. IECE Jpn.* **E-68**, 417–420 (1985)
92. R. Lang, Injection locking properties of a semiconductor-laser. *IEEE J. Quantum Electron.* **QE-18**, 976–983 (1982)
93. A. Tagar, K. Petermann, High-frequency oscillations and self-mode locking in short external-cavity laser diodes. *IEEE J. Quantum Electron.* **30**, 1553–1561 (1994)
94. P. Even, K.A. Ameer, G.M. Stephan, Modeling of an injected gas laser. *Phys. Rev. A* **55**, 1441–1453 (1997)
95. E.G. Lariontsev, I. Zolotoverkh, P. Besnard, G.M. Stephan, Injection locking properties of a microchip laser. *Eur. Phys. J. D* **5**, 107–117 (1999)
96. X.J. Meng, T. Chau, M.C. Wu, Improved intrinsic dynamic distortions in directly modulated semiconductor lasers by optical injection locking. *IEEE Trans. Microwave Theory Techn.* **47**, 1172–1176 (1999)
97. L. Chrostowski, X. Zhao, C.J. Chang-Hasnain, R. Shau, M. Ortsiefer, M.-C. Amann, 50 GHz optically injection-locked 1.55  $\mu\text{m}$  VCSELs. *IEEE Photon. Technol. Lett.* **18**, 367–369 (2006)
98. T. Sogawa, Y. Arakawa, M. Tanaka, H. Sakaki, Observation of a short optical pulse (< 1.3 ps) from a gain switched quantum well laser. *Appl. Phys. Lett.* **53**, 1580–1582 (1988)

99. D. Bimberg, K. Ketterer, E.H. Böttcher, E. Scholl, Gain modulation of unbiased semiconductor lasers: Ultrashort light-pulse generation in the 0.8  $\mu\text{m}$ –1.3  $\mu\text{m}$  wavelength range. *Int. J. Electron.* **60**, 23–45 (1986)
100. H.F. Liu, M. Fukazawa, Y. Kawai, T. Kamiya, Gain-switched picosecond pulse ( $< 10$  ps) generation from 1.3  $\mu\text{m}$  laser diodes. *IEEE J. Quantum Electron.* **25**, 1417–1425 (1989)
101. O. Kjebon, R. Schatz, S. Lourduoss, S. Nilsson, B. Stalnacke, L. Backborn, 30 GHz direct modulation bandwidth in detuned loaded InGaAsP DBR lasers at 1.55  $\mu\text{m}$ . *Electron. Lett.* **33**, 488–489 (1997)
102. L. Bah, W. Kaiser, J.P. Reithmaier, A. Forchel, T.W. Berg, B. Tromborg, Enhanced direct-modulated bandwidth of 37 GHz by a multi-section laser with a coupled cavity-injection-grating design. *Electron. Lett.* **39**, 1592–1593 (2003)
103. J.P. Reithmaier, W. Kaiser, L. Bach, A. Forchel, M. Gioannini, I. Montrosset, T.W. Berg, B. Tromborg, Modulation speed enhancement by coupling to higher order resonances: A road towards 40 GHz bandwidth lasers on InP, *Conf. Indium Phosphide Relat. Mater. (IPRM'05)*, Techn. Digest, 2005, pp. 118–123
104. S. Bauer, O. Brox, M. Biletzke, J. Kreissl, M. Radziunas, B. Sartorius, H.J. Wünsche, Speed potential of active feedback lasers, *Conf. Lasers Electro-Opt. (CLEO)/Europe, OSA Techn. Digest* (2003), p. 176
105. B. Sartorius, M. Möhrle, Mirror modulated lasers: A concept for high speed transmitters. *Electron. Lett.* **32**, 1781–1782 (1996)
106. M. Radziunas, A. Glitzky, U. Bandelow, M. Wolfram, U. Troppenz, J. Kreissl, W. Rehbein, Improving the modulation bandwidth in semiconductor lasers by passive feedback. *IEEE J. Sel. Top. Quantum Electron.* **13**, 136–142 (2007)
107. U. Troppenz, J. Kreissl, W. Rehbein, C. Bornholdt, T. Gaertner, M. Radziunas, A. Glitzky, U. Bandelow, M. Wolfram, 40 Gbit/s directly modulated InGaAsP passive feedback DFB laser, *Proc. 32nd Europ. Conf. Opt. Commun. (ECOC'06)*, Cannes, France (2006), paper Th4.5.5
108. M. Shirai, H. Arimoto, K. Watanbe, A. Taïke, K. Shinoda, J. Shimizu, H. Sato, T. Ido, T. Tsuchiya, M. Aoki, S. Tsuji, N. Sasada, S. Tada, M. Okayasu, 40 Gbit/s electroabsorption modulators with impedance controlled electrodes. *Electron. Lett.* **39**, 734–735 (2003)
109. Y.-J. Chiu, H.-F. Chou, V. Kaman, P. Abraham, J.E. Bowers, High extinction ratio and saturation power traveling-wave electroabsorption modulator. *IEEE Photon. Technol. Lett.* **14**, 792–794 (2002)
110. Y. Akage, K. Kawano, S. Oku, R. Iga, H. Okamoto, Y. Miyamoto, H. Takeuchi, Wide bandwidth of over 50 GHz traveling wave electrode electroabsorption modulator integrated DFB lasers. *Electron. Lett.* **37**, 299–300 (2001)
111. R. Lewén, S. Irmscher, U. Westergren, L. Thylén, U. Eriksson, Segmented transmission-line electroabsorption modulators. *J. Lightw. Technol.* **22**, 172–179 (2004)
112. R.G. Walker, High-speed semiconductor intensity modulators. *IEEE J. Quantum Electron.* **27**, 654–667 (1991)
113. S.R. Sakamoto, A. Jackson, N. Dagli, Substrate removed GaAs/AlGaAs Mach–Zehnder electro-optic modulators for ultra wide bandwidth operation, *Internat. Top. Meeting Microw. Photon.*, 1999, pp. 13–16
114. L. Mörl, D. Hoffmann, K. Matzen, C. Bornholdt, G.G. Mekonnen, F. Reier, Traveling wave electrodes for 50 GHz operation of opto-electronic devices based on InP, *Conf. Indium Phosphide Relat. Mater. (IPRM'99)*, Techn. Digest, WeA1–3, pp. 385–388
115. S. Akiyama, S. Hirose, T. Watanabe, M. Ueda, S. Sekiguchi, N. Morii, T. Yamamoto, A. Kuramata, H. Soda, Novel InP-based Mach–Zehnder modulator for 40 Gbit/s integrated lightwave source, *18th IEEE Internat. Semicond. Laser Conf. (ISLC2002)*, Conf. Digest, Garmisch-Partenkirchen, Germany, 2002, paper TuC1, pp. 57–58
116. K. Tsuzuki, H. Shibata, N. Kikuchi, M. Ishikawa, T. Yasui, H. Ishii, H. Yasaka, 10 Gbit/s, 200 km duobinary SMF transmission using a full C-band tunable DFB laser array co-packaged with InP Mach–Zehnder modulator, *21st IEEE Internat. Semicond. Laser Conf. (ISLC2008)*, Conf. Digest, Waikoloa, HI, USA, 2006, paper MB6

117. H. Arimoto, K. Watanabe, N. Kikuchi, H. Takano, M. Shirai, M. Hashimoto, H. Kudo, T. Kitatani, H. Ohta, R. Mita, R. Takeyari, A 40 Gbit/s electro-absorption modulator with a record modulation efficiency (50 GHz/V) enhanced by a novel technique of hybrid integration on the driver IC, *IEEE 16th Ann. Meeting Lasers Electro-Opt. Soc.*, vol. 2 (2003), pp. 646–647
118. R. Takeyari, N. Kikuchi, Next-generation hybrid design of optoelectronic components with electronic components based on InP and related materials, *Conf. Indium Phosphide Relat. Mater. (IPRM'04)*, Techn. Digest, 2004, pp. 8–9

# Chapter 5

## Widely Tunable Laser Diodes

Hélène Debrégeas-Sillard

**Abstract** The chapter provides a comprehensive overview over widely tunable laser diodes and includes a description of the different tuning mechanisms and relevant implementations: sampled grating- and superstructure grating-DBR lasers, Y-lasers, multiple peak gratings and widely tunable filter lasers. The treatment covers fundamentals of the various solutions, typical performance characteristics, and control issues as well. The focus is primarily on edge-emitting semiconductor lasers; however, vertical cavity surface emitting lasers (VCSELs) and external cavity tunable lasers, integrated tunable laser modulators, and tunable laser subsystems are also contained.

Widespread deployment of dense wavelength division multiplex (DWDM) systems calls for transmitter lasers that can emit with extreme accuracy at any WDM-specific wavelength, as defined by the ITU (International Telecommunication Union) standardization body. Predominantly, these wavelengths cover the whole C-band (1525–1565 nm), but will eventually extend over the L-band (1570–1610 nm) as well. A basic approach consists of using standard DFB lasers, the emission wavelength of which is determined by the Bragg grating pitch, fixed by fabrication. Any DFB laser can be slightly thermally tuned over a small range of typically 4 nm with 0.1 nm/°C tuning efficiency, thus covering a limited number of WDM transmission channels only. A largely superior and preferred solution is to employ widely tunable lasers, which allow adjusting the laser wavelength to any ITU channel within the transmission bands. Such tunable laser devices are mandatory for a large range of applications today.

In long-distance networks, tunable lasers are used either as a spare source to replace any failing DFB laser or as a universal source, dramatically reducing maintenance and inventory management costs. Today, 50 % of newly deployed long-

---

H. Debrégeas-Sillard (✉)  
III-V Lab, Route de Nozay, 91460 Marcoussis, France  
e-mail: helene.debregeas@3-5lab.fr

distance transmitters comprise tunable lasers, and deployment is expected to reach 90 % within the next 10 years.

Tunable lasers provide both flexibility and adaptability in long-distance and metropolitan networks. They represent a key element of reconfigurable optical add and drop multiplexers (ROADMs) – components that can extract or insert any wavelength to dynamically reconfigure wavelength allocation according to traffic evolution. They are used for all-optical routing without the need for optic–electronic–optic conversion, ensuring independence from protocols and bit rates. In packet-switching transmission schemes, they would allow for real-time network reconfiguration with packet granularity, demanding extremely fast wavelength tuning within the guard time of the optical packets ( $\sim 100$  ns).

In future WDM-based access networks, each end user may be equipped with a receiver configured for a specific wavelength. This wavelength can be used as an address to route traffic to the desired user. Tunable lasers are foreseen at the optical line terminal in order to rapidly tune the data for routing to the final users.

For all these applications, performance data similar to standard DFB lasers are required such as 13 dBm coupled output power, more than 40 dB side-mode suppression ratio (SMSR), low noise, linewidths below 5 MHz, wavelength accuracy compliant with the ITU standard, and others. In addition, however, they must be capable of wavelength tuning over the whole 40 nm C-band (48 channels, 100 GHz spaced), and in coming years over the full C+L band (1525–1610 nm). For real mass deployment in DWDM systems, the cost premium compared to fixed wavelength lasers has to remain below 20%, which imposes the following general design requirements:

- To reach high industrial production yield, the tuning mechanism must be based on robust, fabrication-tolerant processes.
- Power, wavelength, and SMSR feedback loops must be simple enough to ensure fast characterization and reliable servo-control algorithms.

Monolithic integration can be advantageous for avoiding costly alignment procedures and multiple bulky mechanical elements. In particular, for metro and access applications, the laser must fit into a TOSA type module (Transmitter Optical Sub-Assembly), that is, compatible with low-cost extended extra flat packaging (e-XFP) modules. Last but not least, the possibility to integrate additional functionalities like external modulation, variable optical attenuation, optical gating, and fast tuning capability are important assets too. They enable compatibility with different networks configurations and reductions in system costs.

Tunable lasers have been studied for several decades, leading to a wide variety of technology solutions based on thermal, mechanical, and current injection tuning mechanisms [1]. Several types of devices are commercially available now while research strongly continues to further improve performance, increase functionalities, and reduce costs.

Tunable lasers based on current injection tuning allow for monolithic integration with additional functionalities, including fast tuning. Derived from distributed



Bragg reflector (DBR) lasers, solutions incorporating several gratings with multiple reflection peaks can provide more than 40 nm wavelength tuning and are widely used in today's networks. Yet, control complexity remains the main drawback, and many studies have been dedicated to propose simpler tuning methods and robust feedback algorithms. Recently, photonic integration has even led to the demonstration of complete subsystems monolithically integrated on InP that comprise tunable lasers, modulators, photodiodes, and optical amplifiers (see Sect. 5.5).

Other approaches rely on the selection of a laser from an array of thermally tuned lasers or use an external cavity with a movable Bragg grating. These device structures are, however, not fully integrable in semiconductor technology, and they are not suited for fast tuning or integrated modulation. Nonetheless, as they are based on robust technologies and use simple control mechanisms, they may be commercially competitive with applications requiring less sophisticated laser functions.

## 5.1 Basics of Current Injection Tuning, DBR Lasers

### 5.1.1 Current Injection Tuning Mechanisms

All tunable laser structures relying on current injection integrate a section with a p-i-n junction containing an intrinsic layer made of quaternary passive material (typically, InGaAsP with 1450 nm photoluminescence wavelength, in the following referred to as Q1.45). Under carrier injection, the nonequilibrium excess carrier concentration creates variations of the index of refraction in this quaternary material via three main mechanisms: free-carrier absorption, bandfilling, and bandgap shrinkage [2]. Physically, these effects are the consequence of a modification of material absorption  $\alpha(E)$  over the whole spectrum which can be linked via the Kramers–Krönig relation to the index variation at the operating energy  $E_0$ :

$$\Delta n(E_0) = \frac{\hbar c}{\pi} \text{Princ} \int_0^{\infty} \frac{\Delta \alpha(E)}{E^2 - E_0^2} dE, \quad (5.1)$$

where ‘Princ’ means principal value of the integral. The effects are represented schematically in Fig. 5.1 and detailed below.

#### 5.1.1.1 Free Carrier Absorption

This intra-band mechanism illustrated in Fig. 5.1a corresponds to the absorption of a photon by a free carrier (electron or hole), raising its energy within the conduction (or valence) band. Conservation of the wavevector  $\mathbf{k}$  is ensured by the interaction with a phonon or an impurity. This absorption at very low energies implies a free-

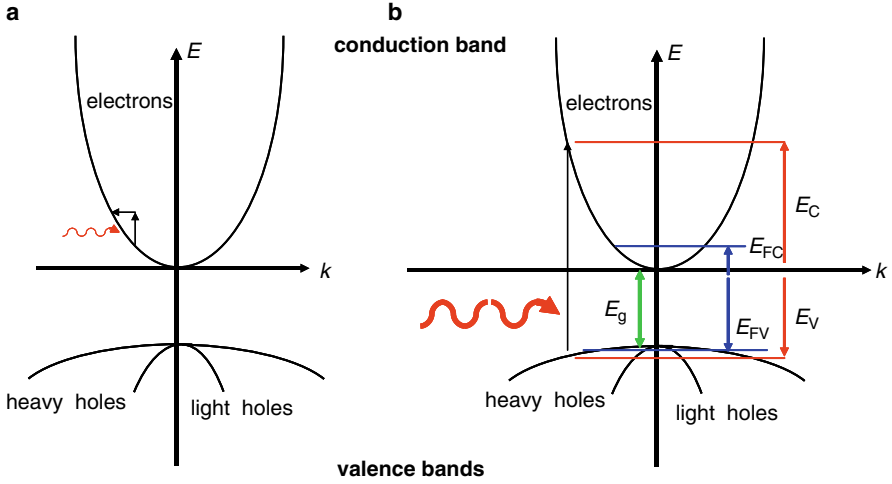


**Fig. 5.1** Schematic representation of the different types of absorption relevant under current tuning. Intra-band free-carrier absorption (a), inter-band absorption (b).  $E$  = carrier energy, indices  $C$  and  $V$  refer to the conduction and valence band, respectively, and  $E_{FC}$  and  $E_{FV}$  represent the Fermi energy levels of the conduction and valence bands, respectively

carrier-related decrease of the refractive index given by [2]

$$\Delta n_{fc} = -\frac{e^2 \lambda^2}{8\pi^2 c^2 \varepsilon_0 n} \left( \frac{N}{m_e} + \frac{P}{\frac{m_{hh}^{3/2} + m_{lh}^{3/2}}{m_{hh}^{1/2} + m_{lh}^{1/2}}} \right) \quad (5.2)$$

with  $n$  denoting the refractive index,  $m_e$ ,  $m_{hh}$ , and  $m_{lh}$ , the effective masses of electrons, heavy and light holes, respectively,  $P$  the hole density,  $N$  the electron density, and  $\varepsilon_0$  the permittivity of free space. As  $m_e \ll m_{lh, hh}$ , the effect is dominated by electron absorption in the conduction band.

### 5.1.1.2 Bandfilling

Assuming a parabolic approximation for the band diagram and using the notations of Fig. 5.1b, absorption without carrier injection  $\alpha(E)$  at an energy  $E$  close to the bandgap,  $E_g$ , is given by [2]

$$\alpha(E) = \frac{C}{E} \sqrt{E - E_g} \text{ if } E \geq E_g \text{ and } \alpha(E) = 0 \text{ otherwise,} \quad (5.3)$$

where  $C$  is a material-dependent constant (given in  $\text{cm}^{-1} \text{eV}^{1/2}$ ).

Under current injection, electrons and holes fill conduction and valence band states at low energy levels (Fig. 5.2a). Now, photon absorption at energy  $E$ , with

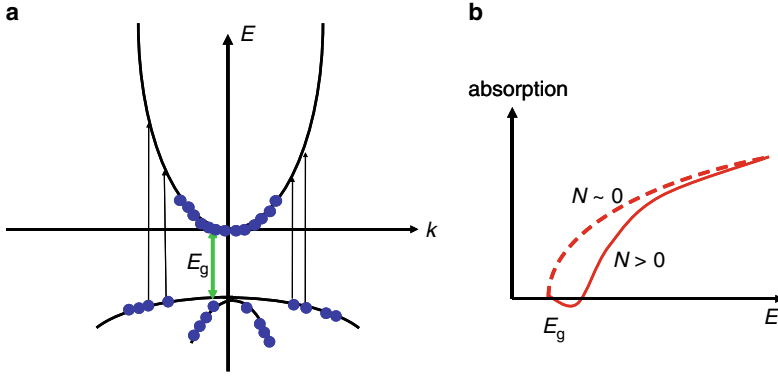


**Fig. 5.2** Illustration of bandfilling: band diagram under current injection (a) and impact on absorption spectrum (b).  $N \sim 0$  and  $N > 0$  correspond to the case without and with current injection, respectively

electron transfer occurring from the valence band energy  $E_V$  to the conduction band energy  $E_C$ , is possible only if, firstly,  $E = E_V + E_C$ , and secondly, if level  $E_V$  is occupied and level  $E_C$  is vacant. Then, (5.3) must be expanded to take into account the occupation probability of either energy state:

$$\alpha(E) = \frac{C}{E} \sqrt{E - E_g} [f_V(E_V) - f_C(E_C)] \quad \text{if } E \geq E_g,$$

$$\alpha(E) = 0 \quad \text{otherwise.} \tag{5.4}$$

Here,  $f_V(E_V)$  and  $f_C(E_C)$  indicate the probability that valence band level  $E_V$  and conduction band level  $E_C$ , respectively, are occupied by an electron. They are expressed by Fermi–Dirac distributions:

$$f_C(E_C) = \frac{1}{1 + e^{(E_C - E_{FC})/kT}}, \quad f_V(E_V) = \frac{1}{1 + e^{(E_V - E_{FV})/kT}}, \tag{5.5}$$

where  $E_{FC}$  and  $E_{FV}$  represent the Fermi levels in the conduction and valence band, respectively. Under carrier injection, the energy values of the Fermi quasilevels tend to increase. For energies  $E$  slightly larger than  $E_g$ ,  $f_C(E_C)$  becomes nonzero and  $f_V(E_V)$  becomes lower than unity. Absorption is no longer possible, and injected carriers can even create gain by stimulated emission as shown in Fig. 5.2b (negative absorption).

### 5.1.1.3 Bandgap Shrinkage

Injected carriers occupy bands of lower energy levels, and their wavefunctions overlap. They repel each other (electrons–electrons, and holes–holes) due to Coulomb forces and for statistical reasons when their spins are identical. These repulsions screen the electric field built-in in the semiconductor crystal network and, as a con-

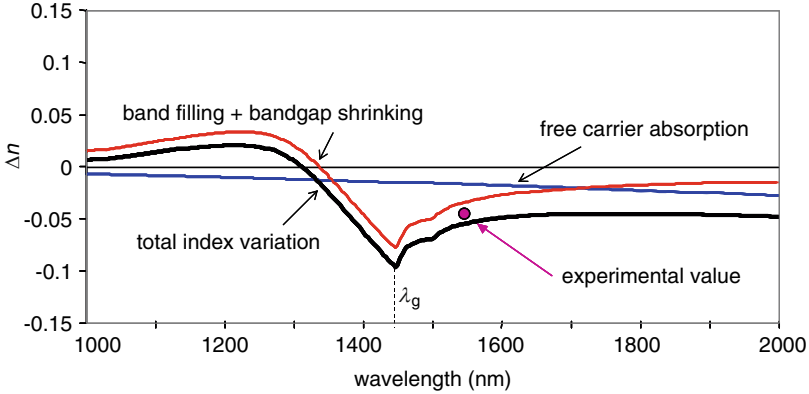


**Fig. 5.3** Index variation calculated as a function of wavelength for  $\text{Ga}_{0.35}\text{In}_{0.65}\text{As}_{0.74}\text{P}_{0.26}$  (Q1.45) at  $N = 3 \times 10^{18} \text{ cm}^{-3}$ . An experimental value at 1550 nm is indicated by the *dot* and  $\lambda_g$  represents the bandgap equivalent wavelength

sequence, the bandgap energy  $E_g$  is reduced. An approximate model gives [2]

$$\Delta E_g = -\frac{e}{2\pi\epsilon_0\epsilon} \left( \frac{3N}{\pi} \right)^{1/3}, \quad (5.6)$$

where  $\epsilon$  represents the dielectric constant of the semiconductor material.

#### 5.1.1.4 Cumulative Impact on Refractive Index Variation

The index variation due to carrier injection corresponds to the sum of the three effects. Simulations of index variation as a function of wavelength are presented in Fig. 5.3 for a bulk layer of Q1.45 composition. For the data shown in Fig. 5.3, the factor  $C$  in (5.3), which determines the absorption coefficient, has been extrapolated from experimental values [3] to be  $2.82 \times 10^4 \text{ cm}^{-1} \text{ eV}^{1/2}$ . Band diagrams are derived from effective electron and hole masses [4] ( $m_e = 0.065m_0$ ,  $m_{hh} = 0.49m_0$  and  $m_{lh} = 0.07m_0$ , with  $m_0 = 9.1095 \times 10^{-31} \text{ kg}$  being the free electron mass), the refractive index  $n$  is 3.49, and the dielectric constant  $\epsilon$  is 13.8.

Bandfilling and bandgap renormalisation result in a modification of the absorption behavior close to the bandgap energy. Due to the denominator  $E^2 - E_0^2$  in the Kramers–Krönig relation (see (5.1)), they generate a maximum index variation around  $E_g$ . On the contrary, the free-carrier plasma leads to an increase of absorption at energies much smaller than the bandgap energy: the impact on index variation around wavelengths corresponding to the bandgap is very weakly dependent on energy. At a typical operation wavelength of 1550 nm, free carrier absorption accounts approximately for one-third of the overall index variation, and bandfilling and bandgap shrinkage for two-thirds. A typical experimental value at 1550 nm is  $\Delta n \sim -0.05$ , plotted in Fig. 5.3 for comparison.

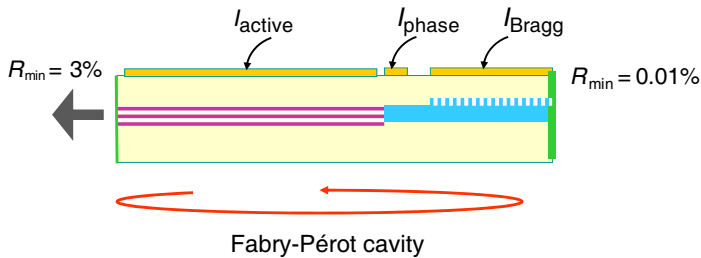


**Fig. 5.4** Schematic cross section of a DBR laser

## 5.1.2 DBR Lasers: Principle of Operation

### 5.1.2.1 DBR Cavity and Mode Selection

Exploiting index variation under carrier injection, the first current injection tunable laser was the DBR laser, proposed in the 1970s and subsequently optimized by many laboratories [5–7]. A typical DBR laser, as shown in Fig. 5.4, comprises three different monolithically integrated sections, each controlled by separate currents: one active and two passive sections, the latter called Bragg and phase section, respectively. The rear facet is antireflection coated and the front facet provides low reflectivity ( $\sim 3\%$ ) to create a Fabry–Pérot (FP) cavity between the front facet and the mirror formed by the Bragg section. The active section has a multi-quantum well (MQW) vertical structure. Injecting the current  $I_{\text{active}}$  gives rise to gain around 1550 nm and generates an FP comb.

The Bragg section is made of bulk Q1.45 material and contains a Bragg grating. This section acts as a wavelength selective mirror with maximum reflectivity at the Bragg wavelength  $\lambda_{\text{Bragg}}$  given by

$$\lambda_{\text{Bragg}} = 2n_{\text{eff}}\Lambda, \quad (5.7)$$

where  $n_{\text{eff}}$  is the effective waveguide index of the Bragg section and  $\Lambda$  the grating pitch. For  $\sim 1550$  nm emission,  $n_{\text{eff}}$  values are typically 3.2, which yields a pitch of around 240 nm. The reflection bandwidth and its maximum value are closely related to the length of the grating and to the coupling coefficient  $\kappa$ , defined as the grating reflectivity per unit length and expressed in  $\text{cm}^{-1}$ . For a rectangular grating, it is given by:

$$\kappa = \frac{2\Delta n_{\text{eff}}}{\lambda}, \quad (5.8)$$

where  $\Delta n_{\text{eff}}$  represents the effective index difference between the mark and space regions of the grating. Figure 5.5 shows the calculated equivalent reflectivity spectrum for a 300  $\mu\text{m}$  long Bragg grating, assuming  $\kappa = 40 \text{ cm}^{-1}$  and  $15 \text{ cm}^{-1}$  material loss.

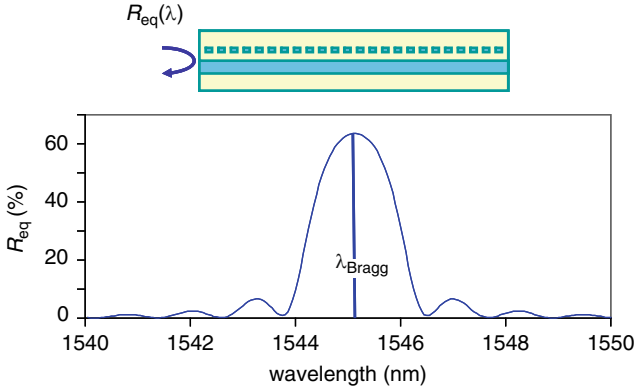


**Fig. 5.5** Equivalent reflectivity  $R_{\text{eq}}$  of a Bragg grating as a function of wavelength ( $\kappa = 40 \text{ cm}^{-1}$ ,  $L = 300 \mu\text{m}$ , loss =  $15 \text{ cm}^{-1}$ )

We define an effective penetration length,  $L_{\text{eff}}$ , into the Bragg grating corresponding to the penetration distance at which the optical power is decreased by a factor  $e$ . For high  $\kappa$  values,  $L_{\text{eff}}$  is equal to  $1/(2\kappa)$ . A laser cavity of length  $L_{\text{cavity}} = L_a + L_{\text{ph}} + L_{\text{eff}}$ , where  $L_a$  and  $L_{\text{ph}}$  represent the length of the active and the phase section, respectively, generates a comb of FP modes separated by a free spectral range (FSR) according to:

$$\text{FSR} = \frac{\lambda^2}{2n_g L_{\text{cavity}}}. \quad (5.9)$$

Here,  $n_g$  indicates the group index that takes into account the wavelength-dependent dispersion of  $n_{\text{eff}}$ :

$$n_g = n_{\text{eff}}(\lambda) - \lambda \frac{dn_{\text{eff}}}{d\lambda} \Big|_{\lambda}. \quad (5.10)$$

The Bragg filter selects the FP mode nearest to  $\lambda_{\text{Bragg}}$  that benefits from lowest cavity losses. As a result, monomode emission occurs at  $\lambda_{\text{emission}}$  (Fig. 5.6).

### 5.1.2.2 DBR Coarse Tuning with Bragg Section

In a DFB laser, the Bragg grating is inside the active section. Above threshold, injected carriers are almost totally consumed by stimulated photon emission so that the carrier density is clamped. Therefore, the effective index cannot be varied through the carrier-related effect anymore, and the only index variation occurs via heating due to current injection, typically leading to a maximum 3 to 4 nm tuning range. The possibility to tune  $\lambda_{\text{Bragg}}$  is specific to DBR lasers. As the Bragg section is made of passive material and separated from the gain section, the carrier density is no longer clamped. When injecting a current  $I_{\text{Bragg}}$ , the carrier density increases and the effec-

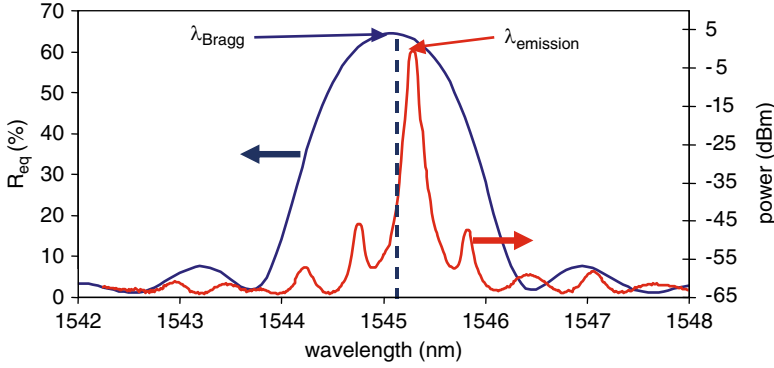


**Fig. 5.6** FP mode selection by a Bragg grating

tive index  $n_{\text{eff}}$  is reduced via the processes presented in Sect. 5.1.1. This gives rise to a decrease of  $\lambda_{\text{Bragg}}$  with a relationship derived from (5.7)

$$\Delta\lambda_{\text{Bragg}} = 2\Delta n_{\text{eff}}\Lambda. \quad (5.11)$$

Maximal achievable  $n_{\text{eff}}$  variation by current injection is in the range of  $4 \times 10^{-2}$ , allowing up to 16 nm tuning. When the Bragg filter is tuned by  $I_{\text{Bragg}}$ , FP modes are successively selected, but this selection leads to tuning characteristics which exhibit mode hops (Fig. 5.7). Apart from those mode hops, corresponding to the case where adjacent FP modes are situated on both sides of the Bragg reflectivity spectrum, the SMSR remains higher than 40 dB.

### 5.1.2.3 DBR Fine-tuning with Phase Section

The FP modes in the DBR cavity are defined by the phase condition

$$2(n_{\text{eff},a}L_a + n_{\text{eff,ph}}L_{\text{ph}} + n_{\text{eff,B}}L_{\text{eff}}) = m\lambda, \quad m \in \mathfrak{N}, \quad (5.12)$$

where  $n_{\text{eff},a}$ ,  $n_{\text{eff,ph}}$ , and  $n_{\text{eff,B}}$  are the effective indices in the active, phase, and Bragg section, respectively. When a current  $I_{\text{ph}}$  is injected into the passive phase section,  $n_{\text{eff,ph}}$  decreases due to the same mechanisms as in the Bragg section. By taking the derivative of (5.12), we obtain

$$\frac{\Delta\lambda_{\text{FP}}}{\lambda} = \frac{\Delta n_{\text{eff,ph}}L_{\text{ph}}}{n_{g,a}L_a + n_{g,ph}L_{\text{ph}} + n_{g,B}L_{\text{eff}}} \quad (5.13)$$

with  $n_{g,a}$ ,  $n_{g,ph}$ , and  $n_{g,B}$  denoting the group indices of the three sections. The FP comb can be continuously shifted to lower wavelengths as illustrated in Fig. 5.7, and the position of the mode hops in the DBR tuning curve can be finely adjusted along the tuning curve. In this way, emission at any wavelength  $\lambda$  in the tuning range

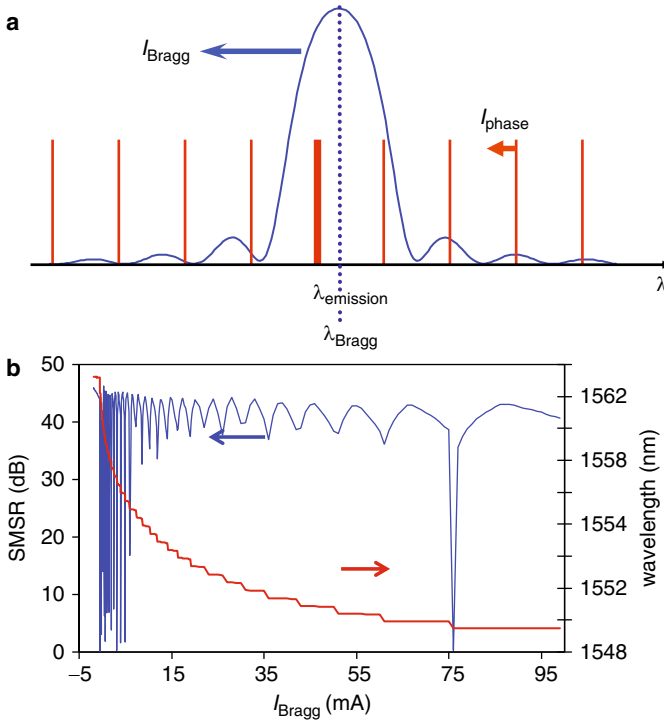


**Fig. 5.7** DBR tuning mechanism, where FP modes are successively selected with decreasing wavelength by injecting current  $I_{\text{Bragg}}$  (a), example of experimental tuning characteristics illustrating emission wavelength and SMSR as a function of  $I_{\text{Bragg}}$  (b)

can be achieved with high accuracy and high SMSR by adjusting  $I_{\text{Bragg}}$  in order to align  $\lambda_{\text{Bragg}}$  with  $\lambda$ , and  $I_{\text{ph}}$  to align an FP mode with  $\lambda$ .

#### 5.1.2.4 Overall DBR Performance

The design of a DBR laser requires multiple compromises in order to simultaneously reach a wide tuning range, high output power, and high SMSR. The tuning range, given by (5.11), can be rewritten as

$$\Delta\lambda_{\text{Bragg}} = 2\Gamma_{\text{Q}} \frac{dn_{\text{Q}}}{dN} \Delta N \Lambda, \quad (5.14)$$

where  $\Gamma_{\text{Q}}$  is the mode's optical confinement factor in the undoped quaternary Q1.45 waveguide material of the Bragg section into which carriers are injected,  $dn_{\text{Q}}/dN$  is the quaternary index variation with changing carrier density (negative value), and  $\Delta N$  represents the increase of carrier density with current injection. In order to maximize the tuning range, one aims at achieving:



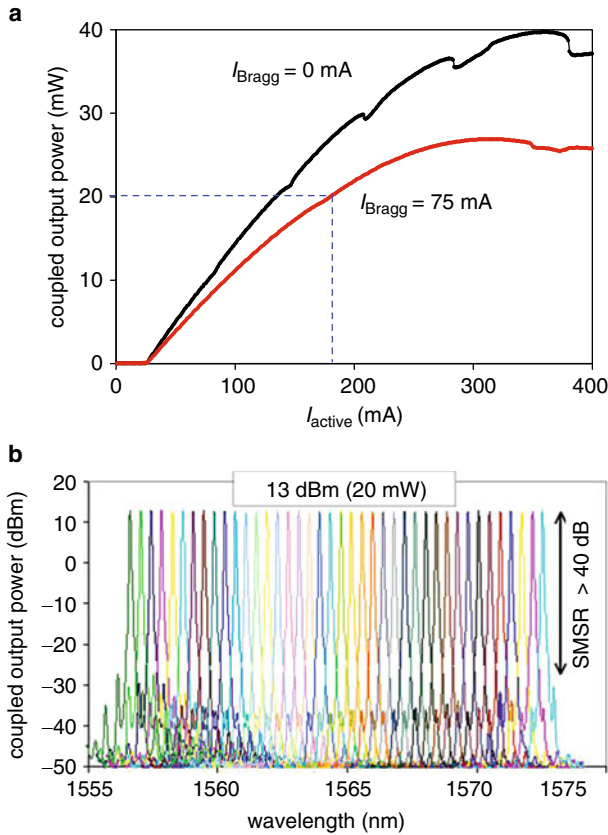


**Fig. 5.8** Coupled output power versus  $I_{\text{active}}$  for minimum (0 mA) and maximum (75 mA)  $I_{\text{Bragg}}$  values (a), superimposed spectra, each at well-adjusted current conditions, for  $I_{\text{active}}$ ,  $I_{\text{phase}}$ , and  $I_{\text{Bragg}}$ , covering a tuning range of 16 nm with 20 mW constant coupled output power and more than 40 dB SMSR (b)

- High  $\Gamma_Q$  by using a thick bulk quaternary guiding layer
- Large  $dn_Q/dN$  by using a quaternary material in the Bragg section which has a bandgap wavelength close to the emission wavelength where the bandfilling effect is particularly pronounced (Fig. 5.3)
- High  $\Delta N$  by reducing current leakage and by reducing the Bragg section length to limit radiative recombination through amplified spontaneous emission.

In order to reach high output power, the following targets must be reached at the same time:

- Maintaining a high mode-overlap between active and passive sections
- Using a quaternary material in the Bragg section with a bandgap wavelength sufficiently shorter than the emission wavelength so that absorption at low  $I_{\text{Bragg}}$  or carrier consumption at high  $I_{\text{Bragg}}$  by stimulated emission is limited
- Increasing fiber coupling efficiency via a spot-size converter in the active section

- Maximizing  $\kappa$  in the Bragg section to ensure high Bragg mirror reflectivity while keeping mode selectivity sufficiently high
- Optimizing the length of the active section regarding the trade-off between a long section ensuring low current threshold density and low thermal effects, and a moderate section length to retain a sufficiently high FSR for efficient Bragg mirror selectivity.

Typical optimized parameters are:

- For the passive sections: 0.42  $\mu\text{m}$ -thick Q1.45 material providing  $T_Q \sim 75\%$ , with  $\kappa \sim 45 \text{ cm}^{-1}$ ,  $L_{\text{Bragg}} \sim 300 \mu\text{m}$ , and  $L_{\text{ph}} \sim 50 \mu\text{m}$
- For the active section: six 8 nm-thick Q1.55 quantum wells with Q1.18 barriers sandwiched between two 100 nm-thick Q1.18 confinement heterostructures, providing 96 % overlap between active and passive section modes.

Such DBR lasers can emit at any ITU channel over a 16 nm tuning range with SMSR  $> 40 \text{ dB}$  and 20 mW of constant coupled output power, as illustrated in Fig. 5.8 [7]. The output power decreases with increasing  $I_{\text{ph}}$  or  $I_{\text{Bragg}}$  (Fig. 5.8a) because of free carrier absorption, but constant output power can be ensured by adjusting  $I_{\text{active}}$  for each channel.

## 5.2 Widely Tunable Lasers by Current Injection

DBR lasers represent basic current-injection-tunable laser devices that exploit a rather simple operation principle relying on the selection of an FP mode with a tunable filter and fine wavelength adjustment by means of a phase section. Their tunability, directly correlated to the limited achievable effective index variation, is limited to around 16 nm, that is nearly half of the C-band. To further increase the tuning range and in particular to cover the whole 40 nm C-band with a monolithic device involving current injection, several approaches have been proposed by different laboratories. Basically, these are utilizing the same principle as DBR lasers, but the Bragg section is replaced by two independently controlled passive sections designed with more complex Bragg gratings. The wavelength tunable selective mirror is the result of the interaction between these two section gratings, thereby widely enhancing the tuning range.

### 5.2.1 Sampled Gratings

The most widely used grating design for such devices is the sampled grating (SG), illustrated in Fig. 5.9. As explained in detail in [8], it consists of a grating with periodically sampled pitch  $\Lambda$ , leading to grating burst lengths  $Z_G$  at a sampling period  $Z_S$ . The resulting reflectivity spectrum is the convolution of the reflectivity of an equivalent Bragg grating with pitch  $\Lambda$  and the reflectivity of a periodic square

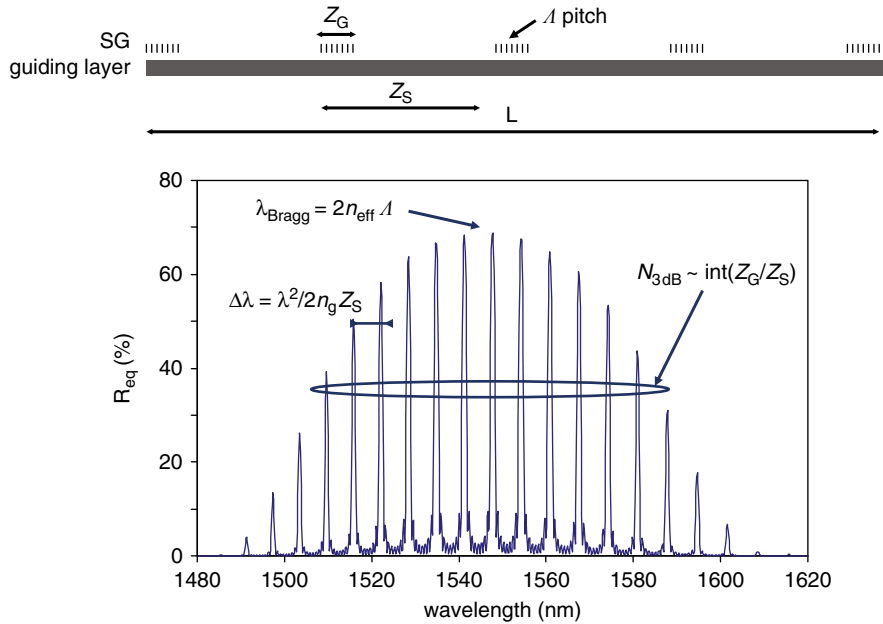


**Fig. 5.9** Sampled grating scheme and calculated reflectivity spectrum ( $L = 580 \mu\text{m}$ ,  $Z_S = 58 \mu\text{m}$ ,  $Z_G = 6 \mu\text{m}$ ,  $\kappa = 300 \text{ cm}^{-1}$ , losses =  $15 \text{ cm}^{-1}$ )

function of length  $Z_G$  and period  $Z_S$ . As a consequence, the reflectivity spectrum shows several reflectivity peaks, centered at  $\lambda_{\text{Bragg}} = 2n_{\text{eff}}\Lambda$  and separated by:

$$\Delta\lambda = \lambda^2 / 2n_g Z_S. \quad (5.15)$$

Each reflectivity peak number  $n$  ( $n = 0$  corresponds to the central peak) is equivalent to the reflectivity of an unsampled Bragg grating with SG length  $L$ , but with a coupling coefficient  $\kappa(n)$  given by

$$\kappa(n) = \kappa_0 \frac{Z_G}{Z_S} \frac{\sin(\pi n Z_G / Z_S)}{\pi n Z_G / Z_S} \exp\left(\frac{-i\pi n Z_G}{Z_S}\right). \quad (5.16)$$

Thus, the peaks are not phase matched, and they correspond to a smaller coupling coefficient rather than that of the central peak which is given by  $\kappa(0) = \kappa_0 Z_G / Z_S$ . The envelope of the reflectivity peaks widens when the duty cycle  $Z_G / Z_S$  is reduced, and the number of peaks in the 3 dB envelope can be approximated by

$$N_{3\text{dB}} \approx \text{int}(Z_G / Z_S). \quad (5.17)$$

To obtain a large number of peaks, the duty cycle must be reduced, which necessitates a higher  $\kappa_0$  in order to retain a sufficiently large  $\kappa(n)$ -value for the required reflectivities. Such SGs typically use  $\kappa_0$  as high as  $300 \text{ cm}^{-1}$ , with a 10%  $Z_G / Z_S$  duty cycle.

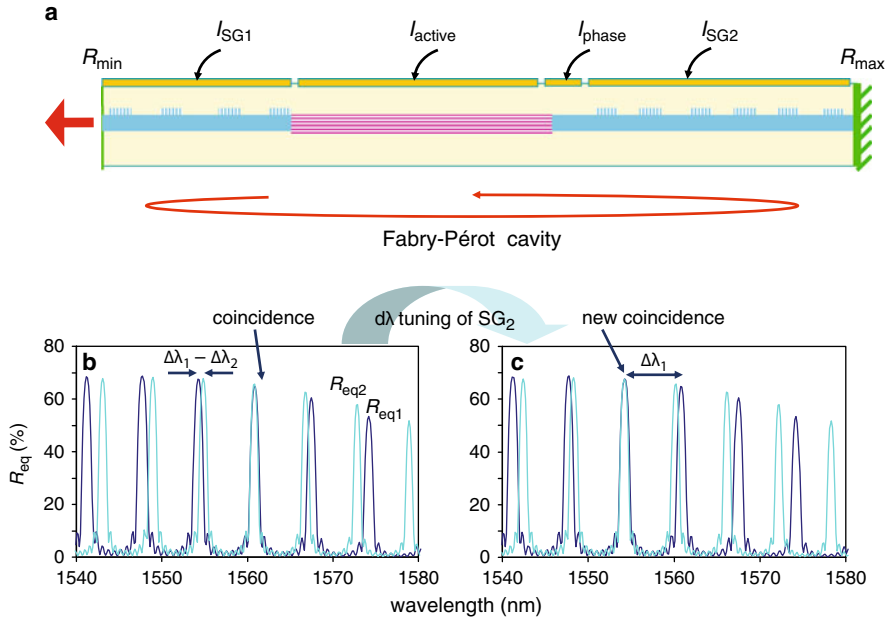


**Fig. 5.10** SG-DBR laser structure. Schematic cross-section (a), superimposed SG spectra providing Vernier effect (b), (c)

### 5.2.2 SG-DBR Lasers

The first device incorporating dual passive grating sections is the SG-DBR structure, initially developed at the University of California at Santa Barbara [8]. It is composed of an active section and an adjacent phase section, sandwiched between two SGs (Fig. 5.10a). The laser cavity itself is delimited by the two SGs: the reflectivity for the FP modes is given by the multiplication of the two SG reflectivities. Both SGs have the same pitch  $\Lambda$ , but their sampling periods  $Z_{S1}$  and  $Z_{S2}$  are slightly different, thus generating different spacings,  $\Delta\lambda_1$  and  $\Delta\lambda_2$ , between the respective reflectivity peaks. By an appropriate choice of  $Z_{S1}$  and  $Z_{S2}$ , one can ensure that only two peaks are in coincidence between the two zeros of the spectrum envelope. This coincidence leads to a higher reflectivity for the specific FP modes and selects the lasing mode (Fig. 5.10b).

By injecting current, for example, into SG<sub>2</sub> corresponding to the smaller  $\Delta\lambda$ , the associated reflectivity comb shifts to lower wavelengths by  $\delta\lambda = \lambda\Delta n_{\text{eff}2}/n_g$  according to (5.11). When  $\delta\lambda$  reaches  $\Delta\lambda_1 - \Delta\lambda_2$ , the coincidence shifts to adjacent peaks to the left side. Tuning one SG by  $\delta\lambda = \Delta\lambda_1 - \Delta\lambda_2$  thus generates a shift of the maximum reflectivity by  $\Delta\lambda_1$ . This behavior is called the Vernier effect and leads to a tuning enhancement given by

$$F = \frac{\Delta\lambda_1}{\Delta\lambda_1 - \Delta\lambda_2}. \quad (5.18)$$

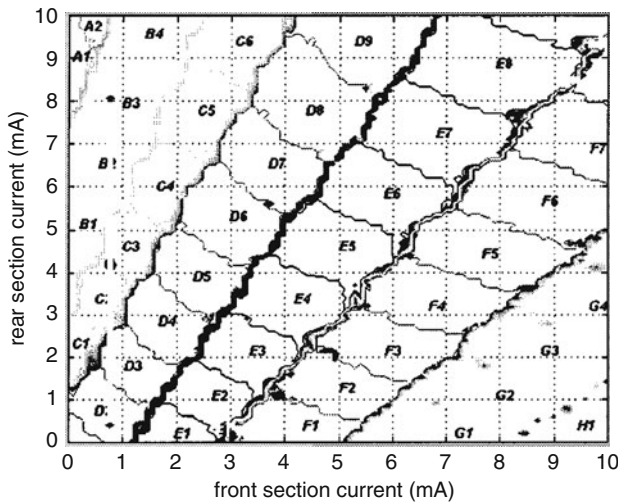


**Fig. 5.11** Two-dimensional tuning map of an SG-DBR (after [9])

By applying the same current density simultaneously to both SGs, the two reflectivity spectra shift equally. Coincidence can be kept on the same peaks, simply tuned by  $\delta\lambda = \lambda \Delta n_{\text{eff}1,2} / n_g$ , and all wavelengths within the reflections' envelope can be reached by an appropriate coincidence.

Sampled grating DBR lasers are hence characterized by two-dimensional tuning curves  $\lambda = f(I_{\text{SG}_1}, I_{\text{SG}_2})$  as illustrated in Fig. 5.11. The diagonals correspond to the same coincidence, with hops between FP cavity modes designated by a number. “Super-mode hops” are observed between diagonals and correspond to a coincidence change designated by a letter.

In order to precisely reach any ITU channel, currents are injected into  $\text{SG}_1$  and  $\text{SG}_2$  to position the emission wavelength in the middle of a mode-hop free area of the 2D tuning curves. Subsequently, the FP wavelength is finely tuned by current injection into the phase section. SG-DBR type tunable lasers demand a precise design in order to simultaneously guarantee stable modal behavior, high SMSR, and a 40 nm tuning range required for covering the whole C-band. To ensure full coverage, the reflection peak spacings  $\Delta\lambda_{1,2}$  are typically chosen to be around 5 nm, leading to SG periods  $Z_{\text{S}1,2}$  of some 60  $\mu\text{m}$ . The overall tuning range is limited by the wavelength spacing between two coincidences, which is given by the enhancement factor  $F$  multiplied by the spacing difference  $\Delta\lambda_1 - \Delta\lambda_2$  between the SG reflectivity peaks. To reach 40 nm, this difference must be kept very small, entailing each reflectivity peak to be extremely narrow in order to avoid SMSR degradation by adjacent channels. This design requirement leads to quite extended SG sections with lengths of around 600  $\mu\text{m}$  and many grating bursts (about 10). Such an optimized design is presented in [10]. There a front grating was applied comprising  $10 \times 6 \mu\text{m}$  bursts and a 58  $\mu\text{m}$  long sampling period, a rear grating with  $11 \times 6 \mu\text{m}$  bursts and a 64  $\mu\text{m}$  long sampling period, and a  $\kappa$  of  $300 \text{ cm}^{-1}$ . Such a de-

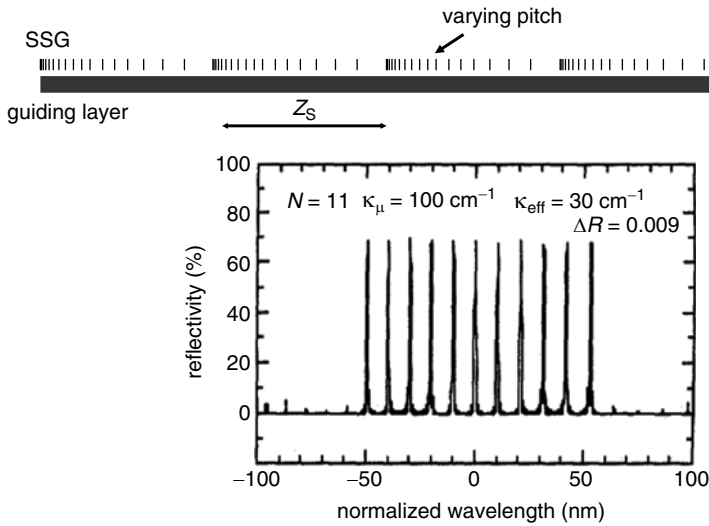


**Fig. 5.12** Super-structure grating scheme and calculated reflectivity spectrum for optimum grating pitch variations [12]

vice provides a tuning enhancement factor  $F$  of 10, and 50 nm tuning range with SMSR > 35 dB.

With the laser light being emitted through the front SG, a semiconductor optical amplifier (SOA) structure (see also Chap. 12) can be inserted between that SG section and the front facet as a booster to enhance the output power. The emitted light is amplified by a single pass through the SOA, while the FP cavity is kept unaffected. Given a typical SOA gain of 15 dB, an input power of 1 mW into the SOA is sufficient to achieve more than 20 mW of optical output power from the laser. Under these conditions, the SOA is operated in the saturation regime: the carrier density in the SOA is low, leading to reduced amplified spontaneous emission and high signal-to-noise ratio. A tilted output and a high quality  $10^{-4}$  antireflection coating are necessary to avoid creating any parasitic cavity between the output facet and the Bragg section, and to ensure a low noise level [10, 11].

### 5.2.3 SSG-DBR Lasers

The overall envelope of the reflectivity peaks represents one of the limitations of SG-DBRs, as it reduces reflectivity far from the central wavelength. To overcome this restriction, it was proposed to replace one or both SGs by more complex gratings, so-called super-structure gratings (SSGs), that consist of periodically repeated gratings with varying pitch (Fig. 5.12). Numerically calculated optimal pitch variations within one period can generate a reflection spectrum with a square envelope [12]. As an example, a device has been designed with a rear SSG to provide uniform

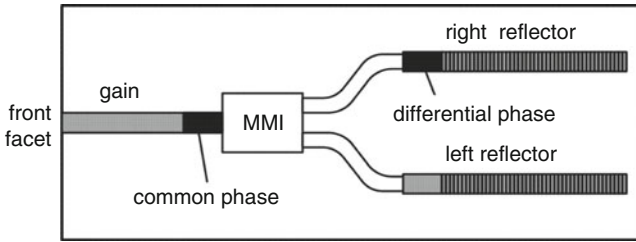


**Fig. 5.13** Schematic structure of a Y-laser (after [14])

reflectivity peaks, and a short front SG to minimize free carrier absorption of the emitted light. In this way, more than 18 mW of output power and 40 dB SMSR over a 30 nm tuning range have been achieved. Even more than 45 mW could be obtained with an integrated booster SOA [13].

#### 5.2.4 Y-Lasers

Another approach very close to the SG-DBR variant consists in using a Y-coupler in order to place the two SGs parallel on the same side of the active section (Fig. 5.13) rather than on either side. Likewise, the Vernier effect is exploited to reach 40 nm tuning, but contrary to SG-DBR lasers, the reflectivity for the FP modes is given by the vector sum of the SG reflectivities, instead of multiplication. With a careful design of the waveguides, the differential phase between both SGs can be adjusted to get opposite phase conditions between competing adjacent channels, and improve super-mode selection. Such a device can deliver an output power of more than 10 mW with more than 40 dB SMSR over a 40 nm tuning range [14, 15], and is now commercially available.

#### 5.2.5 Multiple Peak Grating and Tunable Wide Filter Lasers (GCSR, DS-DBR)

There are other sophisticated solutions that use an active and a phase section sandwiched between a multiple peak grating (SG or SSG) and a tunable wide filter section. Instead of making use of the Vernier effect, the wide filter simply selects one of the reflectivity peaks. The first example of this kind was the grating-assisted codirectional coupled sampled grating reflector (GCSR) laser [16]. The filter is formed by a vertical coupler composed of two waveguides with a long-period grating. The tunability is given by

$$\Delta\lambda = \lambda \frac{\Delta n_1}{n_{g1} - n_{g2}}, \quad (5.19)$$

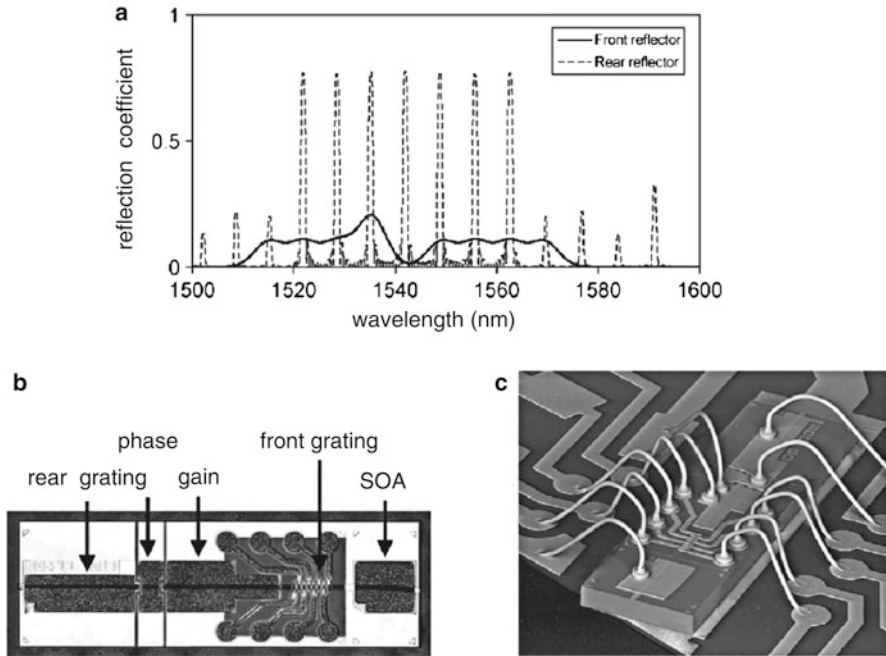


**Fig. 5.14** DS-DBR(-SOA) structure. Tuning mechanism (a), top view (b), photo image of a mounted device (c) [19]

where  $\Delta n_1$  represents the refractive index change of the upper waveguide due to current injection, and  $n_{g1}$ ,  $n_{g2}$  the group indices of the upper and lower waveguide, respectively. Using an optimized coupler design and a specially tailored reflector grating, wavelength tuning over 32 nm was demonstrated, along with SMSR higher than 40 dB and 25 mW output power [17]. This concept has been taken further very recently by employing a grating assisted codirectional coupler filter that is formed by laterally rather than vertically arranged asymmetric waveguides [18]. It was claimed that the adiabatic coupling conditions at the input and output of this filter variant provided more stable characteristics. A very wide quasicontinuous tuning range of 65 nm (1510 nm–1575 nm) with SMSR > 35 dB was obtained at 50 °C and appreciably low operating currents.

Furthermore, the digital supermode DBR (DS-DBR) has been proposed which involves an SSG grating, and a series of eight short Bragg gratings with slightly different pitches (Fig. 5.14) to provide the filter function. Each Bragg grating section is controlled by an individual current. Without current injection, they generate a sequence of reflection peaks separated by 5 nm to result in a wide weak reflectivity spectrum. When current is applied to Bragg section number  $i$ , its reflectivity shifts from  $\lambda_i$  to lower wavelengths and adds to the reflectivity at  $\lambda_{i-1}$  of the adjacent Bragg section  $i - 1$  with lower pitch. As a result, the SG peak closest to  $\lambda_{i-1}$  will be preferentially selected (Fig. 5.14a). Although such a device requires many electrodes, it may be simpler to control than SG-DBR type lasers because it is not



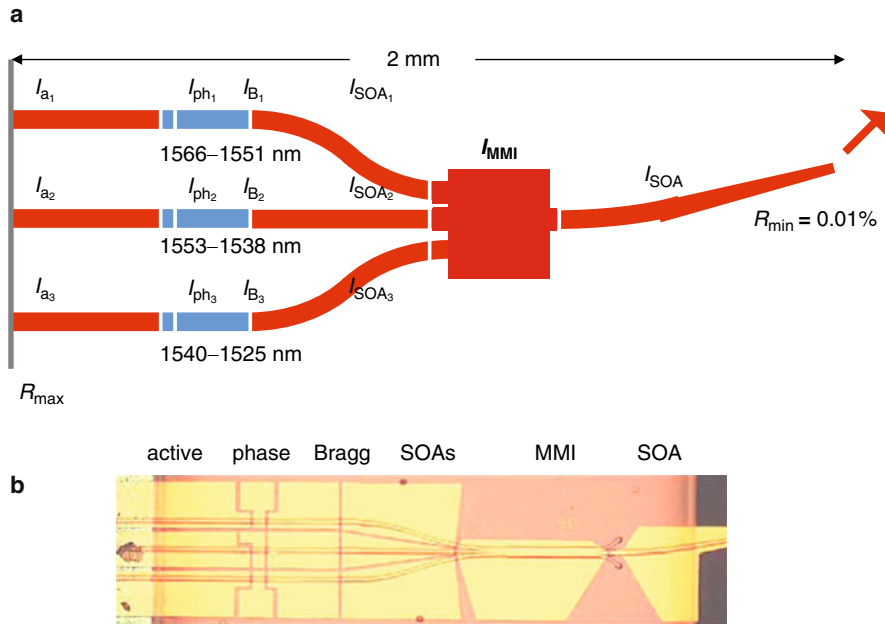


**Fig. 5.15** Wavelength tunable laser design employing three selectable DBR structures combined by an MMI coupler (a), and fabricated device chip (b). Only one of the three branches is operated at the same time

relying on the critical Vernier effect, and the currents controlling the short Bragg sections are digitally fixed at 0 or  $\sim 5$  mA. The drawback of this structure is the poor selectivity of the multiple Bragg peaks. The uniformity of the rear SSG peaks has to be very carefully optimized to ensure efficient peak selectivity. Again, more than 40 nm tuning together with SMSR better than 40 dB has been demonstrated. As with SG-DBR designs, a booster SOA has been incorporated in front of the multiple gratings giving 14 dBm fiber coupled power [19].

### 5.2.6 DBR-MMI

Another means to increase the tuning range consists in using three DBR lasers in parallel, each of them covering one-third of the C-band. A multimode interference (MMI) coupler combines the three outputs, while a common SOA section guarantees high output power (Fig. 5.15). This device requires quite a few electrodes; on the other hand, the tuning scheme proves to be fairly simple. Only one DBR is operated at the same time, and the tuning characteristics are determined by only one Bragg current rather than the two currents simultaneously feeding the grating sections in the aforementioned designs. A total tuning range of 40 nm has been demonstrated whilst maintaining the SMSR level above 40 dB [20].

### 5.3 Control Issues

All current-injection-based tunable lasers described above are very attractive because they are monolithically integrated on InP semiconductors, offering small footprint and packaging costs, and compatibility even with e-XFP modules. They are also well suited for fast-tuning applications as the tuning speed is limited intrinsically only by carrier lifetime ( $\sim 1$  ns). From a practical perspective, however, the major challenge with all these approaches arises from control measures needed to guarantee constant output power, extremely precise emission wavelength, and to avoid any SMSR degradation or even mode hopping. Control accuracy has to be maintained during the full time of operation when the laser is kept running, and when the laser is turned on after a period without operation. To this end, tunable laser components require exhaustive and complex initial characterization to precisely define the optimum operating conditions and feedback loop parameters. Changes in performance and settings due to aging effects are demanded to be limited to levels as low as possible, but nonetheless to be well controlled in order to ensure stability over the entire life cycle. These constraints lead to limited fabrication yield and high characterization costs.

#### 5.3.1 Control Algorithms

Tunable lasers are operated at constant temperature, monitored on submount by means of a temperature-dependent resistive probe, and controlled by a Peltier element. Commonly, a tap coupler is positioned between the front facet and the fiber coupling optics to extract a small amount of light for monitoring purposes. This light is split by a second tap and received by a photodiode  $PD_1$  in the one axis and by another photodiode  $PD_2$  in the other axis after passing a Fabry–Pérot etalon (Fig. 5.16a).  $PD_1$  monitors the output power which is controlled by the drive current of the active laser section or of the booster SOA via a feedback loop. The signal received by  $PD_2$  varies periodically with wavelength, with a period equal to the etalon's free spectral range (typically the 100 GHz ITU spacing, i.e. 0.8 nm at C-band wavelengths). By adjusting the FP etalon transmission characteristic such that the positions of maximum slope coincide with the ITU channels, the ratio  $I_{PD_2}/I_{PD_1}$  can be normalized to unity and used to monitor the position of the emitted wavelength relative to an ITU channel (Fig. 5.16b): if  $I_{PD_2}/I_{PD_1} > 1$ , then  $\lambda_{\text{emission}}$  will be  $> \lambda_{\text{ITU}}$ , whereas  $I_{PD_2}/I_{PD_1} < 1$  indicates  $\lambda_{\text{emission}}$  to be  $< \lambda_{\text{ITU}}$ . In this way, the emission wavelength of the tunable laser is finely tuned to be precisely aligned to the ITU wavelength, controlled by the phase section current in conjunction with a feedback loop.

The major difficulty is to avoid both SMSR degradation and mode hops. For adjusting and maintaining maximum SMSR, it is necessary to extract a monitoring parameter that can easily be measured inside the module. SMSR is optimized when an FP mode matches a maximum of cavity reflectivity, corresponding to the center

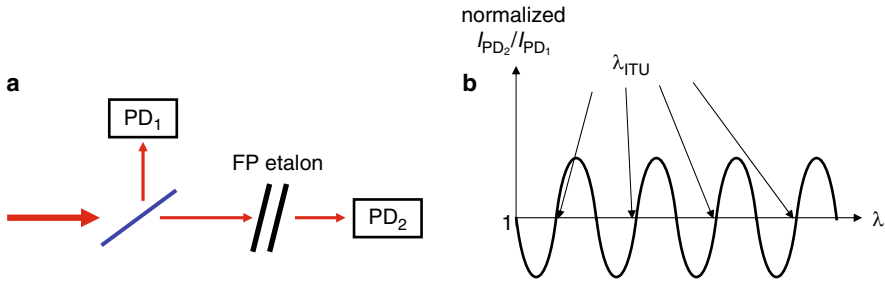


**Fig. 5.16** Scheme of wavelength and power locker inside the module (a), ratio  $I_{PD2}/I_{PD1}$  vs. wavelength characteristic (b)

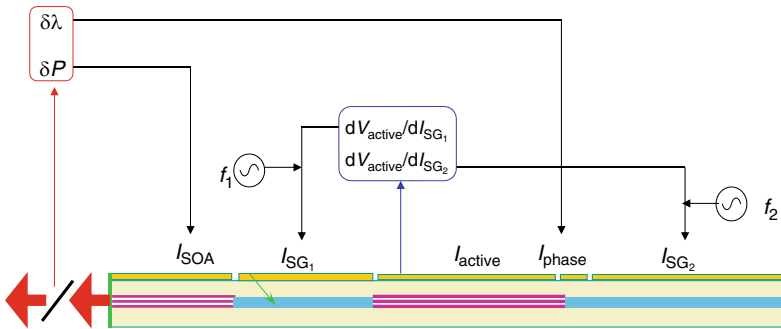


**Fig. 5.17** Servo-control loops for controlling an SG-DBR

of mode-hop-free areas in the 1D or 2D tuning curves. This situation is characterized by minimal loss in the cavity, and accordingly yields minimum threshold current. Then, the voltage at the active section,  $V_{\text{active}}$ , will exhibit a local minimum and the output power a local maximum.

The method used to avoid mode hops in DBRs consists of superimposing a small and slow dithering signal on the current  $I_{\text{Bragg}}$ . Then,  $dP/dI_{\text{Bragg}}$  (or  $dV_{\text{active}}/dI_{\text{Bragg}}$ ) is measured at the same frequency, and maintained on a local extremum by controlling  $I_{\text{Bragg}}$  via a feedback loop. In the case of tunable lasers comprising simultaneously controlled multiple Bragg sections (SG-DBR, Y-laser, or GCSR), the individual currents are dithered at different frequencies, leading to double monitoring of, e.g.,  $dP/dI_{SG1}$  and  $dP/dI_{SG2}$ , involving two feedback loops [21].

Dedicated algorithms are applied to adjust the servo-control loops and to ensure stable behavior. However, these loops, schematically illustrated in Fig. 5.17 for an SG-DBR-SOA, are interdependent. For example, when  $I_{SG}$  is increased to maintain maximum SMSR, the effective refractive index in the SG section is reduced, thus causing the FP modes to shift toward lower wavelengths: the emitted wavelength is decreased. Likewise, when increasing  $I_{\text{phase}}$  or  $I_{SG}$ , cavity losses tend to increase due to free-carrier absorption, and the output power decays. If the power is adjusted by increasing the active current accordingly, the associated heating shifts FP modes and SG reflectivity peaks to higher wavelengths.

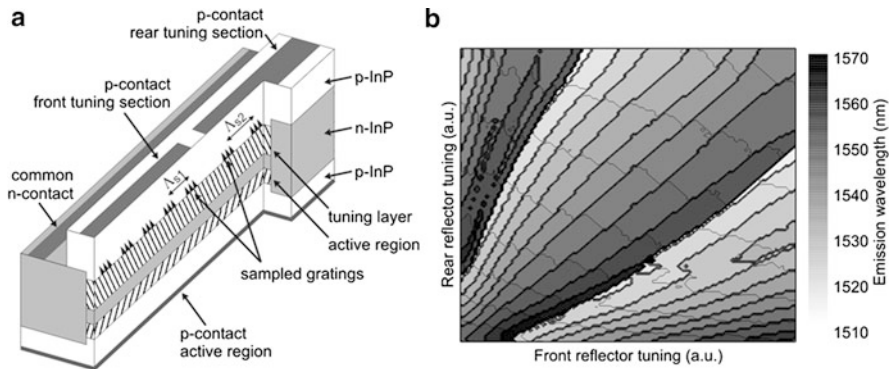


**Fig. 5.18** Scheme of a TTG laser (a) and 2D tuning characteristics (b): the *thin solid lines* within the supermodes indicate 1 nm spaced iso-wavelength contours for visual aid [22]

Adjusting the optical power by using an SOA is advantageous since the SOA is located outside the FP cavity. Any heating effects do not impact the emitted FP mode wavelength. The SOA requires an additional control current; however,  $I_{\text{active}}$  can be set to a constant value (e.g., 50 mA) sufficient for lasing. Hence, the number of adjustable currents is kept unchanged. Moreover, the SOA can fulfill the needed functionality of optical gating: when tuning from one wavelength to another, or when turning on the laser, light is emitted on adjacent channels during the transition interval, which is unacceptable for WDM networks. The SOA can be switched off during those transition time slots and turned on only once the laser is fully stabilized.

Aiming at simplifying the servo-control of SG-DBR type lasers, a tunable twin guide laser (TTG) has been proposed [22]. In this approach, the sampled gratings  $SG_1$  and  $SG_2$  are incorporated in a passive waveguide layer which is placed above the active waveguide (Fig. 5.18). The phase section can be omitted because  $SG_1 + SG_2$  cover the whole cavity length. When  $SG_1$  and  $SG_2$  are simultaneously tuned such that coincidence is retained for the same reflectivity peaks, the FP comb will be tuned similarly and the FP mode remains aligned to this coincidence. Continuous mode-hop free wavelength tuning up to 8 nm is achievable within the supermodes (Fig. 5.18b). The difficulty to be solved in such devices is to achieve efficient, independent current injection into the two successive active and passive p-i-n junctions.

### 5.3.2 Influence of Cavity Length and Nonlinear Effects

The complexity of the control mechanisms is strongly influenced by two factors: the FP cavity length of the tunable laser structure and nonlinear intracavity effects. The free spectral range represents the width of a mode-hop-free area in the tuning characteristics in the center of which the emission wavelength must be kept. According to (5.9) the FSR is inversely proportional to the cavity length. There-

fore, tunable laser designs aim at reducing the cavity length to allow for larger tolerances of the current settings and for more tolerant control algorithms with reduced mode hop risks. As an example, for a DBR laser, the total cavity length  $L_{\text{cavity}} = L_a + L_{\text{ph}} + L_{\text{eff}}$  amounts to  $\sim 400 \mu\text{m} + 50 \mu\text{m} + 150 \mu\text{m} = 600 \mu\text{m}$ . With a typical value of 3.8 for  $n_g$ , this yields an FSR value of  $\sim 0.5 \text{ nm}$ . For widely tunable lasers, on the other hand, such as SG-DBR lasers, the respective length is  $L_{\text{cavity}} = L_a + L_{\text{ph}} + 2L_{\text{eff}}$ ,  $\text{SG} \sim 500 \mu\text{m} + 100 \mu\text{m} + 2 \times 400 \mu\text{m} = 1400 \mu\text{m}$ . Effective lengths in SGs are long due to the reduction of the coupling coefficient by the sampling effect (5.16). The width of mode-hop-free areas is thus reduced to about 0.23 nm.

The other drawback associated with long cavities is the occurrence of nonlinear effects. When experimentally observing SMSR or power maxima on tuning characteristics, they appear not to occur at the center of mode-hop-free areas, but to shift toward a higher wavelength mode. Sometimes, maxima even tend to move outside this area which renders SMSR monitoring impossible (Fig. 5.19). A hysteresis effect may be noticed as well: the currents corresponding to mode hops are different depending on whether the Bragg current is increased or decreased.

This phenomenon was thoroughly studied in [23] and has been attributed to the nonlinear four-wave mixing (FWM) effect. As detailed in [24], the beating of FP modes generates modulation of the carrier density and carrier energies within the conduction or valence bands at a frequency determined by

$$\Delta\nu = \frac{c}{\lambda^2} \text{FSR}. \quad (5.20)$$

For tunable lasers, where the FSR remains within 0.2 to 0.5 nm,  $\Delta\nu$  is in the 25 to 60 GHz range. At these frequencies, the dominant effect turns out to be carrier density pulsation (CDP), whereas intraband effects like spectral hole burning or carrier heating can be neglected. CDP generates an asymmetric gain modification around the emission wavelength [24], as illustrated in Fig. 5.20.

In a tunable laser, assuming the  $m$ th FP mode to be emitted, the gain characteristic behaves asymmetrically, centered at  $\lambda_m$ , in that the gain of mode  $m + 1$  at  $\lambda_{m+1} > \lambda_m$  is larger than the gain of mode  $m - 1$  at  $\lambda_{m-1} < \lambda_m$ . Mode hopping toward decreasing wavelengths is then impeded, while mode hopping toward higher wavelengths is favored. This explains why SMSR and power maxima always tend to shift toward the higher wavelength sides, as mentioned above. When a mode hop occurs, the center of the asymmetric gain characteristic shifts to the new mode and generates an abrupt change in the gain. This results in SMSR or power discontinuities (Fig. 5.19) and causes the hysteresis phenomenon. Indeed, initial gain values for the FP modes are different depending on the initial lasing mode, i.e., whether the Bragg current is being increased or decreased.

Aiming at reducing these nonlinear effects to get regular tuning characteristics with clear power maxima, it proves necessary to shorten the cavity length to increase the spacing of the FP modes and reduce their beating. Secondly, the intracavity power should be reduced. In this respect, the integration of an output SOA is another benefit in that, by providing external amplification, the requirements for

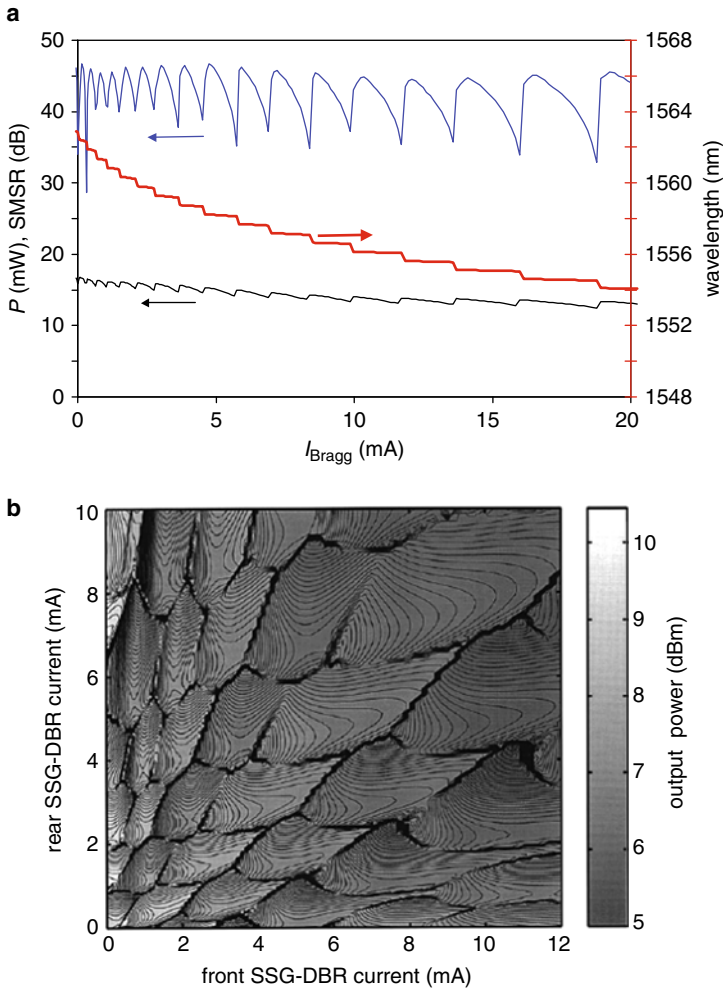
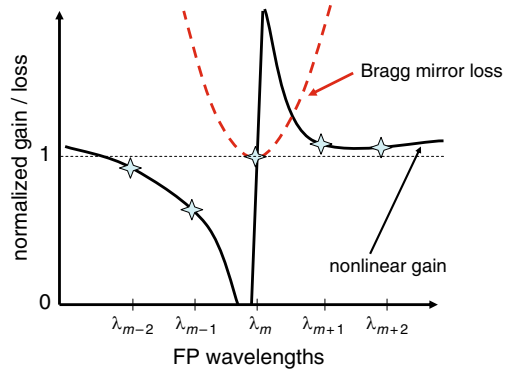


**Fig. 5.19** Tuning characteristics of DBR laser (a): Emission wavelength (red curve), SMSR (blue curve), and output power (black curve). SMSR and output power exhibit a sequence of maxima around 45 dB and 15 mW, respectively, shifted to the left side (lower Bragg current) of mode-hop-free areas (after [20]). Output power characteristics of SSG-DBR laser as a function of current in rear and front SSG-DBR sections (b). Mode-hop-free areas have maximum power away from the center or even no power maximum [21]

the emission power from the cavity itself are highly relaxed. The current driving the active section as well as the section length can be reduced, typically from 600  $\mu\text{m}$  in a DBR to 400  $\mu\text{m}$  for a DBR with SOA. This measure immediately damps nonlinear effects and leads to more regular hysteresis-free characteristics.

Despite all these difficulties, simultaneous control of optical power, wavelength, and SMSR is possible via interleaved feedback loops on control currents of the different sections. This is done at the cost of extremely precise measurements, electronics, and algorithms. Some companies have developed sufficiently reliable algo-

**Fig. 5.20** Normalized gain/loss behavior at the different FP wavelengths around the  $m$ th emitted mode, taking into account the carrier density pulsation (CDP) effect



gorithms to obtain stable behavior despite aging or variation of external conditions (e.g., [25]), and to eventually meet Telcordia qualification standards.

### 5.3.3 Fast Tuning

The transmission of individual packets at different wavelengths leads to very high granularity and offers high flexibility for coping with fast traffic fluctuations in metropolitan or access networks. For such emerging applications to become a reality, the laser tuning speed should be shorter than the 50 ns packet guard time. Current-injection tunable lasers are the only possible candidates for such applications due to the intrinsic fast-tuning mechanism, limited only by carrier lifetime ( $\sim 1$  ns). Studies on widely tunable lasers such as SG-DBR or DS-DBR lasers with optimized electrical current signals have indeed shown extremely fast tuning [9, 26]. Practically, however, the wavelength switching period must also encompass the time needed for precise stabilization of the output power and of the emission wavelength onto the ITU grid including sufficiently good single-mode behavior (SMSR).

The altered injection currents enabling tuning also give rise to transient heating effects, and these are very slow processes. As a consequence, the effective tuning speed for this type of lasers is limited by the servo-control feedback loops. The efficiency of these loops, i.e., the possibility to run them very fast without mode-hop risk, is closely related to the robustness of the tuning mechanisms and to the tolerance with respect to control current variations. With extremely fast electronics, 50 ns tuning with 3 GHz wavelength accuracy has been demonstrated on GCSR lasers [27].

## 5.4 Other Wavelength Tunable/Selectable Lasers

Monolithically integrated tunable lasers based on current injection are attractive as they offer low cost potential, reduced footprint, and fast tuning, and various kinds of such lasers have been introduced into current commercial systems. This has become

possible thanks to a large effort on design, process development, characterization, and electronics that led to devices meeting Telcordia specifications (extrapolated lifetime of 25 years with stable performance) and an industrial yield compatible with commercially viable production. Researchers and manufacturers have suggested many other approaches, including lasers with mechanical or thermal tuning. In general, these devices tend to be larger, though in exchange, they offer relaxed control mechanisms. Depending on their design, they can provide even larger tuning ranges, e.g., over the complete C+L bands, very high output powers, or record low spectral linewidth.

### ***5.4.1 Thermally Tuned DFB Array***

A very simple and yet efficient approach is an array of typically 12 DFB lasers with a stripe-to-stripe wavelength spacing of about 3 nm obtained by an appropriate variation of the grating pitch. For operation, only one of the lasers is selected and electrically turned on while the array temperature is varied within a range of 30 °C to finely tune to the desired wavelength. This solution benefits from an extremely simple control scheme, absence of mode hops, and from the high performance, maturity, and reliability of standard DFB lasers. On the other hand, fabrication of such lasers requires a high level of process control to meet yield requirements. Especially, single-mode behavior must be guaranteed for each laser device of the array (see also Chap. 3). In addition, thermal tuning requires a large operation temperature range and is not compatible with fast-tuning applications.

One option for selecting any of the DFB lasers is to use a monolithically integrated coupler, such as an MMI [28], or alternatively and preferably a funnel combiner (Fig. 5.21a) [29] which relaxes fabrication tolerances. With an integrated output SOA to compensate for around 15 dB coupler losses, achievement of up to 40 mW-coupled output power has been demonstrated over the C-band. Another alternative is to make use of an external microelectro-mechanical system (MEMS) based tilt mirror placed at the focal plane of a collimating lens (Fig. 5.21b) [30]. The InP chip is simplified, losses of the passive combiner are suppressed, and packaging remains simple thanks to an electronic fine alignment of the mirror. Today, this solution has found widespread use in DWDM systems.

### ***5.4.2 Tunable Vertical Cavity Surface Emitting Lasers***

Another very simple-to-control solution is a VCSEL (see Chap. 3) composed of an active structure sandwiched between a bottom Bragg mirror and a movable mirror membrane on top [31], as sketched in Fig. 5.22. Due to the extremely short cavity, only one FP mode exists in the wavelength range where gain is available. This FP mode can be continuously tuned by changing the cavity length accomplished



**Fig. 5.21** DFB array with funnel combiner and output SOA (a) [29], and DFB array with MEMS tilt mirror (b) [30]

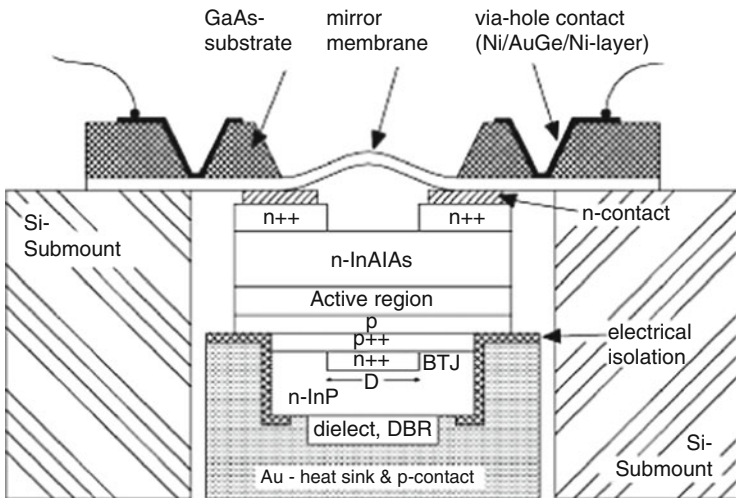
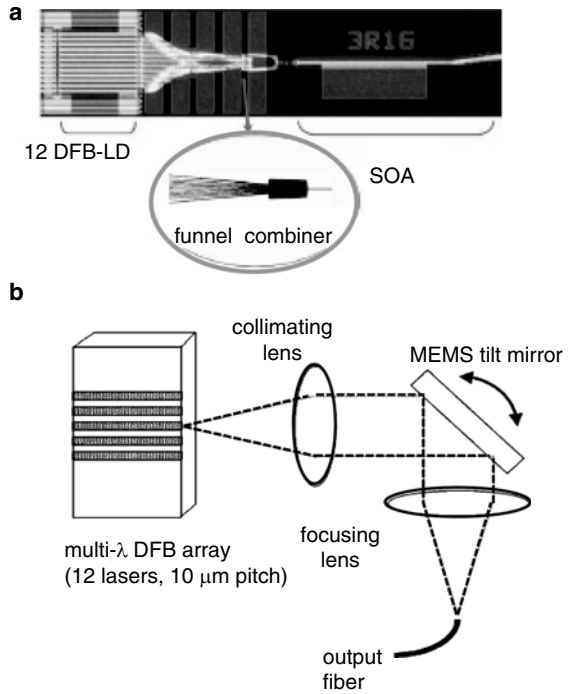


**Fig. 5.22** Tunable VCSEL with a movable top mirror membrane [31] (see also Sect. 3.6.1)

by moving the top mirror. Electrically pumped devices have been realized featuring a 76 nm tuning range, albeit the output power remained limited to a few mW only.

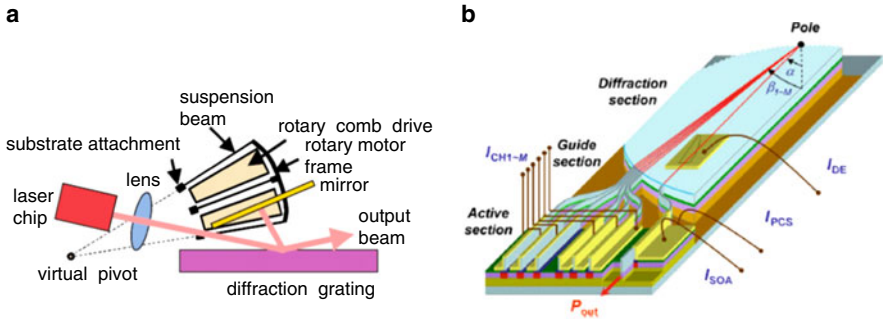


**Fig. 5.23** Designs of external cavity tunable lasers with rotating Bragg grating [32] (a), and with integrated vertical concave grating and dispersive element for fine tuning (b) [33];  $I_{DE}$ ,  $I_{PCS}$ ,  $I_{SOA}$ , and  $I_{CH1-M}$  denote the currents of the dispersive element, phase-controlled section, optical amplifier, and of the active elements (channel 1– $M$ ), respectively

### 5.4.3 External Cavity Tunable Lasers

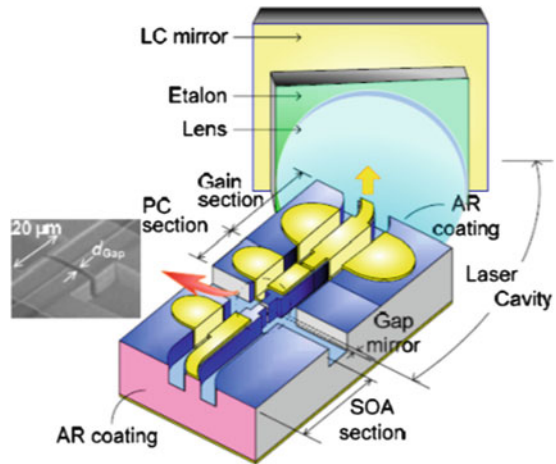
External cavity tunable lasers consist of a long cavity built from discrete elements, including an InP chip as the gain medium (basically an antireflection coated FP laser) and wavelength-selective mirrors. These long cavities have the advantage of enabling fairly small linewidths compared to integrated solutions. However, at the same time, they generate extremely dense FP combs. As a consequence, the laser design must incorporate solutions which ensure that both, the FP modes and the wavelength selective mirror(s), can automatically be tuned in a correlated fashion so that uncontrolled mode hops are avoided.

#### 5.4.3.1 Design with Diffraction Grating

An InP gain chip is placed within a cavity delimited by a fixed mirror and a wavelength tunable external grating. A first example is the Littman/Metcalf cavity configuration depicted in Fig. 5.23a [32]. The beam emerging from a diode with a rear high-reflection coating is collimated by a lens and then diffracted by a grating. A voltage is applied to an MEMS actuator, thereby rotating the grating plane to allow a particular wavelength to be coupled back into the laser diode. The first-order diffracted beam is used to automatically adjust the actuator voltage. By careful choice of the Bragg grating rotation with respect to the pivot point, an equal shift of the cavity FP modes and the Bragg grating can be achieved during tuning, and thereby continuous mode-hop-free tuning over 40 nm along with 55 dB SMSR is provided.

A widely tunable multichannel grating cavity laser is another variant which has been proposed more recently [33]. The laser operates in a Littrow configuration and includes a number of active sections arranged in parallel to each other and all las-

**Fig. 5.24** External cavities based on an FP etalon and an LC tunable mirror [34]



ing at different wavelengths, an output SOA, a phase-controlled section, a current-tunable dispersive element, and an etched vertical diffraction grating, all monolithically integrated on a single InP chip (Fig. 5.23b) [33]. The cavity is formed by the front facets of the active elements and the rear diffraction grating (the center of which is designated by “pole”). Coarse wavelength tuning is accomplished by selecting an appropriate active element while fine-tuning is managed by modifying the angle of the back-reflected beam in that the effective refractive index in the dispersive element is varied via current injection. More than 50 nm tuning without mode hops has already been demonstrated. Nonetheless, the design still needs further improvements so that the output power can be raised above its present values which range from  $-5$  to 0 dBm.

#### 5.4.3.2 Design with Fabry–Pérot Etalon

In another concept, an FP etalon is placed inside the cavity. Its maximum transmittance is adjusted to the ITU wavelengths so that these are the only possible wavelengths to be emitted from the cavity. A widely tunable filter selects the desired ITU channel and again a phase section is used to finely align a cavity mode. In principle, this approach is very similar to the DS-DBR laser, except that the multiple peak grating is replaced by an FP etalon.

A more advanced device consists of a chip with active and phase sections and a front SOA section separated by an on-chip mirror (a deeply etched gap). Light emitted from the active section is collimated by a lens into an FP etalon and reflected by a liquid crystal (LC)-based widely tunable mirror (Fig. 5.24) [34], the reflectivity of which is tuned to the desired transmission peak of the etalon. The phase current is used for fine-tuning in the established way. With the SOA section arranged outside the cavity, external modulation or Variable Optical Attenuator (VOA) functionalities

are feasible, and more than 100 mW output power is achievable over the whole C-band.

Some companies have proposed an external cavity containing two thermally tuned FP etalons of slightly different wavelength periodicity such that tuning is obtained by the Vernier effect between the two FP etalons.

#### **5.4.3.3 Design with Polymer Waveguide Gratings**

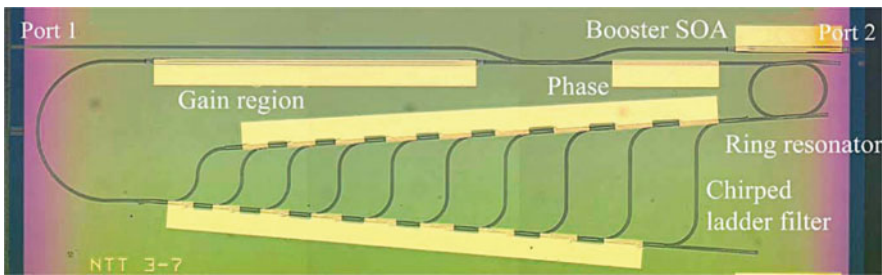
Another type of tunable external cavity laser comprises a thermo-optically tunable waveguide grating that is based on polymer material and coupled to an InP-based gain chip by means of a collimating lens [35] or in a hybrid integration fashion [36, 37]. Such devices offer the potential of very cost-efficient fabrication. Tuning over more than 26 nm was reported [36].

#### **5.4.4 Tunable Lasers with Ring Resonators**

A microring (MR) coupled to a dielectric waveguide represents a microring resonator (MRR) which exhibits periodic high transmission peaks. Their periodicity is determined by the effective refractive index of the MR waveguide and the diameter of the microring (see also Chap. 9, Sect. 9.9). The behavior of such an MRR is similar to that of an FP etalon, and therefore an MRR can also be used for locking laser emission wavelengths to predetermined channels. In the case of widely tunable lasers, it is advantageous to combine an MRR, which transmits channels with narrow spacing, with another element for coarse wavelength selection. One such example is shown in Fig. 5.25 [38].

The monolithic laser structure comprises a gain section, a phase section, a ring resonator, a ladder filter for coarse wavelength selection, and an output booster SOA. The diameter of the ring resonator has been chosen in such a way that the transmission minima coincide with ITU channels. The ladder filter consists of an input and an output waveguide plus a number of interconnecting waveguides coupled via multimode interference (MMI) couplers. The ladder filter is conceptually equivalent to an arrayed waveguide grating (AWG, see also Chap. 9). It may either exhibit periodic peaks with equal transmission [40] or, alternatively, a single transmission peak can be made significantly more pronounced than all the others by chirping (more than 5.4 dB are reported in [38]) so that the coarse wavelength selection is improved. Tuning of this single transmission peak is accomplished by varying the effective refractive index of the input or output waveguide by means of current injection. In essence, the tuning involves three steps: the transmission maximum of the ladder filter assures wide wavelength tuning, the ring resonator selects an ITU channel, and the phase section finely tunes the corresponding cavity mode. A total tuning range of 38 nm and 9 dBm output power thanks to the booster SOA have been demonstrated with this device.

a



b

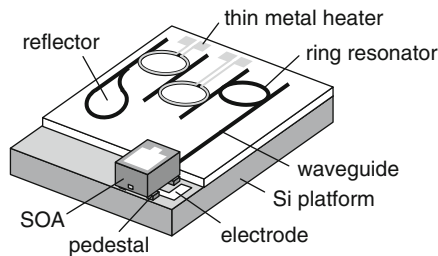


**Fig. 5.25** Ring resonator type tunable lasers: monolithically integrated structure with ladder filter (a) [38], resonator ring reflector laser made on silicon-on-insulator (b) [39]

Another embodiment, consisting of an SOA flip-chipped on a silicon platform with three ring resonators and a waveguide loop mirror (Fig. 5.25b, [39]) provides an even wider tuning range. The three resonators are designed with slightly different peak periodicity: one ring with 100 GHz peak spacing acts as an ITU etalon, the second ring with 100.8 GHz periodicity provides coarse tuning, and the third ring with 110.9 GHz peak separation the fine-tuning. Tuning is obtained via the Vernier effect between the ring resonators, and the individual transmission characteristics are swept by means of thin metal heaters. Such a device delivered an impressive tuning range covering the whole C+L band (115 nm) with more than 40 dB SMSR and better than 13 dBm-coupled output power. Recently, fully integrated versions on InP have been developed which rendered possible 50 nm tuning [41].

## 5.5 Subsystems and Tunable Photonic Integrated Circuits

Tunable lasers covering the C-band have now become commercially available, and, as a next development step, various approaches aim at expanding the tuning range to the C+L bands, at reducing cost, and at simplifying control. In addition, a large amount of current work focuses on the integration of tunable lasers with other optoelectronic devices in order to improve performance and provide new functionalities, apart from cost aspects.

One option is to introduce hybrid integration in optical packaging. For example, an InP Mach–Zehnder modulator (MZM) mounted between collimating lenses has been successfully added to the DFB array with selective MEMS of Fig. 5.21b, and to the DS-DBR-SOA of Fig. 5.14, to implement a 10 Gbit/s transmitter capable of low chirp and adaptable to a small-form-factor optical module. To further reduce footprint and packaging costs, additional optoelectronic devices may be monolithically integrated with the tunable laser chip, leading to so-called photonic integrated circuits (PICs). Each device requires a different material band edge according to its functionality, whether it is an active section with gain, a passive tuning section, a photodetector, an electroabsorption modulator, and maybe others. Different optical integration schemes exist, for example, butt-joint coupling, selective area growth, and quantum well intermixing (QWI) [42] so that materials of different composition can be epitaxially grown on the same wafer. The University of Santa Barbara in California appears to be the most active group in the field of widely tunable PICs. They have focused on the QWI technique and have applied it to demonstrate various PICs around their widely tunable SG-DBR design (see e.g. [42]).

### ***5.5.1 Tunable Laser Integrated with Modulator***

Direct modulation of tunable lasers has been investigated using several designs, but the maximum achievable transmission distances remained limited to around 10 km at 10 Gbit/s due to laser chirp. Improved transmission distances and modulation bit rates can be expected if an external modulator is integrated with a widely tunable laser, similar to the concept of integrating DFB lasers with a modulator.

One example in this respect is an SG-DBR-SOA integrated with a 40 Gbit/s electroabsorption modulator (EAM) as shown in Fig. 5.26a [43]. The EAM bandgap is detuned to 1500 nm by QWI and provides more than 20 dB static extinction ratio for SG-DBR emission ranging between 1540 nm and 1560 nm. 1 V peak-to-peak voltage has been sufficient to provide a clear 40 Gbit/s eye diagram with 8 dB dynamic extinction ratio. However, the integration of EAMs with widely tunable lasers remains critical because the operation of EAMs relies on the quantum confined Stark effect (QCSE) which is a band edge effect and therefore highly dependent on the detuning between the lasing wavelength and the photoluminescence wavelength of the EAM. As a consequence, it is necessary to adapt the driving voltages to the emitted wavelengths, and the performance in terms of power, peak-to-peak voltage, chirp, etc., varies considerably over the whole tuning range.

MZM, which are based upon the interference between two phase-modulated arms (see also Chap. 6), intrinsically provide almost wavelength-independent characteristics and their chirp can be adjusted arbitrarily, allowing for longer reach, virtually penalty-free transmission. The disadvantages of MZM are more stringent processing specifications, higher complexity with monolithic integration, and larger device size. An example of a successful integration is shown in Fig. 5.26b [44] featuring 300  $\mu\text{m}$  long MZ arms, more than 10 GHz bandwidth, and 20 dB static extinction for

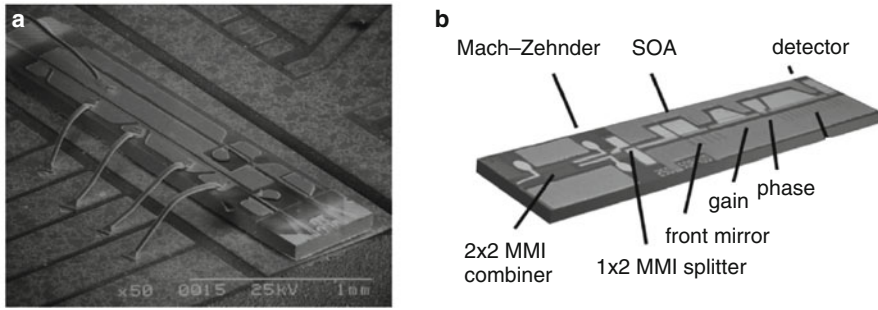


**Fig. 5.26** Photo image of a mounted SG-DBR-SOA-EAM (a) [43], and schematic structure of an SG-DBR-SOA-MZ (b) [44]

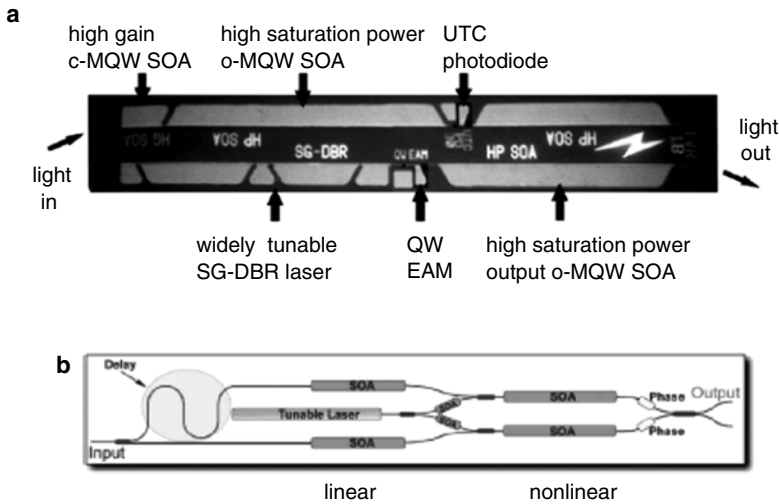


**Fig. 5.27** Complex monolithically integrated 40 Gbit/s components: tunable transceiver (a) [46], and wavelength converter (b) [47]

less than 5 V operation voltage. Higher bandwidth and lower driving voltages can be obtained if the MZM is operated in push-pull configuration and traveling wave electrodes are used on the MZ arms. Clear eye diagrams have been demonstrated at 40 Gbit/s over a tuning range of 34 nm with 3.2 V drive voltage [45].

### 5.5.2 Tunable Subsystems

Monolithic integration can be pushed even further so that complete widely tunable subsystems are obtained as shown in Fig. 5.27a, for example [46]. The transmitter is composed of an SG-DBR laser-integrated with a 125 μm long EAM and an out-

put booster SOA that provides 3 dB penalty only for 40 Gbit/s transmission over 5 km. The tuning range exceeds 30 nm and the driving voltages are as low as 1.5 to 2.5 V. The receiver consisted of two SOAs and a uni-traveling carrier (UTC)-type photodiode yielding  $-20$  dBm sensitivity at 40 Gbit/s.

A 40 Gbit/s tunable all-optical wavelength converter for packet-switched optical networks is illustrated in Fig. 5.27b [47]. The input signal pulses are split into two arms with a relative delay of 10 ps, then amplified by two linear SOAs, and subsequently they generate time-delayed carrier depletion in the nonlinear SOAs of the MZ interferometer. The corresponding phase changes lead to a short time window during which the MZ interferences are constructive. Because the continuous wave (CW) signal emitted by the SG-DBR tunable laser is coupled into both MZ arms and recombined at the output, the resulting signal is a replica of the input pulses, however, converted to the CW wavelength. In this device, QWI for implementing the SG-DBR sections and the linear SOAs is combined with butt-joint technology for integrating nonlinear SOAs containing highly confined bulk material. Very low jitter and more than 12 dB output extinction ratio have been obtained at 40 Gbit/s with less than 1 dB penalty across the whole C-band.

## 5.6 Conclusion

Research has been carried out during the last decade to achieve widely tunable lasers for DWDM systems featuring high performance, reduced footprint, simple control, and cost-efficient fabrication. This topic is extremely rich in terms of overall design innovation, and an impressive variety of approaches has been pursued. None of them, however, appears to be a universal solution so far; instead, there may be optimum designs for different specific applications.

Designs like the SG-DBR or DS-DBR lasers appear to be the prevailing solutions for metropolitan networks and for ROADMs. DFB arrays are widely used solutions that are commercially available. This is especially true for long-distance transmission based upon coherent modulation formats (like QPSK or QAM) where both amplitude and phase are modulated and the signals decoded by interference with a local oscillator (see also Chap. 8). A narrow linewidth is mandatory for these applications in order to assure low phase noise at the detection site.

Tuning can be accomplished thermally, mechanically, and by current injection. The lasers can be monolithically integrated on InP or made of discrete elements. Many embodiments are fundamentally based on the same principles. Most of them comprise an FP cavity and require alignment of a cavity mode to the desired wavelength via a phase section current or via cavity length adjustment (in an external cavity). Coarse tuning relies essentially on three generic concepts and elements:

- Use of highly selective tunable filters. Examples are the current injection tuned Bragg section in a DBR or a Bragg grating with tunable angle in an external cavity.



**Table 5.1** Summary of main tunable lasers approaches, including their tuning characteristics and their state-of-the-art pros and cons. Devices marked with an \* are commercially available

Device	References (companies)	Tuning mechanism	Tuning principle	Pros	Cons	
SG-DBR* SSG-DBR Y-laser*	[8, 10, 12, 13, 14] JD5-Uniphase, Syntune	Current	Vernier	Monolithic integration Fast tuning	Complex control Large linewidth	
DS-DBR* GCSR	[16, 17, 19] Oclaro	Current	Multiple peaks + wide filter			
DBR-MMI	[20]	Current	One filter			1D tuning
TTG	[22]	Current	Vernier			No phase section
DFB array +Funnel*	[28, 29] NTT	Thermal	Selection	Simple control	Slow tuning	
DFB array + MEMS*	[30] Santur	Thermal	Selection		Footprint Slow tuning	
VCSEL	[31]	Voltage	Single FP mode	Simple control Vertical emission	Low power	
Ext. cavity + Bragg	[32]	Mechanical	One filter	Low linewidth	Complex alignment Large footprint Slow tuning	
Ext. cavity + Bragg (integ. solution)	[33]	Current	One filter	Low linewidth Monolithic integration	Slow tuning Low power	
Ext. Cavity+FP etalon+LC mirror	[34]	Voltage	Multiple peaks + wide filter	Low linewidth High power	Large footprint	
Ext. cavity +2 FP etalons		Thermal	Vernier	Low linewidth	Control Slow tuning	
Ladder laser	[38]	Current	Multiple peaks + wide filter	Monolithic integration Simple control Fast tuning	Critical processing High power	
Ring reflector laser	[40, 41]	Thermal	Vernier	Hybrid integration C+L bands or monolithic C-band	Control Slow tuning	

- Use of the Vernier effect between multiple peak elements. Multiple peak elements can be multiple peak gratings such as sampled gratings and SSG in SG-DBR, SSG-DBR, or TTG lasers. Alternatively, they can be formed by Fabry–Pérot etalons in external cavities with dual FPs or by ring resonators in ring reflector lasers.
- Use of a multiple peak element and a widely tunable coarse filter. For example, in DS-DBR lasers, a super-structure grating and multiple Bragg gratings are utilized, in an external cavity laser an FP etalon and a liquid crystal type mirror are employed, and a tunable ring laser involves a ring resonator and a ladder filter.

The main approaches for widely tunable lasers are summarized in Table 5.1, which includes the tuning principles and mechanisms, and state-of-the-art pros and cons for each device.

Some of these tunable lasers are commercially available and deployed in DWDM systems to a varying degree where they offer enhanced flexibility (SG-DBR-, SSG-DBR-, Y-, DS-DBR-, DFB array+Funnel-, DFB array+MEMS-, and External Cavity+FP etalon+LC mirror laser). Other innovative solutions are still in the laboratory stage and these include lasers based upon an external cavity with monolithically integrated concave mirror, with an FP etalon and an LC mirror, and more

recent developments based upon multiple ring resonators. These innovations are expected to further improve performance, e.g., by offering tuning across the full C+L band, allowing for faster switching in future WDM PON access networks, or fitting to very cost-efficient assemblies.

Another important research target is the extension of tunable lasers to PICs to eventually arrive at complete monolithically integrated subsystems. This opens the way toward multiple combinations of various subcomponents and to a wide range of future devices and system functionalities.

## References

1. J. Buus, M.-C. Amann, D.J. Blumenthal, *Tunable Laser Diodes and Related Optical Sources*, 2nd edn. (Wiley, Hoboken, NJ, 2005). ISBN: 978-0-471-20816-7
2. B.R. Bennett, R.A. Soref, J.A. Del Alamo, Carrier-induced change in refractive index of InP, GaAs, and InGaAsP. *IEEE J. Quantum Electron.* **30**, 113–122 (1994)
3. J.-P. Weber, Optimization of the carrier-induced effective index change in InGaAsP waveguides – application to tunable Bragg filters. *IEEE J. Quantum Electron.* **30**, 1801–1816 (1994)
4. S.L. Chuang, *Physics of Optoelectronic Devices*, 2nd edn. (Wiley Interscience, Hoboken, NJ, 2009)
5. A. Yariv, M. Nakamura, Periodic structures for integrated optics. *IEEE J. Quantum Electron.* **QE-13**, 233–253 (1977)
6. T.L. Koch, U. Koren, B.I. Miller, High-performance tunable 1.5  $\mu\text{m}$  InGaAs/InGaAsP multiple quantum well distributed Bragg reflector lasers. *Appl. Phys. Lett.* **53**, 1036–1088 (1988)
7. H. Debrégeas-Sillard, A. Vuong, F. Delorme, J. David, V. Allard, A. Bodéré, O. Legouezigou, F. Gaborit, J. Rotte, M. Goix, V. Voiriot, J. Jacquet, DBR module with 20 mW constant coupled output power over 16 nm (40 channels 50 GHz spaced). *IEEE Photon. Technol. Lett.* **13**, 4–6 (2001)
8. V. Jayaraman, Z.-M. Chuang, L.A. Coldren, Theory, design, and performance of extended tuning range semiconductor lasers with sampled gratings. *IEEE J. Quantum Electron.* **29**, 1824–1834 (1993)
9. R. O’Dowd, S. O’Duill, G. Mulvihill, N. O’Gorman, Y. Yu, Frequency plan and wavelength switching limits for widely tunable semiconductor transmitters. *IEEE J. Sel. Top. Quantum Electron.* **7**, 259–269 (2001)
10. B. Mason, J. Barton, G.A. Fish, L.A. Coldren, S.P. DenBaars, Design of sampled grating DBR lasers with integrated semiconductor optical amplifier. *IEEE Photon. Technol. Lett.* **12**, 762–764 (2000)
11. H. Debrégeas-Sillard, C. Fortin, A. Accard, O. Drisse, E. Derouin, F. Pommereau, C. Kazmierski, Non-linear effects analysis in DBR lasers: applications to DBR-SOA and new double Bragg-DBR. *IEEE J. Sel. Top. Quantum Electron.* **13**, 1142–1149 (2007)
12. H. Ishii, H. Tanobe, F. Kano, Y. Tohmori, Y. Kondo, Y. Yoshikuni, Quasicontinuous wavelength tuning in super-structure-grating (SSG) DBR lasers. *IEEE J. Quantum Electron.* **32**, 433–441 (1996)
13. M. Gotoda, T. Nishimura, Y. Tokuda, Widely tunable SOA-integrated DBR laser with combination of sampled-grating and superstructure grating, *Proc. 19th Internat. Semicond. Laser Conf. (ISLC’04)*, Matsue, Japan, 2004, paper SaA5
14. M. Schilling, W. Idler, E. Kühn, G. Laube, H. Schweizer, K. Wüstel, O. Hildebrand, Integrated interferometric injection laser. Novel fast and broad-band tunable monolithic light source. *IEEE J. Quantum Electron.* **27**, 1616–1624 (1991)
15. J.O. Wesström, G. Sarlet, S. Hammerfeldt, L. Lundqvist, P. Szabo, P.-J. Rigole, State-of-the-art performance of widely tunable modulated grating Y-branch lasers, *Opt. Fiber Commun. Conf. (OFC’04)*, Techn. Digest (Anaheim, CA, USA, 2004), paper TuE2

16. M. Öberg, S. Nilsson, K. Streubel, J. Wallin, L. Bäckbom, T. Klinga, 74 nm wavelength tuning range of an InGaAsP/InP vertical grating assisted codirectional coupler laser with rear sampled grating reflector. *IEEE Photon. Technol. Lett.* **5**, 735–738 (1993)
17. Y. Gustafsson, S. Hammerfeldt, J. Hammersberg, M. Hassler, T. Hörman, M. Isaksson, J. Karlsson, D.E. Larsson, O.D. Larsson, L. Lundqvist, T. Lundström, M. Rask, P.-J. Rigole, E. Runeland, A. Saavedra, G. Sarlet, R. Siljan, P. Szabo, L. Tjemplund, O. Träskman, H. de Vries, J.-O. Wesström, C. Ögren, Record output power (25 mW) across C-band from widely tunable GCSR lasers without additional SOA. *Electron. Lett.* **39**, 292–293 (2003)
18. T. Suzuki, H. Arimoto, T. Kitatani, A. Takei, T. Taniguchi, K. Shinoda, S. Tanaka, S. Tsuji, Wide-tuning (65 nm) semi-cooled (50 °C) operation of a tunable laser based on a novel widely tunable filter, *Opt. Fiber Commun. Conf. and Nat. Fiber Opt. Eng. Conf. (OFC/NFOEC'11)*, Techn. Digest (Los Angeles, CA, USA, 2011), paper OWD7
19. A.J. Ward, D.J. Robbins, G. Busico, E. Barton, L. Ponnampalam, J.P. Duck, N.D. Whitbread, P.J. Williams, D.C.J. Reid, A.C. Carter, M.J. Wale, Widely tunable DS-DBR laser with monolithically integrated SOA: design and performance. *IEEE J. Sel. Top. Quantum Electron.* **11**, 149–156 (2005)
20. H. Debrégeas-Sillard, C. Fortin, F. Pommereau, D. Drugeon, Y. Gottesman, O. Drisse, E. Derouin, N. Lagay, B. Rousseau, F. Martin, J. Landreau, C. Kazmierski, More than 40 nm tuning DBR-MMI-SOA with only one Bragg current control compatible with fast switching, *Proc. 33rd Europ. Conf. Opt. Commun. (ECOC'07)*, Berlin, Germany (2007), paper 9.2.4
21. G. Sarlet, G. Morthier, R. Baets, Wavelength and mode stabilization of widely tunable SG-DBR and SSG-DBR lasers. *IEEE Photon. Technol. Lett.* **11**, 1351–1353 (1999)
22. R. Todt, T. Jacke, R. Meyer, J. Adler, R. Laroy, G. Morthier, M.-C. Amann, Sampled grating tunable twin-guide laser diodes with over 40 nm electronic tuning range. *IEEE Photon. Technol. Lett.* **17**, 2514–2516 (2005)
23. G. Sarlet, Tunable laser diodes for WDM communication – methods for control and characterisation, PhD thesis, University of Ghent and INTEC, Belgium, 2001
24. A. Uskov, J. Mørk, J. Mark, Wave mixing in semiconductor laser amplifiers due to carrier heating and spectral-hole burning. *IEEE J. Quantum Electron.* **30**, 1769–1781 (1994)
25. M.C. Larson, M. Bai, D. Bingo, N. Ramdas, S. Penniman, G.A. Fish, L.A. Coldren, Mode control of widely-tunable SG-DBR lasers, *Proc. 28th Europ. Conf. Opt. Commun. (ECOC'02)*, Copenhagen, Denmark (2002), poster P2.04
26. L. Ponnampalam, N.D. Whitbread, R. Barlow, G. Busico, A.J. Ward, J.P. Duch, D.J. Robbins, Dynamically controlled channel-to-channel switching in a full-band DS-DBR laser. *IEEE J. Quantum Electron.* **42**, 223–230 (2006)
27. J.E. Simsarian, L. Zhang, Wavelength locking a fast-switching tunable laser. *IEEE Photon. Technol. Lett.* **16**, 1745–1747 (2004)
28. H. Hatakeyama, K. Kudo, Y. Yokoyama, K. Naniwae, T. Sasaki, Wavelength-selectable microarray light sources for wide-band DWDM applications. *IEEE J. Sel. Top. Quantum Electron.* **8**, 1341–1348 (2002)
29. H. Ishii, K. Kasaya, H. Oohashi, Y. Shibata, H. Yasaka, K. Okamoto, Widely wavelength-tunable DFB laser array integrated with funnel combiner. *IEEE J. Sel. Top. Quantum Electron.* **13**, 1089–1094 (2007)
30. B. Pezeshki, E. Vail, J. Kubicky, G. Yoffe, S. Zou, J. Heanue, P. Epp, S. Rishton, D. Ton, B. Faraji, M. Emanuel, X. Hong, M. Sherback, V. Agrawal, C. Chipman, T. Razazan, 20 mW widely tunable laser module using DFB array and MEMS selection. *IEEE Photon. Technol. Lett.* **14**, 1457–1459 (2002)
31. S. Jatta, B. Kögel, M. Maute, K. Zogal, F. Riemenschneider, G. Böhm, M.-C. Amann, P. Meißner, Bulk-micromachined VCSEL at 1.55  $\mu\text{m}$  with 76 nm single-mode continuous tuning range. *IEEE Photon. Technol. Lett.* **21**, 1822–1824 (2009)
32. J.D. Berger, Y. Zhang, J.D. Grade, H. Lee, S. Hrinya, H. Jerman, Widely tunable external cavity diode laser based on an MEMS electrostatic rotary actuator, *Opt. Fiber Commun. Conf. (OFC'01)*, Techn. Digest (Anaheim, CA, USA, 2001), paper TuJ2
33. O.K. Kwon, J.H. Kim, K.H. Kim, E.D. Sim, K.R. Oh, Widely tunable multichannel grating cavity laser. *IEEE Photon. Technol. Lett.* **18**, 1699–1701 (2006)

34. M.L. Nielsen, S. Sudo, K. Mizutani, T. Okamoto, K. Tsuruoka, K. Sato, K. Kudo, Integration of functional SOA on the gain chip of an external cavity wavelength tunable laser using etched mirror technology. *IEEE J. Sel. Top. Quantum Electron.* **13**, 1104–1111 (2007)
35. S.H. Oh, K.S. Kim, J.J. Ju, M.-S. Kim, K.-H. Yoon, D.K. Oh, Y.-O. Noh, H.-J. Lee, Tunable external cavity laser employing uncooled superluminescent diode. *Opt. Express* **17**, 10189–10194 (2009)
36. G. Jeong, J.H. Lee, M.Y. Park, C.Y. Kim, S.H. Cho, W. Lee, B.W. Kim, Over 26 nm wavelength tunable external cavity laser based on polymer waveguide platforms for WDM access networks. *IEEE Photon. Technol. Lett.* **18**, 2102–2104 (2006)
37. F.M. Soares, Z. Zhang, G. Przyrembel, M. Lauermann, M. Moehrl, N. Mettbach, C. Zawadzki, B. Zittermann, N. Keil, N. Grote, Hybrid photonic integration of InP-based laser diodes and polymer PLCs, *Proc. 23rd Internat. Conf. Indium Phosphide Relat. Mater.* (IPRM 2011), Berlin, Germany, 2011, paper Th-8.1.3
38. S. Matsuo, S.-H. Jeong, T. Segawa, H. Okamoto, Y. Kawaguchi, Y. Kondo, H. Suzuki, Y. Yoshikuni, Tunable laser using chirped ladder filter. *IEEE J. Sel. Top. Quantum Electron.* **13**, 1122–1128 (2007)
39. R. Todt, S. Watanabe, Y. Deki, M. Takahashi, T. Takeuchi, S. Takaesu, T. Miyazaki, M. Horie, H. Yamazaki, Widely tunable resonated-ring-reflector lasers covering C- and L-bands, *Proc. 33rd Europ. Conf. Opt. Commun.* (ECOC'07), Berlin, Germany (2007), post-deadline paper PDP2.5
40. S. Matsuo, Y. Yoshikuni, T. Segawa, Y. Ohiso, H. Okamoto, A widely tunable optical filter using ladder-type structure. *IEEE Photon. Technol. Lett.* **15**, 1114–1116 (2003)
41. T. Segawa, S. Matsuo, T. Kakitsuka, T. Sato, Y. Kondo, R. Takahashi, Semiconductor double-ring resonator-coupled tunable laser for wavelength routing. *IEEE J. Sel. Top. Quantum Electron.* **7**, 892–898 (2009)
42. E.J. Skogen, J.W. Raring, G.B. Morrison, C.S. Wang, V. Lal, M.L. Mašanovi, L.A. Coldren, Monolithically integrated active components: a quantum-well intermixing approach. *IEEE J. Sel. Top. Quantum Electron.* **11**, 343–355 (2005)
43. J.W. Raring, L.A. Johansson, E.J. Skogen, M.N. Sysak, H.N. Poulsen, S.P. DenBaars, L.A. Coldren, 40 Gbit/s widely tunable low-drive-voltage electroabsorption-modulated transmitters. *J. Lightw. Technol.* **25**, 239–248 (2007)
44. J.S. Barton, E.J. Skogen, M.L. Mašanovi, S.P. DenBaars, L.A. Coldren, A widely tunable high-speed transmitter using an integrated SGDBR laser-semiconductor optical amplifier and Mach-Zehnder modulator. *IEEE J. Sel. Top. Quantum Electron.* **9**, 1113–1117 (2003)
45. J.S. Barton, M.L. Mašanovi, A. Tauke-Pedretti, E.J. Skogen, L.A. Coldren, Monolithically-integrated 40 Gbit/s widely-tunable transmitter using series push-pull Mach-Zehnder modulator SOA and sampled-grating DBR laser, *Opt. Fiber Commun. Conf. and Nat. Fiber Opt. Eng. Conf.* (OFC/NFOEC'05), Techn. Digest (Anaheim, CA, USA, 2005), paper OTuM3
46. J.W. Raring, L.A. Johansson, E.J. Skogen, M.N. Sysak, H.N. Poulsen, S.P. DenBaars, L.A. Coldren, Single-chip 40 Gbit/s widely-tunable transceivers with integrated SG-DBR laser, QW EAM, UTC photodiode, and low confinement SOA, *Proc. 20th Internat. Semicond. Laser Conf.* (ISLC'06), Kohala Coast, HI, USA, 2006, paper TuA1
47. V. Lal, M.L. Mašanovi, J.A. Summers, G. Fish, D.J. Blumenthal, Monolithic wavelength converters for high-speed packet-switched optical networks. *IEEE J. Sel. Top. Quantum Electron.* **13**, 49–57 (2007)

# Chapter 6

## Semiconductor-based Modulators

Hiroshi Yasaka and Yasuo Shibata

**Abstract** The chapter starts with a comparison of methods to generate digital optical signals: direct laser modulation, electroabsorption and Mach–Zehnder interferometer modulators. Next follows an in-depth treatment of physical effects which are utilized for semiconductor-based modulators (Plasma, Franz–Keldysh, quantum-confined Stark, and electro-optic (Pockels) effect), and their exploitation for InP- and GaAs-based modulators with specific emphasis on aspects of high-speed modulator design. Modulator characteristics including eye diagrams obtained for different implementations and various operation conditions illustrate the current state-of-the-art, and the chapter concludes with a section on modulators for higher order modulation formats.

Semiconductor-based modulators are particularly promising for applications in fiber optic communication systems owing to various characteristics which include compactness, low power consumption, and the potential for monolithic integration with other devices.

Key features of semiconductor-based modulators and typical performance parameters will be the topic of this chapter, and it is organized as follows: First, general methods for digital optical signal generation by using semiconductor photonic devices and their features are described (Sect. 6.1). In Sect. 6.2, fundamentals and features of semiconductor-based Mach–Zehnder interferometer (MZI) modulators are elucidated. The way for designing a high-speed semiconductor MZI modulator

---

Hiroshi Yasaka (✉)

Research Institute of Electrical Communication, Tohoku University, 2-1-1 Katahira, Aoba-ku, Sendai-shi, Miyagi Pref., 980-8577, Japan  
e-mail: yasaka@riec.tohoku.ac.jp

Yasuo Shibata

NTT Photonics Laboratories, 3-1 Morinosato Wakamiya, Atsugi-shi, Kanagawa Pref., 243-0198, Japan  
e-mail: shibata.yasuo@lab.ntt.co.jp

is discussed in Sect. 6.3. Properties of current semiconductor-based MZI modulators and high performance modulators for future optical fiber transmission systems are shown in Sects. 6.4 and 6.5, and a general summary is given in the final Sect. 6.6.

## 6.1 Overview of the Methods to Generate a Digital Optical Signal

The generation of high-speed intensity modulated digital optical signals is one of the key functions in fiber optic communication systems. Digital optical signals can either be generated by directly modulating single-mode semiconductor lasers, or by using external intensity modulators, and the characteristics of such signals after transmission through spans of single mode optical fibers (SMFs) significantly depend on the way the digital optical signals had been generated. This will be discussed in more detail below.

The transmission distance of digital optical signals through an SMF is limited by the group velocity (chromatic) dispersion of the SMF and the amount of spectral broadening (spectral width) of the digital optical signal. In principle, the optical spectrum is broadened when the optical intensity is coded by a high-speed digital signal. The spectrum is additionally broadened by the instantaneous frequency change of the signal light, a phenomenon normally designated as ‘chirp.’ The amount of chirp is expressed by using a chirp parameter  $\alpha_{cp}$ , and the parameter is defined by [1]

$$\alpha_{cp} = \Delta n / \Delta n', \quad (6.1)$$

where  $\Delta n$  and  $\Delta n'$  are the relative changes in the real part and the imaginary part of the complex refractive index, respectively. The imaginary part of the complex refractive index  $n'$  is related to the propagation loss or gain of the material. In this chapter, the character  $n$  with no subscript or superscript is used as the real part of the complex refractive index and also the term “refractive index” expresses the real part of the complex refractive index in all cases unless otherwise stated. In an external modulation scheme, an instantaneous frequency change due to a phase change is obtained by using a time differential of the phase:

$$\Delta\omega = -\partial\phi/\partial t, \quad (6.2)$$

where  $\omega$  and  $\phi$  are the angular frequency and the phase of the light, respectively. The phase change is derived by using  $\alpha_{cp}$  according to [2]

$$\frac{d\phi}{dt} = \left(\frac{\alpha_{cp}}{2}\right) \left(\frac{1}{S}\right) \left(\frac{dS}{dt}\right), \quad (6.3)$$

where  $S$  is the intensity of the light. The chirp parameter varies over a certain range depending on the modulation methods used for the digital optical signal generation.

The waveform after SMF transmission can be calculated by using a split step Fourier method (SSFM) [3]. Using this technique, the Fourier component having an instantaneous angular frequency  $\omega$  at the position  $z$ ,  $U(z, \omega)$ , is expressed by using the chromatic dispersion coefficient  $D$  of the SMF:

$$U(z, \omega) = U(0, \omega) \exp\left(-j \frac{\lambda^2}{4\pi c} D \omega^2 z\right), \quad (6.4)$$

where  $\lambda$  and  $c$  are the signal light wavelength and the velocity of light, respectively. The chromatic dispersion coefficient of conventional SMFs takes a value around 17 ps/(nm km) at 1550 nm wavelength.

In the following, we will focus on three ways to generate high-speed digital optical signals: i) direct modulation of semiconductor lasers, ii) external modulation with electroabsorption modulators and iii) external modulation using Mach-Zehnder modulators. We will illustrate characteristics such as waveform, chirp, etc., but we will also discuss features related to SMF transmission such as waveform distortions, eye opening penalties, dispersion tolerances and so forth.

### 6.1.1 Direct Modulation of Semiconductor Lasers

In directly modulated single-mode semiconductor lasers, chirping is slightly different from that in external modulation schemes expressed by (6.2). The lasing wavelength (i.e., the lasing optical frequency) itself changes when the output light intensity is directly modulated with high-speed digital signals superimposed on the injection current. The wavelength change is due to the fact that the carrier density in the laser cavity changes dynamically, and as a consequence, the refractive index in the laser cavity also changes through the plasma effect (see Sect. 6.2.1.1). The chirp parameter  $\alpha_{cp}$  for a semiconductor laser is defined as

$$\alpha_{cp} \equiv \frac{4\pi}{\lambda} \frac{dn/dN}{dg/dN}, \quad (6.5)$$

where  $n$ ,  $g$ , and  $N$  are the real part of the refractive index of the laser cavity, the modal gain of the laser, and the carrier density in the laser cavity, respectively. The parameter  $\alpha_{cp}$  is well-known as the linewidth enhancement factor for semiconductor lasers (see Chap. 4, Sect. 4.3.2), and it typically takes values around 3 to 5 for conventional single-mode semiconductor lasers. The optical frequency change  $\Delta\nu$  due to a carrier density change  $\Delta N$  can be expressed by using the chirp parameter:

$$\Delta\nu = \frac{c}{4\pi n} \alpha_{cp} \Gamma_{oc} A_g \Delta N, \quad (6.6)$$

where  $\Gamma_{oc}$  and  $A_g$  are the optical confinement factors of the laser cavity and the differential gain coefficient of the laser material, respectively.  $\Delta N$  can be derived

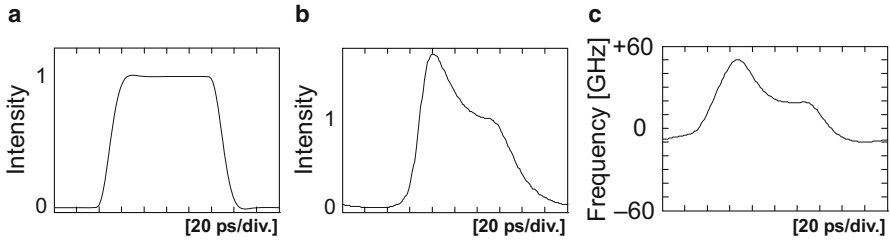


**Fig. 6.1** Calculated output waveforms for a directly modulated semiconductor laser. Input electrical signal with pulse width of 100 ps (a), output waveform from the laser (b), optical frequency change of the laser under modulation (c)

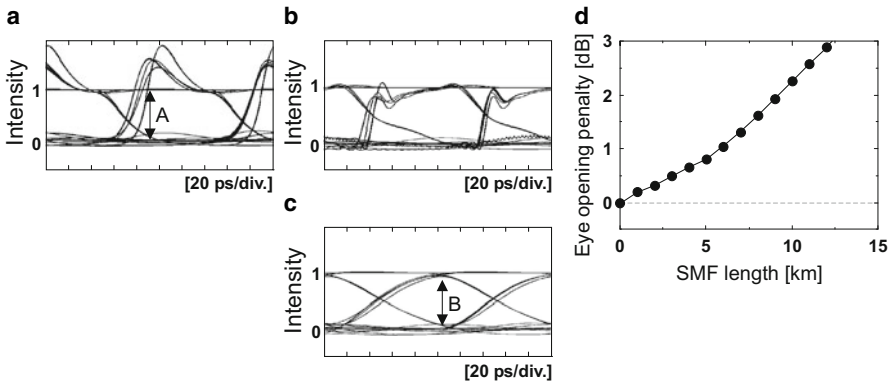


**Fig. 6.2** Calculated characteristics of semiconductor laser output under 10 Gbit/s NRZ signal operation. Output eye diagram from the laser under direct modulation (a), eye diagrams after 6 km SMF transmission for 1550 nm wavelength (total dispersion  $\sim 100$  ps/nm) without and with a low-pass filter (b, c), calculated eye opening penalty as a function of SMF transmission length (d)

by using the well-known semiconductor laser rate equations for the carrier density and the photon density of the laser under the condition that the injection current is modulated by a high-speed digital signal.

Figure 6.1 shows the calculated waveforms for injected and generated pulses with 100 ps width, which corresponds to one bit of a 10 Gbit/s non-return-to-zero (NRZ) signal. Figure 6.1a represents the pulse shape of the input electrical signal with limited bandwidth of some tens of GHz. Figure 6.1b illustrates the corresponding optical output signal from the laser. The waveform is distorted due to the well-known relaxation oscillations. Finally, Fig. 6.1c shows the optical frequency change. In the calculation, a value of three has been used for the chirp parameter. The changes of the optical frequency and that of the optical intensity are correlated by the dynamic carrier density change in the laser cavity. Based on these results, eye diagrams before and after SMF transmission are calculated for a 10 Gbit/s NRZ signal using the semiconductor laser rate equations and the SSFM.

Figure 6.2a represents an eye diagram for the laser output under modulation where relaxation oscillations and pattern effects are clearly visible. Figures 6.2b, c



are the eye diagrams after 6 km SMF transmission for a 1550 nm wavelength signal without and with a low-pass filter (4th order Bessel–Thomson low-pass filter with cut-off frequency  $f_0$  of 7.5 GHz). The total amount of fiber chromatic dispersion is around 100 ps/nm. A pronounced waveform distortion is observed even after a fairly short SMF transmission distance such as 6 km. Figure 6.2d is the calculated eye opening penalty as a function of SMF length. The chromatic dispersion coefficient is approximated to be 17 ps/(nm km). The eye opening penalty, which is used to quantitatively discuss the waveform distortion, is calculated by using

$$\text{Eye opening penalty} = -10 \log_{10} \left( \frac{B}{A} \right), \quad (6.7)$$

where  $A$  and  $B$  are the eye openings of the eye diagrams before (actually, for the filtered eye diagram) and after SMF transmission as shown in Figs. 6.2a, c. The penalty increases drastically as the SMF transmission distance gets longer, while the penalty remains below 1 dB only as long as the SMF transmission distance is shorter than 6 km. This means that a 10 Gbit/s NRZ optical signal generated from a directly modulated single-mode semiconductor laser has a dispersion tolerance of about 100 ps/nm only. As a consequence, directly modulated single-mode semiconductor lasers are mainly used in systems that operate in the 1300 nm wavelength band where the chromatic dispersion of an SMF is almost zero.

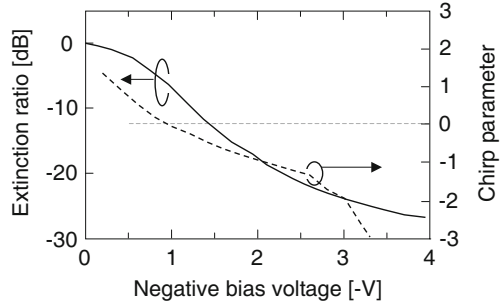
### 6.1.2 Electroabsorption Modulators (EAMs)

Electroabsorption modulators (EAMs) utilize the property of semiconductors that the band-edge wavelength changes under the influence of an applied electric field. The phenomenon is called Franz–Keldysh effect in the case of bulk material [4, 5] and quantum-confined Stark effect (QCSE) for multi-quantum well (MQW) structured materials [6–13]. Until now, the latter one is commonly used for EAMs because the change in the photoabsorption coefficient is steeper for the QCSE compared to the Franz–Keldysh effect, and large optical extinction ratios can be obtained in MQW-EAMs with low bias voltages. Because the EAMs are operated at the band-edge wavelengths, they have large wavelength dependences. Moreover, EAMs also exhibit chirp caused by the refractive index change due to the applied bias voltage. The changes of the refractive index and that of the absorption under the influence of the applied voltage are related to each other by the Kramers–Kronig relations [14, 15]. Figure 6.3 shows an example of the measured extinction of an MQW-EAM as a function of negative bias voltage.

The absorption rises rapidly as the negative bias voltage increases. The chirp parameter measured by utilizing the fiber response method [16, 17] is also shown in the figure. The chirp parameter decreases gradually as the negative bias voltage increases, and it takes negative values when the negative bias voltage exceeds 1 V.

The waveforms for a 10 Gbit/s NRZ signal are calculated by using the characteristics shown in Fig. 6.3, and the corresponding results are illustrated in Fig. 6.4.

**Fig. 6.3** The extinction ratio (solid line) and chirp parameter (dotted line) of an EAM as a function of applied negative bias voltage



In this calculation, the DC bias and modulation voltages are set to  $-1.3$  V and  $2V_{p-p}$ , respectively. The operation wavelength is assumed to be 1550 nm and therefore the chromatic dispersion coefficient is set to 17 ps/(nm km). Figure 6.4a shows the intensity modulated output eye diagram from the EAM. Due to the nonlinear extinction characteristics, the cross-point of the eye diagram becomes low which is one of the drawbacks of EAMs. The instantaneous frequency chirp for a fixed 010 pattern is also calculated and the result is shown in Fig. 6.4b. Pronounced chirp due to the phase change in the EAM can be observed at the leading and falling edges of the pattern. Figures 6.4c, d are the eye diagrams after a 50 km SMF transmission without and with a low-pass filter, respectively. The total amount of fiber dispersion is calculated to be 850 ps/nm. Waveform distortion due to chromatic dispersion is observed, but the eye is still open. Figure 6.4e is the calculated eye opening penalty as a function of propagation distance along the SMF. As expected, the penalty rises as the SMF transmission distance gets longer. Less than 1 dB penalty can be obtained as long as the SMF transmission distance is

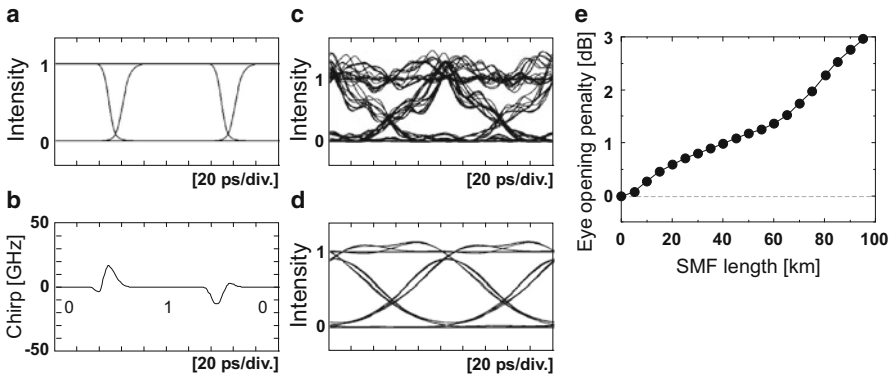


**Fig. 6.4** Calculated characteristics of EAM output under 10 Gbit/s NRZ signal operation. Output eye diagram from the EAM (a), calculated chirp for the fixed 010 pattern (b), eye diagrams after 50 km SMF transmission without and with a low-pass filter (c, d), calculated eye opening penalty as a function of SMF transmission length (e)

shorter than 40 km. This means that a 10 Gbit/s NRZ optical signal generated by an EAM has around 800 ps/nm dispersion tolerance. Research has been devoted to increase the dispersion tolerance. Recently, EAMs having a dispersion tolerance of around 1600 ps/nm have been developed for 10 Gbit/s NRZ optical signals [18–20]. Here, the amount of stress or strain and the thicknesses of the well and barrier layers in the EAM core are designed strictly to make the chirp parameters have negative values. Moreover, core layers are also fabricated in the InGaAlAs material system in order to enlarge the dispersion tolerance and improve the temperature-dependent characteristics. DFB lasers monolithically integrated with a traveling-wave EAM have recently been operated even at 100 Gbit/s, however, no information on chirp nor on maximum transmission distances has been given thus far [21].

### 6.1.3 Mach–Zehnder Interferometer (MZI) Modulators

Mach–Zehnder interferometer (MZI) modulators are very versatile devices which can be used for many purposes, for example, high-speed modulation or the realization of advanced modulation formats, and they have been fabricated in various material systems including III–V semiconductors (to be covered in more detail below), in LiNbO<sub>3</sub> (see Chap. 8) and based upon electro-optic polymers as well [22, 23].

The generic structure of an MZI modulator is that of a symmetric Mach–Zehnder interferometer as schematically shown in Fig. 6.5.

The electric field of an incoming CW light,  $E_{\text{in}}$ , can be represented by

$$E_{\text{in}}(z, t) = E_0 \exp[-j(\beta z - \omega t)] \quad (6.8)$$

with the propagation constant  $\beta$  defined by

$$\beta = \frac{2\pi n_{\text{eff}}}{\lambda}, \quad (6.9)$$

and  $n_{\text{eff}}$  and  $\lambda$  being the effective refractive index of the medium in which the wave propagates (dielectric waveguide for example) and the propagating light's wavelength in vacuum, respectively. Light is assumed to propagate along the  $z$ -direction. The incoming electromagnetic field is equally split into both interferometer arms by a splitter. After traveling along the two branches, it is recombined by a combiner and the output electromagnetic field  $E_{\text{out}}$  at the cross-port output is given by

$$E_{\text{out}}(z, t) = -j \frac{E_0}{2} [\exp(-j\beta_u L) + \exp(-j\beta_l L)], \quad (6.10)$$

where  $\beta_u$  and  $\beta_l$  are the propagation constants along the upper and lower MZI branches, respectively. (The factor  $(-j)$  reflects the fact that the output signal from the cross-port is advanced by 90° with respect to the through-port signal.)

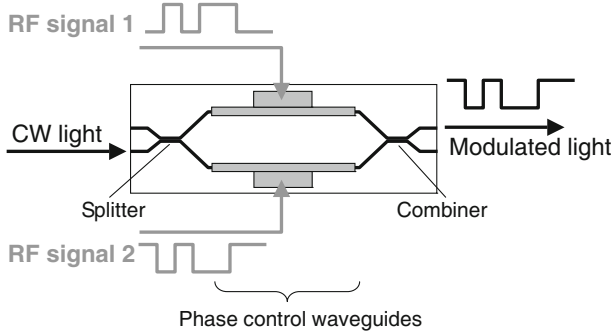


**Fig. 6.5** Schematic structure of an MZI modulator

For the following considerations, it is useful to rewrite the propagation constants as

$$\beta_{u,i} = \beta + \Delta\beta_{u,i}, \quad (6.11)$$

where  $\Delta\beta_{u,i}$  may be positive or negative as well (see below). According to (6.9)  $\Delta\beta_{u,i}$  can be directly related to a change in the effective refractive index,  $\Delta n_{\text{eff}}$ , and as outlined in detail in Sect. 6.2, different physical effects can be used to induce effective refractive index changes  $\Delta n_{\text{eff}}$  by a voltage  $V_{\text{RF}}$  applied to the waveguide arms of the MZI.

Intensity-modulated optical signals are generated by modulating the refractive indices of the two interferometer branches differently, i.e.,

$$\Delta\beta_u \neq \Delta\beta_l, \quad (6.12)$$

which results in a corresponding phase difference between the two light waves interfering at the MZI output. The interferometer branches can thus be designated as phase control waveguides and modulation is normally realized by applying a radio frequency (RF) signal to one or both phase control waveguides of the MZI modulator.

The following cases are of particular interest:

i) a modulation voltage is only applied to one of the MZI arms (“single arm operation”):

$$\beta_u = \beta + \Delta\beta \quad \text{and} \quad \beta_l = \beta \quad (6.13)$$

and under these operation conditions, the output electric field becomes

$$E_{\text{out}} = -jE_0 \cos\left(\frac{\Delta\beta L}{2}\right) \exp\left[-j\left(\beta + \frac{\Delta\beta}{2}\right)L\right]. \quad (6.14)$$

$E_{\text{out}}$  is characterized by a sinusoidal intensity variation plus an additional  $\Delta\beta$ -induced phase change (given by the second term in (6.14)), i.e., the output signal exhibits chirp.

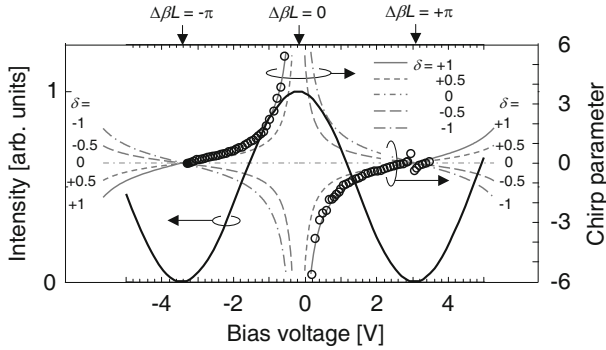


**Fig. 6.6** Output intensity dependence of an MZI modulator as a function of bias voltage applied to phase control waveguide (*black solid curve*). Chirp parameter measured (*black open circles*) and calculated for a differential drive MZI modulator (*gray lines*) for various values of  $\delta$  (see text)

ii) a voltage of equal amplitude but different sign (designated as the “push-pull operation”) is applied to the two MZI arms, i.e.,

$$\Delta\beta_u = +\frac{1}{2}\Delta\beta \quad \text{and} \quad \Delta\beta_l = -\frac{1}{2}\Delta\beta. \quad (6.15)$$

Inserting (6.15) into (6.10) and taking (6.11) into account yields

$$E_{\text{out}}(z, t) = -jE_0 \cos\left(\frac{\Delta\beta L}{2}\right) \exp(-j\beta L). \quad (6.16)$$

This operation mode is characterized by a  $\Delta\beta$ -dependent sinusoidal variation of the output signal without any modulation-induced chirp. In addition, it is worthwhile to note that the required propagation constant change  $\Delta\beta/2$  (which is proportional to the driving voltage swing for each differential RF signal) in the differential drive scheme is half of that needed in the single arm operation scheme,  $\Delta\beta$ .

Figure 6.6 illustrates the output intensity of an MZI modulator which changes sinusoidally as a function of applied bias voltage (black solid curve).

One parameter which characterizes MZI modulators is the so-called half-wavelength voltage  $V_\pi$ , which corresponds to an applied voltage resulting in a  $\pi$ -phase difference between the lightwaves in both phase modulation waveguides. Hence the half-wavelength voltage  $V_\pi$  is defined by the voltage needed to change the output power of MZI modulators from the maximum to the minimum value. In Fig. 6.6, the half-wavelength voltage  $V_\pi$  is  $\sim 3$  V.

The measured chirp parameter under the single arm operation conditions, shown by the black open circles in Fig. 6.6, depends on the bias voltage. The chirp vanishes when the output intensity becomes zero and it diverges when the output intensity gets close to the maximum value. The sign of the chirp parameter depends on the sign of the extinction slope,  $d(\text{Intensity})/dV$ . When the slope is positive, the chirp parameter takes positive values, and the parameter becomes negative when the slope is negative.

Another specific advantage of the differential drive scheme for an MZI modulator is that the chirp of the output optical signal can be freely controlled by adjusting the ratio of the modulation voltages of the differential RF signals. The chirp under unbalanced differential drive conditions can be discussed by introducing an unbalance parameter  $\delta$  into (6.11) as

$$\beta_u = \beta + (1 + \delta) \Delta\beta/2, \quad (6.17)$$

$$\beta_l = \beta - (1 - \delta) \Delta\beta/2 \quad (6.18)$$

with  $-1 \leq \delta \leq +1$ . The single arm (i) and balanced differential drive (ii) operation conditions discussed above are described by setting the parameter  $\delta$  to  $+1$  and to zero, respectively. By inserting (6.17) and (6.18) into (6.10), we get

$$E_{\text{out}} = -jE_0 \cos(\Delta\beta L/2) \exp(-j(\beta + \delta\Delta\beta/2)L). \quad (6.19)$$

The output intensity  $S_{\text{out}}$  and its phase change  $\Delta\phi$  can now be expressed by

$$S_{\text{out}} = E_0^2 \cos^2(\Delta\beta L/2) \quad (6.20)$$

with

$$\Delta\phi = (\Delta\beta L/2) \delta. \quad (6.21)$$

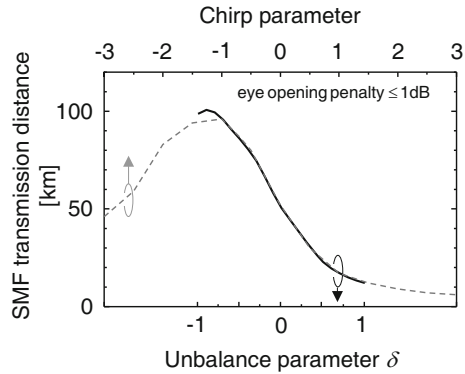
It is worthwhile to note that the output intensity does not depend on the unbalance parameter  $\delta$  and remains constant if the parameter  $\delta$  is changed, while the phase varies linearly with  $\delta$ . The chirp parameter for the MZI modulator defined by (6.3) can be derived by using (6.20) and (6.21) as

$$\alpha_{\text{cp}} = 2S \frac{\Delta\phi}{\Delta S} = -\frac{2 \cos^2(\Delta\beta L/2)}{\sin(\Delta\beta L)} \delta = -\tan^{-1}(\Delta\beta L/2) \delta. \quad (6.22)$$

The calculated chirp parameters for various values of  $\delta$  are shown in Fig. 6.6 as gray curves. The horizontal axis of the calculated chirp parameter is adjusted by fitting the measured and calculated output intensity curves. The calculated chirp parameter for  $\delta = +1$  agrees quite well with the measured one displayed by black open circles. As one can see, the chirp parameter and hence the amount of phase change can be controlled by an appropriate choice of the unbalance parameter  $\delta$  and hence by adjusting the ratio of the modulation swing voltages of the differential RF signals. However, the chirp parameter depends on the bias voltage as well ( $\Delta\beta \sim V_{\text{RF}}$ ), and hence, in a complicated way, on the output intensity of the MZI modulator. Chirpless operation ( $\alpha_{\text{cp}} = 0$ ) can be obtained by setting the parameter  $\delta$  to zero as shown by the dash-dotted line in the figure and also indicated by (6.21).

Calculated SMF transmission characteristics of 10 Gbit/s NRZ optical signals generated by an MZI modulator are illustrated in Figs. 6.7, 6.8 and 6.9. In this calculation, the operation wavelength is set to 1550 nm.

**Fig. 6.7** Calculated maximum SMF transmission distance for an eye opening penalty of  $< 1$  dB as a function of an MZI modulator's unbalance parameter  $\delta$  (black solid curve) and modulated optical signal's chirp parameter (gray dotted curve)



The calculated maximum SMF transmission distance for an eye opening penalty of less than 1 dB is shown by the solid black curve in Fig. 6.7 as a function of the unbalance parameter  $\delta$ .

The transmission distance increases (decreases) as the unbalance parameter decreases (increases) related to a corresponding change of the chirp parameter as shown in Fig. 6.6. Commonly, the SMF transmission characteristics of digital intensity modulated optical signals are discussed by using the approximation that the chirp parameter is constant when changing the optical intensities (see [2, 3]), which helps to clarify the SMF transmission characteristics easily and simply by using the parameter  $\alpha_{cp}$  and the simple relation between the phase change and the optical intensity change given in (6.3). When one adopts the constant chirp parameter approximation to the output from the MZI modulator, the slight distortion of the optical signal waveform in E/O conversion with an MZI modulator caused by the nonlinear transfer function (6.16) and the complicated relation between the chirp parameter and the propagation constant change  $\Delta\beta L$  (see (6.17) and (6.18)) are ignored. In order to find out the validity range of the constant chirp parameter approximation, the dependence of the transmission distance on the unbalance parameter  $\delta$  is fitted by calculated results using the constant chirp parameter approximation. The calculated transmission distances for intensity modulated optical signals with constant chirp parameter are given in Fig. 6.7 by the gray dotted curve. The horizontal

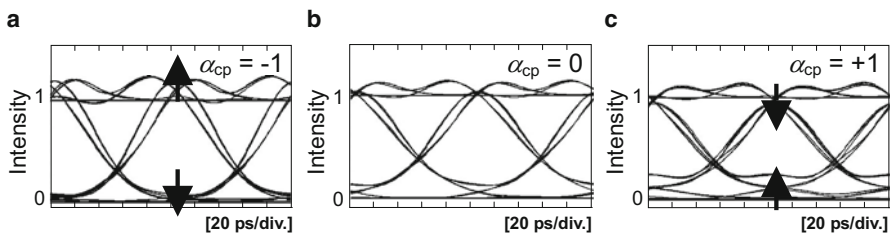


**Fig. 6.8** Calculated eye diagrams after 50 km SMF transmission for various chirp parameter values,  $\alpha_{cp} = -1$  (a),  $\alpha_{cp} = 0$  (b),  $\alpha_{cp} = +1$  (c)

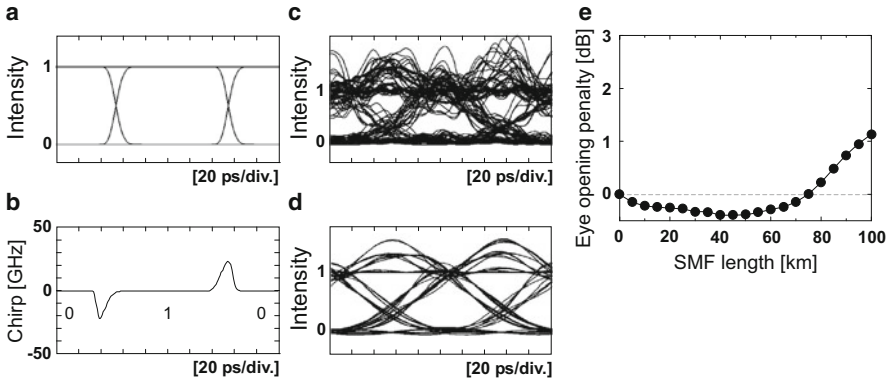


**Fig. 6.9** Calculated characteristics of MZI modulator output with a chirp parameter of  $-1$  under 10 Gbit/s NRZ signal operation. Output eye diagram from an MZI modulator (a), calculated chirp for fixed 010 pattern (b), eye diagrams after 100 km SMF transmission without and with a low-pass filter (c, d), calculated eye opening penalty as a function of SMF transmission length (e)

axes for these results are adjusted in order to gain an optimum agreement between the two calculated curves which turns out to be quite good. The change in the unbalance parameter  $\delta$  from  $-1$  to  $+1$  is approximately equivalent to a change of the chirp parameter of the modulated optical signal from  $-1.4$  to  $+1.4$ . It indicates that the SMF transmission characteristics of the MZI modulator's output can be discussed to a good approximation by using the intensity modulated signal with constant chirp parameter  $\alpha_{cp}$  in the range from  $-1.4$  to  $+1.4$ . To generalize the discussions below, the SMF transmission characteristics for the MZI modulator outputs are discussed by using the chirp parameter  $\alpha_{cp}$ . Here, the chirp parameter is defined for the modulated optical signal and is assumed to be constant. One can see from the figure that a slightly negative value of the chirp parameter (around  $-1$ ) enlarges the SMF transmission distance and raises the chromatic dispersion tolerance. Figure 6.8 shows the eye diagrams of modulated optical signals with various chirp parameter  $\alpha_{cp}$  values after 50 km SMF transmission.

The eye opening is enhanced when  $\alpha_{cp} = -1$  (Fig. 6.8a) compared to the case of  $\alpha_{cp} = 0$  (Fig. 6.8b). On the other hand, it is reduced when  $\alpha_{cp} = +1$ , as shown in Fig. 6.8c. In this case, strong intersymbol interference occurs, which determines the maximum SMF transmission distance. Figure 6.9 summarizes the characteristics of the MZI modulator output having a chirp parameter of  $-1$ .

Figure 6.9a shows the intensity modulated output eye diagram from the MZI modulator. The instantaneous frequency chirp for a fixed 010 pattern is shown in Fig. 6.9b. Clear chirp due to the phase change in the MZI modulator can be observed at the leading and falling edges of the pattern. Figures 6.9c, d are the eye diagrams after 100 km SMF transmission without and with a low-pass filter, respectively. The total amount of the fiber dispersion is 1700 ps/nm. Waveform distortion due to chromatic dispersion is observed, but the eye is still open. Figure 6.9e is the calculated eye opening penalty as a function of SMF transmission length with



a chromatic dispersion coefficient of 17 ps/(nm km). The results suggest that less than a 1 dB penalty can be obtained as long as the SMF transmission distance is shorter than 96 km, and this means that a 10 Gbit/s NRZ optical signal generated by an MZI modulator has a dispersion tolerance of more than 1600 ps/nm if the modulator is operated under proper driving conditions.

## 6.2 Semiconductor-based MZI Modulators

Semiconductor-based MZI modulators offer various advantages including their small size, low driving voltage, and absence of DC drift problems. Additionally, they have been investigated and developed in the GaAs- [24–36] and in the InP-material system as well [37–44]. In this section, fundamentals and relevant features of semiconductor MZI modulators are summarized. The refractive index control methods for semiconductor materials are explained in Sect. 6.2.1. In particular, the plasma (Sect. 6.2.1.1), Franz–Keldysh (Sect. 6.2.1.2), quantum-confined Stark (Sect. 6.2.1.3), and electro-optic (Sect. 6.2.1.4) effects are described. In Sect. 6.2.2, features of GaAs- and InP-based MZI modulators utilizing the effects mentioned above are described.

### 6.2.1 Fundamentals/Refractive Index Control of Semiconductor Materials

Intensity modulation with an MZI modulator is realized by varying the refractive indices of the two phase control waveguides in the MZI modulator. The refractive index of semiconductor materials can be changed in various ways: by injecting carriers through the plasma effect or by applying electric fields via the Franz–Keldysh, the quantum-confined Stark, or the electro-optic effect. The features of these effects are summarized below.

#### 6.2.1.1 Plasma Effect

Free carriers in semiconductor materials change the refractive index of these materials according to [45, 46]

$$\Delta n = -\frac{e^2 \lambda^2}{8\pi^2 c^2 \epsilon_0 n} \left( \frac{N}{m_e} + \frac{P}{m_h} \right), \quad (6.23)$$

where  $e$ ,  $\lambda$ ,  $c$ ,  $\epsilon_0$ ,  $n$ ,  $m_e$ ,  $m_h$ ,  $N$ , and  $P$  are electron charge, incident light wavelength, velocity of light, permittivity of free space, refractive index, electron effective mass, hole effective mass, electron density, and hole density, respectively. The hole effective mass,  $m_h$ , in (6.23) includes contributions of heavy and light holes.

But as the light hole mass is usually much smaller than the heavy hole mass, the hole effective mass is mainly determined by the heavy hole. A precise expression including heavy and light hole masses is given in equation (21) in [46]. According to (6.23), the refractive indices of semiconductors can be varied by changing the amount of free carriers by injection. However, the refractive index change is accompanied by a large increase in free carrier absorption. The absorption coefficient  $\alpha_{fc}$  (in  $\text{cm}^{-1}$ ), for example, has the following dependence on the electron ( $N$  in  $\text{cm}^{-3}$ ) and hole ( $P$  in  $\text{cm}^{-3}$ ) densities for GaAs material [47]:

$$\alpha_{fc} \approx 3 \times 10^{-18} N + 7 \times 10^{-18} P. \quad (6.24)$$

### 6.2.1.2 Franz–Keldysh Effect

When an electric field is applied to a bulk semiconductor, the band structure of the semiconductor is modified and the tails of the electron and hole wave functions penetrate into the forbidden band which is equivalent to a bandgap shrinkage (or a long-wavelength shift of the bandgap-equivalent wavelength) [4, 5]. The refractive index change of the semiconductor material is related to a change in the corresponding absorption spectra, and the following relation between the complex refractive index  $n_c(\omega)$ , the real part of the complex refractive index  $n(\omega)$  and the absorption coefficient  $\alpha(\omega)$  holds

$$n_c(\omega) = n(\omega) + j \frac{c\alpha(\omega)}{2\omega}. \quad (6.25)$$

The change in the real part of the complex refractive index  $\Delta n(\omega)$  can be derived by using the absorption coefficient change  $\Delta\alpha(\omega)$ , following the Kramers–Kronig relations [14, 15, 48]

$$\begin{aligned} \Delta n(\omega) &= \frac{2c}{e^2} P_v \int_0^{\infty} \frac{\Delta\alpha(\omega')}{\omega'^2 - \omega^2} d\omega' \\ &\equiv \frac{2c}{e^2} \lim_{\delta \rightarrow 0} \left( \int_0^{\omega-\delta} \frac{\Delta\alpha(\omega')}{\omega'^2 - \omega^2} d\omega' + \int_{\omega+\delta}^{\infty} \frac{\Delta\alpha(\omega')}{\omega'^2 - \omega^2} d\omega' \right), \end{aligned} \quad (6.26)$$

where  $P_v$  denotes taking the Cauchy principal value. Thus, (6.26) illustrates how the refractive index of a semiconductor can be changed by applying an electric field through the Franz–Keldysh effect. The Franz–Keldysh effect exhibits a pronounced wavelength dependence because it is a band-edge related effect.

### 6.2.1.3 Quantum-confined Stark Effect (QCSE)

The nonlinear electroabsorption characteristics in quantum wells have been studied theoretically and experimentally since the 1980s [6–11]. The absorption spectrum

of a multiquantum-well (MQW) structured semiconductor material shifts to longer wavelengths when an electric field is applied perpendicularly to the MQW structure. The shift, called the Stark shift, is analogous to the energy shift of a hydrogen atom under applied electric fields [6]. In the absorption spectrum of MQW structures, resonance peaks appear at the absorption edge which are due to electron–hole pairs held together by the Coulomb attraction between the opposite charges and which are designated as Wannier excitons. The exciton resonances can be observed even at room temperature due to the confining potential of the barrier material surrounding the quantum wells. The presence of the exciton absorption and its shift in low-dimensional semiconductor systems is referred to as the quantum-confined Stark effect (QCSE). If the applied electric field is weak [12, 13, 46, 49], the bandgap energy shift  $\Delta_{\text{shift}}$  can be expressed as

$$\Delta_{\text{shift}} = \frac{\pi^2 - 15}{24\pi^4 \hbar^2} (m_e + m_h) e^2 E^2 W^4, \quad (6.27)$$

where  $E$  and  $W$  are the applied electric field and the thickness of a well layer, given in units of V/m for  $E$  and in m for  $W$ .  $\Delta_{\text{shift}}$  is then given in J, which can be converted to eV by applying the following relation:  $1 \text{ eV} = 1.6022 \times 10^{-19} \text{ J}$ . The shift is proportional to the square of the applied electric field  $E$  and the fourth power of well width  $W$ . The change of the refractive index of the MQW semiconductor material is accompanied by a change in the absorption spectrum through the Kramers–Kronig relations as given by (6.26). The electric-field induced change in the absorption is much steeper for the QCSE than that due to the Franz–Keldysh effect, and as a consequence, almost all electroabsorption modulators and some semiconductor MZI modulators utilize the QCSE. However, similar to the Franz–Keldysh effect, the QCSE also exhibits a strong wavelength dependence as it is also a band-edge related phenomenon.

#### 6.2.1.4 Electro-optic (Pockels) Effect

The refractive index of semiconductors also changes via the electro-optic (or Pockels) effect when an electric field is applied to the material [50–52]. In anisotropic materials like crystals, an electric displacement field  $D_{0i}$  can be expressed by using the electric field components  $E_j$  as

$$D_{0i} = \sum_{j=1}^3 \varepsilon_{ij} E_j, \quad (6.28)$$

where  $\varepsilon_{ij}$  is the dielectric constant having the form of a symmetric tensor of rank two. Generally, the tensor is expressed as an ellipsoid according to

$$\sum_{i=1}^3 \sum_{j=1}^3 \varepsilon_{ij} x_i x_j = 1, \quad (6.29)$$

where  $x_i$  and  $x_j$  ( $i, j = 1, 2, 3$ ) denote three axes of a rectangular coordinate system. It can be converted into the following standard expression by choosing an appropriate rectangular coordinate system

$$\varepsilon_x x^2 + \varepsilon_y y^2 + \varepsilon_z z^2 = 1. \quad (6.30)$$

This expression is formally equal to the following index ellipsoid whose principal values of the refractive indices are  $n_x$ ,  $n_y$ , and  $n_z$ , that is,

$$\frac{x^2}{n_x^2} + \frac{y^2}{n_y^2} + \frac{z^2}{n_z^2} = 1. \quad (6.31)$$

The relation between the electric displacement field and the electric field can also be written as

$$E_i = \sum_{j=1}^3 b_{ij} D_{0j} \quad (6.32)$$

using coefficients  $b_{ij}$  defined as

$$b_{ij} = \frac{\partial E_i}{\partial D_{0j}}. \quad (6.33)$$

For the case of an electric field applied to a material, the following relation holds with respect to the reciprocal dielectric constant and the electric field:

$$b_{ij} = b_{ij}^0 + \sum_{k=1}^3 \gamma_{ijk} E_k + \frac{1}{2} \sum_{k=1}^3 \sum_{l=1}^3 Q_{ijkl} E_k E_l + \dots, \quad (6.34)$$

where  $\gamma_{ijk}$  and  $Q_{ijkl}$  are called the coefficients of the Pockels and Kerr effect, respectively.  $b_{ij}^0$  is the reciprocal dielectric constant without electric field. The Pockels (or linear electro-optic) effect gives rise to a change in the refractive index which is linearly proportional to the electric field. The Pockels effect requires inversion asymmetry, and thus it is only observed in certain crystalline solids. On the other hand, in the case of the Kerr (or quadratic electro-optic) effect, the change in the refractive index is proportional to the square of the electric field and all materials exhibit the Kerr effect, but it is generally much weaker than the Pockels effect. Thus, electro-optic modulators are usually made from crystals exhibiting the Pockels effect.

III–V semiconductor materials such as GaAs and InP exhibit the Pockels effect. They have zincblende crystal structure with space group of  $T_d^2$ - $F\bar{4}3m$ . The index ellipsoid of this type of crystal structure with no external electric field is a sphere whose principal values of the refractive indices  $n_x$ ,  $n_y$ , and  $n_z$  are equal, which will be designated as  $n_0$  in the following. The crystal structure has determinants for the tensors of rank 2, 3, and 4 and these are given by (6.35)–(6.37) [50–52]. For the

tensor of rank 2 (the reciprocal dielectric constant tensor),

$$b_{ij}^0 = \begin{bmatrix} b_{11} & 0 & 0 \\ 0 & b_{11} & 0 \\ 0 & 0 & b_{11} \end{bmatrix} \quad (6.35)$$

holds, the tensor of rank 3 (coefficient for the linear electro-optic effect) is given by

$$\gamma_{ijk} = \begin{bmatrix} 0 & 0 & 0 \\ 0 & 0 & 0 \\ 0 & 0 & 0 \\ \gamma_{41} & 0 & 0 \\ 0 & \gamma_{41} & 0 \\ 0 & 0 & \gamma_{41} \end{bmatrix}, \quad (6.36)$$

while the tensor of rank 4 (coefficient for the quadratic electro-optic effect) is

$$Q_{ijkl} = \begin{bmatrix} Q_{11} & Q_{12} & Q_{12} & 0 & 0 & 0 \\ Q_{21} & Q_{11} & Q_{12} & 0 & 0 & 0 \\ Q_{21} & Q_{21} & Q_{11} & 0 & 0 & 0 \\ 0 & 0 & 0 & Q_{44} & 0 & 0 \\ 0 & 0 & 0 & 0 & Q_{44} & 0 \\ 0 & 0 & 0 & 0 & 0 & Q_{44} \end{bmatrix}. \quad (6.37)$$

Here, the subscripts for higher rank tensors are expressed as  $\{11\} \rightarrow \{1\}$ ,  $\{22\} \rightarrow \{2\}$ ,  $\{33\} \rightarrow \{3\}$ ,  $\{23\}$ ,  $\{32\} \rightarrow \{4\}$ ,  $\{31\}$ ,  $\{13\} \rightarrow \{5\}$ , and  $\{12\}$ ,  $\{21\} \rightarrow \{6\}$ .

It is interesting to note that the principal values of the refractive indices keep the value  $n_0$  even when an electric field  $\mathbf{E} = (E_x, E_y, E_z)$  is applied, i.e.,

$$b_{11} = \frac{1}{n_0^2} \quad (6.38)$$

holds. This is due to the fact that the components  $\gamma_{11}$ ,  $\gamma_{22}$ , and  $\gamma_{33}$  in (6.36) are equal to zero, and the components  $b_{ij}$  in (6.35) are equal to  $b_{11}$  only when  $i$  is equal to  $j$  (moreover, the Kerr effect has been assumed to be negligible).

For the case of an applied electric field, the index ellipsoid can be expressed as

$$\frac{1}{n_0^2} (x^2 + y^2 + z^2) + 2\gamma_{41} (yzE_x + zxE_y + xyE_z) = 1. \quad (6.39)$$

Here, a rectangular coordinate system has been chosen with the  $x$ -,  $y$ -, and  $z$ -axis oriented along the (100), (010), and (001) crystal axes, respectively.

If an electric field is applied parallel to the (100) direction, which is the standard direction of epitaxial growth of semiconductor material and hence the direction perpendicular to the epitaxial layers,  $E_y$  and  $E_z$  in (6.39) become zero and (6.39)

reduces to

$$\frac{1}{n_0^2} (x^2 + y^2 + z^2) + 2\gamma_{41}yzE_x = 1, \quad (6.40)$$

which means that the Pockels effect does not contribute to the refractive index change when the input light propagates along the  $z$ - or  $y$ -axis because this configuration corresponds to  $y = 0$  or  $z = 0$ . From the discussion it becomes clear that the maximum refractive index change is obtained for light propagating at an angle of  $45^\circ$  from the  $y$ - and  $z$ -axis, that is, along the (011) or the (0 $\bar{1}$ 1) direction. By rotating the  $y$ - and  $z$ -axis to the (011) (new  $y'$ -axis) and (0 $\bar{1}$ 1) direction (new  $z'$ -axis), (6.40) can be converted into

$$\frac{x^2}{n_0^2} + \left( \frac{1}{n_0^2} + \gamma_{41}E_x \right) y'^2 + \left( \frac{1}{n_0^2} - \gamma_{41}E_x \right) z'^2 = 1. \quad (6.41)$$

For the refractive index of a semiconductor under the influence of an electric field and for light propagating along the  $y'$  direction,

$$n_{y'} = \left( \frac{1}{n_0^2} + \gamma_{41}E_x \right)^{-1/2} \quad (6.42)$$

holds, and for light propagating along the  $z'$  direction, one gets

$$n_{z'} = \left( \frac{1}{n_0^2} - \gamma_{41}E_x \right)^{-1/2}. \quad (6.43)$$

By assuming small changes of the refractive index due to the applied electric field, these equations can be expressed as

$$n_{y'} \approx n_0 - \frac{1}{2}n_0^3\gamma_{41}E_x, \quad (6.44)$$

$$n_{z'} \approx n_0 + \frac{1}{2}n_0^3\gamma_{41}E_x. \quad (6.45)$$

According to (6.44) and (6.45), the refractive index experiences opposite changes if the light propagation direction is along the  $y'$  and the  $z'$  directions, while input light having an electric field component parallel to the (100) axis is not affected by the Pockels effect. Thus, semiconductor electro-optic modulators exhibit a strong polarization dependence.

The parameter  $\gamma_{41}$  for III-V semiconductors takes values around  $-1.0$  to  $-2.0 \times 10^{-12}$  m/V, while the parameter for LiNbO<sub>3</sub> is  $10$  to  $30 \times 10^{-12}$  m/V, which is about 20 times larger than that of semiconductor material. However, the larger refractive index in semiconductors helps to raise the Pockels effect ( $n_{\text{LiNbO}_3} \sim 2.2$ ,  $n_{\text{GaAs}} \sim 3.4$ ,  $n_{\text{InP}} \sim 3.2$ ) because the refractive index change is proportional to the third power of the refractive index itself. Moreover, the small dimensions of waveguide structures in semiconductor devices are also favorable for getting a strong electric field at the waveguide core region. Thus, one can obtain a comparable or even larger refractive index change in semiconductor electro-optic modulators compared to the change achievable in LiNbO<sub>3</sub> waveguide devices.

### 6.2.2 GaAs- and InP-based MZI Modulators

In long haul optical fiber transmission systems, the 1550 nm wavelength region is widely used due to the small propagation loss of optical fibers (see Chap. 2). GaAs-based MZI modulators operating in that wavelength region utilize the Pockels effect to control the refractive index and to modulate the optical phase. This is because the GaAs material has a bandgap-equivalent wavelength of 870 nm which is far from the operation wavelength. So band-edge related effects such as the QCSE can not be applied. On the other hand, InP-based MZI modulators can utilize both, the QCSE and the Pockels effect as well. The core layer of InP-based modulators is composed of quaternary materials such as InGaAsP, InGaAlAs, and so forth, whose bandgap wavelengths can be set close to the operation wavelength range. Particularly low driving voltages in InP-based MZI modulators can be obtained by utilizing the QCSE, however, this is achieved at the expense of a strong wavelength dependence. Moreover, an increasing optical absorption under the influence of an applied electric field, which distorts the output optical signal waveform, is also a problem. In order to reduce the wavelength dependence and the optical absorption change in InP-based modulators, it is desirable to only utilize the Pockels effect to control the refractive index of the modulators.

Two types of structures have found widespread use in semiconductor-based MZI modulators in order to efficiently apply the electric field to the core layer and prevent unwanted current flow at the same time.

One solution is a Schottky electrode structure [27–34] as schematically shown in Fig. 6.10a, where a Schottky barrier between a metal electrode and the semiconductor material blocks the unwanted current flow. This option is primarily used for GaAs-based traveling-wave electrode modulators (see Sect. 6.3). A drawback of the structure is that the strength of the electric field applied to the core layer is lower compared to a p-i-n structure (see below) due to the low optical confinement to the core layer and a long distance between the RF electrode and the ground. The second alternative is a p-i-n structure [26, 37–41, 43]. It is schematically shown in Fig. 6.10b. A thin insulating (i) layer (core layer) is sandwiched between p-type and n-type cladding layers. The structure blocks the current flow as a reverse biased diode. The strength of the electric field at the core layer is very high because the electric field is concentrated at the very thin i-layer. This is one of the reasons why p-i-n structure modulators can be made very compact. The electric field applied to the core layer of a p-i-n structure modulator is more than 100 times stronger than in LiNbO<sub>3</sub> modulators because the waveguide width is  $\sim 1/4$  and the thickness of the core layer is less than  $\sim 1/30$  compared to those of LiNbO<sub>3</sub> devices. Drawbacks of the p-i-n structure are:

1. Large absorption loss in the p-doped cladding layer, and
2. A large parasitic capacitance due to the thin i-layer.

The p-type cladding layer has  $\sim 20$  times larger absorption loss than an n-type one due to intervalence band absorption [53, 54]. The resistivity of the p-type cladding layer is also one or two order(s) of magnitude larger than that of n-type

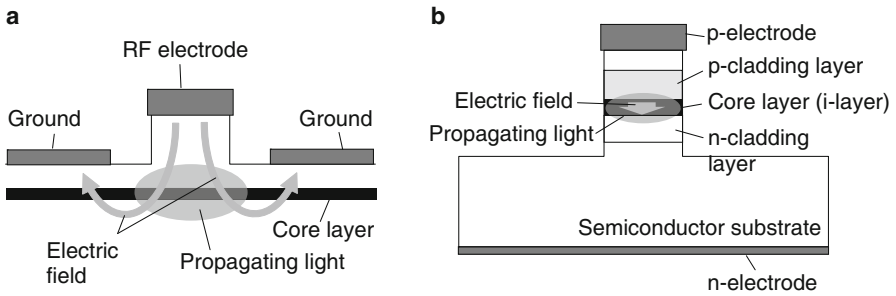


**Fig. 6.10** Schematic structure of Schottky electrode waveguide (a), and p-i-n structure waveguide (b)

layers. Therefore, it is difficult to use sufficiently long traveling-wave electrodes which would meet the velocity and impedance matching conditions in p-i-n structure modulators. The large capacitance due to the thin i-layer is also unfavorable for extending the length of traveling-wave electrodes, and thus lumped electrodes are often used with p-i-n structure modulators, although the maximum achievable operation speed is limited for such designs.

### 6.3 High-speed Modulator Design

Two types of electrode structures are essentially used with semiconductor MZI modulators, as mentioned above. One is the lumped electrode structure which is schematically shown in Fig. 6.11a.

The core and cladding layers of the modulator's waveguide are sandwiched between the lumped electrode, the ground electrode is located at the reverse (substrate) side of the chip, and an electric field is applied between the two. The structure is very simple and can be easily fabricated. The operation speed of the modulator with a lumped electrode structure is usually limited by the parasitic capacitance (CR time constant) of the electrode. The modulation efficiency of the modulator can be increased by extending the length of the phase control waveguide in the MZI modulator. However, a long electrode causes a large parasitic capacitance and the operation speed becomes low, i.e., it is limited to less than 10 Gbit/s for almost all MZI modulators with lumped electrode structure [37, 39, 40].

The other MZI modulator variant is illustrated schematically in Fig. 6.11b: high-speed operation at low driving voltage is enabled by a coplanar traveling-wave structure where the RF drive signal is applied to one side of the electrode and exits from the other side. The output side of the electrode is usually terminated by a terminator resistance which prevents that the RF signal is reflected from the output end. Figure 6.12 shows the principle of the traveling-wave electrode.

The RF signal, which propagates along the electrode, influences the light propagating along the waveguide core. When the velocity of the light is equal to that of



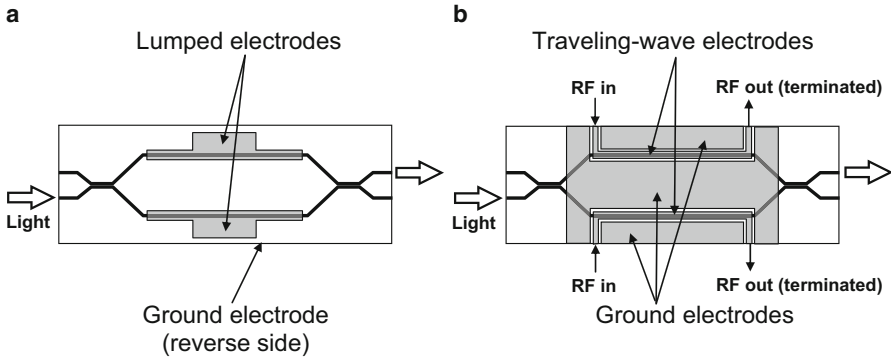


**Fig. 6.11** Schematic structure of electrodes formed on MZI modulators. Lumped electrode structure (a), traveling-wave electrode structure (b)

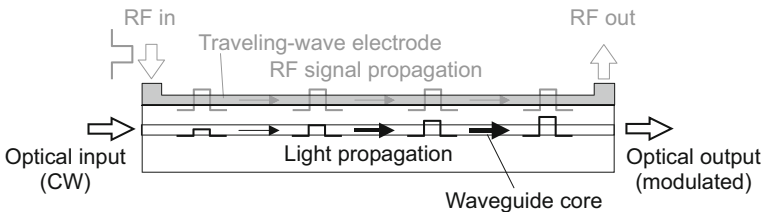


**Fig. 6.12** Principle of a traveling-wave electrode

the RF signal, the RF signal affects the propagating light all along the modulator and the efficiency is highest. Because the change of the refractive index, induced by the electro-optic effect, is smaller than that introduced by the QCSE, it is important to raise the modulation efficiency of the MZI modulator by using the traveling-wave electrode structure. This concept is free from the RC time constant limitation of the electrode, and one can, at least in principle, increase the modulation efficiency by extending the electrode length of the phase control waveguides in the MZI modulator without reducing the bandwidth.

Important requirements when designing traveling-wave electrodes are:

1. Impedance matching between the electrodes and the driving equipment ( $Z_0$ )
2. Velocity matching between the electrical signal and the propagating light ( $\beta$ ), and
3. Sufficiently low transmission loss of the electrode ( $\alpha_0$ ).

The characteristics of a traveling-wave electrode can be discussed conveniently by using a transmission line (distributed element) model based on Maxwell's equations [55] as illustrated schematically in Fig. 6.13a.

The transmission line is divided into small sections and an equivalent circuit segment for a small section with a very short length of  $\Delta x$  is illustrated in Fig. 6.13b. In this figure,  $R$ ,  $L_i$ ,  $G$ , and  $C$  denote resistance, inductance, conductance and capacitance of the electrode, respectively, and the parameters are expressed in values

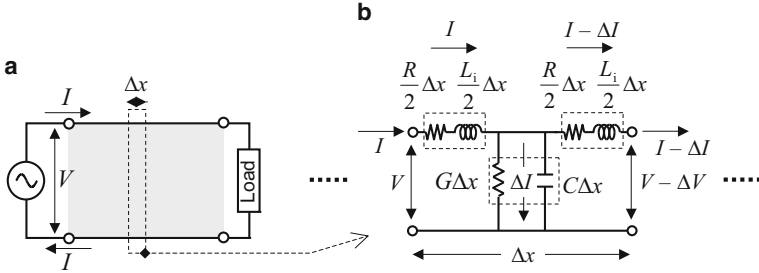


**Fig. 6.13** Schematic of the transmission line (a) and equivalent circuit segment for a small portion in the transmission line with a very short length of  $\Delta x$  (b)

per unit length. These parameters depend on the structure of the electrode (electrode width, gap width between the electrode and ground, etc.), the dielectric constant of the semiconductor material the waveguides are made of, and so forth.

It is assumed that the voltage  $V$ , applied to the equivalent circuit segment, drops to  $V - \Delta V$  due to the resistances  $(R/2)\Delta x$  and the inductances  $(L_i/2)\Delta x$  while the current  $I$ , flowing along the equivalent circuit segment, reduces to  $I - \Delta I$  due to the leakage current  $\Delta I$  through the conductance  $G \Delta x$  and the capacitance  $C \Delta x$ .  $\Delta V$  and  $\Delta I$  are assumed to be small.

The voltage drop  $\Delta V$  in the equivalent circuit segment is given by

$$\begin{aligned} \Delta V &= \left( \frac{R}{2} + j\omega \frac{L_i}{2} \right) I \Delta x + \left( \frac{R}{2} + j\omega \frac{L_i}{2} \right) (I - \Delta I) \Delta x \\ &= (R + j\omega L_i) I \Delta x - \left( \frac{R}{2} + j\omega \frac{L_i}{2} \right) \Delta I \Delta x \\ &\approx (R + j\omega L_i) I \Delta x = Z I \Delta x, \end{aligned} \tag{6.46}$$

where  $Z$  is the impedance per unit length of the equivalent circuit segment. The final result in (6.46) has been obtained by neglecting the second order product of small terms  $\Delta I \Delta x$ . It is straightforward to derive

$$\frac{dV}{dx} = -ZI \tag{6.47}$$

from (6.46).

Analogous to (6.46), the decrease of the current along the equivalent circuit segment,  $\Delta I$ , is given by

$$\begin{aligned} \Delta I &= (G + j\omega C) \left( V - \frac{\Delta V}{2} \right) \Delta x \\ &= (G + j\omega C) V \Delta x - (G + j\omega C) \frac{\Delta V}{2} \Delta x \\ &\approx (G + j\omega C) V \Delta x = Y V \Delta x, \end{aligned} \tag{6.48}$$

where  $Y$  is the admittance per unit length of the equivalent circuit segment. Once again, the final result in (6.48) has been obtained by neglecting the second order product of small terms  $\Delta V \Delta x$ , and (6.48) immediately yields

$$\frac{dI}{dx} = YV. \quad (6.49)$$

The combination of (6.47) and (6.49) leads to

$$\frac{d^2V}{dx^2} = ZYV \quad (6.50)$$

and the general solution of (6.50) is

$$V(x) = V_1 e^{\gamma_e x} + V_2 e^{-\gamma_e x}, \quad (6.51)$$

where  $V_1$  and  $V_2$  are arbitrary values, and  $\gamma_e$  is given by

$$\gamma_e = \sqrt{ZY} = \sqrt{(R + j\omega L_i)(G + j\omega C)}. \quad (6.52)$$

The complex parameter  $\gamma_e$  is normally called the propagation constant, and it is commonly expressed by using an attenuation constant  $\alpha_0$  and a phase constant  $\beta_e$ :

$$\gamma_e = \alpha_0 + j\beta_e. \quad (6.53)$$

Substitution of (6.51) into (6.47) leads to the following equation for the current  $I$ :

$$I(x) = \sqrt{\frac{Y}{Z}} (V_1 e^{\gamma_e x} - V_2 e^{-\gamma_e x}) = \frac{1}{Z_0} (V_1 e^{\gamma_e x} - V_2 e^{-\gamma_e x}), \quad (6.54)$$

where  $Z_0$  is called the characteristic impedance given by

$$Z_0 = \sqrt{\frac{Z}{Y}} = \sqrt{\frac{R + j\omega L_i}{G + j\omega C}}. \quad (6.55)$$

The characteristic impedance and the propagation constant can be controlled by the parameters  $L_i$ ,  $R$ ,  $C$ , and  $G$ . In case that  $G$  is negligibly small and  $R \ll \omega L_i$ , the characteristic impedance  $Z_0$  can be approximated by

$$Z_0 = \sqrt{\frac{L_i}{C} - j\frac{R}{\omega C}} \approx \sqrt{\frac{L_i}{C}} \left(1 - j\frac{R}{2\omega L_i}\right) \approx \sqrt{\frac{L_i}{C}} \quad (6.56)$$

while

$$\gamma_e \approx j\omega \sqrt{L_i C} \left(1 - j\frac{R}{2\omega L_i}\right) \approx j\omega \sqrt{L_i C}. \quad (6.57)$$

This represents a good approximation for the propagation constant  $\gamma_e$  and in this case,

$$\alpha_0 = \frac{R}{2} \sqrt{\frac{C}{L_i}} \approx 0 \quad (6.58)$$

and

$$\beta_e = \omega \sqrt{L_i C} \quad (6.59)$$

hold for the attenuation constant  $\alpha_0$  and the phase constant  $\beta_e$ , respectively. Thus, if the assumptions “small  $G$  and  $R \ll \omega L_i$ ” are justified, the characteristic impedance  $Z_0$  and the propagation constant  $\gamma_e$  are only determined by the parameters  $L_i$  and  $C$ .

From the discussions above, it is obvious that reducing the resistance  $R$  and the conductance  $G$  of the electrode in designing and fabricating traveling-wave electrodes of high-speed modulators is of prime importance. In addition, the characteristic impedance of the traveling-wave electrode should be matched to that of the driving equipment such as driver ICs and so forth. Usually, the impedance of the driving equipment is  $50 \Omega$ . Under these circumstances, the characteristic impedance of the traveling-wave electrode should also be set to  $50 \Omega$ .

The phase velocity of the electrical signal in the transmission line is given by

$$v_p = \frac{\omega}{\beta_e} = \frac{1}{\sqrt{L_i C}} \quad (6.60)$$

and the phase velocity is approximately equal to the group velocity if the losses ( $R$  and  $G$ ) of the transmission line are negligible. If the losses can not be neglected, the group velocity is given by

$$v_g = \frac{\partial \omega}{\partial \beta_e} = v_p + \beta_e \frac{dv_p}{d\beta_e}. \quad (6.61)$$

The following discussion will be based upon the assumption that the losses of the transmission line can be neglected and the phase velocity is equal to the group velocity, which is a good approximation for usual semiconductor MZI modulators with low loss electrodes.

The group velocity of light,  $v_o$ , in a medium with effective refractive index,  $n_{\text{eff}}$ , is given by

$$v_o = \frac{c}{n_{\text{eff}}}, \quad (6.62)$$

where  $c$  is the velocity of light in vacuum. A match as good as possible between the two velocities,  $v_p$  and  $v_o$ , is of key importance for modulators with traveling-wave electrode structure. The dielectric constants of GaAs and InP are around 12.5 and 12.4. Thus,  $v_p$  is normally larger than  $v_o$  in semiconductor-based modulators, and as a consequence, reducing the electrical group velocity  $v_p$  becomes important. In order to reduce the velocity  $v_p$  of GaAs-based MZI modulators with Schottky electrodes, the so-called slow-wave electrode structure has been proposed [26–34]. In this structure, the capacitance can be increased efficiently while the corresponding

inductance change remains small, and as a result, the velocity  $v_p$  of the electrode can be reduced. Using this structure, high-speed GaAs MZI modulators operating up to 40 Gbit/s have been developed [33]. The length of the phase control section of the MZI modulator was 10 mm and the half wavelength voltage was 16.8 V for 1550 nm operation wavelength. Alternatively, a capacitively loaded coplanar strip electrode structure has also been proposed, and corresponding high-speed and low driving voltage MZI modulators on GaAs and InP substrates have been reported [24, 25, 35, 36, 44].

In p-i-n structure MZI modulators, the characteristic impedance of the electrodes becomes small because the modulators have thin i-layers and the capacitances are correspondingly large. In order to increase the characteristic impedance, a segmented electrode structure has been introduced to an InP-based MZI modulator [41]. The phase modulator section of the MZI modulator was divided into small sections, and these have been connected in a series by small capacitance Au electrodes. By introducing the novel structure, 40 Gbit/s operation of the p-i-n InP-MZI modulator has been demonstrated with  $5.3V_{p-p}$  driving voltage. Thanks to the high electric field in the p-i-n structure, the chip was only 5.27 mm long.

The traveling-wave electrode technology has also been introduced to EAMs and it enabled the increase in operation speed of EAMs [56, 57].

## 6.4 Performance of Current MZI Modulators

In this section, specific high performance semiconductor MZI modulators are described which are based upon a novel n-i-n isotype structure in the phase control waveguides. Advanced MZI modulator modules are also described in which the novel structure MZI modulators are installed.

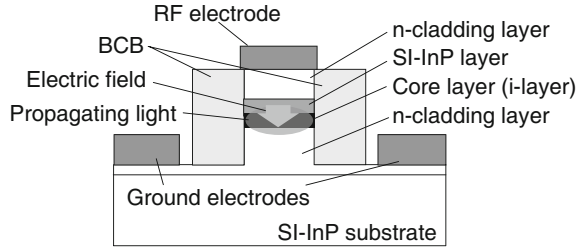
### 6.4.1 *n-i-n Structure MZI Modulators*

The high-speed semiconductor MZI modulators treated in Sect. 6.3 are designed with a rather complicated electrode structure and their fabrication is difficult. Thus, a simpler structure is much more promising for practical applications, provided the following requirements can be fulfilled simultaneously:

1. Simple electrode structure for easy fabrication
2. Capability to apply high electric fields to the core region of the modulator waveguide (similar to the situation with p-i-n waveguides), and
3. Sufficiently low loss of the upper waveguide cladding layer, both for optical and electrical signals.

An n-i-n isotype MZI modulator structure, which meets these requirements, has been fabricated and is described in [42]. The waveguide structure is schematically illustrated in Fig. 6.14.

**Fig. 6.14** Schematic structure of the n-i-n waveguide



A coplanar RF electrode is formed on a high-mesa optical waveguide buried by benzocyclobutene (BCB). The high-mesa optical waveguide consists of an n-doped lower cladding layer, an undoped core layer, an Fe-doped semi-insulating (SI) InP layer, and an n-doped upper cladding layer. The structure is grown on an SI-InP substrate. The waveguide has an n-i-n isotype heterostructure, and since there is no p-doped upper cladding layer, the typically large optical and electrical losses of a p-doped cladding layer are avoided. The concept enables the modulator to not only operate at high-speed, but also at low driving voltage by extending the lengths of the traveling-wave electrode and the phase control waveguide. The SI-InP layer is inserted in order to serve two purposes: as a potential barrier against electrons, it assures blocking of unwanted current flow and, in addition, it assures that a strong electric field is applied to the core layer of the waveguide. The characteristic impedance of the electrodes can be easily controlled by appropriately choosing the thickness of the core and the SI-InP layers, and the width of the high-mesa waveguide, thus determining the parasitic capacitance. Figure 6.15a is an example of the calculated characteristic impedance as a function of the waveguide width.

The calculation is done by using the commercially available high frequency 3-D structure simulator (HFSS<sup>TM</sup>) [58]. In this case, the thicknesses of the core and the SI-InP layers are set to 0.3  $\mu\text{m}$  and 1.0  $\mu\text{m}$ , respectively.

A characteristic impedance of  $50 \pm 5 \Omega$ , corresponding to the hatched area, can be realized by setting the waveguide widths between 1.3  $\mu\text{m}$  and 2.3  $\mu\text{m}$ , i.e., the acceptable waveguide width tolerance is fairly large and consequently the characteristic impedance control is rather straightforward in the case of the n-i-n structure.

In the case of insufficient velocity matching, the electrical bandwidth  $\Delta f$  of the traveling-wave electrode can be approximated by [25]

$$\Delta f \approx \frac{1.4c}{\pi |n_{\text{eff}} - n_m| L}, \quad (6.63)$$

where  $c$  is the velocity of light,  $n_{\text{eff}}$  and  $n_m$  are the optical and microwave effective refractive indices, and  $L$  is the length of the electrode, respectively. According to (6.60), the microwave effective refractive index  $n_m$  is given by

$$n_m = \frac{c}{v_g} = \frac{c}{v_p} = \frac{c\beta_e}{\omega} = c\sqrt{L_i C}. \quad (6.64)$$

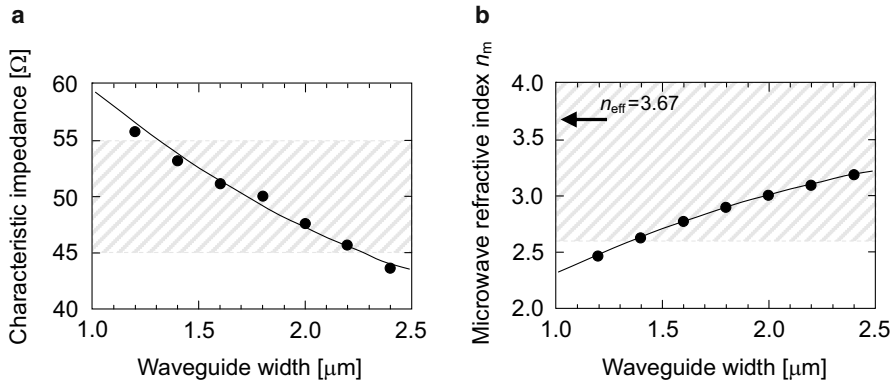


**Fig. 6.15** Calculated results for characteristic impedance (a) and microwave effective refractive index  $n_m$  (b) of the n-i-n structure waveguide with a traveling-wave electrode as a function of waveguide width

In n-i-n structure MZI modulators, a strong electric field can be applied to the core layer and enough efficiency can be obtained even with short phase control waveguides. Thus,  $L$  is set to 3 mm in the following discussion.

If 40 GHz bandwidth is required, the refractive index difference  $|n_{\text{eff}} - n_m|$  must be lower than 1.1 according to (6.63), and for a calculated value  $n_{\text{eff}} = 3.67$  of the optical effective refractive index of the n-i-n structure waveguide, this is equivalent to acceptable microwave effective indices within the range 2.57 to 4.77. Figure 6.15b is an example of the calculated microwave effective refractive index  $n_m$  as a function of the waveguide width. The required range of  $n_m$  for realizing 40 GHz bandwidth is shown by the hatched area. The demands can be seen to be very relaxed, and velocity matching does apparently only require waveguide widths of more than 1.4 μm. Impedance- and velocity-matching of the traveling-wave electrode with the simple structure can thus be realized at the same time by having the width of the n-i-n structure phase control waveguide between 1.4 μm and 2.3 μm. In agreement with these results, the waveguide width has been chosen to be 2 μm in the fabricated n-i-n structure MZI modulator. Figure 6.16 shows the schematic structure of the n-i-n structure MZI modulator.

Input CW light is fed into a  $2 \times 2$  multimode interference (MMI) coupler [59], and passed into two phase control waveguides with equal length. Two traveling-wave electrodes are located on the phase control waveguides. The refractive indices and hence the phases of the light traveling in the two phase control waveguides are modulated by RF signals applied to the two traveling-wave electrodes individually. Finally, light from both waveguides is recombined by another MMI coupler with the light interfering at the MMI coupler's output. The length of the phase control waveguide is 3 mm, and the total size of the MZI modulator chip is 4.5 mm  $\times$  0.8 mm. Figure 6.17 shows the DC extinction ratio of an n-i-n structure MZI modulator as a function of the bias voltage applied to one phase control waveguide. The input wavelength is 1550 nm.

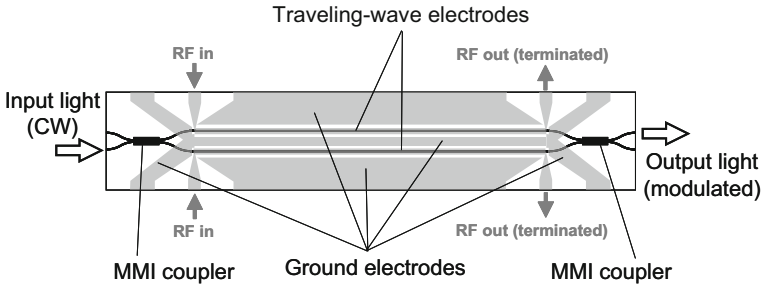
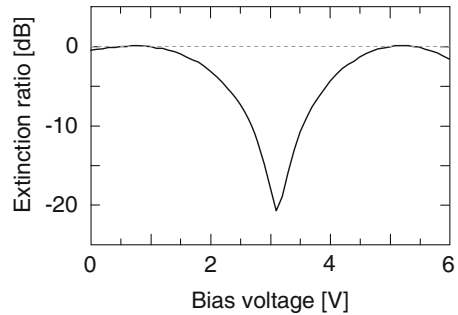


**Fig. 6.16** Schematic view of n-i-n structure MZI modulator

**Fig. 6.17** DC extinction ratio of n-i-n structure MZI modulator as a function of bias voltage applied to a phase control waveguide



A maximum extinction of more than 20 dB is obtained. The half-wavelength voltage,  $V_{\pi}$ , is measured to be 2.3 V. It is worthwhile to note that there is no increase in the optical loss, even at the bias voltage of  $2V_{\pi}$  (around a bias voltage of 5.2 V). Such behavior could not be obtained with the p-i-n structure MZI modulators utilizing the QCSE effect. The small signal Electrical/Optical (E/O) response of the n-i-n modulator is shown in Fig. 6.18a.

The 3 dB bandwidth is measured to be 40 GHz, and a clear eye diagram is obtained for a 40 Gbit/s NRZ signal with a pseudo random binary sequence (PRBS) of  $2^{31} - 1$  (Fig. 6.18b). For measuring the eye diagram, an RF signal with  $2.4V_{p-p}$  driving voltage has been applied to one electrode of the modulator. This modulator exhibits strong potential for high-speed operation with low driving voltage. However, packaging is difficult because of the two input RF electrode pads placed at opposite sides of the modulator chip.

A differential-drive MZI modulator is very important for generating chirpless or chirp-controlled digital optical signals. It is also useful for the generation of phase modulated optical signals which will be utilized in next generation optical transmission systems. To operate the MZI modulator in a differential drive (push-pull) mode, it is important to equalize the RF signal phases, and hence to equalize the lengths of the two electrodes from the chip edge to the two phase control waveguides. In addition, the two electrode pads for the input RF signals should be placed on the same side of the chip for easy connection with differential output driver ICs [60]. A differential-drive InP-MZI modulator is shown schematically in Fig. 6.19.



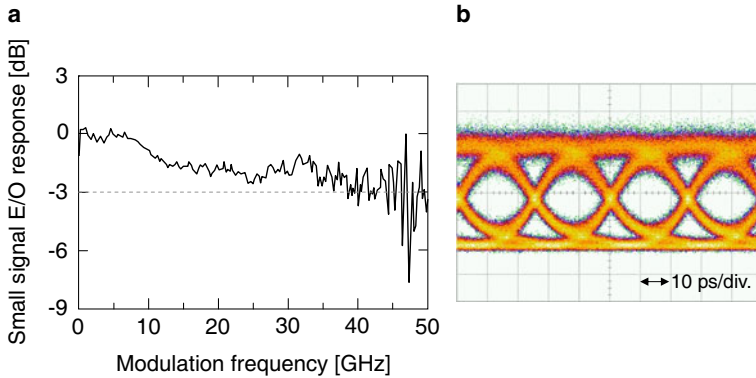


**Fig. 6.18** Small signal E/O response of n-i-n structure MZI modulator (a), output eye diagram of n-i-n structure MZI modulator operated by 40 Gbit/s NRZ signal with PRBS of  $2^{31} - 1$  (b). Waveform measured with a single electrode only driven by the RF signal

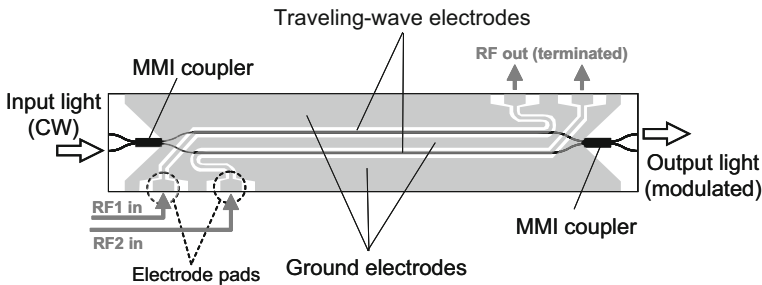


**Fig. 6.19** Schematic structure of differential-drive InP-MZI modulator

Such a modulator has already been fabricated successfully [61], and the design is based upon the n-i-n modulator discussed earlier (Fig. 6.16) with additional microstrip lines (MSLs). The length of the phase control waveguides is 3 mm, and the electrode pads for the input RF signals are both placed on one side (lower side of the figure) of the chip. The pads for the output are placed on the other side (upper side of the figure). MSLs are used in order to equalize the electrode lengths from the pads to the phase control waveguides. The MSLs exhibit small electrical losses only, even when they have bends with small radii of curvature. The chip size of the differential-drive InP-MZI modulator is  $4.5 \text{ mm} \times 0.8 \text{ mm}$ , which is the same as that of the modulator shown in Fig. 6.16. Thus, the MSLs have been added without a need to extend the chip dimensions.

Measurements of the extinction ratio have shown that the same symmetric extinction characteristics can be obtained over the complete C-band if only the DC bias is adjusted linearly as the operation wavelength increases. The results of these experiments are shown in Fig. 6.20a.

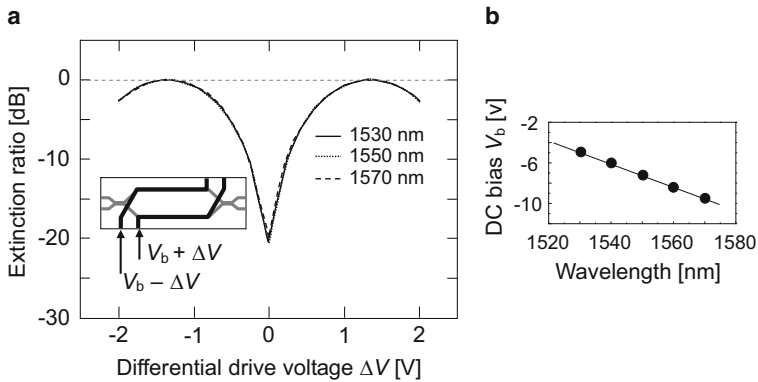
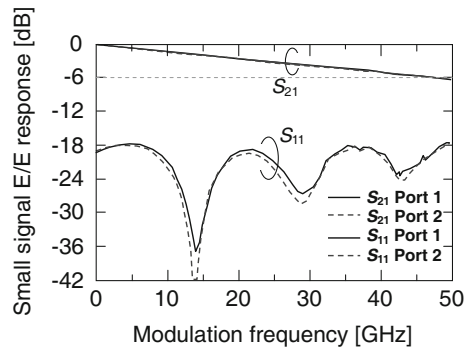


**Fig. 6.20** Extinction characteristics of differential-drive InP-MZI modulator (a). Applied DC bias  $V_b$  as a function of operation wavelength (b)

**Fig. 6.21** Small signal E/E response of differential-drive InP-MZI modulator as a function of modulation frequency.  $S_{21}$  and  $S_{11}$  are E/E transmittance and reflectance, respectively



It is important to note that no adjustment of the RF voltage swing has been necessary and only the linear change of the DC voltage  $V_b$  shown in Fig. 6.20b had to be made.

The experimentally determined small signal Electrical/Electrical (E/E) response for both RF electrodes including traveling-wave electrodes (as shown in Fig. 6.21) exhibits a 6 dB E/E bandwidth (transmittance  $S_{21}$ ) of 46 GHz for both electrodes and reflectance values  $S_{11}$  of less than  $-18$  dB for all modulation frequencies up to 50 GHz.

The characteristics are almost the same for the two electrodes. This indicates that differential-drive InP-MZI modulators can be realized without degradation of the high-speed performance even when MSLs are introduced.

By mounting the MZI modulator in a package, a compact differential-drive InP-MZI modulator module has been fabricated [61]. Figure 6.22a shows a photograph of the module.

The module is 21 mm ( $L$ )  $\times$  17 mm ( $W$ )  $\times$  8 mm ( $H$ ) in size, and its foot print is the same as that of commercially available conventional DFB lasers and EA-DFB lasers in butterfly-type packages. Two RF connectors for differential electrical

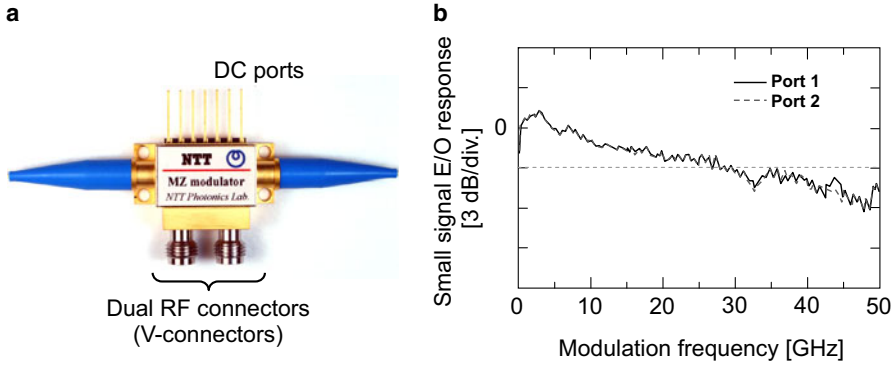


**Fig. 6.22** Photograph of a differential-drive InP-MZI modulator module (a), small signal E/O response of the module (b)

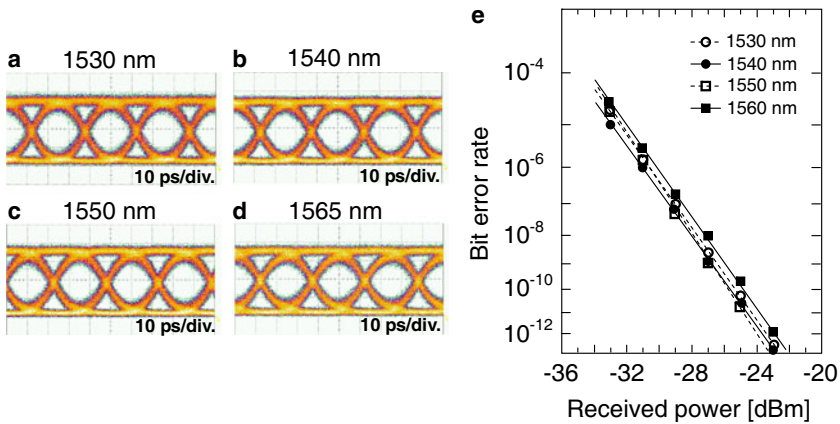


**Fig. 6.23** Eye diagrams (a–d) and bit-error-rate performance (e) of a differential-drive InP-MZI modulator module for 40 Gbit/s NRZ signals and various operation wavelengths

signals are placed at one side of the package while pins for DC bias and other control signals are placed at the opposite side of the package. The module contains 50- $\Omega$  terminations and bias-tees for both RF electrodes in the package, and the fiber-to-fiber insertion loss of the module is 7 dB.

The E/O response of the module measured for both RF ports is illustrated in Fig. 6.22b. Both curves are essentially the same and the 3 dB E/O bandwidth of the module turns out to be 28 GHz which is sufficiently large for 40 Gbit/s operation. Experiments with differential 40 Gbit/s NRZ signals, PRBS of  $2^{31} - 1$ , and 1.3  $V_{p-p}$  drive voltage swing applied to both RF connectors yielded the output eye diagrams shown in Figs. 6.23a–d for various operation wavelengths covering the complete C-band.

Clear eye opening can be observed for all operation wavelength channels. The dynamic extinction ratios are more than 10 dB. The bit error rate (BER) performance

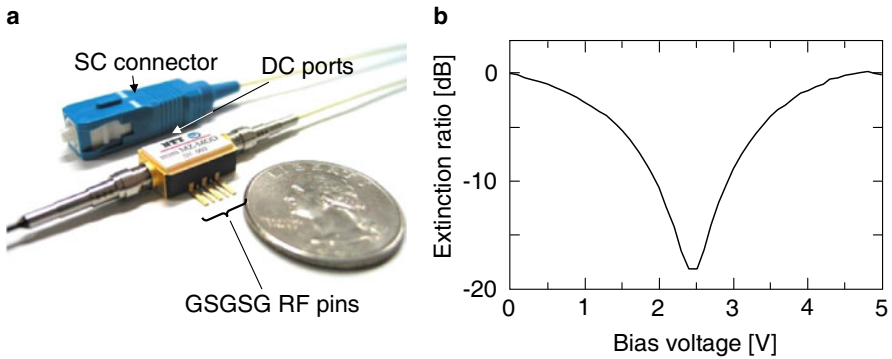


**Fig. 6.24** Photograph of surface-mountable mini 10G MZI modulator module (a) and DC extinction ratio of the module as a function of bias voltage (b). An SC connector (blue box behind the module in the photograph) is also shown as a reference

for the 40 Gbit/s NRZ signals have been measured in a back-to-back configuration, and the results are shown in Fig. 6.23e as a function of received power. The performance is essentially the same for all wavelength channels, no error floors could be observed, and error free operation of the modulator module can be concluded.

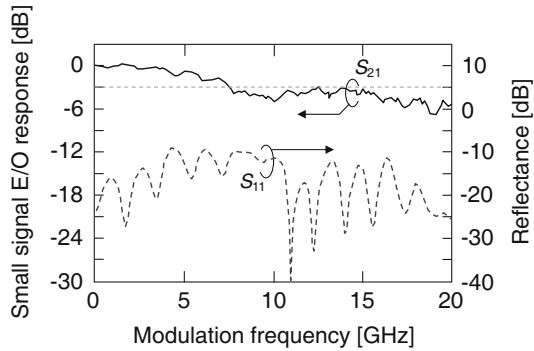
## 6.4.2 Advanced MZI Modulator Modules

### 6.4.2.1 Surface-mountable Mini 10G MZI Modulator Module

Compact MZI modulator modules operating at 10 Gbit/s are desirable for reducing the size of optical transponders and optical transceivers. Semiconductor MZI modulators are promising candidates for that purpose because of their compactness. Although the MZI modulator module shown in Fig. 6.22a is very small compared to commercially available  $\text{LiNbO}_3$  MZI modulator modules, a further reduction of the module size is desired, and thus very small surface mountable differential-drive InP-MZI modulator modules have been developed [62]. A photograph of a corresponding mini 10G MZI modulator module is shown in Fig. 6.24a.

The module is only 13.8 mm ( $L$ )  $\times$  8.9 mm ( $W$ )  $\times$  4.9 mm ( $H$ ) in size, and it consists of an inexpensive ceramic-based package. The RF and DC lead pins are located at the bottom of the package in order to enable its direct mounting onto a printed circuit board. The two RF lead pins for differential drive are located on one side of the package with G-S-G-S-G configuration for high-speed operation. High-speed transmission lines are formed in the wall of the ceramic package to connect the signal (S) lead pins and the two RF electrode pads of the MZI modulator. These lines are designed to have 50- $\Omega$  impedance and the lengths are adjusted to be equal. Figure 6.24b shows the DC extinction ratio of the module as a function of bias voltage. The half-wavelength voltage  $V_\pi$  is estimated to be 2.4 V, and there is no

**Fig. 6.25** Small signal E/O response  $S_{21}$  and reflectance  $S_{11}$  of mini 10G MZI modulator module



increase in the optical loss even at a bias voltage of  $2V_{\pi}$ . The measured small signal E/O response  $S_{21}$  for the module is shown in Fig. 6.25.

The 3 dB E/O bandwidth is 7.5 GHz which is enough for 10 Gbit/s NRZ signal operation. Reflectance is also shown in the figure. It is less than  $-9$  dB, including the reflection from the response measurement equipment. The module is operated by a 10 Gbit/s NRZ signal with PRBS of  $2^{31} - 1$ . The voltage swing of the differential RF signals applied to the two phase control waveguide is  $2.0V_{p-p}$  and  $0.1V_{p-p}$ , respectively. Under these conditions, the output modulated signal is negatively chirped. The input CW light wavelength has been set to 1550 nm. Figure 6.26a shows the eye diagram of the output 10 Gbit/s NRZ signal from the module in a back-to-back configuration.

Clear eye opening is observed. Figure 6.26b shows the eye diagram after 100 km SMF transmission. The eyes are still clearly open. The observed pattern agrees quite well with the calculated results shown in Fig. 6.9c. Measured BER characteristics for back-to-back configuration and after 100 km SMF transmission are shown in

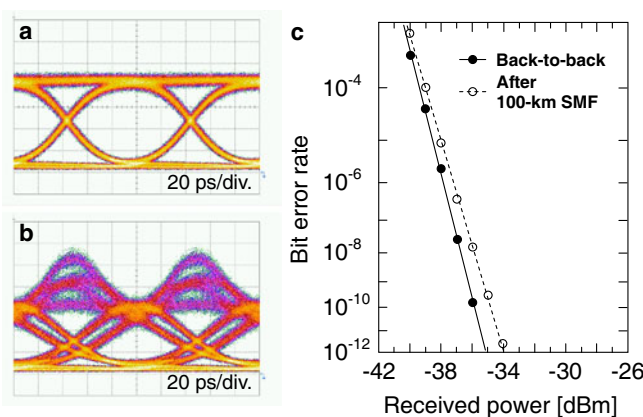


**Fig. 6.26** Eye diagrams of 10 Gbit/s NRZ signal from mini 10G MZI modulator module for back-to-back (a) and after 100 km SMF transmission (b); corresponding bit-error-rate performance (c)

**Fig. 6.27** Tunable transmitter module with InP-MZI modulator. Photograph of module (a), schematic structure (b)

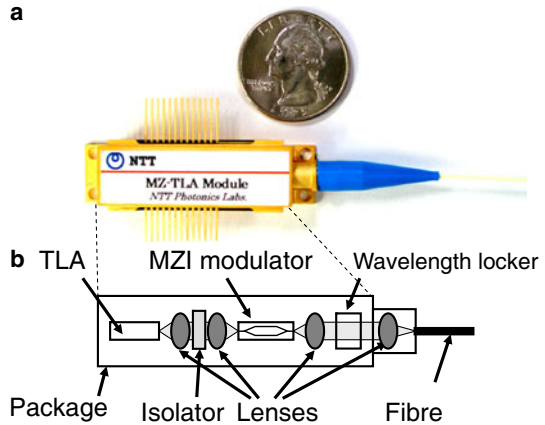


Fig. 6.26c. No error floor can be observed in both cases. The sensitivity degradation after 100 km SMF transmission is measured to be 1.1 dB (@BER =  $10^{-12}$ ).

#### 6.4.2.2 Tunable Transmitter Modules with Semiconductor MZI Modulators

In tunable transmitters and transponders, wavelength tunable laser diodes are used together with MZI modulators. When semiconductor-based MZI modulators are utilized, monolithic [63–65] or hybrid [66–69] integration technologies enable particular compact transmitters, while such compact transmitters cannot be realized with LiNbO<sub>3</sub>-based modulators because the thermal expansion coefficients for semiconductor materials ( $\sim 4.9 \times 10^{-6}/\text{K}$  for InP) and LiNbO<sub>3</sub> ( $\sim 15.0 \times 10^{-6}/\text{K}$ ) are quite different from each other. So laser diodes and LiNbO<sub>3</sub> modulators can not be mounted on the same metal package, whose thermal expansion coefficient is set equal to that of the semiconductor material.

Monolithically integrated, wavelength-tunable transmitters utilize distributed Bragg reflector (DBR) lasers, while those based upon hybrid integration technology have been reported using various sources including a DBR laser [66], a widely tunable DFB laser array (TLA) [67], a tunable laser with external liquid crystal mirror [68], or a DFB laser array with a microelectromechanical system (MEMS) switch [69]. All wavelength tunable transmitters cover the complete C-band. In the following, we will discuss the performance of an example of a compact tunable transmitter module in more detail.

Figure 6.27a illustrates the module with actual package dimensions of 41 mm ( $L$ )  $\times$  13 mm ( $W$ )  $\times$  9 mm ( $H$ ).

The transmitter consists of a widely tunable DFB laser array (TLA) [70, 71] comprising ten DFB lasers hybridly integrated with an InP-MZI modulator and a wavelength locker. This is schematically shown in Fig. 6.27b. The TLA and the MZI modulator are mounted on the same metal carrier and a Peltier cooler. They are cou-

**Fig. 6.28** Output wavelength of the module as a function of TLA temperature

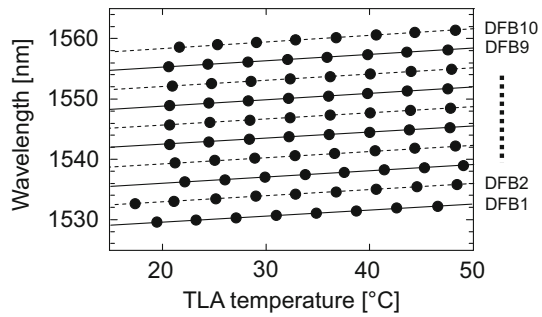
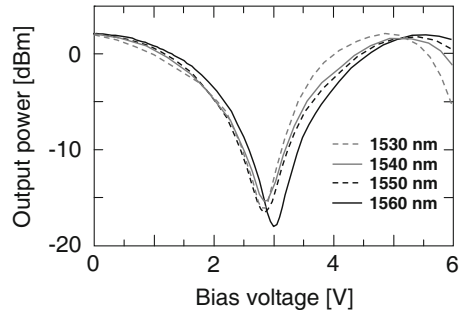


**Fig. 6.29** Extinction characteristics of the module for various output wavelengths



pled by using lenses and include an optical isolator. The modulated output from the MZI modulator is coupled to an optical fiber after passing through the wavelength locker. The wavelength locker has a free-spectral range (FSR) of 50 GHz and assures locking of the output wavelength to any channel of the International Telecommunication Union (ITU) frequency grid defined for wavelength division multiplexing (WDM) systems. The output wavelengths of the transmitter shown can be tuned to 81 channels of the WDM grid with 50 GHz spacing by selecting an appropriate DFB laser for the desired channel from the 10 DFB lasers and setting the TLA chip temperature precisely to the appropriate temperature in the 15 to 50 °C range as shown in Fig. 6.28.

The output power of the module is more than +2 dBm for all channels. Figure 6.29 shows the extinction characteristics of the module for output wavelengths in the range from 1530 to 1560 nm as a function of bias voltage of the MZI modulator. The half-wavelength voltage  $V_{\pi}$  is around 2.5 V for all wavelengths. The module is driven by a 10 Gbit/s NRZ signal with PRBS of  $2^{31} - 1$ . The bias conditions for the MZI modulator have been kept constant during the measurement, even when the output wavelength has been switched. The bias voltages to the MZI modulator's two phase control waveguides were set to  $-3.3$  and  $-2.8$  V, and the driving voltage swing applied to the two waveguides had been fixed to  $0.75$  and  $2.25 V_{p-p}$  for push-pull operation. Under these conditions, the output signal is negatively chirped. Figures 6.30a–d show the eye diagrams for various output wavelengths.

The eyes are clearly open for all wavelengths, even under fixed modulation conditions. Figure 6.30e shows the bit-error-rate performance of the module measured

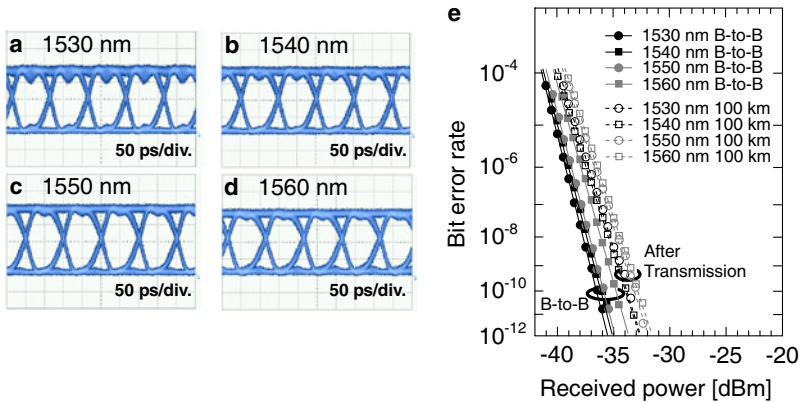


**Fig. 6.30** Eye diagrams of 10 Gbit/s NRZ signals for various output wavelengths (a–d), and corresponding bit-error-rate performance for back-to-back and after 100 km SMF transmission (e). Modulator driving conditions fixed for all wavelength channels

for back-to-back and after 100 km SMF transmission for output wavelengths ranging from 1530 to 1560 nm. No error floors are observed under all conditions. The power penalties resulting from the transmission are less than 3 dB for all wavelength channels.

## 6.5 High Performance Modulators for Advanced Modulation Formats

The maximum transmission distance of standard high-speed digital optical signals is limited by various factors, and one of particular relevance is the chromatic dispersion of the optical fiber (see Sect. 6.1 and also Chap. 2, Sect. 2.2.5). Thus, systems performance is expected to be improved if modulation formats are introduced which are less sensitive to chromatic dispersion. The optical duobinary (ODB) [72–77] format is such a solution. Coherent transmission systems are another option where the information is carried by the optical phase and improvements in sensitivity are expected [78, 79]. It has already been a research topic of high interest in the 1980s and 1990s. Formats that have been investigated include optical phase-shift keying (PSK) and differential phase-shift keying (DPSK) [78, 80–83], differential quadrature phase-shift keying (DQPSK) [84–100] and even multilevel modulation formats such as multi-quadrature amplitude modulation (QAM) [101–105]. A more detailed coverage of advanced modulation formats within the present book is given in Chap. 8 and in a more compact fashion in Chap. 13.

Transmitters for advanced modulation formats must enable optical amplitude and phase modulation as well, and MZI modulators can be used for that purpose. In the following section, various advanced modulation formats and the applicability of semiconductor MZI modulators for their generation will be discussed.



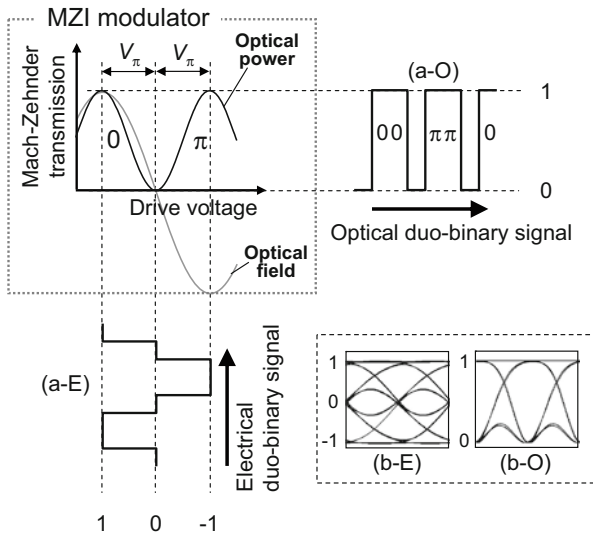


**Fig. 6.31** Principle of optical duobinary signal generation. Duobinary encoded three-level electrical signal (a-E) and generated optical duobinary signal (a-O). Eye diagram of electrical duobinary signal (b-E) and eye diagram of optical duobinary signal (b-O)

### 6.5.1 Optical Duobinary (ODB) Modulation

Optical duobinary (ODB) signals can be generated by using MZI modulators driven with a three-level electrical signal as shown in Fig. 6.31 which is generated by using the sequence shown in Fig. 6.32.

First, a bit sequence with NRZ format (Fig. 6.32a) is precoded using an EXNOR operator. The converted bit sequence (Fig. 6.32b) is then duobinary coded by adding the bit sequence with one bit delay to the original one (Fig. 6.32c). The final duobinary encoded signal has three levels of  $+1$ ,  $0$  and  $-1$ . By comparing the original bit pattern (Fig. 6.32a) with the encoded pattern (Fig. 6.32c), one can see that the absolute value of the encoded signal is equal to the original NRZ signal. When the three-level electrical duobinary encoded signal is applied to an MZI modulator, the bias voltages for the  $+1$ ,  $0$ , and  $-1$  levels are set in such a way that they correspond to the first maximum transmission point, the null point and the second maximum transmission point of the MZI modulator, respectively (see Fig. 6.31). The bias voltage differences from  $+1$  to  $0$  and from  $0$  to  $-1$  are  $V_\pi$ , and thus  $2V_\pi$  total voltage swing is required for using an MZI modulator for ODB modulation. The resulting optical signals are shown in Fig. 6.31 (a-O) and Fig. 6.32d. The phases of the modulated optical signals corresponding to the first ( $+1$ ) and the second ( $-1$ ) maximum transmission points have a phase difference of  $\pi$ . Thus, the ODB signal has the same intensity pattern as the original NRZ signal, but the ‘mark’ signals have two optical phases,  $0$  and  $\pi$ . ODB signals are detectable with conventional NRZ receivers because the intensity modulated bit pattern of the ODB signal (Fig. 6.32d) is identical to that of the corresponding NRZ bit pattern (Fig. 6.32a).

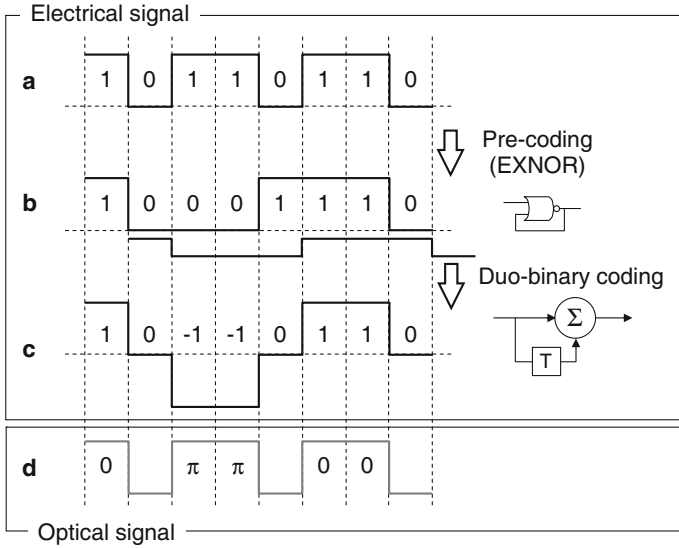


**Fig. 6.32** Principle of duobinary encoding (a–c), and generated optical duobinary signal (d)

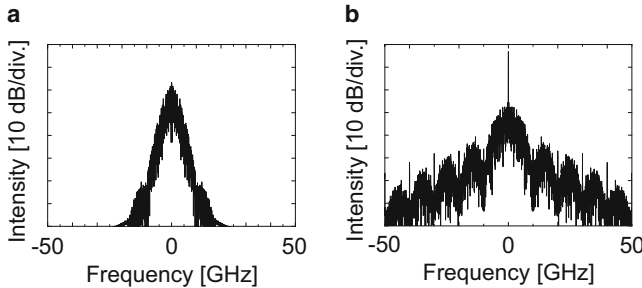


**Fig. 6.33** Calculated optical spectra for 10 Gbit/s optical duobinary signal (a) and 10 Gbit/s NRZ signal (b)

For completeness, eye diagrams for 10 Gbit/s input electrical three-level duobinary (b-E) and corresponding ODB (b-O) signals are also shown in Fig. 6.31. Furthermore, Fig. 6.33a shows the calculated optical spectrum for the 10 Gbit/s ODB signal and as a reference, the calculated optical spectrum for a 10 Gbit/s NRZ signal as well (Fig. 6.33b).

The spectral broadening for the ODB signal is small compared to that of the NRZ signal, and there is no carrier frequency component in the spectrum for the ODB signal. These results clearly indicate that ODB signals are superior to NRZ signals with respect to chromatic dispersion tolerance of an optical fiber.

Differential-drive InP-based MZI modulators are particularly promising for ODB signal generation [62]. They can be operated at low driving voltage, chirp-less modulation can be achieved under differential drive conditions, and the increase

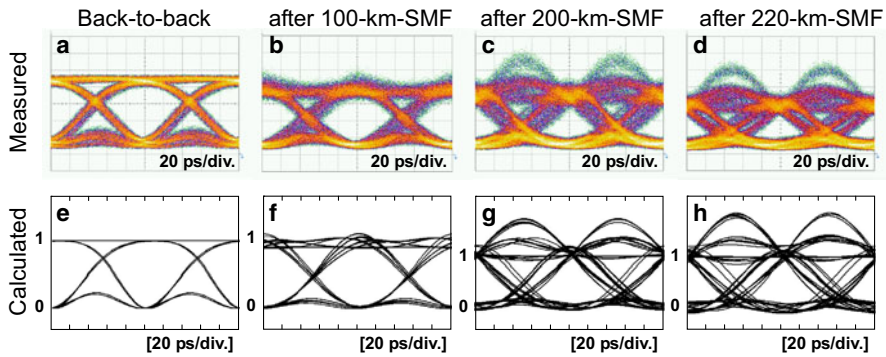
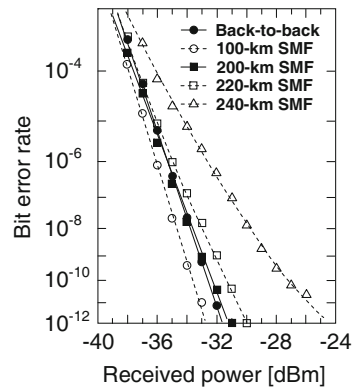


**Fig. 6.34** Measured 10 Gbit/s eye diagrams for generated optical duo-binary signal (a), and after SMF transmission of 100 km (b), 200 km (c), and 220 km (d), respectively. Lower figures are calculated eye diagrams for generated optical duo-binary signal (e), and after SMF transmission of 100 km (f), 200 km (g), and 220 km (h), respectively

**Fig. 6.35** Measured bit-error-rate performance of 10 Gbit/s optical duobinary signal as a function of received power



in transmission loss is negligibly low even if the driving voltage is raised above  $2V_{\pi}$  (see for example Fig. 6.20 and Fig. 6.24). The last feature is important for the generation of ODB signals without waveform distortion because the signals require  $2V_{\pi}$  drive voltage swing. Eye diagrams of 10 Gbit/s ODB signals measured with  $2.3V_{p-p}$  drive voltage swing are shown in Fig. 6.34a.

The large tolerance of ODB signals with respect to chromatic dispersion is illustrated by eye diagrams measured after 100 km, 200 km, and 220 km transmission over standard SMF at 1550 nm operation wavelength as shown in Figs. 6.34a–d. Clear eye openings are observed in all cases. Figures 6.34e–h are the calculated eye diagrams for the ODB signals at back-to-back (Fig. 6.34e), after 100 km (Fig. 6.34f), 200 km (Fig. 6.34g), and 220 km (Fig. 6.34h) SMF transmission. The calculated curves are in good agreement with the measured data Figs. 6.34a–d. These results indicate that the differential-drive InP-MZI modulator does not add any extra chirp nor any additional signal distortion. Figure 6.35 illustrates the measured bit-error-rate performance as a function of received power.

An error floor starts to develop after 240 km SMF transmission while error-free transmission can be achieved up to about 220 km transmission distance. The sensitivity degradation is less than 1.7 dB (@BER =  $10^{-12}$ ), even when the transmission distance is 220 km. These results indicate that the differential-drive InP-MZI modulator is suited as a compact and low drive voltage ODB signal generator.

### 6.5.2 Optical DPSK Modulation

In the optical phase-shift keying (PSK) format, bit information of digital optical signals is carried by optical phases. In coherent PSK systems [78, 80–83], an absolute phase reference is required at the receiver in order to read out the bit information. On the other hand, the optical differential PSK (DPSK) format utilizes the optical phase change to recognize the bit information and uses the phase of the preceding bit as a phase reference. The DPSK format offers several benefits such as low bit-pattern-dependent nonlinear effects, high sensitivity and large tolerance for tight optical filtering.

Optical DPSK signals can be generated by using a phase modulator or an MZI modulator, where the latter option is superior to the former with respect to chirping characteristics and reshaping of the electrical signal [94]. The method to generate DPSK signals by using an MZI modulator will be discussed in the following and Fig. 6.36 illustrates the concept.

The precoded electrical signal (a) in Fig. 6.36, generated by a precoder, is applied to an MZI modulator. The drive voltage swing of the precoded electrical signal is set to twice the half-wavelength voltage ( $2V_{\pi}$ ), while the DC bias is set to the null point of the MZI modulator. Under these conditions, the MZI modulator is operated between the first (phase 0) and the second (phase  $\pi$ ) maximum transmission points, and the output signal of the MZI is the optical DPSK signal as shown in Fig. 6.36b. The intensity dip observed in the optical DPSK signal when the phase changes does not significantly affect the decoded signal at the receiver. The concept illustrated in Fig. 6.36 can also be modified in such a way that an additional intensity modulator is used as a pulse carver so that a return-to-zero (RZ) DPSK signal is generated which is more tolerant to optical fiber nonlinearities [106].

DPSK signal demodulation can be accomplished by using a Mach–Zehnder delay interferometer (MZDI) and a balanced receiver as shown in Fig. 6.37.

The MZDI has an asymmetric MZI structure with one arm of the MZI being longer than the other one, where the time needed by the optical signals to travel the extra length corresponds to exactly one bit. As a consequence, two subsequent bits of the DPSK signal interfere at the output of the MZDI, i.e., the preceding bit acts as a phase reference to demodulate the DPSK encoded optical signal. The MZDI has two output ports and the interfering signals yields a nonzero output in one of these outputs depending on their relative phase. When subsequent bits are in-phase (antiphase), a nonzero optical signal leaves the MZDI from the lower (upper) port as illustrated in Fig. 6.37. (It should be noted that, due to the MZDI's asymmetric

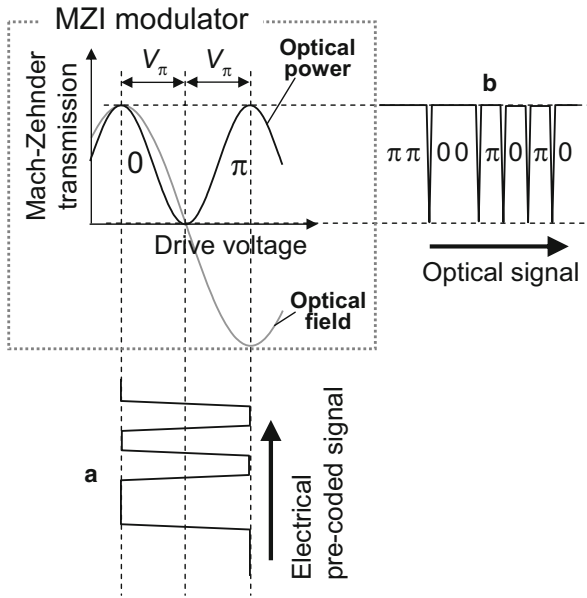


**Fig. 6.36** Principle of optical DPSK signal generation using an MZI modulator. Electrical pre-coded signal (a), generated optical DPSK signal (b)

nature, one can achieve (by precisely controlling the device temperature) that CW light either leaves the MZDI from the cross port or from the through port. The latter is the case for the device shown in Fig. 6.37, and this is different from the behavior of symmetric MZIs (cf. Fig. 6.5).) The output signals are detected by means of a balanced detector, and because the demodulated electrical output signal of the balanced detector is twice as large as for conventional direct detection, a 3 dB sensitivity improvement of the signal-to-noise ratio (SNR) is expected in DPSK systems compared to conventional on-off keying (OOK).

Figure 6.38 compiles the calculated eye diagrams and optical spectra for three modulation formats, NRZ, DPSK, and RZ-DPSK, for 10 Gbit/s. Figures 6.38a, c, e

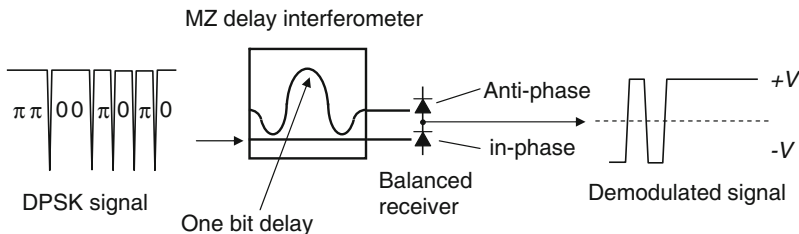


**Fig. 6.37** Principle of demodulation of optical DPSK signal using a Mach-Zehnder delay interferometer and a balanced receiver

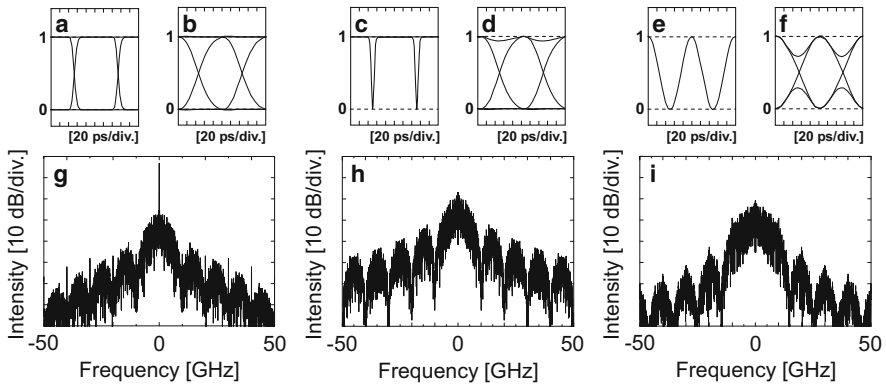


**Fig. 6.38** Calculated 10 Gbit/s eye diagrams and optical spectra for NRZ (a, b, g), optical DPSK (c, d, h), and optical RZ-DPSK signals (e, f, i). Eye diagram of directly detected NRZ signal with a low-pass filter (b). Eye diagrams for generated optical DPSK and RZ-DPSK signals (c, e). Eye diagrams of demodulated DPSK and RZ-DPSK signals with low-pass filter (d, f), and calculated optical spectra for NRZ (g), DPSK (h), and RZ-DPSK signals (i)

are the generated optical waveforms for NRZ, DPSK, and RZ-DPSK formats. The mark ratio is 0.5,  $\sim 1$ , and 0.5 when the original electrical signals have a mark ratio of 0.5. In the diagrams in Figs. 6.38c, e, the optical power is the same for each bit while the optical power of the bits of the NRZ signal (Fig. 6.38a) is random, where the latter is due to the fact that in the case of NRZ signals, bits are easily affected by neighboring bits (pattern effect). Figure 6.38b represents the eye diagram of directly detected NRZ signals using a low-pass filter having a bandwidth of 0.7 times the bit rate. Figures 6.38d, f are the eye diagrams of demodulated DPSK and RZ-DPSK signals with a low-pass filter. Figures 6.38g–i are the calculated optical spectra for NRZ, DPSK and RZ-DPSK signals, and the comparison of Figs. 6.38g, h demonstrates that the carrier frequency component of the spectrum for DPSK (Fig. 6.38h) is well suppressed in contrast to the case of the NRZ-related spectrum (Fig. 6.38g). The carrier frequency component of the RZ-DPSK spectrum (Fig. 6.38i) is also suppressed, but a slight spectral broadening is observed.

Finally, Fig. 6.39 compiles experimental data illustrating the performance of a differential-drive InP-MZI modulator operated in a 40 Gbit/s DPSK system.

Figure 6.39a represents the measured optical spectrum of the 40 Gbit/s DPSK signal. The carrier frequency component is well suppressed. Figures 6.39b, c are the demodulated eye diagram and the bit-error-rate performance, respectively. Clear eye opening can be observed in the demodulated optical signal (Fig. 6.39b), and Fig. 6.39c illustrates that error-free operation can be obtained with 40 Gbit/s DPSK signals generated by a differential-drive InP-MZI modulator, and it clearly demonstrates the potential of MZI modulators in high-speed DPSK systems. Similar results obtained with an InP-based InGaAlAs-InAlAs n-i-n modulator have been reported in [107].

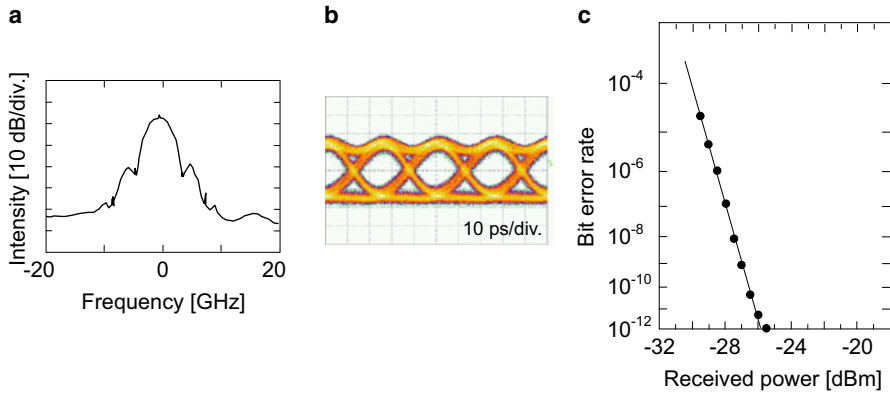


**Fig. 6.39** Measured results for a differential-drive InP-MZI modulator under 40 Gbit/s DPSK operation. Optical spectrum for generated optical DPSK signal (a). Eye diagram for demodulated optical DPSK signal (b) and corresponding bit-error-rate performance (c)

### 6.5.3 Semiconductor Optical DQPSK Modulators

Differential quadrature PSK (DQPSK) is a modulation format slightly more complex than DPSK and the principle can be explained by using the constellation diagrams shown in Fig. 6.40.

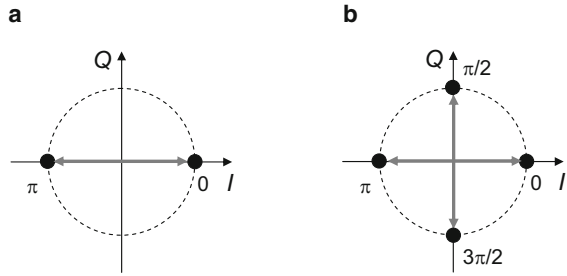
The intensity of all signals is unity, and in the case of DPSK, Fig. 6.40a, there are two possible states corresponding to the phase either being  $0$  or  $\pi$  on the  $I$ -axis. On the other hand, DQPSK signals, Fig. 6.40b, may take four phase values:  $0$  or  $\pi$  on the  $I$ -axis and  $\pi/2$  and  $3\pi/2$  on the  $Q$ -axis to express a two-bit signal. The benefits of the DQPSK modulation format compared with DPSK format are:

1. The symbol rate becomes half compared to that of the DPSK format for the same data rate because the bit rate in the DQPSK format is twice that of the symbol rate
2. Spectral broadening becomes smaller which results in higher chromatic dispersion tolerance and reduction of the bandwidth needed for transmitters and receivers, and
3. An increase in spectral efficiency can also be expected.

As outlined in more detail in Chap. 8, a DQPSK transmitter and a corresponding receiver can be designed as illustrated in Fig. 6.41.

The modulator consists of two parallel sub-MZI modulators and a  $\pi/2$  phase shifter which are arranged in two branches of a Mach-Zehnder interferometer. The input CW light is divided equally into the two branches, both branches are DPSK-modulated by the two sub-MZI modulators (in-phase ( $I$ ) MZI modulator and quadrature-phase ( $Q$ ) MZI modulator), and the  $\pi/2$  phase shifter in the  $Q$ -arm assures that the signal obtained after recombining both branches exhibits four different points in the constellation diagram.

**Fig. 6.40** Signal constellations for a DPSK signal (a) and DQPSK signal (b)



DQPSK signals can be detected by two MZDIs and two balanced receivers as shown at the right side of Fig. 6.41. The phase differences in the delay lines of the two MZDIs are set to  $+\pi/4$  and  $-\pi/4$  [94, 96, 100]. Alternatively, novel  $90^\circ$  hybrids with delay lines are proposed and demonstrated as DQPSK receivers [95, 97–99], see also Chap. 8, Sect. 8.3.2.

Optical DQPSK systems utilize the optical phase, so the spectral linewidth (phase noise) of the CW light sources discussed in [1] affects the performance of the system, and the requirements for the linewidth of the CW light sources are rather demanding as discussed in more detail in [93].

Semiconductor-based DQPSK modulators have been realized on GaAs [108] and InP substrates [109, 110]. The DQPSK modulators correspond to  $I-Q$  modulators with two sub-MZI modulators at the branches of the main MZI [108, 110] or a novel three-arm-interferometer structure with two EAMs [109] where four DQPSK signal phase levels are produced by turning the EAMs on and off. 107 Gbit/s operation is demonstrated by the very compact chip ( $1500\ \mu\text{m} \times 250\ \mu\text{m}$  in size). The drawback of the modulator is its large insertion loss of  $\sim 34\ \text{dB}$  excluding fiber coupling loss. The GaAs/AlGaAs DQPSK modulator reported in [108] uses microwave slow-wave electrodes to achieve wide bandwidth with low driving voltage. The chip is  $52\ \text{mm} \times 3.5\ \text{mm}$  in size and exhibits a half-wavelength voltage  $V_\pi$  of 3.5 V. 10 Gbit/s ( $5\ \text{Gbit/s} \times 2$ ) operation has been demonstrated.

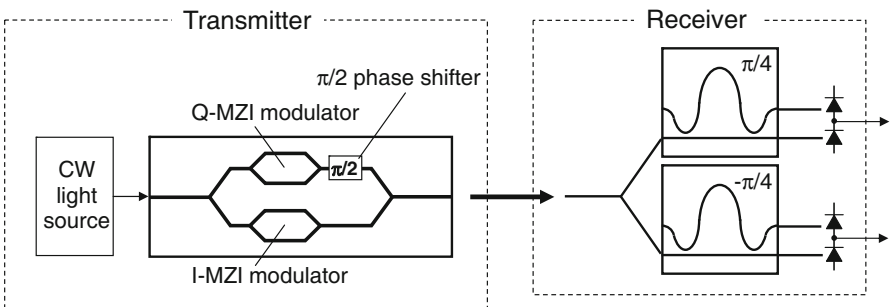


**Fig. 6.41** Conventional optical DQPSK transmitter with a DQPSK modulator and receiver for optical DQPSK signals



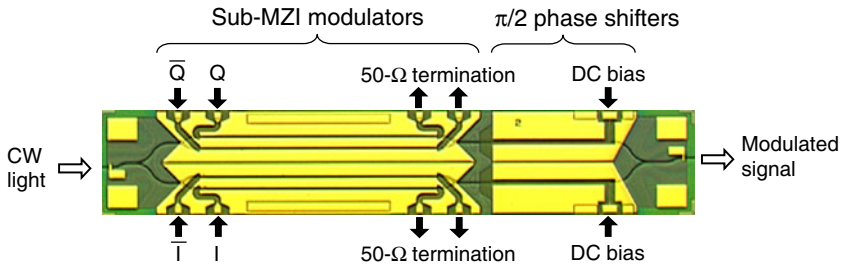
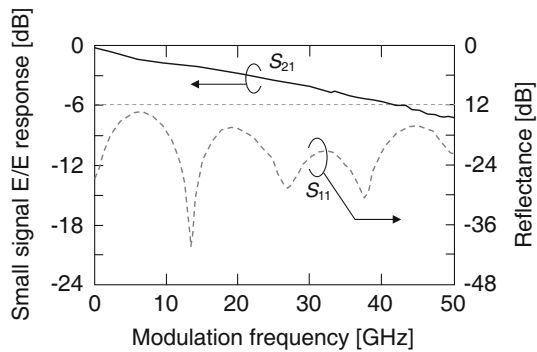


**Fig. 6.42** Photograph of InP-DQPSK modulator chip. The size is 7.5 mm  $\times$  1.3 mm

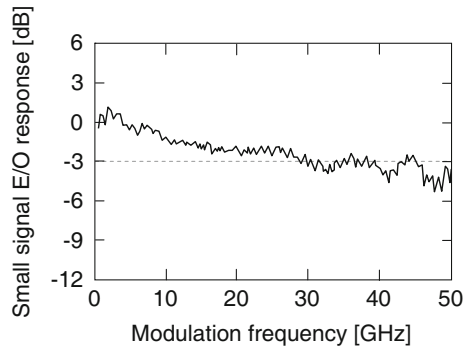
**Fig. 6.43** Small signal E/E response  $S_{21}$  and reflectance  $S_{11}$  of an electrode of the InP-DQPSK modulator



The InP-based DQPSK modulator reported in [110] integrates differential-drive InP-MZI modulators as  $I$  and  $Q$  modulators. The structure is shown in Fig. 6.42.

Two parallel differential-drive InP-MZI modulators (sub-MZI modulators) and two  $\pi/2$  phase shifters are monolithically integrated at the branches of the main Mach-Zehnder interferometer. The two sub-MZI modulators are used for the generation of two optical DPSK signals, and the  $\pi/2$  phase shifters are used to adjust the phase difference of the two DPSK signals to  $\pi/2$ . The length of the phase control waveguides of the sub-MZI modulators is 3 mm, and the length of the  $\pi/2$  phase shifters is 1.5 mm. The chip is only 7.5 mm  $\times$  1.3 mm in size. It is small enough for being installed into a small package such as a conventional 14-pin butterfly package [111] or into compact modules normally used for mounting conventional lasers and having RF connectors in addition to the standard electrical contacts [112]. Moreover, such InP-based n-p-i-n MZ modulators have also been co-packaged with a widely tunable laser into a transmitter module which enabled full C-band 40 Gbit/s DPSK operation [113]. The waveguide in the InP-DQPSK modulator is realized by introducing a novel n-p-i-n structure where a thin p-doped layer (chosen instead of the SI layer in the corresponding n-i-n structure) acts as a potential barrier against electron carriers. For the integration with semiconductor photonic active devices such as laser diodes, this new structure is more suitable than an n-i-n structure. Figure 6.43 shows the small signal E/E response  $S_{21}$  and reflectance  $S_{11}$  of a traveling-wave electrode on the modulator.

**Fig. 6.44** Small signal E/O response of a sub-MZI modulator



The 6 dB E/O bandwidth exceeds 40 GHz, and the reflectance is below  $-14$  dB up to 50 GHz. Figure 6.44 shows the small signal E/O response of the sub-MZI modulator. The 3 dB E/O bandwidth is measured to be 30 GHz. Thus, the modulator is sufficiently fast for 80 Gbit/s ( $40 \text{ Gbit/s} \times 2$ ) operation, and the results also indicate that the sub-MZI modulators in the InP-DQPSK modulator have essentially the same characteristics as solitary differential-drive InP-MZI modulators. 80 Gbit/s optical DQPSK signal generation by using the InP-DQPSK modulator is illustrated in Fig. 6.45.

The  $I$  and  $Q$  modulators are operated at 40 Gbit/s, and the phases of the generated signals are controlled by the  $\pi/2$  phase shifters. Figure 6.45a shows the optical spectrum for an 80 Gbit/s optical DQPSK signal. The carrier frequency component is well suppressed, and the spectrum corresponds quite well to that of the 40 Gbit/s optical DPSK signal shown in Fig. 6.39a. This is a clear indication that the 80 Gbit/s optical DQPSK signal has indeed a large chromatic dispersion tolerance. Figures 6.45b, c are the demodulated eye diagrams of the 80 Gbit/s optical DQPSK signal, obtained by using two MZDIs and balanced receivers. The eyes are clearly open, and these results indicate that the InP-DQPSK modulator has high potential for being utilized in future high-speed, highly functional optical communication systems.

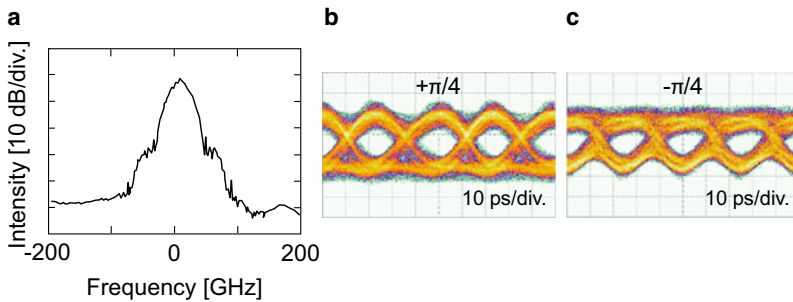


**Fig. 6.45** Measured results of the InP-DQPSK modulator under 80 Gbit/s operation. Optical spectrum of 80 Gbit/s optical DQPSK signal (a), demodulated signals' eye diagrams (b, c)

### 6.5.4 Semiconductor Multilevel Modulators

Multilevel modulation formats are considered as one promising option for improving the spectral efficiency of optical communication systems and raising the total single channel transmission capacity towards 100 Gbit/s and beyond (see also Chap. 8, Sect. 8.1.2). 16 quadrature amplitude modulation (16QAM) is one example which has received specific current interest and corresponding transmitters have already been realized in different ways, including a monolithic dual-drive (DD) InP Mach–Zehnder modulator [114]. The device reported in [114] used an EAM in each of the two arms of the DD MZM as a 6 dB amplitude attenuator and 50 Gbit/s (12.5 Gbaud  $\times$  4 bit) 16QAM signal generation was successfully demonstrated.

## 6.6 Summary and Future Issues

Semiconductor MZI modulators offer a number of advantages such as small size, low driving voltage, and the capability of high-speed operation. Their key properties and recent progress in the development of semiconductor MZI modulators have been described in this chapter. The performance of the semiconductor MZI modulators is expected to improve even further, and they will be deployed in commercial optical communication systems in the near future.

Semiconductor-based MZI modulators can be monolithically integrated with other semiconductor active/passive optoelectronic devices on the same substrate. In this respect, InP-based MZI modulators have an advantage because the laser diodes for optical communication systems are made in the InGaAsP material system using InP substrates (see Chaps. 3–5). Monolithically integrated InP-MZI modulators with tunable lasers are corresponding examples [63–65]. High performance InP-MZI modulators have also been integrated with semiconductor optical amplifiers (SOA) and very promising performance has been demonstrated [115, 116]. Highly functional semiconductor photonic devices will rely on semiconductor MZI modulators and semiconductor phase modulators, and increasingly complex monolithic photonic integrated circuits comprising modulators will be an R&D topic of high relevance in the years to come.

**Acknowledgements** The authors wish to thank Dr. Ken Tsuzuki and Dr. Nobuhiro Kikuchi in the NTT Photonics Laboratories, NTT Corporation for their work on the semiconductor modulators and for their fruitful discussions.

## References

1. C.H. Henry, Theory of the phase noise and power spectrum of a single mode injection laser. *IEEE J. Quantum Electron.* **QE-19**, 1391–1397 (1983)
2. F. Koyama, K. Iga, Frequency chirping in external modulators. *J. Lightw. Technol.* **6**, 87–93 (1988)

3. G.P. Agrawal, *Nonlinear Fiber Optics* (Academic Press, New York, 1989)
4. K. Tharmalingham, Optical absorption in the presence of a uniform field. *Phys. Rev.* **130**, 2204–2206 (1963)
5. B.O. Seraphin, N. Bottoka, Franz–Keldysh effect of the refractive index in semiconductors. *Phys. Rev. A* **139**, 560–565 (1965)
6. D.A.B. Miller, D.S. Chemla, T.C. Damen, A.C. Gossard, W. Wiegmann, T.H. Wood, C.A. Burrus, Electric field dependence of optical absorption near the band gap of quantum-well structures. *Phys. Rev. B* **32**, 1043–1060 (1985)
7. D.A.B. Miller, D.S. Chemla, D.J. Eilenberger, P.W. Smith, A.C. Gossard, W.T. Tsang, Large room-temperature optical nonlinearity in GaAs/Ga<sub>1-x</sub>Al<sub>x</sub>As multiple quantum well structures. *Appl. Phys. Lett.* **41**, 679–681 (1982)
8. D.S. Chemla, D.A.B. Miller, P.W. Smith, A.C. Gossard, W. Wiegmann, Room temperature excitonic nonlinear absorption and refraction in GaAs/AlGaAs multiple quantum well structures. *IEEE J. Quantum Electron.* **QE-20**, 265–275 (1984)
9. D.A.B. Miller, D.S. Chemla, S. Schmitt-Rink, Relation between electroabsorption in bulk semiconductors and in quantum wells: The quantum-confined Franz–Keldysh effect. *Phys. Rev. B* **33**, 6976–6982 (1986)
10. D.A.B. Miller, J.S. Weiner, D.S. Chemla, Electric-field dependence of linear optical properties in quantum well structures: Waveguide electroabsorption and sum rules. *IEEE J. Quantum Electron.* **QE-22**, 1816–1830 (1986)
11. S. Schmitt-Rink, D.S. Chemla, W.H. Knox, D.A.B. Miller, How fast is excitonic electroabsorption. *Opt. Lett.* **15**, 60–62 (1990)
12. D.A.B. Miller, D.S. Chemla, T.C. Damen, A.C. Gossard, W. Wiegmann, T.H. Wood, C.A. Burrus, Electric field dependence of optical absorption near the band gap of quantum-well structures. *Phys. Rev. B* **32**, 1043–1060 (1985)
13. T.H. Wood, C.A. Burrus, D.A.B. Miller, D.S. Chemla, T.C. Damen, A.C. Gossard, W. Wiegmann, High-speed optical modulation with GaAs/AlGaAs quantum wells in a p-i-n diode structure. *Appl. Phys. Lett.* **44**, 16–18 (1994)
14. R. de L. Kronig, On the theory of dispersion of X-rays. *J. Opt. Soc. Am. Rev. Scient. Instrum.* **12**, 547–558 (1926)
15. H.A. Kramers, La diffusion de la lumiere par les atomes. *Atti Cong. Intern. Fisica Como* **2**, 545–557 (1927)
16. F. Devaux, Y. Sorel, J.F. Kerdiles, Chirp measurement and transmission experiment at 10 Gbit/s with Wannier–Stark modulator. *Electron. Lett.* **29**, 814–816 (1993)
17. F. Devaux, Y. Sorel, J.F. Kerdiles, Simple measurement of fiber dispersion and of chirp parameter of intensity modulated light emitter. *J. Lightw. Technol.* **11**, 1937–1940 (1993)
18. Y. Miyazaki, T. Yamatoya, K. Matsumoto, K. Kuramoto, K. Shibata, T. Aoyagi, T. Ishikawa, High-power ultralow-chirp 10-Gb/s electroabsorption modulator integrated laser with ultrashort photocarrier lifetime. *IEEE J. Quantum Electron.* **42**, 357–362 (2006)
19. S. Makino, K. Shinoda, T. Shiota, T. Kitatani, T. Fukamachi, M. Aoki, N. Sasada, K. Naoe, K. Uchida, H. Inoue, Wide temperature (15 °C to 90 °C), 80-km SMF transmission of a 1.55- $\mu$ m, 10-Gbit/s InGaAlAs electroabsorption modulator integrated DFB laser, *Opt. Fiber Commun. Conf. and Nat. Fiber Opt. Eng. Conf. (OFC/NFOEC'07)*, Techn. Digest (Anaheim, CA, USA, 2007), paper OMS1
20. 10 Gbit/s EML (Electroabsorption modulator integrated lasers), SUMITOMO ELECTRIC Device Innovations USA, <http://www.sei-device.com/products/laser/eml-pt.asp>. Accessed March 2012
21. M. Chacinski, U. Westergren, B. Stoltz, R. Driad, R.E. Makon, V. Hurm, J. Rosenzweig, J. Li, A.G. Steffan, Transceiver modules utilizing travelling-wave electro-absorption modulator, *Opt. Fiber Commun. Conf. and Nat. Fiber Opt. Eng. Conf. (OFC/NFOEC'10)*, Techn. Digest (San Diego, CA, USA, 2010), paper OWN4
22. J. Mallari, C. Wei, D. Jin, G. Yu, A. Barklund, E. Miller, P. O'Mathuna, R. Dinu, A. Motafakker-Fard, B. Jalali, 100 Gbps eo polymer modulator product and its characterization using a real-time digitizer, *Opt. Fiber Commun. Conf. and Nat. Fiber Opt. Eng. Conf. (OFC/NFOEC'10)*, Techn. Digest (San Diego, CA, USA, 2010), paper OThU2

23. <http://www.gigoptix.com>
24. R.G. Walker, I. Bennion, A.C. Carter, Low-voltage, 50  $\Omega$ , GaAs/AlGaAs travelling-wave modulator with bandwidth exceeding 25 GHz. *Electron. Lett.* **25**, 1549–1550 (1989)
25. R.G. Walker, High-speed III–V semiconductor intensity modulators. *IEEE J. Quantum Electron.* **27**, 654–667 (1991)
26. J.S. Cites, P.R. Ashley, High-performance Mach–Zehnder modulators in multiple quantum well GaAs/AlGaAs. *J. Lightw. Technol.* **12**, 1167–1173 (1992)
27. N.A.F. Jaeger, Z.K.F. Lee, Slow-wave electrode for use in compound semiconductor electrooptic modulators. *IEEE J. Quantum Electron.* **28**, 1778–1784 (1992)
28. R. Spickermann, N. Dagli, Experimental analysis of millimeter wave coplanar waveguide slow wave structures on GaAs. *IEEE Trans. Microwave Theory and Techniques* **42**, 1918–1924 (1994)
29. S.R. Sakamoto, R. Spickermann, N. Dagli, Narrow gap coplanar slow wave electrode for travelling wave electro-optic modulators. *Electron. Lett.* **31**, 1183–1185 (1995)
30. R. Spickermann, N. Dagli, M.G. Peters, GaAs/AlGaAs electro-optic modulator with bandwidth > 40 GHz. *Electron. Lett.* **31**, 915–916 (1995)
31. N.A.F. Jaeger, F. Rahmatian, H. Kato, R. James, E. Berolo, Z.K.F. Lee, Velocity-matched electrodes for compound semiconductor traveling-wave electrooptic modulators: Experimental results. *IEEE Microwave and Guided Wave Lett.* **6**, 82–84 (1996)
32. R. Spickermann, M.G. Peters, N. Dagli, A polarization independent GaAs–AlGaAs electrooptic modulator. *IEEE J. Quantum Electron.* **32**, 764–769 (1996)
33. R. Spickermann, S.R. Sakamoto, M.G. Peters, N. Dagli, GaAs/AlGaAs travelling wave electro-optic modulator with an electrical bandwidth > 40 GHz. *Electron. Lett.* **32**, 1095–1096 (1996)
34. H.R. Khazaei, E. Berolo, F. Ghannouchi, High-speed slow-wave coplanar strip GaAs/AlGaAs electro-optic laser modulator. *Microw. Opt. Technol. Lett.* **19**, 184–186 (1998)
35. L. Mörl, C. Bornholdt, D. Hoffmann, K. Matzen, G.G. Mekonnen, F.W. Reier, A travelling wave electrode Mach–Zehnder 40 Gb/s demultiplexer based on strain compensated GaInAs/AlInAs tunnelling barrier MQW structure, *Proc. 10th Internat. Conf. Indium Phosphide Relat. Mater.* (IPRM'98), Tsukuba, Japan, WA3–4
36. Y. Cui, P. Berini, Modeling and design of GaAs traveling-wave electrooptic modulators based on capacitively loaded coplanar strips. *J. Lightw. Technol.* **24**, 544–554 (2006)
37. C. Rolland, R.S. Moore, F. Shepherd, G. Hiller, 10 Gbit/s, 1.56  $\mu\text{m}$  multiquantum well InP/InGaAsP Mach–Zehnder optical modulator. *Electron. Lett.* **29**, 471–472 (1993)
38. M. Fetterman, C.-P. Chao, S.R. Forrest, Fabrication and analysis of high-contrast InGaAsP–InP Mach–Zehnder modulators for use at 1.55- $\mu\text{m}$  wavelength. *IEEE Photon. Technol. Lett.* **8**, 69–71 (1996)
39. D.M. Adams, C. Rolland, N. Puetz, R.S. Moore, F.R. Shepherd, H.B. Kim, S. Bradshaw, Mach–Zehnder modulator integrated with a gain-coupled DFB laser for 10 Gbit/s, 100 km NDSF transmission at 1.55  $\mu\text{m}$ . *Electron. Lett.* **32**, 485–486 (1996)
40. O. Leclerc, C. Duchet, P. Brindel, M. Goix, E. Grard, E. Maunand, E. Desurvire, Polarisation-independent InP push-pull Mach–Zehnder modulator for 20 Gbit/s soliton regeneration. *Electron. Lett.* **34**, 1011–1013 (1998)
41. S. Akiyama, S. Hirose, T. Watanabe, M. Ueda, S. Sekiguchi, N. Morii, T. Yamamoto, A. Kuramata, H. Soda, Novel InP-based Mach–Zehnder modulator for 40 Gb/s integrated light-wave source, *Proc. 18th IEEE Internat. Semicond. Laser Conf. (ISLC'02)*, Garmisch, Germany (2002), pp. 57–58
42. K. Tsuzuki, T. Ishibashi, T. Ito, S. Oku, Y. Shibata, R. Iga, Y. Kondo, Y. Tohmori, 40 Gbit/s n-i-n InP Mach–Zehnder modulator with a  $\pi$  voltage of 2.2 V. *Electron. Lett.* **39**, 1464–1466 (2003)
43. I. Betty, M.G. Boudreau, R.A. Griffin, A. Feckes, An empirical model for high yield manufacturing of 10 Gb/s negative chirp InP Mach–Zehnder modulators, *Opt. Fiber Commun. Conf. (OFC'05)*, Techn. Digest (Anaheim, CA, USA, 2005), paper OWE5

44. S. Akiyama, H. Itoh, T. Takeuchi, A. Kuramata, T. Yamamoto, Low-chirp 10 Gbit/s InP-based Mach-Zehnder modulator driven by 1.2 V single electrical signal. *Electron. Lett.* **41**, 40–41 (2005)
45. C.H. Henry, R.A. Logan, K.A. Bertness, Spectral dependence of the change in refractive index due to carrier injection in GaAs lasers. *J. Appl. Phys.* **52**, 4457–4461 (1981)
46. B.R. Bennett, R.A. Soref, J.A. del Alamo, Carrier-induced change in refractive index of InP, GaAs, and InGaAsP. *IEEE J. Quantum Electron.* **26**, 113–122 (1990)
47. H.C. Casey, Jr., M.B. Panish, *Heterostructure Lasers* (Academic Press, New York, 1978)
48. H.M. Nussenzveig, *Causality and Dispersion Relations* (Academic Press, New York, 1972)
49. T. Hiroshima, R. Lang, Well size dependence of Stark shifts for heavy-hole and light-hole levels in GaAs/AlGaAs quantum wells. *Appl. Phys. Lett.* **49**, 639–641 (1986)
50. S. Namba, Electro-optical effect of zincblends. *J. Opt. Soc. Am.* **51**, 76–79 (1961)
51. J.F. Nye, *Physical Properties of Crystals* (Oxford University Press, New York, 1975)
52. A. Yariv, P. Yeh, *Optical Waves in Crystals* (Wiley, New York, 1984)
53. C.H. Henry, R.A. Logan, H. Temkin, F.R. Merritt, Absorption, emission, and gain spectra of 1.3  $\mu\text{m}$  InGaAsP quaternary lasers. *IEEE J. Quantum Electron.* **QE-19**, 947–952 (1983)
54. H.C. Casey, Jr., P.L. Carter, Variation of intervalence band absorption with hole concentration in p-type InP. *Appl. Phys. Lett.* **44**, 82–83 (1984)
55. B.C. Wadell, *Transmission Line Design Handbook* (Artec House, Norwood, 1991)
56. Y.-J. Chiu, T.-H. Wu, W.-C. Cheng, F.J. Lin, J.E. Bowers, Enhanced performance in traveling-wave electroabsorption modulators based on undercut-etching the active-region. *IEEE Photon. Technol. Lett.* **17**, 2065–2067 (2005)
57. H. Fukano, T. Yamanaka, M. Tamura, Design and fabrication of low-driving-voltage electroabsorption modulators operating at 40 Gb/s. *J. Lightw. Technol.* **25**, 1961–1969 (2007)
58. HFSS™ – Simulation software for high-performance electronic design, Ansoft Corp., <http://www.ansoft.com/products/hf/hfss/>. Accessed March, 2012
59. L.B. Soldano, E.C.M. Pennings, Optical multi-mode interference devices based on self-imaging: Principles and applications. *J. Lightw. Technol.* **13**, 615–627 (1995)
60. K. Tsuzuki, K. Sano, N. Kikuchi, N. Kashio, E. Yamada, Y. Shibata, T. Ishibashi, M. Tokumitsu, H. Yasaka, 0.3  $V_{pp}$  single-drive push-pull InP Mach-Zehnder modulator module for 43-Gbit/s systems, *Opt. Fiber Commun. Conf. (OFC'06)*, Techn. Digest (Anaheim, CA, USA, 2006), paper OWC2
61. K. Tsuzuki, H. Kikuchi, E. Yamada, H. Yasaka, T. Ishibashi, 1.3- $V_{pp}$  push-pull drive InP Mach-Zehnder modulator module for 40 Gbit/s operation, *Proc. 31st Europ. Conf. Opt. Commun. (ECOC'05)*, Glasgow, UK (2005), vol. 4, paper Th2.6.3, pp. 905–906
62. K. Tsuzuki, N. Kikuchi, Y. Shibata, W. Kobayashi, H. Yasaka, Surface mountable 10-Gb/s InP Mach-Zehnder modulator module for SFF transponder. *IEEE Photon. Technol. Lett.* **20**, 54–56 (2008)
63. Y.A. Akulova, G.A. Fish, P. Koh, P. Kozodoy, M. Larson, C. Schow, E. Hall, H. Marchand, P. Abraham, L.A. Coldren, 10 Gb/s Mach-Zehnder modulator integrated with widely-tunable sampled grating DBR Laser, *Opt. Fiber Commun. Conf. (OFC'04)*, Techn. Digest (Los Angeles, CA, USA, 2004), paper TuE4
64. A. Tauke-Pedretti, M.N. Sysak, J.S. Barton, J.W. Raring, L. Johansson, L.A. Coldren, 40-Gb/s series-push-pull Mach-Zehnder transmitter on a dual-quantum-well integration platform. *IEEE Photon. Technol. Lett.* **18**, 1922–1924 (2006)
65. C-band tunable 10 Gb/s transmitter, S7500, <http://ignis.com/products/tuneable-lasers/s7500/>, <http://www.finisar.com/products/optical-components/Tunable-Lasers/S7500>. Accessed March, 2012
66. R.A. Griffin, B. Pugh, J. Fraser, I.B. Betty, K. Anderson, G. Busico, C. Edge, T. Simmons, Compact, high power, MQW InP Mach-Zehnder transmitters with full-band tunability for 10 Gb/s DWDM, *Proc. 31st Europ. Conf. Opt. Commun. (ECOC'05)*, Glasgow, UK (2005), vol. 4, paper Th2.6.2, pp. 903–904
67. K. Tsuzuki, N. Kikuchi, H. Sanjoh, Y. Shibata, K. Kasaya, H. Oohashi, H. Ishii, K. Kato, Y. Tohmori, H. Yasaka, Compact wavelength tunable laser module integrated with n-i-n structure Mach-Zehnder modulator, *Proc. 32nd Europ. Conf. Opt. Commun. (ECOC'06)*, Cannes, France (2006), paper Tu3.4.3, pp. 79–80

68. M.L. Nielsen, K. Tsuruoka, T. Kato, T. Morimoto, S. Sudo, T. Okamoto, K. Mizutani, K. Sato, K. Kudo, Demonstration of 10-Gb/s C+L-band InP-based Mach-Zehnder modulator. *IEEE Photon. Technol. Lett.* **20**, 1270–1272 (2008)
69. Low profile 10 Gb/s tunable transmitter engine, Santur TLMZ-LP, [http://www.neophotonics.com/products/product\\_131.aspx](http://www.neophotonics.com/products/product_131.aspx). Accessed March, 2012
70. H. Oohashi, Y. Shibata, H. Ishii, Y. Kawaguchi, Y. Kondo, Y. Yoshikuni, Y. Tohmori, 46.9-nm wavelength-selectable arrayed DFB lasers with integrated MMI coupler and SOA, *Proc. 13rd Internat. Conf. Indium Phosphide Relat. Mater. (IPRM'01)*, Nara, Japan (2001), pp. 575–578, paper FB1–2
71. H. Oohashi, H. Ishii, K. Kasaya, Widely tunable DFB laser array (TLA), *Proc. Internat. Conf. Optical Internet and Next Gen. Network (COIN-NGNCON'06)*, Jeju, Korea (2006), pp. 286–288, paper TuB1–2
72. M. Rocks, Calculation of duobinary transmission systems with optical waveguides. *IEEE Trans. Commun.* **30**, 2464–2470 (1982)
73. S. Kuwano, K. Yonenaga, K. Iwashita, 10 Gbit/s repeaterless transmission experiment of optical duobinary modulated signal. *Electron. Lett.* **31**, 1359–1361 (1995)
74. X. Gu, S.J. Dodds, L.C. Blank, D.M. Spirit, S.J. Pycoc, A.D. Ellis, Duobinary technique for dispersion reduction in high capacity optical systems – modelling, experiment and field trial. *IEE Proc. Optoelectron.* **143**, 228–236 (1996)
75. K. Yonenaga, S. Kuwano, Dispersion-tolerant optical transmission system using duobinary transmitter and binary receiver. *J. Lightw. Technol.* **15**, 1530–1537 (1997)
76. M. Shtaif, A.H. Gnauck, The relation between optical duobinary modulation and spectral efficiency in WDM Systems. *IEEE Photon. Technol. Lett.* **11**, 712–714 (1999)
77. Y. Miyamoto, K. Yonenaga, A. Hirano, H. Toba, K. Murata, H. Miyazawa, 100 GHz-spaced  $8 \times 43$  Gbit/s DWDM unrepeaters transmission over 163 km using duobinary-carrier-suppressed return-to-zero format. *Electron. Lett.* **37**, 1395–1396 (2001)
78. R.A. Linke, B.L. Kasper, N.A. Olsson, R.C. Alferness, Coherent lightwave transmission over 150 km fiber lengths at 400 Mb/s and 1 Gb/s data rates using phase modulation. *Electron. Lett.* **22**, 30–31 (1986)
79. K. Emura, S. Yamazaki, S. Fujita, I. Mito, K. Minemura, Over 300 km transmission experiment on an optical FSK heterodyne dual filter detection system. *Electron. Lett.* **22**, 1096–1097 (1986)
80. A.H. Gnauck, R.A. Linke, B.L. Kasper, K.J. Pollock, K.C. Reichmann, R. Valenzuela, R.C. Alferness, Coherent lightwave transmission at 2 Gbit/s over 170 km of optical fibre using phase modulation. *Electron. Lett.* **23**, 286–287 (1987)
81. S. Yamazaki, S. Murata, K. Komatsu, Y. Koizumi, S. Fujita, K. Emura, 1.2 Gbit/s optical DPSK heterodyne detection transmission system using monolithic external-cavity DFB LDs. *Electron. Lett.* **23**, 860–862 (1987)
82. T. Chikama, T. Naitou, H. Onaka, T. Kiyonaga, S. Watanabe, M. Suyama, M. Seino, H. Kuwahara, 1.2 Gbit/s, 201 km optical DPSK heterodyne transmission experiment using a compact, stable external fiber cavity DFB laser module. *Electron. Lett.* **24**, 636–637 (1988)
83. T. Chikama, S. Watanabe, T. Naito, H. Onaka, T. Kiyonaga, Y. Onoda, H. Miyata, M. Suyama, M. Seino, H. Kuwahara, Modulation and demodulation techniques in optical heterodyne PSK transmission system. *J. Lightw. Technol.* **8**, 309–322 (1990)
84. H. Kim, P.J. Winzer, Robustness to laser frequency offset in direct-detection DPSK and DQPSK systems. *J. Lightw. Technol.* **21**, 1887–1891 (2003)
85. M. Serbay, C. Wree, W. Rosenkranz, Implementation of differential precoder for high-speed optical DQPSK transmission. *Electron. Lett.* **40**, 1288–1289 (2004)
86. Y. Han, G. Li, Impact of RZ pulse carver phase errors on optical DQPSK, *Opt. Fiber Commun. Conf. (OFC'05)*, Techn. Digest (Anaheim, CA, USA, 2005), paper OThO4
87. I. Morita, N. Yoshikane, Merits of DQPSK for ultrahigh capacity transmission, *Proc. 18th Annual Meeting of the IEEE Lasers & Electro-Optics Society (LEOS'05)*, Sydney, Australia (2005), paper WE5

88. H.G. Weber, S. Ferber, M. Kroh, C. Schmidt-Langhorst, R. Ludwig, V. Marembert, C. Boerner, F. Futami, S. Watanabe, C. Schubert, Single channel 1.28 Tbit/s and 2.56 Tbit/s DQPSK transmission. *Electron. Lett.* **42**, 178–179 (2006)
89. A. Sano, H. Masuda, Y. Kisaka, S. Aisawa, E. Yoshida, Y. Miyamoto, M. Koga, K. Hagimoto, T. Yamada, T. Furuta, H. Fukuyama, 14-Tb/s (140 × 111-Gb/s PDM/WDM) CSRZ-DQPSK transmission over 160 km using 7-THz bandwidth extended L-band EDFAs, *Proc. 32nd Europ. Conf. Opt. Commun.* (ECOC'06), Cannes, France (2006), paper Th4.1.1
90. A.H. Gnauck, P.J. Winzer, L.L. Buhl, T. Kawanishi, T. Sakamoto, M. Izutsu, K. Higuma, 12.3-Tb/s C-band DQPSK transmission at 3.2 b/s/Hz spectral efficiency, *Proc. 32nd Europ. Conf. Opt. Commun.* (ECOC'06), Cannes, France (2006), paper Th4.1.2
91. C. Fürst, J.-P. Elbers, M. Camera, H. Wernz, H. Griesser, S. Herbst, F. Cavaliere, A. Ehrhardt, D. Breuer, D. Frizsche, S. Vorbeck, M. Schneiders, W. Weiershausen, R. Leppla, J. Wendler, M. Schrödel, T. Wuth, C. Fludger, T. Duthel, B. Milivojevic, C. Schullien, 43 Gb/s RZ-DQPSK DWDM field trial over 1047 km with mixed 43 Gb/s and 10.7 Gb/s channels at 50 and 100 GHz channel spacing, *Proc. 32nd Europ. Conf. Opt. Commun.* (ECOC'06), Cannes, France (2006), paper Th4.1.4
92. A.H. Gnauck, G. Charlet, P. Tran, P.J. Winzer, C.R. Doerr, J.C. Centanni, E.C. Burrows, T. Kawanishi, T. Sakamoto, K. Higuma, 25.6-Tb/s WDM transmission of polarization-multiplexed RZ-DQPSK signals. *J. Lightw. Technol.* **26**, 79–84 (2008)
93. S. Savory, A. Hadjifotiou, Laser linewidth requirements for optical DQPSK systems. *IEEE Photon. Technol. Lett.* **16**, 930–932 (2004)
94. A.H. Gnauck, P.J. Winzer, Optical phase-shift-keyed transmission. *J. Lightw. Technol.* **23**, 115–130 (2005)
95. C.R. Doerr, D.M. Gill, A.H. Gnauck, L.L. Buhl, P.J. Winzer, M.A. Cappuzzo, A. Wong-Foy, E.Y. Chen, L.T. Gomez, Monolithic demodulator for 40-Gb/s DQPSK using a star coupler. *J. Lightw. Technol.* **24**, 171–174 (2006)
96. G. Bosco, P. Poggiolini, On the joint effect of receiver impairments on direct-detection DQPSK systems. *J. Lightw. Technol.* **24**, 1323–1333 (2006)
97. C.R. Doerr, L. Zhang, S. Chandrasekhar, L.L. Buhl, Monolithic DQPSK receiver in InP with low polarization sensitivity. *IEEE Photon. Technol. Lett.* **19**, 1765–1767 (2007)
98. M. Oguma, Y. Nasu, H. Takahashi, H. Kawakami, E. Yoshida, Single MZI-based 1 × 4 DQPSK demodulator, *Proc. 33rd Europ. Conf. Opt. Commun.* (ECOC'07), Berlin, Germany (2007), paper 10.3.4
99. H. Kawakami, E. Yoshida, Y. Miyamoto, M. Oguma, T. Itoh, Simple phase offset monitoring technique for 43 Gbit/s optical DQPSK receiver. *Electron. Lett.* **44**, 437–438 (2008)
100. I. Lyubomirsky, C.-C. Chien, Y.-H. Wang, Optical DQPSK receiver with enhanced dispersion tolerance. *IEEE Photon. Technol. Lett.* **20**, 511–513 (2008)
101. N. Chand, L. Bakker, D. van Veen, R.D. Yadavish, Significant performance advantage of electroabsorption modulator integrated distributed feedback laser (EML) transmitter in transporting multicarrier QAM signals. *J. Lightw. Technol.* **19**, 1462–1468 (2001)
102. M. Ohm, J. Speidel, Quaternary optical ASK-DPSK and receivers with direct detection. *IEEE Photon. Technol. Lett.* **15**, 159–161 (2003)
103. X. Liu, X. Wei, Y.-H. Kao, J. Leuthold, C.R. Doerr, Y. Su, L.F. Mollenauer, Return-to-zero quaternary differential-phase amplitude-shift-keying for long-haul transmission, *Opt. Fiber Commun. Conf. (OFC'04)*, Techn. Digest (Los Angeles, CA, USA, 2004), paper FN2
104. K. Sekine, N. Kikuchi, S. Sasaki, S. Hayase, C. Hasegawa, T. Sugawara, 40 Gbit/s, 16-ary (4 bit/symbol) optical modulation/demodulation scheme. *Electron. Lett.* **41**, 430–432 (2005)
105. M. Yoshida, H. Goto, K. Kasai, M. Nakazawa, 64 and 128 coherent QAM optical transmission over 150 km using frequency-stabilized laser and heterodyne PLL detection. *Opt. Express* **16**, 829–840 (2008)
106. J.-X. Cai, C.R. Davidson, D.G. Foursa, L. Liu, Y. Cai, B. Bakhshi, G. Mohs, W.W. Patterson, P.C. Corbett, A.J. Lucero, W. Anderson, H. Li, M. Nissov, A.N. Pillpetskii, N.S. Bergano, Experimental comparison of the RZ-DPSK and NRZ-DPSK modulation formats, *Opt. Fiber Commun. Conf. (OFC'05)*, Techn. Digest (Anaheim, CA, USA, 2005), paper OThO1



107. Y. Shibata, N. Kikuchi, K. Tsuzuki, W. Kobayashi, H. Yasaka, 40 Gbit/s DPSK modulation using an InGaAlAs-InAlAs MQW n-i-n Mach-Zehnder modulator. *Electron. Lett.* **44**, 1269–1271 (2008)
108. R.A. Griffin, Integrated DQPSK transmitters, *Opt. Fiber Commun. Conf. (OFC'05)*, Techn. Digest (Anaheim, CA, USA, 2005), paper OWE3
109. C.R. Doerr, L. Zhang, P.J. Winzer, J.H. Sinsky, A.L. Adamiecki, N.J. Sauer, G. Raybon, Compact high-speed InP DQPSK modulator. *IEEE Photon. Technol. Lett.* **19**, 1184–1186 (2007)
110. N. Kikuchi, H. Sanjoh, Y. Shibata, K. Tsuzuki, T. Sato, E. Yamada, T. Ishibashi, H. Yasaka, 80-Gbit/s InP DQPSK modulator with an n-p-i-n structure, *Proc. 33rd Europ. Conf. Opt. Commun. (ECOC'07)*, Berlin, Germany (2007), paper 10.3.1
111. N. Kikuchi, K. Tsuzuki, Y. Shibata, M. Ishikawa, T. Yasui, H. Ishii, H. Oohashi, T. Ishibashi, T. Akeyoshi, H. Yasaka, F. Kano, Full L-band 40-Gbit/s operation of compact InP-DQPSK modulator module with low constant driving voltage of  $3.5 V_{pp}$ , *Proc. 34th Europ. Conf. Opt. Commun. (ECOC'08)*, Brussels, Belgium (2008), paper Mo.3.C.4
112. N. Kikuchi, K. Tsuzuki, T. Kurosaki, Y. Shibata, H. Yasaka, High-speed, low-driving voltage dual-drive InP-based Mach-Zehnder modulator. *IEICE Trans. Electron.* **E92-C**, 205–211 (2009)
113. E. Yamada, A. Ohki, N. Kikuchi, Y. Shibata, T. Yasui, K. Watanabe, H. Ishii, R. Iga, H. Oohashi, Full C-band 40-Gbit/s DPSK tunable transmitter module developed by hybrid integration of tunable laser and InP n-p-i-n Mach-Zehnder modulator, *Opt. Fiber Commun. Conf. and Nat. Fiber Opt. Eng. Conf. (OFC/NFOEC'10)*, Techn. Digest (San Diego, CA, USA, 2010), paper OWU4
114. E. Yamada, Y. Shibata, K. Watanabe, T. Yasui, A. Ohki, H. Mawatari, S. Kanazawa, R. Iga, H. Ishii, Demonstration of 50 Gbit/s 16QAM signal generation by novel 16QAM generation method using a dual-drive InP Mach-Zehnder modulator, *Opt. Fiber Commun. Conf. and Nat. Fiber Opt. Eng. Conf. (OFC/NFOEC'11)*, Techn. Digest (Los Angeles, CA, USA, 2011), paper OMU1
115. T. Yasui, Y. Shibata, K. Tsuzuki, N. Kikuchi, M. Ishikawa, Y. Kawaguchi, M. Arai, H. Yasaka, 10-Gb/s 100-km SMF transmission using InP Mach-Zehnder modulator monolithically integrated with semiconductor optical amplifier. *IEEE Photon. Technol. Lett.* **20**, 1178–1180 (2008)
116. T. Yasui, Y. Shibata, N. Kikuchi, K. Tsuzuki, Y. Kawaguchi, M. Arai, H. Yasaka, 10-Gbit/s optical duobinary transmission using lossless InP n-p-i-n Mach-Zehnder modulator with semiconductor optical amplifier, *Proc. 20th Internat. Conf. Indium Phosphide Relat. Mater. (IPRM'08)*, Versailles, France (2008), paper ThA1.2

# Chapter 7

## Photodetectors

Andreas Beling and Joe C. Campbell

**Abstract** The chapter provides an overview of recent research on photodetectors for fiber optic communication systems. Following an introduction on basic properties (responsivity, bandwidth, noise) and material systems, photodiode structures including p-i-n photodiode (PD), metal–semiconductor–metal (MSM) photodetector and low-noise avalanche PD (APD) are discussed. The third section focuses on the design and performance of high-speed photodetectors and covers uni-traveling carrier (UTC) PDs, waveguide PDs, traveling wave photodetectors, and integrated photoreceivers.

### 7.1 Introduction

In optical communication systems semiconductor photodetectors are used for the optoelectronic conversion of the modulated light signal into the electrical domain. This chapter focuses on junction photodiodes including p-i-n and avalanche photodiodes (APD) and metal–semiconductor–metal (MSM) photodetectors. The basic concepts of the light receiving process as well as advanced high-speed photodetector types are introduced.

#### 7.1.1 Fundamentals

The light absorption process in a semiconductor photodetector for photogeneration of electron–hole pairs is based on the internal photoelectric effect and requires the

---

Andreas Beling (✉) · Joe C. Campbell  
Department of Electrical & Computer Engineering, University of Virginia, 351 McCormick Road,  
PO Box 400743, Charlottesville, VA 22904, USA  
e-mail: ab3pj@virginia.edu, jccuva@virginia.edu

photon energy  $h\nu$  to be at least equal to the bandgap energy  $E_g$  of the absorber material. Only then is the available energy of one photon sufficient to excite an electron from the valence band to the conduction band leaving a hole in the valence band. For this band-to-band transition, the upper wavelength limit for photon absorption is given by:

$$\lambda_g [\mu\text{m}] = \frac{1.24}{E_g [\text{eV}]} \quad (7.1)$$

Under the influence of an electric field, that is established by an applied bias voltage, electrons and holes are swept across the absorber which results in a flow of photocurrent in the external circuit [1]. The external quantum efficiency  $\eta_{\text{ext}}$  quantifies the ability of the photodiode (PD) to transform light into an electrical current and is defined as the number of charge carrier pairs generated per incident photon:

$$\eta_{\text{ext}} = \frac{I_{\text{pd}} h\nu}{q P_{\text{opt}}}, \quad (7.2)$$

where  $I_{\text{pd}}$  is the photogenerated current by the absorption of the optical input power  $P_{\text{opt}}$  at frequency  $\nu$ , and  $q$  is the elementary charge ( $1.602 \times 10^{-19}$  C). Ideally  $\eta_{\text{ext}} = 1$ , that is each photon generates one electron hole pair. However, it will be shown below that in practice photodiodes usually exhibit  $\eta_{\text{ext}} < 1$  because of several effects including finite absorber thickness, carrier recombination, optical reflections and coupling losses. A common figure of merit is the responsivity  $R_{\text{pd}}$ , defined as the ratio of photocurrent to optical input power. On the basis of (7.2) we write:

$$R_{\text{pd}} = \frac{I_{\text{pd}}}{P_{\text{opt}}} = \frac{\eta_{\text{ext}} \lambda [\mu\text{m}]}{1.24} \frac{\text{A}}{\text{W}}. \quad (7.3)$$

Using (7.3),  $\eta_{\text{ext}} = 1$  and a wavelength of  $\lambda = 1.55 \mu\text{m}$  we find that the maximum achievable responsivity is  $R_{\text{pd}} = R_{\text{ideal}} = 1.25 \text{ A/W}$ . Whenever  $R_{\text{pd}}$  depends on the state of polarization of the incoming light, the definition of the polarization-dependent loss (PDL) is useful:

$$\text{PDL} = 10 \log \left( \frac{R_{\text{max}}}{R_{\text{min}}} \right) [\text{dB}]. \quad (7.4)$$

Here,  $R_{\text{max}}$  and  $R_{\text{min}}$  are the maximum and minimum responsivities for all states of polarization.

In telecommunication systems photodiodes are required to detect optical signals modulated at high data rates. Thus, another important figure of merit is the opto-electrical 3 dB bandwidth, which is defined as the frequency range from DC to the cut-off frequency  $f_{3\text{dB}}$ . The latter is the frequency at which the electrical output power has dropped by 3 dB below the power value at very low frequency. The resistance-capacitance (RC) time constant and the carrier transit times are the two crucial bandwidth limitations of a photodiode. Considering the RC-effect, Fig. 7.1

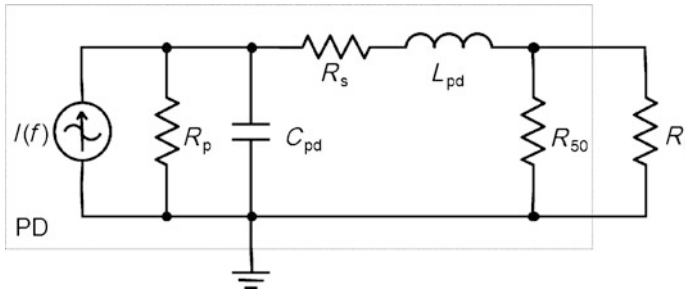


**Fig. 7.1** Equivalent circuit of a lumped-element photodetector

shows a simple equivalent circuit of a lumped-element photodetector for which the device length is much shorter than the electrical signal wavelength.

The photodiode is described as an ideal current source  $I(f)$  in parallel with the junction capacitance,  $C_{pd}$ , and resistance,  $R_p$ , and a series resistance,  $R_s$ .  $R_l$  is the external load resistor and is usually  $50 \Omega$ . In order to achieve a matched transition to the load impedance,  $R_l$ , an optional termination resistor,  $R_{50}$  ( $= 50 \Omega$ ), may be implemented close to the photodiode. Thus, the effective load is reduced to  $25 \Omega$ , but at the expense of losing half the output current. In most cases the parallel leakage current is small compared to the photocurrent and therefore  $R_p$  becomes very high and can be omitted. The inductance  $L_{pd}$  may originate from electrical interconnections or air bridges. It is usually in the pH-range and can be neglected in photodetectors with bandwidths up to 20 GHz. With these simplifications the RC-limited 3 dB cut-off frequency is calculated from the equivalent circuit as

$$f_{RC} = \frac{1}{2\pi R_{eff} C_{pd}} \quad (7.5)$$

with  $R_{eff} = R_s + R_l R_{50} / (R_l + R_{50})$ .

The second bandwidth constraint is the carrier transit time, which is the time a photogenerated electron or hole takes to travel through the active region prior to being collected by the contacts. Assuming uniform photogeneration in an absorber with thickness  $d_{abs}$ , the transit time-limited bandwidth can be well estimated using [2]:

$$f_t \approx \frac{3.5\bar{v}}{2\pi d_{abs}}, \quad (7.6)$$

where  $\bar{v}$  is the averaged carrier velocity. The resulting 3 dB bandwidth is given by the expression:

$$f_{3dB} \approx \sqrt{\frac{1}{\frac{1}{f_{RC}^2} + \frac{1}{f_t^2}}}. \quad (7.7)$$

Taking the product of the bandwidth (7.7) and quantum efficiency (7.2) one can define the bandwidth-efficiency product in units of GHz. As will be shown in the

following paragraphs, the bandwidth-efficiency product of photodiodes is generally limited.

In the absence of light the photodiode's dark or leakage current dominates. Generally several effects contribute to the dark current with their actual magnitudes depending on the bias voltage, material properties and detector design. The current that is common to all junction diodes is the diffusion current. However, in most photodiodes the diffusion current is considerably smaller than the generation current [3, 4], which originates in the depleted absorption layer from impurities within the bandgap and can be reduced by improving material quality. Additionally, tunneling and impact ionization currents can be observed once the electric field exceeds 100 kV/cm. While the tunneling current is generally undesirable, impact ionization can be used to provide an internal gain mechanism to amplify the photocurrent. Photodiodes that exploit impact ionization effects are referred to as avalanche photodiodes (APD) and will be discussed in Sect. 7.2.3.

Photocurrent and dark current generate shot noise, which, together with thermal noise, degrades the sensitivity of the photodiode. Shot noise accompanies any generated current within a photodetector and is related to the statistical nature of the carrier transport and the photon detection process. The mean square noise current of shot noise for a photodiode is given by

$$\langle i_{\text{shot}}^2 \rangle = 2q(I_{\text{pd}} + I_{\text{d}})\Delta f. \quad (7.8)$$

$I_{\text{pd}}$  is the photocurrent,  $I_{\text{d}}$  the dark current, and  $\Delta f$  is the bandwidth.

The thermal noise or Johnson noise is due to the thermal motion of electrons in conductors and is generated in all resistances of the photodiode. The mean square thermal noise current of a resistor  $R$  for a given bandwidth  $\Delta f$  is given by the expression

$$\langle i_{\text{th}}^2 \rangle = \frac{4kT\Delta f}{R}, \quad (7.9)$$

where  $k$  is Boltzmann's constant and  $T$  is the temperature. It is worth noting that  $\langle i_{\text{th}}^2 \rangle$  does not depend on the photocurrent and dark current whereas  $\langle i_{\text{shot}}^2 \rangle$  does. Since shot noise and thermal noise are uncorrelated, the total noise is found from adding individual noise contributions as sums of squares. Once the total noise in a photodiode is known, the signal-to-noise ratio, SNR, can be determined. The electrical SNR is defined as the ratio of signal power to noise power and can be computed for a given average photocurrent,  $I_{\text{pd}}$ , using the relation

$$\text{SNR} = \frac{I_{\text{pd}}^2}{\langle i_{\text{shot}}^2 \rangle + \langle i_{\text{th}}^2 \rangle} \quad (7.10)$$

which assumes that the power varies as the square of the current.

An important measure in digital communication systems is the bit-error rate (BER) given by the probability of false identification of a bit by the decision circuit in the receiver. The decision circuit compares the sampled signal to a reference

value, the decision threshold. If the signal is greater than the decision threshold, it indicates that a “1” was detected, otherwise a “0.” As in binary systems there are only two possible signal levels, that for a “1,”  $I_1$ , and that for a “0,”  $I_0$ . Each of these signal levels may have a different average noise associated with it. In order to calculate the overall probability of a bit error, the SNRs of both signal levels have to be taken into account which leads to the definition of the  $Q$ -factor:

$$Q = \frac{I_1 - I_0}{\sqrt{\langle i_1^2 \rangle} + \sqrt{\langle i_0^2 \rangle}}. \quad (7.11)$$

In this expression  $I_1$ ,  $I_0$ , and  $\langle i_1^2 \rangle$ ,  $\langle i_0^2 \rangle$  are the photocurrents and the Gaussian mean square noise currents associated with the received bits “1” and “0,” respectively. Assuming a constant but optimum threshold level in the decision circuit, the BER is related to the  $Q$ -factor by the following equation:

$$\text{BER} = \frac{1}{2} \operatorname{erfc} \left( \frac{Q}{\sqrt{2}} \right) \approx \frac{\exp(-Q^2/2)}{Q\sqrt{2\pi}}, \quad (7.12)$$

where  $\operatorname{erfc}$  represents the complementary error function. The approximate form of (7.12) is accurate for  $Q > 3$ . A bit-error rate of  $10^{-12}$  or a  $Q$ -factor of 7 corresponds to a probability of  $1 : 10^{12}$  that a bit is identified incorrectly and is commonly called “error-free” reception (see also Chap. 1, Sect. 1.2.6).

The receiver sensitivity is a common figure in optical communication systems. It is the minimum received average optical power  $P_{\text{rec}}$  that is necessary to achieve error-free detection at a given bitrate. Considering on-off modulated signals with optical power  $P_1$  and  $P_0$  in bits “1” and “0,” respectively, the average power is  $0.5(P_1 + P_0)$ . Here we consider a more general case, that is  $P_0 \neq 0$ . The fact that some optical power is received during “0” bits is common to most fiber links and is quantified by the extinction ratio,  $r_e = P_0/P_1$ . Using (7.3) and (7.11), the receiver sensitivity can be approximated as:

$$P_{\text{rec}} = \left( \frac{1 + r_e}{1 - r_e} \right) \frac{Q}{2R} \left( \sqrt{\langle i_1^2 \rangle} + \sqrt{\langle i_0^2 \rangle} \right) \approx \left( \frac{1 + r_e}{1 - r_e} \right) \frac{Q}{R} \sqrt{\langle i_{\text{th}}^2 \rangle}, \quad (7.13)$$

where shot noise from  $I_{\text{pd}}$  and  $I_{\text{d}}$  has been neglected.

It should be noted, that the sensitivity is usually used to characterize the entire optical frontend including photodiode and electrical amplifiers. This requires modification of (7.13) in order to include noise contributions from the amplifier. Similarly, if the receiver contains an optical pre-amplifier, the amplifier’s noise figure has to be taken into account. In this case  $P_{\text{rec}}$  is typically referred to the optical power before amplification.

The ultimate detection limit of an ideal receiver (i.e., no thermal noise, no dark current, 100 % quantum efficiency, and  $r_e = 0$ ) is given by the quantum limit. Assuming an ideal receiver, the sensitivity for a BER of  $10^{-12}$  is given by [5]:

$$P_{\text{min}}^* \approx 13.5 \cdot h\nu \cdot B, \quad (7.14)$$

where  $h\nu$  is the photon energy,  $B$  is the bitrate, and 13.5 is the average number of photons per bit. For example, at a bitrate of 40 Gbit/s and an optical signal wavelength of 1.55  $\mu\text{m}$ , the quantum limited sensitivity  $P_{\text{min}}^*$  is  $-42$  dBm.

Noise contributions from the receiver components and, ultimately, the quantum noise limit the performance of an optical frontend at very low optical input powers. Conversely, at very high optical input powers the detection capability is restricted by saturation effects in the photodiode or the amplifier circuitry. It is worth noting that operating photodiodes at high photocurrent levels offers distinct advantages. High receiver sensitivity at 40 Gbit/s has been achieved by increasing the incident optical power with Er-doped fiber amplifiers [6, 7] and semiconductor optical amplifiers (SOA) [8] to the extent that the voltage swing at the output of the photodiode can directly drive digital decision circuits without any electrical post-amplification. In analog applications high-output photocurrent levels help to minimize the noise figure and hence increase the dynamic range [9, 10]. However, there are several physical mechanisms that impact saturation in photodiodes, including space-charge screening [11, 12], and thermal [11, 13] effects. The thermal limit is determined by the heat dissipation characteristics of the constituent semiconductor layers, the photodiode geometry, and by the heat sink design. Joule heating can result in temperatures as high as 500  $^{\circ}\text{C}$  in the depletion region [14], which can cause device thermal and/or electrical failure. The space charge effect has its origin in the spatial distribution of the photogenerated carriers as they transit the depletion layer. At high current densities, as electrons and holes travel in opposite directions, an internal space-charge field is generated that opposes the bias electric field. For sufficiently high optical input power levels, the space-charge-induced electric field can be strong enough to make the bias electric field collapse, which will result in reduced carrier drift velocities, longer transit times, and hence radio frequency (RF) photocurrent compression [15]. When large output photocurrent is delivered to the load, the voltage drop across the load and the device series resistance can effectively remove the available voltage bias from the depletion region and thus negatively impact the photodiode saturation. A measure of the photodiode saturation is the saturation current which is defined as the average photocurrent at which the electrical output power at the cut-off frequency deviates by  $-1$  dB from an ideal current-power relation at the load resistor.

### 7.1.2 Material Systems

The appropriate material system for photodiodes is determined, to a great extent, by the application and depends on system parameters including the signal wavelength, the signal bandwidth, and noise requirements. In high-speed long-haul fiber-optic links the required material system for photodetectors is determined by the characteristics of today's optical silica fibers with the spectral windows at 1.3  $\mu\text{m}$  and 1.55  $\mu\text{m}$  wavelength. This constraint narrows the selection to InGaAs, Ge, or other absorber materials with similar bandgaps. The III-V group direct-bandgap semicon-

ductor InP with its lattice-matched compound semiconductors (InGaAs, InGaAsP, InGaAlAs) is currently thought to be the most appropriate material system for the fabrication of high-performance optoelectronic devices. Varying compositions of the alloys allow the bandgap to be varied between 0.75 eV (1.65  $\mu\text{m}$ ) and 1.35 eV (0.92  $\mu\text{m}$ ). The relevant lattice-matched ternary composite is  $\text{In}_{0.53}\text{Ga}_{0.47}\text{As}$ , which exhibits an absorption coefficient of  $7000\text{ cm}^{-1}$  at 1.55  $\mu\text{m}$  wavelength [16]. Thus, the material system allows a composition of highly absorbing and transparent layers at telecommunication wavelengths. An important property that significantly impacts the speed of the photodiode is the saturation drift velocity of electrons and holes. For InGaAs values of  $6.5 \times 10^6\text{ cm/s}$  and  $4.8 \times 10^6\text{ cm/s}$  for electrons and holes, respectively, have been reported [17]. Much higher electron drift velocities can be achieved in both InGaAs and InP when velocity overshoot effects are exploited at lower electric fields [18–20]. Another advantage of the InP material system arises from the potential for monolithic integration. To date monolithic integration of all active and passive optical functions and electronic devices has been demonstrated. Hence, InP is the leading platform for photonic integrated circuits (PICs) and optoelectronic integrated circuits (OEICs) which have the potential to enhance performance, reduce footprint, and decrease packaging costs of complex photonic devices [21–24]. Because of the steady progress in the field of components and manufacturing, even large-scale PICs have reached sufficient reliability for deployment in optical networks [25, 26].

It should be noted, however, that Ge and Si-Ge-based photodetectors have recently drawn attention as they have become promising alternatives to InGaAs-based high-speed detectors for 1.55  $\mu\text{m}$  detection. Since Ge can be grown on silicon substrate, this approach promises large-scale monolithic integration of photodiodes with Si receiver electronic circuits using mature CMOS technology [27–29]. Although Ge has an indirect bandgap, responsivities as high as 1 A/W have been demonstrated on 40 GHz devices with selectively re-grown Ge [30]. In system applications that are not limited by fiber dispersion and attenuation (e.g., short reach and free-space links) the signal wavelengths can be shorter (e.g., 850 nm) and thus other materials such as GaAs or Si may be successfully deployed.

## 7.2 Photodiode Types

### 7.2.1 *p-i-n Photodiode*

In order to achieve a high optoelectronic conversion efficiency and high bandwidth the p-i-n photodiode is widely used. The p-i-n PD consists of an intrinsic absorber, sandwiched between highly doped  $n^+$ - and  $p^+$ -layers which give rise to a space charge region. Compared to a simple p-n-junction, this design allows for a lower junction capacitance and provides an additional degree of freedom in designing the thickness of the depleted high-field region. In contrast to a homojunction PD where



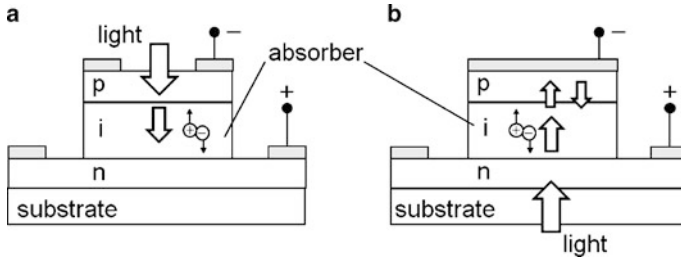


**Fig. 7.2** Top (a) and back (b) illuminated p-i-n photodiode

the p-, i- and n-layers have the same bandgap, a heterostructure p-i-n PD potentially provides higher speed as slow diffusion photocurrents arising from carriers generated in undepleted material are suppressed. In this design the contact layers exhibit bandgap energies higher than the photon energy and are consequently transparent at the operation wavelength. In order to avoid slow carrier trapping effects at the heterojunction interfaces, grading of the bandgap can be employed to smooth the discontinuities in the band structure [31].

A schematic of a top-illuminated p-i-n photodiode is shown in Fig. 7.2a; this simple structure has become a standard commercial product.

For high-speed operation the device is reverse biased by an externally applied voltage to completely deplete the absorber and create an electric field to facilitate carrier transport. Once an electron-hole pair is created, the carriers drift at their saturation velocities in opposite directions toward the electrodes and contribute to the photocurrent. The device responsivity can be written as

$$R_{\text{pd}} = R_{\text{ideal}} (1 - R_0) (1 - e^{-\alpha d_{\text{abs}}}), \quad (7.15)$$

where  $\alpha$  is the absorption coefficient,  $d_{\text{abs}}$  is the absorber thickness, and  $R_0$  is the reflectance at the air-semiconductor interface. Assuming negligible carrier trapping at energy band discontinuities the bandwidth is well approximated by (7.7).

It is well known that for this device structure there is a performance trade-off between quantum efficiency and bandwidth associated with the thickness of the absorber region. A thicker absorption layer provides higher quantum efficiency and this also results in longer carrier transit time which reduces the bandwidth. A second bandwidth constraint is due to the photodiode RC time constant. Since the resistance is usually governed by the fixed load resistor ( $50 \Omega$ ), reducing the RC time constant is achieved by decreasing the device capacitance. In a p-i-n photodiode this can be achieved by minimizing the active junction area ( $C_{\text{pd}} \sim A$ ) and maximizing the depleted absorber thickness ( $C_{\text{pd}} \sim d^{-1}$ ), which, in turn, results in longer transit times. As a result of these considerations, the bandwidth-efficiency-product of normal-incidence p-i-n photodiodes is limited to approximately 20 GHz [32], which enables operation up to 40 Gbit/s. However, because of device miniaturization, integration of matching circuits on chip and improvements in the vertical layer structure, several very high-speed vertically illuminated p-i-n photodiodes with ac-

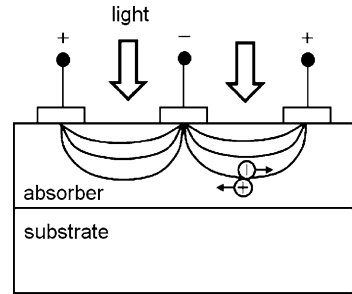
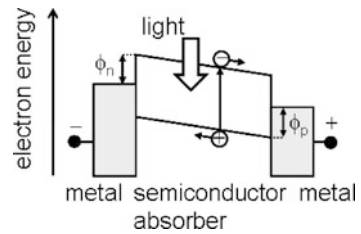
ceptable quantum efficiencies have been demonstrated. Wey et al. achieved a 3 dB bandwidth of 110 GHz with a back-illuminated p-i-n PD [31]. Even though a thin absorber (200 nm) was employed, the external quantum efficiency was 30 % as an enhanced efficiency was obtained by “double pass” of the light from the top electrode (Fig. 7.2b). To increase the RC-bandwidth limitation a matched resistor ( $50 \Omega$ ) was integrated on chip. Hence, the effective load was reduced to  $25 \Omega$ , however, since the resistor forms a current divider with the load, half the output current was lost which resulted in a 6 dB reduction in output power at low frequencies. If a reduced spectral width can be accepted, the resonant cavity enhanced (RCE) photodetector represents another solution. With the integration of mirrors at the top and bottom of the structure multipass absorption can be achieved, leading to doubled quantum efficiency as reported in [33].

### 7.2.2 Metal–semiconductor–metal Photodetector

A metal–semiconductor–metal (MSM) photodetector consists of an undoped semiconductor absorption layer on which two interdigitated metal electrodes have been deposited. Hence, it can be basically described as two Schottky diodes connected back-to-back. For operation a voltage has to be applied to the electrodes to completely deplete the absorber and generate an electric field within the absorber (Fig. 7.3).

Since one of the diodes is in reverse bias while the other is forward biased, the MSM detector exhibits symmetric current-voltage and capacitance-voltage characteristics. Figure 7.4 shows the simplified band structure of an MSM detector under bias condition.

Because of the Schottky barriers,  $\Phi_n$  and  $\Phi_p$ , formed at the metal–semiconductor interfaces, carriers are prevented from entering the semiconductor from the metal contacts which lowers the dark current. This is in contrast to photoconductors which consist of Ohmic metal–semiconductor contacts. Under illumination photogenerated carriers drift to the electrodes and contribute to the photocurrent. Compared to p-i-n PDs this type of planar photodetector generally exhibits lower capacitance, a simple fabrication process, and is well suited for monolithic integration with metal semiconductor field effect transistors (MESFET). However, the responsivity of top-illuminated MSM photodetectors is significantly lower compared to p-i-n PDs due to shadowing of the electrode fingers. This issue has been addressed by using either semitransparent electrodes made, for example, from cadmium tin oxide [34] or thin metal [35], or by back-illumination [36, 37]. Using back-illumination through the substrate, the responsivity can be at least doubled [37]. Similar to p-i-n photodiodes the bandwidth of an MSM photodetector is generally governed by RC- and carrier transit time effects. Since the MSM PD has lower capacitance per unit area compared to PDs based on p-n junctions, its bandwidth is usually determined by carrier transit times. Although the optical radiation propagates perpendicular to the direction of the charge carrier transport (Fig. 7.3), the MSM PD suffers from a trade-off

**Fig. 7.3** MSM photodetector**Fig. 7.4** Schematic band diagram of MSM PD

between quantum efficiency and bandwidth: In order to increase the quantum efficiency of a front-illuminated MSM detector the absorber has to be made thicker and the electrode finger spacing needs to be enlarged, which, in turn, leads to an increase in carrier transit times and hence lower bandwidth. Back-illuminated MSM photodetectors are even more adversely affected by longer transit times since the carriers are predominantly generated further away from the high electric field regions near the top electrodes. Compared to their front-illuminated counterparts they achieve lower bandwidths. In some cases the bandwidth reduction is as great as 50 % [37].

In the last two decades, high-performance GaAs-based MSM photodetectors operating in the 0.85  $\mu\text{m}$  wavelength window have been extensively studied. Owing to their large Schottky barrier of 0.7 eV, these MSM photodetectors have achieved low dark currents and high speed [38]. Monolithically integrated optical receivers consisting of MSM photodetectors and GaAs MESFET or AlGaAs/GaAs HEMT amplifiers suitable for the detection of data rates up to 20 Gbit/s have been reported [39]. For operation at the longer telecommunication wavelengths MSM photodetectors with a narrow-bandgap InGaAs absorber are required. However, as the Schottky barrier height of undoped InGaAs is only 0.2 eV, the direct deposition of the electrode on the InGaAs results in unacceptably large leakage currents at low bias voltage. To solve this problem a thin undoped barrier-enhancement layer (GaAs, InAlAs, or InP) has been introduced between the electrode and the absorption layer [40]. Since the resulting bandgap discontinuity may be responsible for some performance degradation due to charge pile-up at the interface, additional compositionally graded layers or a graded superlattice region have been placed between the hetero-interfaces to improve device performance [41].

Because of the low capacitance of the MSM structure very large area detectors with notable bandwidth have been reported. In [42] a  $350 \times 350 \mu\text{m}^2$  MSM detector with 0.4 A/W responsivity and 900 MHz bandwidth has been achieved. A  $1 \times 1 \text{mm}^2$  area MSM photodetector with 1.02 A/W responsivity at 1.53  $\mu\text{m}$  wavelength and 210 MHz bandwidth was reported in [43]. To reduce carrier transit times and thus achieve higher speed the electrode finger widths and gaps were further downscaled into the sub-micron range. By applying direct electron beam lithography, front-illuminated InGaAs MSM photodetectors with 0.2  $\mu\text{m}$  feature size finger electrodes with 70 GHz bandwidth have been demonstrated [44].

Similar to the p-i-n photodiode the MSM photodetector suffers from the space charge effect under high optical input power. However, because of the nonuniform electrical field in the absorber, MSM photodetectors tend to saturate at an earlier stage compared to p-i-n PDs [45].

### 7.2.3 Avalanche Photodiodes

Unlike the previously described photodiode structures, the avalanche photodiode (APD) can achieve substantially better sensitivity due to an internal gain mechanism. In an APD the photogenerated carriers are accelerated in a high-field drift region to such an extent that they generate new electron–hole pairs by impact ionization. Thus, a single photon is able to produce multiple electron–hole pairs. The multiplication factor  $M$  quantifies the photocurrent enhancement and is typically between 10 and 100 for fiber optic receivers. Although APDs require more complex epitaxial wafer structures and bias circuits, they have been successfully deployed in optical receivers that operate up to 10 Gbit/s. Because of their gain APDs provide higher sensitivity in optical receivers (PD + amplifier) than p-i-n photodiodes [46–49]. This advantage, however, applies only to thermal-noise-limited receivers since the gain mechanism is accompanied by an excess noise, which depends on the carrier multiplication statistics. The excess noise also affects the speed of an APD through the avalanche build-up time, which gives rise to the gain-bandwidth product of an APD.

The multiplication region of an APD plays a critical role in determining its performance, specifically the gain, the multiplication noise, and the gain-bandwidth product. According to McIntyre’s local-field avalanche theory [50–52], both the noise and the gain-bandwidth product of APDs are determined by the electron,  $\alpha$ , and hole,  $\beta$ , ionization coefficients of the semiconductor in the multiplication region, or more specifically, the ionization coefficient ratio,  $k = \beta/\alpha$  if  $\beta < \alpha$  and  $k = \alpha/\beta$  if  $\beta > \alpha$ . The shot noise current for mean gain  $M$  is given by

$$\langle i_{\text{shot,APD}}^2 \rangle = 2qM^2(I_{\text{pd}} + I_{\text{d}})F(M)\Delta f, \quad (7.16)$$

where  $F(M)$  is the excess noise factor, which arises from the random nature of impact ionization. Under the conditions of uniform electric fields and injection of

the carrier with the highest ionization coefficient, the excess noise factor is:

$$F(M) = kM + (1 - k) \left( 2 - \frac{1}{M} \right). \quad (7.17)$$

Equation (7.17) has been derived under the condition that the ionization coefficients are in local equilibrium with the electric field, hence, the designation “local field” model. This model assumes that the ionization coefficients at a specific position are determined solely by the electric field at that position. It is clear from (7.17) that lower noise is achieved when  $k \ll 1$ . The gain-bandwidth product results from the time required for the avalanche process to build up or decay; the higher the gain, the higher the associated time constant and, thus, the lower the bandwidth. Emmons [53] has shown that the frequency-dependent gain can be approximated by the expression

$$M(2\pi f) = \frac{M_0}{\sqrt{1 + (2\pi f M_0 k \tau)^2}}, \quad (7.18)$$

where  $M_0$  is the DC gain and  $\tau$  is approximately (within a factor of  $\sim 2$ ) the carrier transit time across the multiplication region. It follows from this expression that for  $M_0 > \alpha/\beta$  the frequency response is characterized by a constant gain bandwidth-product that increases as  $k$  decreases. There are three documented methods to achieve low excess noise in an avalanche photodiode. The best-known approach is to select a material with low-noise characteristics such as Si [54–57] that has  $k \ll 1$ . Si APDs were widely used in first-generation optical fiber communication systems, which operated in the wavelength range 800 to 900 nm [58]. However, at long wavelengths tunneling at the high electric fields required for impact ionization in InGaAs homojunctions [59, 60] led to the development of separate absorption and multiplication (SAM) APD structures [61]. In these APDs the p-n junction and thus the high-field multiplication region is located in a wide bandgap semiconductor such as InP where tunneling is insignificant and absorption occurs in an adjacent InGaAs layer. By properly controlling the charge density in the multiplication layer, it is possible to maintain a high enough electric field to achieve good avalanche gain while keeping the field low enough to minimize tunneling and impact ionization in the InGaAs absorber. However, the frequency response of SAM APDs, as originally implemented, was very poor owing to accumulation of photogenerated holes at the absorption/multiplication heterojunction interface [62]. To eliminate the slow release of trapped holes a transition region consisting of one or more latticed-matched, intermediate-bandgap InGaAsP layers was introduced [63, 64]. A second modification to the original SAM APD structure has been the inclusion of a high-low doping profile in the multiplication region [65–67]. In this structure the wide-bandgap multiplication region consists of a lightly doped layer where the field is high and an adjacent, doped charge layer or field control region. This type of APD, which is frequently referred to as the SACM structure with the “C” representing the charge layer, decouples the thickness of the multiplication region from the charge density constraint in the SAM APD.

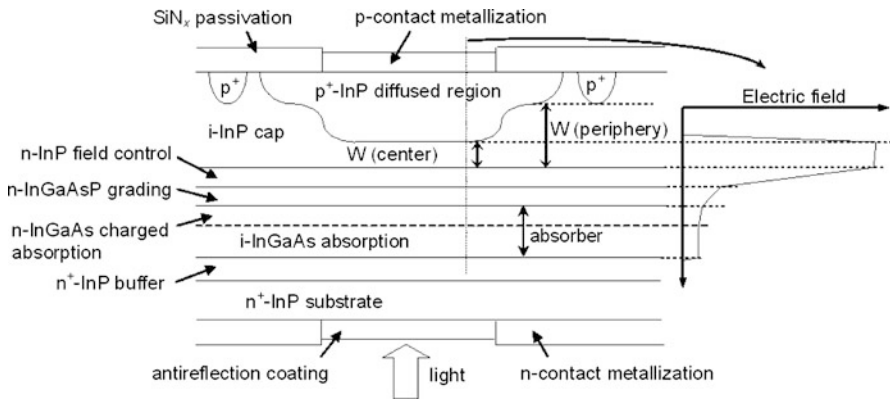
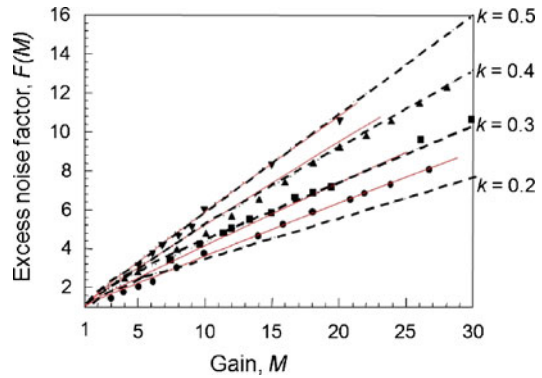


**Fig. 7.5** Schematic cross section of InP/InGaAsP/InGaAs SACM APD with double-diffused floating guard ring configuration [68]

Most of the initial work on InP/InGaAsP/InGaAs SAM and SACM APDs utilized mesa structures because of their fabrication simplicity and reproducibility. However, the consensus that planar structures can effectively suppress edge breakdown spurred the development of this type of APD. Figure 7.5 shows a schematic cross section of an InP/InGaAsP/InGaAs SACM APD with a double diffused floating guard ring [68]. The adjacent graph shows the electric field profile normal to the surface and illustrates how the charge layer is used to tailor the relative fields in the multiplication and absorption layers.

Low excess noise and high gain-bandwidth product have also been achieved by submicron scaling of the thickness of the multiplication region,  $w_m$ . This is somewhat counterintuitive since it appears to contradict the local field model. As  $w_m$  is reduced, in order to maintain the same gain, the electric field intensity must increase in order to reduce the distance between ionization events. However, for high electric fields the electron and hole ionization coefficients tend to merge so that  $k$  approaches unity. Consequently, based on the excess noise expression in (7.17), higher excess noise would be expected for the same gain. However, in contrast to the basic assumption of the local-field model, it is well known that impact ionization is nonlocal in that carriers injected into the high field region are “cool” and require a certain distance to attain sufficient energy to ionize [69]. This also applies to carriers immediately after ionization because their final states are typically near the band edge. The distance in which essentially no impact ionization occurs is frequently referred to as the “dead space.” If the multiplication region is thick, the dead space can be neglected and the local field model provides an accurate description of APD characteristics. However, for thin multiplication layers the nonlocal nature of impact ionization has a profound impact as the ionization process becomes more deterministic. Several models [70–76] have successfully been developed to accurately include the effect of the dead space. Practical noise reduction in thin APDs has been demonstrated for a wide range of materials [77–79]. Figure 7.6 shows the excess

**Fig. 7.6** Comparison of calculated noise curves (*solid lines*) with experimental data for GaAs homojunction APD of different thickness  $0.1\ \mu\text{m}$  ( $\bullet$ ),  $0.2\ \mu\text{m}$  ( $\blacksquare$ ),  $0.5\ \mu\text{m}$  ( $\blacktriangle$ ), and  $0.8\ \mu\text{m}$  ( $\blacktriangledown$ ) [72]



noise figure versus gain for GaAs APDs with  $w_m$  in the range  $0.1\ \mu\text{m}$  to  $0.8\ \mu\text{m}$  [72]. The dashed lines are plots of (7.17) for  $k = 0.2$ – $0.5$ . These lines are not representative of the actual  $k$  values; they are presented solely for reference because the  $k$  value has become a widely used indirect figure of merit for excess noise. For constant gain, it is clear that the excess noise falls significantly with decreasing  $w_m$ .

While shrinking the multiplication region thickness is an effective approach to noise reduction, it should be noted that this is relative to the characteristic noise of the bulk (thick) material. Thus, it appears that lower noise can be achieved by beginning with “low-noise” semiconductors. For this reason, InAlAs, which can be grown lattice-matched on InP substrates, is an attractive candidate for telecommunications APDs. Watanabe et al. [80] have measured the ionization coefficients for InAlAs and found that  $k = \beta/\alpha \sim 0.3$ – $0.4$  for electric field in the range  $400$ – $650\ \text{kV/cm}$ , which compares favorably with  $k = \alpha/\beta \sim 0.4$ – $0.5$  for InP. Thin layers of InAlAs have also been incorporated into the multiplication region of SACM APDs. Ning Li et al. [81] reported that mesa-structure undepleted-absorber InAlAs APDs with  $180\ \text{nm}$ -thick multiplication regions exhibited excess noise equivalent to  $k = 0.15$  and a gain-bandwidth product of  $160\ \text{GHz}$ . Several planar InAlAs/InGaAs SACM APDs have also been developed. Recently an AlInAs/InGaAs planar SACM APD without a guard ring has been reported [82, 83]. These APDs have achieved gain  $> 40$ , high external quantum efficiency (88%),  $10\ \text{GHz}$  low-gain bandwidth, and a gain-bandwidth product of  $120\ \text{GHz}$ . Recently, the SACM structure was successfully applied to a monolithically grown Ge/Si APD in which light absorption and carrier multiplication occur inside Ge and Si, respectively. At  $1.3\ \mu\text{m}$  wavelength a gain-bandwidth product of  $340\ \text{GHz}$  with  $k = 0.09$  was demonstrated [84].

It has been shown that the noise of APDs with thin multiplication regions can be reduced even further by incorporating new materials and impact ionization engineering ( $\text{I}^2\text{E}$ ) with appropriately designed heterostructures [85–92]. Structurally,  $\text{I}^2\text{E}$  is similar to a truncated multiple quantum well, however, operationally there is a fundamental difference in that these APDs do not invoke heterojunction band discontinuities. Their function relies instead on the differences in threshold energies for impact ionization between adjacent wide-bandgap and narrower-bandgap

**Fig. 7.7** Layer structure of SACM InAlAs/InGaAlAs APD with I<sup>2</sup>E multiplication region [92]

InGaAs, contact, $p^+ > 9 \times 10^{18}$ , 30 nm	} 420-nm absorption layer
InAlAs, $p^+ : 4 \times 10^{18}$ , 500 nm	
InGaAs, $p: 1.0 \times 10^{16}$ , 270 nm	
InGaAs, $p: 4.0 \times 10^{16}$ , 150 nm	
InGaAlAs, $p: 1.0 \times 10^{16}$ , 50 nm	} I <sup>2</sup> E multiplication region
InAlAs, $p: 2.2 \times 10^{17}$ , 80 nm	
InGaAlAs, Q1.1, $p: 2.2 \times 10^{17}$ , 120 nm	
InGaAlAs, Q1.1, un-doped, 80 nm	
InAlAs, un-doped, 80 nm	
InAlAs, $n^+ : 5 \times 10^{18}$ , 500 nm	
InAlAs buffer, $n^+$ , 500 nm	
InAlAs buffer, un-doped, 100 nm	
Semi-insulating InP substrate	

materials. The structures that have achieved the lowest excess noise, to date, utilize multiplication regions in which electrons are injected from a wide bandgap semiconductor into adjacent low bandgap material. Recently, InGaAlAs/InP implementations that operate at the telecommunications wavelengths have been reported. Using both a single-well structure and a pseudo-graded bandgap based on InAlAs/InGaAlAs materials Wang et al. [91] demonstrated excess noise equivalent to  $k \sim 0.12$  and dark current comparable to that of homojunction InAlAs APDs. Duan et al. have incorporated a similar I<sup>2</sup>E multiplication region into an MBE-grown InAlAs/InGaAlAs I<sup>2</sup>E SACM APD [92]. A cross section of the layer structure is shown in Fig. 7.7.

The compound I<sup>2</sup>E multiplication region consisted of an unintentionally doped layer of In<sub>0.52</sub>Al<sub>0.48</sub>As with a thickness of 80 nm, an unintentionally doped In<sub>0.53</sub>Ga<sub>0.17</sub>Al<sub>0.3</sub>As layer with a thickness of 80 nm, a p-type (Be,  $2.2 \times 10^{17} \text{ cm}^{-3}$ ) 120 nm-thick In<sub>0.53</sub>Ga<sub>0.17</sub>Al<sub>0.3</sub>As and an 80 nm-thick In<sub>0.52</sub>Al<sub>0.48</sub>As layer with the same p-type doping level. The latter two layers also served as the field control or “charge” region. A 420 nm-thick unintentionally doped In<sub>0.53</sub>Ga<sub>0.47</sub>As layer was grown as the absorbing layer. Undoped InGaAlAs grading layers (50 nm) were inserted to reduce the barrier between In<sub>0.52</sub>Al<sub>0.48</sub>As and In<sub>0.53</sub>Ga<sub>0.47</sub>As. The absorber was slightly p-doped in order to suppress impact ionization in the absorption region. Ideally, the doping in the absorber would be graded to provide a slightly higher field in the direction of the multiplication region. This was approximated by step doping the absorber in two regions, one at  $1 \times 10^{16} \text{ cm}^{-3}$  and the other at  $4 \times 10^{16} \text{ cm}^{-3}$ . On the basis of Monte Carlo simulations of similar GaAs/AlGaAs I<sup>2</sup>E APDs [88], it can be inferred that there are relatively few ionization events in the In<sub>0.52</sub>Al<sub>0.48</sub>As layer, owing to the combined effects of “dead space” and the higher threshold energy in In<sub>0.52</sub>Al<sub>0.48</sub>As. Figure 7.8 shows the excess noise factor,  $F(M)$ , versus gain.

The dotted lines in Fig. 7.8 are plots of  $F(M)$  for  $k = 0$  to 5. For  $M \leq 4$ , it appears that  $k < 0$ , which is unphysical and simply reflects the inapplicability of the local field model for this type of multiplication region. At higher gain, the excess



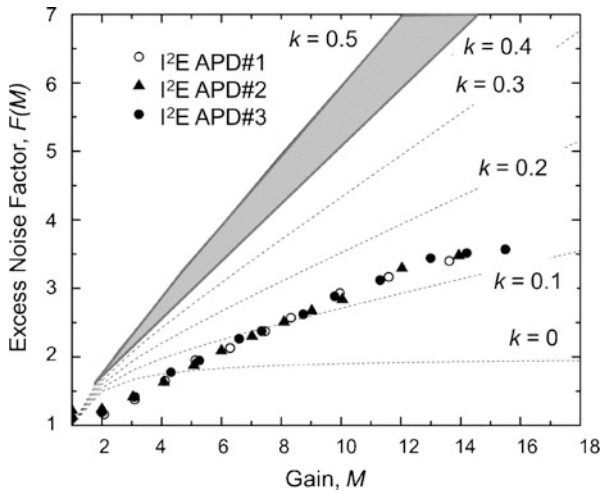


**Fig. 7.8** Excess noise factor vs. gain for an SACM APD with I<sup>2</sup>E InGaAlAs/InAlAs multiplication region [92]

noise is equivalent to a  $k$  value of  $\sim 0.12$ . For reference, the excess noise factor for InP/In<sub>0.53</sub>Ga<sub>0.47</sub>As SACM APDs is shown as the shaded region in Fig. 7.8.

## 7.3 High-speed Photodetectors

### 7.3.1 Advanced Photodiode Structures

The evolution of optical communication and microwave photonic applications to higher and higher speed has driven the demand for new photodiode structures that can achieve the requisite bandwidths without sacrificing responsivity or output power signal levels. To this end several photodiode structures have been developed including the dual-depletion region (DDR) photodiode [93], the uni-traveling carrier (UTC) photodiode [94, 95], and the partially depleted absorber (PDA) photodiode [96].

The DDR PD is characterized by a transparent drift layer between the intrinsic absorber and the n-type contact layer (Fig. 7.9a).

Compared to a p-i-n PD with the same depleted absorber thickness the DDR PD allows for a reduced junction capacitance for the same hole transit time. In the structure the photogenerated holes transit only the InGaAs absorbing layer whereas the electrons travel across both the absorbing layer and the InP drift layer. Since electrons are faster than holes, the overall bandwidth in otherwise RC-limited devices can be reasonably increased when the layer thicknesses are designed properly. To date, DDR PDs with bandwidths up to 50 GHz and 0.7 A/W responsivity have been

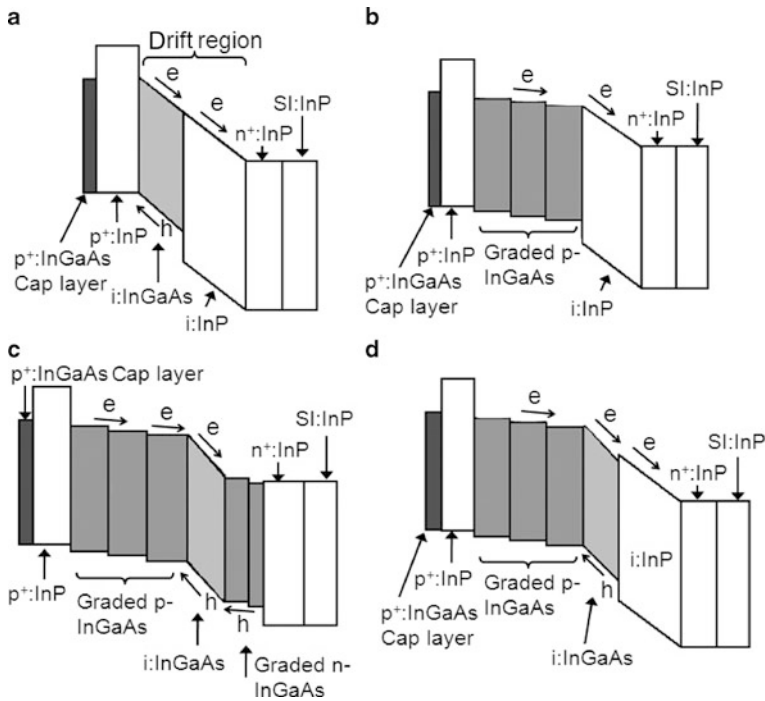


**Fig. 7.9** Schematic band diagrams of (a) DDR PD, (b) UTC PD, (c) PDA PD and (d) MUTC PD with InGaAs absorbing layers and InP contact layers on semi-insulating (SI) InP substrate. The transit paths of photogenerated electrons (e) and holes (h) are indicated

published [97]. Using a graded-index (GRIN) lens for uniform illumination, which mitigates the space-charge effect [98], saturation photocurrents of 45 mA at 10 GHz were achieved [99].

In 1996, Davis et al. [94] proposed a photodetector with an undepleted absorber and a transparent depletion region to improve the photodiode saturation behavior. This device has subsequently been given the appellation uni-traveling photodiode (UTC PD). The band diagram of the UTC PD is schematically shown in Fig. 7.9b. The active part of the UTC PD consists of a p-type narrow-bandgap light absorption layer and an undoped, wide-bandgap (transparent) depleted carrier-collection layer. The photogenerated minority electrons in the neutral absorption layer are transported by diffusion and/or drift into the depleted collection layer. In order to accelerate the electron diffusion process, a built-in electric field can be generated in the p-doped absorber by well-controlled bandgap- or doping-grading. Once the electrons reach the high-field collection layer, they drift toward the n-contact at a high saturation velocity. Conversely, since the absorption layer is quasi-neutral, photogenerated majority holes respond very fast within the dielectric relaxation time by their collective motion. This is an essential difference from the conventional p-i-n PD, in which both electrons and holes contribute to the response current and the

low-velocity hole-transport dominates the speed performance and exacerbates the space-charge effect [100]. Since electrons maintain their high velocity at relatively low electric fields, the UTC PD can achieve high speed and high saturation output photocurrent even at low bias voltage [101].

The original UTC PD reported by Davis et al. [94] had a diameter of  $500\ \mu\text{m}$  with a  $3\ \mu\text{m}$ -thick p-type InGaAs absorber and a  $5\ \mu\text{m}$  depleted InP drift layer. It achieved a dc photocurrent as high as  $150\ \text{mA}$ , however, the bandwidth was only  $295\ \text{MHz}$ . Through layer design optimization and device miniaturization Ishibashi et al. demonstrated that this type of photodiode could achieve high saturation current *and* high-speed operation [95]. In 1998, they reported a  $20\ \mu\text{m}^2$  back-illuminated UTC PD with a 3 dB bandwidth of  $152\ \text{GHz}$ , an output peak voltage of  $0.7\ \text{V}$ , and 13 % external quantum efficiency [102]. A UTC PD with bandwidth of  $220\ \text{GHz}$  at  $25\ \Omega$  effective load and  $0.13\ \text{A/W}$  was presented in [103]. In addition, the carrier transit time in UTC photodiodes can be further reduced by exploiting the velocity overshoot of electrons in the depletion layer [104]. By introducing an additional p-type charge layer between collector and n-contact layer, the electric field inside the structure can be adjusted to benefit from the electron velocity overshoot [105]. Using this structure Wu et al. have reported a  $64\ \mu\text{m}^2$  device having a 3 dB bandwidth of  $120\ \text{GHz}$  at  $25\ \Omega$  effective load. The back-illuminated PD with an integrated micro-lens on the substrate showed a responsivity of  $0.15\ \text{A/W}$  [105]. Recently, a similar device flip-chip bonded on an AlN substrate for improved heat sinking achieved a saturation photocurrent of  $37\ \text{mA}$  [106].

In [107] Li et al. proposed a structure where a thin InGaAs depletion layer was combined with undepleted InGaAs absorbers to increase responsivity (Fig. 7.9c). This structure is called a partially depleted absorber (PDA) photodiode and provides higher responsivity than a UTC PD with the same undepleted absorber thickness. Balancing the hole and electron densities within the depletion region was previously suggested as a technique for minimizing the space charge effect and for increasing photocurrents [15]. In the PDA, photodiode charge balance is accomplished by the p-doped absorber and an n-doped absorber on each side of the i-region. The p-doped absorber injects electrons into the i-region while the n-doped absorber injects holes. In the implementation, electron injection is stronger than that of holes due to the different thicknesses of the absorbers on each side of the i-layer. Since thin depletion layers are essential to obtain high currents, the PDA PD was designed with a thinned i-layer ( $250\ \text{nm}$ ), which reduces space-charge screening and minimizes thermal effects across the depletion layer [100]. Because of the poor thermal conductivity of InGaAs high-power InP/InGaAs PDs need to avoid thick InGaAs depletion layers to prevent thermally induced degradation and potential device failure at high optical photocurrents [15]. The measured compression photocurrent of a back-illuminated  $8\ \mu\text{m}$ -diameter PDA PD was  $24\ \text{mA}$  at  $48\ \text{GHz}$  with responsivity of  $0.6\ \text{A/W}$  [107].

Recently, a hybrid structure of UTC and PDA has been proposed by Jun et al. [108]. This structure, called a modified UTC (MUTC), is formed by inserting an undoped i-InGaAs layer between the p-type InGaAs absorber and the InP drift layer (Fig. 7.9d). Thus, the MUTC PD provides an additional design parameter which allows higher responsivity and higher bandwidth when the layer design is optimized.

**Fig. 7.10** Epitaxial layer structure of MUTC PD [109]. The doping concentrations are given in  $\text{cm}^{-3}$

p <sup>+</sup> InGaAs:Zn, $2 \times 10^{19}$ , 50 nm
p InP:Zn, $3 \times 10^{18}$ , 1000 nm
p InGaAs:Zn, $2 \times 10^{18}$ , 100 nm
p InGaAs:Zn, $1 \times 10^{18}$ , 150 nm
p InGaAs:Zn, $5 \times 10^{17}$ , 200 nm
p InGaAs:Zn, $2.5 \times 10^{17}$ , 200 nm
n InGaAs:Si, $1 \times 10^{16}$ , 200 nm
i InGaAsP Q1.4, 15 nm
i InGaAsP Q1.1, 15 nm
n InP:Si, $1 \times 10^{16}$ , 605 nm
n <sup>+</sup> InP:Si, $1 \times 10^{19}$ , 1000 nm
n <sup>+</sup> InGaAs:Si, $1 \times 10^{19}$ , 20 nm
n <sup>+</sup> InP:Si, $1 \times 10^{19}$ , 200 nm
Semi-insulating InP substrate, double side polished

Wang et al. [109] have shown that this type of PD can also achieve high saturation characteristics. The epitaxial layer structure of the reported device is shown in Fig. 7.10.

The InGaAs absorber region with a thickness of 850 nm is comprised of a 200 nm depleted n layer and four step-graded p-doped layers. The latter create a quasidelectric field that enhances the electron diffusion toward the drift region. The 605 nm InP electron drift layer is slightly n-type doped for space charge compensation. By doping the depletion region, the electric field can be pre-conditioned to be higher at the location where ultimately it will tend toward zero in the presence of high space charge [15]. The responsivity of the reported back-illuminated MUTC PD was 0.75 A/W. The measured results are summarized in Table 7.1. At a bias of 6 V the 20  $\mu\text{m}$ -diameter MUTC PD exhibited 30 GHz bandwidth, 60 mA saturation current, and +15.5 dBm RF output power.

**Table 7.1** Measured bandwidth, saturation photocurrent, and RF output power of 40  $\mu\text{m}$ , 34  $\mu\text{m}$ , 28  $\mu\text{m}$ , and 20  $\mu\text{m}$  diameter MUTC PD devices under 5 V, 6 V, and 7 V reverse bias.  $I_s$  and  $P_{\text{out}}$  are the saturation current and RF output power, respectively [109]

Diameter ( $\mu\text{m}$ )	Bandwidth (GHz)	$I_s$ (mA) and $[P_{\text{out}} \text{ (dBm)}]$ at 5 V	$I_s$ (mA) and $[P_{\text{out}} \text{ (dBm)}]$ at 6 V	$I_s$ (mA) and $[P_{\text{out}} \text{ (dBm)}]$ at 7 V
40	14	120 [23.0]	130 [24.5]	Failure @ 140 mA [25.2 @ 130 mA]
34	17	100 [21.9]	110 [23.0]	Failure @ 120 mA
28	23	80 [18.3]	90 [19.2]	Failure @ 80 mA
20	30	52 [14.0]	60 [15.5]	

Driven by the requirements of coherent fiber optic links and high-speed analog systems there has been increased interest in the linearity of high-power PDs [110–112]. To date, both UTC and MUTC PDs have been demonstrated having excellent linear transfer characteristics at high photocurrent levels and multi-GHz modulation frequencies [113–115].

### 7.3.2 High-speed Side-illuminated Photodiodes

To overcome the bandwidth-efficiency trade-off side-illuminated waveguide-photodiodes (WGPD) have been developed for p-i-n [116, 117], MSM [44], UTC [118–121], PDA [122], and APD photodiodes [123–126]. WGPD structures are illustrated in Fig. 7.11.

The primary benefit of this type of photodetector is that high efficiency and short carrier transit times can be achieved simultaneously [127]. Waveguide-photodiodes utilize an input optical waveguide with embedded absorbing layer. The photogenerated carriers transit only the thin absorption/depletion region perpendicular to the epitaxial layers, which enables high bandwidths. Since electrical and optical transports are not collinear, the carrier transit times are determined by the thickness of the absorber while the length of the detector primarily controls the responsivity. Assuming a single-mode WGPD the responsivity is given by [32]:

$$R_{\text{WGPD}} = R_{\text{ideal}} (1 - R_0) \eta_c [1 - \exp(-\Gamma_{xy} \alpha l_{\text{abs}})]. \quad (7.19)$$

Here,  $\eta_c$  is the input coupling efficiency determined from the overlap integral between the optical fields of the input (fiber) and WGPD,  $\Gamma_{xy}$  is the confinement factor in the  $xy$ -plane (perpendicular to the propagation direction) which quantifies the fraction of power confined within the absorbing layer, and  $l_{\text{abs}}$  is the PD length. For high-speed WGPDs with thin absorbers ( $< 1 \mu\text{m}$ ) either  $\eta_c$  or  $\Gamma_{xy}$  is  $< 1$ . This is because the diameter of the fiber input light spot, even when focused by lenses, is no less than  $2 \mu\text{m}$ , while the optical field distribution well confined within the absorbing layer is narrower than  $1 \mu\text{m}$ . Conversely, having a wider optical field distribution in the WG-PD improves  $\eta_c$ , however, at the expense of a reduced  $\Gamma_{xy}$ .

Using a double core, i.e., large multimode optical cavity, Kato et al. presented a WGPD with a record bandwidth-efficiency product of 55 GHz in 1994 [128]. The  $12 \mu\text{m}$ -long p-i-n WGPD achieved a quantum efficiency as high as 50%. The mushroom mesa approach developed for this photodiode yielded low resistance ( $10 \Omega$ ) while minimizing the p-n junction area to realize very low capacitance ( $\sim 15 \text{fF}$ ), which enabled an RC-limited bandwidth of 110 GHz.

The disadvantages of WGPDs are the limited high-power capability due to nonuniform carrier distribution along the optical path and the low tolerance to lateral and vertical displacement of the input signal. The latter implies the use of additional optics or a tapered fiber in order to efficiently illuminate the small active region. Thus, in general, a low tolerance to lateral and vertical displacement of the input

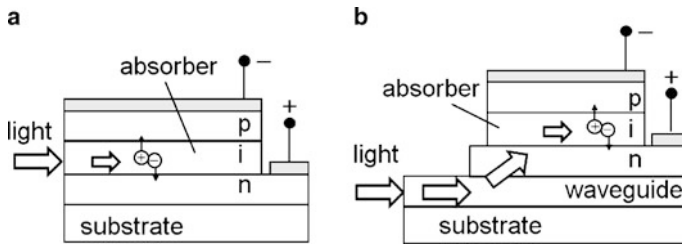


**Fig. 7.11** Side-illuminated (a) and evanescently coupled (b) WGPD

signal is obtained which makes the fiber-chip coupling more crucial and complex. To solve this problem, Fukano et al. proposed the edge-illuminated refracting facet photodiode (RFPD) in which the incident light that is parallel to the top surface is refracted at an angled facet and transits the absorption layer with a certain refracted angle [129]. With this design, the fiber-chip  $-1$  dB-misalignment tolerances in the horizontal and vertical direction were as large as  $13.4\ \mu\text{m}$  and  $3.3\ \mu\text{m}$ , respectively. Furthermore, since this design leads to an increased absorption length compared to a vertically illuminated photodiode, a high responsivity of  $1\ \text{A/W}$  with  $< 0.3$  dB polarization-dependent loss (PDL) was measured for a p-i-n RFPD with a  $1\ \mu\text{m}$  thick absorber [130]. Applying the UTC structure to the RFPD and further downscaling of the active area has led to high-speed, high-power UTC PDs with 3 dB bandwidths up to 310 GHz (at  $12.5\ \Omega$  effective load) [131]. In [132] a refracting-facet UTC PD module with responsivity of  $0.21\ \text{A/W}$  and 0.5 dB PDL for the detection of 100 and 160 Gbit/s return-to-zero (RZ) data rates was reported. Similar detector modules have been further optimized for W-band (75–110 GHz) [133], F-band (90–140 GHz) [134], and D-band (110–170 GHz) [135] operation; the latter exhibited a maximum RF output power of 2 dBm at 150 GHz.

In contrast to these side-illuminated devices the evanescently coupled WGPD consists of a photodiode located on top of a passive waveguide. In the structure shown in Fig. 7.11b the light couples evanescently from a single mode input waveguide to the PD mesa which ensures a more uniform absorption along the device length and leads to an improved high-power capability [138]. This WGPD is well suited for monolithic integration with additional components such as planar light-wave circuits resulting in advanced detector structures with increased functionality [139, 140]. Furthermore, independent of the active device, a mode field transformer (taper) can be integrated in order to improve the fiber-chip coupling efficiency. This enables the use of a cleaved fiber instead of a tapered/lensed fiber which simplifies the fiber-chip coupling process and also provides large alignment tolerances of  $\pm 2.5\ \mu\text{m}$  and  $\pm 3.5\ \mu\text{m}$  in the vertical and horizontal directions, respectively [116]. A highly efficient waveguide-integrated p-i-n photodiode was reported in [136]. The photodiode chip comprised a p-i-n photodiode with an active area of  $5 \times 20\ \mu\text{m}^2$  and an InGaAsP/InGaAs heterostructure absorption layer stack, a vertically tapered mode field transformer, a biasing network, and a  $50\ \Omega$  load resistor. An optimized impedance of the electrical output line of the detector led to

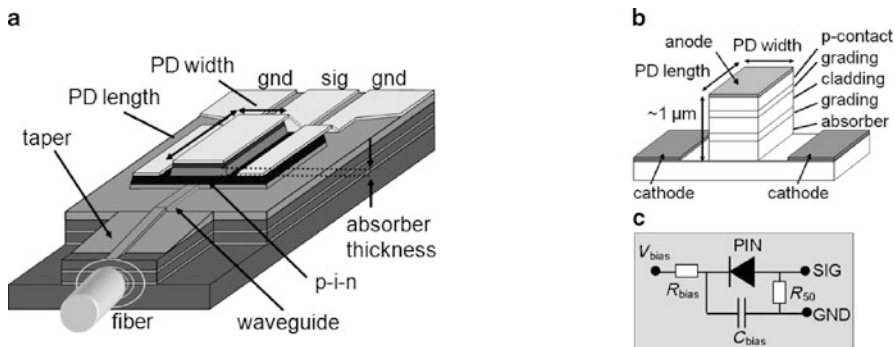
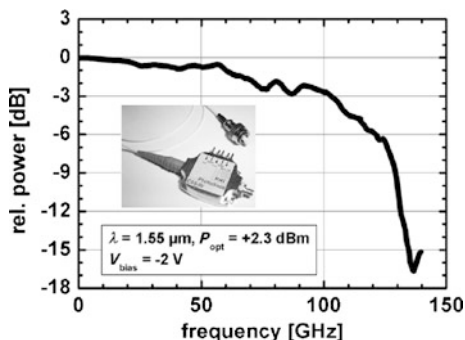


**Fig. 7.12** Evanescently coupled WGPD [136] (a), p-i-n mesa (b), and monolithically integrated bias circuitry (c)

**Fig. 7.13** Relative frequency response of the PD module (+2.3 dBm optical input power), *inset*: photograph of the PD module [137]

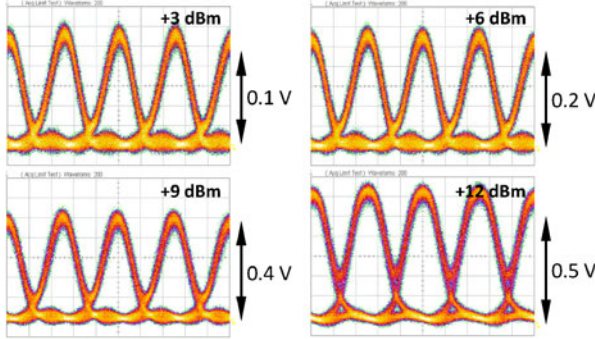


an increase of the cut-off frequency to >100 GHz. Figure 7.12a shows a schematic of this photodiode structure, Fig. 7.12b shows the p-i-n layer stack, and Fig. 7.12c shows the monolithically integrated bias circuitry.

The chip was assembled into a package equipped with a 1 mm coaxial output connector and a fiber pigtail (Fig. 7.13, inset). A responsivity of 0.73 A/W with a PDL of only 0.4 dB was obtained. Figure 7.13 shows the calibrated frequency response of the photodetector module at  $-2$  V bias. A 3 dB bandwidth of 100 GHz with a maximum RF output power of  $-7$  dBm was measured with an optical heterodyne setup [137].

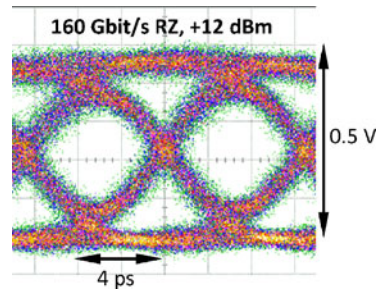
Similar PD modules have been evaluated in several back-to-back transmission experiments [141]. Figure 7.14 shows the received electrical 80 Gbit/s return-to-zero (RZ) eye patterns at different optical input power levels using a 70 GHz sampling oscilloscope. All measured eye patterns exhibit wide opening with a peak voltage up to 0.6 V revealing only negligible saturation effects at +12 dBm.

Figure 7.15 shows the detected 160 Gbit/s RZ data stream at +12 dBm optical input power. Because of the insufficient bandwidth of the sampling head and the PD module an RZ-to-NRZ conversion can be observed. Nevertheless, the eye amplitude is still notable and the inner eye opening reached 160 mV.



**Fig. 7.14** Electrical 80 Gbit/s return-to-zero (RZ) eye pattern at 3, 6, 9, and 12 dBm optical input power detected by the PD module at  $-2.5$  V bias ( $x$ : 5 ps/div) [141]

**Fig. 7.15** Detected eye pattern under 160 Gbit/s RZ excitation [141]



To further enhance the bandwidth of this type of evanescently coupled WGPD the p-n junction capacitance was reduced by downscaling the PD mesa to  $5 \times 7 \mu\text{m}^2$  [142]. To avoid a decrease in responsivity, which generally follows the reduction in PD length, the n-contact layer was extended by a well-defined length  $L$  toward the single-mode input waveguide (Fig. 7.16).

Since both, the PD mesa and the protruding section  $L$  form multimode waveguides, mode-beating effects can be exploited in order to facilitate an efficient coupling from the single-mode waveguide into the absorber [143, 144], and thus increase  $\Gamma_{xy}$ . Since  $\Gamma_{xy}$  is a function of  $z$  (in propagation direction) and  $L$ , the responsivity of the evanescently coupled WGPD can be estimated using the relation:

$$R_{e\text{WGPD}} = R_{\text{ideal}} (1 - R_0) \eta_c \left[ 1 - \exp \left( -\alpha \int_0^{l_{\text{abs}}} \Gamma_{xy}(z, L) dz \right) \right], \quad (7.20)$$

where the input waveguides are assumed to be lossless.

Numerical simulations of the optimized structure showed that illumination, and thus absorption, are strong in the first few microns of the absorber (Fig. 7.16, insets) [145]. For maximum responsivity the protrusion length  $L$  can be estimated from the beat length of the two most prominent modes in the multimode structure



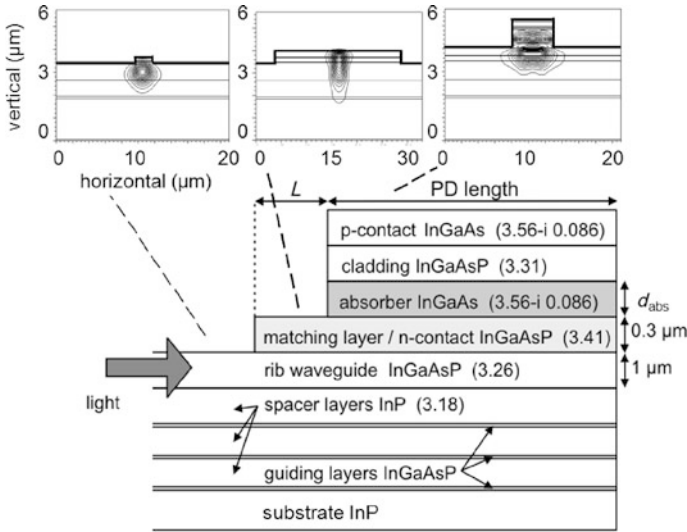
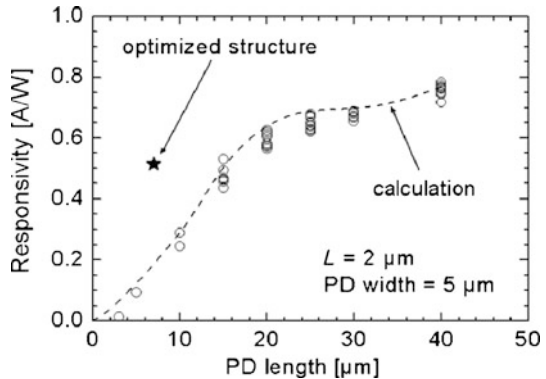


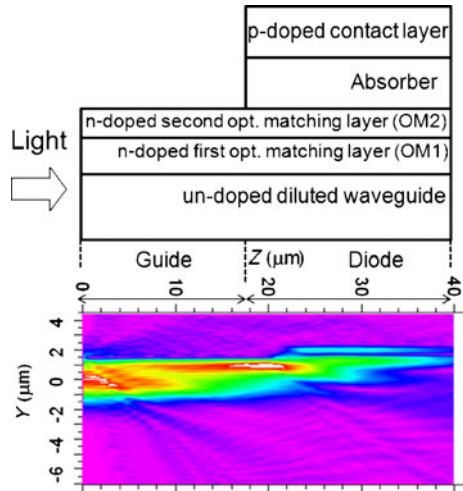
**Fig. 7.16** Cross-sectional view of the PD with extended n-contact layer (matching layer). Numbers given in parentheses are refractive indices at  $1.55 \mu\text{m}$  wavelength. The light is injected from the left into the mode field transformer (not shown) and couples evanescently from the semi-insulating waveguide into the p-i-n mesa. The insets depict the optical 2D field intensity profiles calculated in the single-mode waveguide (left), multimode matching layer (center), and multimode PD mesa (right)

**Fig. 7.17** Responsivity vs. PD length. Each circle displays experimental data for a different device from a previously fabricated wafer with  $L = 2 \mu\text{m}$ . The star indicates the optimized design with  $L = 7 \mu\text{m}$  [145]



reduced by the PD length. Experimentally  $L = 7 \mu\text{m}$  was found for a  $7 \mu\text{m}$  long PD which is in good agreement with the calculation using a numerically determined beat length of  $13 \mu\text{m}$ . Compared to previous devices with  $L = 2 \mu\text{m}$  a twofold responsivity increase to  $0.51 \text{ A/W}$  was reached with the optimized structure (Fig. 7.17). The reduced capacitance of these small area photodiodes enabled transit-time limited bandwidths at  $25 \Omega$  effective load of  $120 \text{ GHz}$  and  $145 \text{ GHz}$  for p-i-n structures with  $350 \text{ nm}$  and  $200 \text{ nm}$  thick absorbers, respectively [142, 146].

**Fig. 7.18** Schematic of photodiode with planar multimode input waveguide and two optical matching layers. The lower image is the simulated optical intensity as light propagates through the integrated waveguide/PD structure [149]



In contrast to the vertically tapered mode field transformer shown in Fig. 7.12a, Xia et al. [147] proposed the asymmetric twin-waveguide photodiode using a lateral taper. In this device the incident light is collected by a diluted large-fiber guide followed by transfer to a thin-coupling waveguide using a lateral-taper coupler. From there the light couples evanescently into the absorption layer. Using a lensed fiber for optical coupling a responsivity of 0.75 A/W, 0.4 dB polarization dependence, and a  $-1$  dB alignment tolerance of  $1\ \mu\text{m}$  were reported. The bandwidth was 42 GHz.

Recently, it has been shown that the mode field transformer can be omitted when using a short multimode input waveguide [119, 148]. Figure 7.18 depicts a schematic of an evanescently coupled photodiode that utilizes a planar diluted waveguide and two optical matching layers.

The diluted waveguide is a stack of 10-periods of un-doped InP/InGaAsP ( $1.1\ \mu\text{m}$  bandgap) layers. The number of periods was optimized to achieve high coupling efficiency with an input fiber and low TE/TM polarization dependence. The two optical matching layers are n-doped InGaAsP with band gaps corresponding to  $1.1\ \mu\text{m}$  and  $1.4\ \mu\text{m}$  for the first and second optical matching layers, respectively. This provides a gradual increase of the optical refractive index from the diluted waveguide to the absorbing layer (as illustrated by the simulated optical intensity in the lower part of Fig. 7.18), which results in a significant enhancement in the quantum efficiency. For this approach, since the waveguide to photodiode coupling is based on mode-beating effects, the coupling efficiency oscillates along the propagation direction. The solid line in Fig. 7.19 presents the responsivity simulation of  $20\ \mu\text{m}$  long photodiodes versus the input waveguide length.

Oscillations related to inter-modal interferences are clearly visible in this figure. In agreement with the modeling, the optimal waveguide length was found to be  $20\ \mu\text{m}$ .  $1.07\ \text{A/W}$  responsivity with PDL less than 0.5 dB were achieved with a lensed fiber at  $1.543\ \mu\text{m}$  wavelength [149]. Since the crucial beat lengths of the

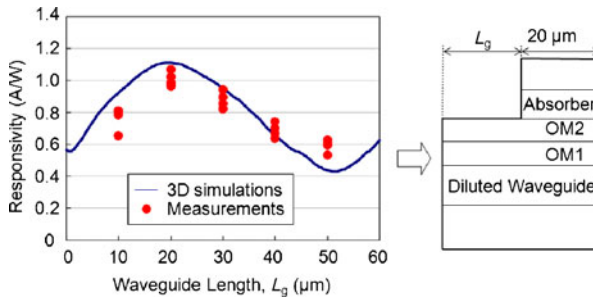


**Fig. 7.19** Responsivity of photodiode with planar multimode input waveguide vs. guide length for a 20  $\mu\text{m}$ -long active region: the *solid line* is the simulated responsivity and the *filled circles* are measurements [149]

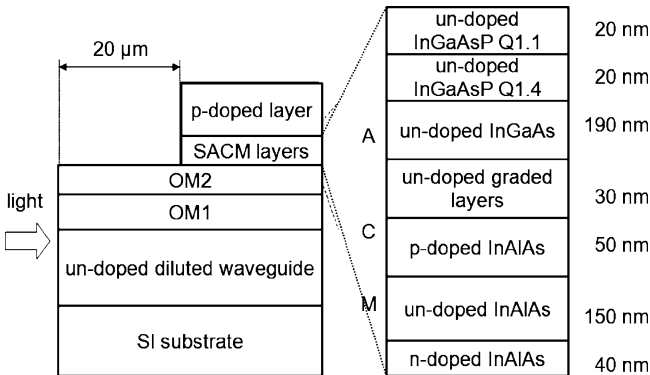


**Fig. 7.20** Schematic cross section of evanescently coupled InAlAs/InGaAs waveguide APD [151]

relevant optical modes show only a weak dependence on the wavelength, it was found that the efficiency changed  $< 0.2$  dB from 1500 to 1600 nm. Both, heterodyne measurements and electro-optic sampling verified a bandwidth of 65 GHz. As shown in Fig. 7.19 the responsivity is a function of the length of the input multimode waveguide which is determined by cleaving. It has been demonstrated that the use of etched V-grooves can control the input waveguide length to  $\pm 2 \mu\text{m}$ . However, by using a dual-step coupling region, that separates the input waveguide region from the coupling-waveguide region, the dependence of the responsivity on the length of the input waveguide has been essentially eliminated [150]. Recently, Wu et al. [150] demonstrated a dual-step evanescently coupled UTC-PD with bandwidth of 60 GHz at 50  $\Omega$  load. Using a tapered fiber with 3  $\mu\text{m}$  spot size, they achieved a high responsivity ( $\sim 1.0$  A/W) with a large tolerance to variations in cleaving ( $\sim 50 \mu\text{m}$ ).

The WGPD approach has also been applied to APDs. Demiguel et al. [151] have reported an evanescently coupled  $\text{In}_{0.52}\text{Al}_{0.48}\text{As}/\text{In}_{0.53}\text{Ga}_{0.47}\text{As}$  SACM APD having a planar short multimode input waveguide. A schematic cross section of this APD is shown in Fig. 7.20.

**Fig. 7.21** Photocurrent, dark current, and gain vs. reverse bias of evanescently coupled InAlAs/InGaAs waveguide APD [151]

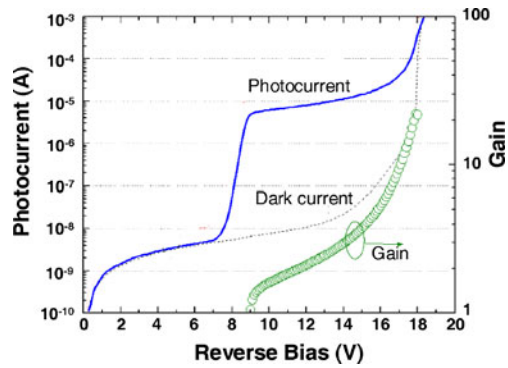
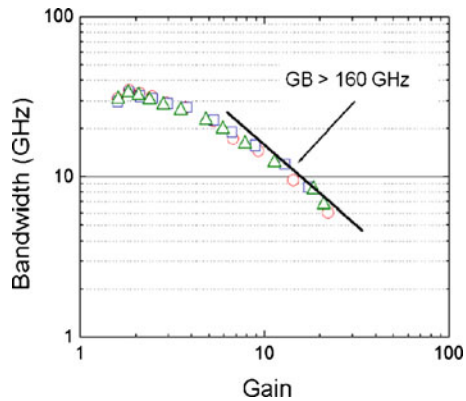


**Fig. 7.22** Bandwidth vs. gain of evanescently coupled InAlAs/InGaAs waveguide APD [151]



The input diluted waveguide is similar to that reported for p-i-n PDs in [149]. The photocurrent, dark current, and gain versus reverse bias are plotted in Fig. 7.21.

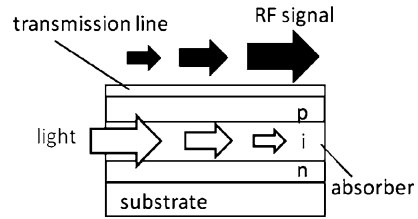
The breakdown occurred at  $\sim 18.5$  V and the dark current at 90% of the breakdown was in the range 100 to 500 nA. The responsivity was 0.62 A/W with a PDL  $< 0.5$  dB. Figure 7.22 shows the bandwidth versus gain; at low gain the maximum bandwidth was 35 GHz and the high-gain response exhibits a gain-bandwidth product of 160 GHz.

Nakata et al. [124] have reported an edge-coupled InAlAs/InGaAs APD that achieved 0.73 A/W responsivity, low-gain bandwidth of 35 GHz, and 140 GHz gain-bandwidth product. A similar waveguide APD with a gain-bandwidth product of 170 GHz and a minimum received power of  $-19.6$  dBm at 40 Gbit/s (for BER of  $10^{-9}$ ) was recently reported in [152].

### 7.3.3 Traveling Wave Photodetectors

Resistance, capacitance, and inductance (RCL) of conventional, lumped-element photodiodes determine their bandwidth in the absence of carrier transit-time limita-

**Fig. 7.23** Schematic of TWPD with co-propagating optical and electrical signals



tions. For these photodiodes it is imperative to reduce the device size to minimize capacitance while simultaneously maintaining low series and contact resistances. While this approach has yielded devices with bandwidths greater than 100 GHz, it has also imposed narrow constraints on design parameters in order to also achieve acceptable responsivity and practical input alignment tolerances. An alternative is to adopt traveling wave structures [153, 154]. The traveling wave photodetector (TWPD) is a distributed structure in that optical and photogenerated electrical signals co-propagate along the device (Fig. 7.23).

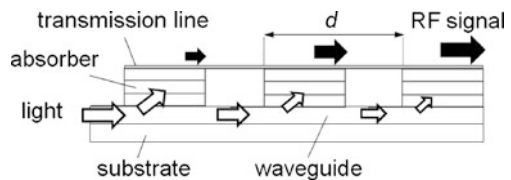
The electrical contacts are designed as a transmission line with characteristic impedance matched to that of the external microwave circuit ( $50\ \Omega$ ). Hence, the requirement to optimize the trade-off between the RCL bandwidth and the transit-time bandwidth can effectively be eliminated [155–159].

TWPDs were first reported for GaAs-based p-i-n photodiodes that operated between 800 and 1060 nm wavelength [157–159]. In [158], a  $7\ \mu\text{m}$  long WGPD integrated with a microwave electrode designed to support traveling electrical waves with characteristic impedance matched to that of the external circuit achieved an FFT-deduced bandwidth of 172 GHz and a record bandwidth-efficiency product of 76 GHz.

For traveling wave photodiodes the bandwidth is determined by the carrier transit times and the velocity mismatch. Velocity mismatch results from the difference between the group velocity of the optical wave in the device and the electrical signal in the transmission line [154]. The fact that both, the characteristic impedance and the electrical signal velocity depend on the capacitance of the photodiode, make a velocity match difficult. Thus, it has been suggested that in practical devices a residual velocity mismatch is inevitable which can lead to bandwidth degradations in long devices [154, 157, 160].

A second type of TWPD, referred to as periodic TWPD, divides the absorption length into several photodiodes (Fig. 7.24).

**Fig. 7.24** Periodic TWPD with serial optical feed



In this design discrete photodiodes located on top of an optical waveguide are combined to a traveling wave structure [160–162]. The variation of the spacing between the PDs provides an additional degree of freedom in the device design. Thus, by optimizing the geometries of the photodiodes, their spacing, and the transmission line independently, the electrical velocity  $v_{el}$  and characteristic impedance  $Z_0$  can be matched to the optical signal velocity  $v_{opt}$  and external load  $R_1$ , respectively [160, 161, 163]. With the PD junction capacitance  $C_{pd}$  and assuming that the electrical signal wavelength is in the order of the device length, the periodic TWPD can be described as a capacitively loaded transmission line with  $v_{el}$  and  $Z_0$  given by:

$$v_{el} = \sqrt{\frac{1}{L' \left( C' + \frac{C_{pd}}{d} \right)}} \cong v_{opt} \quad (7.21)$$

$$Z_0 = \sqrt{\frac{L'}{C' + \frac{C_{pd}}{d}}} \cong R_1. \quad (7.22)$$

Here  $C'$  and  $L'$  represent the capacitance and inductance per unit length of a lossless transmission line, respectively, and  $d$  is the photodiode spacing.

Because of the periodic nature of the device this approach is valid for electrical signal frequencies below the Bragg frequency, which is defined as [164]:

$$f_{Bragg} = \frac{1}{\pi \sqrt{d \cdot L' (d \cdot C' + C_{pd})}}. \quad (7.23)$$

Since reflections of the backward-propagating electrical signal wave at the input of the transmission line lead to reduced bandwidth, periodic TWPDs necessitate a termination at the input end of the transmission line to minimize reflections. Only then can the bandwidth of the discrete photodiodes be retained, to a large extent, within the Bragg frequency. Using this approach and an integrated matching resistor for termination, three  $2 \mu\text{m} \times 5 \mu\text{m}$  InAlGaAs/InGaAs UTC PDs, and an InAlGaAs waveguide, Hirota et al. reported 115 GHz bandwidth with 0.15 A/W responsivity [163]. In [165], Murthy et al. reported a multisection coplanar strip transmission line to avoid the internal resistor. In their device multisection coplanar strips with step-reduced impedances connected three discrete photodiodes spaced by  $300 \mu\text{m}$ . The design of the transmission line discontinuities was optimized to cancel the backward-propagating electrical waves. The measured bandwidth, linear DC photocurrent, and responsivity were 38 GHz, 12 mA, and 0.24 A/W, respectively. The lengths of the photodiodes (8, 10, and  $20 \mu\text{m}$ ) were designed to achieve uniform photocurrent distribution. This is desirable since the maximum saturation photocurrent in the periodic TWPD is often limited by the heat-induced failure of the first PD which is exposed to the highest optical power [166].

An efficient way to achieve a uniform photocurrent distribution and thus high saturation photocurrents is to symmetrically distribute the optical signal to several

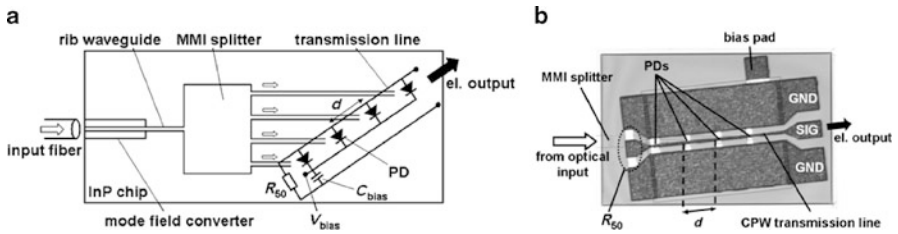
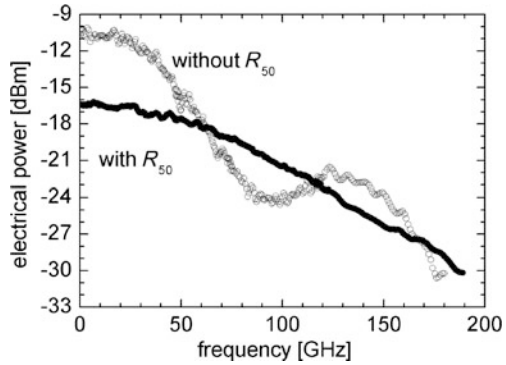


**Fig. 7.25** Schematic view of the parallel-fed TWPD (a), and micrograph of the fabricated TWPD chip with  $d = 90\mu\text{m}$  (b). The input signal is fed from the left via the mode field converter and rib waveguide (not shown) into the MMI splitter. The RF output pads are in ground-signal-ground configuration [146]

photodiodes. In this configuration the optical signal is split by a power divider and fed into several discrete photodiodes which are connected by an output transmission line [167]. Now, because of the uniform optical power distribution, the photocurrent flowing through each photodiode in the periodic TWPD scales inversely with the number of PDs. Using this approach and a TWPD with  $40\mu\text{m}$ -diameter back-illuminated MUTC photodiodes a saturation photocurrent as high as  $114\text{ mA}$  at  $-3.5\text{ V}$  bias voltage was demonstrated in [168]. The responsivity and bandwidth of the 2-element TWPD with integrated matching resistor were  $0.55\text{ A/W}$  and  $17\text{ GHz}$ , respectively. In [169], the monolithic integration of a multimode interference (MMI) power splitter and a TWPD with four  $80\mu\text{m}$ -long p-i-n PD was reported. A linear DC photocurrent of  $52\text{ mA}$  and an unsaturated RF power of  $9\text{ dBm}$  at  $10\text{ GHz}$  signal frequency were achieved. A similar approach was adopted in [146]. Here, the traveling wave photodetector chip comprised a mode field converter and a  $1 \times 4$  MMI power splitter of which output waveguides fed four high-speed evanescently coupled p-i-n PDs, each with an active area of  $4 \times 7\mu\text{m}^2$ . Figure 7.25a, b show the schematic chip layout and a micrograph of a fabricated TWPD, respectively.

The coplanar waveguide (CPW) transmission line, which connects the PDs in parallel, was designed with an impedance of  $85\Omega$  and a phase velocity of  $126\mu\text{m/ps}$ . As the integration of the discrete PDs within the CPW leads to an additional capacitive loading of the transmission line due to the PD's junction capacitance, the overall TWPD characteristic impedance and the electrical phase velocity were reduced to  $49\Omega$  and  $73\mu\text{m/ps}$ , respectively. The latter agrees sufficiently with the optical group velocity in the single-mode waveguide of  $86\mu\text{m/ps}$ , which has been derived from measurements using a Fabry-Pérot resonance method. The impedance match to  $50\Omega$  was verified experimentally to be  $> 84\%$  up to  $50\text{ GHz}$ . The electrical Bragg frequency was determined to be  $> 200\text{ GHz}$  for this particular design, which is high enough to provide a smooth frequency response to more than  $100\text{ GHz}$ . In order to eliminate electrical reflections at the input of the transmission line, which lead to a reduced bandwidth, a matching resistor  $R_{50}$  was integrated. For convenient biasing and to avoid the short-circuit current at the matching resistor a bias capacitor  $C_{bias}$  was implemented to decouple the bias voltage from RF ground. Figure 7.26 compares the results of two TWPDs with identical design, but

**Fig. 7.26** Electrical output power vs. frequency for a TWPD with (*closed circles*) and without (*open circles*) termination resistor measured at an (average) DC photocurrent of 2 mA [146]



one without termination resistor. In the latter case, a 3 dB bandwidth of 41 GHz is obtained which is mainly limited due to the interaction of the forward and the reflected traveling waves.

By implementing the matching resistor at the input of the CPW the backward traveling wave is terminated and the bandwidth can be significantly enhanced up to 80 GHz [146]. However, this results in loss of half of the photocurrent, which results in a reduction of 6 dB in output power at low frequencies. Figure 7.27 shows the high-power characteristics of this TWPD measured at several fixed beat frequencies.

At 150 GHz signal frequency, a maximum electrical output power of  $-2.5$  dBm is measured. Compared to a single PD from the same wafer with an active area of  $4 \times 7 \mu\text{m}^2$  (open circles in Fig. 7.27), this is an improvement of 7 dB in available power. An enhancement up to 12 dB (= four times the current) can be expected if both devices have identical frequency responses. The 1 dB compression point amounts to 6 mA and 22 mA for the single PD and the TWPD, respectively. At 200 GHz, the available power from the TWPD was as high as  $-9$  dBm, and even at 400 GHz a power of  $-32$  dBm was detected [170]. From these devices a fully packaged TWPD module with 0.24 A/W and 0.2 dB PDL was fabricated and operated in 80 Gbit/s back-to-back experiments [171]. Although the chip's 3 dB bandwidth was

**Fig. 7.27** Electrical output power vs. DC photocurrent for a single PD at 150 GHz and a TWPD at 150 GHz, 200 GHz, 300 GHz, and 400 GHz; both devices with integrated termination resistor [171]

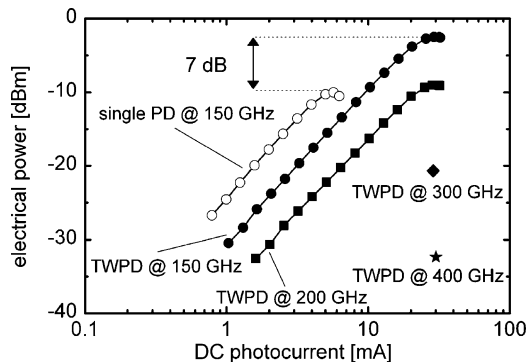
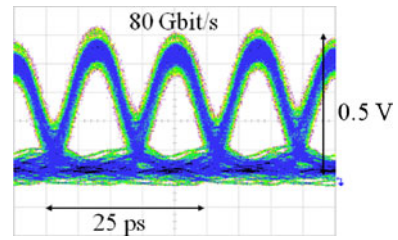




**Fig. 7.28** Eye diagram at 80 Gbit/s RZ modulation format detected by the TWPDP module [171]



notably reduced due to some additional losses in the packaging, a well-opened eye diagram with a peak voltage  $> 0.5$  V was received at 80 Gbit/s RZ and an average optical input power of +12 dBm (Fig. 7.28).

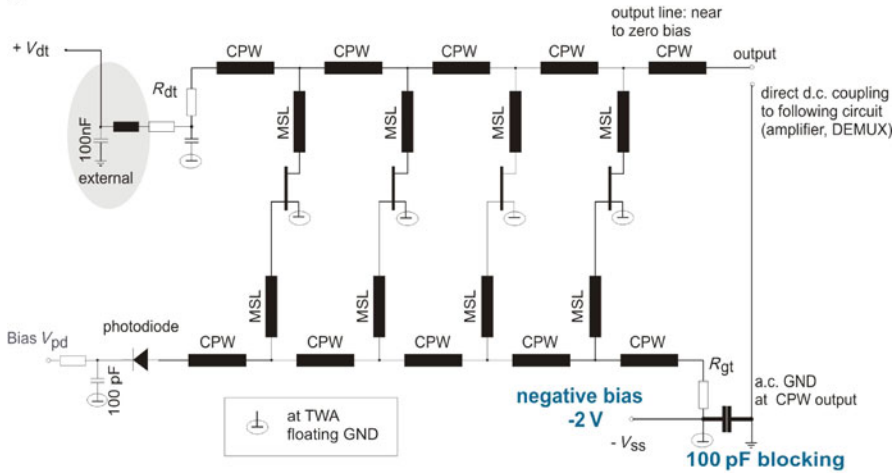
### 7.3.4 Photoreceivers

Most telecommunication applications require significant signal amplification on the receiver side prior to demultiplexing and decision thresholding. An optical front-end providing both, detection and amplification of the signal, will be referred to in the following as a photoreceiver. To date, the combination of a photodetector with a subsequent electrical amplifier is the preferred solution for 40 Gbit/s photoreceivers. In its simplest form the photoreceiver consists of a high-speed p-i-n photodiode co-packaged with a transimpedance amplifier (TIA) connected by bond wires (p-i-n TIA photoreceiver). This hybrid approach offers the ability to choose the PD and amplifier independent of their material system and thus allows for separate optimization of the fabrication processes.

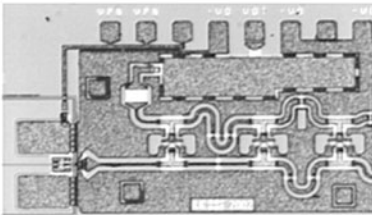
In order to reach the common goal of high receiver sensitivity, amplifiers in photoreceivers are required to provide high gain of electrical amplification, broad bandwidth, low group delay scatter, and low noise. Since the sensitivity of electrically amplified photoreceivers is typically dominated by electronic circuit noise, it can be approximated with (7.13) when replacing  $\langle i_{in}^2 \rangle$  with the input equivalent noise current of the amplifier.

Particularly for very high-speed applications the integrated photoreceiver, i.e., the monolithic or flip-chip integration of the photodetector and the electronic amplifier on the same chip, is a promising approach. Compared to hybrid solutions the integrated photoreceiver is more compact and provides potentially better speed performance as parasitics arising from device-interconnects can be reduced. Various integration schemes have been demonstrated including p-i-n and MSM photodiodes with bipolar transistors (HBTs) or high electron mobility transistors (HEMTs) [39, 173–175]. A very high-speed monolithic p-i-n-traveling wave amplifier (p-i-n TWA) photoreceiver for 80 Gbit/s operation was demonstrated in [172]. The device comprised a wide-bandwidth evanescently coupled WGPDP and a traveling wave amplifier based on four HEMTs. The TWA is a distributed amplifier and provides large bandwidth potential since the transistor input and output capacitances

a



b



Photodiode traveling wave amplifier

**Fig. 7.29** Circuit diagram of the photoreceiver with negative bias and GND-isolated output port (MSL: microstrip line) (a), partial view of photoreceiver chip [172] (b)

can be included into the distributed capacitances of the input and output transmission lines [176]. Figure 7.29a shows the circuit diagram of the photoreceiver with a negative bias and ground (GND)-isolated output port which allows DC-coupling to the following circuit. Figure 7.29b shows a micrograph of the fabricated chip. The amplifier transimpedance, the overall conversion gain, and the bandwidth of the fully packaged photoreceiver were  $71 \Omega$ ,  $45.4 \text{ V/W}$  ( $= 0.91 \text{ A/W}$ ), and  $70 \text{ GHz}$ , respectively.

Another concept to enhance the signal level is the previously mentioned optical pre-amplifier in conjunction with a high-power photodetector. Using this approach photoreceivers have been demonstrated to reach the highest sensitivities due to the excellent gain and noise characteristics of erbium-doped fiber amplifiers (EDFA) [6, 7]. However, the large size and large pump power of fiber-based amplifiers make these photoreceivers less attractive for commercial application. A more compact solution is the semiconductor optical amplifier (see e.g., [8] and Chap. 12 of this book), which can also be monolithically integrated with photodiodes on InP [177]. SOAs require less power, however, they have typically lower gain

and higher noise than EDFAs. A monolithically integrated SOA p-i-n photoreceiver with 39 GHz bandwidth and a total conversion gain of 800 V/W (= 16 A/W) was demonstrated in [178].

The increasing interest in high-serial-bitrate systems has recently driven research on photoreceivers operating at 100 Gbit/s and above [179–181]. In [182], a co-packaged optical demultiplexing photoreceiver comprising a 100 GHz evanescently coupled WGPLD, a SiGe 85 Gbit/s 1 : 2 electrical demultiplexer, and a SiGe traveling wave clock amplifier with a bandwidth of approximately 55 GHz was reported. To minimize performance reduction at the chip interconnects all internal RF-connections were realized with carefully designed microstrip and coplanar waveguide circuits. The optically pre-amplified photoreceiver was successfully operated at 107 Gbit/s. The required optical signal-to-noise ratio for a BER of  $10^{-3}$  (corresponding to the required threshold for enhanced forward error correction) was 24 dB.

## 7.4 Summary

Undiminished demand for higher and higher speed has pushed the development of new photodiode structures and devices. As conventional normal-incidence p-i-n photodiodes cannot achieve the requisite bandwidth-efficiency products and output power levels, the move to side-illuminated PDs and novel device structures has paved the way for very high bitrate, high-power photodetectors. To date, high-efficiency side-illuminated UTC-PDs, evanescently coupled p-i-n WGPLDs, and distributed periodic TWPDs have been successfully operated at bitrates as high as 160 Gbit/s.

At 1.55  $\mu\text{m}$  wavelength APD-TIA photoreceivers have become a standard solution for high-sensitivity 10 Gbit/s systems. Although WG-APDs with sufficient bandwidth for 40 Gbit/s operation have been reported, their gain-bandwidth products do not permit operation at the gain values ( $M > 10$ ) required to achieve sufficient receiver sensitivities. As a result, pending a breakthrough that produces APDs with gain-bandwidth products  $\sim 400$  GHz, 10 Gbit/s appears to be a transition point where APDs still prove beneficial with a switch to high-speed p-i-n PDs at higher bitrates.

## References

1. S. Ramo, Currents induced by electron motion. Proc. IRE **27**, 584–585 (1939)
2. K. Kato, S. Hata, K. Kawano, A. Kozen, Design of ultrawide-band, high-sensitivity p-i-n photodetectors. IEICE Trans. Electron. **E76-C**, 214–221 (1993)
3. W. Shockley, W.T. Read, Statistics of the recombination of holes and electrons. Phys. Rev. **87**, 835–839 (1952)
4. R.N. Hall, Electron-hole recombination in germanium. Phys. Rev. **87**, 387–391 (1952)

5. G.P. Agrawal, *Fiber-Optic Communication Systems* (Wiley, New York, 2002)
6. Y. Miyamoto, M. Yoneyama, K. Hagimoto, T. Ishibashi, N. Shimizu, 40 Gbit/s high sensitivity optical receiver with uni-travelling-carrier photodiode acting as decision IC driver. *Electron. Lett.* **34**, 214–215 (1998)
7. Y. Miyamoto, K. Yonenaga, A. Hirano, N. Shimizu, M. Yoneyama, H. Takara, K. Noguchi, K. Suzuki, 1.04-Tbit/s DWDM transmission experiment based on alternate-polarization 80-Gbit/s OTDM signals, *Proc. 24th Europ. Conf. Opt. Commun. Conf. (ECOC'98)*, Madrid, Spain (1998), vol. 3, pp. 55–57
8. S. Takashima, H. Nakagawa, S. Kim, F. Goto, M. Okayasu, H. Inoue, 40-Gbit/s receiver with  $-21$  dBm sensitivity employing filterless semiconductor optical amplifier, *Opt. Fiber Commun. Conf. (OFC'03)*, Techn. Digest (Atlanta, GA, USA, 2003), vol. 2, pp. 471–472
9. K.J. Williams, L.T. Nichols, R.D. Esman, Photodetector nonlinearity on a high-dynamic range 3 GHz fiber optic link. *J. Lightw. Technol.* **16**, 192–199 (1998)
10. A.J. Seeds, K.J. Williams, Microwave photonics. *J. Lightw. Technol.* **24**, 4628–4641(2006)
11. K.J. Williams, R.D. Esman, Design considerations for high-current photodetectors. *J. Lightw. Technol.* **17**, 1443–1454 (1999)
12. K.J. Williams, R.D. Esman, M. Dagenais, Effects of high space-charge fields on the response of microwave photodetectors. *IEEE Photon. Technol. Lett.* **6**, 639–641 (1994)
13. J. Paslaski, P.C. Chen, J.S. Chen, C.M. Gee, N. Bar-Chaim, High-power microwave photodiode for improving performance of RF fiber optic links, *Proc. SPIE Photon. Radio Freq.*, Denver, CO (1996), vol. 2844, pp. 110–119
14. N. Duan, X. Wang, N. Li, H.-D. Liu, J.C. Campbell, Thermal analysis of high-power InGaAs-InP photodiodes. *IEEE J. Quantum Electron.* **42**, 1255–1258 (2006)
15. K.J. Williams, Comparison between dual-depletion-region and uni-travelling-carrier p-i-n photodetectors. *IEE Proc. Optoelectron.* **149**, 131–137 (2002)
16. S. Adachi, *Physical Properties of III–V Semiconductor Compounds* (Wiley, New York, 1992)
17. J.E. Bowers, C.A. Burrus, Ultrawide-band long-wavelength p-i-n photodetectors. *J. Lightw. Technol.* **LT-5**, 1339–1350 (1987)
18. M. Dentan, B. de Cremoux, Numerical simulation of the nonlinear response of a p-i-n photodiode under high illumination. *J. Lightw. Technol.* **8**, 1137–1144 (1990)
19. T.H. Windhorn, L.W. Cook, G.E. Stillman, Temperature dependent electron velocity-field characteristics for InGaAs at high electric fields. *J. Electron. Mater.* **11**, 1065–1082 (1982)
20. P. Hill, J. Schlafer, W. Powazinik, M. Urban, E. Eichen, R. Olshansky, Measurement of hole velocity in n-type InGaAs. *Appl. Phys. Lett.* **50**, 1260–1262 (1987)
21. M.K. Smit, InP photonic integrated circuits, *Proc. Annual Meeting IEEE (LEOS 2002)*, Glasgow, U.K. (2002), vol. 2, pp. 843–844
22. M.K. Smit, E.A.J.M. Bente, M.T. Hill, F. Karouta, X.J.M. Leijtens, Y.S. Oei, J.J.G.M. van der Tol, R. Nötzel, P.M. Koenraad, H.S. Dorren, H. de Waardt, A.M.J. Koonen, G.D. Khoe, Current status and prospects of photonic IC technology, *Proc. 19th Internat. Conf. Indium Phosphide Relat. Mater. (IPRM'07)*, Matsue, Japan, paper PL1 (2007), pp. 3–6
23. R. Kaiser, Photonic integration on InP for telecom and datacom applications, *Opt. Fiber Commun. Conf. (OFC'05)*, Techn. Digest (Anaheim, CA, USA, 2005), paper OTuM1
24. H. Yoshimura, Future photonic networks and the role of InP-based devices, *Proc. 12th Internat. Conf. Indium Phosphide Relat. Mater. (IPRM'00)*, Williamsburg, VA, USA (2000), pp. 3–6
25. R. Nagarajan, M. Kato, V.G. Dominic, J. Pleumeekers, A.G. Dentai, P. Evans, S. Hurr, J. Baeck, D. Lambert, M. Missey, A. Mathur, S. Murthy, R.A. Salvatore, C. Joyner, R.P. Schneider, M. Ziari, J. Bostak, M. Kauffman, H.-S. Tsai, M. Van Leeuwen, A. Nilsson, R. Taylor, S.G. Grubb, D. Mehuys, F.A. Kish, D.F. Welch, Large scale InP photonic integrated circuits for high speed optical transport, *Proc. 18th Internat. Conf. Indium Phosphide Relat. Mater. (IPRM'06)*, Princeton, NJ, USA, paper WA2.1 (2006), 237–240
26. R. Nagarajan, M. Kato, V. Dominic, J. Pleumeekers, A. Dentai, P. Evans, S. Hurr, J. Bäck, D. Lambert, M. Missey, A. Mathur, S. Murthy, R. Salvatore, C. Joyner, R. Schneider, M. Ziari, J. Bostak, M. Kauffman, H.-S. Tsai, M. Van Leeuwen, A. Nilsson, R. Taylor,

- S. Grubb, D. Mehuys, F. Kish, D. Welch, Monolithic, 10 and 40 channel InP receiver photonic integrated circuits with on-chip amplification, *Opt. Fiber Commun. Conf. and Nat. Fiber Opt. Eng. Conf. (OFC/NFOEC'07)*, Techn. Digest (Anaheim, CA, USA, 2007), post-deadline paper PDP32
27. G. Masini, G. Capellini, J. Witzens, C. Gunn, High-speed, monolithic CMOS receivers at 1550 nm with Ge on Si waveguide photodetectors, *Proc. Annual Meeting IEEE (LEOS 2007)*, Lake Buena Vista, FL (2007), paper ThU1, pp. 848–849
  28. S. Klinger, M. Berroth, M. Kaschel, M. Oehme, E. Kasper, Ge-on-Si p-i-n photodiodes with a 3-dB bandwidth of 49 GHz. *IEEE Photon. Technol. Lett.* **21**, 920–922 (2009)
  29. D. Liang, J.E. Bowers, Photonic integration: Si or InP substrates?. *Electron. Lett.* **45**, 578–581 (2009)
  30. L. Vivien, J. Osmond, J.-M. Fédéli, D. Marris-Morini, P. Crozat, J.-F. Damlencourt, E. Casan, Y. Lecunff, S. Laval, 42 GHz p-i-n germanium photodetector integrated in a silicon-on-insulator waveguide. *Opt. Express* **17**, 6252–6257 (2009)
  31. Y.-G. Wey, K. Giboney, J. Bowers, M. Rodwell, P. Silvestre, P. Thiagarajan, G. Robinson, 110-GHz GaInAs/InP double heterostructure p-i-n photodetectors. *J. Lightw. Technol.* **13**, 1490–1499 (1995)
  32. K. Kato, Ultrawide-band/high-frequency photodetectors. *IEEE Trans. Microwave Theory Tech.* **47**, 1265–1281 (1999)
  33. I. Kimukin, N. Biyikli, B. Butun, O. Aytur, S.M. Ünlü, E. Ozbay, InGaAs-based high-performance p-i-n photodiodes. *IEEE Photon. Technol. Lett.* **14**, 366–368 (2002)
  34. W. Gao, A.-S. Khan, P.R. Berger, R.G. Hunsperger, G. Zydzik, H.M. O'Bryan, D. Sivco, A.Y. Cho,  $\text{In}_{0.53}\text{Ga}_{0.47}\text{As}$  metal–semiconductor–metal photodiodes with transparent cadmium tin oxide Schottky contacts. *Appl. Phys. Lett.* **65**, 1930–1932 (1994)
  35. M.A. Matin, K.C. Song, B.J. Robinson, J.G. Simmons, D.A. Thompson, F. Gouin, Very low dark current InGaP/GaAs MSM photodetector using semi-transparent and opaque contacts. *Electron. Lett.* **32**, 766–767 (1996)
  36. J.H. Kim, T. Griem, R.A. Friedman, E.Y. Chan, S. Ray, High-performance back-illuminated InGaAs/InAlAs MSM photodetector with a record responsivity of 0.96 A/W. *IEEE Photon. Technol. Lett.* **4**, 1241–1243 (1992)
  37. M.C. Hargis, S.E. Ralph, J. Woodall, D. McInturff, A.J. Negri, P.O. Haugsjaa, Temporal and spectral characteristics of back-illuminated InGaAs MSM photodetectors. *IEEE Photon. Technol. Lett.* **8**, 110–112 (1996)
  38. J. Burm, K.I. Litvin, D.W. Woodard, W.J. Schaff, P. Mandeville, M.A. Jaspan, M.M. Gitin, L.F. Eastman, High-frequency, high-efficiency MSM photodetectors. *IEEE J. Quantum Electron.* **31**, 1504–1509 (1995)
  39. V. Hurm, W. Benz, M. Berroth, W. Bronner, G. Kaufel, K. Köhler, M. Ludwig, E. Olander, B. Raynor, J. Rosenzweig, 20 Gbit/s fully integrated MSM-photodiode AlGaAs/GaAs-HEMT optoelectronic receiver. *Electron. Lett.* **32**, 638–685 (1996)
  40. Z. Lao, V. Hurm, W. Bronner, A. Hülsmann, T. Jakobus, K. Köhler, M. Ludwig, B. Raynor, J. Rosenzweig, M. Schlechtweg, A. Thiede, 20-Gb/s 14-k transimpedance long-wavelength MSM-HEMT photoreceiver OEIC. *IEEE Photon. Technol. Lett.* **10**, 710–712 (1998)
  41. Y.G. Zhang, A.Z. Li, J.X. Chen, Improved performance of InAlAs-InGaAs-InP MSM photodetectors with graded superlattice structure grown by gas source MBE. *IEEE Photon. Technol. Lett.* **8**, 830–832 (1996)
  42. F. Hieronymi, E.H. Böttcher, E. Dröge, D. Kuhl, D. Bimberg, High-performance large-area InGaAs MSM photodetectors. *IEEE Photon. Technol. Lett.* **5**, 910–913 (1993)
  43. J. Kim, W.B. Johnson, S. Kanakaraju, L.C. Calhoun, C.H. Lee, Improvement of dark current using InP/InGaAsP transition layer in large-area InGaAs MSM photodetectors. *IEEE Trans. Electron Devices* **51**, 351–356 (2004)
  44. E. Dröge, E.H. Böttcher, D. Bimberg, O. Reimann, R. Steingrüber, 70 GHz InGaAs MSM photodetectors for polarization-insensitive operation. *Electron. Lett.* **34**, 1421–1422 (1998)
  45. D. Kuhl, F. Hieronymi, E.H. Böttcher, T. Wolf, D. Bimberg, J. Kuhl, M. Klingenstein, Influence of space charges on the impulse response of InGaAs MSM photodetectors. *J. Lightw. Technol.* **10**, 753–759 (1992)

46. S.D. Personick, Receiver design for digital fiber-optic communication systems, Parts I and II. *Bell Syst. Tech. J.* **52**, 843–886 (1973)
47. R.G. Smith, S.D. Personick, Receiver design for optical fiber communications systems, in *Semiconductor Devices for Optical Communication*, ed. by H. Kressel (Springer, New York, 1980), Chap. 4
48. S.R. Forrest, Sensitivity of avalanche photodetector receivers for high-bit-rate long-wavelength optical communication systems, in *Semiconductors and Semimetals*, ed. by W.T. Tsang. *Lightwave Communications Technology*, vol. 22 (Academic Press, Orlando, 1985), Part D, Chap. 4
49. B.L. Kasper, J.C. Campbell, Multigigabit-per-second avalanche photodiode lightwave receivers. *J. Lightw. Technol.* **LT-5**, 1351–1364 (1987)
50. R.J. McIntyre, Multiplication noise in uniform avalanche diodes. *IEEE Trans. Electron Devices* **13**, 154–158 (1966)
51. R.J. McIntyre, The distribution of gains in uniformly multiplying avalanche photodiodes: Theory. *IEEE Trans. Electron Devices* **19**, 703–713 (1972)
52. R.J. McIntyre, Factors affecting the ultimate capabilities of high speed avalanche photodiodes and a review of the state-of-the-art, *Tech. Dig. Internat. Electron Dev. Mtg.* **19**, 213–216 (1973)
53. R.B. Emmons, Avalanche-photodiode frequency response. *J. Appl. Phys.* **38**, 3705–3714 (1967)
54. C.A. Lee, R.A. Logan, R.L. Batdorf, J.J. Kleimack, W. Weigmann, Ionization rates of holes and electrons in silicon. *Phys. Rev. A* **134**, 761–773 (1964)
55. J. Conradi, The distributions of gains in uniformly multiplying avalanche photodiodes: experimental. *IEEE Trans. Electron Devices* **19**, 713–718 (1972)
56. W.N. Grant, Electron and hole ionization rates in epitaxial silicon at high electric fields. *Solid-State Electron.* **16**, 1189–1203 (1973)
57. T. Kaneda, H. Matsumoto, T. Yamaoka, A model for reach-through avalanche photodiodes (RAPD's). *J. Appl. Phys.* **47**, 3135–3139 (1976)
58. H. Melchior, A.R. Hartman, D.P. Schinke, T.E. Seidel, Planar epitaxial silicon avalanche photodiode. *Bell Syst. Tech. J.* **57**, 1791–1807 (1978)
59. S.R. Forrest, M. DiDomenico, Jr., R.G. Smith, H.J. Stocker, Evidence of tunneling in reverse-bias III–V photodetector diodes. *Appl. Phys. Lett.* **36**, 580–582 (1980)
60. H. Ando, H. Kaaba, M. Ito, T. Kaneda, Tunneling current in InGaAsP and optimum design for InGaAs/InP avalanche photo-diodes. *Jpn. J. Appl. Phys.* **19**, 1277–1280 (1980)
61. K. Nishida, K. Taguchi, Y. Matsumoto, InGaAsP heterojunction avalanche photodiodes with high avalanche gain. *Appl. Phys. Lett.* **35**, 251–253 (1979)
62. S.R. Forrest, O.K. Kim, R.G. Smith, Optical response time of In<sub>0.53</sub>Ga<sub>0.47</sub>As avalanche photodiodes. *Appl. Phys. Lett.* **41**, 95–98 (1982)
63. J.C. Campbell, A.G. Dentai, W.S. Holden, B.L. Kasper, High-performance avalanche photodiode with separate absorption, grading, and multiplication regions. *Electron. Lett.* **18**, 818–820 (1983)
64. Y. Matsushima, A. Akiba, K. Sakai, K. Kushirn, Y. Node, K. Utaka, High-speed response InGaAs/InP heterostructure avalanche photodiode with InGaAsP buffer layers. *Electron. Lett.* **18**, 945–946 (1982)
65. F. Capasso, A.Y. Cho, P.W. Foy, Low-dark-current low-voltage 1.3–1.6  $\mu\text{m}$  avalanche photodiode with high-low electric field profile and separate absorption and multiplication regions by molecular beam epitaxy. *Electron. Lett.* **20**, 635–637 (1984)
66. P. Webb, R. McIntyre, J. Scheibling, M. Holunga, A planar InGaAs APD fabricated using Si implantation and regrowth techniques, *Opt. Fiber Commun. Conf. (OFC'88)*, Techn. Digest (New Orleans, LA, USA, 1988), vol. 1, paper WQ32
67. L.E. Tarof, Planar InP-InGaAs avalanche photodetectors with n-multiplication layer exhibiting a very high gain-bandwidth product. *IEEE Photon. Technol. Lett.* **2**, 643–645 (1990)
68. M.A. Itzler, K.K. Loi, S. McCoy, N. Codd, N. Komaba, Manufacturable planar bulk-InP avalanche photodiodes for 10 Gb/s applications, *Proc. Annual Meeting IEEE LEOS 1999*, San Francisco, CA, USA (1999), pp. 748–749

69. Y. Okuto, C.R. Crowell, Ionization coefficients in semiconductors: a nonlocalized property. *Phys. Rev. B* **10**, 4284–4296 (1974)
70. M.M. Hayat, B.E.A. Saleh, M.C. Teich, Effect of dead space on gain and noise of double-carrier multiplication avalanche photodiodes. *IEEE Trans. Electron Devices* **39**, 546–552 (1992)
71. R.J. McIntyre, A new look at impact ionization – part 1: a theory of gain, noise, breakdown probability and frequency response. *IEEE Trans. Electron Devices* **48**, 1623–1631 (1999)
72. X. Li, X. Zheng, S. Wang, F. Ma, J.C. Campbell, Calculation of gain and noise with dead space for GaAs and  $\text{Al}_x\text{Ga}_{1-x}\text{As}$  avalanche photodiodes. *IEEE Trans. Electron Devices* **49**, 1112–1117 (2002)
73. B. Jacob, P.N. Robson, J.P.R. David, G.J. Rees, Fokker-Planck model for nonlocal impact ionization in semiconductors. *J. Appl. Phys.* **90**, 1314–1317 (2001)
74. A. Spinelli, A.L. Lacaita, Mean gain of avalanche photodiodes in a dead space model. *IEEE Trans. Electron Devices* **43**, 23–30 (1996)
75. G.M. Dunn, G.J. Rees, J.P.R. David, S.A. Plimmer, D.C. Herbert, Monte Carlo simulation of impact ionization and current multiplication in short GaAs  $\text{p}^+\text{-i-n}^+$  diodes. *Semicond. Sci. Technol.* **12**, 111–120 (1997)
76. S.A. Plimmer, J.P.R. David, D.S. Ong, K.F. Li, A simple model for avalanche multiplication including deadspace effects. *IEEE Trans. Electron Devices* **46**, 769–775 (1999)
77. K.F. Li, S.A. Plimmer, J.P.R. David, R.C. Tozer, G.J. Rees, P.N. Robson, C.C. Button, J.C. Clark, Low avalanche noise characteristics in thin InP  $\text{p}^+\text{-i-n}^+$  diodes with electron initiated multiplication. *IEEE Photon. Technol. Lett.* **11**, 364–366 (1999)
78. M.A. Saleh, M.M. Hayat, P.O. Sotirelis, A.L. Holmes, J.C. Campbell, B. Saleh, M. Teich, Impact-ionization and noise characteristics of thin III–V avalanche photodiodes. *IEEE Trans. Electron Devices* **48**, 2722–2731 (2001)
79. C.H. Tan, J.C. Clark, J.P.R. David, G.J. Rees, S.A. Plimmer, R.C. Tozer, D.C. Herbert, D.J. Robbins, W.Y. Leong, J. Newey, Avalanche noise measurements in thin Si  $\text{p}^+\text{-i-n}^+$  diodes. *Appl. Phys. Lett.* **76**, 3926–3928 (2000)
80. T. Watanabe, K. Torikai, K. Makita, T. Fukushima, T. Uji, Impact ionization rates in  $(100)\text{Al}_{0.48}\text{In}_{0.52}\text{As}$ . *IEEE Electron Device Lett.* **11**, 437–439 (1990)
81. N. Li, R. Sidhu, X. Li, F. Ma, X. Zheng, S. Wang, G. Karve, S. Demiguel, A.L. Holmes, Jr., J.C. Campbell, InGaAs/InAlAs avalanche photodiode with undepleted absorber. *Appl. Phys. Lett.* **82**, 2175–2177 (2003)
82. E. Yagyu, E. Ishimura, M. Nakaji, T. Aoyagi, Y. Tokuda, Simple planar structure for high-performance AlInAs avalanche photodiodes. *IEEE Photon. Technol. Lett.* **18**, 76–78 (2006)
83. E. Yagyu, E. Ishimura, M. Nakaji, T. Aoyagi, K. Yoshiara, Y. Tokuda, Investigation of guardring-free planar AlInAs avalanche photodiodes. *IEEE Photon. Technol. Lett.* **18**, 1264–1266 (2006)
84. Y. Kang, H.-D. Liu, M. Morse, M.J. Paniccia, M. Zadka, S. Litski, G. Sarid, A. Pauchard, Y.-H. Kuo, H.-W. Chen, W.S. Zaoui, J.E. Bowers, A. Beling, D.C. McIntosh, X. Zheng, J.C. Campbell, Monolithic germanium/silicon avalanche photodiodes with 340 GHz gain–bandwidth product. *Nat. Photon.* **3**, 59–63 (2008)
85. P. Yuan, S. Wang, X. Sun, X.G. Zheng, A.L. Holmes, Jr., J.C. Campbell, Avalanche photodiodes with an impact-ionization-engineered multiplication region. *IEEE Photon. Technol. Lett.* **12**, 1370–1372 (2000)
86. O.-H. Kwon, M.M. Hayat, S. Wang, J.C. Campbell, A.L. Holmes, Jr., B.E.A. Saleh, M.C. Teich, Optimal excess noise reduction in thin heterojunction  $\text{Al}_{0.6}\text{Ga}_{0.4}\text{As}$ -GaAs avalanche photodiodes. *IEEE J. Quantum Electron.* **39**, 1287–1296 (2003)
87. C. Groves, C.K. Chia, R.C. Tozer, J.P.R. David, G.J. Rees, Avalanche noise characteristics of single  $\text{Al}_x\text{Ga}_{1-x}\text{As}$  ( $0.3 < x < 0.6$ )-GaAs heterojunction APDs. *IEEE J. Quantum Electron.* **41**, 70–75 (2005)
88. S. Wang, R. Sidhu, X.G. Zheng, X. Li, Sun, A.L. Holmes, Jr., J.C. Campbell, Low-noise avalanche photodiodes with graded impact-ionization-engineered multiplication region. *IEEE Photon. Technol. Lett.* **13**, 1346–1348 (2001)

89. S. Wang, F. Ma, X. Li, R. Sidhu, X.G. Zheng, X. Sun, A.L. Holmes, Jr., J.C. Campbell, Ultra-low noise avalanche photodiodes with a 'centered-well' multiplication region. *IEEE J. Quantum Electron.* **39**, 375–378 (2003)
90. M.M. Hayat, O.-H. Kwon, S. Wang, J.C. Campbell, B.E.A. Saleh, M.C. Teich, Boundary effects on multiplication noise in thin heterostructure avalanche photodiodes: theory and experiment. *IEEE Trans. Electron Devices* **49**, 2114–2123 (2002)
91. S. Wang, J.B. Hurst, F. Ma, R. Sidhu, X. Sun, X.G. Zheng, A.L. Holmes, Jr., J.C. Campbell, A. Huntington, L.A. Coldren, Low-noise impact-ionization-engineered avalanche photodiodes grown on InP substrates. *IEEE Photon. Technol. Lett.* **14**, 1722–1724 (2002)
92. N. Duan, S. Wang, F. Ma, N. Li, J.C. Campbell, C. Wang, L.A. Coldren, High-speed and low-noise SACM avalanche photodiodes with an impact-ionization engineered multiplication region. *IEEE Photon. Technol. Lett.* **17**, 1719–1721 (2005)
93. F.J. Effenberger, A.M. Joshi, Ultrafast, dual-depletion region, InGaAs/InP p-i-n detector. *J. Lightw. Technol.* **14**, 1859–1864 (1996)
94. G.A. Davis, R.E. Weiss, R.A. LaRue, K.J. Williams, R.D. Esman, A 920–1650 nm high current photodetector. *IEEE Photon. Technol. Lett.* **8**, 1373–1375 (1996)
95. T. Ishibashi, N. Shimizu, S. Kodama, H. Ito, T. Nagatsuma, T. Furuta, Uni-traveling-carrier photodiodes, in *Ultrafast Electronics and Optoelectronics, 1997*. OSA Trends in Optics and Photonics Series, vol. 13 (Opt. Soc. America, Washington, 1997), paper UC3
96. X. Li, N. Li, X. Zheng, S. Demiguel, J.C. Campbell, D. Tulchinsky, K.J. Williams, High-speed high-saturation-current InP/InGaAs photodiode with partially depleted absorber, *Opt. Fiber Commun. Conf. (OFC'03)*, Techn. Digest (Atlanta, GA, USA, 2003), vol. 1, pp. 338–339
97. A.M. Joshi, X. Wang, DC to 50 GHz wide bandwidth InGaAs photodiodes and photoreceivers, in *Reliability of Optical Fibers and Optical Fiber Systems*, ed. by D.K. Paul. Proc. SPIE, vol. CR73 (1999), pp. 181–196
98. K.J. Williams, R.D. Esman, Design considerations for high-current photodetectors. *J. Lightw. Technol.* **17**, 1443–1454 (1999)
99. A.M. Joshi, D. Becker, GRIN lens-coupled top-illuminated photodetectors for high-power applications, *2007 IEEE Internat. Topical Meeting on Microwave Photonics*, Victoria, BC, Canada (2007), pp. 18–20
100. T. Furuta, H. Ito, T. Ishibashi, Photocurrent dynamics of uni-traveling-carrier and conventional pin photodiodes. *Inst. Phys. Conf. Ser.* **166**, 419–422 (2000)
101. H. Ito, T. Furuta, S. Kodama, T. Ishibashi, Zero-bias high-speed and high-output-voltage operation of cascade-twin uni-travelling-carrier photodiode. *Electron. Lett.* **36**, 2034–2036 (2000)
102. N. Shimizu, N. Watanabe, T. Furuta, T. Ishibashi, InP-InGaAs uni-traveling-carrier photodiode with improved 3 dB bandwidth of over 150 GHz. *IEEE Photon. Technol. Lett.* **10**, 412–414 (1998)
103. H. Ito, T. Furuta, S. Kodama, N. Watanabe, T. Ishibashi, InP/InGaAs uni-travelling-carrier photodiode with 220 GHz bandwidth. *Electron. Lett.* **35**, 1556–1557 (2004)
104. T. Ishibashi, High speed heterostructure devices, in *Semiconductors and Semimetals*, vol. 41 (Academic Press, San Diego, 1994), Chap. 5
105. Y.-S. Wu, J.-W. Shi, Dynamic analysis of high-power and high-speed near-ballistic untraveling carrier photodiodes at W-band. *IEEE Photon. Technol. Lett.* **20**, 1160–1162 (2008)
106. J.-W. Shi, F.-M. Kuo, C.-J. Wu, C.L. Chang, C.-Y. Liu, C.Y. Chen, J.-I. Chyi, Extremely high saturation current-bandwidth product performance of a near-ballistic uni-traveling-carrier photodiode with a flip-chip bonding structure. *IEEE J. Quantum Electron.* **46**, 80–86 (2010)
107. X. Li, S. Demiguel, N. Li, J.C. Campbell, D.L. Tulchinsky, K.J. Williams, Backside illuminated high saturation current partially depleted absorber photodetectors. *Electron. Lett.* **39**, 1466–1467 (2003)
108. D.-H. Jun, J.-H. Jang, I. Adesida, J.-I. Song, Improved efficiency-bandwidth product of modified uni-traveling carrier photodiode structures using an undoped photo-absorption layer. *Jpn. J. Appl. Phys.* **45**, 3475–3478 (2006)



109. X. Wang, N. Duan, H. Chen, J.C. Campbell, InGaAs/InP photodiodes with high responsivity and high saturation power. *IEEE Photon. Technol. Lett.* **19**, 1272–1274 (2007)
110. J. Klamkin, Y.-C. Chang, A. Ramaswamy, L.A. Johansson, J.E. Bowers, S.P. DenBaars, L.A. Coldren, Output saturation and linearity of waveguide unitraveling-carrier photodiodes. *IEEE J. Quantum Electron.* **44**, 354–359 (2008)
111. M. Chtioui, A. Enard, D. Carpentier, S. Bernard, B. Rousseau, F. Lelarge, F. Pommereau, M. Achouche, High-power high-linearity uni-traveling-carrier photodiodes for analog photonic links. *IEEE Photon. Technol. Lett.* **20**, 202–204 (2008)
112. A. Beling, H. Pan, H. Chen, J.C. Campbell, Linearity of modified uni-traveling carrier photodiodes. *J. Lightw. Technol.* **26**, 2373–2378 (2008)
113. H. Pan, A. Beling, J.C. Campbell, High-linearity uni-traveling-carrier photodiodes. *IEEE Photon. Technol. Lett.* **21**, 1855–1857 (2009)
114. A. Beling, H. Pan, H. Chen, J.C. Campbell, Measurement and modeling of a high-linearity modified uni-traveling carrier photodiode. *IEEE Photon. Technol. Lett.* **20**, 1219–1221 (2008)
115. M. Chtioui, D. Carpentier, B. Rousseau, F. Lelarge, A. Enard, M. Achouche, Experimental and theoretical linearity investigation of high-power unitraveling-carrier photodiodes. *IEEE Photon. Technol. Lett.* **21**, 1247–1249 (2009)
116. A. Umbach, D. Trommer, R. Steingrüber, S. Seeger, W. Ebert, G. Unterbörsch, Ultrafast, high-power 1.55  $\mu\text{m}$  side-illuminated photodetector with integrated spot size converter, *Opt. Fiber Commun. Conf. (OFC'2000)*, Techn. Digest (Baltimore, MD, USA, 2000), pp. 117–119
117. T. Takeuchi, T. Nakata, K. Makita, T. Torikai, High-power and high-efficiency photodiode with an evanescently coupled graded-index waveguide for 40 Gb/s applications, *Opt. Fiber Commun. Conf. (OFC'01)*, Techn. Digest (Anaheim, CA, USA, 2001), vol. 3, paper WQ2–1-3
118. Y.-S. Wu, P.-H. Chiu, J.-W. Shi, High-speed and high-power performance of a dual-step evanescently-coupled uni-traveling-carrier photodiode at 1.55  $\mu\text{m}$  wavelength, *Opt. Fiber Commun. Conf. and Nat. Fiber Opt. Eng. Conf. (OFC/NFOEC'07)*, Techn. Digest (Anaheim, CA, USA, 2007), paper OThG1
119. M. Achouche, V. Magnin, J. Harari, F. Lelarge, E. Derouin, C. Jany, D. Carpentier, F. Blanche, D. Decoster, High performance evanescent edge coupled waveguide unitraveling-carrier photodiodes for > 40 Gb/s optical receivers. *IEEE Photon. Technol. Lett.* **16**, 584–586 (2004)
120. Y. Muramoto, K. Kato, M. Mitsuhashi, O. Nakajima, Y. Matsuoka, N. Shimizu, T. Ishibashi, High output voltage, high speed, high efficiency uni-travelling carrier waveguide photodiode. *Electron. Lett.* **34**, 122–123 (1998)
121. C.C. Renaud, D. Moodie, M. Robertson, A.J. Seeds, High output power at 110 GHz with waveguide uni-travelling carrier photodiode, *Proc. Annual Meeting IEEE LEOS 2007*, Lake Buena Vista, FL (2007), pp. 782–783
122. S. Demiguel, X. Li, N. Li, H. Chen, J.C. Campbell, J. Wei, A. Anselm, Analysis of partially depleted absorber waveguide photodiodes. *J. Lightw. Technol.* **23**, 2505–2512 (2005)
123. C. Cohen-Jonathan, L. Giraudet, A. Bonzo, J.P. Praseuth, Waveguide AlInAs/GaAlInAs avalanche photodiode with a gain-bandwidth product over 160 GHz. *Electron. Lett.* **33**, 1492–1493 (1997)
124. T. Nakata, T. Takeuchi, K. Maliita, Y. Amamiya, T. Kalo, Y. Suzuki, T. Torikai, High-sensitivity 40-Gbps receiver with a wideband InAlAs waveguide avalanche photodiode, *Proc. 28th Europ. Conf. Opt. Commun. (ECOC'02)*, Copenhagen, DK (2002), paper 10.5.1
125. G.S. Kinsey, J.C. Campbell, A.G. Dentai, Waveguide avalanche photodiode operating at 1.55  $\mu\text{m}$  with a gain-bandwidth product of 320 GHz. *IEEE Photon. Technol. Lett.* **13**, 842–844 (2001)
126. J. Wei, F. Xia, S.R. Forrest, A high-responsivity high-bandwidth asymmetric twin-waveguide coupled InGaAs-InP-InAlAs avalanche photodiode. *IEEE Photon. Technol. Lett.* **14**, 1590–1592 (2002)

127. J.E. Bowers, C.A. Burrus, High-speed zero-bias waveguide photodetectors. *Electron. Lett.* **22**, 905–906 (1986)
128. K. Kato, A. Kozen, Y. Muramoto, Y. Itaya, T. Nagatsuma, M. Yaita, 110-GHz, 50 %-efficiency mushroom-mesa waveguide p-i-n photodiode for a 1.55- $\mu\text{m}$  wavelength. *IEEE Photon. Technol. Lett.* **6**, 719–721 (1994)
129. H. Fukano, A. Kozen, K. Kato, O. Nakajima, Edge-illuminated refracting-facet photodiode with high responsivity and low-operation voltage. *Electron. Lett.* **32**, 2346–2347 (1996)
130. H. Fukano, Y. Matsuoka, A low-cost edge-illuminated refracting-facet photodiode module with large bandwidth and high responsivity. *J. Lightw. Technol.* **18**, 79–83 (2000)
131. H. Ito, T. Furuta, S. Kodama, T. Ishibashi, InP/InGaAs uni-travelling-carrier photodiode with 310 GHz bandwidth. *Electron. Lett.* **36**, 1809–1810 (2000)
132. Y. Muramoto, K. Yoshino, S. Kodama, Y. Hirota, H. Ito, T. Ishibashi, 100 and 160 Gbit/s operation of uni-travelling-carrier photodiode module. *Electron. Lett.* **40**, 378–379 (2004)
133. H. Ito, T. Furuta, T. Ito, Y. Muramoto, K. Tsuzuki, K. Yoshino, T. Ishibashi, W-band uni-travelling-carrier photodiode module for high-power photonic millimeter-wave generation. *Electron. Lett.* **38**, 1376–1377 (2002)
134. H. Ito, T. Ito, Y. Muramoto, T. Furuta, T. Ishibashi, Rectangular waveguide output unitraveling-carrier photodiode module for high-power photonic millimeter-wave generation in the F-band. *J. Lightw. Technol.* **21**, 3456–3462 (2003)
135. T. Furuta, T. Ito, Y. Muramoto, H. Ito, M. Tokumitsu, T. Ishibashi, D-band rectangular-waveguide-output uni-travelling-carrier photodiode module. *Electron. Lett.* **41**, 715–716 (2005)
136. H.-G. Bach, A. Beling, G.G. Mekonnen, R. Kunkel, D. Schmidt, W. Ebert, A. Seeger, M. Stollberg, W. Schlaak, InP-based waveguide-integrated photodetector with 100-GHz bandwidth. *IEEE J. Sel. Top. Quantum Electron.* **10**, 668–672 (2004)
137. A. Beling, H.-G. Bach, G.G. Mekonnen, T. Eckhardt, R. Kunkel, D. Schmidt, C. Schubert, Highly efficient PIN photodetector module for 80 Gbit/s and beyond, *Opt. Fiber Commun. Conf. (OFC'05)*, Techn. Digest (Anaheim, CA, USA, 2005), paper OFM1
138. G. Unterbörsh, D. Trommer, A. Umbach, R. Ludwig, H.-G. Bach, High-power performance of a high-speed photodetector, *Proc. 24th Europ. Conf. Opt. Commun. (ECOC'98)*, Madrid, Spain (1998), pp. 67–68
139. A. Beling, D. Schmidt, H.-G. Bach, G.G. Mekonnen, R. Ziegler, V. Eisner, M. Stollberg, G. Jacumeit, E. Gottwald, C.-J. Weiske, A. Umbach, High power 1550 nm twin-photodetector modules with 45 GHz bandwidth based on InP, *Opt. Fiber Commun. Conf. (OFC/IOOC'02)*, Techn. Digest (Anaheim, CA, USA, 2002), paper WN4, pp. 274–275
140. H.-G. Bach, A. Matiss, C.C. Leonhardt, R. Kunkel, D. Schmidt, M. Schell, A. Umbach, Monolithic 90° hybrid with balanced PIN photodiodes for 100 Gbit/s PM-QPSK receiver applications, *Opt. Fiber Commun. Conf. and Nat. Fiber Opt. Eng. Conf. (OFC/NFOEC'09)*, Techn. Digest (San Diego, CA, USA, 2009), pp. 1–3
141. A. Beling, PIN photodiode modules for 80 Gbit/s and beyond, *Opt. Fiber Commun. Conf. (OFC'06)*, Techn. Digest (Anaheim, CA, USA, 2006), paper OFI1
142. A. Beling, H.-G. Bach, G.G. Mekonnen, R. Kunkel, D. Schmidt, Miniaturized waveguide-integrated p-i-n photodetector with 120-GHz bandwidth and high responsivity. *IEEE Photon. Technol. Lett.* **17**, 2152–2154 (2005)
143. R.J. Hawkins, R.J. Deri, O. Wada, Optical power transfer in vertically integrated impedance-matched waveguide/photodetectors: physics and implications for diode-length reduction. *Opt. Lett.* **16**, 470–472 (1991)
144. R.J. Deri, W. Döldissen, R.J. Hawkins, R. Bhat, J.B.D. Soole, L.M. Schiavone, M. Seto, N. Andreadakis, Y. Silberberg, M.A. Koza, Efficient vertical coupling of photodiodes to InGaAsP rib waveguides. *Appl. Phys. Lett.* **58**, 2749–2751 (1991)
145. A. Beling, InP-based 1.55  $\mu\text{m}$  waveguide-integrated photodetectors for high-speed applications, in *Integrated Optics: Devices, Materials, and Technologies X*, ed. by Y. Sidorin, C.A. Waechter. Proc. SPIE, vol. 6123 (2006), pp. 156–167

146. A. Beling, H.-G. Bach, G.G. Mekonnen, R. Kunkel, D. Schmidt, High-speed miniaturized photodiode and parallel-fed traveling-wave photodetectors based on InP. *IEEE J. Sel. Top. Quantum Electron.* **13**, 15–21 (2007)
147. F. Xia, J.K. Thomson, M.R. Gokhale, P.V. Studenkov, J. Wei, W. Lin, S.R. Forrest, An asymmetric twin-waveguide high-bandwidth photodiode using a lateral taper coupler. *IEEE Photon. Technol. Lett.* **13**, 845–847 (2001)
148. M. Achouche, V. Magnin, J. Harari, D. Carpentier, E. Derouin, C. Jany, F. Blanche, D. Decoster, Design and fabrication of a p-i-n photodiode with high responsivity and large alignment tolerances for 40 Gb/s applications. *IEEE Photon. Technol. Lett.* **18**, 556–558 (2006)
149. S. Demiguel, N. Li, X. Li, X. Zheng, J. Kim, J.C. Campbell, H. Lu, A. Anselm, Very high-responsivity evanescently coupled photodiodes integrating a short planar multimode waveguide for high-speed applications. *IEEE Photon. Technol. Lett.* **15**, 1761–1763 (2003)
150. Y.-S. Wu, J.-W. Shi, P.-H. Chiu, W. Lin, High-performance dual-step evanescently coupled uni-traveling-carrier photodiodes. *IEEE Photon. Technol. Lett.* **19**, 1682–1684 (2007)
151. S. Demiguel, X.-G. Zheng, N. Li, X. Li, J.C. Campbell, J. Decobert, N. Tschertner, A. Anselm, High-responsivity and high-speed evanescently-coupled avalanche photodiodes. *Electron. Lett.* **39**, 1848–1849 (2003)
152. K. Makita, K. Shiba, T. Nakata, E. Mizuki, S. Watanabe, Recent advances in ultra-high-speed waveguide photodiodes for optical communications. *IEICE Trans. Electron.* **E92-C**, 922–927 (2009)
153. H.F. Taylor, O. Eknayan, C.S. Park, K.N. Choi, K. Chang, Traveling wave photodetectors, in *Optoelectronic Signal Processing for Phased-Array Antennas II*, ed. by B.M. Hendrickson, G.A. Koepf. Proc. SPIE, vol. 1217 (1990), pp. 59–63
154. K.S. Giboney, M.J.W. Rodwell, J.E. Bowers, Traveling-wave photodetectors. *IEEE Photon. Technol. Lett.* **4**, 1363–1365 (1992)
155. K.S. Giboney, M.J.W. Rodwell, J.E. Bowers, Traveling-wave photodetector theory. *IEEE Trans. Microw. Theory Tech.* **45**, 1310–1319 (1997)
156. A. Stöhr, A. Malcoci, A. Sauerwald, I.C. Mayorga, R. Güsten, D.S. Jäger, Ultra-wide-band traveling-wave photodetectors for photonic local oscillators. *J. Lightw. Technol.* **21**, 3062–3070 (2003)
157. V.M. Hietala, A. Vawter, T.M. Brennan, B.E. Hammons, Traveling-wave photodetectors for high-power, large-bandwidth applications. *IEEE Trans. Microw. Theory Tech.* **43**, 2291–2298 (1995)
158. K.S. Giboney, R.L. Nagarajan, T.E. Reynolds, S.T. Allen, R.P. Mirin, M.J.W. Rodwell, J.E. Bowers, Travelling-wave photodetectors with 172-GHz bandwidth and 76-GHz bandwidth-efficiency product. *IEEE Photon. Technol. Lett.* **7**, 412–414 (1995)
159. Y.-J. Chiu, S.B. Fleischer, J.E. Bowers, High-speed low-temperature-grown GaAs p-i-n traveling-wave photodetector. *IEEE Photon. Technol. Lett.* **10**, 1012–1014 (1998)
160. L.Y. Lin, M.C. Wu, T. Itoh, T.A. Vang, R.R. Muller, D.L. Sivco, A.Y. Cho, High-power high-speed photodetectors—Design, analysis, and experimental demonstration. *IEEE Trans. Microw. Theory Tech.* **45**, 1320–1331 (1997)
161. M.S. Islam, S. Murthy, T. Itoh, M.C. Wu, D. Novak, R.B. Waterhouse, D.L. Sivco, A.Y. Cho, Velocity-matched distributed photodetectors with p-i-n photodiodes. *IEEE Trans. Microw. Theory Tech.* **49**, 1914–1920 (2001)
162. E. Dröge, E.H. Böttcher, S. Kollakowski, A. Strittmatter, D. Bimberg, O. Reimann, R. Steingrüber, 78 GHz distributed MSM photodetector. *Electron. Lett.* **34**, 2241–2242 (1998)
163. Y. Hirota, T. Ishibashi, H. Ito, 1.55  $\mu\text{m}$  wavelength periodic traveling-wave photodetector fabricated using untraveling-carrier photodiode structures. *J. Lightw. Technol.* **19**, 1751–1758 (2001)
164. M.J.W. Rodwell, S.T. Allen, R.Y. Yu, M.G. Case, U. Bhattacharya, M. Reddy, E. Carman, M. Kamegawa, Y. Konishi, J. Pusz, R. Pulella, Active and nonlinear wave propagation devices in ultrafast electronics and optoelectronics. Proc. IEEE **82**, 1037–1059 (1994)
165. S. Murthy, S.-J. Kim, T. Jung, Z.-Z. Wang, W. Hsin, T. Itoh, M.C. Wu, Backward-wave cancellation in distributed traveling-wave photodetectors. *J. Lightw. Technol.* **21**, 3071–3077 (2003)

166. A. Nespola, T. Chau, M.C. Wu, G. Ghione, Analysis of failure mechanisms in velocity-matched distributed photodetectors. *IEE Proc. Optoelectron.* **146**, 25–30 (1999)
167. C.L. Goldsmith, G.A. Magel, R.J. Baca, Principles and performance of traveling-wave photodetector arrays. *IEEE Trans. Microw. Theory Tech.* **45**, 1342–1350 (1997)
168. A. Beling, H. Chen, H. Pan, J.C. Campbell, High-power monolithically integrated traveling wave photodiode array. *IEEE Photon. Technol. Lett.* **21**, 1813–1815 (2009)
169. S. Murthy, M.C. Wu, D. Sivco, A.Y. Cho, Parallel feed traveling wave distributed pin photodetectors with integrated MMI couplers. *Electron. Lett.* **38**, 78–79 (2002)
170. A. Beling, H.-G. Bach, G.G. Mekonnen, R. Kunkel, D. Schmidt, J.C. Campbell, High-frequency performance of a high-power traveling wave photodetector with parallel optical feed, *65th Ann. Device Res. Conf. (DRC'07)*, South Bend, IN (2007), pp. 187–188
171. A. Beling, J.C. Campbell, H.-G. Bach, G.G. Mekonnen, D. Schmidt, Parallel-fed traveling wave photodetector for > 100-GHz applications. *J. Lightw. Technol.* **26**, 16–20 (2008)
172. G.G. Mekonnen, H.-G. Bach, A. Beling, R. Kunkel, D. Schmidt, W. Schlaak, 80-Gb/s InP-based waveguide-integrated photoreceiver. *IEEE J. Sel. Top. Quantum Electron.* **11**, 356–360 (2005)
173. A. Huber, D. Huber, T. Morf, H. Jackel, C. Bergamaschi, V. Hum, M. Ludwig, M. Schlechtweg, Monolithic, high transimpedance gain (3.3 k $\Omega$ ), 40 Gbit/s InP-HBT photoreceiver with differential outputs. *Electron. Lett.* **35**, 897–898 (1999)
174. A. Leich, V. Hurm, J. Sohn, T. Feltgen, W. Bronner, K. Kohler, H. Walcher, J. Rosenzweig, M. Schlechtweg, 65 GHz bandwidth optical receiver combining a flip-chip mounted waveguide photodiode and GaAs-based HEMT distributed amplifier. *Electron. Lett.* **38**, 1706–1707 (2002)
175. W. Schlaak, G.G. Mekonnen, H.-G. Bach, C. Bornholdt, C. Schramm, A. Umbach, R. Steingrüber, A. Seeger, G. Unterbörsch, W. Passenberg, P. Wolfram, 40 Gbit/s eye pattern of a photoreceiver OEIC with monolithically integrated spot size converter. *Opt. Fiber Commun. Conf. (OFC'01)*, Techn. Digest (Anaheim, CA, USA, 2001), vol. 3, paper WQ4-1-3
176. Th.T.Y. Wong, *Fundamentals of Distributed Amplification* (Artech, Boston, 1993)
177. F. Xia, J. Wei, V. Menon, S.R. Forrest, Monolithic integration of a semiconductor optical amplifier (SOA) and a high-speed p-i-n photodiode using asymmetric twin-waveguide technology. *Opt. Fiber Commun. Conf. (OFC'03)*, Techn. Digest (Atlanta, GA, USA, 2003), vol. 1, pp. 189–190
178. B. Mason, J.M. Geary, J.M. Freund, A. Ougazzaden, C. Lentz, K. Glogovsky, G. Przybylek, L. Peticolas, F. Walters, L. Reynolds, J. Boardman, T. Kercher, M. Rader, D. Monroe, L. Ketelsen, S. Chandrasekhar, L.L. Buhl, 40 Gb/s photonic integrated receiver with  $-17$  dBm sensitivity. *Opt. Fiber Commun. Conf. (OFC'02)*, Techn. Digest (Anaheim, CA, USA, 2002), post-deadline paper FB10
179. R.H. Derksen, G. Lehmann, C. Weiske, C. Schubert, R. Ludwig, S. Ferber, C. Schmidt-Langhorst, M. Möller, J. Lutz, Integrated 100 Gbit/s ETDM receiver in a transmission experiment over 480 km DMF. *Opt. Fiber Commun. Conf. (OFC'06)*, Techn. Digest (Anaheim, CA, USA, 2006), post-deadline paper PDP37
180. C. Schubert, R.H. Derksen, M. Möller, R. Ludwig, C.-J. Weiske, J. Lutz, S. Ferber, C. Schmidt-Langhorst, 107 Gbit/s transmission using an integrated ETDM receiver. *Proc. 32nd Europ. Conf. Opt. Commun. (ECOC'06)*, Cannes, France (2006), paper Tu1.5.5
181. P.J. Winzer, G. Raybon, M. Duelk, 107 Gb/s optical ETDM transmitter for 100 G Ethernet transport. *Proc. 31st Europ. Conf. Opt. Commun. (ECOC'05)*, Glasgow, UK (2005), vol. 6, paper Th4.1.1
182. J.H. Sinsky, A. Adamiecki, L. Buhl, G. Raybon, P. Winzer, O. Wohlgenuth, M. Duelk, C.R. Doerr, A. Umbach, H.-G. Bach, D. Schmidt, A 107-Gbit/s optoelectronic receiver utilizing hybrid integration of a photodetector and electronic demultiplexer. *J. Lightw. Technol.* **26**, 114–119 (2008)

# Chapter 8

## Systems with Higher-order Modulation

Yaakov Achiam, Arkady M. Kaplan, and Matthias Seimetz

**Abstract** The chapter covers concepts, systems aspects, and key components for higher-order modulation. The introductory section presents relevant variants of higher-order modulation formats and includes coherent detection and coherent optical orthogonal frequency-division multiplexing as well. The next section is devoted to system configurations with particular emphasis on transmitter structures and receiver concepts, whereas the subsequent chapter focuses on key components. Included are LiNbO<sub>3</sub>-based quadrature modulators, integrated coherent receivers, in particular 90° hybrids, ranging from new concepts to proven implementations. A treatment of integrated balanced four-branch receivers ranges from theoretical analysis to the presentation of commercially available devices. The chapter concludes with a discussion of system trends and expected future developments.

### 8.1 Introduction

The emerging demand for digital video over the Internet, as well as the need for storage networking, carrier wholesaling, and science applications, is prompting an *exploding need for optical data transmission capacity* and is transferring the Internet granularity from 10 Gbit/s to 100 Gbit/s.

---

Yaakov Achiam (✉)  
4 Tseelas St., Omer 8496500, Israel  
e-mail: Yachiam@gmail.com

Arkady Morris Kaplan  
CeLight Inc., 12200 Tech Road, Silver Spring, 20904 MD, USA  
e-mail: arkady0@yahoo.com

Matthias Seimetz  
Beuth Hochschule für Technik Berlin, FB VII: Elektrotechnik – Mechatronik – Optometrie,  
Luxemburger Str. 10, 13353 Berlin, Germany  
e-mail: matthias.seimetz@beuth-hochschule.de

With the objective of reducing cost per information bit in optical communication networks, per-fiber transmission capacities and optical transparent transmission lengths have been stepped up by the *introduction of new technology* in recent years. The innovation of the Erbium-doped fiber amplifier (EDFA) at the beginning of the nineties facilitated long distances to be bridged without electro-optical conversion. Furthermore, the wavelength division multiplex (WDM) technology, which allows a lot of wavelength channels to be simultaneously transmitted over one fiber and to be amplified by one EDFA with high bandwidth, cut the cost of the transport network and offered wide bandwidth. Since there is no drive for high spectral efficiency at that moment, the modulation format is straightforward “on-off keying” (OOK). The Internet traffic growth during the nineties required increasing transmission rates which were limited by the transmission properties of the optical fiber. In that context, the application of differential binary phased shift keying (DBPSK) became an issue, providing for a higher robustness against nonlinear effects [1]. Moreover, the transmission behavior of binary intensity modulation was optimized by using alternative optical pulse shapes like return-to-zero (RZ) and by employing schemes with auxiliary phase coding, for instance, optical duobinary (see also Chap. 6, Sect. 6.5.1) which exhibits a higher tolerance against chromatic dispersion. The capacity-distance product was further enhanced by applying optical dispersion compensation, Raman amplification and advanced optical fibers, as well as through electronic means such as forward error correction (FEC) and the adaptive compensation of chromatic dispersion (CD) and polarization mode dispersion (PMD). Using these technologies, the 10 Gbit/s line rate has become the standard of today’s network, with the acknowledgment that pushing these technologies to the 40 Gbit/s range is not economical. Some system vendors are trying to increase the capacity by using ultra-dense WDM, e.g., 160 wavelengths at 25 GHz channel spacing in the C-band. By using highly integrated components, this approach yields price competitive systems. However, nonlinear effects limit the transmission range, and the need to switch and route many carriers places the burden on the switching/routing elements. To further increase the fiber capacity, the *spectral efficiency*, which is defined as the ratio of bit-rate per WDM channel to channel spacing, should be addressed and increased.

Emerging technologies on the way to 100 Gbit/s line rates and to highest spectral efficiency are *higher-order optical modulation formats*, which lead to a reduction of symbol rate and spectral width of a WDM channel, as well as *coherent detection* in combination with electrical equalization. The latter allows compensating for optical transmission impairments in the electrical domain and permits one to operate the next generation of optical transmission systems close to the ultimate limits of spectral efficiency [2]. On the other hand, when employing these new technologies, the complexity of the transmitters and receivers increases, so that the benefits arising from higher spectral efficiency have to be weighed up against higher hardware costs.

The goal of advanced modulation formats is to set up a high bit-rate communication link that combines high spectral efficiency and long distance transmission capability. The overall link economy is described by a figure of merit (FoM), which

is equal to the spectral efficiency multiplied by the link distance (without amplification):

$$\text{FoM} = [\text{km}] \times [\text{bits}]/([\text{s}] \times [\text{Hz}]).$$

From the link economy perspective, low cost fibers and a minimum number of amplification stages are preferable. The type of fiber is not reflected in the FoM, as well as the end-equipment, and should be considered separately. Therefore, each advanced communication format has to be evaluated with respect to its link tolerance. Following the trend in RF communication, the on-off-keying (OOK) format and its variants should be abandoned in favor of formats that utilize the phase of the electric field, either solely or in combination with the amplitude.

### ***8.1.1 Coherent Detection***

A coherent receiver exploits information contained in the amplitude, frequency, phase and polarization of the optical carrier during demodulation. Coherent detection is performed by mixing the modulated carrier signal with a local oscillator (LO) and is widely used in RF wireline and wireless telecommunication systems. The signal is amplified by the LO and subsequently down converted, including appropriate filtering if needed. In conjunction with optical fiber communication, coherent systems were extensively studied in the late eighties and early nineties, for instance, in [3–5]. However, with the emergence of the EDFA in the early nineties, the former advantage of higher receiver sensitivity – compared to direct detection – disappeared. For transmission rates up to 10 Gbit/s, comparable sensitivities could also be achieved by direct detection receivers with optical preamplifiers [6] which required relatively low-cost components. Thus, research in this area ceased until the beginning of the 21st century.

With coherent detection, all the optical field parameters (amplitude, phase, frequency and polarization) are available in the electrical domain. Therefore, the demodulation schemes are not limited to the detection of phase differences as for direct detection, but arbitrary modulation formats and modulation constellations can be received. Moreover, the preservation of the temporal phase enables more effective methods for the adaptive electronic compensation of transmission impairments like chromatic dispersion [7, 8] and nonlinearities even at the electrical baseband. When used in WDM systems, coherent receivers can offer tunability and enable very small channel spacing since channel separation can be accomplished by highly selective electrical filtering.

Nowadays, coherent optical systems are reappearing as an area of interest [9] and are already deployed by carrier companies. Many limitations which existed in the past for the deployment of the coherent detection disappeared: The carrier linewidth requirements have relaxed with increasing channel data rates, and standard commercial communication lasers can be used [10]. In addition, currently available high-speed digital signal processing allows one to perform critical operations such as

phase locking, frequency synchronization and polarization control in the electronic domain through digital means, thus lifting the main barrier which has thus far prevented one from benefiting from the advantages of coherent detection.

### 8.1.2 Higher-order Optical Modulation

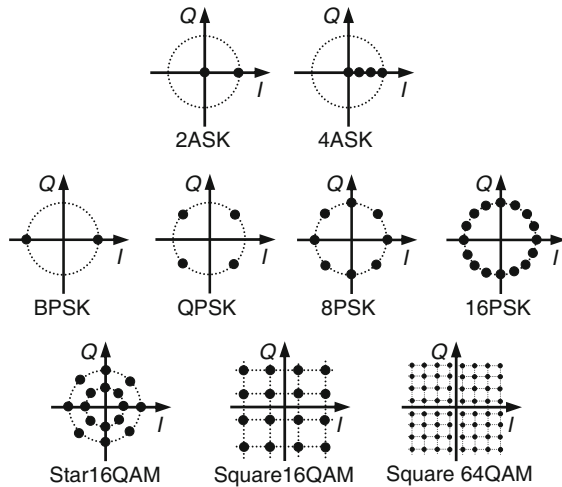
Through the deployment of optical *higher-order modulation formats*, which encode  $m = \log_2 M$  data bits on  $M$  symbols, the symbol rate is reduced by  $m$  compared to the data rate, and higher spectral efficiencies can be obtained due to spectral narrowing. One of the  $M = 2^m$  symbols is assigned to each symbol interval of length  $T_S = m \cdot T_B$ , where  $r_B = 1/T_B$  is the data rate. The assignment of appropriate combinations of  $m$  bits to symbols with particular amplitude and phase states (bit mapping) is defined in a so-called *constellation diagram*. For the best noise performance, bit mapping should be arranged in such a way that only one bit per symbol differs from a neighboring symbol (Gray coding). The symbols are transmitted on the reduced symbol rate  $r_S = 1/T_S = r_B/m$ . Figure 8.1 illustrates the constellation diagrams of selected higher-order modulation formats which are possible candidates for future applications in optical fiber networks.

A simple optical multilevel signaling scheme is *M-ary amplitude shift keying MASK*. The constellation diagrams of binary ASK (2ASK) and quaternary ASK (4ASK) are shown in the upper part of Fig. 8.1. Information is encoded here in several intensity levels. The 2ASK, usually denoted as on-off keying, is the standard modulation format in currently deployed optical transmission systems and defines only two symbol points (just one bit is assigned to each symbol). *M-ary ASK* was shown in [11] and [12] to require high optical signal to noise ratios (OSNR) for direct detection, especially in optically amplified links, due to the intensity dependence of the signal-spontaneous beat noise. For instance, a 2.5 times higher dispersion tolerance compared to OOK can be achieved by 4ASK, but only at the expense of a 5 dB power penalty due to noise. Thus, the use of *M-ary ASK* formats should mainly be considered for short reach applications and will not be considered further in this chapter.

The constellation diagrams of different *phase modulation formats* are illustrated in the second row of Fig. 8.1. In the case of phase modulation, all constellation points lie on one circle and all symbols exhibit the same amplitude level, but different phase states. The first optical multilevel phase modulation format whose transmission characteristics were intensively examined, for instance, in [13], is the *quadrature phase shift keying (QPSK)*. Since it features good transmission performance and doubled spectral efficiency, the differential version of QPSK (differential quadrature phase shift keying, DQPSK) is presently used for 40 Gbit/s networks. DQPSK does not need a local oscillator at the receiver since each of its symbols uses the previous one as a phase reference. However, the nonlinear recovery of the optical field for DQPSK detection forbids the efficient use of digital signal processing (DSP) methods for optical impairment compensation. Furthermore, DQPSK can ei-



**Fig. 8.1** Constellation diagrams of selected modulation formats applicable in future optical networks



ther be combined with polarization multiplexing or operated with a single polarization only. The latter option is particularly attractive because no polarization control is needed, while the former option requires polarization control but provides twice the spectral efficiency of the corresponding single polarization scheme. Nowadays, the QPSK format, which is detected with coherent receivers, is currently starting to be commercially applied, mostly in combination with polarization multiplexing (dual-polarization QPSK, DP-QPSK).

Encouraged by the current trends and today's progress in high-speed electronics and digital signal processing technology, even higher-order modulation formats are being investigated. With direct detection, *8-ary differential phase shift keying* (8DPSK) has been theoretically examined by Ohm [14] and Yoon et al. [15], and experimentally demonstrated by Serbay et al. [16]. By using coherent detection, 8-ary PSK has been experimentally reported by Tsukamoto et al. [17], Seimetz et al. [18], Freund et al. [19], Zhou et al. [20] and Yu et al. [21]. The 16PSK/16DPSK formats which exhibit relatively poor OSNR performance have only been investigated by computer simulations [22, 23].

By combining intensity and phase modulation, the number of phase states can be reduced for the same number of symbols, leading to larger Euclidean distances between the symbols. As shown in the lower part of Fig. 8.1, the symbols can be arranged in different circles (Star quadrature amplitude modulation, 'Star QAM') or can be positioned in a square (Square QAM). In *Star QAM* constellations, first suggested by Cahn in 1960 [24], the same number of symbols is placed on different concentric circles. The phases can be arranged with equal spacing, as shown in Fig. 8.1 for Star 16QAM (which can also be denoted as 2ASK-8PSK/2ASK-8DPSK), so the phase difference of any two symbols corresponds to a phase state defined in the constellation diagram and phase information can be differentially encoded as for DPSK formats. Thus, Star QAM signals with differentially encoded phases can be

detected by receivers with differential detection. On the other hand, Star QAM constellations are not optimal with respect to noise performance because symbols on the inner ring are closer together than symbols on the outer ring. In order to improve noise performance, Hancock and Lucky suggested placing more symbols on the outer ring than on the inner ring [25], leading to constellations with more balanced Euclidean distances. However, they came to the conclusion that such systems are more complicated to implement. For optical transmission, Star QAM experiments have been reported with four phase levels in [26] and [27, 28] for 2ASK-DQPSK and 4ASK-DQPSK, respectively. The Star 16QAM format shown in Fig. 8.1 has been investigated by computer simulations [22, 23] and experimentally as well [29]. Moreover, the 8QAM format with two rings – each of them containing four symbols that are shifted by  $45^\circ$  against each other – has been experimentally demonstrated in [30].

Formats widely used in electrical communication systems are the *Square QAM formats*, where the symbols are arranged in a square, leading to larger Euclidean distances between the symbols and thus to an improvement of noise performance. Square QAM constellations, shown in Fig. 8.1 for Square 16QAM and Square 64QAM, were introduced for the first time in 1962 by Campopiano and Glazer [31]. Square QAM signals are conveniently detected by coherent synchronous receivers, although they can also be detected by differential detection when phase preintegration is employed at the transmitter [32]. Thinking in terms of two quadrature carriers, relatively simple modulation and demodulation schemes are possible due to the regular structure of the constellation projected onto the in-phase axis and quadrature axis. In contrast to electrical transmission systems, higher-order Square QAM is still far from commercial implementation in optical systems. However, recently, Square QAM has also been successfully demonstrated for optical fiber transmission: Square 16QAM signals were transmitted over large distances of more than 1000 km for single-channel transmission [33, 34], as well as with a high baud rate of 28 GBd and high spectral efficiency for WDM transmission [35]. Even very high-order Square 256QAM transmission has already been performed at a lower baud rate of 4 GBd [36].

It is widely agreed by the communication society that capacity growth based on the use of 100 Gbit/s line rates and the deployment of advanced modulation formats will lead to very highly spectrally efficient networks which will be compatible with existing systems [37].

### **8.1.3 Coherent Optical Orthogonal Frequency-division Multiplexing**

Within this chapter, optical “single-carrier systems” where optical carriers are higher-order phase and quadrature amplitude modulated by a complex electrical baseband signal are described, whereas “multicarrier systems” with several electrical subcarriers like OFDM are not considered in detail although they are a very

promising future technology providing for very high spectral efficiency as well. Coherent optical orthogonal frequency-division multiplexing (CO-OFDM) is a specific technique where orthogonal subcarriers are combined in the electrical domain and the resulting waveform is mixed (at the modulator) with an optical carrier [38]. At the receiver side, CO-OFDM signals are detected by a digital coherent receiver. The subcarriers may use QPSK or even higher-order QAM modulation, and different architectures using single side-band modulation have been proposed [39, 40]. RF OFDM modulation is a mature technology widely used in wireless communications, and digital audio and video broadcasting due to its resilience to fading. Therefore, the required DSP algorithms exist and can be readily used in CO-OFDM systems. CO-OFDM is on the one hand considered promising for long-haul transmission as it enables very high total transmission rates and high spectral efficiency [41, 42], but it is also considered a competitive solution for the access network regime.

The main deployment barrier for CO-OFDM is the lack of suitable off-the-shelf electronics, a Fast/Inverse-Fast Fourier Transformation chip in particular. Therefore, most of the hero experiments are not real-time experiments, but rather demonstrations that use off-line data processing. In the scope of very high spectral efficiency, Liu et al. [43] demonstrated a transmission of a 448 Gbit/s CO-OFDM signal with 16QAM subcarrier modulation over a distance of 2000 km with spectral efficiency of 7 bit/(s Hz).

CO-OFDM exhibits extreme robustness against chromatic dispersion and polarization mode dispersion, two of the main detrimental effects in high-bit rate optical communication links [36]. Furthermore, theoretical studies have shown that four wave mixing, one of the main impairments of CO-OFDM, can be mitigated using appropriate algorithms at the base-band [44, 45].

Simulations that compared 100 Gbit/s DP-QPSK and CO-OFDM systems found that the transceiver electrical bandwidth required for CO-OFDM is narrower than that for DP-QPSK and the resolution needed for the analogue-to-digital converters tends to be slightly smaller for CO-OFDM compared to DP-QPSK (R. Noé, private communication). The main disadvantage of CO-OFDM is its sensitivity to nonlinear effects, however, advanced techniques can mitigate this weakness.

## 8.2 System Configurations

### 8.2.1 Transmitter Structures

Optical higher-order modulation signals can be generated by many different transmitter types. Generally, the migration to higher-order formats brings about an increase in transmitter complexity. The upgrade can be performed by adding optical modulators and accordingly creating more elaborate optical modulator structures or by providing more complex electrical level generators for the generation of mul-

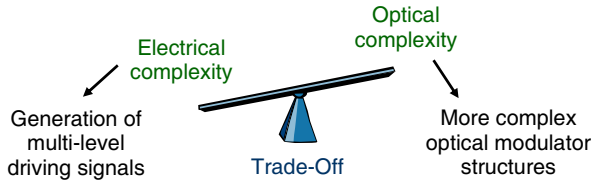


**Fig. 8.2** Transmitter complexity: trade-off between the optical and electrical parts

tilevel electrical driving signals. As illustrated in Fig. 8.2, the overall complexity of transmitters for higher-order modulation can be traded-off between the optical and electrical parts. Optical complexity can be reduced through increased electrical complexity and vice versa.

Theoretically, a single dual-drive Mach–Zehnder modulator (MZM) is sufficient to generate arbitrary higher-order modulation signals [46]. However, multilevel electrical driving signals are required in this case. Their generation raises the electrical effort and is problematic since high-speed digital-to-analogue converters just start appearing. An analogue creation of multilevel electrical driving signals with sufficient high power for the modulator inputs is also quite challenging since overlapping different binary electrical signals to generate a multilevel signal leads to increased eye spreading and thus to a degradation of system performance [46]. Another option suitable for generating arbitrary higher-order modulation signals is to use a single optical IQ-modulator [47]. In this case, the necessary number of states of electrical driving signals corresponds to the number of projections of the symbols onto the in-phase- and the quadrature axis. The IQ-modulator is not the best choice for the generation of higher-order PSK and Star QAM signals where the in-phase and quadrature driving signals have a high number of signal states and the distances between these signal states are small. On the other hand, due to the regular structure of the Square QAM constellation projected onto the in-phase- and quadrature axis, the optical IQ-modulator is a suitable device for generating Square QAM signals. However, the generation of multilevel driving signals is required here (quaternary driving signals must be generated for Square 16QAM, and 8-ary driving signals for Square 64QAM).

Because multilevel electrical driving signals are hard to generate at high data rates, transmitter configurations which require solely binary electrical driving signals are attractive. However, this increases the necessary number of optical modulators and thus the complexity of the optical transmitter part. As will be shown in the next subchapters, transmitter configurations with binary electrical driving signals are possible for arbitrary PSK/DPSK, Star QAM and Square QAM formats.

### 8.2.1.1 Phase Modulation Transmitters

A simple way of generating optical PSK/DPSK signals with binary electrical driving signals is to use several consecutive phase modulators (PM). After the first PM

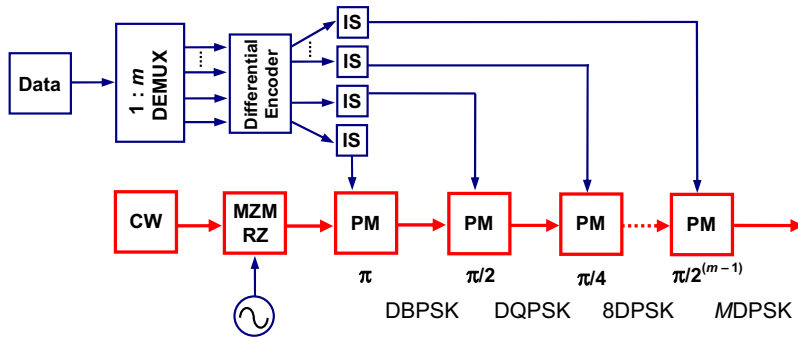


**Fig. 8.3** Higher-order DPSK transmitter composed of consecutive phase modulators, CW: continuous wave laser, IS: impulse shaper, PM: phase modulator, MZM: Mach-Zehnder modulator, RZ: return-to-zero

(phase shift  $\pi$ ), a signal with binary phase modulation is obtained, and after the second PM (phase shift  $\pi/2$ ) a signal with quaternary phase modulation, and so on. Figure 8.3 illustrates this kind of transmitter, including the electrical transmitter part which is shown here with differential encoding.

In the electrical part of the transmitter, the data signal is first parallelized with a demultiplexer. Then, the parallelized data bits are fed into a differential encoder, whose complexity and configuration generally depend on the order of the DPSK modulation [48]. The differential encoding allows for differential detection at the receiver side or to resolve phase ambiguity within the carrier synchronization (optical phase locked loop or digital phase estimation) when homodyne synchronous detection is applied. Otherwise, the differential encoding can be omitted. In the optical domain, an MZM can be additionally used for carving RZ pulses. The first PM accomplishing the phase modulation by  $\pi$  can also be replaced by an MZM, as done in the experiment reported in [20]. This leads to higher phase accuracy and to a better transmission performance in the case of NRZ pulse shape [48]. The performance of the PM is temperature dependent and since the phase changes linearly with the applied voltage, the burden of maintaining the linearity is transferred to the electronic driving circuit. For example, to drive a 2PSK phase modulator, a two-level signal is sufficient. However, this signal has to be shifted by the  $V_\pi$  voltage with high accuracy; any variation in the amplitude of the driving voltage will appear as phase noise in the optical signal.

Another transmitter configuration suitable for generating arbitrary PSK/DPSK signals, which has been employed in recent experiments with higher-order phase modulation [18], also uses binary electrical driving signals and is composed of a combination of an optical IQ-modulator and consecutive phase modulators, as depicted in Fig. 8.4. The optical IQ-modulator, whose MZMs are driven at the minimum transmission point, accomplishes a quaternary phase modulation, and higher-order phase modulation signals are generated by the consecutive PMs. The electrical transmitter part (not shown in Fig. 8.4) is identical to the one for the transmitter shown in Fig. 8.3, with the exception of the internal setup of the differential encoder.

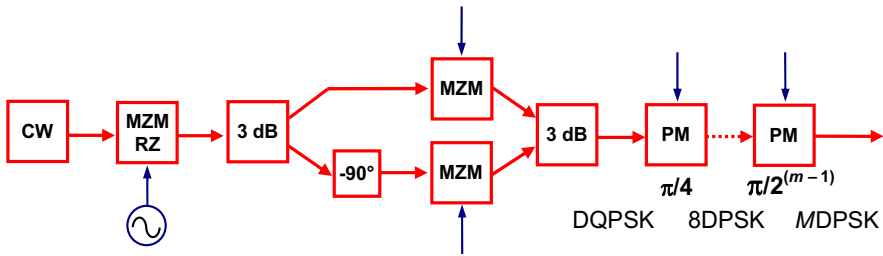


**Fig. 8.4** Optical part of a higher-order PSK/DPSK transmitter composed of an optical IQ-modulator and consecutive phase modulators (PM)

### 8.2.1.2 Star QAM Transmitters

For the generation of Star QAM signals using binary driving signals, almost the same transmitter structures as described in the last section can be employed. The PSK/DPSK transmitters described above only have to be extended by an additional intensity modulator, usually an MZM. This modulator allows for placing symbols on different intensity levels. For instance, a transmitter for Star 16QAM (2ASK-8PSK) can be composed of an 8PSK transmitter extended by an additional MZM. In the case of Star QAM constellations with only two intensity rings, the driving signal of the MZM is binary. Otherwise, in the case of more than two rings, the driving signal of the MZM is multilevel. To differentially encode the phases of Star QAM signals, the same differential encoders can be used as for the respective DPSK format with the same number of phase states. An important parameter, which can optimize the OSNR performance for Star QAM formats with only two amplitude states is the ring ratio  $RR = r_2/r_1$ , where  $r_1$  and  $r_2$  are the amplitudes of the inner and outer circle, respectively. In practice, it can be adjusted by changing the driving and bias voltages of the MZM.

### 8.2.1.3 Square QAM Transmitters

In the case of Square QAM, various options exist for signal generation. As mentioned above, the use of a single optical IQ-modulator is beneficial for Square QAM due to the regular structure of the constellation projected onto the in-phase and quadrature axis. The whole transmitter configuration including the optical and electrical parts and denoted here as conventional IQ-transmitter is illustrated in Fig. 8.5.

Both coders – the differential DQPSK encoder and the Square QAM coder (creating a bit mapping symmetric in rotation) in the electrical transmitter part – become necessary if a quadrant ambiguity must be resolved in the carrier synchronization of the transmitter [48]. The electrical level generators are used for generation of multilevel electrical driving signals for the MZMs and can be implemented by analogue driving circuits or digitally using digital-to-analogue converters. The number

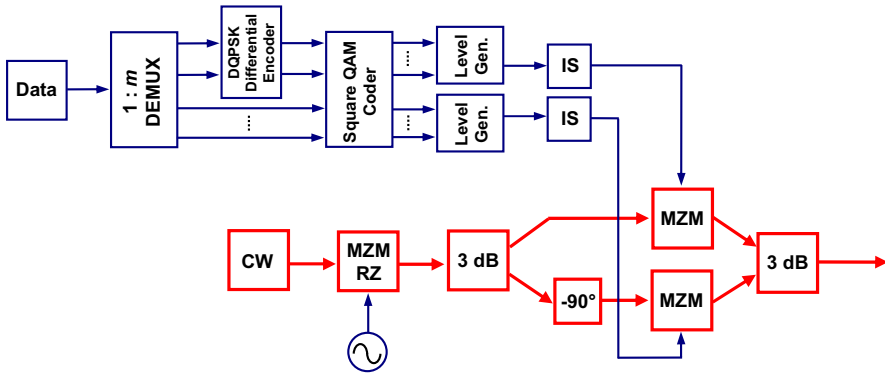


**Fig. 8.5** Generating optical Square QAM signals using an optical IQ-transmitter and multilevel electrical driving signals

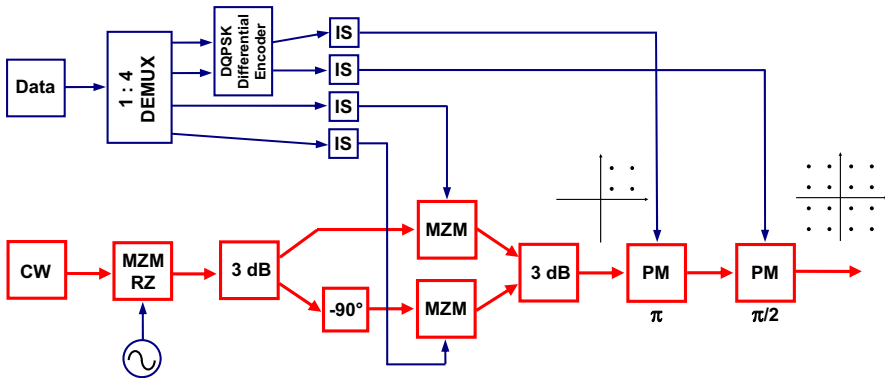


**Fig. 8.6** “Tandem-QPSK transmitter” for generating optical Square 16QAM constellations using binary driving signals

of necessary signal levels corresponds to the number of projections of the symbols onto the in-phase- and quadrature axis.

In contrast to Star QAM, the phases are arranged unequally spaced in Square QAM constellations, so that it is not possible to adjust all the phase states of the symbols by driving consecutive phase modulators with binary electrical signals. However, transmitter configurations which are based on binary electrical driving signals are also possible for Square QAM. Different configurations, denoted as enhanced IQ transmitter, Tandem-QPSK transmitter and multiparallel MZM transmitter are described in detail in [48]. Exemplarily, Fig. 8.6 shows the Tandem-QPSK transmitter for generation of Square 16QAM signals using binary driving signals. A first IQ-modulator is employed to generate a constellation with four points in the first quadrant. This is achieved by using the MZMs of the IQ-modulator as intensity modulators. Using a consecutive QPSK modulator, which can be realized using another IQ-modulator or by using two PMs as shown in Fig. 8.6, for instance, the

four-point constellation in the first quadrant can be shifted into the other three quadrants, thereby generating a complete Square 16QAM constellation. It is a beneficial side-effect of this transmitter type that – initiated through signal generation – the resulting constellation is inherently symmetric in rotation, so that – in addition to the differential encoder – no further coder is required to handle a quadrant ambiguity at the receiver [48].

Choosing a particular transmitter structure is not only a matter of trading off complexities and looking at the transmitter's practical feasibilities. The respective transmitters can also be rated by considering the influence of their individual signal properties such as intensity shape, symbol transitions and chirp characteristics on the overall system performance. Especially for NRZ pulse shape, different transmitter configurations exhibit different system performance, whereas the differences are only small for RZ. More details can be found in [48].

## **8.2.2 Receiver Concepts**

An overview about receiver schemes applicable for the detection of optical higher-order modulation signals is given in Fig. 8.7. They can be roughly divided into two basic groups: direct detection and coherent detection. In the latter case, two fundamental coherent detection principles can be distinguished: homodyne and heterodyne detection. In the case of homodyne detection, the carrier frequencies of the signal laser and the LO laser aspire to be identical and the optical spectrum is directly converted to the electrical baseband. In the case of heterodyne detection, the frequencies of the signal laser and the LO are chosen to be different, so that the field information of the optical signal wave is transferred to an electrical carrier at an intermediate frequency which corresponds to the frequency difference between the signal laser and the LO. On the one hand, heterodyne detection permits simple demodulation schemes and enables carrier synchronization with an electrical phase locked loop. On the other, the occupied electrical bandwidth for heterodyne detection is more than twice as high as for homodyne detection, and image-rejection techniques are required to allow for acceptable spectral efficiency for WDM. Therefore, when considering spectral efficiency and the practical feasibility at high data rates, homodyne receivers are superior to their heterodyne counterparts and seem to be a better choice for future optical networks. For this reason, only homodyne detection will be discussed in the following sections.

### **8.2.2.1 Direct Detection**

Direct detection receivers are convincingly simple. No phase, frequency or polarization control is necessary. Although, only the intensity of the optical field can be detected by a simple photodiode, the information encoded in the optical phase can also be obtained when employing additional optics. By using an optical interferometer,



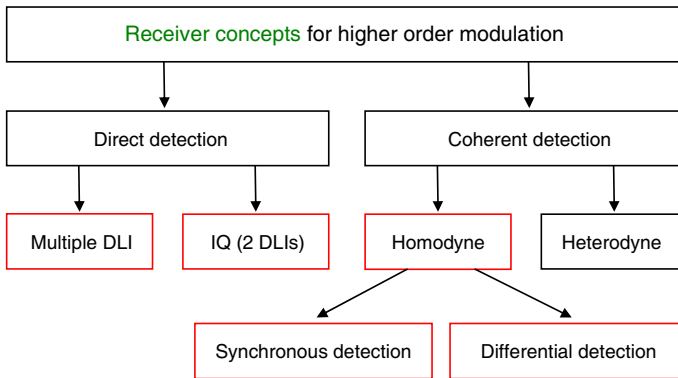


**Fig. 8.7** Detection schemes for higher-order modulation signals

the phase difference information of two consecutive symbols can be converted into intensity information, which can then be detected by a photodiode. This allows for the detection of arbitrary DPSK signals. With a separate intensity detection branch, arbitrary Star QAM signals with differentially encoded phases can also be received when appropriate data recovery methods are employed [48, 49]. Square QAM signals have recently been detected by differential detection using an additional phase preintegration at the transmitter [32].

The usual way for constructing direct detection receivers is employing delay line interferometers (DLIs) to convert differential phase modulation into intensity modulation before photodiode square-law detection. One receiver option – whose optical part is shown in Fig. 8.8 – is to use  $N_{\text{ph}}/2$  DLIs with appropriate phase shifts, where  $N_{\text{ph}}$  represents the number of phase states ( $N_{\text{ph}} = M$  for an  $M$ DPSK signal). For the detection of DPSK signals, only the branch with the DLIs (phase detection branch) is needed. Another branch (intensity detection branch) must be provided for a separate evaluation of the intensity when detecting Star QAM signals. Phase information can be demodulated by performing binary decisions on the resulting  $N_{\text{ph}}/2$  electrical photocurrents.

The receiver concept with multiple DLIs was investigated for 8DPSK in [15]. Unfortunately, the optical effort becomes quite high for modulation formats with a high number of phase states. Four DLIs are needed for 8DPSK, and as many as eight DLIs for 16DPSK.

The complexity of the optical receiver part can be reduced by employing a receiver structure with only two DLIs, which is sufficient to obtain the phase difference information of arbitrary DPSK and Star QAM signals by detecting their in-phase and quadrature components (IQ receiver). However, the data recovery becomes more complicated in that case. Decisions on multilevel electrical signals with multiple thresholds become necessary for modulation formats with  $N_{\text{ph}} > 4$ . Moreover, decision thresholds are no longer located at zero under these circumstances. The setup of the optical receiver part of a Star QAM direct detection IQ receiver is shown in Fig. 8.9.

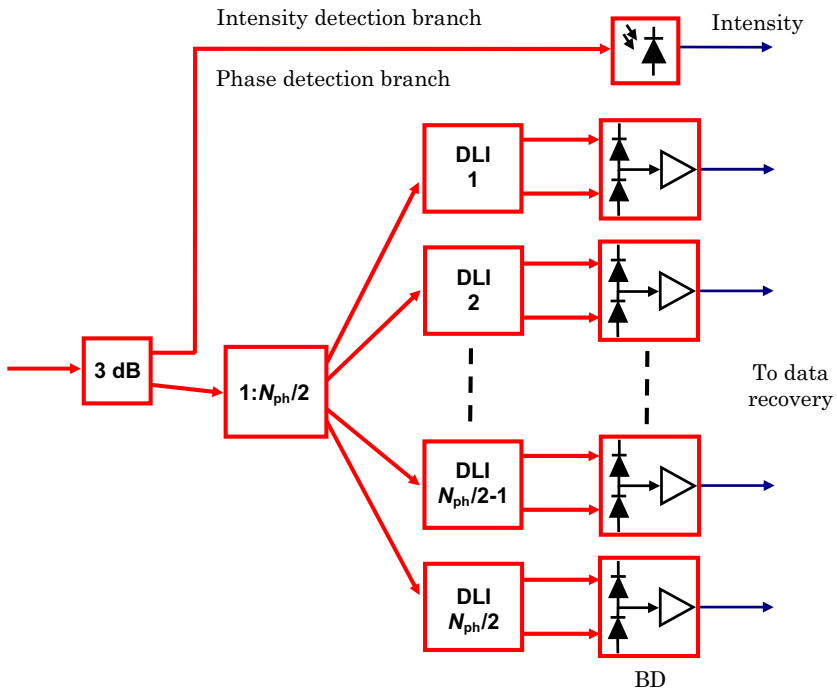


**Fig. 8.8** Optical part of a Star QAM direct detection receiver composed of an array of delay line interferometers (DLIs); BD: Balanced detector

To enhance the sensitivity, an optical preamplifier, commonly followed by an optical filter, is typically placed in front of the receiver (not shown in Fig. 8.9). For the detection of DQPSK signals, for instance, the phase shifts of the upper and lower DLI in the phase detection branch should be set to  $-45^\circ$  and  $-135^\circ$  so that information retrieval can be accomplished based upon binary signals in the in-phase and quadrature arms. More general, the in-phase and quadrature components of arbitrary DPSK constellations can be obtained by choosing the phase shifts of the DLIs as  $0^\circ$  and  $-90^\circ$ . Electrical data recovery from the in-phase and quadrature photocurrents for arbitrary DPSK and Star QAM formats is described in detail in [48].

Alternatively to the use of two DLIs, the direct detection IQ receiver can also be composed of a  $2 \times 4$   $90^\circ$  hybrid, combined with a delay of one symbol duration in front of one of the hybrid inputs [48]. The choice of a specific configuration will depend on practical implementation considerations.

Advantages of the direct detection scheme are its simplicity and the lower linewidth requirements in comparison with coherent detection schemes. On the other hand, attainable receiver sensitivities are not as high as for receivers with homodyne synchronous detection. Moreover, since coherent detection enables an optical signal's phase and polarization to be measured and processed, the transmission impairments that previously presented challenges to accurate data reception can, in

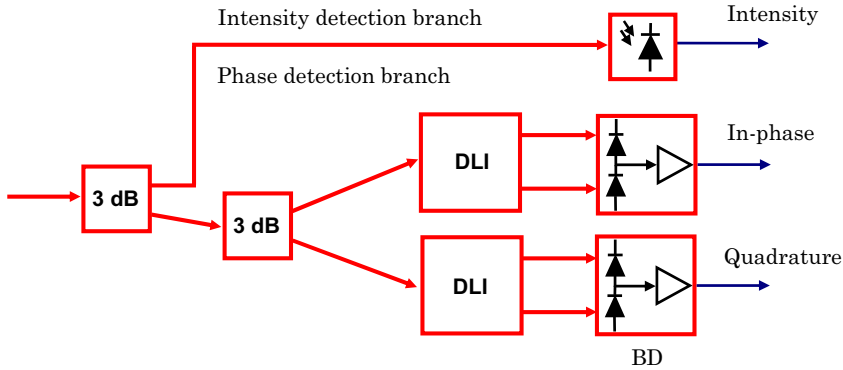


**Fig. 8.9** Optical part of a Star QAM direct detection IQ receiver composed of two delay line interferometers (DLIs); BD: Balanced detector

principle, be mitigated electronically when an optical signal is converted into the electronic domain. Tier-1 network providers have now realized the potential of optical coherent systems by deploying QPSK systems with improved DSP receiving circuits.

### 8.2.2.2 Homodyne Detection

In the case of homodyne detection, the optical information signal is interfered with the light of an LO laser before photodetection, for instance, in a simple 3 dB coupler or in a  $90^\circ$  hybrid for detection of the in-phase and quadrature components of an optical signal. The optical spectrum is directly converted to the electrical baseband (the carrier frequencies of the signal laser and the LO laser aspire to be identical). All the information of the optical signal wave (amplitude, frequency, phase and polarization) is thereby transferred to the electrical domain. This has the advantage that demodulation of higher-order modulation signals can be performed completely electrically. Moreover, this enables enhanced possibilities for electronic compensation of transmission impairments. On the other hand, coherent detection schemes do not only enable the availability of the desired field parameters in the electrical domain, but also necessitate a controlled state of the remaining field parameters in order to be able to evaluate the information in demand. In comparison with direct detection, additional effort must be spent on tasks like phase synchronization, frequency synchronization and polarization control. However, these tasks can all be accomplished using signal processing. Since carrier linewidth requirements have relaxed with increasing channel data rates, and current high-speed digital signal processing allows to accomplish critical operations such as phase locking, frequency synchronization and polarization control in the electronic domain through digital means, coherent receivers have reappeared as a topic of great interest in the last few years.

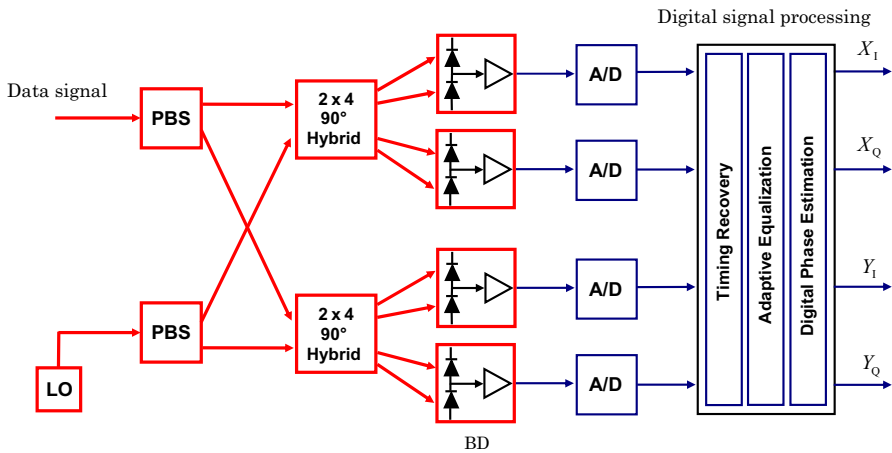


**Fig. 8.10** Digital coherent receiver with homodyne synchronous detection employing timing recovery, adaptive equalization, polarization de-multiplexing and digital phase estimation

### Receivers with Homodyne Synchronous Detection

Figure 8.10 shows the basic setup of a digital coherent receiver with homodyne synchronous detection and polarization division de-multiplexing. The signal launched into the receiver is split by a polarization beam splitter (PBS) first. Afterwards, both polarization components are interfered with the LO light in two  $2 \times 4$   $90^\circ$  hybrids. The splitting of the LO light by another PBS in Fig. 8.10 has to be understood schematically. In practice, both separated polarization components of the information signal at the PBS outputs exhibit the same linear polarization state, and it is sufficient if the LO light, whose polarization must then be aligned to the polarization of the signal at the two PBS outputs, is equally split with a 3 dB coupler. Since carrier synchronization is performed by digital means in the electrical part of the receiver, a free running LO which does not have to be phase locked by an optical phase locked loop (OPLL) can be used in modern homodyne receivers based on digital signal processing. The output signals of the two  $2 \times 4$   $90^\circ$  hybrids are detected by two pairs of balanced detectors which provide the in-phase and quadrature photocurrents of both polarization components at the outputs of the optical receiver front end.

In the electrical receiver part, the in-phase and quadrature signals are sampled by A/D-converters and then further processed by elaborate digital signal processing. Generally, the first functional block in the digital signal processing part is a nonadaptive time or frequency domain equalizer (not shown in Fig. 8.10) which compensates for the main part of chromatic dispersion having accumulated along the fiber link [50, 51]. Afterwards, a timing recovery is accomplished in order to synchronize the sample rate with the signal's symbol rate. Algorithms widely used here are the Gardner [52] and the square timing recovery [53]. Timing recovery is

typically followed by an adaptive time domain equalizer, which compensates for degradation effects and performs the polarization de-multiplexing. The equalizer is usually implemented as an FIR (finite impulse response) butterfly equalizer [54] whose coefficients are adapted using the constant modulus algorithm (CMA) or the decision-directed least mean square (LMS) algorithm. In order to ensure a proper operation of the equalizers, a sample rate of at least twice the symbol rate is mostly chosen (fractionally spaced equalizer). For digital phase estimation – the functional block behind the adaptive equalizer – just one sample per symbol is required which must be properly selected for the case that more than one sample per symbol is utilized for equalization. Phase estimation can be performed by treating both polarizations independently (selected algorithms are described in [48], for instance) or by using a joint-polarization approach [55]. After carrier synchronization, the constellation diagrams are appropriately aligned, and data can be recovered from the received symbols by evaluating their amplitudes and absolute phase states (synchronous detection) as described in detail for PSK, Star QAM and Square QAM formats in [48]. In the case of single-polarization systems, the optical effort is approximately half (the PBS, one  $2 \times 4$   $90^\circ$  hybrid and two balanced detectors can be saved). Moreover, the digital signal processing becomes less complex.

The described receiver concept with homodyne synchronous detection offers several advantages. Firstly, arbitrary modulation formats can be demodulated since demodulation is based upon absolute phases. For the detection of any modulation format, the same optical front end can be used. The digital algorithms, however, as well as the data recovery, must be adapted in accordance with the particular format received. Secondly, receiver sensitivity is increased in comparison with receivers based on differential detection. Furthermore, the availability of the optical phase information in the electrical domain enables an efficient digital equalization to compensate for transmission impairments. On the other hand, homodyne receivers with synchronous detection show the disadvantage of more stringent laser linewidth requirements [48].

### Receivers with Homodyne Differential Detection

If laser linewidth requirements cannot be fulfilled using a homodyne receiver with synchronous detection but the advantage of an efficient equalization shall still be exploited, receivers with homodyne differential detection are an interesting option. Differential detection in the electrical part of the receiver can be accomplished by analogue means (phase diversity receivers, see [48, 56, 57]) or by applying digital signal processing, as shown for the single-polarization case in Fig. 8.11.

After sampling the in-phase and quadrature signals at the outputs of the optical front end by A/D-converters, an arg-operation is performed on the in-phase and quadrature samples to calculate the instantaneous phase of the current symbol. By subtracting the phase sample delayed by one symbol time from the current phase sample, the current phase difference can be determined. In practice, these steps necessitate only a table-lookup for phase determination and a subtraction operation

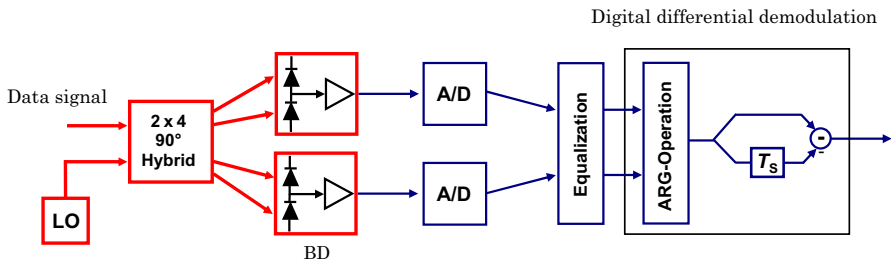


**Fig. 8.11** Homodyne receiver with digital differential demodulation, illustrated here for single-polarization and the reception of arbitrary DPSK signals

for phase differentiation, so the signal processing part is less complex than for homodyne synchronous detection. It should be noted that digital equalization of transmission impairments can be performed here in the same manner as in receivers with homodyne synchronous detection. Since differential demodulation is employed, arbitrary DPSK signals can be demodulated with this receiver concept. Of course, Star QAM signals with differentially encoded phases can be demodulated just as well by simply calculating additionally the amplitude from the in-phase and quadrature samples.

Due to the differential demodulation, the absolute phase is not important and laser phase noise remains uncritical unless the phase noise induced phase change takes considerable values within the symbol duration, which is the same as for direct detection. In comparison with direct detection, laser linewidth requirements are doubled when the same linewidth is assumed for the signal laser and the LO [48]. Frequency offsets and frequency offset drifts, which lead to corresponding fixed phase rotations and to slow varying rotations of the constellation diagram, respectively, can be compensated by an automatic frequency control (AFC) loop and digital frequency estimation [58]. Moreover, a polarization control must be implemented to align polarizations of the signal laser and the LO. The drawback of the homodyne differential detection scheme in comparison with homodyne synchronous detection is the lower receiver sensitivity, which is in the range of direct detection receivers only.

## 8.3 Key Components for Higher-order Modulation

### 8.3.1 Quadrature Modulators

A simple structure capable of *M*PSK modulation is a single waveguide phase modulator (PM) [59]. For example, a voltage applied to a straight LiNbO<sub>3</sub> (LN) waveguide creates a linear refractive index change that corresponds to a linear phase change of the light in the waveguide. This scheme, which appears simple, suffers

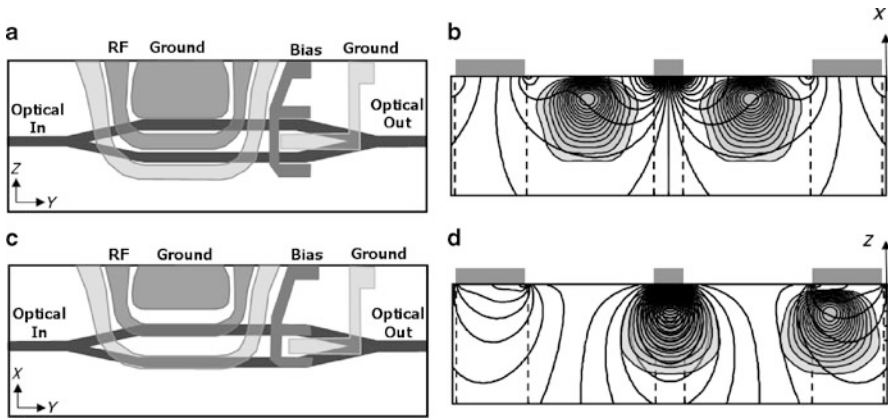


**Fig. 8.12** LiNbO<sub>3</sub> modulator: **a,b** *X*-cut symmetric layout: tangential index perturbation and TE optical field; **c,d** *Z*-cut asymmetric layout: normal index perturbation and TM optical field. **a,c** top view, **b,d** cross-sectional view

from practical embodiment problems. The performance of the device is temperature dependent and, since the phase changes linearly with the applied voltage, the burden of maintaining the linearity is transferred to the electronic driving circuit. By utilizing the principle of interference, the process of phase modulation can also be used to cause intensity modulation of the optical lightwave when the interferometric structure shown in Fig. 8.12 is used, which represents a Mach–Zehnder modulator (MZM) and is described in more detail in Sect. 8.3.1.1. Another generic modulator structure is the optical IQ-modulator consisting of two MZMs and one PM. Using an IQ-modulator, any *MPSK* and *MQAM* constellation can be constituted. This type of modulator is covered in detail in Sect. 8.3.1.2.

### 8.3.1.1 LiNbO<sub>3</sub> MZM Modulators/Transmitters

High-speed wide-bandwidth LN modulators are typically based on either an *X*-cut or *Z*-cut (both *Y*-propagating) Mach–Zehnder interferometer with traveling wave electrodes. The single-mode optical waveguides can be fabricated by either Ti indiffusion at about 1000 °C [60] or annealed proton exchange [61]. The single modulator has two parallel waveguides in which the refractive index is changed by an externally applied voltage. The two layouts are shown in Fig. 8.12.

The detected optical output power of the single Mach–Zehnder modulator is

$$P_{\text{out}}(t) = \frac{\alpha}{2} P_0(t) \{1 + \cos[\pi(V_s(t) + V_b)/V_\pi]\}, \quad (8.1)$$

where  $P_0$  is the input optical power,  $\alpha$  is insertion loss,  $V_s(t)$  is the RF drive signal, and  $V_b$  is the bias voltage. To generate an optical BPSK signal (and other higher-order phase modulation formats using an IQ-modulator, see Sect. 8.3.1.2), the MZM

bias is set to the null transmission point with  $V_b = V_\pi$ , and  $V_s$  varies between  $\pm V_\pi$  where  $V_\pi$  is the half-wave voltage (i.e., the voltage needed to induce a  $\pi$  phase shift). Devices with low  $V_\pi$  are desirable in order to minimize the voltage swing required to drive  $V_s$ .

The LN  $Z$ -cut devices take advantage from an improved overlap of the driving electric field and the optical waveguide, which results in a lower  $V_\pi$  device. However, the nonsymmetric structure of the travelling wave electrodes with respect to the waveguides creates a chirp with a typical chirp parameter of 0.7–0.8 [62].  $X$ -cut devices, on the other hand, have a close to zero chirp parameter. In order to achieve low-chirp  $Z$ -cut modulation, a domain inversion, in which the active region in the  $Z$ -cut device is divided into two parts with opposite travelling wave electrode orientation, has been proposed [63].  $V_\pi$  is inversely proportional to the modulator effective length, the span over which the optical wave is influenced by the drive voltage. This effective length is a function of velocity-mismatch between propagating light and RF waves. The velocity matching plays a crucial role in the reduction of  $V_\pi$  especially when very high-rate, wideband modulation is required. Better matching can be achieved by controlling the thickness and composition of the dielectric buffer between the electrodes and the LN substrate, controlling the thickness and shape of the electrodes, as well as by implementing ridge waveguide structures [64]. With respect to the electrodes, balancing the velocity-matching and impedance-matching requires relatively thick electrodes, which present a significant challenge for manufacturing. In addition, an appropriate charge dissipation layer [65] can reduce the DC-drift of  $V_b$ , a phenomenon that modulators of both orientations suffer from, although it is more severe in the  $Z$ -cut orientation [60].

The modulator optical insertion losses are affected by the device length, the performance of the  $Y$  branches connecting the two waveguides, and the fiber-waveguide coupling. Typical values for commercial devices are about 0.2 dB/cm in propagation, about 0.5 dB per  $Y$  branch [66], and about 0.25 dB at the fiber/chip interface. A typical commercial device, e.g., the 12.5 Gbit/s model FTM7926FB modulator from Fujitsu, has a  $V_\pi$  less than 5 V (less than 3 V at dual drive) and an insertion loss less than 5 dB. These values should be compared to values reported in the literature such as a  $V_\pi$  of 1.8 V at dual drive [67] and straight waveguide insertion loss of 0.03 dB/cm [68].

A more detailed review of integrated MZI modeling, fabrication, and applications can be found in [69].

### 8.3.1.2 LiNbO<sub>3</sub> IQ-modulators

A widely used concept for the generation of (four-level) QPSK constellations is the use of two (nested) MZIs. The optical input signal is split between these two MZIs, and one of them ensures the in-phase and the other the quadrature modulation, and a phase shifter keeps a constant  $\pi/2$  phase difference between the two MZIs (see Fig. 8.13). The decoupling between the two arms enables the use of two independent binary electrical drive signals, in contrast to the straight phase modulator that would



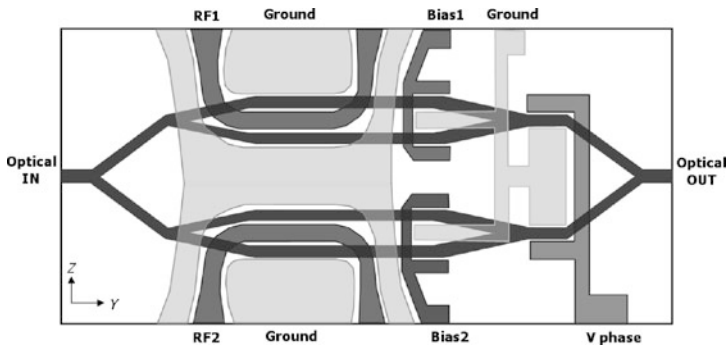


**Fig. 8.13** Schematic design of an  $X$ -cut LN IQ-modulator

require a high-speed digital-to-analogue converter to generate multiple drive levels for QPSK modulation. The differential operation makes the device temperature insensitive, except for the phase shifter. The phase shifter can be kept at its working point by a simple and relatively slow control circuit [70]. The described modulator structure consisting of two nested MZMs and a  $\pi/2$  phase shifter is commonly denoted as “IQ-modulator” and can also be used to create arbitrary higher-level  $M$ PSK and  $M$ QAM constellations, such as the ones shown in Fig. 8.1, by employing appropriate digital-to-analogue converters providing multi-level electrical driving signals at the RF inputs.

It might be worthwhile to note that the terminology for this modulator found in the literature is not always identical. Since this device was used for generation of QPSK signals at first, it was initially denoted as “QPSK modulator”. However, since this device can be employed to generate arbitrary higher-order  $M$ PSK and  $M$ QAM constellations by modulating the in-phase and quadrature components (as mentioned above), it is more generally denoted as “IQ-modulator”. We will adopt the term “IQ-modulator” in the rest of this chapter.

Today, the most frequently used substrate material for IQ-modulators is  $\text{LiNbO}_3$ . InP modulators offer the potential to be monolithically integrated with other sub-components including sources (lasers) and detectors and are covered in detail in Chap. 6.

The key building block for a  $\text{LiNbO}_3$  IQ-modulator is the standard MZM that was described in the previous section. Figure 8.13 shows a schematic of an  $X$ -cut IQ-modulator having two push-pull type MZMs with RF and DC bias electrodes. The two MZMs are nested in an MZI that introduces a  $\pi/2$ -phase shift between the MZM outputs for generating the quadrature signal output. In terms of the integrated modulator structure, there is no difference between QPSK modulators,  $M$ PSK modulators,  $M$ QAM modulators and differential phase shift keying (DQPSK,  $M$ DPSK) modulators. Differences in generating these different formats only exist in the electrical transmitter part (coders, generation of the electrical driving signals). By applying a multilevel driving signal to the two RF input ports of the single MZI modulators, any digital advanced signal format can principally be generated.

For higher-order modulation formats ( $M > 4$ ), a digital-to-analogue converter is required at the RF inputs in order to generate the multilevel signals. The digital-to-analogue converter is also required for CO-OFDM. In OFDM, the baseband is divided into many lower-rate subcarrier tones to convey the data stream. This format has very high optical spectral efficiency, is more resilient to chromatic dispersion and polarization mode dispersion than the DP-QPSK, and is well adapted to many network architectures. For CO-OFDM, the DSP includes Fast/Inverse Fast Fourier Transform (FFT/IFFT) for the receiver/transmitter. The embodiment of a full 100 GBd CO-OFDM transponder results in a less power-consuming transponder compared to the dual-polarization QPSK (DP-QPSK) format, a tendency for less demanding digital-to-analogue converters and much higher tolerances for mechanical design and calibration/stabilization algorithms (Y. Achiam, unpublished results).

The nested MZIs increase the overall footprint of the modulator. The wide  $Y$ -branches introduce additional optical losses in addition to the higher propagation loss due to the added length of the device. The length of the chip together with the differences in the thermal expansion coefficients of the LN and standard optoelectronic packaging materials make the manufacturing and packaging of such IQ-modulators a challenging task. Moreover, the need to feed the MZMs with two wide-band high-rate RF signals requires strict mechanical tolerances and an advanced RF design.

Advanced modulation formats are often based on RZ signals [71]. In an optical system, the IQ-modulator can be connected to an additional narrow-band modulator, which carves out the RZ pulses. With respect to creating an integrated device, combining an IQ-modulator and an RZ pulse carver in series would result in a structure that is too large to be practically implemented using a standard 4" LN wafer. In order to overcome this limitation, two different techniques are used to fit the integrated RZ-IQ-modulator into a 4" wafer. One uses the reflective edges at the facets of the chip [72]. The second uses a ridge waveguide, a well-confined waveguide that allows a much smaller radius of curvature (lower bending losses) [73]. An example of using the reflecting-edge technology for the integration of two single-polarization IQ-modulators into a dual-polarization IQ-modulator (for DP-QPSK) has recently been proposed by Kaplan et al. [74].

The DSP engine in the transponder available in modern coherent communication systems enables maintaining the modulator at its working point by using an appropriate algorithm as well as relaxing some manufacturing tolerances. Thus, the two MZMs as well as the  $\pi/2$  phase shifter can be biased and kept at their working points.

The currently available commercial modulators target the 40 Gbit/s QPSK/DQPSK systems market and have bandwidths of about 20 GHz. A short list of manufacturers is given in Table 8.1 and the performance of some LN IQ-modulators is given in Table 8.2.

While only LN-based IQ-modulators are commercially available, there are experimental versions of modulators that use different materials. The leading alternative material is InP. The ability to integrate lasers, waveguides, and phase modulators on the same substrate leads to compact device design and potentially lower cost.

**Table 8.1** Manufacturers of IQ-modulators

Lithium Niobate ( $X$ -cut)	Lithium Niobate ( $Z$ -cut)	InP	GaAs/AlGaAs
Sumitomo JDSU Keopsys Covega(Gemfire) CeLight	Fujitsu Photline	Infinera Oclaro NTT Alcatel – Lucent	u <sup>2</sup> t Photonics

**Table 8.2** Properties of typical LN IQ-modulators

Company Model		Photline QPSK-LN-40	Covega Mach-10060	JDSU DPMZ	Sumitomo $X$ -cut LN SSB-SC	Fujitsu FTM7960EX <sup>a</sup>	CeLight CL-QM-12.5
Insertion Loss (max)	dB	8	7	6	7	9	12
Insertion Loss (typ)	dB	7	5.5				10
Optical Return Loss (min)	dB	40	40	35	30	30	15
Bandwidth (min)	GHz	14	10	16	16	25	10
RF $V_{\pi}$ @ 1 GHz (max)	V	6.0 <sup>b</sup>	7.5	6	5.5 <sup>c</sup>	4 <sup>a</sup> (8)	
RF $V_{\pi}$ @ 1 GHz (typ)	V	5.5 <sup>b</sup>	6.5				7.5
Electrical Return Loss (max)	dB	-10	-10	-10		-10	-10
Electrical Return Loss (typ)	dB	-12	-12				
DC $V_{\pi}$ (max)	V	9 <sup>b</sup>	5.5	6		14	
DC $V$ (typ)	V	8.5 <sup>b</sup>	4.5		4 <sup>c</sup>		5
Extinction Ratio (min)	dB	20	20	25		20	20

<sup>a</sup> the Fujitsu device is dual parallel dual drive (4 RF inputs)

<sup>b</sup> Photline: RF  $V_{\pi}$  @ 10 GHz. DC  $V_{\pi}$ : 18 V (typ) 20 V (max)

<sup>c</sup> Sumitomo: RF  $V_{\pi}$  @ 20 GHz. DC  $V_{\pi}$ : 7 V

The InP high integration and tightly confined optical fields (large refractive index contrast) can, potentially, compensate for larger propagation and insertion losses compared to LN waveguide devices.

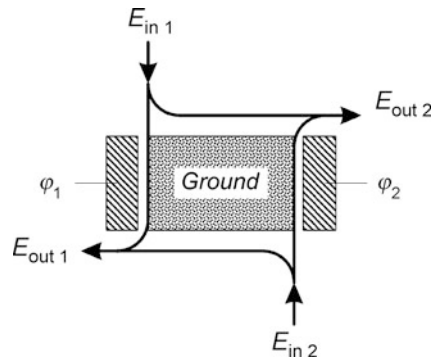
Oclaro has recently announced a device composed of an InP-based IQ-modulator that is co-packaged with a tunable distributed feedback (DFB) laser [75]. The size of

the modulator is  $1 \times 5 \text{ mm}^2$ . Infinera Inc. has developed a monolithically integrated InP-based transmitter chip which comprises 10 DQPSK modulators, each of them composed of two nested MZIs for modulation of the in-phase and quadrature components, respectively, plus 10 tunable DFB lasers plus an arrayed waveguide grating (AWG) serving as wavelength combiner [76]. A different approach for an MPSK modulator was presented by Doerr and coworkers [77, 78], where the modulator is based on two star-coupled devices. A set of waves with fixed phases produced by one device is guided into a second device that performs a combining function. The waveguides pass via electroabsorbers. By absorbing different phase components, the phase of the recombined wave can be controlled. Unfortunately, this approach suffers from high insertion loss. NTT presented an InGaAlAs/InAlAs multi-quantum well (MQW) IQ-modulator with a footprint of  $7.5 \times 1.3 \text{ mm}^2$  [79]. It has a DC extinction ratio of 18 dB,  $V_\pi$  of 3 V, and a 6 dB electro-optical bandwidth of 41 GHz. The optical loss is as high as 13 dB. In the first half of 2010, Oclaro [80] started shipping InP-based 43 Gbit/s RZ-DQPSK transponder modules suited for C-band applications.

u<sup>2</sup>t Photonics has recently announced a GaAs-based IQ-modulator which is the latest from an established area of development previously worked on by GEC-Marconi [81, 82] (now part of Oclaro), QinetiQ, Nortel Networks, Filtronic [83], and RF Micro Devices (RFMD). A significant benefit of GaAs is the availability of larger wafer sizes and high volume commercial processes which offer high yield, high reproducibility and a route to integration on a commercial cost base [83]. Because its absorption band-edge is not close to the operating wavelength at 1550 nm, the linearity of the modulation characteristics is better compared to InP, which will be increasingly important as more complex modulation formats are used. In comparison with LiNbO<sub>3</sub>, devices of similar drive voltage are smaller or, for comparable device length, the drive voltage can be lower because the combined figure of merit for the coupling to the optical mode and the size of the electro-optic effect is better for GaAs. A typical GaAs-based IQ-modulator manufactured by u<sup>2</sup>t consists of a pair of MZMs arranged within a Mach–Zehnder super-structure [84]. It has a fiber-to-fiber loss of around 5–6 dB, a DC extinction ratio of more than 20 dB, DC  $V_\pi$  of 3 V, and a 3 dB electro-optical bandwidth of greater than 20 GHz (and a 6 dB electro-optical bandwidth of greater than 30 GHz). Furthermore, because the dielectric constant of GaAs is similar at RF and optical frequencies, the RF traveling wave phase velocity can be matched very well to the optical group velocity in GaAs modulators (without compromising the voltage sensitivity). This means that GaAs modulators can be operated to very high speeds and operating speeds up to 100 GHz can be expected [81].

The transmission capacity and at the same time the spectral efficiency of fiber optic systems can be doubled if two orthogonal polarization states are used as separate data channels (polarization division multiplexing), and corresponding dual-polarization modulators can be realized as integrated devices. It is worthwhile to mention that systems comprising polarization division multiplexing are starting to be deployed, e.g., as 100 Gbit/s links using dual-polarization QPSK [85].

**Fig. 8.14** Functional scheme of a  $2 \times 2$  optical hybrid (“ $180^\circ$ -hybrid,” when  $\varphi_1 = 0$  and  $\varphi_2 = 180^\circ$ , or “ $90^\circ$ -hybrid” for  $\varphi_1 = 0$  and  $\varphi_2 = 90^\circ$ )



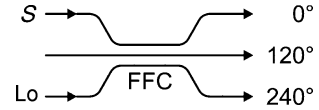
### 8.3.2 Integrated Coherent Receivers

There are new, commercially feasible, optical hybrid solutions that revise the previous rationales that restrained coherent detection from adoption and implementation. The optical hybrid is the critical part of the coherent receiver needed to combine a local oscillator wave,  $Lo$ , with the signal,  $S$ , and such optical hybrids are used in phase- or polarization-diversity schemes as well. A functional scheme of a particularly simple optical hybrid is illustrated in Fig. 8.14.

Its functionality is as follows: Signals are fed into input ports 1 and 2, split within the hybrid, and are subsequently added with different phase shifts at output ports 1 and 2. The device shown can be implemented, for example, in an integrated electro-optical material where the electro-optic effect enables introducing appropriate phase shifts  $\varphi_1$  and  $\varphi_2$ . For  $\varphi_1 = 0$  and  $\varphi_2 = 90^\circ$ , one gets a  $90^\circ$  (or quadrature)  $2 \times 2$  optical hybrid where the two output signals are designated as in-phase ( $I$ ) and quadrature ( $Q$ ), respectively. For the case of a  $180^\circ$  hybrid ( $\varphi_1 = 0$  and  $\varphi_2 = 180^\circ$ ) the following cases are of relevance: If identical (coherent) signals are launched into input 1 and input 2, they will add and appear at output 1 while no signal will appear at output 2. Alternatively, if the same input signals are  $180^\circ$  out of phase, all power will appear at output 2.

Optical hybrids can be implemented with more than just two output ports, and more generally speaking, they are designated as “ $m \times N$   $\alpha$ -degree hybrid” where  $m$  and  $N$  are the number of input and output ports, respectively, and  $\alpha$  represents the difference of the relative phase shifts with which the input signals are vectorially added at the hybrid outputs. In all hybrids – in the ideal case – the input power is equally distributed among the output ports and therefore it seems to be desirable to keep the number  $N$  of branches small since the larger  $N$ , the more local oscillator power is needed to suppress receiver noise, and  $N = 2$  looks the most advantageous from this point of view. However, receivers based on two-branch  $90^\circ$  hybrids have some disadvantages, such as a 3 dB penalty (2.3 dB theoretical limit [4]) and high sensitivity to hybrid imperfections such as LO intensity noise, reflections, and polarization misalignment, compared to hybrids with  $N > 2$ .

**Fig. 8.15** Three-branch 120° hybrid, implementation in fiber technology (FFC: fused fiber coupler), after [57, 87]



Three-branch  $3 \times 3$  120° hybrids ( $N = 3$ ) as illustrated in Fig. 8.15 have been realized, e.g., by three symmetrically fused fibers [57, 87]. They do not suffer from intrinsic losses and they are less sensitive to hybrid imperfections compared to two-branch hybrids. Moreover, it is possible to deduce two signals of equal amplitude which are 90° out of phase from the three hybrid outputs [48]. However, altogether, such receivers require more electronic signal processing hardware and as a consequence they have gained only minor relevance.

### 8.3.2.1 Optical Four-branch 90° Hybrids

Four-branch receivers ( $N = 4$ ) are presently the most widely accepted in coherent communications and will therefore be described in more detail below. Optical four-branch  $2 \times 4$  90° hybrids (sometimes also called six-port hybrids) have been used for coherent microwave and millimeter-wave detection systems since the mid-1990s. In principle, such four-branch hybrids consist of linear dividers and combiners interconnected in such a way that the incoming signal is mixed (by vectorial addition) with the four quadrature states associated with the reference signal. In typical applications, the optical hybrid then delivers the resulting four signals to two pairs of balanced detectors (the configuration comprising the four-branch  $2 \times 4$  90° hybrid and the balanced detectors will be denoted as “balanced four-branch receiver” in the following sections) and by applying suitable base-band signal processing algorithms, the amplitude and phase of the unknown signal can be determined. Although a balanced four-branch receiver needs four photodetectors, it has only two electronic branches (amplifier, filter, squarer, AD-converter, signal-processing, etc.). While a four-branch hybrid has no intrinsic losses, it requires higher LO power in comparison with  $N < 4$  hybrids.

$2 \times 4$  90° hybrids can be realized according to many different concepts, and a selection of four-branch receiver solutions will be briefly illustrated in the following sections. Figure 8.16 illustrates a 90° hybrid where the different output phase states are a consequence of properly polarized input states. Linear and circular polariza-

**Fig. 8.16** 90° hybrid exploiting polarization properties (after [89])

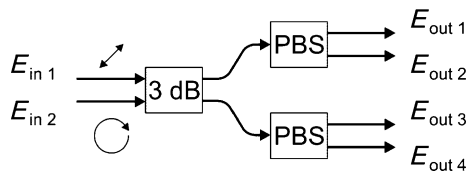


**Fig. 8.17** Michelson-interferometer based bulk optics  $90^\circ$  hybrid

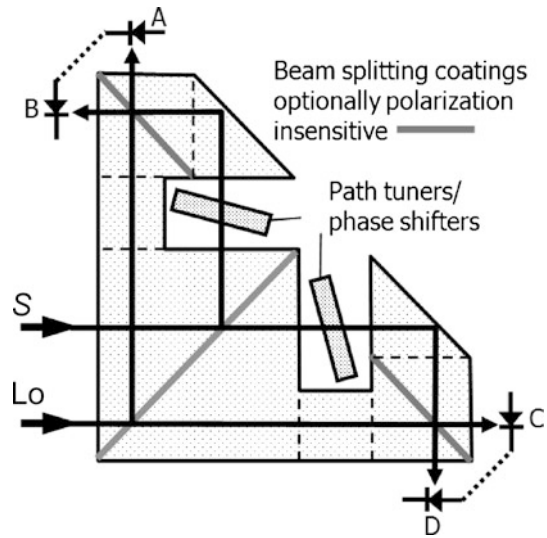
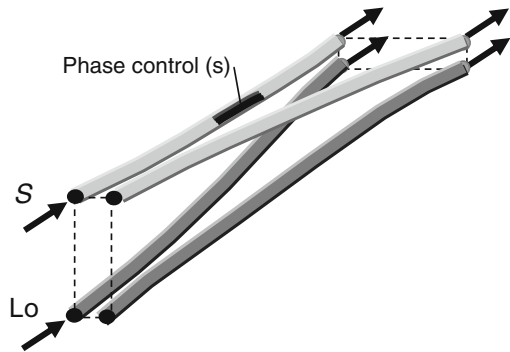


**Fig. 8.18** Three-dimensional hybrid (conceptual view)



tion of the signal and LO fields are required at the inputs, respectively, as illustrated in Fig. 8.16 [48, 89].

An example of a bulk-optics miniature implementation of a Michelson interferometer to serve as a  $90^\circ$  hybrid [90–92] can be seen in Fig. 8.17. The device includes three beam-splitters and light beams that are twice totally internally reflected before interference occurs. This makes the phase difference of the interfering beams independent of the polarization if the beam splitters themselves do not introduce any polarization dependent phase. This can be achieved by a “symmetrical” (i.e., two-sided) coating of the beam splitters. In addition, as shown in Fig. 8.17, the optical phase shifters/optical-path-tuners (index matched or mechanical) can be implemented externally. Devices of this type are very sensitive to angular misalignments.

Figure 8.18 shows a conceptual view of a three-dimensional hybrid. It could be implemented either using fibers or, alternatively, by waveguides integrated into bulk optical substrate (silica, as an example).

**Fig. 8.19** 90° hybrid based on a multimode interference (MMI) coupler



Figure 8.19 represents an interferometric hybrid structure based on multimode interference (MMI) waveguides that will be discussed in more detail in a separate section (see Sect. 8.3.2.2).

Finally, a typical integrated four-branch/six-port 90° balanced receiver [93, 94] consisting of the  $2 \times 4$  90° hybrid with four 3 dB (optionally adjustable) couplers and at least one tunable phase shifter, as well as two pairs of balanced detectors, is illustrated in Fig. 8.20.

Hybrid devices corresponding to Fig. 8.20 have been fabricated as fully integrated structures using well-developed planar waveguiding technology [94, 95] and using various materials such as glass, semiconductors and ferroelectric substrates. Either electro-optic or thermo-optic effects can be utilized to effectively tune coupling ratios and/or control the phase of at least one phase-shifter, and this kind of structure will be presented in more detail in Sects. 8.3.3.3 and 8.3.3.4.

In the next paragraphs, the signals within the receiver shown in Fig. 8.20 will be analytically described. The time and location dependence of propagating electromagnetic waves will be taken as  $\exp[j(\beta z - \omega t)]$  for the following considerations, where  $\beta$  is the propagation constant. Neglecting location dependence and assuming the same frequency  $\omega$  for the signal and the local oscillator, the electric fields of the signal and that of the local oscillator at the input ports of the  $2 \times 4$  90° hybrid,  $S$  and  $Lo$ , can be written as

$$\begin{aligned} S &= E_S \exp [j(-\omega t + \varphi_S + \varphi(t))], \\ Lo &= E_{Lo} \exp [j(-\omega t + \varphi_{Lo})], \end{aligned} \quad (8.2)$$

where  $E_S$  and  $E_{Lo}$  are the field amplitudes of signal and LO, respectively, and  $\varphi_S$  and  $\varphi_{Lo}$  the initial phases of signal and LO, respectively.  $\varphi(t)$  describes the phase modulation of the signal. After combining these fields in the hybrid, we get the following four electric fields at the hybrid outputs:

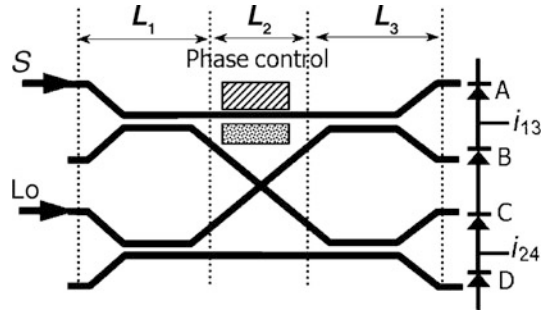
$$E_{out k}(t) = \sqrt{\alpha/N} \left[ S + Lo \exp \left( \frac{j2\pi(k-1)}{N} \right) \right], \quad 1 \leq k \leq 4, \quad (8.3)$$

where  $E_{out k}$  is the output field of the  $k$ th branch,  $\alpha$  the insertion loss of the hybrid,  $N$  the number of output ports (here  $N = 4$ ), and the relative phase of the signal electric field,  $S$ , has been taken to be  $0^\circ$  at all outputs. The functionality of a  $2 \times 4$  90° hybrid is illustrated more clearly if we write the output electric fields in the following way:

$$[E_{out 1}; E_{out 2}; E_{out 3}; E_{out 4}] \equiv [S + Lo; S + jLo; S - Lo; S - jLo]. \quad (8.4)$$



**Fig. 8.20** Balanced four-branch receiver with integrated planar single-polarized balanced  $90^\circ$  phase-diversity hybrid



For the optical power in the  $k$ th branch,  $P_k(t)$ , we obtain

$$P_k(t) = E_{\text{out}k}(t) \cdot E_{\text{out}k}^*(t) \\ \propto P_S + P_{L_o} + 2\sqrt{P_S P_{L_o}} \cos\left(\varphi_S - \varphi_{L_o} + \varphi(t) - \frac{\pi}{2}(k-1)\right), \quad 1 \leq k \leq 4, \quad (8.5)$$

where  $P_S$  and  $P_{L_o}$  are the signal and LO power, respectively.

After detecting the four optical signals with the two balanced detectors, as illustrated in Fig. 8.20, the following photocurrents can be readily generated:

$$i_{13} \equiv i_1 - i_3 \propto 4R\sqrt{P_S P_{L_o}} \cos(\varphi_S - \varphi_{L_o} + \varphi(t)), \\ i_{24} \equiv i_2 - i_4 \propto 4R\sqrt{P_S P_{L_o}} \sin(\varphi_S - \varphi_{L_o} + \varphi(t)), \quad (8.6)$$

where  $R$  is the detector responsivity, and indices 1/3 and 2/4 refer to the hybrid output branches A/B and C/D, respectively (see Fig. 8.20). The two photocurrents encompassing the amplitude and phase information of the optical signal are fed to the transimpedance amplifiers (TIA).

The detailed operation and calibration of the hybrid shown in Fig. 8.20 is discussed below (see Sect. 8.3.3.4).

### 8.3.2.2 MMI-based $2 \times 4$ $90^\circ$ Hybrid

MMI couplers, similar to the one shown in Fig. 8.19, based upon single-mode input/output waveguides and a strongly-guiding MMI waveguide section, have been realized in different materials and can be used to form multiple images at certain lengths of the MMI coupler [96–98]. The phase and amplitude profile of the images can be arranged by accurate adjustment of the MMI structure parameters. It has also been demonstrated that the desired performance can be maintained fairly independently of polarization and over a relatively wide range of operational wavelengths and temperatures.

Let us consider a  $4 \times 4$  MMI coupler, schematically shown in Fig. 8.19. The strongly guided eigenmodes of the MMI section have the form

$$E_k(x) = \sin\left(\pi(k+1)\frac{x}{W}\right), \quad (8.7)$$

where  $k = 0, 1, 2, \dots$  is an MMI mode-number index,  $x$  is a lateral dimension, and  $W$  is the lateral width of the MMI section. The *shortest self imaging* length of the MMI coupler  $L_{\text{MMI}}$  can be given as [98]

$$L_{\text{MMI}} = \frac{3L_b}{4}, \quad (8.8)$$

where  $L_b$  is the beat length between the two lowest-order modes of the MMI section given by

$$L_b = \pi / |\beta_0 - \beta_1|. \quad (8.9)$$

The MMI-section longitudinal (effective) propagation constants in the paraxial, strongly guided approximation are given by

$$\beta_k \cong nk_0 - \frac{\pi^2}{2nk_0W^2} [1 - k(k+2)], \quad k = 1, 2, 3, \dots, \quad (8.10)$$

where  $n$  is the MMI section refractive index, and  $k_0 = 2\pi/\lambda$  is the wavevector corresponding to the vacuum wavelength  $\lambda$ . Strongly guided modes (with low  $k$  numbers) are confined to their lateral mode profiles and will contain an integer number of half-periods within the waveguide. Within the structure, the input field  $F_{\text{In}}$  (either  $S$  or  $Lo$ ) is interfering while being expanded into eigenmodes of the MMI section.

The input field (either  $S$  or  $Lo$ ) is defined within the interval equal to the width of the MMI coupler:  $0 \leq x \leq W$ . However, because  $E_k(x)$  in (8.7) is periodic and antisymmetric, it can be extended over the entire  $x$ -dimension with  $2W$  periodicity. Figure 8.21a (schematically) illustrates the case when the first and third input waveguides are excited.

Now, using a spatial Fourier expansion, the input signal into the MMI-section can be represented as a superposition of an infinite number of strongly guided eigenmodes  $E_k(x)$ :

$$F_{\text{In}}(x) = \sum_{k=0}^{\infty} a_k E_k(x), \quad a_k = \frac{2}{W} \int_0^W F_{\text{In}}(x) E_k^*(x) dx. \quad (8.11)$$

The input field is expanded into eigenmodes (8.11) that propagate the distance  $L_{\text{MMI}}$  (see (8.8)) with the propagation constants given by (8.10). In the extended lateral dimension, the eigenmodes within the MMI section form an output field  $F_{\text{Out}}$  at the

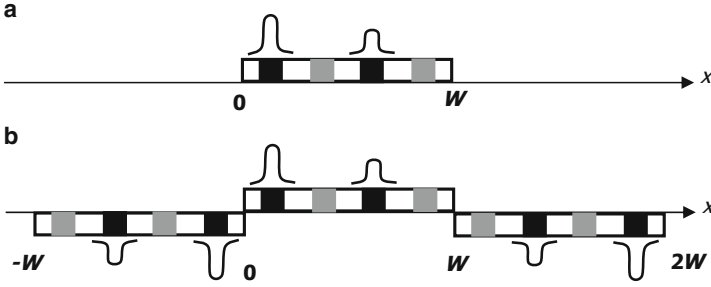


**Fig. 8.21** **a** Schematic example of the actual input power distribution for the MMI structure. **b** Extended input power distribution for the same MMI structure used in the analysis

distance  $L_{\text{MMI}}$ :

$$F_{\text{Out}}(x) = \sum_{k=0}^{\infty} a_k A_k E_k(x), \quad A_k = \exp\left(j\beta_0 L_{\text{MMI}} + j\pi \frac{k(k+2)}{4}\right). \quad (8.12)$$

This output distribution can be represented in a different form [98] to make the extraction of *position, phases and amplitudes* of the output images more convenient. Thus, for the case when  $N = 4$ , we get

$$F_{\text{Out}}(x) = \frac{1}{C} \sum_{p=0}^3 F_{\text{In}}(x - X_p) \exp(j\Phi_p), \quad (8.13)$$

where  $C$  is a complex normalization constant. There is a superposition of the four images with equal amplitudes at the output of the MMI section, and the *position and phases* of these four images are given, respectively, by

$$X_p = \frac{p-2}{2}W, \quad \Phi_p = p\left(1 - \frac{p}{4}\right)\pi. \quad (8.14)$$

The output intensities of the MMI structure depend on the relative phases of the inputs. For  $4 \times 4$  MMI couplers, the mixed signals at the output channels are in phase quadrature. Indeed, (8.13) and (8.14) together with the function  $F_{\text{In}}(x)$  (see Fig. 8.21b) can be used to describe the hybrid shown in Fig. 8.19 when the first and third input waveguides are excited by the inputs  $S$  and  $Lo$ , producing a mixed four-guide quadrature output in the form

$$[E_{\text{out } 1}; E_{\text{out } 2}; E_{\text{out } 3}; E_{\text{out } 4}] \equiv [-S + \xi Lo; -\xi S - Lo; \xi S - Lo; -S - \xi Lo], \\ \xi = \exp(j3\pi/4). \quad (8.15)$$

Equation (8.15) is, essentially, a  $\pi/4$ -shifted quadrature output compared to (8.4). Note that the connection of the balanced detectors is different for the cases shown in Figs. 8.20 and 8.19, and described by (8.4) and (8.15), respectively.

### 8.3.3 Integrated Balanced Four-branch Receivers

The hybrid device that is shown in Fig. 8.20 will be considered in more detail in the following sections. Corresponding hybrids can be effectively integrated using well-developed planar waveguiding technology [73, 74, 76] and based upon different materials including glass, semiconductors and ferroelectric substrates. Either electro-optical or thermo-optical effects can be utilized to effectively tune coupling ratios and/or control the phase of at least one phase-shifter (see Fig. 8.20). The model can be applied to various structures based on multiple waveguides, including coupled, connected or split/combined configurations.

#### 8.3.3.1 Tunable Coupling Model

Relying on the basic assumptions of coupled mode theory (CMT), the evolution of the  $N$ -mode set in coupled waveguides can be described as

$$U_{\text{Out}} = \prod_S \exp(jL_S \mathbf{M}_S) U_{\text{In}} \equiv \prod_S \mathbf{T}_S U_{\text{In}}, \quad (8.16)$$

where multiplication is taken with respect to consecutive sections of the coupled array,  $U$  denotes the vector of (complex) distributed field amplitudes characterizing the  $x$ -propagation of radiation in each waveguide.  $\mathbf{M}_S$  is a  $[2N \times 2N]$  coupling operator for the longitudinal  $s$ -section of the coupler, having the corresponding effective interaction length of  $L_S$  and, hence,  $\mathbf{T}_S$  is a transfer operator describing the guiding section of the coupled section.

Matrix  $\mathbf{T}_S(\mathbf{M}_S)$  depends uniquely on the properties of the waveguiding structure and its modes. In the case of single-mode/polarization waveguides, the dimension of  $\mathbf{T}(\mathbf{M})$  is equal to the number of guides in the coupler cross section. As mentioned, the interaction between different pairs of optical modes can be considered independently. The diagonal and off-diagonal elements of  $\mathbf{M}$  are defined as propagation constants and overlap integrals of the guided modes, respectively. For the two generic coupled modes, the transfer operator has the following form:

$$\mathbf{M} = \begin{bmatrix} \beta_1 & \kappa_{12} \\ \kappa_{21} & \beta_2 \end{bmatrix} = \beta_0 \mathbf{I} + \begin{bmatrix} \delta\beta & \kappa_{12} \\ \kappa_{21} & -\delta\beta \end{bmatrix}. \quad (8.17)$$

Here,  $\kappa_{ij}$  is the mode coupling coefficient,  $\beta_{1/2}$  are mode propagation constants and  $\delta\beta$  is the perturbation of the propagation constants within the coupler. Assuming the coupling between two identical single-mode waveguides, the perturbation of the propagation constants can be described as

$$\delta\beta = (\beta_1 - \beta_2)/2; \quad \beta_0 = (\beta_1 + \beta_2)/2. \quad (8.18)$$

The first term in (8.17) corresponds to a common phase shift that can be ignored and for most practical cases  $\kappa_{ij} = \kappa_{ji} = \kappa$  (weak-mode coupling and small

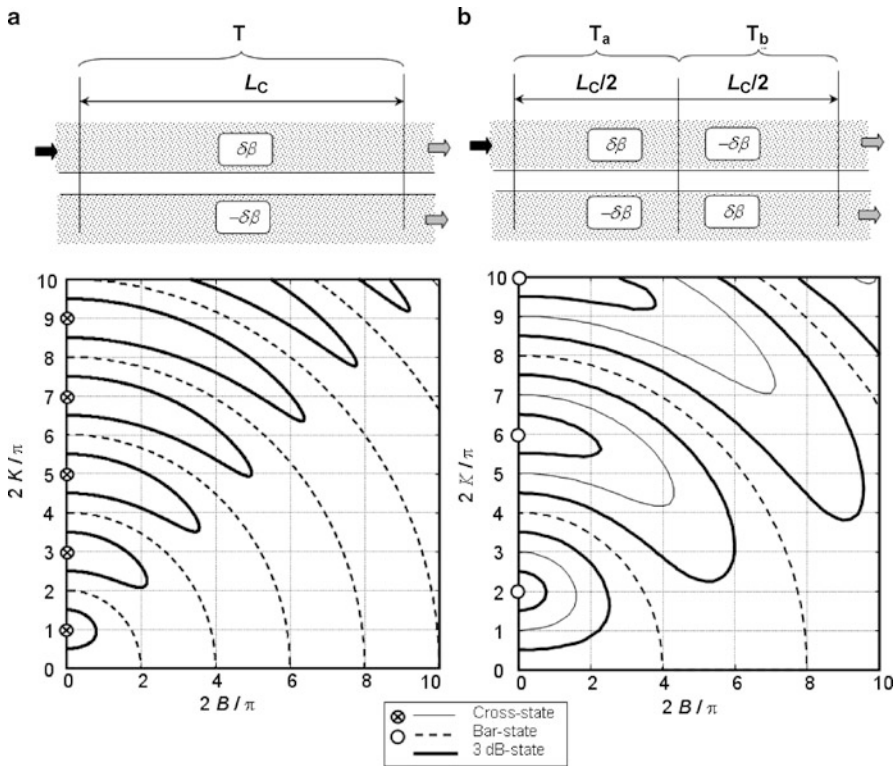


**Fig. 8.22** Tuning diagram for conventional coupler (a) and  $\delta\beta$ -reversal coupler (b)

coupled mode asymmetry approximations). The propagation constant perturbation (mismatch)  $\delta\beta$  may have a different nature and, in general, can be externally induced by different means. The unitary transfer operator  $\mathbf{T}_S$  in (8.16) for two coupled modes is given by

$$\mathbf{T}_S \equiv \exp(jL_S M_S). \tag{8.19}$$

The resulting coupler operator will depend on the coupling coefficients  $\kappa_{ij}$ , propagation constants  $\beta_{1/2}$  and the *tuning scheme of the coupler*, as will be discussed below. Also, losses must be taken into account by using proper factors where necessary.

### 8.3.3.2 Active Couplers

The most typical configurations for a coupler’s external tuning are a) conventional coupler and, b)  $\delta\beta$ -reversal coupler. The tuning diagrams for these two types of couplers are shown in Fig. 8.22 [99], where  $L_c$  is the coupler’s effective coupling length.

Explicitly, the transfer operator (8.19) for these two cases can be written as

$$\mathbf{T} = \begin{bmatrix} \cos(H) + j\frac{B}{H} \sin(H) & j\frac{K}{H} \sin(H) \\ j\frac{K}{H} \sin(H) & \cos(H) - j\frac{B}{H} \sin(H) \end{bmatrix}, \quad (8.20)$$

$$\begin{aligned} \mathbf{T}_{\pm\delta\beta} &\equiv \mathbf{T}_b \mathbf{T}_a \\ &= \begin{bmatrix} \left(\frac{K}{H}\right)^2 \cos(H) + \left(\frac{B}{H}\right)^2 & -\frac{KB}{H^2} (1 - \cos(H)) + j\frac{K}{H} \sin(H) \\ \frac{KB}{H^2} (1 - \cos(H)) + j\frac{K}{H} \sin(H) & \left(\frac{K}{H}\right)^2 \cos(H) + \left(\frac{B}{H}\right)^2 \end{bmatrix}, \end{aligned} \quad (8.21)$$

where the following dimensionless parameters were used for each coupler, that is,

$$K = \kappa L_c, \quad B = \delta\beta L_c, \quad H = \sqrt{B^2 + K^2}. \quad (8.22)$$

$L_c$  and  $\kappa$  are corresponding effective coupling lengths and coupling coefficients, respectively, and  $\delta\beta$  is the induced perturbation of the modes propagation constant within the couplers.

The switching diagram in Fig. 8.22 is correct for the input couplers in the phase-diversity hybrid shown in Fig. 8.20, where only a single input is excited. However, the transfer operators (8.20) to (8.22) characterize any coupled waveguides in a hybrid, within the framework of the valid CMT.

### 8.3.3.3 Tunable Balanced Receiver

The functional scheme of a detector based on a four-branch  $90^\circ$  hybrid is shown in Fig. 8.20 and Fig. 8.23a. The photo of such a manufactured and packaged integrated  $90^\circ$  hybrid with balanced receivers is shown in Fig. 8.23b [94]. The two-input, four-output  $90^\circ$  optical hybrid consists of a pair of input couplers, the waveguide intersection area with two phase modulators and one pair of output couplers, having interactions lengths  $L_1$ ,  $L_2$  and  $L_3$ , respectively (see Fig. 8.20), as well as two balanced photodetectors with a bias removal control, as shown in Fig. 8.23a. Accordingly, the transfer operators  $\{\mathbf{T}(L_3), \mathbf{T}(L_2), \mathbf{T}(L_1)\}$ , which are used in (8.16) for  $N = 4$ , may have the form: have

$$\begin{aligned} \bar{\mathbf{T}}(L_1) &= \begin{bmatrix} T_{11}^1(v_1) & T_{12}^1(v_1) & 0 & 0 \\ T_{21}^1(v_1) & T_{22}^1(v_1) & 0 & 0 \\ 0 & 0 & T_{11}^2(v_2) & T_{12}^2(v_2) \\ 0 & 0 & T_{21}^2(v_2) & T_{22}^2(v_2) \end{bmatrix}; \\ \bar{\mathbf{T}}(L_3) &= \begin{bmatrix} T_{11}^3(v_3) & T_{12}^3(v_3) & 0 & 0 \\ T_{21}^3(v_3) & T_{22}^3(v_3) & 0 & 0 \\ 0 & 0 & T_{11}^4(v_4) & T_{12}^4(v_4) \\ 0 & 0 & T_{21}^4(v_4) & T_{22}^4(v_4) \end{bmatrix} \end{aligned} \quad (8.23a)$$

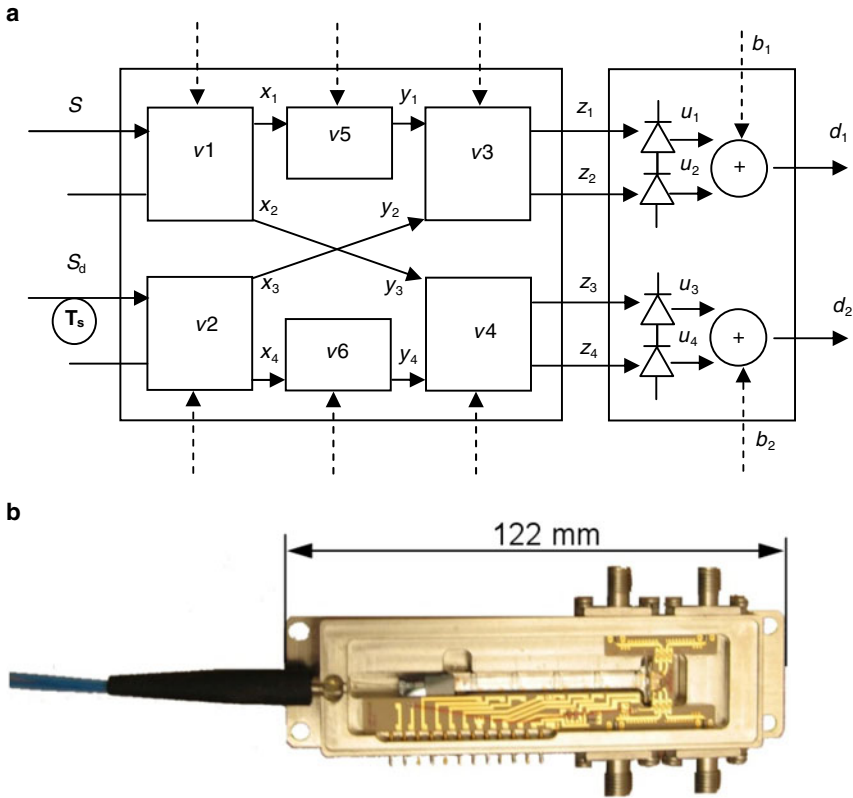


**Fig. 8.23** Functional scheme of a six-port hybrid-based detector with coupler biases  $\{v_1-v_4\}$ , phase-shifters biases  $\{v_5, v_6\}$  and detector biases  $\{b_1, b_2\}$ .  $S_d$  is a symbol-delayed signal  $S$  (a), and picture of an actual device (b) [94]

and for the middle section with intersecting waveguides:

$$\bar{\mathbf{T}}(L_2) = \begin{bmatrix} \exp\{j\varphi_1(v_5) + j\psi_1\} & 0 & 0 & 0 \\ 0 & \eta & (1 - \eta) \exp(j\psi_2) & 0 \\ 0 & (1 - \eta) \exp(j\psi_3) & \eta & 0 \\ 0 & 0 & 0 & \exp\{j\varphi_2(v_6) + j\psi_4\} \end{bmatrix}. \tag{8.23b}$$

The elements  $T_{ik}$  in (8.23a) are given by (8.20) or (8.21) for the regular and  $\delta\beta$ -reversed coupler, respectively;  $(1 - \eta)$  is the  $X$ -junction crosstalk parameter,  $\psi_{1-4}$  are phases accumulating in each optical path. The applied voltages are  $\{v_1-v_6\}$ , see Fig. 8.23a. The attenuation losses of the respective optical paths should also be taken into account by respective factors, including the material propagation losses [dB] and random components related to possible fabrication errors.

### 8.3.3.4 Optical Tunable Balanced Receiver Transfer Function

The receiver transfer function of the described  $90^\circ$  hybrid can be evaluated and used for device initialization, calibration and real-time adjustment. As an example, a one-symbol delayed ( $T_s$ ) input signal  $S_d$  can be used as a local input, see Fig. 8.23a. As described earlier, the  $S$  and  $S_d$  inputs result in four hybrid outputs [ $S + S_d$ ,  $S - S_d$ ,  $S + jS_d$ ,  $S - jS_d$ ]. The first two outputs will give the cosine of the relative phase between  $S$  and  $S_d$  after the balanced detectors, and the last two will give the sine of the relative phase. The outputs of the detectors can be sampled and processed.

By applying (8.21) to a lossless coupler, the hybrid transfer function can be defined. Thus, after the first set of couplers we have

$$\begin{aligned}
 x &= \begin{bmatrix} \cos(\beta_1) \exp(j\mu_1) & j \sin(\beta_1) & 0 & 0 \\ j \sin(\beta_1) & \cos(\beta_1) \exp(-j\mu_1) & 0 & 0 \\ 0 & 0 & \cos(\beta_2) \exp(j\mu_2) & j \sin(\beta_2) \\ 0 & 0 & j \sin(\beta_2) & \cos(\beta_2) \exp(-j\mu_2) \end{bmatrix} \cdot \begin{bmatrix} S \\ 0 \\ S_d \\ 0 \end{bmatrix} \\
 &= \begin{bmatrix} S \cos(\beta_1) \exp(j\mu_1) \\ jS \sin(\beta_1) \\ S_d \cos(\beta_2) \exp(j\mu_2) \\ jS_d \sin(\beta_2) \end{bmatrix}, \tag{8.24}
 \end{aligned}$$

where  $\gamma = \sqrt{\delta\beta^2 + \kappa^2}$ ,  $\kappa = \sqrt{\kappa_{21}\kappa_{21}^*}$ ,  $\sin(\beta) = \frac{\kappa}{\gamma} \sin(\gamma)$ ,  $\tan(\mu) = \frac{\delta\beta}{\gamma} \tan(\gamma)$ .

The values  $\{\beta_1 - \beta_4\}$  of the four couplers are controlled by a set of applied voltages  $\{v_1 - v_4\}$ , respectively. Signals  $S$ ,  $S_d$  are time varying. The delayed signal is described by

$$S_d(t) = D \cdot S(t - T_s) \cdot \exp(j\psi), \tag{8.25}$$

where  $D$  is the couplers imbalance parameter,  $\psi$  is a phase difference induced by the delay, and  $T_s$  is the duration of a single bit. At the input to the second set of couplers we have

$$y = \begin{bmatrix} x_1 \exp(j\zeta_1) \\ x_3 \exp(j\sigma_1) \\ x_2 \exp(j\sigma_2) \\ x_4 \exp(j\zeta_2) \end{bmatrix} = \begin{bmatrix} S \cos(\beta_1) \exp[j(\zeta_1 + \mu_1)] \\ S_d \cos(\beta_2) \exp[j(\sigma_1 + \mu_2)] \\ jS \sin(\beta_1) \exp(j\sigma_2) \\ jS_d \sin(\beta_2) \exp(j\zeta_2) \end{bmatrix} \tag{8.26}$$

where  $\sigma_1$  and  $\sigma_2$  are phases induced by the different optical signal paths. The two other similar phases were included in  $\zeta_1$  and  $\zeta_2$  and can be actively controlled by applied voltages  $\{v_5, v_6\}$  of the phase-shifters, respectively. At the output of the



optical hybrid, we have

$$\begin{aligned}
 z &= \begin{bmatrix} \cos(\beta_3) \exp(j\mu_3) & j \sin(\beta_3) & 0 & 0 \\ j \sin(\beta_3) & \cos(\beta_3) \exp(-j\mu_3) & 0 & 0 \\ 0 & 0 & \cos(\beta_4) \exp(j\mu_4) & j \sin(\beta_4) \\ 0 & 0 & j \sin(\beta_4) & \cos(\beta_4) \exp(-j\mu_4) \end{bmatrix} \cdot y \\
 &= \begin{bmatrix} S \cos(\beta_1) \cos(\beta_3) \exp[j(\zeta_1 + \mu_1 + \mu_3)] + jS_d \cos(\beta_2) \sin(\beta_3) \exp[j(\varphi_1 + \mu_2)] \\ jS \cos(\beta_1) \sin(\beta_3) \exp[j(\zeta_1 + \mu_1)] + S_d \cos(\beta_2) \cos(\beta_3) \exp[j(\varphi_1 + \mu_2 - \mu_3)] \\ jS \sin(\beta_1) \cos(\beta_4) \exp[j(\varphi_2 + \mu_4)] - S_d \sin(\beta_2) \sin(\beta_4) \exp(j\zeta) \\ -S \sin(\beta_1) \sin(\beta_4) \exp(j\varphi_2) + jS_d \sin(\beta_2) \cos(\beta_4) \exp[j(\zeta_2 - \mu_4)] \end{bmatrix}.
 \end{aligned} \tag{8.27}$$

In addition, the bias to the detectors (one for each pair) may be controlled. The output of the hybrid detector is (see Fig. 8.23a)

$$\begin{aligned}
 d &= \begin{bmatrix} (u_2 + u_1 \cos(2\beta_3)) |S|^2 \cos^2(\beta_1) + (u_2 - u_1 \cos(2\beta_3)) |S_d|^2 \cos^2(\beta_2) + b_1 \\ (u_4 + u_3 \cos(2\beta_4)) |S|^2 \sin^2(\beta_1) + (u_4 - u_3 \cos(2\beta_4)) |S_d|^2 \sin^2(\beta_2) + b_2 \end{bmatrix} \\
 &+ \begin{bmatrix} 2u_1 \cos(\beta_1) \cos(\beta_2) \sin(2\beta_3) \cdot \text{Re} \{ S S_d^* \exp[j(\gamma_1 + \psi)] \} \\ 2u_3 \sin(\beta_1) \sin(\beta_2) \sin(2\beta_4) \cdot \text{Im} \{ S S_d^* \exp[j(\gamma_2 + \psi)] \} \end{bmatrix}
 \end{aligned} \tag{8.28}$$

where the following definitions hold:  $\gamma_1 \equiv \zeta_1 - \varphi_1 + \mu_1 + \mu_3 - \mu_2 - \psi - \frac{\pi}{2}$ ,  $\gamma_2 \equiv \varphi_2 - \zeta_2 + \mu_4 - \psi$ ,  $b_1$  and  $b_2$  are the detectors' biases (if applicable), and  $u_i$  ( $i = 1, 2, 3, 4$ ) are the output signals at photodetectors 1–4 (see Fig. 8.23).

Equation (8.28) describes the output of the receiver as a function of couplers biases  $\{v_1-v_4\}$ , hybrid phase-shifter biases  $\{v_5, v_6\}$  and biases of the detectors  $\{b_1, b_2\}$  and can be used for various kinds of numerical analyses. Examples include the calculation of the SNR in the presence of additive white Gaussian noise and statistical analyses. Specific applications will require an optimized algorithm for initialization and real-time adjustment of the pairs  $\{\beta_3, \beta_4\}$ ,  $\{\beta_1, \beta_2\}$ ,  $\{\gamma_1, \gamma_2\}$ , as well as mitigation of parameter ambiguity effects. The calibration algorithm can be built accordingly, relying on the statistics of the received signals over transmitted data. The received signal can be sampled for the calibration algorithm during either payload transmission or a training period. The calibration procedure may also work with payload transmission at a lower sampling rate. Further work will require establishing the exact operational parameters (sampling rate, training sequences, power levels, number of samples, etc.) and will be application dependent.

### 8.3.3.5 Balanced Receiver DSP Control

As mentioned (see Sect. 8.1.1), coherent communication formats offer several advantages, in particular amplification of the incoming signal by the LO and linear baseband transformation, which is particularly useful as it allows disturbances in the optical band to be compensated for in the RF domain. Coherent detection relies on locking the received signal to the LO in polarization and frequency so that any relative phase changes which are not connected to the transferred data are eliminated.

Polarization fluctuations and line-induced phase changes have a time scale much smaller than the bit rate, so that by applying digital signal processing (DSP) techniques, these fluctuations can be estimated and their effect on the received signal can be canceled out at the baseband [100]. A full coherent system, in contrast to a differential one, requires a DSP engine. The DSP capability, together with the linear transformation, can be used to mitigate different link-impairments, such as chromatic dispersion and polarization mode dispersion [101]. The electronics that are needed for the DSP layer of balanced receivers operating in 40–100 Gbit/s networks function at rates of 10–50 GHz. These electronics, which are beyond the scope of this book, are beginning to be commercially available, thus enabling commercial use of the advanced modulation formats.

### 8.3.3.6 Commercial Balanced Receivers

The first commercial application of an optical QPSK modulation scheme, the 40 Gbit/s DQPSK that didn't require four-branch balanced receivers or advanced DSP engines, was initiated during the years 2008–2010. Therefore, while a relatively large variety of commercial IQ-modulators appeared during this period, commercial four-branch balanced receivers emerged only with the need for 100 Gbit/s systems in about 2010. Prior to 2010, only two companies had commercial four-branch balanced receivers, both for 40 Gbit/s DP-QPSK, CeLight [102] and Nortel [103]. During the 2010 Optical Fiber Communication Conference (OFC/NFOEC, San Diego) exhibition, additional companies announced their coherent receivers.

A short list of manufacturers includes Optoplex that uses free-space  $90^\circ$  optical hybrid, NeoPhotonics that uses Silica-on-Silicon technology, and Fujitsu, u<sup>2</sup>t, and NTT Photonics Labs that did not detail the internal structure. Most of the coherent receivers are in the status of samples or prototypes, and their full specifications cannot be found at present. A common denominator for the published specifications is that they target the 40/100 Gbit/s DP-QPSK market. The receivers are typically integrated versions with two polarizations and some include internal polarization splitters. Their  $90^\circ$  optical hybrids have a  $\pm 5^\circ$  error. Unpublished calculations show that  $90 \pm 5^\circ$  can lead to 0.2 dB penalty in the signal to noise ratio in QPSK systems. While this value is tolerated in most of the communication systems, a larger penalty, which is expected for the more advanced constellations, is not acceptable. For these constellations,  $90^\circ$  optical hybrids that have a minimal error will be needed, like the one of CeLight that can control the phase dynamically, or appropriate DSP methods should be used.

## 8.4 Trends in System Performance

The migration from traditionally used modulation formats to higher-order formats with more bits per symbol leads to a reduction of symbol rate and spectral width. Therefore, higher spectral efficiencies and per fiber capacities can be achieved. At

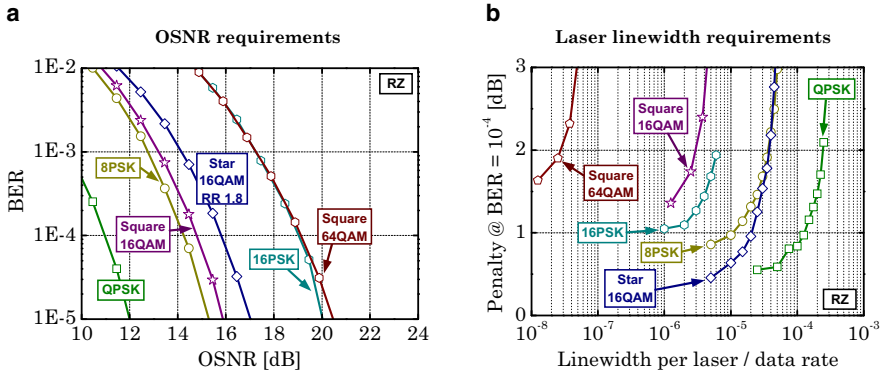


**Fig. 8.24** OSNR requirements (a) and laser linewidth requirements with  $M$ th power feed forward phase estimation (b) of various modulation formats when using homodyne receivers with synchronous detection

the same time, migration to higher-order modulation strongly influences system performance. This section discusses the basic trends in system performance resulting from migration to higher-order modulation formats, regarding relevant parameters such as noise, laser linewidth requirements, chromatic dispersion (CD) tolerance, self phase modulation (SPM) tolerance and attainable transmission distances. The discussion presented here is based on computer simulations for 40 Gbit/s systems employing homodyne receivers with synchronous detection and RZ pulse shape.

Figure 8.24a shows the back-to-back OSNR requirements of various modulation formats for homodyne synchronous detection (ideal carrier synchronization) at 40 Gbit/s, assuming the use of second-order Gaussian optical bandpass filters and fifth-order electrical Bessel filters within the receiver, with 3 dB bandwidths of 2.5 and 0.75 times the symbol rate, respectively. It can be observed that – when assuming a fixed data rate – the noise performance degrades with increasing number of bits per symbol as the Euclidean distances between the symbols become smaller. Higher-order QAM formats exhibit a significantly better noise performance than higher-order phase modulation formats for a certain number of bits per symbol, in particular Square QAM formats. In comparison with 16PSK, Square 16QAM has an OSNR performance gain of about 4 dB, for instance.

Another important system parameter which can become critical in systems with higher-order modulation is the laser linewidth. As illustrated in Fig. 8.24b, the requirements on laser linewidth increase with an increasing number of phase states since a certain level of laser phase noise is more problematic for closer phase distances. In addition – if the different formats are compared at the same data rate – the reduction of the symbol rate makes the laser phase noise more critical for modulation formats with a higher number of bits per symbol. In systems with homodyne synchronous detection, requirements on laser phase noise are stringent for higher-order formats such as 16PSK, Square 16QAM and Square 64QAM, even when using feed forward digital phase estimation which is not impaired by process-

ing delay. When the feed forward  $M$ th power block scheme is employed for phase estimation (for Square QAM: calculation of the phase error after class partitioning, for details see [48, 104]), the required linewidths at 40 Gbit/s are in the range of 240 kHz, 120 kHz and 1 kHz for 16PSK, Square 16QAM and Square 64QAM, respectively. These requirements cannot be fulfilled with currently available low-cost lasers. As a consequence, a commercial application of those modulation formats in systems with homodyne synchronous detection necessitates the development of low-cost lasers with very low linewidths. Moreover, the application of improved phase estimation schemes offers a way of further relaxing the requirements on laser linewidth [105, 106]. In [10] double polarization coherent 40 Gbit/s QPSK transmission with standard DFB lasers has become possible by using appropriate phase estimation. In comparison with systems with homodyne synchronous detection, the linewidth requirements are relatively relaxed in systems with direct detection. Even 16DPSK can tolerate a linewidth of about 1 MHz at 40 Gbit/s [48]. In the case of homodyne differential detection, the effective phase noise which affects the electrical differential demodulation process is determined by the beat-linewidth. The linewidth requirements on each laser are approximately doubled in comparison with direct detection when the same linewidths are assumed for the signal laser and the LO.

In the following paragraphs, the tolerance of different modulation formats regarding two important fiber transmission effects is outlined: chromatic dispersion (CD) and self phase modulation (SPM). Due to the reduced symbol rates and the longer symbol durations therewith aligned, modulation formats of higher order feature an improved tolerance against chromatic dispersion. The same is true for tolerance against polarization mode dispersion (PMD). Figure 8.25a illustrates the CD tolerances of a wide range of modulation formats at 40 Gbit/s for RZ pulse shape when digital homodyne synchronous receivers without equalization are used. It can be observed that – at a fixed data rate – CD tolerances improve when the order of the modulation format is increased.

Figure 8.25b illustrates the self phase modulation (SPM) tolerances of various modulation formats. These were determined by transmitting the signals over a single dispersive and nonlinear fiber link (standard single mode fiber) with a length of 80 km. The chromatic dispersion was completely compensated for after the link and the average fiber input power was varied. Generally, SPM tolerances tend to become worse as the number of phase states increases in modulation formats. Self phase modulation induces a power dependent phase shift on a signal propagating through the fiber. Each symbol of an idealized phase modulated signal with constant power would be affected by the same nonlinear phase shift during fiber propagation if there was no other effect than SPM. In this case, the received constellation would be rotated, but not distorted. However, chromatic dispersion and SPM interact during propagation. Power fluctuations induced by chromatic dispersion cause the nonlinear phase shifts experienced by the symbols to become different so that the received constellation diagrams become distorted in amplitude and phase. Since phase distances are getting smaller, the robustness against SPM decreases with increasing order of the PSK/DPSK format. When QAM signals have been propagated through

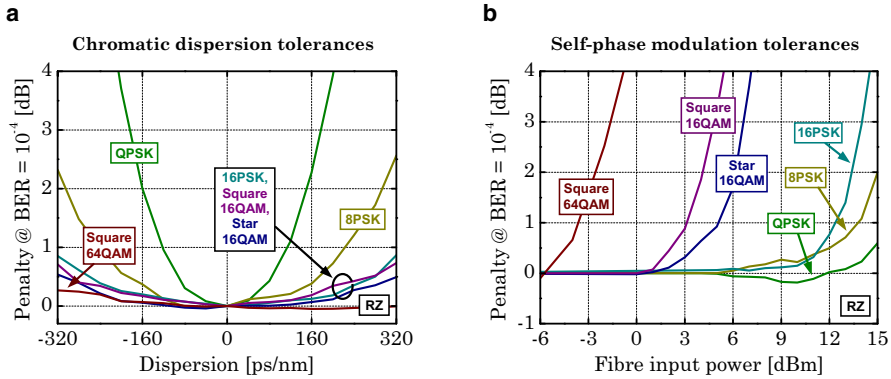


**Fig. 8.25** Chromatic dispersion tolerance (a) and self phase modulation tolerance (b) of various modulation formats for 40 Gbit/s; parameters: RZ pulse shape, homodyne synchronous detection with  $M$ th power feed forward digital phase estimation

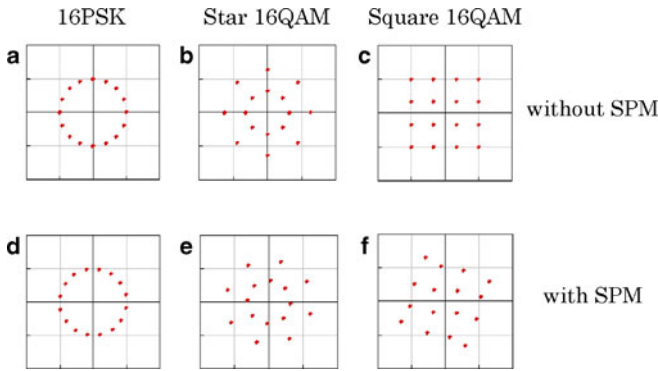


**Fig. 8.26** Deformation of the signal constellations of 16PSK (a, d), Star 16QAM (b, e) and Square 16QAM (c, f) caused by the SPM-induced nonlinear phase shift. a–c without SPM, d–f with SPM

the fiber, the constellation diagrams are deformed even in the absence of chromatic dispersion since symbols with different power levels are affected by different mean nonlinear phase shifts, as shown in Fig. 8.26. This phenomenon constitutes an inherent problem of optical QAM transmission and is the reason for the very poor SPM performance of all QAM formats (see Fig. 8.25b). However, relatively simple techniques can be employed to compensate for this effect [48, 107].

In conclusion, the migration to modulation formats with more bits per symbol leads to higher spectral efficiencies and higher chromatic dispersion and polarization mode dispersion tolerances. At the same time, laser linewidth requirements get more stringent, noise performance deteriorates and self phase modulation tolerances go down. The latter two effects essentially determine the distances achievable for single-channel multispan long-haul transmission. Thus, systems applying

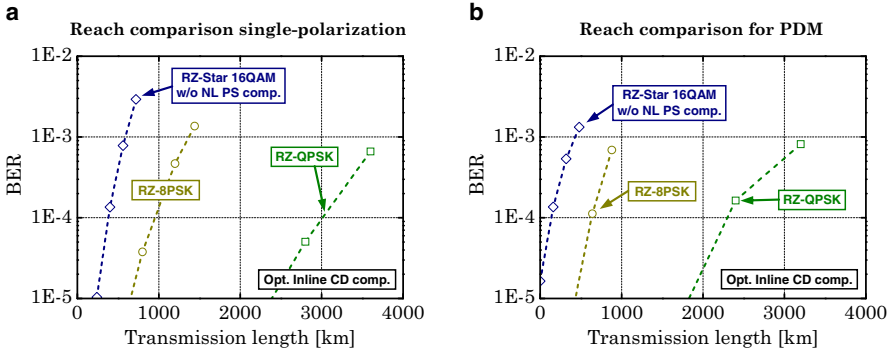


**Fig. 8.27** Transmission distances achieved with RZ-QPSK, RZ-8PSK and RZ-Star 16QAM for multispan transmission with optical inline CD compensation for single-polarization (a) and polarization division multiplexing (PDM) (b), assuming a common symbol rate of 10 Gbd (after [29])

higher-order modulation formats show a reduced transmission reach. The evaluation of transmission distances attainable using higher-order modulation formats represents an important field of current and future research. Corresponding recent experimental results are shown in Fig. 8.27 [29]. These confirm the expected reduction of transmission reach when migrating to higher-order formats. In multispan transmission systems with optical inline CD compensation, transmission distances of 3700 km/1360 km/600 km and 3200 km/960 km/400 km could be bridged with RZ-QPSK/RZ-8PSK/RZ-Star 16QAM for single-polarization (Fig. 8.27a) and polarization division multiplexing (Fig. 8.27b), respectively, assuming a common symbol rate of 10 GBd, single-channel transmission and a BER reference of  $10^{-3}$ . In the case of single-polarization, the transmission distance for RZ-Star 16QAM could be increased to about 1000 km by applying compensation of the mean nonlinear phase shift [29]. For all formats, transmission lengths can be further increased by replacing optical inline CD compensation with an electrical CD compensation at the receiver. In this way, transmission distances of > 6000 km/2800 km/950 km could be attained for single-polarization RZ-QPSK/RZ-8PSK/RZ-Star 16QAM [48]. The transmission distance of 950 km for RZ-Star 16QAM was achieved in a five-channel WDM environment and could even be extended to 1400 km by using adaptive electronic equalization [108]. Results from computer simulations indicate that a further extension of transmission reach is possible for the higher-order formats by optimizing the practical system setups. Generally, a compensation of the SPM-induced mean nonlinear phase shift is essential for achieving longer optical QAM transmission distances [107].

It should be noted that the comparison of transmission distances made is based upon a common symbol rate for all the modulation formats. The differences between maximum transmission distances would be smaller if the comparison were made at the same data rate.

## 8.5 Issues of Future Research

A continuous extension of network capacities while maintaining an attractive system reach is of high relevance, and it can be achieved by applying higher-order modulation formats which provide a higher spectral efficiency. The reduction of transmission distances aligned with this can be mitigated by optimization and high-quality fabrication of the system components required for generating and detecting optical signals with higher-order modulation, but also by reducing transmission impairments such as noise and fiber nonlinearities using low-noise optical amplification and Kerr effect compensation. Future research should cover the following areas:

**Transmission distances achievable with higher-order modulation formats** Analysis of multispan fiber transmission systems with higher-order modulation is still at an early stage, and corresponding further investigations are indispensable. Link configurations must be optimized for optimal fiber input powers and dispersion maps in systems with optical inline chromatic dispersion compensation. Moreover, a key issue is the development of techniques which will efficiently compensate for fiber nonlinearities.

**Behavior of higher-order modulation formats in WDM systems** The transmission lengths and channel spacings achievable with higher-order modulation formats in WDM systems are a matter of particular interest. Attention must be paid to channel filtering, crosstalk and interchannel nonlinearities. The channel spacing attainable depends on the signal bandwidth and on how narrowly optical signals can be filtered. Narrower channel spacing induces higher penalties due to cross phase modulation and four wave mixing. Thus, the system penalty induced by narrow optical filtering and the impact of linear and nonlinear interchannel crosstalk must be determined for the various modulation formats.

**Capacity, spectral efficiency and capacity-distance product attainable in WDM systems** If the fiber were linear and there were no system degradation through fiber nonlinearities, spectral efficiency could theoretically be increased to infinity by applying modulation formats of higher and higher order. Thereby, the expected increase of spectral efficiency would be about the ratio of the data rate to the symbol rate. More demanding noise requirements of the higher-order formats could then be met by simply launching more and more power into the fiber. However, in real transmission systems, performance degrades due to fiber nonlinearities when the fiber input power is increased. Simulations show that spectral efficiencies attainable in WDM fiber transmission systems are limited due to inter-channel nonlinear effects [109]. Moreover, it is an open question whether the capacity-distance product can be improved through the application of higher-order modulation formats as a consequence of the reduced transmission distances. The capacity-distance product of 11.25 Pbit/(s km) reported for 8PSK modulation [21] is four times smaller than the record product of 41.82 Pbit/(s km) obtained with QPSK [110]. However, there is potential for further optimization of systems applying higher-order modulation.

**System optimization** One key challenge on the way towards widespread deployment of systems using higher-order modulation is the optimization of system components at low cost. Signal distortions caused by pattern effects and accumulating in multiple modulator stages lead to implementation penalties. Multilevel electrical driving signals are not being generated easily. Thus, in order to realize transmitters performing close to the theoretical performance limits, high-speed integrated optical modulator structures and electrical level generators of high quality are currently being developed. At the receiver end, developments aim at integrating the whole optical receiver front end in a single chip, and to exploit digital signal processing technology to compensate for performance degradation effects and facilitate the recovery of information.

**Utilization of polarization** Polarization information provides an additional degree of freedom in optical fiber transmission systems and by utilizing polarization division multiplexing the spectral efficiency of any modulation format can be doubled. The extent to which crosstalk between the multiplexed channels degrades the performance of systems applying higher-order modulation will be a topic of future research. In addition, modulation formats exploiting all the parameters of the electrical field and encoding information additionally into the polarization are available for optical transmission and should also be considered in future investigations.

## References

1. M. Rohde, C. Caspar, N. Heimes, M. Konitzer, E.-J. Bachus, N. Hanik, Robustness of DPSK direct detection transmission format in standard fiber WDM systems. *Electron. Lett.* **36**, 1483–1484 (2000)
2. J.M. Kahn, K.P. Ho, Spectral efficiency limits and modulation/detection techniques for DWDM systems. *IEEE J. Sel. Top. Quantum Electron.* **10**, 259–272 (2004)
3. P.W. Hooijmans, *Coherent Optical System Design* (Wiley, Chichester, 1994)
4. L.G. Kazovsky, R. Welter, A.F. Elrefaie, W. Sessa, Wide-linewidth phase diversity homodyne receivers. *J. Lightw. Technol.* **6**, 1527–1536 (1988)
5. S. Norimatsu, K. Iwashita, K. Noguchi, An 8 Gb/s QPSK optical homodyne detection experiment using external-cavity laser diodes. *IEEE Photon. Technol. Lett.* **4**, 765–767 (1992)
6. O.K. Tonguz, R.E. Wagner, Equivalence between Pre-amplified Direct Detection and Heterodyne Receivers. *IEEE Photon. Technol. Lett.* **3**, 835–837 (1991)
7. J.H. Winters, Equalization in coherent lightwave systems using a fractionally spaced equalizer. *J. Lightw. Technol.* **8**, 1487–1491 (1990)
8. B. Spinnler, P.M. Krummrich, E.-D. Schmidt, Chromatic dispersion tolerance of coherent optical communication systems with electrical equalization, *Opt. Fiber Commun. Conf. (OFC'06)*, Techn. Digest (Anaheim, CA, USA, 2006), paper OWB2
9. L.G. Kazovsky, G. Kalogerakis, W.T. Shaw, Homodyne phase-shift-keying systems: past, challenges and future opportunities. *J. Lightw. Technol.* **24**, 4876–4884 (2006)
10. T. Pfau, S. Hoffmann, R. Peveling, S. Bhandare, S.K. Ibrahim, O. Adamczyk, M. Porrmann, R. Noe, Y. Achiam, First real-time data recovery for synchronous QPSK transmission with standard DFB lasers. *IEEE Photon. Technol. Lett.* **18**, 1907–1909 (2006)
11. S. Walklin, J. Conradi, Multilevel signaling for increasing the reach of 10 Gb/s lightwave systems. *J. Lightw. Technol.* **17**, 2235–2248 (1999)



12. J. Zhao, L. Huo, C. Chan, L. Chen, C. Lin, Analytical investigation of optimization, performance bound, and chromatic dispersion tolerance of 4-amplitude-shifted-keying format, *Opt. Fiber Commun. Conf. (OFC'06)*, Techn. Digest (Anaheim, CA, USA, 2006), paper JThB15
13. C. Wree, J. Leibrich, W. Rosenkranz, Differential quadrature phase-shift keying for cost-effective doubling of the capacity in existing WDM systems, *Proc. 4th ITG Conf. Photonic Networks*, Leipzig, Germany (2003), pp. 161–168
14. M. Ohm, Optical 8-DPSK and receiver with direct detection and multilevel electrical signals, *IEEE/LEOS Workshop on Advanced Modulation Formats*, San Francisco, USA, CA (2004)
15. H. Yoon, D. Lee, N. Park, Performance comparison of optical 8-ary differential phase-shift keying systems with different electrical decision schemes. *Opt. Express* **13**, 371–376 (2005)
16. M. Serbay, C. Wree, W. Rosenkranz, Experimental investigation of RZ-8DPSK at  $3 \times 10.7$  Gb/s, *18th Annual Meeting of the IEEE Lasers & Electro-Optics Society*, Sydney (2005), paper WE3
17. S. Tsukamoto, K. Katoh, K. Kikuchi, Coherent demodulation of optical 8-phase shift-keying signals using homodyne detection and digital signal processing, *Opt. Fiber Commun. Conf. (OFC'06)*, Techn. Digest (Anaheim, CA, USA, 2006), paper OThR5
18. M. Seimetz, L. Molle, D.-D. Gross, B. Auth, R. Freund, Coherent RZ-8PSK transmission at 30 Gbit/s over 1200 km employing homodyne detection with digital carrier phase estimation, *Proc. 33rd Europ. Conf. Opt. Commun. (ECOC'07)*, Berlin, Germany (2007), paper 8.3.4
19. R. Freund, D.-D. Groß, M. Seimetz, L. Molle, C. Caspar, 30 Gbit/s RZ-8-PSK transmission over 2800 km standard single mode fiber without inline dispersion compensation, *Opt. Fiber Commun. Conf. and Nat. Fiber Opt. Eng. Conf. (OFC/NFOEC'08)*, Techn. Digest (San Diego, CA, USA, 2008), paper OMI5
20. X. Zhou, J. Yu, D. Qian, T. Wang, G. Zhang, P. Magil,  $8 \times 114$  Gb/s, 25-GHz-spaced, PolMux-RZ-8PSK transmission over 640 km of SSMF employing digital coherent detection and EDFA-only amplification, *Opt. Fiber Commun. Conf. and Nat. Fiber Opt. Eng. Conf. (OFC/NFOEC'08)*, Techn. Digest (San Diego, CA, USA, 2008), paper PDP1
21. J. Yu, X. Zhou, M.-F. Huang, Y. Shao, D. Qian, T. Wang, M. Cvijetic, P. Magill, L. Nelson, M. Birk, S. Ten, H.B. Matthew, S.K. Mishra, 17 Tb/s ( $161 \times 114$  Gb/s) PolMux-RZ-8PSK transmission over 662 km of ultra-low loss fiber using C-band EDFA amplification and digital coherent detection, *Proc. 34th Europ. Conf. Opt. Commun. (ECOC'08)*, Brussels, Belgium (2008), paper Th.3.E.2
22. M. Seimetz, M. Noelle, E. Patzak, Optical systems with high-order DPSK and star QAM modulation based on interferometric direct detection. *J. Lightw. Technol.* **25**, 1515–1530 (2007)
23. M. Seimetz, Optical fiber transmission systems with high-order phase and quadrature amplitude modulation, PhD thesis, Technical University of Berlin, Germany (2008)
24. C.R. Cahn, Combined digital phase and amplitude modulation communication system. *IRE Trans. Commun. Syst.* **8**, 150–155 (1960)
25. J.C. Hancock, R.W. Lucky, Performance of combined amplitude and phase modulated communication system, *IRE Trans. Commun. Syst.* **8**, 232–237 (1960)
26. M. Ohm, J. Speidel, Receiver sensitivity, chromatic dispersion tolerance and optimal receiver bandwidths for 40 Gbit/s 8-level optical ASK-DQPSK and optical 8-DPSK, *Proc. 6th Conf. Photonic Networks*, Leipzig, Germany (2005), pp. 211–217
27. K. Sekine, N. Kikuchi, S. Sasaki, S. Hayase, C. Hasegawa, T. Sugawara, Proposal and demonstration of 10-Gsymbol/sec 16-ary (40 Gbit/s) optical modulation/demodulation scheme, *Proc. 30th Europ. Conf. Opt. Commun. (ECOC'04)*, Stockholm, Sweden (2004), paper We3.4.5
28. M. Serbay, T. Tokle, P. Jeppesen, W. Rosenkranz, 42.8 Gbit/s, 4 bits per symbol 16-ary inverse-RZ-QASK-DQPSK transmission experiment without polmux, *Opt. Fiber Commun. Conf. and Nat. Fiber Opt. Eng. Conf. (OFC/NFOEC'07)*, Techn. Digest (Anaheim, CA, USA, 2007), paper OThL2
29. M. Seimetz, L. Molle, M. Gruner, R. Freund, Transmission reach attainable for single-polarization and PolMux coherent star 16QAM systems in comparison to 8PSK and QPSK

- at 10 Gbaud, *Opt. Fiber Commun. Conf. and Nat. Fiber Opt. Eng. Conf. (OFC/NFOEC'09)*, Techn. Digest (San Diego, CA, USA, 2009), paper OTuN2
30. X. Zhou, J. Yu, M.-F. Huang, Y. Shao, T. Wang, P. Magill, M. Cvijetic, L. Nelson, M. Birk, G. Zhang, S. Ten, H.B. Matthew, S.K. Mishra, 32 Tb/s ( $320 \times 114$  Gb/s) PDM-RZ-8QAM transmission over 580 km of SMF-28 ultra-low-loss fiber, *Opt. Fiber Commun. Conf. and Nat. Fiber Opt. Eng. Conf. (OFC/NFOEC'09)*, Techn. Digest (San Diego, CA, USA, 2009), paper PDPB4
  31. C.N. Campopiano, B.G. Glazer, A coherent digital amplitude and phase modulation system, *IRE Trans. Commun. Syst.* **10**, 90–95 (1962)
  32. N. Kikuchi, S. Sasaki, Optical dispersion-compensation free incoherent multilevel signal transmission over single-mode fibre with digital pre-distortion and phase pre-integration techniques, *Proc. 34th Europ. Conf. Opt. Commun. (ECOC'08)*, Brussels, Belgium (2008), paper Tu.1.E.2
  33. L. Molle, M. Seimetz, D.D. Gross, R. Freund, M. Rohde, Polarization multiplexed 20 Gbaud Square 16QAM long-haul transmission over 1120 km using EDFA amplification, *Proc. 35th Europ. Conf. Opt. Commun. (ECOC'09)*, Vienna, Austria (2009), paper 8.4.4
  34. T. Kobayashi, A. Sano, H. Masuda, K. Ishihara, E. Yoshida, Y. Miyamoto, H. Yamazaki, T. Yamada, 160-Gb/s Polarization-multiplexed 16-QAM long-haul transmission over 3,123 km using digital coherent receiver with digital PLL based frequency offset compensator, *Opt. Fiber Commun. Conf. and Nat. Fiber Opt. Eng. Conf. (OFC/NFOEC'10)*, Techn. Digest (San Diego, CA, USA, 2010), paper OTuD1
  35. A.H. Gnauck, P.J. Winzer, S. Chandrasekhar, X. Liu, B. Zhu, D.W. Peckham,  $10 \times 224$  Gb/s WDM transmission of 28 Gbaud PDM 16 QAM on a 50 GHz grid over 1,200 km of fiber, *Opt. Fiber Commun. Conf. and Nat. Fiber Opt. Eng. Conf. (OFC/NFOEC'10)*, Techn. Digest (San Diego, CA, USA, 2010), paper PDPB8P
  36. M. Nakazawa, S. Okamoto, T. Omiya, K. Kasai, M. Yoshida, 256 QAM (64 Gbit/s) coherent optical transmission over 160 km with an optical bandwidth of 5.4 GHz, *Opt. Fiber Commun. Conf. and Nat. Fiber Opt. Eng. Conf. (OFC/NFOEC'10)*, Techn. Digest (San Diego, CA, USA, 2010), paper OMJ5M
  37. S.J. Trowbridge, High-Speed Ethernet transport. *IEEE Commun. Mag.* **45**, 120–125 (2007)
  38. W. Shieh, H. Bao, Y. Tang, Coherent optical OFDM: theory and design. *Opt. Express* **16**, 841–859 (2008)
  39. X. Yi, W. Shieh, Y. Ma: Phase noise on coherent optical OFDM systems with 16-QAM and 64-QAM beyond 10 Gb/s, *Proc. 33th Europ. Conf. Opt. Commun. (ECOC'07)*, Berlin, Germany (2007), paper 5.2.3
  40. A.J. Lowery, L.B. Du, J. Armstrong, Performance of optical OFDM in ultralong-haul WDM lightwave systems. *J. Lightw. Technol.* **25**, 131–136 (2007)
  41. R. Dischler, F. Buchali, Transmission of 1.2 Tb/s continuous waveband PDM-OFDM-FDM signal with spectral efficiency of 3.3 bit/s/Hz over 400 km of SSMF, *Opt. Fiber Commun. Conf. and Nat. Fiber Opt. Eng. Conf. (OFC/NFOEC'09)*, Techn. Digest (San Diego, CA, USA, 2009), paper PDPC2
  42. M. Nölle, L. Molle, D.-D. Gross, R. Freund, Transmission of  $5 \times 62$  Gbit/s DWDM coherent OFDM with a spectral efficiency of 7.2 bit/s/Hz using joint 64-QAM and 16-QAM modulation, *Opt. Fiber Commun. Conf. and Nat. Fiber Opt. Eng. Conf. (OFC/NFOEC'10)*, Techn. Digest (San Diego, CA, USA, 2010), paper OMR4
  43. X. Liu, S. Chandrasekhar, B. Zhu, P.J. Winzer, A.H. Gnauck, D.W. Peckham, Transmission of a 448-Gb/s reduced-guard-interval CO-OFDM signal with a 60-GHz optical bandwidth over 2000 km of ULAF and five 80-GHz-grid ROADMs, *Opt. Fiber Commun. Conf. and Nat. Fiber Opt. Eng. Conf. (OFC/NFOEC'10)*, Techn. Digest (San Diego, CA, USA, 2010), paper PDPC2
  44. M. Nazarathy, J. Khurgin, R. Weidenfeld, Y. Meiman, P. Cho, R. Noe, I. Shpantzer, V. Karagodsky, Phased-array cancellation of nonlinear FWM in coherent OFDM dispersive multi-span links. *Opt. Express* **16**, 15777–15810 (2008)

45. R. Weidenfeld, M. Nazarathy, R. Noe, I. Shpantzer, Volterra nonlinear compensation of 112 Gb/s ultra-long-haul coherent optical OFDM based on frequency-shaped decision feedback, *Proc. 35th Europ. Conf. Opt. Commun. (ECOC'09)*, Vienna, Austria (2009), paper 2.3.3
46. K.P. Ho, H.-W. Cui, Generation of arbitrary quadrature signals using one dual-drive modulator. *J. Lightw. Technol.* **23**, 764–770 (2005)
47. A. Kaplan, Y. Achiam, A. Greenblatt, I. Shpantzer, P. S. Cho, M. Tseytlin, A. Salamon, Electro-optical integrated transmitter chip for arbitrary quadrature modulation of optical signals, US Patent 7272271 (2003)
48. M. Seimetz, *High-Order Modulation for Optical Fiber Transmission*. Springer Series in Optical Sciences, vol. 143 (Springer, Berlin, 2009). ISBN: 978-3-540-93770-8
49. M. Seimetz, Optical receiver for reception of M-ary star-shaped quadrature amplitude modulation with differentially encoded phases and its application, Patent DE 10 2006 030 915.4, German Patent and Trade Mark Office (2006)
50. M. Kuschnerov, F.N. Hauske, K. Piyawanno, B. Spinnler, E.-D. Schmidt, B. Lankl, Joint equalization and timing recovery for coherent fiber optic receivers, *Proc. 34th Europ. Conf. Opt. Commun. (ECOC'08)*, Brussels, Belgium (2008), paper Mo.3.D.3
51. S.J. Savory, Compensation of fibre impairments in digital coherent systems, *Proc. 34th Europ. Conf. Opt. Commun. (ECOC'08)*, Brussels, Belgium (2008), paper Mo.3.D.1
52. F.M. Gardner, A BPSK/QPSK timing-error detector for sampled receivers. *IEEE Trans. Commun.* **34**, 423–429 (1986)
53. M. Oerder, H. Meyr, Digital filter and square timing recovery. *IEEE Trans. Commun.* **36**, 605–612 (1988)
54. S.J. Savory, G. Gavioli, R.I. Killey, P. Bayvel, Transmission of 42.8 Gbit/s polarization multiplexed NRZ-QPSK over 6400 km of standard fiber with no optical dispersion compensation, *Opt. Fiber Commun. Conf. and Nat. Fiber Opt. Eng. Conf. (OFC/NFOEC'07)*, Techn. Digest (Anaheim, CA, USA, 2007), paper OTuA1
55. M. Kuschnerov, D. Van den Borne, K. Piyawanno, F. N. Hauske, C.R.S. Fludger, T. Duthel, T. Wuth, J.C. Geyer, C. Schullien, B. Spinnler, E.-D. Schmidt, B. Lankl, Joint-polarization carrier phase estimation for XPM-limited coherent polarization-multiplexed QPSK transmission with OOK-neighbors, *Proc. 34th Europ. Conf. Opt. Commun. (ECOC'08)*, Brussels, Belgium (2008), paper Mo.4.D.2
56. L.G. Kazovsky, Phase- and polarization-diversity coherent optical techniques. *J. Lightw. Technol.* **7**, 279–292 (1989)
57. A.W. Davis, M.J. Pettitt, J.P. King, S. Wright, Phase diversity techniques for coherent optical receivers. *J. Lightw. Technol.* **LT-5**, 561–572 (1987)
58. U. Koc, A. Leven, Y. Chen, N. Kaneda, Digital coherent quadrature phase-shift-keying (QPSK), *Opt. Fiber Commun. Conf. (OFC'06)*, Techn. Digest (Anaheim, CA, USA, 2006), paper OTh11
59. R.E. Tench, J.-M.P. Delavaux, L.D. Tzeng, R.W. Smith, L.L. Buhl, R.C. Alferness, Performance evaluation of waveguide phase modulators for coherent systems at 1.3 and 1.5  $\mu\text{m}$ . *J. Lightw. Technol.* **LT-5**, 492–501 (1987)
60. J.W. Minford, O. Sneh, Apparatus and method for dissipating charge from lithium niobate devices, U.S. Patent 5,949,944 (1997)
61. P.G. Suchoski, T.K. Findakly, F.J. Leonberger, Stable low-loss proton-exchanged LiNbO<sub>3</sub> waveguide devices with no electro-optic degradation. *Opt. Lett.* **13**, 1050–1052 (1988)
62. F. Koyama, K. Iga, Frequency chirping in external modulators. *J. Lightw. Technol.* **6**, 87–93 (1988)
63. N. Courjal, A. Martinez, H. Porte, A LiNbO<sub>3</sub> modulator with chirp adjusted by domain inversion, *Proc. Integrated Photonics Research*, ed. by A. Sawchuk. OSA Trends in Optics and Photonics, vol. 78 (Opt. Soc. America, 2002), paper IFA3
64. K. Noguchi, O. Mitomi, H. Miyazawa, S. Seki, A broadband Ti:LiNbO<sub>3</sub> optical modulator with a ridge structure. *J. Lightw. Technol.* **13**, 1164–1168 (1995)

65. H. Nagata, N.F. Oapos, Brien, W.R. Bosenberg, G.L. Reiff, K.R. Voisine, DC-voltage-induced thermal shift of bias point in LiNbO<sub>3</sub> optical modulators. *IEEE Photon. Technol. Lett.* **16**, 2460–2462 (2004)
66. N. Grossard, J. Hauden, H. Porte, Low-loss and stable integrated optical Y-junction on lithium niobate modulators, *Proc. 13th Europ. Conf. Integr. Optics (ECIO'07)*, Copenhagen, Denmark (2007), paper ThG08
67. M. Sugiyama, S. Doi, S. Taniguchi, T. Nakazawa, H. Onaka, Driver-less 40 Gb/s LiNbO<sub>3</sub> modulator with sub-1 V drive voltage, *Opt. Fiber Commun. Conf. (OFC/IOOC'02)*, Techn. Digest (Anaheim, CA, USA, 2002), paper PD-FB6
68. R. Schiek, M.L. Sundheimer, D.Y. Kim, Y. Baek, G.I. Stegeman, H. Seibert, W. Sohler, Direct measurement of cascaded nonlinearity in lithium niobate channel waveguides. *Opt. Lett.* **19**, 1949–1951 (1994)
69. E.L. Wooten, K.M. Kissa, A. Yi-Yan, E.J. Murphy, D.A. Lafaw, P.F. Hallemeier, D. Maack, D.V. Attanasio, D.J. Fritz, G.J. McBrien, D.E. Bossi, A Review of lithium niobate modulators for fiber-optic communications systems. *IEEE J. Sel. Top. Quantum Electron.* **6**, 69–82 (2000)
70. P.S. Cho, J.B. Khurgin, I. Shpantzer, Closed-loop control of LiNbO<sub>3</sub> quadrature modulator for coherent communications, *OSA Topical Meeting: Coherent Optical Technologies and Applications (COTA-2006)* Whistler, BC, Canada (2006), paper CThC2
71. P.S. Cho, G. Harston, C.J. Kerr, A.S. Greenblatt, A. Kaplan, Y. Achiam, G. Levy-Yurista, M. Margalit, Y. Gross, J.B. Khurgin, Investigation of 2-bit/s/Hz 40-Gb/s DWDM transmission over 4 × 100-km SMF-28 fiber using RZ-DQPSK and polarization multiplexing. *IEEE Photon. Technol. Lett.* **16**, 656–658 (2004)
72. M.M. Howerton, R.P. Moeller, A.S. Greenblatt, R. Krähenbühl, Fully packaged broad-band LiNbO<sub>3</sub> modulator with low drive voltage. *IEEE Photon. Technol. Lett.* **12**, 792–794 (2000)
73. M. Sugiyama, M. Doi, T. Hasegawa, T. Shiraishi, K. Tanaka, K. Tanaka, Low-drive-voltage and compact RZ-DQPSK LiNbO<sub>3</sub> Modulator, *Proc. 33rd Europ. Conf. Opt. Commun. (ECOC'07)*, Berlin, Germany (2007), paper 10.3.3
74. A. Kaplan, I. Shpantzer, Single chip two-polarization quadrature synthesizer analyser and optical communication system using the same, US Patent US 2009/0185810 A1 (2009)
75. R. Griffin, Integrated InP devices for advanced optical modulation formats, *Proc. 14th Europ. Conf. Integr. Optics (ECIO'08)*, Eindhoven, The Netherlands (2008), paper ThA1
76. S. Corzine, P. Evans, M. Kato, G. He, M. Fisher, M. Raburn, A. Dentai, I. Lyubomirsky, A. Nilsson, J. Rahn, R. Nagarajan, C. Tsai, J. Stewart, D. Christini, M. Missey, V. Lal, H. Dinh, A. Chen, J. Thomson, W. Williams, P. Chavarkar, S. Nguyen, D. Lambert, S. Agashe, J. Rossi, P. Liu, J. Webjorn, T. Butrie, M. Reffle, R. Schneider, M. Ziari, C. Joyner, S. Grubb, F. Kish, D. Welch, 10-Channel × 40 Gb/s per channel DQPSK monolithically integrated InP-based transmitter PIC, *Opt. Fiber Commun. Conf. and Nat. Fiber Opt. Eng. Conf. (OFC/NFOEC'08)*, Techn. Digest (San Diego, CA, USA, 2008), paper PDP18
77. C.R. Doerr, P.J. Winzer, L. Zhang, L. Buhl, N.J. Sauer, Monolithic InP 16-QAM modulator, *Opt. Fiber Commun. Conf. and Nat. Fiber Opt. Eng. Conf. (OFC/NFOEC'08)*, Techn. Digest (San Diego, CA, USA, 2008), paper PDP20
78. C.R. Doerr, Compact advanced modulation format InP modulators and receivers, *OSA Topical Meeting: Coherent Optical Technologies and Applications (COTA-2008)* Boston, MA, USA (2008), paper IMA1
79. N. Kikuchi, InP Mach-Zehnder modulators for advanced modulation formats, *OSA Topical Meeting: Coherent Optical Technologies and Applications (COTA-2008)* Boston, MA, USA (2008), paper IMA4
80. <http://www.oclaro.com>
81. R.G. Walker, High-speed III–V semiconductor intensity modulators. *IEEE J. Quantum Electron.* **27**, 654–667 (1991)
82. R.A. Griffin, R.G. Walker, R.I. Johnstone, Integrated devices for advanced modulation formats, *Proc. IEEE/LEOS Workshop Advanced Modulation Formats*, San Francisco, CA, 2004, pp. 39–40

83. J.M. Heaton, Y. Zhou, H. Gao, G. Murdoch, A. Miller, C. Main, D. Hannan, S.J. Clements, Gallium arsenide linearised electro-optic waveguide modulators for RF-on-fibre applications, *Proc. SPIE Conf. on Electro-Optical Remote Sensing, Photonic Technologies, and Applications II*, ed. by G.W. Kamerman, O.K. Steinvall, K.L. Lewis, T.J. Merlet, R.C. Hollins, Cardiff, UK, September 2008. Proc. SPIE, vol. 7114, 71140M. doi: 10.1117/12.802211
84. R.A. Griffin, Integrated DQPSK transmitters, *Opt. Fiber Commun. Conf. (OFC'05)*, Techn. Digest (Anaheim, CA, USA, 2005), paper OWE3
85. www.lightwaveonline.com, Lightwave, **27**(1), **27**(2) (2010)
86. A. Davis, M. Pettitt, J.King, S. Wright, Phase diversity techniques for coherent optical receivers. *J. Lightw. Technol.* **LT-5**, 561–572 (1987)
87. R.P. Rickard, Coherent optical receiver, US Patent 7,085,501, assigned to Nortel Networks Ltd. (2006)
88. R. Epworth, J. Whiteaway, S.J. Savory, 3 Fibre I and Q coupler, US Patent 6,859,586, assigned to Nortel Networks Ltd. (2005)
89. L.G. Kazovsky, L. Curtis, W.C. Young, N.K. Cheung, All-fiber 90° optical hybrid for coherent communication. *Appl. Opt.* **26**, 437–439 (1987)
90. C. Hsieh, Free-space optical hybrid, US Patent 0223932, assigned to Optoplex Corporation (2007)
91. E.C.M. Pennings, D. Schouten, G.D. Khoe, R.A.J.C.M. van Gils, G.F.G. Depovere, Ultra fabrication tolerant fully packaged micro-optical polarization diversity hybrid. *J. Lightw. Technol.* **13**, 1985–1991 (1995)
92. R. Langenhorst, W. Pieper, M. Eiselt, D. Rohde, H.G. Weber, Balanced phase and polarization diversity coherent optical receiver. *IEEE Photon. Technol. Lett.* **3**, 814–816 (1991)
93. D. Hoffman, H. Heidrich, G. Wenke, R. Langenhorst, E. Dietrich, Integrated optics eight-port 90° hybrid on LiNbO<sub>3</sub>. *J. Lightw. Technol.* **7**, 794–798 (1989)
94. A. Kaplan, Y. Achiam, A.S. Greenblatt, G. Harston, P.S. Cho, LiNbO<sub>3</sub> integrated optical QPSK modulator and coherent receiver, *Proc. 11th Europ. Conf. Integr. Optics (ECIO'03)*, Prague, CZ (2003), pp. 79–82
95. D. Hoffman, H. Heidrich, G. Wenke, R. Langenhorst, E. Dietrich, Integrated optics eight-port 90° hybrid on LiNbO<sub>3</sub>. *J. Lightw. Technol.* **7**, 794–798 (1989)
96. E.C.M. Pennings, R.J. Deri, R. Bhat, T.R. Hayes, N.C. Andreadakis, Ultracompact, all-passive optical 90°-hybrid on InP using self-imaging. *IEEE Photon. Technol. Lett.* **5**, 701–703 (1993)
97. Th. Niemeier, R. Ulrich, Quadrature outputs from fiber interferometer with 4 × 4 coupler. *Opt. Lett.* **11**, 677–679 (1986)
98. M. Bachmann, P.A. Besse, H. Melchior, Overlapping-image multimode interference couplers with a reduced number of self-images for uniform and non-uniform power splitting. *Appl. Opt.* **34**, 6898–6910 (1995)
99. A. Kaplan, Design of ring resonators with tunable couplers. *IEEE Sel. Top. Quantum Electron.* **12**, 86–95 (2006)
100. T. Pfau, R. Peveling, F. Samson, J. Romoth, S. Hoffmann, S. Bhandare, S. Ibrahim, D. Sandel, O. Adamczyk, M. Porrmann, R. Noé, J. Hauden, N. Grossard, Y. Achiam, Polarization-multiplexed 2.8 Gbit/s synchronous QPSK transmission with real-time digital polarization tracking, *Proc. 33rd Europ. Conf. Opt. Commun. (ECOC'07)*, Berlin, Germany (2007), paper 8.3.3
101. H. Sun, K.-T. Wu, K. Roberts, Real-time measurements of a 40 Gb/s coherent system. *Opt. Express* **16**, 873–879 (2008)
102. P.S. Cho, G. Harston, A. Greenblatt, A. Kaplan, Y. Achiam, R.M. Bertenburg, A. Brenemann, B. Adoram, P. Goldgeier, A. Hershkovits, Integrated optical coherent balanced receiver, *OSA Topical Meeting: Coherent Optical Technologies and Applications (COTA-2006)* Whistler, BC, Canada (2006), paper CThB2
103. K. Roberts, Real time 40 Gb/s coherent system, *OSA Topical Meeting: Coherent Optical Technologies and Applications (COTA, 2008)* Boston, MA USA (2008), paper CWC1

104. M. Seimetz, Laser linewidth limitations for optical systems with high-order modulation employing feed forward digital carrier phase estimation, *Opt. Fiber Commun. Conf. and Nat. Fiber Opt. Eng. Conf. (OFC/NFOEC'08)*, Techn. Digest (San Diego, CA, USA, 2008), paper OTuM2
105. H. Louchet, K. Kuzmin, A. Richter, Improved DSP algorithms for coherent 16-QAM transmission, *Proc. 34th Europ. Conf. Opt. Commun. (ECOC'08)*, Brussels, Belgium (2008), paper Tu.1.E.6
106. T. Pfau, S. Hoffmann, R. Noé, Hardware-efficient coherent digital receiver concept with feed-forward carrier recovery for M-QAM constellations. *J. Lightw. Technol.* **27**, 989–999 (2009)
107. M. Seimetz, System degradation by the SPM-induced mean nonlinear phase shift in optical QAM transmission, *Opt. Fiber Commun. Conf. and Nat. Fiber Opt. Eng. Conf. (OFC/NFOEC'09)*, Techn. Digest (San Diego, CA, USA, 2009), paper JWA38
108. R. Freund, H. Louchet, M. Gruner, L. Molle, M. Seimetz, A. Richter, 80 Gbit/s/ $\lambda$  polarization multiplexed Star-16QAM WDM transmission over 720 km SSMF with electronic distortion equalization, *Proc. 14th OptoElectron. Commun. Conf. (OECC-2009)*, Hong Kong (2009), paper WP2
109. R.-J. Essiambre, G.J. Foschini, P.J. Winzer, G. Kramer, Exploring capacity limits of fibre-optic communication systems, *Proc. 34th Europ. Conf. Opt. Commun. (ECOC'08)*, Brussels, Belgium (2008), paper We.1.E.1
110. G. Charlet, J. Renaudier, H. Mardoyan, P. Tran, O.B. Pardo, F. Verluise, M. Achouche, A. Boutin, F. Blache, J.-Y. Dupuy, S. Bigo, Transmission of 16.4 Tbit/s capacity over 2550 km using PDM QPSK modulation format and coherent receiver, *Opt. Fiber Commun. Conf. and Nat. Fiber Opt. Eng. Conf. (OFC/NFOEC'08)*, Techn. Digest (San Diego, CA, USA, 2008), paper PDP3

# Chapter 9

## Wavelength Filters

Herbert Venghaus

**Abstract** The chapter reviews filters (to be) used in fibre optic communication: Fibre coupler filters, diffraction gratings, arrayed waveguide gratings, fibre Bragg gratings, Fabry–Pérot interferometers, thin-film and microring filters, interleavers, and acousto-optic filters. The presentations include the underlying basic physics, implementations of filters and modules, and typical performance data in the wavelength domain, but relevant phase properties are discussed as well. Attention is also given to system implications of the various device characteristics.

### 9.1 Introduction

The transmission capacity of a single optical fibre is in the range of several 10 Tbit/s, and in order to make best use of this several strategies have been followed in the past. One developmental path has been to raise the bit rate in a single channel. 10 Gbit/s systems have already been widely deployed, 40 Gbit/s links can also be seen in the field, and higher-order modulation formats (see Chap. 8) will enable a further increase of the transmission capacity per optical channel.

A second approach in parallel to raising bit rates has been and still is transmitting different wavelengths along a single fibre where each wavelength carries information independently from all other wavelengths. The corresponding technique is called wavelength division multiplexing (WDM), and it has been pursued from the early days of fibre optic communication [1–4]. WDM experienced a particularly strong developmental push through the availability of the erbium-doped fibre amplifier (EDFA, cf. Chap. 11) in the 1990s. The parallel transmission of up to several tens of WDM channels represents the current state-of-the-art, but significantly more

---

Herbert Venghaus (✉)  
c/o Fraunhofer Institute for Telecommunications, Heinrich Hertz Institute, Einsteinufer 37, 10587  
Berlin, Germany  
e-mail: herbert.venghaus@hhi-extern.fraunhofer.de

channels have already been transmitted in parallel along a single fibre in different laboratories. Examples are the successful transmission of more than 1000 ultra-dense WDM channels with 6.25 GHz channel separation and 2.5 Tbit/s total bit rate [5] or 160 wavelength channels on a 50 GHz grid with polarization-multiplexed RZ-DQPSK signals, which enabled 25.6 Tbit/s transmission over 240 km [6]. More details and additional examples are given in Chap. 8 of this book. WDM systems on the one hand require wavelength-selective transmitters (see Chaps. 3 and 5), but on the other they also require wavelength filters that enable the selection, adding/dropping, and routing of individual wavelengths or wavelength bands as key elements, and these filters will be the topic of the current chapter.

The demands on wavelength filters depend strongly on their functionality and the respective system specifications, and a variety of different types of wavelength filters have been developed in the past and are continuously being further improved. Wavelength filters include adaptations of previously known concepts to the specific requirements of fibre optics (e.g. diffraction and transmission gratings or thin-film filters), planar integrated optics devices (such as arrayed waveguide gratings (AWGs) or microring filters), or they may be closely related to the optical fibre itself (such as fibre coupler filters, fibre Bragg gratings (FBGs), or fibre Fabry–Pérot filters). Filters are normally developed for the spatial separation of a larger number of wavelength channels. However, filters can also be designed with periodic response in such a way that a sequence of incoming wavelength channels is sequentially directed towards  $2^N$  ( $N = 1, 2, \dots$ ) outputs resulting in  $2^N$  data streams with  $2^N$ -times larger channel spacing than the original one. Such devices are called interleavers and enable a cost-efficient upgrading of WDM systems (see Sect. 9.10).

All filters mentioned above will be covered in more detail in the following sections. The treatment will include short summaries of relevant physical principles, the technological realization of the different filters, and typical performance parameters as well. In accordance with the overall focus of the present book the treatment will be restricted to filters that are relevant to the 1.3 to 1.6  $\mu\text{m}$  wavelength region, and we will consider linear passive optical filters only.

Filters used in WDM systems can be classified as band-pass-, notch-, low-pass-, high-pass-, and all-pass filters which exhibit the following generic characteristics:

**Band-pass filters** transmit optical power within a certain wavelength window only while all other wavelengths are reflected or redirected elsewhere. In the case of a single optical channel the role of a band-pass filter is the rejection of noise at all wavelengths other than the optical channel. In multi-wavelength systems band-pass filters are key components for multiplexing and demultiplexing different wavelengths.

**Low-pass and high-pass filters** provide a sharp cut-off either above or below a particular wavelength and are therefore used for selecting (or rejecting) specific wavelength regions. A low-pass filter transmits long wavelength radiation while short wavelengths are reflected, and for a high-pass filter it is the other way round.

**Notch filters** reflect a specific wavelength or narrow wavelength band and exhibit high transmission elsewhere.



**Power-equalization filters** assure that wavelength channels in WDM systems have equal optical power. Adding and dropping of channels, non-uniform gain of optical amplifiers, power inequalities of laser sources are among the causes making channel power unequal. Power variations may be small after one span, however, they tend to accumulate and lead to large variations after a number of spans, and therefore power equalization is of high relevance.

**All-pass filters** transmit a complete wavelength band without any wavelength-dependent attenuation, but they induce a specific wavelength-dependent phase change. Such filters can, for example, be designed to compensate group velocity dispersion.

## 9.2 Phase Effects

Wavelength filters are fully characterized by their complex wavelength-dependent response, i.e. how the intensity and the phase of transmitted and/or reflected radiation is modified by the filter.

Filters used in fibre optics have traditionally been described primarily with respect to their wavelength-dependent intensity characteristics, while the associated phase variations have received significantly less attention. This has been adequate for sufficiently large channel separations and moderate bit rates. However, as the separations between adjacent channels in WDM systems come down to as low as 25 GHz or even less ( $100 \text{ GHz} \equiv 0.8 \text{ nm}$  wavelength separation at  $1.55 \mu\text{m}$ ) with the bit rates increasing at the same time, the phase characteristics of wavelength filters can no longer be ignored in leading-edge fibre optic systems. Phase-related effects become more pronounced the narrower the respective filters are, and in addition, the narrower the filters are the closer the channel wavelengths come to the filter edges where phase effects tend to be strongest.

In most cases phase effects are unwanted although the phase characteristics can sometimes be taken advantage of, one corresponding example being fibre Bragg gratings tailored for dispersion compensation.

### 9.2.1 General Considerations

Filters are described mathematically (see e.g. [7, 8]) in a convenient fashion by means of a complex transfer function  $H(\omega) = |H(\omega)| \exp[i\varphi(\omega)]$ . If the angular frequency  $\omega$  is replaced by the complex variable  $z = \exp(i\omega)$ , designated as ‘z-transform’, the new transfer function of digital filters,  $H_z(z)$ , can be represented as a ratio of polynomials which is true for the filters under consideration in this chapter. Depending on the location of the zeros and poles with respect to the unit circle ( $|z| = 1$ ) filters fall into the two categories of ‘minimum-phase’ and ‘non-minimum-phase’ filters.

A minimum-phase filter results if all zeros are located inside the unit circle, and if a filter is minimum-phase, its amplitude and phase are correlated and can be inferred from each other by a relation analogous to the Kramers–Kronig relation (which links the real and imaginary parts of the dielectric function). The phase and amplitude of minimum-phase filters are said to constitute a Hilbert transform pair [7, 8].

Conversely, non-minimum-phase filters do not obey the Kramers–Kronig relation. The property of a filter being minimum-phase or not is of high relevance in fibre optics for the following reason: In many cases filters should be narrow, have steep edges, and at the same time the corresponding filters should exhibit negligible dispersion. Non-minimum-phase filters can in principle meet this demand. However, if a filter is minimum-phase, these features cannot be optimized at the same time since steep roll-off implies strong dispersion due to the very nature of Hilbert transform pairs.

Interference filters such as Fabry–Pérot and thin-film filters (TFF) are inherently minimum phase while generalized Mach–Zehnder filters including AWGs are in general not minimum phase. However, the latter statement only holds for ‘ideal’, i.e. loss-less AWGs, while ‘real’ AWGs which exhibit a certain amount of loss satisfy the minimum-phase condition. Grating filters are minimum-phase in transmission, but this is not always the case when they are used in reflection [8–10]. One possibility to reconcile the conflicting demands for steep filter band edges and concurrent flat dispersion even for minimum-phase filters is the combination of a minimum-phase filter with an appropriate all-pass filter which compensates the filter-induced dispersion [11].

The local slope of the phase response is called the group delay  $\tau_g$ , and it is defined as the negative derivative of the phase response with respect to the angular frequency  $\omega$

$$\tau_g = -d\varphi/d\omega. \quad (9.1)$$

*(Note: the definition of the group delay is also found with a positive sign in the literature, and it is a consequence of the choices of the sign for the phase in the definition of the transfer function and that of the time dependence in the complex representation of the electric field.)*

The derivative  $D$  of the group delay with respect to wavelength

$$D = d\tau_g/d\lambda \quad (9.2)$$

is called the filter dispersion, typically given in ps/nm. The dispersion slope of filters,  $dD/d\lambda$ , (given in ps/nm<sup>2</sup>), normally also has a significant impact on the performance of high-bit-rate optical networks (see Sect. 9.2.4) and must therefore be compensated (designated commonly as “third-order compensation”). In addition, it might be worthwhile to note that the dispersion of optical fibres is generally normalized with respect to length, and the corresponding units are [ps/(nm km)].

### 9.2.2 Phase Characterization Techniques

The dispersion of passive optical devices can be determined in different ways. One experimental method to derive the dispersion of optical components including optical fibres and wavelength filters is the so-called modulation phase-shift or simply phase-shift method [8, 12–15]. Corresponding experiments provide the group delay  $\tau_g$ , and the dispersion has to be derived from  $\tau_g$  by differentiation. The method has two limitations: First, there is an averaging effect due to the fact that the two sidebands of the amplitude-modulated signal probe the dispersion of the device at two different wavelengths and this is a fundamental issue. Second, it might be difficult to numerically differentiate the measured curves in the case of noisy experimental data. The need for numerical differentiation can be overcome by application of the “differential phase-shift technique” which adds a low-speed modulation of the laser wavelength to the otherwise unchanged phase-shift measurement set-up, and this approach enables a direct determination of the dispersion of the device under investigation (fibre, wavelength filter, ...) [16, 17].

Another option for determining the dispersion of optical components including filters is low-coherence interferometry [18], and the so-called dispersion offset method is a further technique, which was initially proposed for the characterization of optical fibres and later extended to the determination of the dispersion of wavelength filters [19], however, it is not much used in practice.

Finally, dual-wavelength heterodyne measurements have also been shown to directly provide the spectral phase and therefore the chromatic dispersion of optical filters with high precision, and the concept has been illustrated for the case of fibre Bragg gratings and thin-film filters as well [20].

### 9.2.3 Typical Group Delay Characteristics

In the following a few examples of experimental results will illustrate the dispersion characteristics of various filter types (AWG, FBG, TFF, volume-phase holographic grating).

Standard AWGs exhibit Gaussian passbands and ideally have zero dispersion ([7], Sect. 4.4.2, [8], Sect. 2.4.4). Flat-top AWGs, which have a passband shape with more favourable properties for system applications (see Sect. 9.5.1), may have residual dispersion in the order of a few ps/nm only [21], however, experimentally observed values can be significantly higher. One corresponding example is illustrated in Fig. 9.1. A flat-top silicon-on-insulator- (SOI)-based AWG initially exhibited fairly large dispersion (long dashes), which turned out to be essentially due to a systematic phase error of the waveguides. After removing this phase error the dispersion appeared to be significantly improved (and the filter transmission became more symmetric as well).

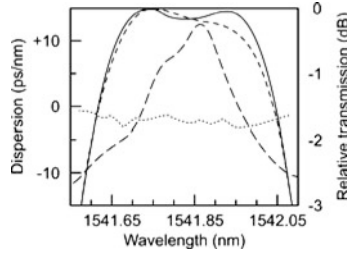


**Fig. 9.1** Comparison of dispersion and transmission across passband of AWG without and with phase-error correction. *Long-dashed*: dispersion, no correction; *dotted*: dispersion with correction; *short-dashed*: transmission, no correction; *full curve*: transmission with correction; after [22]

The relative group delay (measured using the phase-shift technique with 2 GHz modulation frequency) of two commercial-grade apodized fibre Bragg gratings designed for 100 GHz and 50 GHz channel separation is shown in Fig. 9.2.

The significantly higher group delay observed for the narrower filter is in agreement with expectation.

FBGs are routinely optimized towards two completely different goals: On the one hand, FBGs are designed for operation as filters reflecting a single band. For that purpose dispersion should be as small as possible, and residual dispersion of a few ps/nm has already been reported [23, 24]. On the other hand, one key application of FBGs is for dispersion compensation, and for that purpose FBGs are designed to exhibit very large dispersion as treated in more detail in Sect. 9.6.5.

The group delay and related chromatic dispersion of a thin-film “4-skip-1” filter (see Sect. 9.8.4 and Fig. 9.23) is shown in Fig. 9.3, which elucidates the strong increase of the group delay towards the filter band edges and the corresponding increase of the chromatic dispersion as well. 100 GHz thin-film filters are typically specified with 30 ps/nm dispersion while this value increases to about 60 ps/nm for TFFs with an enlarged flat top region (see Sect. 9.8.3).

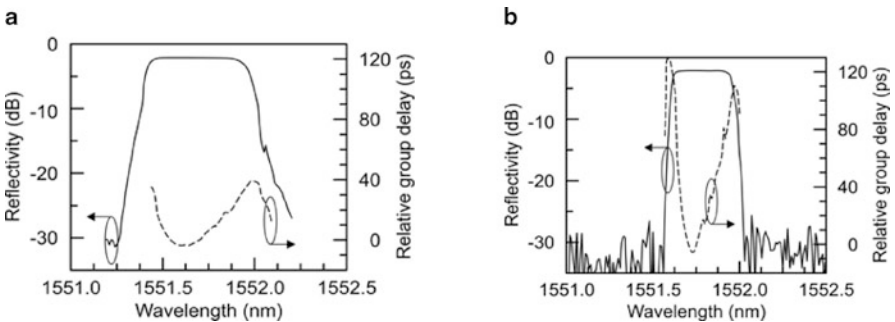


**Fig. 9.2** Experimentally determined reflectivity and group delay of apodized fibre Bragg gratings designed for 100 GHz (a) and 50 GHz (b) channel separation (after [8])

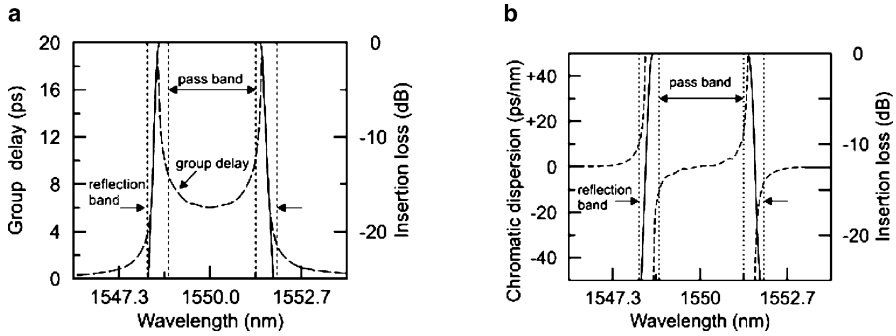
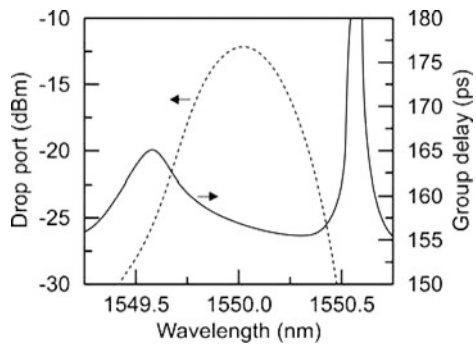


**Fig. 9.3** Group delay (a) and chromatic dispersion (b) of thin-film 4-skip-1 filter [25]

**Fig. 9.4** Group delay (*full line*) and drop port intensity (*broken line*) of a tunable volume-phase holographic grating (after [26])



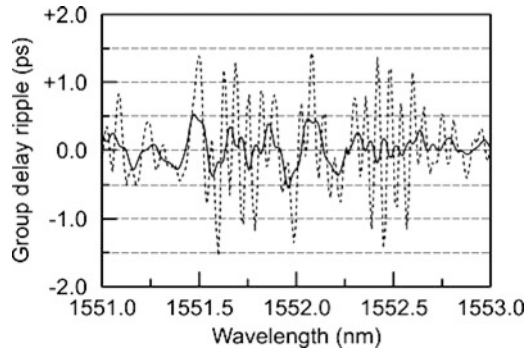
Finally, measurements of the group delay of volume-phase holographic gratings (see Sect. 9.4.3) [26] reveal group delay variations of a few ps across the reflected channel, and the results also illustrate a strong increase of the dispersion towards the passband edges which is the more pronounced the steeper the passband roll-off is (Fig. 9.4).

### 9.2.4 Group Delay Ripple

WDM filters, in particular gain-flattening and dispersion-compensating filters based upon thin-film and fibre-grating technologies, do typically exhibit in-band time delay ripples, (“group delay ripple(s)”, GDR) which can equivalently be characterized by the corresponding dispersion, the group delay, or the phase spectrum. Figure 9.5 illustrates (as an example) the GDR of an FBG-based gain-flattening filter [27].

Sources of GDR may be design compromises and imperfections such as spurious reflections at the grating ends of FBGs, which can be reduced by appropriate apodization [28] (see Sect. 9.6.3). Conversely, GDR may be due to manufacturing imperfections/variations. Correspondingly, the ripple amplitude of cascaded gain-flattening filters (GFF) was found to correspond essentially to the square root

**Fig. 9.5** Group delay ripple of an FBG-based gain-flattening filter; as measured (*broken line*) and averaged over 100 pm (*solid line*), after [27]



of the sum of individual ripple amplitudes squared, indicating that the GDR was not systematic in the GFFs investigated but varied randomly from one GFF to another [27, 29, 30].

A more careful inspection (e.g. by Fourier analysis of the GDR) reveals that a number of different frequency components contribute to the total GDR, and they have different consequences. The low-frequency ripple essentially gives rise to a broadening of the input pulse while a high-frequency ripple tends to create leading and trailing edge satellite pulses.

### 9.2.5 System Implications of Non-ideal Filter Characteristics

The estimation or evaluation of the adverse effects, which non-ideal filter phase characteristics have on system performance, is in general a challenging task, and it is not only the characteristics of the filter itself which matters, but other effects may also be important. For example (i) filters in real systems are not perfectly aligned (in contrast to re-circulating loop experiments), and (ii) the channel wavelengths of the transmitters are not perfectly aligned to the filter centre wavelengths. As a consequence the filter characteristics off the band centre become more important, and this is particularly relevant for higher bit rates and smaller channel separations. (iii) Signal distortions do not only occur due to passband dispersion [31], but in the case of add-drop multiplexers filter dispersion may also affect signals outside the filter bandwidth [32], in particular those adjacent to the channel selected by the filter.

Investigations (e.g. [32–34]) have further proven that it is not only the filter dispersion itself but the dispersion slope or even higher derivatives of the dispersion, and in particular the group delay ripple which can and normally do significantly degrade network performance.

The influence of GDR on system performance is extremely complex and consequently difficult to assess in a generic fashion. In addition to the GDR-induced broadening of signal bits or the creation of additional spurious spikes, a large number of other dependences have been reported in the literature. Higher GDR ampli-

tudes tend to have larger detrimental effects, and therefore it is generally attempted to make the GDR amplitude as small as possible. The period of the GDR is also of high relevance, and adverse effects are particularly pronounced if the GDR period is close to that of the bit rate (i.e. corresponds to 10 or 40 Gbit/s, which is equivalent to 80 and 320 pm periodicity, respectively). The relative position of the ripple amplitudes with respect to the transmitted bits is important as well [35], and the system impact of GDR depends on the modulation format used [29, 36], on the specific combination of modulation and signal detection scheme [37], and on pulse shape. The GDR-related penalty is also affected by interactions between phase ripples and fibre non-linearities, and as a consequence the maximum transmission distance decreases with increasing input power to the fibre [38]. Finally, all-optical 2R signal regeneration experiments performed in order to correct pulse distortions introduced by GDR, have demonstrated a dependence of the achievable results on the concept of 2R regeneration applied: Four-wave-mixing-based regenerators achieved better performance than their self-phase-modulation-based counterparts [39].

## 9.3 Fibre Couplers

### 9.3.1 Basics of Coupled Mode Theory

Fibre couplers can serve different purposes in fibre optic networks. They can be used for passive functionalities as outlined in Chap. 10, and they also exhibit wavelength-dependent characteristics which can be exploited to fabricate wavelength filters, and this will be the topic of the following section.

If two dielectric waveguides (WG) are located close enough to each other so that the evanescent fields of the modes guided in one of the WGs overlap with the core of the other WG, this arrangement is called a directional coupler, and an appropriately designed directional coupler constitutes a wavelength multiplexer/demultiplexer (MUX/DEMUX) as explained below. More detailed descriptions based on coupled-mode theory are found in many textbooks (e.g. [7, 40–42]), and we will summarize here the most relevant results only.

Let us designate the upper WG in the insert of Fig. 9.6a (leading from port 1 to port 3) as WG ‘*a*’ and the lower WG (leading from port 2 to port 4) as ‘*b*’ and represent the electric fields propagating along WG *a* and *b* as

$$E(x, y, z) = E^{(a)}(x, y)a(z) \quad \text{and} \quad E(x, y, z) = E^{(b)}(x, y)b(z), \quad (9.3)$$

where  $E^{(j)}(x, y)$  (with  $j = a, b$ ) characterizes the modal distribution of the electric fields in the  $x, y$ -plane.

*(Please note that in standard S-parameter terminology ‘b’ normally represents back-reflected power, which is different from the definition convention used here!)*

For the amplitudes  $a(z)$  and  $b(z)$  we assume

$$a(z) = a_0 \exp(i\beta_a z) \quad \text{and} \quad b(z) = b_0 \exp(i\beta_b z), \quad (9.4)$$

where  $\beta_j$  ( $j = a, b$ ) are the propagation constants (see (9.24), below). The total field of the coupled mode  $E(z)$  is given by

$$E(x, y, z) = E^{(a)}(x, y)a(z) + E^{(b)}(x, y)b(z) \quad (9.5)$$

and the amplitudes  $a(z)$  and  $b(z)$  satisfy

$$\frac{d}{dz}a = i\beta_a a + i\kappa_{ab}b \quad \text{and} \quad \frac{d}{dz}b = i\kappa_{ba}a + i\beta_b b. \quad (9.6)$$

Since we are not interested in the  $x, y$ -dependence but the coupling between the WGs only, we will omit the  $x, y$ -dependence in the following, and we will further assume that the electric field intensity has been normalized to 1. If we then make the substitution

$$\begin{bmatrix} a(z) \\ b(z) \end{bmatrix} = \begin{bmatrix} A \\ B \end{bmatrix} \exp(i\beta z) \quad (9.7)$$

assume symmetric coupling, i.e.  $\kappa_{ab} = \kappa_{ba} = \kappa$ , convert (9.6) into a matrix equation, and solve for non-trivial solutions of the corresponding determinant, we get

$$\beta = \frac{\beta_a + \beta_b}{2} \pm q \quad (9.8)$$

or, rewriting the two solutions of (9.8),

$$\beta_+ = \frac{\beta_a + \beta_b}{2} + q \quad \text{and} \quad \beta_- = \frac{\beta_a + \beta_b}{2} - q \quad (9.9)$$

with

$$q = \sqrt{\Delta^2 + \kappa^2} \quad \text{and} \quad \Delta = \frac{\beta_a - \beta_b}{2}. \quad (9.10)$$

The two modes corresponding to the propagation constants  $\beta_+$  and  $\beta_-$  are designated as “even” and “odd” modes. After finding the eigenvectors corresponding to  $\beta_+$  and  $\beta_-$ , the general solution for the guided waves can be expressed as

$$\begin{bmatrix} a(z) \\ b(z) \end{bmatrix} = \mathbf{S}(z) \begin{bmatrix} a(0) \\ b(0) \end{bmatrix}, \quad (9.11)$$

where the matrix  $\mathbf{S}(z)$  is given by

$$\mathbf{S} = \begin{bmatrix} \cos(qz) + i\frac{\Delta}{q} \sin(qz) & i\frac{\kappa}{q} \sin(qz) \\ i\frac{\kappa}{q} \sin(qz) & \cos(qz) - i\frac{\Delta}{q} \sin(qz) \end{bmatrix} \exp(i\varphi z) \quad (9.12)$$



with

$$\varphi = \frac{\beta_a + \beta_b}{2}. \quad (9.13)$$

If the input power is launched into the upper waveguide (designated as ‘a’), we have

$$a(0) = 1 \quad \text{and} \quad b(0) = 0 \quad (9.14)$$

and for the variation of the electric field amplitudes in the waveguides and the corresponding guided power in the case of identical WGs ( $\beta_a = \beta_b$ ) we get

$$a(z) = \cos(\kappa z) \exp(i\beta z), \quad b(z) = \sin(\kappa z) \exp(i\beta z) \quad (9.15)$$

and

$$P_a = \cos^2(\kappa z), \quad P_b = \sin^2(\kappa z). \quad (9.16)$$

Equations (9.15) and (9.16) represent a periodic power transfer between the two WGs, and the distance after which complete coupling occurs for the first time is called the coupling length  $L_c$ , given by

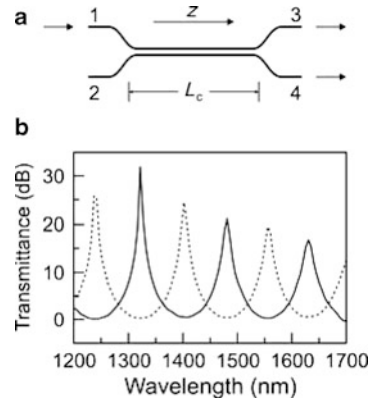
$$L_c = \frac{\pi}{2\kappa}. \quad (9.17)$$

The coupling constant  $\kappa$  depends on the distribution of the propagating fields (in particular their evanescent tails), and  $\kappa$  can be considered (to a good approximation) as being proportional to  $1/\lambda$ . As a consequence, the output power in each port of the directional coupler varies periodically as a function of frequency/wavelength if the length of the directional coupler is fixed.

### 9.3.2 Fabrication of Fibre Couplers

Fibre couplers are most frequently realized as fused biconical taper couplers. Fabrication of the fibre couplers starts with a removal of the cladding in the region where the coupling is intended to occur, and the next fabrication steps are essentially heating, stretching, and tapering of the two fibres. Through this stretching the fibre core diameters become smaller in the coupling region and as a consequence the confinement of the guided radiation is reduced which enables stronger coupling. The coupling region is typically multi-mode in contrast to the single-mode characteristics in the feeding branches of the coupler, and therefore it is a key issue in designing and fabricating directional couplers – beyond assuring the proper wavelength-dependent coupling – to make sure that essentially no power is coupled from the fundamental mode to higher order ones in the coupling region as this would give rise to unwanted losses [43, 44].

**Fig. 9.6** Schematic presentation of a directional coupler (a), wavelength-dependent transmission of a fibre coupler (b) (1550/1625 nm MUX/DEMUX) [45]



### 9.3.3 Characteristics of Fibre Coupler-based Wavelength Filters

The typical parameters of optical fibres exhibit moderate wavelength-dependent variations, and as a consequence standard fibre coupler filters operate for rather large channel separations. Fibre couplers are commercially available for demultiplexing the 1.3  $\mu\text{m}$  and 1.55  $\mu\text{m}$  channels, demultiplexing a 1625 nm monitoring channel from the 1.3  $\mu\text{m}$  or 1.55  $\mu\text{m}$  band, as pump wavelength combiners for erbium-doped fibre amplifiers (980 nm/1550 nm, 1480 nm/1550 nm, 1054 nm/1550 nm, and 1065 nm/1550 nm multiplexers), and as 1017 nm/1300 nm multiplexers for Pr-doped fibre amplifiers. In addition, fibre-coupler based wavelength filters are offered for CATV or various measurement applications (see also Chap. 10, Sect. 10.2.4 and Fig. 10.15).

Figure 9.6b illustrates the periodic characteristics of a fibre coupler which has been designed and specified as a 1550/1625 nm MUX/DEMUX, and it also illustrates that the wavelength characteristics of standard fibre couplers do not enable high wavelength discrimination over a larger wavelength range (a crosstalk of the order of 20 dB is a typical requirement). One means to improve performance and in particular to achieve better crosstalk is cascading, and cascaded 1310/1550 nm fibre couplers with crosstalk better than 40 dB have already been demonstrated [46].

### 9.3.4 Applications Beyond Wavelength Channel Filters

Fibre couplers also enable the splitting of the guided power into any ratio desired. Power splitters or tap couplers are typically offered with splitting ratios ranging from 50:50 to 99:1, and such splitters can be fabricated for any wavelength wanted [47, 48], see also Chap. 10, Sect. 10.2.4. Figure 9.7 illustrates the generic wavelength dependence of different types of power splitters: single wavelength, wavelength flattened and broadband. The example chosen is for 1300 nm

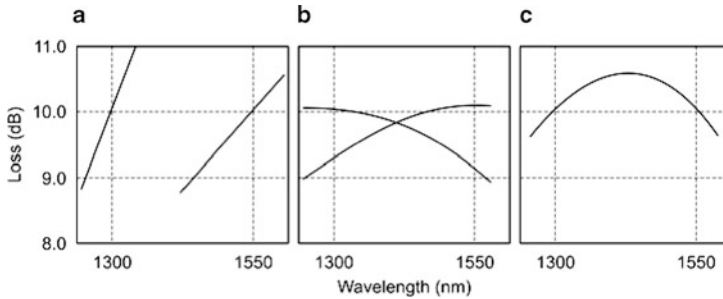


**Fig. 9.7** Wavelength-dependence of fibre-coupler based power splitters. Single wavelength (a), wavelength flattened (b), broadband (c) [47]

and 1550 nm as operation wavelengths and 10 : 90 splitting ratio, however, the wavelength dependence for other splitting ratios is very much the same.

Furthermore, fibre couplers can be designed as pump combiners which enable the combination of two different pump waves into a single fibre or alternatively combining two orthogonally polarized pumps at the same wavelength, and finally, fibre couplers can be designed as gain flattening filters (cf. also thin-film filters, Sect. 9.8) which assure gain flatness from 1530 nm to 1560 nm with less than  $\pm 0.25$  dB deviation from the target value [48].

## 9.4 Diffraction Gratings

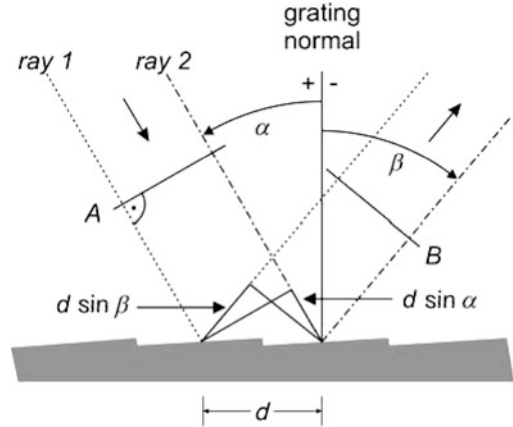
### 9.4.1 Planar Diffraction Gratings

A diffraction grating is an arrangement of reflecting (or transmitting) elements separated by a distance comparable to the wavelength of the light (or in more general terms: electromagnetic radiation) under investigation. Typical structures under discussion in the subsequent section are two-dimensional collections of parallel transparent slits or reflecting grooves on an optical surface while fibre Bragg gratings will be discussed in Sect. 9.6.

The characteristic property of a diffraction grating is its ability to diffract light into different, wavelength-dependent directions. As a consequence, different wavelengths of an incoming beam are angularly separated, and this constitutes the basis for many kinds of spectroscopic investigations and for the fabrication of wavelength filters as well.

Diffraction gratings have been manufactured for more than 200 years, starting with the fabrication of the first diffraction grating by the American astronomer David Rittenhouse in 1785 and spurred by the pioneering work of Joseph von Fraunhofer at the beginning of the 19th century, so that by the end of that century diffraction gratings had become distinctly superior to prisms and interferometers for spec-

**Fig. 9.8** Diffraction of planar wave fronts from a reflection grating (schematic). A planar wave front is represented by parallel rays such as “ray 1” and “ray 2”. Angles measured (counter-) clockwise are defined as negative (positive). Lines labelled ‘A’ and ‘B’ represent incoming and diffracted wave fronts, respectively



trosopic applications. In the early days the periodic structures had been grooves scratched on a blank surface while different grating variants subsequently emerged. Gratings can be operated from the UV over the visible range until far into the IR regime, they are used in many different areas of science, and more recently diffraction gratings have found applications in fibre-optic communication systems where they serve as wavelength MUX/DEMUX in WDM systems.

The operation of a reflection grating is illustrated in Fig. 9.8 (see e.g. [49–51]). Ray 1 and ray 2 correspond to light diffracted from adjacent grooves separated by a distance  $d$ , and constructive interference occurs (i.e. these rays are in-phase) if their path difference after diffraction is an integral number of wavelengths. This relationship is expressed by the grating equation

$$m\lambda = d(\sin \alpha + \sin \beta) \quad (9.18)$$

(please note that  $\sin \beta$  is negative since  $\beta < 0$ ).  $m$  is an integer and is called the diffraction order, and  $m = 0$  is the special case of normal reflection. A frequently used configuration corresponds to  $\alpha = \beta$ , i.e. light is diffracted back towards the direction from which it came, and this is called the *Littrow configuration*.

### 9.4.2 Relevant Parameters of Diffraction Gratings

The range of wavelengths for a given diffraction order without any superposition of light from adjacent orders is called the *free spectral range* (FSR). For telecom applications the FSR of diffraction gratings (typically operated in the first diffraction order) is much larger than the range of all wavelengths used in WDM systems, and thus there is no unwanted coincidence of any telecom channel/wavelength with higher orders of other wavelengths.

The diffraction efficiency of a grating into different orders  $m$  exhibits a pronounced wavelength dependence, and as a consequence, the efficiency is also strongly wavelength dependent for a given diffraction order. The efficiency of reflection gratings is particularly high if the directions of the incident and diffracted rays correspond to specular reflection from the grating facets. The corresponding angle  $\theta_{\text{bl}}$  which satisfies the condition

$$m\lambda_{\text{bl}} = 2d \sin \theta_{\text{bl}} \quad (9.19)$$

is called the *blaze angle* and  $\lambda_{\text{bl}}$  is called the *blaze wavelength*, and diffraction gratings are normally designed/chosen in such a way that  $\lambda_{\text{bl}}$  corresponds to the centre of the wavelength range the diffraction grating is expected to cover in the application under consideration.

Diffraction gratings also exhibit a strong polarization dependence, however, this dependence can be kept acceptably low over a limited range of wavelengths by an appropriate design. States of polarization are normally designated as s- and p-polarized, however, there are two different definitions: The most widely accepted one is that s- and p-polarization correspond to radiation having the electric field vector orthogonal and parallel to the plane of incidence, respectively. However, s- and p-polarization are also defined as orthogonal and parallel to the grooves of the diffraction grating, and the latter definition is just the opposite of the former for the common configuration where the plane of incidence is orthogonal to the plane of the grooves. If the plane of incidence is not orthogonal to the grooves, there is no relation at all between the two definitions. We will use the former definition throughout this chapter, although the latter is the one more frequently used with diffraction gratings. Alternatively, s- (and p-) polarization are also called TE- (TM-) polarization.

The *resolving power*  $R$  or ability of a grating to resolve two closely spaced wavelengths is given by

$$R = \lambda/\Delta\lambda = |m|N \quad (9.20)$$

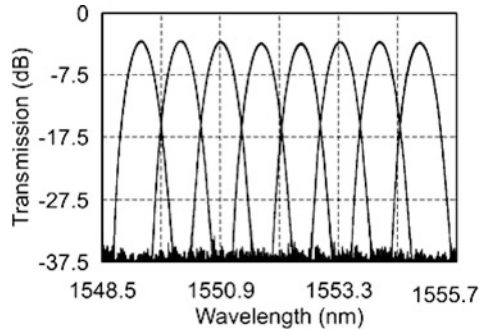
with  $m$  being the diffraction order and  $N$  the total number of illuminated grooves (see e.g. [49]). A slightly different expression for the maximum attainable resolving power  $R_{\text{max}}$  is derived in [50]:

$$R_{\text{max}} = \frac{2Nd}{\lambda}, \quad (9.21)$$

where  $Nd$  is simply the width of the ruled area. Equation (9.21) holds for  $|\alpha| \approx 90^\circ$  and  $|\alpha| \approx |\beta|$ , i.e. for grazing incidence in the Littrow configuration, and it is interesting to note that (9.21) does not depend on the diffraction order  $m$ .

*Echelle gratings* represent a special type of diffraction grating with high groove spacing and are optimized for high diffraction orders. Planar gratings fabricated in the InP material system or in SOI are typical examples of such gratings (see Sect. 9.12.2).

**Fig. 9.9** Transmission of diffraction-grating-based 8-channel 100 GHz DEMUX ([52], fabrication discontinued recently)



### 9.4.3 Diffraction Gratings Used in Fibre Optic Communication

Diffraction gratings used in fibre optics fall into two categories: surface relief gratings and volume phase (holographic) gratings.

Figure 9.8 is an example of a surface relief grating operated in reflection. Such gratings are typically composed of a substrate material, for example glass with low thermal expansion coefficient, an epoxy or photoresist structured in such a way as to exhibit the desired surface profile, and a metallic highly reflecting coating on top. Multiplexers and demultiplexers based upon reflection gratings have become commercially available for the C-, the L-, and the C+L-bands with 50, 100 or 200 GHz channel spacing, channel numbers ranging from 8 to 96, and polarization-dependent loss < 0.3 dB. The characteristics of a corresponding grating-based 8-channel 100 GHz demultiplexer is shown in Fig. 9.9.

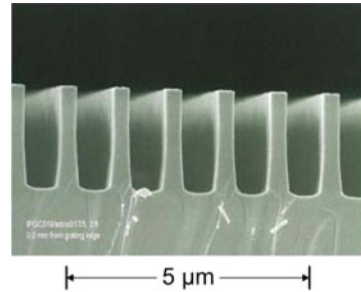
Another variety of surface relief gratings are surface relief transmission gratings. They are used in many different areas because they can be operated from about 200 nm (or even 157 nm) into the mid-IR, exhibit very low absorption loss, are particularly stable with respect to environmental influences, can tolerate high temperature (up to 1000 °C) and high input power of the light to be dispersed, and there are specific designs for telecom applications as well.

A surface relief transmission grating designed for operation in the C-band (1525–1575 nm) is shown in Fig. 9.10.

MUX/DEMUX based upon surface relief transmission gratings have already achieved > 97 % efficiency and < 0.05 dB polarization-dependent loss (PDL) over the whole C-band, and more than 99 % efficiency has been predicted theoretically [53]. Specific details, however, depend on customer requirements and on the overall design and implementation of the MUX/DEMUX.

A third type of diffraction gratings are volume-phase holographic (VPH) gratings consisting of a thin layer with modulated refractive index sandwiched between two glass substrates which makes such gratings particularly rugged. VPH gratings for telecom applications may be fabricated by optically replicating a previously recorded interference pattern, or alternatively, each grating may be an original where a thin film of dichromated gelatine is exposed to a laser interference pat-

**Fig. 9.10** SEM picture of fused-silica surface relief transmission grating [53]



tern and laminated with a protective glass cover after proper processing of the film. VPH gratings encapsulated between parallel glass plates may additionally be sandwiched between two precision prisms in such a way that the beam cross-section is enhanced at the grating (providing higher resolution) and the Bragg condition is fulfilled for a particular wavelength, for example 1550 nm for telecom applications. VPH gratings are commercially available optimized for operation in the C-, L-, or the S-band [54, 55]. A diffraction-limited resolution of 12.5 GHz over the whole C-band has been achieved already, and L- and S-band performance is comparable. Thus VPH gratings can be used in DWDM systems for combining/demultiplexing channels with separations as low as 25 GHz.

Other relevant characteristics of VPH gratings are 0.3 dB PDL, 1 dB uniformity over the complete wavelength range covered, and the total insertion loss may amount to a few dB but can be reduced to as low as 1 dB if required. Angular resolution at around 1550 nm is typically in the range from 0.1 to 0.3°/nm. VPH gratings exhibit a temperature dependence which is essentially that of the substrate. Zero expansion material, which is well suited for reflection gratings, is insufficient for transmission gratings with respect to optical clarity and homogeneity. Better (and common) choices are fused silica with a coefficient of thermal expansion  $\text{CTE}_{\text{SiO}_2} = 0.5 \times 10^{-6}/\text{K}$  or BK7 ( $\text{CTE}_{\text{BK7}} = 7.5 \times 10^{-6}/\text{K}$ ) where the latter is obviously less favourable, however, significantly less expensive.

Volume-phase holographic gratings can also be used for optical channel monitoring, and devices are commercially available covering the complete C- or L-bands and enabling channel monitoring with 50 GHz channel separation. For such applications the grating as the spectral dispersive element is typically combined with an extremely sensitive detector array (e.g. GaInAs, [54]).

#### 9.4.4 InP- and Si-based Planar Gratings

Planar (echelle) diffraction gratings have been fabricated in the InP-material system, for example as part of multi-wavelength lasers [56] or as a demultiplexer in integrated channel monitors [57–59], and they have been developed in silica-on-silicon (SoS) [60] and in SOI in the context of silicon photonics [61–64]. As will be out-

lined in more detail in Sect. 9.12, remarkably good results have been achieved more recently in the latter case, after progress in the development of planar, integratable echelle gratings had been moderate for many years before.

## 9.5 Arrayed Waveguide Gratings

Arrayed waveguide gratings are planar (lightwave) structures based upon an array of waveguides that exhibit both imaging and dispersive properties. The field of an input WG is imaged onto an array of output WGs in such a way that different input wavelengths are imaged onto different output WGs. AWGs were first reported by Smit [65], followed by Takahashi [66] and Dragone [67]. Besides “AWG” other names such as phased array (PHASAR) and waveguide grating router have also been proposed but AWG has become the most commonly used designation.

AWGs are fabricated in various material systems: SoS, InP, SOI, and polymer. SoS-based AWGs are the most relevant ones, they have been commercially available since 1994 and can be considered to represent by far the best technology for MUX/DEMUX applications in high-channel-count DWDM systems because they offer lowest cost per channel, highest uniformity, and lowest loss ( $< 0.05$  dB/cm propagation loss and about 0.1 dB fibre-chip coupling loss for appropriately chosen parameters, see below).

### 9.5.1 Basics of AWGs

#### Operation Principle

A schematic of an AWG demultiplexer is shown in Fig. 9.11, and its operation can be understood as follows [68, 69]: After entering the AWG by the input WG, light propagates across the initial free propagation region (FPR) without lateral guidance so that the incoming intensity gets evenly distributed at the input aperture of the waveguide array before it propagates along the individual WGs towards the output aperture. The waveguide array is designed in such a way that the optical path difference between adjacent WGs is equal to an integer multiple of the AWG’s (vacuum) centre wavelength ( $\lambda_c$ ), and this is equivalent to

$$\Delta L = m \frac{\lambda_c}{n_{\text{eff}}}. \quad (9.22)$$

Here  $\Delta L$  is the length difference between adjacent waveguides, the integer  $m$  is called the order of the array,  $n_{\text{eff}}$  is the effective refractive (phase) index of the guided mode, and  $\lambda_c/n_{\text{eff}}$  represents the wavelength inside the array WGs. For the operation wavelength  $\lambda_c$ , the fields at the exit of the individual WGs have identical



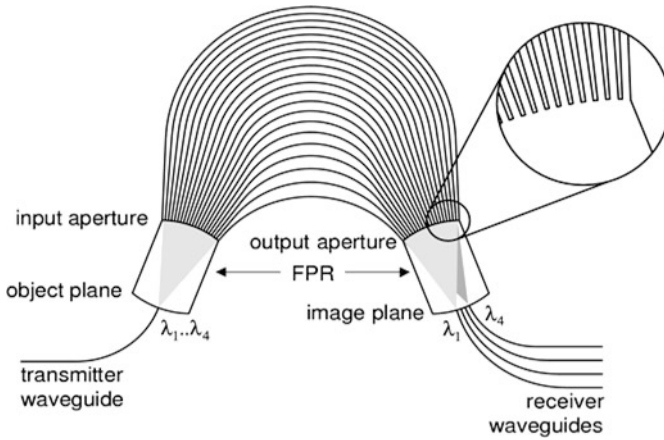


**Fig. 9.11** AWG (schematic, after [69]). FPR: free propagation region

phase (mod  $2\pi$ ) and as a consequence the field distribution at the output aperture is a reproduction of that at the input aperture. Thus, the divergent beam at the input aperture is transformed into a convergent beam at the output aperture, and the input field at the entrance of the input FPR gives rise to an image at the exit of the output FPR, i.e. the array behaves like a lens. If the operation wavelength  $\lambda$  is varied, the length increment  $\Delta L$  of the array gives rise to a phase difference  $\Delta\phi$  according to

$$\Delta\phi = \Delta\beta\Delta L, \tag{9.23}$$

where

$$\beta = 2\pi\nu n_{\text{eff}}/c \tag{9.24}$$

is the propagation constant in the waveguides,  $\nu = c/\lambda$  the frequency of the propagating waves,  $\lambda$  their (vacuum) wavelength, and  $c$  the vacuum speed of light. The wavelength-dependent phase difference  $\Delta\phi$  causes a wavelength-dependent tilt of the outgoing wave front, and this leads to a wavelength-dependent shift of the focal point along the image plane.

The horizontal shift  $ds$  of the image point per unit frequency interval  $d\nu$  is called the AWG's spatial dispersion  $D_{\text{sp}}$  and it is given by (as outlined in more detail in [70])

$$D_{\text{sp}} = \frac{ds}{d\nu} = \frac{1}{\nu_c} \frac{n_g}{n_{\text{FPR}}} \frac{\Delta L}{\Delta\alpha}. \tag{9.25}$$

Here  $\nu_c$  is the frequency corresponding to the centre (vacuum) wavelength,  $n_{\text{FPR}}$  is the slab mode index in the free propagation region,  $\Delta\alpha$  is the divergence angle between the array waveguides in the fan-in and the fan-out sections, and  $n_g$  is the

group refractive index of the waveguide mode given by

$$n_g = n_{\text{eff}} + v \frac{dn_{\text{eff}}}{dv}. \quad (9.26)$$

If the change of the input wavelength introduces a phase difference of  $\Delta\phi = 2\pi$  between adjacent waveguides, the transfer characteristics of the AWG will be the same as before, i.e. the response is periodic or cyclic. The period is called the free spectral range (FSR), and  $\Delta\beta\Delta L = 2\pi$  combined with (9.22) leads to

$$\text{FSR} = \frac{v_c}{m} \left( \frac{n_{\text{eff}}}{n_g} \right). \quad (9.27)$$

Crosstalk problems with adjacent orders are avoided if the FSR is chosen larger than the whole frequency range covered by all channels. As an example, for a demultiplexer with 8 channels and 200 GHz channel spacing, the FSR should amount to at least 1600 GHz. For  $\lambda_c \approx 1550$  nm, (9.27) suggests that the order of the array should be about 120 (with  $n_{\text{eff}}/n_g \approx 0.975$  for the SoS- and  $n_{\text{eff}}/n_g \approx 0.9$  for the InP-material system, respectively).

The passband shape of standard AWGs is Gaussian which is not optimum for optical networks where signals typically pass a certain number of wavelength filters and the effective width of cascaded Gaussian filters becomes fairly narrow. Consequently AWGs are also designed with so-called “flat top” characteristics, which can be accomplished in different ways, examples are by using a multi-mode interference (MMI) coupler before the input slab region [71, 72] or alternatively a parabolic horn [73]. However, the enhanced channel width goes along with an extra loss of about 2 to 2.5 dB in the centre of the transmission band.

Birefringence (and consequently polarization dependence) and temperature-dependent behaviour are important issues in many cases and different approaches have been developed to cope with these phenomena as will be outlined in Sect. 9.5.2.

## Applications

AWGs serve a number of different purposes in fibre optic networks. The most straightforward functionality is combining different wavelengths in multi-wavelength sources or combining and/or separating different wavelength channels in optical add-drop multiplexers (OADM). OADMs have been designed in many different ways, and various architectures are explained in more detail in [69, 74]. AWGs are a particularly favourable choice for OADMs designed for handling larger numbers of channels ( $> 8$ ).

Furthermore, passive optical networks (PONs) can be upgraded using AWGs as they support the overlay of additional WDM channels [75, 76] and AWGs can be used for routing applications, for example in optical cross-connects [69].

### 9.5.2 AWGs in Silica-on-Silicon

As already mentioned, SoS-based AWGs are the variety most widely used in today's fibre-optic communication networks. These AWGs are typically fabricated on crystalline flat silicon wafers having 6" or 8" diameter, and this size offers the possibility to fabricate multiple devices on a single wafer and favours cost-efficient processing. Fabrication of AWGs is essentially a sequence of glass and silica layer deposition combined with horizontal structuring, i.e. standard pattern transfer based on optical lithography and etching. For depositing the glass and silica layers two different processes are primarily used: flame hydrolysis and chemical vapour deposition (CVD) including low-pressure CVD (LPCVD) and plasma-enhanced CVD (PECVD) [69].

One key design (and fabrication) parameter of AWGs is the refractive index contrast  $\Delta n$  between the WG core and the cladding. The higher  $\Delta n$  the more compact an AWG can be made as bend radii can be made smaller without unacceptably high (bending) losses. However, larger  $\Delta n$  implies stronger confinement of the guided waves with two unfavourable consequences: (i) scattering losses due to WG sidewall roughness increase, and (ii) the size difference of modes guided in the AWG and in standard single-mode fibre (SMF) become more pronounced which leads to narrower fibre-chip coupling tolerances and larger fibre-chip coupling losses (unless tapers are used for improving the coupling).

Commercially available AWGs are essentially designed and fabricated with the following different choices of refractive index contrast:

- $\Delta n = 0.30\%$  ( $8 \times 8 \mu\text{m}^2$  WG core size and 25 mm minimum bend radius) and
- $\Delta n = 0.45\%$  ( $7 \times 7 \mu\text{m}^2$  WG core size and 15 mm minimum bend radius).

Corresponding WGs enable very good coupling to standard SMF and have shown losses as low as 0.017 dB/cm [77], but these favourable characteristics go along with rather large total device size.

- $\Delta n = 0.75\%$  ( $6 \times 6 \mu\text{m}^2$  WG core dimension and 5 mm minimum bend radius) represents a good compromise between fairly compact overall device size, relatively low propagation loss (0.035 dB/cm [78]) and still relatively good fibre-chip coupling characteristics. It can therefore be considered the "standard" choice. Typical AWG chip sizes are  $30 \times 50 \text{ mm}^2$  for 40 channel-,  $25 \times 40 \text{ mm}^2$  for 16 channel-, and  $20 \times 20 \text{ mm}^2$  for  $4 \times 4$  channel devices (*private communication, Enablence Technologies Inc.* [79]).
- AWGs with  $\Delta n = 1.5$  to  $2\%$  ( $4.5 \times 4.5$ – $3 \times 3 \mu\text{m}^2$  WG core size and 2 mm minimum bend radius) can be made really compact but efficient fibre-chip coupling requires tapers and propagation losses are about 0.1 dB/cm.

### Polarization and Temperature Dependence

Waveguides are normally designed with square cross section, but different thermal expansion coefficients of glass and silicon induce compressive stress in the AWG

structures so that the propagation constants for TE- and TM-polarized waves vary ( $\beta_{\text{TE}} \neq \beta_{\text{TM}}$ ). As a consequence a wavelength separation  $\Delta\lambda$  between the peak transmission for TE- and TM-polarized waves is observed which is given by

$$\Delta\lambda = \frac{1}{m} \Delta L (n_{\text{TE}} - n_{\text{TM}}), \quad (9.28)$$

where  $n_{\text{TE}}$  and  $n_{\text{TM}}$  are the effective refractive indices for TE- and TM polarization, respectively. A typical value for the polarization-dependent peak transmission difference of SoS AWGs is about 30 GHz which is too high for standard channel separations (100 GHz or even smaller) and consequently various concepts have been reported to compensate unwanted birefringence so that  $< 2.5$  GHz variation can be assured [69].

The centre wavelength of any output WG of standard SoS AWGs exhibits a temperature-dependent shift  $d\lambda/dT \approx -1.5$  GHz/K, and this variation is primarily due to the temperature dependence of the refractive index of the silica glass ( $dn/dT = 1.1 \times 10^{-5}$ /K). In order to avoid temperature-dependent adverse effects on system performance several options exist:

AWGs may be operated with a temperature control using either a Peltier cooler or a heater. This is a proven concept, however, specific equipment and electrical power at the site of the AWG are needed.

So-called ‘athermal’ AWGs need no extra equipment nor electrical power, and as a consequence athermal AWGs are attractive for long-haul, METRO, and for WDM-PON applications as well. In order to be suited for outdoor applications, athermal AWGs are required to work in a temperature range from  $-30^\circ\text{C}$  to  $+70^\circ\text{C}$ . Athermal behaviour has been obtained by various means, for example by fabricating part of the AWG using a material with refractive index variation  $dn/dT < 0$  [80], or by mechanically compensating the temperature drift of the grating [81, 82].

## Commercially Available AWGs

SoS-based AWGs are commercially available from various suppliers worldwide. They are offered for operation in all wavelength bands (O-, E-, S-, C-, and L-band), but there is a clear focus on the  $1.55 \mu\text{m}$  range (C-band). The channel count ranges from 4 to 80, and up to 128 channels are available on customer demand. Most commercial products are offered for 50, 100 and 200 GHz channel separation although other variants (down to 12.5 GHz) are also on sale, and the passband shape is most frequently Gaussian or flat top. An example of the wavelength characteristics of a commercial 40 channel AWG is shown in Fig. 9.12.

Commercial AWGs normally require active temperature control, but athermal AWGs are also commercially available.

The cyclic behaviour of AWGs enables the fabrication of so-called ‘colourless’ AWGs. The design of these AWGs is made in such a way that the FSR exactly matches the channel separation times the number of output channels. If a sequence

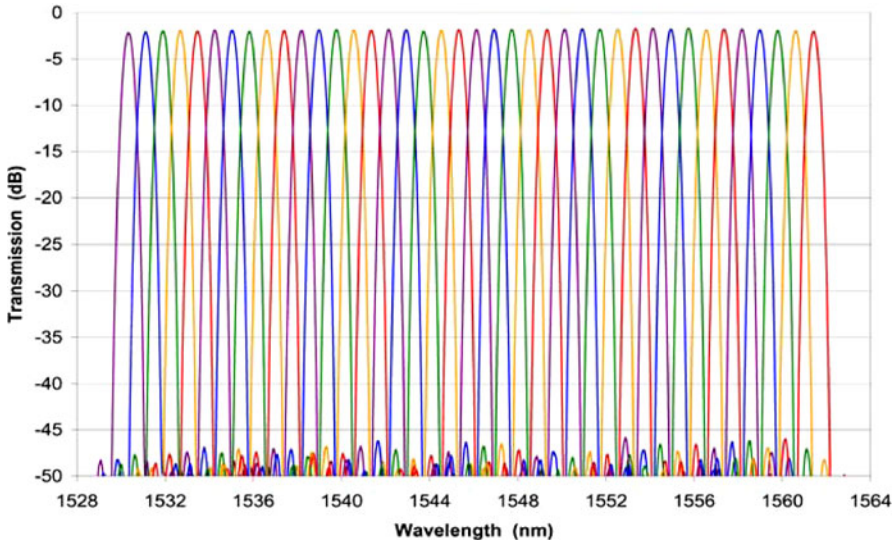


**Fig. 9.12** Wavelength characteristics of a 40 channel AWG with Gaussian passband [79]

of evenly spaced channels enters a colourless AWG with  $m$  output ports, the first  $m$  channels leave the AWG via output channels  $1, \dots, m$ , and in general the  $k$ th channel leaves the AWG via output port  $k \pmod{m}$ . In practice, colourless AWGs are mostly designed having eight output- and one or two input ports.

The high interest in colourless AWGs comes from cost-saving arguments: The complete C-band can accommodate about 96 channels with 50 GHz spacing, however, such a large number of channels is normally not installed at once. Instead, carriers start with a single band comprising eight channels and add more bands as traffic demand grows. If an appropriately designed colourless AWG is available, the same type of AWG can be taken for multiplexing/demultiplexing the individual channels of any of these bands, and thus inventory cost is significantly reduced.

The transmission of a colourless AWG with eight output ports and 50 GHz channel separation is illustrated in Fig. 9.13, where the cyclic characteristics with an 8-channel periodicity can be clearly seen.

Additional typical parameters of commercial AWGs not mentioned so far include 0.2 dB PDL,  $< 10$  ps/nm chromatic dispersion, and 0.5 ps differential group delay. 3 dB can be considered a typical total insertion loss value, and it is also worthwhile to note that the insertion loss varies across the output ports by an amount of 2 to 3 dB, referred to as ‘non-uniformity’.

Various types of AWGs have been reported in the literature with performance characteristics significantly exceeding those of commercial devices. Examples are AWGs with channel count as high as 400 in a single stage [84] or even 4200 channels in two-stage configurations [85]. AWGs have further been developed for coarse WDM (CWDM) applications with 10 or 20 nm channel separation [86], and con-

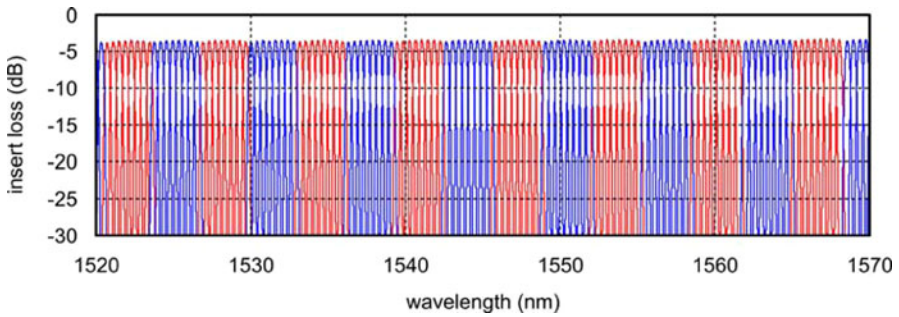


**Fig. 9.13** Wavelength characteristics of colourless AWG with 50 GHz channel separation and 400 GHz free spectra range [83]

versely an AWG with 1 GHz channel spacing operating in  $m = 11,818$  grating order has also been reported [87].

### 9.5.3 AWGs in InP

AWGs fabricated in the InP material system exhibit a number of pronounced differences compared to SoS-based ones. Most important is a significantly higher refractive index contrast of InP-based waveguides which leads to very compact structures (InP-based AWGs are about two orders of magnitude smaller than SoS-AWG). Conversely, the small dimensions of InP-based WGs make the fibre-chip coupling much more demanding. Efficient coupling with moderate alignment tolerances requires spot size converters integrated onto the InP chip, which renders these chips rather complex. The first AWG fabricated in the GaInAsP material system was reported as early as 1992 [88], but performance of InP-based AWGs is (still) inferior with respect to crosstalk, polarization dependence is also a serious issue, and InP-based AWGs have not (yet) reached commercial status as stand-alone components although they are continuously being further improved [89].

The recent interest in InP-based AWGs is to a significant extent due to the fact that they can be monolithically integrated with active InP-based components such as lasers, SOAs, detectors, or modulators. The fabrication of InP-based AWGs is comparatively simple (standard sequence of epitaxial layer deposition and pattern transfer using optical or electron beam lithography and dry etching), however, monolithic integration of AWGs with other subcomponents becomes more demanding the greater the number of different types of subcomponents with specific vertical layer structure are to be combined on a single InP chip to form photonic integrated circuits (PICs). Since 1992 a large number of PICs comprising AWGs has been developed [90] with most recent examples being an optical router [91] and a monolithic 40-channel transmitter [92, 93], the latter representing the most complex InP-based PIC reported so far.

### 9.5.4 AWGs in Other Material Systems

AWGs have also been developed in other material systems such as polymer [94–96] and in particular in SOI. The former is a particularly low-cost solution while AWGs in SOI are an important building block for the realization of wavelength-agile silicon photonics chips which is outlined in more detail in Sect. 9.12 and in Chap. 14.

## 9.6 Fibre Bragg Gratings

In 1978 Hill, Kawasaki and coworkers reported the discovery of photosensitivity of Germanium-doped optical fibre [97, 98], later it was found that intense UV irradiation of photosensitive fibres created permanent index changes [99], and this spurred the development of fibre Bragg gratings which have found widespread applications since then, in particular in sensing, fibre lasers, and in fibre optic communication as well.

### 9.6.1 Generic Properties

An FBG is essentially a piece of single-mode optical fibre with a periodic variation of the core refractive index. In the most simple case the planes of equal refractive index are parallel to the longitudinal axis of the optical fibre and the index variations have constant period as illustrated in Fig. 9.14.

Light guided by the core and propagating along the FBG will be scattered by each of the grating planes, and in general light scattered from different planes will add up out of phase and will eventually cancel out. Conversely, if

$$\lambda_B = 2n_{\text{eff}}\Lambda \quad (9.29)$$

holds, (where  $\lambda_B$  is the “Bragg wavelength”,  $n_{\text{eff}}$  is the (mean) effective refractive index experienced by an optical wave propagating along the fibre, and  $\Lambda$  is the period of the index modulation), the small amounts of light scattered from each plane add up constructively and give rise to a back scattered wave. The Bragg condition (9.29) is a straightforward consequence of energy and momentum conservation [100] and leads to a characteristic pit in the transmission spectrum as well as a peak in the reflection spectrum around  $\lambda_B$ .

Typical reflection spectra of fibre Bragg gratings are illustrated in Fig. 9.15. The different spectra correspond to different values of refractive index contrast (ranging from  $10^{-4}$  to  $10^{-3}$ ), the grating is 5.4 mm long, and  $\lambda_B = 1500$  nm [101].

One characteristic and important parameter of any FBG is the width of the reflection band, and neglecting the fact that the detailed characteristics of FBGs depend on various design parameters in a complex manner [100], a good approximation for

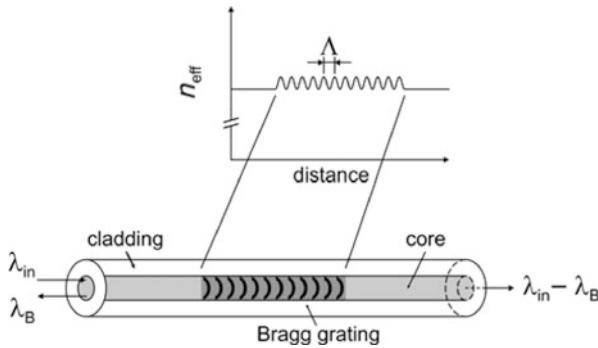


**Fig. 9.14** Fibre Bragg grating (schematic)

the full-width at half-maximum of the reflection band,  $\Delta\lambda_{\text{FWHM}}$ , is given by [102]

$$\Delta\lambda_{\text{FWHM}} = \lambda_B S \sqrt{\left(\frac{\Delta n}{2n_{\text{eff}}}\right)^2 + \left(\frac{1}{N}\right)^2} \quad (9.30)$$

where  $\Delta n$  is the variation of the effective refractive index  $n_{\text{eff}}$ ,  $N$  is the number of grating planes and  $S$  is a parameter varying between 0.5 for weak and 1.0 for strong gratings.

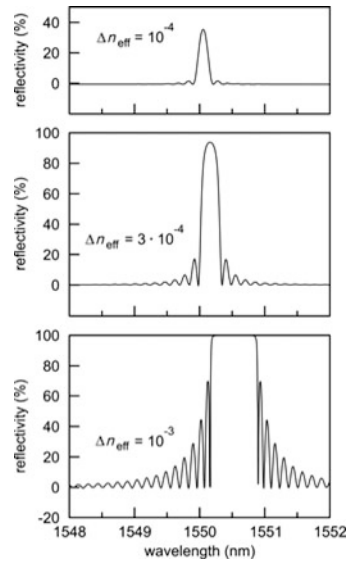
A number of key characteristics of FBGs are illustrated by Fig. 9.15: (i) the reflectance increases with higher index contrast, and essentially 100% reflectance can be achieved with appropriate contrast and sufficiently long gratings, (ii) the reflectance curve can be made flat-top as well by these means. (iii) Uniform gratings exhibit pronounced side lobes next to the main reflectance maximum. These side lobes are unwanted for many applications, in particular for channel selection in telecom applications, however, the side lobes can be removed by appropriate grating design as outlined in Sect. 9.6.3. (iv) The shift of the reflectance to longer wavelengths as  $\Delta n_{\text{eff}}$  increases is essentially a consequence of the correspondingly larger average effective index in the grating region.

Furthermore, (9.30) suggests that FBG filters become narrower the longer the gratings are (as long as the index variation is sufficiently weak). This is in principle equivalent to the fact that the resolving power of a diffraction grating rises with increasing number of illuminated grooves. For higher index variation this is no longer true because a wave entering a high-index contrast grating region is already completely reflected before reaching the end of the grating so that only a fraction of the grating planes determines the spectral shape of the reflected wave.

The fundamental characteristics of FBGs are a consequence of coupling between modes propagating in the forward direction with back-reflected ones. However, the forward-propagating mode can also couple to radiation modes, and this effect gives rise to dips in the transmission spectrum on the short-wavelength side of the main transmission minimum without corresponding spectral features in the reflected spectrum [100], but these dips are very much reduced in appropriately designed state-of-the-art FBGs.



**Fig. 9.15** (Calculated) reflectance of a 5.4 mm long FBG with different refractive index contrast [101]



Another phenomenon is coupling to cladding modes, which is particularly pronounced in long-period gratings and will be discussed in Sect. 9.6.6.

### 9.6.2 Types of Gratings

Fibre Bragg gratings are fabricated from fibres with different photosensitivity conditioning, and different inscription procedures are also being used. As a result different types of FBGs are obtained which are normally classified as type I, IA, II, and IIA.

Type I gratings are generated in normal photosensitive fibres with moderate illumination intensities. The transmission and reflection spectra are complementary, i.e. type I FBGs do not exhibit unwanted loss. They are thermally stable up to about 200 °C and represent the most common variant of FBGs [103].

Type IA gratings are typically formed after relatively long UV exposure in hydrogenated germanosilicate fibre. The index change, attributed to the creation of colour centres, is particularly strong and gives rise to a pronounced red shift of the Bragg wavelength. Type IA are the least stable FBGs [104, 105].

The formation of type IIA gratings builds upon the type I inscription process and eventually results in gratings due to material compaction in the grating region [106] so that these gratings are stable up to about 500 °C.

Finally, the refractive index changes giving rise to type II FBGs are introduced by single excimer laser light pulses of  $> 0.5 \text{ J/cm}^2$  fluence [107]. The index changes are rather large (up to about  $10^{-2}$ ) and are attributed to localized fusion in the fibre core region. Wavelengths longer than  $\lambda_B$  transmitted by type II gratings are essen-

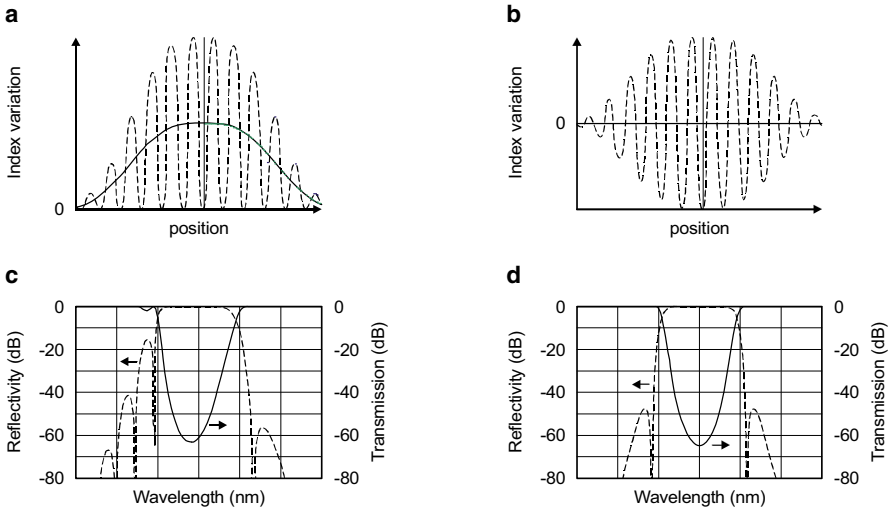


**Fig. 9.16** Apodization of FBGs (schematic), with varying (a, c) and constant (b, d) average effective refractive index and corresponding reflectance spectra (after [109]). a, b: dashed lines: local index variation, full lines: average refractive index

tially unaffected while for  $\lambda < \lambda_B$  strong coupling to cladding modes occurs associated with pronounced attenuation. The grating structure is stable beyond 800 °C which makes these gratings a particularly good choice for high ambient temperature applications.

### 9.6.3 Apodization

The strong side lobes observed in the reflectance spectra of FBGs with uniform gratings (Fig. 9.15) can be efficiently reduced by ‘apodization’. Apodized gratings are characterized by a short-period index variation (with period length  $\Lambda$ , cf. (9.29)) plus a long-range variation which may have different shape (e.g. Gaussian or ‘raised-cosine’ [108]), and the local variation of the average effective refractive index may be zero or non-zero. Two schematic examples of apodized FBGs are illustrated in Fig. 9.16, one with raised index profile and one without change of the average refractive index. The efficient side lobe suppression is obvious in both cases.

### 9.6.4 Temperature and Strain Dependence

FBGs exhibit a temperature-dependent shift of the reflection band of about 13 pm/K which is essentially due to the coefficient of thermal expansion of the glass form-

ing the fibre core [100]. For telecom applications such a pronounced temperature-induced variation of the FBG channel wavelength(s) is unacceptable, and one straightforward means to suppress this shift is by fixing the FBG onto a sub-mount which exhibits a negative CTE so that the resulting temperature variation is reduced. Typical residual temperature dependence is  $< 0.5$  to  $1$  pm/K for  $-5^\circ\text{C} \leq T \leq 70^\circ\text{C}$  [110–114].

Conversely, the temperature-induced shift of the reflected wavelength is widely exploited for temperature sensing using FBGs.

In a similar way, the reflectance peak of FBGs exhibits a pronounced change due to mechanical strain which is taken advantage of in FBG-based stress sensors.

### 9.6.5 Chirped Gratings

A chirped grating is an FBG with a refractive index continuously varying across the grating region for example as [100]

$$n(z) = n_{\text{eff}} + \Delta n_{\text{mod}} f_{\text{apod}}(z) \cos\left(\frac{2\pi}{\Lambda} z - \frac{\pi}{2n_{\text{eff}}\Lambda^2} \Lambda_{\text{ch}} z^2\right), \quad (9.31)$$

where  $n(z)$  is the index variation along the fibre axis,  $\Delta n_{\text{mod}}$  is the index modulation amplitude,  $f_{\text{apod}}(z)$  is the apodization function, and  $\Lambda_{\text{ch}}$  is the (dimensionless) so-called chirp parameter (of the Bragg grating). Because of the variation of the pitch and/or the effective refractive index (characterized by  $\Lambda_{\text{ch}}$ ) different wavelengths are reflected from different parts of the grating, and the choice of the chirp parameter determines whether a given grating compensates positive or negative (residual) dispersion. Dispersion-compensating FBGs (DCG) are normally designed to simultaneously compensate the dispersion and the dispersion slope [115–117]. The compensation of higher order dispersion derivatives is not an issue for telecom applications while in chirped fibres designed for pulse compression higher order dispersion derivatives are being compensated as well.

### 9.6.6 Long-period Fibre Bragg Gratings

Period lengths  $\Lambda$  of ‘standard’ FBGs (cf. (9.29)) are in the order of several 100 nm while the periodicity of long-period FBGs (LPG) is in the several 10  $\mu\text{m}$  to several 100  $\mu\text{m}$  range. Such long-range periodic index variations do not induce coupling of counter-propagating modes as ‘normal’ FBGs do, but they give rise to coupling between co-propagating modes [118–121]. In particular, the core-guided modes couple to forward-propagating cladding modes and the latter experience pronounced attenuation due to absorption and scattering which can be observed as an attenuation of the transmitted intensity.

Depending on the details of the grating, coupling to different modes is supported. This is a strongly wavelength-dependent process and correspondingly offers high design flexibility so that LPGs can be fabricated with essentially any spectral shape in transmission without creating any back-reflected light. Telecom applications of LPGs include their use as non-reflecting band rejection filters and as gain flattening filters for EDFAs and Raman amplifiers, in addition, they offer attractive characteristics for sensing applications [122–124].

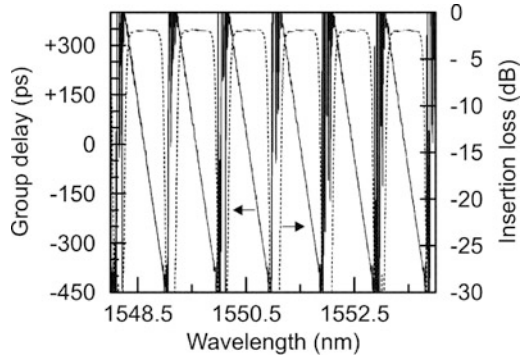
### ***9.6.7 Commercially Available Devices***

The most relevant commercial application of FBGs is using chirped gratings for dispersion compensation. An alternative solution for dispersion compensation has been (and still is) the use of dispersion-compensating fibre (DCF). However, large strands of DCF (many km) are needed which makes this solution fairly bulky. In addition, because of the DCF's small core dimensions non-linear interactions (four-wave mixing, self-phase modulation, . . .) introduce signal distortions, and DCF also adds a significant amount of signal attenuation. Conversely, FBG-based dispersion compensation does not suffer from any of these shortcomings and thus it is the preferred choice.

DCGs are offered (i) in channelized versions, where the dispersion compensation is tailored to the ITU grid (50 GHz or 100 GHz are standard, but other separations such as e.g. 25 GHz or 33 GHz are available on customer demand), and these DCGs may cover the complete C-band (from 32 to about 50 channels). A close-up taken from a channelized dispersion-compensating Bragg grating which covers the complete C-band (51 channels with 100 GHz separation) is shown in Fig. 9.17. (ii) DCGs are available for continuous dispersion compensation over a wider wavelength range, for example the full C-band, or (iii) they come as single-channel tunable dispersion compensators. In the latter case the dispersion to be compensated may be as high as  $\pm 3000$  ps/nm, alternatively dispersion as low as 0.1 ps/nm can be compensated with high precision.

Fibre Bragg grating-based band filters are commercially available ranging from broadband (several 10 nm) down to very narrowband filters (about 20 pm), and they are also offered for channel selection (primarily for 50 GHz and 100 GHz but for 25 GHz channel separation as well). The separation of individual channels is by no means straightforward when FBGs are used: OADMs for handling a single channel can either be built using two optical circulators (which is a fairly expensive solution) or for example using a less-expensive twin-core fibre based Mach–Zehnder interferometer design [109]. Therefore, as far as channel filtering is concerned, FBGs seem to be inferior from a cost point of view to thin-film filters (for moderate channel counts or for stepwise upgrade of fibre optic systems) or to AWGs (for higher channel count).

**Fig. 9.17** Close-up of channelized dispersion-compensating fibre Bragg grating (100 GHz channel spacing, selected part of 51-channel device, [113]). *Full curves*: group delay (dispersion), *dashed curves*: insertion loss



Finally, FBGs are also available for locking the wavelengths of EDFA pump lasers or the emission wavelength of DFB lasers where they compete with Fabry–Pérot-based solutions (see following paragraph).

## 9.7 Fabry–Pérot Interferometers

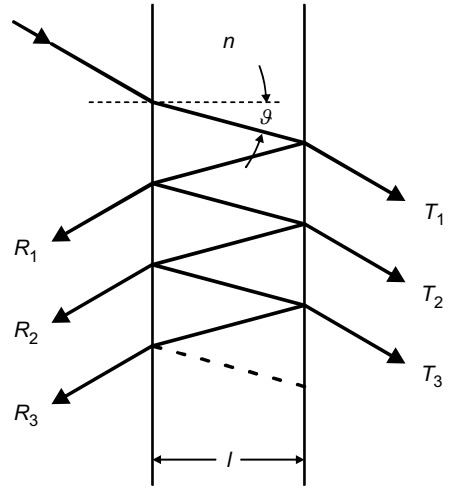
A Fabry–Pérot interferometer (FPI) or etalon consists of a transparent cavity bounded by two reflecting surfaces or by two parallel highly reflecting mirrors. To be more precise, the former is an etalon and the latter represents an interferometer, but this distinction is not always made in the literature. The transmission spectrum of an FPI as a function of wavelength or frequency is characterized by peaks of large transmission corresponding to resonances of the FPI/etalon. The FPI is named after Charles Fabry and Alfred Pérot [125].

FPI filters have found widespread applications. They enable spectroscopic applications with specific high demands on spectral resolution, they are used in astronomy for generating pictures at selected wavelengths, and they are found in fibre-optic communication systems as well, for example for precise locking of laser emission wavelengths in DWDM and ultra DWDM transmitters, wavelength monitoring, laser stabilization for tunable laser modules, and for DWDM channel frequency and optical power monitoring.

### 9.7.1 Multiple-reflection Cavities

The wavelength- (or frequency-) dependent transmission of an FPI is due to the interference of multiple reflections of the radiation between the two reflecting surfaces as illustrated schematically in Fig. 9.18.

**Fig. 9.18** Fabry–Pérot etalon (schematic) illustrating multiple transmitted ( $T_i$ ) and reflected ( $R_i$ ) beams



If the transmitted beams are in phase, constructive interference occurs which gives rise to transmission maxima, while low transmission is observed if the transmitted beams are out of phase.

The phase difference between subsequent reflections,  $\delta$ , is given by

$$\delta = \left( \frac{2\pi}{\lambda} \right) 2nl \cos \vartheta, \quad (9.32)$$

where  $\lambda$  is the light wavelength in vacuum,  $\vartheta$  is the angle between the light propagation direction and the normal to the reflecting planes within the cavity,  $l$  is the thickness of the cavity, and  $n$  is the refractive index of the material within the cavity.

The various transmitted beams constitute a geometrical series and can therefore be summed up easily. This is outlined in detail in numerous (text-)books (e.g. [49], Chap. 7.6 and [126]) and we will present here the final results only. If  $r$  and  $t$  represent, respectively, the electric field reflection and transmission factors of the mirror plates, and  $a$  represents the field attenuation factor of the light travelling through the medium between the mirrors, and with  $R = |r|^2$ ,  $T = |t|^2$ ,  $A = |a|^2$  being the corresponding intensities, the transmitted intensity  $T_{\text{FP}}$  of the FPI is given by

$$T_{\text{FP}} = \frac{T_0}{1 + \left[ \frac{2}{\pi} F_R \sin\left(\frac{\delta}{2}\right) \right]^2}, \quad (9.33)$$

where  $F_R$  is defined as

$$F_R = \frac{\pi \sqrt{AR}}{1 - AR} \quad (9.34)$$

and  $T_0$  is given by

$$T_0 = \frac{AT^2}{(1-AR)^2} = \frac{A(1-R)^2}{(1-AR)^2}. \quad (9.35)$$

Losses are normally negligible in standard devices. For that reason we will assume zero loss (i.e.  $A = 1$ ) in the following discussion in order to keep the formulae simpler.

### 9.7.2 Wavelength/Frequency Characteristics

According to (9.33) an FPI exhibits periodic spectral characteristics, and the separation between adjacent transmission peaks represents the free spectral range of the FPI. With  $\lambda_0$  being the central wavelength of the FPI and  $c$  the vacuum speed of light, the FSR is given in terms of wavelength or frequency, respectively, by

$$\text{FSR}_\lambda = \frac{\lambda_0^2}{2nl \cos \vartheta + \lambda_0} \approx \frac{\lambda_0^2}{2nl \cos \vartheta} \quad \text{and} \quad \text{FSR}_\nu \approx \frac{c}{2nd \cos \vartheta}. \quad (9.36)$$

The ratio of the FSR to the full-width half-maximum of any of the transmission bands is called the finesse (FIN). For the wavelength domain we get

$$\text{FIN} = \frac{\text{FSR}_\lambda}{\Delta\lambda_{\text{FWHM}}} = \frac{\pi}{2 \arcsin[(1-R)/2\sqrt{R}]} \quad (9.37)$$

which can be approximated (for  $R > 0.5$ ) by

$$\text{FIN} \approx \frac{\pi\sqrt{R}}{(1-R)}. \quad (9.38)$$

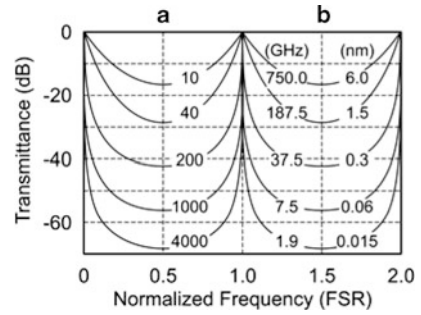
It is worthwhile to note that the effective finesse of an FPI filter may be lower than given by (9.38), for example if the mirrors are not perfectly flat or not perfectly aligned, and the finesse is also lower than (9.38) in the presence of loss.

Another important performance parameter is the contrast factor  $C$  representing the ratio of maximum to minimum intensity transmission and given by

$$C = \frac{T_{\text{FP,max}}}{T_{\text{FP,min}}} = \left( \frac{1+AR}{1-AR} \right)^2. \quad (9.39)$$

The contrast factor  $C$  determines the maximum achievable crosstalk attenuation if an FPI is used for selecting a single channel wavelength out of different channels.

**Fig. 9.19** Spectral transmission characteristics of FPI filters with fixed FSR (60 nm) for different finesse values ranging from 10 to 4000 (a), and corresponding 3 dB bandwidth (b), see [127]



Typical transmission characteristics of FPI filters for different finesse values (or corresponding 3 dB bandwidth for fixed FSR) are illustrated in Fig. 9.19.

### 9.7.3 Implementations

Fabry–Pérot interferometers for telecommunication applications are normally made tunable over a reasonable spectral range by providing a means to vary the cavity length. An example of a piezoelectrically driven, tunable, lenseless all-fibre design is illustrated in Fig. 9.20 [127].

With passive temperature compensation the device operation temperature is in the range of  $-20$  to  $+80$  °C.

The mirrors of FPI filters can either be metallic or alternatively dielectric multi-layer structures. In the latter case these constitute a special case of dielectric or thin-film multi-layer filters/structures covered in more detail in Sect. 9.8.

A specific type of FP interferometer is the Gires–Tournois interferometer (GTI) [128]. As for the normal FPI, the cavity of the GTI consists of two parallel reflective plates, but one of them is only partly reflective while the other is fully reflective so that the GTI can only work in the reflection mode. Apart from that a GTI behaves in the same way as an FPI does. An example of a telecom application is the insertion of a GTI into a Michelson interferometer in such a way that the combination serves as an optical channel interleaver (see Sect. 9.10).

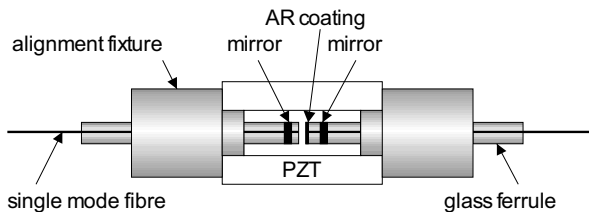


**Fig. 9.20** FPI filter (schematic, cf. [127])



### 9.7.4 Typical Performance Characteristics

Typical performance characteristics of FPI filters can be summarized as follows:

FPI filters are commercially available covering the complete range of the O-, E-, S-, C-, and L-bands, i.e. the wavelength range from 1280 to 1620 nm which corresponds to an FSR of 340 nm or 51 THz. Conversely, the FSR may be as small as 10 GHz (corresponding to 80 pm), and the full range in between is either covered by standard devices or ones built on customer demand. The finesse may be up to several 1000 or even beyond 10,000 on special request. The total insertion loss is typically between 1.5 and 3 dB, and the PDL is  $< 0.2$  dB.

### 9.7.5 Applications

#### Optical Channel Selection and Performance Monitoring

Tunable FP filters enable fast and precise channel selection in dynamic multi-wavelength systems. This can either simply be the selection of a single narrowband channel or the dropping of selected channels in WDM networks. For these purposes the FSR should be larger than the wavelength band over which the channels are spread, and the finesse should be large enough to assure sufficiently low crosstalk. As a rule of thumb this demand is fulfilled if the finesse is about three times the number of channels.

Continuously tuned FPI filters can be used for optical channel monitoring, and with appropriately chosen resolution up to 400 channels in the C-band can be supervised.

#### FP Etalons for Wavelength Locking

As channel spacings in DWDM systems get smaller and smaller, the requirements on wavelength stability, as far as wavelength sources are concerned, become more and more demanding. For systems with 100 GHz channel separation a wavelength drift of  $< |0.1|$  nm over the complete laser lifetime is acceptable and this can be assured by current chip technology. However, if the channel spacing is reduced to 50 GHz, the maximum acceptable drift is  $\pm 2.5$  to 3 GHz (20 to 24 pm) only, and this requires active wavelength locking which is typically implemented using an FP etalon as a reference. Any deviation of the laser emission from the resonance wavelength of the etalon causes an error signal and this is taken as an input for the wavelength control (cf. Chap. 5, Sect. 5.3.1). Normally the laser operation temperature is adjusted in order to get the proper emission wavelength. Typical frequency stability achieved with wavelength lockers is about  $\pm 2.5$  GHz and it can be improved to about  $\pm 1.25$  GHz with more sophisticated designs.

## 9.8 Thin-film Filters

Thin-film filter technology started in the 1930s with the development of dielectric multi-layer anti-reflective coatings for military purposes during World War II. Since then TFFs (also designated as dielectric multi-layer filters) have been developed for applications in many different areas (e.g. aerospace, spectroscopy, microscopy, and lasers) and TFFs also entered the field of fibre optic communication after they had reached a sufficient maturity in the 1990s. TFFs used in fibre optics include band-pass (single or multiple), short-pass, long-pass and gain-flattening filters, and these will be covered in more detail below. Properties of TFFs, which are particularly appreciated, include their proven reliability and long-term stability, and their excellent wavelength stability makes them even suitable for the stabilization of the emission wavelengths of wavelength sources (DFB lasers) [129].

TFFs also enable the fabrication of non-resonant structures such as anti-reflection coatings/filters or beam splitters, but these will not be discussed any further herein. A comprehensive and general treatment of TFFs can be found in [130, 131] for example, and more details with a particular focus on telecom applications are given in [129].

### 9.8.1 Generic Functionalities of TFFs

#### High Reflector Coatings

The generic structure of an HR coating is a sequence of alternating layers of two materials, one of which has a high and the other a low refractive index. If the thickness of an individual layer made of high- and low-index material (and referred to as quarter-wave layer) is given by

$$H = \frac{\lambda_c}{4n_H} \quad \text{and} \quad L = \frac{\lambda_c}{4n_L}, \quad (9.40)$$

respectively, with  $\lambda_c$  being the desired centre wavelength and  $n_H$  and  $n_L$  the refractive indices of the high- and low-index material, the basic HR design can be represented as [129]

$$\text{HR} \equiv \text{Substrate} \mid (HL)^p \mid \text{Ambient}, \quad (9.41)$$

where the power  $p$  indicates how often the period is repeated. HR layers exhibit a reflection band (designated as ‘stop band’) around  $\lambda_c$ , the width of which depends on the contrast between  $n_H$  and  $n_L$ . Filters become more square-shaped as  $p$  gets larger, and the maximum reflection  $R_{\max}$  of the stop band depends on both, the contrast between  $n_H$  and  $n_L$  and on the number of layer periods as well according to

$$R_{\max} \cong 1 - 4 \left( \frac{n_L}{n_H} \right)^{2p} \frac{n_S}{n_A}. \quad (9.42)$$

Here  $n_S$  and  $n_A$  are the refractive indices of the substrate and the ambient medium, respectively.

### Band-pass Filters

A thin-film band-pass filter is either simply a single thin-film FP filter or consists, in general, of several coupled thin-film FP filters. The generic structure of a TF FP filter is a central layer designated as the *spacer* plus an HR structure on either side of the spacer. The thickness  $d_{sp}$  of the spacer is given by

$$d_{sp} = 2L = m \frac{\lambda_c}{2n_L} \quad (m = 1, 2, 3, \dots) \quad (9.43)$$

and the generic structure of a band-pass filter can be represented as

$$\text{Substrate} \mid (LH)^p (2L)^m (HL)^p \mid \text{Ambient}. \quad (9.44)$$

For a first-order filter ( $m = 1$ ) the spacer thickness is one half-wave, for  $m = 2$  it is two half-waves, etc. The band-pass filter shape is determined essentially by the reflectance of the HR structures and by the order  $m$  of the spacer, and band-pass filters become more square shaped and flat top the higher  $m$  gets. Proper coupling of multiple FP filters is a critical issue and has received considerable attention by many research groups [129].

### Band-edge Filters

Band-edge filters can be fabricated according to two different approaches: The edge can either be one of the stop band edges of an appropriately designed HR structure. For example, a short-pass filter is obtained if the low-wavelength edge is aligned with the desired band edge (i.e.  $\lambda_c$  is moved to longer wavelengths). If needed, the stopband width can be extended by cascading two (or more) HR structures with different centre wavelengths. Alternatively, one might design a sufficiently wide band-pass structure where the cut-on and cut-off features of the band-pass determine the edge.

### Gain-flattening Filters

Gain-flattening filters exploit the fact that it has become possible to model essentially any kind of TFF function and fabricate the corresponding very complex layer stacks with extremely high precision. Gain equalization using TFFs started in the 1990s for flattening the gain of EDFAs and has since then made significant progress so that TFF-based GFFs have become an attractive alternative to FBG-based GFFs (see Sect. 9.6.6).

## 9.8.2 Fabrication of TFFs

### Substrates

TFFs are normally fabricated on glass substrates which should be sufficiently stable (mechanically, environmentally), have a smooth surface (no defects as defects might grow larger during layer deposition), and should assure good adhesion of the deposited layers. The size may be as large as 300 mm in diameter, and smaller dices are cut after the thin-film layer stack has been deposited. If the temperature of a TFF is raised, the refractive index  $n$  and the effective layer thickness  $d_{\text{sp}}$  normally increase which gives rise to a long wavelength shift of  $\lambda_c$  (according to (9.43)), and the shift amounts to about 10–15 pm/K [129, 132]. However, it has been shown that this shift can successfully be suppressed by the use of substrates which have a coefficient of thermal expansion capable of counteracting the unwanted wavelength variation [133]. As the temperature increases, the substrate expands, stretches the filter layers and reduces the physical layer thickness. By proper substrate selection and overall device design the temperature-dependent variation of the optical path length  $d_{\text{sp}} \times n$  can be made so small that this approach allows minimizing the temperature-induced shift to levels that meet typical specifications of  $\leq 1$  pm/K for narrow channel filters (50, 100 GHz) and  $\leq 3$  pm/K for CWDM or edge filters without need of any active control. Substrate materials meeting these demands are offered by various suppliers.

### Materials

Thin film coatings should be highly durable, and one class of materials which perfectly meet this requirement are the refractory oxides, examples of which are  $\text{SiO}_2$ ,  $\text{TiO}_2$ ,  $\text{ZrO}_2$ ,  $\text{HfO}_2$ ,  $\text{Nb}_2\text{O}_5$ , and  $\text{Ta}_2\text{O}_5$ .  $\text{SiO}_2$  has a rather low refractive index ( $n = 1.44$ – $1.49$  at  $1.5 \mu\text{m}$  [129, 134]) while the other oxides listed have significantly higher refractive indices. Therefore,  $\text{SiO}_2$  is generally used as the low-index material and it is frequently combined with  $\text{Ta}_2\text{O}_5$  ( $n = 2.10$  at  $1.55 \mu\text{m}$  [134]) for the fabrication of wavelength filters.

### Deposition Processes

Thin film layers are typically grown by physical vapour deposition (PVD) although chemical vapour deposition has also been reported for the fabrication of telecom filters [129]. The three PVD processes most widely used for TFF fabrication are ion-assisted deposition (IAD), ion beam sputtering (IBS) and reactive magnetron sputtering. Details of these processes are reported elsewhere (see [129] and references therein) and we will recall the most relevant requirements for these fabrication processes.

Demands on filter tolerances may be as high as  $\pm 0.1$  nm for the filter edge wavelength which corresponds to a maximum tolerable variation of the operation wavelength (1.55  $\mu\text{m}$  range) of about 0.01 %, and this requires both well-defined layer thicknesses and non-porous layers with bulk-like density. These specifications have to be met over a sufficiently large substrate area in order to assure acceptable overall yield, and this is normally enabled by fully automating the deposition process combined with optical in situ monitoring. On the basis of these developments single deposition runs may last up to multiple days (if required), and providing filters with correspondingly complex structure has become possible [129, 132].

### ***9.8.3 Filters for Telecom Applications***

As already stated, thin-film filters used in fibre optic networks comprise band-pass-, multiple-band-, edge-, and gain-flattening filters, and TFFs are used as wavelength lockers for DFB lasers.

#### **Band-pass Filters**

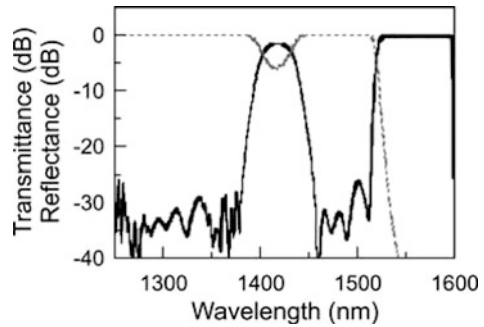
TFF-based band-pass filters cover the complete range of filters from CWDM to (D)WDM applications, and as far as CWDM channels are concerned, TFFs are essentially the only solution with commercial relevance. For (D)WDM applications TFFs are typically offered for 100 GHz and 200 GHz channel spacings but are available for 50 GHz channel separation as well. The clear channel passband of 100 GHz filters is typically about 25 GHz, but TFFs with 50 GHz clear channel passband are also available ('wide-top' filters). The latter tend to have higher chromatic dispersion (e.g. 60 ps/nm) which is about twice the value of standard 100 GHz filters and therefore it is evident that filter dispersion has to be given proper attention with the deployment of 40 Gbit/s systems. More detailed information on dispersion is compiled in [129] for example or is given by the respective manufacturers.

CWDM filters are commercially available for single channels (and about 15 nm passband), but they are also available for numbers of adjacent channels, for example four or eight, and they are offered with various degrees of roll-off at the band edges [135].

#### **Multiple-band Filters**

Multiple-band filters are filters designed for transmitting or reflecting more than one band or wavelength regime. For spectroscopy applications filters are offered with multiple blocking bands while developments for telecom applications include dual band filters (e.g. transmitting the O- and C-bands, and reflecting elsewhere), or transmitting two CWDM channels (1510 and 1570 nm) and reflecting all other

**Fig. 9.21** Transmittance (grey, dotted curve) and reflection (full curve) characteristics of short-pass tri-band filter [136]



channels. Tri-band filters are a variety for supporting the deployment of FTTx [136]. One concept for bringing optical fibre to the residential customer are broadband passive optical networks (BPON, cf. Chap. 1, Sect. 1.5.1) with the 1260–1360 nm and 1480–1500 nm wavelength ranges reserved for digital upstream and digital downstream traffic, respectively, and the 1.55  $\mu\text{m}$  band provided for downstream analogue signals. For use in such systems filters capable of handling three bands have been developed. They are offered either as long-pass- or short-pass (SP) tri-band filters, and an example of a corresponding SP filter, which reflects the 1550–1560 nm wavelength range and passes both, the 1260–1360 nm and the 1480–1500 nm ranges, is illustrated in Fig. 9.21.

### Edge Filters

Edge filters are commercially available both, as short-pass- and as long-pass filters (SPF, LPF), and they are essentially available for the separation of any wavelength range into a reflected and a transmitted regime. The range between the reflected and the transmitted wavelengths, which cannot be used for transmission channels because neither the reflection nor the transmission are adequate, is typically a few nm wide. This is due to the fact that the roll-off of filters gets less steep as the filter bandwidth increases (and edge filters are in essence very broadband filters, as stated above).

### Gain-flattening Filters

Commercially available GFFs are primarily designed for covering the C-band (1525–1565 nm), but are available for the S- and L-band as well. The output power/gain variation of an EDFA plus GFF cascade can be made  $< 0.5$  dB over the complete wavelength range specified, the difference between the designed transmission of a GFF and its actual value can be made as small as about  $\pm 0.1$  dB, and PDL is typically  $< 0.1$  dB [129, 132, 136, 137].

### TFFs for hybrid PLC modules

Thin-film filters have been used in hybrid planar lightwave circuit (PLC) modules, for example for separating 1.3/1.55  $\mu\text{m}$  wavelengths in FTTH transceivers, for a number of years already ([138] and references therein) and a very recent variety are TFFs to be used with a polymer optical integration platform [139, 140]. Such a PLC platform is highly flexible and may be particularly suited for low-cost optoelectronic modules to be used in access networks. The TFF elements can be designed with a wide range of application-specific spectral characteristics, including CWDM filters, “triple play” filters, and reflectors for OTDR monitoring. In contrast to the common TFFs these PLC embedded TFFs have to be extremely thin ( $< 20$  to  $25 \mu\text{m}$ ) to minimize optical excess loss. To this end they are deposited on a thin polymer “substrate” film using ion beam sputtering. If the same kind of polymer is used as for the PLC waveguides, unwanted residual reflection at the WG/TFF interfaces can be largely suppressed, and it is further improved by inserting the TFF under a small angle (e.g.  $8^\circ$ ), so that better than  $-30$  dB crosstalk levels can be achieved.

Polymer-based multi-layer structures have also been designed for polarization handling purposes, namely as a polarization rotator and polarization beam splitter. The former has proven to efficiently compensate for polarization effects for example in AWGs whereas with the latter  $> 20$  dB discrimination between TE- and TM-polarized guided waves over the 1535–1600 nm wavelength range have already been demonstrated [140].

#### 9.8.4 Filter Modules

As thin-film filters have no wavelength-dispersive properties and can only discriminate between transmitted and reflected wavelengths, they are essentially three-port devices as illustrated in Fig. 9.22.

In order to enable the spatial separation of the incoming and the reflected light without the need of an optical circulator, the incoming light hits the TFF at an angle. However, the characteristics of TFFs depend on the angle of incidence: (i) the transmission wavelength shifts to longer wavelengths with increasing incidence angle (which may be used for (fine-) tuning the centre wavelength if this is wanted or acceptable), and (ii) the characteristics become polarization dependent which is generally unwanted. As a consequence, TFFs are normally mounted under very small angles of incidence (around  $1^\circ$ ). The beam shaping and focusing is typically achieved by using GRIN (gradient-index) lenses, but as outlined in [129], there are various additional restrictions and design considerations to be taken into account.

Optical add-drop multiplexers (OADM) are key building blocks in WDM networks, and they have to combine or separate larger numbers of wavelength channels. In order to accomplish that functionality using TFFs they have to be cascaded, and one corresponding option is illustrated in Fig. 9.22b.

Different wavelength channels to be separated by a TFF-based DEMUX travel different paths and experience a different number of reflections until they are even-

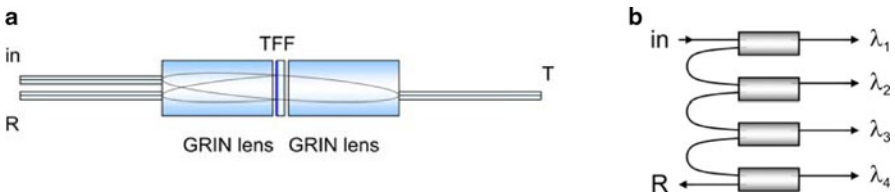


**Fig. 9.22** Three-port TFFs. Single device: in, T, R represent incoming, transmitted and reflected signals (a), four-channel MUX/DEMUX:  $\lambda_1, \dots, \lambda_4$  are transmitted via different output ports, any other wavelength is reflected (R) (b)

tually transmitted (or leave by the reflection output port). Each reflection causes an average loss of typically 0.3 dB and as a consequence the overall attenuation of the wavelength transmitted first ( $\lambda_1$ ) is correspondingly lower than that of the last wavelength transmitted ( $\lambda_4$  in Fig. 9.22 or  $\lambda_n$  in general). One possibility to compensate this variation without significant effort is by using appropriate MUX and DEMUX pairs which have a complementary arrangement of wavelengths so that the total loss for any channel is almost the same after one MUX/DEMUX pair has been traversed. Because of this inherent asymmetry of TFF-based MUX/DEMUXs, a standard cascade comprises a maximum of eight three-port devices, and MUX/DEMUXs for higher channel counts are a combination of such cascades with band splitting couplers or interleavers.

Another issue concerning cascaded TFFs is chromatic dispersion (CD) where each reflection and the final transmission contribute to the total CD of a channel. CD accumulation can be mitigated by choosing proper cascade architectures, and one example is the combination of a 3 dB coupler with two legs of interleaved channels [141]. As the adjacent channel separation is doubled by the interleaver structure, the reflection CD is significantly reduced, however, at the expense of an extra 3 dB loss.

Band-splitting couplers, (also designated as wave-band or wideband couplers), are TFF-based band filters with rather large bandwidth so that they can be used to transmit or reflect a number of WDM channels with one element, and they also support a “pay-as-you-grow” strategy. Such filters come in two varieties (cf. Fig. 9.23). Either all channels having the fundamental separation from each other are used (“ $x$ -skip-0”), or  $n$  channels next to the edges of the banded filter are skipped (“ $x$ -skip- $n$ ”) with  $n > 0$ . The reason for using skip- $n$  filters is the following: with increasing width of the transmission band it becomes more and more difficult to assure a sufficiently steep roll-off at the band edges of the filters so that the corresponding fabrication effort and related costs go up. At the same time detrimental effects of chromatic dispersion increase with steeper band edges (because of the fact that TFFs are minimum-phase filters in transmission with transmission and phase response constituting a Hilbert transform pair, cf. Sect. 9.2.1). Compared to  $x$ -skip-0 filters  $x$ -skip- $n$  solutions are beneficial in two respects: they allow for less-steep filter edges, which reduces CD, and in addition, the maxima of CD can be moved further away from the band filter edges resulting in lower overall CD within the filter band [141].



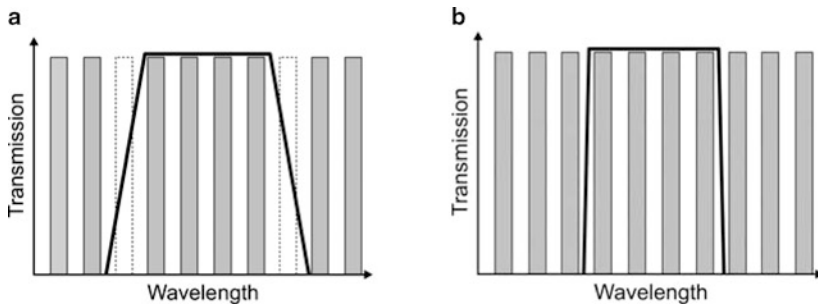


**Fig. 9.23** Schematic representation of 4-skip-1 (a) and 4-skip-0 (b)

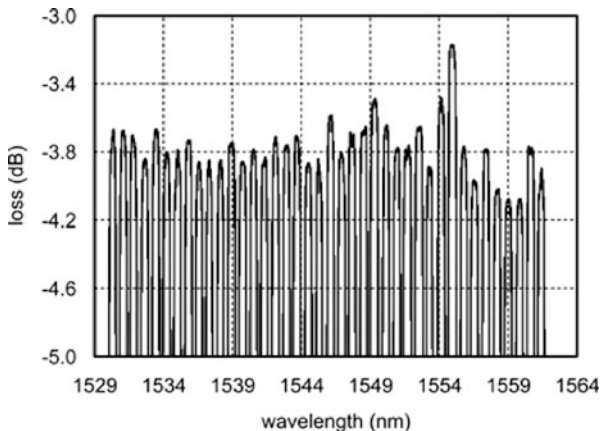


**Fig. 9.24** Channel-dependent variation of insertion loss in a TFF-based 40-channel DEMUX [142]

The most common varieties are  $x$ -skip-1 and  $x$ -skip-2 filters, but for example 20-skip-4 devices are also commercially available [137]. On the basis of the concepts illustrated MUX/DEMUXs with a maximum channel count of 40 are offered from different manufacturers. Because the different channels traverse different filters, there is a certain variation of the individual channel's insertion loss as illustrated in Fig. 9.24.

Other approaches to building TFF-based MUX/DEMUXs have been reported in the literature [129, 143, 144], however, they have not yet found commercial relevance.

## 9.9 Microrings

Microring resonators (MRR) optically coupled to dielectric waveguides represent a class of filters with characteristics very similar to Fabry–Pérot filters. They are particularly easy to fabricate as no gratings, facets, or high-reflecting structures

are needed for building the cavity. Typical dimensions are in the several  $10\mu\text{m}$  up to a few  $100\mu\text{m}$  range which allows for compact one- or two-dimensional arrays. MRRs enable a wide range of applications. Examples related to fibre optic communication include optical channel filtering [145, 146], planar dispersion compensation [147], all-optical wavelength/frequency conversion [148–150], all-optical switching [151, 152], and cascaded microring (MR) modulators for WDM optical interconnects [153]. MRRs are considered promising beyond telecom applications as well, and one particularly prominent area of current interest is sensing of (bio)molecules [124, 154–156]. Materials used for the fabrication of MRs include  $\text{SiON}_x$  [147], SOI [152, 155], glass [145], or semiconductor material systems such as GaAlAs [151] and GaInAsP [150, 157].

### 9.9.1 Key Features of Microring Resonators

The most simple MRR configuration is a single microring coupled to a dielectric waveguide which represents an all-pass filter. The design can be horizontal (as illustrated in Fig. 9.25a) but vertical coupling (where the MR and the feeding WG are vertically arranged in layers one on top of the other) is an equivalent option. Another generic MRR configuration is the add-drop multiplexer shown in Fig. 9.25b which consists of an MR coupled to two dielectric WGs.

The characteristics of waveguide-coupled microrings can be derived by different approaches. Details are given in various textbooks [7, 42, 158] and the most relevant results for the add-drop multiplexer, which also include the characteristics of simple MRRs, are given below.

The formulae given hold for the (idealistic) case of polarization-independent behaviour or TE- (TM-) polarized light launched into the feeding waveguide and full polarization conservation while polarization-dependent effects will be briefly discussed in Sect. 9.9.2.

For the add-drop multiplexer illustrated in Fig. 9.25b the following relations hold [42]:

$$T_{\text{out}} = \left| \frac{b_1}{a_1} \right|^2 = \frac{|t_1|^2 + |at_2|^2 - 2a|t_1t_2|\cos(\theta - \theta_{t_1} - \theta_{t_2})}{1 + |at_1t_2|^2 - 2a|t_1t_2|\cos(\theta - \theta_{t_1} - \theta_{t_2})}, \quad (9.45)$$

$$T_{\text{drop}} = \left| \frac{c_2}{a_1} \right|^2 = \frac{(1 - |t_1|^2)(1 - |t_2|^2)a}{1 + |at_1t_2|^2 - 2a|t_1t_2|\cos(\theta - \theta_{t_1} - \theta_{t_2})}, \quad (9.46)$$

where  $T_{\text{out}}$  and  $T_{\text{drop}}$  are the intensities at the (forward) output and the drop port, respectively,  $t_1$  and  $t_2$  characterize the fraction of light amplitude propagating along the straight WGs in the coupling regions,  $a$  represents the attenuation which the propagating fields experience after travelling once along the ring length  $L$ , and  $a$  is related to the field attenuation coefficient  $\alpha/2$  by

$$a = \exp(-\alpha L/2), \quad (9.47)$$

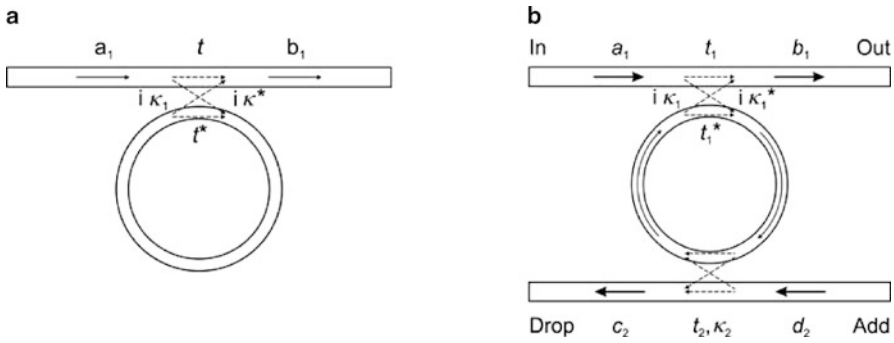


**Fig. 9.25** Generic microring resonator structure (a) and principle of MR-based add-drop multiplexer (b)

i.e.  $a = 1$  corresponds to zero loss.  $\theta$  and  $\theta_{t_j}$  are defined by

$$\theta = \frac{2\pi\nu}{c}n_{\text{eff}}L \quad \text{and} \quad t_j = |t_j| \exp(i\theta_{t_j}), \quad j = 1, 2, \quad (9.48)$$

respectively, where  $\nu = c/\lambda$  is the frequency of the propagating wave. The coupling between the straight WGs and the MR is characterized by coupling constants  $\kappa_1$  and  $\kappa_2$  which satisfy the relation

$$|t_j|^2 + |\kappa_j|^2 = 1 \quad \text{with } j = 1, 2. \quad (9.49)$$

The behaviour of a microring coupled to a single WG only (Fig. 9.25a) is obtained from (9.45) to (9.49) by setting  $t_1 = t$ ,  $t_2 = 1$ ,  $\theta_{t_1} = \theta$ ,  $\theta_{t_2} = 0$ ,  $\kappa_1 = \kappa$ , and  $\kappa_2 = 0$ .

The waveguide-coupled MRs characterized by (9.45) and (9.46) exhibit periodic characteristics, in particular periodic dips in the transmission spectra and corresponding maxima at the drop port in the case of the add-drop multiplexer according to

$$\theta - \theta_{t_1} - \theta_{t_2} = 2m\pi = \frac{2\pi\nu}{c}n_{\text{eff}}L - \theta_{t_1} - \theta_{t_2} \quad (9.50)$$

with  $m$  being an integer. The frequency spacing between two adjacent transmission minima is called the free spectral range (FSR), and the FSR is given in the frequency domain by

$$\text{FSR} = \frac{c}{n_g L} \quad (9.51)$$

i.e. the free spectral range is determined by the ring dimension and the group refractive index  $n_g$  (see (9.26)).

The intensity at the ‘through’ output port vanishes if

$$a = \left| \frac{t_1}{t_2} \right| \quad \text{or} \quad a = |t| \quad (9.52)$$

holds for the add-drop multiplexer or the MR coupled to a single WG, respectively. This condition is called “critical coupling”, and in this case light coupling back from the ring to the (‘through’) output waveguide is equal in amplitude but has opposite phase compared to the directly propagating light so that complete destructive interference occurs.

As far as phase effects are concerned, MRRs exhibit pronounced phase variations around the resonance, i.e. the group delay exhibits a peak at the resonance wavelength (see e.g. [7]).

### ***9.9.2 Polarization-dependent Effects***

The effective refractive index  $n_{\text{eff}}$  of straight or bent waveguides is normally different for TE- and TM-polarized light and as a consequence the resonance frequencies and the FSR of MRRs are polarization dependent. But, more importantly, MRRs may also rotate the state of polarization so that an initially purely TE- (TM-) polarized wave launched into the feeding WG will leave the WG-coupled MR structure partly (or even completely) TM- (TE-) polarized [159]. The extent of polarization rotation depends on many parameters including WG geometry (cross sectional shape and bend radius), refractive index contrast, degree of vertical asymmetry, MR loss, and wavelength (near resonance polarization rotation may be particularly pronounced) [160]. Bent WG and MRR designs exist which favour polarization rotation or even enable complete polarization conversion [161, 162], but conversely, by proper design, polarization rotation can be suppressed to a large extent as well. As a consequence, polarization-dependent characteristics have to be taken into account in the design of MRR-based devices with sharp resonances while these effects tend to be less relevant in filters with fairly broad add-drop bands such as the higher order filters described below.

### ***9.9.3 Higher Order Filters***

Single microrings in an arrangement as shown in Fig. 9.25b are not particularly useful for most filter applications, but cascaded microrings exhibit significantly more favourable properties. Two examples of generic higher order filter structures (add-drop multiplexers) are illustrated in Fig. 9.26.

A large number of different arrangements of MRs have already been fabricated and reported in the literature, comprising rings of the same size and different radii as well [163]. Tuning of individual MR parameters has already been implemented [164], and architectures with two-dimensional arrangements, for example as dynamically configurable add-drop multiplexers, as well [165].

The wavelength-dependent properties of cascaded MRs can be evaluated and represented by different concepts. The transfer function of serially coupled MRs which

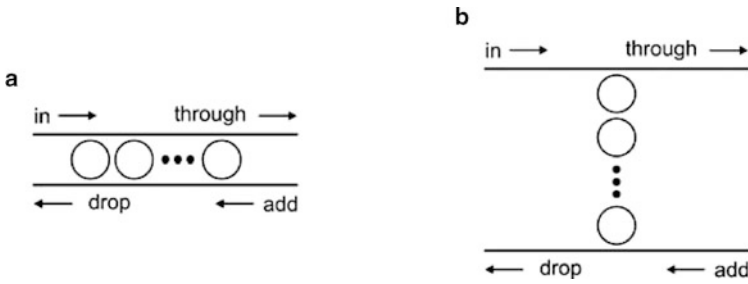


**Fig. 9.26** Parallel (a) and serially (b) cascaded MRs as generic add-drop multiplexer structures

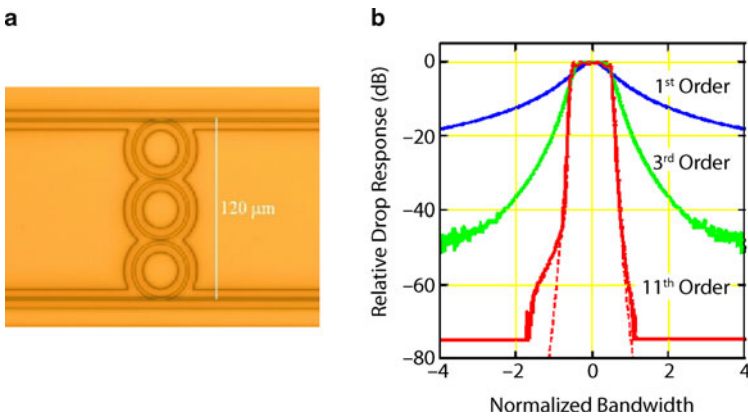


**Fig. 9.27** Top view of 3-ring serially cascaded MR filter (a) and experimentally determined drop-response of serially cascaded microring filters with different numbers of MRs (b), all fabricated in Hydex® [145, 146, 170]

is a configuration enabling filters with particularly steep edges and flat top transmission characteristics (see Fig. 9.27), has been derived based upon the Z-transform and using the transfer matrix [7, 166], the characteristic matrix concept [167], or by performing time-dependent analyses [158, 168]. The final results can conveniently be written as a set of recursive formulae [169] or continued-fractions expressions [145, 158].

### 9.9.4 Experimental Results

Serially cascaded MRs with excellent filter characteristics have been fabricated in a glass called Hydex®. Hydex® is a high-index material ( $n = 1.7$ ) and offers the possibility to vary the index contrast between the core and the silica cladding in the range from 1 to 25% [170] so that tight bends with radii down to about 5 μm are possible which enables the fabrication of compact and complex microstructures.

The transmission characteristics of filters built from different numbers of equally sized rings are shown in Fig. 9.27.

In a parallel all-pass filter arrangement the phase characteristics of the individual rings add and this property can be exploited for the fabrication of MR-based dispersion compensators [147].

### ***9.9.5 Microring-based Filters with Extended FSR***

For typical applications in fibre optic systems filters should have FSRs in the range of several 10 nm, i.e. comparable to the width of the C-band for example. This is not easy to accomplish as it is equivalent to rather low ring radii which is challenging from a technological point of view. A way to overcome these difficulties is the combination of MRs with different radii in such a way that resonances only occur where the resonances of all individual MRs involved coincide (Vernier effect). This is essentially equivalent to designing widely tunable lasers by using gratings with slightly different pitch so that super modes only develop if both gratings are matched (see Chap. 5, Sect. 5.2.2). A corresponding filter has been fabricated in the SiO<sub>2</sub>/Si material system comprising two rings with 28.5 μm radius coupled to one ring with 39.3 μm radius. The FSRs of the individual rings were 8 nm and 6 nm, respectively while the filter based upon the coupled rings exhibited about 20 nm FSR [171]. For widely tunable lasers using ring resonator structures see also Chap. 5, Sect. 5.4.4.

### ***9.9.6 Prospects and Further Developments of MR-based Filters***

At present there is little evidence that MR-based filters will achieve greater relevance as stand-alone components in fibre optic communications, however, they are highly promising with respect to monolithically integrated filter solutions due to their small size, compactness and the possibility for cascading so that their transmission (or phase) characteristics can be shaped almost arbitrarily. With these targets in mind integrated MRs have more recently received particular attention in the field of Silicon Photonics (see Sect. 9.12) [172].

## **9.10 Interleavers**

### ***9.10.1 Operation Principle***

Interleavers are used in wavelength routing but for (de)multiplexing and prefiltering as well. The latter application is based upon the fact that an ongoing trend in the development of WDM systems is to locate transmission channels closer to each

other to make better use of the transmission capacity of a single optical fibre. Correspondingly optical filters have to cope with ever-decreasing channel separations which makes their fabrication more and more demanding. One smart way out of this dilemma is the use of optical interleavers in combination with standard filters.

An interleaver operates as follows: If a stream of wavelength channels at carrier frequencies  $\nu_1, \nu_2, \dots, \nu_n$  and constant channel separation  $\Delta\nu$  enters a standard interleaver, frequencies  $\nu_1, \nu_3, \nu_5, \dots$  exit from one port of the interleaver while frequencies  $\nu_2, \nu_4, \nu_6, \dots$  come out from the other port. The frequency separation is  $2\Delta\nu$  for the data streams at output ports 1 and 2. Interleavers can also be cascaded if even larger channel separations are required (a cascade of  $N$  interleaver stages splits the original data stream into  $2^N$  channels with  $2^N \Delta\nu$  channel separation). Once the initial channel spacing has been widened, the requirements on subsequent filtering are less demanding compared to the case without the interleaver, and standard filters, OADMs etc. can be utilized. Interleavers have consequently been used for the highest total transmission capacity systems which have been upgraded from 100 GHz to 50 GHz channel separation, thus doubling the overall system bit rate (see also [6]).

If an interleaver is operated in the reverse direction, it can combine two (or  $2^N$ ,  $N = 2, 3, \dots$ ) streams of frequency channels with channel separation of  $2\Delta\nu$  ( $2^N \Delta\nu$ ) into a single data stream with  $\Delta\nu$  channel separation.

In principle, any kind of optical filter that exhibits a periodic response with respect to frequency may be used as an interleaver. However, for real applications there are additional requirements, in particular: flat top band shape, large channel width, high adjacent band isolation, low polarization dependence (i.e. low polarization-dependent loss and low polarization dependence of the channel centre frequency/wavelength), low chromatic dispersion, and low overall insertion loss. Furthermore, the channel separation of the interleaver has to match the ITU grid with sufficient accuracy over the whole operation range, and interleavers meeting all these demands require careful design and mature manufacturing.

### 9.10.2 Interleaver Types

As already mentioned, interleavers fall into different categories according to their functionality. The simplest design, designated as a 1:2 interleaver, separates the even and odd channels of an incoming wavelength comb (or combines these two groups of channels into a single one if operated in the reverse direction).

The next category are 1:  $2^N$  interleavers (i.e. cascades of  $N$  interleaver stages) which separate a single DWDM comb into  $2^N$  data streams (or combine  $2^N$  sequences of wavelength channels into a single data stream).

A third category are banded interleavers which separate (or combine) bands of channels. In this case it is particularly demanding to assure a steep roll-off at the end of the bands to be separated over a wavelength interval corresponding to a single channel spacing (which is significantly narrower than the range covered by the individual bands).

Finally, interleavers may be asymmetric, i.e. they may single out one channel from a larger number of channels  $N$ , or more generally speaking, they separate (or combine) channels with freely chosen passband width (e.g. 60%/40%, 70%/30%, ...).

Interleavers also fall into different categories according to the physical principles they are based upon [173]. One class of interleavers are the so-called lattice filters, which may be based upon a cascade of birefringent waveplates located between two polarizers. This design is inherently polarization dependent, but polarization-independent operation, which is a must for telecom applications, can be assured by polarization diversity. Another variant of this interleaver type relies on polarization beam splitting rhombs and glass delay prisms and offers the possibility to choose the refractive indices, their thermal dependencies and the physical dimensions in such a way that the interleaver exhibits a very small residual temperature dependence. Operational details of these interleavers are given in [173].

Cascaded Mach–Zehnder interferometers (MZI) with properly chosen delay and coupling between the individual MZIs is another variant. Such interleavers are primarily realized in planar lightwave technology [174], and the concept is equivalent to birefringent filters.

One more category of interleavers is based upon Michelson interferometers (MI) where the mirror(s) in one or both arm(s) is/are replaced by (a) Gires–Tournois interferometer(s), cf. Sect. 9.7.3. Corresponding non-linear Michelson interferometers are also designated as ‘step-phase MI’ because the phase change introduced by the GTI exhibits a step-like behaviour.

Gires–Tournois interferometer-based interleavers can either be of interferometric or of birefringent type. The former variant operates on the phase returned from the two MI arms [173, 175] while the functionality of the latter is based upon the polarization returned from each arm [173]. GTI-based interleavers can be built with standard MI set-ups and using thin-film GTIs, but the same kind of structure has also been reported as an all-fibre solution with one of the mirrors being a chirped FBG and the other a distributed Gires–Tournois etalon (DGTE) [176]. The gratings were written into the two arms of a fibre coupler, and the DGTE consisted of a weak fibre grating (acting as front mirror) and a strong fibre grating (acting as rear mirror).

Finally, properly designed microring resonators coupled to a Mach–Zehnder interferometer [177–179] can be considered as another variety of GTI-type interleaver, and interleavers have also been designed as AWGs [180] which offer particular application potential as single-state  $1 : 2^N$  interleavers.

### ***9.10.3 Characteristics of Commercially Available Interleavers***

Interleavers are fabricated by a number of suppliers and have been implemented using different technologies. These include designs using crystals, fibres (with cascaded MZIs or FBGs for example), and planar lightwave circuits as well. In a number of cases suppliers do not disclose their concept and the technology used, and one



**Table 9.1** Typical performance data of commercially available 50/100 GHz interleavers

Parameter	Unit	Typical values
Wavelength accuracy	nm	0.02
Insertion loss	dB	$\leq 2.0$
0.5 dB passband width/Clear channel	GHz	20–30
Isolation/Crosstalk	dB	$> 20$ –25
Return loss	dB	$> 40$
Directivity	dB	$> 45$ –55
Polarization-dependent loss	dB	$< 0.2$ –0.5
Polarization mode dispersion	ps	$< 0.2$ –0.3
Chromatic dispersion	ps/nm	$< \pm 20$ –30

can make guesses only. A comprehensive overview has been published some time ago [181] and the data are still relevant although one or the other supplier listed has since then discontinued its interleaver business.

Interleavers are primarily offered for 25/50 and 50/100 GHz channel spacings, but they are also available for 12.5/25 GHz [182] or 100/200 GHz operation, with asymmetric channel widths [182] or as 1:4 interleavers [183]. Channel spacings down to 6.25 GHz have so far only been published in the literature (see [173]). Interleavers typically cover the C- or the L-band with 80 channels for example in the case of 50/100 GHz interleavers.

A number of key performance parameters for commercially available 50/100 GHz interleavers are listed in Table 9.1. The parameter variations are partly due to different technologies and implementations, but also due to slightly different definitions of the parameters themselves.

The improvement of interleavers is very likely to go on as interleavers represent an efficient means for upgrading the channel count of communication systems without the need to improve the performance of each individual wavelength filter.

## 9.11 Acousto-optic Tunable Filters

Acousto-optic tunable filters (AOTF), sometimes also designated as acoustically tunable optical filters (ATOF), are passband transmission filters based upon the acousto-optic interaction inside an anisotropic medium. An applied radio-frequency causes acoustical vibrations in a corresponding crystal (e.g.  $\text{TeO}_2$ ,  $\text{LiNbO}_3$ ) and creates a bulk transmission diffraction grating. AOTFs offer the unique property of multiple-band filtering by mixing multiple radio frequencies, and arbitrary wavelength selection can be accomplished within microseconds. AOTFs are available for operation within the visible or near/mid infra-red spectral region and have been developed for applications in fibre-optic communication systems as well [184–187]. However, they could not satisfactorily meet the demands of (D)WDM systems, and as there is no application where the unique properties of AOTFs can compensate their shortcomings, these filters are currently considered of essentially no relevance

for fibre-optic communication systems although AOTFs have found various other useful applications [188].

## 9.12 Filters for Silicon Photonics

### 9.12.1 *General and Technological Aspects*

So far filters have been described by the concepts they are based upon, and filters are typically fabricated in material systems that yield the overall performance needed at the lowest possible cost. Devices are either stand-alone solutions or are integrated into modules. This strategy enables one to obtain the best filter performance from the specific systems and applications point of view, but at the same time this approach has limited the total sales volumes for each individual filter solution in the past and has limited cost-saving potential as well.

Silicon photonics (or more precisely CMOS based photonics) offers the potential to fabricate strongly miniaturized PLCs due to a very high index contrast, and it lends itself to large volume production and corresponding cost savings because existing CMOS fabrication facilities can be used. Particularly promising is the eventual monolithic integration of silicon photonics PLCs with electronics on a single chip as it enables the fabrication of versatile and cost-efficient optoelectronic integrated circuits (OEICs) with applications anticipated in many areas including the field of fibre optic communication. Attractive low-cost solutions are expected in access and metropolitan area networks, 10, 40 Gbit/s or even higher bit rate transponders for up to about 100 km reach is one specific application example and cost-efficient broad band fibre-to-the-home delivery represents another opportunity. Silicon photonics is also expected to support the development of optical cross connects, high-capacity short-reach data links between storage units, or radio-over-fibre, to name a few future applications only.

Considerable progress has been made in the last few years, but before silicon photonics will acquire substantial market shares significant further improvements are still needed, in particular with respect to optical sources and modulators (see e.g. Chap. 14), but also as far as detectors and optical filters are concerned. Filters, which are particularly promising and have received the highest attention in this respect, are planar diffraction (echelle) gratings, AWGs, microring-based filters, and Mach-Zehnder interferometer-based filters. Bragg gratings of various kinds have also been part of different silicon photonics solutions, however, not for MUX/DEMUX applications but for example for the definition of resonator cavities or as reflecting elements within echelle gratings [189].

Waveguides/wires are typically fabricated in a 220 nm-thick silicon (waveguiding) layer with refractive index  $n = 3.45$  which is separated from the Si substrate by a buried oxide layer of about 1 to 2  $\mu\text{m}$  thickness with a refractive index  $n = 1.45$  [190]. The approach is commonly designated as silicon-on-insulator (SOI). As a consequence of the large index contrast the waveguiding structures can be made extremely compact and with very sharp waveguide bends without undue

losses. But at the same time devices are very sensitive to minor process variations: 1 nm width variation may result in about 1 nm shift of the wavelength characteristics, and phase errors tend to degrade the maximum achievable crosstalk [190].

Fabrication is typically made in CMOS fabrication lines with either 248 nm or 193 nm lithography. The latter enables fabrication with significantly higher precision and consequently superior optical performance (e.g. straight WG losses have been reduced to 2.7 dB/cm with 193 nm technology compared to about 7 dB/cm for 248 nm processing [190]). The use of e-beam lithography is an alternative, however, it is primarily used in research environments.

### ***9.12.2 Examples of CMOS-based Filters***

For the demultiplexing of larger numbers of wavelength channels two concepts are particularly promising and compatible with silicon photonics: echelle gratings (also designated as planar concave gratings, PCG) and AWGs [190] while the ultimate performance of other concepts, for example multi-channel filters based upon sampled gratings [191] is so far difficult to assess. If filters are required for single wavelengths or for lower channel count, microring resonator-based filters are apparently a good choice.

#### **Echelle Gratings**

Among all filters used in silicon photonics echelle gratings are considered to be the least sensitive to process variations. This is due to the fact that the crucial region, where dispersion typically accumulates, is a slab waveguide or free-space region without laterally confining waveguides. Echelle gratings can be designed in different ways, including different variants for the reflecting elements [189, 192]. Device footprint, insertion loss, channel crosstalk, and channel uniformity depend on the specific design, but the following recently reported characteristics of echelle gratings can be considered to represent the current state-of-the-art: 8 channels with 3.2 nm (400 GHz) separation and  $250 \times 200 \mu\text{m}^2$  footprint [192] or 30 channels, again with 400 GHz separation, and  $0.5 \text{ mm}^2$  footprint [190], adjacent channel crosstalk close to 20 dB, and insertion loss in the 3–4 dB range (achieved by using strong Bragg mirrors in the reflecting facets). Planar echelle gratings are strongly polarization dependent and the design is normally made for TE-polarization. One generic shortcoming of echelle gratings for MUX/DEMUX applications is the fact that they exhibit Gaussian passbands [193] whereas a flat top shape would generally be preferred.

#### **Arrayed Waveguide Gratings**

AWGs, representing another type of simultaneous multi-channel MUX/DEMUX, have also been realized in SOI already [190, 194–198]. AWGs are a particu-

larly good choice for narrower channel spacings (200 GHz have already been realized), larger overall channel count, and AWGs can also be fabricated polarization-insensitive [199]. Characteristics of recently reported AWGs, both with 200 GHz channel separation, are: 8 channels, 1.1 dB insertion loss for the central channel and 1.3 dB roll-off towards the outer channels, 25 dB crosstalk, and  $200 \times 350 \mu\text{m}^2$  footprint [190] or 32 channels, 2.5 dB on-chip transmission loss, better than 18 dB crosstalk, and  $400 \times 500 \mu\text{m}^2$  footprint [200], clearly illustrating the potential of AWGs for integrated chips. The fact that the optimum achievable crosstalk of SOI-based AWGs is limited to about 20–25 dB is a consequence of the high refractive index contrast, which leads to a strong influence of fabrication variations on phase changes in the waveguide arms.

### **Microring Filters**

Microring filters are attractive for silicon photonics applications (1) due to their very low footprint, for example  $0.0007 \text{ mm}^2$  for a 5th order cascaded MRR filter (similar to the one shown in Fig. 9.27) with flat top characteristics and 1.8 dB insertion loss only [201], and (2) because they can be thermally tuned with low power consumption [202–204]. 1 mW per nm and  $< 10 \mu\text{s}$  tuning time constant have been achieved using trenches for thermal isolation [202], and placing heaters directly on top of the silicon resonator without any oxide buffer layer also enables low-power thermal tuning. Beyond varying the centre wavelength this has also been applied for adjusting the filter extinction ratio and the individual channel bandwidth [203]. The strong confinement of the light within the high contrast Si waveguides/wires is advantageous for making very compact MRR filters, but in combination with the normally chosen high Q-factors of the MRs even moderate signal powers give rise to strong non-linear effects which is important to be taken into account [190].

### **MZI Filters**

Mach–Zehnder interferometer-based filters have also been fabricated based upon silicon waveguides [64, 205, 206]. So far satisfactory device performance requires an individual (e.g. thermal) control of each channel and this has been successfully implemented for an 8-channel demultiplexer with 400 GHz channel spacing, 13 dB adjacent channel isolation, 1.5 dB channel uniformity and 2.6 dB excess loss [206].

## **9.13 Conclusions**

The enormous transmission capability of today's fibre-optic communication systems relies to a significant extent on the application of wavelength division multiplexing, and this technique itself is crucially dependent on wavelength filters. As

a consequence various types of filters have been developed in the past, each with specific favourable and less wanted properties. Different solutions have already been deployed in actual systems, others have not yet reached commercial status or have even more recently experienced a declining interest.

Filters are primarily described with respect to their channel selection capability, however, with increasing system bit rates and with decreasing channel separations (requiring steeper filter edges) the phase characteristics (dispersion) of filters become more and more important. In many cases filter dispersion is an unwanted property to be mitigated, however, it can also be a useful quantity for example to be exploited for compensating fibre dispersion or for pulse compression.

Fibre coupler filters constitute a very simple solution for the separation of two (fairly broad) wavelength bands or for the separation of a monitoring or a pump wavelength channel from wavelength bands. However, in general more sophisticated filter solutions are required for more demanding applications, in particular for channel separation or combination in (D)WDM systems.

Dielectric multi-layer (or thin film) filters are widely used as single or multiple band-pass-, short- or long-pass-, and gain-flattening filters. They are the preferred choice for lower channel counts ( $\leq 8$  channels) and are particularly suited for systems where additional channels are gradually lit.

Fibre Bragg gratings can also be used as single channel filters and for equalizing purposes (long-period gratings), however, their predominant application is in chromatic (channelized) fibre dispersion compensators based upon chirped FBGs.

In contrast to TFF or FBG filters, which select one channel at a time, arrayed waveguide gratings separate (or combine) a large number of channels simultaneously and for that reason they are primarily used as add/drop multiplexers with larger numbers ( $> 8$ ) of wavelength channels. AWGs can also be used for routing purposes, for example in optical cross-connects, and they enable the upgrade of passive optical networks via overlay of additional WDM channels. Finally, GaInAsP-based AWGs have become subcomponents of various photonic integrated circuits ranging from fairly simple multi-wavelength sources to a complete monolithic 40-channel transmitter.

Fabry–Pérot interferometers/filters have been known for many years already and have found different applications in fibre optic systems. These include wavelength locking of emitters for DWDM or ultra DWDM transmitters, wavelength monitoring, and fast and precise channel selection in dynamic multi-wavelength systems. One specific variety of FPIs are Gires–Tournois interferometers which can be combined with a Michelson interferometer in such a way that an optical channel (de-)interleaver is obtained. However, optical interleavers can also be built based upon a number of other approaches. Interleavers are particularly suited for upgrading existing WDM systems by halving the minimum system channel separation (via the interleaver) without the need to individually upgrade any of the other wavelength filters.

3D diffraction gratings (surface relief reflection, surface relief transmission, and volume-phase holographic gratings) are key components for many (spectroscopic) applications and they have also been adapted to the specific needs of fibre-optic

communication systems, however, the corresponding interest has apparently declined in the last few years. Planar diffraction gratings have been developed in various material systems as subcomponents for OEICs; commercial product status has not yet been reached, but planar gratings have found renewed and strong interest in the field of silicon photonics. Microring resonator-based filters are also estimated to have particularly good future prospects for silicon photonics solutions primarily due to their cascadability and their very small footprint.

## References

1. W.J. Tomlinson, Wavelength multiplexing in multimode optical fibers. *Appl. Opt.* **16**, 2180–2194 (1977)
2. K. Kobayashi, M. Seki, Microoptic grating multiplexers and optical isolators for fiber-optic communications. *IEEE J. Quantum Electron.* **QE-16**, 11–22 (1980)
3. J. Lipson, C.A. Young, P.D. Yeates, J.C. Masland, S.A. Wartonick, G.T. Harvey, P.H. Read, A four-channel lightwave subsystem using wavelength division multiplexing. *J. Lightw. Technol.* **LT-3**, 16–20 (1985)
4. N. Lewis, M. Miller, J. Ravita, R. Winfrey, M. Page, W. Lewis, A four channel bi-directional data link using wavelength division multiplexing, *9th Internat. Fiber Optic Communications and Local Area Networks Exposition (FOCLAN85)*, San Francisco, CA, USA, 18–20 Sept. 1985. *Proc. SPIE*, vol. 574 (1985), pp. 47–54
5. T. Ohara, H. Takahara, T. Yamamoto, H. Masuda, T. Morioka, M. Abe, H. Takahashi, Over 1000 channel, 6.25 GHz-spaced ultra-DWDM transmission with supercontinuum multi-carrier source, *Opt. Fiber Commun. Conf. (OFC'2005)*, Techn. Digest (Anaheim, CA, USA, 2005), paper OWA6
6. A.H. Gnauck, G. Charlet, P. Tran, P.J. Winzer, C.R. Doerr, J.C. Centanni, E.C. Burrows, T. Kawanishi, T. Sakamoto, K. Higuma, 25.6-Tb/s WDM transmission of polarization-multiplexed RZ-DQPSK signals. *J. Lightw. Technol.* **26**, 79–84 (2008)
7. C.K. Madsen, J.H. Zhao, *Optical Filter Design and Analysis, a Signal Processing Approach* (Wiley, New York, 1999)
8. C. Peucheret, Phase characteristics of optical filters, in *Wavelength Filters in Fibre Optics*, ed. by H. Venghaus (Springer, Berlin, Heidelberg, 2006), Chap. 2
9. G. Lenz, B.J. Eggleton, C.R. Giles, C.K. Madsen, R.E. Slusher, Dispersive properties of optical filters for WDM systems. *IEEE J. Quantum. Electron.* **34**, 1390–1402 (1998)
10. L. Poladian, Group delay reconstruction for fiber Bragg gratings in reflection and transmission. *Opt. Lett.* **22**, 1571–1573 (1997)
11. M. Tilsch, C.A. Hulse, F.K. Zernik, R.A. Modavis, C.J. Addiego, R.B. Sargent, N.A. O'Brien, H. Pinkney, A.V. Turukhin, Experimental demonstration of thin-film dispersion compensation for 50-GHz filters. *IEEE Photon. Technol. Lett.* **15**, 66–68 (2003)
12. B. Costa, D. Mazzoni, M. Puleo, E. Vezzoni, Phase shift technique for the measurement of chromatic dispersion in optical fibers using LED's. *IEEE J. Quantum Electron.* **QE-18**, 1509–1514 (1982)
13. S. Ryu, Y. Horichi, K. Mochizuki, Novel chromatic dispersion measurement method over continuous gigahertz tuning range. *J. Lightw. Technol.* **7**, 1177–1180 (1989)
14. G. Genty, T. Niemi, H. Ludvigsen, New method to improve the accuracy of group delay measurements using the phase-shift technique. *Opt. Commun.* **204**, 119–126 (2002)
15. X. Yi, F. Wei, Y. Wang, C. Lu, W.D. Zong, Group delay measurement of WDM components using photonic microwave technique. *Microwave Opt. Technol. Lett.* **35**, 346–348 (2002)
16. A.J. Barlow, R.S. Jones, K.W. Forsyth, Technique for direct measurement of single-mode fiber chromatic dispersion. *J. Lightw. Technol.* **LT-5**, 1207–1213 (1987)

17. S.E. Mechels, J.B. Schlager, D.L. Franzen, Accurate measurements of the zero-dispersion wavelength in optical fibers. *J. Res. Natl. Inst. Stand. Technol.* **102**, 333–347 (1997)
18. S.D. Dyer, K.B. Rochford, A.H. Rose, Fast and accurate low-coherence interferometric measurement of fiber Bragg grating dispersion and reflectance. *Opt. Express* **5**, 262–266 (1999)
19. C. Peucheret, F. Liu, R.J.S. Pedersen, Measurement of small dispersion values in optical components. *Electron. Lett.* **35**, 409–411 (1999)
20. K. Ogawa, Characterization of chromatic dispersion of optical filters by high-stability real-time spectral interferometry. *Appl. Opt.* **45**, 6718–6722 (2006)
21. D. Dai, W. Mei, S. He, Using a tapered MMI to flatten the passband of an AWG. *Opt. Commun.* **219**, 233–239 (2003)
22. M.G. Thompson, D. Brady, S.W. Roberts, Chromatic dispersion and bandshape improvement of SOI flatband AWG multi/demultiplexers by phase-error correction. *IEEE Photon. Technol. Lett.* **15**, 924–926 (2003)
23. H.-J. Deyerl, C. Peucheret, B. Zsigri, F. Floreani, N. Plougmann, S.J. Hewlett, M. Kristensen, P. Jeppesen, A compact low dispersion fiber Bragg grating with high detuning tolerance for advanced modulation formats. *Opt. Commun.* **247**, 93–100 (2005)
24. M. Ibsen, R. Fececi, P. Petropoulos, M.N. Zervas, High reflectivity linear-phase fibre Bragg gratings, *Proc. 26th Europ. Conf. Opt. Commun. (ECOC'00)*, Berlin, Germany (2000), vol. 1, pp. 53–54
25. X.X. Zhang, Thin film optical filter – an enabling technology for modern optical communication systems, white paper, [www.auxora.com](http://www.auxora.com), in *Active and Passive Optical Components for WDM Communications IV*, ed. by A.K. Dutta, A.A.S. Awwal, N.K. Dutta, Y. Ohishi. *Proc. SPIE*, vol. 5595 (2004), pp. 349–358. doi: 10.1117/12.580087
26. F. Havermeyer, W. Liu, C. Moser, D. Psaltis, G.J. Steckman, Volume holographic grating-based continuously tunable optical filter. *Opt. Eng.* **43**, 2017–2021 (2004)
27. H. Chotard, Y. Painchaud, A. Mailloux, M. Morin, F. Trépanier, M. Guy, Group delay ripple of cascaded Bragg grating gain flattening filters. *IEEE Photon. Technol. Lett.* **14**, 1130–1132 (2002)
28. L. Poladian, Understanding profile-induced group-delay ripple in Bragg gratings. *Appl. Opt.* **39**, 1920–1923 (2000)
29. S. Jamal, J.C. Cartledge, Variation in the performance of multispan 10-Gb/s systems due to the group delay ripple of dispersion compensating fiber Bragg gratings. *J. Lightw. Technol.* **20**, 28–35 (2002)
30. L.-S. Yan, T. Luo, Q. Yu, Y. Xie, K.-M. Feng, R. Khosravani, A.E. Willner, Investigation of performance variations due to the amplitude of group-delay ripple in chirped fiber Bragg gratings. *Opt. Fiber Technol.* **12**, 238–242 (2006)
31. H. Geiger, M. Ibsen, Complexity limitations of optical networks from out-of-band dispersion of grating filters, *Proc. 24th Europ. Conf. Opt. Commun. (ECOC'98)*, Madrid, Spain (1998), pp. 405–406
32. G. Castanon, T. Hoshida, Impact of filter dispersion slope in NRZ, CS-RZ, IMDPSK and RZ formats on ultra high bit-rate systems, *Proc. 28th Europ. Conf. Opt. Commun. (ECOC'02)*, Copenhagen, Denmark (2002), vol. 4, paper 9.6.1
33. M. Lee, N. Antoniadis, On the impact of filter dispersion slope on the performance of 40 Gbps DWDM systems and networks. *Photon. Netw. Commun.* **14**, 97–102 (2007). doi: 10.1007/s11107-006-0051-0
34. M. Kuznetsov, N.M. Froberg, S.R. Henion, K.A. Rauschenbach, Power penalty for optical signals due to dispersion slope in WDM filter cascades. *IEEE Photon. Technol. Lett.* **11**, 1411–1413 (1999)
35. C. Riziotis, M.N. Zervas, Effect of in-band group delay ripple on WDM filter performance, *Proc. 27th Europ. Conf. Opt. Commun. (ECOC'01)*, Amsterdam, The Netherlands (2001), paper Th.M.1.3, pp. 492–493
36. A. Dochhan, G. Göger, S. Smolorz, H. Rohde, W. Rosenkranz, The influence of FBG phase ripple distortions – comparisons of different modulation formats, *Opt. Fiber Commun. Conf. and Nat. Fiber Opt. Eng. Conf. (OFC/NFOEC'2008)*, Techn. Digest (San Diego, CA, USA, 2008), paper JWA60

37. V. Veljanovski, M. Alfiad, D. van den Borne, S.L. Jansen, T. Wuth, Equalization of FBG-induced group-delay ripples penalties using a coherent receiver and digital signal processing, *Opt. Fiber Commun. Conf. and Nat. Fiber Opt. Eng. Conf. (OFC/NFOEC'2009)*, Techn. Digest (San Diego, CA, USA, 2009), paper JThA40
38. A. Dochhan, S. Smolorz, H. Rohde, W. Rosenkranz, Electronic equalization of FBG phase ripple distortions in 43 Gb/s WDM systems, *Proc. 10th ITG Topical Meeting Photon. Networks*, 04–05 May, 2009, Leipzig, Germany (2009), pp. 175–181
39. J.T. Mok, J.L. Blows, B.J. Eggleton, Investigation of group delay ripple distorted signals transmitted through all-optical 2R regenerators. *Opt. Express* **12**, 4411–4422 (2004)
40. D. Marcuse, *Theory of Dielectric Optical Waveguides*, 2nd edn. (Academic, New York, 1991)
41. H. Kogelnik, Theory of optical waveguides, in *Guided-Wave Optoelectronics*, ed. by T. Tamir (Springer, Berlin, 1988), Chap. 2
42. S.L. Chuang, *Physics of Photonic Devices*, 2nd edn. (Wiley, Hoboken, 2009)
43. K. Jędrzejewski, Biconical fused taper – a universal fibre devices technology. *Opto-Electr. Rev.* **8**, 153–159 (2000)
44. M. Rusu, O.G. Okhotnikov, Practical method for fabricating dense WDM fiber couplers with arbitrary wavelength channels, in *Advanced Topics in Optoelectronics, Microelectronics, and Nanotechnologies*, ed. by O. Iancu, A. Manea, D. Cojoc. *Proc. SPIE*, vol. 5227 (2003), pp. 402–409
45. [www.foc-fo.de](http://www.foc-fo.de)
46. J.H. Chang, B.G. Jeon, J.K. Kang, J.H. Jung, Y.K. Kim, Characteristics of optical fiber WDM with high isolation, *Proc. 1999 IEEE Region 10 Conf.*, The Silla Cheju, Cheju Islands, Korea, Sept. 15–17, 1999
47. [www.newport.com](http://www.newport.com)
48. [www.itflabs.com](http://www.itflabs.com)
49. M. Born, E. Wolf, *Principles of Optics*, 6th edn. (Pergamon, Oxford, 1980)
50. *Diffraction Gratings Handbook*, 6th edn., ed. by C. Palmer, 1st edn. (E. Loewen, Newport, 2005)
51. J.P. Laude, Diffraction gratings WDM components, in *Wavelength Filters in Fibre Optics*, ed. by H. Venghaus (Springer, Berlin, 2006), Chap. 3
52. [www.yenista.com](http://www.yenista.com)
53. [www.ibsen.dk](http://www.ibsen.dk)
54. [www.kosi.com](http://www.kosi.com)
55. [www.wasatchphotonics.com](http://www.wasatchphotonics.com)
56. J.B.D. Soole, K.R. Poguntke, A. Scherer, H.P. LeBlanc, C. Chang-Hasnain, J.R. Hayes, C. Caneau, R. Bhat, M.A. Koza, Wavelength-selectable laser emission from a multistripe array grating integrated cavity laser. *Appl. Phys. Lett.* **61**, 2750–2752 (1992)
57. C. Cremer, N. Emeis, M. Schier, G. Heise, G. Ebbinghaus, L. Stoll, Grating spectrograph integrated with photodiode array in InGaAsP/InP. *IEEE Photon. Technol. Lett.* **4**, 108–110 (1992)
58. H. Jian-Jun, B. Lamontagne, A. Delage, L. Erickson, M. Davies, E.S. Koteles, Monolithic integrated wavelength demultiplexer based on a waveguide Rowland circle grating in InGaAsP/InP. *J. Lightw. Technol.* **16**, 631–638 (1998)
59. A. Densmore, V.I. Tolstikhin, K. Primenov, DWDM data receiver based on monolithic integration of an echelle grating demultiplexer and waveguide photodiodes. *Electron. Lett.* **41**, 766–767 (2005)
60. S. Janz, A. Balakrishnan, S. Charbonneau, P. Cheben, M. Cloutier, A. Delâge, K. Dossou, L. Erickson, M. Gao, P.A. Krug, B. Lamontagne, M. Packirisamy, M. Pearson, D.X. Xu, Planar waveguide echelle gratings in silica-on-silicon. *IEEE Photon. Technol. Lett.* **16**, 503–505 (2004)
61. W. Wang, Y. Tang, Y. Wang, H. Qu, Y. Wu, T. Li, J. Yang, Y. Wang, M. Liu, Etched-diffraction-grating-based planar waveguide demultiplexer on silicon-on-insulator. *Opt. Quantum Electron.* **36**, 559–566 (2004)



62. E. Bissaillon, D.T. Tan, J. Laniel, A. Jugessur, L. Chrostowski, A.G. Kirk, A shallow-etched distributed-grating wavelength demultiplexer in SOI, in *Integrated Photonics Research and Applications/Nanophotonics*, Techn. Digest (CD) (Optical Society of America, 2006), paper IWA2
63. J. Brouckaert, W. Bogaerts, P. Dumon, D. Van Thourhout, R. Baets, Planar concave grating demultiplexer fabricated on a nanophotonic silicon-on-insulator platform. *J. Lightw. Technol.* **25**, 1269–1275 (2007)
64. F. Horst, Silicon integrated waveguide devices for filtering and wavelength demultiplexing, *Opt. Fiber Commun. Conf. and Nat. Fiber Opt. Eng. Conf. (OFC/NFOEC'10)*, Techn. Digest (San Diego, CA, USA, 2010), paper OWJ3
65. M.K. Smit, New focusing and dispersive planar component based on an optical phased array. *Electron. Lett.* **24**, 385–386 (1988)
66. H. Takahashi, S. Suzuki, K. Kato, I. Nishi, Arrayed-waveguide grating for wavelength division multi/demultiplexer with nanometer resolution. *Electron. Lett.* **26**, 87–88 (1990)
67. C. Dragone, An NxN optical multiplexer using a planar arrangement of two star couplers. *IEEE Photon. Technol. Lett.* **3**, 812–815 (1991)
68. C. van Dam, InP-based polarization independent wavelength demultiplexers, PhD thesis, Delft University of Technology, The Netherlands (1997). ISBN: 90-9010798-3
69. X.J.M. Leitjens, B. Kuhlou, M.K. Smit, Arrayed waveguide gratings, in *Wavelength Filters in Fibre Optics*, ed. by H. Venghaus (Springer, Berlin, 2006), Chap. 4
70. M.K. Smit, C. van Dam, PHASAR-based WDM-devices: principles, design and applications. *IEEE J. Sel. Top. Quantum Electron.* **2**, 236–250 (1996)
71. J.B.D. Soole, M.R. Amersfoort, H.P. LeBlanc, N.C. Andreadakis, A. Rajhel, C. Caneau, R. Bhat, M.A. Koza, C. Youtsey, I. Adesida, Use of multimode interference couplers to broaden the passband of wavelength-dispersive integrated WDM filters. *IEEE Photon. Technol. Lett.* **8**, 1340–1342 (1996)
72. M.R. Amersfoort, J.B.D. Soole, H.P. LeBlanc, N.C. Andreadakis, A. Rajhel, C. Caneau, Passband broadening of integrated arrayed waveguide filters using multimode interference couplers. *Electron. Lett.* **32**, 449–451 (1996)
73. K. Okamoto, A. Sugita, Flat spectral response arrayed-waveguide grating multiplexer with parabolic waveguide horns. *Electron. Lett.* **32**, 1661–1662 (1996)
74. C.G.P. Herben, X.J.M. Leitjens, D.H.P. Maat, H. Blok, M.K. Smit, Crosstalk performance of integrated optical cross-connects. *J. Lightw. Technol.* **17**, 1126–1134 (1999)
75. U. Hilbk, T. Hermes, J. Saniter, F.-J. Westphal, High capacity WDM overlay on a passive optical network. *Electron. Lett.* **32**, 2162–2163 (1996)
76. S. Das, B. Grek, J. Sun, M. Jain, L.G. Kazowski, MAWG: Multicasting arrayed waveguide grating for WDM-PON applications, *Opt. Fiber Commun. Conf. and Nat. Fiber Opt. Eng. Conf. (OFC/NFOEC'2008)*, Techn. Digest (San Diego, CA, USA, 2008), paper JWA35
77. Y. Hida, Y. Hibino, H. Okazaki, Y. Ohmori, 10 m-long silica-based waveguide with a loss of 1.7 dB/m, *Integrated Photonics Research (IPR'95)*, Techn. Digest (Dana Point, CA, USA, 1995), pp. 49–51
78. Y. Hibino, H. Okazaki, Y. Hida, Y. Ohmori, Propagation loss characteristics of long silica-based optical waveguides on 5-inch Si wafers. *Electron. Lett.* **29**, 1847–1848 (1993)
79. [www.enablence.com](http://www.enablence.com)
80. Y. Inoue, A. Kaneko, F. Hanawa, H. Takahashi, K. Hattori, S. Sumida, Athermal silica-based arrayed-waveguide grating multiplexer. *Electron. Lett.* **33**, 1945–1947 (1997)
81. G. Heise, H.W. Schneider, P.C. Clemens, Optical phased array filter module with passively compensated temperature dependence, *Proc. 24th Europ. Conf. Opt. Commun. (ECOC'98)*, Madrid, Spain (1998), pp. 319–320
82. A.J. Ticknor, B.P. McGinnis, T. Tarter, M. Yan, Efficient passive and active wavelength-stabilization techniques for AWGs and integrated optical filters, *Opt. Fiber Commun. Conf. (OFC'2005)*, Techn. Digest (Anaheim, CA, USA, 2005), paper NThL3
83. [www.neophotonics.com](http://www.neophotonics.com)

84. Y. Hida, Y. Hibino, T. Kitoh, Y. Inoue, T. Shibata, A. Himeno, 400-channel 25-GHz spacing arrayed-waveguide grating covering a full range of C- and L-bands, *Opt. Fiber Commun. Conf. (OFC'2001)*, Techn. Digest (Anaheim, CA, USA, 2001), paper WB2
85. K. Takada, M. Abe, T. Shibata, K. Okamoto, 5 GHz-spaced 4200-channel two-stage tandem demultiplexer for ultra-multi-wavelength light source using supercontinuum generation. *Electron. Lett.* **38**, 572–573 (2002)
86. NTT Photonics Labs, Annual Report 2005
87. K. Takada, M. Abe, T. Shibata, K. Okamoto, 1-GHz-spaced 16-channel arrayed-waveguide grating for a wavelength reference standard in DWDM network systems. *J. Lightw. Technol.* **20**, 850–853 (2002)
88. M. Zirngibl, C. Dragone, C.H. Joyner, Demonstration of a  $15 \times 15$  arrayed waveguide multiplexer on InP. *IEEE Photon. Technol. Lett.* **4**, 1250–1253 (1992)
89. F.M. Soares, W. Jiang, N.K. Fontaine, S.W. Seo, J.H. Baek, R.G. Broeke, J. Cao, K. Okamoto, F. Olsson, S. Lourdudoss, S.J.B. Yoo, InP-based arrayed-waveguide grating with a channel spacing of 10 GHz, *Opt. Fiber Commun. Conf. and Nat. Fiber Opt. Eng. Conf. (OFC/NFOEC'2008)*, Techn. Digest (San Diego, CA, USA, 2008), paper JThA.23
90. R. Nagarajan, M. Smit, Photonic integration. *IEEE LEOS Newsletter* **21**, 4–10 (2007)
91. S.C. Nicholes, M.L. Mašanović, B. Jevremović, E. Lively, L.A. Coldren, D.J. Blumenthal, The world's first InP  $8 \times 8$  monolithic tunable optical router (MOTOR) operating at 40 Gbps line rate per port, *Opt. Fiber Commun. Conf. and Nat. Fiber Opt. Eng. Conf. (OFC/NFOEC 2009)*, Techn. Digest (San Diego, CA, USA, 2009), post-deadline paper PDP.B1
92. R. Nagarajan, M. Kato, S. Corzine, P. Evans, C. Joyner, R. Schneider, F. Kish, D. Welch, Monolithic, multi-channel DWDM transmitter photonic integrated circuits, *Proc. 21st IEEE Int. Semicond. Laser Conf. (ISLC2008)*, Sorrento, Italy, 14–18 Sept. 2008, paper MA3. doi: 10.1109/ISLC.2008.4635981
93. www.infinera.com
94. J. Kobayashi, Y. Inoue, T. Matsuura, T. Maruno, Tunable and polarization-insensitive arrayed-waveguide grating multiplexer fabricated from fluorinated polyimides. *IEICE Trans. Electron.* **E81-C**, 1020–1026 (1998)
95. Jia Jiang, C.L. Callender, C. Blanchetiere, J.P. Noad, S. Chen, J. Ballato, D.W. Smith, Jr., Arrayed waveguide gratings based on perfluorocyclobutane polymers for CWDM applications. *IEEE Photon. Technol. Lett.* **18**, 370–372 (2006)
96. J.-M. Lee, J.T. Ahn, S. Park, M.-H. Lee, Athermal polymeric arrayed-waveguide grating by partial detachment from a Si substrate. *ETRI Journal* **26**, 281–284 (2004)
97. K.O. Hill, Y. Fujii, D.C. Johnson, B.S. Kawasaki, Photosensitivity in optical fiber waveguides: Application to reflection filter fabrication. *Appl. Phys. Lett.* **32**, 647–649 (1978)
98. B.S. Kawasaki, K.O. Hill, D.C. Johnson, Y. Fujii, Narrow-band Bragg reflectors in optical fibers. *Opt. Lett.* **3**, 66–68 (1978)
99. G. Meltz, W.W. Morey, W.H. Glenn, Formation of Bragg gratings in optical fibers by a transverse holographic method. *Opt. Lett.* **14**, 823–825 (1989)
100. A. Othonos, K. Kalli, *Fiber Bragg Gratings: Fundamentals and Applications in Telecommunications and Sensing* (Artech, Boston, 1999)
101. R. Paschotta, *Encyclopedia of Laser Physics and Technology* (Wiley-VCH, Berlin, 2008)
102. P.St.J. Russell, J.L. Archambault, L. Reekie, Fiber gratings, *Physics World*, October 1993 issue, 41–46 (1993)
103. H. Patrick, S.L. Gilbert, Growth of Bragg gratings produced by continuous-wave ultraviolet light in optical fiber. *Opt. Lett.* **18**, 1484–1486 (1993)
104. Y. Liu, J.A.R. Williams, L. Zhang, I. Bennion, Abnormal spectral evolution of fibre Bragg gratings in hydrogenated fibres. *Opt. Lett.* **27**, 586–588 (2002)
105. A.G. Simpson, K. Kalli, K. Zhou, L. Zhang, I. Bennion, Formation of type IA fibre Bragg gratings in germanosilicate optical fibre. *Electron. Lett.* **40**, 163–164 (2004)
106. I. Riant, F. Haller, Study of the photosensitivity at 193 nm and comparison with photosensitivity at 240 nm. Influence of fiber tension: type IIA aging. *J. Lightw. Technol.* **15**, 1464–1469 (1997)

107. J.L. Archambault, L. Reekie, P.St.J. Russell, High reflectivity and narrow bandwidth fibre gratings written by single excimer pulse. *Electron. Lett.* **29**, 28–29 (1993)
108. T. Erdogan, Fiber grating spectra. *J. Lightw. Technol.* **15**, 1277–1294 (1997)
109. A. Othonos, K. Kalli, D. Pureur, A. Mugnier, Fibre Bragg gratings, in *Wavelength Filters in Fibre Optics*, ed. by H. Venghaus (Springer, Berlin, 2006), Chap. 5
110. www.gouldfo.com
111. www.broptics.com
112. www.aos-fiber.com
113. www.teraxion.com
114. www.redferncomponents.com
115. M. Li, H. Li, Reflection equalization of the simultaneous dispersion and dispersion-slope compensator based on a phase-only sampled fiber Bragg grating. *Opt. Express* **16**, 9821–9828 (2008)
116. M. Li, T. Takahagi, K. Ogusu, H. Li, Y. Painchaud, A comprehensive study of the chromatic dispersion measurement of the multi-channel fiber Bragg grating based on an asymmetrical Sagnac loop interferometer. *Opt. Commun.* **281**, 5165–5172 (2008)
117. Y. Painchaud, A. Mailloux, H. Chotard, E. Pelletier, M. Guy, Multi-channel fiber Bragg gratings for dispersion and slope compensation, *Opt. Fiber Commun. Conf. (OFC'02)*, Techn. Digest (Anaheim, CA, USA, 2002), paper ThAA5, pp. 581–582
118. A.M. Vengsarkar, P.J. Lemaire, J.B. Judkins, V. Bhatia, T. Erdogan, J.E. Sipe, Long-period fiber gratings as band-rejection filters. *J. Lightw. Technol.* **14**, 58–65 (1996)
119. K.O. Hill, B. Malo, K. Vineberg, F. Bilodeau, D. Johnson, I. Skinner, Efficient mode-conversion in telecommunication fiber using externally written gratings. *Electron. Lett.* **26**, 1270–1272 (1990)
120. S.A. Vasiliev, E.M. Dianov, A.S. Kurkov, O.I. Medvedkov, V.N. Protopopov, Photoinduced in-fibre refractive-index gratings for core-cladding mode coupling. *Quantum Electron.* **27**, 146–149 (1997)
121. T. Erdogan, Cladding-mode resonances in short- and long-period fiber grating filters. *J. Opt. Soc. Am. A* **14**, 1760–1773 (1997)
122. S.W. James, R.P. Tatam, Optical fiber long-period grating sensors: characteristics and application. *Meas. Sci. Technol.* **14**, R49–R61 (2003)
123. P.-S. Jian, E. Smela, Modeling the performance of a long-period Bragg grating ambient-index sensor. *Smart Mater. Struct.* **15**, 821–828 (2006)
124. X. Fan, I.M. White, S.I. Shopova, H. Zhu, J.D. Suter, Y. Sun, Sensitive optical biosensors for unlabeled targets: A review. *Anal. Chim. Acta* **620**, 8–26 (2008)
125. C. Fabry, A. Pérot, Théorie et applications d'une nouvelle méthode de spectroscopie différentielle. *Ann. Chim. Phys.* **16**, 115–144 (1899)
126. T. Koonen, Fabry–Perot interferometer filters, *Wavelength Filters in Fibre Optics*, ed. by H. Venghaus (Springer, Berlin, 2006), Chap. 6
127. www.micronoptics.com
128. F. Gires, P. Tournois, Interféromètre utilisable pour la compression d'impulsions lumineuses modulées en fréquence. *C.R. Acad. Sci. Paris* **258**, 6112–6115 (1964)
129. M.K. Tilsch, R.B. Sargent, C.A. Hulse, Dielectric multilayer filters, *Wavelength Filters in Fibre Optics*, ed. by H. Venghaus (Springer, Berlin, 2006), Chap. 7
130. H.A. Macleod, *Thin Film Optical Filters* (Institute of Physics Publishing, Dirac House, Temple Back, Bristol, 2001)
131. A. Thelen, *Design of Interference Coatings* (McGraw-Hill, New York, 1989)
132. A. Badeen, M. Briere, P. Hook, C. Montcalm, R. Rinfret, J. Schneider, B.T. Sullivan, Advanced optical coatings for telecom and spectroscopic applications, *Conf. Opt. Systems Design*, 01–05 Sept. 2008, Glasgow, UK/*Advances in Opt. Thin Films III*, ed. by N. Kaiser, M. Lequime, H.A. Macleod. *Proc. SPIE*, vol. 7101 (2008), paper 71010H
133. H. Takahashi, Temperature stability of thin-film narrow-bandpass filters produced by ion assisted deposition. *Appl. Opt.* **34**, 667–675 (1995). Note that the author's last name is misspelled as Takashashi in the article; the correct spelling is Takahashi

134. [www.oxfordplasma.de](http://www.oxfordplasma.de)
135. [www.auxora.com](http://www.auxora.com)
136. [www.iridian.ca](http://www.iridian.ca)
137. [www.jdsu.com](http://www.jdsu.com)
138. N. Kawakami, J. Kobayashi, M. Hikita, A. Kudo, F. Yamamoto, S. Imamura, Filter-embedded four-channel WDM module fabricated from fluorinated polyimide. *J. Lightw. Technol.* **24**, 2388–2393 (2006)
139. N. Keil, Z. Zhang, C. Zawadzki, C. Wagner, A. Scheibe, H. Ehlers, D. Ristau, J. Wang, W. Brinker, N. Grote, Ultra low-loss  $1 \times 2$  multiplexer using thin-film filters on polymer integration platform. *Electron. Lett.* **45**, 1167–1168 (2009)
140. N. Keil, C. Zawadzki, Z. Zhang, J. Wang, N. Mettlich, N. Grote, M. Schell, Polymer PLC as an optical integration bench, *Opt. Fiber Commun. Conf. and Nat. Fiber Opt. Eng. Conf. (OFC/NFOEC'11)*, Techn. Digest (Los Angeles, CA, USA, 2011), paper OWM1
141. R.M. Fortenberry, M.A. Scobey, D.J. Derickson, L.F. Stokes, P.C. Egerton, Chromatic dispersion of thin film filters, *Opt. Fiber Commun. Conf. (OFC'2005)*, Techn. Digest (Anaheim, CA, USA, 2005), paper OFL2
142. [www.oclaro.com](http://www.oclaro.com)
143. K. Nosu, H. Ishio, K. Hashimoto, Multireflection optical multi/demultiplexer using interference filters. *Electron. Lett.* **15**, 414–415 (1979)
144. Y. Okabe, H. Sasaki, A simple wide wavelength division multi/demultiplexer consisting of optical elements, *Opt. Fiber Commun. Conf. (OFC/IOOC'2002)*, Techn. Digest (Anaheim, CA, USA, 2002), pp. 322–323
145. B.E. Little, S.T. Chu, P.P. Absil, J.V. Hryniewicz, F.G. Johnson, F. Seifert, D. Gill, V. Van, O. King, M. Trakalo, Very high-order microring resonator filters for WDM applications. *IEEE Photon. Technol. Lett.* **16**, 2263–2265 (2004)
146. P.P. Absil, S.T. Chu, D. Gill, J.V. Hryniewicz, F. Johnson, O. King, B.E. Little, F. Seifert, V. Van, Very high order integrated optical filters, *Opt. Fiber Commun. Conf. (OFC'2004)*, Techn. Digest (Los Angeles, CA, USA, 2004), paper TuL3
147. G.L. Bona, F. Horst, R. Germann, B.J. Offrein, D. Wiesmann, Tunable dispersion compensator realized in high-refractive-index-contrast SiON technology, *Proc. 28th Europ. Conf. Opt. Commun. (ECOC'02)*, Copenhagen, Denmark (2002), vol. 2, paper 4.2.1
148. M. Ferrera, L. Razzari, D. Duchesse, R. Morandotti, Z. Yang, M. Liscidini, J.E. Sipe, S. Chu, B.E. Little, D.J. Moss, Ultra-low power frequency conversion in two-photon-absorption free micro ring resonator, *Proc. Progress in Electromagn. Res. Symposium (PIERS)* (Beijing, China, 2009), pp. 1291–1294
149. P.P. Absil, J.V. Hryniewicz, B.E. Little, P.S. Cho, R.A. Wilson, L.G. Joneckis, P.-T. Ho, Wavelength conversion in GaAs micro-ring resonators. *Opt. Lett.* **25**, 554–556 (2000)
150. M. Hamacher, U. Troppenz, H. Heidrich, D.G. Rabus, Active ring resonators based on InGaAsP/InP. *Proc. SPIE*, vol. 4947 (2003), pp. 212–222
151. V. Van, T.A. Ibrahim, K. Ritter, P.P. Absil, F.G. Johnson, R. Grover, J. Goldhar, P.-T. Ho, All-optical nonlinear switching in GaAs-AlGaAs microring resonators. *IEEE Photon. Technol. Lett.* **14**, 74–76 (2002)
152. V.R. Almeida, C.A. Barrios, R.R. Panepucci, M. Lipson, All-optical control of light on a silicon chip. *Nature* **431**, 1081–1084 (2004)
153. Q. Xu, B. Schmidt, J. Shakya, M. Lipson, Cascaded silicon micro-ring modulators for WDM optical interconnection. *Opt. Express* **14**, 9430–9435 (2006)
154. A. Chen, H. Sun, A. Pyayt, X. Zhang, J. Luo, A. Jen, P.A. Sullivan, S. Elangovan, L.R. Dalton, R. Dinu, D. Jin, D. Huang, Chromophore-containing polymers for trace explosive sensors. *J. Phys. Chem. C* **112**, 8072–8078 (2008)
155. K. De Vos, I. Bartolozzi, E. Schacht, P. Bienstman, R. Baets, Silicon-on-Insulator microring resonator for sensitive and label-free biosensing. *Opt. Express* **15**, 7610–7615 (2007)
156. A. Yalçın, K.C. Papat, J.C. Aldridge, T.A. Desai, J. Hryniewicz, N. Chbouki, B.E. Little, O. King, V. Van, S. Chu, D. Gill, M. Anthes-Washburn, M.S. Ünlü, B.B. Goldberg, Optical sensing of biomolecules using microring resonators. *IEEE J. Sel. Top. Quantum Electron.* **12**, 148–155 (2006)

157. G. Grover, P. Absil, V. Van, J. Hryniewicz, B.E. Little, O. King, L. Calhoun, F. Johnson, P. Ho, Vertically coupled GaInAsP-InP microring resonators. *Opt. Lett.* **26**, 506–508 (2001)
158. D.G. Rabus, *Integrated Ring Resonators* (Springer, Berlin, 2007)
159. W.W. Lui, T. Hirono, K. Yokohama, W.-P. Huang, Polarization rotation in semiconductor bending waveguides: A coupled-mode theory formulation. *J. Lightw. Technol.* **16**, 929–936 (1998)
160. F. Morichetti, A. Melloni, M. Martinelli, Effects of polarization rotation in optical ring-resonator-based devices. *J. Lightw. Technol.* **24**, 573–585 (2006)
161. C. van Dam, L.H. Spiekman, F.P.G.M. van Ham, G.H. Groen, J.J.G.M. van der Tol, I. Moerman, W.W. Pascher, M. Hamacher, H. Heidrich, C.M. Weinert, M.K. Smit, Novel compact polarization converters based on ultra short bends. *IEEE Photon. Technol. Lett.* **8**, 1346–1348 (1996)
162. F. Morichetti, A. Melloni, Polarization converters based on ring-resonator phase-shifters. *IEEE Photon. Technol. Lett.* **18**, 923–925 (2006)
163. D.H. Geuzebroek, A. Driessen, Ring-resonator-based wavelength filters, in *Wavelength Filters in Fibre Optics*, ed. by H. Venghaus (Springer, Berlin, 2006), Chap. 8
164. B. Little, S. Chu, Wei Chen, J. Hryniewicz, D. Gill, O. King, F. Johnson, R. Davidson, K. Donovan, Wenlu Chen, S. Grubb, Tunable bandwidth microring resonator filters, *Proc. 34th Europ. Conf. Opt. Commun.* (ECOC'08), Brussels, Belgium (2008), vol. 4, paper Th.2.C.2, pp. 81–82
165. Z. Wang, W. Chen, Y.J. Chen, Unit cell design of crossbar switch matrix using micro-ring resonators, *Proc. 30th Europ. Conf. Opt. Commun.* (ECOC'04), Stockholm, Sweden (2004), vol. 3, pp. 462–463
166. A. Melloni, M. Martinelli, Synthesis of direct-coupled-resonators bandpass filters for WDM systems. *J. Lightw. Technol.* **20**, 296–303 (2002)
167. Wei Chen, Wenlu Chen, Y.J. Chen, A characteristic matrix approach for analyzing resonant ring lattice devices. *IEEE Photon. Technol. Lett.* **16**, 458–460 (2004)
168. B.E. Little, H.A. Haus, J.S. Foresi, L.C. Kimmerling, E.P. Ippen, D.J. Ippen, Wavelength switching and routing using absorption and resonance. *IEEE Photon. Technol. Lett.* **10**, 816–818 (1998)
169. H. Shen, J.-P. Chen, X.-W. Li, Y.-P. Wang, Group delay and dispersion analysis of compound high order microring resonator all-pass filters. *Opt. Commun.* **262**, 200–205 (2006)
170. B.E. Little, A VLSI photonics platform, *Opt. Fiber Commun. Conf.* (OFC'2003), Techn. Digest (Atlanta, GA, USA, 2003), vol. 2, paper ThD1, pp. 444–445
171. Y. Yanagase, S. Suzuki, Y. Kokubun, S.T. Chu, Box-like filter response by vertically series coupled microring resonator filter, *Proc. 27th Europ. Conf. Opt. Commun.* (ECOC'01), Amsterdam, The Netherlands (2001), vol. 4, pp. 634–635
172. L.C. Kimerling, L. Dal Negro, S. Saini, Y. Yi, D. Ahn, S. Akiyama, D. Cannon, J. Liu, J.G. Sandland, D. Sparacin, J. Michel, K. Wada, M.R. Watts, Monolithic silicon microphotronics, in *Silicon Photonics*, ed. by L. Pavesi, D.J. Lockwood (Springer, Berlin, 2004), pp. 89–120
173. S. Cao, J. Chen, J.N. Damask, C.R. Doerr, L. Guiziuo, G. Harvey, Y. Hibino, H. Li, S. Suzuki, K.-Y. Wu, P. Xie, Interleaver technology: Comparisons and applications requirements. *J. Lightw. Technol.* **22**, 281–289 (2004)
174. H. Arai, H. Nonen, K. Ohira, T. Chiba, PLC wavelength splitter for a dense WDM transmission system. *Hitachi Cable Rev.* **21**, 11–16 (2002)
175. B. Dingel, M. Izutsu, Multifunctional optical filter with a Michelson-Gires–Tournois interferometer for wavelength-division-multiplexed system applications. *Opt. Lett.* **23**, 1099–1101 (1998)
176. X. Shu, K. Sugden, I. Bennion, Flattop multi-passband filter based on all-fiber Michelson-Gires–Tournois interferometer, *Proc. 30th Europ. Conf. Opt. Commun.* (ECOC'04), Stockholm, Sweden (2004), paper Tu1.3.1
177. M. Kohtoku, S. Oku, Y. Kadota, Y. Shibata, Y. Yoshikuni, 200-GHz FSR periodic multi/demultiplexer with flattened transmission and rejection band by using a Mach–Zehnder interferometer with a ring resonator. *IEEE Photon. Technol. Lett.* **12**, 1174–1176 (2000)

178. J. Song, Q. Fang, S.H. Tao, M.B. Yu, G.Q. Lo, L. Kwong, Proposed silicon wire interleaver structure. *Opt. Express* **16**, 7849–7859 (2008)
179. J. Song, Q. Fang, S.H. Tao, M.B. Yu, G.Q. Lo, D.L. Kwong, Passive ring-assisted Mach-Zehnder interleaver on silicon-on-insulator. *Opt. Express* **16**, 8359–8365 (2008)
180. D. Dai, S. He, Novel ultrasmall Si-nanowire-based arrayed-waveguide grating interleaver with spirals. *Opt. Commun.* **281**, 3471–3475 (2008)
181. R.M. de Ridder, C.G.H. Roeloffzen, Interleavers, in *Wavelength Filters in Fibre Optics*, ed. by H. Venghaus (Springer, Berlin, 2006), Chap. 9
182. <http://www.optoplex.com>
183. <http://www.hitachi-cable.co.jp>
184. D.A. Smith, J.E. Baran, J.J. Johnson, K.-W. Cheung, Integrated-optic acoustically-tunable filters for WDM networks. *IEEE J. Sel. Areas Commun.* **8**, 1151–1159 (1990)
185. S.F. Su, R. Olshansky, G. Joyce, D.A. Smith, J.E. Baran, Gain equalization in multiwavelength lightwave systems using acoustooptic tunable filters. *IEEE Photon. Technol. Lett.* **4**, 269 (1992)
186. J.L. Jackel, M.S. Goodman, J.E. Baran, W.J. Tomlinson, G.-K. Chang, M.Z. Iqbal, G.H. Song, K. Bala, C.A. Brackett, D.A. Smith, R.S. Chakravarthy, R.H. Hobbs, D.J. Fritz, R.W. Ade, K.M. Kissa, Acousto-optic tunable filters (AOTF's) for multiwavelength optical cross-connections: crosstalk considerations. *J. Lightw. Technol.* **14**, 1056–1066 (1996)
187. M.K. Smit, T. Koonen, H. Hermann, W. Sohler, Wavelength-selective devices, in *Fibre Optic Communication Devices*, ed. by N. Grote, H. Venghaus (Springer, Berlin, 2001), Chap. 7
188. <http://www.goochandhousego.com/products/prod/16>
189. J. Brouckaert, W. Bogaerts, S. Selvaraja, P. Dumon, R. Baets, D. Van Thourhout, Planar concave grating demultiplexer with high reflective Bragg reflector facets. *IEEE Photon. Technol. Lett.* **20**, 309–311 (2008)
190. W. Bogaerts, S.K. Selvaraja, P. Dumon, J. Brouckaert, K. De Vos, D. Van Thourhout, R. Baets, Silicon-on-insulator spectral filters fabricated with CMOS technology. *IEEE J. Sel. Top. Quantum Electron.* **16**, 33–44 (2010)
191. I. Giuntioni, P. Ballardares, R. Steingrüber, J. Bruns, K. Petermann, WDM multi-channel filter based on sampled gratings in silicon-on-insulator, *Opt. Fiber Commun. Conf. and Nat. Fiber Opt. Eng. Conf. (OFC/NFOEC'11)*, Techn. Digest (Los Angeles, CA, USA, 2011), paper OThV3
192. F. Horst, W.M.J. Green, B.J. Offrein, Y.A. Vlasov, Silicon-on-insulator echelle grating WDM demultiplexers with two stigmatic points. *IEEE Photon. Technol. Lett.* **21**, 1743–1745 (2009)
193. R. März, *Integrated Optics – Design and Modeling* (Artech, Boston, 1994)
194. [www.luxtera.com](http://www.luxtera.com)
195. J.-M. An, Y.-D. Wu, J. Li, J.-G. Li, H.-J. Wang, J.-Y. Li, X.-W. Hu, Fabrication of triplexers based on flattop SOI AWG. *Chin. Phys. Lett.* **25**, 1717–1719 (2008)
196. K. Sasaki, F. Ohne, A. Motegi, T. Baba, Arrayed waveguide grating of  $70 \times 60 \mu\text{m}^2$  size based on Si photonic wire waveguides. *Electron. Lett.* **41**, 801–802 (2005)
197. P. Cheben, J.H. Schmid, A. Delâge, A. Densmore, S. Janz, B. Lamontagne, J. Lapointe, E. Post, P. Waldron, D.-X. Xu, A high-resolution silicon-on-insulator arrayed waveguide grating microspectrometer with sub-micrometer aperture waveguides. *Opt. Express* **15**, 2299–2306 (2007)
198. L. Wosinski, Nanophotonic devices based on silicon-on-insulator nanowire waveguides, *Proc. 8th Int. Conf. Transparent Opt. Netw. (ICTON 2006)*, Nottingham, UK (2006), paper We.C1.2
199. D. Hirahara, K. Sasaki, T. Ishii, T. Baba, Large birefringence in SOI layer and its application to polarization-insensitive AWG, *5th IEEE Conf. Group IV Photonics*, Sorrento, Italy, 2008, paper FD3
200. Q. Fang, T.-Y. Liow, J.F. Song, K.W. Ang, Y.T. Phang, M.B. Yu, G.Q. Lo, D.L. Kwong, Monolithic silicon photonic DWDM receiver for Terabit data communications, *Opt. Fiber Commun. Conf. and Nat. Fiber Opt. Eng. Conf. (OFC/NFOEC'10)*, Techn. Digest (San Diego, CA, USA, 2010), paper OMI4

201. F. Xia, M. Rooks, L. Sekaric, Y. Vlasov, Ultra-compact high order ring resonator filters using submicron silicon photonic wires for on-chip optical interconnects. *Opt. Express* **15**, 11934–11941 (2007)
202. P. Dong, W. Qian, H. Liang, R. Shafiha, N.-N. Feng, D. Feng, X. Zheng, A.V. Krishnamoorthy, M. Asghari, Low power and compact reconfigurable multiplexing devices based on silicon microring resonators. *Opt. Express* **18**, 9852–9858 (2010)
203. H. Shen, M.H. Khan, L. Fan, L. Zhao, Y. Xuan, J. Ouyang, L.T. Varghese, M. Qi, Eight-channel reconfigurable microring filters with tunable frequency, extinction ratio and bandwidth. *Opt. Express* **18**, 18067–18076 (2010)
204. X. Zheng, I. Shubin, G. Li, T. Pinguet, A. Mekis, J. Yao, H. Thacker, Y. Luo, J. Costa, K. Raj, J.E. Cunningham, A.V. Krishnamoorthy, A tunable  $1 \times 4$  silicon CMOS photonic wavelength multiplexer/demultiplexer for dense optical interconnects. *Opt. Express* **18**, 5151–5160 (2010)
205. T. Tsuchizawa, K. Yamada, H. Fukuda, T. Watanabe, J.-I. Takahashi, M. Takahashi, T. Shoji, E. Tamechika, S.-I. Itabashi, H. Morita, Microphotonics devices based on silicon microfabrication technology. *IEEE J. Sel. Top. Quantum Electron.* **11**, 232–240 (2005)
206. D.W. Kim, A. Barkai, R. Jones, N. Elek, H. Nguyen, A. Liu, Silicon-on-insulator eight-channel optical multiplexer based on a cascade of asymmetric Mach–Zehnder interferometers. *Opt. Lett.* **33**, 530–532 (2008)

# Chapter 10

## Passive Devices

Wolfgang Coenning and François Caloz

**Abstract** The chapter presents devices which ensure the following generic functionalities: i) physically connecting devices, ii) splitting and coupling of light, iii) separating and redirecting light travelling into opposite directions (optical circulators), and iv) isolating light travelling into one direction from that travelling into the reverse direction (optical isolators). The coverage includes theoretical aspects, practical implementations, standardisation issues, and typical characteristics of fibres and fibre-optic cables. The treatment of optical isolators includes their fundamental principles, polarisation-independent, and planar integrated waveguide-based solutions as well.

Fibre-optic networks have experienced tremendous growth during the last few years, starting with backbone or long haul networks over Metro nets and having reached the residential area more recently. The enabling components for this development include lasers, modulators, detectors for example, but passive devices as well and the latter will be the topic of this chapter. The most relevant functionalities of passive devices are i) physically connecting devices, ii) splitting and coupling, but also iii) separating and redirecting light travelling into opposite directions (optical circulators), and iv) isolating light travelling into one direction from that travelling into the reverse direction (optical isolators), and corresponding solutions will be covered in the subsequent paragraphs.

---

Wolfgang Coenning (✉)  
Hochschule Esslingen, Flandernstraße 101, 73732 Esslingen, Germany  
e-mail: wolfgang.coenning@hs-esslingen.de

François Caloz  
Diamond SA, via dei Patrizi 5, 6616 Losone, Switzerland  
e-mail: francois.caloz@diamond-fo.com



## 10.1 Optical Connectors

### 10.1.1 Introduction

The optical fibre connecting devices most widely used are splices and connectors. Splices are permanent connections; they may be fusion splices, where the two fibres are fused together or mechanical splices, where the fibres are mechanically positioned in a semi-permanent way. Optical connectors are passive optical components designed to connect two or more optical fibres in a non-permanent way that may be easily detached and reconnected several times.

Requirements on optical connectors are increasing steadily in parallel with the improvement of fibre-optic technologies. Main technical requirements are low insertion loss, low return loss, stable performance with respect to temperature and during mechanical stress as well as after disconnecting and re-establishing the connection. In addition, connectors have to be reliable, safe and easy to use, and small. They should offer dust protection and protection against wrong handling, and last but not least, the price of optical connectors should be low since that may have a significant influence on the overall price of the system as large quantities of connectors are used in modern fibre-optic networks.

### 10.1.2 Connecting Different Types of Fibres

The main challenge for optical connectors' manufacturers is related to the dimension of the optical fibre and its core since the role of an optical connection is to align the cores of the fibres to be connected. Dimensions of fibre cores range from a few micrometres up to hundreds of micrometres, and as a consequence the requirements on precision of the mechanical alignment range from a few tens of nanometres to tens of micrometres, depending on the fibre type.

Since most of the applications covered by this book are based on single-mode (SM) optical fibre designed to be operated in the wavelength range between 1200 and 1650 nm, we will primarily concentrate on this type of fibre in this chapter. Examples of connector applications using other types of fibres are discussed in Sect. 10.1.9.

Fibres to be connected have to be aligned properly, but a number of alignment errors may negatively affect the performance of the optical connection, and Fig. 10.1 illustrates the most relevant alignment errors: An air gap, fibre core offset and angular misalignment are extrinsic parameters and may be corrected by using the right positioning technology. Mode field diameter mismatch is due to fabrication tolerances of optical fibres, this parameter is intrinsic and can not be corrected by aligning the fibres.

The two key performance parameters that characterise any optical connection are attenuation and return loss. Both place different physical demands on the positioning of the optical fibre in the optical connection interface.

**Fig. 10.1** Main alignment errors affecting performances of fibre-optical connections

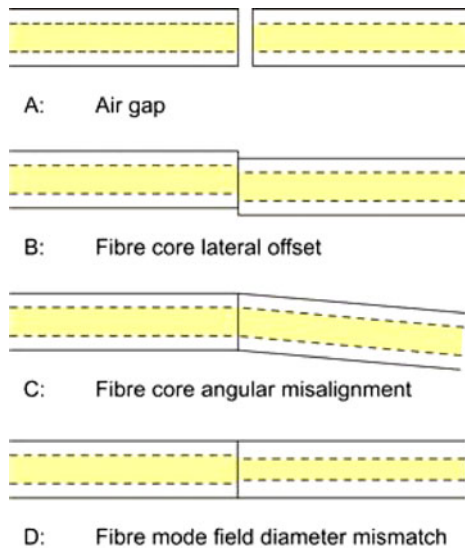
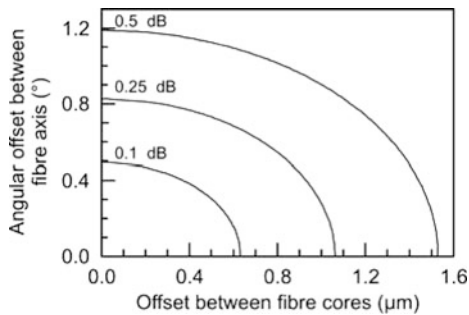


**Fig. 10.2** Lines of equal attenuation of two coupled standard single-mode fibres as a function of lateral and angular offset for 1310 nm operation wavelength

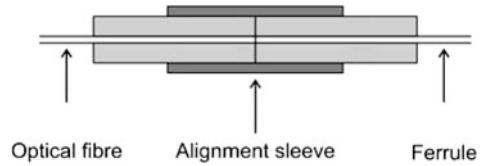


Return loss is primarily affected by end face separation, lateral offset and angular misalignment. Figure 10.2 illustrates the dependence of the coupling loss on lateral and angular offset of two standard non-dispersion shifted single-mode fibres operated at 1310 nm. The curves are obtained under the assumption that both, input and output fibres, are in physical contact (no air gap between the fibres).

The most significant parameters affecting return loss are end face separation, end face high index layer conditions (high index layer thickness and index of refraction) and end face condition.

Environmental conditions may also affect the characteristics of the optical interface. As a consequence, connectors are specified for working under different physical and mechanical conditions, including device classes which ensure that specified performance is guaranteed even under extreme environmental conditions (see Sect. 10.1.4).

**Fig. 10.3** Simplified (schematic) scheme of an optical connection



### 10.1.3 Basics of FO-Connectors

Since fibre dimensions are small (125  $\mu\text{m}$  diameter in the case of standard telecom fibre), they are difficult to handle, process, polish and align. The most common way of solving these difficulties is to fix the fibre in an object of larger dimensions (ferrule) prior to proceeding to any further handling of the fibre.

Ferrules are high precision tubes with outer diameter controlled with sub-micron precision and a hole in the centre which has a diameter of the optical fibre cladding, and they are available for one single fibre only or up to 72 fibres being handled. In this chapter, we will mainly focus on single fibre connectors.

So far, three different types of ferrules are standardised:

- Mono-bloc ferrules, that are one material (ceramics) ferrules, usually referred to as full zirconium ferrule (IEC 61755-3-1/IEC 61755-3-2).
- Multi-material ferrules, which are composed by an outer ceramic tube with a Cu/Ni metallic insert in the centre. These ferrules are referred to as composite ferrules (IEC 61755-3-5/IEC 61755-3-6).
- Multi-material ferrules, which are composed by an outer ceramic tube with a titanium metallic insert in the centre. These ferrules are referred to as composite ferrules (IEC 61755-3-7/IEC 61755-3-8).

Single fibre connectors usually rely on cylindrical ferrules with diameters ranging from 1.25 mm up to 3.2 mm (the most frequently used ferrule diameters are 2.5 and 1.25 mm). The fibre is fixed in the ferrule hole, and the end faces of the ferrules are then polished in order to enable physical contact between the two fibres to be connected. Two ferrules are then brought into contact through a precision sleeve which has the role of guiding them one in front of the other, as illustrated in Fig. 10.3. The reference surface for the alignment is the outer diameter of the ferrule. Therefore, if the fibre cores are positioned exactly in the centre of the ferrules, aligning the two ferrules' outer diameters will perfectly align the two fibre cores.

The ferrule is then assembled into a connector body which has the function of guiding the ferrules' axial positions as well as to orientate them in order to bring them into the right position and to guarantee the necessary compression force. Most of the optical connections have a plug-adapter-plug design, where the spring-loaded ferrules are assembled in the plug-part (also called "connector"), whereas the alignment sleeve is contained in the adapter.

Polishing of the ferrule end face may be straight or angled, depending on the optical performance requirement and particularly the return loss.

**Table 10.1** Examples of performance categories (IEC 61753-standard series)

Category	Environment	Operating conditions
C	indoor controlled	Operating temperature: $-10\text{ }^{\circ}\text{C} \leq T \leq +60\text{ }^{\circ}\text{C}$ Relative humidity: 5–93 %
U or O	outdoor uncontrolled	Operating temperature: $-40\text{ }^{\circ}\text{C} \leq T \leq +75\text{ }^{\circ}\text{C}$ Relative humidity: 0–100 %
I	industrial	Operating temperature: $-40\text{ }^{\circ}\text{C} \leq T \leq +70\text{ }^{\circ}\text{C}$ Relative humidity: 0–95 %
E	extreme	Proposal: $-45\text{ }^{\circ}\text{C} \leq T \leq +85\text{ }^{\circ}\text{C}$

### 10.1.4 Relevant Standards for Optical Connectors

Different standard series have been developed by international standardisation bodies (IEC, CENELEC, TIA, . . .) to specify optical connectors, in particular their optical and mechanical characteristics as well as performance, reliability and test and measurement procedures in order to determine these quantities. The main purpose of these standards is to ensure that products conforming to the standard will work together repeatedly to a known level of optical performance without the need for compatibility testing or cross checking, and this has to be true for the combination of any products from any manufacturer.

The optical interface standard (IEC 61755-series) defines the location of the fibre core in relation to the datum target and the following key parameters: lateral offset, end face separation, end face angle, end face high index layer condition. If these requirements are met, (in particular) attenuation and return loss performance in a randomly mated pair of fibres of the same type will be within the appropriate specifications.

Performance standards (IEC 61753-series) describe different service environments in which connectors may be used as illustrated in Table 10.1. Connectors are generally designed for operation in specific categories, and materials may also be suitable for specific categories only. For example, zirconium ferrule material is suited for all environmental categories, while the polymer material specified for some rectangular ferrules may only be applicable for controlled indoor environment.

The categories given in Table 10.1 are related to the following typical environments:

- C: Office, equipment room, telecommunication centre or building, not subjected to condensed water.
- U or O: Outdoors but enclosed or covered. Locations: shacks, lofts, telephone booths, street cabinets, garages, cellars, building entrances and unattended equipment stations. Subject to condensed water and limited wind driven precipitation, in close proximity of sand or dust.
- I: Automation islands.
- E: Outside plants with direct exposure of components to the environment.

**Table 10.2** Attenuation grades for single-mode fibre-optical connectors (IEC 61755-1)

Attenuation Grade	Attenuation ( $\geq 97\%$ ) <sup>a</sup>	Average	Note
A	–	–	Reserved for future applications
B	$\leq 0.25$ dB	$\leq 0.12$ dB	
C	$\leq 0.5$ dB	$\leq 0.25$ dB	
D	$\leq 1$ dB	$\leq 0.5$ dB	

<sup>a</sup> The probability of a random mated connector set of meeting or exceeding the specified level of attenuation will be  $\geq 97\%$ . This performance is reached considering a statistical distribution of connectors' parameters (MFD, eccentricity and tilt angle) and using a nominal value for the wavelength.

Finally, there exist reliability and test standards similar to the ones for other OE-ICs as well and these will not be described in more detail here.

Mechanical interface standards (IEC 61754-series) provide both manufacturer and user with all the information required to manufacture or use the product in conformity with the physical features foreseen by that standard interface. Mechanical interface standards fully define and dimension the features essential for the mating and un-mating of optical fibre connectors and other components.

### ***10.1.5 Optical Requirements for Single-mode FO-Connectors***

#### **10.1.5.1 Insertion Loss and Alignment Requirements**

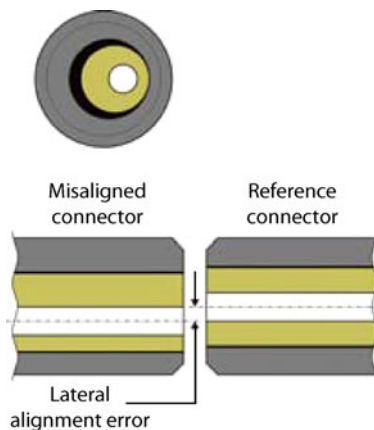
Connectors fall into different attenuation grade categories as illustrated in Table 10.2 and applicable to any pair of randomly mated connectors. For example, any grade B connector mated with any other grade B connector will have an insertion loss smaller than 0.25 dB with a probability of better than 97%.

The achievable insertion loss (attenuation) for fibre-optic connectors is directly related to the precision of the alignment of the two connecting fibres.

Ferrule hole concentricity and diameter, fibre cladding diameter and fibre core concentricity are the main contributions to the eccentricity of the fibre core position relative to the centre of the ferrule. The sum of all these tolerances usually leads to overall values for fibre eccentricity in the order of typically 1 to 2  $\mu\text{m}$ . However, dedicated composite ferrule technology allows centring of the fibre core by deformation of a metallic insert in such a way that the residual fibre core eccentricity is lower than 0.1  $\mu\text{m}$  and therefore high performance, low loss connectors become possible (see [1]).

Figure 10.4 displays a ferrule with an eccentric connector core, and a solution, which enables one to experimentally determine the eccentricity, as illustrated in Fig. 10.5.

**Fig. 10.4** Sketch of a ferrule with off-centred fibre, in comparison with an ideally perfect “reference connector”



During the measurement, the fibre core is illuminated and the ferrule is rotated in a precision sleeve in front of a microscope and a CCD camera. The fibre core concentricity is defined as the diameter of the circular trajectory of the fibre core image. The position of the fibre core may be corrected using a special crimping tool. Using this technology, Diamond was able to develop a low loss connector class that was named “0.1 dB”, allowing reaching random attenuation values smaller than 0.1 dB [1].

#### 10.1.5.2 Return Loss and End Face Geometry Requirements for Contacting Fibres

In order to achieve a stable optical connection, physical contact between the input and output fibres is needed. Lack of optical contact would result in high and unstable insertion loss of the connection, and it would have an even larger effect on the return loss (see Fig. 10.6). As a consequence, it is essential to avoid any air gap

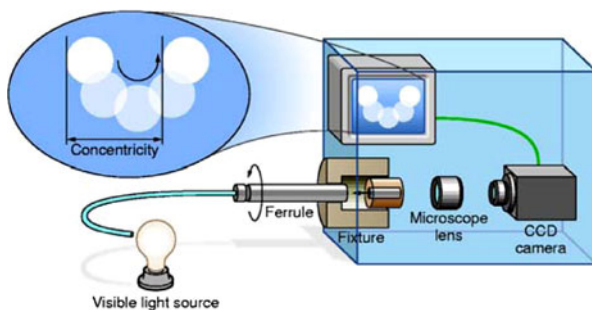


**Fig. 10.5** Schematic sketch of a ferrule concentricity measurement instrument

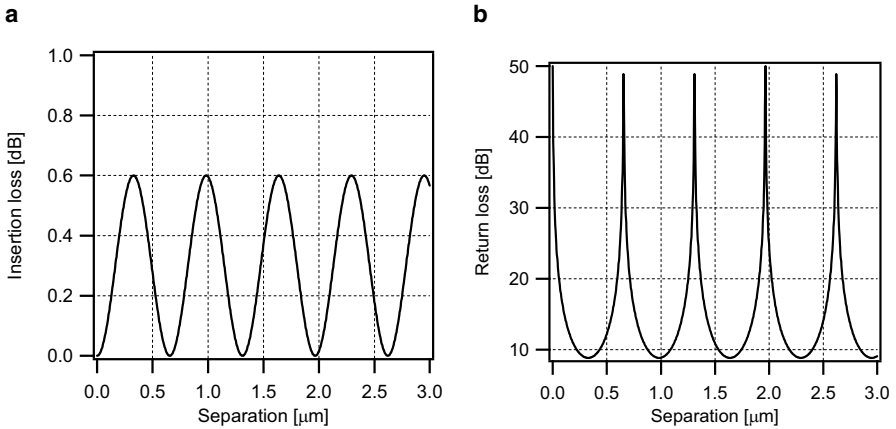
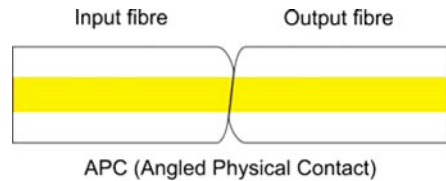


**Fig. 10.6** Calculated induced insertion loss (a) and return loss (b) for two perfectly aligned fibres separated by an air gap

**Fig. 10.7** Scheme of APC-polished connector end face



between the two connected fibres. This can be accomplished by spherically polishing of the two ferrules and pressing them together in an optical connection so that an elastic deformation of the spherical ferrules leads to physical contact of the two fibres.

### 10.1.5.3 PC- and APC-polished Connectors

In the previous discussion, we only mentioned physical-contact (PC)-polished connectors, where the fibre is polished  $90^\circ$  towards its axis. In order to reduce reflections at the connection interface, the connector industry developed the so-called angled PC (APC) connectors, which are polished with a tilt of  $8^\circ$ , as displayed in Fig. 10.7.

In APC-connectors, the input and output fibres have to be in physical contact, exactly in the same way as for PC connectors. The additional angle allows a reduction of the amount of reflected light which is coupled back into the input optical fibre by several orders of magnitude. APC connectors' return loss (RL)-values are specified in the standards to be below  $-65$  dB. In reality, well polished APC connectors reach RL-values well below  $-100$  dB!

### ***10.1.6 Mechanical and Climatic Requirements for FO-Connectors***

Ideal optical connectors provide stable and repeatable alignment between fibres which must be detachable and repeatable over hundreds or even thousands of connection cycles without deterioration. Handling by operators may include pulling, torsion, twisting, etc., and the optical connection may not only be placed in air-conditioned rooms, but in unprotected locations as well, which may exhibit extreme variations in temperature and humidity. Appropriate (long-term) operation under all these conditions is ensured by test standards (e.g. IEC 61300-2-xx) which connectors have to pass.

### ***10.1.7 Available Standard Connector Types***

Standard connector types to be mentioned are based on three different ferrule types:

- Cylindrical 2.5 mm ferrules (E-2000, FC, SC, LSA, ...),
- Cylindrical 1.25 mm ferrules (LC, F-3000, MU, LX.5),
- Rectangular multi-fibre ferrule, ranging from 2 to 12 fibres (MT, MT-RJ, MPO, MF ...).

Table 10.3 shows a few examples of some of the most frequently used connector types.

Recently developed connectors usually use a push pull latching mechanism as opposed to a screw coupling nut, allowing better accessibility, space reduction and therefore higher connection density.

Standard connections may be simplex, allowing one to connect an input and one output connector. Duplex connections, where the number of input and output connectors is two, are often used in the case where there is a downstream and an upstream fibre to be connected.






Backplane connectors are used in interconnect systems for connecting printed circuit boards or electro-optic circuit boards to backplanes. Depending on the construction, they may range from one connection up to six connections. When using MT-ferrule technology (see beginning of this section), one backplane connection is capable to interconnect up to several tens of fibres.

### ***10.1.8 FO-cables for Patch Cords***

Cord is a general term for terminated cable assembly, whatever the expected use is. Examples of cords are equipment cord, work area cord or patch cords. Equipment cords are cords connecting equipment to a distributor. A patch cord (see Fig. 10.8) is a cord used within cross-connect implementations at distributors. A work area cord is a cord connecting the telecommunications outlet to the terminal equipment.



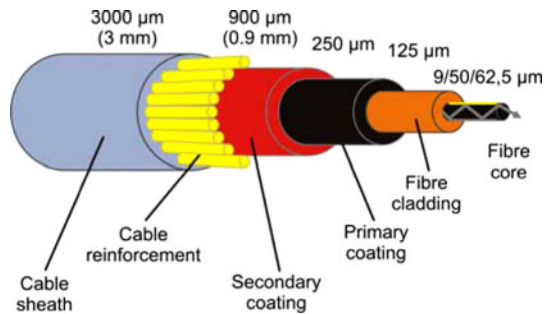
**Table 10.3** Examples of most frequently used fibre-optic connectors (courtesy Diamond SA [1])

Figure	Connector name	Mechanical interface standard
	E-2000	IEC 61754-15
	F-3000 LC compatible	IEC 61754-20
	SC	IEC 61754-4
	MPO (Multi-fibre connector using rectangular MT ferrule technology)	IEC 61754-7
	FC	IEC 61754-13

Cords represent a very important product family in which optical connectors are used. They often are assemblies of connectors and cable which are not produced by the same manufacturer. In many cases, both the cable and connector are qualified products, performing well separately. However, as soon as the two are combined into a patch cord, problems may appear:

- Problems may be caused by the fact that connectors are two fixed points in a patch cord, therefore not allowing the cable sheath or other polymer layers to shrink or

**Fig. 10.8** Typical simplex patch cord cable construction



move as a function of temperature, thus leading to bending of the fibre in the cable causing high attenuation variations.

- Connector ferrules are usually spring loaded. In a connector assembly, the fibre (including primary and secondary coating) is fixed to the ferrule, and the cable reinforcement and sheath are fixed to the connector body. In a connection cycle, the two ferrules come into contact and push each other back into the connector body. This movement is pushing back the fibre, whereas the other cable layers are fixed. In some cable constructions, this movement of the fibre is not allowed due to dimensions or to friction. In this case, the fibre usually bends within the connector body, causing high attenuation.

For the reasons mentioned above, terminated patch cords need to be qualified as such. The connector and the cable used in the assembly have to be qualified products, and the subsequent patch cord qualification is a repetition of selected tests used for the connector testing. (Patch cord performance standards: e.g. IEC 61753-121 document series).

### ***10.1.9 Connectors for Special Fibres or Special Use***

Thus far, the discussion has been focussed on connectors for standard single-mode fibres, the most widely used fibre for telecom applications. However, there are also connectors for other types of fibres (polarisation maintaining, specialty fibres at shorter wavelengths), for special applications such as very high optical power or particularly harsh environment requiring a hardened connector design.

#### **10.1.9.1 Polarisation-maintaining Connectors**

Standard single-mode fibres do not maintain a well-defined state of polarisation (SOP) of the light because many effects including reflection from surfaces or stress within the transmitting media (due to moving the fibre or temperature variations) can affect the polarisation of the propagating light.

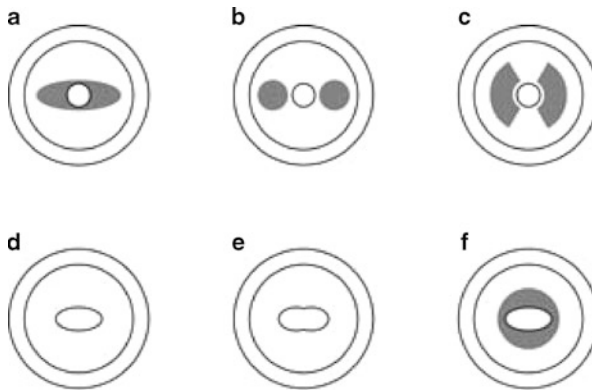


**Fig. 10.9** Examples of polarisation-maintaining fibres: **a** elliptical-cladding-, **b** PANDA-, **c** “bow-tie”-, **d** elliptical-core-, **e** double-core-, and **f** elliptical-core circular-cladding fibre

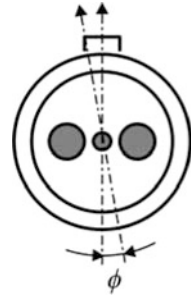
On the other hand, many systems such as fibre interferometers and sensors, fibre-optic gyroscopes, fibre lasers and electro-optic modulators depend on a well-defined SOP, which can be assured by polarisation maintaining (PM) fibre plus corresponding connectors and a careful overall assembly so that polarisation-dependent losses, which normally degrade system performance, can be avoided.

In response to these requirements, several manufacturers have developed polarisation-maintaining fibres which exhibit birefringence within the core that is characterised by two orthogonal axes corresponding to different propagation constants of light polarised parallel to these axes (frequently designated as fast and slow axis, respectively). If the input light into a PM fibre is linearly polarised and orientated along one of these two axes, the output light from the fibre will remain linearly polarised and parallel to the principal axis, even when subjected to external stress.

Birefringence within a PM fibre is obtained by breaking the circular symmetry, and this can either be done by forming a non-circular fibre core (shape induced birefringence), or by inducing constant stress within the fibre (stress induced birefringence) by fabricating the fibre with two highly doped regions located on opposite sides of the core. Corresponding examples are illustrated in Fig. 10.9. Currently, the most popular SM fibre is the so-called PANDA fibre (where PANDA stands for ‘polarisation-maintaining and absorption-reducing’) which relies on stress-induced birefringence. One particular advantage of PANDA fibres compared to most other variants is the fact that the PANDA core size and numerical aperture are compatible with regular single-mode fibre. This ensures minimum loss in devices using both types of fibre.

While one can produce perfectly linearly polarised light in theory, this is not the case in practice. Instead, there is always some residual polarisation (random or elliptical) present in the output beam, and a measure of beam quality is its polarisation extinction ratio (PER). The extent to which a fibre maintains polarisation depends on

**Fig. 10.10** For FO connectors assembled on PM-fibre, the orientation of the birefringence axes is a key parameter



the input launch conditions, in particular, on the alignment between the polarisation axes of the light and the fibre principal axes.

If a perfectly polarised beam is launched into an ideal fibre misaligned by an angle  $\phi$  with respect to the slow (fast) axis of the fibre (see Fig. 10.10), this misalignment causes a small amount of light being transmitted along the fast (slow) axis of the fibre and consequently degrades the PER of the output beam.

The optimum achievable value of the output extinction ratio (ER) is thus limited by

$$ER \leq -10 \cdot \log(\tan^2 \phi). \quad (10.1)$$

Therefore, to achieve output extinction ratios better than 20 dB, the angular misalignment must be less than  $6^\circ$ . For 30 dB extinction ratio, the angular misalignment must be less than  $1.8^\circ$ .

As a consequence, in PM connector assemblies, it is not only important to align fibre cores, but also to orient the fibre axes (see Fig. 10.10), so that in a connection, both fibres have their main axes aligned. In addition, since most PM fibres are stress-induced high birefringence fibres, care should be taken not to excessively stress them because this would decrease their efficiency in maintaining polarisation states.

For these connectors orientation of fibre concentricity, as described in Sect. 10.1.5.1, is no longer possible because priority has to be given to the principle axis orientation. Therefore, this type of fibre is most conveniently terminated using centred technology connectors, which allow both, to position the fibre core in the centre of the ferrule and then to orient the fibre axis.

Very often, PM-applications also require shorter wavelengths, usually related to smaller fibre core and mode field diameter as compared to standard single-mode fibre. For these applications, the alignment of the fibre core is even more challenging. A general rule of thumb is that if the mode field diameter is two times smaller, the same offset error is leading to a four times larger attenuation in a connection. The only possible way of manufacturing low loss PM-connectors on small core fibres is by using centring technology, as developed by Diamond SA (see Sect. 10.1.5.1).

### 10.1.9.2 High Power Connectors

The transmission of high power signals through single-mode fibres raises new challenges, not only for the fibre manufacturers, but for the in-line components manufacturers as well. Within the core of the fibres and in the areas where the light beam is focussed, the power density can reach more than  $10 \text{ GW/m}^2$  (as a reference, this is more than hundred times the power density dissipated on the surface of the sun). This can have catastrophic consequences for the materials that cannot withstand such a high power density.

One very critical component is the single-mode connector. Good connectors only provide a much reduced hindrance to the transmitted signal (the best connectors guarantee a maximum attenuation as low as 0.1 dB). These small losses are mostly induced by a mismatch of the fibre core parameters (numerical aperture, diameter) or a lateral and angular misalignment, and the energy that gets lost this way is not a threat to the connector reliability as it is dissipated through the fibre cladding.

Problems arise when the connectors are not perfectly clean. Contamination particles that are located at the connector interface can absorb part of the transmitted energy and convert it into heat. When the heat produced this way is high enough, the temperature of the fibre can rise over the melting point of silica, causing the collapse of the connection.

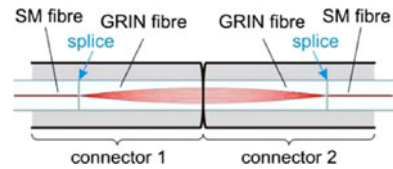
To avoid these problems, a connector that has to bear high power signals must ensure perfect cleanliness conditions. A visual inspection of the ferrule's end face before every mating is essential. There should not be any metallic wear parts; metal sleeves and threads are to be avoided. When the connectors are unmated, there must be a protection cap for the ferrules in order to avoid any contamination on the fibre. The mating adapter must also have a protection cap to prevent dust particles to enter the sleeve, and connectors exhibiting all these features are already commercially available [1].

Cleanliness and the above mentioned features may still not be sufficient to guarantee a flawless functioning of the connectors as small particles that may be overlooked with a field inspection microscope could still cause the connector to fail. The only way to eliminate this risk is to reduce the power density at the connector interface, i.e. to enlarge the beam diameter. For this reason, connector manufacturers propose a connector design based on expanded beam technology.

Expanded beam connectors that use collimating lenses have been on the market for many years. They are constructed for use in harsh environments, so they usually have rugged bodies and provide higher insertion loss values. Some manufacturers offer expanded beam connectors as high power connectors based on the use of a piece of gradient index fibre instead of an external lens to collimate the light beam. This way, the expanded beam system can be integrated in a standard cylindrical ferrule (2.5 mm or 1.25 mm), as illustrated in Fig. 10.11.

The GRIN fibre is spliced to a standard SM fibre and cut at the right length in order to achieve the desired focal length. At the connector interface, the beam is collimated and has a large mode field diameter dependent on the magnification

**Fig. 10.11** High power connector based on grin lens design using gradient index fibre



of the GRIN fibre (typical magnification factors 4–5, leading to a power density decrease of a factor 16–25). In the other connector, the second GRIN fibre focuses the beam back into the SM fibre.

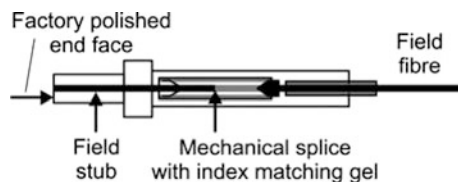
It has been demonstrated that connectors based on the design described above can withstand high power signals (up to 1 W) under standard contamination conditions (same cleaning procedure and same inspection procedure) and show low insertion loss values (similar to standard SM connectors). This technology may be coupled to the E-2000™ connector body, offering a good protection of the ferrule from the environment thanks to its protection cap.

### 10.1.9.3 Field Termination

Most of the fibre-optic connectors are assembled in the factory and then spliced (pigtail) or patched in the field, but there are applications where it is needed to assemble the connector in the field. Since connector assembly requires specialised tools and skills, it is usually not possible to assemble connectors in the field using the same technologies as in the factory. Therefore, alternative solutions have been developed for field terminations:

- Optimised, “quick assembly” tools, which allow the field assembly of standard connectors.
- Field termination connectors based on mechanical splices: A connector assembly that is factory terminated and polished may be field terminated on a cable end. The connection to the cable fibre is accomplished through a mechanical splice (see Fig. 10.12).
- Field termination connectors based on fusion splices: The principle is similar to the termination mentioned above with the difference that the mechanical splice is replaced by a fusion splice which increases performance and reliability of the termination. Some manufacturers offer this kind of solution with similar performance as for standard connectors. Usual installations rely on a 1–

**Fig. 10.12** Schematics of a field termination based on mechanical splice



3 m pigtail which is spliced to the cable end. However, in the case of a fusion field termination, the pigtail is significantly shorter (10–20 mm) and the connector housing integrates splice protection features. This makes this solution very similar in performance to what is usually achieved with factory-assembled connectors.

### ***10.1.10 Cleaning and Inspection***

A single particle mated into the core of a fibre can cause significant back reflection, insertion loss, and equipment damage. If high optical power is involved, contamination may even cause a permanent damage. As a consequence, it is of high importance to prevent contamination of connector end faces which may be due to:

- Mishandling, such as accidental touching of connector end faces or inappropriate cleaning
- Connectors left open for a while and subject to dust or other environmental contaminations
- Travelling contamination where one contaminated connector used for measurements on a patch panel may contaminate a large series of initially clean connectors
- Contaminated connector adapters where contamination is usually not bound to the adapter parts.

Accessible connector end faces (when the connector can be hold in a hand) may be cleaned using fabric and/or composite material wipes which combine mechanical action and absorbency to remove contamination. Wipes should be used with a resilient pad in order avoid potential scratching of the connector end face and assist the cleaning material in conforming to the connector end-face geometry, and wipes should be lint free and non-debris producing.

The use of a solvent with a dry wipe is advantageous for various reasons: it adds chemical action to the mechanical function of the wipe which increases its cleaning ability. In addition, the use of a static dissipative solvent eliminates the problem that dry wipes may leave a static charge on the end face of connectors which can subsequently attract particulate contamination.

If the connector end face is assembled in a port, it can only be accessed through the adapter aperture. In such cases, purpose-built swabs or mechanical port cleaning devices provide mechanical action and absorbency to remove contamination. Again, the cleaning end of the swab or cleaning material used in the port cleaning device should be lint free and non-debris generating. Particular care has to be taken that saturating the connector interface is avoided when solvents are used.

Cleaning of connector end faces and adapters is a process which usually does not have 100% yield and may therefore require several iterations, which require observation of the end faces with an adequate inspection microscope. Today's microscopes usually use a CCD camera and may be connected to measurement in-

struments (e.g. OTDR, power meter), to a computer or a portable screen, and in some cases, image analysis is used to facilitate the detection of any defect or contamination.

## 10.2 Fibre-optical Couplers

### 10.2.1 Introduction

Routing signals to their appropriate destination is one important functionality in communication networks, and combining, distributing or tapping optical channels is equally important. Passive optical couplers offer this functionality (see Fig. 10.13) and are therefore widely used in fibre-optic networks.

Some designs are inherently directional, such as couplers where several fibres are fused in the middle, routing signals from a group of input fibres to a separate group of output fibres. Others are not directional, taking inputs from all fibres and distributing them among all fibres. Therefore,  $2 \times N$  couplers and  $1 \times N$  couplers (tree couplers) are special cases of star couplers. In the four-port directional coupler, an incoming signal at each of the input ports 1 or 2 reaches both output ports 3 and 4; otherwise, an incoming signal from each of the output ports 3 or 4, propagating in the opposite direction, reaches both input ports 1 and 2.

The behaviour of these coupler structures is the result of reciprocity. Reciprocity is essential for the correct interpretation of incoming signals at the output ports. We will see that using fused-fibre technology, a T-coupler is nothing more than a directional coupler terminating the second input fibre. Fused-fibre couplers may be further characterised by the wavelength dependence of coupling. In this chapter, we will only discuss power splitters with a wavelength-independent behaviour over a specified wavelength range and not wavelength-selective splitters (filters). Such devices are discussed in Chap. 9.

### 10.2.2 Modelling of Optical Directional Couplers/Power Splitters

A generic model of a directional coupler, which is independent of the coupler type, is shown in Fig. 10.14 with ports numbered 1, 2, 3, and 4.

Based upon this model, the directional coupler can be characterised by a scattering matrix. The scattering matrix is commonly used in the field of microwave technology [2], and it is also used with the same definitions in fibre-optics. Two complex quantities,  $a_j$  and  $b_j$ , associated with each port  $j$ , represent the complex amplitudes for the input and the reflected light waves, respectively. The relation between the input and the reflected light waves is given by

$$\mathbf{b} = \mathbf{S}\mathbf{a} \quad (10.2)$$



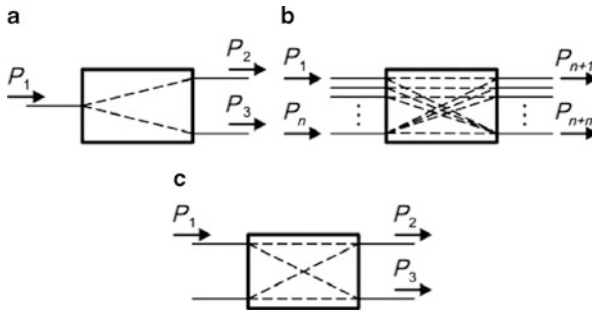
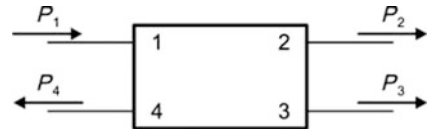


**Fig. 10.13** Coupler types: T- or Y-coupler (a), star coupler (b), directional coupler (c)

**Fig. 10.14** Four-port model of a directional coupler



with vectors  $\mathbf{a} = [a_1, a_2, a_3, a_4]$  and  $\mathbf{b} = [b_1, b_2, b_3, b_4]$  and the scattering matrix  $\mathbf{S}$  given by

$$\mathbf{S} = \begin{bmatrix} s_{11} & s_{12} & s_{13} & s_{14} \\ s_{21} & s_{22} & s_{23} & s_{24} \\ s_{31} & s_{32} & s_{33} & s_{34} \\ s_{41} & s_{42} & s_{43} & s_{44} \end{bmatrix}, \tag{10.3}$$

all corresponding to the four-port case. If the coupler is made of identical fibres,

$$s_{jk} = s_{kj} \tag{10.4}$$

holds due to geometric symmetry and reciprocity of the device. Therefore, we get for the scattering matrix

$$\mathbf{S} = \begin{bmatrix} s_1 & s_2 & s_3 & s_4 \\ s_2 & s_1 & s_4 & s_3 \\ s_3 & s_4 & s_1 & s_2 \\ s_4 & s_3 & s_2 & s_1 \end{bmatrix} \tag{10.5}$$

with

- $s_1 = s_{11} = s_{22} = s_{33} = s_{44}$ : self-reflection coefficient,
- $s_2 = s_{12} = s_{21} = s_{34} = s_{43}$ : transmission coefficient,
- $s_3 = s_{13} = s_{31} = s_{24} = s_{42}$ : coupling coefficient,
- $s_4 = s_{14} = s_{41} = s_{23} = s_{32}$ : blocking coefficient.

For an ideal directional coupler with no reflections and no loss, the corresponding scattering matrix  $\mathbf{S}_{\text{ideal}}$  is known to be a unitary matrix given by

$$\mathbf{S}_{\text{ideal}} = \begin{bmatrix} 0 & c_1 & ic_2 & 0 \\ c_1 & 0 & 0 & ic_2 \\ ic_2 & 0 & 0 & c_1 \\ 0 & ic_2 & c_1 & 0 \end{bmatrix}, \quad (10.6)$$

where  $c_1$  and  $c_2$  are real constants and

$$c_1^2 + c_2^2 = 1 \quad (10.7)$$

holds.

In the following paragraph, we will show how the scattering matrix formalism can be applied to the description of (biconical fused) fibre couplers (see also Sects. 10.2.3 and 10.2.4).

The coupling region can support two fundamental modes, the even and the odd one, which are characterised by different propagation constants  $\beta$  given by

$$\beta_{\text{even}} = \frac{2\pi n_{\text{even}}}{\lambda} \quad \text{and} \quad \beta_{\text{odd}} = \frac{2\pi n_{\text{odd}}}{\lambda} \quad \text{with} \quad \frac{\beta_{\text{even}} + \beta_{\text{odd}}}{2} = \beta_{\text{av}} \quad (10.8)$$

with  $n_{\text{even}}$  and  $n_{\text{odd}}$  being the effective refractive indices of the even and odd modes, respectively, and  $\lambda$  being the vacuum wavelength of the wave under consideration. A plane electromagnetic wave propagating into the  $z$ -direction is represented by

$$E(z, t) = E_0 \exp[-i(\beta z - \omega t)] \quad (10.9)$$

with  $\omega = 2\pi c/\lambda$  and  $c$  being the vacuum speed of light. Light propagating in the odd mode will travel faster in the coupling area because its electrical field extends further into the low-index cladding of the fibre. As a consequence, a phase difference as given by (10.10) accumulates between the even and odd modes as they propagate a distance  $L$  along the coupler, that is,

$$\varphi = L(\beta_{\text{even}} - \beta_{\text{odd}}) = \frac{2\pi L}{\lambda}(n_{\text{even}} - n_{\text{odd}}). \quad (10.10)$$

If a common phase delay of both modes, i.e.  $\exp(-i\beta_{\text{av}}L)$ , is neglected, the total electrical fields at the output arms 2 and 3 are given by

$$\begin{aligned} E_2 &= \frac{E}{2} + \frac{E}{2} \exp(i\varphi) = \frac{E}{\sqrt{2}} \sqrt{1 + \cos \varphi} \exp\left(\frac{i\varphi}{2}\right) \\ E_3 &= \frac{E}{2} - \frac{E}{2} \exp(i\varphi) = \frac{E}{\sqrt{2}} \sqrt{1 + \cos \varphi} \exp\left(\frac{i\varphi}{2} - \frac{i\pi}{2}\right). \end{aligned} \quad (10.11)$$

Equation (10.11) demonstrates that the output of arm 3 is always delayed by  $90^\circ$  with respect to arm 2. This behaviour is independent of the coupling length and the

strength of the coupling mechanism and therefore independent of the coupling factor.<sup>1</sup> Another important result is that the angle  $\varphi$  determines the coupling ratio of the coupler where the following cases are of particular relevance:  $\varphi = 0$  corresponds to no coupling at all,  $\varphi = 90^\circ$  characterises a splitting ratio of 50 %, i.e. this represents an ideal 3 dB coupler, and  $\varphi = 180^\circ$  is equivalent to a splitting ratio of 100 %, i.e. 100 % of the input power appears in arm 3 and no power is observed in arm 2. According to (10.10) and (10.11), for a given set of fibre parameters, the periodic exchange of the output power between the arms 2 and 3 only depends on the length of the coupling region. Neglecting the common phase shift (i.e.  $\exp(i\varphi/2)$ ), we get

$$\begin{aligned} E_2 &= c_1 E_1 + ic_2 E_4, \\ E_3 &= ic_2 E_1 + c_1 E_4. \end{aligned} \quad (10.12)$$

The quadratic terms  $c_1^2$  and  $c_2^2$  represent the power coupling coefficients between connected or coupled arms.

Directional couplers can also be analysed using the coupled mode theory, as outlined in Chap. 9, Sect. 9.3.1.

If ports 2, 3 and 4 are terminated without any reflection, the power  $P_j$  at each port can easily be calculated using the incoming wave  $a_1$  at port 1 and the outgoing waves  $b_2$ ,  $b_3$  and  $b_4$  at the other ports, leading to

$$\begin{aligned} P_1 &= |a_1|^2, \\ P_2 &= |b_2|^2 = |s_2|^2 |a_1|^2, \\ P_3 &= |b_3|^2 = |s_3|^2 |a_1|^2, \\ P_4 &= |b_4|^2 = |s_4|^2 |a_1|^2. \end{aligned} \quad (10.13)$$

Besides the coupling ratio, there are three other parameters which characterise the behaviour of a coupler and which are usually expressed in units of dB: the coupling ratio CR, the excess loss EL, the return loss RL, and the directivity  $D$ , which are given by

$$\begin{aligned} \text{CR} &= -10 \log \left( \frac{P_3}{P_1} \right) = -20 \log (|s_3|), \\ \text{EL} &= -10 \log \left( \frac{P_2 + P_3}{P_1} \right) = -10 \log (|s_2|^2 + |s_3|^2), \\ \text{RL} &= -10 \log \left( \frac{P_r}{P_1} \right), \\ D &= -10 \log \left( \frac{P_4}{P_1} \right) = -20 \log (|s_4|), \end{aligned} \quad (10.14)$$

---

<sup>1</sup> It might be worthwhile to note that the sign of the phase change of the wave leaving the coupler via the cross port depends on the sign in the exponent of (10.9). Conventions using positive or negative sign for the wave propagation are both found in the literature giving rise to different signs of the phase change, which might cause confusion.

where  $P_r$  results from the outgoing wave at port 1 due to internal reflections in the coupling zone. In general, EL, RL, and  $D$  result from internal imperfections of the device because there are no incoming waves except at port 1. Other figures of merit, which are relevant for the characterisation of couplers, are independence (or negligible residual dependence) on fibre modes and on the state of polarisation. The first is a very important requirement for multimode couplers because different excitation conditions can often result in a large change of the coupling ratio. Polarisation independence is naturally a topic for single-mode couplers only. One rule of thumb is that the shorter the tapered zone of the fibres the larger the residual polarisation dependence. As a consequence, the overall size of couplers should not be reduced too much.

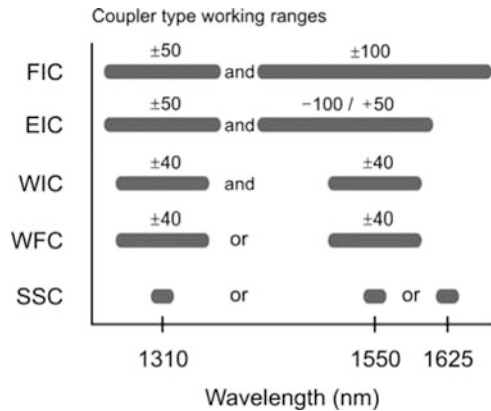
### ***10.2.3 Fibre Coupler Technologies***

The most common type of fibre coupler is the evanescent field coupler which uses a narrow spacing between two adjacent fibre cores. Because the electromagnetic field extends beyond the cores, coupling between the cores happens. Fibre-based couplers are produced using essentially two different techniques. Most popular is the fused biconical taper technique, producing fused biconical couplers (FBCs). Two fibres are fused together and stretched at high temperature. To achieve an approach of the fibre cores due to a force, the fibres must be twisted in or outside the coupling area. The stretching decreases the diameter of the fibres and therefore, proportionally, the diameter and the distance of the cores. At the beginning and at the end of the coupling zone, a tapered zone occurs. This causes an extension of the electromagnetic field and therefore the possibility of coupling. The coupling length is the major parameter to define the coupling ratio. Fused biconical couplers are primarily used as power splitters for telecommunication applications, but they also serve as wavelength division multiplexers and demultiplexers. The other popular approach to fabricate fibre couplers relies on polishing the fibres. The two fibres, which will build the coupler, are first embedded into a glass plate and then polished down to the cores. Joining the glass plates brings the cores into proximity. The lateral spacing can be freely chosen which allows the definition of essentially any coupling ratio wanted. Due to a perfectly manageable polishing process, it is easier and more repeatable to create couplers using different fibre types with different diameters. Therefore, this technique is very important for the fabrication of couplers which use special fibres, for example, for high power or sensors applications.

### ***10.2.4 Classification***

By appropriate design of the manufacturing process and pre-treatment of the fibres, which constitute the coupler, it is possible to create couplers with different coupling

**Fig. 10.15** Fibre coupler categories [3]



ratio and transmission characteristics, and the following categories can be distinguished:

- Standard single-mode couplers (SSCs), specified for one wavelength and a (small) bandwidth of typically  $\pm 5$  nm
- Wavelength flattened couplers (WFCs), specified for one wavelength and a (wider) bandwidth of typically  $\pm 40$  nm
- Wavelength independent couplers (WICs), specified for two wavelengths (for example: 1310 nm and 1550 nm) and for a bandwidth of typically  $\pm 40$  nm at each wavelength
- Extended wavelength independent couplers (EIC), specified for two wavelengths and larger unequal bandwidths of typically  $\pm 50$  nm and  $-100 / +50$  nm
- Full range wavelength independent couplers (FIC), specified for two wavelengths and large equal bandwidths of typically  $\pm 50$  nm and  $\pm 100$  nm.

These fibre coupler categories are illustrated in Fig. 10.15.

Due to the coupling principle, it is not possible to narrow the gap between the two transmission windows to less than 75 nm because a smaller separation would at the same time narrow the transmission windows themselves which is not acceptable.

The typical coupling behaviour of fused biconical couplers using standard single-mode fibres or pre-treated fibres as a function of pull length during the pulling process is illustrated in Fig. 10.16.

Continuous monitoring of the power at the output ports enables one to stop the pulling process at the desired pull length in order to get the requested coupling behaviour. For example, point A and B indicate pull lengths representing a 50/50% power splitting for 1310 nm or 1550 nm. At point D, the power splitting is 80/20% for both wavelengths. In the case of identical fibres (Fig. 10.16a) the coupling ratio exhibits a large wavelength dependence due to the steep slopes of the curves. If different fibre types are used (Fig. 10.16b), the wavelength dependence is significantly lower. Finally, the same basic structure could also be used as a wavelength multiplexer as point E in (Fig. 10.16a) illustrates.

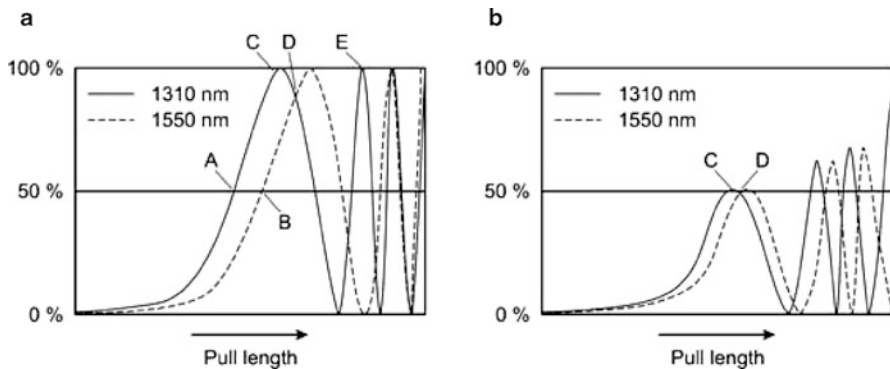


**Fig. 10.16** Coupling behaviour of fused biconical couplers made of identical fibres (a) and different fibres (b) [3]

**Table 10.4** Typical values observed at output ports 2 and 3 for the coupling ratios indicated [3]

Wavelength [nm]	FIC		EIC		WIC		WFC		SSC	
	O <sub>2</sub>	O <sub>3</sub>	O <sub>2</sub>	O <sub>3</sub>	O <sub>2</sub>	O <sub>3</sub>	O <sub>2</sub>	O <sub>3</sub>	O <sub>2</sub>	O <sub>3</sub>
1310 ± 50 and 1550 ± 100	4.2	4.2	4.0	4.0	3.6	3.6	3.4	3.4	3.4	3.4
1310 ± 50 and 1550 ± 100	3.2	5.4	3.0	5.2	2.7	4.7	2.5	4.3	2.5	4.3
1310 ± 50 and 1550 ± 100	2.7	6.4	2.5	6.2	2.2	5.6	2.0	5.2	2.0	5.2
1310 ± 50 and 1550 ± 100	2.4	7.0	2.2	6.8	2.0	6.1	1.8	5.6	1.8	5.6
1310 ± 50 and 1550 ± 100	1.7	9.2	1.5	9.0	1.4	8.4	1.1	7.4	1.1	7.4
1310 ± 50 and 1550 ± 100	1.1	13.0	0.9	12.8	0.8	11.7	0.6	10.6	0.6	10.6
1310 ± 50 and 1550 ± 100	0.8	16.8	0.6	16.6	0.5	15.3	0.4	13.8	0.4	13.8
1310 ± 50 and 1550 ± 100	0.1	24.7	0.4	24.5	0.2	23.1	0.2	22.0	0.2	22.0

Minimum directivity (in dB): 55 for 1 × 2, 60 for 2 × 2

Minimum return loss (in dB): 55 for 1 × 2, 60 for 2 × 2

Polarisation dependent loss<sup>1,2</sup> [dB]: typical 0.05

<sup>1</sup> maximum 0.1 dB for port O<sub>2</sub> and maximum 0.2 dB for port O<sub>3</sub>

<sup>2</sup> FIC, EIC: measured at 1310 nm and 1550 nm, WIC, WFC, SSC: measured at central wavelength of wavelength range

Typical and best performance values of the different fibre coupler types and for various splitting ratios are compiled in Table 10.4.

### 10.2.5 Star Couplers

Multipoint couplers can – in theory – be made by fusion of many fibres. Large variations of the power distribution at the different outputs and an often poor repeatability of the manufacturing processes have prevented the commercial implementation of

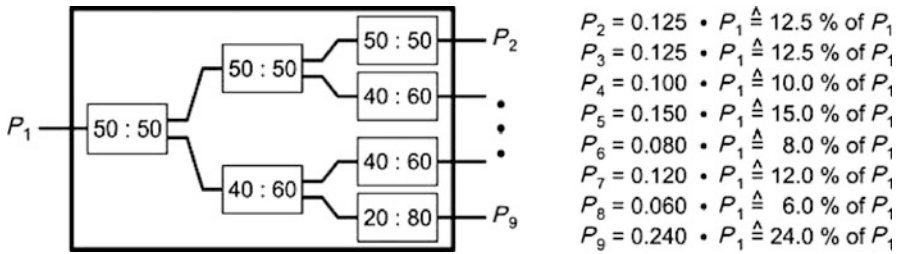


**Fig. 10.17** Drawing of a  $1 \times 8$  star coupler and output power distribution

the theoretic concepts so far. In practice, the manufacturing process has acceptable yield for a maximum of four fibres or even less. Therefore, transmissive star couplers, which are key devices for star-type networks, are mostly built by a cascade of equal or different T-couplers. One particular advantage of this approach is the flexibility to create individual power distributions at the output ports, and lower cost is an additional argument in favour of this approach. There is only one shortcoming of transmissive star couplers which favours the use of fused couplers with more than two fibres: the latter require less space. Figure 10.17 shows a drawing of a transmissive  $1 \times 8$  star coupler, built from  $1 \times 2$  couplers with different coupling ratios.

### 10.3 Optical Circulators

An optical circulator is a non-reciprocal, passive multiport device, and its key functionality is directing light sequentially from port to port which results in the separation of signals which travel along an optical fibre in opposite directions. Sub-components, of which optical circulators are assembled from, are a selection from polarising beam splitters, phase shifters, Faraday rotators, optical isolators, walk-off polarisers, prisms, and lenses.

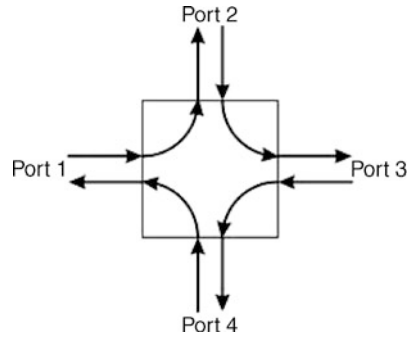
Optical circulators are typically three- or four-port devices, and an “ideal” four-port circulator is schematically illustrated in Fig. 10.18 where “ideal” means that light may enter by any input and is routed to the subsequent port in all cases.

Various implementations of optical circulators have been published as early as the late 70s and early 80s, and have continued since then, including different “ideal” four-port circulators [4–7]. One design is illustrated in Fig. 10.19.

Typical characteristics of these early devices were about 2 dB insertion loss, 25–35 dB isolation (sometimes < 25 dB), and the operation wavelength was typically around 1.3  $\mu\text{m}$ .

In practice, the full functionality of an “ideal” circulator requires a very sophisticated and complex design. However, this is not generally needed, and as a consequence, optical circulators are normally offered with reduced functionality [8]. In the case of four-port circulators, the corresponding routing characteristics can be

**Fig. 10.18** Functionality of an “ideal” four-port optical circulator (schematic)



represented by  $1 \rightarrow 2, 2 \rightarrow 3, 3 \rightarrow 4$ , i.e. port 1 is an input port only, ports 2 and 3 serve as input and output ports while port 4 is an output-only port. Three-port circulators generally correspond to  $1 \rightarrow 2, 2 \rightarrow 3$  routing, i.e. they have one input-only port (1), one output-only port (3) while port 2 serves both, as an input and an output port.

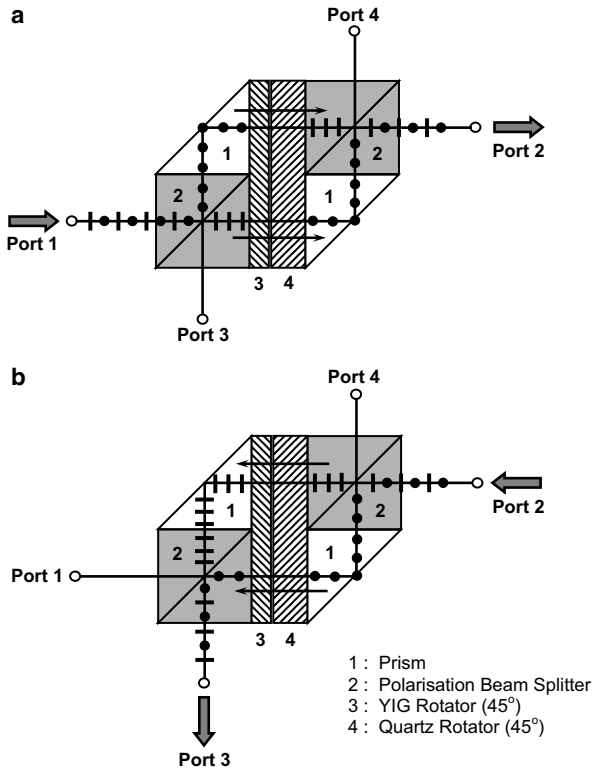


**Fig. 10.19** Design example of an “ideal” four-port optical circulator [4]



**Table 10.5** Typical characteristics of commercially available optical circulators. Numbers given apply to three-port and four-port circulators as well (for the former case all entries containing “4” should be removed)

Wavelength ranges	1310 ± 30 nm 1525–1565 nm 1570–1610 nm
Insertion loss (1 → 2, 2 → 3, 3 → 4)	0.8–1.2 dB
Channel isolation (2 → 1, 3 → 2, 4 → 3)	
peak:	> 50 dB
complete operation range	> 40 dB
Directivity (1 → 3, 2 → 4)	> 50 dB
Return loss	> 55 dB
Polarisation-dependent loss (PDL)	< 0.1–0.15 dB
Polarisation mode dispersion (PMD)	0.06–0.1 ps
Wavelength-dependent loss (WDL)	0.15–0.2 dB
Polarisation extinction ratio*	20–23 dB
Typical dimensions	

\* applies for polarisation-maintaining circulators

Typical parameters of commercially available circulators for operation at telecom wavelengths are compiled in Table 10.5.

The wavelength ranges over which optical circulators are specified may vary by several nm, and there are also products on the market which cover the complete C+L bands. Dimensions of typical circular modules are about 5.5 mm in diameter and 60 to 65 mm length.

## 10.4 Optical Isolators

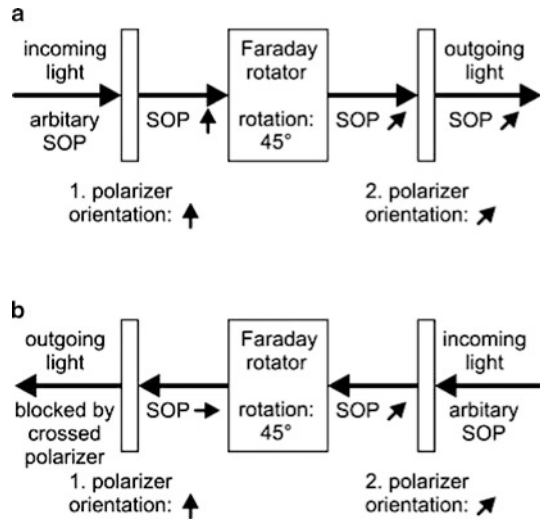
### 10.4.1 General Characteristics

Optical isolators transmit light in one direction only. They play an important role in fibre-optic systems by preventing back-reflected and scattered light from reaching the sensitive cavity of transmitter lasers, which might otherwise strongly affect the performance of lasers, and optical isolators assure stable performance of EDFAs. An isolator is a two-port optical circuit and its behaviour can be characterised by a scattering matrix according to

$$\mathbf{S} = \begin{bmatrix} s_{11} & s_{12} \\ s_{21} & s_{22} \end{bmatrix}. \quad (10.15)$$

Key elements of an optical isolator (as illustrated in Fig. 10.20) are a pair of linear polarisers separated by a Faraday rotator, which shifts the plane of polarisation by

**Fig. 10.20** Generic set-up and operation of an optical isolator. **a** illustrates light transmission, **b** corresponds to blocking



$45^\circ$ . The polarisers are orientated in such a way that their planes of polarisation differ by  $45^\circ$ .

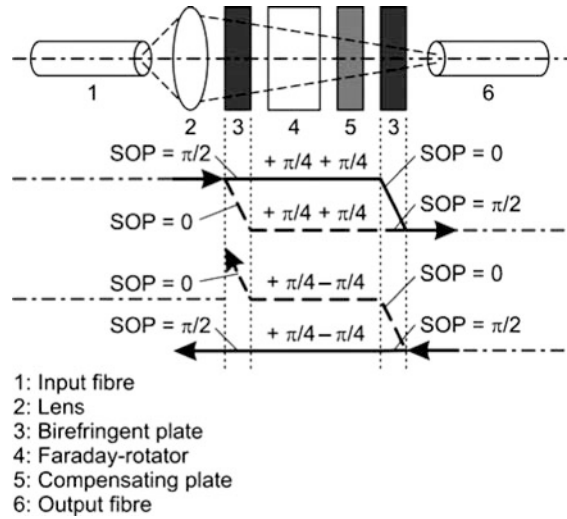
The functionality of an optical isolator can be understood as follows: Light coming from the left in the example will pass the first polariser (provided their polarisations match while any polarisation mismatch leads to extra insertion loss (see Sect. 10.4.2)). Next, the light enters the Faraday rotator (usually an yttrium-iron-garnet = YIG or a terbium-gallium-garnet = TGG) material which rotates the light polarisation by  $45^\circ$ . At the output, the light beam passes the second polariser which is intended to operate as an analyser and which is orientated at an angle of  $45^\circ$  with respect to the first polariser.

Light coming from the right can only pass the second polariser if the light polarisation and the optical axis of the polariser are parallel. Reciprocity would now demand that the polarisation of the backward passing light were changed to the polarisation of the input polariser. However, the Faraday rotator rotates the polarisation of the back-travelling beam by another  $45^\circ$ , which results in an overall rotation of  $90^\circ$  compared to the first polariser so that the back-travelling light beam is blocked by the polariser. It is easy to understand that the performance of an isolator is primarily defined by the quality of the two polarisers, although the quality of the anti-reflection-coating of each surface inside the isolator is another important issue.

It might be worthwhile to mention that a Faraday rotator could not be replaced by an optically active or liquid-crystal polarisation rotator because in those devices the sense of rotation is such that the polarisation of the reflected wave retraces that of the incident wave so that the reflected wave is transmitted back through the polariser to the entrance of the device.

Figures of merit which essentially characterise isolators are isolation  $I$  and insertion loss  $IL$ . Typical values of isolation (i.e. the suppression of back-reflection)

**Fig. 10.21** Configuration and behaviour of a polarisation-independent isolator after [9]



are about 50–60 dB, and  $I$  and IL are related to the scattering parameters  $s_{11}$  and  $s_{12}$  by

$$I = -10 \log(|s_{12}|^2),$$

$$IL = -10 \log\left(\frac{|s_{21}|^2}{1 - |s_{11}|^2}\right). \quad (10.16)$$

### 10.4.2 Polarisation-independent Optical Isolators

One serious drawback of optical isolators using polarisers and a Faraday rotator is their polarisation dependence. This issue will increase the insertion loss. Therefore, implementations of optical isolators without polarisation dependence are very interesting for future transmission systems.

For the first time, a polarisation-independent isolator was proposed in 1979 [9]. The configuration of the suggested fibre-based isolator is shown in Fig. 10.21.

The device uses two birefringent plates with equal thickness, a Faraday rotator and a compensating plate which shifts the phase of the light by  $\lambda/4$ . The light beam with two orthogonal polarisations propagates in the directions indicated by the solid and dotted lines in the figure. The birefringent plates produce a spatial separation for the orthogonally polarised components of the light. In case of the forward travelling light, these parts of light interchange their polarisation before the second birefringent plate and then they are combined at the second fibre. In the case of backward travelling light, the two orthogonally polarised components of light do not change their polarisation due to the non-reciprocal characteristics of a Faraday rota-

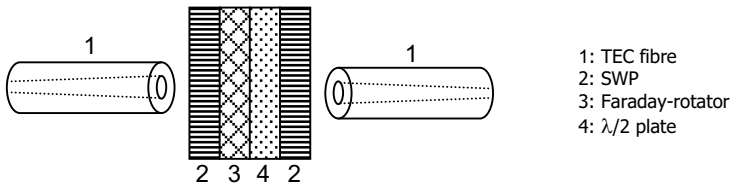


**Fig. 10.22** Setup of a polarisation-independent optical isolator after [10]

tor. Therefore, they are not combined by the birefringent plate and consequently also not coupled into the input fibre (fibre 1). The principle used in this configuration is that the backward travelling light is focussed on points with a spatial offset with respect to the core of fibre 1. Based on the same principle, a very small fibre-embedded polarisation-independent isolator has also been fabricated [10]. This configuration is shown in Fig. 10.22.

An isolator chip is inserted between TEC (thermal expanded core) fibres. The chip consists of spatial walk-off polarisers (SWP), a half-wave plate ( $\lambda/2$ -plate) and a Faraday rotator. Rutile plates were used as an SWP and a garnet crystal of  $(YbTbBi)_3Fe_5O_{12}$  was used as a Faraday rotator. The isolator exhibited about 2.5 dB insertion loss and over 40 dB of isolation at  $\lambda = 1550$  nm.

Another type of polarisation-independent isolator has been proposed which is based upon a polarisation-dependent isolator, two SWPs, and two half-wave plates [11], see Fig. 10.23. Forward travelling light with orthogonal polarisations is separated by the first SWP and then set to the same polarisation using a half-wave plate in one path before the light passes through the polarisation-dependent isolator. Then, one of the light beams is rotated again by a half-wave plate before the second SWP will combine the two beams. Backward travelling light is blocked completely by the polarisation-dependent isolator because after travelling through the SWP and through the half-wave plate, both light beams have the same polarisation orientation which is blocked by the isolator. The performance of this isolator configuration is about 60 dB of isolation with about 0.3 dB insertion loss at 1300 nm and 1550 nm.

An acousto-optic cell as illustrated in Fig. 10.24 can serve as an isolator without the drawback of the exact positioning of several elements. The optical signal

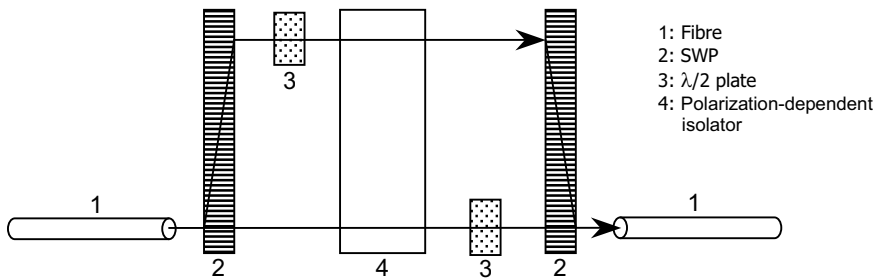


**Fig. 10.23** Polarisation-independent optical isolator after [11]

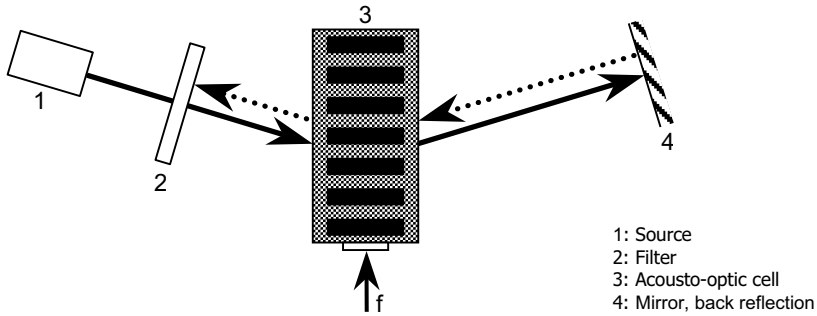


**Fig. 10.24** Polarisation-independent optical isolator using an acousto-optic cell after [12]

transmitted from a laser or travelling in the transmission system is frequency-up-shifted by the acousto-optic modulator and Bragg-diffracted. Coming to a reflection face part of the light is reflected onto itself and traces its path back into the cell. The backward-travelling light undergoes a second Bragg diffraction accompanied by a second frequency up-shift. Since the frequency of the returning light differs from that of the original light by twice the acoustic frequency used in the cell, a filter may be used to block it. Depending on the acoustic frequency used to modulate the light, even without a filter, the laser will be insensitive to the frequency-shifted light.

### 10.4.3 Planar Integrated Waveguide-based Optical Isolators

In addition to optical isolators as stand-alone devices, solutions which are suited for incorporation into optoelectronic integrated circuits (OEICs) have been a research topic for more than two decades already [13]. Beyond the bonding of garnet films onto InP or GaAs substrates [14, 15], or hybrid integration of garnets on silica-based planar lightwave circuits [16], the most promising concept relies on the non-reciprocal loss in semiconductor optical amplifier (SOA) structures combined with a ferromagnetic layer magnetised parallel to the light propagation direction. Designs have been proposed with a ferromagnetic layer on top of the WG ridge or at one of the side walls as well. In the former case, the reflectivity at the semiconductor guiding layer and the ferromagnetic layer is propagation-direction dependent for TM-polarised waves. As a consequence, the TM-mode travelling into the forward direction can be amplified while the backward travelling mode is absorbed. TE-polarised light can be suppressed by making the gain higher for TM than for TE [17]. An in-depth modelling of InP-based SOA structures with  $\text{Co}_x\text{Fe}_{1-x}$  layers on top of the ridge led to the conclusion that for a 2.825 mm long device driven with 116.5 mA/ $\mu\text{m}$  ridge width, 25 dB isolation should be achievable [18]. Alternatively,

a ferromagnetic (e.g. Fe-) layer has been located at the side wall of an SOA ridge and such a device operates with respect to TE-polarised waves. A corresponding isolator exhibited more than 10 dB/mm isolation over the complete C-band (1530–1560 nm) and a peak TE-mode non-reciprocal attenuation of 14.7 dB/mm [19], and it has also been monolithically integrated with a laser diode resulting in 4 dB optical isolation [20].

## References

1. www.diamond-fo.com
2. R.E. Collin, *Foundations of Microwave Engineering*, 2nd edn. (Wiley, Hoboken, 2001). ISBN: 978-0-7803-6031-0
3. www.foc-fo.de
4. H. Iwamura, H. Iwasaki, K. Kubodera, Y. Torii, J. Noda, Simple polarisation-independent optical circulator for optical transmission systems. *Electron. Lett.* **15**, 830–831 (1979)
5. T. Matsumoto, Polarisation-independent optical circulator coupled with multimode fibres. *Electron. Lett.* **16**, 8–9 (1980)
6. Y. Fujii, Polarization-independent optical circulator having high isolation over a wide wavelength range. *IEEE Photon. Technol. Lett.* **4**, 154–156 (1992)
7. J.-H. Chen, D.-C. Su, J.-C. Su, Holographic spatial walk-off polarizer and its application to a 4-port polarization-independent optical circulator. *Opt. Express* **11**, 2001–2006 (2003)
8. W.L. Emkey, A polarization-independent optical circulator for 1.3  $\mu\text{m}$ . *J. Lightw. Technol.* **LT-1**, 466–469 (1983)
9. T. Matsumoto, Polarization-independent isolators for fiber optics. *Trans. IECE Japan* **E62**, 516–517 (1979)
10. K. Shiraiishi, T. Chuzenji, S. Kawakami, Polarization-independent in-line optical isolator with lens-free configuration. *J. Lightw. Technol.* **10**, 1839–1842 (1992)
11. K. Shiraiishi, New configuration of polarization-independent isolator using a polarization-dependent one. *Electron. Lett.* **27**, 302–303 (1991)
12. B.E.A. Saleh, M.C. Teich, *Fundamentals of Photonics*, 3rd edn. (Wiley, Hoboken, 2007). ISBN: 0471358320
13. K. Ando, Nonreciprocal devices for integrated optics. *Proc. SPIE*, vol. 1126 (1989), pp. 58–65
14. H. Yokoi, T. Mizumoto, K. Maru, Y. Naito, Direct bonding between InP and rare earth iron garnet grown on GdGaO substrate by liquid phase epitaxy. *Electron. Lett.* **31**, 1612–1613 (1995)
15. M. Levy, R.M. Osgood, A. Kumar, H. Bakhru, Epitaxial liftoff of thin oxide layers: Yttrium iron garnets onto GaAs. *Appl. Phys. Lett.* **71**, 2617–2619 (1997)
16. N. Sugimoto, H. Terui, A. Tate, Y. Katoh, Y. Yamada, A. Sugita, A. Shibukawa, Y. Inoe, A hybrid integrated waveguide isolator on a silica-based planar lightwave circuit. *J. Lightw. Technol.* **14**, 2537–2546 (1996)
17. W. Zaets, K. Ando, Optical waveguide isolator based on nonreciprocal loss/gain of amplifier covered by ferromagnetic layer. *IEEE Photon. Technol. Lett.* **11**, 1012–1014 (1999)
18. M. Vanwolleghem, P. Gogol, P. Beauvillain, W. Van Parys, R. Baets, Design and optimization of a monolithically integratable InP-based optical waveguide isolator. *J. Opt. Soc. Am. B* **24**, 1–12 (2007)
19. H. Shimizu, Y. Nakano, Fabrication and characterization of an InGaAsP/InP active waveguide optical isolator with 14.7 dB/mm TE mode nonreciprocal attenuation. *J. Lightw. Technol.* **24**, 38–43 (2006)
20. H. Shimizu, Y. Nakano, Monolithic integration of a waveguide optical isolator with a distributed feedback laser diode in the 1.5- $\mu\text{m}$  wavelength range. *IEEE Photon. Technol. Lett.* **19**, 1973–1975 (2007)

# Chapter 11

## Fiber Amplifiers

Karsten Rottwitt

**Abstract** The chapter gives a detailed treatment of erbium-doped fiber amplifiers (EDFA), Raman amplifiers, and parametric amplifiers. Each section comprises the fundamentals including the basic physics and relevant in-depth theoretical modeling, amplifier characteristics and performance data as a function of specific operation parameters. Typical applications in fiber-optic communication systems and the improvements achievable through the use of fiber amplifiers are illustrated.

Since the early days of optical communication much effort has been put into making optical fibers with as low an intrinsic attenuation as possible. State-of-the-art high-capacity transmission optical fibers have a minimum attenuation close to 0.2 dB/km at the wavelength 1555 nm. Figure 11.1 illustrates the attenuation as a function of wavelength in a state-of-the-art high-capacity optical fiber.

For wavelengths in the range from 500 to 1550 nm the attenuation is mainly due to Rayleigh scattering whereas the loss at wavelengths beyond 1550 nm is mainly due to infrared absorption [1].

Even though 0.2 dB/km is a very low attenuation, it is obvious that there is a need for optical amplification when transmitting an optical signal over long distances. For this reason it is clear that the development of the erbium-doped fiber amplifier led to huge progress within the field of optical communication. It may be fair to state that the erbium-doped fiber amplifier enabled tremendous progress in the field of optical communication, progress, which emphasized the need for more and more bandwidth. This together with the availability of high-power fiber lasers, powered by erbium-doped fiber amplifiers, led to the interest in Raman amplifiers which again enabled further increase in the capacity of optical communication systems. Even though the Raman amplifier has proven strong benefits it appears to be a safe

---

Karsten Rottwitt (✉)

DTU Fotonik, Department of Photonics Engineering, Technical University of Denmark, DTU, 2800 Kgs. Lyngby, Denmark  
e-mail: karo@fotonik.dtu.dk

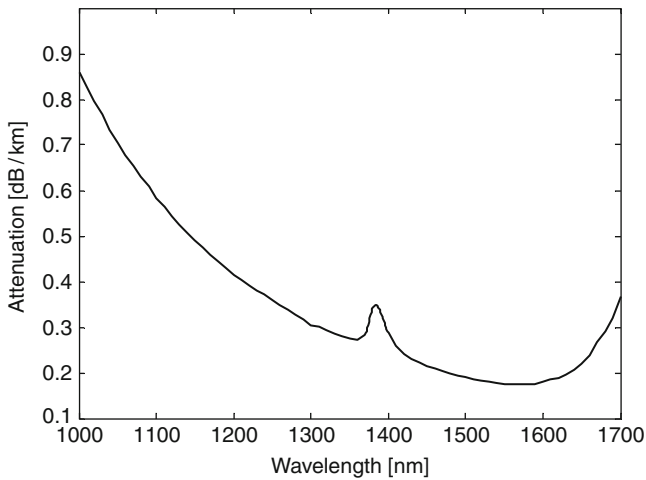


**Fig. 11.1** The attenuation in a standard single-mode optical fiber versus wavelength. Data adapted from [1]

statement that the erbium-doped fiber amplifier will continue to be one of the most important components within optical communication systems.

Lately the search for even higher capacity has seeded a strong interest in novel modulation schemes and consequently also a search for optical amplifiers which may assist in improved system performance. Such an amplifier may be the parametric amplifier which in addition to being able to amplify an optical signal also may enable further signal processing such as regeneration or wavelength conversion of a signal.

In the following chapter the above mentioned three optical fiber amplifier schemes are discussed. Section 11.1 is dedicated to the erbium-doped fiber amplifier, Sect. 11.2 to the fiber Raman amplifier and Sect. 11.3 to the fiber optical parametric amplifier. The chapter is concluded in Sect. 11.4 with a short summary of the three methods of optical amplification.

## 11.1 The EDFA

In the erbium-doped fiber amplifier (EDFA) the core of the optical fiber is co-doped with erbium ions. These have energy levels separated by energies corresponding to optical frequencies. The energy levels are defined by the angular momentum of the electrons of the ions together with their spin. When an ion makes a transition between two energy levels, light may be emitted. This together with the fact that the host fiber is a silica-based optical fiber makes an EDFA an obvious component to splice to passive fibers for achieving amplification.



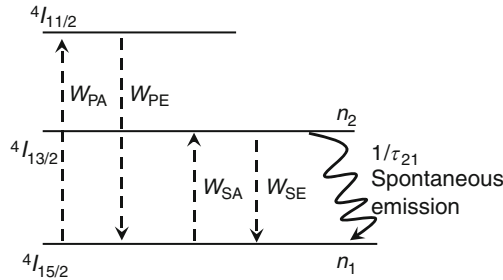


**Fig. 11.2** The energy levels of  $\text{Er}^{3+}$  are characterized by quantum numbers for the orbital momentum  $L$  and spin-momentum  $S$ . For  $\text{Er}^{3+}$   $L = 6$  and  $S = 3/2$ . The total angular momentum,  $J$ , varies between  $L - S = 9/2$  and  $L + S = 15/2$  [3, 4], the latter being the ground level. The notation for the energy levels is:  $2S+1L_J$ , where  $L$  is quoted with a letter rather than a number ( $I$  represents 6). The energy of one electron is changed, between the different energy levels either by pumping or due to emission. An electron may exist in the  $4I_{13/2}$  level for up to about 10 ms

The EDFA has numerous advantages of which the most important ones are listed below:

- Gain at 1555 nm coinciding with the loss minimum of optical fibers
- Large gain, and large gain efficiency, tens of dB per mW of pump power
- Low noise figure, 3 dB at high gain
- Low polarization dependence
- Low channel-to-channel crosstalk.

The EDFA was heavily researched in the late 1980s and in the early 1990s, see for example [2–4]. The EDFA may be one of the most important inventions for optical communication, and it is for example less likely that we would have trans-oceanic transmission links employing wavelength-division multiplexed signals, nor metro/access networks, without the EDFA.

### 11.1.1 Energy Levels

The erbium-ion may be described using a simplified energy level diagram as depicted in Fig. 11.2. When optically pumped at 980 nm the EDFA acts as a 3-level laser system which means that the  $\text{Er}^{3+}$  ion is excited from the ground state level  $4I_{15/2}$  to the third energy level  $4I_{11/2}$  with rate  $W_{PA}$  (index PA indicates absorption at pump wavelength) from which it rapidly, instantaneous in the figure, decays to the upper laser level  $4I_{13/2}$  where the ion exists for a finite time (10 ms). Conversely the erbium ion may also decay to the ground state energy level with rate  $W_{PE}$  (index PE indicates emission at pump wavelength). While in the  $4I_{13/2}$  state, the erbium ion may decay back to the ground level either in a spontaneous process with rate  $1/\tau_{21}$  ( $\tau_{21}$  is the lifetime of the energy level  $4I_{13/2}$ ) or stimulated by a signal with rate  $W_{SE}$  (index SE indicates emission at signal wavelength). The signal may also cause the erbium ion to change energy level from  $4I_{15/2}$  to  $4I_{13/2}$  with rate  $W_{SA}$  (index SA indicates absorption at signal wavelength).

It is noted that one may also pump the erbium-doped fiber amplifier using light at 1480 nm, in which case the  $\text{Er}^{3+}$  ions are excited directly into the upper energy level  ${}^4I_{13/2}$ .

### 11.1.2 Rate Equations

In any practical case the population levels at the relevant energy levels are determined from rate equations. Assuming that the decay from  ${}^4I_{11/2}$  to  ${}^4I_{13/2}$  is instantaneous or that one is pumping using the pump wavelength at 1480 nm, the rate equation for the population of ions in the lower energy level  $n_1(r, \phi, z)$  is

$$\begin{aligned} \frac{dn_1(r, \phi, z)}{dt} = & - [W_{SA}(r, \phi, z) + W_{PA}(r, \phi, z)] n_1(r, \phi, z) \\ & + \left[ W_{SE}(r, \phi, z) + W_{PE}(r, \phi, z) + \frac{1}{\tau_{21}} \right] n_2(r, \phi, z), \end{aligned} \quad (11.1)$$

where the rates  $W_{SE}$ ,  $W_{SA}$ ,  $W_{PE}$ ,  $W_{PA}$  and  $1/\tau_{21}$  are as described in Fig. 11.2. A similar rate equation exists for the population of ions in the upper energy level  $n_2(r, \phi, z)$ , which may be found using Fig. 11.2 or simply by using  $n_2 = \rho - n_1$ , where  $\rho$  is the total erbium concentration level of the fiber. When evaluating the steady state case, i.e.,  $dn_1/dt = 0$  and  $dn_2/dt = 0$ , the population  $n_2(r, \phi, z)$  has the solution

$$n_2 = \rho \frac{W_{SA} + W_{PA}}{W_{SE} + W_{SA} + W_{PE} + W_{PA} + 1/\tau_{21}}. \quad (11.2)$$

The evolution of signal and spontaneous emission determines the signal gain and the noise performance. In the following these equations are described together with their solutions.

As discussed above, the two wavelengths used for pumping are 1480 nm or 980 nm, respectively. When pumping at 1480 nm the EDFA acts as a two-level laser system and the inversion, defined as the number of excited Er-ions relative to the total number of ions:  $x = n_2/(n_1 + n_2)$ , can not exceed a maximum level of 70 %. If instead erbium is pumped at 980 nm, the rate  $W_{PE}$  approximates zero and consequently the maximum inversion may be 100 %.

### 11.1.3 Signal Propagation

In the signal mode the power may be separated into a sum of pure signal and spontaneous emission. The pure signal power is governed by

$$\frac{dP_s}{dz} = [\gamma_e(\nu_s, z) - \gamma_a(\nu_s, z)] P_s, \quad (11.3)$$

where  $\nu_s$  is the frequency of the signal and  $z$  the position coordinate. The emission and absorption factors  $\gamma_e$  and  $\gamma_a$  are defined through the material emission and absorption cross factors ( $\sigma_e(\nu)$ ,  $\sigma_a(\nu)$ ), together with the overlap integrals between the populations  $n_1$  and  $n_2$  and the transverse signal mode  $I_s(r)$

$$\gamma_e(\nu, z) = \sigma_e(\nu) 2\pi \int_0^{a_d} n_2(r, z) I_s(r) r dr, \quad (11.4)$$

$$\gamma_a(\nu, z) = \sigma_a(\nu) 2\pi \int_0^{a_d} n_1(r, z) I_s(r) r dr. \quad (11.5)$$

It is noted that the signal is assumed to be in the fundamental fiber mode, i.e., the integration over the angular coordinate  $\phi$  equals  $2\pi$ . The intrinsic fiber loss is omitted in the propagation equation (11.3), but may be included as an additional term  $-\alpha_i P_s$ , where  $\alpha_i$  is the loss rate.

The intensity of the electric field representing the signal is

$$I_s(r, \phi, z) = P_s(z) |E_s^{01}(r, \phi)|^2, \quad (11.6)$$

where  $P_s(z)$  is the signal power, and the index '01' on  $E_s^{01}(r, \phi)$  shows that the transverse distribution of the electrical field of the signal is in the fundamental mode, i.e., the LP<sub>01</sub> mode. The electrical field is normalized according to

$$\int_0^{2\pi} \int_0^b |E_s^{01}(r, \phi)|^2 r dr d\phi = 1, \quad (11.7)$$

where  $b$  is the radius of the cladding. The solution to the propagation equation for the signal is:

$$P_s(z) = P_s(z=0) \exp \left\{ \int_0^z [\gamma_e(\nu_s, x) - \gamma_a(\nu_s, x)] dx \right\} = P_s(z=0) G. \quad (11.8)$$

Equation (11.8) defines the signal gain  $G$  as the output signal power relative to the input signal power.

In analogy to the propagation equation for the signal, a similar propagation equation exists for the pump, i.e.,

$$\frac{dP_p}{dz} = [\gamma_e(\nu_p, z) - \gamma_a(\nu_p, z)] P_p \quad (11.9)$$

where  $\gamma_e$  and  $\gamma_a$  are now determined by replacing the signal frequencies by the pump frequency and by replacing the signal intensity distribution by the pump intensity

distribution in (11.4) and (11.5), using as above that the intensity of the pump is

$$I_p(r, \phi, z) = P_p(z) |E_p^{01}(r, \phi)|^2, \quad (11.10)$$

where  $P_p(z)$  is the pump power which is in the fundamental fiber mode.

### 11.1.4 Emission and Absorption Cross Sections

Rather than using the comprehensive model described above, which requires numerical analysis, alternative semi-analytical models have found their use to predict amplifier gain, gain saturation, and noise properties [5–7]. In these models the gain per unit length is given as

$$\frac{G(\lambda)}{L} = [g^*(\lambda) + \alpha(\lambda)] \text{Inv} - \alpha(\lambda), \quad (11.11)$$

where  $\alpha(\lambda) = \sigma_a(\lambda)\Gamma(\lambda)\rho$  is the absorption per unit length with no inversion, and  $g^*(\lambda) = \sigma_e(\lambda)\Gamma(\lambda)\rho$  is the gain per unit length with full inversion. Figure 11.3a shows examples of absorption and gain per unit length for a specific fiber.  $\rho$  is the total erbium concentration and  $\Gamma(\lambda)$  is the overlap between the optical mode and the transverse distribution of the erbium ions. Inv is the average inversion of ions in the amplifier when operating under signal-induced gain compression and  $\text{Inv} = \frac{1}{L} \int_0^L (n_2/\rho) dz$ . Figure 11.3b shows gain as a function of inversion level as obtained in an EDFA.

**Material Systems** A silica-based optical fiber consists of a core surrounded by a silica cladding. The core material is silica to which a codopant is added to raise the refractive index. In standard passive fibers germanium is typically used as the codopant, however, in erbium-doped fibers aluminum is a commonly used codopant material. The reason is that the absorption and emission spectra depend on the core material and it has been found that by using aluminum it is possible to obtain advantages with respect to the spectral properties of the amplifier.

In erbium-doped fibers, the fiber is obviously doped with erbium in addition to the index raising dopant, i.e., germanium/aluminum. With this material system amplification around 1555 nm is obtained. The erbium-doped fiber is pumped with either 1480 nm or 980 nm. Other active materials may also be used including ytterbium, neodymium, praseodymium, or thulium. All of these have been demonstrated for applications at different wavelengths. As it is of relevance to this chapter, it should be noted that ytterbium may be used in combination with erbium, referred to as Er:Yb. The resulting fiber is pumped using 980 nm, and the pump energy is first used to excite the ytterbium system and then energy is transferred to the erbium system. This material combination offers much higher pump absorption per unit length, and the constructed amplifier may provide more gain per unit length as compared to a fiber where erbium is the only rare earth dopant.

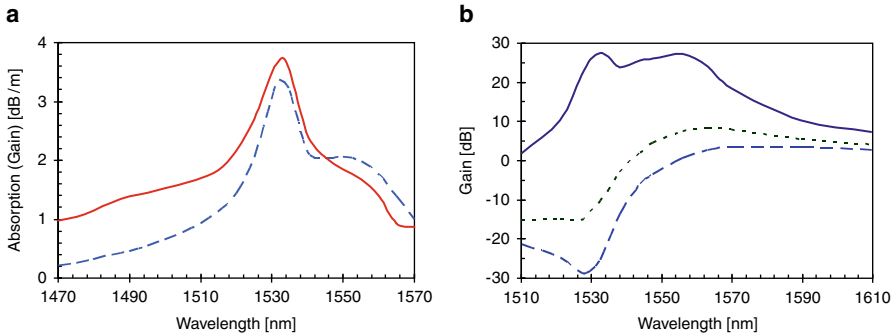


**Fig. 11.3** Absorption (*solid*) and gain (*dashed*) spectra versus wavelength [5–7] (a), and gain as a function of wavelength for different average levels of inversion: upper trace 63 %, middle trace 45 %, lower trace 38 % (b). The data are a courtesy of OFS Fitel Denmark. Both figures are for aluminum-germanium-erbium-doped silica fibers

Fibers doped solely with ytterbium are often used to obtain very high output power amplifiers. The ytterbium system is pumped at 980 nm and provides gain from 1000 to 1100 nm. For further details regarding different material systems see for example [3, 4].

### 11.1.5 Characteristics

**Polarization Dependence** The polarization dependence of erbium-doped amplifiers is very weak, and as noted in [2] only becomes significant when many amplifiers are cascaded. The polarization-dependent gain manifests itself when a signal with a well-defined state of polarization saturates the amplifier. As an example, the spontaneous emission in the polarization state orthogonal to the signal then experiences a gain higher than the signal and the spontaneous emission in the same state of polarization as the signal. Consequently, the spontaneous emission in the orthogonal state increases faster than the spontaneous emission in the same state of polarization as the signal. A polarization-dependent gain of 0.01 dB was reported by V.L. Mazurczyk and coworkers [8].

**Time Response** The response time of erbium is defined by the lifetime of the excited state  $^4I_{13/2}$  in Fig. 11.2. This is a metastable state and consequently it has a rather long lifetime of 10 ms, which is much longer than the time for one bit in a communication signal, for example a 40 Gbit/s non return to zero signal where a bit slot equals 25 ps. Consequently, the performance of an amplifier is well predicted by considering the signal as a continuous wave. An additional benefit of the long lifetime of the metastable state is that the pump source may be rather noisy without any noise transfer from the pump to the signal, assuming that the frequency of the pump noise exceeds the kHz erbium response defined by the metastable lifetime.

It should be noted that in a long chain of amplifiers used to amplify a WDM signal, the dynamic behavior may create transients that potentially could create detrimental power spikes [9].

**Dispersion** Whenever a material has a significant absorption or gain peak in the wavelength space, it may also have significant group velocity dispersion. This could impact propagation of short pulses through the material. In addition, when designing a fiber laser aiming at a high repetition rate, the fiber length is critical. Consequently, in such amplifiers, a high erbium concentration is desired. In relation to this it is noted that the erbium concentration has an upper limit due to effects such as clustering which results in reduced gain efficiency [10]. In a recent work by B. Pálsdóttir concentration levels as high as  $5 \times 10^{25}$  ions/m<sup>3</sup> to  $10 \times 10^{25}$  ions/m<sup>3</sup> (corresponding to 75–150 dB/m absorption at 1530 nm) have been reported [10].

Most often erbium-doped fibers have normal dispersion and can be used to compensate for anomalous dispersion in standard single-mode fibers used in laser cavities. However, when the inversion changes in a pumped EDFA, the dispersion changes significantly. For a passive fiber with an NA of 0.27 the dispersion equals  $-40$  ps/(nm km) at 1550 nm, though it is almost independent of wavelength from 1520 to 1620 nm. When the fiber is pumped, the dispersion changes significantly and may even be normal or anomalous, depending on the used pump power, for further details the reader is referred to [10].

### 11.1.6 Amplifier Performance

**Amplified Spontaneous Emission** A signal may be amplified in an erbium-doped fiber amplifier only because of stimulated emission. However, stimulated emission is accompanied by spontaneous emission. The spontaneous emission propagates in both directions of the optical fiber. Obviously, the spontaneous emission generated in the first infinitesimal section of the optical fiber is amplified in the succeeding fiber section. Thus, the power of the spontaneous emission at the output of the amplifier is referred to as amplified spontaneous emission (ASE). In the following, the forward-propagating ASE is denoted ASE<sup>+</sup> whereas the backward-propagating ASE is denoted ASE<sup>-</sup>.

Compared to the equation for the signal, the propagation equation for spontaneous emission includes a source term. The propagation equations are:

$$\frac{dP_{\text{ASE}\pm}}{dz} = \pm 2h\nu\gamma_e(\nu, z)B_0 \pm [\gamma_e(\nu_s, z) - \gamma_a(\nu_s, z)] P_{\text{ASE}\pm}, \quad (11.12)$$

where  $h\nu B_0$  is the power of one photon per unit bandwidth accumulated within bandwidth  $B_0$ . By solving the propagation equation (11.12), the power of the ASE may be predicted.

**Noise Figure** The performance of an amplifier is characterized by its gain but equally important also by its noise performance. It is customary to quantify the noise performance of an amplifier by its degradation of the signal-to-noise ratio when the signal is amplified by the amplifier. The degradation of the signal-to-noise ratio is called the noise figure [3, 4]. The signal-to-noise ratio is defined as the squared mean photon number  $\langle n \rangle$  relative to the variance of the photon number  $V_n$ . At the output of an erbium amplifier the mean and variance of the photon number are:

$$\begin{aligned}\langle n \rangle &= Gn_0 + M\tilde{n}, \\ V_n &= G^2(V_0 - n_0) + Gn_0(2\tilde{n} + 1) + M\tilde{n}(\tilde{n} + 1),\end{aligned}\quad (11.13)$$

where  $G$  is the gain of the amplifier and  $n_0$  is the mean signal photon number at launch.  $\tilde{n}$  is the noise photon number while  $M$  is the number of signal modes the detector is sensitive to, and  $V_0$  the variance of the photon number at launch [3, 4]. Assuming the signal is quasi-monochromatic with frequency  $\nu_s$ , the noise power in the signal mode is related to the noise photon number through  $\tilde{P} = h\nu_s\tilde{n}B_0$ , where  $B_0$  is the bandwidth of the signal. It should be noted that for the signal mode  $B_0$  equals  $1/T$ , where  $T$  is the time duration of the signal. Assuming furthermore that  $V_0 = n_0$ , then the electrical signal-to-noise ratio is given by

$$\text{SNR}_e = \frac{Gn_0}{2\tilde{n} + 1 + \frac{M\tilde{n}}{Gn_0}(\tilde{n} + 1)} \approx \frac{Gn_0}{2\tilde{n} + 1} \approx \frac{Gn_0}{2\tilde{n}}. \quad (11.14)$$

The first approximation is true when the noise power is much less than the signal power, i.e.,  $Gn_0/M\tilde{n} \gg 1$ , whereas the second approximation is valid when the added spontaneous emission is significant, i.e.,  $\tilde{n} \gg 1/2$ . The ratio  $Gn_0/\tilde{n}$  represents the optical signal-to-noise ratio at the output of the amplifier. When the input signal is shot-noise limited and therefore has Poissonian statistics i.e.,  $V_0 = n_0$ , the noise figure  $F = \text{SNR}_{\text{in}}/\text{SNR}_{\text{out}}$  equals

$$F = \frac{2\tilde{n} + 1 + \frac{M\tilde{n}}{Gn_0}(\tilde{n} + 1)}{G} \approx \frac{2\tilde{n} + 1}{G}. \quad (11.15)$$

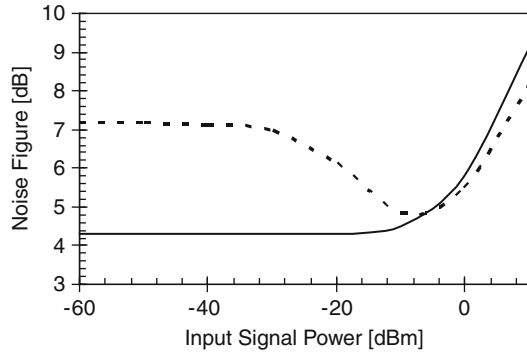
This approximation is valid if the output signal power exceeds the noise power, i.e.,  $Gn_0/M\tilde{n} \gg 1$ , which is true in almost all cases. Expressing the added noise in terms of power, the noise figure in (11.15) may be written as

$$F = \frac{2\tilde{P}}{Gh\nu B_0} + \frac{1}{G}, \quad (11.16)$$

where  $\tilde{P}$  is the spontaneously emitted power within the bandwidth  $B_0$  and in the signal polarization.

**Amplifier Efficiency** The erbium-doped fiber amplifier is characterized by its high gain efficiency of several dB of gain per mW of pump power. In addition, this is obtained in amplifiers that are only tens of meters long. Moreover, the EDFA is also

**Fig. 11.4** Noise figure as a function of input signal power for a saturated amplifier. The signal wavelength is 1550 nm whereas the pump is at 1470 nm and a pump power of 60 mW has been assumed. The *dashed line* characterizes an amplifier without components to reduce ASE, the *solid line* represents the case with an isolator in the amplifier. Data adopted from [8]



characterized by noise figures close to 3 dB for high gain amplifiers. Consequently the EDFA is ideal for discrete amplifiers, and a large effort has been made to optimize such amplifiers by including ASE suppression filters, optical isolators [11], and dividing the amplifier into different wavelength bands, C band amplifiers, L band amplifiers etc. [12].

**Optimum Length** If the case is considered where the pump power is given and the signal power fixed, then the signal gain increases as the fiber length increases and as long as the fiber is sufficiently short. However, for long lengths the inversion level can not be maintained and the gain drops because of absorption, erbium absorption as well as intrinsic fiber loss, at the signal wavelength. Consequently, there exists an optimum fiber length.

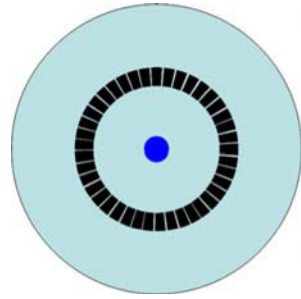
**Depletion** For a given amplifier design, i.e., for an amplifier with a fixed length and a fixed pump power, the gain is constant for low input signal power levels. However, as the input signal power increases, the gain decreases and the output signal power approaches a constant value. When this happens, the amplifier is saturated. The input signal power level where the gain has dropped by 3 dB, is referred to as the saturation power level. This power level increases linearly with pump power and inversely with the emission cross section at the signal wavelength [2].

When the amplifier is operated in depletion, the inversion level drops and consequently the noise performance of the amplifier worsens. Figure 11.4 illustrates the noise figure of an amplifier as a function of input signal power. Two graphs are shown. In the dashed curve a simple amplifier design is considered whereas the solid curve illustrates the noise figure obtained if additional noise reduction filters/isolators are inserted into the amplifier [11].

The spectral gain profile depends on the input signal power level which in effect is the inversion of the amplifier. Consider a fixed fiber length and a fixed pump power level. In this case the inversion changes as the signal input power level increases because an increased signal power level uses the pump power over a shorter distance compared to the undepleted power level. As a consequence the inversion level changes and the spectral shape is modified.



**Fig. 11.5** An illustration of an air-clad fiber. In [13] the pump guide is  $50\ \mu\text{m}$  with a cladding defined by a ring of air holes, and the single-mode core has a mode field diameter of  $10\ \mu\text{m}$ . The outer diameter of the fiber is  $125\ \mu\text{m}$



### 11.1.7 Recent Applications

The erbium-doped fiber amplifier has proven itself to be one of the most important components within optical communication systems. The amplifier is now (readily) commercially available and applied in almost all communication system architectures, and most research on this type of commodity amplifiers is directed toward production parameters such as uniformity and consistency during fabrication and splicing to other fibers [10].

In addition to being used as an amplifier in communication systems, the erbium-doped fiber amplifier is also widely used in fiber lasers. In the mid 1990s focus was directed toward low-power fiber lasers, including single-frequency narrow-linewidth fiber lasers. However, within the last decade focus has been directed toward high-power fiber lasers, continuous wave as well as short-pulsed lasers, and new fibers for these applications are still being researched. These fibers include fibers that may handle high powers for example for high-power delivery, fibers that may be used for pulse compression, so-called air-clad fibers, higher order mode (HOM) fibers and rod-like fibers. In the following a short state-of-the-art regarding such erbium-doped fibers is provided.

**Air-Clad Fibers** To increase the output power of an erbium amplifier it has been suggested to use a so-called air-clad fiber, see Fig. 11.5 [10]. This fiber type consists of an inner core which is highly doped with erbium and surrounded by a cladding, defining an active single-mode fiber for the signal. The cladding is surrounded by an additional cladding which is a ring of air holes. This gives a high NA, 0.5 to 0.6, for the multimode waveguide for the pump beam.

In [13] F. Koch and coworkers demonstrate a 30 dBm output power amplifier providing 40 dB gain from 1530 to 1568 nm. The result was achieved by combining a preamplifier pumped by 750 mW at 974 nm succeeded by an air-clad erbium-doped fiber pumped by 8 W at 976 nm. The length of the air-clad fiber was 20 m.

**Rod-Type Amplifiers** Air-clad fibers may also be achieved with microstructuring not only of the air cladding but also of the cladding of the single-mode core [14]. By using microstructuring of the fiber it has been possible to enlarge the core as well as the cladding region and consequently increase the pump absorption.

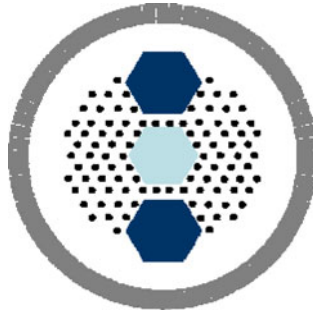


**Fig. 11.6** Illustration of the cross section of a PM rod-type fiber. The center of the fiber has a hexagonal structure of Yb/Al doping with a corner-to-corner distance of  $70\ \mu\text{m}$ . The pump waveguide has a diameter of  $200\ \mu\text{m}$  and is surrounded by 90 air holes which define the cladding for the pump. Two stress zones, top and bottom, of the microstructured area, enable the polarization state of the light to be maintained during propagation [15]

In 2008 O. Schmidt and coworkers demonstrated an ytterbium-doped polarization-maintaining (PM) rod-type amplifier [15]. A figure of the fiber cross section is shown in Fig. 11.6.

The center of the fiber has a hexagonal structure of Yb/Al doping with a corner-to-corner distance of  $70\ \mu\text{m}$  resulting in a mode field area of  $2300\ \mu\text{m}^2$ , and a beam quality factor  $M^2$  equal to 1.2, where a diffraction limited beam has an  $M^2$  of 1, which is the lower limit of  $M^2$ . The pump waveguide has a diameter of  $200\ \mu\text{m}$  and is surrounded by 90 air holes, which defines the cladding for the pump. This results in an NA for the pump waveguide of 0.6 at 976 nm. The ratio of the pump to active cross sectional area leads to a small signal absorption of 30 dB/m at 976 nm. The air cladding is surrounded by a 1.5 mm outer cladding. By using the rod-type amplifier an output power of 163 W, with a degree of polarization of 85 %, has been reported [15].

**Higher Order Mode Fibers** To achieve very high output power fiber lasers including high-energy pulsed fiber lasers, a significant effort has been made to make large-mode-area fibers, for example using microstructured fibers. Such a fiber allows mitigation of nonlinear effects such as Raman scattering, Brillouin scattering, self-phase modulation, and four wave mixing. Recently, another approach, which relies on using higher order modes of the optical fiber, has been demonstrated. Mode areas up to  $3200\ \mu\text{m}^2$  at 1600 nm have been demonstrated [16].

In 2007 S. Ramachandran and coworkers gave the first demonstration of amplification in higher order mode fibers [17]. In their experiment they propagated a signal in the  $\text{LP}_{07}$  mode with an effective mode area of  $2040\ \mu\text{m}^2$ . The HOM fiber was doped with Yb and the signal was at 1083 nm while the amplifier was pumped using conventional pumps at 975 nm launched into the cladding surrounding the inner core, see Fig. 11.7. A signal gain of 3.9 dB with a slope efficiency (rate of change of output power per unit change in absorbed pump power) of 62 % was achieved for

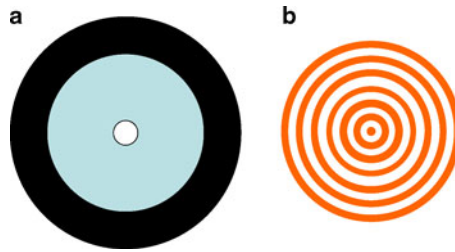


**Fig. 11.7** Cross section of the HOM fiber used in [17] (a), illustration of the intensity distribution of the LP<sub>07</sub> mode propagating in the fiber (b). The fiber consists of a single-mode-like central core which is surrounded by a 40  $\mu\text{m}$  inner cladding doped with Yb. Finally, this structure is surrounded by an outer cladding. In [17] the length of the HOM fiber was 4.75 m

an input power of 6 W, while a signal gain of 8.2 dB and a slope efficiency of 48 % were obtained for an input power of 1 W.

## 11.2 Raman Amplifiers

Within optics communication, Raman scattering in optical fibers may be applied to obtain amplification. This is achieved by simultaneously launching light at two frequencies separated by a frequency corresponding to the energy of the phonons in the glass fiber. Hereby light is transferred from the high frequency beam to the low frequency beam. The benefits of Raman amplification include:

- Gain at any wavelength: The Raman scattering process only depends upon the frequency shift between pump and signal. In silica this is 13 THz.
- Wide bandwidth: By launching multiple pump wavelengths a composite spectrum is obtained. In this way it is possible to broaden the gain bandwidth [18].
- Distributed gain medium: The Raman gain per unit length is relatively weak. Hence it is possible to counterbalance the loss along the transmission. This distributed amplification has unique noise properties [19].
- Intrinsic to silica: Silica has a Raman efficiency that is sufficient to achieve gain such that a transmission fiber may be turned into an amplifier in itself, i.e., no special doping is necessary [20].

Figure 11.8 displays a generic fiber Raman amplifier.

In the simplest configuration only one pump is used and the amplifier is either forward or backward pumped. In short discrete amplifiers the amplifier may consist of multiple stages, gain equalization filters, isolators etc.

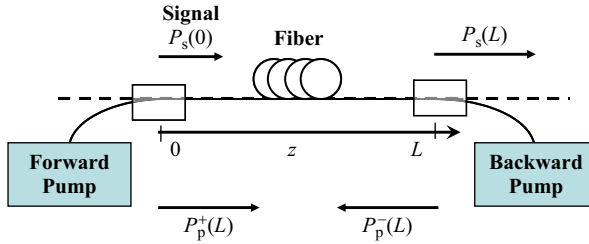


**Fig. 11.8** Generic set-up of Raman amplifier. Forward and backward pump coupled together with the signal in wavelength-dependent couplers. The signal is propagating in one direction only. Bi-directional signal transmission is not considered in this chapter

The amplifier fiber is characterized with respect to its Raman gain coefficient and the attenuation of the fiber at the pump and signal wavelength. Finally, the dispersion properties may also be important for the amplifier performance when using multiple pump wavelengths, due to cross-coupling among pumps and between pumps and signals.

### 11.2.1 Propagation Equations

In the following an approach is presented which enables the prediction of the performance of a Raman amplifier based on the evolution of optical power. The propagation equation of the signal is

$$\frac{dP_s}{dz} = g_R P_p P_s - \alpha_s P_s, \quad (11.17)$$

where  $g_R$  is the Raman gain coefficient,  $P_p$  and  $P_s$  are the powers of the pump and signal, respectively.  $P_p$  may be a sum of a forward-  $P_p^+$  and a backward-propagating  $P_p^-$  pump beam. Finally,  $\alpha_s$  is the intrinsic loss at the wavelength of the signal. In (11.17) the first term on the right hand side represents the Raman gain while the second term represents the intrinsic loss.

The equation for the forward- and the backward-propagating pump power is

$$\pm \frac{dP_p^\pm}{dz} = -\frac{\nu_p}{\nu_s} g_R P_p^\pm P_s - \alpha_p P_p^\pm, \quad (11.18)$$

where the first term on the right hand side represents depletion due to the signal and the second term on the right hand side describes the attenuation at the pump wavelength described by  $\alpha_p$ .

Equation (11.17) may be solved analytically, and the signal gain, i.e., the signal output power relative to the signal input power, at the output end of a fiber of

length  $L$  is

$$G(L) = \exp\left(\int_0^L g_R P_p(\tilde{z}) d\tilde{z} - \alpha_s L\right). \quad (11.19)$$

Assuming that the pump is independent of the signal and determined solely by the intrinsic fiber loss, i.e., the pump decays exponentially with the intrinsic fiber loss, the gain may be evaluated analytically. This situation is referred to as the undepleted pump regime, and the propagation of the pump power is described simply through

$$P_p(z) = P_p^0 \exp(-\alpha_p z) \quad (11.20)$$

when the pump propagates in the positive  $z$ -direction which means that it is launched from the signal input end, and it is referred to as the co-pumped or the forward-pumped Raman amplifier. Alternatively, the pump propagates according to

$$P_p(z) = P_p^L \exp(-\alpha_p(L - z)) \quad (11.21)$$

when the pump propagates in the negative  $z$ -direction or opposite to the signal, referred to as the counter-pumped, or the backward-pumped Raman amplifier.

The signal gain in the undepleted forward-pumped Raman amplifier is given by

$$G(L) = \exp(g_R L_{\text{eff}} P_p^0) \exp(-\alpha_s L), \quad (11.22)$$

where  $P_p^0$  is the launched pump power, and  $L_{\text{eff}}$  is the effective fiber length for the Raman amplifier, in the following referred to as the Raman effective length, given by

$$L_{\text{eff}} = \frac{1 - \exp(-\alpha_p L)}{\alpha_p}. \quad (11.23)$$

In a typical transmission fiber, the loss at the pump wavelength is  $\sim 0.25$  dB/km, and therefore the Raman effective length is about 17 km.

The gain of the undepleted backward-pumped Raman amplifier is identical to the gain in (11.22) only with  $P_p^0$  replaced by  $P_p^L$ .

Equation (11.22) shows that the gain in decibels increases linearly with the pump power in Watts. For a typical dispersion-shifted transmission fiber (with  $A_{\text{eff}} \approx 75 \mu\text{m}^2$ ), and an optical fiber much longer than the effective length, the Raman gain is approximately 55 dB/W when the intrinsic loss is omitted and an unpolarized pump is assumed. This number represents a typical value for the gain efficiency of Raman amplifiers.

The undepleted pump approximation is very powerful and may be used to estimate the levels of gain and spontaneous emission. The criterion for its validity is

that the loss of the pump should be dominated solely by the intrinsic loss [21], i.e.:

$$\frac{\nu_p}{\nu_s} g_R P_s \ll \alpha_p. \quad (11.24)$$

In a typical dispersion-shifted fiber with  $\alpha_p \approx 0.057 \text{ km}^{-1}$  ( $= 0.25 \text{ dB/km}$ ) and  $g_R \approx 0.7 \text{ (W km)}^{-1}$ , the undepleted pump approximation is valid for  $P_s \ll 80 \text{ mW}$ . It should be noted that in (11.24) depletion due to spontaneous emission is neglected which is a valid approximation since the signal is typically orders of magnitude higher than the spontaneous emission.

The Raman gain is often quoted in terms of the On-Off Raman gain which is the ratio of the signal output power with the pump on to the signal output power with the pump off. The On-Off Raman gain is easily calculated in the undepleted pump regime by omitting the factor  $\exp(-\alpha_s L)$  in (11.22).

**Multiple Pump Wavelengths** One of the advantages of the Raman amplifier is that pump sources at different wavelengths may be combined to form an amplifier with a wide bandwidth. In one example, gain over 92 nm was achieved in a 45 km-long dispersion-shifted fiber by combining a pump at 1453 nm (206 mW) with a pump at 1495 nm (256 mW) [18]. This property of the Raman process may be utilized not only to achieve a wide bandwidth amplifier but equally well to achieve a flat gain spectrum [22] or a flat noise spectrum [23].

When multiple pumps propagate together, the propagation gets slightly more complicated compared to the case when only one pump beam propagates since they all mutually interact with each other through Raman scattering. However, mathematically the propagation equations are easily extended to multiple pumps as described in [22]. In general, the Raman process transfers energy from shorter to longer wavelengths. As a consequence, to achieve a gain spectrum as wide and as flat as possible by using multiple pumps, more pump power should be launched within the shorter wavelengths of a pump spectrum. For the signals in a wideband amplifier the transfer of energy from shorter to longer wavelengths also impacts the signal-to-noise ratio differently from shorter toward longer wavelengths. In general the longer signal wavelengths are favored compared to the shorter signal wavelengths.

### 11.2.2 The Raman Gain Coefficient

From the previous discussion it is obvious that the Raman gain coefficient  $g_R$  is of key relevance. Figure 11.9 displays the Raman gain coefficient for different fiber types. All have been measured using unpolarized pump light at the wavelength 1453 nm. The pure silica fiber, labeled Pure-silica, which has a fiber core of silica and a cladding with a lower refractive index, displays the lowest gain coefficient of approximately  $0.5 \text{ (W km)}^{-1}$  at its peak. The dispersion-compensating fiber, labeled DCF, which has a small core area, a silica cladding, and a core of silica glass heavily doped with germanium, displays the largest Raman gain coefficient of ap-

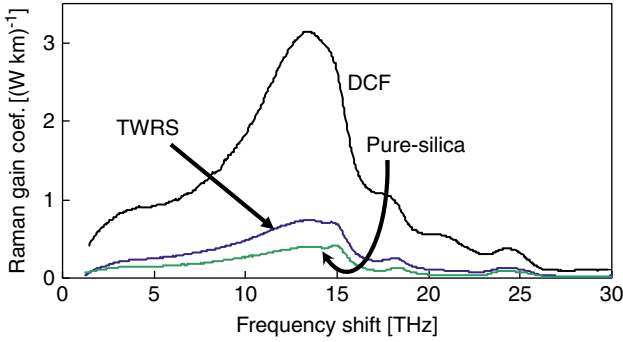


**Fig. 11.9** Raman gain coefficient versus frequency shift between pump and signal for different fiber types. In the dispersion-compensating fiber, DCF, the germanium content is higher and the effective area less than in the high-capacity transmission fiber, the TrueWave Reduced Slope fiber, TWRS. The Pure-silica fiber has no germanium in the core (data adopted from [21])

proximately  $3 \text{ (W km)}^{-1}$  at its peak. The higher gain coefficient compared to the silica core fiber is caused by the germanium content and the effective area of the fiber [20, 24]. In typical high-capacity transmission fibers, in Fig. 11.9 exemplified by an OFS TrueWave Reduced Slope fiber, labeled TWRS, the gain coefficient is close to  $0.7 \text{ (W km)}^{-1}$  at its peak. This fiber has a lower concentration of germanium compared to the dispersion-compensating fiber and an effective area of approximately  $75 \times 10^{-12} \text{ m}^2$ .

The composite spectrum of any germano-silicate fiber with moderate fractional germanium concentration (less than 50%) [20], may be predicted and scaled according to the operating wavelength [24]. The gain coefficient depends on the wavelength and the spatial overlap of the pump and signal wave which not only varies with wavelength, but even more strongly if the signal and/or the pump power are not in the fundamental mode [25].

### 11.2.3 Characteristics

**Time Response** Since the Raman scattering is an interaction between the pump, signal and molecular vibrations, the response time is not instantaneous. By taking the inverse Fourier transform of the frequency domain response, i.e., the gain spectrum as the imaginary part and the Raman-induced refractive index as the real part, see below, the Raman response in the time domain may be predicted. From this it is derived that the Raman response is in the order of a hundred femtoseconds [25].

**Raman-induced Kerr Effect** In the Raman scattering process energy is not only transferred from the short wavelength beam, the pump, to the long wavelength beam, the signal. In the process, the pump also induces a phase shift on the signal with a wavelength dependence as shown in Fig. 11.10. The induced refractive

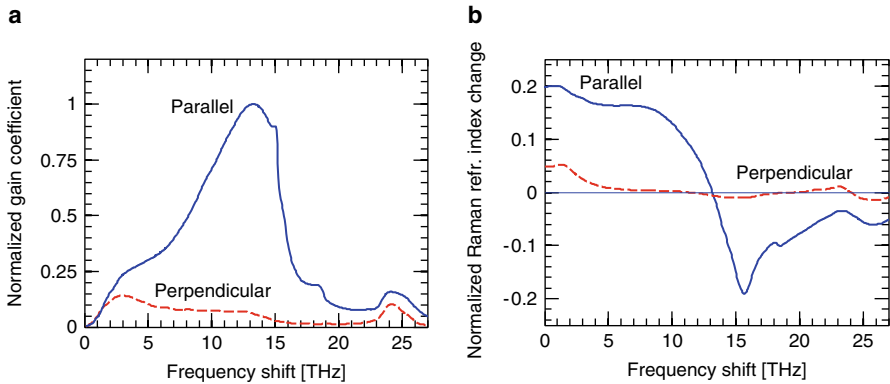


**Fig. 11.10** Raman gain coefficient (a), corresponding Raman-induced refractive index change (b), both sets of curves as a function of the frequency shift between the pump and the signal. The data are from [26] using values for fused quartz. In both figures two curves are displayed, one labeled ‘parallel’, which is recorded by measuring the scattered light in the same linear state of polarization as the launched light, and one labeled ‘perpendicular’, which is recorded by measuring the scattered light in a state of polarization perpendicular to the launched light. The curves of the Raman gain coefficient are normalized to the peak gain coefficient for the parallel measurement whereas the Raman-induced refractive index change is normalized relative to the intensity-dependent refractive index of pure silica [27]

index change is evaluated using the Kramers–Kronig relation which is also valid in the case of Raman scattering, even though the scattering is a nonlinear phenomenon [25]. The reason for this is that the Raman scattering from the signal point of view may be considered as an effective first-order nonlinearity.

**Polarization Dependence** The Raman gain spectrum of silica depends on the relative polarization of the pump and signal beams. When they are co-polarized, the peak gain is approximately 10 times higher than when they are orthogonally polarized, see Fig. 11.10. This may cause a polarization-dependent gain (PDG), which may lead to transmission impairments, for example, amplitude fluctuations, if the relative polarization of pump and signal vary randomly. However, the small amount of PDG produced in Raman amplifiers consisting of long lengths of fibers is typically not as large as in bulk samples because of intrinsic polarization-mode dispersion (PMD) of fibers. Even when the pump and signal polarizations are aligned at the input, PMD causes both polarizations to evolve differently, consequently changing the strength of the Raman coupling along the fiber. This produces an averaging effect that is larger if the pump and signals propagate in opposite directions [28–30].

In [30] Lin and Agrawal consider a 10 km long forward, respectively backward, pumped Raman amplifier pumped using 1 W. An average gain of 8 dB is achieved assuming an unpolarized pump. If the pump and signal are polarized, the gain depends on the polarization states of the pump and the signal. In the absence of PMD the pump and the signal maintain their state of polarization. The intrinsic fiber loss is 2 dB and the signal experiences a maximum gain of 17.6 dB, that is 19.6 dB



On-Off Raman gain if the pump and the signal are co-polarized. On the contrary, the signal experiences a loss of 1.7 dB when the pump and the signal are orthogonally polarized, corresponding to an On-Off Raman gain of 0.3 dB.

PMD has the effect of making PDG vanish as a consequence of the averaging of the Raman gain. This averaging is weaker in a forward-pumped amplifier compared to backward pumping for the following reason: pump and signal propagate along with each other in the forward-pumped amplifier in contrast to the counter-pumped amplifier where one time sequence of the signal experiences many different time sequences of the pump which leads to strong averaging. As a consequence there is a significant benefit in using a backward-pumped amplifier configuration. In the latter case a PMD of  $0.001 \text{ ps}/(\text{km})^{1/2}$  only is sufficient to essentially eliminate the impact of PDG while under forward-pumping conditions a PMD of  $0.01 \text{ ps}/(\text{km})^{1/2}$  is needed for the suppression of unwanted PDG effects [30].

However, the suggestion to increase the PMD leads to a trade-off since a significant amount of fiber PMD may in itself directly impair the transmission. Thus, other methods should be considered to reduce PDG. This includes simple measures to depolarize the pump light such as polarization-multiplexing the same wavelength outputs of two independent pump lasers [31].

### 11.2.4 Amplifier Performance

**Spontaneous Raman Scattering** The signal gain is determined by the difference between stimulated emission and stimulated absorption, however, this is accompanied by spontaneous emission which leads to a significant signal distortion. In the simplest model the amplified spontaneous emission in bandwidth  $B_0$  is given by:

$$\pm \frac{dP_{\text{ASE}\pm}}{dz} = g_{\text{R}} P_{\text{p}} P_{\text{ASE}\pm} + h\nu B_0 (1 + n_{\nu}) g_{\text{R}} P_{\text{p}} - \alpha_{\text{ASE}} P_{\text{ASE}\pm}, \quad (11.25)$$

where  $P_{\text{ASE}+}$  and  $P_{\text{ASE}-}$  characterize the amplified spontaneous emission co-propagating or counter-propagating with the signal, respectively,  $h$  is Planck's constant,  $\nu$  the frequency of the signal,  $B_0$  the bandwidth of the signal  $P_s$ ,  $g_{\text{R}}$  the Raman gain coefficient,  $P_{\text{p}}$  the pump power, and  $(1 + n_{\nu})$  is the thermal phonon population number. At room temperature  $(1 + n_{\nu}) \approx 1.14$  [24], the sign ( $\pm$ ) in front of  $dP_{\text{ASE}\pm}/dz$  accounts for power propagating in the forward (+) and backward (-) direction, respectively. The first term on the right hand side represents amplification of spontaneous emission, the second term represents generation of spontaneous emission, and the last term is the fiber attenuation at the wavelength of the ASE power described by the attenuation coefficient  $\alpha_{\text{ASE}}$ .

It should be noted that a factor of 2 may be included in the spontaneous emission (second term in (11.25)) to account for the fact that the signal typically occupies one state of polarization whereas the spontaneous emission is equally generated in both polarizations guided by single-mode optical fibers.

At the output end ( $z = L$ ) the noise power  $P_{\text{ASE}^+}$ , propagating with the signal in the signal polarization state, is given by

$$P_{\text{ASE}^+}(L) = G(L) (1 + n_\nu) h\nu_s B_0 g_R \int_0^L \frac{P_p(z)}{G(z)} dz, \quad (11.26)$$

where  $G(L)$  is the Raman gain, i.e., the signal output power relative to the input power.

The design of broadband amplifiers suitable for WDM applications requires consideration of several factors. An appropriate model that includes interactions among multiple pumps, Rayleigh backscattering, and spontaneous Raman scattering considers each frequency component separately and solves the relevant set of coupled equations [22].

**The Noise Figure** Following Sect. 11.1.6, the noise figure of the Raman amplifier is in general given by

$$F = \frac{2\tilde{n} + 1}{G}, \quad (11.27)$$

where  $\tilde{n} = P_{\text{ASE}}/(h\nu B_0)$  is the number of ASE photons emitted into the signal mode, and  $G$  is the signal gain i.e., the signal output power relative to the signal input power, for more details, see [21].

When Raman scattering is used to convert a fiber into a distributed amplifier, where the signal is amplified as it propagates through the transmission fiber, the degradation of the signal-to-noise ratio is typically much larger than the degradation produced by a discrete amplifier with a gain comparable to the On-Off gain of the Raman amplifier. That is, the noise figure of the pumped span may be many dB worse than the noise figure of a typical discrete amplifier. For comparative purposes the concept of an effective discrete amplifier with an effective noise figure and effective gain was introduced [32] as outlined below.

**Effective Noise Figure** To understand the concept of an effective noise figure, the noise performance of the distributed amplifier is represented as the signal-to-noise ratio performance of a passive fiber with the same length as the distributed amplifier, followed by a discrete amplifier with a noise figure equal to the effective noise figure.

The effective noise figure,  $F_{\text{eff}}$ , is then  $F_{\text{eff}} = F/T_{\text{sp}}$ , where  $T_{\text{sp}}$  is the transmission (in dB) through the passive fiber span from the signal input to the point where the effective discrete amplifier is located. For example, in a 100 km long fiber with an intrinsic loss of 0.2 dB/km, the effective noise figure in decibels is  $F_{\text{eff}}(\text{dB}) = F(\text{dB}) - 20 \text{ dB}$ .

When evaluating a distributed Raman amplifier, for example by comparing it with a discrete amplifier, it is important to make the comparison based on the same transmission length, and furthermore the comparison should be based on the same path average power for the signal and hence (presumably) equal nonlinear impairments. For these conditions it has been shown that the distributed Raman amplifier

performs better than any other solution with discrete amplifiers. This is a very important result [21].

**Pump Depletion** In many realistic Raman amplifiers the rate at which pump power is lost exceeds the exponential decay rate originating from the intrinsic fiber loss. This pump depletion occurs when a significant fraction of the pump power is transferred to the signal via Raman amplification. Examples are the amplification of a large number of signal channels, the amplification of a very high power signal, or an amplifier providing a very high gain. Under such conditions the simple model described above is not appropriate.

Relative to the simple undepleted case the differential equation which describes the propagation of the pump (11.18) needs to be solved. Neglecting spontaneously emitted Raman light the coupled propagation equations for the signal and pump are

$$\frac{dP_s}{dz} = g_R (P_p^+ + P_p^-) P_s - \alpha_s P_s \quad (11.28)$$

$$\pm \frac{dP_p^\pm}{dz} = \frac{\nu_p}{\nu_s} g_R P_p^\pm P_s - \alpha_p P_p^\pm. \quad (11.29)$$

The ratio  $\nu_p/\nu_s$  in the first term on the right hand side of (11.29) accounts for the energy lost to the fiber in the form of phonons when pump light scatters to signal light. The sign accounts for the forward- and backward-propagating pump power, respectively.

The coupled equations in (11.28) and (11.29) may only be solved numerically. However, considering only the forward-pumped amplifier, and assuming that the loss at the signal and pump wavelengths are identical, the coupled equations may be solved by counting photons rather than calculating power. From this, the number of signal photons is

$$n_s(z) = n_s(z=0) \frac{1+r}{r + G_R^{-(1+r)}} \exp(-\alpha z), \quad (11.30)$$

where  $r$  is the ratio of signal to pump photons at launch  $r = n_s(z=0)/n_p(z=0)$ , and  $G_R$  the On-Off Raman gain [33, 34].

Using real values for the intrinsic fiber loss, the effects of depletion must be evaluated numerically. Figure 11.11 a illustrates the effect of pump depletion in a counter-pumped fiber Raman amplifier. In the figure the On-Off Raman gain versus signal input power is shown. The figure shows three curves, each calculated for fixed launched pump powers of 150 mW, 300 mW, and 600 mW. Figure 11.11b illustrates the effective noise figure corresponding to the cases in Fig. 11.11a.

Figure 11.11a illustrates that the On-Off Raman gain decreases as the launched signal becomes sufficiently powerful. This can be explained by the rate of loss of the pump. At any position along the fiber, the intrinsic fiber loss and the product of the signal power and the Raman gain coefficient determine the rate of loss of the pump. For a sufficiently powerful signal, the rate of pump loss is enhanced

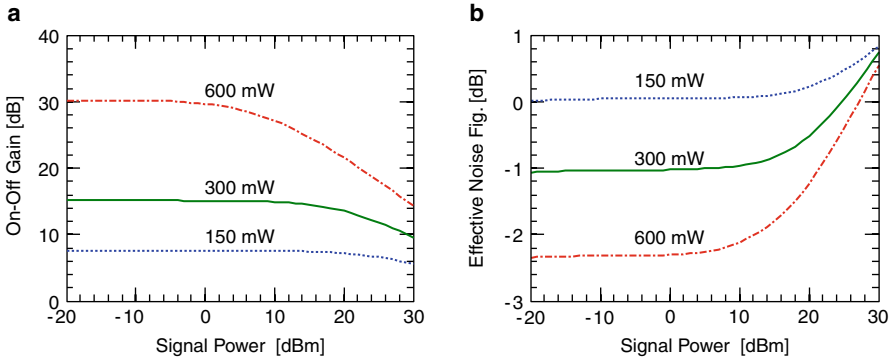


**Fig. 11.11** On-Off Raman gain versus input signal power for three different pump power levels (a) and corresponding effective noise figures as a function of input signal power (b). Each data point is calculated for a 100 km-long counter-pumped Raman amplifier. The signal wavelength is 1555 nm and the pump wavelength is 1455 nm. The loss coefficient at the pump wavelength is 0.25 dB/km creating an effective Raman length of 17 km, and the Raman gain coefficient is  $0.7(\text{W km})^{-1}$ . From [21]

by the term including the signal power times the Raman gain coefficient, i.e., the Raman scattering. As the pump is more quickly attenuated, the effective length of the Raman interaction is reduced, leading to a reduction in the On-Off Raman gain.

From Fig. 11.11b it is seen that the effective noise figure of the Raman amplifier increases as the pump is depleted. This is explained by the enhanced decay of the pump power due to pump depletion. As the length of the Raman interaction is reduced, the signal power is allowed to drop to a lower minimum value within the span, resulting in a higher span noise figure.

### 11.2.5 System Considerations

The Raman amplifier is a distributed amplifier in the sense that its efficiency is very low, and Raman amplification occurs in silica-based transmission fibers without additional doping. It is in fact this distributed gain that enables improved noise properties since the gain is pushed into a transmission span, and consequently the signal power does not drop as much as it otherwise would have done if there were no amplification. However, the distributed gain also causes the average path signal power to be higher.

In typical high-capacity digital transmission systems, the signal power launched into a fiber span is adjusted to minimize the bit-error rate (BER) of the received signal. Often the BER does not only worsen at lower launched signal power due to accumulation of spontaneous emission, but also at higher launched signal power due to optical nonlinear impairments, including pulse distortion from self- and cross-phase modulation in addition to generated four-wave mixing waves and subsequent depletion of the generating waves. In general, the launched power is adjusted until

the complicated interplay between the various sources of noise and pulse distortion results in a minimum BER [35].

In [21, 23] it is demonstrated that the linear accumulation of spontaneous emission is worse in a discrete amplified system compared to a distributed Raman amplified system. However, the nonlinear impairments are slightly worse in a Raman amplified system compared to a discrete amplified system. The balance between the accumulated linear noise and the nonlinear noise defines the maximum achievable spectral efficiency which turns out to be higher in a distributed Raman amplified system compared to a lumped amplified system.

**Impact of Rayleigh Scattering** A major fraction of the intrinsic loss in an optical fiber is due to Rayleigh scattering. In this process light is scattered and a fraction of the optical power is lost. However, a small part of the scattered light is recaptured, half of which propagates in the original direction and the other half propagates in the opposite direction. In a Raman amplifier this causes a severe penalty as the signal and the backward-propagating spontaneous emission are reflected figuratively an even or an odd number of times, respectively. Especially the Rayleigh reflected signal may cause a severe penalty because it appears as an echo of the signal exactly at the signal frequency. In distributed amplifiers the effect due to Rayleigh reflections may be enhanced relative to a discretely amplified system because of the long distances over which gain is accumulated.

**Rayleigh-reflected ASE** When the Raman gain approaches 25 dB, the reflected ASE is comparable to the forward-propagating ASE giving rise to a 3 dB increase in the total spontaneous emission in the signal mode [23]. Consequently, the electrical signal-to-noise ratio is expected to increase until it is impacted by Rayleigh reflections when the Raman gain exceeds 25 dB. At the same time the system performance is expected to degrade due to an increase in the signal effective length when more and more Raman gain is applied.<sup>1</sup> Thus, a Raman amplifier improves the system performance up to an upper limit in the On-Off Raman gain only. In [23] the electrical signal-to-noise ratio is predicted in a 100 km-long backward-pumped Raman amplifier as a function of the On-Off Raman gain, and the optimum gain is shown to be close to 20 dB where the difference between the improvement due to an increased signal-to-noise ratio including Rayleigh-reflected ASE and the increased signal effective length is close to 6.4 dB.

**Rayleigh Reflected Signal** The Rayleigh double-reflected signal power at  $z = L$ , denoted  $P_{\text{dbr}}$ , relative to the transmitted signal power  $P_{\text{T}} = G(L)P_{\text{s}}^0$ , where  $P_{\text{s}}^0$  is the launched power, is [21, 36]

$$\frac{P_{\text{dbr}}(L)}{P_{\text{T}}} = (B_{\text{R}}\alpha_{\text{s}}^{\text{R}})^2 \int_0^L \frac{1}{G^2(\tilde{z})} \int_{\tilde{z}}^L G^2(x) dx d\tilde{z}, \quad (11.31)$$

<sup>1</sup> The signal length  $L_{\text{eff}}^{\text{s}}$  is defined through the relation  $P_{\text{s}}^0 L_{\text{eff}}^{\text{s}} = \int_0^L P_{\text{s}}(z) dz$ , where  $P_{\text{s}}^0$  is the signal power at  $z = 0$ . In the absence of gain and assuming that the loss rate at the signal and pump wavelength are identical, the signal effective length equals the Raman effective length in (11.23).

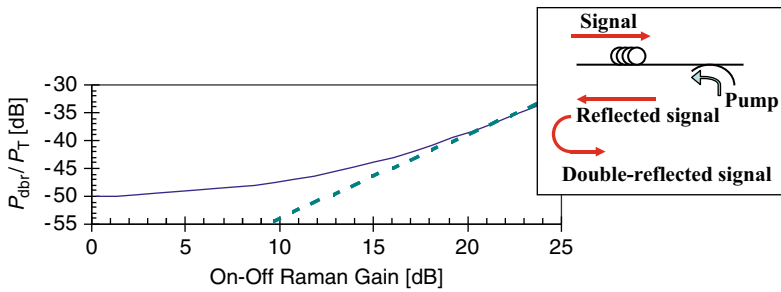


**Fig. 11.12** Ratio of double-reflected signal power to forward-propagating signal power versus the On-Off Raman gain in a 100 km long fiber. A peak Raman gain coefficient of  $0.7 \text{ W km}^{-1}$  and a loss coefficient for the signal and pump of  $\alpha_s = 0.2 \text{ km}^{-1}$  and  $\alpha_p = 0.25 \text{ km}^{-1}$  were used. The dashed line has the slope corresponding to a  $G_R^{3/2}$  dependence. Data from [21]

where again  $G(x)$  is the net gain, not the On-Off Raman gain, and  $B_R \alpha_s^R$  is the Rayleigh backscatter coefficient times the recapture fraction of the fiber. Figure 11.12 illustrates the ratio of the double-reflected signal power,  $P_{\text{dbr}}$ , relative to the unscattered signal at the end of the transmission fiber.

The double-reflected signal power is critical to the performance of a system applying distributed Raman amplifiers. One way to reduce the double Rayleigh scattering is to apply bi-directional pumping. In effect this splits the gain into two sections, one close to the input end and one close to the output end with a loss element in between. In an example of a 100 km-long distributed Raman amplifier pumped to transparency, this may lead to an improvement of 7 dB in the ratio of Rayleigh reflected power relative to the signal output power [21]. However, the use of forward pumping is accompanied by a noise contribution originating from the coupling of noise on the pump to noise on the signal [37]. Consequently, most system demonstrations using Raman amplifiers have been based on backward-pumped amplifiers only.

In the treatment above all considerations regarding polarization have been neglected. However, assuming that the distance between two successive reflections is long, the reflected power, that beats with the signal, needs to be multiplied by  $5/9$  [38] to take the polarization dependence into account.

### 11.2.6 Recent Applications

Some of the first long haul transmission experiments were carried out using Raman gain to counterbalance the intrinsic fiber losses. In 1988 Mollenauer and Smith used Raman gain to counterbalance the loss in a 4000 km transmission experiment [39]. The transmission experiment was carried out in a loop configuration where each

roundtrip in the loop was a 41.7 km-long Raman amplifier. The pump laser was a color center laser and the required pump power was 300 mW.

Because of the poor pump power efficiency work on Raman amplifiers was abandoned when the erbium-doped fiber amplifier matured. However, in the late 1990s high-power fiber lasers became available and the interest in Raman amplifiers was renewed.

**High-Capacity Transmission** The Raman amplifier applied as a distributed amplifier has proven its capabilities and found its way into commercial 40 Gbit/s products [40]. However, research on Raman-assisted high-capacity optical communication systems continues.

In 2005 G. Charlet and coworkers demonstrated a 6 Tbit/s experiment over a transatlantic transmission distance of 6120 km [41]. The capacity was obtained by multiplexing 149 channels each carrying 42.7 Gbit/s. The modulation format was differential phase-shift keying. A spectral efficiency of 0.8 bit/(s Hz) was achieved. The repeaters in their experiment were based on distributed backward-pumped Raman amplifiers each being 65 km long which was claimed to be the optimum length. 16 dB of Raman gain was provided by five pump sources operated at the wavelengths 1429 nm, 1439.5 nm, 1450 nm, 1461 nm, and 1493 nm.

In a more recent system experiment a capacity of 25.6 Tbit/s was demonstrated by A.H. Gnauck et al. [42]. In this experiment 160 channels, each containing two polarization multiplexed 85.4 Gbit/s signals, were transmitted over 240 km. The experiment demonstrated a spectral efficiency as high as 3.2 bit/(s Hz). The 240 km transmission was made up of three 80 km fiber spans. Raman amplification was added together with erbium-doped fiber amplifiers to counterbalance loss from 1530 nm through 1600 nm. Each span included a dispersion-compensating fiber. Consequently, the Raman amplification enabled an increase in the received optical signal-to-noise ratio, and in addition, the Raman amplification was also used to simplify the design of the optical repeaters.

In 2009 G. Charlet and coworkers demonstrated a record in capacity times distance product of 41.8 Pbit/s km [43]. The system capacity was 16.4 Tbit/s obtained through wavelength multiplexing of 164 channels each carrying 100 Gbit/s. The modulation format was 50 Gbit/s polarization-division-multiplexed quadrature phase-shift keying. The signals were transmitted in a loop experiment and after a total distance of 2550 km a BER better than  $10^{-13}$  (using forward error correction) was achieved. Each loop contained 65 km-long bidirectional pumped Raman amplifiers using 25 % forward and 75 % backward pumping.

**Silicon Raman Photonics** In addition to silica-based fiber Raman amplifiers, Raman gain in silicon waveguides has recently become of interest. In 2002 R. Claps and coworkers demonstrated amplification and lasing in silicon waveguides [44]. Since then the topic has attracted much attention. The reason for this is the fact that the Raman cross section is three to four orders of magnitude higher in silicon compared to silica. In addition the effective area of the waveguide is about 100 times smaller in a silicon waveguide compared to a silica-based fiber. In [44] a gain co-

efficient of  $2 \times 10^{-8}$  cm/W at a pump wavelength of 1427 nm was demonstrated. This should be compared with a gain coefficient for silica of  $10^{-13}$  m/W. However, it should be noted that the two gain coefficients just quoted for silicon and silica do not include the effective waveguide area. In silicon the gain peak occurs at a frequency shifted by 15.6 THz and with a bandwidth of 105 GHz only in contrast to several THz bandwidth and 13 THz shift for silica.

Dimitropoulos and coworkers calculated the noise figure of silicon Raman amplifiers in the presence of nonlinear losses [45] and predicted a noise figure close to 4 dB. This result was obtained considering a 1 cm long waveguide pumped with  $200 \text{ MW/cm}^2$ , a gain coefficient of  $15 \text{ cm/GW}$ , and a nonlinear absorption of  $0.7 \text{ cm/GW}$ . One of the main challenges is the nonlinear optical loss that competes with the Raman gain. Besides competing with the Raman gain, the nonlinear loss also affects the signal-to-noise ratio.

## 11.3 Parametric Amplifiers

Parametric amplification is based on four-wave mixing which is a mutual interaction of four waves through the intensity-dependent refractive index, also referred to as the optical Kerr effect. In a degenerate case the process involves three waves only [34]. The effect may classically be described as a third-order nonlinear process as it depends on the electrical field raised to the third power. Parametric amplification is well known from second-order nonlinear materials. The efficiency relies heavily on phase matching and thus the dispersion properties of the optical fiber are as important as the nonlinear strength of the fiber.

The development of high-power lasers and highly nonlinear fibers with tailored dispersion properties have seeded renewed interest in fiber devices based on parametric processes. These devices include regenerators, wavelength converters and amplifiers, phase-sensitive as well as phase-insensitive ones.

In this section the focus is directed toward a general discussion of fiber-optical parametric amplifiers. The section also includes a subsection on recent applications.

### 11.3.1 Propagation Equations

In the degenerate parametric amplifier gain is obtained by transfer of energy between three propagating waves, a signal, the pump, and a so-called idler. That is, the energy goes from the pump to the signal and the idler, and if the fiber is too long, the energy goes back to the pump.

The propagation of signal, pump and idler is governed by three coupled differential equations. If the amplitude of the signal power is  $A_s$  in units  $\sqrt{W}$  and likewise the amplitude of the pump is  $A_p$  and the idler is  $A_i$ , then the coupled equations



are [34]

$$\begin{aligned}
 \frac{dA_p}{dz} &= \gamma[(|A_p|^2 + 2(|A_s|^2 + |A_i|^2))A_p + 2A_s A_i A_p^* \exp\{i\Delta\beta z\}], \\
 \frac{dA_s}{dz} &= \gamma[(|A_s|^2 + 2(|A_i|^2 + |A_p|^2))A_s + A_i^* A_p^2 \exp\{-i\Delta\beta z\}], \\
 \frac{dA_i}{dz} &= \gamma[(|A_i|^2 + 2(|A_s|^2 + |A_p|^2))A_i + A_s^* A_p^2 \exp\{-i\Delta\beta z\}],
 \end{aligned} \tag{11.32}$$

where  $\gamma$  is the nonlinear strength  $\gamma = 2\pi n_2/(\lambda A_{\text{eff}})$ ,  $n_2$  is the intensity-dependent refractive index,  $A_{\text{eff}}$  is the effective area of the fiber, and  $\Delta\beta = \beta(\omega_s) + \beta(\omega_i) - 2\beta(\omega_p)$  is the phase mismatch between the three waves. All three equations (11.32) are weighted by the same nonlinear strength. This is an approximation which is valid under the assumption that the amplifier is operated at wavelengths where the idler, the pump as well as the signal are in the fundamental fiber mode. In addition, the amplitude equations are all scalar which emphasizes the assumption that the signal, pump and idler are all launched in the same state of polarization and remain in the same state of polarization throughout propagation through the amplifier. Finally, the nonlinearity is assumed to be instantaneous and only continuous wave (CW) beams are considered. The amplitude equations (11.32) may be rewritten as power equations:

$$\begin{aligned}
 \frac{dP_p}{dz} &= -4\gamma P_p \sqrt{P_s P_i} \sin \theta, \\
 \frac{dP_s}{dz} &= 2\gamma P_p \sqrt{P_s P_i} \sin \theta, \\
 \frac{dP_i}{dz} &= 2\gamma P_p \sqrt{P_s P_i} \sin \theta, \\
 \frac{d\theta}{dz} &= \Delta\beta + \gamma (2P_p - P_s - P_i) \\
 &\quad + \gamma (P_p \sqrt{P_s/P_i} + P_p \sqrt{P_i/P_s} - 4\sqrt{P_s P_i}) \cos \theta,
 \end{aligned} \tag{11.33}$$

where  $\theta = \Delta\beta z - 2\phi_p(z) + \phi_s(z) + \phi_i(z)$ , and  $P_p$ ,  $P_s$ ,  $P_i$  are the power levels of the pump, signal and idler. By having a signal, idler and pump present at the fiber input and by adjusting the relative phase between them it is possible to control whether the signal is amplified or attenuated – this gives a possibility to create a phase-sensitive amplifier. However, if the idler is zero at the input, then  $\theta = \pi/2$  may be assumed since there is always a zero point field that satisfies this condition. In this case the amplification becomes phase in-sensitive, and the relative gain defined as the output power relative to the input power may be expressed as:

$$G = 1 + \left( \gamma P_p L \frac{\sinh(gL)}{gL} \right)^2, \tag{11.34}$$

where  $\gamma$  is the nonlinear coefficient,  $L$  the fiber length,  $P_p$  the pump power and  $g$  a phase parameter that describes the phase-matching condition between the pump,

idler and signal according to

$$g^2 = [(\gamma P_p)^2 - (\kappa/2)^2] \quad \text{with } \kappa = \Delta\beta + 2\gamma P_p. \quad (11.35)$$

In (11.34) it is assumed that there is no pump depletion, and that there is no intrinsic fiber attenuation.

The gain exhibits a maximum when  $g$  is maximum, that is when  $\kappa = 0$ . At this point

$$G = 1 + (\sinh(\gamma P_p L))^2 \approx \exp(2\gamma P_p L)/4. \quad (11.36)$$

This gives a gain efficiency of  $G = 8.7\gamma P_p L - 6$  dB, when  $G$  is expressed in dB.

For state-of-the-art highly nonlinear fibers a nonlinear strength  $\gamma$  of  $11 \text{ (W km)}^{-1}$  is realistic, and for a 500 m long fiber this gives a gain efficiency of  $G = 47.9P_p - 6$  dB where  $P_p$  is given in units of W.

### 11.3.2 Amplifier Gain Spectrum

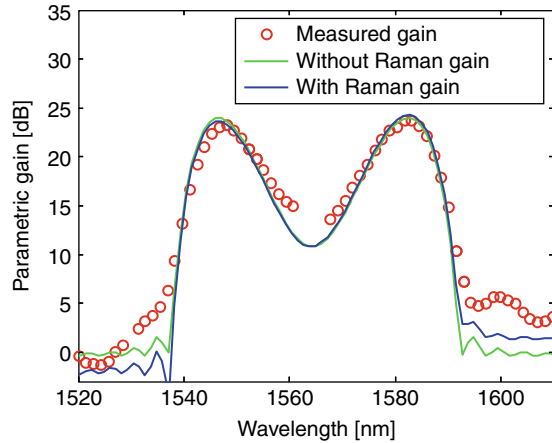
The operation wavelength and the bandwidth of the amplifier are related to each other through the dispersion properties of the optical fiber that is used in the amplifier. The reason for this is that the pump wavelength has to be chosen close to the wavelength where the group-velocity-dispersion of the amplifier fiber equals zero, and the bandwidth of the amplifier is determined by the phase-matching of the interacting waves. Mathematically this is seen from (11.34) and (11.35) in which the parameter  $\kappa$  may be expressed through the slope of the group-velocity-dispersion

$$\kappa = - (2\pi c/\lambda_0^2) S(\lambda_p - \lambda_0)(\lambda_p - \lambda_s)^2 + 2\gamma P_p, \quad (11.37)$$

where  $S$  is the slope of the group velocity dispersion at the wavelength where the group velocity dispersion equals zero,  $\lambda_0$ .  $\lambda_s$  is the signal wavelength,  $\lambda_p$  is the pump wavelength,  $\gamma$  is the nonlinear strength of the optical fiber as defined below (11.32) and  $P_p$  is the pump power. By considering the bandwidth of the amplifier as the distance between the gain peaks i.e., where  $\kappa = 0$ , it is evident, as expected, that the bandwidth of the amplifier is determined by the slope of the group velocity dispersion with respect to wavelength, the lower the slope the larger the bandwidth. In addition, the bandwidth also depends on the nonlinear strength and the pump power.

Figure 11.13 illustrates the gain spectrum of a parametric amplifier. The fiber used was 500 m long with a zero dispersion wavelength at 1561 nm, a dispersion slope of  $0.015 \text{ ps}/(\text{nm}^2 \text{ km})$ , and a pump power of 29 dBm at 1564 nm. The fiber had a nonlinear strength of  $11.5 \text{ (W km)}^{-1}$ . The figure illustrates measured as well as predicted data. The predicted data are found by solving the coupled amplitude equations as in (11.32). In addition, the figure also shows the predicted gain if Raman scattering in the fiber is included.

**Fig. 11.13** Parametric gain as a function of wavelength. Circles are measured data, the symmetric green line represents predicted data without taking Raman scattering into account, and the blue unsymmetrical curve represents predictions when Raman scattering is included [46]



### 11.3.3 Characteristics

**Response Time** The response time is defined by the nonlinearity and hence for all practical purposes assumed to be instantaneous. However, a small contribution to the nonlinearity comes from Raman scattering. This is not included in the propagation equations (11.32) and is typically neglected.

**Polarization Dependence** The parametric interaction between the pump, the signal and the idler is strongly polarization dependent. To get the maximum (degenerate) four-wave mixing, the state of polarizations of the pump, the signal and the idler need to be aligned. If they are orthogonal to each other, the (degenerate) four-wave mixing is minimized. Experimentally, the polarization states of the beams may be aligned by adjusting the input state of polarization for maximum output signal power. However, if the state of polarization does not remain aligned during propagation, the efficiency is reduced.

### 11.3.4 Amplifier Performance

**Spontaneous Emission** Optical amplification is always accompanied by spontaneous emission and as a general rule, the signal-to-noise ratio can never be improved. This is also the case for a parametric amplifier. However, since the amplifier may be operated as a phase-sensitive amplifier, it may not be sufficient to characterize the amplifier based on its noise figure, it may also require information describing the phase degradation experienced during propagation.

The amplifier has proven its validity as a regenerator in transmission systems utilizing phase-shift-keyed modulation formats. The reason is that, since the amplifier has a fast response time and at the same time it may operate in depletion, it is capa-

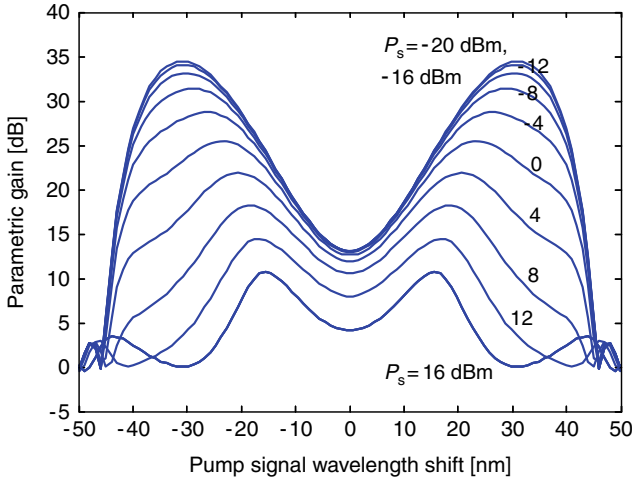


**Fig. 11.14** Parametric gain versus pump signal wavelength shift. The fiber was 500 m long with a zero dispersion wavelength at 1561 nm, a dispersion slope of 0.015 ps/(nm<sup>2</sup> km), and a nonlinear strength  $\gamma$  of 11.5 (W km)<sup>-1</sup>. A pump power of 29 dBm at 1564 nm was used. Data from [48]

ble of acting as a limiter which means that the amplitude of individual pulses will be nearly identical after propagation through the amplifier. As a consequence the accumulation of nonlinear phase shift on each pulse amounts to the same and each bit will experience less phase noise.

The spontaneous emission in a parametric amplifier is more complicated to predict than the spontaneous emission in an EDFA or Raman amplifier.

**Noise Figure** McKinstrie and coworkers have calculated the noise figure of a degenerate (single-pumped) as well as a double-pumped parametric amplifier under the assumption that the amplifier is unsaturated. McKinstrie et al. [47] show that the noise figure equals

$$F = \frac{\langle n_0 \rangle (G^2 \langle n_0 \rangle + G(G - 1)(\langle n_0 \rangle + 1))}{(G \langle n_0 \rangle + (G - 1))^2}, \tag{11.38}$$

where  $G$  is the gain of the parametric amplifier and  $\langle n_0 \rangle$  the mean number of input signal photons. For a high gain and a large signal input photon number the noise figure is 3 dB.

**Saturation Performance** The results in Fig. 11.13 were obtained using a very low input signal power level of -30 dBm. As the signal input power is increased, the transfer of energy from the pump to the signal and idler happens over shorter distances and the analytical expression in (11.34) is no longer valid. However, the coupled equations are still valid and may be used to predict the saturation behavior of the parametric amplifier numerically.

Using the same amplifier configuration as in Fig. 11.13, the saturation performance illustrated in Fig. 11.14 is found.

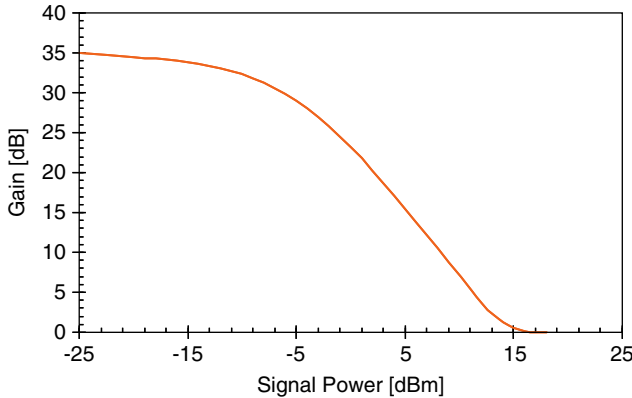


**Fig. 11.15** Gain of parametric amplifier as a function of input signal power. The amplifier configuration is as in Fig. 11.13. From [48]

When the parametric amplifier is operated in depletion, its performance gets more complicated. The spectral shape changes which is in contrast to the Raman amplifier. On consequence of this is that the bandwidth of the amplifier reduces.

Figure 11.15 shows the gain as a function of signal power. The calculations are performed for a 500 m-long highly nonlinear fiber using  $\gamma = 11.5 (\text{W km})^{-1}$  and a dispersion slope of  $0.015 \text{ ps}/(\text{nm}^2 \text{ km})$ , similar to Figs. 11.13 and 11.14. The signal wavelength is chosen where the gain under undepleted operation conditions is maximum. At low signal power levels the gain is constant whereas the gain has dropped by 3 dB for a signal input power of approximately  $-7 \text{ dBm}$ . As the input signal power is raised further, the gain eventually drops to the background loss of the fiber.

### 11.3.5 Application Issues

**Forward Pumping** The only viable configuration for a parametric amplifier is as a forward-pumped amplifier. Since its response time is instantaneous for all practical purposes, intensity fluctuations of the pump are transferred to the signal. In [49] it is shown that the noise figure may be dominated by contributions from the pump signal crosstalk. However, it is also shown that the ratio of pump-induced noise and spontaneous emission depends on the fiber-optic parametric amplifier (FOPA) gain and the signal power level.

**Brillouin Scattering** Stimulated Brillouin scattering is a significant issue in the application of parametric amplifiers.

Because of the low efficiency of the parametric process, high pump power is required. This leads to the onset of Brillouin scattering and consequently limits the maximum achievable gain. Various methods have been proposed to mitigate the

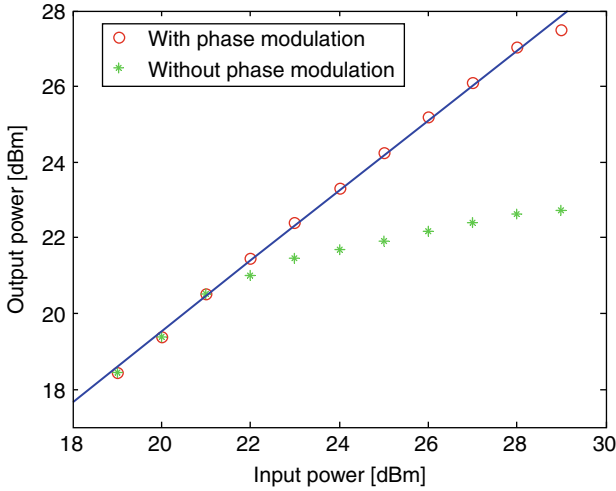


**Fig. 11.16** Output power as a function of input power through a 500 m long fiber of the same type as in Fig. 11.13. The *circles* represent measurements applying 4-tone phase modulation (see details in the main text) to suppress Brillouin scattering while the *diamonds* represent the case when no phase modulation is applied, after [50]

impact of stimulated Brillouin scattering (SBS) including fiber designs with other index-raising codopants, for example aluminum instead of germanium, the use of phase modulation, applying a strain along the fiber or applying a temperature gradient along the fiber. To date the most frequently applied SBS suppression method is to apply a phase modulation.

Figure 11.16 shows measurements of transmitted power through 500 m of highly nonlinear fiber: When no measure has been taken to suppress SBS, the maximum input power is limited to approximately 22 dBm before the onset of SBS. However, when applying a phase modulation consisting of four tones (100 MHz, 330 MHz, 1 GHz, and 3 GHz), the onset of SBS is strongly reduced and only appears as the input pump power exceeds 30 dBm.

### 11.3.6 Recent Applications

The topic of parametric amplification has attracted more and more interest within recent years. This has been spurred by demonstrations of various applications and the development of high-power fiber lasers and specifically tailored highly nonlinear, dispersion engineered optical fibers. The FOPA is an attractive device since it not only provides phase-insensitive amplification but also phase-sensitive amplification, wavelength conversion, and has an almost instantaneous response as well. Some of the recent demonstrations of applications are highlighted below.

**Wavelength Conversion** Parametric amplifiers have great potential as devices for wavelength conversion since a signal is copied by nature to the idler as it propagates through the parametric fiber amplifier.

In 2008 J.M. Chavez Boggio and coworkers demonstrated a conversion over 700 nm [51]. In their experiment a 15 m long highly nonlinear fiber with very low fourth-order dispersion was used. The nonlinear strength  $\gamma$  was  $11.5 (\text{W km})^{-1}$ , the wavelength of zero dispersion of the fiber was at 1582.8 nm, and the dispersion slope was  $0.027 \text{ ps}/(\text{nm}^2 \text{ km})$ . The third- and fourth-order dispersion coefficients were  $0.038 \text{ ps}^3/\text{km}$  and  $1.4 \times 10^{-5} \text{ ps}^4/\text{km}$ , respectively. In order to achieve the wavelength conversion a pulsed pump was used. The peak power of each pump pulse was 200 W. In one example a signal at 1312.6 nm was converted to 1999 nm with a conversion efficiency of 30 dB.

**Waveform Sampling** Another promising application of the parametric process is as a sampling of a signal. To this end, in principle, a wavelength converter is designed, however, with the only purpose of generating an idler, which is a sample of the signal. The power generated in the idler is proportional to the power of the signal. P. Andrekson and coworkers have demonstrated this approach and have shown high-resolution optical waveform sampling for example of a 640 Gbit/s RZ data stream. The method may be further extended to include phase information in constellation diagrams also [52, 53].

**Broadband Amplification** One of the benefits of parametric amplifiers is that their bandwidth is determined by the fiber design, more specifically, by the slope of the group velocity dispersion as a function of wavelength, and the available pump power. In addition, their operation wavelength is determined by the wavelength of zero group velocity dispersion around which the gain is symmetrically centered.

In 2008 Chavez Boggio and coworkers demonstrated a parametric amplifier providing gain over 81 nm [54]. The amplifier was a 2 pump configuration where each pump wavelength was located symmetrically around the zero dispersion wavelength of the fiber which was measured to be 1561.9 nm, with a dispersion slope of  $0.025 \text{ ps}/(\text{nm}^2 \text{ km})$ . One pump wavelength was at 1511.29 nm while the other was at 1613.85 nm. Approximately 1 W of pump power was used in each of the two pump beams. The fiber in their experiment was 350 m long with a nonlinear strength  $\gamma = 14 (\text{W km})^{-1}$ .

**Regeneration** Recently, application of advanced modulation formats such as phase-shift keying have proven superior transmission properties and enabled record high-capacity transmission. However, one of the limiting factors in such high-capacity communication links is signal distortion due to the nonlinear phase shift accumulated during transmission. Because of intensity fluctuations of the signal, a phase-shift keyed signal will be distorted significantly since the induced nonlinear phase shift will fluctuate in accordance with the intensity of the signal. However, by employing a method to reduce the intensity fluctuations, the phase distortion may be reduced leading to a further improved transmission capacity if phase-shift keyed signals are used.

**Table 11.1** Main characteristics of different types of fiber amplifiers

	EDFA	Raman	FOPA
Efficiency	dB/mW	60 dB/W	40 dB/W
Time response	10 ms	100 fs	instantaneous
Pump configuration	co/counter; arbitrary	(co)counter	co
Length	meters	kilometers	hundreds of meters
Operation wavelength	1530–1610 nm	13 THz separation between pump and signal	pump close to the wavelength of zero dispersion
Bandwidth	100 nm	~ 13 THz	(tens to hundreds of nm) depends on dispersion slope and pump power
Polarization dependence	very weak	strong but mitigated when counter pumped	strong

In 2008 C. Peucheret and coworkers [55] demonstrated experimentally that a parametric amplifier may be used as a limiter and consequently mitigate the accumulated phase penalties. In [55] the dynamic range of a 40 Gbit/s return-to-zero differential phase-shift-keyed (RZ-DPSK) signal was enhanced. An optical signal-to-noise ratio penalty of 3.5 dB was reduced to 0.2 dB by using a single-pumped FOPA with a 22 dB small signal gain. The improvement in the optical signal-to-noise ratio was experimentally found through BER measurements.

## 11.4 Conclusion

Optical fiber amplifiers are one of the most important fiber devices if not the most important ones. They have played a significant role in the evolution that has led to the high-capacity optical communication systems which constitute one of the most important carriers in today's information society where fiber to the home is now becoming a reality around the globe.

The chapter has discussed (i) the erbium-doped fiber amplifier which has been a research topic throughout the late 1980s but is still subject to research with respect to specific applications including high-power amplifiers; (ii) the Raman amplifier, which attracted significant research interest in the late 1990s which still continues with a particular focus on novel fiber types, systems applications and novel materials, and finally (iii) the parametric amplifier which is currently a topic of research in many groups around the world.

The aim of the chapter has been to highlight the fundamental physical mechanism of each amplifier type including a brief discussion of the important amplifier properties such as gain, noise performance and noise sources, and finally to illustrate some of the most recent results with respect to the three amplifier types.

A short summary of the main characteristics of the discussed amplifiers is shown in Table 11.1.



## References

1. A.T. Pedersen, L. Grüner-Nielsen, K. Rottwitt, Measurement and modeling of low wavelength losses of silica fibers and their impact at communication wavelengths. *J. Lightw. Technol.* **27**, 1296–1300 (2009)
2. P.C. Becker, N.A. Olson, J.R. Simpson, *Erbium-Doped Fiber Amplifiers, Fundamentals and Technology* (Academic Press, San Diego, 1999)
3. E. Desurvire, *Erbium Doped Fiber Amplifiers, Principles and Applications* (Wiley, New York, 1994)
4. M.J.F. Digonet, *Rare-Earth-Doped Fiber Lasers and Amplifiers*, 2nd edn. (Marcel Dekker, New York, 1993)
5. C.R. Giles, E. Desurvire, Modeling erbium-doped fiber amplifiers. *J. Lightw. Technol.* **9**, 271–283 (1991)
6. Y. Sun, J.L. Zyskind, A.K. Srivastava, Average inversion level, modeling, and physics of erbium-doped fiber amplifiers. *J. Sel. Top. Quantum Electron.* **3**, 991–1007 (1997)
7. P.F. Wysocki, J.R. Simpson, D. Lee, Prediction of gain peak wavelength for Er-doped fiber amplifiers and amplifier chains. *IEEE Photon. Technol. Lett.* **6**, 1098–1100 (1994)
8. V.L. Mazurczyk, J.L. Zyskind, Polarization dependent gain in erbium doped-fiber amplifiers. *IEEE Photon. Technol. Lett.* **6**, 616–618 (1994)
9. J. Nagel, The dynamic behaviour of amplified systems, *Opt. Fiber Commun. Conf. (OFC'98)*, Techn. Digest (San Jose, CA, USA, 1998), paper ThO3
10. B. Pálsdóttir, Erbium doped AirClad fibers for high power broad band amplifiers and single mode erbium doped fibers for high performance amplifiers and lasers, *Opt. Fiber Commun. Conf. and Nat. Fiber Opt. Eng. Conf. (OFC/NFOEC'08)*, Techn. Digest (San Diego, CA, USA, 2008), paper OTuJ1
11. O. Lumholt, J.H. Povlsen, K. Schüsler, A. Bjarklev, S. Dahl-Pedersen, T. Rasmussen, K. Rottwitt, Quantum limited noise figure operation of high gain erbium doped fiber amplifiers. *J. Lightw. Technol.* **11**, 1344–1352 (1993)
12. Y. Sun, A.K. Srivastava, J. Zhou, J.W. Sulhoff, Optical fiber amplifiers for WDM networks. *Bell Labs Tech. J.* **4**, 187–206 (1999)
13. F. Koch, B. Palsdottir, J.O. Olsen, T. Veng, B. Flintham, R. Keys, 30 dBm wideband air-clad EDFA using two pump lasers, *Opt. Fiber Commun. Conf. and Nat. Fiber Opt. Eng. Conf. (OFC/NFOEC'08)*, Techn. Digest (San Diego, CA, USA, 2008), paper OWU3
14. K.P. Hansen, J. Broeng, P.M.W. Skovgaard, J.R. Folkenberg, M.D. Nielsen, A. Pedersen, T.P. Hansen, H.R. Simonsen, High-power photonic crystal fiber lasers: Design, handling and sub-assemblies, in *Fiber Lasers II: Technology, Systems and Applications*. Proc. SPIE (2005), pp. 273–283
15. O. Schmidt, J. Rothhardt, T. Eidam, F. Röser, J. Limpert, A. Tünnermann, K.P. Hansen, C. Jakobsen, J. Broeng, Single-polarization ultra-large-mode-area Yb-doped photonic crystal fiber. *Opt. Express* **16**, 3918–3923 (2008)
16. S. Ramachandran, J.W. Nicholson, S. Ghalmi, M.F. Yan, P. Wisk, E. Monberg, F.E. Dimarcello, Light propagation with ultralarge modal areas in optical fibers. *Opt. Lett.* **31**, 1797–1799 (2006)
17. S. Ramachandran, K. Brar, S. Ghalmi, K. Aiso, M. Yan, D. Trevor, J. Flemming, C. Headley, P. Wisk, G. Zyzdik, M. Fisteyn, E. Monberg, F. Dimarcello, High-power amplification in a 2040  $\mu\text{m}^2$  higher order mode. Proc. SPIE, vol. 6453 (2007), 64532G
18. K. Rottwitt, H.D. Kidorf, A 92 nm bandwidth Raman amplifier, *Opt. Fiber Commun. Conf. (OFC'98)*, Techn. Digest (San Jose, CA, USA, 1998), post-deadline paper PD6
19. K. Rottwitt, J.H. Povlsen, A. Bjarklev, O. Lumholt, B. Pedersen, T. Rasmussen, Noise in distributed erbium doped fibers. *IEEE Photon. Technol. Lett.* **5**, 218–221 (1993)
20. J. Bromage, K. Rottwitt, M.E. Lines, A method to predict the Raman gain spectra of germanosilicate fibers with arbitrary index profiles. *IEEE Photon. Technol. Lett.* **14**, 24–26 (2002)

21. K. Rottwitt, A. Stentz, Raman amplification in lightwave communication systems, in *Optical Fiber Telecommunication IV A*, ed. by I.P. Kaminov, T. Li (Academic Press, San Diego, 2002), Chap. 5
22. H. Kidorf, K. Rottwitt, M. Nissov, M. Ma, E. Rabarrijoana, Pump interactions in a 100 nm bandwidth Raman amplifier. *IEEE Photon. Technol. Lett.* **11**, 530–532 (1999)
23. K. Rottwitt, Distributed Raman amplifiers, in *Raman Amplification*, ed. by C. Headley, G.P. Agrawal (Academic Press, San Diego, 2005), Chap. 3
24. K. Rottwitt, J. Bromage, A.J. Stentz, L. Leng, M.E. Lines, H. Smith, Scaling the Raman gain coefficient: Applications to germanosilicate fibers. *J. Lightw. Technol.* **21**, 1652–1663 (2003)
25. K. Rottwitt, J.H. Povlsen, Analyzing the fundamental properties of Raman amplification in optical fibers. *J. Lightw. Technol.* **23**, 3597–3605 (2005)
26. R.W. Hellwarth, Third-order optical susceptibilities of liquids and solids. *Prog. Quantum Electron.* **5**(1), 1–68 (1977)
27. R.H. Stolen, J.P. Gordon, W.J. Tomlinson, H.A. Haus, Raman response function of silica-core fibers. *J. Opt. Soc. Am. B* **6**, 1159–1166 (1989)
28. S. Popov, E. Vanin, G. Jacobsen, Influence of polarization mode dispersion value in dispersion-compensating fibers on the polarization dependence of Raman gain. *Opt. Lett.* **27**, 848–850 (2002)
29. Q. Lin, G.P. Agrawal, Statistics of polarization-dependent gain in fiber-based Raman amplifiers. *Opt. Lett.* **28**, 227–229 (2003)
30. Q. Lin, G.P. Agrawal, Vector theory of stimulated Raman scattering and its application to fiber-based Raman amplifiers. *J. Opt. Soc. Am. B* **20**, 1616–1631 (2003)
31. J. Bromage, Raman amplification for fiber communication systems. *J. Lightw. Technol.* **22**, 79–93 (2004)
32. P.B. Hansen, L. Eskildsen, A.J. Stentz, T.A. Strasser, J. Judkins, J.J. DeMarco, R. Pedrazzani, D.J. Digiovanni, Rayleigh scattering limitations in distributed Raman pre-amplifiers. *IEEE Photon. Technol. Lett.* **10**, 159–161 (1998)
33. J. Auyeng, A. Yariv, Spontaneous and stimulated Raman scattering in long low loss fibers. *IEEE J. Quantum Electron.* **QE-14**, 347–352 (1978)
34. G.P. Agrawal, *Nonlinear Fiber Optics*, 3rd edn. (Academic Press, San Diego, 1995)
35. J. Stark, P. Mitra, A. Sengupta, Information capacity of nonlinear wavelength division multiplexing fiber optic transmission line. *Opt. Fiber Technol.* **7**, 275–288 (2001)
36. M. Nissov, K. Rottwitt, H. Kidorf, F. Kerfoot, Rayleigh crosstalk in long cascades of distributed unsaturated Raman amplifiers. *Electron. Lett.* **35**, 997–998 (1999)
37. C.R.S. Fludger, V. Handerek, R.J. Mears, Pump to signal RIN transfer in Raman fiber amplifiers. *J. Lightw. Technol.* **18**, 1140–1148 (2001)
38. M.O. van Deventer, Polarization properties of Rayleigh backscattering in single-mode fibers. *J. Lightw. Technol.* **11**, 1895–1899 (1993)
39. L.F. Mollenauer, K. Smith, Demonstration of soliton transmission over more than 4000 km in fiber with loss periodically compensated by Raman gain. *Opt. Lett.* **13**, 675–677 (1988)
40. D. Fishman, W.A. Thompson, L. Vallone, LambdaXtreme transport system; R&D of a high capacity system for low cost ultra long haul DWDM transport. *Bell Labs Tech. J.* **11**, 27–53 (2006)
41. G. Charlet, E. Corbel, J. Lazaro, A. Klekamp, R. Dischler, P. Tran, W. Idler, H. Mandoyan, A. Konczykowska, F. Jorge, S. Bigo, WDM transmission at 6 Tbit/s capacity over transatlantic distance, using 42.7-Gbit/s differential phase-shift keying without pulse carver. *J. Lightw. Technol.* **23**, 104–107 (2005)
42. A.H. Gnauck, G. Charlet, P. Tran, P.J. Winzer, C.R. Doerr, J.C. Centanni, E.C. Burrows, T. Kawanishi, T. Sakamoto, K. Higuma, 25.6 Tbit/s WDM transmission of polarization multiplexed RZ-DQPSK signals. *J. Lightw. Technol.* **26**, 79–84 (2008)
43. G. Charlet, J. Renaudier, H. Mardoyan, P. Tran, O.B. Pardo, F. Verluise, M. Achouche, A. Boutin, F. Blache, J.-Y. Dupuy, S. Bigo, Transmission of 16.4 bit/s capacity over 2550 km using PDM QPSK modulation format and coherent receiver. *J. Lightw. Technol.* **27**, 153–157 (2009)

44. R. Claps, D. Dimitropoulos, V. Raghunathan, Y. Han, B. Jalali, Observation of stimulated Raman amplification in silicon waveguides. *Opt. Express* **11**, 1731–1739 (2003)
45. D. Dimitropoulos, D.R. Solli, R. Claps, O. Boyraz, B. Jalali, Noise figure of silicon Raman amplifiers. *J. Lightw. Technol.* **26**, 847–852 (2008)
46. D. Noordegraaf, M. Lorenzen, C.V. Nielsen, K. Rottwitt, Brillouin scattering in fiber optical parametric amplifiers, *Proc. 9th Internat. IEEE Conf. Transparent Optical Netw. (ICTON '07)*, vol. 1, pp. 197–200
47. C.J. McKinstrie, S. Radic, M.G. Raymer, Quantum noise properties of parametric amplifiers driven by two pump waves. *Opt. Express* **12**, 5037–5066 (2004)
48. K. Rottwitt, M.R. Lorenzen, D. Noordegraaf, C. Peucheret, Gain characteristics of a saturated fiber optic parametric amplifier, *Proc. 10th Internat. IEEE Conf. Transparent Optical Netw. (ICTON '08)*, vol. 1, pp. 62–64, paper Mo.D1.1
49. P. Kylemark, P.O. Hedekvist, H. Sunnerud, M. Karlsson, P.A. Andrekson, Noise characteristics of fiber optical parametric amplifiers. *J. Lightw. Technol.* **22**, 409–416 (2004)
50. M. Lorenzen, D. Noordegraaf, C.V. Nielsen, O. Odgaard, L. Grüner-Nielsen, K. Rottwitt, Brillouin suppression in a fiber optical parametric amplifier by combining temperature distribution and phase modulation, *Opt. Fiber Commun. Conf. and Nat. Fiber Opt. Eng. Conf. (OFC/NFOEC'08)*, Techn. Digest (San Diego, CA, USA, 2008), paper OML1
51. J.M. Chavez Boggio, J.R. Windmiller, M. Knutzen, R. Jiang, C. Bres, N. Alic, B. Stossel, K. Rottwitt, S. Radic, 730-nm optical parametric conversion from near- to short-wave infrared band. *Opt. Express* **16**, 5435–5443 (2008)
52. P.A. Andrekson, M. Westlund, H. Sunnerud, High resolution optical waveform sampling using fiber-optic parametric amplifiers, *Proc. 2008 IEEE/LEOS Winter Topical Meeting* (2008), pp. 55–56, paper MB3
53. P.A. Andrekson, M. Westlund, Nonlinear optical fiber based high resolution all-optical waveform sampling, *Laser & Photon. Rev.* **1**, 231–248 (2007)
54. J.M. Chavez Boggio, C. Lundström, J. Yang, H. Sunnerud, P.A. Andrekson, Double-pumped FOPA with 40 dB flat gain over 81 nm bandwidth, *Proc. 34th Europ. Conf. Opt. Commun. (ECOC'08)*, Brussels, Belgium (2008), paper Tu.3.B.5
55. C. Peucheret, M. Lorenzen, J. Seonne, D. Noordegraaf, C.V. Nielsen, L. Grüner-Nielsen, K. Rottwitt, Amplitude regeneration of RZ-DPSK signals in single pump fiber optic parametric amplifiers. *IEEE Photon. Technol. Lett.* **21**, 872–874 (2009)

# Chapter 12

## Linear Semiconductor Optical Amplifiers

René Bonk, Thomas Vallaitis, Wolfgang Freude, Juerg Leuthold, Richard V. Penty, Anna Borghesani, and Ian F. Lealman

**Abstract** The chapter reviews properties and applications of linear semiconductor optical amplifiers (SOA). Section 12.1 covers SOA basics, including working principles, material systems, structures and their growth. Booster or inline amplifiers as well as low-noise preamplifiers are classified. Section 12.2 discusses the influence of parameters like gain, noise figure, gain saturation, gain and phase dynamics, and alpha-factor. In Sect.12.3, the application of a linear SOA as a reach extender in future access networks is addressed. The input power dynamic range is introduced, and measurements for on-off keying and phase shift keying signals are shown. Section 12.4 presents the state of the art for commercially available SOA and includes a treatment of reflective SOAs (RSOA) as well.

---

René Bonk (✉)  
Alcatel-Lucent Deutschland AG, Bell Labs/Optical Access, Lorenzstr. 10, 70435 Stuttgart, Germany  
e-mail: Rene.Bonk@alcatel-lucent.com

Thomas Vallaitis  
Infinera, 1322 Bordeaux Drive, Sunnyvale, CA 94089  
e-mail: tvallaitis@infinera.com

Wolfgang Freude · Juerg Leuthold  
Karlsruhe Institute of Technology (KIT), Institute of Photonics & Quantum Electronics (IPQ), Engesserstr. 5, 76131 Karlsruhe, Germany  
e-mail: W.Freude@kit.edu, juerg.leuthold@kit.edu

Richard Penty  
Cambridge University Engineering Department, Electrical Engineering, Building, 9 JJ, Thomson Ave, Cambridge, CB3 0FA, UK  
e-mail: rvp11@cam.ac.uk

Anna Borghesani · Ian F. Lealman  
CIP Technologies, Phoenix House, Adastral Park, Martlesham Heath, Ipswich, IP5 3RE, UK  
e-mail: anna.borghesani@huawei.com, Ian.Lealman@huawei.com

## 12.1 Introduction

Linear semiconductor optical amplifiers (SOAs) have attracted much interest in the last few years due to their ability to amplify signals over the whole spectral range from 1250 nm up to 1600 nm at a reasonable cost [1].

Optical fiber communications systems, especially in the metro and access networks, take advantage of semiconductor-based optical amplifiers because of their compact size, high efficiency, the required amplification wavelength region and bandwidth. Currently, SOAs show promise as inline amplifiers (reach extender) in fiber-to-the-home (FTTH) applications [2] and in photonic integrated circuits (PICs) [3] to boost a data signal from a directly modulated laser source or to compensate losses in optical switches to name but a few applications.

Depending on the desired application, SOAs can offer power gains  $G$  exceeding 25 dB [4]. SOAs with a polarization dependent gain (PDG) down to 0.2 dB are available commercially today [5]. Low PDG is important in many cases, for example, within a fiber communications network, the state of polarization of the data signal is typically unknown. An unavoidable effect which occurs during the data signal amplification is that noise is added to the signal. The corresponding parameter is the noise figure (NF) which typically has values between 5–8 dB [6]. Additionally, in networks in which multiple data signals are transmitted on different wavelengths, an SOA needs to be able to amplify these data signals simultaneously. Here, the SOA gain bandwidth and the input saturation power  $P_{\text{in}}^{\text{sat}}$  determine the maximum number of channels which can be handled. An SOA gain bandwidth of up to 100 nm [7] and high saturation input powers exceeding 10 dBm [8] have been demonstrated.

The first section of this chapter discusses SOA basics. The concept of an SOA including SOA working principles, material systems, structures and their growth, is discussed. The use of SOAs in PICs and their classification as booster, inline amplifier and preamplifier devices are addressed.

In the second section, all key parameters that characterize the performance of an SOA are discussed in more detail. A simple but efficient model is used to determine the power gain  $G$ , the noise figure NF, the saturation power  $P_s$ , the SOA dynamics (covering interband as well as intraband effects) and finally, the time-dependent effective alpha-factor  $\alpha_{\text{eff}}$ .

In the third section, the important application of linear SOAs as reach extender in future access networks is addressed. The input power dynamic range (IPDR) is introduced, and measurements for on-off keying and phase shift keying (PSK) signals are shown.

In the fourth section, the performance of commercial devices for communications applications is presented, also including reflective SOAs (R-SOA).

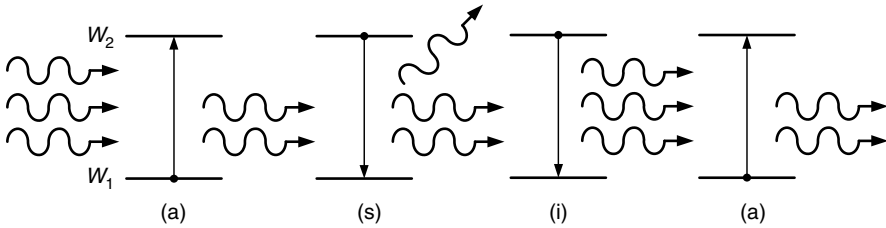


**Fig. 12.1** Interaction of a two-level microsystem with electromagnetic radiation, photon energy  $hf_s = W_2 - W_1$ . A sequence of processes is shown with absorption (a), spontaneous emission (s), induced (= stimulated) emission (i), and absorption of photons (a)

## 12.2 SOA Basics

In this section, the semiconductor optical amplifier (SOA) operating principle is introduced. The condition of achieving optical gain, the more common compound semiconductor heterostructures and the active-region materials to grow such SOAs are discussed, along with the SOA device structure and design. The packaging of SOAs into 14-pin butterfly cases together with SOA applications, including booster, inline and preamplification are outlined.

### 12.2.1 Absorption and Emission of Light

An SOA is a semiconductor waveguide with a gain medium. In SOAs, the gain is obtained by injecting carriers from a current source into the active region. These injected carriers occupy energy states in the conduction band of the active material, leaving holes in the valence band. Electrons and holes recombine either nonradiatively or radiatively, in this case, releasing the recombination energy in form of a photon. Three radiative processes are important in such structures, namely, induced (= stimulated) absorption, spontaneous emission and induced (= stimulated) emission of photons.

We first discuss these processes for a two-level system and subsequently illustrate the situation for a semiconductor material. The three radiative types of transitions from a high to a low energy state a microsystem can undergo are schematically explained in Fig. 12.1.

**Absorption** A microsystem in its ground state  $W_1$  can absorb radiation at a frequency  $f_s = (W_2 - W_1)/h$  (photon energy  $hf_s$ , Planck's constant  $h$ ) and make an upward transition to its higher energy level  $W_2$ . This absorption process is obviously induced or stimulated by an existing electromagnetic wave. The absorption rate depends on the electromagnetic energy density, and on the number of microsystems in the ground state, Fig. 12.1(a).

**Spontaneous Emission** An excited microsystem in energy level  $W_2$  can make a downward transition to the ground state  $W_1$  “spontaneously” (apparently without any interaction with other photons) by emitting a photon with energy  $hf_s = W_2 - W_1$ , Fig. 12.1(s). The spontaneous emission rate depends on the number of excited microsystems. The spontaneous emission can be regarded as being induced by so-called zero-point fluctuations. This energy fluctuation around the electromagnetic field expectation zero represents a perturbation for an excited microsystem and may therefore induce random transitions to the ground state. The spontaneously emitted photons will be found with equal probability in any possible mode of the electromagnetic field.

**Induced Emission** A microsystem in an excited level  $W_2$  can also make a downward transition to the ground state  $W_1$  in the presence and induced by an external radiation (incident photon) of frequency  $f_s = (W_2 - W_1)/h$ . As in the case of (induced) absorption, the emission rate depends on the electromagnetic energy density and on the number of microsystems in the excited state, Fig. 12.1(i). In contrast to the spontaneous emission process, the emitted radiation is in all respects coherent to the stimulating radiation. Therefore, the induced radiation adds with the same polarization and phase to the stimulating field which thus becomes amplified.

For a microsystem in thermal equilibrium, the occupation probability  $w(W_i)$  of the various energy levels  $W_i$  at any temperature  $T$  is given by the Maxwell–Boltzmann statistics (degeneracy  $g_i$  of level  $W_i$ , Boltzmann’s constant  $k = 1.380658 \times 10^{-23}$  W s/K)

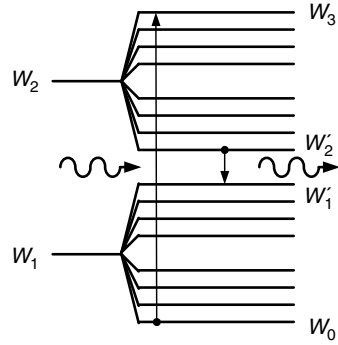
$$w(W_i) = \frac{g_i \exp[-W_i/(kT)]}{\sum_i g_i \exp[-W_i/(kT)]}. \quad (12.1)$$

For nondegenerate ( $g_i = 1$ ) two-level microsystems, as in Fig. 12.1, the relative occupation probability numbers  $N_{1,2}$  of microsystems with energy states  $W_{1,2}$  in thermal equilibrium can be derived from (12.1), that is,

$$\frac{N_2}{N_1} = \exp\left[\frac{-(W_2 - W_1)}{(kT)}\right], \quad N = N_1 + N_2. \quad (12.2)$$

The quantity  $N$  is the total number of microsystems. As seen from (12.2), in thermal equilibrium, the excited state is less densely populated than the ground state. With induced absorption as described in Fig. 12.1(a), the population number  $N_2$  may be increased in proportion to the photon number  $N_p$ , and in proportion to the time  $t$ . Spontaneous emission reduces  $N_2$  in proportion to  $t$ , and stimulated emission diminishes  $N_2$  in proportion to  $N_p$ , and  $t$ . Therefore, in the presence of an electromagnetic field of photon energy  $hf_s$ , a dynamic equilibrium will be reached for which the number of spontaneous and induced emission processes equals the number of stimulated absorption processes. If  $N_p$  is so large that spontaneous emission may be neglected, a state of dynamic equilibrium with  $N_2 = N_1$  (including spontaneous emission  $N_2 \leq N_1$  holds) may be reached so that the number of stimulated emission processes equals the number of stimulated absorption processes. The

**Fig. 12.2** Pump mechanism using energy levels inside the energy level group (pseudo-four-level system)



medium is called *transparent* in this case. However, with a two-level system, it is impossible to achieve what is called “population inversion” with  $N_2 > N_1$ , where the number of stimulated emission processes is potentially larger than the number of absorption processes. It is exactly this case that would lead to a net amplification of an electromagnetic wave propagating in such a medium.

**Semiconductors** The situation is significantly different with a semiconductor material. In the following, we show that population inversion and therefore a net medium power gain can be obtained.

The valence band (VB) and conduction band (CB) states of the semiconductor can be associated with multiple closely spaced levels centered at  $W_1$  and  $W_2$  in a low and high energy state, respectively. According to the equilibrium distribution (12.1), the occupation probability of the lowest energy sublevel ( $W_0$ ) is highest, and of the highest energy sublevel ( $W_3$ ) is lowest, so that the absorption from the lowest energy states to the highest ones is a most probable process, see Fig. 12.2. If an electron is excited to a  $W_3$  sublevel, it would relax quickly within the band to the lower energy sublevel  $W_2'$  (in technical terms, one would say that the intraband carrier relaxation is short). This way, all excitations to a level  $W_3$  will almost instantaneously be transferred to level  $W_2'$  which becomes more densely populated while level  $W_3$  stays lowly populated.

On the other hand, emission from a strongly populated sublevel ( $W_2'$ ) to a sparsely populated sublevel ( $W_1'$ ) is very probable. Therefore, the maximum for absorption is found at higher frequencies (shorter wavelength) than the maximum for spontaneous emission.

This way, pump light with photon energy  $hf_s^{(a)} = W_3 - W_0$  can be absorbed, thereby generating electron–hole pairs. If the pumping is strong enough, then population inversion can be achieved. Optical pumping is not the only way to arrive at population inversion. It is also possible, and indeed preferable, by injecting electrons and holes electronically into a forward biased semiconductor pn-junction. For a hypothetical temperature  $T = 0$  K, the “pump energy”  $hf_s^{(a)} = eU$  provided by the forward voltage  $U$  (elementary charge  $e = 1.602 \times 10^{-19}$  C) would define the energetic difference at which electrons and holes could be injected, i.e., the difference of the quasi-Fermi levels  $W_{Fn} - W_{Fp} = hf_s^{(a)} = eU$  for electrons in the CB



( $W_{Fn}$ ) and for holes in the VB ( $W_{Fp}$ ), respectively. The energy  $hf_s^{(e)} = W_2' - W_1'$  of the emitted photons is therefore smaller than  $W_{Fn} - W_{Fp}$ , but necessarily larger than the bandgap  $W_G$  [9]. Therefore, the general inversion condition for amplification of an electromagnetic wave by a semiconductor is determined by

$$W_G < hf_s^{(e)} \leq W_{Fn} - W_{Fp}. \quad (12.3)$$

### 12.2.2 Compound Semiconductors and Heterostructures

In the previous section we discussed general material properties for generation and amplification of light. Such properties are, e.g., found in the III–V compound semiconductor (In,Ga)(As,P), a material system which will be discussed here.

In this material system, the bandgap  $W_G$ , and hence the bandgap wavelength  $\lambda_G$  and the refractive index  $n$ , depend on the composition. In all practical instances, the compounds have radiative direct band-to-band transitions without the need of phonon interactions. Further, the lattice constant of the compound may be chosen to match the lattice constant of a binary substrate semiconductor. Lattice matching is very important for several reasons:

- A close lattice match is necessary in order to grow high-quality crystal structures.
- Excess lattice mismatch between the heterostructure layers (adjacent semiconductor layers with different  $W_G$ ) would result in crystal imperfections which lead to nonradiative recombinations.
- A moderate lattice mismatch (including either tensile or compressive strain) enables bandgap engineering and parameter optimization, as is outlined in more detail below and also in Chap. 3.

By varying the compound's composition, the bandgap as well as the refractive index and the lattice constant can be engineered. SOAs realized with the (In<sub>1-x</sub>Ga<sub>x</sub>)(As<sub>y</sub>P<sub>1-y</sub>) material system operate in the wavelength range of  $\lambda = 0.92\text{--}1.65\ \mu\text{m}$  and are typically grown on lattice-matched indium phosphide (InP) substrates. Alternatively, gallium arsenide (GaAs) substrates may be chosen which provide amplification in the wavelength region from  $\lambda = 0.87\ \mu\text{m}$  (GaAs) down to  $\lambda = 0.68\ \mu\text{m}$  (In<sub>0.49</sub>Ga<sub>0.51</sub>P). Table 12.1 provides a summary [10].

**Heterostructures** SOAs typically consist of heterojunction structures [11] composed of doped semiconductors with different bandgap energies  $W_G$ . When an impurity atom is implanted into a crystal, its perfect periodicity is destroyed and additional energy levels for electrons located near the band edges are created. These levels are either near the conduction band edge for donating an electron to the conduction band (n-doping), or they are near the valence band edge where they can accept an electron from the valence band (acceptor, p-doping), see the position of the Fermi-energy  $W_F$  in Fig. 12.3.

An energy-band diagram of a typical heterostructure as a function of the layer growth direction  $x$  is shown in Fig. 12.3 for thermal equilibrium. The active

**Table 12.1** Material system  $(\text{In}_{1-x}\text{Ga}_x)(\text{As}_y\text{P}_{1-y})$ .  $W_G$  bandgap,  $\lambda_G$  bandgap equivalent wavelength,  $n$  refractive index,  $a$  lattice constant

Semiconductor	$W_G/\text{eV}$ ( $\lambda_G/\mu\text{m}$ )	$n$ at $\lambda_G$	$a/\text{nm}$
GaAs, direct	1.424 (0.871)	3.655	0.5653
InAs, direct	0.36 (3.444)	3.52	0.6058
InP, direct	1.35 (0.918)	3.45	0.5869
GaP, indirect	2.261 (0.548)	3.452	0.5451
$(\text{In}_{1-x}\text{Ga}_x)(\text{As}_y\text{P}_{1-y})$	$1.35 - 0.72y + 0.12y^2$	$3.45 + 0.256y - 0.095y^2$	0.5869
lattice-matched to InP	$1.35 \dots 0.75$	$3.45 \dots 3.61$	
direct: $y \leq 1$	$(0.918 \dots 1.653)$		
$x = y/(2.2091 - 0.06864y)$			

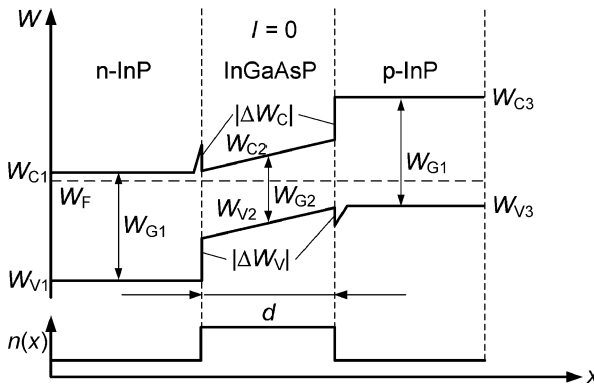


**Fig. 12.3** Energy-band diagram of an InGaAsP/InP double-heterostructure in thermal equilibrium and the schematic of refractive index  $n$  as a function of the growth direction  $x$

InGaAsP region thickness,  $d$ , is typically in the range 0.1–0.5  $\mu\text{m}$ . The active layer is not intentionally doped. However, due to diffusion of p-dopants, it typically is slightly p-doped. The neighboring layers consist of InP which has a larger bandgap  $W_G = W_C - W_V$  (with the CB edge energy  $W_C$  and the VB edge energy  $W_V$ ), and therefore comes with a lower refractive index  $n$ , see Fig. 12.3. The band edge energies (and therefore the carrier concentrations) are not continuous, but exhibit steps by  $|\Delta W_C|$ ,  $|\Delta W_V|$  which lead to spikes and jumps in the band diagram.

In detail, this heterostructure exhibits the following features:

**Potential Wells** The low bandgap of the active medium creates a potential well for carriers which become confined to the active region. If the difference of the quasi-Fermi levels exceeds the bandgap,  $W_{Fn} - W_{Fp} > W_G$ , population inversion occurs and optical amplification results.

**Larger  $W_G$  in the InP Cladding Layers** The larger bandgap in the InP regions prevents reabsorption in the noninverted cladding regions.

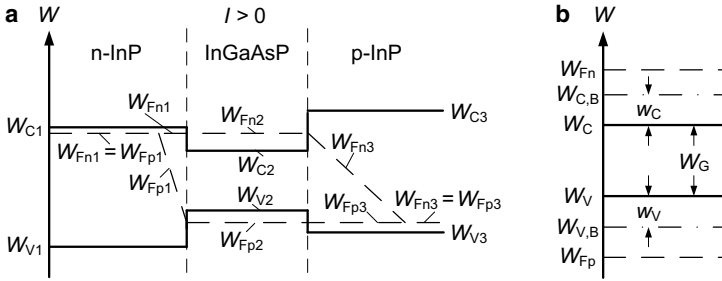


**Fig. 12.4** Energy-band diagram of a double-heterojunction with a forward bias voltage  $U$  ( $T = 0$  K and flat-band case assumed). The quantities  $w_c$  and  $w_v$  are energies measured from the respective band edges into the bands

**Smaller  $n$  in the InP Cladding Layers** A structure with a larger refractive index in the core which is clad by a lower refractive index material forms a slab waveguide that provides guiding in the vertical direction. Lateral guiding results from the lateral gain profile, or by additionally adding low-index regions laterally.

For the three-layer structure presented in Fig. 12.3, both the carrier and the field confinement are determined by the thickness  $d$  of the active layer and by the bandgap energy  $W_G$ .

Figure 12.4 shows the energy band diagram of the double-heterojunction of Fig. 12.3 for the case of a large forward current so that the flat-band case is approximately reached. Far away from the junction, the quasi-Fermi levels of electrons and holes are practically identical. However, inside the thin active p-InGaAsP, we have  $W_{Fn} > W_{Fp}$  due to the carrier injection. The electrons and holes are confined to the potential well inside the active p-InGaAsP layer. Due to current injection, the semiconductor may be population-inverted and the quasi-Fermi level for electrons  $W_{Fn}$  shifted towards or beyond the CB, while the quasi-Fermi level for holes  $W_{Fp}$  is shifted towards or beyond the VB edge.

**Physics of Gain – Material Power Gain** The material power gain  $g_m$  is equivalent to the fractional increase of photons per unit length. It can be approximately calculated by Fermi’s golden rule, a quantum mechanical expression for the transition probability of electrons from the conduction to the valence band [12–15]

$$g_m \sim \int_0^\infty |M_{ave}|^2 \rho(k_{tr}) [f_C(w_V(k_{tr})) + f_V(w_C(k_{tr})) - 1] L(hf_s - w_{cv}(k_{tr})) dk_{tr}. \tag{12.4}$$

The terms in the integral in (12.4) are:

- $k_{tr}$  is the electron–hole transition wave vector.
- $|M_{ave}|^2$  is the squared dipole matrix element describing the quantum mechanical properties of the interband transition.

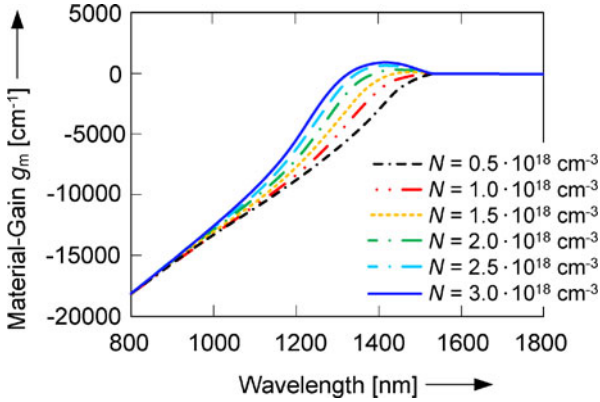


**Fig. 12.5** Calculated material gain  $g_m$  for different carrier densities for 1.55  $\mu\text{m}$  bandgap InGaAsP

- The number of available states per energy interval to be occupied at a certain energy level in the semiconductor material is described by the density of states (DOS). The DOS in the  $k_{\text{tr}}$ -space is  $\rho(k_{\text{tr}})$ .
- The occupation probabilities for CB electrons and VB holes under nonequilibrium conditions (forward bias supplied to pn-junction) are described by the Fermi functions of the CB  $f_c$  or VB  $f_v$ , respectively.
- $L(hf_s - w_{\text{CV}}(k_{\text{tr}}))$  is the linewidth broadening function that takes into account the finite lifetime of the carriers due to scattering effects. The photon energy is  $hf_s$ ,  $w_{\text{CV}} = w_c + W_G + w_v$  is the transition energy from the CB to the VB with the bandgap energy  $W_G$  and the energies of the electrons in the CB and the holes in VB given by  $w_c$  and  $w_v$ , respectively.

Details of the calculation of  $g_m$  can be found in [16]. Figure 12.5 shows the spectral dependence of the material gain for InGaAsP [15]. The gain region occurs at 1.5  $\mu\text{m}$ . The curves have been calculated for carrier densities ranging from  $N = 0.5 \times 10^{18} \text{ cm}^{-3}$  to  $3.0 \times 10^{18} \text{ cm}^{-3}$  in steps of  $0.5 \times 10^{18} \text{ cm}^{-3}$ . It is assumed that the electron and hole densities are equal, i.e.,  $N = P$ . Obviously, the material power gain increases with increasing carrier injection, and the maximum of the material gain shifts to lower wavelengths basically due to band-filling effects. In all practical instances, the material gain is not directly calculated by (12.4). One normally goes back to parameterized material gain curves that have been derived from experiments [16].

### 12.2.3 Properties of the Active Region

Semiconductor optical amplifiers require an active region consisting of a direct bandgap material which gives a high probability for radiative recombinations. SOAs can differ in the dimensionality of the electronic system of their active region. The

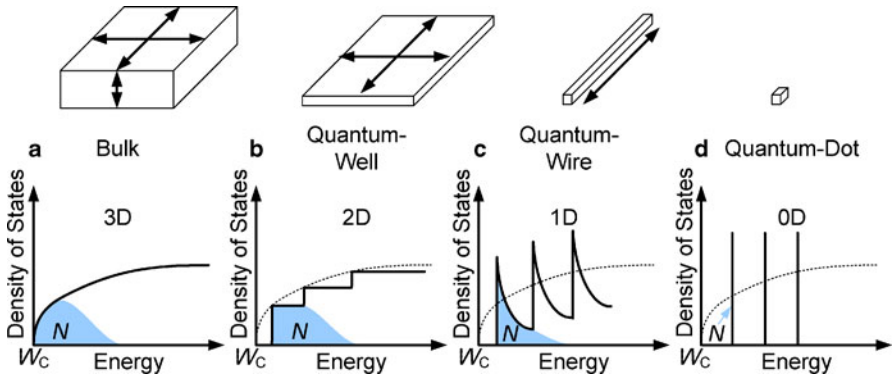


**Fig. 12.6** Density of states (DOS) for SOAs. **a** In bulk material, the carriers are not restrained in their movement. However, this is different if the carriers experience a spatially dependent potential, the dimension of which is smaller than the mean free path length of the carriers. **b** In a quantum well if the carrier motion is limited to a plane, **c** in a quantum wire (or quantum dash) if the carrier motion is limited to one direction, and **d** in a quantum dot, the carrier motion is fully restricted in all dimensions. The corresponding electron concentration  $N$  (blue area) is shown.  $W_c$  is the conduction band edge

classification is done in terms of the mean free path length  $l_{fp}$  of the carriers in the active region with respect to the de Broglie wavelength  $\lambda_{dBr}$  of the carriers. In this sense, if the carrier motion is not restricted, we talk about bulk SOAs. Figure 12.6a shows the density of states (DOS) as a function of energy  $W$  for such a three-dimensional (3D) structure as well as the carrier concentrations of electrons  $N$  (blue area under the curve). The DOS shows a square root dependency on the energy. If the carrier motion is limited to a layer of a thickness  $d$ , which is in the order of the de Broglie wavelength (10–100 nm), discrete energy levels occur for this direction [17]. If the carrier motion is restricted to two dimensions (2D), it is common to talk about a quantum “well” SOA (QW, strictly speaking, it is a quantum film or quantum layer). The DOS corresponding to such discrete energy states is constant as depicted in Fig. 12.6b. If the carrier motion is restricted to one dimension (1D), a quantum wire or quantum dash (QDash) active region results. The quantum wire DOS is proportional to  $1/\sqrt{W}$  as shown in Fig. 12.6c. Finally, if the carrier motion is fully restricted (zero dimension 0D), we talk of a quantum dot (QD) SOA. The atom-like DOS for a QD is expressed by a delta function  $\delta(W)$  as depicted in Fig. 12.6d.

The advantages in reducing the dimensionality of the electronic systems are manifold. In particular, the need of a temperature independent material power gain as well as a reduction in the operating current density for a certain material power gain drives these approaches.

**Bulk SOAs** The active region thickness  $d$  of a bulk double-heterostructure SOA is typically 100–500 nm. As mentioned in Sect. 12.2.2, a common compound used to fabricate such bulk SOA structures for the wavelength region of 1.3  $\mu\text{m}$  or

1.55  $\mu\text{m}$  is based on an  $\text{In}_{1-x}\text{Ga}_x\text{As}_y\text{P}_{1-y}$  active layer with adjacent InP layers grown on an InP substrate. The gain bandwidth is determined by the relationship of the material fractions ( $x$  and  $y$  in Table 12.1). Further, lattice matching is needed to reduce nonradiative recombination at imperfections. However, if bulk SOAs are fabricated with a slab-like waveguide, strong polarization dependent gain will be found due to different optical confinement factors (fraction of light in the active region) for the fundamental transverse electric (TE) and transverse magnetic (TM) propagating modes. Since a low PDG is very important due to the unknown state of polarization at the amplifier input, several approaches are used to reduce PDG. One possibility is the fabrication of virtually ideal square waveguide cross-sections (strip waveguide) to achieve identical confinement factors for the TE and TM mode. However, since such square waveguides are difficult to fabricate, a strained active bulk layer can be grown to adjust the material power gains for the TE and TM mode. Such strained layers result from choosing the material composition with a slight mismatch in the lattice constant relative to the substrate material [5]. If properly chosen, the generated difference in the power gain for the TE mode and TM mode counteracts the difference in optical confinement for the TE mode and TM mode. In effect, these bulk SOAs have virtually polarization independent gain. In [5], it is shown that a tensile strain for the active bulk layer increases the TM material power gain relative to the TE material power gain, and the PDG is minimized. Another approach, which is widely used to achieve low PDG, is the growth of a thin layer with higher bandgap material on either side of the active region, a so-called separate confinement heterostructure (SCH) [5]. This layer has a refractive index between that of the active region (InGaAsP) and the cover (InP) or substrate layer (InP). The inclusion of an SCH structure gives control over the confinement factor ratio for the TE and TM mode via its refractive index and thickness, but it also changes the dynamic characteristics of the SOA.

**QW SOAs** If the carrier motion normal to the active region is restricted by properly choosing the layer thickness  $d$  (down to 10–100 nm), the carriers are confined in a potential “well.” Quantum-well (QW) SOAs or multiquantum-well (MQW) SOAs with lattice matching are strongly polarization dependent with high gain for the TE polarization and considerably lower gain for the TM polarization. Typically, polarization insensitive operation has been shown using both compressive and tensile strained wells based on InGaAsP/InP [18–20], tensile strained QW SOA based on AlGaInAs/InP for the wavelength region of 1.3  $\mu\text{m}$  [21–23] and MQW SOA tensile strained wells based on AlGaInAs/InP for operation at 1.55  $\mu\text{m}$  [24]. For a reduced temperature dependence of the material gain, AlGaInAs/InP is used instead of InGaAsP/InP. The larger conduction band offset with AlGaInAs results in a higher electron confinement in the QW. Another promising material system is GaInNAs on lattice-matched GaAs substrates. The GaInNAs compound is particularly promising for uncooled amplifier operation because the material’s temperature dependence of the gain is superior to that of conventional InP-based structures. At a wavelength of 1.3  $\mu\text{m}$ , QW SOA have been demonstrated with (Al)GaInP or

(Al)GaAs cladding layers on GaAs substrates [25], and 1.5  $\mu\text{m}$  MQW SOA were reported with GaInNAs/GaInAs layers on InP substrates [26].

So far, SOAs were mostly developed on the InGaAsP/InP or AlGaInAs/InP material systems. However, the overall energy efficiency of these devices is unsatisfactory and becomes worse still at elevated temperatures. One of the principal causes of the poor electro-optical conversion efficiency is that a large fraction of the pump energy is converted into unwanted heat via nonradiative recombinations. It is predicted that new materials such as bismides and diluted nitrides on InP and GaAs offer exciting possibilities to reduce or remove the detrimental effects of, e.g., Auger recombination [27]. It has been further shown for the case of GaAsBi that about 10 % Bi is needed to suppress the problematic Auger process [28], and optically pumped lasing has already been demonstrated [29]. Photoluminescence in the wavelength range used for fiber-optic communication and a beneficially weak temperature dependent variation of the energy gap compared to InGaAsP were reported for the quaternary compound  $\text{Ga}(\text{N}_{0.34}\text{Bi}_{0.66})_z\text{As}_{1-z}/\text{GaAs}$  [30]. These new material systems are currently investigated in a number of research projects to determine to what extent the theoretically predicted benefits can be realized.

**QD SOAs** Quantum-dot SOAs with InAs QDs on InP substrates are fabricated using a self-organized growth technique for operation wavelengths at 1.55  $\mu\text{m}$  [31–33]. Also, InAs QDs on InGaAs/GaAs layers [34, 35] are available for operation wavelengths around 1.3  $\mu\text{m}$ . The typical size of these QDs is 10 nm in height and 50 nm in width [31]. Usually, several QD layers are vertically stacked and separated with a spacer layer having a thickness exceeding 30 nm [34]. QD shapes are neither cubic nor ball-shaped which results in strong PDG. One approach to counteract this PDG is the fabrication of columnar quantum dots by vertically stacking QD layers with a spacer layer thickness of only around 1–3 nm. This approach has successfully been used to show polarization independent gain in QD SOAs [36–38].

Several techniques exist to grow SOAs. Typically, metal-organic chemical vapor deposition (MOCVD) or molecular beam epitaxy (MBE) are used. Beside the growth of lattice-matched structures, the strained layer epitaxial growth is also used for special purposes as explained previously. Lattice mismatch between the epitaxial layers and the substrate compared to the substrate lattice constant is around 1.5 %. In contrast to the growth of several nm thick layers on top of a planar substrate for QW SOAs, SOA devices with QD active regions are fabricated by a self-organized growth process, where the lateral dimensions of the quantum dots can be controlled simply by choosing the appropriate growth parameters. The Stranski–Krastanov (SK) growth regime, in which self-assembled quantum dots are formed, is based on a slight lattice mismatch between the substrate and the quantum dot material. In the case of InAs dots on a GaAs substrate, this lattice mismatch is  $\sim 7\%$ . At the beginning of the SK self-assembled quantum dot growth mode, a compressively strained film (wetting layer) is formed. At a critical InAs coverage of around 0.5 nm, the accumulated strain is elastically relieved by the formation of small 3D islands. Beyond the critical InAs thickness, the additional InAs can migrate freely on the sample surface, adding to the 3D island growth. The growth of a capping layer fin-

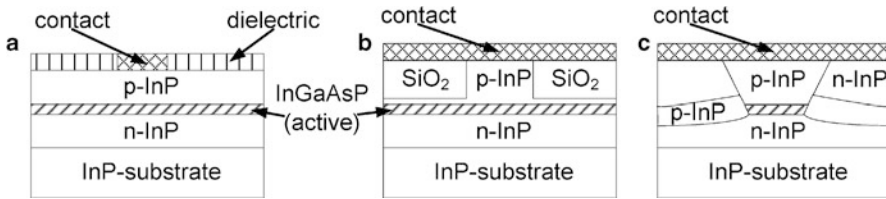


**Fig. 12.7** Typical SOA structures. **a** Stripe-geometry structure for gain-guiding, **b** ridge waveguide structure for weak index-guiding and **c** buried heterostructure for strong index-guiding. The figures are modified from [40], and not drawn to scale

ishes the dot formation. If the capping layer material has a smaller bandwidth than the substrate, a quantum well structure around the dots is formed. This technique is used to extend the emission wavelength of the dots (dot-in-a-well-structure) [39].

Quantum dot SOAs promise several advantages, such as an ultra-fast QD gain response in the order of 1–25 ps due to a fast QD refilling through the carrier reservoir represented by the wetting layer [41]. The ideal QD SOA also offers a large gain bandwidth exceeding 120 nm which is due to QD size fluctuations during the growth [7], low temperature dependence of the gain [42], and low chirp even under gain saturation [43]. The enhanced multi-wavelength capability which is expected compared to bulk/QW SOA has up to now been found in simulations only [44, 45].

#### 12.2.4 SOA Structures and Devices

SOAs are fabricated with an active region material (nominally undoped, i.e., intrinsic) with a larger refractive index compared to its n-cladding and p-cladding layer materials. Such a structure forms a pin-junction. In general, the refractive index difference between core and cladding material is around 0.3 for InGaAsP/InP structures. This strong index difference leads to a vertical guiding of the optical mode. However, with a slab waveguide, the light is unconfined in the lateral direction, parallel to the pin-junction plane. This issue can be solved by tailoring the SOA device structure. In Fig. 12.7, various SOA cross sections with lateral light confinement are presented: (a) stripe-geometry for a gain-guided SOA, (b) ridge waveguide for a weakly index-guided SOA, and (c) buried heterostructure for a strongly index-guided SOA.

The technically simplest and cheapest solution for guiding the light is a gain-guided structure which limits the current injection to a narrow region [46]. This stripe-geometry (Fig. 12.7a) is easy to fabricate since a contact region is required only after the growth process of the n-cladding layer, the active region and the p-cladding layer.

The contact consists of a dielectric layer which has an opening of 4–6  $\mu\text{m}$  through which the current is injected via a metal contact. In the direction parallel to the pin-junction plane, the lateral spread of injected carriers introduces a lateral gain



profile. Since the active region has large absorption losses beyond the central stripe, the light is confined to the stripe region which shows gain (active region). As the light-confinement is influenced by the injected carriers, a so-called gain-guiding structure is fabricated in which the mode is weakly guided [40]. The counteracting antiguiding due to the higher carrier concentration below the contact stripe and its associated reduction of the refractive index usually has a lesser effect.

In order to improve the performance, stronger waveguiding is achieved with so-called index-guided structures. Here, an index step is introduced also in the lateral direction, i.e. parallel to the pin-junction plane. A ridge waveguide (Fig. 12.7b) is comparatively simple to fabricate. After the growth of the n-cladding, the active region and the p-cladding a ridge is formed by etching parts of the p-layer. The ridge width (waveguide width  $w$ ) is typically 2–4  $\mu\text{m}$ . Next, a dielectric layer ( $\text{SiO}_2$  or  $\text{Si}_3\text{N}_4$ ) is deposited to block the current flow and to introduce a refractive index difference of around 0.03 between the p-InP and the dielectric material. In this way, the mode is confined to the ridge waveguide by weak index-guiding. Finally, the metal contact layer is fabricated.

Strong index-guiding SOAs have a buried heterostructure (Fig. 12.7c). Here, the InGaAsP active layer is “buried” by surrounding it on all sides by InP regions which have a lower refractive index [13, 40]. The layers are fabricated such that any current is efficiently blocked between the n-InP/p-InP, and thus a good current confinement is guaranteed. The index difference between the core and cladding regions is around 0.3. However, the fabrication of buried-heterostructure SOAs is complex, and several growth and etching steps are required to form the current blocking layers and the contacts.

After the definition of a gain-guided or an index-guided structure, the SOA chip is fabricated. Normally, SOA devices are fabricated as traveling-wave amplifiers. In ideal traveling wave amplifiers (no facet reflectivities as opposed to resonant Fabry–Perot amplifiers), the optical wave makes only a single pass through the active layer. Typically, an SOA has a length of roughly 0.5–4 mm. Antireflection multilayer dielectric coatings with a thickness of approximately a quarter of a wavelength reduce the total facet reflectivity down to around  $10^{-4}$ . However, residual facet reflectivities are always present, so the SOA becomes a laser oscillator if the gain is sufficiently high. To further suppress lasing, the waveguide is often tilted by 7–10° with respect to the facet normal, thereby reducing the residual reflection from the end facets even more.

Besides preventing lasing, a low facet reflectivity is also desirable to avoid periodic variations of the gain with the cavity mode spacing, so-called gain ripple. The larger the reflectivity of the input and output facets, the larger the gain ripple is. However, the use of antireflection coated facets as well as tilted waveguides lead to an SOA with gain ripple below 0.2 dB.

Typically, SOA chips are mounted on a heat sink to efficiently remove the dissipated heat. Further, single-mode operation of the SOA is desirable which sets limits for the maximum waveguide height  $d$ , the waveguide width  $w$  and the maximum refractive index difference between core and cladding material, respectively.

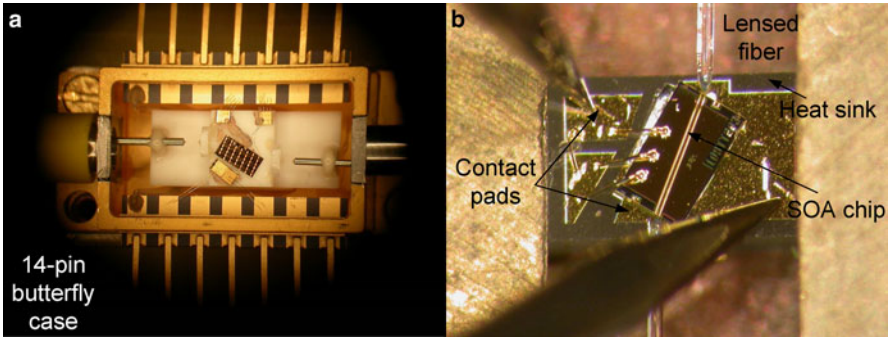


**Fig. 12.8** SOA packaging and fiber-to-chip coupling. **a** Top view of an SOA package using typical butterfly cases. **b** Close-up of the top view of an SOA chip with fiber-to-chip coupling

### 12.2.5 Packaging and Photonic Integrated Circuits

Semiconductor optical amplifier chips are typically packaged into hermetic 14-pin butterfly cases which are free of organic materials (Fig. 12.8a). This technology ensures high operation stability, long term reliability, low power consumption, and supports operating temperatures in the range from  $-30$  to  $+60$  °C. SOA packaging follows similar rules as the packaging of laser diodes. A lensed input fiber is mechanically stabilized and fixed to the input facet, Fig. 12.8b. The SOA chip is temperature stabilized with a thermoelectric cooler (TEC) to keep the chip at the operation temperature. The temperature is measured using a thermistor located close to the sample. The contact pads of the pin-junction are wire-bonded to the butterfly pads of the case for current supply. The lensed output fiber is also mechanically stabilized and permanently fixed.

Today, SOAs are also often found as subcomponents of photonic integrated circuits (PIC). A PIC is a highly integrated device performing multiple functions on a single chip. PICs are gaining interest due to the small footprint, the low power consumption and potentially due to lower cost compared to discrete solutions. PICs are built based upon substrate materials such as InP, GaAs, lithium niobate ( $\text{LiNbO}_3$ ), silicon and also glass. To guarantee cost-effective chip integration, the performance of PICs must be competitive with discrete solutions and the yield of each element must be very high.

While the InP system is not inexpensive, it reliably integrates active and passive optical devices using standard batch-semiconductor manufacturing processes. InP supports key optoelectronic functions such as light generation, amplification, modulation and detection as well as passive components such as arrayed-waveguide gratings (AWG), filters and waveguides. To date, the speed of active components is limited due to carrier dynamics in the range of tens to hundreds of ps. Recently, a PIC transmitter with a capacity of  $10 \times 40$  Gbit/s (on-off keying format) has been shown which nicely demonstrates the high integration potential of this material system [3, 47, 48].

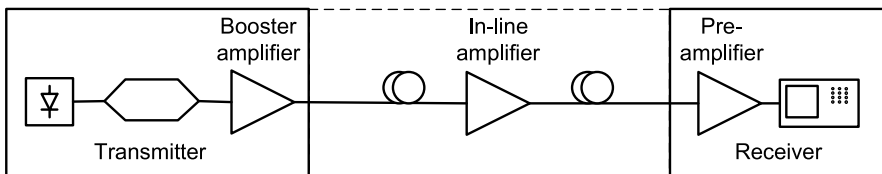


**Fig. 12.9** SOA can be used at different positions within a network. An SOA booster raises the power level of the signal at the transmitter, the inline SOA compensates for fiber losses and the preamplifier SOA increases the power level at the receiver to increase the receiver sensitivity

### 12.2.6 Applications as Booster, Inline and Preamplifiers

Linear SOAs maintain proportionality between output and input field. They can be used at different locations within a network. In metro networks, linear SOAs can be used in optical-electric-optical (OEO) converters to boost the optical signal, or in optical add-drop multiplexers (OADM) to increase the tolerable loss budget. SOAs are also good reach extenders in access networks for increasing the distances between the central office and the customer locations, and for providing an increased fan-out (split ratio) to serve a higher number of customers.

Figure 12.9 shows three common SOA applications in networks [49]. A booster amplifier (postamplifier) increases the power level of a signal at the transmitter prior to transmission. In general, the output power of a laser diode or a tunable laser source is moderate, especially if an external modulator is used. Therefore, the booster should have a high saturation output power. Further, the booster should provide pattern free amplification of the data signal. In WDM systems, it should amplify all signals alike across the spectrum. Booster amplifiers normally are polarization sensitive. This is not an issue for boosters as the input signal polarization is known. Booster SOAs typically have small-signal gains in the order of 10 dB with a saturation output power of more than 10 dBm.

An inline amplifier mainly compensates for fiber losses or splitter losses in an optical transmission system. The most important performance parameters are saturation output power and noise figure because the incoming signals are weak. The polarization dependence of the gain should be as small as possible due to the random state of polarization within a network. Also, inline SOAs need to cope with several wavelength channels simultaneously. Further, inline SOAs should process the data signal “transparently” which means that all kinds of modulation formats at any data-rate should be amplified without significant degradation. Typical saturation output powers are 8 dBm for small-signal gains in the order of 10–20 dB and a noise figure between 5–7 dB. In addition, there is an increasing interest in low wall-plug power consumption since inline amplifiers might be placed outside of network central offices.

A preamplifier SOA raises the power level of an incoming data signal to enhance the receiver sensitivity. The most important parameters of these SOAs are gain and

noise figure as well as low residual polarization dependence of the gain. Typical small-signal gains are between 25–30 dB. Noise figures lie in the region 5–7 dB.

In today's optical networks, fiber amplifiers predominate (see Chap. 11). Fiber amplifiers are usually based on rare-earth doped fibers (Erbium (EDFA) for C-band operation). In contrast to SOAs, fiber amplifiers not only need a doped fiber, but also an optical pump laser. Also, the gain bandwidth is limited to anything between 30–70 nm. Especially in the upstream path of access networks, where the traffic is bursty (bursts in the milli- and microsecond time scales), fiber amplifiers induce strong signal degradations since the fluorescent lifetimes in the fiber amplifiers are on the same time scale (10 ms in an EDFA). An advantage of fiber amplifiers is a large small-signal gain of up to 40 dB and low noise figures down to 4 dB or even less (see Chap. 11). They are polarization independent and widely used in multi-wavelength applications due to their low channel crosstalk. Patterning effects at high speed applications (10 Gbit/s and even higher bitrates) are avoided due to the long fluorescent lifetimes.

In contrast, SOAs do not have such good performance parameters, but they can be designed to operate over a wide range of wavelengths, are very compact and can be modulated (their gain can be turned on and off) very rapidly (in time scales of the order of 1 ns) so they can be used to blank signals when necessary.

## 12.3 Parameters of Semiconductor Optical Amplifiers

The absolute performance of SOAs for linear applications is determined by parameters such as the power gain, the noise figure, the saturation power, the gain and phase dynamics as well as the chirp described by the so-called alpha-factor. In this section, we will discuss the concepts and the assumptions used to define these parameters. We start the description with the basic wave equation for an active medium, and afterwards define power gain and phase, and then calculate the SOA noise figure in direct detection systems as well as the SOA saturation power. The carrier dynamics in an SOA due to interband and intraband contributions are described by rate equations and finally the alpha-factor relating gain and phase changes are introduced.

### 12.3.1 Physics of Media with Gain

A signal propagating in a sufficiently pumped SOA is amplified. Starting from the general form of Maxwell's equations [50], a couple of practical assumptions are made to simplify the analysis of light propagation in an SOA:

- The SOA material is nonmagnetic, has a sufficiently low free carrier concentration so that the carriers do not affect the optical properties, and is only weakly inhomogeneous and isotropic.
- The medium response to an electric field is described by a medium susceptibility  $\chi$ .

We start with the description of a homogeneous, weakly amplifying (or attenuating) medium. The complex relative dielectric constant  $\bar{\epsilon}_r$  and the complex refractive index  $\bar{n}$  are related by

$$\bar{\epsilon}_r(\omega) = \epsilon_r(\omega) - j\epsilon_{ri}(\omega), \quad \bar{n}(\omega) = n(\omega) - jn_i(\omega), \quad \bar{\epsilon}_r(\omega) = \bar{n}^2(\omega), \quad (12.5)$$

where  $\epsilon_r$ ,  $n$  are the real parts and  $-\epsilon_{ri}$ ,  $-n_i$  are the imaginary parts of relative frequency-dependent dielectric constant and refractive index, respectively [46, 51]. We investigate signal propagation in a sufficiently narrow spectral range, so that  $\bar{\epsilon}_r(\omega)$  and  $\bar{n}(\omega)$  can be replaced by their values  $\bar{\epsilon}_r = \bar{\epsilon}_r(\omega_s)$  and  $\bar{n} = \bar{n}(\omega_s)$  at the optical carrier frequency  $\omega_s = 2\pi f_s$ .

The unpumped SOA medium is described by a constant (carrier independent) complex background refractive index  $\bar{n}_b = n_b - j\alpha_L/(2k_0)$  with real part  $n_b$  and an imaginary part  $-\alpha_L/2k_0$  determined by the material power loss  $\alpha_L$  and the vacuum wave number  $k_0 = \omega_s/c_0$  ( $c_0$  speed of light in vacuum). When the medium is pumped, the additional charge carriers (density  $N$ ) slightly reduce the real part of the background refractive index by  $n_N$  and provide gain with a material power gain  $g_m$ . The complex refractive index due to carrier injection is a perturbation to the complex background refractive index,  $\bar{n}_N = -n_N + jg_m/(2k_0)$ . Then, we can write considering the net power gain  $g = g_m - \alpha_L$ ,

$$\begin{aligned} \bar{\epsilon}_r &= (\bar{n}_b + \bar{n}_N)^2 = \left( n_b - n_N + j\frac{g_m - \alpha_L}{2k_0} \right)^2 \\ &\approx n_b^2 - 2n_b n_N + jn_b \frac{g_m - \alpha_L}{k_0} = n_b^2 - 2n_b n_N + jn_b \frac{g}{k_0}. \end{aligned} \quad (12.6)$$

With increasing  $N$  the carrier-related complex refractive index changes from  $\bar{n}_N$  to  $\bar{n}_N + \Delta\bar{n}_N \approx -n_N + \Delta n + j(g_m + \Delta g_m)/(2k_0)$ , where  $\Delta n < 0$  and  $\Delta g_m > 0$  hold in this case.

The real and the imaginary parts of the refractive index are related by the Kramers–Kronig relation [52–54]. This relation is a result of causality in physical systems. Phenomenologically, it has been found that this relation can be simplified for a fixed operating point, and expressed by the linewidth enhancement factor, also known as the Henry factor or alpha-factor  $\alpha$  [55, 56] which relates the change of the refractive index  $\Delta n$  and the change of the material power gain  $\Delta g_m$  (assumption:  $\alpha_L \ll g_m$ , (12.6) or  $\partial\alpha_L/\partial N = 0$ ),

$$\alpha = \frac{\partial n_N/\partial N}{\partial n_{i,N}/\partial N} \approx -2k_0 \frac{\partial n_N/\partial N}{\partial g_m/\partial N} \approx -2k_0 \frac{\Delta n}{\Delta g_m} = -2k_0 \frac{\Delta n}{\Delta g}. \quad (12.7)$$

The alpha-factor depends on parameters such as wavelength and current density. Further, the SOA active material strongly influences the alpha-factor.

A monochromatic guided wave in a transparent SOA is described by a complex electric field  $E_y$  linearly polarized in  $y$ -direction, defined parallel to the substrate plane. The field can be written as a product of a transverse modal function  $F(x, y)$ ,

an envelope  $A(z, t)$ , wave propagating terms, and a normalization constant  $c_p$  [50],

$$E_y(x, y, z, t) = E_y(x, y)E_y(z, t) = c_p F(x, y) \exp(j\omega_s t) A(z, t) \exp(-jk_0 n_b z). \quad (12.8)$$

In (12.8) and for the following considerations, the background refractive index has to be interpreted as an effective refractive index  $n_b = \beta/k_0$  representing the guided-wave propagation constant  $\beta$ . As a next approximation step, we only focus on the evolution of  $A(z, t)$ . We fix  $c_p F(x, y)$  such that  $|A(z, t)|^2$  equals the total power  $P(z, t)$  of the optical field propagating in  $z$ -direction.

With the free space impedance  $Z_0 = \sqrt{\mu_0/\varepsilon_0}$  ( $\mu_0$  is the magnetic permeability and  $\varepsilon_0$  the permittivity of free space), we write

$$|A(z, t)|^2 =: P(z, t) = \frac{n_b}{2Z_0} \iint_{-\infty}^{\infty} |E_y(x, y, z, t)|^2 dx dy, \quad (12.9)$$

$$\frac{|c_p|^2 n_b}{2Z_0} \iint_{-\infty}^{\infty} |F(x, y)|^2 dx dy = 1.$$

In an SOA, the optical mode overlaps only partially with the active volume. The fraction of power propagating in the active region area  $C$  (having width  $w$  and height  $d$ ) related to the totally guided power is known as optical confinement factor  $\Gamma$ ,

$$\Gamma = \frac{\int_0^w \int_0^d |F(x, y)|^2 dx dy}{\int_{-\infty}^{+\infty} |F(x, y)|^2 dx dy}. \quad (12.10)$$

Therefore, quantities relevant for the interaction of amplifying medium and optical field have to be modified, leading to an effective net power gain  $g_e$  (modal gain) and an effective real part of the refractive index  $n_{eN}$ ,

$$\begin{aligned} g &\rightarrow g_e = \Gamma g, \\ n_N &\rightarrow n_{eN} = \Gamma n_N. \end{aligned} \quad (12.11)$$

Actually, we want to approximately describe the field in an amplifying guiding medium. The electric field is then represented by an equivalent plane wave with amplitude  $A(z, t)$  (neglecting the phase front curvature of the actual guided wave) that propagates along the  $z$ -direction. Integrating (12.9) over the cross-section area, we can isolate the complex electric field  $E(z, t) = A(z, t) \exp(j\omega_s t) \exp(-jk_0 n_b z)$ , which is a solution of the wave equation

$$\frac{\partial^2 E(z, t)}{\partial z^2} - \frac{1}{c_0^2} (n_b^2 - 2n_b \Gamma n_N + jn_b \Gamma g/k_0) \frac{\partial^2 E(z, t)}{\partial t^2} = 0. \quad (12.12)$$

The wave equation (12.12) can be further simplified using the following assumptions:

- The ideal traveling-wave amplifier only guides the fundamental mode in the active region, and the polarization of the field is conserved.
- The bias current supplies carriers, which under all conditions remain uniformly distributed in the active volume.
- The envelope  $A(z, t)$  of the propagating wave varies slowly in space compared to the wavelength of light (slowly varying envelope approximation) [50],

$$\left| \frac{\partial^2}{\partial z^2} A(z, t) \right| \ll \left| 2k_0 n_b \frac{\partial}{\partial z} A(z, t) \right|. \quad (12.13)$$

If we neglect group-velocity dispersion, because its effect on the optical field envelope is negligible for a typical amplifier length of approximately 1 mm, and then introduce the retarded time  $t' = t - z/v_g$  (group velocity  $v_g$ ) and an amplitude  $A'(z, t') = A(z, t)$ , a simplified version of the nonlinear Schrödinger equation (NLSE) results [57],

$$\frac{\partial A'(z, t')}{\partial z} = \left( jk_0 \Gamma n_N + \frac{\Gamma g}{2} \right) A'(z, t'). \quad (12.14)$$

Equation (12.14) describes the slowly varying amplitude of the wave during propagation in the active medium of an SOA. In the following, we understand that an input amplitude  $A'(0, 0)$  at  $z = 0$  and  $t = 0$  leads to a time-delayed output amplitude  $A'(L, t - L/v_g)$  at  $z = L$ . However, because  $n_N$  and  $g$  are regarded as  $z$ -independent global quantities, we drop the retarded-time argument. Any changes of the output amplitude  $A'$  are then due to temporal changes  $n_N(t)$  and  $g(t)$  only. This implies that the SOA length  $L$  is much shorter than the length scale, on which  $A'(z, t')$  varies. In this spirit, and because we neglect dispersion, we replace in the following  $A'(z, t')$  by  $A(z)$ .

More elaborate SOA models take into account the photon density variations along the SOA waveguide by means of longitudinal segmentation. Thus, the SOA is subdivided along the propagation direction into a number of sections for which the differential equations for carrier density and photon number are solved. The results are evaluated at the boundaries and handed over to the following section [51].

### 12.3.2 Gain and Phase

In an active material, it is essential to learn about the photon density  $S(z)$  or the optical power  $P(z)$  and the phase  $\varphi(z)$  at the SOA output. A phasor representation of the envelope  $A(z)$  is introduced to separate  $\sqrt{P(z)}$  from the phase  $\varphi(z)$  of the wave,

$$A(z) = \sqrt{P(z)} \exp(j\varphi(z)). \quad (12.15)$$

By substituting (12.15) into (12.14) and performing a separation of variables, we obtain differential equations for the power

$$\frac{dP(z)}{dz} = \Gamma g P(z) \quad (12.16)$$

and for the phase

$$\frac{d\varphi(z)}{dz} = k_0 \Gamma n_N. \quad (12.17)$$

In this simplified model, the net power gain  $g$  and the confinement factor  $\Gamma$  are assumed to be independent of the propagation distance  $z$ , so that an integration of (12.16) yields an expression for the SOA output power  $P(L) = P_{\text{out}}$  for a propagation length  $L$  (power at SOA input  $P(0) = P_{\text{in}}$ ). This leads to the definition of the single-pass power gain  $G$  of the device,

$$P(L) = P(0) \exp\left(\int_0^L \Gamma g dz\right) = P(0) \exp(\Gamma g L) = GP(0), \quad G = \frac{P(L)}{P(0)}. \quad (12.18)$$

As mentioned before, also the real part  $n_N$  of the refractive index is assumed to be independent of the propagation distance  $z$ , so that an integration of (12.17) yields the output phase  $\varphi(L)$  for a waveguide of length  $L$  (reference phase at SOA input  $\varphi(0) = 0$ )

$$\varphi(L) = \varphi(0) + k_0 \Gamma n_N L, \quad \varphi(0) = 0. \quad (12.19)$$

From (12.9), (12.18) and (12.19), it can be seen that the power increases exponentially with the SOA length while the phase only increases linearly.

If the carrier density is increased from  $N_1$  to  $N_2$  due to carrier injection, the net power gain increases by  $\Delta g > 0$ . The additional charge carriers slightly reduce the real part of the refractive index from  $n_{N_1}$  to  $n_{N_2}$ , so that  $\Delta n < 0$ . With the help of the alpha-factor  $\alpha$  (12.7), we may express the change of the phase  $\Delta\varphi(L, N) = \varphi(L, N_1) - \varphi(L, N_2) := \Delta\varphi(N)$  at the output of the SOA by the gain change

$$\Delta\varphi(N) = k_0 \Gamma (n_{N_1} - n_{N_2}) L = -k_0 \Gamma \Delta n L = \alpha \Gamma \Delta g L / 2. \quad (12.20)$$

The absolute values of the gain must be derived from experiments by measurements of the input and output powers. Care must be taken to subtract the noise that may be superimposed. If noise cannot easily be subtracted, then a more complicated measurement approach may be used which is presented in Sect. 12.3.3 on “Noise Figure.”

Figure 12.10 shows a typical dependency of the power gain on the (a) wavelength and (b) input power. Today, typical power gains between 10 dB and 30 dB are found



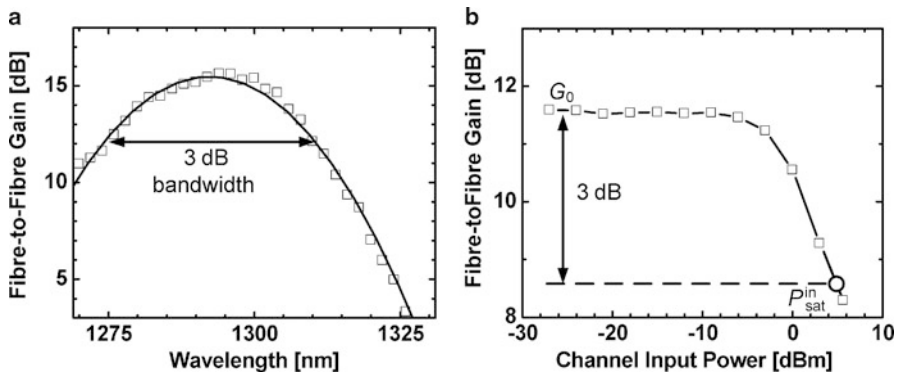


**Fig. 12.10** Typical power gain  $G$  characteristics as measured with fibers connected to the input and output of the SOA (fiber-to-fiber power gain). **a** The bandwidth is around 40 nm with a peak gain of 15 dB at 1295 nm. The parameters have been derived at a temperature of 20 °C, with a bias current of 490 mA and a continuous wave (cw) input power of  $-10$  dBm. **b** Power gain  $G$  as a function of the input power. The 3 dB saturation input power level is indicated by a circle

in practice [4, 33]. In wavelength-division-multiplexing (WDM) systems, signals on different wavelengths are simultaneously amplified which requires a large full width half maximum (FWHM) bandwidth of the SOA. From Fig. 12.10a, it can be seen that this specific amplifier offers a bandwidth of 35–40 nm. However, gain bandwidths exceeding 100 nm are reported [7, 26].

In Fig. 12.10b, also the 3 dB saturation input power level  $P_{\text{sat}}^{\text{in}}$ , which determines the input power at which the unsaturated power gain  $G_0$  is halved, is indicated by a circle. A discussion on the saturation power follows in the respective Sect. 12.3.4 on “Gain Saturation.”

### 12.3.3 Noise Figure

SOAs are also limited by spontaneous emission. This spontaneous emission adds to any input signal, it limits the overall number of amplifiers in a system and confines operation to signals with sufficient input powers.

If spontaneously emitted photons happen to propagate along the active region of an SOA, they are amplified and this noise is called amplified spontaneous emission (ASE) noise. The noise characteristic of an amplifier is generally described by a parameter called the noise factor ( $F$ ) or in logarithmic units by the noise figure (NF), respectively [58–60].

In this paragraph, we will follow a noise figure definition which is valid for phase-insensitive amplifiers [61] that are discussed herein. In a semiclassical interpretation for the case of reasonable power gain values, we will obtain the noise figure definition widely accepted within the optical amplifier community. This definition can also be used for amplifier cascades [60].

The noise figure is defined as the ratio of the (extractable, i.e., measurable) optical output noise power inside the optical amplifier bandwidth  $B_O$  and the (nonextractable, i.e., not directly measurable) optical power fluctuations of an ideal coherent signal in the same bandwidth. Equivalently, this ratio can be expressed by relating the signal-to-noise ratio (SNR) at the amplifier input to the SNR at the amplifier output,

$$F = \frac{\text{SNR}_{\text{in}}}{\text{SNR}_{\text{out}}}. \quad (12.21)$$

For the noise factor  $F$ , it is customary to use logarithmic units

$$\text{NF} = 10 \log_{10}(F). \quad (12.22)$$

The average photon number corresponds to the average optical signal power  $P$ , which is proportional to the average photocurrent  $\langle i \rangle$ . The electrical power  $P_e$  is proportional to the square of the average photocurrent  $\langle i \rangle^2$ .

In the following, we assume ideally coherent signal light, the photon statistic of which is Poissonian. The associated quantum (shot) noise can be described by the variance  $\sigma_i^2 = \langle \Delta i^2 \rangle_{\text{shot}}$  of the photocurrent  $i$ , where the photocurrent fluctuations  $\Delta i = i - \langle i \rangle$  are defined with respect to the average current  $\langle i \rangle$  [58].

We introduce the relation between the average photocurrent and the average optical signal power  $\langle i \rangle = RP$ , and define the sensitivity (responsivity)  $R = \eta e / (hf_s)$  of a photodiode having a quantum efficiency  $\eta$ . Then, we write for the effective electrical photocurrent noise power in an electrical bandwidth  $B$  [59]

$$\langle \Delta i^2 \rangle_{\text{shot}} = 2e \langle i \rangle B = 2eRPB. \quad (12.23)$$

For a quantum (shot) noise limited reception, the SNR at the input of the SOA is defined for a quantum efficiency  $\eta = 1$  by

$$\text{SNR}_{\text{in}} = \frac{\langle i \rangle^2}{\langle \Delta i^2 \rangle_{\text{shot}}} = \frac{R^2 P_{\text{in}}^2}{2eRP_{\text{in}}B} = \frac{P_{\text{in}}}{2hf_s B}. \quad (12.24)$$

Electrical and optical SNR are the same for an ideal detector with quantum efficiency  $\eta = 1$ . However, the equivalent optical input noise power  $2hf_s B$  cannot be measured directly. Two measurement techniques lead to the same result: Either  $\text{SNR}_{\text{in}}$  is determined by measuring  $P$  and by inferring the equivalent input noise power  $2hf_s B$  from quantum theory, or the square  $\langle i \rangle^2$  of the average photocurrent is measured along with its shot noise fluctuation  $\langle \Delta i^2 \rangle_{\text{shot}}$ , corrected for the real quantum efficiency  $\eta$  of the photodetector.

The output SNR from the SOA is given by the optical signal power at the amplifier output divided by the total optical noise power measured at the output in a bandwidth  $B$ . These quantities can be measured directly with an optical spectrum analyzer (OSA), or an electrical method can be employed, again using a photodetector and analyzing the resulting photocurrent.

The photocurrent fluctuations have to be subdivided into several contributions due to the fact that a photodiode is a square-law detector inducing mixing of the received components. Here, we consider contributions from the signal with shot noise (shot), as well as the beat-noise terms arising from signal-spontaneous (s-sp) noise and spontaneous-spontaneous (sp-sp) noise mixing [61].

To calculate the output SNR after the SOA, we assume that an optical filter is used prior to detection having an optical bandwidth  $B_O$  and a rectangular transfer function. This assumption is valid as the optical filters used in practice have bandwidths much narrower than typical SOA spectral bandwidths.

Furthermore, the ASE noise at the amplifier output is assumed to have a uniform optical power spectral density  $\rho_{ASE}$  over the filter bandwidth. The ASE noise power spectral density in one polarization only (here:  $\rho_{ASE\parallel}$  copolarized with the signal) is  $\rho_{ASE}/2$  and can be written with the inversion factor  $n_{sp}$  and  $N_{1,2}$  as the number of excited microsystems in the lower and upper energy states, respectively [60],

$$\rho_{ASE} = 2\rho_{ASE\parallel} = n_{sp}2hf_s(G-1) = 2P_{ASE\parallel}/B_O, \quad n_{sp} = \frac{N_2}{N_2 - N_1}. \quad (12.25)$$

The different contributions to the photocurrent noise power in one polarization at the amplifier output are ( $B_O \gg B$ )

$$\langle \Delta i'^2 \rangle_{\text{shot}} = 2eRGP_{\text{in}}B, \quad (12.26)$$

$$\langle \Delta i'^2 \rangle_{\text{s-sp}} = 4R^2GP_{\text{in}}\rho_{ASE\parallel}B, \quad (12.27)$$

$$\langle \Delta i'^2 \rangle_{\text{sp-sp}} = 2R^2\rho_{ASE\parallel}^2(B_O - B/2)B \approx 2R^2\rho_{ASE\parallel}^2B_OB. \quad (12.28)$$

The square of the amplified signal current is  $\langle i' \rangle^2 = R^2G^2P_{\text{in}}^2$ . Then, the output SNR is written by

$$\text{SNR}_{\text{out}} = \frac{R^2G^2P_{\text{in}}^2}{2eRGP_{\text{in}}B + 4R^2GP_{\text{in}}\rho_{ASE\parallel}B + 2R^2\rho_{ASE\parallel}^2B_OB}. \quad (12.29)$$

Thus, the noise factor  $F$  is obtained,

$$F = \frac{1}{G} + \frac{2\rho_{ASE\parallel}}{hf_sG} + \frac{\rho_{ASE\parallel}^2B_O}{hf_sG^2P_{\text{in}}} = \frac{1}{G} + \frac{2\rho_{ASE\parallel}}{hf_sG} + \frac{n_{sp}hf_s(G-1)}{hf_sG} \frac{P_{ASE\parallel}}{GP_{\text{in}}}. \quad (12.30)$$

This expression for the noise factor depends on the input signal. However, because  $n_{sp}$  is in the order of 1 and the signal output power  $GP_{\text{in}}$  is typically much larger than the copolarized ASE power  $P_{ASE\parallel}$ , the last term in (12.30) can be safely neglected to yield the usual noise factor definition

$$F = F_{\text{shot}} + F_{\text{excess}} = \frac{1}{G} + \frac{2\rho_{ASE\parallel}}{hf_sG} = \frac{1}{G} + \frac{2P_{ASE\parallel}}{hf_sGB_O} = \frac{1}{G} + 2n_{sp} \frac{G-1}{G} \quad (12.31)$$

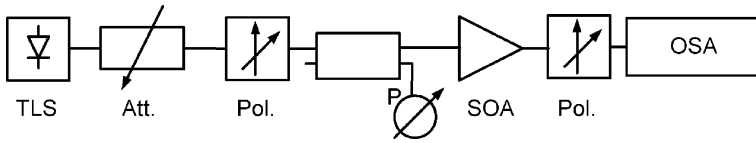


**Fig. 12.11** Setup to measure the device power gain and the noise figure of an SOA as a function of different input power levels and wavelengths. The wavelength-tunable laser source (TLS) provides a continuous wave signal. The input power to the SOA is varied by an optical attenuator (Att.) and measured with a power meter (P) after a polarizer (Pol.) and a 50 : 50 coupler. The output signal power and the amplified spontaneous emission (ASE) power are measured by an optical spectrum analyzer (OSA). The second polarizer transmits only ASE noise which is co-polarized with the signal

which is independent of the input signal, obeys the cascading rules for amplifiers, and may be also derived from quantum mechanical first principles [59].

From (12.31), it can be seen that the minimum achievable excess noise figure of an optical amplifier is  $F = 2$  (NF = 3 dB) for the case of maximum inversion  $n_{sp} = 1$  and a large single-pass power gain ( $G \gg 1$ ).

In specific network applications, it is of interest to cascade SOAs in a link. To evaluate the total noise factor  $F_{tot}$  of the amplifiers in the link, we must consider a number of  $m$  SOAs, each with single-pass power gain  $G_q \geq 1$  and excess noise factor  $F_q$  ( $q = 1, \dots, m$ ), followed by a fiber section with a linear power “gain” of  $0 < a_q \leq 1$ . Assuming narrowband optical filters after each SOA,  $F_{tot}$  can be written as

$$F_{tot} = F_{shot}^{total} + F_{excess}^{total} = \frac{1}{\prod_{q=1}^m a_q G_q} + \left[ F_1 + \frac{F_2}{G_1 a_1} + \dots + \frac{F_m}{(\prod_{q=1}^{m-1} a_q G_q)} \right]. \tag{12.32}$$

Assuming  $a_q = 1$  and  $m = 2$  in (12.32), it can be seen that a low-noise, high output amplifier can be constructed by combining a low-noise high-gain first stage amplifier section followed by a high output power amplifier, the noise of which can be larger.

Of important practical interest is the measurement technique to determine the power gain and the noise figure of an SOA. The measurement setup is depicted in Fig. 12.11. A continuous-wave signal from a tunable laser source (TLS) is fed to an attenuator (Att.) which allows the accurate control of the SOA input power, measured with a power meter (P) and a 50 : 50 coupler. The input polarization to the SOA is adjusted with a polarizer (Pol.). After the SOA, the output signal power and the ASE power are measured with an optical spectrum analyzer (OSA). The second polarizer (Pol.) enables the measurement of the ASE noise which is co-polarized with the signal only.

In Fig. 12.12a, the measurement principle is explained. The OSA detects the output power  $P_{out} + P_{ASE\parallel}$  at the coherent-carrier wavelength  $\lambda_s$  in a resolution bandwidth  $B_O$  usually set to an equivalent wavelength interval of 0.1 nm. To sep-

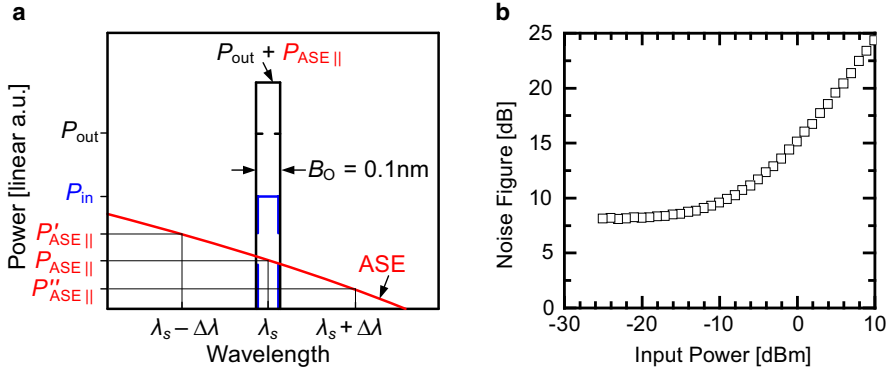


**Fig. 12.12** Schematic for determining power gain  $G = P_{out}/P_{in}$ , ASE noise power and noise figure (NF) of an SOA with typical NF measurement results. Spectral data refer to a resolution bandwidth  $B_O = 0.1$  nm. **a** Measured input power  $P_{in}$ , total output power  $P_{out} + P_{ASE||}$ , and spectral dependence of ASE noise power. The actual coherent output power  $P_{out}$  is retrieved by subtracting the ASE noise power  $P_{ASE||}$ , which is obtained by a linear interpolation of the ASE noise powers  $P'_{ASE||}$  and  $P''_{ASE||}$  measured in a distance  $\Delta\lambda$  from the coherent carrier wavelength  $\lambda_s$ . **b** Measured NF increases for increasing input power due to a decreasing power gain

arate  $P_{out}$  and  $P_{ASE}$ , the co-polarized ASE powers  $P'_{ASE||}$  and  $P''_{ASE||}$  are measured in a distance of  $\Delta\lambda = 1$  nm to the left and the right of  $\lambda_s$ , respectively. A linear interpolation  $(P'_{ASE||} + P''_{ASE||})/2$  gives an estimate of the ASE power  $P_{ASE||}$  at  $\lambda_s$ . From the measured quantities  $P_{in}$  and  $P_{out}$ , the power gain  $G$  can be calculated in addition, (12.18). From  $G$ ,  $P_{ASE||}$  and  $B_O$  the noise figure (12.31) is calculated.

Figure 12.12b shows a typical result of a noise figure characterization. We find a noise figure of  $NF = 7$  dB for low input powers. The noise figure increases for increasing input powers due to the associated decrease in single-pass power gain. Commercially, SOAs are available with noise figures in the region of  $NF = 5 \dots 10$  dB [62, 63].

### 12.3.4 Gain Saturation

Since an SOA provides a limited amount of extractable power at a constant bias current only, the gain saturates if the SOA input power is sufficiently large. To describe the saturation power of an SOA a small-signal model is introduced in this section.

With the help of a rate equation model that governs the interaction of photons and electrons inside the active region, the so-called saturation input power is calculated. The saturation input power of an SOA describes the input power at which the unsaturated single-pass power gain reduces by 3 dB. In this section, the rate equations are specified heuristically by considering the phenomena through which the number of carriers changes with time inside the active volume. The dominant pro-

cess is the electronic carrier injection and the resultant effective carrier lifetime  $\tau_c$ , i.e., the time for an interband transition. Under steady state operation, the injection and relaxation of carriers are in equilibrium and occur on a nanosecond to hundreds of picoseconds time scale. Intraband phenomena which can also contribute to gain saturation are disregarded here, but are considered in the following section on “SOA dynamics.” The model can be considerably simplified by assuming an SOA input signal with a pulse width  $\tau_p$  much longer than the effective carrier lifetime  $\tau_c \approx 1$  ns. Then, the intraband dynamics of carriers (leading to an effective intraband relaxation time  $\tau_{\text{intra}}$ ) can be neglected since the associated intraband relaxation time scale is typically in the range of hundreds of femtoseconds up to a few picoseconds. The assumption  $\tau_p \gg \tau_c \gg \tau_{\text{intra}}$  is typically justified for steady-state (continuous wave) or low bitrate (large pulse width) operation. Furthermore, longitudinal and transverse carrier diffusion is neglected, and a uniform distribution of the bias current  $I$  across the active region is assumed [64].

Equation (12.33) relates the temporal change of the carrier density  $N$  to the carrier injection rate  $I/e$  per active volume  $V = CL = wdL$  (waveguide cross section area  $C$ , active region length  $L$ ) and to the carrier recombination rates  $R_c$  and  $R'_s$ , which are due to spontaneous recombination (radiative and nonradiative [65]), and to stimulated (radiative) transitions, respectively. The stimulated recombination rate due to the amplification of the signal is  $R_s$ , and the recombination rate due to ASE noise is  $R_{\text{ASE}}$ . The quantity  $\tau_c$  is the so-called effective carrier lifetime,  $v_g$  the group velocity,  $g$  the net power gain and  $S'$  the total photon density. The total photon density  $S'$  consists of the signal photon density  $S$  and the ASE photon density  $S_{\text{ASE}}$ . Because of charge neutrality, the carrier density  $N$  represents both, the electron and the hole concentration. Further, it needs to be mentioned that  $v_g g = G'$  is the gain rate. The carrier rate equation reads

$$\begin{aligned} \frac{dN}{dt} &= \frac{I}{eV} - R_c - R'_s = \frac{I}{eV} - \frac{N}{\tau_c} - \Gamma g v_g S', \\ R'_s &= R_s + R_{\text{ASE}}, \quad S' = S + S_{\text{ASE}}. \end{aligned} \quad (12.33)$$

We assume that the net power gain  $g$  [1/cm] linearly depends on the density of carriers injected from an external current supply. The quantity  $a$  is the differential gain, and  $N_t$  is the carrier density at transparency. The net power gain can be approximated by

$$g \approx \frac{dg}{dN}(N - N_t) = a(N - N_t), \quad a = \frac{dg}{dN}. \quad (12.34)$$

This linear relation is a good approximation at a wavelength corresponding to the gain peak of the SOA [64]. If the SOA is operated at other spectral positions inside its gain bandwidth, (12.34) can be replaced by a polynomial model with quadratic and cubic dependencies on the carrier density and wavelength [16, 51].

**Saturation Input Power** For small input signal powers, the output power of an amplifier depends linearly on the input power if we disregard noise as is the case

for the following. Beyond the so-called saturation input power, the output power increases sublinearly (it “saturates”) because the power gain starts decreasing (“gain suppression”). Gain suppression is explained by the fact that the carrier injection rate which is fixed by the external current source sets a limit to the number of electron–hole pairs that can possibly recombine per time. Therefore, the rate of generated photons is also limited.

Using (12.34) and rewriting the total photon density  $S$  averaged over the active volume in terms of an average optical power  $P = Shf_s v_g C$ , the relation (12.33) can be written as

$$\frac{dN}{dt} = \frac{I}{eV} - \frac{N}{\tau_c} - \Gamma g v_g S = \frac{I}{eV} - \frac{N}{\tau_c} - \Gamma a(N - N_t) \frac{P}{Chf_s}. \quad (12.35)$$

Equation (12.35) is solved for a time-independent carrier concentration  $dN/dt = 0$  by

$$N = \frac{\tau_c I}{eV} \frac{P_s}{P_s + P} + N_t \frac{P}{P_s + P}, \quad P_s = \frac{Chf_s}{a\Gamma\tau_c}. \quad (12.36)$$

Substituting (12.36) in (12.34) modifies (12.16) to

$$\begin{aligned} \frac{dP}{dz} &= \Gamma a \left( \frac{\tau_c I}{eV} - N_t \right) \frac{P_s}{P_s + P} P = \Gamma g(P) P, \quad g(P) = a \left( \frac{\tau_c I}{eV} - N_t \right) \frac{P_s}{P_s + P}, \\ \frac{dP}{dz} &= \Gamma g_0 \frac{P_s}{P_s + P} P, \quad g = g_0 \frac{1}{1 + \frac{P}{P_s}}, \quad g_0 = a(N_0 - N_t), \quad N_0 = \frac{\tau_c I}{eV}, \\ g &= g_0 \frac{1}{1 + \frac{S}{S_s}} = \frac{g_0}{1 + \varepsilon_c S}, \quad \varepsilon_c = \frac{1}{S_s} = v_g a \tau_c. \end{aligned} \quad (12.37)$$

For small input powers  $P \ll P_s$ , the quantities  $g_0$  and  $N_0$  represent the net gain and the average carrier concentration in analogy to the more general relation (12.34). From (12.37), it can be seen that the parameter  $P_s$  is the power level at which the power-dependent net gain  $g = g(N) = g(N(S))$  is half of its unsaturated value  $g_0$ . As an alternative to the saturation power  $P_s$ , the nonlinear gain compression factor  $\varepsilon_c$  (the inverse saturation photon density  $S_s$ ) can be used, which then transforms (12.35) into

$$\frac{dN}{dt} = \frac{I}{eV} - \frac{N}{\tau_c} - v_g \Gamma g S = \frac{I}{eV} - \frac{N}{\tau_c} - v_g \Gamma \frac{g_0 S}{1 + \varepsilon_c S}. \quad (12.38)$$

Equation (12.37) can be solved by employing the boundary conditions  $P(z=0) = P_{in}$  and  $P(z=L) = P_{out}$ , and substituting the single-pass power gain  $G$  from (12.18) and the unsaturated single-pass power gain  $G_0$ ,

$$\frac{P_{out}}{P_{in}} = G = G_0 \exp \left[ -(G - 1) \frac{P_{in}}{P_s} \right], \quad G_0 = \exp(\Gamma g_0 L). \quad (12.39)$$

From (12.39), we see that as long as the SOA output power  $GP_{\text{in}}$  with  $G \geq 1$  is much lower than the saturation power,  $GP_{\text{in}} \ll P_s$ , the first exponential term in (12.39) is close to one and the amplifier gain is almost  $G_0$ . However, when the output power exceeds the saturation power, the amplifier gain decreases. The input  $P_{\text{in}}^{\text{sat}}$  and output  $P_{\text{out}}^{\text{sat}} = (G_0/2) P_{\text{in}}^{\text{sat}}$  saturation powers, for which the unsaturated single-pass power gain is halved, can be calculated to be

$$P_{\text{in}}^{\text{sat}} = \frac{2 \ln 2}{G_0 - 2} P_s = \frac{2hf_s \ln 2 C}{G_0 - 2} \frac{1}{\Gamma a \tau_c}, \quad (12.40)$$

$$P_{\text{out}}^{\text{sat}} = \frac{G_0 \ln 2}{G_0 - 2} P_s = \frac{hf_s \ln 2 G_0 C}{G_0 - 2} \frac{1}{\Gamma a \tau_c}. \quad (12.41)$$

The saturation input or output powers can be easily determined from a single-pass power gain measurement. Typical values for the saturation input power are  $-15$  dBm to  $0$  dBm depending on the unsaturated single-pass power gain and the saturation power of the device.

Unlike linear SOAs, nonlinear SOAs are optimized for very low input saturation powers. This helps in performing all-optical switching at highest-speed with low input powers. By using ideal nonlinear configurations, low optical switching powers of  $-17.5$  dBm or  $0.45$  fJ/bit at  $40$  Gbit/s are recorded [66].

### 12.3.5 SOA Dynamics

For a linear amplifier, the gain does not depend on the amplifier input power if it is much smaller than the input saturation power  $P_{\text{in}}^{\text{sat}}$ . Therefore, in an arbitrary sequence of “1”s and “0”s, each bit experiences the same small-signal gain, and there is no dependency on the bit pattern. Similarly, if multiple signals with differing wavelengths are amplified simultaneously, there is no crosstalk between the wavelength channels. In both cases, the situation would be different if larger average input powers led to carrier depletion and therefore to a gain lower than the small-signal gain. A series of “1”s would lead to a temporal gain decrease, and high average input power in one wavelength channel would reduce the gain for signals at a different wavelengths. This may result in undesirable signal patterning and wavelength channel crosstalk. It should be noticed though, that such crosstalk may be exploited for nonlinear optical operations such as 2R [67] and 3R all-optical wavelength conversion [68, 69], for performing logical optical operations [70] or all-optical demultiplexing [71].

Even if the input power exceeds the saturation power  $P_{\text{in}}^{\text{sat}}$ , a quasilinear operation is possible, depending on the gain dynamics and therefore depending on the temporal change of the charge carriers. If the SOA carrier recovery between subsequent “1”s is sufficiently fast, then the power gain for each “1”-bit remains the same. On the other hand, if the amplifier dynamics are sufficiently slow, an average input power larger than  $P_{\text{in}}^{\text{sat}}$  leads to a stationary gain compression. If “1”s and



“0”s are equally distributed, the power gain would remain constant, though at a level smaller than the small-signal gain. This is the case in, e.g., doped fiber amplifiers which show fluorescence lifetimes of a few milliseconds [72]. Thus, such fiber amplifiers are successfully used in today’s fiber communications systems in which the transmission bit period of, e.g., a 10 Gbit/s data signal is 100 ps.

In the case of an SOA, the situation is more involved since the typical gain recovery time is in the order of 100 ps. Therefore, if SOAs are used to amplify high bitrate ( $> 10$  Gbit/s) data signals, bit pattern effects and channel crosstalk will occur if the input power exceeds  $P_{in}^{sat}$ .

In the following section, the SOA gain recovery due to slow interband and fast intraband processes is discussed.

**Interband Effects** Typical effective carrier lifetimes for spontaneous interband transitions are in the range of  $\tau_c = 100$  ps–1 ns. Assume a pulse sequence where the bit period is of the order of the impulse width  $\tau_p$  which is much larger than the effective carrier lifetime,  $\tau_p \gg \tau_c$ . If the power of an input pulse is sufficiently large so that it reduces the SOA gain, the time to re-establish the gain to its original level is of interest. This time is called gain recovery time and will be specified in the following.

The SOA carrier density evolution is described by the rate equation (12.35) for the case that only interband effects are considered. Since the carrier density  $N$  and the net power gain  $g$  are assumed to be linearly related as in (12.34), the gain evolution can be derived from (12.35) as well. To simplify the description, we combine the effective lifetime  $\tau_c$  for radiative and nonradiative spontaneous recombinations with the lifetime  $\tau_s'$  for stimulated recombination to a *total* effective carrier lifetime  $\tilde{\tau}_c$  [73],

$$\frac{1}{\tilde{\tau}_c} = \frac{R_c + R_s'}{N} = \frac{R_c}{N} + \frac{R_s + R_{ASE}}{N} = \frac{1}{\tau_c} + \frac{1}{\tau_s'}, \quad R_s \sim S, \quad R_{ASE} \sim S_{ASE}. \quad (12.42)$$

The value of  $\tilde{\tau}_c$  strongly depends on the SOA operating point, i.e., on the carrier concentration  $N$ .

The effective carrier lifetime  $\tau_c$  is determined by nonradiative recombination via impurity levels in the forbidden band (Shockley–Read–Hall recombination, subscript SRH), by interband radiative spontaneous recombination (subscript sp), by nonradiative Auger recombination (subscript Au), and by a term that takes carrier leakage through the active region into account (subscript Leak) [51]. The terms have the corresponding coefficients  $A_{SRH}$ ,  $B_{sp}$ ,  $C_{Au}$  and  $D$

$$\frac{1}{\tau_c} = \frac{1}{\tau_{SRH}} + \frac{1}{\tau_{sp}} + \frac{1}{\tau_{Au}} + \frac{1}{\tau_{Leak}} = A_{SRH} + B_{sp}N + C_{Au}N^2 + DN^{5.5}. \quad (12.43)$$

The dominant contribution in (12.42) strongly depends on the SOA operating point. For short SOA lengths (no significant ASE) and zero input power (no amplified signal), the total effective carrier lifetime  $\tilde{\tau}_c$  is dominated by the effective carrier

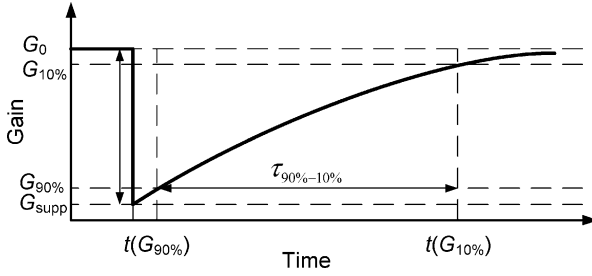


**Fig. 12.13** Schematic for determining the 90–10% gain recovery time. After an abrupt transition from the small-signal power gain  $G_0$  to a suppressed gain  $G_{\text{supp}}$ , a 90–10% gain recovery time  $\tau_{90-10\%} = |t(G_{90\%}) - t(G_{10\%})|$  measures the effective rise time of the gain back towards  $G_0$

lifetime  $\tau_c = N/R_c$  due to spontaneous radiative and nonradiative recombinations. For long SOA length (significant ASE) and zero input power, the ASE recombination rate  $R_{\text{ASE}} \sim S_{\text{ASE}}$  dominates. If an input signal is present, the stimulated emission rate due to the signal  $R_s \sim S$  dominates.

From a practical point of view, the total effective carrier lifetime  $\tilde{\tau}_c$  is not used to determine the SOA speed limitation in system experiments. This is because the SOA gain recovery time should also take into account the strength of gain saturation. After an abrupt transition from the small-signal power gain  $G_0$  to a suppressed gain  $G_{\text{supp}}$ , a 90%-to-10% gain recovery time  $\tau_{90-10\%}$  measures the effective rise time of the gain towards  $G_0$ . It is defined by the difference of the time at which the actual gain is  $G_{90\%} = G_0 - 0.9(G_0 - G_{\text{supp}})$  and the time where the gain is re-established to  $G_{10\%} = G_0 - 0.1(G_0 - G_{\text{supp}})$ .

The gain recovery time  $\tau_{90-10\%} = |t(G_{90\%}) - t(G_{10\%})|$  (see Fig. 12.13) is related to the total effective carrier lifetime. In detail, one finds [73]

$$\tau_{90-10\%} \approx \tilde{\tau}_c \ln \left[ \frac{\ln(0.1 + (0.9G_{\text{supp}}/G_0))}{\ln(0.9 + (0.1G_{\text{supp}}/G_0))} \right], \quad (12.44)$$

$$\lim_{G_0 \gg 9G_{\text{supp}}} \tau_{90-10\%} = \tilde{\tau}_c \ln \left( \frac{\ln 0.1}{\ln 0.9} \right) \approx 3\tilde{\tau}_c.$$

From (12.44), it can be seen that the gain recovery time depends on the degree of gain suppression. A short total effective carrier lifetime implies faster gain recovery, while a larger gain suppression  $G_0/G_{\text{supp}}$  leads to a slower recovery. For  $G_0/G_{\text{supp}} \gg 9$ ,  $\tau_{90-10\%}$  approaches  $3\tilde{\tau}_c$ .

Ordinarily, the gain recovery time is in the range of a few picoseconds (ps) up to several hundreds of ps. It has been found that a couple of mechanisms can be used to reduce this gain recovery time for an SOA. For example, a bias current increase reduces the recovery time because the increase in the carrier number leads to a larger  $R_c$  [74]. For a constant net gain  $g$ , an increase in the device length increases the power gain  $G = \exp(\Gamma gL)$ . Therefore, the spectral density of the ASE noise (12.25) increases, and the resulting larger recombination rate  $R_{\text{ASE}} \sim S_{\text{ASE}} \sim \rho_{\text{ASE}}$

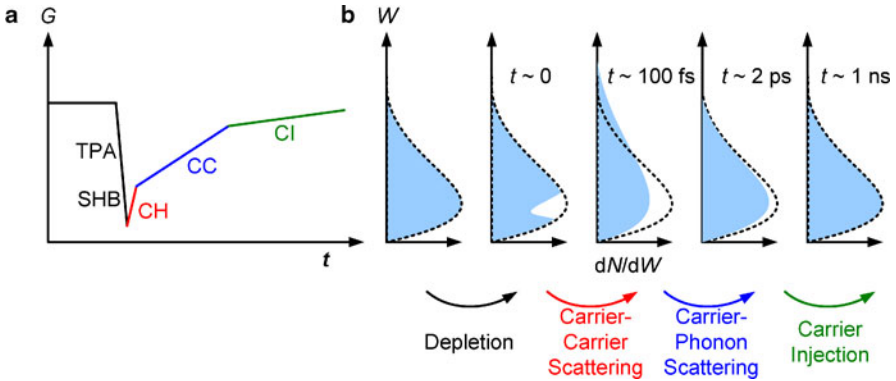


**Fig. 12.14** Gain as a function of time and explanation of intraband effects, modified from [80]. **a** Gain suppression due to spectral hole burning and two-photon absorption. Gain recovery is caused by carrier heating, carrier cooling and carrier injection. **b** The corresponding energy versus the density of electrons  $N$  per energy interval in the conduction band

(12.42) reduces the recovery time [75, 76]. Another technique to reduce the recovery time is the use of a holding beam to enhance the stimulated emission rate  $R_s$  [74, 77]. Further, the SOA material properties are often tailored by n-doping or p-doping of the active region to increase  $R_c$  [78].

In recent years, it was found that the use of quantum-dots in the active SOA region can also reduce the recovery time down to a few ps. The QDs are embedded in a so-called wetting layer which acts as a carrier reservoir for the QD states [6, 41]. In principle, by a proper population of the reservoir states, the fast refilling of QD states from the wetting layer dominates the gain recovery process. The refilling of wetting layer states follows the physics as discussed above and is ultimately limited by the supply rate of carriers through the injection current.

**Intraband Effects** Fast intraband transitions come into play if pulses with a duration shorter than the effective carrier lifetime  $\tau_c$  are investigated. Intraband effects are characterized by a nonequilibrium carrier distribution within the bands, whereas interband effects are characterized by a nonequilibrium carrier distribution between the conduction and the valence band.

Before an optical pulse is launched to a forward-biased SOA, the CB and VB carriers inside each band are in equilibrium, Fig. 12.14b, and follow a Fermi–Dirac distribution. When an optical beam with a short duration (few ps) is launched in the SOA, CB electrons at the appropriate photon energies are depleted because of stimulated recombinations [80–82]. Therefore, at these photon energies, the carrier number and consequently the gain is reduced, Figs. 12.14a and 12.13. A (nearly symmetrical) spectral “hole” is “burned” into the carrier distribution, and therefore this effect is called spectral hole burning (SHB). It is an ultra-fast effect on a time scale of a few femtoseconds (fs).

In addition, pairs of photons are absorbed, a process which generates an electron–hole pair. For this so-called two-photon absorption (TPA), the sum of the two photon

energies is larger than the bandgap energy. The TPA-generated free carriers absorb light (free carrier absorption, FCA) [73] and move to higher energy states within the same band. SHB, TPA and FCA alter the carrier distributions from intraband equilibrium to nonequilibrium, so that the Fermi–Dirac distribution function is not applicable any more. SHB eliminates carriers which need to be refilled by carrier-carrier scattering from higher energy states, so that the carrier distributions flatten out and the effective carrier temperature rises. Furthermore, carriers hotter than the average are added by TPA and FCA, thereby additionally increasing the average carrier energy beyond the one associated with the lattice temperature [51]. The process is named carrier heating (CH in Fig. 12.14a) and occurs on a time scale of 100 fs, e.g., 78 fs in a 1.55  $\mu\text{m}$  bulk SOA or 95 fs in a 1.3  $\mu\text{m}$  bulk SOA have been reported [15]) named the SHB relaxation time  $\tau_{\text{SHB}}$ . The hot carriers cool down (carrier cooling (CC) in Fig. 12.14a) by carrier-phonon scattering on a time scale of up to several ps characterized by a CH relaxation time  $\tau_{\text{CH}}$  (e.g., 700 fs in a 1.55  $\mu\text{m}$  bulk SOA or 1000 fs in a 1.55  $\mu\text{m}$  MQW SOA [15]). Finally, carrier injection fills the depleted states on a nanosecond scale (CI in Fig. 12.14a) until the initial intraband equilibrium state is eventually reached. The associated time constant is the effective carrier lifetime  $\tau_c$ .

In the following, we incorporate short-time intraband carrier effects into a theory of the SOA carrier dynamics. We distinguish two cases related to the pulse width  $\tau_p$ . First, if the pulse width is smaller than the effective carrier lifetime  $\tau_c$  and larger than the effective intraband relaxation time  $\tau_{\text{intra}}$ , then on the scale of the pulse width the intraband effects occur instantaneously. We include the various intraband effects phenomenologically by a gain compression that becomes the more pronounced the larger the photon density  $S$  is, see (12.37). Second, if the pulse width is comparable to the effective intraband relaxation time, intraband memory effects must be taken into account by rate equations.

**Case 1,  $\tau_c \gg \tau_p \gg \tau_{\text{intra}}$**  Here, we consider saturation by SHB and CH with its associated relaxation times [81, 83, 84]. For this case, the nonlinear gain compression factor  $\varepsilon_c$  for interband effects in (12.37) is supplemented with the corresponding factors  $\varepsilon_{\text{SHB}}$  and  $\varepsilon_{\text{CH}}$  for SHB and CH [81, 83, 84],

$$g = \frac{g_0}{1 + (\varepsilon_c + \varepsilon_{\text{SHB}} + \varepsilon_{\text{CH}})S}. \quad (12.45)$$

The rate equation (12.35) for the time dependence of the carrier density  $N$  is then modified by the power-dependent net gain  $g(S)$  from (12.37) in analogy to (12.38),

$$\frac{dN}{dt} = \frac{I}{eV} - \frac{N}{\tau_c} - v_g \Gamma g S = \frac{I}{eV} - \frac{N}{\tau_c} - v_g \Gamma \frac{g_0 S}{1 + (\varepsilon_c + \varepsilon_{\text{SHB}} + \varepsilon_{\text{CH}})S}. \quad (12.46)$$

This approach is often used to model the behavior of the SOAs dynamic in system experiments for up to 100 Gbit/s on-off keying data signals.

**Case 2,  $\tau_p \sim \tau_{\text{intra}}$**  Now, the data pulse width of interest is in the order of the effective intraband relaxation times [83]. Intraband effects modify the modal gain from  $\Gamma g(N(t)) = \Gamma g(t)$ , see (12.34) and (12.37), to  $\Gamma g_{\text{tot}}(t)$ , so that the time-dependent single-pass power gain now reads

$$G(t) = \exp \left( \Gamma \int_0^L g_{\text{tot}}(t) dz \right) = \exp (\Gamma g_{\text{tot}}(t)L), \quad (12.47)$$

and (12.35), (12.38) changes to

$$\frac{dN}{dt} = \frac{I}{eV} - \frac{N}{\tau_c} - v_g \Gamma g_{\text{tot}} S. \quad (12.48)$$

It is convenient to introduce a dimensionless gain coefficient  $h_{\text{tot}}(t)$ , which is expressed as a sum of the bias-dependent interband term  $h(t) = \Gamma g(t)L$  and the additional contributions of SHB and CH to the compression of the gain,  $\Delta h_{\text{SHB}}(t) = \Gamma \Delta g_{\text{SHB}}(t)L$  and  $\Delta h_{\text{CH}}(t) = \Gamma \Delta g_{\text{CH}}(t)L$ , respectively. Following [73, 83], we write for  $h_{\text{tot}}(t)$

$$h_{\text{tot}}(t) = \Gamma \int_0^L g_{\text{tot}}(t) dz = \Gamma g_{\text{tot}}(t)L = h(t) + \Delta h_{\text{SHB}}(t) + \Delta h_{\text{CH}}(t), \quad (12.49)$$

$$G(t) = \exp (h_{\text{tot}}(t)).$$

The time-dependence of the integrated modal gain  $h(t)$  for the interband effects is determined as before by the dynamics of the carrier density  $N$  which is given by (12.35). The corresponding rate equation for  $h(t)$  is derived by starting from the time-dependent rate equation for the carrier density  $N$  (12.35). We substitute  $N$  by the net power gain  $g$  from (12.34) and integrate the resulting differential equation for the modal gain  $\Gamma g$  over the SOA length  $L$ . We then rewrite the differential equation for the spatially dependent power (12.16) in terms of the photon density  $S$ , where the total gain  $g_{\text{tot}}$  replaces  $g$  which is determined by interband effects only. After an integration over the SOA length, we end up with a differential equation for  $h(t)$ . Having introduced the SOA input photon density  $S = S_{\text{in}}(t)$  and the nonlinear gain compression factor  $\varepsilon_c = v_g a \tau_c$  from (12.37), we find

$$\tau_c \frac{dh(t)}{dt} = h_0 - h(t) - (G(t) - 1) \varepsilon_c S_{\text{in}}(t), \quad h_0 = \Gamma g_0 L, \quad \frac{dS(z)}{dz} = \Gamma g_{\text{tot}} S(z),$$

$$S_{\text{out}}(t) = S(t, L) = G(t) S(t, 0) = G(t) S_{\text{in}}(t),$$

$$\int_0^L \Gamma g_{\text{tot}} S dz = (G(t) - 1) S(t, 0). \quad (12.50)$$

The rate equation for  $h(t)$  can be directly compared to (12.33) and (12.35). Via (12.34), the proportionality  $h \sim g \sim N$  holds, and  $h_0 \sim g_0 \sim N_0 \sim I$  is connected to the fixed bias current  $I$ . The induced emission term incorporates all gain compression effects in its total power gain  $G(t)$ . If for a small integrated total modal gain  $h_{\text{tot}} \ll 1$  the approximation  $G(t) - 1 = \exp(h_{\text{tot}}(t)) - 1 \approx h_{\text{tot}}(t)$  holds true, the photon density  $S(z)$  does not significantly change along  $z$ . Therefore, the integral over  $z$  need not to be executed, and an approximation to (12.50) follows directly by substituting (12.33) in (12.48).

The intraband effects are described by nonlinear gain compression factors  $\varepsilon_{\text{SHB}}$  and  $\varepsilon_{\text{CH}}$  for SHB and CH, respectively. Conduction band carriers are considered, and effects such as TPA and FCA are neglected. Using the SHB relaxation time  $\tau_{\text{SHB}}$  and the CH relaxation time  $\tau_{\text{CH}}$ , we write, following [51, 73, 82, 83],

$$\tau_{\text{SHB}} \frac{\partial \Delta h_{\text{SHB}}}{\partial t} = -\Delta h_{\text{SHB}} - (G(t) - 1) \varepsilon_{\text{SHB}} S_{\text{in}}(t) - \tau_{\text{SHB}} \left( \frac{\partial \Delta h_{\text{CH}}}{\partial t} + \frac{\partial h}{\partial t} \right), \quad (12.51)$$

$$\tau_{\text{CH}} \frac{\partial \Delta h_{\text{CH}}}{\partial t} = -\Delta h_{\text{CH}} - (G(t) - 1) \varepsilon_{\text{CH}} S_{\text{in}}(t). \quad (12.52)$$

Carrier heating due to an input impulse  $S_{\text{in}}$ , which instantaneously burns a spectral hole, reduces the integrated modal gain by  $|\Delta h_{\text{CH}}|$  according to (12.52);  $|\Delta h_{\text{CH}}|$  then relaxes back to zero due to carrier cooling on a time scale  $\tau_{\text{CH}}$ . On the other hand, the spectral hole burned by the input impulse reduces the integrated modal gain by  $|\Delta h_{\text{SHB}}|$  according to (12.51);  $|\Delta h_{\text{SHB}}|$  then relaxes back to zero due to carrier heating on a time scale  $\tau_{\text{SHB}}$ . If carrier cooling has a small effect, this relaxation time is large (see last but one term in (12.51)). The same is true if carriers are injected at a low rate only, (see last term in (12.51)).

### 12.3.6 Alpha-factor

So far, the alpha-factor was assumed to be time-independent. This implies that at the time scale considered in (12.7), refractive index changes and gain changes were identically related to a carrier concentration change. Following a carrier depletion, the total number of carriers recovers on a time scale fixed by the external injection rate, and so does the refractive index  $n_N$ . However, as was discussed in the previous section, there are various time scales for gain recovery. As a consequence, the alpha-factor becomes time-dependent and is renamed to be an effective time-dependent alpha-factor  $\alpha_{\text{eff}}(t)$ . This approach is contrary to most publications in which the alpha-factor is tacitly assumed to be constant in time. For linear low data rate applications, e.g for a 10 Gbit/s fiber-to-the-home (FTTH) reach extender, this approximation is good enough. However, for describing SOAs at highest data rates ( $> 100$  Gbit/s) and smallest pulse widths, the time-dependent alpha-factor approach

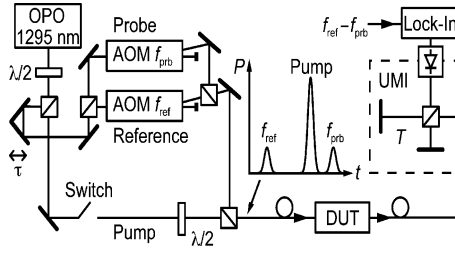


**Fig. 12.15** Schematic of the heterodyne pump-probe setup. Short pulses are generated by an optical parametric oscillator (OPO) and split into pump, probe and reference pulses. Probe and reference pulses are tagged by a frequency shift  $f_{\text{prb}}$  and  $f_{\text{ref}}$ , respectively, which is induced by acousto-optic modulators (AOM). A strong pump pulse drives the SOA into its nonlinear regime. A weak pulse probes these nonlinearities in gain and phase. After the device under test (DUT), the pulse train is split and recombined in a Michelson interferometer with unbalanced arm lengths such that the resulting probe-reference beat signal with frequency  $f_{\text{ref}} - f_{\text{prb}}$  can be detected in amplitude and phase by a lock-in amplifier

offers higher accuracy. More details on time dependency and modeling of the effective alpha-factor for wavelength conversion can be found in [85]. Typical reported values for SOAs are in the range of  $\alpha = 0\text{--}2$  for QD SOAs and  $\alpha = 2\text{--}8$  for QW or bulk SOAs.

In the following, we discuss the time dependence of the SOA phase change  $\Delta\phi(N(t))$  resulting from carrier and subsequent gain changes. Starting from the definition (12.7) and in the spirit of the previous section, we interpret the integrated modal gain change  $\Gamma\Delta gL$  as the change  $\Delta h_{\text{tot}}(t)$  of the time-dependent integrated modal gain  $h_{\text{tot}}(t)$  in (12.49). In analogy to (12.20), we write

$$\Delta\varphi(t) = \alpha_{\text{eff}}(t)\Gamma\Delta g_{\text{tot}}(t)L/2 = \alpha_{\text{eff}}(t)\Delta h_{\text{tot}}(t)/2, \quad \Gamma\Delta g_{\text{tot}}(t)L = \Delta h_{\text{tot}}(t). \quad (12.53)$$

The time-dependent effective alpha-factor is defined as

$$\alpha_{\text{eff}}(t) = \frac{2\Delta\varphi(t)}{\Delta h_{\text{tot}}(t)} = \frac{2\Delta\varphi(t)}{\Delta(\ln G(t))}. \quad (12.54)$$

A detailed discussion of the constituents of  $\alpha_{\text{eff}}(t)$  comprising SHB ( $\alpha_{\text{SHB}}$ ), carrier heating ( $\alpha_{\text{CH}}$ ) and band-filling ( $\alpha$ ), and the respective changes of the refractive indices  $\Delta n_{\text{SHB}}$ ,  $\Delta n_{\text{CH}}$ ,  $\Delta n$  together with the changes in the gain  $\Delta g_{\text{SHB}}$ ,  $\Delta g_{\text{CH}}$ ,  $\Delta g$  is found in [85]. The contribution  $\alpha_{\text{SHB}}$  is almost zero since SHB produces a nearly symmetrical spectral hole centered at the signal wavelength, so that the Kramers–Kronig integrand becomes antisymmetric around the operating frequency, and the Kramers–Kronig integral remains small. The contribution  $\alpha_{\text{CH}}$  may be approximated by a constant [51]. The band-filling term  $\alpha$  finally shows a more complicated behavior, and it strongly depends on the signal wavelength as well as on the carrier density  $N$ . An appropriate parameterization to model this alpha-factor as a function of wavelength and carrier density may be found in [85]. In summary,

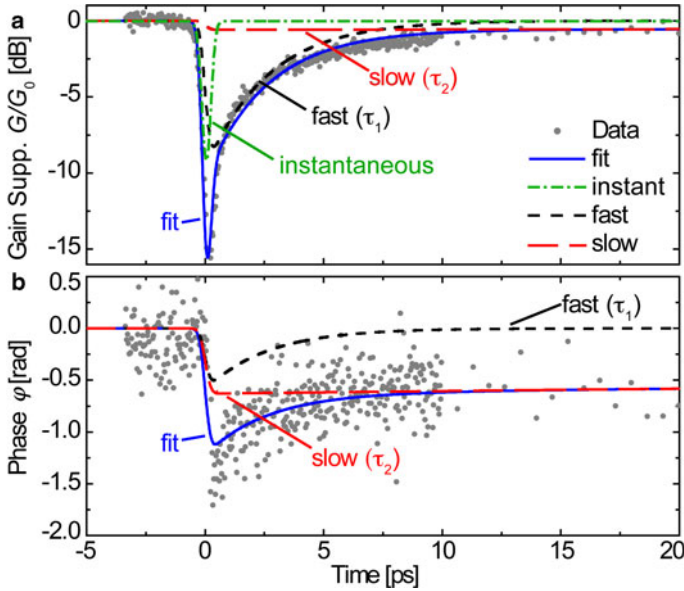


**Fig. 12.16** Time evolution of **a** gain suppression  $G/G_0$  and **b** phase dynamics of a typical QD SOA device. The fit (solid line) well reproduces the measured data (gray dots). The model assumes a fast process (dashed line), a slow process (long-dashed line) and instantaneous two-photon absorption (TPA, dash-dotted line) [41]

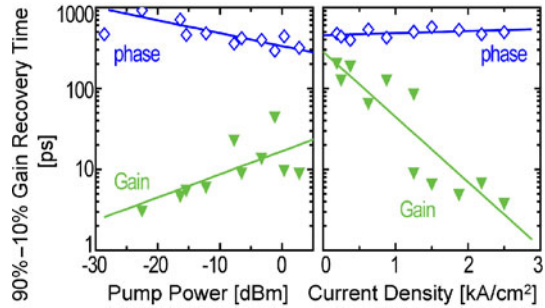
it is to be expected that initially the alpha-factor is small due to SHB, and that it increases for larger times.

**Pump-Probe Measurement Setup and Results** For determining gain and phase recovery times of an SOA, a heterodyne pump-probe technique with subpicosecond resolution has been employed as shown in Fig. 12.15 [41].

Pulses with a full width half maximum (FWHM) of 130 fs are generated by an optical parametric oscillator (OPO) and split into pump, probe and reference pulses. Probe and reference pulses are tagged by frequency shifts  $f_{\text{prb}}$  and  $f_{\text{ref}}$ , respectively, which are induced by acousto-optic modulators (AOM). The pulse repetition rate is 80 MHz. The pulses are coupled into a polarization-maintaining (PM) fiber, from where they are launched into the SOA. First, the weak reference pulse is guided through the unperturbed device under test (DUT). Next, a strong pump pulse drives the SOA into its nonlinear, gain-depleted regime. A weak pulse probes these nonlinearities in gain and phase. After the device, the pulse train is split in a Michelson interferometer with unbalanced arm lengths. Both copies of the pulse train are then superimposed in such a way that the reference pulse leaving the long arm coincides with the probe pulse leaving the short arm. Because of the respective frequency shifts, the lock-in amplifier detects amplitude and phase of the photodiode current at the difference frequency  $f_{\text{ref}} - f_{\text{prb}}$ . By varying the optical delay between 10 ps and 300 ps, the temporal evolution of gain and phase can be measured.



**Fig. 12.17** Dependence of effective 90–10 % power gain and phase recovery time on input power and bias current density. The phase recovery is dominated by the slow process. The gain recovery is fastest for a low input power and high current densities [41]



The typical gain and phase dynamics of an SOA (in this case, especially a QD SOA) are shown in Fig. 12.16. However, in pump-probe experiments, the number of measurable time constants is limited by temporal resolution and by noise. Therefore, it is only possible to draw conclusions regarding the dominant relaxation processes, the time dependence of which is usually approximated by an exponential function.

Figure 12.16 shows the gain and phase dynamics of a QD SOA. Here, two processes with different relaxation times are found: A fast one associated with the quantum dot carrier capture time  $\tau_1$  in the order of a few ps, and a slow one associated with the wetting layer capture time  $\tau_2$  in the order of several hundred ps. Both processes influence the material gain and the phase change simultaneously, but with different magnitudes.

As discussed in Fig. 12.13, the 90 %-to-10 % recovery time  $\tau_{90-10\%}$  of the power gain after a gain compression is a useful metric. In Fig. 12.17, the dependence of  $\tau_{90-10\%}$  on pump power and bias current density is displayed. The phase recovery is clearly dominated by the slow process. It shows an effective recovery time of hundreds of picoseconds and cannot be improved considerably by changing the in-

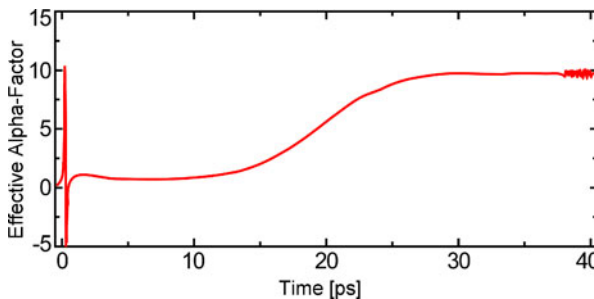


**Fig. 12.18** Time-dependent effective alpha-factor for an SOA, here for a QD SOA. The dynamic response of the first 10 ps is governed by fast QD refill processes with an alpha-factor close to zero. Later on, the depleted reservoir states lead to an alpha-factor, which remains at a high level until the reservoir is slowly refilled by externally injected carriers [41]

put power or the bias current density. The gain recovery is considerably faster. The associated effective time constant increases with input power, because the gain depletion is much stronger, but it rapidly decreases for higher bias current densities, as the capture efficiency of the QD states becomes larger.

Eventually, the slowest gain recovery time in an SOA, namely, the refilling of the carriers from an external current supply, limits the linear amplifier speed in a data communication system.

From the pump-probe measurement results, we know that in a QD SOA fast and slow processes influence the material power gain and the phase dependence simultaneously, but with different magnitudes: The material power gain depletes strongly, but recovers fast. In contrast, the phase recovers slowly. Therefore, the effective alpha-factor changes with time, see Fig. 12.18 [41]. The alpha-factor of the first 10 ps is governed by the refilling of the depleted QD states from the reservoir. This depletion can be described as an SHB process with an alpha-factor close to zero. The depleted reservoir states lead to an increased alpha-factor ( $t > 20$  ps) which remains large until the reservoir states are slowly refilled by external carrier injection.

## 12.4 Linear SOAs in Optical Networks

In this section, we discuss the influence of SOA parameters and their relevance in optical networks. The limitations for signal amplification with an SOA are outlined for on-off keying (OOK) and phase-shift keying (PSK) modulation formats. Measurement results of the input power dynamic range (IPDR) for 2.5 Gbit/s, 10 Gbit/s and 40 Gbit/s OOK and for 28 GBd differential quadrature PSK (DQPSK) data signals are presented. Finally, the use of an SOA as a reach extender in an access network is demonstrated.

### 12.4.1 Parameters of SOAs for Network Applications

Reach extenders in future access networks require linear SOAs. In order to get linear amplification across the largest possible spectral range parameters such as power gain, noise figure, saturation power, SOA dynamics as well as the alpha-factor need to be optimized.

**Important Parameters of a Linear SOA for Access Networks** The required SOA *single-pass power gain*  $G$  strongly depends on the SOA position in the network and the network topology itself. However, an unsaturated gain  $G_0$  exceeding 10 dB is ordinarily sufficient to extend the power budget of the network enabling an extended reach from 20 km to 60 km or an increased split ratio in a PON access network from 1 : 16 to 1 : 128.

The *noise figure* NF should be as small as possible for amplifying the usually low input power levels. An NF around 5–6 dB is achievable today in commercial devices.

The *saturation input power*  $P_{\text{in}}^{\text{sat}}$  should be as high as possible. This way, saturation of the amplifier can be avoided as well as patterning and interchannel crosstalk. A large saturation input power is of particular importance for an upstream reach-extender amplifier where data signals from the customer locations are sent to the central office. Due to the distance variations of the customer locations, the power at the SOA input varies. For future networks [2] input power variations in the order of  $> 40$  dB are envisaged. Therefore, an SOA requires a large input power dynamic range (IPDR) to cover these distance variations of the customer locations.

The 90 %-to-10 % *gain recovery time* is of limited interest since the SOA is operated in the linear gain regime to avoid gain saturation.

Lastly, a small *alpha-factor* has advantages as well. It guarantees that there are little if no phase variations upon a change in the gain. This way, a transition from one point in the constellation diagram to another will not be accompanied by phase changes. This is of particular importance for networks with PSK modulation formats since PSK encodes the information on the phase only, but amplitude transitions from one symbol to the other still might go through the constellation zero [86–88].

**Influence of Dimensionality of the Electronic System on the Linearity of an SOA** With respect to their suitability for a linear amplifier, we now compare the parameters such as gain, noise figure, saturation input power, SOA recovery time and alpha-factor for the mature bulk SOA and QW SOA technologies, along with the relatively novel QD SOAs. This is done from a theoretical point of view as based on the equations given in the Sect. 12.3, but also relying on experimental studies performed in recent years [2, 4, 6, 33, 41, 84–88].

The *single-pass power gain*  $G$  of both bulk and QD SOAs can be made comparable, though their lengths, however, are quite different. This can be understood from the definition of power gain  $G$  (12.18) and net power gain  $g$  (12.34)

$$G = \exp(\Gamma g L) = \exp[\Gamma a(N - N_t)L]. \quad (12.55)$$

Thus, the power gain  $G$  of an SOA depends on the carrier density  $N$ , the differential gain  $a$ , the amplifier length  $L$  and the confinement factor  $\Gamma$  (12.10). While quite a few sources state that the differential gain of the different devices is comparable with  $a \sim 2 \times 10^{-20} \text{ m}^2$  [6, 89], the confinement factor is not. The confinement factor of a QD SOA is in the order of 1% per layer [43] and in the order of 20–50% in bulk and QW SOAs [43]. However, this typically is compensated by stacking QD layers (5–15 layers are typical), and by making QD SOA devices longer. Typically QW and bulk SOA lengths are in the range 0.5–1 mm and thus have about  $\sim 25\%$  of the length of a QD SOA (2–4 mm).

One disadvantage of QD SOAs is that they show large PDG of up to 10 dB. However, this PDG can be eliminated with a polarization diversity schemes.

In theory, the *noise figure* NF of a QD SOA should be better than the noise figure of a bulk SOA. Equations (12.56) actually shows that the NF of an SOA basically

depends on the inversion factor  $n_{\text{sp}}$  and the power gain  $G$ ,

$$\text{NF} = 10 \log_{10} \left( \frac{1}{G} + 2n_{\text{sp}} \frac{G-1}{G} \right). \quad (12.56)$$

While the gain of a bulk and a QD SOA could be made similar, the (population) inversion factor of a QD SOA is close to ideal ( $n_{\text{sp}} \approx 1$ ). This is due to the carrier reservoir (wetting layer) in QD SOAs which allows an efficient filling of the QD states even for the low current densities compared to the bulk SOA. In practice, however, a typical noise figure of a QD SOA is in the order of 5 dB [33], a number which is comparable to the noise figure of the best bulk and QW SOAs [4].

The *saturation input power*  $P_{\text{in}}^{\text{sat}}$  (see (12.57)) of an SOA depends on the modal cross section  $C/\Gamma$ , the differential gain  $a$  and the effective carrier lifetime  $\tau_c$  if only interband effects are considered,

$$P_{\text{in}}^{\text{sat}} = \frac{2hf_s \ln 2 C}{G_0 - 2} \frac{1}{\Gamma} \frac{1}{a} \frac{1}{\tau_c}. \quad (12.57)$$

- Large values of  $P_{\text{in}}^{\text{sat}}$  are achievable with a large modal cross section. QD SOAs intrinsically offer large  $C/\Gamma$  of, i.e.,  $6 \times 10^{-13} \text{ m}^2$ , for example, [90], due to their low optical confinement factor  $\Gamma$  of 1 % per layer. However, it needs to be mentioned that also broad-area structures with bulk active media are reported to have large values of  $P_{\text{in}}^{\text{sat}}$ , where a small  $\Gamma$  increases the saturation power as well [49].
- Low differential gain  $a$  also contributes to large saturation powers. In theory,  $a$  is expected to increase if the dimensionality of the electronic system of the active medium reduces [14]. This is, i.e., in QD active regions due to the delta-function like density of states which should lead to quite a strong change in the gain even for small carrier density variations. However, in practice, the differential gain of QD SOAs are not as large because the size of quantum dots varies significantly, and the QD energy states are thus spread across a larger spectral range. It needs to be mentioned that the experimental results for the differential gain  $a$  for QW, bulk and QD SOAs are comparable for the time being, and it is still a research topic to compare actual devices in terms of the differential gain.
- An effective carrier lifetime of  $\tau_c \sim 100 \text{ ps} - 1 \text{ ns}$  is similar for QD, QW and bulk SOAs. The effective carrier lifetime  $\tau_c$  is related to the total effective carrier lifetime  $\tilde{\tau}_c$  which influences the 90 %-to-10 % gain recovery time. Therefore, a speed enhancement of SOA devices is achieved with an increase in bias current or with a lifetime doping in bulk SOA and an associated reduction in  $\tau_c$ . Further, longer SOA are preferable since the higher number of photons in the active medium causes the total effective carrier lifetime  $\tilde{\tau}_c$  to decrease [91].
- It needs to be mentioned that the characteristic time in the saturation power relation changes for a QD SOA if ultra-fast effects are considered and a full population inversion (high number of carriers in the reservoir states) is assumed. Then,  $\tau_c$  has to be substituted by the carrier capture time  $\tau_1 \sim 1 - 10 \text{ ps}$  from the wetting layer (reservoir states) into the QD states (see Sect. 12.3.6 “pump-probe measure-

ment setup and results”), and  $\tau_1 \approx \tau_{\text{SHB}} \sim \varepsilon_{\text{SHB}}$  has to be associated with the SHB relaxation time. The significant reduction of this characteristic time causes QD SOA saturation powers to be larger by factors 30–100 (continuous wave applications) or 5–10 (50 ps pulse width applications) than for bulk SOAs [84].

The *phase change* at the output of an SOA  $\Delta\varphi$  depends on the confinement factor  $\Gamma$ , the net power gain change  $\Delta g$ , the device length  $L$  and the SOA *alpha-factor*  $\alpha$

$$\Delta\varphi(N) = \alpha\Gamma\Delta gL/2. \quad (12.58)$$

Typically, in bulk or QW structures, a high confinement factor and an alpha-factor  $\alpha$  of value 2–8 are observed. Contrary to that, QD SOAs with a population inversion of  $n_{\text{sp}} = 1$  have an alpha-factor  $\alpha \approx 0$  mostly due to SHB, so that gain change and phase change are decoupled. Here, no or only small phase changes are imposed on the signal. This makes the QD SOA a promising device for linear amplification, i.e., for amplification without phase or amplitude distortion.

Recent publications of novel columnar QD SOA structures also report the possibility to observe a considerably high alpha-factor. Such devices have been successfully used to achieve high-speed wavelength conversion and regeneration [92].

It can be concluded that, in general, the use of QD SOA is advantageous for linear applications. However, it needs to be mentioned that a well engineered bulk or QW SOA could be better than its QD SOA counterpart [93].

### 12.4.2 Linear Amplification Range

The capability of an SOA to perform linear amplification is limited to input signals that do not exceed a lowest and a highest input power level, independently of the modulation format, the symbol rate or the number of wavelength channels.

For low input signal powers, error-free amplification (with signal quality  $Q^2 = 15.6$  dB corresponding to a bit error probability (BER) of  $10^{-9}$ ) becomes an issue. The limitations are due to amplified spontaneous emission (ASE) noise which is almost independent of the signal input power (for low SOA input powers). Therefore, if the input power decreases while the ASE remains constant, it will lead to a poor optical-signal-to-noise ratio (OSNR) for input signal powers that decrease below a certain value. An example of such OSNR limitation is presented in Fig. 12.19a for on-off keying (OOK) and quadrature phase shift keying (QPSK) modulation formats. The eye diagram of the 10 Gbit/s return-to-zero (RZ) OOK single channel signal shows strong noise on the one and zero level indicating degraded eye quality. Further, the constellation diagram of the 20 GBd (40 Gbit/s) QPSK single channel signal shows a symmetrical broadening of the constellation points which causes an increase of the error-vector-magnitude (EVM).

For large input powers, limitations occur as well. In this case, the strong input powers will induce gain suppression, leading to amplitude patterning and induces phase changes between subsequent bits. For example, the OOK format shown in

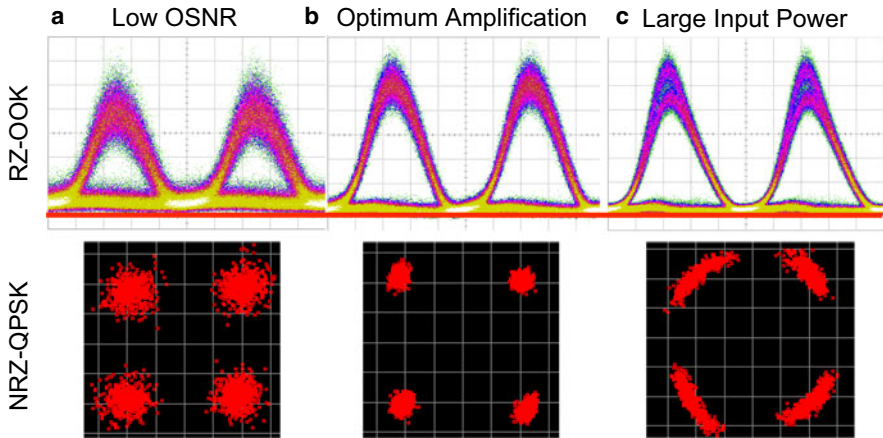


**Fig. 12.19** Eye diagrams and constellations showing the limitations for linear amplification of data signals. **a–c** show the eye diagrams for a 10 Gbit/s RZ-OOK signal as well as the constellation diagrams of an NRZ-QPSK signal. In **a**, the input signal into the SOA is very low, resulting in a bad OSNR level at the output of the amplifier. In **b**, error-free amplification of the data signal is observed, whereas in **c**, for high input powers, patterning effects due to compression of the gain occur and distort the OOK signals. In QPSK signals, the phase change induced by a refractive index change within the SOA causes a rotation of the constellation points

Fig. 12.19c shows patterning. Such patterning is manifested by overshoots in the eye diagram and could lead to signal quality degradations. Patterning is seen when subsequent ones experience different power gains which happens when the recovery time between bits is comparable or exceeds the bit-slot duration. Since typical SOA recovery times are in the order of a few tens to hundreds of picoseconds, signal degradations are already visible at bitrates of a few Gbit/s. At highest input powers, even PSK encoded signals can degrade. The signal degradation by amplification of PSK signals is caused by SOA induced phase changes, as may be seen in Fig. 12.19c. The degradation has its origin in the fast amplitude transitions that a PSK signal will undergo when switching from one symbol to another. These transitions may even go through the constellation zero. Such transitions then introduce fast gain changes which induce carrier density variations and therefore cause refractive index changes and phase errors. SOAs with lower alpha-factors induce less amplitude-to-phase conversion, and therefore show higher resilience with respect to phase errors. If higher orders of advanced modulation formats are used, e.g., 16-QAM, phase errors are accompanied by amplitude errors. This is due to the fact that the power gain for the three different amplitude levels in a 16-QAM signal is different leading to magnitude errors due to gain saturation [88].

The situation where the input signal power is neither too low nor too high is shown in Fig. 12.19b.

If more wavelength channels are involved, cross-gain modulation (XGM) and cross-phase-modulation (XPM) can cause signal quality degradations by interchan-

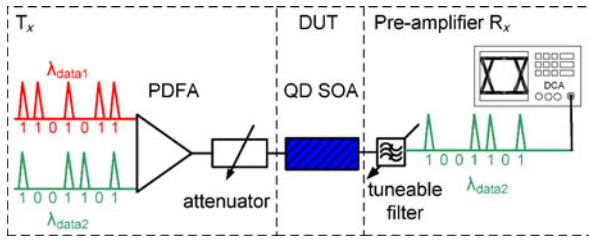


**Fig. 12.20** Setup for measuring  $Q^2$ -factors of data signals after amplification in an SOA

nel crosstalk. Such distortions are only relevant if one of the channels is operated in saturation.

The range of input powers for error-free amplification is called input power dynamic range (IPDR).

### 12.4.3 SOA Dynamic Range for Different Modulation Formats

In this section, we discuss the input power dynamic range (IPDR) for different modulation formats, different speeds and different SOA types. In particular, measurements are performed for on-off keying (OOK) and PSK modulations formats and for single-channel as well as wavelength-division-multiplexing (WDM) systems. Finally, a scenario of an application with linear amplifiers and a large dynamic range for fiber-to-the-home (FTTH) is presented.

**Input Power Dynamic Range (IPDR) of OOK Signals at Different Speed** The IPDR for amplification of single and multiple data signals with a  $1.3\ \mu\text{m}$  QD SOA has been studied by evaluating the  $Q^2$ -factor under various input power conditions. Experiments were performed with the setup shown in Fig. 12.20. Two decorrelated data signals were adjusted to various power levels before launching the composite signal into the QD SOA. After the QD SOA, one channel is blocked by a tunable filter, while the  $Q^2$ -factor of the remaining data channel is analyzed with a digital communications analyzer (DCA). The receiver was operated at its optimum operation point, i.e., 10 dB above the sensitivity threshold of  $Q^2 = 15.6\ \text{dB}$  for all of the experiments.

Two different cases in terms of power levels at the SOA input are investigated for bitrates of 2.5 Gbit/s NRZ-OOK, 10 Gbit/s NRZ-OOK, and 40 Gbit/s RZ-OOK. Firstly, a single data signal at a wavelength of 1310 nm is generated. Its power at the SOA input is varied, and the quality of the received signal is measured. Secondly, two decorrelated data signals at a wavelength of 1310 nm and 1290 nm are generated with identical power levels at the SOA input and the same bitrates.

For the single channel case, the  $Q^2$ -factor is plotted against the SOA input power, as shown in Fig. 12.20a. Experiments have been performed with a QD SOA at a wavelength of 1310 nm. An IPDR exceeding 25 dB has been found for all bitrates (the gray line within the figure marks a  $Q^2$ -factor of 15.6 dB) [94].

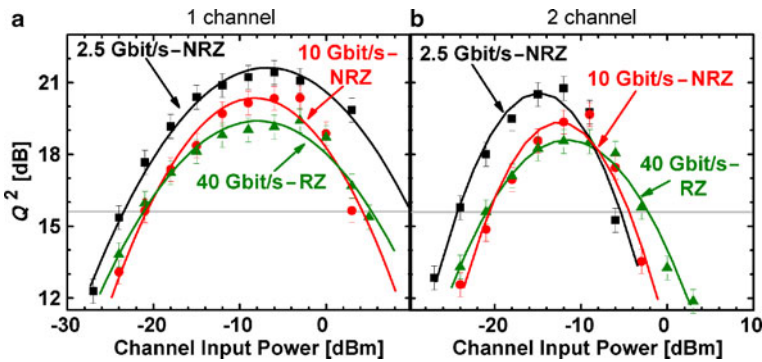


**Fig. 12.21**  $Q^2$ -factor of a QD SOA versus channel input power for one and two channel systems. **a** A large IPDR (horizontal gray line) between 34 dB and 25 dB is found for bitrates of 2.5 Gbit/s, 10 Gbit/s and 40 Gbit/s for the one channel case at 1310 nm. **b**  $Q^2$ -factor for two decorrelated data signals at 1310 nm and 1290 nm entering the SOA with equal power levels. IPDRs in the range of 19 dB to 16 dB for bitrates of 2.5, 10 and 40 Gbit/s at 1310 nm are found [94]

At high input power levels (gain saturation), the signal quality decreases due to patterning introduced by the slow components in the QD SOA. The slow effects are due to the refilling of the reservoir states (wetting layer). They have a time constant in the order of 100–200 ps. Therefore, these slow gain dynamic effects have a particular strong impact on signals with the same or shorter bit duration which means that the signals at 10 and 40 Gbit/s are affected most. However, at 2.5 Gbit/s, the performance is enhanced compared to 10 Gbit/s or 40 Gbit/s data rates because an input signal can now follow the slow gain dynamics of the wetting layer.

The results of the two-channel experiments are plotted in Fig. 12.21b. The  $Q^2$ -factor is evaluated under the same operating conditions as for the single-channel experiment, which is performed at a wavelength of 1310 nm, now under the influence of a second decorrelated data signal at 1290 nm. The IPDR exceeds 16 dB for all bitrates. At low input powers, the signal quality is similar to what was found for the single-channel case. Under deep gain saturation, patterning and interchannel crosstalk degrade the signal quality. The worst-case IPDR is found at 10 Gbit/s.

**Input Power Dynamic Range of PSK Signals for Different SOA Types** A new and interesting question is the ability of an SOA to amplify phase-encoded signals. It has been suggested that the constant envelope of differential phase encoded signals provides higher tolerance towards SOA nonlinear impairments such as cross-gain (XGM) and cross-phase modulation (XPM) compared to on-off keying (OOK) formats. Indeed, there is a higher tolerance for PSK signals, yet it has its limit once the SOA is operated in saturation where nonlinear impairments reduce the input power dynamics. Here, a study of the IPDR improvement for a 28 GBd NRZ-DQPSK signal amplified in a 1.5  $\mu\text{m}$  QD SOA compared to a similar bulk SOA (similar in terms of small-signal gain and OOK performance) is presented. The IPDR is defined as the range of input power levels with less than 2 dB power penalty compared to the back-to-back case.



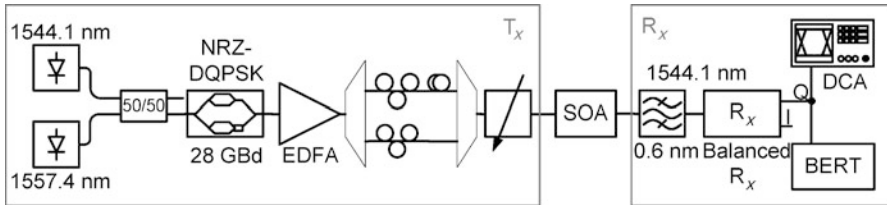


**Fig. 12.22** Experimental setup. Two 28 GBd NRZ-DQPSK channels are equalized and decorrelated using 0.5 m of fiber. The average power in both channels is varied and launched into a bulk or QD SOA. A single channel is selected, amplified and demodulated in a DQPSK receiver ( $R_x$ ), consisting of a delay interferometer (DI) followed by a balanced detector. The electrical signal is then analyzed using a digital communications analyzer (DCA) and a bit error ratio tester (BERT)

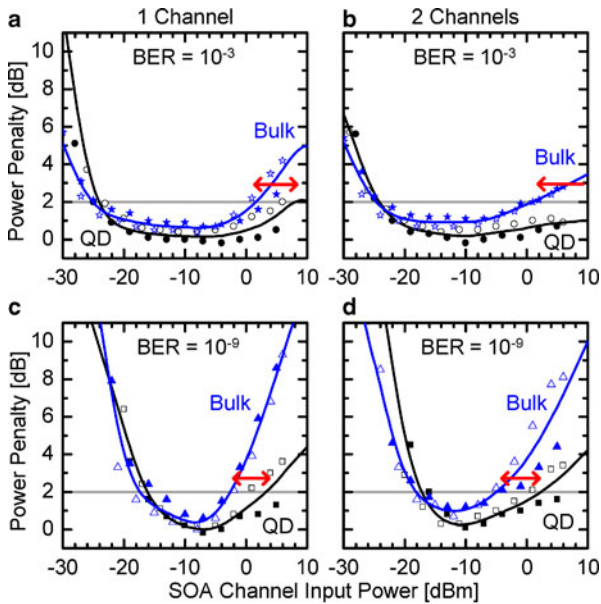
The IPDR for amplification of one and two 28 GBd NRZ-DQPSK data signals is studied by evaluating the BER. The experimental setup (Fig. 12.22) comprises two decorrelated data signals at 1554 nm (channel 1) and 1557 nm (channel 2). The power levels of both channels are adjusted alike before launching them into the device under test (DUT). After amplifying both data signals in the DUT, the 1557 nm channel is blocked by a tunable filter, while the BER of the remaining data channel is analyzed. The DQPSK receiver consists of a demodulator based on a delay interferometer (DI) followed by a balanced detector and a bit-error ratio tester.

Figure 12.23 shows the power penalty as a function of the SOA channel input power for one and two channel(s) at two specific BERs. Figure 12.23a, b shows an IPDR improvement of the QD SOA over the bulk SOA of 5 dB for the single channel case and  $> 10$  dB for the two channel case at a BER of  $10^{-3}$  [86–88]. Figure 12.23c, d exhibits about 6 dB IPDR improvement for the QD SOA compared to the bulk SOA for one and for two NRZ-DQPSK channels at a BER of  $10^{-9}$ , respectively. The full symbols correspond to the I-channel whereas the open symbols represent the Q-channel. The QD SOA proves to have a large IPDR of about 20 dB for BER =  $10^{-9}$  and exceeds 30 dB for BER =  $10^{-3}$ .

The power penalty and phase errors in DQPSK systems are related. In our case, where we use devices with similar gain saturation properties, the difference in the performance of the QD SOA and the bulk SOA must obviously stem from the different amount of phase errors. The origin is found in the difference of the devices' alpha-factors. The QD SOA clearly has a lower alpha-factor than the bulk SOA.

**An Example: Power Budget from an SOA Reach Extender in an Access Network** The FTTH market is rapidly increasing due to a fast growing demand of high bandwidth applications. A promising technology for fiber access systems is the gigabit passive optical network (GPON). Today, it offers a physical reach of 20 km between the central office and the customer, a split ratio of 1 : 32 and a loss budget of 28 dB.

It would be highly desirable to expand both the reach and the split ratio in order to bring costs down [94–96]. Such long-reach PONs would allow the consolidation of thousands of central offices to a few metro nodes. Also, split ratios up



**Fig. 12.23** Power penalty vs. channel input power levels. The input power dynamic range (IPDR) is defined as the range of input power levels with less than 2 dB power penalty compared to the back-to-back case. *Red arrows* indicate the IPDR enhancement of the QD SOA (*black*) over the bulk SOA (*blue*). **a, b** the QD SOA improves the IPDR at a BER of  $10^{-3}$  by 5 dB and  $> 10$  dB compared to the bulk SOA for one and two 28 GBd NRZ-DQPSK channels, respectively. **c, d** For a BER of  $10^{-9}$ , the QD SOA IPDR is enhanced by 5 dB. The *filled symbols* correspond to the I-channel, whereas the *open symbols* represent the Q-channel [86, 87]

to 128 would significantly reduce the cost per subscriber. To enable such systems, reach extenders are needed. Especially critical is a reach extender in the upstream path, from the customer to the central office, because – as already mentioned – a high dynamic range is required due to the distance variations of the customer locations.

And indeed, typical extended-reach WDM/TDM GPON architectures require optical amplification. This can be provided by an SOA as plotted in the GPON setup of Fig. 12.24. This GPON setup comprises the central office (CO) with the optical line terminations (OLT), an up to 50 km (SMF-28) fiber trunk, the amplifier extender box with the QD SOAs, the WDM de-/multiplexer followed by a 1 : 32 passive splitter and the optical network terminations (ONT). Four ONTs are 10 km away from the extender box. Since the losses in the trunk and the losses in the access branch are interrelated, we determined the acceptable losses after the QD SOA as a function of the given losses in front of the QD SOA, both for upstream and downstream. The losses are acceptable as long as the quality factor  $Q^2$  is better than 15.6 dB [2].

Figure 12.25a depicts the branch access loss versus the acceptable loss in the trunk for a 1.31  $\mu\text{m}$  QD SOA (blue curve), and Fig. 12.25c shows the dependence of

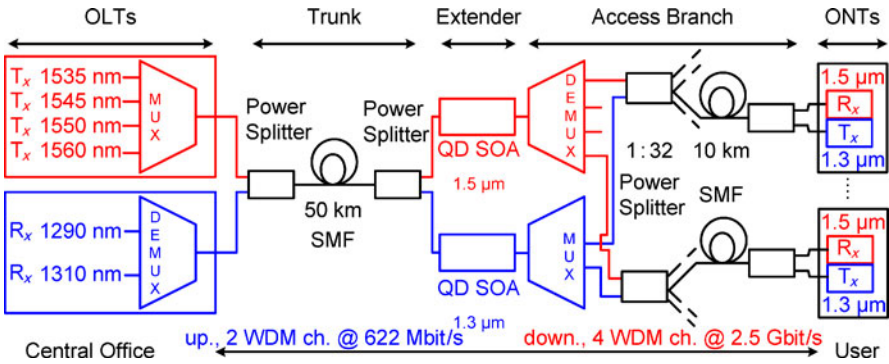


**Fig. 12.24** Extended WDM/TDM GPON testbed with four downstream and two upstream channels, each serving 32 subscribers with 60 km reach using QD SOA technology for bi-directional amplification [2]

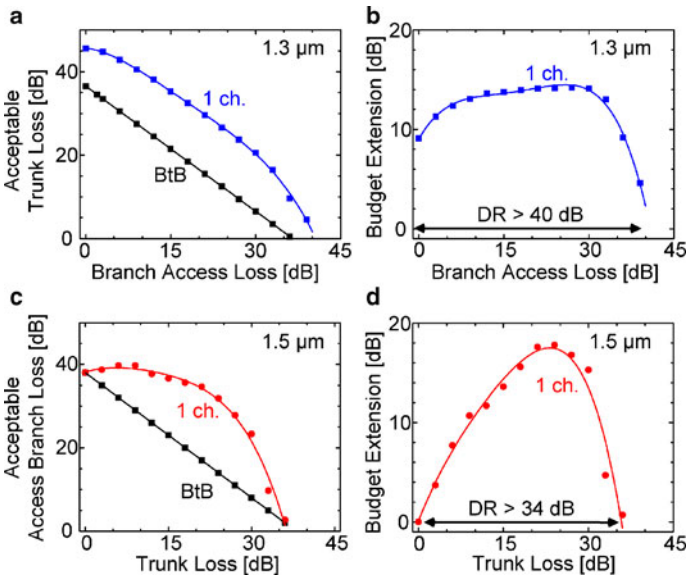


**Fig. 12.25** **a** Access branch loss plotted against acceptable trunk losses for the upstream path for which the BER is always better than  $1 \times 10^{-9}$ . **c** Trunk loss plotted against acceptable access branch loss for the downstream path. The OLT and ONT launch powers are 5 dBm. **b** and **d** show the budget extension of maximal 17 dB (**d**) and 14 dB (**b**) by the QD SOA. The dynamic range (DR) is 40 dB (**b**) and 34 dB (**d**)

loss in the trunk line as a function of the acceptable access branch loss for a  $1.55 \mu\text{m}$  QD SOA (red curve). The results with QD SOA are compared to the case without amplification (black curves). For high losses in the order of 20 dB before the amplifier, the QD SOAs extend the loss budget up to 17 dB and 14 dB for downstream and upstream, respectively. At these optimum operating points, the total accept-

able loss after the amplifier exceeds 30 dB for downstream and upstream. Therefore, state-of-the-art QD SOAs support a total loss budget exceeding 50 dB. The data in Fig. 12.25 are measured with signals at 2.5 Gbit/s-NRZ (1550 nm) and at 622 Mbit/s-NRZ (1310 nm). A power of +5 dBm for each channel is launched at the OLT and ONT, respectively. The receiver sensitivity is  $-33$  dBm at  $1.55 \mu\text{m}$  and  $-31.5$  dBm at  $1.31 \mu\text{m}$ . Figure 12.25b, d gives insight into the dependence of the reach extension offered by the QD SOA as a function of the loss budget. For low losses in front of the QD SOA, the high input power causes gain saturation. Therefore, the loss budget extension is small, but still exceeds 8 dB in the upstream case. If the losses in front of the amplifiers are increased beyond 30 dB, then the optical-signal-to-noise-ratio of the data signal becomes too low, and consequently the loss budget extension decreases. The optimum loss budget extension is obtained for losses of about 20 dB in front of the amplifier. Figure 12.25b further shows that the  $1.3 \mu\text{m}$  QD SOA offers a large IPDR of 40 dB, so that it tolerates input powers between +5 dBm and  $-35$  dBm with  $\text{BER} < 10^{-9}$ . This dynamic range is large enough to handle the total power variations by users at differently remote locations in the network.

## 12.5 Commercial SOAs

SOAs have been a subject of intense research interest for many years, but it is only recently that commercial devices have become available on the market. Whilst EDFAs have technical advantages over SOAs as high gain ( $> 25$  dB typical), low noise figure (4... 5 dB) and high saturation power ( $> 30$  dBm), for a long time, SOA gain blocks have been said to be cheaper since they require only one semiconductor component. However, economies of scale enabled by mass production made the price of the EDFA comparable to that of the SOA. It is therefore only by the advent of important wavelength regimes outside the 1530... 1560 nm EDFA gain band, such as those needed for PONs and coarse WDM (CWDM), that significant commercial volumes of SOAs have become available.

SOAs are delivered from companies such as CIP [97], Kamelian [98], Thorlabs [99] or QD Laser [100], amongst others. As described in Sect. 12.2.6, commercial linear SOAs are typically designed so that they are optimized for preamplification, inline amplification or as booster amplifiers. There are also markets emerging for reflective SOAs which are often used as reflective colorless amplifying modulators for WDM-PON applications. In addition, SOAs can be integrated with other components in a PIC (e.g., a tunable laser monolithically integrated with a booster SOA), as sold by Oclaro [101]). The following subsections describe commercial SOAs (Fig. 12.26 shows a packaged CIP SOA as an example) used as single-channel 40 Gbit/s signal amplifier, 10 Gbit/s WDM power booster, and the use of reflective SOAs as a colorless modulator within WDM-PONs.

CIP's linear SOAs are typically designed with a low confinement factor, buried heterostructure (BH), multiple quantum well (MQW) angled facet structure. The

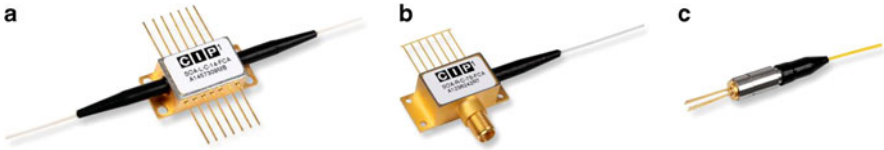


**Fig. 12.26** **a** Photograph of CIP SOA in 14-pin butterfly package, **b** reflective SOA in butterfly package, and **c** reflective SOA in pigtailed coaxial module

SOAs are packaged with optical fibers matched to the device output spatial mode to enable coupling losses of  $\sim 1$  dB per facet. This allows low noise figures (NF) of typically 6.5 dB. Also, the variation of the gain with the polarization of the input signal (PDG) is very low across the C-band (typically  $< 1$  dB). This makes it attractive for use in optical networks, where usually the input signal polarization is not controlled. In addition to this, SOAs can offer a wide gain bandwidth, making them ideal as colorless and wide band amplifier for WDM and CWDM applications.

Another class of SOAs is the reflective SOA. These are curved waveguide devices that are designed to work with a single fiber and can be used as gain blocks for external cavity lasers or as colorless modulators in WDM-PON applications. These devices are supplied either as butterfly modules for lab-based applications or as a pigtailed coaxial module for more cost sensitive ones (see Fig. 12.26b, c).

### 12.5.1 SOAs for High Data Rate Signal Amplification

In today's metro and access networks, where bands of wavelengths are transmitted over tens of kilometers, SOAs can play an important role. Provided the SOA is operated in its linear regime, not only is its gain independent of the number of wavelengths being amplified, but also the gain is not affected by dynamic effects of network reconfiguration or by bursty data, such as that experienced in IP packet transmission. An amplifier with high saturation input power is therefore necessary. A possible candidate is CIP's linear SOA. It is a low confinement factor device optimized for moderate gain in the C-band, low noise and high saturated output power. In order to ensure the device suitability for high capacity network amplification, a careful assessment of the amplifier characteristics versus input power must be done.

The particular device described here (SOA-L-OEC-1550 3061) offers the characteristics illustrated in Fig. 12.27 and in Table 12.2.

If we observe the close relationship between Gain and ASE profile, shown in Fig. 12.27b, this device will offer 18 dB gain in the S-band. The NF is low in the C-band, but expected to be higher at shorter wavelengths. The device's PDG is below 1.5 dB across the C-band and finally, the saturation output power is quite high, even at shorter wavelengths. From Fig. 12.28, we can see that the SOA is in its

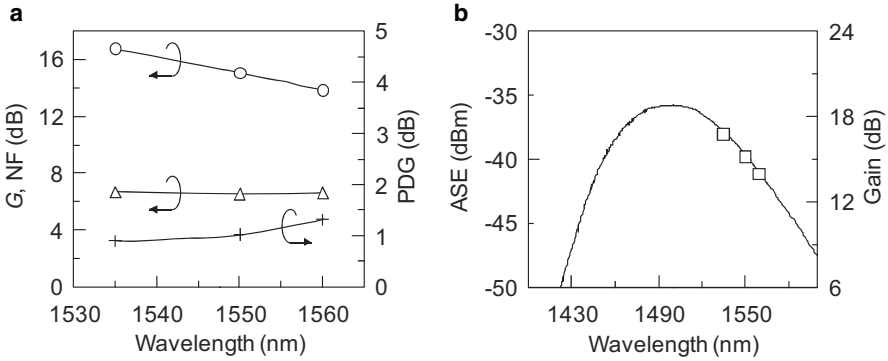


**Fig. 12.27** **a** SOA C band gain (*open circles*), noise figure (*open triangles*) and polarization dependent gain (+) versus wavelength. **b** amplified spontaneous emission (ASE) versus wavelength; C band gain is shown as well. The SOA under test is kept at 20 °C and biased at 500 mA

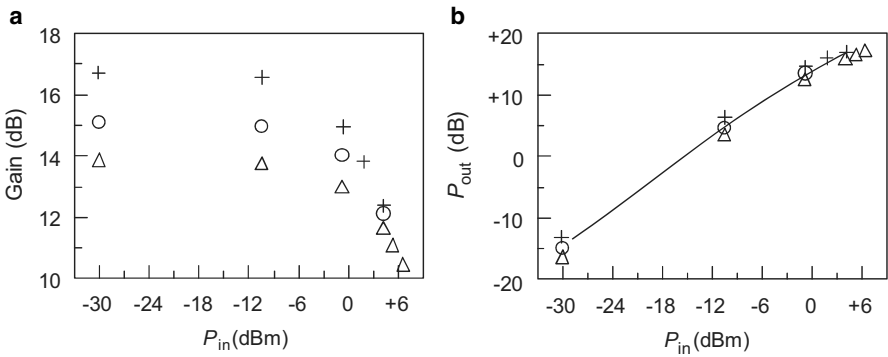


**Fig. 12.28** **a** SOA gain curves versus input power for 1535 (+), 1550 (*open circles*) and 1560 nm (*triangles*) and **b** linearity of SOA output power versus input power in C-band, both at 20 °C and at a bias current of 500 mA

**Table 12.2** SOA CW characteristics at 1550 nm at 20 °C

Item	Value	Unit
Gain ( $G$ )	15.2	dB
Noise figure (NF)	6.6	dB
Polarization dependent gain (PDG)	1	dB
Saturation output power ( $P_{out}^{sat}$ )	16.2	dBm

linear regime, at 1550 nm, for input powers up to approximately 0 dBm and with a correspondent output power of +14 dBm.

It is interesting to note how the system performance at 40 Gbit/s varies in terms of BER, sensitivity and  $Q$ -factor as a function of input power to the SOA to study the effects of SOA saturation as shown in Fig. 12.29.

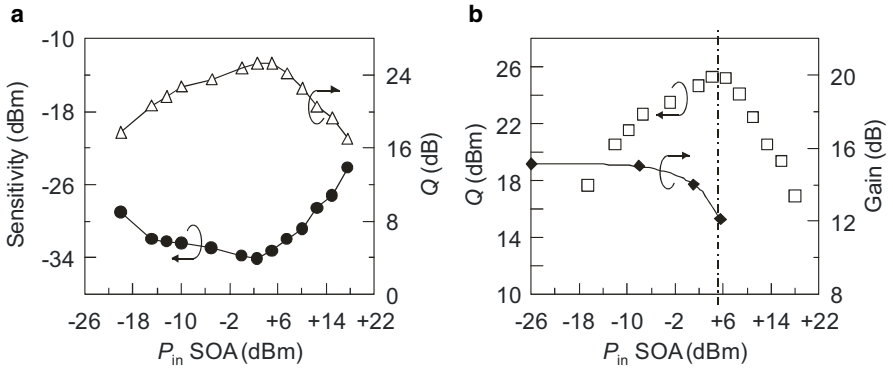


**Fig. 12.29** a System sensitivity and  $Q$  versus SOA input power and b  $Q$  performance and CW SOA gain versus SOA input power

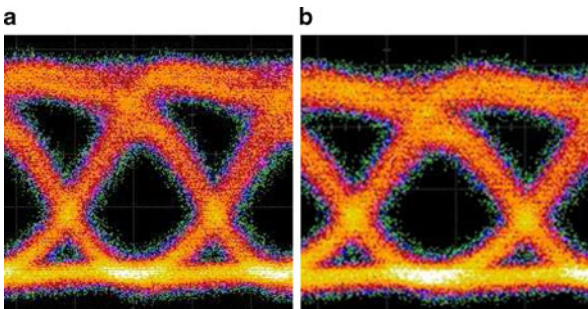


**Fig. 12.30** From left to right, 40 Gbit/s eye diagrams for a system with a no SOA and b with SOA (SOA  $P_{in} = 5$  dBm)

The best system performances are achieved when the SOA is over 2 dB in saturation ( $P_{in} = 2.5$  dBm) with a total SOA output power  $P_{out} = 15$  dBm. The system is still error free for SOA  $P_{in} = 12.5$  dBm (corresponding to an SOA  $P_{out} = 18.4$  dBm) when the SOA is deeply saturated. For low input power (when  $P_{in} \ll$  saturation input power), the system  $Q$  increases in direct proportion to the signal power. As the power increases, the contribution from the SOA to the overall OSNR becomes insignificant and the  $Q$ -factor does not follow the increase in SOA input power, becoming limited by the input OSNR. Beyond 2 dB into saturation ( $P_{in} > 3$  dBm), the signal quality reduction arising from distortions caused by the SOA nonlinearities overcome the benefit of an increased OSNR given by a higher SOA output power. Finally, the eye diagrams for the system with and without the SOA are compared in Fig. 12.30 (for an SOA input power equal to  $-5$  dBm). The eye from the SOA does not show any degradation effects due to the amplifier.

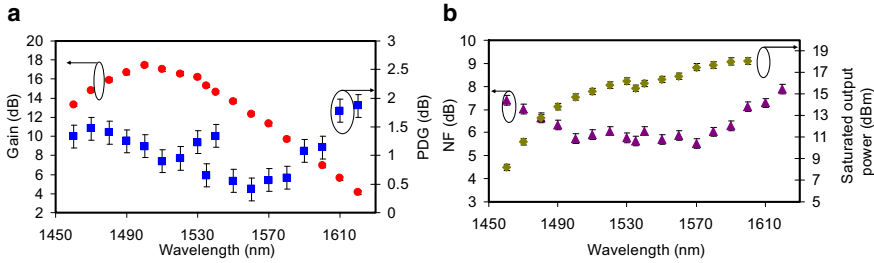


**Fig. 12.31** **a** Measured gain and PDG and **b** NF and saturated output power for a typical SOA-L-OEC-1550 over the S-band, C-band and L-band. (Bias current = 500 mA and  $T = 20^\circ\text{C}$ )

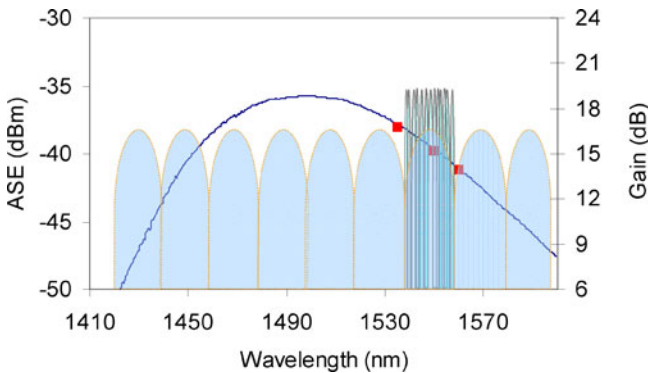


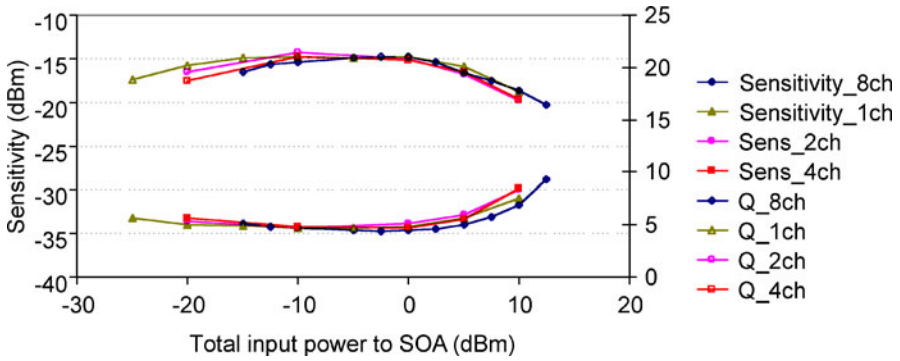
**Fig. 12.32** SOA gain (red markers) and ASE profile compared with DWDM and CWDM wavelength grids

### 12.5.2 Extended Wavelength Range and Multi-wavelength Operation

Although the SOA-L-OEC-1550 is optimized for operation across the C-band, the extended wavelength data in Fig. 12.31a, b show how the NF is maintained below 8 dB, that PDG stays below 2 dB across a wavelength bandwidth of 160 nm, and that the saturated output power is greater than 10 dBm over a bandwidth of 150 nm. This wavelength coverage includes the telecommunication S-band (1450–1520 nm) and L-band (1565–1610 nm). These characteristics make the SOA a strong candidate for multi-channel systems.

A common misconception is that SOAs cannot be used for simultaneous amplification of several optical wavelengths due to interchannel crosstalk. However, this is not true. An SOA can successfully simultaneously amplify several optical wavelengths as long as the total amplified power does not greatly exceed the saturation power of the SOA. Also, due to the broad optical bandwidth, the device can amplify not only the DWDM, 50 GHz or 100 GHz spaced, channels, but also 20 nm spaced, CWDM channels (as shown in Fig. 12.32).





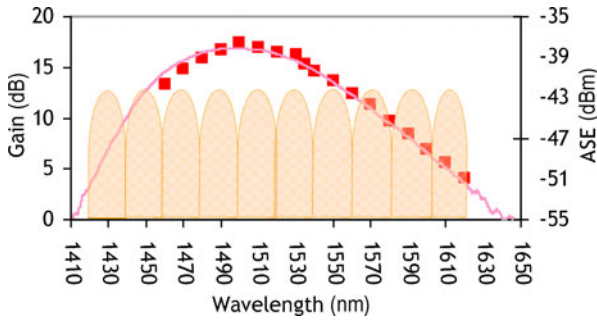
**Fig. 12.33** System sensitivity ( $S$ ) and  $Q$ -factors for 10 Gbit/s signals as a function of the total input power into the SOA (for wavelength channel counts of 1, 2, 4 and 8). SOA bias is 500 mA and temperature is 20 °C, corresponding to an SOA gain  $\sim 13$  dB

Figure 12.33 shows that there is very little variation in the performance between the results for a single-channel and the eight 100 GHz spaced channels operating at 10 Gbit/s. This confirms that when the linear SOA is operated in the correct regime, there is no crosstalk induced between the different wavelength channels under multi-wavelength amplification. This excellent performance will extend to higher channel count systems as long as the total amplified power remains within the saturation constraints.

The wide spectral width of 80 nm offered by the SOA-L-OEC-1550 at high drive currents also makes the device ideal for CWDM applications, where each wavelength channel is widely spaced ( $\sim 20$  nm) to allow the wavelength of the laser sources to vary with temperature, and this optical networking technology has made substantial progress over the past few years. In contrast to the capabilities of SOAs, the narrow bandwidth of an EDFA limits these amplifiers to a couple of CWDM wavelength channels, while the broad spectral width of the SOA-L-OEC-1550 provides optical gain across 10 CWDM channels as shown in Fig. 12.34.

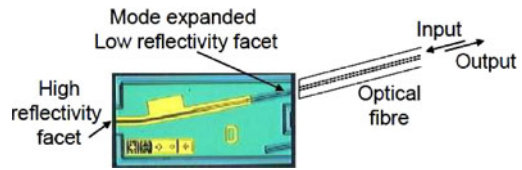
### 12.5.3 Reflective SOAs for WDM-PON Applications

The fast SOA gain dynamics allow for the device to be directly modulated. Thus, an SOA can be used as a modulated reflective device if one facet of the chip has a high reflection facet rather than a more usual low reflectivity at both facets. In this configuration, the inputs of the SOA and the amplified light from the SOA are coupled to the same optical fiber, as shown in Fig. 12.35. Because of the back facet reflection, reflective SOAs are very susceptible to optical feedback. In order to prevent any lasing effects, the device facet has been designed with an ultra-low reflectivity ( $< 10^{-5}$ ), and the angled waveguide has a curved design with an integrated mode



**Fig. 12.34** Diagram showing overlay of 10 CWDM channels with the measured ASE (*line*) and gain (*points*) of a typical SOA-L-OEC-1550 at bias of 500 mA

**Fig. 12.35** Schematic diagram of reflective SOA operation



expander. This type of SOA has applications in optical access networks, such as WDM-PON. In this scenario, the reflective SOA is used as an amplifying modulator for the upstream data at the customer optical network unit (ONU). The unmodulated cw seed source is placed at the central office (CO).

Due to its large optical bandwidth (approximately 50 nm for a 3 dB bandwidth), the SOA offers the advantage of “colorless” amplification, i.e., the performance of the device is independent of the wavelength of the input optical signal.

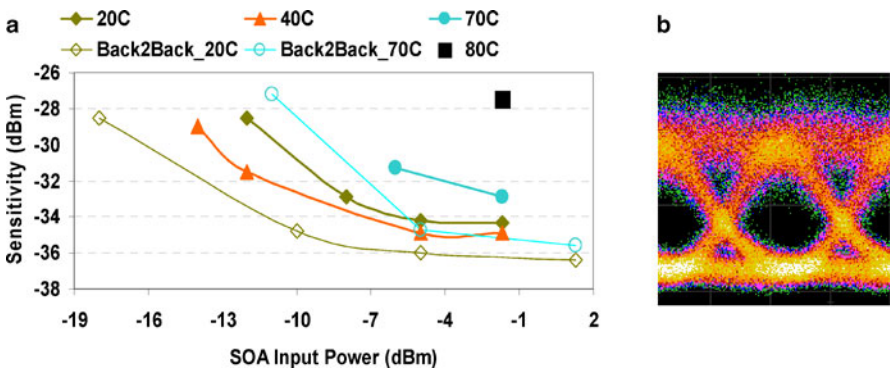


**Fig. 12.36** RSOA as upstream transmitter. **a** Receiver sensitivity over temperature for back-to-back and over 10 km of SMF-28 at 2.5 Gbit/s for a WDM-PON sliced system. **b** A received eye diagram

The seed source at the CO can be a bank of narrowband lasers or a sliced broadband source [102]. The two approaches offer different advantages and also require different types of reflective SOAs. The latter is economically more attractive, while the former reduces the impact of chromatic dispersion for the return channel in long reach applications and avoids the excess noise produced by the spectral slicing process. While the broadband source, if unpolarized, does not require any polarization control, the narrowband approach requires the use of an SOA with low polarization sensitivity.

A reflective SOA (SOA-R-OEC-1550) has been successfully tested as a 2.5 Gbit/s ONU transmitter up to 80 °C [103]. Another feature of the device is that the gain saturation mechanism in the SOA reduces the amplitude noise of the injected signal. This is very beneficial for noise reduction on spectrally sliced PON systems [104]. An example of the performance of this RSOA is shown in Fig. 12.36a, b.

## 12.6 Conclusion

This chapter has described the basic operation of linear SOAs, namely, absorption and emission processes in semiconductors, and suitable active region materials for a linear SOA design. We explained modification of those materials using quantum confinement and how they can be incorporated into waveguide structures and the packaging of these. Simple models were used to derive some of the important operating performance parameters, such as power gain, phase change, noise figure and dynamic range. Experimental results were presented, illustrating how a QD linear SOA performs for single and multiple wavelength channels. The suitability of SOAs in amplifying signals encoded with advanced modulation formats was demonstrated and it was shown that the reduced alpha-factor of a QD SOA relative to its bulk counterpart can give an improved dynamic range for an NRZ-DQPSK signal. In a WDM TDM PON, an SAO proves to be useful. Finally, a range of commercial SOAs for high data rate signal amplification, extended wavelength range and multi-wavelength operation as well as reflective SOAs for colorless WDM-PON applications were presented.

## References

1. D.R. Zimmerman, L.H. Spiekman, Amplifiers for the masses: EDFA, EDWA, and SOA amplifiers for metro and access applications. *J. Lightw. Technol.* **22**, 63–70 (2004)
2. R. Bonk, R. Brenot, C. Meuer, T. Vallaitis, A. Tussupov, J. C. Rode, S. Sygletos, P. Vorreau, F. Lelarge, G.H. Duan, H.-G. Krimmel, Th. Pfeiffer, D. Bimberg, W. Freude, J. Leuthold, 1.3/ 1.5  $\mu\text{m}$  QD-SOAs for WDM/TDM GPON with extended reach and large upstream/downstream dynamic range, *Opt. Fiber Commun. Conf. and Nat. Fiber Opt. Eng. Conf.* (OFC/NFOEC'09), Techn. Digest (San Diego, CA, USA, 2009), paper OWQ1

3. L.A. Coldren, S.C. Nicholes, L. Johansson, S. Ristic, R.S. Guzzon, E.J. Norberg, U. Krishnamachari, High performance InP-based photonic ICs – A tutorial. *J. Lightw. Technol.* **29**, 554–570 (2011)
4. K. Morito, High-power semiconductor optical amplifier, *Opt. Fiber Commun. Conf. and Nat. Fiber Opt. Eng. Conf.* (OFC/NFOEC'09), Techn. Digest (San Diego, CA, USA, 2009), paper OWQ4 (tutorial)
5. C. Michie, A.E. Kelly, J. McGeough, I. Armstrong, I. Andonovic, C. Tombling, Polarization-insensitive SOAs using strained bulk active regions. *J. Lightw. Technol.* **24**, 3920–3927 (2006)
6. M. Sugawara, H. Ebe, N. Hatori, M. Ishida, Y. Arakawa, T. Akiyama, K. Otsubo, Y. Nakata, Theory of optical signal amplification and processing by quantum-dot semiconductor optical amplifiers. *Phys. Rev. B* **69**, 235332 (2004)
7. R. Brenot, F. Lelarge, O. Legouezigou, F. Pommereau, F. Poingt, L. Legouezigou, E. Derouin, O. Drisse, B. Rousseau, F. Martin, G.H. Duan, Quantum dots semiconductor optical amplifier with a  $-3$  dB bandwidth of up to 120 nm in semi-cooled operation, *Opt. Fiber Commun. Conf. and Nat. Fiber Opt. Eng. Conf.* (OFC/NFOEC'08), Techn. Digest (San Diego, CA, USA, 2008), paper OTuC1
8. K. Morito, M. Ekawa, T. Watanabe, Y. Kotaki, High-output-power polarization-insensitive semiconductor optical amplifier. *J. Lightw. Technol.* **21**, 176–181 (2003)
9. M.G.A. Bernard, G. Duraffourg, Laser conditions in semiconductors. *phys. stat. sol. (b)* **1**, 699–703 (1961)
10. N. Nakamura, S. Tsuji, Single-mode semiconductor injection lasers for optical fiber communications. *IEEE J. Quantum Electron.* **QE-17**, 994 (1981)
11. Z.I. Alferov, Nobel Lecture: The double heterostructure concept and its applications in physics, electronics, and technology. *Rev. Mod. Phys.* **73**, 767–782 (2001)
12. G. Lasher, F. Stern, Spontaneous and stimulated recombination radiation in semiconductors. *Phys. Rev. A* **133**, 553–563 (1964)
13. N.K. Dutta, Q. Wang, *Semiconductor Optical Amplifiers* (World Scientific Publishing, Singapore, 2006)
14. *Quantum Well Lasers*, ed. by P.S. Zory, Jr. (Academic Press, Boston, 1993)
15. J. Leuthold, *Advanced indium-phosphide waveguide Mach-Zehnder interferometer all-optical switches and wavelength converters*, Series in Quantum Electronics, vol. 12 (Hartung-Gorre, Konstanz, 1999)
16. J. Leuthold, M. Mayer, J. Eckner, G. Guekos, H. Melchior, Ch. Zellweger, Material gain of bulk 1.55  $\mu\text{m}$  InGaAsP/InP semiconductor optical amplifiers approximated by a polynomial model. *J. Appl. Phys.* **87**, 618–620 (2000)
17. D. Bimberg, M. Grundmann, N.N. Ledentsov, *Quantum Dot Heterostructures* (Wiley, Chichester, 1999)
18. M.A. Newkirk, B.I. Miller, U. Koren, M.G. Young, M. Chien, R.M. Jopson, C.A. Burrus, 1.5  $\mu\text{m}$  multiquantum-well semiconductor optical amplifier with tensile and compressively strained wells for polarization-independent gain. *IEEE Photon. Technol. Lett.* **4**, 406–408 (1993)
19. K. Magari, M. Okamoto, Y. Suzuki, K. Sato, Y. Noguchi, O. Mikami, Polarization-insensitive optical amplifier with tensile-strained-barrier MQW structure. *IEEE J. Quantum Electron.* **30**, 695–702 (1994)
20. D. Leclerc, P. Brosseau, F. Pommereau, R. Ngo, P. Doussière, F. Mallécot, P. Gavignet, I. Wamsler, G. Laube, W. Hunziker, W. Vogt, H. Melchior, High-performance semiconductor optical amplifier array for self-aligned packaging using Si V-groove flip-chip technique. *IEEE Photon. Technol. Lett.* **7**, 476–478 (1995)
21. C.-E. Zah, R. Bhat, B.N. Pathak, F. Favire, W. Lin, M.C. Wang, N.C. Andreadakis, D.M. Hwang, M.A. Koza, T.-P. Lee, Z. Wang, D. Darby, D. Flanders, J.J. Hsieh, High-performance uncooled 1.3- $\mu\text{m}$   $\text{Al}_x\text{Ga}_y\text{In}_{1-x-y}\text{As}/\text{InP}$  strained-layer quantum-well lasers for subscriber loop applications. *IEEE J. Quantum Electron.* **30**, 511–523 (1994)
22. M. Yamada, T. Anan, K. Tokutome, S. Sugou, High-temperature characteristics of 1.3- $\mu\text{m}$  InAsP-InAlGaAs ridge waveguide lasers. *IEEE Photon. Technol. Lett.* **11**, 164–166 (1999)

23. P. Koonath, S. Kim, W.-J. Cho, A. Gopinath, Polarization-insensitive optical amplifiers in AlInGaAs. *IEEE Photon. Technol. Lett.* **13**, 779–781 (2001)
24. H. Ma, X. Yi, S. Chen, 1.55  $\mu\text{m}$  AlGaInAs/InP polarization-insensitive optical amplifier with tensile strained wells grown by MOCVD. *Opt. and Quantum Electron.* **35**, 1107–1112 (2003)
25. J. Hashimoto, K. Koyama, T. Katsuyama, Y. Tsuji, K. Fujii, K. Yamazaki, A. Ishida, 1.3  $\mu\text{m}$  GaInNAs bandgap difference confinement semiconductor optical amplifiers. *Jpn. J. Appl. Phys.* **45**, 1635–1639 (2006)
26. S. Tanaka, A. Uetake, S. Yamazaki, M. Ekawa, K. Morito, Polarization-insensitive GaInNAs–GaInAs MQW-SOA with low noise figure and small gain tilt over 90-nm bandwidth (1510–1600 nm). *IEEE Photon. Technol. Lett.* **20**, 1311–1313 (2008)
27. S.J. Sweeney, patent WO 2010/149978 A1
28. S.J. Sweeney, Bismide-alloys for higher efficiency infrared semiconductor lasers, *Proc. 22nd IEEE Int. Semicond. Laser Conf. (ISLC2010)*, Conf. Digest (Kyoto, Japan, 2010), paper P24
29. Y. Tominaga, K. Oe, M. Yoshimoto, Low temperature dependence of oscillation wavelength in GaAs<sub>1-x</sub>Bi<sub>x</sub> laser by photo-pumping. *Appl. Phys. Express* **3**, 062201 (2010)
30. M. Yoshimoto, W. Huang, G. Feng, K. Oe, New semiconductor alloy GaNAsBi with temperature-insensitive bandgap. *phys. stat. sol. (b)* **243**, 1421–1425 (2006)
31. J.P. Reithmaier, G. Eisenstein, A. Forchel, InAs/InP quantum-dash lasers and amplifiers. *Proc. IEEE* **95**, 1779–1790 (2007)
32. F. Lelarge, B. Dagens, J. Renaudier, R. Brenot, A. Accard, F. van Dijk, D. Make, O.L. Gouezigou, J.-G. Provost, F. Poingt, J. Landreau, O. Drisse, E. Derouin, B. Rousseau, F. Pommereau, G.-H. Duan, Recent advances on InAs/InP quantum dash based semiconductor lasers and optical amplifiers operating at 1.55  $\mu\text{m}$ . *IEEE J. Sel. Top. Quantum Electron.* **13**, 111–124 (2007)
33. T. Akiyama, M. Sugawara, Y. Arakawa, Quantum-dot semiconductor optical amplifiers. *Proc. IEEE* **95**, 1757–1766 (2007)
34. A.R. Kovsh, N.A. Maleev, A.E. Zhukov, S.S. Mikhlin, A.P. Vasil'ev, E.A. Semenova, Y.M. Shernyakov, M.V. Maximov, D.A. Livshits, V.M. Ustinov, N.N. Ledentsov, D. Bimberg, Z.I. Alferov, InAs/InGaAs/GaAs quantum dot lasers of 1.3  $\mu\text{m}$  range with enhanced optical gain. *J. Cryst. Growth* **251**, 729–736 (2003)
35. D. Bimberg, G. Fiol, M. Kuntz, C. Meuer, M. Laemmlin, N.N. Ledentsov, A.R. Kovsh, High speed nanophotonic devices based on quantum dots. *phys. stat. sol. (a)* **203**, 3523–3532 (2006)
36. T. Kita, O. Wada, H. Ebe, Y. Nakata, M. Sugawara, Polarization-independent photoluminescence from columnar InAs/GaAs self-assembled quantum dots. *Jpn. J. Appl. Phys.* **41**, L1143–L1145 (2002)
37. N. Yasuoka, K. Kawaguchi, H. Ebe, T. Akiyama, M. Ekawa, K. Morito, M. Sugawara, Y. Arakawa, 1.55- $\mu\text{m}$  polarization-insensitive quantum dot semiconductor optical amplifier, *Proc. 34th Europ. Conf. Opt. Commun. (ECOC'08)*, Brussels, Belgium (2008), paper Th.1.C.1
38. N. Yasuoka, K. Kawaguchi, H. Ebe, T. Akiyama, M. Ekawa, K. Morito, M. Sugawara, Y. Arakawa, Quantum-dot semiconductor optical amplifiers with polarization-independent gains in 1.5- $\mu\text{m}$  wavelength bands. *IEEE Photon. Technol. Lett.* **20**, 1908–1910 (2008)
39. D. Litvinov, H. Blank, D. Schneider, D. Gerthsen, T. Vallaitis, J. Leuthold, T. Passow, A. Grau, H. Kalt, C. Klingshirm, M. Hetterich, Influence of InGaAs cap layers with different In concentration on the properties of InGaAs quantum dots. *J. Appl. Phys.* **103**, 083532 (2008)
40. G.P. Agrawal, *Fiber-Optic Communication Systems* (Wiley, New York, 2002)
41. T. Vallaitis, C. Koos, R. Bonk, W. Freude, M. Laemmlin, C. Meuer, D. Bimberg, J. Leuthold, Slow and fast dynamics of gain and phase in a quantum dot semiconductor optical amplifier. *Opt. Express* **16**, 170–178 (2008)
42. H. Wang, E. Aw, M. Xia, M. Thompson, R. Penty, I. White, A. Kovsh, Temperature independent optical amplification in uncooled quantum dot optical amplifiers, *Opt. Fiber Commun. Conf. and Nat. Fiber Opt. Eng. Conf. (OFC/NFOEC'08)*, Techn. Digest (San Diego, CA, USA, 2008), paper OTuC2

43. R. Brenot, M.D. Manzanedo, J.-G. Provost, O. Legouezigou, F. Pommereau, F. Poingt, L. Legouezigou, E. Derouin, O. Drisse, B. Rousseau, F. Martin, F. Lelarge, G.H. Duan, Chirp reduction in quantum dot-like semiconductor optical amplifiers, *Proc. 33rd Europ. Conf. Opt. Commun.* ('07), Berlin, Germany (2007), paper We08.6.6
44. M. Spyropoulou, S. Sygletos, I. Tomkos, Simulation of multi-wavelength regeneration based on QD semiconductor optical amplifiers. *IEEE Photon. Technol. Lett.* **19**, 1577–1579 (2007)
45. S. Sygletos, M. Spyropoulou, P. Vorreau, R. Bonk, I. Tomkos, W. Freude, J. Leuthold, Multi-wavelength regenerative amplification based on quantum-dot semiconductor optical amplifiers, *Proc. 9th Intern. Conf. on Transparent Optical Netw. (ICTON'07)* (Rome, Italy, 2007), paper We.D2.5
46. G.P. Agrawal, N.K. Dutta, *Semiconductor Lasers*, 2nd edn. (Van Nostrand Reinhold, New York, 1993)
47. Photonic integrated circuits – A technology and applications primer, Infinera, white paper (2005). [www.infinera.com](http://www.infinera.com)
48. R. Nagarajan, M. Kato, J. Pleumeekers, P. Evans, D. Lambert, A. Chen, V. Dominic, A. Mathur, P. Chavarkar, M. Missey, A. Dentai, S. Hurtt, J. Bäck, R. Muthiah, S. Murthy, R. Salvatore, C. Joyner, J. Rossi, R. Schneider, M. Ziari, H.-S. Tsai, J. Bostak, M. Kaufmann, S. Pennypacker, T. Butrie, M. Reffle, D. Mehuys, M. Mitchell, A. Nilsson, S. Grubb, F. Kish, D. Welch, Large-scale photonic integrated circuits for long-haul transmission and switching. *J. Opt. Netw.* **6**, 102–111 (2007)
49. M.J. Connelly, *Semiconductor Optical Amplifiers* (Kluwer Academic, Boston, 2002)
50. T. Kremp, *Split-step wavelet collocation methods for linear and nonlinear optical wave propagation*, PhD thesis, University of Karlsruhe (TH) (2002)
51. J. Wang, *Pattern effect mitigation techniques for all-optical wavelength converters based on semiconductor optical amplifiers*, PhD thesis, University of Karlsruhe (TH) (2008)
52. H.A. Kramers, Diffusion of light by atoms, *Atti. Congr. Internat. Fisici* **2**, 545–57 (1927)
53. R. de L. Kronig, On the theory of the dispersion of X-rays. *J. Opt. Soc. Am.* **12**, 547–557 (1926)
54. D.C. Hutchings, M. Sheik-Bahae, D.J. Hagan, E.W. van Stryland, Kramers-Krönig relations in nonlinear optics. *Opt. Quantum Electron.* **24**, 1–30 (1992)
55. C.H. Henry, Theory of the linewidth of semiconductor lasers. *IEEE J. Quantum Electron.* **QE-18**, 259–264 (1982)
56. L. Occhi, L. Schares, G. Guekos, Phase modeling based on the  $\alpha$ -factor in bulk semiconductor optical amplifiers. *IEEE J. Sel. Top. Quantum Electron.* **9**, 788–797 (2003)
57. G. Agrawal, *Nonlinear Fiber Optics*, 3rd edn. (Academic Press, New York, 2001)
58. H.A. Haus, Noise figure definition valid from RF to optical frequencies. *IEEE J. Sel. Top. Quantum Electron.* **6**, 240–247 (2000)
59. D.M. Baney, P. Gallion, R.S. Tucker, Theory and measurement techniques for the noise figure of optical amplifiers. *Optical Fiber Technol.* **6**, 122–154 (2000)
60. E. Desurvire, *Erbium-doped Fiber Amplifiers: Principles and Applications* (Wiley, New York, 1994)
61. N.A. Olsson, Lightwave systems with optical amplifiers. *J. Lightw. Technol.* **7**, 1071–1082 (1989)
62. A. Borghesani, N. Fensom, A. Scott, G. Crow, L.M. Johnston, J.A. King, L.J. Rivers, S. Cole, S.D. Perrin, D. Scrase, G. Bonfrate, A.D. Ellis, I.F. Lealman, G. Crouzel, L.H.K. Chun, A. Lupu, E. Mahe, P. Maigne, High saturation power ( $> 16.5$  dBm) and low noise figure ( $< 6$  dB) semiconductor optical amplifier for C-band operation, *Opt. Fiber Commun. Conf. (OFC'03)*, Techn. Digest (Atlanta, GA, USA, 2003), paper ThO1
63. K. Morito, S. Tanaka, Record high saturation power ( $+22$  dBm) and low noise figure (5.7 dB) polarization-insensitive SOA module. *IEEE Photon. Technol. Lett.* **17**, 1298–1300 (2005)
64. G.P. Agrawal, N.A. Olsson, Self-phase modulation and spectral broadening of optical pulses in semiconductor laser amplifiers. *IEEE J. Quantum Electron.* **25**, 2297–2306 (1989)

65. R. Olshansky, C.B. Su, J. Manning, W. Powazinik, Measurement of radiative and nonradiative recombination rates in InGaAsP and AlGaAs light sources. *IEEE J. Quantum Electron.* **QE-20**, 838–854 (1984)
66. J. Leuthold, D.M. Marom, S. Cabot, J.J. Jaques, R. Ryf, C.R. Giles, All-optical wavelength conversion using a pulse reformatting optical filter. *J. Lightw. Technol.* **22**, 186–192 (2004)
67. J. Leuthold, C.H. Joyner, B. Mikkelsen, G. Raybon, J.L. Pleumeekers, B.I. Miller, K. Dreyer, C.A. Burrus, 100 Gbit/s all-optical wavelength conversion with integrated SOA delayed-interference configuration. *Electron. Lett.* **36**, 1129–1130 (2000)
68. J. Leuthold, L. Møller, J. Jaques, S. Cabot, L. Zhang, P. Bernasconi, M. Cappuzzo, L. Gomez, E. Laskowski, E. Chen, A. Wong-Foy, A. Griffin, 160 Gbit/s SOA all-optical wavelength converter and assessment of its regenerative properties. *Electron. Lett.* **40**, 554–555 (2004)
69. J. Leuthold, G. Raybon, Y. Su, R. Essiambre, S. Cabot, J. Jaques, M. Kauer, 40 Gbit/s transmission and cascaded all-optical wavelength conversion over 1 000 000 km. *Electron. Lett.* **38**, 890–892 (2002)
70. H. Chen, G. Zhu, Q. Wang, J. Jaques, J. Leuthold, A.B. Piccirilli, N.K. Dutta, All-optical logic XOR using differential scheme and Mach–Zehnder interferometer. *Electron. Lett.* **38**, 1271–1273 (2002)
71. J.P. Sokoloff, P.R. Prucnal, I. Glesk, M. Kane, A terahertz optical asymmetric demultiplexer (TOAD). *IEEE Photon. Technol. Lett.* **5**, 787–790 (1993)
72. A. Bjarklev, *Optical Fiber Amplifiers: Design and System Applications* (Artech, Norwood, 1993)
73. L. Occhi, *Semiconductor optical amplifiers made of ridge waveguide bulk InGaAsP/InP: Experimental characterization and numerical modeling of gain, phase and noise*, PhD thesis, ETH Zürich (2002)
74. R.J. Manning, D.A.O. Davies, J.K. Lucek, Recovery rates in semiconductor laser amplifiers: Optical and electrical bias dependencies. *Electron. Lett.* **30**, 1233–1235 (1994)
75. F. Girardin, G. Guekos, A. Houbavlis, Gain recovery of bulk semiconductor optical amplifiers. *IEEE Photon. Technol. Lett.* **10**, 784–786 (1998)
76. J. Slovak, C. Bornholdt, U. Busolt, G. Bramann, Ch. Schmidt, H. Ehlers, H.P. Nolting, B. Sartorius, Optically clocked ultra long SOAs: A novel technique for high speed 3R signal regeneration. *Opt. Fiber Commun. Conf. (OFC'04)*, Techn. Digest (Los Angeles, CA, USA, 2004), paper WD4
77. R. Gutiérrez-Castrejón, L. Schares, L. Occhi, G. Guekos, Modeling and measurement of longitudinal gain dynamics in saturated semiconductor optical amplifiers of different length. *IEEE J. Quantum Electron.* **36**, 1476–1484 (2000)
78. A. Kapoor, E.K. Sharma, W. Freude, J. Leuthold, Investigation of the saturation characteristics of InGaAsP-InP bulk SOA. *Proc. SPIE*, vol. 7597 (2010), 759711
79. M. Sugawara, H. Ebe, N. Hatori, M. Ishida, Y. Arakawa, T. Akiyama, K. Otsubo, Y. Nakata, Theory of optical signal amplification and processing by quantum-dot semiconductor optical amplifiers. *Phys. Rev. B* **69**, 235332 (2004)
80. J. Mørk, M.L. Nielsen, T.W. Berg, The dynamics of semiconductor optical amplifiers, modeling and applications. *Opt. Photon. News* **14**, 43–48 (2003)
81. A. Mecozzi, J. Mørk, Saturation induced by picosecond pulses in semiconductor optical amplifiers. *J. Opt. Soc. Am. B* **14**, 761–770 (1997)
82. J. Mørk, A. Mecozzi, Theory of the ultrafast optical response of active semiconductor waveguides. *J. Opt. Soc. Am. B* **13**, 1803–1816 (1996)
83. A. Mecozzi, J. Mørk, Saturation effects in nondegenerated four-wave mixing between short optical pulses in semiconductor laser amplifiers. *IEEE J. Sel. Top. Quantum Electron.* **3**, 1190–1207 (1997)
84. A.V. Uskov, E.P. O'Reilly, M. Laemmlin, N.N. Ledentsov, D. Bimberg, On gain saturation in quantum dot semiconductor optical amplifiers. *Opt. Commun.* **248**, 211–219 (2005)
85. J. Wang, A. Maitra, C.G. Poulton, W. Freude, J. Leuthold, Temporal dynamics of the alpha factor in semiconductor optical amplifiers. *J. Lightw. Technol.* **25**, 891–900 (2007)

86. R. Bonk, T. Vallaitis, J. Guetlein, D. Hillerkuss, J. Li, W. Freude, J. Leuthold, Quantum dot SOA dynamic range improvement for phase modulated signals, *Opt. Fiber Commun. Conf. and Nat. Fiber Opt. Eng. Conf. (OFC/NFOEC'10)*, Techn. Digest (San Diego, CA, USA, 2010), paper OThK3
87. T. Vallaitis, R. Bonk, J. Guetlein, D. Hillerkuss, J. Li, R. Brenot, F. Lelarge, G.H. Duan, W. Freude, J. Leuthold, Quantum dot SOA input power dynamic range improvement for differential-phase encoded signals. *Opt. Express* **18**, 6270–6276 (2010)
88. R. Bonk, G. Huber, T. Vallaitis, R. Schmogrow, D. Hillerkuss, C. Koos, W. Freude, J. Leuthold, Impact of alfa-factor on SOA dynamic range for 20 GBd BPSK, QPSK and 16-QAM signals, *Opt. Fiber Commun. Conf. and Nat. Fiber Opt. Eng. Conf. (OFC/NFOEC'11)*, Techn. Digest (Los Angeles, CA, USA, 2011), paper OML4
89. A. Fiore, A. Markus, Differential gain and gain compression in quantum-dot lasers. *IEEE J. Quantum Electron.* **43**, 287–294 (2007)
90. T. Vallaitis, R. Bonk, J. Guetlein, C. Meuer, D. Hillerkuss, W. Freude, D. Bimberg, J. Leuthold, Optimizing SOA for large input power dynamic range with respect to applications in extended GPON, *OSA Topical Meeting: Access Networks and In-house Communications (ANIC'10)*, Techn. Digest (Karlsruhe, Germany, 2010), paper AThC4
91. P. Runge, Nonlinear effects in ultralong semiconductor optical amplifiers for optical communications: physics and applications, PhD thesis, University of Berlin (TH) (2010)
92. G. Contestabile, A. Maruta, S. Sekiguchi, K. Morito, M. Sugawara, K. Kitayama, Cross-gain modulation in quantum-dot SOA at 1550 nm. *IEEE J. Quantum Electron.* **46**, 1696–1703 (2010)
93. J. Leuthold, R. Bonk, T. Vallaitis, A. Marculescu, W. Freude, C. Meuer, D. Bimberg, R. Brenot, F. Lelarge, G.-H. Duan, Linear and nonlinear semiconductor optical amplifiers, *Opt. Fiber Commun. Conf. and Nat. Fiber Opt. Eng. Conf. (OFC/NFOEC'10)*, Techn. Digest (San Diego, CA, USA, 2010), paper OThI3
94. R. Bonk, C. Meuer, T. Vallaitis, S. Sygletos, S. Ben-Ezra, S. Tsadka, A.R. Kovsh, I.L. Krestnikov, M. Laemmlin, D. Bimberg, W. Freude, J. Leuthold, Single and multiple channel operation dynamics of linear quantum-dot semiconductor optical amplifier, *Proc. 34th Europ. Conf. Opt. Commun. (ECOC'08)*, Brussels, Belgium (2008), paper Th1.C.2
95. S. Koenig, J. Pfeiffle, R. Bonk, T. Vallaitis, C. Meuer, D. Bimberg, C. Koos, W. Freude, J. Leuthold, Optical and electrical power dynamic range of semiconductor optical amplifiers in radio-over-fiber networks, *Proc. 36th Europ. Conf. Opt. Commun. (ECOC'10)*, Torino, Italy (2010), paper Th.10.B.6
96. S. Koenig, M. Hoh, R. Bonk, H. Wang, P. Pahl, T. Zwick, C. Koos, W. Freude, J. Leuthold, Rival signals in SOA reach-extended WDM-TDM-GPON converged with RoF, *Opt. Fiber Commun. Conf. and Nat. Fiber Opt. Eng. Conf. (OFC/NFOEC'11)*, Techn. Digest (Los Angeles, CA, USA, 2011), paper OWT1
97. [http://www.ciphotonics.com/cip\\_semiconductor.htm](http://www.ciphotonics.com/cip_semiconductor.htm)
98. <http://www.kamelian.com/products.html>
99. [http://www.thorlabs.de/Navigation.cfm?Guide\\_ID=2105](http://www.thorlabs.de/Navigation.cfm?Guide_ID=2105)
100. <http://qdlaser.com/product01.html>
101. [http://www.oclaro.com/product\\_pages/TL5000DCJ.html](http://www.oclaro.com/product_pages/TL5000DCJ.html)
102. A. Borghesani, Reflective based active semiconductor components for next generation optical access networks, *Proc. 36th Europ. Conf. Opt. Commun. (ECOC'10)*, Torino, Italy (2010), paper Mo.1.B.1
103. A. Borghesani, I.F. Lealman, A. Poustie, D.W. Smith, R. Wyatt, High temperature, colourless operation of a reflective semiconductor optical amplifier for 2.5 Gbit/s upstream transmission in a WDM-PON, *Proc. 33rd Europ. Conf. Opt. Commun. (ECOC'07)*, Berlin, Germany (2007), paper 6.4.1
104. P. Healey, P. Townsend, C. Ford, L. Johnston, P. Townley, I. Lealman, L. Rivers, S. Perrin, R. Moore, Spectral slicing WDM-PON using wavelength-seeded reflective SOAs. *Electron. Lett.* **37**, 1181–1182 (2001)



# Chapter 13

## Optical Signal Processing for High-speed Data Transmission

Hans-Georg Weber and Reinhold Ludwig

**Abstract** The chapter describes high-speed optical data transmission based on optical time-division multiplexing (OTDM) with the focus on optical signal processing in the key building blocks of OTDM transmission systems. The OTDM transmitter is described including pulse generation, pulse shaping, and modulation of an optical pulse train. The OTDM receiver is discussed for direct detection and coherent detection systems. This includes signal processing using various optical gates, timing extraction devices, and optoelectronic base rate receivers, as well as the operation of phase-diversity homodyne receivers and coherent receivers as OTDM demultiplexers. A final section focuses on combating impairments in fiber links, i.e., using optical signal processing for the compensation of linear and higher order chromatic dispersion and polarization-mode dispersion as well.

### 13.1 Introduction

A most challenging view as regards future optical transmission technology is that optical networks will evolve into “photonic networks,” in which high-speed optical data signals of any bit rate and modulation format will be transmitted and processed from end to end without optical-electrical-optical (O/E/O) conversion. With this view as the target, the transmission technology of optical time-division multiplexing (OTDM) explores the feasibility of high-speed data transmission in fibers in a single wavelength channel. Already in 1993, the first 100 Gbit/s OTDM trans-

---

Hans-Georg Weber (✉)  
Sudetenstrasse 16, 63916 Amorbach, Germany  
e-mail: hans-georg.weber@gmx.de

Reinhold Ludwig  
Picowave Microelectronics GmbH, Möwenweg 17, 12359 Berlin, Germany  
e-mail: ludwig@picowave.de

mission experiment over a 36 km fiber link was reported [1]. Since then, OTDM transmission technology has made a lot of progress towards much higher bit rates and much longer transmission links, as has been described in several review articles [2–6]. OTDM transmission technology succeeded in the transmission of optical data signals at data rates of 1.28 Tbit/s [7–9], 2.4 Tbit/s [9], 5.1 Tbit/s [10, 11], and recently up to 10.2 Tbit/s [12] in a single wavelength channel.

The transmission of high-speed optical data signals in a single wavelength channel is an important task in the development of optical communication systems. The transmission capacity per fiber is given by the number of wavelength-division multiplexing (WDM) channels multiplied by the bit rate per WDM channel, also called TDM bit rate. For very large numbers of WDM channels (e.g., a few thousand) such factors as wavelength management, power consumption, and footprint will probably limit the usefulness of increasing the number of WDM channels and will favor a high TDM bit rate per WDM channel. Another motivation for a high TDM bit rate arises from the effort to reduce the cost per transmitted information bit. Indeed, in the past the TDM bit rate per WDM channel was steadily increased in installed fiber transmission systems. In the early 1990s and in about 1995, respectively, TDM bit rates of 2.5 Gbit/s and 10 Gbit/s were introduced in commercial fiber transmission systems. Since about 2006 commercial systems with a TDM bit rate of 40 Gbit/s have been in operation, and presently the introduction of 100 Gbit/s per WDM channel is being considered.

Commercial systems of today do not use OTDM technology but electrical time-division multiplexing (ETDM) transmission technology. However, the operation speed of ETDM systems is limited for example by the energy consumption. Even if electrical signal processing at 160 Gbit/s would be available, it will be difficult to provide terminal equipment that is cheaper and less energy consuming than the terminal equipment based on optical signal processing at 160 Gbit/s. OTDM receivers perform better than ETDM receivers already at data rates of 80 Gbit/s. ETDM technology must work hard to compete with OTDM systems for instance as regards receiver sensitivity. It is therefore reasonable to see OTDM technology not only as a tool to explore the feasibility of ultra-high-speed data transmission in fibers but also as a technology, which possibly will provide solutions for high-speed data transmission in future transmission systems.

An essential ingredient of OTDM transmission technology is signal processing of high-speed optical data signals. This includes in particular signal processing in the terminal equipment. At the transmitter side, this means the generation and the modulation of an appropriate optical pulse train as well as the multiplexing of low bit rate optical data signals to a high bit rate data signal. At the receiver side, the high bit rate data signal has to be separated into its tributaries and then converted to an electrical signal. The signal processing involved in manipulating the optical pulses appropriately is either an electrically or optically controlled processing of the optical pulses.

Transmission at data rates beyond 160 Gbit/s not only requires appropriate terminal equipment at the transmitter and the receiver but also improved transmission

links including fiber and repeater or amplifier stages. With higher TDM bit rates, data transmission in fibers is more strongly affected by chromatic dispersion (CD), polarization-mode dispersion (PMD), fiber nonlinearity, and by the limited bandwidth of channel filters, routers, repeaters, or amplifiers in the transmission link. One solution to combat these problems is by the application of advanced (multi-state) modulation formats (see also Chap. 8). These advanced modulation formats increase the transmitted bit rate but keep the pulse rate low. For instance, modulation of the phase of an optical pulse allows one to associate several information bits with one pulse (one symbol). This enables a lower pulse rate (symbol rate) for a given bit rate and causes therefore less impairments by the transmission properties of the fiber link. Conversely, these modulation formats need a higher optical signal-to-noise ratio (OSNR), are more sensitive to distortions, and the amount of optical signal processing increases due to the generation and evaluation of the multilevel modulated optical pulses.

Another challenge for OTDM technology is its optimized combination with WDM technology. The bandwidth of each WDM-channel is restricted by the WDM multiplexers and demultiplexers in the system. This restricts the bandwidth of each OTDM signal. Upgrading the data rate per WDM-channel requires data signals with higher spectral efficiency. The installment of high bit rate data signals with high spectral efficiency requires techniques like phase stable multiplexing, polarization multiplexing and again advanced modulation formats. An additional advantage is the combination of OTDM technology with coherent detection technology. Coherent detection technology is compatible with spectrally efficient modulation formats, allows for the mitigation of transmission impairments in the receiver and provides high spectral selectivity as well as high sensitivity.

This chapter discusses optical signal processing for point-to-point transmission. However, an optical network also comprises networking components, such as add-drop multiplexers, 3R-regenerators, or wavelength converters etc. The principal operation of these networking components has been shown so far based on optical signal processing at data rates up to 160 Gbit/s. However, up to now, the reported solutions for these networking components have not shown much promise. A weakness of optical signal processing is the lack of appropriate optical buffers, which seem to be required to realize practical solutions for all-optical networking components. Therefore, the “photonic network” is still a target for the distant future and a guide line for finding innovative solutions.

This chapter is organized as follows: Sect. 13.2 gives a description of OTDM systems. We introduce the so-called “conventional” and the “coherent” OTDM receiver. In Sect. 13.3 we compile some fundamentals of optical signal processing, which will be used in the subsequent sections. This is followed by a discussion of optical signal processing in the OTDM transmitter in Sect. 13.4 and of the “conventional” and “coherent” OTDM receiver in Sects. 13.5 and 13.6, respectively. Section 13.7 deals with optical signal processing for combating impairments due to transmission on the fiber link. Finally, Sect. 13.8 summarizes our conclusions on the present state of optical signal processing associated with OTDM technology.

## 13.2 OTDM Transmission Systems

The principle of an OTDM transmission system is as follows. In an OTDM transmitter,  $N$  optical data signals (called base rate data signals or TDM channels) are optically combined (multiplexed) to one optical bit stream. Each TDM channel has the same bit rate  $B$ . Therefore, the combined (multiplexed) data signal has the aggregate bit rate  $NB$ . The multiplexed data signal with bit rate  $NB$  is transmitted over the fiber link. In the OTDM receiver, the multiplexed data signal is decomposed into the  $N$  tributaries for further signal processing. In order to simplify the discussion of OTDM transmission systems, we describe in the following subsections experiments with special bit rates, namely 40 Gbit/s for the base rate  $B$  and 160 Gbit/s or 1.28 Tbit/s for the OTDM aggregate transmission rate  $NB$ . However, the underlying principles can be scaled to any reasonable bit rate.

### 13.2.1 OTDM Transmission System Using OOK Modulation

Figure 13.1a is a schematic illustration of a 160 Gbit/s OTDM transmission system. It is represented by the three blocks: transmitter, fiber link, and receiver. On the transmitter side, the essential component is an optical pulse source. The repetition frequency of the generated pulse train is assumed to be 40 GHz. In general, the repetition frequency depends on the base data rate (or on the symbol rate, see Sect. 13.4.1), at which the subsequent modulators (MOD) are driven by an electrical data signal (base rate signal). The 40 GHz optical pulse train is coupled into four optical branches, in which four 40 Gbit/s nonreturn-to-zero (NRZ) electrical data signals drive four modulators and generate four 40 Gbit/s optical return-to-zero (RZ) data signals. The simplest modulation format is on-off keying (OOK). A pulse is either transmitted (for a “1”) or not transmitted (for a “0”). The four optical data signals (TDM channels) are combined into a multiplexed 160 Gbit/s optical data signal by bit-interleaving with use of an appropriate delay in the four optical branches. The bit period (minimum pulse separation) of a 40 Gbit/s data signal is 25 ps. In the multiplexed 160 Gbit/s data signal the bit period is reduced to 6.25 ps. Multiplexing (MUX) can be such that all bits of the multiplexed data signal have the same polarization (single polarization signal, SP multiplexing) or adjacent bits have alternating (orthogonal) polarization (AP multiplexing). On the receiver side, the essential component is an optical demultiplexer (DEMUX), which separates the four base rate data signals (tributaries or TDM channels) again for subsequent detection and electrical signal processing. The fiber link requires in general compensation for chromatic dispersion and polarization-mode dispersion, which both depend on the type of single-mode fiber used in the transmission system.

The DEMUX shown in Fig. 13.1 comprises two parts, an optical gate and a clock recovery device. The optical gate is a fast switch with a switching time that is shorter than the bit period (6.25 ps for 160 Gbit/s) of the multiplexed data signal. The clock recovery device provides the timing signal for the optical gate. In Sects. 13.4–13.7

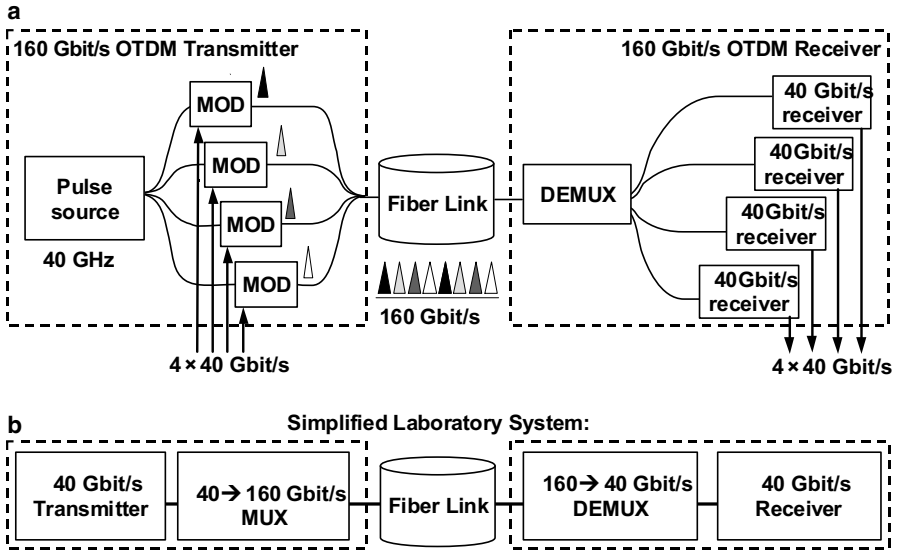


**Fig. 13.1** Schematic view of a 160 Gbit/s OTDM transmission system (a) and of a simplified laboratory system (b)

we discuss the OTDM transmitter, the OTDM receiver, and the fiber transmission line in more detail.

Laboratory systems are frequently simplified systems (see Fig. 13.1b): On the transmitter side, only one modulator is used and combined with the pulse source for a 40 Gbit/s optical transmitter. The generated optical data signal is then multiplexed by a fiber delay line multiplexer (MUX) to a 160 Gbit/s data signal using either SP or AP multiplexing. The internal delay in the MUX needs to be properly chosen to de-correlate the four tributaries. On the receiver side, the DEMUX selects only one 40 Gbit/s tributary, which is detected by one 40 Gbit/s optoelectronic receiver at a given time. In a proper experiment all four tributaries (TDM channels) are measured successively in this way.

### 13.2.2 1.28 Tbit/s OTDM Transmission System with Conventional Receiver

A (simplified) 1.28 Tbit/s OTDM transmission system, comprising the three blocks: transmitter, fiber link and receiver, is schematically illustrated in Fig. 13.2a. The system resembles the 160 Gbit/s transmission system shown in Fig. 13.1b. In particular, the receiver consists of two parts: a demultiplexer and a low bit rate receiver. We call this combination a “conventional” receiver. However, the system depicted in Fig. 13.2a does not use the modulation format on-off keying (OOK) but the mod-

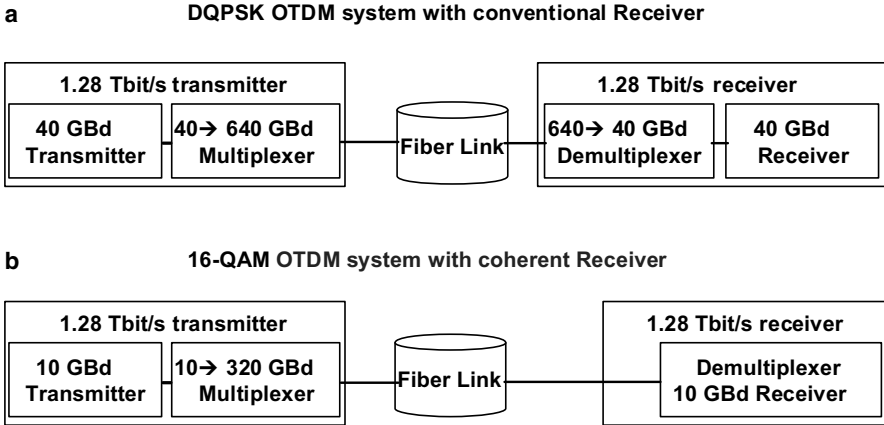


**Fig. 13.2** Schematic view of a 1.28 Tbit/s OTDM transmission system with a conventional receiver (a) and coherent receiver (b)

ulation format differential quadrature phase shift keying (DQPSK). In a DQPSK-system the modulator transmits all pulses, however modulated in the phase with  $n \times \pi/2$ ,  $n \in \{0, 1, 2, 3\}$ . Consequently, in a DQPSK modulated signal, each optical pulse (symbol) carries 1 out of 4 logical states instead of 1 out of 2 logical states as in an OOK-system. In this case one has to take into account that the bit rate (expressed in bit/s) is twice the symbol rate (expressed in baud and often abbreviated by Bd, for details see Sect. 13.4.4). For OOK, the data rate is equal to the symbol rate, whereas for DQPSK the data rate is twice the symbol rate.

1.28 Tbit/s OTDM transmission experiments were first performed using the modulation format OOK [7, 8]. However, the use of DQPSK has the advantage that only half the symbol rate is necessary. That is, the minimum pulse separation of a 1.28 Tbit/s data signal is 0.78 ps for the OOK and 1.56 ps for the DQPSK modulation format. Therefore, the required pulse width is less critical for DQPSK modulation format (see Sect. 13.4.1). Consequently, the 1.28 Tbit/s DQPSK transmission experiment [9] enables a larger transmission span than the before-mentioned OOK transmission experiment. However, the advanced (as compared to OOK) modulation format DQPSK requires additional devices in the transmitter and the receiver for optical signal processing as will be discussed in the following sections.

### ***13.2.3 1.28 Tbit/s OTDM Transmission System with Coherent Receiver***

Figure 13.2b depicts schematically a (simplified) 1.28 Tbit/s OTDM transmission system comprising again the three blocks: transmitter, fiber link, and receiver. However, the system differs by the receiver and the applied modulation format.

The receiver uses “coherent” detection. In coherent detection, the incident signal is demodulated by mixing the incident signal with an optical reference signal (local oscillator, LO) and detecting the resulting beat frequency signals by pairs of balanced photodiodes. The resulting electrical output signals of the coherent detector have to be digitized and postprocessed to decode the incident signal. Coherent detection using a pulsed LO allows for ultra-high speed time-division demultiplexing.

The higher order modulation format used in this system is  $m$ -ary quadrature amplitude shift keying ( $m$ -QAM) with  $m = 16$ . It allows a symbol rate, which is 4 times smaller than the transmitted bit rate. This modulation format will be discussed in Sect. 13.4.4. Transmission of 1.28 Tbit/s 16-QAM modulated data signals has been performed over 480 km dispersion managed fiber (DMF) and over 800 m multimode fiber [13].

### 13.3 Introduction to Optical Signal Processing for OTDM Systems

Before we start discussing optical signal processing in OTDM systems we will compile a few relevant properties of nonlinear optics [14–17]. Light propagation through a dielectric medium can be described by the relation between the polarization  $P(r, t)$  and the electric field  $E(r, t)$  as:

$$P(r, t) = \varepsilon_0 \chi^{(1)} E(r, t) + \varepsilon_0 \chi^{(2)} E(r, t) E(r, t) + \varepsilon_0 \chi^{(3)} E(r, t) E(r, t) E(r, t) + \dots \quad (13.1)$$

Higher order terms are in general not considered. To simplify the expression, we did not indicate explicitly that  $E$  and  $P$  are vectors, that the susceptibilities  $\chi^{(m)}$  with  $m = 1, 2, 3$  are in general tensors of order  $m + 1$ , that the  $\chi^{(m)}$  are also time and space dependent, and that a proper expression requires a convolution integral over time.  $\varepsilon_0$  is the electric permittivity. The rules of linear optics are valid if the susceptibilities  $\chi^{(m)}$  with  $m > 1$  can be neglected. The index of refraction and the attenuation coefficient are related with the real and imaginary part of  $\chi^{(1)}$ , respectively. In an isotropic medium  $\chi^{(1)}$  is a scalar. Conversely, the phenomena of nonlinear optics appear if the susceptibilities  $\chi^{(m)}$  with  $m > 1$  become important. Several optical effects are observed, which do not appear in the regime of linear optics. In particular the superposition of two light signals in the same spatial region may cause one signal to affect the other one. One light signal can be switched or controlled by another light signal. This enables all-optical switching.

Isotropic media have  $\chi^{(2)} \equiv 0$  because of inversion symmetry. For instance, all nonlinear optical effects in optical fibers or semiconductor optical amplifiers are solely due to  $\chi^{(3)}$ . Conversely, crystals (e.g., LiNbO<sub>3</sub>) are typical media showing nonlinear optical effects due to  $\chi^{(2)}$ . The  $\chi^{(3)}$ -dependent processes are also present but are weaker.

The formalism described by (13.1) applies to all materials used for optical signal processing in optical communications. However, the physical mechanism of the nonlinear optical response is different in the various materials. The optical nonlinearity in the fiber has its origin in the electronic polarization and has consequently an ultra-short response time of about  $10^{-15}$  s. Conversely, the optical nonlinearity of the semiconductor optical amplifiers (SOA) has a response time of about  $10^{-10}$  s. The origin of the optical nonlinearity of the SOA is a carrier density effect in the active waveguide. The gain coefficient  $g$  and the refractive index  $n$  of the SOA are a function of the carrier density, i.e., they will change, when the carrier density in the SOA is varied, for example by the injection of an optical wave into the SOA. The dynamics of the changes of  $g$  and  $n$  is important for switching applications of the SOA. The carrier density in the conduction band is almost instantaneously reduced by stimulated emission if an optical pulse having a narrow width ( $\sim 1$  ps) is injected into the SOA. This causes an almost instantaneous change of  $g$  and  $n$ . However, the recovery of the gain and of the index of refraction is governed by several processes with different time constants, which are as slow as some 100 ps depending on the geometry and the operating conditions of the SOA [18–20].

### 13.3.1 Self-phase Modulation (SPM) and Cross-phase Modulation (XPM)

Here we discuss effects due to  $\chi^{(3)}$  in an optical fiber. The same effects appear also in an SOA for example, however, the functional dependencies (the derived equations) differ in some cases, because the tensor components may differ, for instance. The most important effect of  $\chi^{(3)}$  is that the index of refraction  $n$  becomes dependent on the optical power as  $n = n_0 + n_2 P/A$ . Here  $n_0$  is the linear index of refraction determined by  $\chi^{(1)}$ , and  $n_2$  is a quantity proportional to the real part of a tensor component of  $\chi^{(3)}$ . Moreover,  $P$  is the power and  $A$  the cross-sectional area of the light wave injected into the fiber. In a waveguide,  $n_0$  is the effective index of refraction and  $A$  is the effective area.

An optical wave (wavelength in vacuum  $\lambda_0$ ) traveling a distance  $L$  in a medium experiences a phase shift  $\varphi = \varphi(L, t) = -(2\pi n L)/\lambda_0$ . Inserting the nonlinear index of refraction  $n$  gives  $\varphi(L, t) = \varphi_L + \varphi_{NL}$  with the linear phase shift  $\varphi_L = -(2\pi n_0 L)/\lambda_0$  and the nonlinear phase shift  $\varphi_{NL}$ . An exact calculation of  $\varphi_{NL}$  has to take into account, that the optical power decreases along the length  $L$  according to  $P(L) = P(0) \exp(-\alpha L)$  where  $\alpha$  is the attenuation constant. The correct expression for  $\varphi_{NL}$  is obtained if  $L$  is replaced by  $L_{\text{eff}} = \frac{1 - \exp(-\alpha L)}{\alpha}$ . This gives

$$\varphi_{NL} = -\gamma P L_{\text{eff}} \quad (13.2)$$

for the nonlinear phase shift with the nonlinear parameter  $\gamma = (\omega n_2)/(c_0 A)$  and  $P = P(0)$ . Here  $c_0 = \lambda_0 \omega / 2\pi$  is the velocity of light in vacuum and  $\omega$  the angular



frequency of the light wave. The effect that generates the nonlinear phase  $\varphi_{\text{NL}}$  is called Self-Phase Modulation (SPM).

The superposition of several co-propagating optical waves in the same spatial volume leads to the effect of Cross-Phase Modulation (XPM). As an example, we consider two optical waves  $E(\omega_1, P_1)$  and  $E(\omega_2, P_2)$  where  $\omega$  and  $P$  are the angular frequency and power, respectively, and  $\omega_1 \neq \omega_2$ . The nonlinear phase shift, which  $E(\omega_1, P_1)$  experiences due to the presence of  $E(\omega_2, P_2)$ , is

$$\varphi_{\text{NL}}(\omega_1) = -\xi \gamma P_2 L_{\text{eff}}. \quad (13.3)$$

Here  $\xi = 2$  if both waves have the same state of linear polarization and  $\xi = 2/3$  if the two linear polarization states are orthogonal to each other. This polarization dependence is due to the tensor properties of  $\chi^{(3)}$ .

SPM and XPM have many applications in optical signal processing. SPM is involved in the generation of optical solitons, various kinds of pulse shaping, and supercontinuum generation. XPM finds many applications, in particular in optically controlled switching of optical data signals. We will discuss various applications in the following sections. SPM and XPM also cause very detrimental effects in the transmission of data signals over an optical fiber. XPM causes crosstalk in WDM systems between data signals transmitted at different wavelengths, and SPM causes a chirp of optical pulses and a broadening of the spectra of optical pulses.

A particularly interesting effect of SPM in combination with chromatic dispersion of the optical fiber is the generation of solitons. An optical pulse traveling along an optical fiber in general continuously changes its shape, because its constituent frequency components travel at different velocities due to group velocity dispersion of the fiber ( $n = n(\omega)$ ). Consequently the different frequency components of the pulse experience different linear phase shifts  $\varphi_{\text{L}}$ . In addition, because of the effect of  $\chi^{(3)}$ , the parts of the pulse having high power (e.g., the pulse peak) and the parts having low power (e.g., the pulse wings) experience different nonlinear phase shift  $\varphi_{\text{NL}}$ . The interplay between SPM and chromatic dispersion of the fiber can therefore result in pulse compression or increased pulse spreading depending on the magnitudes and signs of both effects. It is also possible that both effects compensate each other if the power and shape of the pulse have appropriate values. An optical pulse with this property travels along the fiber without ever altering its shape. This pulse is called a fundamental or first-order soliton. The fundamental soliton has a  $\text{sech}^2$  pulse shape and the following relation holds

$$N^2 = \gamma P_0 (T_0)^2 / |\beta_2|, \quad (13.4)$$

where  $P_0$  is the peak power of the pulse,  $T_0$  the pulse width,  $\gamma$  the nonlinear parameter,  $\beta_2$  the group velocity dispersion parameter and finally  $N = 1$  corresponds to the fundamental soliton while higher order solitons have  $N = 2, 3, \dots$ . However, the shape of the higher order solitons changes periodically while they travel along the fiber. Solitons have many applications in optical signal processing. In Sect. 13.4.2 we describe their use for a pulse compressor to generate fs-pulses.

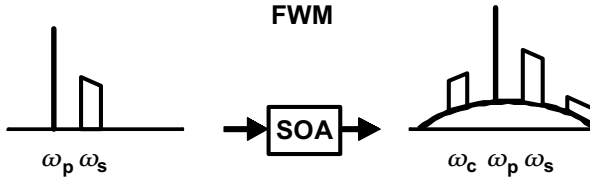


**Fig. 13.3** Four-wave mixing in an SOA. The output spectrum shows the FWM-components superimposed on the background of amplified spontaneous emission

### 13.3.2 Four-Wave Mixing (FWM)

The term with the susceptibility  $\chi^{(3)}$  in (13.1) leads also to the generation of new optical waves with frequencies other than those of the injected optical waves. For instance, the mixing of three optical waves generates field components with the sum and difference frequencies of the injected optical waves. Not all of these newly generated optical waves are of interest for applications in optical signal processing. However, the effect of Four-Wave Mixing (FWM) has gained particular interest. FWM is the wave mixing effect by which three incident optical waves with frequencies  $\omega_1, \omega_2, \omega_3$  and with  $\omega_1, \omega_2 \neq \omega_3$  generate a new wave with frequency  $\omega_4$ , which is given by  $\omega_4 = \omega_1 + \omega_2 - \omega_3$ . A special case is the so-called nearly degenerate FWM in which  $\omega_1 = \omega_2, |\omega_1 - \omega_3| \ll \omega_1$  and  $\omega_4 = 2\omega_2 - \omega_3$ . We discuss this case in more detail in the following and assume  $\omega_1 = \omega_2 = \omega_p$  and  $\omega_3 = \omega_s$  with  $E(\omega_p, P_p)$  and  $E(\omega_s, P_s)$  being the pump and the signal wave, respectively. Both waves are co-propagating with the same state of linear polarization and are injected into a medium with the susceptibility  $\chi^{(3)}$ , for example an SOA. These waves generate the conjugate wave  $E(\omega_c, P_c)$  where  $\omega_c = 2\omega_p - \omega_s = \omega_p + \Delta\omega$  with  $\Delta\omega = \omega_p - \omega_s$ . In Fig. 13.3, we assume  $\omega_p < \omega_s$ . Calculations show that  $E(\omega_c, P_c)$  is proportional to the conjugate complex of  $E(\omega_s, P_s)$ :

$$E(\omega_c, P_c) \propto E(\omega_p, P_p)E(\omega_p, P_p)E^*(\omega_s, P_s). \quad (13.5)$$

If  $E(\omega_p, P_p)$  is a monochromatic wave, the spectrum of  $E(\omega_c, P_c)$  is an inverted replica of the spectrum of  $E(\omega_s, P_s)$  shifted in frequency by  $2(\omega_p - \omega_s) = 2\Delta\omega$ . An optical wave is also generated with  $\omega = 2\omega_s - \omega_p = \omega_s - \Delta\omega$ , which has similar properties as  $E(\omega_c, P_c)$  if we interchange  $E(\omega_p, P_p)$  and  $E(\omega_s, P_s)$ .

An efficient generation of the optical wave  $E(\omega_c, P_c)$  requires so-called phase matching. The optical waves in (13.5) are each associated with a propagation constant  $\beta = \omega n_0/c_0$  in the waveguide. The propagation constants  $\beta_c, \beta_p,$  and  $\beta_s$  have to fulfill the condition:  $\beta_c = 2\beta_p - \beta_s$ , which follows from (13.5), where the propagation constant  $\beta$  of the complex conjugate field  $E^*(\omega_s, P_s)$  has to be chosen with negative sign. This condition is required for a constructive generation of the optical wave  $E(\omega_c, P_c)$  along the whole interaction length  $L_{\text{int}}$  in the medium. More generally, the phase matching condition is given by  $|\Delta\beta L_{\text{int}}| \ll 1$  with  $\Delta\beta = 2\beta_p - \beta_s - \beta_c$ . Thus, the short interaction length  $L_{\text{int}}$  in SOAs enables still efficient FWM also for  $\Delta\beta \neq 0$ .

The application of FWM in optical communications includes wavelength conversion of optical data signals, demultiplexing of optical data signals, parametric amplification, and dispersion compensation by phase conjugation. Some of these applications will be discussed in the following sections. FWM has also very detrimental effects for transmission of data signals over an optical fiber. FWM causes crosstalk in WDM systems between data signals transmitted with different wavelengths, and it also causes the so-called ghost pulses in the transmission of high bit rate data signals.

## 13.4 OTDM Transmitter

This section deals with the OTDM transmitter including the OTDM transmitter of the 1.28 Tbit/s DQPSK transmission system as well as the OTDM transmitter of the 1.28 Tbit/s 16-QAM transmission system, which are both depicted in Fig. 13.2. The subsystems of an OTDM transmitter comprising the pulse source, the modulator and the multiplexer are schematically shown in Fig. 13.4.

The subsystems have to be adjusted to each particular transmission system. For instance, the pulse source in Fig. 13.4 comprises three parts: the optical pulse generator, the pulse compressor, and the pulse cleaner. This is the pulse source, which is needed in the 1.28 Tbit/s DQPSK transmission system. The OTDM transmitter of the 1.28 Tbit/s 16-QAM transmission system needs a simpler pulse source, which comprises only the optical pulse generator. The pulse compressor and the pulse cleaner are missing in this case. The reason is that the transmitted symbol rate for the 16-QAM modulation format is, by a factor of two, smaller than the symbol rate for the DQPSK modulation format. Consequently, the requirements on the pulse source (see Sect. 13.4.1) are reduced and pulse compression is not necessary. It is evident, that also the modulators for the 16-QAM or DQPSK modulation format are different as we will see in Sect. 13.4.4.

### 13.4.1 Optical Pulse Generator

An optical pulse source appropriate for an OTDM transmitter has to satisfy several conditions:

The pulse width  $\Delta t$  (Full-Width Half-Maximum, FWHM) must be less than  $1/3$  of the pulse separation of the multiplexed data signal. This provides sufficient separation of adjacent optical pulses to prevent coherent superposition of the pulse slopes and consequently disturbing effects [21, 22].

The optical pulses should preferably have a  $\text{sech}^2$  pulse shape (in the temporal domain) and an optical spectrum with the spectral width (FWHM)  $\Delta\nu$  close to the transformation limit leading to a time-bandwidth product  $\Delta\nu \cdot \Delta t = 0.3148$ . The  $\text{sech}^2$  pulse shape is especially attractive as its time-bandwidth product is smaller than that of pulses with Gaussian shape and because the pulse slopes are steeper

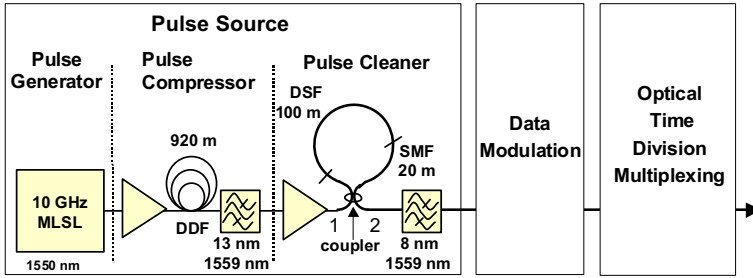


**Fig. 13.4** Schematic view of the transmitter of an OTDM system. Only the pulse source, comprising the pulse generator, the pulse compressor and the pulse cleaner, is shown in detail. The pulse compressor and the pulse cleaner are required in particular transmission systems only

than for example for Lorentzian-shaped pulses. Both properties allow applications which require high spectral efficiency. Moreover, for high pulse peak powers the formation of solitons is expected (see Sect. 13.3.1).

The optical pulse source needs to generate a pulse train with a well-controlled repetition frequency at the standard clock rates near 10 GHz or 40 GHz and it needs to have long-term stability to avoid frequency drifts. The standard clock at 10 GHz is defined by the standard transmission module (STM64) to be 9.95328 GHz. Forward error correction (FEC) schemes with some data overhead are often introduced to relax the requirement on the tolerable bit error rate from  $10^{-9}$  to  $10^{-3}$  for experimental systems. Because of the overhead the required data rate increases by 7 to 11 % depending on the specific correction scheme used. Consequently the pulse repetition frequency has to be adjusted correspondingly.

The optical pulse train needs to have a high extinction ratio which is the ratio of the optical power at the pulse peak to the optical power of a constant background. This is particularly important if pulse carving (i.e., cw-lasers externally modulated) is used for pulse generation. Some pulse sources produce trailing pulses (a small accompanying pulse) or a pulse pedestal. The suppression of trailing pulses and the pulse pedestal is very important to achieve a high signal-to-noise ratio.

The generated pulse train needs to have a low timing jitter and a low amplitude noise. The timing jitter describes deviations of the pulse position from the expected time slot. This is particularly disturbing if a pulse train is multiplexed to a high bit rate data signal. In the 1.28 Tbit/s DQPSK system described above a symbol rate of 640 GBd requires a timing jitter of less than 65 fs.

The pulse generator in Fig. 13.4 is a mode-locked solid-state laser (MLSL) generating a 10 GHz train of optical pulses which have a pulse width of 2.0 ps. The MLSL consists of a diode-pumped, solid-state erbium-glass passively mode-locked laser with a semiconductor saturable absorber as mode-locker. The cavity design provides stable fundamental mode-locking, resulting in optical pulses with low jitter ( $< 100$  fs) [23].

Besides the MLSL other pulse sources have also been used for high bit rate transmission experiments including mode-locked laser diodes (MLLD) either as exter-

nal cavity devices (e.g., [24–26]) or monolithically integrated ones (e.g., [27, 28]), mode-locked fiber lasers (MLFL) (e.g., [29–31]), and cw-lasers externally modulated (pulse carving) for example by an electro-absorption modulator (e.g., [32, 33]). For WDM/OTDM applications, a multi-wavelength pulse source is of particular interest, and such a pulse source is obtained by supercontinuum generation (SC-pulses) (e.g., [34]). In this case, a high power pulse can generate a supercontinuum spectrum and spectral slicing provides the multi-wavelength pulse source.

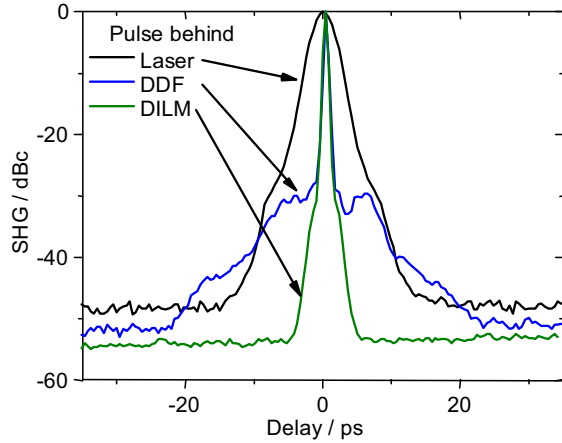
In general the optical pulse sources do not fulfill all of the requirements described above, and as a consequence further improvements are necessary. For instance, the MLSL has a sufficiently low timing jitter but an insufficient pulse width for the 1.28 Gbit/s DQPSK transmission experiment considered above. In this case the symbol rate is 640 GBd and consequently the pulse separation is 1.56 ps. A pulse width (FWHM) of less than 0.52 ps is required. The MLSL does not provide this pulse width. Therefore, the pulses of the MLSL are improved by a pulse compressor and a pulse cleaner as depicted in Fig. 13.4.

### 13.4.2 Optical Pulse Compressor and Pulse Cleaner

There are several methods for optical pulse compression. For fiber optic communication applications the most common technique is adiabatic soliton compression using a dispersion-decreasing fiber (DDF) [35–39]. We restrict our discussion to the soliton pulse compressor illustrated in Fig. 13.4. The soliton pulse compressor uses a particular property of optical solitons mentioned in (13.4). For the fundamental soliton ( $N = 1$ ), (13.4) can be written as  $(P_0 T_0) T_0 = \beta_2 / \gamma$  with  $P_0$  the peak power of the soliton,  $T_0$  the width of the soliton (the FWHM is  $\Delta t = 1.763 T_0$ ),  $\gamma$  the non-linearity parameter of the fiber, and  $\beta_2$  the group-velocity dispersion parameter of the fiber.  $\beta_2$  is related to the fiber dispersion parameter  $D$  by:  $D = -(2\pi c_0 / \lambda^2) \beta_2$  (see Sect. 13.7.2). A soliton propagating in a lossless ( $P_0 T_0 = \text{constant}$ ) fiber remains a soliton even if  $T_0$  decreases as  $\beta_2$  gets smaller. In a dispersion-decreasing fiber the soliton develops to a pulse with narrower pulse width  $T_0$  and increased peak power  $P_0$ . Changes of  $\gamma$  are much lower than those of  $\beta_2$  over the length of the DDF. An experimental example of pulse compression is shown in Fig. 13.5.

In this example the length of the DDF is 920 m and the dispersion  $D$  decreases linearly from 10 ps/(nm km) to 0.6 ps/(nm km). Thus, a compression ratio of 17 is expected. At the input of the compressor an optical pulse is amplified to sufficient optical power to generate a fundamental soliton. The optical filter at the output of the compressor suppresses the Amplified Spontaneous Emission (ASE) of the high-power optical amplifier. Moreover, the center wavelength of the optical filter is slightly shifted as a consequence of a wavelength shift in the compression operation. The experimental results reveal a compression factor of 13. There are several reasons for this discrepancy from the expected compression factor. In particular, higher order dispersion and the power dissipation in the DDF cause deviations from an ideal pulse compressor. This is also indicated by the pulse pedestal in Fig. 13.5.

**Fig. 13.5** Autocorrelation traces of OTDM pulse source after pulse generator (laser), compression stage (DDF), and pulse cleaning (DILM)



The imperfections of the pulse compressor produce a narrow pulse with a pedestal. In a next step, the pulse pedestal has to be removed by use of the pulse cleaner. At high bit rate transmission, the most common method is pedestal reduction by a dispersion-imbalanced loop mirror (DILM, also called DI-NOLM) (e.g., [40–42]). This device has the configuration of a nonlinear optical loop mirror (NOLM) or all-fiber-based Sagnac interferometer [43]. It is constructed by connecting a long piece of fiber to the two output ports of a fiber coupler to form a loop. In Fig. 13.4 (pulse cleaner) the input ports of the coupler are indicated by 1 and 2. The coupler used here is a 50 : 50 fiber coupler. An optical pulse at the input (port 1) of the NOLM is split into two equal components in the fiber coupler, one left-circulating in the loop and the other right-circulating in the loop. After a round trip, these two pulse components meet again at the coupler, interfere with one another and exit the NOLM in one or both of the two coupler ports 1 and 2, depending on the phase difference  $\Delta\varphi = (\varphi_L + \varphi_{NL})_{\text{right}} - (\varphi_L + \varphi_{NL})_{\text{left}}$  of right- and left-circulating pulses after a round trip. These phases comprise a linear phase  $\varphi_L$  and a nonlinear phase  $\varphi_{NL}$  as discussed in Sect. 13.3.1. In the NOLM, the transmittance (from port 1 to port 2) is given by  $T = P_{\text{out}}/P_{\text{in}} = (1/2)(1 - \cos \Delta\varphi)$ , where  $P_{\text{in}}$  is the input power at port 1 and  $P_{\text{out}}$  is the output power at port 2. In the NOLM we have  $\Delta\varphi = 0$  and therefore  $T = 0$  because the NOLM is symmetric for both round trips. The NOLM reflects the incoming pulse totally like a mirror [43]. An output signal is only present if one of the left- and right-circulating signal components exhibits a different  $\varphi_{NL}$  which is realized in the DILM arrangement.

Contrary to an NOLM, in the DILM the fiber connected to the coupler comprises two fiber pieces with different chromatic dispersion (dispersion-imbalance). The set-up in Fig. 13.4 uses 100 m DSF and 20 m SMF. The DSF (dispersion-shifted fiber) has a very low dispersion at the considered wavelength as compared to the SMF (standard single-mode fiber, for details see Sect. 13.7.1). Because of this asymmetry in the DILM, the left- and right-circulating pulse components are very different when arriving at the coupler after one round trip. The left-circulating pulse com-

ponent propagating first through the low-dispersion fiber (DSL) is not significantly broadened, keeps its high peak power over the whole length of the DSL, and accumulates a large  $\varphi_{\text{NL}}$ . Conversely, the right-circulating pulse is immediately broadened in the strong dispersion fiber SMF, its peak power is strongly reduced when it passes the DSF, and it accumulates a small  $\varphi_{\text{NL}}$  only. The linear phase shift is the same for both pulse components. A transmittance  $T = 1$  is obtained if the power of the input pulse into the DILM is properly adjusted to a phase difference  $\Delta\varphi = \pi$  between both components. However, this applies to the narrow pulse contribution only and not to the pulse pedestal. The power in the pulse pedestal is always too low to significantly take part in the nonlinear interaction along the fiber. For the pedestal the phase difference is  $\Delta\varphi = 0$ , and the pedestal is reflected.

An important requirement for the pulse compression and pulse cleaning units is to preserve the phase coherence of the pulse train as required for the generation of phase-modulated data signals. The following subsection describes techniques to assure the phase coherence.

### 13.4.3 Characterization of Optical Pulses

The characterization of the generated pulse train is essential for a successful transmission at high data rates. A convenient technique to characterize the pulses in the time domain is a photodiode and an electrical sampling oscilloscope. An optical pulse with a pulse width of  $\Delta t = 1$  ps requires a detector bandwidth of more than 500 GHz for a reasonable recovery of the pulse shape. Today, the fastest photodiodes and electrical sampling systems available do not provide this bandwidth.

An alternative is the application of the optical sampling technique. Here a fast optical gate samples the signal directly in the optical domain. This technique enables a bandwidth of 500 GHz and beyond [44]. The optical sampling technique is a direct application of optical signal processing technology, which was developed in conjunction with the development of OTDM transmission systems. Several of the optical gates initially developed for OTDM-demultiplexers (see Sect. 13.5.2) have also been applied as optical sampling gates. In addition, the techniques of time extraction (see Sect. 13.5.3) and coherent signal detection (see Sect. 13.6) have also been applied in optical sampling systems. It is obvious that the techniques for detection of high bit rate data signals can also be used for the characterization of high-speed data signals.

Autocorrelation measurements provide a convenient technique to estimate the pulse width in the time domain if the pulse shape is known. In this measurement a pulse is superimposed by its delayed replica in a nonlinear crystal for second harmonic generation (SHG) [45]. A related but more advanced technique is frequency-resolved optical gating (FROG) [46]. This technique provides, in addition to the width, the chirp of the optical pulses which characterizes the spectral distribution within a pulse. In general it is desirable to generate optical pulses with zero chirp because these pulses have minimum pulse width.

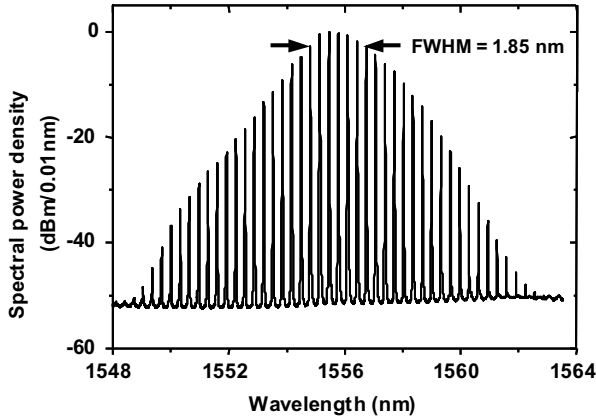


**Fig. 13.6** Optical spectrum of OTDM pulse source (monolithically integrated mode-locked laser diode)

Next to measurements in the time domain, there are also measurements in the frequency domain. Figure 13.6 shows the optical spectrum (mode comb spectrum measured with 0.01 nm resolution) of a 40 GHz pulse train (pulse width 1.8 ps) generated by a monolithically integrated MLLD.

A clean mode-comb structure is an indication for the preservation of the coherent phase relation in an optical pulse train. A small linewidth (i.e., the width of the narrow lines) and a large contrast ratio of the mode comb indicate a pulse train with low phase and amplitude noise. If phase modulation formats such as DPSK or DQPSK are used, it is mandatory that this spectrum has a long-term stability in the wavelength position as well which meets the requirements for the phase-demodulator in the receiver (see Sect. 13.5.4). This is a problem frequently encountered with MLFLs: These lasers operate with harmonic mode locking and long-term stability is a critical issue [47].

The noise of the pulse train comprises amplitude noise and phase noise. A frequently used method to estimate the timing jitter is the measurement of the single-sideband (SSB) phase noise. The SSB phase noise level per 1 Hz bandwidth relative to the carrier,  $L(f)$ , can be measured using a photo detector and an RF-spectrum analyzer. From  $L(f)$ , the RMS timing jitter of the pulse source can be calculated [48].

#### ***13.4.4 Modulation of an Optical Pulse Train***

The pulses of an optical pulse train need to be modulated for the transport of information. An optical pulse can be modulated in amplitude, phase, polarization and carrier frequency [49]. In the various applications one uses either one or a combination of these methods to optimize the system design in view of throughput, link budget, OSNR margin, nonlinearity, spectral efficiency, and cost. However, espe-



cially for high-speed systems it is very difficult to achieve clean optical multistate data signals with analog electrical driving signals. Therefore, sophisticated modulator structures have been developed which can be driven with use of binary data signals. In the following, we will discuss amplitude and phase modulation only, which are the most frequently applied techniques and which were both used in the systems considered in Fig. 13.2. Modulation of polarization and carrier frequency including a comparison of the various formats are considered in [49, 50].

The simplest modulation format is amplitude shift keying (ASK). In binary ASK (2-ASK or on-off keying, OOK), the pulse train passes a modulator having a transmittance  $T = P_{\text{out}}/P_{\text{in}}$ , which is switched between  $T = 1$  and  $T = 0$  by an electrical data signal. A convenient description is to represent the operation of the modulator by a set of numbers  $\{a_k\}$  by which the optical pulses are multiplied. For 2-ASK there are only two values for  $\{a_k\}$ :  $a_1 = 1$  and  $a_0 = 0$ . Each optical pulse (symbol) carries 1 out of 2 logical states, i.e., the pulse in a given time slot represents a “1” for  $T = 1$  and it represents a “0” for  $T = 0$ . In 4-ary ASK (4-ASK), the transmittance can be switched between  $T = 1$ ,  $T = 2/3$ ,  $T = 1/3$  and  $T = 0$ . In other words, the operation of the modulator is represented by  $\{a_k\}$ , where the  $a_k$  are the numbers 1,  $2/3$ ,  $1/3$ , 0, which the pulses are multiplied with. Each optical pulse carries 1 out of 4 logical states 00, 01, 11, 10 and represents 2 bits (Grey-coded). In this example the transmitted bit rate is twice the pulse rate (symbol rate). In an  $n$ -ASK-system with  $n = 2^k$  the bit rate is  $k$  times the symbol rate. We will often use the symbol rate, which is expressed in “baud,” abbreviated Bd. The demodulation of a 2-ASK-modulated data signal needs a photo detector and a simple (one-level) decision gate. The demodulation of a 4-ASK-modulated data signal requires a more complicated decision gate, and a higher signal-to-noise ratio is required for a good separation of the pulse power levels. This is even more problematic for  $n$ -ASK with  $n > 4$ .

In phase shift keying (PSK) modulation format the phase is digitally modulated by a phase modulator. For instance, in  $n$ -PSK the operation of the modulator is described by multiplying the pulses with the set of numbers  $\{a_k\}$  where  $a_k = \exp(j\varphi_k)$  and  $k = 1, 2, \dots, n$ . For  $n = 2$  the  $\{a_k\}$  are obtained with  $\varphi_1 = 0$  and  $\varphi_2 = \pi$ , and in the 4-PSK case the corresponding phases are  $\varphi_k = 0, \pi/2, \pi, 3\pi/2$ . Sometimes, for instance in Fig. 13.7, we use the values  $a_k = \exp(j\varphi_k)$  with  $\varphi_k = \pi/4, 3\pi/4, 5\pi/4, 7\pi/4$  in 4-PSK because a constant phase shift is allowed. Consequently, in 2-PSK each pulse carries 1 out of 2 logical states, and in 4-PSK each symbol (optical pulse) carries 1 out of 4 logical states. However, PSK is not so common in optical communication systems today because the receiver needs the reference to an absolute phase value. It is more common to use differential phase shift keying modulation formats instead and to have a receiver employing delay demodulation or differential detection. Differential binary phase shift keying (DBPSK or simply DPSK) encodes information on the binary phase change between two adjacent pulses. A “1” bit is encoded onto a  $\pi$  phase change, whereas a “0” is encoded by the absence of a phase change of two adjacent pulses. The encoding is similar in DQPSK, where the phase values between two adjacent pulses are  $\varphi = 0, \pi/2, \pi, 3\pi/2$ . For a given modulation format, the possible states of modu-

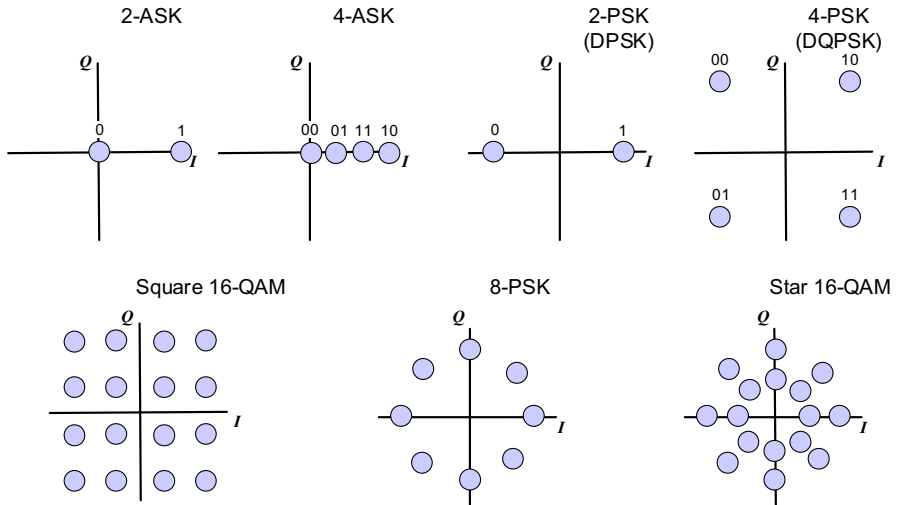


**Fig. 13.7** Constellation diagrams for various modulation formats

lation are depicted in the so-called constellation diagram. This diagram represents the modulation states by the numbers  $\{a_k\}$ , which the modulator can “multiply” to the transmitted pulses. In general,  $\{a_k\}$  are complex numbers and the constellation diagram is a representation of  $\{a_k\}$  in the complex plane. The real axis is called the in-phase ( $I$ ) component and the imaginary axis is called the quadrature-phase ( $Q$ ) component. Figure 13.7 shows the constellation diagrams of a number of modulation formats including 2-ASK, 4-ASK, 2-PSK, DPSK, 4-PSK, DQPSK, 8-PSK, and two other modulation formats described below, see also Chap. 8, Sect. 8.1.2.

For ASK, all  $\{a_k\}$  are real and lying on the  $I$ -axis. For PSK and DPSK, all  $\{a_k\}$  are represented by  $\{A \exp(j\varphi_k)\}$  where  $A$  is a real and constant number. For 2-PSK and DPSK the phases in Fig. 13.7 are set to  $\varphi_k = 0, \pi$ , and for 4-PSK (or DQPSK) the phases are set to  $\varphi_k = \pi/4, 3\pi/4, 5\pi/4, 7\pi/4$ .

Amplitude modulation and phase modulation can be combined into one modulation format which is called quadrature amplitude modulation (QAM). In this modulation format the constellation points are distributed over the full complex  $IQ$ -plane. Since the distance between the constellation points represents the decision space and therefore the immunity against noise and other distortions, one tries to optimize the QAM for maximum distance between the constellation points, which would lead to an arrangement with equilateral triangles in the  $IQ$ -plane. However, up to now this has not been shown experimentally.

Figure 13.7 also shows the constellation diagram of the modulation format square 16-QAM. The modulation states in this format are arranged in a Cartesian grid. This QAM-type is frequently used in mobile communications but it is difficult to realize such a grid for high-speed operation in the optical regime. Therefore, sometimes the star 16-QAM grid structure is chosen, which is easy to realize experimentally by combining the 8-PSK modulation format ( $\{a_k\}$  with  $a_k = \exp(j\varphi_k)$ ) and

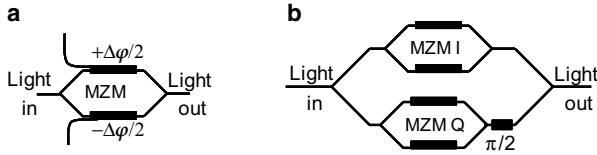


**Fig. 13.8** Schematic of a Mach-Zehnder modulator (a) and an  $IQ$  modulator (b)

$\varphi_k = k\pi/4, k = 0, \dots, 7$ ) and the 2-ASK modulation format ( $\{a_n\}$  with  $a_n = n/2$  and  $n = 1, 2$ ) to one modulation format  $\{a_n \exp(j\varphi_k)\}$ .

Next, we will discuss how the modulation formats described above are realized by modulators. Today two basic modulator technologies are widely used in OTDM systems: electroabsorption modulators (EAMs) and Mach-Zehnder modulators (MZMs). EAMs work by the principle of absorption whereas MZMs work by the principle of interference. EAMs predominantly modulate the amplitude whereas MZMs can be used to modulate all quantities of the optical field. Here, we discuss the MZM only, while EAMs are treated in Chap. 6, Sect. 6.1.2 for example.

The generic set-up of a push-pull operated MZM is shown in Fig. 13.8a. This modulator comprises a Mach-Zehnder interferometer with an electro-optic phase modulator (linear electro-optic effect, see also Chap. 6) in each branch of the interferometer. The whole structure is implemented using optical waveguides fabricated in  $\text{LiNbO}_3$ . The incoming light is split into two paths at an input coupler. In both paths the optical fields experience a phase change due to a refractive index change induced by electric fields (modulation voltages plus a DC voltage to adjust the desired operation point). In the output coupler the signals from both paths interfere. The output signal depends on the phase difference  $\Delta\varphi$  accumulated in the two interferometer arms. Push-pull-operation means, that the phase change is  $+\Delta\varphi/2$  in one path and  $-\Delta\varphi/2$  in the other path. Depending on the applied electrical voltage, the interference varies from destructive to constructive. The push-pull-operated Mach-Zehnder modulator offers several advantages, for example a chirp-free amplitude modulation or a nearly perfect  $\pi$  phase shift in DPSK modulation if the modulator is biased at zero transmission and driven by two times the “ $\pi$ ”-switching voltage [51, 52].

In principle, the Mach-Zehnder-modulator can generate all modulation states in the  $IQ$ -plane including the DQPSK modulation format. However, it is common to use the so-called nested MZM (nMZM) or  $IQ$  modulator for DQPSK modulation because it allows simpler and in particular binary driving signals [49, 53, 54]. An  $IQ$  modulator is depicted in Fig. 13.8b. It comprises an outer MZM structure with an “inner” push-pull-operated MZM in each branch and with a constant phase difference of  $\pi/2$  between both branches of the outer MZM. The two inner MZM generate binary PSK signals with the phase states  $\varphi = 0, \pi$ . Because of the constant phase shift of  $\pi/2$  in one interferometer branch one obtains the phase states  $\varphi = \pi/2, 3\pi/2$  as well.

The  $IQ$  modulator is the appropriate modulator for the 1.28 Tbit/s DQPSK transmission system shown in Fig. 13.2a. A different modulator is needed in the

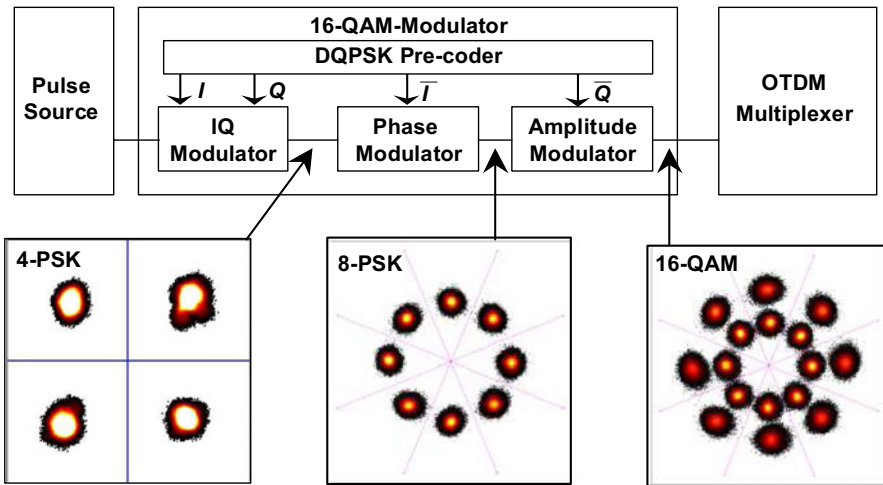


**Fig. 13.9** Schematic view of a modulator for the star-16-QAM modulation format and the constellation diagrams for the cascaded modulators

1.28 Tbit/s 16-QAM transmission system illustrated in Fig. 13.2b. This difference in the modulators is the main difference in the transmitters of both transmission systems. The modulator used in the 1.28 Tbit/s 16-QAM transmission system is realized by a concatenation of three modulators (see Fig. 13.9) using the star 16-QAM grid structure which is a combination of the 8-PSK and the 2-ASK modulation format. 8-PSK modulation is obtained by the concatenation of an  $IQ$  modulator and a binary phase modulator. In the experiment, the four electrical driving signals for the modulators (two signals for the  $IQ$  modulator) were generated by pseudo random bit sequences from a 4-channel PRBS pattern generator.

In principle it is possible to realize even more complicated modulation formats including  $m$ -ary phase shift keying ( $m$ -PSK) and  $m$ -ary quadrature amplitude shift keying ( $m$ -QAM) by using either sophisticated electrical driver circuits for the  $IQ$  modulator or cascaded  $IQ$ -, phase- and amplitude modulators (8-PSK, star 16-QAM). However, these modulation formats need a very high optical signal-to-noise ratio (OSNR). Recently, a theoretical study of multilevel modulation formats has been published [50]. This study shows, that the 16-QAM modulation format performs much worse than a so-called polarization-switched QPSK (PS-QPSK) modulation format. At present, it is very difficult to predict the best modulation format.

### 13.4.5 OTDM-multiplexer

In real OTDM systems, different data signals are combined with a delay (Fig. 13.1a) to provide a multiplexed data signal. An example of such a “real multiplexer” is

reported in [55, 56]. This multiplexer enables the multiplexing of eight different 20 Gbit/s OOK data signals to one multiplexed 160 Gbit/s OOK data signal by using an integrated planar lightwave circuit. Yet another “real multiplexer” is reported in [57]. It provides independent modulation of all TDM-channels and optical phase alignment between adjacent bits. We have to note here that in these “real” systems in general the multiplexer and the modulators constitute a single unit.

Most laboratory experiments are performed using “test multiplexers,” which combine several replicas of one data signal with different relative delays to a high bit rate test signal as already indicated in Fig. 13.1b. A schematic set-up of a “test multiplexer” (MUX) for multiplexing the symbol rate from 40 GBd to 160 GBd is shown in Fig. 13.10. The MUX comprises two stages with a multiplexing factor of two for each stage. Multiplexing the symbol rate from 40 GBd to 640 GBd requires four stages. Each stage has the configuration of a Mach–Zehnder interferometer with a relative delay of an odd multiple of  $(1/2)T_B$  where  $T_B$  is the period of the symbol rate of the signal at the input of the stage.

The MUX is realized by using  $2 \times 2$  optical couplers and optical delay lines either as fiber devices or as planar lightwave circuits. The set-up illustrated in Fig. 13.10 is a fiber-based device. The lower branch of the interferometer configuration includes an adjustable free space optical delay line ( $\approx 200$  ps), a polarization controller ( $\lambda/4$ ,  $\lambda/2$ ,  $\lambda/4$  plates), and a shutter. These tools enable a precise adjustment of the relative delay and of the polarization of the output signal, i.e., the adjustment for a single polarization signal or an alternating polarization signal. There is an additional attenuator in the upper branch to compensate for the loss in the free beam optics in the lower branch to provide constant amplitude for all pulses.

An important requirement for these “test multiplexers” is that there is strong decorrelation between adjacent bits of the multiplexed data signal. This is obtained by employing a delay time which is long compared to the period of the symbol rate of the input signal (which is not possible in general if a planar lightwave circuit is used). Laboratory experiments are usually performed using PRBS (pseudo-random bit stream) data signals at the base rate. The PRBS structure is preserved if the relative delay in one stage equals half the word length of the PRBS word at the input of this stage. For a PRBS word with  $2^7 - 1 = 127$  bit, this gives a delay time of  $(127/2)T_B = 1.595$  ns for an input STM-rate of 39.813 GBd. This delay corresponds to about 32 cm fiber in the first stage and 16 cm in the second stage in Fig. 13.10. A PRBS word length of  $2^{15} - 1$  corresponds already to a delay length of 82 m. Consequently the construction of multiplexers, which preserve the PRBS structure of longer PRBS word lengths, is not reasonable.

In constructing a fiber based “test multiplexer” for very high symbol rates, for example 640 GBd, the effect of chromatic dispersion has to be taken into account as illustrated by the following considerations. The optical pulses at the output of the “test multiplexer” have passed different fiber lengths. Thus, they experience different pulse broadening due to chromatic dispersion. The generation of data signals having a symbol rate of 640 GBd from a base symbol rate of 10 GBd requires a 10 to 640 GBd multiplexer. Using a delay as determined by a PRBS word length of  $2^7 - 1$

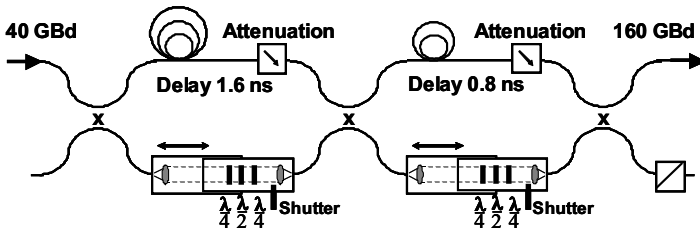


**Fig. 13.10** Set-up of a 40 to 160 Gb/s laboratory multiplexer (delays chosen to preserve a PRBS  $2^7 - 1$  sequence)

bits requires delays with fiber lengths of 1.28 m, 0.64 m, 0.32 m, 0.16 m, 0.08 m, and 0.04 m. The maximum length difference passed by the pulses in the six stages of the “test multiplexer” adds up to 2.52 m. An optical pulse with a pulse width of 0.4 ps is broadened to 0.58 ps over a fiber length of 2.52 m assuming a chromatic dispersion of  $D = 17$  ps/(nm km). As a consequence such a multiplexer already requires some sort of dispersion compensation in the first stages. Conversely, an MUX starting at the first stage with 40 Gb/s does in general not require any additional dispersion compensation in the first stages.

In general, the delay line multiplexer provides an arbitrary relative phase of adjacent pulses in the multiplexed data signal because usually no effort is made in these experiments to adjust and stabilize the delay line multiplexer for a well-defined relative phase of adjacent pulses. The effect of a well-defined relative phase of adjacent data pulses in the multiplexed data signal is expected to increase the tolerance of the transmission system with respect to chromatic dispersion and fiber nonlinearity, and it will increase the spectral efficiency as well [58]. Therefore, the controllability of the optical phase alignment between adjacent pulses in the multiplexed data signal is an important feature of a transmission system. Techniques for realizing optical phase alignment have been introduced [59, 60], and several OTDM and OTDM/WDM transmission experiments have been performed using such formats as “carrier-suppressed return-to-zero (CS-RZ)” in which the optical pulses in adjacent bit slots have a relative phase shift of  $\pi$  [57, 61–64]. Conversely, the improvement for the transmission system is not significant enough to justify the effort of adjustment and stabilization of a “test-multiplexer,” even not for phase-modulated data signals. In DPSK and DQPSK transmission systems the well-defined phase of adjacent pulses is only required behind the demultiplexer (i.e., within the base rate-channel) and is independent of the adjustment of the delay line “test multiplexer.”

### 13.5 Conventional OTDM Receiver

The goal of this section is to discuss optical signal processing in conventional OTDM receivers. An example is the receiver of the 1.28 Tbit/s transmission systems with DQPSK modulation format, introduced in Fig. 13.2 in Sect. 13.2. How-

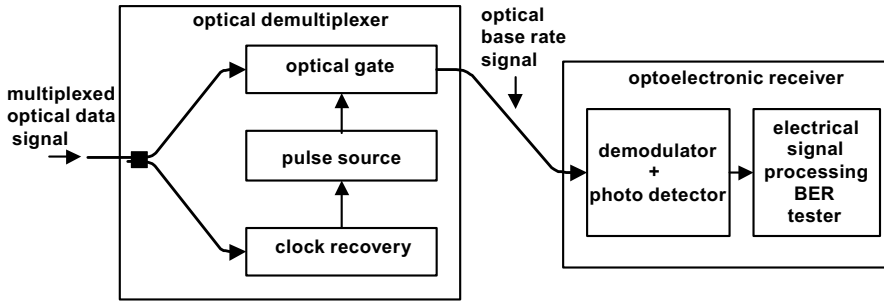


Fig. 13.11 Structure and key components of a conventional OTDM receiver

ever, the discussion also includes alternatives to this special receiver. The coherent OTDM receiver of the 1.28 Tbit/s transmission system with the 16-QAM modulation format will be discussed in Sect. 13.6. According to Fig. 13.2, a conventional OTDM receiver comprises two subsystems, an optical demultiplexer and an optoelectronic receiver for the base symbol rate. In Fig. 13.11 the receiver is shown with these two subsystems in more detail.

The demultiplexer selects (drops) one data channel (one tributary) of the transmitted multiplexed OTDM data signal. The selected data channel is subsequently passed to the optoelectronic receiver for signal processing in the electrical domain. To select a tributary from the transmitted multiplexed data signal, the demultiplexer has to periodically drop single pulses of a pulse train in well-defined time slots with a switching time shorter than the bit period of the multiplexed data signal (3.12 ps for 320 GBd). Therefore, the demultiplexer comprises an optical gate and a timing extraction device (clock recovery). The clock recovery device extracts the timing signal for the optical gate from the multiplexed data signal. Most optical gates need an optical control signal to drive the optical gate. Therefore, the clock recovery synchronizes an optical pulse source which drives the optical gate.

In Sect. 13.5.1 we discuss the optical gate which was used in the 1.28 Tbit/s transmission systems with DQPSK modulation while some alternative optical gates are treated in Sect. 13.5.2. Section 13.5.3 deals with the timing extraction unit and Sect. 13.5.4 covers the optoelectronic receiver.

### 13.5.1 NOLM as the Optical Gate

An important property of the optical gate is the amplitude transfer characteristic, the so-called switching window. In the ideal case, the control signal generated by the timing extraction unit changes the transmittance  $T = P_{\text{out}}/P_{\text{in}}$  of the gate for the train of data pulses at a given time instantly from  $T = 0$  to  $T = 1$  and after a time interval  $\tau$  back from  $T = 1$  to  $T = 0$  in such a way that only a single pulse passes the gate. The switching window is the variation of  $T$  versus time. The switching

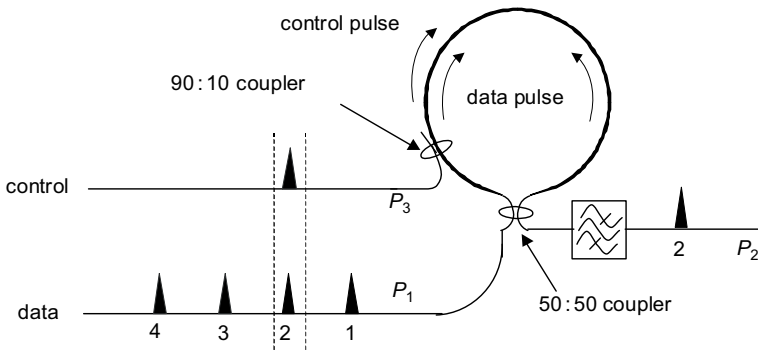


**Fig. 13.12** Nonlinear optical loop mirror (NOLM) as the optical gate

windows of real optical gates do not have this ideal form. The steepness of the slopes is limited and the transmittance is less than  $T = 1$ . The important parameters of the switching windows of real optical gates are the contrast and the width (FWHM) of the switching window where the former is defined as the ratio of transmitted signal power for maximum transmittance  $T$  to the transmitted signal power far off the maximum transmittance  $T$ , while the latter is the temporal interval in which the transmitted data power exceeds half of the maximum transmitted power.

The most important optical gate for symbol rates beyond 160 GBd is based on the Nonlinear Optical Loop Mirror (NOLM) [43, 65]. The NOLM is applied as a demultiplexer for symbol rates up to 640 GBd, the fastest optical gate reported so far [7, 9, 42, 66, 67]. The NOLM is also the optical gate which was used in the 1.28 Tbit/s DQPSK transmission experiment. Figure 13.12 is a schematic illustration of the NOLM. It has the configuration of a fiber Sagnac interferometer and is constructed by connecting a long piece of fiber (typical length 300 to 1000 m) to the two output ports of a fiber coupler to form a loop. In Fig. 13.12 the input ports of the fiber coupler are indicated by  $P_1$  and  $P_2$ . The fiber coupler used here is a 50 : 50 coupler. An optical pulse at the input (port  $P_1$ ) of the NOLM is split by the coupler into two pulses of equal power, one left-circulating in the loop and the other right-circulating. After a round trip, these two pulses meet again at the coupler where they interfere and exit the NOLM in one or both of the two coupler ports  $P_1$  and  $P_2$ , depending on the phase difference  $\Delta\varphi$  of left- and right-circulating pulses after a round trip. The transmittance (from port  $P_1$  to port  $P_2$ ) is given by  $T = P_{\text{out}}/P_{\text{in}} = (1/2)(1 - \cos \Delta\varphi)$ , where  $P_{\text{in}}$  is the input power at port  $P_1$  and  $P_{\text{out}}$  is the output power at port  $P_2$ . In the NOLM we have  $\Delta\varphi = 0$  and therefore  $T = 0$ , because the optical path in the NOLM is the same for the left- and right-circulating pulse. This is different in the DILM (see Sect. 13.4.2). The NOLM reflects the incoming pulse totally like a mirror.

To operate the NOLM as an optical gate, an additional fiber coupler is inserted into the fiber loop as shown in Fig. 13.12. This fiber coupler often has a splitting ratio of about 1/10 to keep the loss of the circulating pulses in the fiber loop low. The pulses circulating in the loop lose 1/10 of their power at the coupler. Con-



versely, an optical pulse at port  $P_3$  couples only 1/10 of its power into the loop. The pulse train representing the transmitted multiplexed data signal is input at  $P_1$ . To switch a selected pulse of this pulse train (for instance pulse 2 in Fig. 13.12) to  $P_2$ , a control pulse is input in  $P_3$ , which is co-propagating with the left circulating pulse component of pulse 2 in the fiber loop. This control pulse changes the phase of the left circulating pulse 2 component by cross-phase modulation (XPM) according to (13.3) (see Sect. 13.3.1) such that  $\Delta\varphi = \varphi_{NL} = -\xi\gamma P_C L_{eff}$ . If the power  $P_C$  of the control pulse (in the loop) is properly adjusted, one obtains  $\Delta\varphi = \pi$  and consequently  $T = 1$  for the selected data pulse 2, whereas  $T = 0$  for all other data pulses. The required power for  $\Delta\varphi = \pi$  is given by  $P_C L_{eff} \approx 1 \text{ W km}$  and with  $L_{eff} = L$  to a good approximation. The control pulse has a wavelength which is different from the wavelength of the data pulses and does not pass the optical filter at port  $P_2$  of the NOLM. The exact timing for the control pulse is provided by the timing extraction unit.

The fiber nonlinearity is extremely fast. It has about the duration of the pulse width. The switching window is solely determined by the shape and width of the control pulse and by the walk-off between the data and control pulse. The walk-off is caused by chromatic dispersion of the fiber in the loop. Because of chromatic dispersion, the data pulse and control pulse do not have a constant overlap in the fiber during the propagation along the loop length. This broadens the width of the switching window and restricts the application as a demultiplexer for very high bit rates. The walk-off can be reduced by fibers having an appropriate chromatic dispersion profile with the same dispersion for the wavelength of control and data signal or by constructing a fiber loop which is a concatenation of multiple short fiber sections having an alternating walk-off along the length of the fiber loop [42]. Another problem of the NOLM-switch represents the factor  $\xi$  in (13.3). The factor  $\xi$  expresses the dependence of XPM in the fiber on the relative states of polarization of the data pulse and the control pulse. There are techniques to construct polarization-independent NOLM-based demultiplexers [68]. The NOLM is not the only optical gate based on the optical nonlinearity of the fiber. Also four-wave mixing (FWM) in a fiber was applied to operate as a demultiplexer [69]. This optical gate is not discussed here. See, however, Sect. 13.5.2.

## 13.5.2 SOA- and EAM-based Optical Gates

### 13.5.2.1 Optical Gates Using XPM in SOA

Fiber-based optical gates are very bulky. In general, a fiber length of some 100 m is required because the nonlinearity of the fiber is comparatively low. The semiconductor optical amplifier (SOA) offers a much higher optical nonlinearity and enables very compact switching devices. The operation speed of these switching devices is restricted by the slow nonlinear response time of the SOA (see Sect. 13.3). To overcome this problem SOA-based optical gates were used in specific config-

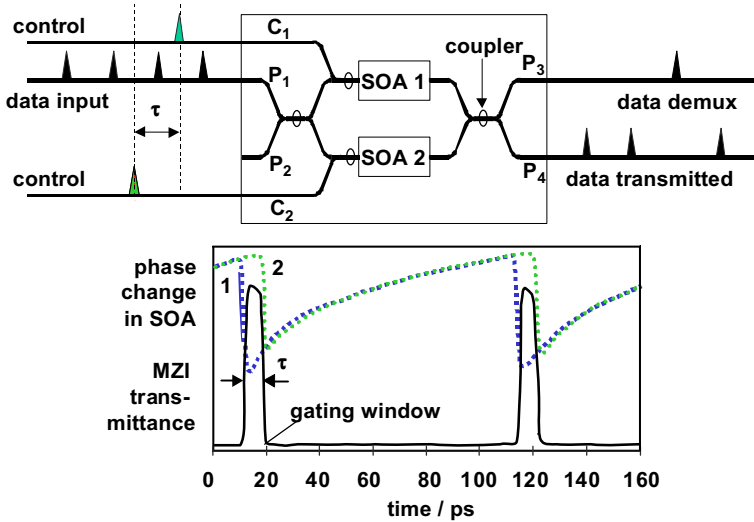


**Fig. 13.13** Mach-Zehnder structure for an optical gate based on XPM in SOAs

urations as demultiplexers [70–76]. The most prominent SOA-based optical gate uses cross-phase modulation (XPM) in an SOA and is realized by incorporating the SOA into an interferometer configuration in which the phase modulation is transferred into an amplitude modulation. The Sagnac and Mach-Zehnder interferometer configurations were frequently applied [20]. In particular the SOA-based optical gate in the configuration of a Mach-Zehnder interferometer was successfully realized as a monolithically integrated Mach-Zehnder interferometer having a size of about  $1 \text{ mm} \times 5 \text{ mm}$  (e.g., [70, 71]). In [70], the two SOA sections (length  $1.0 \text{ mm}$ ) comprised a buried heterostructure (with band gap equivalent wavelength  $\lambda_g = 1.50 \mu\text{m}$ ) InGaAsP bulk layer. The passive sections consisted of a buried heterostructure  $\lambda_g = 1.25 \mu\text{m}$  InGaAsP bulk layer and included 3 dB multimode interference (MMI) couplers, S-bends, straight waveguides, and spot size converters (taper). The active waveguide was a strained bulk material with a cross-section of  $0.2 \mu\text{m} \times 0.8 \mu\text{m}$  to provide polarization-insensitive gain. The passive waveguide was a wide double-mode waveguide ( $0.35 \mu\text{m} \times 2 \mu\text{m}$ ). Demultiplexing of data signals up to 320 Gbit/s was reported [72, 73]. Optical signal processing using SOAs and in particular the application for demultiplexing are described in a review article [20].

In the following we describe the principle of operation of an SOA-based interferometer switch using the Mach-Zehnder interferometer configuration illustrated in Fig. 13.13.

The Mach-Zehnder interferometer comprises a 50 : 50 coupler with the two input ports P<sub>1</sub> and P<sub>2</sub> and a 50 : 50 coupler with the two output ports P<sub>3</sub> and P<sub>4</sub>. Additionally, there is a 50 : 50 coupler in each interferometer branch to provide a direct coupling of the control pulses into each branch via the ports C<sub>1</sub> and C<sub>2</sub>. The

data signal (data pulse) is injected into port  $P_1$ . The interferometer is balanced such that the data signal emerges from port  $P_4$  in the absence of a control pulse. The control pulses, which both come from the same pulse source, are coupled (ports  $C_1$  and  $C_2$ ) with a relative time delay  $\tau$  into the SOAs. As already reported, the nonlinear response time of the SOA is slow as compared to the nonlinear response time of the fiber. In the SOA, the control pulse induces a fast change of the refractive index of the SOA. Subsequently the refractive index recovers slowly with a response time of some 100 ps. The data pulses experience this change of the refractive index as a corresponding change of the phases  $\varphi_1$  and  $\varphi_2$  (depicted in the lower part of Fig. 13.13). The changes of  $\varphi_1$  and  $\varphi_2$  affect the balance of the interferometer such that the data pulse is switched to port  $P_3$ .

The switching scheme in Fig. 13.13 is called a differential switching scheme. It provides a transmission to port  $P_3$  which is only determined by the difference of  $\varphi_1$  and  $\varphi_2$  and not limited by the slow recovery. The resulting switching window is nearly symmetric and has a width determined by the relative time delay  $\tau$  because the differential phase shift  $\Delta\varphi = \varphi_1 - \varphi_2$  is nearly zero outside  $\tau$  by proper adjustment of the various device parameters. The change of the transmittance to port  $P_3$  is the switching window and the complementary change of transmittance to port  $P_4$  is called the complementary switching window. The minimum width (FWHM) of the switching window achieved so far was 3 ps and the highest switching contrast amounted to 27 dB.

### 13.5.2.2 Optical Gates Using FWM in an SOA

The nonlinear optical effect of FWM has also been exploited for various functional operations in high bit rate transmission systems. For instance the operation of a demultiplexer based on FWM in an SOA was reported in experiments with data rates up to 200 Gbit/s [77]. The FWM-effect is strongly dependent on the relative states of polarization of the two injected optical waves, as described in Sect. 13.3.2. However, such a polarization dependence is not acceptable for a demultiplexer. In the following we describe the principle of operation of an FWM-based demultiplexer which operates independently of the state of polarization of the incoming data signal. Figure 13.14 illustrates the set-up of this demultiplexer in a schematic fashion.

The clock and the data signal (6.3 GHz and 200 Gbit/s, respectively, in the example shown) are input via a polarization-maintaining coupler (not shown in Fig. 13.14) in a polarization-maintaining fiber (PM fiber) having a length of 6 m (differential group delay of 16 ps). The state of polarization of the clock signal is linear polarized under  $45^\circ$  with respect to the slow and fast axis of the PM-fiber. The state of polarization of the data signal is not fixed. Because of polarization dispersion in the PM fiber the components of clock and data signal along the fast and slow axis separate in time. The fast components of the clock and the data signal arrive earlier (16 ps) at the SOA and generate a new frequency component via FWM (FWM-component  $F$ ). Similarly the slow components of clock and data signal generate a new frequency component (FWM-component  $S$ ). At the output of the SOA

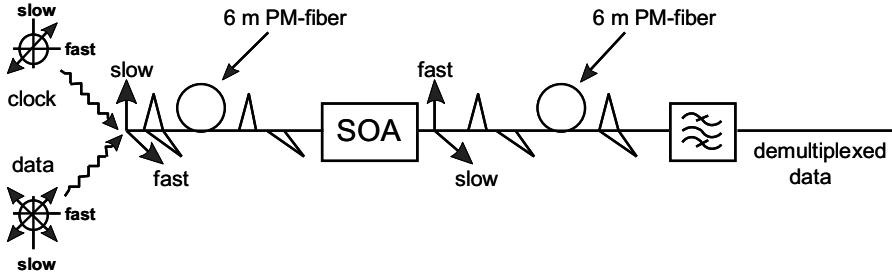


Fig. 13.14 Polarization-insensitive SOA demultiplexer based on FWM

is another PM fiber (length 6 m). The axes of this fiber are adjusted such, that the FWM-component  $F$  is coupled into the slow axis and the FWM-component  $S$  is coupled into the fast axis. Thus, at the output of the PM fiber, the FWM components  $F$  and  $S$  overlap in time and result in an FWM-signal that is independent of the state of polarization of the data signal. The resulting FWM signal passes an optical filter, which separates the clock pulses.

In the experiment, the gain of the SOA in the TE and TM modes was slightly different ( $< 1$  dB). The adjustment of the slow and fast axes to the TE and TM modes was such that equal FWM efficiency was excited in each mode. The sources for clock and data signal were supercontinuum pulse sources providing clock pulses ( $\lambda = 1543.5$  nm, pulse width 1.7 ps, average optical power 7.3 dBm) and data pulses ( $\lambda = 1553.1$  nm, 1.7 ps, 2.3 dBm) at the input of the demultiplexer. Error-free, polarization-independent ( $< 0.5$  dB dependency) operation was confirmed.

Whereas in an XPM-based optical gate the selected optical pulse of the input pulse train passes the optical gate, this is different in the FWM-based optical gate. In this gate not the original pulse is transmitted but a replica of this pulse is generated and transmitted to the output. This replica is shifted in wavelength with respect to the original pulse and is a phase conjugate replica of the original pulses.

### 13.5.2.3 Optical Gates Based on EAM

The optical gates discussed above are gates based on nonlinear optical effects in fibers or in semiconductor optical amplifiers. These gates use all-optical switching. An optical pulse controls the transmittance of the gate for the optical data signal. Also the electro-absorption modulator (EAM) was used as an optical gate. In the EAM, however, an electrical control signal controls the transmittance of the gate for the optical data signal. Therefore, this gate does not require the pulse source indicated in Fig. 13.11. The electrical signal from the timing extraction unit controls the EAM gate directly. This is an enormous simplification of the demultiplexer because appropriate optical pulse sources are expensive and difficult to handle. The EAM is a commercially available device. In the application as an optical gate it is charac-

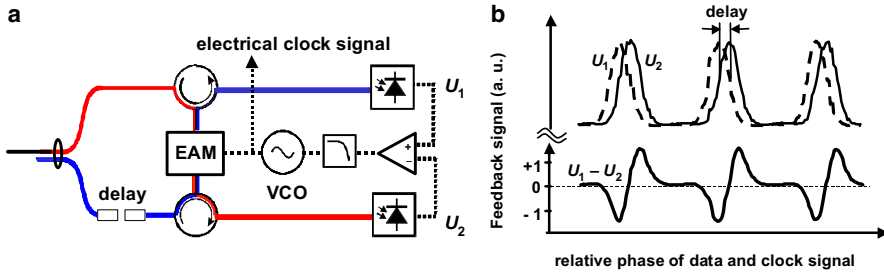


**Fig. 13.15** Optoelectronic clock recovery with EAM as the phase detector (a). Both signals versus the relative phase of the data signal and the 40 GHz RF signal taken while the PLL was not closed (b)

terized by a switching window which typically has a width (FWHM) of about 5 ps and a switching contrast of about 20 dB for a DC-bias voltage of about 3.5 V and for a 40 GHz clock signal with an RF power of about 26 dBm. The width of the switching window depends on the frequency of the clock signal. Demultiplexing of 160 GBd to 10 GBd with a 10 GHz clock signal requires in general a cascade of two EAMs. The EAM is a polarization-independent gate. More details on EAM-based 160 GBd demultiplexing are described in [33, 78]. The EAM also has the potential for application as a demultiplexer for symbol rates up to 500 GBd if an optical control signal is used [79].

The demultiplexers described above are capable of selecting only one TDM channel (one tributary) of the multiplexed data signal (single channel output operation). Multiple channel output operation can be achieved by a serial-parallel configuration of several of these switches. Examples for multichannel output operation using only one device are reported in [3, 80, 81].

### 13.5.3 Timing Extraction Devices

Timing extraction or clock recovery is an essential operation in a demultiplexer and in other functional devices, for example in a regenerator. Among the many timing extraction techniques proposed and demonstrated so far, a phase-locked loop (PLL) with an optical or optoelectronic phase comparator is a promising method especially for subharmonic clock extraction from data signals beyond 100 Gbit/s [82–84]. Clock recovery has been reported using an optical phase comparator based on four-wave mixing in an SOA at data rates up to 400 Gbit/s [82]. In this section we discuss optoelectronic clock recovery using an EAM as the optical phase comparator.

The clock recovery shown in Fig. 13.15a is a prescaled optoelectronic timing extraction device using a PLL configuration and an EAM as the phase comparator. The optical data signal with a symbol rate of for example 320 GBd is split into

two branches and fed into the EAM via two circulators. The two light paths are indicated by different colors of the two solid lines. The switched output signals of the EAM are detected by two low bandwidth (100 MHz) photo detectors. The two electrical signals  $U_1$  and  $U_2$  are subtracted from each other by a difference amplifier to generate the bipolar feedback signal  $U_1 - U_2$  for the voltage controlled oscillator (VCO) operating for instance at 40 GHz. The paths of the electrical signals are indicated by broken lines. The PLL comprises a low-pass filter with a bandwidth of 50 kHz. The electrical 40 GHz VCO signal is finally fed into the electrical input of the EAM to close the loop of the PLL. This electrical 40 GHz signal is the output signal of the timing extraction unit and controls for example the EAM gate directly or the NOLM gate by synchronizing a 40 GHz optical pulse source as indicated in Fig. 13.11.

In this set-up, the EAM acts as an ultra-fast electro-optical phase comparator. The optical power transmitted through the EAM to both sides is determined by the phase difference between the data signal and the 40 GHz RF-signal driving the EAM. Thus, the two electrical signals  $U_1$  and  $U_2$  depend on this phase difference. Figure 13.15b shows both signals versus the relative phase of the data signal and the 40 GHz RF signal taken while the PLL was not closed. There is a shift between  $U_1$  and  $U_2$  because of the optical delay in one of the two signal branches at the input of the EAM. The bipolar feedback signal  $U_1 - U_2$  is within the locking-range proportional to the relative phase of the data signal and the 40 GHz RF signal. This clock recovery was successfully operated at symbol rates up to 320 Gbd [83, 84].

Many transmission experiments were also performed without recovering the clock signal from the multiplexed data signal because an appropriate clock recovery device was unavailable. Two alternative approaches were used. A clock signal was generated at the transmitter and transmitted together with the data signal over the fiber at a separate wavelength (“transmitted clock signal” [85]), or the multiplexer at the transmitter end was adjusted for slightly different pulse amplitudes (“clock modulation,” e.g., [86]) such that a simple photo detector was able to detect the clock signal at the receiver end. These two approaches are, however, not applicable in real systems.

### ***13.5.4 Optoelectronic Base Rate Receiver***

In an OTDM receiver, the output signal of the demultiplexer is passed to the optoelectronic base rate receiver for signal processing in the electrical domain as indicated in Fig. 13.11. The first stage of the optoelectronic receiver in Fig. 13.11 comprises the demodulator and the photo detector. In a system with ASK modulation format (e.g., 2-ASK or OOK) this stage of the optoelectronic receiver comprises only the photo detector (together with an optical amplifier and an optical filter) because a demodulator is not necessary for this modulation format. Conversely, the DPSK and the DQPSK OTDM-receiver require a demodulator before the photo de-

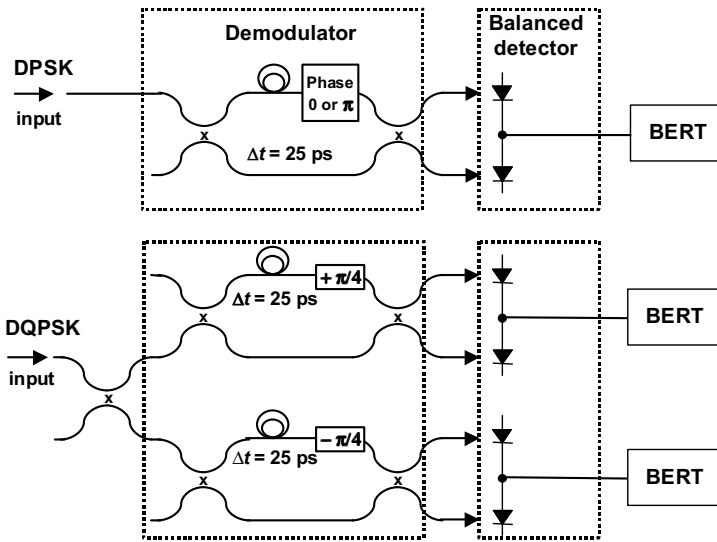


**Fig. 13.16** Conventional receiver with demodulator for DPSK or DQPSK

detector. The demodulator converts the phase-modulated data signal into two complementary amplitude-modulated data signals. The demodulators for these two modulation formats are depicted in Fig. 13.16. In the DPSK receiver, the demodulator is a Mach-Zehnder interferometer with a delay between both interferometer arms of one period at the symbol base rate, for instance 25 ps for a symbol base rate of 40 GBd.

Adjacent pulses with zero phase difference, which carry the logical information “0” (see Sect. 13.4.4), interfere constructively at one port (e.g., upper port in Fig. 13.16) and destructively at the other port (lower port in Fig. 13.16) of the interferometer, whereas adjacent pulses with  $\pi$  phase difference, which carry the logical information “1,” interfere constructively at the lower port and destructively at the upper port. If the two complementary signals are detected by a balanced photo detector, an improvement in receiver sensitivity of 3 dB as compared with OOK is obtained [87].

The demodulator for a DQPSK signal is also shown in Fig. 13.16. It comprises two Mach-Zehnder interferometers each with a differential delay (in the interferometer arms) of one period at the symbol base rate (i.e., 25 ps for 40 GBd) plus an additional phase shift of  $+\pi/4$  or  $-\pi/4$  to detect the in-phase or quadrature component, respectively.

The DPSK or DQPSK demodulator needs to be actively matched to the transmitter wavelength for proper operation. This requires a control loop for the demodulator and also a pulse source in the transmitter which is highly stable in terms of the carrier wavelength.

## 13.6 Coherent OTDM Receiver

Figure 13.17 shows the coherent OTDM receiver schematically as it was used in the 1.28 Tbit/s, 16-QAM, OTDM transmission experiment reported in Sect. 13.2 and Fig. 13.2. The set-up of the coherent receiver is subdivided into two main blocks, the optical frontend (used for demultiplexing, demodulation, and e-o conversion) and the electrical signal processing unit. In the coherent receiver, the output of the optical frontend is an electrical tributary signal contrary to the conventional receiver (see Fig. 13.11), where the output of the optical demultiplexer is an optical tributary signal. The essential difference of the two receivers is that the optical gate in the conventional receiver is replaced by the polarization-diversity and phase-diversity homodyne receiver in the coherent receiver. In Fig. 13.17 there is also a clock recovery unit to extract the base clock from the OTDM signal and an optical pulse generator which is synchronized by the clock recovery unit to generate a train of control pulses with a repetition frequency at the base symbol rate of the multiplexed data signal. However, in a complete coherent OTDM receiver, where all tributaries are present in the electrical signal processing unit, no synchronization of the control pulses to the data stream is required as long as an appropriate oversampling rate is used. This also enables the compensation of transmission impairments like chromatic dispersion and polarization-mode dispersion in the electrical signal processing unit.

### 13.6.1 Principle of the Phase-diversity Homodyne Receiver

The principle of operation of the phase-diversity homodyne receiver is described with use of Fig. 13.18 [88, 89]. The figure shows a 90° optical hybrid and two balanced photo detectors.

For the discussion we assume that an optical data signal  $E_s(t)$  and an optical continuous wave  $E_c(t)$  given by

$$E_s(t) = A_s \exp(j\theta_s + j\theta_n) \exp(j\omega_s t) \quad (13.6)$$

and

$$E_c(t) = A_c \exp(j\theta_c) \exp(j\omega_c t) \quad (13.7)$$

are coupled into two input ports of the 90° optical hybrid. Here,  $j$  is the imaginary unit with  $j^2 = -1$ .  $E_c$  is often called the local oscillator wave and will be later replaced by a pulse train to enable optical demultiplexing. In (13.6) and (13.7)  $A_s$  and  $A_c$  are real amplitudes,  $\theta_s$  represents the phase modulation and  $\theta_n$  the phase noise of the data signal,  $\theta_c$  is the phase of the LO-wave, and  $\omega_s$  and  $\omega_c$  are the angular frequencies of  $E_s(t)$  and  $E_c(t)$ , respectively. In particular, it is assumed that amplitude noise may be neglected and that both  $E_s$  and  $E_c$  have the same state of polarization (SOP). The optical signals at the four outputs of the 90° optical



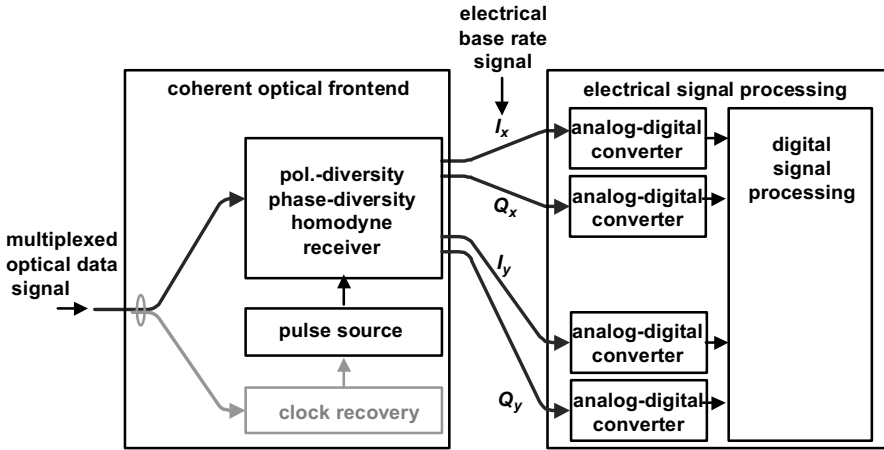


Fig. 13.17 Coherent receiver with pulsed local oscillator

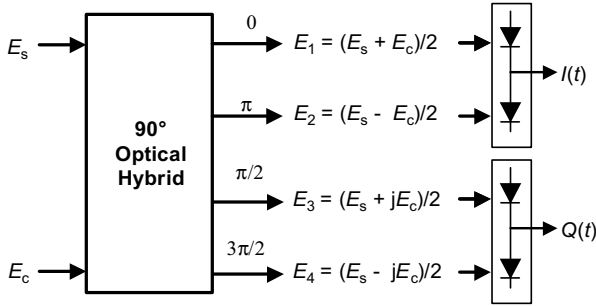


Fig. 13.18 Phase relations after 90° optical hybrid

hybrid are:  $E_1 = (E_s + E_c)/2$ ,  $E_2 = (E_s - E_c)/2$ ,  $E_3 = (E_s + jE_c)/2$ , and  $E_4 = (E_s - jE_c)/2$  [88, 89]. There are several realizations of the optical 90° hybrid (e.g., [90–92]). Optical 90° hybrids monolithically integrated with balanced photo receivers are also commercially available now [93].

The outputs of the two balanced photo detectors connected to the 90° hybrid are [89]

$$I(t) = R (P_s P_c)^{1/2} \cos(\omega_{IF}t + \theta_s + \theta_n - \theta_c), \quad (13.8)$$

$$Q(t) = R (P_s P_c)^{1/2} \sin(\omega_{IF}t + \theta_s + \theta_n - \theta_c). \quad (13.9)$$

Here,  $R$  is the responsivity of the photodiode,  $P_s = (1/2)A_s^2$  and  $P_c = (1/2)A_c^2$  are the optical powers, and  $\omega_{IF} = \omega_s - \omega_c$  is the intermediate angular frequency. In a homodyne coherent receiver  $\omega_s = \omega_c$  and therefore the intermediate frequency is  $\omega_{IF} = 0$ .

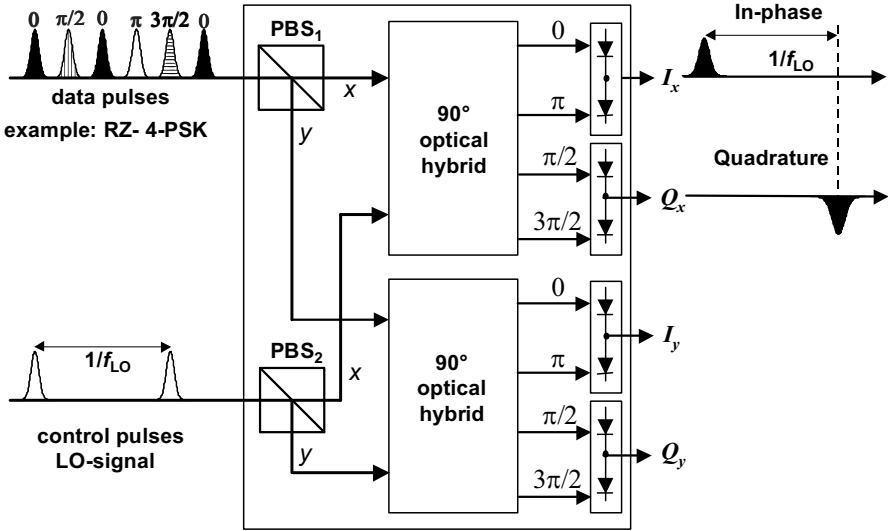


Fig. 13.19 Polarization- and phase-diversity homodyne receiver with pulsed LO

In a homodyne receiver, the quantity

$$I_g(t) = I(t) + jQ(t) = (1/2)RAcA_s \exp[j(\theta_s + \theta_n - \theta_c)]$$

is proportional to the complex amplitude  $A_s \exp(j\theta_s)$  if  $\theta_n - \theta_c = 0$ . Here,  $A_s \exp(j\theta_s)$  is the information content of the input data signal  $E_s(t)$ . One way to obtain  $\theta_n - \theta_c = 0$  is to operate an optical phase-locked loop that locks the phase  $\theta_c$  of the local oscillator to the phase  $\theta_s(t)$  of the data signal. This is a very difficult task, and no practical solutions are presently known for high bit rate data signals. Recently, high-speed digital signal processing (DSP) has been successfully applied to solve this problem in a different way [89]. In the phase-diversity receiver, the optical phase is not lost in the detection process and can be tracked also in the electrical domain, thus enabling  $\theta_n - \theta_c = 0$ . Moreover, DSP is also able to handle a frequency offset  $\omega_{IF} \neq 0$  as long as  $|\omega_{IF}| \ll \omega_b/2$ , where  $\omega_b$  is the modulation bandwidth of the optical carrier determined by the bit rate [94]. These examples show that problems appearing in optical signal processing are partly alleviated by the use of digital signal processing in the electrical domain.

Finally, there is still the assumption that both  $E_s(t)$  and  $E_c(t)$  have the same state of polarization. In a real system the SOP of the transmitted data signal changes irregularly with time. One solution to this problem is the application of polarization-diversity [89]. The principle of polarization-diversity is discussed with use of Fig. 13.19, which shows schematically the set-up of the polarization-diversity and phase-diversity homodyne receiver applied in the 1.28 Tbit/s, 16-QAM, OTDM transmission experiment reported in Sect. 13.2 and Fig. 13.2.

In this figure a pulse train (control signal) is used as local oscillator  $E_c$  instead of a continuous wave LO (see Sect. 13.6.2). The set-up in Fig. 13.19 comprises two

phase-diversity receivers of the kind discussed before and two polarization beam splitters (PBS<sub>1</sub> and PBS<sub>2</sub>). The data signal having an arbitrary SOP is split at PBS<sub>1</sub> into two orthogonal SOPs with linear polarization, called the  $x$ - and  $y$ -components in the following. The relative strength of these two components varies between 1 and 0 depending on the SOP of the data signal at the input. Figure 13.19 shows a particular situation where only the  $x$ -component is present in the input data signal. The  $y$ -component is zero. The LO-signal is adjusted to an SOP, which is split at PBS<sub>2</sub> into an  $x$ -component and a  $y$ -component of equal strength. Thus, the polarization-diversity scheme provides the same linear SOP for the data signal and the LO-signal at the input of each 90° optical hybrid. In general, the  $x$ -branch of the polarization-diversity and phase-diversity receiver provides an  $I_x$ -signal and a  $Q_x$ -signal in the  $x$ -branch and an  $I_y$ -signal and a  $Q_y$ -signal in the  $y$ -branch. In the electrical signal processing unit (see Fig. 13.17) these signals are separately processed and later added together.

### 13.6.2 Coherent Receiver as an OTDM Demultiplexer

The coherent receiver is used as an OTDM demultiplexer by applying a pulse train (control signal) as local oscillator instead of a continuous wave LO. This is schematically shown in Fig. 13.19 for the polarization-diversity and phase-diversity homodyne receiver.

In this figure, we assume an OTDM data signal comprising four tributaries with a 4-PSK modulation format. The SOP of the data signal is assumed to have only an  $x$ -component in the polarization-diversity set-up. The hatching of the data pulses indicates the different states of the phase of the OTDM signal. The LO pulses are assumed to all have the same state “0” of the phase. The LO-pulse train is adjusted in the time domain (by a variable optical delay line) to overlap one of the tributaries of the OTDM data signal. In the example in Fig. 13.19 the output signals are  $I_x \propto \cos(\theta_s)$  and  $Q_x \propto \sin(\theta_s)$  with  $\theta_s = 0, 3\pi/2$ .

The output signals  $I_x$ ,  $Q_x$ ,  $I_y$ , and  $Q_y$  of the four balanced receivers are zero if no interference signal between data pulses and LO pulses is detected. In the example considered in Fig. 13.19, this interference signal can only appear in the  $x$ -branch of the polarization diversity set-up and it can only appear for the data pulses which overlap with the LO pulses. However, the LO pulses and the data pulses have to overlap not only in the time domain but also in the frequency domain to enable homodyne detection. Figure 13.20 shows an example of spectra of data pulses and LO pulses.

An overlap of both spectra is needed for the envelope as well as for the mode combs of the spectra. Ideally, for homodyne detection the frequency offset  $\Delta f$  of the mode combs should be zero, but a  $\Delta f \neq 0$  can be corrected for by high-speed digital signal processing in the postdetection electrical signal processing unit. The LO pulses define a “switching window” which is mainly given by the pulse width of the LO signal. Similar to the switching of a conventional OTDM demultiplexer

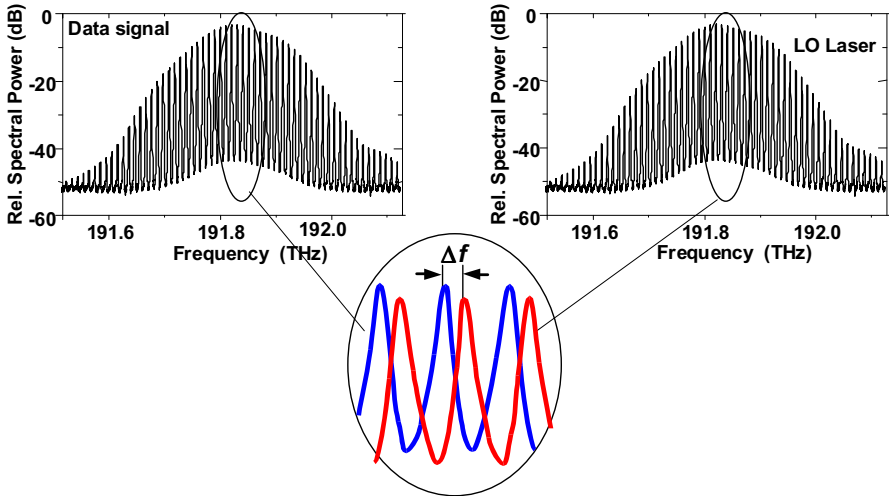


**Fig. 13.20** Wavelength allocation of the mode combs of the (unmodulated) transmitter laser and the LO

an appropriate shape of the LO pulses with a very low pedestal is essential to avoid crosstalk from the neighboring time slots.

The use of a pulsed local oscillator in the coherent digital receiver was proposed in [94, 95] and applied in transmission experiments up to a data rate of 10.2 Tbit/s using the 16-QAM modulation format [12, 96]. Fiber transmission has been reported up to a data rate of 640 Gbit/s over 1073 km dispersion-managed fiber using the QPSK modulation format as well as at the data rate 1.28 Tbit/s over 480 km DMF using the 16-QAM modulation format [10, 97, 98] and over 800 m multimode fiber [13].

### 13.6.3 Postdetection Electrical Signal Processing

Electrical signal processing of the detected data signal was already being discussed 20 years ago for applications to mitigate signal distortions induced in the optical domain [99]. Of particular importance was postdetection electrical signal processing of the photodiode signal for the compensation of polarization-mode dispersion (see Sect. 13.7.4) by application of electrical equalizers within the receiver [100]. However, at this time, the photodiode signal was the result of a simple square law detection process and the information transported in the optical phase was lost. Consequently, postdetection electrical signal processing was not very successful, in particular for high-speed optical data transmission systems.

With the use of a coherent receiver and the application of postdetection high-speed digital signal processing the situation is different [89]. The output signals  $I_x$ ,

$Q_x$ ,  $I_y$ , and  $Q_y$  of the four balanced receivers are fed into the electrical signal processing unit. In four analog-digital converters (ADC) the four signals are sampled and digitized. Then digital signal processing is performed. As the four input signals represent the complex amplitude  $A_s \exp(j\theta_s)$  of the data signal  $E_s(t)$ , the full information transported in the optical data signal can be used for electrical signal processing. Therefore, various kinds of signal processing can be performed: timing skew corrections, compensation of the  $IQ$ -imbalance of the  $90^\circ$ -hybrid, compensation of transmission impairments (e.g., chromatic dispersion and polarization-mode dispersion), re-timing, correction of the optical frequency offset between signal and LO, digital carrier-phase estimation, decoding and bit-error ratio (BER) calculation [89, 94].

### 13.7 Optical Signal Processing for Combating Impairments in the Fiber Link

For applications in commercial systems a fiber link length of the order of 1000 km is desirable. For these fiber lengths, the fiber needs to be a single-mode fiber. The transmission properties are determined by the transmission loss, the optical nonlinearity, the chromatic dispersion, and the polarization-mode dispersion.

#### 13.7.1 Fiber Nonlinearity and Choice of Appropriate Transmission Fiber

Various types of transmission fiber in combination with their associated dispersion-compensating fiber (DCF) have been investigated for high-speed data transmission near 1550 nm. Examples are standard single-mode fiber (SMF,  $D \approx 17$  ps/(nm km)), dispersion-shifted fiber (DSF,  $D \approx 0.1$  ps/(nm km)), and various types of nonzero dispersion-shifted fiber (NZDSF,  $D \approx 2$  to 8 ps/(nm km)).

The DCF is a fiber with opposite (reversed) chromatic dispersion compared to the associated transmission fiber (see Sect. 13.7.2). The DCF compensates for the path-averaged chromatic dispersion  $D$  and the path-averaged dispersion slope  $dD/d\lambda$  of the associated transmission fiber. Generally, the DCF is localized as a module in the repeaters and does not contribute to the transmission length. Conversely, DCF has further evolved into inline dispersion-managed fiber transmission lines. The DMF represents a pair of transmission fibers, which together compensate for the path-averaged  $D$  and  $dD/d\lambda$  over a wide wavelength range. There are several types of DMF such as SMF/RDF (SMF/reverse dispersion fiber) or SLA/IDF. The latter comprises “Super large area fiber” (SLA,  $D \approx 20$  ps/(nm km)) and “Inverse dispersion fiber” (IDF,  $D \approx -40$  ps/(nm km)).

Fibers with low chromatic dispersion are not favorable for high-speed data transmission because of the optical nonlinearity of the fiber. High-speed transmission experiments are commonly performed in the quasi-linear (pseudo-linear) transmission regime, where the nonlinear length is much greater than the dispersion length (e.g., [60]). A high local dispersion is advantageous for this transmission regime provided that the path-averaged  $D$  and  $dD/d\lambda$  are close to zero. The short pulses of the data signal disperse very quickly in the fiber, spreading into many adjacent timeslots before the original pulse sequence is restored by dispersion compensation. Therefore, the peak power of the pulses is low for most of the path along the fiber. Conversely, the nonlinear interaction of the pulses stretched over many adjacent timeslots causes distortions due to intrachannel four-wave mixing. Consequently, there exists an optimum fiber dispersion depending on the data rate. However, it is more important to use fibers with a low nonlinearity (large effective area). Because of the physical constraints in the fiber design all available nonlinearity fibers have high local dispersion. For example, 160 Gbit/s DPSK data transmission was successful with transmission distances of up to 2000 km using NZDSF [86]. Conversely, 160 Gbit/s DPSK data transmission over the SLA/IDF fiber with its high local dispersion and low nonlinearity achieved a transmission distance of more than 4000 km [101].

### ***13.7.2 Compensation of Chromatic Dispersion by DCF***

In general, chromatic dispersion causes a broadening of the width of a pulse which is propagating in an optical fiber because the different frequency components of the pulse spectrum travel with different velocities. Already for a system with a symbol rate of 160 GBd, it is necessary to compensate for both the path-averaged CD (i.e.,  $D = 0$ ) at the center wavelength of the pulse and for the path-averaged CD slope (i.e.,  $dD/d\lambda = 0$ ), because the dispersion slope produces oscillations near the trailing edge of the data pulse even if  $D = 0$  for the center wavelength of the pulse. Currently, the most mature dispersion compensation technique is based on dispersion-compensating fiber. A detailed discussion of fiber-based dispersion compensators is given in [102].

The propagation of a pulse in a fiber is determined by the propagation constant  $\beta$ . The frequency dependence of  $\beta$  is discussed by expressing  $\beta$  in a Taylor series as

$$\begin{aligned} \beta = \beta_0 + \beta_1 (\omega - \omega_0) + \frac{1}{2}\beta_2 (\omega - \omega_0)^2 \\ + \frac{1}{6}\beta_3 (\omega - \omega_0)^3 + \frac{1}{24}\beta_4 (\omega - \omega_0)^4 + \dots, \end{aligned} \quad (13.10)$$

where  $\omega_0$  is the center frequency of the pulse spectrum and  $\beta_n = d^n\beta/d\omega^n$  at  $\omega = \omega_0$ . The time delay of a pulse component with frequency  $\omega$  over a fiber of

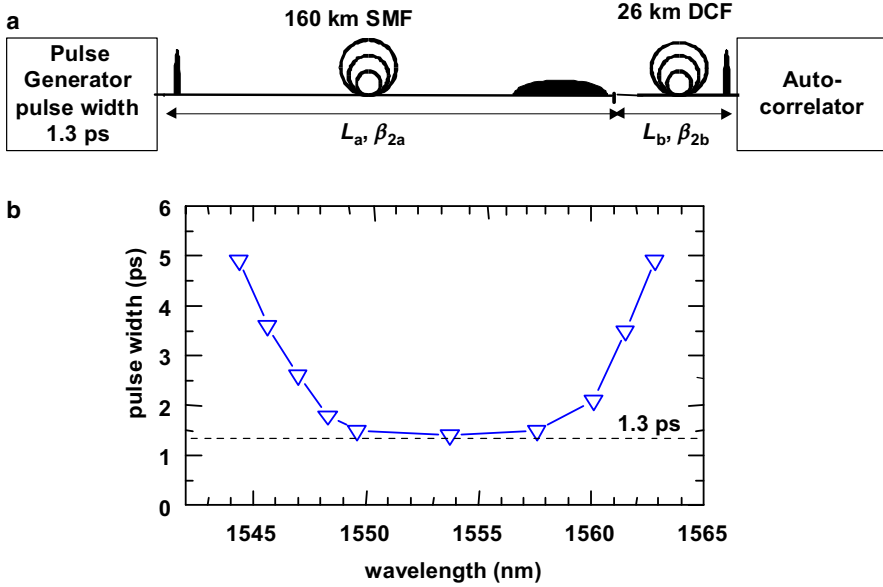


**Fig. 13.21** Dispersion-compensated fiber link (a) and wavelength dependence due to residual dispersion slope (b)

length  $L$  is given by

$$\begin{aligned} \tau(\omega) &= L \frac{d\beta}{d\omega} \\ &= L \left\{ \beta_1 + \beta_2(\omega - \omega_0) + \frac{1}{2}\beta_3(\omega - \omega_0)^2 + \frac{1}{6}\beta_4(\omega - \omega_0)^3 + \dots \right\}. \end{aligned} \quad (13.11)$$

The center ( $\omega = \omega_0$ ) of the pulse travels with the group velocity  $v_g = 1/\beta_1$ , and its time delay  $\tau_g = \tau(\omega_0) = L\beta_1$  is called group delay. Chromatic dispersion is defined as  $D = d\beta_1/d\lambda = -(2\pi c/\lambda^2)\beta_2$ . The objective of dispersion compensation by a DCF is to add to the transmission fiber of length  $L_a$  a DCF of length  $L_b$  such that the sum  $\tau_a(\omega) + \tau_b(\omega)$  of the time delays in the two concatenated fiber lengths  $L_a$  and  $L_b$  becomes independent of  $\omega$ . This is obtained if  $L_a\beta_{2a} = -L_b\beta_{2b}$ ,  $L_a\beta_{3a} = -L_b\beta_{3b}$ ,  $L_a\beta_{4a} = -L_b\beta_{4b}$ , etc. Here,  $\beta_{2a}$  designates  $\beta_2$  for the fiber of length  $L_a$ , and  $\beta_{2b}$  designates  $\beta_2$  for the fiber of length  $L_b$ , and similar for all other  $\beta_n$ . DCF enables one to compensate simultaneously for both the path-averaged CD ( $D = 0$ , or  $\beta_2 = 0$ , averaged over  $L_a + L_b$ ) at the center wavelength of the pulse and for the path-averaged CD slope ( $dD/d\lambda = \beta_3(2\pi c/\lambda^2)^2 - 2D/\lambda = 0$ , or  $\beta_3 = 0$  additionally to  $\beta_2 = 0$ ). Conversely, the DCF is in general not able to compensate for  $\beta_4$ .

We discuss the application of dispersion compensation based on DCF using the example in Fig. 13.21.

A pulse generator generates optical pulses with a pulse width (FWHM) of 1.3 ps. These pulses propagate through a standard fiber (SMF,  $D = 17 \text{ ps}/(\text{nm km})$ ) of length  $L_a = 160 \text{ km}$ , followed by a dispersion-compensating fiber ( $D = -105 \text{ ps}/(\text{nm km})$ ) of length  $L_b \approx 26 \text{ km}$ . Before the pulse enters the DCF, its width is broadened by CD to about 2600 ps. If a data signal with a symbol rate of 160 GBd is transmitted, this broadened pulse covers more than 400 symbol periods. The pulses overlap strongly. After propagation through the DCF the pulse width is again about 1.3 ps, and the pulses are well separated at the input of the demultiplexer.

The adjustment of the transmission link to minimum pulse width at the receiver is a prerequisite of all high bit rate OTDM transmission experiments. In the example shown in Fig. 13.21 the pulse width is measured with use of an autocorrelation measurement versus the center wavelength of the optical pulses generated in a wavelength-tunable pulse generator. The figure shows the useful spectral range (e.g., pulse width  $< 1.6 \text{ ps}$ ) for data transmission of 160 GBd over the given fiber link.

The length  $L_b$  of the DCF has to be carefully adjusted to the length  $L_a$  of the SMF. The tolerances as regards residual dispersion or residual SMF or DCF length are particularly crucial for high-speed systems. For instance, for a single polarization signal at the symbol rate of 160 GBd (pulse width 1.5 ps), simulations yield a tolerance (eye opening penalty of 1 dB for  $\text{BER} = 10^{-9}$ ) of  $\pm 2.5 \text{ ps}/\text{nm}$ , which corresponds to an SMF length of  $\pm 150 \text{ m}$  [103]. However, in experiments a fine tuning of  $\pm 50 \text{ m}$  is appropriate. To maintain such tolerances over a large environmental temperature range requires automatic dispersion compensation in addition to the DCF. Various tunable dispersion compensators have been proposed [104–107].

### 13.7.3 Compensation of Higher Order Chromatic Dispersion

For symbol rates of 640 GBd and beyond, higher order dispersion terms ( $d^2D/d\lambda^2$  or  $\beta_4$ ) cause substantial pulse broadening in most fibers and also in transmission links with exact compensation of  $D$  and  $dD/d\lambda$ . It is very difficult to construct DCFs, which are able to simultaneously compensate  $D$ ,  $dD/d\lambda$  and  $d^2D/d\lambda^2$  [102]. Therefore, other techniques for the compensation of the higher order dispersion term  $d^2D/d\lambda^2$  were investigated. The most important technique is dispersion compensation using prechirping by a phase modulator [108–110]. In an OTDM transmitter, the prechirping unit is placed between the signal generator (e.g., 10 Gbit/s) and the OTDM multiplexer (e.g., 10 Gbit/s to 1.28 Tbit/s) [7]. The prechirping unit comprises three elements: a piece of SMF of length  $L_s$ , a phase modulator, and a piece of RDF (reverse dispersion fiber, see Sect. 13.7.1) of length  $L_r$ . The phase modulator is driven by a 10 GHz sinusoidal RF signal generator, which is synchronized to the 10 Gbit/s data signal. In the SMF, chromatic dispersion broadens the signal pulses and induces a strong linear chirp with the fast frequency components at the front and the slow frequency components at the tail of the pulse. This enables phase modulation in the spectral domain of each signal pulse by the phase modulator, for example



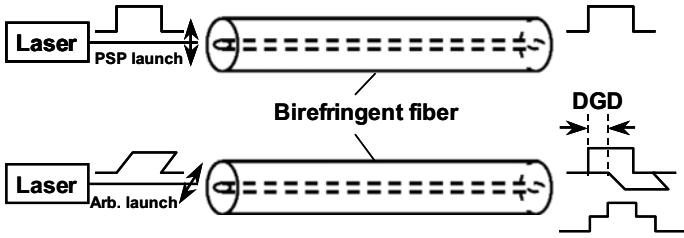


**Fig. 13.22** Pulse distortion due to first-order PMD in a fiber. The figure shows a single birefringent section

$\varphi_m = A \cos[B(\omega - \omega_0)] = A\{1 - (1/2)[B(\omega - \omega_0)]^2 + (1/24)[B(\omega - \omega_0)]^4 + \dots\}$ . The two fiber lengths  $L_s$  and  $L_r$  as well as the two modulation parameters  $A$  and  $B$  have to be properly adjusted to the length  $L_a$  of the transmission fiber to make the phase  $\beta(L_a + L_s + L_r)$  independent of  $(\omega - \omega_0)$  up to the 4th order  $(\omega - \omega_0)^4$  according to (13.10). This dispersion compensation technique was successfully realized in a 1.28 Tbit/s OOK transmission experiment over a 70 km SMF/RDF fiber link [7, 8].

Modern fibers like the SLA/IDF fiber (see Sect. 13.7.1) are more suitable for high-speed data transmission. A 2.56 Tbit/s DQPSK data signal, corresponding to a symbol rate of 1.28 TBd, was transmitted over 160 km SLA/IDF fiber without application of higher order dispersion compensation using prechirping by a phase modulator [9].

### 13.7.4 Compensation of Polarization-mode Dispersion

Polarization-mode dispersion is an effect in which polarization-dependent time delays of optical pulses in fibers lead to distorted signals at the receiver. PMD is caused by birefringence of the fiber and of other components in the transmission line. Birefringence is induced in the fiber for example by mechanical stress or an elliptical core profile of the waveguide. PMD is a severe limitation for high-speed data transmission. It results in broadening and depolarization of optical pulses. Unlike CD, PMD is much more difficult to compensate for because it changes with time and wavelength in a nondeterministic way. A common way to describe PMD is the so-called “retarder plate” or “wave-plate” model. In this model, the fiber is viewed as a series of concatenated birefringent sections (i.e., retarder plates or wave-plates, see Fig. 13.22).

We consider a single section of length  $L_n$ . It is characterized by its two main axes, say the  $x$ - and  $y$ -axes, which are perpendicular to the propagation direction ( $z$ -axis). An optical pulse with a state of polarization parallel to the  $x$ - or  $y$ -axis experiences the propagation constant  $\beta_x$  or  $\beta_y$ , respectively.  $\beta_x$  and  $\beta_y$  are different due to linear birefringence. Therefore, the group delays  $\tau_{gx} = L_n \beta_{1x}$  and  $\tau_{gy} = L_n \beta_{1y}$  differ.

The difference  $\Delta\tau = \tau_{gx} - \tau_{gy}$  is the retardation of the birefringent section (see Fig. 13.22). In the “retarder plate” model, the concatenated sections all have the same  $z$ -axis, but the orientation of the  $x$ - and  $y$ -axis as well as the retardation varies randomly and time dependently from section to section.

The fiber has similar properties as the sum of all concatenated sections. At a given time and over a given narrow wavelength range, there are two principal states of polarization (PSP), such that an optical pulse with an SOP parallel to these PSPs experiences the maximum or minimum group delay, respectively. The difference between these group delays is called the differential group delay (DGD). Theory shows that the PSPs and the DGD are both represented by one quantity, the so-called PMD vector (in Stokes space) [111]. The PMD vector is wavelength dependent and in general expanded in a Taylor series about the center frequency of the pulse spectrum. In the first order of this expansion (first-order PMD), the PSPs and the DGD are independent of wavelength as in a single retarder plate. With first-order PMD only, an optical pulse with an arbitrary SOP at the input of the fiber can be resolved into components along these two orthogonal PSPs such that two orthogonal components of the pulse propagate with different propagation constants through the fiber and appear at the output of the fiber separated by the DGD. If second-order PMD is also taken into account, the wavelength dependence of the DGD causes the two PSP-components of a pulse to see different chromatic dispersion while a wavelength dependence of the PSPs will yield a depolarization of a pulse at the output even in the case of PSP pulse launching [112]. In the following, we consider first-order PMD only because PMD compensation is mostly restricted to first-order PMD.

A fiber is often characterized by the so-called PMD value of a fiber. The PMD value is the mean value of the DGD, i.e., the average over wavelength and time. Even for fiber links with low PMD value, instantaneous DGD values can exceed the tolerable margin and cause system outages if the PMD value of the fiber link is higher than approximately  $0.1T_B$  [111]. Here  $1/T_B$  is the symbol rate of the transmitted (multiplexed) data signal. This shows that PMD becomes a serious impairment at high symbol rates.

In most ultra-high-speed transmission experiments (in the laboratory), PMD (first order) was compensated for by manually adjusting the SOP of the data signal at the input of the transmission line to a PSP. In real systems, however, an automatic and dynamic approach for PMD compensation is necessary since PMD is influenced by environmental conditions and varies on different time scales. The PMD compensation techniques can be classified into electrical and optical compensation techniques. Electrical PMD compensation is based on postdetection electrical signal processing of the photodiode signal, i.e., processing after detection. We considered this approach shortly in Sect. 13.6.3, and refer to [100]. Here we discuss optical PMD compensation based on optical signal processing, i.e., before the data signal is detected at the receiver.

The set-up of an optical PMD compensator is schematically shown in Fig. 13.23.

It consists of a polarization controller (PC), a PMD equalizer, an error detector, and a control unit. A simple example of an equalizer is indicated in the box representing the PMD equalizer. This example comprises two polarization beam

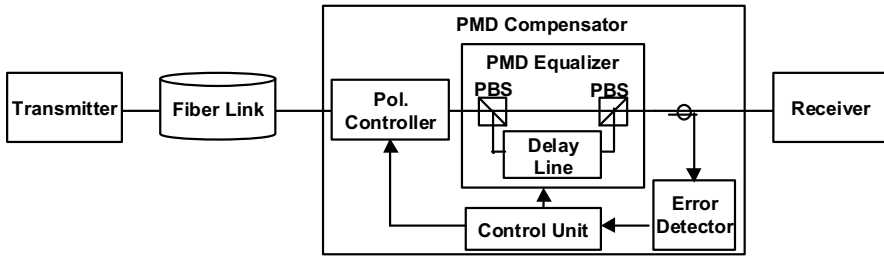


**Fig. 13.23** PMD compensator

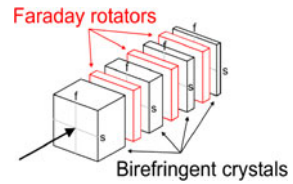
splitters and a motor-driven variable optical delay line. The polarization controller (e.g., a  $\text{LiNbO}_3$  polarization controller) adjusts the input polarization to the PMD equalizer such that the DGD of the fiber link is compensated for by the retardation of the variable delay line. Both, the polarization controller and the PMD equalizer, are driven by the control unit. The input to the control unit is a signal from the error detector. The error detector measures the “quality” of the data signal before the receiver and gives a feedback signal to the control unit. In the control unit, an algorithm optimizes adaptively the parameter settings of the equalizer and the polarization controller. The parameter settings are typically dithered around the current operating point, and the gradient of the feedback signal is used to approach a minimum of first-order PMD of the sum of both the fiber link and PMD compensator. In addition to this feedback structure of the PMD compensator, there are also applications of a feed-forward structure of the PMD compensator [112].

There are several techniques to measure the “quality” of the data signal and to generate the feedback signal. A frequently used technique is the measurement of the degree of polarization (DOP) with use of a Stokes polarimeter. PMD reduces the DOP of a data signal strongly. The PMD-induced pulse splitting in a fast and a slow component leads to a time varying SOP along the pulse as follows. The leading fast pulse component may have a linear vertical SOP, and the trailing slow pulse component consequently has a linear horizontal SOP. In this case, the DOP approaches zero if both pulse components have the same strength and do not overlap in time ( $|\text{DGD}| > \text{FWHM}$ ). If these pulse components partly overlap in time, the overlapping part may have an arbitrary elliptical SOP. In the control unit, a maximum-search control algorithm adjusts the polarization controller and the DGD of the equalizer to maximum mean DOP.

Several realizations for PMD equalizers have been investigated [112]. Here, we discuss a PMD compensator that enabled error-free single-channel 160 Gbit/s RZ-DPSK transmission over a 75 km SMF link (comprising 45 km installed fiber) with a PMD-value of  $0.34T_B$  [113]. The equalizer illustrated in Fig. 13.24 consists of an alternating cascade of birefringent  $\text{YVO}_4$ -crystals and tunable Faraday rotators and was designed to cover a DGD range from 0.31 ps to 4.70 ps in steps of 0.63 ps.

The magneto-optical polarization rotators have a response time of less than 1 ms and were used to couple light from one main axis of a crystal to one of the main axes

**Fig. 13.24** PMD compensator based on  $\text{YVO}_4$ -crystals and tunable Faraday rotators



of the next crystal, requiring driving currents of less than 100 mA each, consuming less than 250 mW. The crystal thickness (and thus the DGD of the birefringent elements) varies in powers of two, allowing for a sufficiently small step size which is important for minimizing second-order PMD as well as frequency-independent changes of the PSPs of the PMD compensator during switching. Neglecting small wavelength dependencies of the Faraday rotators, there will be no polarization-dependent chromatic dispersion and the depolarization rate can be kept low due to the small step size. It is important, however, that the crystals are placed in order of descending thickness since otherwise the input PSPs of the compensator will be interchanged during each switching process, causing additional transmission impairments. The insertion loss of the equalizer is 5 dB and its polarization-dependent loss is less than 0.5 dB.

In the considered 160 Gbit/s RZ-DPSK transmission experiment, the transmitter and the receiver were equipped with additional polarization controllers. At the output of the transmitter, a  $\text{LiNbO}_3$ -based polarization controller was used to scramble the polarization. This ensures that changes of the instantaneous DGD will be detected independently from the input polarization in the fiber link. Otherwise, the DOP may be unaffected by PMD if the input polarization by chance matches one of the PSPs of the fiber link. At the input of the receiver, another polarization controller was placed together with a polarimeter to provide a constant SOP of the data signal, because the delay line interferometer in the DPSK receiver was slightly polarization sensitive.

## 13.8 Concluding Remarks

In this chapter, optical signal processing was discussed for high-speed data transmission using optical time-division multiplexing (OTDM) technology. We considered OTDM systems employing a conventional OTDM receiver or a coherent OTDM receiver both operating at data rates up to several Tbit/s. The combination of OTDM technology with coherent technology is very promising. In particular, the coherent receiver is useful in conjunction with advanced modulation formats such as  $m$ -PSK and  $m$ -ary-QAM. Moreover, the application of the coherent receiver promises compensation of transmission impairments by postdetection signal processing in the electrical regime, thus alleviating optical signal processing. However, we do not expect optical signal processing to be strongly alleviated by the application of coherent

technology. The demultiplexing operation of the coherent receiver is a key process. Postdetection signal processing requires a clear amplitude and phase replica of the selected tributary signal of the multiplexed data signal. To obtain this amplitude and phase replica undisturbed for example by channel crosstalk, the demultiplexer requires signal processing in the optical domain in front of the demultiplexer. Up to now only a few transmission experiments have been performed using coherent receiver technology. It is not possible to judge how much optical signal processing will be replaced by postdetection electrical signal processing. But in any case, a promising new research area has opened.

## References

1. S. Kawanishi, H. Takara, K. Uchiyama, M. Saruwatari, T. Kitoh, Single polarization completely time-division-multiplexed 100 Gbit/s optical transmission experiment, *Proc. 19th Europ. Conf. Opt. Commun. (ECOC'93)*, Montreux, Switzerland (1993), vol. 3, pp. 53–56
2. S. Kawanishi, Ultrahigh-speed optical time-division-multiplexed transmission technology based on optical signal processing. *IEEE J. Quantum Electron.* **34**, 2064–2079 (1998)
3. M. Saruwatari, All-optical signal processing for Terabit/s optical transmission. *IEEE J. Sel. Top. Quantum Electron.* **6**, 1363–1374 (2000)
4. H.G. Weber, R. Ludwig, S. Ferber, C. Schmidt-Langhorst, M. Kroh, V. Marembert, C. Boerner, C. Schubert, Ultrahigh-speed OTDM-transmission technology. *J. Lightw. Technol.* **24**, 4616–4627 (2006)
5. H.G. Weber, M. Nakazawa, Introduction to ultra-high-speed optical transmission technology, in *Optical and Fiber Communication Reports 3, Ultrahigh-Speed Optical Transmission Technology*, ed. by H.G. Weber, M. Nakazawa (Springer, LLC, New York, 2007), pp. 1–20. ISBN: 978-3-540-23878-2
6. H.G. Weber, R. Ludwig, Ultra-high-speed OTDM transmission technology, in *Optical Fiber Telecommunications VB*, ed. by I.P. Kaminow, T. Li, A.E. Willner, (Academic Press, London, 2008), pp. 201–232. ISBN: 978-0-12-374172-1
7. M. Nakazawa, T. Yamamoto, K.R. Tamura, 1.28 Tbit/s-70 km OTDM transmission using third- and fourth-order simultaneous dispersion compensation with a phase modulator. *Electron. Lett.* **36**, 2027–2029 (2000)
8. T. Yamamoto, M. Nakazawa, Ultrafast OTDM transmission using novel fiber devices for pulse compression, shaping, and demultiplexing. *J. Opt. Fiber Commun. Rep.* **2**, 209–225 (2005). ISSN: 1619-8638 (online)
9. H.G. Weber, S. Ferber, M. Kroh, C. Schmidt-Langhorst, R. Ludwig, V. Marembert, C. Boerner, F. Futami, S. Watanabe, C. Schubert, Single channel 1.28 Tbit/s and 2.56 Tbit/s DQPSK transmission. *Electron. Lett.* **42**, 178–179 (2006)
10. C. Schmidt-Langhorst, R. Ludwig, D.-D. Groß, L. Molle, M. Seimetz, R. Freund, C. Schubert, Generation and coherent time-division demultiplexing of up to 5.1 Tbit/s single-channel 8-PSK and 16-QAM signals, *Opt. Fiber Commun. Conf. and Nat. Fiber Opt. Eng. Conf. (OFC/NFOEC'09)*, Techn. Digest (San Diego, CA, USA, 2009), paper PDPC6
11. H.C. Hansen Mulvad, M. Galili, L.K. Oxenløwe, H. Hu, A.T. Clausen, J.B. Jensen, C. Peucheret, P. Jeppesen, Error-Free 5.1 Tbit/s data on a single-wavelength channel using a 1.28 Tbaud symbol rate, *22nd Meeting IEEE Phot. Soc.*, 4–8 Oct. 2009, Antalya, Turkey, paper PD2.1
12. T. Richter, E. Palushani, C. Schmidt-Langhorst, M. Nölle, R. Ludwig, C. Schubert, Single wavelength channel 10.2 Tbit/s TDM-data capacity using 16-QAM and coherent detection, *Opt. Fiber Commun. Conf. and Nat. Fiber Opt. Eng. Conf. (OFC/NFOEC'11)*, Techn. Digest (Los Angeles, CA, USA, 2011), paper PDPA9

13. R. Freund, D.-D. Groß, R. Ludwig, C. Schmidt-Langhorst, 1.28 Tbit/s single wavelength star-16-QAM transmission over up to 800 m of graded-index multimode fibre, *Proc. OECC*, 13–17 July 2009, Hong Kong (China), post-deadline paper
14. G.P. Agrawal, *Nonlinear Fiber Optics* (Academic Press, London, 1995)
15. Y.R. Shen, *The Principles of Nonlinear Optics* (Wiley, New York, 1984)
16. G.I. Stegeman, Nonlinear guided wave optics, in *Contemporary Nonlinear Optics*, ed. by G.P. Agrawal, R.W. Boyd (Academic Press, Boston, 1992), pp. 1–40
17. G.I. Stegeman, A. Miller, Physics of all-optical switching devices, in *Photonics in Switching*, vol. 1, ed. by J.E. Midwinter (Academic Press, Boston, 1993), pp. 81–145
18. M.J. Adams, D.A.O. Davies, M.C. Tatham, M.A. Fisher, Nonlinearities in semiconductor laser amplifiers. *Opt. Quantum Electron.* **27**, 1–13 (1995)
19. R. Manning, A. Ellis, A. Poustie, K. Blow, Semiconductor laser amplifier for ultrafast all-optical signal processing. *J. Opt. Soc. Am. B* **14**, 3204–3216 (1997)
20. C. Schubert, R. Ludwig, H.G. Weber, High-speed optical signal processing using semiconductor optical amplifiers, in *Optical and Fiber Communication Reports 3, Ultrahigh-Speed Optical Transmission Technology*, ed. by H.G. Weber, M. Nakazawa (Springer, LLC, New York, 2007), pp. 103–140. ISBN: 978-3-540-23878-2
21. R. Ludwig, W. Pieper, H.G. Weber, D. Breuer, K. Petermann, F. Küppers, A. Mattheus, Unrepeated 40 Gbit/s RZ single channel transmission over 150 km of standard fiber at 1.55  $\mu\text{m}$ . *Electron. Lett.* **36**, 1405–1406 (2000)
22. A.T. Clausen, H.N. Poulsen, L.K. Oxenløwe, A.I. Siahlo, J. Seoane, P. Jeppesen, Pulse source requirements for OTDM systems, *IEEE LEOS Annual Meeting Conf. Proc.*, Tucson, AZ, USA, 2003, vol. 1, pp. 27–28
23. S.C. Zeller, L. Krainer, G.J. Spühler, K.J. Weingarten, R. Paschotta, U. Keller, Passively mode-locked 40-GHz Er:Yb:glass laser. *Appl. Phys. B* **76**, 787–788 (2003)
24. R. Ludwig, S. Diez, A. Ehrhardt, L. Kueller, W. Pieper, H.G. Weber, A tunable femtosecond modelocked semiconductor laser for applications in OTDM-systems. *IEICE Trans. Electron.* **E81-C**, 140–145 (1998)
25. H. Yokoyama, Highly reliable mode-locked semiconductor lasers. *IEICE Trans. Electron.* **E85-C**, 27–36 (2002)
26. L.A. Jiang, E.P. Ippen, H. Yokoyama, Semiconductor mode-locked lasers as pulse sources for high bit rate data transmission, in *Optical and Fiber Communication Reports 3, Ultrahigh-Speed Optical Transmission Technology*, ed. by H.G. Weber, M. Nakazawa (Springer, LLC, New York, 2007), pp. 21–51. ISBN: 978-3-540-23878-2
27. S. Arahira, Y. Ogawa, 40 GHz actively mode-locked distributed Bragg reflector laser diode module with an impedance-matching circuit for efficient RF signal injection. *Jpn. J. Appl. Phys.* **43**, 1960–1964 (2004)
28. H. Heidrich, B. Huettl, R. Kaiser, M. Kroh, C. Schubert, G. Jacumeit, Optical 40 GHz pulse source module based on a monolithically integrated mode locked DBR laser, *SPIE Proc. Asia-Pacific Optical Communications (APOC) 2005*, Session 12b, paper 6020-79
29. K. Tamura, H.A. Haus, E.P. Ippen, Self-starting additive pulse mode-locked erbium fibre ring laser. *Electron. Lett.* **28**, 2226–2228 (1992)
30. M. Nakazawa, E. Yoshida, Y. Kimura, Ultrastable harmonically and regeneratively mode-locked polarisation-maintaining erbium fibre laser. *Electron. Lett.* **30**, 1603–1604 (1994)
31. M. Nakazawa, Ultrafast mode-locked fiber lasers for high-speed OTDM transmission and related topics, in *Optical and Fiber Communication Reports 3, Ultrahigh-Speed Optical Transmission Technology*, ed. by H.G. Weber, M. Nakazawa (Springer, LLC, New York, 2007), pp. 53–87. ISBN: 978-3-540-23878-2
32. M.D. Pelusi, Y. Matsui, A. Suzuki, Femtosecond optical pulse generation from an electro-absorption modulator with repetition rate and wavelength tuning, *Proc. 25th Europ. Conf. Opt. Commun. (ECOC'99)*, Nice, France (1999), vol. II, pp. 26–27
33. E. Lach, K. Schuh, M. Schmidt, Application of electroabsorption modulators for high-speed transmission systems, in *Optical and Fiber Communication Reports 3, Ultrahigh-Speed Optical Transmission Technology*, ed. by H.G. Weber, M. Nakazawa (Springer, LLC, New York, 2007), pp. 347–377. ISBN-13: 978-3-540-23878-2

34. T. Morioka, K. Uchiyama, S. Kawanishi, S. Suzuki, M. Saruwatari, Multiwavelength picosecond pulse source with low jitter and high optical frequency stability based on 200 nm supercontinuum filtering. *Electron. Lett.* **31**, 1064–1066 (1995)
35. W.J. Tomlinson, R.H. Stolen, C.V. Shank, Compression of optical pulses chirped by self-phase modulation in fibers. *J. Opt. Soc. Am. B* **1**, 139–149 (1984)
36. S.V. Chernikov, D.J. Richardson, E.M. Dianov, D.N. Payne, Picosecond soliton pulse compressor based on dispersion decreasing fiber. *Electron. Lett.* **28**, 1842–1844 (1992)
37. A. Mostofi, H. Hatami-Hanza, P.L. Chu, Optimum dispersion profile for compression of fundamental solitons in dispersion decreasing fibers. *IEEE J. Quantum Electron.* **33**, 620–628 (1997)
38. M. Nakazawa, E. Yoshida, K. Kubota, Y. Kimura, Generation of a 170 fs, 10 GHz transform-limited pulse train at 1.55  $\mu\text{m}$  using a dispersion-decreasing, erbium-doped active soliton compressor. *Electron. Lett.* **30**, 2038–2039 (1994)
39. K.R. Tamura, M. Nakazawa, 54-fs, 10 GHz soliton generation from a polarization-maintaining dispersion-flattened dispersion-decreasing fiber compressor. *Opt. Lett.* **26**, 762–764 (2001)
40. W.S. Wong, S. Namiki, M. Margalit, H.A. Haus, E.P. Ippen, Self-switching of optical pulses in dispersion-imbalanced nonlinear loop mirrors. *Opt. Lett.* **22**, 1150 (1997)
41. I.Y. Khrushchev, I.D. Phillips, A.D. Ellis, R.J. Manning, D. Nesses, D.G. Moodie, R.V. Penty, I.H. White, Dispersion-imbalanced fiber loop mirror for high bit-rate OTDM, *Proc. 25th Europ. Conf. Opt. Commun. (ECOC'99)*, Nice, France (1999), vol. II, pp. 24–25
42. T. Yamamoto, M. Nakazawa, Ultrafast OTDM transmission using novel fiber devices for pulse compression, shaping, and demultiplexing, in *Optical and Fiber Communication Reports 3, Ultrahigh-Speed Optical Transmission Technology*, ed. by H.G. Weber, M. Nakazawa (Springer, LLC, New York, 2007), pp. 379–395. ISBN: 978-3-540-23878-2
43. N.J. Doran, D. Wood, Nonlinear optical loop mirror. *Opt. Lett.* **13**, 56–58 (1988)
44. C. Schmidt-Langhorst, H.G. Weber, Optical sampling techniques, in *Optical and Fiber Communication Reports 3, Ultrahigh-Speed Optical Transmission Technology*, ed. by H.G. Weber, M. Nakazawa (Springer, LLC, New York, 2007), pp. 453–481. ISBN: 978-3-540-23878-2
45. K.L. Sala, W.A. Kenny, G.E. Hall, CW autocorrelation measurements of picosecond laser pulses. *IEEE J. Quantum Electron.* **QE-16**, 990–996 (1980)
46. R. Trebino, *Frequency Resolved Optical Gating: the Measurement of Ultrashort Laser Pulses* (Kluwer Academic, Dordrecht, 2002)
47. M. Kroh, Semiconductor mode-locked laser for high-speed OTDM transmission, PhD Thesis, Technical University Berlin (2006). <http://opus.kobv.de/tuberlin/volltexte/2006/1268/>
48. D. von der Linde, Characterization of the noise in continuously operating mode-locked lasers. *Appl. Phys. B* **39**, 201–217 (1986)
49. P.J. Winzer, R.-J. Essiambre, Advanced optical modulation formats, in *Optical Fiber Telecommunications VB*, ed. by I.P. Kaminow, T. Li, A.E. Willner (Academic Press, London, 2008), pp. 23–93. ISBN 978-0-12-374172-1
50. E. Agrell, M. Karlsson, Power-efficient modulation formats in coherent transmission systems. *J. Lightw. Technol.* **27**, 5115–5126 (2009)
51. T. Chikama, S. Watanabe, T. Naito, H. Onaka, T. Kiyonaga, Y. Onoda, H. Miyata, M. Suyama, M. Seino, H. Kuwahara, Modulation and demodulation techniques in optical heterodyne PSK transmission systems. *J. Lightw. Technol.* **8**, 309–321 (1990)
52. A.H. Gnauck, S. Chandrasekhar, J. Leuthold, L. Stulz, Demonstration of 42.7-Gbit/s DPSK receiver with 45 photons/bit sensitivity. *IEEE Photon. Technol. Lett.* **15**, 99–101 (2003)
53. A. H. Gnauck, P.J. Winzer, Optical phase-shift-keyed transmission. *J. Lightw. Technol.* **23**, 115–130 (2005)
54. R. Griffin, A. Carter, Optical differential phase shift key (oDQPSK) for high capacity optical transmission, *Opt. Fiber Commun. Conf. (OFC/IEOC'02)*, Techn. Digest (Anaheim, CA, USA, 2002), paper WX6, pp. 367–368

55. T. Ohara, H. Takara, I. Shake, K. Mori, S. Kawanishi, S. Mino, T. Yamada, M. Ishii, T. Kitoh, T. Kitagawa, K.R. Parameswaran, M.M. Fejer, 160 Gbit/s optical-time-division multiplexing with PPLN hybrid integrated planar lightwave circuit. *IEEE Photon. Technol. Lett.* **15**, 302–304 (2003)
56. T. Ohara, H. Takara, I. Shake, K. Mori, K. Sato, S. Kawanishi, S. Mino, T. Yamada, M. Ishii, I. Ogawa, T. Kitoh, K. Magari, M. Okamoto, R.V. Roussev, J.R. Kurz, K.R. Parameswaran, M.M. Fejer, 160-Gbit/s OTDM transmission using integrated all-optical MUX/DEMUX with all-channel modulation and demultiplexing. *IEEE Photon. Technol. Lett.* **16**, 650–652 (2004)
57. H. Murai, M. Kagawa, H. Tsuji, K. Fujii, Single channel 160 Gbit/s carrier-suppressed RZ transmission over 640 km with EA modulator based OTDM module, *Proc. 29th Europ. Conf. Opt. Commun. (ECOC'03)*, Rimini, Italy (2003), paper Mo.3.6.4
58. S. Randel, B. Konrad, A. Hodzic, K. Petermann, Influence of bitwise phase changes on the performance of 160 Gbit/s transmission systems, *Proc. 28th Europ. Conf. Opt. Commun. (ECOC'02)*, Copenhagen, Denmark (2002), vol. 3, paper P3.31
59. M. Kagawa, H. Murai, H. Tsuji, K. Fujii, Performance comparison of bitwise phase-controlled 160 Gbit/s signal transmission using an OTDM multiplexer with phase-correlation monitor, *Proc. 30th Europ. Conf. Opt. Commun. (ECOC'04)*, Stockholm, Sweden (2004), paper We 4.P.109
60. Y. Su, L. Möller, C. Xie, R. Ryf, X. Liu, X. Wei, S. Cabot, Ultra high-speed data signals with alternating and pairwise alternating optical phases. *J. Lightw. Technol.* **23**, 26–31 (2005)
61. M. Schmidt, K. Schuh, E. Lach, M. Schilling, G. Veith,  $8 \times 160$  Gbit/s (1.28 Tbit/s) DWDM transmission with 0.53 bit/s/Hz spectral efficiency using single EA-modulator based RZ pulse source and demux, *Proc. 29th Europ. Conf. Opt. Commun. (ECOC'03)*, Rimini, Italy (2003), paper Mo3.6.5
62. E. Lach, K. Schuh, M. Schmidt, B. Junginger, G. Charlet, P. Pecci, G. Veith,  $7 \times 170$  Gbit/s (160 Gbit/s + FEC overhead) DWDM transmission with 0.53 bit/s/Hz spectral efficiency over long haul distance of standard SMF, *Proc. 29th Europ. Conf. Opt. Commun. (ECOC'03)*, Rimini, Italy (2003), paper PD Th4.3.5
63. M. Daikoku, T. Otani, M. Suzuki, 160 Gbit/s four WDM quasi-linear transmission over 225 km NZ-DSF with 75 km spacing. *IEEE Photon. Technol. Lett.* **15**, 1165–1167 (2003)
64. M. Schmidt, M. Witte, F. Buchali, E. Lach, E. Le Rouzic, S. Salaun, S. Vorbeck, R. Leppla,  $8 \times 170$  Gbit/s DWDM field transmission experiment over 430 km SSMF using adaptive PMD compensation, *Proc. 30th Europ. Conf. Opt. Commun. (ECOC'04)*, Stockholm, Sweden (2004), PDP Th4.1.2
65. K.J. Blow, N.J. Doran, B.P. Nelson, Demonstration of the nonlinear fibre loop mirror as an ultrafast all-optical demultiplexer. *Electron. Lett.* **26**, 962–963 (1990)
66. M. Nakazawa, E. Yoshida, T. Yamamoto, E. Yamada, A. Sahara, TDM single channel 640 Gbit/s transmission experiment over 60 km using 400 fs pulse train and walk-off free, dispersion flattened nonlinear optical loop mirror. *Electron. Lett.* **34**, 907–908 (1998)
67. T. Yamamoto, E. Yoshida, K.R. Tamura, K. Yonenaga, M. Nakazawa, 640 Gbit/s optical TDM transmission over 92 km through a dispersion managed fiber consisting of single-mode fiber and reverse dispersion fibre. *IEEE Photon. Technol. Lett.* **12**, 353–355 (2000)
68. K. Uchiyama, H. Takara, S. Kawanishi, T. Morioka, M. Saruwatari, Ultrafast polarization-independent all-optical switching using a polarization diversity scheme in the nonlinear optical loop mirror. *Electron. Lett.* **28**, 1864–1865 (1992)
69. T. Morioka, H. Takara, S. Kawanishi, T. Kitoh., M. Saruwatari, Error-free 500 Gbit/s all-optical demultiplexing using low-noise, low-jitter supercontinuum short pulses. *Electron. Lett.* **32**, 833–834 (1996)
70. E. Jahn, N. Agrawal, M. Arbert, H.-J. Ehrke, D. Franke, R. Ludwig, W. Pieper, H.G. Weber, C.M. Weinert, 40 Gbit/s all-optical demultiplexing using a monolithically integrated Mach-Zehnder interferometer with semiconductor laser amplifiers. *Electron. Lett.* **31**, 1857–1858 (1995)



71. R. Hess, M. Caraccia-Gross, W. Vogt, E. Gamber, P.A. Besse, M. Duell, E. Gini, H. Melchior, B. Mikkelsen, M. Vaa, K.S. Jepsen, K.E. Stubkaer, S. Bouchoule, All-optical demultiplexing 80 to 10 Gbit/s signals with monolithic integrated high performance Mach-Zehnder interferometer. *IEEE Photon. Technol. Lett.* **10**, 165–167 (1998)
72. A. Suzuki, X. Wang, Y. Ogawa, S. Nakamura,  $10 \times 320$  Gbit/s (3.2 Tbit/s) DWDM/OTDM transmission by semiconductor based devices, *Proc. 30th Europ. Conf. Opt. Commun. (ECOC'04)*, Stockholm, Sweden (2004), paper Th4.1.7
73. K. Tajima, S. Nakamura, A. Furukawa, Hybrid-integrated symmetric Mach-Zehnder all-optical switches and ultrafast signal processing. *IEICE Trans. Electron.* **E87-C**, 1119–1125 (2004)
74. C. Schubert, S. Diez, J. Berger, R. Ludwig, U. Feiste, H.G. Weber, G. Toptchiyski, K. Petermann, V. Krajinovic, 160 Gbit/s all-optical demultiplexing using a gain-transparent ultrafast-nonlinear interferometer (GT-UNI). *IEEE Photon. Technol. Lett.* **13**, 475–477 (2001)
75. U. Feiste, R. Ludwig, C. Schubert, J. Berger, C. Schmidt, H.G. Weber, B. Schmauss, A. Munk, B. Buchold, D. Briggmann, F. Kueppers, F. Rumpf, 160 Gbit/s transmission over 116 km field-installed fibre using 160 Gbit/s OTDM and 40 Gbit/s ETDM. *Electron. Lett.* **37**, 443–445 (2001)
76. J.P. Sokoloff, P.R. Prucnal, I. Glesk, M. Kane, A terahertz optical asymmetric demultiplexer (TOAD) *IEEE Photon. Technol. Lett.* **5**, 787–790 (1993)
77. T. Morioka, H. Takara, S. Kawanishi, K. Uchiyama, M. Saruwatari, Polarization-independent all-optical demultiplexing up to 200 Gbit/s using four-wave-mixing in a semiconductor laser amplifier. *Electron. Lett.* **32**, 840–842 (1996)
78. H. Murai, M. Kagawa, H. Tsuji, K. Fuji, EA modulator based optical multiplexing/demultiplexing techniques for 160 Gbit/s OTDM signal transmission. *IEICE Trans. Electron.* **E88-C**, 309–318 (2005)
79. S. Kodama, T. Yoshimatsu, H. Ito, 500-Gbit/s demultiplexing operation of monolithic PD-EAM gate, *Proc. 29th Europ. Conf. Opt. Commun. (ECOC'03)*, Rimini, Italy (2003), post-deadline paper Th4.2.8
80. M. Saruwatari, All-optical time-division multiplexing technology. in *Fiber Optic Communication Devices*, ed. by N. Grote, H. Venghaus (Springer, Berlin, 2001), Chap. 9
81. I. Shake, H. Takara, K. Uchiyama, I. Ogawa, T. Kitoh, T. Kitagawa, M. Okamoto, K. Magari, Y. Suzuki, T. Morioka, 160 Gbit/s full optical time-division demultiplexing using FWM of SOA-array integrated on PLC. *Electron. Lett.* **38**, 37–38 (2002)
82. O. Kamatani, S. Kawanishi, Prescaled timing extraction from 400 Gbit/s optical signal using a phase lock loop based on four-wave mixing. *IEEE Photon. Technol. Lett.* **8**, 1094–1096 (1996)
83. C. Boerner, V. Marenbert, S. Ferber, C. Schubert, C. Schmidt-Langhorst, R. Ludwig, H.G. Weber, 320 Gbit/s clock recovery with electro-optical PLL using a bidirectionally operated electroabsorption modulator as phase comparator, *Opt. Fiber Commun. Conf. (OFC'05)*, Techn. Digest (Anaheim, CA, USA, 2005), paper OTuO3
84. C. Boerner, Clock recovery for optical high bit-rate return-to-zero datsignals by differential signal processing, PhD Thesis (in German), Technical University Berlin (2009). <http://opus.kobv.de/tuberlin/volltexte/2009/2071/>
85. U. Feiste, R. Ludwig, C. Schubert, J. Berger, C. Schmidt, H.G. Weber, B. Schmauss, A. Munk, B. Buchold, D. Briggmann, F. Kueppers, F. Rumpf, 160 Gbit/s transmission over 116 km field-installed fibre using 160 Gbit/s OTDM and 40 Gbit/s ETDM. *Electron. Lett.* **37**, 443–445 (2001)
86. A.H. Gnauck, G. Raybon, P.G. Bernasconi, J. Leuthold, C.R. Doerr, L.W. Stulz, 1 Tbit/s ( $6 \times 170.6$  Gbit/s) transmission over 2000 km NZDF using OTDM and RZ-DPSK. *IEEE Photon. Technol. Lett.* **15**, 1618–1620 (2003)
87. A.H. Gnauck, P.J. Winzer, Optical phase-shift-keyed transmission. *J. Lightw. Technol.* **23**, 115–130 (2005)
88. T. Okoshi, K. Kikuchi, *Coherent Optical Fiber Communications* (Kluwer, Boston, 1988)

89. K. Kikuchi, Coherent optical communication systems, in *Optical Fiber Telecommunications V B*, ed. by I.P. Kaminow, T. Li, A.E. Willner (Academic Press, London, 2008), pp. 95–129. ISBN: 978-0-12-374172-1
90. W.R. Leeb, Realization of 90° and 180° hybrids for optical frequencies. *Archiv Elektron. Übertrag.* (AEÜ) **37**, 203–208 (1983)
91. R. Langenhorst, G. Wenke, Compact bulk optical 90° hybrid for balanced phase diversity receiver. *Electron. Lett.* **22**, 1518–1519 (1989)
92. D. Hoffmann, H. Heidrich, G. Wenke, R. Langenhorst, E. Dietrich, Integrated optics eight port 90° hybrid on LiNbO<sub>3</sub>. *J. Lightw. Technol.* **7**, 794–798 (1989)
93. A. Matiss, R. Ludwig, J.K. Fischer, L. Molle, C. Schubert, C.C. Leonhardt, H.G. Bach, R. Kunkel, A. Umbach, Novel integrated coherent receiver module for 100G serial transmission, *Opt. Fiber Commun. Conf. and Nat. Fiber Opt. Eng. Conf.* (OFC/NFOEC'10), Techn. Digest (San Diego, CA, USA, 2010), paper PDPB3
94. K. Kikuchi, Phase-diversity homodyne detection of multi-level optical modulation with digital carrier phase estimation. *IEEE J. Sel. Top. Quantum Electron.* **12**, 563–570 (2006)
95. C. Zhang, Y. Mori, K. Igarashi, K. Katoh, K. Kikuchi, Ultrafast operation of digital coherent receivers using their time-division demultiplexing function. *J. Lightw. Technol.* **27**, 224–232 (2009)
96. C. Zhang, Y. Mori, K. Igarashi, K. Katoh, K. Kikuchi, Demodulation of 1.28-Tbit/s polarization-multiplexed 16-QAM signals on a single carrier with digital coherent receiver, *Opt. Fiber Commun. Conf. and Nat. Fiber Opt. Eng. Conf.* (OFC/NFOEC'09), Techn. Digest (San Diego, CA, USA, 2009), paper OTuG3
97. C. Zhang, Y. Mori, K. Igarashi, K. Katoh, K. Kikuchi, Straight-line 1,073-km transmission of 640-Gbit/s dual-polarization QPSK signals on a single carrier, *Proc. 35th Europ. Conf. Opt. Commun.* (ECOC'09), Vienna, Austria (2009), paper PD2.8
98. C. Schmidt-Langhorst, R. Ludwig, H. Hu, C. Schubert, Single-channel 1-Tbit/s transmission over 480 km DMF for future Terabit Ethernet systems, *Opt. Fiber Commun. Conf. and Nat. Fiber Opt. Eng. Conf.* (OFC/NFOEC'09), Techn. Digest (San Diego, CA, USA, 2009), paper OTuN5
99. J.H. Winters, R.D. Gitlin, Electrical signal processing techniques in long-haul fiber-optic systems. *Trans. Commun.* **38**, 1439–1453 (1990)
100. H. Bülow, S. Lanne, PMD compensation techniques, *Optical and Fiber Communication Reports, Polarization Mode Dispersion*, ed. by A. Galtarossa, C.R. Menyuk (Springer, New York, 2005), pp. 225–245. ISBN: 978-0387-23193-8
101. S. Weisser, S. Ferber, L. Raddatz, R. Ludwig, A. Benz, C. Boerner, H.G. Weber, Single- and alternating polarization 170 Gbit/s transmission up to 4000 km using dispersion-managed fiber and all-Raman amplification. *IEEE Photon. Technol. Lett.* **18**, 1320–1322 (2006)
102. M. Nishimura, Optical fibers and fiber dispersion compensators in optical communication systems, in *Optical and Fiber Communication Reports 3, Ultrahigh-Speed Optical Transmission Technology*, ed. by H.G. Weber, M. Nakazawa (Springer, LLC, New York, 2007), pp. 251–275. ISBN: 978-3-540-23878-2
103. S. Vorbeck, R. Leppla, Dispersion and dispersion slope tolerance of 160-Gbit/s systems, considering the temperature dependence of chromatic dispersion. *IEEE Photon. Technol. Lett.* **15**, 1470–1472 (2003)
104. B.J. Eggleton, B. Mikkelsen, G. Raybon, A. Ahuja, J.A. Rogers, P.S. Westbrook, T.N. Nielsen, S. Stulz, K. Dreyer, Tunable dispersion compensation in a 160 Gbit/s TDM system by voltage controlled chirped fiber Bragg grating. *IEEE Photon. Technol. Lett.* **12**, 1022–1024 (2000)
105. C.K. Madsen, Integrated waveguide allpass filter tunable dispersion compensator, *Opt. Fiber Commun. Conf.* (OFC/IOOC'02), Techn. Digest (Anaheim, CA, USA, 2002), paper TuT1
106. T. Inui, T. Komukai, M. Nakazawa, K. Suzuki, K.R. Tamura, K. Uchiyama, T. Morioka, Adaptive dispersion slope equalizer using a nonlinearly chirped fiber Bragg grating pair with a novel dispersion detection technique. *IEEE Photon. Technol. Lett.* **14**, 549–551 (2002)

107. S. Wakabayashi, A. Baba, H. Moriya, X. Wang, T. Hasegawa, A. Suzuki, Tunable dispersion and dispersion slope compensator based on two twin chirped FBGs with temperature gradient for 160 Gbit/s transmission. *IEICE Trans. Electron.* **E87-C**, 1100–1105 (2004)
108. M.D. Pelusi, X. Wang, F. Futami, K. Kikuchi, A. Suzuki, Fourth-order dispersion compensation for 250-fs pulse transmission over 139-km optical fiber. *IEEE Photon. Technol. Lett.* **12**, 795–798 (2000)
109. M.D. Pelusi, A. Suzuki, Higher-order dispersion compensation using phase modulators, in *Optical and Fiber Communication Reports 3, Ultrahigh-Speed Optical Transmission Technology*, ed. by H.G. Weber, M. Nakazawa (Springer, LLC, New York, 2007), pp. 301–321. ISBN: 978-3-540-23878-2
110. T. Yamamoto, M. Nakazawa, Third- and fourth-order active dispersion compensation with a phase modulator in a terabit-per-second optical time-division multiplexed transmission. *Opt. Lett.* **26**, 647–650 (2001)
111. L.E. Nelson, R.M. Jopson, Introduction to polarization mode dispersion in optical systems, in *Optical and Fiber Communication Reports, Polarization Mode Dispersion*, ed. by A. Galatarossa, C.R. Menyuk (Springer, New York, 2005), pp. 1–33. ISBN 978-0387-23193-8
112. H. Rosenfeldt, E. Brinkmeyer, PMD-compensation techniques, in *Optical and Fiber Communication Reports 3, Ultrahigh-Speed Optical Transmission Technology*, H.G. Weber, M. Nakazawa (Springer, LLC, New York, 2007), pp. 323–346. ISBN: 978-3-540-23878-2
113. S. Kieckbusch, S. Ferber, H. Rosenfeldt, R. Ludwig, A. Ehrhardt, E. Brinkmeyer, H.G. Weber, Automatic PMD compensator in a single-channel 160 Gbit/s transmission over deployed fiber using RZ-DPSK modulation format. *J. Lightw. Technol.* **23**, 165–171 (2005)

# Chapter 14

## Silicon Lasers and Photonic Integrated Circuits

Di Liang, Alexander W. Fang, and John E. Bowers

**Abstract** The chapter discusses photonic integration on silicon from the material property and device points of view and reviews the numerous efforts including bandgap engineering, Raman scattering, monolithic heteroepitaxy and hybrid integration to realize efficient light emission, amplification and lasing on silicon. The state of the art technologies for high-speed modulation are also discussed in order to unfold a picture of future transmitters on silicon.

This chapter discusses photonic integration on silicon from the material property and device points of view. The progressive growth of silicon-based electronic integrated circuits (ICs) has been governed by Moore's Law and historicized by the roadmap of conventional electronic ICs. Silicon is arguably the primary host material platform for future photonic integrated circuits (PICs) as well, particularly for applications beyond conventional fiber-optical telecommunications. Until recently, the lack of a laser source on silicon has been seen as the key hurdle limiting the usefulness and complexity of silicon photonic integrated circuits. In this chapter, we review the numerous efforts including bandgap engineering, Raman scattering, monolithic heteroepitaxy and hybrid integration to realize efficient light emission, amplification and lasing on silicon. The state of the art technologies for high-speed modulation are also discussed in order to unfold a picture of future transmitters on silicon.

---

Di Liang (✉) · John E. Bowers

Electrical and Computer Engineering Department, University of California (UCSB), Santa Barbara, CA 93106, USA

e-mail: dliang@ece.ucsb.edu, bowers@ece.ucsb.edu

Alexander W. Fang

Aurrion, 130 Robin Hill Rd, Suite 300, Goleta, CA 93117, USA

e-mail: alexander.fang@aurrion.com

## 14.1 Silicon as a Platform for PICs

An integrated circuit (IC) is a miniaturized electronic circuit that consists of a large number of individual components, fabricated side-by-side on a common substrate and wired together to perform a particular circuit function. In 1943, the first working transistor was demonstrated [1], and 11 years later, the invention of the IC began a new era. The inherent advantages in *cost and performance* have been the driving force in the IC industry since then. Moore's Law has set the progressive pace in these advances. Gordon Moore foresaw exponential growth, with the number of transistors on an IC doubling approximately every two years [2], as illustrated in Fig. 14.1a. Large-scale integration and mass production also resulted in the enormous reduction of the chip size and system cost, and tremendous improvement in performance and applications. The first UNIVAC computer in 1951 weighed 13 metric tons and occupied more than 35 m<sup>2</sup> of floor space with a clock speed of 2.25 MHz [3]. Sixty years later, a personal computer now easily delivers 1000× faster speed and is small and light enough to fit into a shirt pocket. Moore's Law was actually the fifth paradigm to provide accelerating price-performance [4]. The exponential technology advance in computing devices (computing speed per unit cost) has existed for the entire past century. Integration is the leading driver in the semiconductor world in the 20th and 21st centuries, both technologically and economically.

While the term IC generally refers to microelectronics, the analogous term photonic integrated circuit (PIC), also sometimes referred to as planar lightwave circuit (PLC), offers functionality of information signals imposed on an optical carrier from ultraviolet to near infrared. Though the growth of PICs can also be depicted and predicted by a photonic "Moore's Law" [5, 6], several figures of merit including critical dimensions, integration scale, complexity of function, and cost per unit component show that present PICs are several generations behind the electronic ICs. PICs appeared much later than ICs and have grown more slowly (Fig. 14.1b). The reasons that PIC integration advances have occurred more slowly are partially market based, partially technology based, and partially the result of the choice of host material. Most telecom devices are based on Indium Phosphide (InP) substrates, which have required the construction of custom fabrication lines dedicated to InP photonics.

The first transistor and one of the first two ICs were demonstrated on germanium (Ge), but silicon (Si) quickly became the dominant host material for electronic ICs. Si is the second most abundant element on earth, but more importantly, Si has outperformed Ge and even many compound semiconductors from the early stage of IC development due to large bandgap and thermal conductivity, stable and high crystal quality/purity, excellent mechanical properties and an ideal native oxide, SiO<sub>2</sub>. Unlike Si-dominated electronic ICs, PICs have been fabricated in a variety of host material systems, including element semiconductors (Si- and Ge-related), compound semiconductors (InP- and Gallium Arsenide (GaAs)-based), dielectrics (SiO<sub>2</sub> and SiN<sub>x</sub>-related), polymers and nonlinear crystal materials (e.g., LiNbO<sub>3</sub>). The material properties of different material systems place them into desirable but discrete functionality regimes. For example, InP and GaAs are flagship materials for light

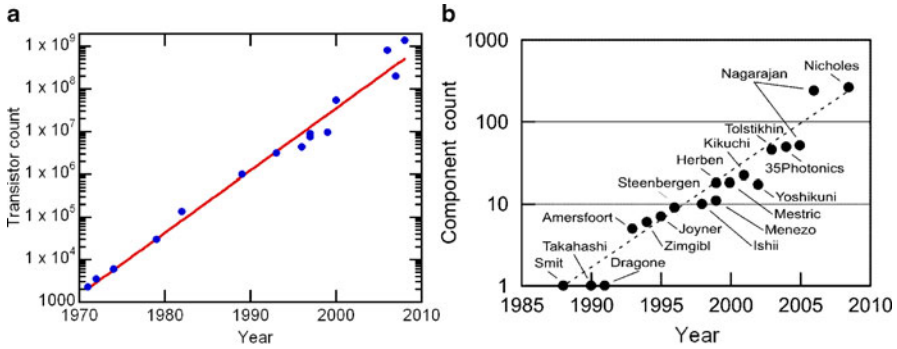


**Fig. 14.1** Electronic [1] (a) and photonic (b) integrated circuit evolution [7, 8]

sources, while silica- and Si-based waveguides exhibit more than an order of magnitude lower propagation loss than III–V counterparts with the same dimensions.

Material incompatibility in different material systems has been the largest barrier to singling out a unitary host material for large-scale PICs. Analogous to a long-term debate in electronic ICs about whether to integrate high-performance electronics on Si, InP or GaAs, the same question surfaced lately in the PIC community. This debate did not shake the dominance of Si in electronic ICs, though several successful compound semiconductor-based IC chip companies, such as Vitesse, RF Micro Devices, Skywork solutions, and Broadcom, etc., were successful in target markets. The success of Si-based electronic ICs proves the wisdom in determination of a primary host material, which is reflected by the International Technology Roadmap for Semiconductors (ITRS) [9]. The solidification of silicon's role resulted in rational technology development and deployment, drastically reducing the uncertainties in investments, critical research directions and resource allocations. The past half-century technology revolution in design tools, circuit architecture, substrate manufacturing and epitaxy, device processing, packaging, testing and quality control led to the present Si IC industry with about 200 billion U.S. dollars in revenue per year [10]. The annual research and development investment in electronic ICs, particularly in device innovation, is about \$45 bio/year. This level of R&D spending is unaffordable for the PIC industry due to a much smaller volume and revenue.

It is therefore important to determine the primary host material for PICs. InP-based compound semiconductors and Si compete for the mainstream adoption as the host material for future PICs. A 40 Gbit/s InP-based single-chip all-photonic transceiver has been demonstrated recently [11]. It includes a high-gain, high-saturation power semiconductor optical amplifier (SOA), a uni-traveling carrier (UTC) photodiode-based receiver, and a widely tunable transmitter that combines a sampled grating-distributed Bragg reflector (DBR) laser with an electroabsorption modulator (EAM) [11, 12]. The first InP monolithic tunable optical router with error-free 40 Gbit/s operation per port was just demonstrated successfully by Nicholes et al. [7]. The device has eight wavelength converters and an  $8 \times 8$  arrayed-waveguide grating router (see Chap. 9, Sect. 9.5), yielding more than 200 on-chip

functional elements. InP chip maker Infinera launched 10-channel and 40-channel 10 Gbit/s per channel transmitters and receivers for dense wavelength-division multiplexing (DWDM) data communication at an aggregate rate of 400 Gbit/s followed by 40-channel InP transmitters at an aggregate rate of 1.6 Tbit/s. Luxtera, an industrial leader in complementary metal oxide semiconductor (CMOS) photonics, announced the industry's first single chip 100 Gbit/s optoelectronic transceiver in the end of 2011. It contains a  $4 \times 28$  Gbit/s, 0.13  $\mu\text{m}$  CMOS Si-on-insulator (SOI) integrated optoelectronic transceiver chip co-packaged with a semiconductor laser for an aggregate unencoded data rate of up to 112 Gbit/s. The diode laser is the only component not fabricated in a CMOS production line and flip-chip bonded onto the CMOS chip later on. PICs are presently moving forward on parallel Si and III–V platforms, but the future requirement for higher capacity, lower power on-chip and off-chip *optical* interconnects in microprocessors may tilt the balance. Larger bandwidth, lower power consumption (i.e., lower heat dissipation), smaller interconnect delays, and better resistance to electromagnetic interference are attractive advantages over the conventional Cu and Al electrical interconnects [13]. By leveraging the mature CMOS technology, low-cost and high-quality Si substrates, duplicate investment in money and time for fundamental research, infrastructure, and business model development can be largely reduced. With the compensation and assistance of mature electronic ICs, Si PICs are able to tolerate more error, lowering the design and fabrication criteria. Furthermore, the potentially enormous volume of optical interconnects (on-chip, interchip, rack-to-rack) is several orders of magnitude larger than the sum of conventional PIC markets. Exciting results in CMOS optical components, such as continuous-wave (CW) Si Raman lasers, modulators, detectors, optical buffers and switches, have been demonstrated in succession in university and industrial labs in the past few years. The basic operation principles of key devices for transmitters are discussed in the following sections, starting from a major question still being investigated: how to deploy a high-performance electrically driven CW light source on Si?

## 14.2 Lasers (Emitters) and Amplifiers on Silicon

As discussed in Sect. 14.1, GaAs- and InP-based III–V materials have been dominant candidates for semiconductor light-emitting devices for nearly half a century. Si has not been widely used because it has an indirect bandgap, and hence is a poor light-emitting material. The band structure for Si is shown in Fig. 14.2a where it can be seen that free electrons tend to reside at the  $X$  valley which is the lowest point in the conduction band. However, the  $X$  valley doesn't align with the peak of the valence band where holes find their lowest energy to stay. This momentum mismatch determines that free electrons have to bridge to the  $\Gamma$  valley through phonons in order to recombine with holes in the valence band *radiatively*. This transition has a low probability, resulting in a long radiative lifetime of  $\sim$  ms. Meanwhile, these free carriers (electrons and holes) can recombine nonradiatively, resulting in

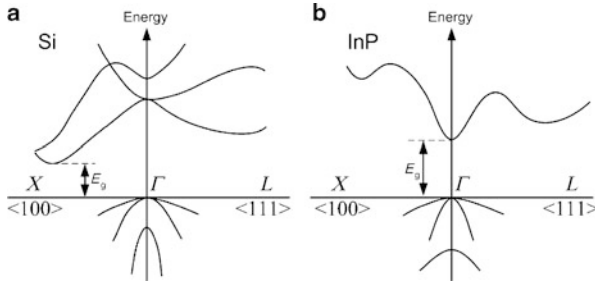


**Fig. 14.2** Energy band diagrams of Si (a) and InP (b) at 300 K

extremely poor internal quantum efficiency  $\eta_i$  of light emission in Si, which is in the order of  $10^{-6}$  and is defined as [14]

$$\eta_i = \frac{\tau_{\text{nonrad}}}{\tau_{\text{nonrad}} + \tau_{\text{rad}}}, \quad (14.1)$$

where  $\tau_{\text{nonrad}}$  and  $\tau_{\text{rad}}$  are recombination lifetimes for nonradiative and radiative processes, respectively.

The band diagram of InP is shown in Fig. 14.2b, and has a direct bandgap, which means electrons and holes can recombine radiatively with high efficiency ( $\eta_i \sim 1$ ).

A major source of nonradiative recombination in processed Si is trap recombination. Another major nonradiative process is Auger recombination where an electron (or hole) is excited to a higher energy level by absorbing the released energy from an electron-hole recombination. The Auger recombination rate  $R$  increases with injected free carrier density  $\Delta N$  and is inversely proportional to the bandgap. Since the Auger recombination is a three-particle process, the Auger recombination rate for high-level carrier injection with  $\Delta N \approx \Delta P$  is proportional to  $\Delta N^3$

$$\tau_a = N/R = N/C_a \Delta N^3 \approx 1/C_a \Delta N^2, \quad (14.2)$$

where  $C_a$  is the ambipolar Auger coefficient around  $10^{-30} \text{ cm}^6/\text{s}$  [15]. It is the dominant recombination mechanism for high-level carrier injection ( $\Delta N \sim 10^{19} \text{ cm}^{-3}$ ) in Si.

Free carrier absorption represents another hurdle to realizing lasing in Si. The free electrons in the conduction band can jump to higher energy levels by absorbing photons. This process leads to higher optical loss as governed by (14.3) [16],

$$\alpha_f = \frac{q^3 \lambda_0^2}{4\pi^2 c^3 n \epsilon_0} \left( \frac{N_e}{m_{\text{ce}}^{*2} \mu_e} + \frac{N_h}{m_{\text{ch}}^{*2} \mu_h} \right), \quad (14.3)$$

where  $q$  is the electronic charge,  $\lambda_0$  is the vacuum wavelength,  $n$  is the refractive index of Si,  $\epsilon_0$  is the permittivity of free space,  $N_e(N_h)$  is the free electron (hole) concentration,  $\mu_e$  ( $\mu_h$ ) is the electron (hole) mobility, and  $m_{\text{ce}}^*$  ( $m_{\text{ch}}^*$ ) is the conductivity effective mass of electrons (holes). In high-level carrier injection devices (e.g.,



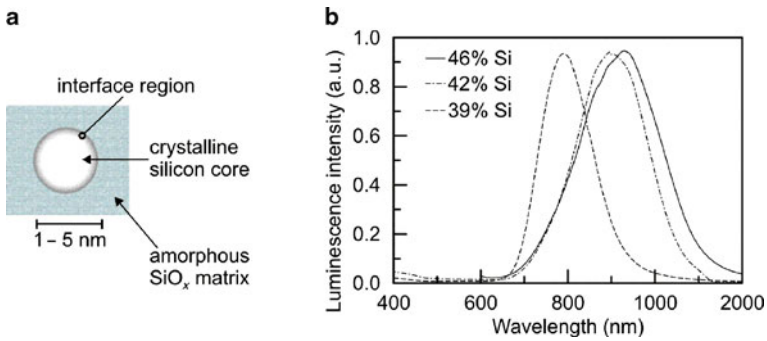


**Fig. 14.3** TEM cross-section of a typical Si-nc embedded in an  $\text{SiO}_x$  dielectric (a) (courtesy Lorenzo Pavesi, University of Trento, Italy), and luminescence spectrum of Si-nc in the dielectric [17] (b)

lasers and semiconductor optical amplifiers) or heavily doped situations, free carrier loss is orders of magnitudes higher than the material gain [16]. It explains why intrinsic or lightly doped Si has served as low-loss waveguide material, but excessively high free carrier absorption stands as another major limitation for achieving lasing in heavily doped cases.

### 14.2.1 Low-dimensional Silicon Approaches

Recently, a number of groups have reported enhanced light-emitting efficiency in low-dimensional (i.e., in the order of the de Broglie wavelength) Si including porous Si [18–21], Si nanocrystals [22, 23], SOI superlattices [24], and Si nanopillars [25, 26]. The motivation is to achieve the quantum confinement of excitons in a nanometer-scale crystalline structure [27]. The spatial localization of carriers reduces the probability of nonradiative recombination, i.e., increases  $\tau_{\text{nonrad}}$  and  $\eta_i$ , and forms radiative states [28].

For the first time Pavesi et al. reported the observation of optical net gain and modal gain in Si nanoclusters (Si-nc) dispersed in a silica matrix [23]. The Si-nc can be formed by introducing Si nanoparticles into ultra-pure quartz, thermal  $\text{SiO}_2$  or plasma-enhanced chemical vapor deposition (PECVD)  $\text{SiO}_2$ , etc. by deposition, sputtering, ion implantation, cluster evaporation, etc. The excess Si (excess with respect to the  $\text{SiO}_2$  stoichiometric quantity) clusterizes after a thermal annealing process ( $\sim 1100^\circ\text{C}$ ) which leads to phase separation. The thermal process and the starting excess Si content determine the final sizes of the clusters and the Si-nc crystalline nature. As shown in Fig. 14.3a, the Si-nc embedded in an amorphous  $\text{SiO}_x$  matrix have a core-shell structure with a crystalline Si core (1–5 nm) and a thin ( $\sim 0.5$  nm) transition layer of a suboxide (Si-nc interface) [29]. Figure 14.3b shows luminescence spectra of Si-nc for various Si concentrations [17]. As can be seen the emission shifts to shorter wavelengths with decreasing Si concentration which

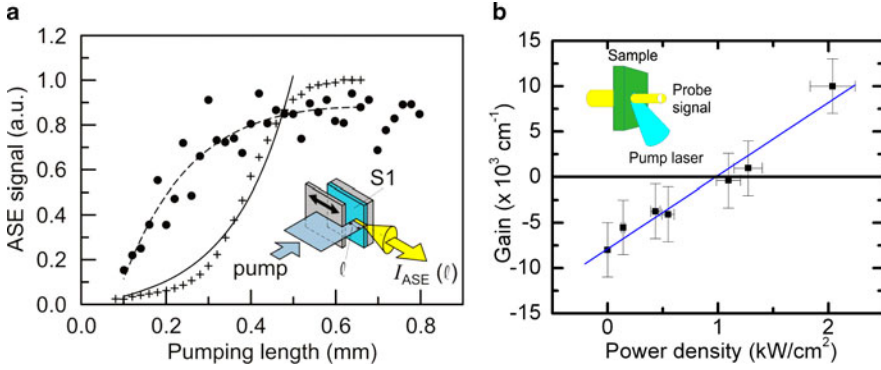


**Fig. 14.4** ASE vs. pumping length of Si-nc for pump powers of  $10 \text{ W/cm}^2$  (●) and  $1 \text{ kW/cm}^2$  (+). Corresponding modal gain at  $800 \text{ nm}$ ,  $g = -20 \text{ cm}^{-1}$  and  $g = 100 \text{ cm}^{-1}$ , respectively (a), dependence of material gain on pump power density (b); *inset*: schematic of variable stripe length (VSL) method [32] (a) and pump-probe technique [33] (b) (courtesy Lorenzo Pavesi, University of Trento, Italy)

goes along with a smaller mean Si-nc radius. Furthermore, the width of the luminescence bands gets narrower and the luminescence intensity increases as the Si-nc size decreases [17]. It is believed that the luminescence comes from confined exciton recombination in the Si-nc at around  $800 \text{ nm}$  [30] and radiative interface states around  $700 \text{ nm}$  [31]. The spectral broadening of the luminescence is intrinsic in nature [23].

The optical gain from Si-nc formed by many different techniques was measured by the variable stripe length (VSL) method [32] and the pump-probe technique [33], as shown schematically in Fig. 14.4a, inset, and Fig. 14.4b, inset, respectively. The VSL method measures the amplified spontaneous emission (ASE) signal coming out of an edge of a waveguide with a Si-nc-rich core. Figure 14.4a shows the ASE signal intensity  $I_{\text{ASE}}$  vs. pump length  $l$  for Si-nc formed by PECVD. The ASE signal intensity increases sublinearly with the pumping length when the pump power ( $\lambda = 390 \text{ nm}$ ) is lower than a threshold. But when the pump power is above this threshold and net modal gain becomes positive, the ASE signal increases more than exponentially, which can be fitted with [23]:

$$I_{\text{ASE}}(l) = \frac{I_{\text{sp}}(\theta) \cdot l}{g_{\text{mod}}} (g_{\text{mod}} l - 1), \quad (14.4)$$

$$g_{\text{mod}} = \Gamma g - \alpha, \quad (14.5)$$

where  $I_{\text{sp}}$  is the spontaneous emission intensity emitted within the observation angle ( $\theta$ ) per unit length,  $\alpha$  is the overall loss coefficient,  $\Gamma$  is the optical confinement factor in the active layer, and  $g$  is the net material gain. A modal gain  $g_{\text{mod}}$  of  $-20 \text{ cm}^{-1}$  (i.e., loss) at  $800 \text{ nm}$  emission wavelength was deduced when the pump power was  $10 \text{ W/cm}^2$ , while  $1 \text{ kW/cm}^2$  pump power leads to  $100 \text{ cm}^{-1}$  modal gain. For pump length  $l > 0.5 \text{ mm}$ ,  $I_{\text{ASE}}$  saturates as expected for any finite power supply amplification mechanism.

The pump-probe transmission measurement (Fig. 14.4b, inset) involves the use of an intense laser pump beam (390 nm in this case [23]) to excite the Si-nc to reach population inversion while a weak probe signal at  $\sim 800$  nm simultaneously passes through the sample with active region thickness  $d$ . The Si-nc in the quartz substrate are formed by negative ion implantation and thermal anneal [23]. In the presence (absence) of a sufficiently strong pump beam the probe signal is amplified (absorbed). Figure 14.4b shows the net material gain extracted from (14.6) as a function of pump power.

$$I_{\text{tr}} = I_{\text{in}} \exp(g - \alpha) d, \quad (14.6)$$

where  $I_{\text{tr}}$  and  $I_{\text{in}}$  refer to transmitted and incident probe beam intensities, respectively. Up to  $10\,000\text{ cm}^{-1}$  average material gain is obtained, comparable to that of self-assembled quantum dots made of III–V semiconductors [34]. No change in probe signal intensity is observed when the same measurement is performed on an identical quartz sample without Si-nc. A four-level system model has been proposed to interpret the population inversion scheme in Si-nc. A more detailed discussion can be found in [14].

Several approaches have been demonstrated lately to achieve electrically injected light emission, including a light-emitting diode (LED) structure [35] and a field-effect LED [36, 37] with recent demonstration of 1 MHz direct modulation speed [38]. The critical design element of all is to embed Si-nc into an ultrathin dielectric layer which is sandwiched by a poly-Si layer and a single crystalline Si substrate to allow efficient carrier injection by tunneling. A large amount of effort is focused on reducing leakage current in the dielectric and achieving high enough current density without excessive device heating and premature failure for amplifiers and lasers. Another intrinsic limitation for Si-nc-based emitters is the difficulty of integration with conventional SOI waveguides due to emission around 800 nm.

Incorporating rare earth doping (e.g., Er, Tb, Yb, Gd) into Si-nc is a way to shift emission to the important communication wavelengths of 1.3–1.6  $\mu\text{m}$  [39]. Following the revolution that the Er-doped fiber amplifier (EDFA) led in fiber optic telecommunications, research in Si emitters has been concentrated on doping Si with rare earth elements [40, 41]. However, it has been shown that Si is not a good host material to accommodate rare earth elements. Dopant clustering and back transfer of energy from the rare earth element are the main obstacles to obtaining high emission efficiency [42]. Therefore, an  $\text{SiO}_2$  dielectric with Si-nc seems to be a better host choice for  $\text{Er}^{3+}$  [39] because the  $\text{SiO}_2$  environment is an excellent natural host material for  $\text{Er}^{3+}$ , and Si-nc are shown to act as a good sensitizer as well [39, 43]. The energy of excitons excited by optical or electrical pumping from Si-nc is transferred to  $\text{Er}^{3+}$  ions which are coupled to adjacent Si-nc. Up to 70% energy transfer efficiency has been reported from Si-nc to  $\text{Er}^{3+}$  [44]. By employing a light-emitting device structure with  $5.5\text{ A/cm}^2$  injection current density in Fig. 14.5a, room-temperature electroluminescence (EL) at 1.54  $\mu\text{m}$ , corresponding to typical Er first-excited multiplet  ${}^4I_{13/2}$  to the ground state  ${}^4I_{15/2}$  transitions, is demonstrated [42]. Two metal rings provide the electrical contacts to the n-type

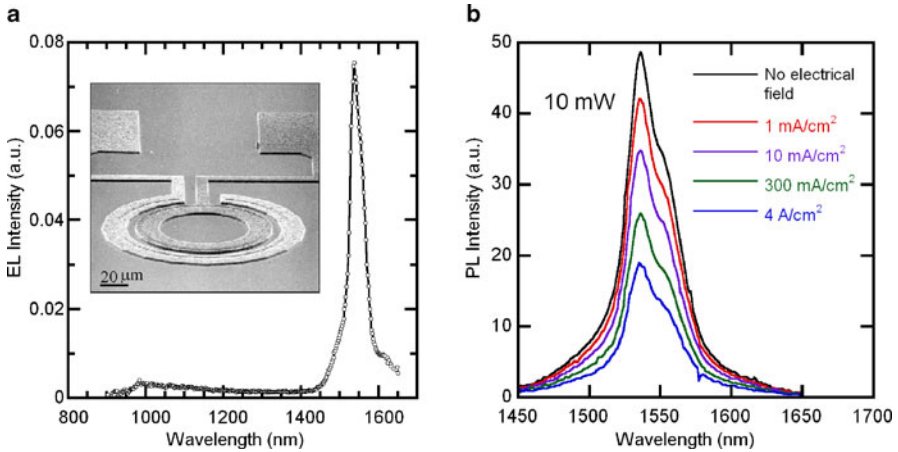


**Fig. 14.5** EL spectrum of a device based on Er-doped Si-nc obtained at room temperature under forward bias conditions with a current density of  $5.5 \text{ A/cm}^2$ . *Inset*: SEM image of an LED device structure with ring-type electrodes (a). PL spectra of a device based on Er-doped amorphous Si-nc for the unbiased device (*black line*) and in the presence of different current densities flowing through the device (b) (courtesy Fabio Iacona, Center of Materials and Technologies for Information and Communication Science (MATIS CNR-INFN), Catania, Italy)

poly-Si and to the p-type Si substrate. Emission is detected from the metal-free central area. The disappearance of the intrinsic EL peak around 800–900 nm for Si-nc in Er-doped Si-nc samples clearly proves the efficient energy transfer from excitons formed in Si-nc to the rare earth ions.

However, significant light emission diminishes quickly from low temperature (30 K) to room temperature under electrical pumping, a much faster decay than in the case of optical pumping [42]. Studies of PL (488 nm, 10 mW) under different electrical biases have been performed to investigate the effect of injected carriers on the luminescence properties. Figure 14.5b shows PL spectra with the device under different forward bias, compared with that of the unbiased case. A clear quenching of the PL signal with increasing electrical pumping is noticed, indicating the new possible nonradiative paths with the presence of electrically injected carriers. Iacona et al. [42] believe that independent but unbalanced electron and hole injection causes the Auger de-excitation of Er ions. Conversely, for the conventional PL, electron-hole pairs are generated simultaneously in the active region and then undergo a rapid recombination with subsequent Er excitation. For electrical pumping, measurements suggest that more electrons than holes are injected into the active region in these devices. This results in wasting a certain amount of current since they do not recombine with holes and cause the Auger de-excitation of Er ions [42]. In addition to the major challenge of increasing the injection current density in all Si-nc-based light-emitting devices, how to overcome the EL efficiency degradation with increasing injected current density is a problem for Er-doped devices.

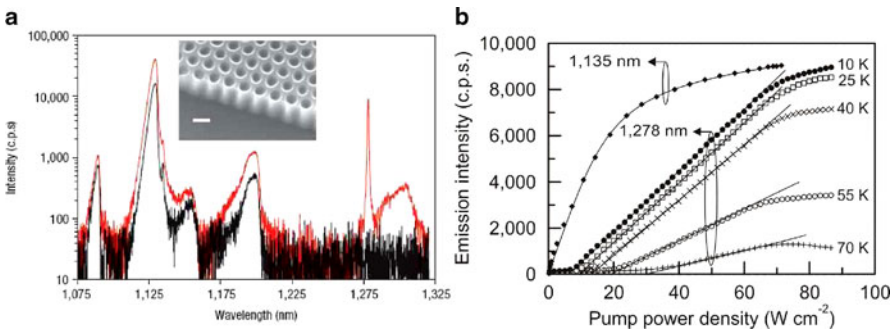


**Fig. 14.6** Edge-emission spectra from cleaved nanopatterned (*red*) and unpatterned (*black*) samples at 10 K. *Inset*: Side-view SEM image of nanopatterned Si; *scale bar*: 100 nm (a). Evolution of the edge-emission intensity of the 1278 nm line as a function of pump power at 10, 25, 40, 55, and 70 K temperatures. Evolution of the 1135 nm phonon-assisted free-exciton line at 10 K is shown for comparison, its intensity has been divided by 7 to plot all curves on the same scale (b) (reproduced from [45] with permission from Macmillan Publishers Ltd.)

Another promising attempt to utilize low-dimensional Si is the observation of optical gain and stimulated emission in nanopatterned crystalline Si by Cloutier et al. [45]. Figure 14.6a, inset, is an SEM side-view of periodic nanopatterned Si with a highly ordered array of holes in the top Si layer of a conventional SOI wafer. The top Si is about 100 nm thick with 3  $\mu\text{m}$  buried oxide underneath. An anodic aluminum oxide nanopore membrane serves as a mask for patterning holes with 60 nm diameter and 110 nm center-to-center spacing in  $\text{Cl}_2\text{-BCl}_3$  plasma dry etch. Figure 14.6a shows the edge emission from a CW optically pumped sample at 10 K. In the spectrum of this gain-guided slab waveguide, a sharp peak at 1278 nm is observed and remains detectable till 80 K. The other emission bands in the spectrum below 1250 nm, believed to be emission from the crystalline Si substrate, are similar to the classical spontaneous PL emission bands of an unpatterned reference SOI sample. The temperature-dependent 1278 nm-peak intensity vs. CW pump power density characteristic is shown in Fig. 14.6b. Transition from spontaneous to stimulated emission is observed in the 10–70 K range. Linewidth narrowing in Fig. 14.6b, inset, after passing the pump power threshold represents additional evidence of stimulated emission. The phonon-assisted free-exciton recombination PL band at 1135 nm is also plotted to show no stimulated emission observable at this wavelength. The optical gain in nanopatterned Si is measured with the variable stripe length method discussed previously. Modal gains  $g_{\text{mod}}$  of 260, 247, 230, 165, and  $88 \pm 5 \text{ cm}^{-1}$  [46] are measured at 10, 25, 40, 55, and 70 K, respectively, with a fixed pump power density of  $65 \text{ W/cm}^2$ . In contrast, a modal loss of  $-31 \pm 5 \text{ cm}^{-1}$  at 10 K is measured when the pump power density is only  $8 \text{ W/cm}^2$ , i.e., below pump threshold [45].

The optical gain and stimulated emission in nanopatterned Si is attributed to the bistable carbon-substitutional-carbon-interstitial ( $\text{C}_s\text{C}_i$ ) complex known as the *G-center* [46]. It is well known that substitutional carbon ( $\text{C}_s$ ) atoms occur naturally

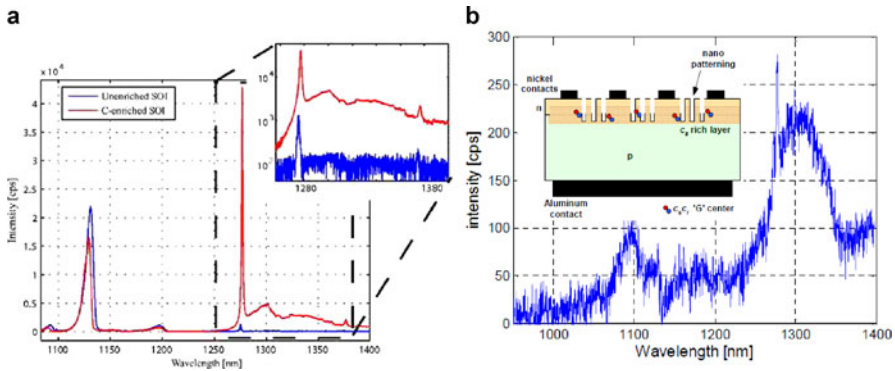


**Fig. 14.7** Photoluminescence spectrum at 25 K of nanopatterned Si and nanopatterned C-enriched Si. The *inset* shows a semi-logarithmic plot of the region containing the G line and phonon replicas (a). Electroluminescence spectrum of *G-center* LED at 60 K and a current of 50 mA. *Inset*: Schematic of the *G-center* LED in nanopatterned Si (b) (reproduced from [46] with permission from the American Institute of Physics)

in Si wafers at concentrations between  $10^{15}$  and  $10^{17}$   $\text{cm}^{-3}$  depending on the crystal growth technique [47], and are necessary for *G-center* formation. A *G-center* is created when a mobile interstitial carbon atom ( $\text{C}_i$ ) binds with a substitutional carbon atom ( $\text{C}_s$ ), a consequence of a damage event and following  $\text{C}_s$ - $\text{Si}_i$  exchange (where  $\text{Si}_i$  represents a Si interstitial) [48]. The density of *G-centers* depends on the densities of  $\text{C}_s$  in the lattice and introduced  $\text{C}_s$ - $\text{Si}_i$ . Recent studies show that nanopatterned carbon-rich Si generates higher gain. Figure 14.7a exhibits a  $33\times$  enhancement in the PL intensity at 25 K for a nanopatterned Si with  $\sim 10^{19}$   $\text{cm}^{-3}$  carbon atoms implanted (background carbon concentration:  $2.5 \times 10^{16}$   $\text{cm}^{-3}$ ), compared with the PL response from a base-line nanopatterned SOI sample with background carbon concentration. These results confirm that carbon in the silicon crystal is responsible for the creation of *G-centers*, rather than the dry etching process [46]. It also provides a path for increasing the efficiency and gain of this material. Electroluminescence at 1287 nm is demonstrated in the nanopatterned Si pn junction with a 100 nm-thick carbon-rich layer at the junction interface (Fig. 14.7b, inset) [49]. Figure 14.7b shows the electroluminescence from the device at 60 K with a current of 50 mA. The mechanism of the electroluminescence can be described briefly in the following way: the *G-center* is bistable and can be excited below 50 K. The excited/injected carriers occupy the *G-center*-induced acceptor and donor states existing inside the conventional Si bandgap, resulting in a sub-bandgap of 0.97 eV. The trapped electrons and holes can recombine directly producing a phonon-less emission at 1278 nm, or indirectly producing an emission band extending from 1250 nm to 1350 nm. However, emission is quickly diminished at higher temperatures when carriers in the *G-center*-induced states move back to the conduction and valence bands [49].

With the availability of nanotechnology, the phonon-selection rule can be relaxed or broken by crystal-symmetry breaking or phonon localization; however, it

still remains challenging to achieve room-temperature CW lasing based on these temperature-dominated processes.

### 14.2.2 Raman Effect

Raman scattering is an inelastic scattering mechanism where photons give up energy to or gain energy from optical phonons in the medium they are propagating through. This results in a frequency-shifted output photon of  $-15.6$  THz or  $+15.6$  THz in bulk silicon for the Stokes and anti-Stokes, respectively [50]. The anti-Stokes can typically be neglected over the Stokes under equilibrium temperature conditions and no external crystal phonon excitation due to Boltzmann statistics.

Spontaneous Raman emission occurs in a linear regime where the scattered light intensity is linearly proportional to the pump light intensity. Above a certain threshold this interaction is no longer linear and Stimulated Raman Scattering (SRS) occurs. The SRS relation for the change in Raman power can be written as:

$$\frac{dP_R}{dz} = g_R \cdot P_R \cdot P_p, \quad (14.7)$$

where  $P_R$  is the power of the Raman signal at the Stokes wavelength,  $P_p$  is the pump power, and  $g_R$  is the SRS gain coefficient. The Raman gain coefficient is [50]:

$$g_R = \frac{8\pi c^2 \omega_p}{\hbar \omega_S^4 n_S^2 \omega_S (N + 1) \Delta \omega_S} S, \quad (14.8)$$

where  $\omega_p$  and  $\omega_S$  are the frequencies of the pump and Stokes wavelengths, respectively.  $n_S$ ,  $N$ , and  $\Delta \omega_S$  are the index of refraction at the Stokes wavelength, the Bose occupation factor (0.1 at room temperature), and the full-width-half-maximum of the spontaneous Raman spectrum, respectively.  $S$  is the spontaneous scattering efficiency.

Although the 1.3 and 1.5  $\mu\text{m}$  operating wavelengths are well below the bandgap energy of silicon and single photons are not absorbed, two photon absorption (TPA) still occurs. TPA is a nonlinear loss mechanism that increases as the number of photons increases in a waveguide. During TPA, two photons are absorbed by an electron in the valence band, exciting it as a free carrier in the conduction band. The free carriers generated through TPA add an additional carrier-induced loss, free carrier absorption (FCA), as discussed previously, to the signal [51].

The first demonstration of a pulsed silicon Raman laser [52] overcame TPA by using a long delay within the laser cavity (an 8 m long cavity), and a short optical pulse such that the carriers generated during TPA would recombine prior to the next pass of the optical pulse (Fig. 14.8a). The experimental light output versus pump light ( $L-L$ ) characteristic is shown in Fig. 14.8b. Most demonstrations in silicon have been conducted with a pump wavelength of  $\sim 1550$  nm and a lasing wavelength near 1690 nm.

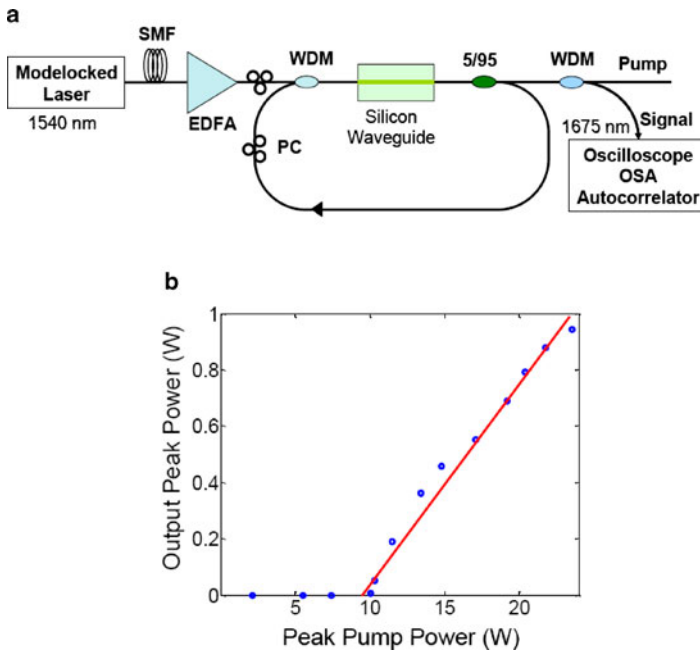


**Fig. 14.8** Experimental setup (a) and laser light vs. pump light (b) from the first pulsed silicon Raman laser [52] (reproduction under permission of the Optical Society of America)

In order to achieve net gain under continuous wave operation, the conduction band carrier lifetime needs to be reduced. This can be achieved in a few ways. One method is to reduce the volume-to-surface ratio of the waveguide in order to increase the surface recombination rate of the carriers. Imbedding a p-i-n structure into the waveguide to sweep carriers away [53] resulted in the first CW demonstration of a silicon Raman laser [54] and this is the approach most widely used [55]. Figure 14.9a shows the cross-section of a waveguide with an imbedded p-i-n structure, along with the first CW  $L$ - $L$  curve [54]. Although the p-i-n structure reduces the carrier lifetime to achieve lasing, TPA and FCA increase the cavity loss at higher pump powers leading to compression of the  $L$ - $L$  curve (Fig. 14.9b).

Further improvements in laser performance have been made by utilizing a specially designed ring cavity that enhances the pump wavelength in the cavity while still allowing power at the lasing wavelength to efficiently exit the cavity [55]. This has led to a reduction in threshold pump power from 200 mW to 20 mW while increasing the maximum laser output power from 10 mW to 18 mW (Fig. 14.9c). Another configuration of this ring has been used to generate lasing at longer wavelengths (1848 nm) not typically accessible by InP- or GaAs-based semiconductor lasers [56]. The cavity is designed such that lasing at 1680 nm acts as a pump for second-order lasing at 1848 nm. Figure 14.10 shows the spectra of the pump, the first-order lasing mode, and the second-order lasing mode.



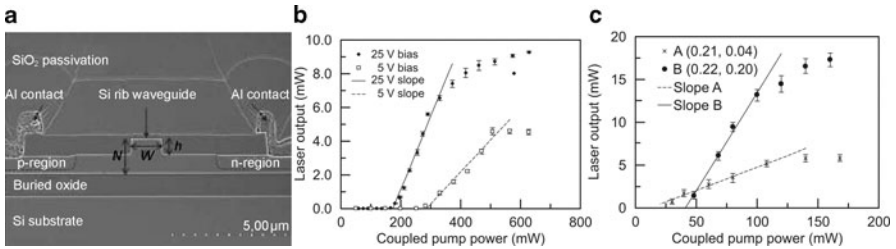


**Fig. 14.9** Waveguide cross-section with imbedded p-i-n cross-section for carrier lifetime reduction (a),  $L$ - $L$  curve of first continuous wave silicon Raman laser [54] (b),  $L$ - $L$  curve of racetrack Raman laser [56] (c) (reproduction under permission of Macmillan Publishers Ltd. and the American Institute of Physics)

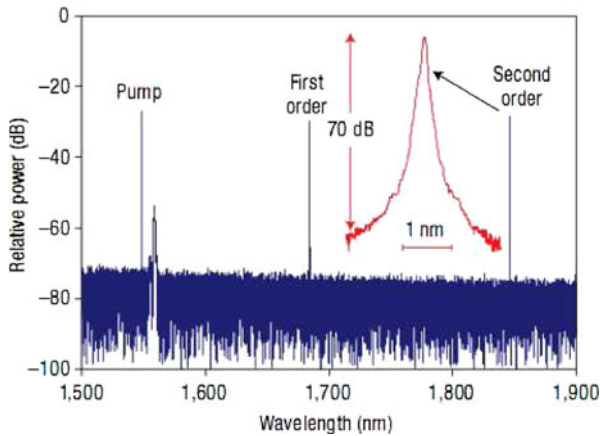


**Fig. 14.10** Cascaded silicon Raman laser output spectrum measured with a grating-based optical spectrum analyzer with a resolution of 0.01 nm, showing three peaks corresponding to the pump, the first- and the second-order laser outputs. *Inset*: high-resolution scan of the second-order lasing peak, showing 70 dB side-mode suppression ratio (SMSR) [56] (reproduced with permission from Macmillan Publishers Ltd.)

Silicon Raman amplifiers and lasers are unlikely to be integrated with CMOS chips due to the optical pump sources required. However, their excellent wavelength purity and emission wavelength are of interest in medical or sensing applications.

### 14.2.3 Monolithic Integration Approaches

An on-going effort for nearly four decades has been to achieve epitaxially grown compound direct bandgap materials on Si substrates. However, overcoming the mismatch in lattice constant and thermal expansion coefficient is a major challenge to achieving sufficiently low threading dislocation density [57]. Table 14.1 compares these two parameters of several important semiconductors. GaAs and InP

**Table 14.1** Linear thermal expansion coefficients (TEC) and bandgaps (300 K) of selected important semiconductors as a function of their lattice constants (300 K)

Semi-conductor	Lattice constant (nm)	Lattice mismatch to Si (%)	Bandgap (eV)	Linear TEC ( $10^{-6}/\text{K}$ )	Linear TEC (relative)
GaN	0.3189	-41.2815	3.20	3.17	1.22
Si	0.5431	0.0000	1.12	2.60	<b>1.00</b>
GaP	0.5451	0.3683	2.26	4.65	1.79
Ge	0.5646	3.9588	0.66	5.90	2.27
GaAs	0.5653	4.0876	1.42	5.73	2.20
InP	0.5869	8.0648	1.35	4.60	1.77
InAs	0.6058	11.5448	0.36	4.52	1.74

have a lattice (thermal expansion coefficient) mismatch of 4.1 % (120.4 %) and 8.1 % (76.9 %), respectively. This leads to  $10^8$ – $10^{10}$   $\text{cm}^{-2}$  threading or misfit dislocation density when GaAs or InP is grown on Si substrates [58]. Numerous approaches including special surface treatment [59], strained superlattices [60, 61], low-temperature buffers [62] and growth on patterned substrates [63] have been employed to reduce the dislocation density to around  $10^5$ – $10^6$   $\text{cm}^{-2}$ , still two orders of magnitude higher than the typical number ( $< 10^4$   $\text{cm}^{-2}$ ) in InP- or GaAs-based epitaxial wafers used to achieve room-temperature CW lasers. In this section we discuss several recent innovative approaches to achieving high-quality heteroepitaxial thin films for Si photonics applications.

GaP is the binary compound semiconductor with the smallest lattice mismatch with Si. Kunert et al. recently demonstrated monolithic integration of a Ga(NAsP)-based MQW active region on Si with a (BGa)P/GaP buffer layer [64]. Ga(NAsP) pseudomorphically grown on GaP substrates has been introduced as a direct bandgap material [65]. By incorporating small percentages of N or B into GaP, it is also possible to adjust the lattice constant to match with Si. Tensile (BGa)P was selected to be buffer and barrier material to balance the compressive strain of Ga(NAsP) quantum wells. The inset in Fig. 14.11a shows the MQW structure with a 100 nm GaP nucleation layer on (001)Si, followed by a  $1\ \mu\text{m}$  ( $\text{B}_{0.0032}\text{Ga}$ )P buffer. Each 4.5 nm Ga(NAsP) quantum well is sandwiched by a 5 nm GaP intermediate layer to avoid the formation of N-B bonds and a 60 nm ( $\text{B}_{0.0043}\text{Ga}$ )P barrier layer. Figure 14.11a shows the room-temperature PL spectra of the sample, exhibiting a strong peak at 930 nm originating from the active region in addition to a broad peak at the Si bandgap. The relative intensity of the peak at 930 nm from 13 nm quantum wells is evidence of appreciable material gain. High-resolution X-ray diffraction (XRD) is employed to probe the dislocation-induced MQW satellite fringe shifting or broadening. The good agreement between experimental and simulated data in Fig. 14.11b indicates excellent integrity of the active region. It is promising to obtain high-quality active region growth on a Si substrate when utilizing quaternary or even higher order compound semiconductor material systems, which gives more freedom to compensate lattice mismatch and thermal expansion mismatch of materials.

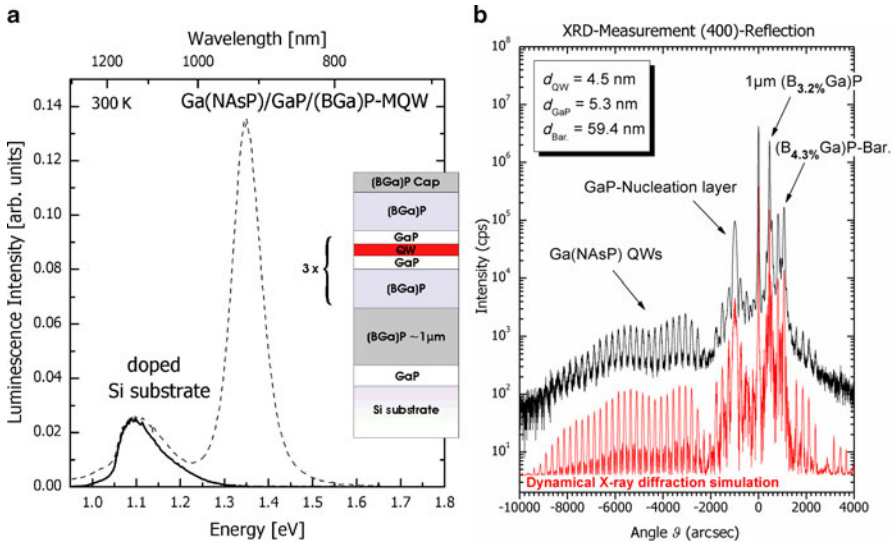


**Fig. 14.11** Room-temperature PL spectra of Ga(NaSP)/GaP/(BGa)P MQWs (*dashed line*) in comparison to doped Si substrate (*solid line*). *Inset*: Epitaxial layer structure (a). High-resolution XRD pattern around (400)-reflection of Si (*upper trace*: experimental, *lower trace*: modeling by dynamical X-ray diffraction theory) [64] (b) (courtesy Wolfgang Stolz, Philipps-Universität Marburg, Germany)

Since the debut of the first transistor and integrated circuits on Ge, Ge(SiGe)-on-Si heteroepitaxy has been of great interest for building light emitters on a Si substrate. Compatibility with modern CMOS technology and potential  $\sim 1.55 \mu\text{m}$  emission from direct band-to-band transitions (0.8 eV) are important reasons for corresponding research. Crystalline Ge is an indirect bandgap material with a minimum bandgap energy of 0.66 eV, close to the direct transition band. Theoretically, a 2% tensile strain is required for converting Ge into a direct bandgap material, while experiment shows a large emission wavelength red shift to  $2.5 \mu\text{m}$  (0.5 eV) [66], which is of less interest for optical interconnects and telecommunications.

Strain engineering and heavy n-type doping were recently used to achieve room-temperature direct bandgap electroluminescence [67, 68]. Sun et al. selectively grew Ge on  $\text{p}^+\text{Si}$  substrates with moderate tensile strain of 0.2 to 0.25% to reduce the direct bandgap between the minimum of the direct  $\Gamma$  valley and the maximum of the light-hole band to 0.76 eV [67]. Heavily doped poly-Si was used for the electrode, resulting in a p-i-n diode structure as shown schematically in Fig. 14.12, inset. Figure 14.12 demonstrates a superlinear dependence of the integral direct bandgap room-temperature electroluminescence intensity on the injected current. The electroluminescent intensity is proportional to both the total injected carrier concentration and the fraction of electrons scattered to the direct  $\Gamma$  valley. A model based on the Fermi-Dirac distribution has been developed to fit the experimental data very well [67]. An important question is whether the relatively high threading disloc-

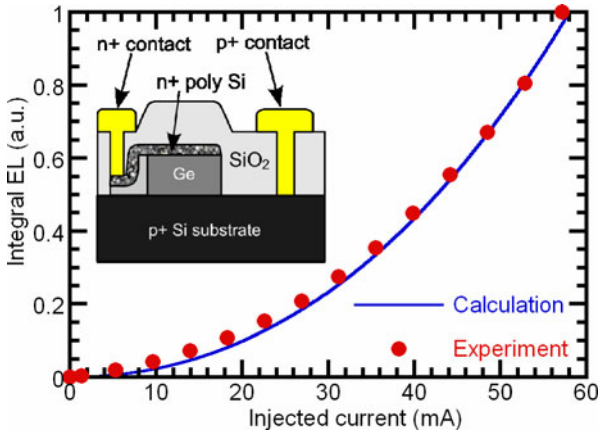


**Fig. 14.12** Integral EL intensity of a  $20\ \mu\text{m} \times 100\ \mu\text{m}$  0.2% tensile-strained Ge/Si p-i-n LED increases superlinearly with injected current, which agrees with theoretical calculations. *Inset:* Schematic cross-section of the Ge/Si LED [67] (courtesy Xiaochen Sun, MIT, Cambridge, MA, USA)

tion density of around  $1.7 \times 10^7\ \text{cm}^{-2}$  could be a major hurdle to realizing diode lasers on this Ge-on-Si substrate.

Another room-temperature Ge LED has been demonstrated using heavy n-type doping, resulting in a Fermi level above the indirect  $L$  valley and good electron occupation of the direct  $\Gamma$  valley [68] of Ge. An  $n^+$ /p Ge homojunction LED structure ( $300\ \mu\text{m}$  in diameter) on a Si substrate is employed. The doping concentrations of phosphorous and boron are  $7.5 \times 10^{18}\ \text{cm}^{-3}$  and  $3.6 \times 10^{17}\ \text{cm}^{-3}$ , respectively, accomplished by in situ doping to achieve an abrupt junction profile. Room-temperature EL spectra of the Ge LED with different applied biases (Fig. 14.13a, inset) show an EL peak located near  $1.6\ \mu\text{m}$ , indicating emission from the direct bandgap of Ge. The onset of the EL is at  $0.75\ \text{V}$ , closely matching the indirect bandgap ( $0.66\ \text{eV}$ ) of Ge. The corresponding injected current density vs. EL intensity in Fig. 14.13a exhibits a superlinear current density-EL intensity dependence and a fitting exponent  $m$  of 1.48 is observed for currents greater than  $300\ \text{A}/\text{cm}^2$ . This implies that the device is more effective when operating under high current, contrary to typical LEDs which suffer from low radiative efficiency at higher injection current levels due to enhanced Auger recombination. The hypothesis of this enhanced EL intensity is Joule heating-induced larger overlap of the Fermi–Dirac distribution of the carriers in the  $\Gamma$  valley, which is confirmed by temperature-dependent EL in Fig. 14.13b. The wavelength peak shifts towards longer wavelengths due to shrinkage of the direct bandgap. The observation of this band-filling effect in Ge LEDs is inverse to the EL quenching in devices which rely on quantum confinement effects like Si-Ge quantum-dot and quantum-well devices [69] and those discussed in Sect. 14.2.1, giving an edge to achieve room-temperature lasing in the future. The use of high-Q ring cavities together with these structures holds promise for room-temperature lasing.

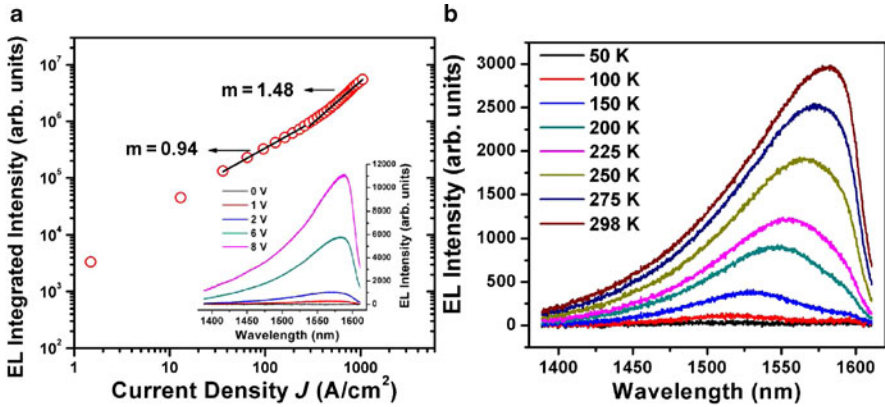


**Fig. 14.13** Integrated luminescence vs. current density ( $L-J^m$ ) characteristics of a Ge LED. *Inset:* Electroluminescence spectra of the Ge LED under different applied biases (a). EL spectra measured at various temperatures, better radiative efficiencies are observed for higher temperatures (b) (courtesy Szu-Lin Cheng, Stanford University, Stanford, CA, USA)

Another exciting approach is the epitaxial growth of direct gap III–V semiconductors directly on silicon substrates [70, 71] with the use of epitaxial layer overgrowth (ELO) to achieve high-quality III–V layers. The next section describes a wide variety of high-performance photonic devices, which were demonstrated by bonding III–V layers onto SOI. These structures could be demonstrated by epitaxial growth once this technology becomes sufficiently advanced. The major problems of lattice mismatch and thermal stress mismatch (Table 14.1) may be overcome by ELO on a Si substrate.

#### 14.2.4 Hybrid Integration Approach

In Sects. 14.2.1 and 14.2.2 we reviewed a few of the major efforts to make silicon lase by manipulating the material properties of silicon or by utilizing other physical mechanisms to obtain optical gain. Recent progress in monolithic integration of direct bandgap materials on Si substrates is also highlighted in Sect. 14.2.3 though only LEDs are demonstrated. Although much progress has been made in this area and optically pumped Si Raman lasers have been demonstrated, room-temperature electrically pumped lasers with useful powers for optical communication applications have not been demonstrated. Hybrid integration is a promising approach where III–V compound semiconductors are used to provide electrically pumped gain and are coupled into passive lightwave circuits on silicon.

The traditional approach to hybrid integration is to take prefabricated III–V lasers and amplifiers and die bond these elements onto a passive planar lightwave circuit (PLC). Since the waveguides on the host substrate, the PLC, and the laser die are already defined, the alignment accuracy during placement needs to be a fraction of

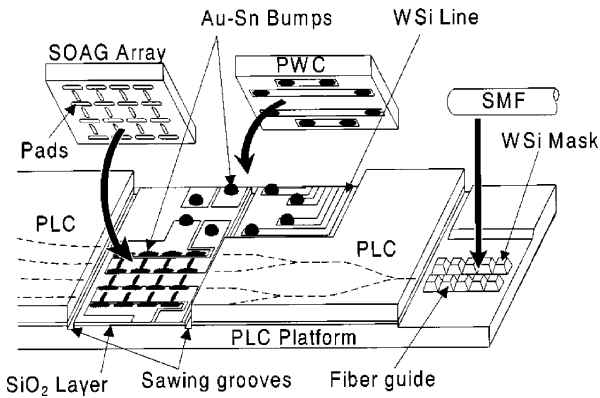


**Fig. 14.14** Schematic of proposed hybrid integration scheme for switching [74]. SOAG: semiconductor optical amplifier gate, PWC: printed wiring chips (reproduced with permission from the Institute of Electrical and Electronic Engineers)

the mode width. This is typically within a few hundred nanometers for silicon waveguides, making alignment a challenge for high-volume manufacturing and leading to substantial variation in coupling power and back reflections between the two waveguides. Efforts have been made to reduce the sensitivity of this coupling by increasing the mode size through spot size converters [72]. Precision cleaving the III–V active die and creating a perfectly matched trench in the PLC host substrate have been explored in order to create assembly methods that allow for self alignment of the optical modes [73].

Figure 14.14 illustrates a PLC utilizing hybrid integration for switching [74]. In this work, self alignment with  $\pm 1 \mu\text{m}$  precision is achieved by placing solder-wettable pads on both the host PLC substrate and the III–V chips. During bonding, the surface tension of the Au–Sn solder bumps pulls the two chips into alignment. This demonstration yielded coupling losses of 4 to 5 dB when used with spot size converters. However, the production efficiency and chip yield result in expensive integration cost, preventing this hybrid integration approach from being widely adopted by the industry.

A new hybrid integration methodology is the transfer of thin crystalline III–V films onto an SOI host substrate. The silicon is typically patterned prior to the transfer, and the III–V films are processed after transfer allowing for the use of standard lithography-based patterning techniques used to fabricate III–V lasers. The alignment of the optical modes is determined by the lithography, which allows for an extremely repeatable fabrication process and coupling efficiencies near  $\sim 1$  dB between the III–V regions and the passive silicon regions as demonstrated by Park et al. [75]. The following section will focus on the new hybrid platforms and devices.

Direct wafer bonding is commonly used to mate lattice-mismatched semiconductors such as AlGaAs and GaP for high-power LEDs, InGaAsP, AlAs and GaAs for improved mirror reflectivity in long-wavelength vertical cavity surface emitting

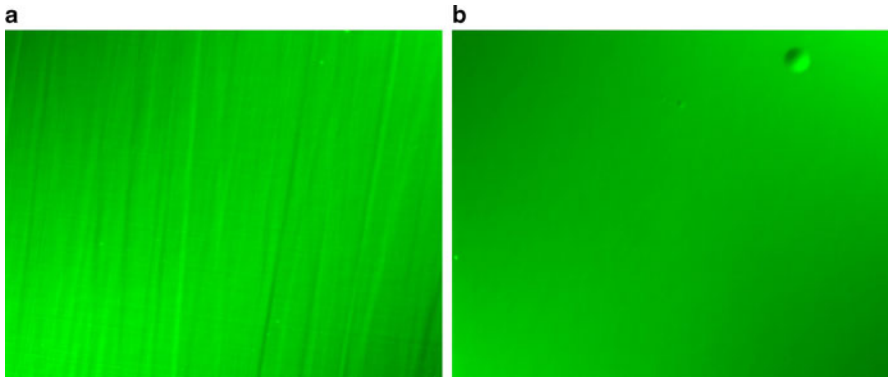
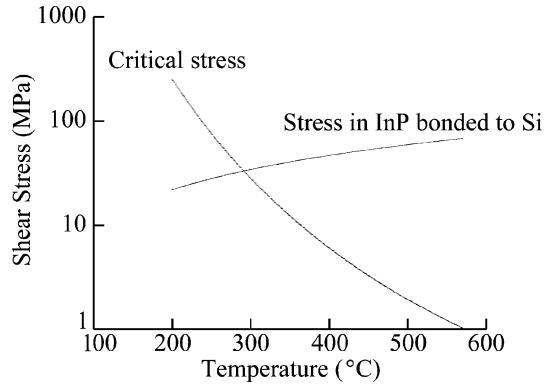


**Fig. 14.15** Nomarski microscope images showing the surface roughness of the transferred III-V surface (InGaAs) at bonding temperatures of 600 °C (a) and 250 °C (b)

lasers (VCSELs), and InGaAsP and AlGaAs for high characteristic temperature  $T_0$  lasers [76]. This process consists of a thorough cleaning of the sample surface to remove all semiconductor particles that were generated during dicing or cleaving as well as all organics on the surface. Next a chemical surface treatment is employed to remove any surface native oxides or other stable surface states. The samples are then placed in physical contact with each other and undergo spontaneous bonding and are held together with Van der Waals forces. This bond is relatively strong, depending on the two material systems being bonded, but is further strengthened through a high-temperature anneal (typically 600 °C or higher) while applying pressure on the bonded sample. The high-temperature anneal results in the formation of covalent bonds at the bonded interface, while the pressure on the sample compensates for any waviness or surface roughness and ensures greater surface area contact between the two materials. The substrate of one of the material systems is then removed by using a wet etch resulting in the transfer of one epitaxial layer structure to another.

The difference in the thermal expansion coefficient of silicon ( $\alpha_{\text{Si}} = 2.6 \times 10^{-6}/\text{K}$ ) and InP ( $\alpha_{\text{InP}} = 4.8 \times 10^{-6}/\text{K}$ , cf. Table 14.1), thermal damage, and doping diffusion pose a large challenge for achieving high quality with active region transfer to silicon through direct wafer bonding. As samples cool from 600 °C to room temperature, the InP begins to fracture since the thermal stress built up was larger than the fracture energy of the InP. Mild success in preserving the III-V material can be achieved by thinning the substrate of the InP to  $\sim 150 \mu\text{m}$  between the spontaneous bonding step and high-temperature anneal steps. The thinned III-V materials conform more easily to the silicon without accumulating enough stress to fracture the III-V but show cross hatching and material waviness in the transferred III-V materials (Fig. 14.15a). Figure 14.15b shows a Nomarski-mode microscope image of the top surface of an InAlGaAs active region layer structure transferred to silicon after a 250 °C anneal. The Nomarski mode of the microscope shows the

**Fig. 14.16** Critical dislocation generation stress in InP and shear stress between InP bonded to silicon vs. temperature [77] (reproduced with permission from the Institute of Electrical and Electronic Engineers)



polarization dependence of the surface reflection and is useful for seeing surface particles and roughness.

The thermal mismatch stress  $\sigma$  of the bonded wafers is given by:

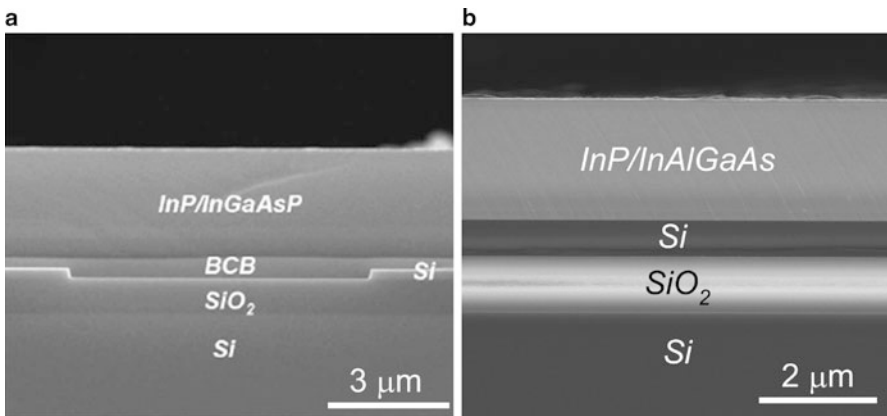
$$\sigma = \frac{E}{1 - \nu^2} \left( \frac{\frac{E_{\text{InP}}}{1 - \nu_{\text{InP}}^2} \alpha_{\text{InP}} h_{\text{InP}} + \frac{E_{\text{Si}}}{1 - \nu_{\text{Si}}^2} \alpha_{\text{Si}} h_{\text{Si}}}{\frac{E_{\text{InP}}}{1 - \nu_{\text{InP}}^2} h_{\text{InP}} + \frac{E_{\text{Si}}}{1 - \nu_{\text{Si}}^2} h_{\text{Si}}} - \alpha \right) \Delta T, \quad (14.9)$$

where  $\alpha$  is the thermal expansion coefficient,  $h$  is the thickness of the substrate,  $E$  is Young's modulus,  $\nu$  is Poisson's ratio, and  $\Delta T$  is the difference between the bonding temperature and room temperature. The critical stress  $\tau_{\text{critical}}$  required to generate dislocations in InP is empirically formulated by Pasquariello et al. using the theory of stress-induced dislocation generation [78] as:

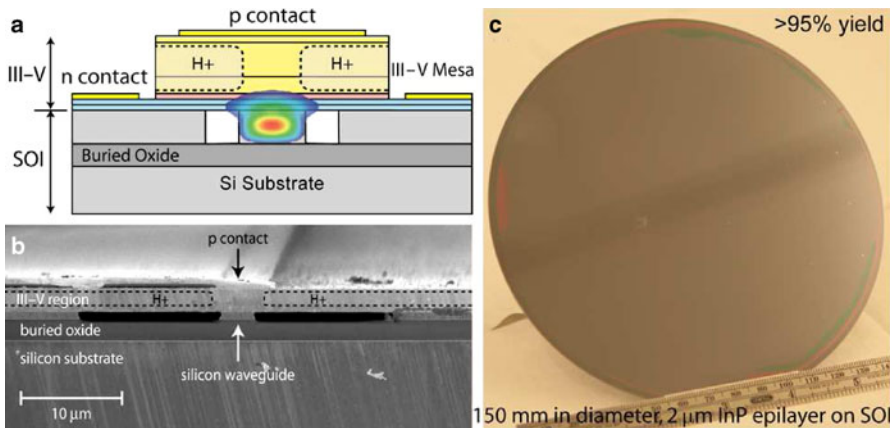
$$\tau_{\text{critical}} = 898 \exp\left(\frac{5934}{T}\right). \quad (14.10)$$

Figure 14.16 shows a plot of the critical stress and the shear stress as a function of temperature. In order to prevent the generation of dislocations in the InP, the bonding temperature must be kept below 300 °C. Two low-temperature III–V film transfer approaches have been used to yield electrically pumped lasers on silicon. The first uses polymers such as divinyl-tetramethyldisiloxane-benzocyclobutene (DVS-BCB) as a 300 nm thin adhesive layer between the III–V region and the waveguide as shown in Fig. 14.17a [79], and the second uses low-temperature oxygen plasma-assisted (LTOPA) wafer bonding where the interfacial oxide with around 15 nm thickness is too thin to be seen in the SEM image of Fig. 14.17b [80]. Detailed studies of polymer-based and LTOPA bonding can be found in [81] and [82], respectively. The transferred InP-based epitaxial thin film acts as a gain medium to generate photons when carriers are injected optically or electrically. Then the light can be evanescently coupled into the SOI waveguide underneath as long as the interface material (i.e., polymer or oxide) is thin.





**Fig. 14.17** SEM cross-sectional images of DVS-BCB (a) and LTOPA bonding (b) to integrate InP thin epitaxial films on an SOI substrate



**Fig. 14.18** Cross-sectional schematic (a) and SEM image (b) of hybrid Si evanescent platform; 150 mm diameter, 2 μm thick InP epitaxial transfer on SOI with > 95 % yield (c)

Figure 14.18a, b are the LTOPA wafer bonding-based hybrid silicon evanescent platform (HSEP) cross-sectional schematic and SEM image, showing a hybrid waveguiding structure formed by bonding III–V epitaxial layers onto the SOI substrate. The typical anneal temperature is kept at 300 °C in all devices made on this platform and discussed in this section. The small index difference between Si and III–V materials enables a large freedom in manipulating modal confinement in Si and the III–V semiconductor, which is realized by adjusting the III–V layer thickness, the SOI waveguide dimension [83], and the rib etch depth. The large index contrast for SOI waveguides can tremendously reduce the chip size and power consumption, and enhance the integration complexity and yield. Unlike the conventional flip-chip die bond to place discrete active components on passive chips, HSEP

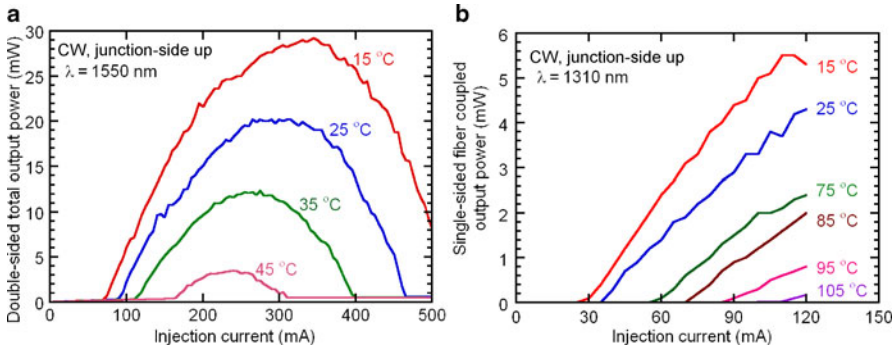


**Fig. 14.19** LI curves for a 1550 nm FP silicon evanescent laser (a), LI curves for a 1310 nm FP silicon evanescent laser (b)

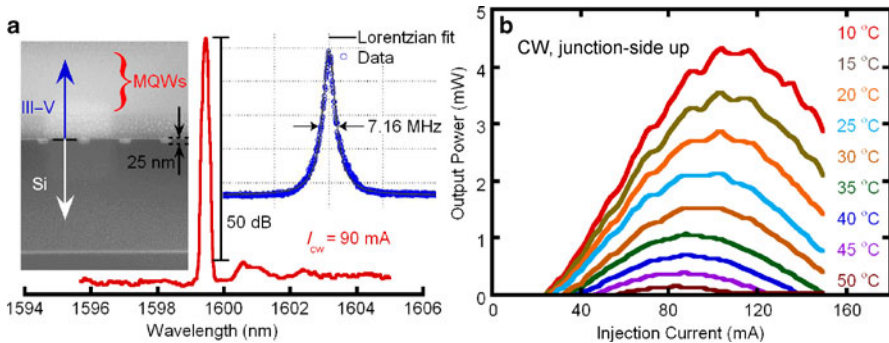


**Fig. 14.20** Experimental spectrum of a Si DFB laser at 90 mA CW injection current. *Left inset*: image of longitudinal cross-section, *right inset*: Delayed-self heterodyned line width trace at 1.8 mW laser output power (a), LI curve for stage temperatures of 10 to 50 °C (b)

eliminates effort and loss in alignment and modal mismatch and literally millions of devices can be made with one bond. Proton implantation in III–Vs creates a current flow channel resulting in good gain and optical mode overlap. Scale-independent integration [82] is demonstrated up to the presently largest InP substrates of 150 mm diameter shown in Fig. 14.18c [84]. No degradation in bonding quality or increase of processing complexity was observed as the process was scaled up to 150 mm, indicating the possibility for low-cost mass production. Bonding and III–V device back-end processing, both conducted at temperatures less than 350 °C, are completely CMOS-compatible.

Figure 14.19a demonstrates the CW LI characteristics of InAlGaAs-MQW hybrid silicon lasers with emission wavelength around 1550 nm [85]. The waveguide height, width, rib etch depth, and cavity length were 0.7  $\mu\text{m}$ , 2  $\mu\text{m}$ , 0.5  $\mu\text{m}$ , and 850  $\mu\text{m}$ , respectively. The calculated confinement factors in the silicon and the quantum-well region are 63 % and 4 %, respectively. The Fabry–Pérot (FP) cavity for these lasers was made by dicing the ends of the hybrid waveguide and polishing them to a mirror finish. The CW single-sided output power for this device is

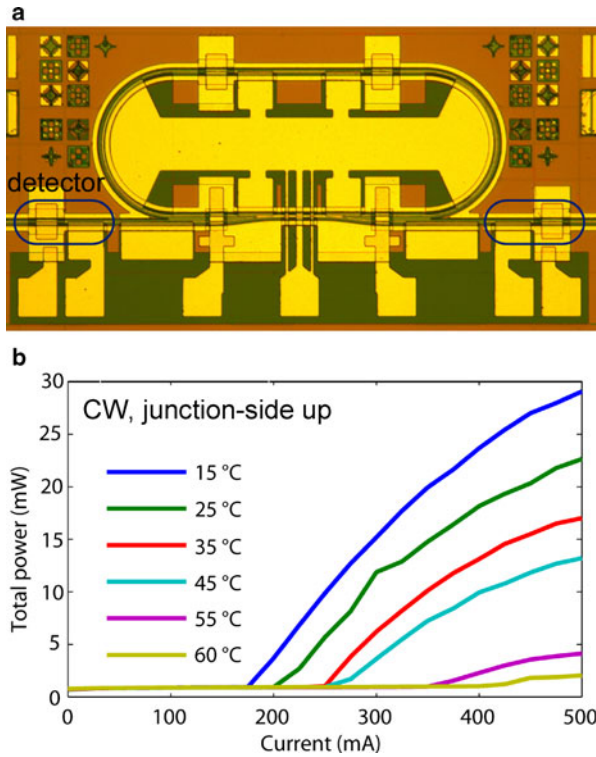


**Fig. 14.21** **a** Top-view microscopic image of a silicon racetrack ring laser, **b** CW LI characteristics of the device as a function of stage temperature

collected on one side with an integrating sphere. Total power is a result of doubling the measured power assuming equal outputs at both sides. It can be seen that the maximum laser output power, threshold, and differential efficiency at 15 °C are 32.8 mW, 70 mA, and 26 %, respectively. Figure 14.19b shows the performance of corresponding devices in the 1310 nm emission wavelength regime. The threshold current at 15 °C is 30 mA [86]. Single-side output power is measured by coupling the light to a single-mode lensed fiber. The total power can be estimated by taking ~ 5 dB coupling loss and then doubling the result. Lasing is observed up to a stage temperature of 105 °C. The higher temperature performance is due to a higher confinement factor, a larger conduction band offset than that of the 1550 nm epitaxial design in Fig. 14.19a, and the intrinsic advantage of 1310 nm lasers for reduced intravalence band absorption and Auger scattering [86].

Grating-based on-chip lasers, distributed feedback (DFB) and distributed Bragg reflector (DBR)-types, are fabricated on the HSEP as well. DFB lasers with a ~ 25 nm surface corrugated grating pattern with a 238 nm pitch and 71 % duty cycle were formed on Si for a grating stop-band designed at around 1600 nm shown by the SEM image and the single-mode spectrum in Fig. 14.20a [87]. 50 dB SMSR,

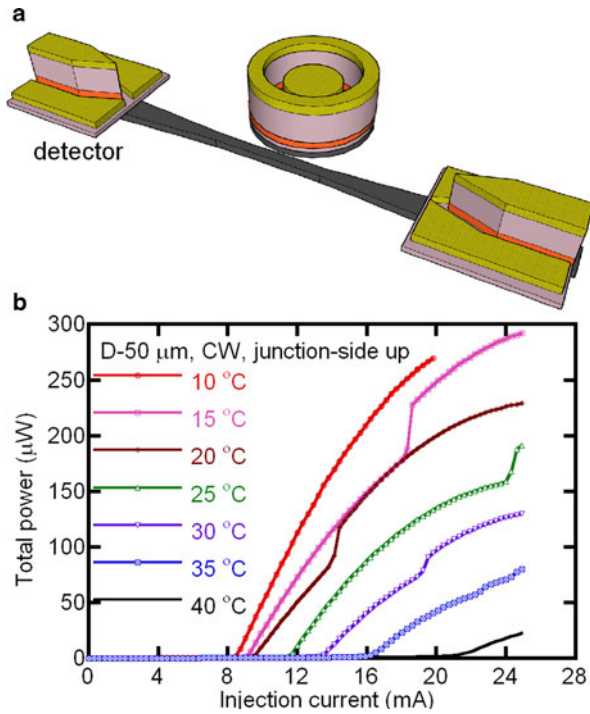


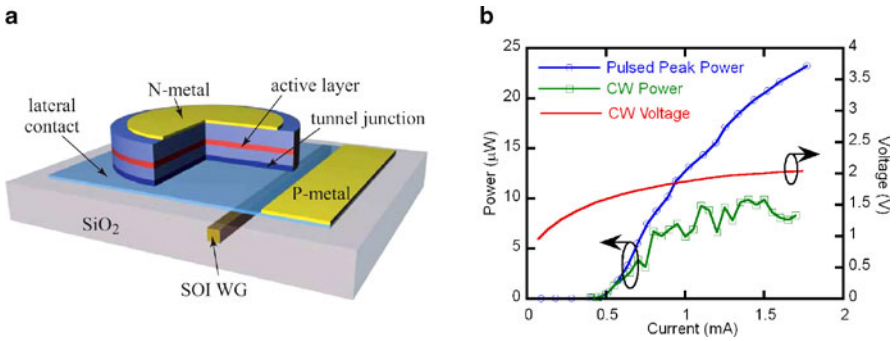
**Fig. 14.22** Schematic of silicon microring laser with integrated photodetectors (a), and CW LI characteristics of the device as a function of stage temperature (b)

over 100 nm single-mode operation span, and 3.5 MHz linewidth are comparable to III–V DFB lasers. Figure 14.20b shows the LI curves of the device exhibiting lasing up to 50 °C. Output power is measured by integrated photodetectors with a responsivity of  $\sim 1$  A/W [88]. More than 4 mW output power was obtained. Recently optimized DFB devices showed over 10 mW maximum output power and up to 80 °C CW lasing temperature [89], and 2.5 GHz direct modulation bandwidth was demonstrated in similar DBR devices [90].

Another type of on-chip lasers plus integrated photodetectors with ring cavity geometry was also developed prior to the DFB and DBR devices. As illustrated by the top-view microscopic image in Fig. 14.21a, the bending radius and directional coupling interaction length of the device are 200 and 400  $\mu\text{m}$ , respectively.

A 12.6% outcoupling is expected based on simulations, and Fig. 14.21b shows CW lasing up to 60 °C with a minimum threshold of 175 mA and a maximum power of 29 mW at 15 °C for a hybrid racetrack ring laser [91].

The long cavity length  $\sim 2.6$  mm limits the minimum threshold and high-speed modulation that can ultimately be achieved. After demonstrating the first on-chip light source on HSEP, a more compact microring structure was then utilized to reduce the cavity length and threshold current as illustrated by the device schematic in Fig. 14.22a [92].



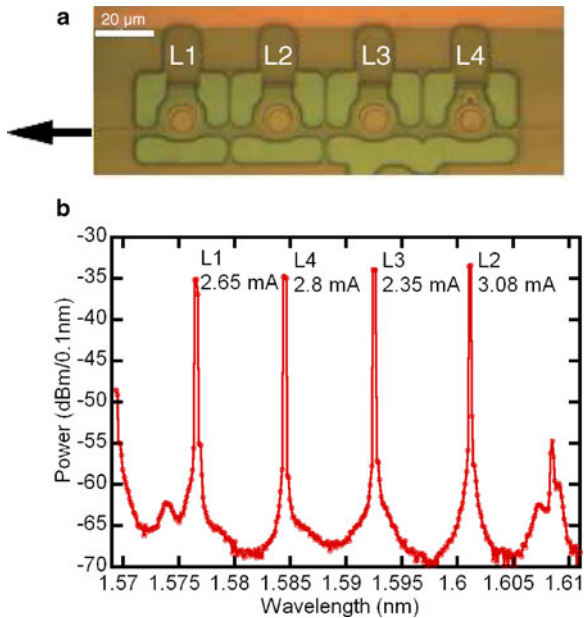
**Fig. 14.23** Schematic of disk laser with vertically coupled SOI waveguide underneath (a), pulsed and CW light-current-voltage (LIV) characteristics at 20 °C for 7.5  $\mu\text{m}$  disk laser [94] (b) (courtesy Joris Van Campenhout, Ghent University, Belgium)

Figure 14.22b shows the CW temperature-dependent LI characteristics of a 50  $\mu\text{m}$  diameter device with a 150 nm coupling gap between the resonator and the bus waveguide. Finite-difference time-domain (FDTD) simulations indicate 1–2 % out-coupling in this geometry. The output power is the sum of the photocurrent measured at both photodetectors for stage temperatures of 10, 15, 20, 25, 30, 35, and 40 °C. The minimum threshold current is 8.37 mA at 10 °C, corresponding to a threshold current density of 2.24 kA/cm<sup>2</sup>. A threshold current as low as 5 mA and a lasing temperature as high as 65 °C have been observed with further reduction of the outcoupling by increasing the coupling gap, although with lower output power. More recent optimization work by selectively reducing the active region volume demonstrated less than 4 mA CW threshold and over 3 mW maximum output power [93].

Sub-mA threshold operation has recently been demonstrated in a DVS-BCB bonded disk laser with 7.5  $\mu\text{m}$  disk diameter by Van Campenhout et al. as shown schematically in Fig. 14.23a [94].

A threshold current of 0.5 mA is achieved under both pulsed and CW operation at 20 °C in Fig. 14.23b, leading to a threshold current density of 1.13 kA/cm<sup>2</sup> for uniform injection. The output power was collected at one end of the output SOI waveguide using a fiber grating coupler. The maximum CW and pulsed output power are 10 and 100  $\mu\text{W}$ , respectively. By optimizing the III–V epitaxial structure and dry etch technique, 0.3 mA threshold and 300  $\mu\text{W}$  output power were achieved by the same research group recently [95]. The early thermal roll-over in the CW regime is caused by a high thermal resistance, which was measured to be 10,000 K/W [94].

A multi-wavelength laser (MWL) source with four cascaded microdisk lasers was also demonstrated [96]. Shown by a top-view microscopic image in Fig. 14.24a, the nominal microdisk diameters were 7.632, 7.588, 7.544, and 7.5  $\mu\text{m}$  for lasers L1, L2, L3, and L4, respectively, such that the laser peaks are uniformly spread within the free-spectral range of a single microdisk.



**Fig. 14.24** Microscope image of a multi-wavelength laser source consisting of four microdisk lasers coupled to a common, underlying SOI waveguide (a) and balanced output spectrum obtained by adjusting the individual microdisk drive currents [96] (b) (courtesy Joris Van Campenhout, Ghent University, Belgium)

The uniform MWL output spectrum is achieved by tuning the individual microdisk lasers with different bias currents as shown in Fig. 14.24b. Although the measured thermal impedance was about 6,400 K/W, the wavelength shift of one laser by changing the bias does not lead to a drifting of the others, meaning that the thermal crosstalk is negligible [96].

To summarize, the silicon laser with the possibility of integration with other CMOS-compatible components is the most important component in the silicon photonics toolbox. It may become a crucial component for the microprocessor industry to deploy low-cost, high-speed optical interconnects in microelectronic chips for larger communication bandwidth and lower power consumption. The highest performance to date has been demonstrated with hybrid silicon approaches, but rapid progress is being made in all of the approaches described here.

### 14.3 High-speed Signal Processing in Silicon

The progress in high-speed silicon modulators has been extraordinary in the past decade. Though conventional electro-optic effects are either unavailable (i.e., the

Pockels effect [97]), or weak (i.e., the Kerr and Franz–Keldysh effects) in silicon, the free carrier plasma effect has been successfully employed to provide index changes  $\Delta n$  in the order of  $10^{-4}$  to  $10^{-3}$  with reasonable applied voltages. The change of free carrier concentration not only causes the loss variation as given by (14.3), but also determines the index change by (14.11) [98].

$$\Delta n = \frac{-q^2 \lambda_0^2}{8\pi^2 c^2 n \epsilon_0} \left( \frac{N_e}{m_{ce}^*} + \frac{N_h}{m_{ch}^*} \right). \quad (14.11)$$

Soref et al. derived the useful empirical equations (14.12)–(14.15) to relate the free carrier plasma effect to the change of index  $\Delta n$  and absorption loss  $\Delta\alpha$  in the telecommunication windows at 1.31 and 1.55  $\mu\text{m}$ .

At  $\lambda_0 = 1.31 \mu\text{m}$ :

$$\Delta n = \Delta n_e + \Delta n_h = -6.2 \times 10^{-22} \Delta N_e - 6.0 \times 10^{-18} (\Delta N_h)^{0.8}, \quad (14.12)$$

$$\Delta\alpha = \Delta\alpha_e + \Delta\alpha_h = 6.0 \times 10^{-18} \Delta N_e + 4.0 \times 10^{-18} \Delta N_h. \quad (14.13)$$

At  $\lambda_0 = 1.55 \mu\text{m}$

$$\Delta n = \Delta n_e + \Delta n_h = -8.8 \times 10^{-22} \Delta N_e - 8.5 \times 10^{-18} (\Delta N_h)^{0.8}, \quad (14.14)$$

$$\Delta\alpha = \Delta\alpha_e + \Delta\alpha_h = 8.5 \times 10^{-18} \Delta N_e + 6.0 \times 10^{-18} \Delta N_h, \quad (14.15)$$

where  $\Delta N_e$  and  $\Delta N_h$  are the respective concentration changes of electrons and holes. Please note the  $(\Delta N)^{0.8}$  dependence for holes in the refractive index calculation [98]. An appreciable index change  $\Delta n > 1 \times 10^{-3}$  is readily achievable in a moderate doping range of  $5 \times 10^{17} \text{cm}^{-3}$ , making the plasma effect the primary phase modulation mechanism in silicon. A more detailed derivation of carrier change-induced index and absorption variations from the Kramers–Kronig relations can be found in [99], followed by an excellent review of the history of silicon modulator development. The following sections highlight a few of the most recent innovative high-speed optical modulators on a Si substrate.

### 14.3.1 Silicon Optical Modulators

The first two silicon modulators passing the 10 Gbit/s data transmission benchmark utilized a forward-biased MOS capacitor structure, and a ring-resonator p-i-n diode structure, respectively [100, 101]. Further improvement in bandwidth in the former case is limited by large capacitances in MOS capacitors, while the latter case suffers from slow minority carrier generation and/or recombination [102].

A recent pn diode-based Mach–Zehnder interferometer (MZI) design demonstrated 40 Gbit/s data transmission and more than 30 GHz bandwidth [103]. The device operates in a carrier depletion mode (i.e., reverse-biased), so the depletion region, whose width is  $W_D$ , replaces the MOS capacitor, resulting in a reduction of

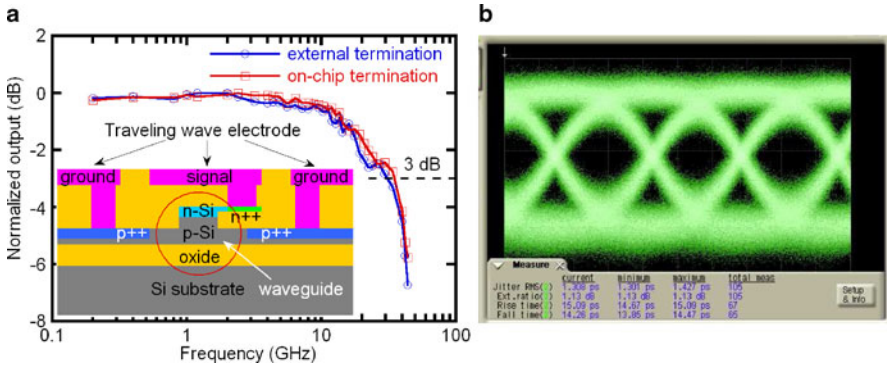


**Fig. 14.25** Frequency response of an MZI with 1 mm-long phase shifter with on-chip and external termination. *Inset*: Cross-sectional schematic of the phase shifter (a). Optical eye diagram of the device at 40 Gbit/s data transmission rate [102] (b) (courtesy Ansheng Liu, Intel. Corp., Santa Clara, CA, USA)

device capacitance [104].  $W_D$  is given by

$$W_D = \sqrt{\frac{2\epsilon_0\epsilon_r(V_{Bi} + V)}{qN_A}}, \quad (14.16)$$

where  $\epsilon_r$ ,  $V_{Bi}$  and  $V$  are the low-frequency relative permittivity of silicon, the built-in voltage and applied reverse bias voltage, respectively. The change of depletion region width leads to a change of free carrier concentration and to a related change of the refractive index as well. This subsequently results in an optical phase change  $\Delta\phi$

$$\Delta\phi = \frac{2\pi\Delta n_{\text{eff}}L}{\lambda_0}, \quad (14.17)$$

where  $\Delta n_{\text{eff}}$  and  $L$  are the effective modal index change and the device length, respectively. The MZI geometry converts the phase modulation into an optical intensity modulation.

The inset of Fig. 14.25a is a cross-sectional schematic of the phase shifter, showing a  $0.6\ \mu\text{m}$ -wide p-doped rib with an epitaxially grown  $0.1\ \mu\text{m}$  thick n-doped silicon cap. A special doping profile is designed to place the pn junction in an optimal position for good optical mode overlap and results in the highest depletion in a p-doped rib because the hole density change gives rise to a large index change as described by (14.12) and (14.14). The traveling wave electrode design based on a coplanar waveguide structure is utilized to realize similar propagation speed of electrical and optical signals [103]. The single-sided asymmetric silicon cap layer is for reducing the capacitance of the phase shifter. A phase efficiency  $V_\pi L_\pi \sim 4\ \text{V cm}$  is obtained in 1, 3, and 5 mm-long phase shifters. Figure 14.25a shows the frequency response of 1 mm long devices either packaged onto a printed circuit board with external resistors or integrated with on-chip thin-film resistors. Both devices demon-



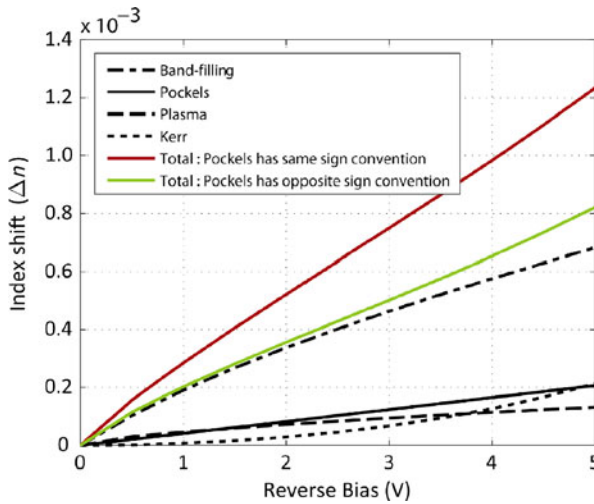


**Fig. 14.26** Estimated index shift (TE polarization) of a carrier depletion phase modulator in InAlGaAs MQW [105]

strate over 30 GHz 3 dB bandwidth at 1550 nm. Figure 14.25b shows the eye diagram of this modulator's optical output at a bit rate of 40 Gbit/s. The extinction ratio is measured to be 1.1 dB with a rise/fall time of  $\sim 14$  ps. The open eye diagram shows that the modulator is capable of transmitting data at 40 Gbit/s, which is consistent with a 3 dB bandwidth  $> 30$  GHz [102].

### 14.3.2 Hybrid Silicon Modulators

A similar carrier depletion-mode is also implemented based upon the HSEP discussed in Sect. 14.2.4. The III–V MQW epitaxial layer is transferred onto the SOI waveguide and the carrier density is modulated by the reverse bias. Once the carriers deplete out of the MQW, several physical effects, such as the band-filling, plasma, Pockels, and Kerr effect, all contribute to the index change. Among all of them, the Pockels effect is the only phenomenon which is sensitive to crystal orientation. In other words, this effect can be additive to the other effects if the optical signal propagates along the right direction; if otherwise, it can reduce the overall index change. On the hybrid silicon platform, the direction of patterned silicon waveguides needs to be aligned to the [011] direction of the III–V material so that the phase shift is maximized, or under the correct angle to make it polarization independent. Figure 14.26 shows simulation results with consideration of all these effects [105]. As can be seen, the index change is proportional to the magnitude of the reverse bias. Moreover, the introduced index shift in the case of orientation match is approximately 1.5 times larger than in the mismatch case.

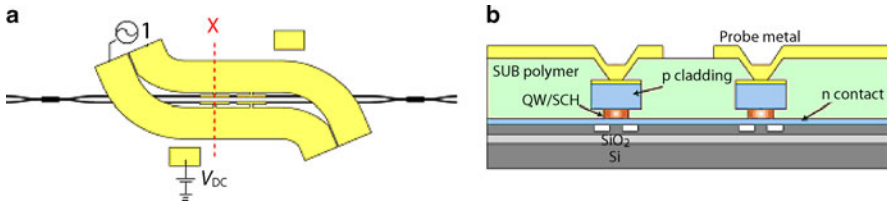


**Fig. 14.27** Top view of a device with a CL-slotline electrode (a), Cross-section (along  $x$ ) of the hybrid waveguide [107] (b)

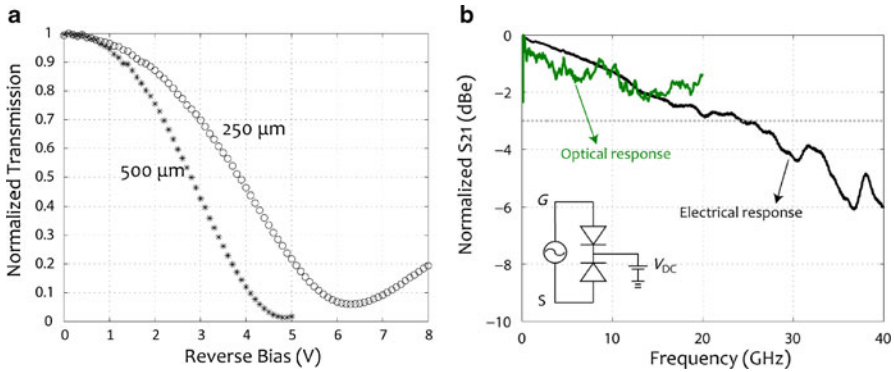


**Fig. 14.28** Modulation efficiency of 250  $\mu\text{m}$  and 500  $\mu\text{m}$  devices at 1550 nm (a), electrical and modulation response of a 250  $\mu\text{m}$  device (b)

Because of the same reverse-bias operation, a 16 period MQW active region is designed with a PL peak at 1.36  $\mu\text{m}$  in order to achieve high optical confinement in the MQWs and low absorption at 1.55  $\mu\text{m}$  [106]. Both, the top SCH layer and the MQWs, are n-type doped in order to introduce free carriers. The thickness and doping of the top SCH layer are carefully designed to result in complete depletion of this layer at zero bias. Thus, all applied bias voltage will be used to deplete carriers in the MQW region only. As shown in Fig. 14.27a, a capacitively loaded (CL) traveling wave electrode (TWE) based on a slotline architecture is adopted to prevent the electrical field from overlapping with the doped semiconductor underneath the metal electrode.

The device capacitance is reduced by half by using a push-pull scheme because the two diodes on both arms are in series [107]. The cross-section of the loaded region is depicted in Fig. 14.27b. The signal and ground of the slotline are on top of each arm, respectively. The two arms have a common ground formed by connecting the n-contact layers together. The cladding mesa is 4  $\mu\text{m}$  wide, and the active region is intentionally under-cut to 2  $\mu\text{m}$  to reduce the device capacitance. The silicon waveguides have a height of 0.47  $\mu\text{m}$ , a slab height of 0.2  $\mu\text{m}$ , and a width of 1  $\mu\text{m}$ .

The normalized transmission as a function of reverse bias for two devices is shown in Fig. 14.28a.

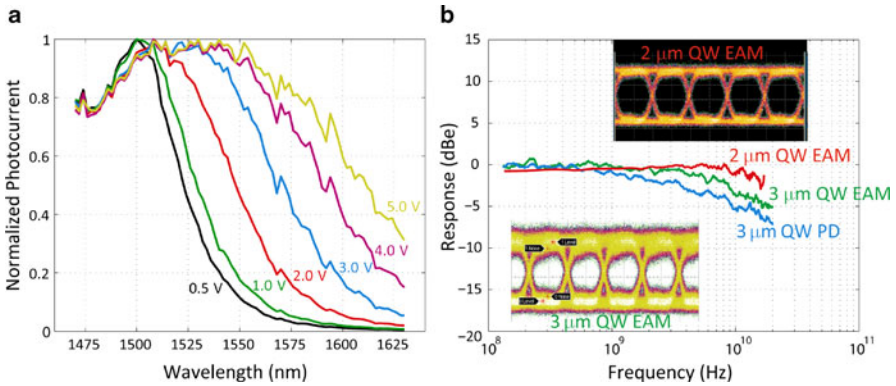


**Fig. 14.29** Photocurrent of 100  $\mu\text{m}$  long EAM at different bias voltages (a), and experimental frequency response of 100  $\mu\text{m}$  long device. *Insets:* 10 Gbit/s eye diagram of devices with different MQW undercut: (1) 3  $\mu\text{m}$  wide MQW and (2) 2  $\mu\text{m}$  wide MQW (b)

As can be seen, the  $V_{\pi}$  of a 250  $\mu\text{m}$  and a 500  $\mu\text{m}$  long modulator are 6.3 V and 4.8 V, respectively. This results in voltage length products of 1.6 V mm and 2.4 V mm, respectively. The static ER of a 250  $\mu\text{m}$  and a 500  $\mu\text{m}$  long modulator are 12.2 dB and 18.4 dB, respectively. The frequency response of a 250  $\mu\text{m}$  modulator with  $-3$  V bias across the diode is shown in Fig. 14.28b. The inset of Fig. 14.28b illustrates the circuit model for the device under test. The transmission curve indicates a 3 dB cutoff frequency around 25 GHz, which is about three times larger than that of the previously demonstrated device [106]. The optical modulation response follows the trend of the electrical response and shows more than 20 GHz bandwidth in Fig. 14.28b. 40 Gbit/s modulation speed with 11.4 dB extinction ratio have been observed in most recent devices [108].

Conversely, the transferred InAlGaAs-based MQWs also make a strong quantum-confined Stark effect (QCSE) available for electroabsorption modulation due to a large conduction band offset for high ER. The MQW section of the electroabsorption modulator (EAM) contains 10 wells and 11 barriers with a PL peak at 1478 nm and is slightly different from the epitaxial structure of the hybrid silicon MZI modulators. The top SCH is slightly doped to assure most of the voltage drop across the MQWs, while the bottom SCH remains undoped to prevent dopant diffusion from highly doped n-InP and also help reducing overall capacitance. The conduction band offset in the MQWs is designed to be larger than that of MZI structures for larger ER [109].

The absorption shift due to the QCSE can be observed by measuring the photocurrent at different wavelengths as shown in Fig. 14.29a. The device, which shares the same cross-sectional geometry as the MZI in Fig. 14.27b, has a 100  $\mu\text{m}$  long absorber and the optical input power is kept at 0.5 mW across all wavelengths. The absorption edge shifts about 20 nm for each additional volt applied to the device, resulting in over 10 dB static ER when biased at 4 V or less [109].

As shown in Fig. 14.29b, two 100  $\mu\text{m}$  long EAMs with different MQW undercuts were measured. The device with a 3  $\mu\text{m}$  wide MQW section has a series resistance around 30  $\Omega$  and capacitance of 0.2 pF at 2 V bias, which corresponds to a cut-off frequency around 10 GHz. The modulators have also been driven with a  $2^{31}-1$  pseudorandom bit sequence (PRBS) to explore the performance of large signal modulation. A peak-to-peak driving voltage of 0.82 V has been used to produce a clear eye diagram with 5 dB ER. In the device with a 2  $\mu\text{m}$  wide MQW section the capacitance drops to around 0.1 pF and produces a 3 dB bandwidth > 16 GHz, though the reduction of the MQW volume causes an increase of driving voltage. The open eye diagram with 6 dB ER has been taken with much higher voltage swing of 3.2 V peak-to-peak. After increasing the reverse bias to 4 V, the EAM turns into an efficient photodetector with on-chip responsivity greater than 0.8 A/W and bandwidth over 4.5 GHz. The estimated photo-carrier generation in the taper region is about 10% of the total photocurrent. A traveling-wave electrode design was employed very recently, resulting in a 3 dB bandwidth of around 42 GHz with 23 GHz/V modulation efficiency. A dynamic extinction ratio of 9.8 dB with a driving voltage swing of only 2 V was demonstrated at a transmission rate of 50 Gbit/s [110].

The QCSE has also recently been utilized in strained Ge/SiGe MQW structures monolithically integrated on Si substrates though the absorption coefficient in SiGe MQWs is still lower than in InP-based materials [111]. Furthermore, it has been reported that strained silicon also exhibits linear electro-optic refractive index modulation [112]. It is realistic to believe that 40 Gbit/s or faster data processing speed with low-power consumption and high ER will be soon accomplished in silicon modulators on both monolithic and hybrid platforms. Each of them will find its appropriate role in a variety of applications.

Because of the space limit here, this chapter primarily focuses on transmitters. Photodetection in Si is not presented, although it is important for communication links. An important breakthrough in avalanche photodiodes (APD), though, is worth mentioning here as extremely high gain-bandwidth products up to 850 GHz have been demonstrated in monolithic SiGe APDs [113, 114]. These devices will be important for telecommunication and data communication links.

## 14.4 Summary

The developmental roadmap of the microelectronics industry indicates that Si is unlikely to be replaced by other materials. The urgent need to break the “brick wall” of interconnect bandwidth and power consumption in microprocessors plus emerging markets (e.g., fiber-to-the-home applications) should be a compelling force to make Si the primary host material for PICs as well. Equipped with recently developed Si lasers, modulators and photodetectors, plus other necessary components demonstrated already or under development, sophisticated Si PICs should become widespread.

**Acknowledgements** The authors thank Brian Koch, Hui-Wen Chen, Hsu-Hao Chang, Hyundai Park, Jag Shah, Mario Paniccia, Matthew Sysak, Mike Haney, Ray Zaroni, Richard Jones, and Ying-Hao Kuo, for valuable discussions, and Jared Bauters, Martijn Heck and Molly Piels for careful proofreading. We thank DARPA MTO, Intel, Hewlett Packard and Rockwell Collins for supporting this research.

## References

1. J.D. Plummer, M.D. Deal, P.B. Griffin, *Silicon VLSI Technology: Fundamentals, Practice, and Modeling* (Prentice Hall, New York, USA, 2000)
2. G.E. Moore, Cramming more components onto integrated circuits. *Electronics* **19**, 114–117 (1965)
3. [http://en.wikipedia.org/wiki/UNIVAC\\_I](http://en.wikipedia.org/wiki/UNIVAC_I)
4. <http://www.kurzweilai.net/articles/art0134.html?printable=1>
5. M.K. Smit, Past and future of InP-based photonic integration, *LEOS Annual Meeting*, Newport Beach, CA, USA (2008), paper MF1
6. L. Thylen, A Moore's law for photonics, *Intern. Symp. Biophoton., Nanophoton. Metamater.*, Hangzhou, China (2006), pp. 256–263
7. S.C. Nicholes, M.L. Maanovi, B. Jevremovi, E. Lively, L.A. Coldren, D.J. Blumenthal, The world's first InP  $8 \times 8$  monolithic tunable optical router (Motor) operating at 40 Gbps line rate per port, *Opt. Fiber Commun. Conf. and Nat. Fiber Opt. Eng. Conf. (OFC/NFOEC'09)*, Techn. Digest (San Diego, CA, USA, 2009), post-deadline paper PDPB1
8. M.K. Smit, Lecture at the University of California, Santa Barbara, CA, USA (2008)
9. <http://www.itrs.net/>
10. <http://www.eetimes.com/showArticle.jhtml?articleID=214502894>
11. J.W. Raring, L.A. Coldren, 40-Gbit/s widely tunable transceivers. *IEEE J. Sel. Top. Quantum Electron.* **13**, 3–14 (2007)
12. L.A. Coldren, InP-based photonic integrated Circuits, *CLEO/QELS*, San Jose, CA, USA (2008), paper CTuBB1
13. D. Liang, A.W. Fang, H.-W. Chen, M. Sysak, B.R. Koch, E. Lively, Y.-H. Kuo, R. Jones, J.E. Bowers, Hybrid silicon evanescent approach to optical interconnects. *Appl. Phys. A* **95**, 1045–1057 (2009)
14. L. Pavesi, Optical gain and lasing in low dimensional silicon: the quest for an injection laser, in *Device Applications of Silicon Nanocrystals and Nanostructures*, ed. by N. Koshida (Springer, New York, 2009), Chap. 4
15. P. Jonsson, H. Bleichner, M. Isberg, E. Nordlander, The ambipolar Auger coefficient: measured temperature dependence in electron irradiated and highly injected n-type silicon. *J. Appl. Phys.* **81**, 2256–2262 (1997)
16. R. Soref, J.P. Lorenzo, All-silicon active and passive guided-wave components for  $\lambda = 1.3$  and  $1.6 \mu\text{m}$ . *IEEE J. Quantum Electron.* **QE-22**, 873–879 (1986)
17. L. Dal Negro, M. Cazzanelli, N. Daldosso, Z. Gaburro, L. Pavesi, F. Priolo, D. Pacifici, G. Franzo, F. Iacona, Stimulated emission in plasma-enhanced chemical vapour deposited silicon nanocrystals. *Phys. E* **16**, 297–308 (2003)
18. U. Gösele, V. Lehmann, Light-emitting porous silicon. *Mater. Chem. Phys.* **40**, 253–259 (1995)
19. L.T. Canham, Silicon quantum wire array fabrication by electrochemical and chemical dissolution of wafers. *Appl. Phys. Lett.* **57**, 1046–1048 (1990)
20. A.G. Cullis, L.T. Canham, Visible light emission due to quantum size effects in highly porous crystalline silicon. *Nature* **353**, 335–338 (1991)
21. K.D. Hirschman, L. Tsybeskov, S.P. Duttagupta, P.M. Fauchet, Silicon-based visible light-emitting devices integrated into microelectronic circuits. *Nature* **384**, 338–341 (1996)

22. W.L. Wilson, P.F. Szajowski, L.E. Brus, Quantum confinement in size-selected, surface-oxidized silicon nanocrystals. *Science* **262**, 1242–1244 (1993)
23. L. Pavesi, L. Dal Negro, C. Mazzoleni, G. Franzo, F. Priolo, Optical gain in silicon nanocrystals. *Nature* **408**, 440–444 (2000)
24. Z.H. Lu, D.J. Lockwood, J.M. Baribeau, Quantum confinement and light emission in SiO<sub>2</sub>/Si superlattices. *Nature* **378**, 258–260 (1995)
25. A.G. Nassiopoulos, S. Grigoropoulos, D. Papadimitriou, Electroluminescent device based on silicon nanopillars. *Appl. Phys. Lett.* **69**, 2267–2269 (1996)
26. A. Malinin, V. Ovchinnikov, S. Novikov, C. Tuovinen, A. Hovinen, Fabrication of a silicon based electroluminescent device. *Mater. Sci. Eng. B* **74**, 32–35 (2000)
27. O. Bisi, S. Ossicini, L. Pavesi, Porous silicon: a quantum sponge structure for silicon based optoelectronics. *Surf. Sci. Rep.* **38**, 1–126 (2000)
28. M.V. Wolkin, J. Jorne, P.M. Fauchet, G. Allan, C. Delerue, Electronic states and luminescence in porous silicon quantum dots: the role of oxygen. *Phys. Rev. Lett.* **82**, 197–200 (1999)
29. A. Zimina, S. Eisebitt, W. Eberhardt, J. Heitmann, M. Zacharias, Electronic structure and chemical environment of silicon nanoclusters embedded in a silicon dioxide matrix, *Appl. Phys. Lett.* **88**, 163103 (2006)
30. J. Heitmann, F. Müller, L. Yi, M. Zacharias, D. Kovalev, F. Eichhorn, Excitons in Si nanocrystals: confinement and migration effects. *Phys. Rev. B* **69**, 195309 (2004)
31. K. Leonid, R. Markku, N. Sergei, K. Olli, S. Juha, Raman scattering from very thin Si layers of Si/SiO<sub>2</sub> superlattices: experimental evidence of structural modification in the 0.8–3.5 nm thickness region. *J. Appl. Phys.* **86**, 5601–5608 (1999)
32. L. Dal Negro, M. Cazzanelli, L. Pavesi, S. Ossicini, D. Pacifici, G. Franzo, F. Priolo, F. Iacona, Dynamics of stimulated emission in silicon nanocrystals. *Appl. Phys. Lett.* **82**, 4636–4638 (2003)
33. L. Dal Negro, M. Cazzanelli, B. Danese, L. Pavesi, F. Iacona, G. Franzo, F. Priolo, Light amplification in silicon nanocrystals by pump and probe transmission measurements. *J. Appl. Phys.* **96**, 5747–5755 (2004)
34. C. Lingk, G. von Plessen, J. Feldmann, K. Stock, M. Arzberger, G. Böhm, M.-C. Amann, G. Abstreiter, Dynamics of amplified spontaneous emission in InAs/GaAs quantum dots. *Appl. Phys. Lett.* **76**, 3507–3509 (2000)
35. S. Fujita, N. Sugiyama, Visible light-emitting devices with Schottky contacts on an ultrathin amorphous silicon layer containing silicon nanocrystals. *Appl. Phys. Lett.* **74**, 308–310 (1999)
36. R.J. Walters, G.I. Bourianoff, H.A. Atwater, Field-effect electroluminescence in silicon nanocrystals. *Nat. Mater.* **4**, 143–146 (2005)
37. R.J. Walters, J. Carreras, F. Tao, L.D. Bell, H.A. Atwater, Silicon nanocrystal field-effect light-emitting devices. *IEEE J. Sel. Top. Quantum Electron.* **12**, 1647–1656 (2006)
38. C. Josep, J. Arbiol, B. Garrido, C. Bonafos, J. Montserrat, Direct modulation of electroluminescence from silicon nanocrystals beyond radiative recombination rates. *Appl. Phys. Lett.* **92**, 091103 (2008)
39. F. Minoru, Y. Masato, K. Yoshihiko, H. Shinji, Y. Keiichi, 1.54 μm photoluminescence of Er<sup>3+</sup> doped into SiO<sub>2</sub> films containing Si nanocrystals: evidence for energy transfer from Si nanocrystals to Er<sup>3+</sup>. *Appl. Phys. Lett.* **71**, 1198–1200 (1997)
40. G. Franzò, F. Priolo, S. Coffa, A. Polman, A. Camera, Room-temperature electroluminescence from Er-doped crystalline Si. *Appl. Phys. Lett.* **64**, 2235–2237 (1994)
41. G. Franzò, S. Coffa, F. Priolo, C. Spinella, Mechanism and performance of forward and reverse bias electroluminescence at 1.54 μm from Er-doped Si diodes. *J. Appl. Phys.* **81**, 2784–2793 (1997)
42. F. Iacona, A. Irrera, G. Franz, D. Pacifici, I. Crupi, M.P. Miritello, C.D. Presti, F. Priolo, Silicon-based light-emitting devices: properties and applications of crystalline, amorphous and Er-doped nanoclusters. *IEEE J. Sel. Top. Quantum Electron.* **12**, 1596–1606 (2006)
43. G. Franzò, V. Vinciguerra, F. Priolo, The excitation mechanism of rare-earth ions in silicon nanocrystals. *Appl. Phys. A* **69**, 3–12 (1999)

44. D. Pacifici, G. Franzò, F. Priolo, F. Iacona, L. Dal Negro, Modeling and perspectives of the Si nanocrystals-Er interaction for optical amplification. *Phys. Rev. B* **67**, 245301 (2003)
45. S.G. Cloutier, P.A. Kosyrev, J.M. Xu, Optical gain and stimulated emission in periodic nanopatterned crystalline silicon. *Nat. Mater.* **4**, 887–891 (2005)
46. E. Rotem, J.M. Shainline, J.M. Xu, Enhanced photoluminescence from nanopatterned carbon-rich silicon grown by solid-phase epitaxy. *Appl. Phys. Lett.* **91**, 051127–051129 (2007)
47. G. Davies, The optical properties of luminescence centres in silicon. *Phys. Rep.* **176**, 83–188 (1989)
48. G.D. Watkins, Defects in irradiated silicon: EPR and electron-nuclear double resonance of interstitial boron. *Phys. Rev. B* **12**, 5824–5839 (1975)
49. E. Rotem, J.M. Shainline, J.M. Xu, Electroluminescence of nanopatterned silicon with carbon implantation and solid phase epitaxial regrowth. *Opt. Express* **15**, 14099–14106 (2007)
50. R. Claps, D. Dimitropoulos, V. Raghunathan, Y. Han, B. Jalali, Observation of stimulated Raman amplification in silicon waveguides. *Opt. Express* **11**, 1731–1739 (2003)
51. T.K. Liang, H.K. Tsang, Role of free carriers from two-photon absorption in Raman amplification in silicon-on-insulator waveguides. *Appl. Phys. Lett.* **84**, 2745–2747 (2004)
52. O. Boyraz, B. Jalali, Demonstration of a silicon Raman laser. *Opt. Express* **12**, 5269–5273 (2004)
53. R. Jones, H. Rong, A. Liu, A.W. Fang, M.J. Paniccia, D. Hak, O. Cohen, Net continuous wave optical gain in a low loss silicon-on-insulator waveguide by stimulated Raman scattering. *Opt. Express* **13**, 519–525 (2005)
54. H. Rong, R. Jones, A. Liu, O. Cohen, D. Hak, A.W. Fang, M.J. Paniccia, A continuous-wave Raman silicon laser. *Nature* **433**, 725–728 (2005)
55. S. Fathpour, K.K. Tsia, B. Jalali, Energy harvesting in silicon Raman amplifiers. *Appl. Phys. Lett.* **89**, 061109 (2006)
56. H. Rong, S. Xu, Y.-H. Kuo, V. Sih, O. Cohen, O. Raday, M.J. Paniccia, Low-threshold continuous-wave Raman silicon laser. *Nat. Photon.* **1**, 232–237 (2007)
57. C.P. Kuo, S.K. Vong, R.M. Cohen, G.B. Stringfellow, Effect of mismatch strain on bandgap in III–V semiconductors. *J. Appl. Phys.* **57**, 5428–5432 (1985)
58. H. Kawanami, Heteroepitaxial technologies of III–V on Si. *Sol. Energy Mater.* **66**, 479–486 (2001)
59. Y.H. Xie, K.L. Wang, Y.C. Kao, An investigation on surface conditions for Si molecular beam epitaxial (MBE) growth. *J. Vac. Sci. Technol. A* **3**, 1035–1039 (1985)
60. K. Samonji, H. Yonezu, Y. Takagi, K. Iwaki, N. Ohshima, J.K. Shin, K. Pak, Reduction of threading dislocation density in InP-on-Si heteroepitaxy with strained short-period superlattices. *Appl. Phys. Lett.* **69**, 100–102 (1996)
61. Y. Masafumi, S. Mitsuru, I. Yoshio, Misfit stress dependence of dislocation density reduction in GaAs films on Si substrates grown by strained-layer superlattices. *Appl. Phys. Lett.* **54**, 2568–2570 (1989)
62. K. Nozawa, Y. Horikoshi, Low threading dislocation density GaAs on Si(100) with InGaAs/GaAs strained-layer superlattice grown by migration-enhanced epitaxy. *Jpn. J. Appl. Phys.* **30**, L668–L671 (1991)
63. E. Yamaichi, T. Ueda, Q. Gao, C. Yamagishi, M. Akiyama, Method to obtain low-dislocation-density regions by patterning with SiO<sub>2</sub> on GaAs/Si followed by annealing. *Jpn. J. Appl. Phys.* **33**, L1442–L1444 (1994)
64. B. Kunert, S. Zinnkann, K. Volz, W. Stolz, Monolithic integration of Ga(NAsP)/(BGa)P multi-quantum well structures on (001) silicon substrate by MOVPE. *J. Cryst. Growth* **310**, 4776–4779 (2008)
65. B. Kunert, K. Volz, J. Koch, W. Stolz, Direct-bandgap Ga(NAsP)-material system pseudomorphically grown on GaP substrate. *Appl. Phys. Lett.* **88**, 182108 (2006)
66. V.G. TalalaeV, G.E. Cirlin, A.A. Tonkikh, N.D. Zakharov, P. Werner, Room temperature electroluminescence from Ge/Si quantum dots superlattice close to 1.6  $\mu\text{m}$ . *phys. stat. sol. (a)* **198**, R4–R6 (2003)

67. X. Sun, J. Liu, L.C. Kimerling, J. Michel, Room-temperature direct bandgap electroluminescence from Ge-on-Si light-emitting diodes. *Opt. Lett.* **34**, 1198–1200 (2009)
68. S.-L. Cheng, J. Lu, G. Shambat, H.-Y. Yu, K. Saraswat, J. Vuckovic, Y. Nishi, Room temperature 1.6  $\mu\text{m}$  electroluminescence from Ge light emitting diode on Si substrate. *Opt. Express* **17**, 10019–10024 (2009)
69. L. Tsybeskov, E.-K. Lee, H.-Y. Chang, D.J. Lockwood, J.-M. Baribeau, X. Wu, T.I. Kamins, Silicon–germanium nanostructures for on-chip optical interconnects, *Appl. Phys. A.* **95**, 1015–1027 (2009)
70. F. Olsson, M. Xie, S. Lourdudoss, I. Prieto, P.A. Postigo, Epitaxial lateral overgrowth of InP on Si from nano-openings: theoretical and experimental indication for defect filtering throughout the grown layer. *J. Appl. Phys.* **104**, 093112 (2008)
71. M. Deura, T. Hoshii, T. Yamamoto, Y. Ikuhara, M. Takenaka, S. Takagi, Y. Nakano, M. Sugiyama, Dislocation-free InGaAs on Si(111) using micro-channel selective-area metal-organic vapor phase epitaxy. *Appl. Phys. Express* **2**, 011101–011103 (2009)
72. L. Yan, L. Yan, F. Zhongchao, X. Bo, Y. Yude, Y. Jinzhong, Fabrication and optical optimization of spot-size converters with strong cladding layers. *J. Opt. A* **11**, 085002 (2009)
73. E.E.L. Friedrich, M.G. Oberg, B. Broberg, S. Nilsson, S. Valette, Hybrid integration of semiconductor lasers with Si-based single-mode ridge waveguides. *J. Lightw. Technol.* **10**, 336–340 (1992)
74. J. Sasaki, M. Itoh, T. Tamanuki, H. Hatakeyama, S. Kitamura, T. Shimoda, T. Kato, Multiple-chip precise self-aligned assembly for hybrid integrated optical modules using Au-Sn solder bumps. *IEEE Trans. Adv. Packag.* **24**, 569–575 (2001)
75. H. Park, A.W. Fang, S. Kodama, J.E. Bowers, Hybrid silicon evanescent laser fabricated with a silicon waveguide and III–V offset quantum wells. *Opt. Express* **13**, 9460–9464 (2005)
76. A. Black, A.R. Hawkins, N.M. Margalit, D.I. Babic, A.L. Holmes, Jr., Y.L. Chang, P. Abraham, J.E. Bowers, E.L. Hu, Wafer fusion: materials issues and device results. *IEEE J. Sel. Top. Quantum Electron.* **3**, 943–951 (1997)
77. D. Pasquariello, K. Hjort, Plasma-assisted InP-to-Si low temperature wafer bonding. *IEEE J. Sel. Top. Quantum Electron.* **8**, 118–131 (2002)
78. D. Pasquariello, M. Camacho, F. Ericsson, K. Hjort, Crystalline defects in InP-to-silicon direct wafer bonding. *Jpn. J. Appl. Phys.* **40**, 4837–4844 (2001)
79. G. Roelkens, D. Van Thourhout, R. Baets, R. Nötzel, M.K. Smit, Laser emission and photodetection in an InP/InGaAsP layer integrated on and coupled to a silicon-on-insulator waveguide circuit. *Opt. Express* **14**, 8154–8159 (2006)
80. A.W. Fang, H. Park, O. Cohen, R. Jones, M.J. Paniccia, J.E. Bowers, Electrically pumped hybrid AlGaInAs-silicon evanescent laser. *Opt. Express* **14**, 9203–9210 (2006)
81. I. Christiaens, G. Roelkens, K. De Mesel, D. Van Thourhout, R. Baets, Thin-film devices fabricated with benzocyclobutene adhesive wafer bonding. *J. Lightw. Technol.* **23**, 517–523 (2005)
82. D. Liang, J.E. Bowers, Highly efficient vertical outgassing channels for low-temperature InP-to-silicon direct wafer bonding on the silicon-on-insulator (SOI) substrate. *J. Vac. Sci. Technol. B* **26**, 1560–1568 (2008)
83. H. Park, A.W. Fang, O. Cohen, R. Jones, M.J. Paniccia, J.E. Bowers, Design and fabrication of optically pumped hybrid silicon-AlGaInAs evanescent lasers. *IEEE J. Sel. Top. Quantum Electron.* **12**, 1657–1663 (2006)
84. D. Liang, J.E. Bowers, D.C. Oakley, A. Napoleone, D.C. Chapman, C.-L. Chen, P.W. Juodawlkis, O. Raday, High-quality 150 mm InP-to-silicon epitaxial transfer for silicon photonic integrated circuits. *Electrochem. Solid-State Lett.* **12**, H101–H104 (2009)
85. H. Park, A.W. Fang, D. Liang, Y.-H. Kuo, H.-H. Chang, B.R. Koch, H.-W. Chen, M.N. Sysak, R. Jones, J.E. Bowers, Photonic integration on the hybrid silicon evanescent device platform. *Adv. Opt. Technol.* **2008**, 682978 (2008)
86. H.-H. Chang, A.W. Fang, M.N. Sysak, H. Park, R. Jones, O. Cohen, O. Raday, M.J. Paniccia, J.E. Bowers, 1310 nm silicon evanescent laser. *Opt. Express* **15**, 11466–11471 (2007)
87. A.W. Fang, E. Lively, Y.-H. Kuo, D. Liang, J.E. Bowers, A distributed feedback silicon evanescent laser. *Opt. Express* **16**, 4413–4419 (2008)



88. H. Park, A.W. Fang, R. Jones, O. Cohen, O. Raday, M.N. Sysak, M.J. Paniccia, J.E. Bowers, A hybrid AlGaInAs-silicon evanescent waveguide photodetector. *Opt. Express* **15**, 6044–6052 (2007)
89. H. Park, M.N. Sysak, H.-W. Chen, A.W. Fang, D. Liang, L. Liao, B.R. Koch, J. Bovington, Y. Tang, K. Wong, M. Jacob-Mitos, R. Jones, J.E. Bowers, Device and integration technology for silicon photonic transmitters. *IEEE J. Sel. Top. Quantum Electron.*, online article (2011). doi: 10.1109/JSTQE.2011.2106112
90. A.W. Fang, B.R. Koch, R. Jones, E. Lively, L. Di, Y.-H. Kuo, J.E. Bowers, A distributed Bragg reflector silicon evanescent laser. *IEEE Photon. Technol. Lett.* **20**, 1667–1669 (2008)
91. A.W. Fang, R. Jones, H. Park, O. Cohen, O. Raday, M.J. Paniccia, J.E. Bowers, Integrated AlGaInAs-silicon evanescent race track laser and photodetector. *Opt. Express* **15**, 2315–2322 (2007)
92. D. Liang, M. Fiorentino, T. Okumura, H.-H. Chang, D.T. Spencer, Y.-H. Kuo, A.W. Fang, D. Dai, R.G. Beausoleil, J.E. Bowers, Electrically-pumped compact hybrid silicon microring lasers for optical interconnects. *Opt. Express* **17**, 20355–20364 (2009)
93. D. Liang, M. Fiorentino, S. Srinivasan, J.E. Bowers, R.G. Beausoleil, Low threshold electrically-pumped hybrid silicon microring lasers. *IEEE J. Sel. Top. Quantum Electron.*, online article (2011). doi: 10.1109/JSTQE.2010.2103552
94. J. Van Campenhout, P. Rojo Romeo, P. Regreny, C. Seassal, D. Van Thourhout, S. Verstuyft, L. Di Cioccio, J.M. Fedeli, C. Lagae, R. Baets, Electrically pumped InP-based microdisk lasers integrated with a nanophotonic silicon-on-insulator waveguide circuit. *Opt. Express* **15**, 6744–6749 (2007)
95. T. Spuesens, L. Liu, T. de Vries, P.R. Romeo, P. Regreny, D.J. Van Thourhout, Improved design of an InP-based microdisk laser heterogeneously integrated with SOI, *Proc. 6th IEEE Internat. Conf. Group IV Photonics*, Techn. Digest (San Francisco, CA, USA, 2009), paper FA3
96. J. Van Campenhout, L. Liu, P.R. Romeo, D. Van Thourhout, C. Seassal, P. Regreny, L. Di Cioccio, J.M. Fedeli, R. Baets, A compact SOI-integrated multiwavelength laser source based on cascaded InP microdisks. *IEEE Photon. Technol. Lett.* **20**, 1345–1347 (2008)
97. G.T. Reed, A.P. Knights, *Silicon Photonics: An Introduction* (Wiley, Chichester, 2004)
98. R. Soref, B. Bennett, Electrooptical effects in silicon. *IEEE J. Quantum Electron.* **QE-23**, 123–129 (1987)
99. G.T. Reed, *Silicon Photonics: The State of the Art* (Wiley, Chichester, 2008)
100. A. Liu, R. Jones, L. Liao, D. Samara-Rubio, D. Rubin, O. Cohen, R. Nicolaescu, M.J. Paniccia, A high-speed silicon optical modulator based on a metal-oxide-semiconductor capacitor. *Nature* **427**, 615–618 (2004)
101. Q. Xu, B. Schmidt, S. Pradhan, M. Lipson, Micrometre-scale silicon electro-optic modulator. *Nature* **435**, 325–327 (2005)
102. J. Basak, L. Liao, A. Liu, D. Rubin, Y. Chetrit, H. Nguyen, D. Samara-Rubio, R. Cohen, N. Izhaky, M.J. Paniccia, Developments in gigascale silicon optical modulators using free carrier dispersion mechanisms. *Adv. Opt. Technol.* **2008**, Article ID 678948 (2008). doi: 10.1155/2008/678948
103. A. Liu, L. Liao, D. Rubin, B. Juthika, H. Nguyen, Y. Chetrit, R. Cohen, N. Izhaky, M.J. Paniccia, High-speed silicon modulator for future VLSI interconnect, *OSA Topical Meeting, Integrated Photonics and Nanophotonics Research and Applications (IPNRA)*, Techn. Digest (Salt Lake City, UT, USA, 2007), paper IMD3
104. A. Liu, L. Liao, D. Rubin, H. Nguyen, B. Ciftcioglu, Y. Chetrit, N. Izhaky, M.J. Paniccia, High-speed optical modulation based on carrier depletion in a silicon waveguide. *Opt. Express* **15**, 660–668 (2007)
105. H.-W. Chen, Y. Kuo, J.E. Bowers, Hybrid silicon modulators. *Chin. Opt. Lett.* **7**, 280–285 (2009)
106. H.-W. Chen, Y.-H. Kuo, J.E. Bowers, A hybrid silicon-AlGaInAs phase modulator. *IEEE Photon. Technol. Lett.* **20**, 1920–1922 (2008)

107. H.-W. Chen, Y.-H. Kuo, J.E. Bowers, High speed Mach–Zehnder silicon evanescent modulator using capacitively loaded traveling wave electrode, *Proc. 6th IEEE Internat. Conf. Group IV Photonics*, Techn. Digest (San Francisco, CA, USA, 2009), paper FC4
108. H.-W. Chen, J.D. Peters, J.E. Bowers, Forty Gbit/s hybrid silicon Mach–Zehnder modulator with low chirp. *Opt. Express* **19**, 1455–1460 (2011)
109. Y.-H. Kuo, H.-W. Chen, J.E. Bowers, High speed hybrid silicon evanescent electroabsorption modulator. *Opt. Express* **16**, 9936–9941 (2008)
110. Y. Tang, H.-W. Chen, S. Jain, J.D. Peters, U. Westergren, J.E. Bowers, 50 Gbit/s hybrid silicon traveling-wave electroabsorption modulator. *Opt. Express* **19**, 5811–5816 (2011)
111. J.E. Roth, O. Fidaner, R.K. Schaevitz, Y.-H. Kuo, T.I. Kamins, J.S. Harris, D.A.B. Miller, Optical modulator on silicon employing germanium quantum wells. *Opt. Express* **15**, 5851–5859 (2007)
112. R.S. Jacobsen, K.N. Andersen, P.I. Borel, J. Fage-Pedersen, L.H. Frandsen, O. Hansen, M. Kristensen, A.V. Lavrinenko, G. Moulin, H. Ou, C. Peucheret, B. Zsigri, A. Bjarklev, Strained silicon as a new electro-optic material. *Nature* **441**, 199–202 (2006)
113. Y. Kang, H.-D. Liu, M. Morse, M.J. Paniccia, M. Zadka, S. Litski, G. Sarid, A. Pauchard, Y.-H. Kuo, H.-W. Chen, W.S. Zaoui, J.E. Bowers, A. Beling, D.C. McIntosh, X. Zheng, J.C. Campbell, Monolithic germanium/silicon avalanche photodiodes with 340 GHz gain-bandwidth product. *Nat. Photon.* **3**, 59–63 (2009)
114. W.S. Zaoui, H.-W. Chen, J.E. Bowers, Y. Kang, M. Morse, M.J. Paniccia, A. Pauchard, J.C. Campbell, Frequency response and bandwidth enhancement in Ge/Si avalanche photodiodes with over 840 GHz gain-bandwidth-product. *Opt. Express* **17**, 12641–12649 (2009)

## About the Authors

**Yaakov Achiam** has over 32 years of experience in photonics research and development at world-class academic and industrial institutions. Dr. Achiam has served for the last 10 years as the Vice President of Photonics, for CeLight Inc., a company that specializes in coherent optical technologies. During this period he has been involved in the development of components and systems for coherent optical communication, standoff detection of explosives, and signal analysis. Collaboratively with CeLight, he holds patents on the QPSK modulator and Coherent Receiver. Prior to joining CeLight, Dr. Achiam served as the Joint Head of the Coherent Light Source Laboratory for Ben Gurion University and Israel's Nuclear Research Center, where he conducted work on advanced lasers and materials. From 1992 to 1999, Dr. Achiam was the Director of the Laser Department for the Nuclear Research Center in Israel. Dr. Achiam received his B.Sc., M.Sc., and Ph.D. from Tel Aviv University's Department of Physics and Astronomy.

**Masahiro Aoki** received the B.E., M.E., and Ph.D. degrees in physical electronics from the Tokyo Institute of Technology, Tokyo, Japan, in 1987, 1989, and 1999, respectively.

In 1989, he joined the Central Research Laboratory of Hitachi Ltd., Tokyo, Japan, where he has been engaged in the research, development and commercialization of semiconductor lasers and related monolithic/hybrid integrated components/modules for telecommunications/data communications, information, and industry applications. From 1999 to 2000, he was a Visiting Researcher at the Heinrich-Hertz-Institute, Berlin, Germany, where he was engaged in the advanced monolithic integration of Indium Phosphide-based photonic ICs. From 2006, he headed a Nano-Electronics R&D team and his interests extended to new material and new functional devices such as organic electronics, power electronics, and Micro Electro Mechanical Systems (MEMS) and related subsystems. He is now with the Telecommunications & Network Systems Division of Hitachi Ltd., Yokohama, Japan, and his current focus is on global business development and operation in the field of communication networks.

Dr. Aoki is a member of the Japan Society of Applied Physics and the Institute of Electronics, Information and Communication Engineers (IEICE) of Japan. He received Best Paper Awards from the Third Optoelectronics Conference in 1990, the Second Optoelectronics and Communication Conference in 1997, and the Seventh Optoelectronics and Communication Conference in 2004. He also received the Scientific Encouragement Award in 1994, the Excellent Paper Award in 1995, and the Achievement Award in 2007, all from IEICE, the R&D100 Award in 1996, and the IPRM 10th Anniversary Paper Award in 1998 from the IEEE Lasers and Electro-Optics Society.

**Andreas Beling** received the Dipl.-Phys. degree (M.Sc.) in physics from the University of Bonn, Germany, in 2000 and the Dr.-Ing. degree (Ph.D.) in electrical engineering from the Technical University Berlin, Germany, in 2006. In 2000 he worked as a Research Assistant at the Max-Planck-Institute for Radioastronomy, Bonn, Germany. From 2001 to 2006 he was a staff scientist in the photonics division at the Heinrich-Hertz-Institut für Nachrichtentechnik (HHI) in Berlin, Germany. At HHI, he was engaged in the design and characterization of high-speed optoelectronic circuits. From 2006 to 2008 he was a Research Associate in Prof. Joe C. Campbell's group at the University of Virginia, Charlottesville. At UVA he worked on high-power high-linearity photodiodes and microwave photonics. He joined u<sup>2</sup>t Photonics AG in Berlin, Germany, in late 2008 where he worked as a project manager on the development of new optoelectronic receivers for 40 and 100 G applications. He returned to UVA in 2010 where he is currently a Research Scientist in the Department of Electrical and Computer Engineering. Andreas Beling has authored or co-authored more than 65 technical papers and was a member of the technical program committee of the Optical Fiber Communication Conference in 2010 and 2011. Andreas Beling is a member of the IEEE Photonics Society (formerly IEEE LEOS).

**René Bonk** was born in August 1979 in Germany. In 2006 he received the Diploma degree in Physics from the Technical University of Braunschweig (Germany) for work in the field of quantum transport in low-dimensional electronic systems. In 2012 he received the Dr.-Ing. (Ph.D.) degree in Electrical Engineering from the Karlsruhe Institute of Technology (KIT). From 2006 to 2009 he managed the European FP6 project "TRIUMPH" (Transparent Ring Interconnection Using Multi-wavelength PHotonic switches). During his Ph.D. studies he was working in the area of all-optical signal processing and linear and non-linear semiconductor optical amplifiers (SOA). Currently, he is with Alcatel-Lucent Deutschland AG, Bell-Labs Germany, where he is working as a research engineer in the field of optical access networks.

**Anna Borghesani** obtained the degree of Doctor in Physics at the University of Genova (Physics Department), Italy, in 1999, following the completion of a one year thesis project on particle physics experiments in Italy and in the US. She has worked in the photonics industry for 12 years. She joined Corning Research Cen-

tre in Ipswich, UK, in 2000 where she worked as a System Scientist working on high-speed –10 and 40 Gbit/s tests of optoelectronic components. She then joined CIP Technologies in Ipswich, UK, at its foundation in 2003 as a High-Speed Systems Scientist and product manager for CIP's Monolithic R-SOA-EAM Product. Her expertise in photonics has focused on optoelectronic device characterisation and optical high speed systems up to 40 Gbit/s, implementing new test-beds and measurement techniques. Her work also focused on high frequency component testing including high speed detector and modulator characterisation up to 110 GHz. She has been strongly involved in ongoing EU research projects studying semiconductor optical amplifiers, electro-absorption modulators and ultra high speed photo detectors. She has continued her work since CIP's acquisition by Huawei in early 2012, taking the role of Test and Measurement manager. She is author and co-author of over 30 several technical papers.

**John E. Bowers** holds the Fred Kavli Chair in Nanotechnology, and is the Director of the Institute for Energy Efficiency and a Professor in the Department of Electrical and Computer Engineering at UCSB. He is a co-founder of Aurrion, Aerius Photonics and Calient Networks. Dr. Bowers received his M.Sc. and Ph.D. degrees from Stanford University and worked for AT&T Bell Laboratories and Honeywell before joining UC Santa Barbara. Dr. Bowers is a member of the National Academy of Engineering, a fellow of the IEEE, OSA and the American Physical Society, and a recipient of the OSA Holonyak Prize, the IEEE LEOS William Streifer Award and the South Coast Business and Technology Entrepreneur of the Year Award. He has published eight book chapters, 450 journal papers, 700 conference papers and has received 52 patents. He and coworkers received the EE Times Annual Creativity in Electronics (ACE) Award for Most Promising Technology for the hybrid silicon laser in 2007.

**François Caloz** received a diploma in applied physics from the Swiss Federal Institute of Technology in Zurich in 1991 and a Ph.D. in physical chemistry from the Swiss Federal Institute of Technology in Lausanne in 1997. From 1997–1999 he was a post-doctoral fellow at the Jet Propulsion Laboratory (Pasadena, Los Angeles, CA), and since 1999 he has been with Diamond SA, a worldwide leader in developing and supplying passive fibre optic components and high-precision fibre optic solutions. François Caloz was employed by Diamond SA as the fibre optic laboratory manager, where he was mainly involved in the development, test and measurement of passive optical components, as well as in the implementation and development of new test and measurement equipment. He is currently involved in the standardization of fibre optic connectors with the IEC 86B committee “Fibre optic interconnecting devices and passive components,” which is responsible for the preparation of international standards for fibre optic interconnecting devices and passive components, related test and measurement methods and functional interfaces, including all mechanical, environmental and optical requirements to ensure interoperability and reliable performance of fibre optic interconnecting devices and passive components.

**Joe C. Campbell** received the B.Sc. Degree in Physics from the University of Texas at Austin in 1969, and the M.Sc. and Ph.D. degrees in Physics from the University of Illinois at Urbana-Champaign in 1971 and 1973, respectively. From 1974 to 1976 he was employed by Texas Instruments where he worked on integrated optics. In 1976 he joined the staff of AT&T Bell Laboratories in Holmdel, New Jersey. In the Crawford Hill Laboratory he worked on a variety of optoelectronic devices including semiconductor lasers, optical modulators, waveguide switches, photonic integrated circuits, and photodetectors with emphasis on high-speed avalanche photodiodes for high-bit-rate lightwave systems. In January of 1989 he joined the faculty of the University of Texas at Austin as Professor of Electrical and Computer Engineering and Cockrell Family Regents Chair in Engineering. In January of 2006, Professor Campbell joined the faculty of the University of Virginia in Charlottesville as the Lucian Carr, III Chair of Electrical Engineering and Applied Science. Professor Campbell's research has focused on the optoelectronic components that are used to generate, modulate, and detect the optical signals. At present he is actively involved in single-photon-counting avalanche photodiodes, Si-based optoelectronics, high-speed, low-noise avalanche photodiodes, ultraviolet photodetectors, and quantum-dot IR imaging. To date he has co-authored seven book chapters, 350 articles for refereed technical journals, and more than 300 conference presentations.

**Wolfgang Coenning** was born in Reutlingen, Germany, in 1962. He received his diploma degree in electrical communication engineering and Ph.D. from the University of Stuttgart, Germany, in 1987 and 1995, respectively. From 1987 to 2001 he was with the Institute of Electrical and Optical Communication Engineering of the University of Stuttgart working on optoelectronic devices and optical communication systems. From 2001 to 2006 he has with DIAMOND GmbH in Leinfelden-Echterdingen, Germany, a subsidiary of DIAMOND SA in Losone, Switzerland. He has been responsible for research and development of customized optical systems in different areas as well as for production of these devices. Further he established the training center "Glasfaserschule" at DIAMOND GmbH for internal and external education in optics. In 2008 he finished off additional training in scientific teaching and has been with the University of Applied Sciences Esslingen, Germany since 2008.

**Hélène Debrégeas-Sillard** was born in France in 1972. She received the engineer degree from the Ecole Nationale Supérieure des Télécommunications (ENST) of Paris in 1994, and passed the aggregation of Mathematics in 1995. She joined Alcatel in 1997, where she focused on conception, simulations and characterizations of semiconductor InP telecommunications components. She was first in charge of 10 Gbit/s Electro-Absorption Modulator Lasers until an industrial transfer to Alcatel Optronics in 1999. Then she worked on tunable lasers within the joined laboratory Alcatel Thales III-V Lab, and passed her Ph.D. on that topic in 2006. Since then, she has been developing within Bell Labs Photonic Integrated Circuits for 100 Gbit/s applications, with ten laser sources independently modulated

at 10Gbit/s, flip-chipped on a Si submount, hybridized with SiO<sub>2</sub> Arrayed Waveguides.

**Alexander W. Fang** is the CEO and co-founder of Aurrion. He received his B.Sc. in Electrical Engineering with minors in Physics and Mathematics in 2003 from San Jose State University and his M.Sc. and Ph.D. in Electrical Engineering from the University of California, Santa Barbara (UCSB) in 2005 and 2008, respectively. His dissertation was on “Silicon Evanescent Lasers.” Alex is a leader in the field of silicon photonics and photonic integrated circuits. Alex has authored/coauthored over 70 papers in the field and has filed six patents. He has won a number of awards for the technology he developed together with Prof. Bowers and colleagues. Dr. Fang worked for Lawrence Livermore National Laboratory and Intel prior to founding Aurrion.

**Wolfgang Freude** was born in June 1944 in Germany. He received the Dipl.-Ing. (M.Sc.E.E.) and the Dr.-Ing. (Ph.D.E.E.) degrees in Electrical Engineering from the University of Karlsruhe in 1969 and 1975, respectively. He is Professor at the Institute of Photonics and Quantum Electronics and at the Institute of Microstructure Technology, Karlsruhe Institute of Technology (KIT). His research activities are in the area of optical OFDM, high-density integrated-optics with a focus on silicon photonics, photonic crystals and semiconductor optical amplifiers, and in the field of low-energy opto-electronic devices and protocols for optical access networks. He has published more than 190 papers, co-authored a book entitled “Optical Communications” (Berlin, Germany, Springer-Verlag 1991, in German), and authored and co-authored two book chapters on “Multimode Fibres” (Handbook of Optical Communications, Berlin, Springer-Verlag 2002, in German) and “Microwave Modeling of Photonic Crystals” (Photonic Crystals – Advances in Design, Fabrication, and Characterization, Berlin, Wiley-VCH 2004). Prof. Freude is an Honorary Doctor of the Kharkov National University of Radioelectronics, Kharkov, Ukraine, and a member of VDE/ITG (Verband der Elektrotechnik Elektronik Informationstechnik Informationstechnische Gesellschaft, Germany), IEEE, and OSA. Until 2010 he was Vice Chair of the IEEE Germany Photonics Society Chapter. From 2002 to 2006 he served as spokesman of the Research Training Group “Mixed fields and nonlinear interactions,” which was funded by the Deutsche Forschungsgemeinschaft (DFG) to support young researchers in their pursuit of a doctorate.

**Norbert Grote** studied physics at the Technical University of Aachen, Germany, from which he earned the M.Sc. (Dipl. Phys.) and Ph.D. degree in 1974 and 1977, respectively, working on III–V (GaAs, GaInP, GaAlP) based light-emitting diode lasers and related liquid-phase epitaxial material growth. In 1980 he joined the Heinrich-Hertz-Institut in Berlin where he was among the first to help establish the Integrated Optics Department, aiming at developing components for optical telecommunication systems, primarily on an InP basis. In this framework he has been engaged in III–V epitaxy and a variety of photonic and electronic (HBT) devices, including laser devices, and optical devices relying on polymer material. Cur-

rently, he is deputy head of the department, now named the Photonic Components Department after HHI became a member institute of the Fraunhofer Association in 2002. In this position he is supervising different R&D groups focusing on InP materials technology, laser devices, PICs, and hybrid integration technology using a PLC polymer platform. Over the years he has been extensively involved in the initiation and coordination of photonics-related national R&D programmes/projects in the public domain and of collaborative projects with companies. He has coordinated the EC funded FP-6 project MEPHISTO, and currently he is actively engaged in the EC projects EuroPIC and PARADIGM covering monolithic optical integration technology.

**Werner Hofmann** received his Dipl.-Ing. (M.Sc.) degree in electrical engineering and information technology in 2003 and the Dr.-Ing. (Ph.D.) degree in 2009, both from the Technical University of Munich, Germany. From 2003 to 2008 he has been with the Walter Schottky Institute where he was engaged in research on InP-based vertical-cavity surface-emitting lasers (VCSELs) including design, manufacturing and characterization. Subsequently he joined Connie Chang-Hasnain's group at the University of California, Berkeley, via a postdoctoral fellowship program granted by the DAAD (German Academic Exchange Service). At UCB he worked on the incorporation of high-contrast gratings (HCG) into long-wavelength VCSEL devices. Since 2010 he has been with the faculty of the Technical University of Berlin, Germany, working on ultra-high-speed surface emitters. Concurrently, he is a CTO of the Center of Nanophotonics at TU Berlin. He has authored or co-authored some 100 articles (including several invited) in scientific journals, conference proceedings and books. He is a recipient of the E.ON Future Award 2009, one of the most highly esteemed research awards sponsored by the German Industry. Dr. Hofmann is a member of the Association of German Engineers (VDI), and a member of the IEEE Photonics Society.

**Arkady Kaplan** is a photonics Design Lead in CeLight Inc. (USA, MD) responsible for the company core electro-optical components, utilizing more than 15 years of experience in R&D of advanced integrated electro-optical components and subsystems for the defense and commercial markets as well as academic research. Previously, he was with Elbit Systems Ltd., and at Tel Aviv University, Faculty of Engineering, where he received his Ph.D. (1999). He received his M.Sc. (1994) in Physics and Optical Engineering (Magna Cum Laude) from the Institute of Fine Mechanics and Optics, St. Petersburg, Russia. He is an author of multiple publications and inventor on about 25 patents and patent applications.

**Ian F. Lealman** became a Member of the IEEE in 2000. He graduated with a B.Sc. (Hons) in Physics from Southampton University, UK, in 1985 and received a Ph.D. in Physics from the University of Essex, UK, in 1999. He joined British Telecom (BT) labs in 1985 where he worked on the development of BH laser technology and was seconded to BT&D in 1989 to transfer the device it into production. He returned to BT labs in 1990 to continue research into a wide range of optoelectronic devices



including high speed semiconductor lasers, monolithic widely tuneable lasers and mode expanded lasers and semiconductor optical amplifiers. In 1996 he also became the project manager for BT's photonics research. From 2000 to 2003 Ian was Department Manager for active design and fabrication at the Corning research centre in the UK. From its inception in 2003 he was VP of Device Development as well product manager for semiconductor optical amplifiers at CIP. He has continued to work on the development and project management of optoelectronic devices since CIP's acquisition by Huawei in early 2012. He is a named inventor on nine granted patents and over 80 publications in journals and international conference proceedings.

**Juerg Leuthold** was born in July 1966 in Switzerland. He was awarded a Ph.D. degree in Physics from the Swiss Federal Institute of Technology (ETH) Zürich for work in the field of integrated optics and all-optical communications. From 1999 to 2004 he was affiliated with Bell Labs, Lucent Technologies in Holmdel, USA, where he performed device and system research employing III–V semiconductors and silicon optical bench technology for applications in high-speed telecommunications. Since July 2004 he has been a full Professor at Karlsruhe Institute of Technology (KIT), where he is heading both the Institute of Photonics and Quantum Electronics, and the Institute of Microstructure Technology. Juerg Leuthold is a Fellow of the Optical Society of America, a member of the Heidelberg Academy of Science, and has and is serving the community in many technical programme committees such as OFC, ECOC, CLEO and others. Besides these activities in committees he is currently chairing the Photonics Division of the Optical Society of America.

**Di Liang** received his B.Sc. degree in Optical Engineering from the Zhejiang University, Hangzhou, China, in 2002, and his M.Sc. and Ph.D. degrees both in Electrical Engineering from the University of Notre Dame, Indiana, USA, in 2004 and 2006, respectively. He studied silicon-on-insulator waveguide devices in his M.Sc. project, and switched to designing and fabricating GaAs-based, high-index-contrast in-plane lasers for high-power lasers and dense photonic integration in his Ph.D. project. He then joined Prof. John Bowers' silicon photonics group at the University of California, Santa Barbara, as a research specialist. Record-large InP-to-silicon direct wafer bonding and compact low-threshold hybrid silicon microring lasers have been demonstrated by him. At the end of 2009, he joined Hewlett-Packard Labs in Palo Alto, California, USA, to continue developing silicon photonic components and integrated circuits for future silicon optical interconnect systems. His research interests include silicon photonics, diode lasers, photodiodes and modulators, semiconductor materials, hybrid integration techniques and nanofabrication. He holds/has filed eight patents in total so far, and authored and co-authored over 80 papers, and has been a member of IEEE since 2002.

**Reinhold Ludwig** was born in 1952 in Lahnstein, Germany. He received the Ing. grad. degree from the Fachhochschule Koblenz in 1974 and the Dipl.-Ing. and Dr.-Ing. degrees from the Technical University Berlin in 1985 and 1993. In 1985 he

joined the Heinrich-Hertz-Institute (HHI) Berlin where he is involved in research on photonic components and systems. He worked as a visiting scientist at Nippon Telephone&Telegraph Co. (NTT), Japan, in 1991 and at Bell Labs, USA, in 1993. Since 1985 he has authored and co-authored more than 350 scientific papers, contributed to several book chapters and served in the TPC of the OFC. In 1996 he founded the first HHI spin-off company, LKF Advanced Optics GmbH, and served as CEO until the merger of LKF and u2t Innovative Optoelectronic Components GmbH in 2001. In 1999 his group received the Philip-Morris-Science Award and he was nominated for the Innovation Award of the German Bundespraesident. Dr. Ludwig is a member of the German Association for Electrical, Electronic & Information Technologies (VDE).

**Martin Möhrle** received his diploma degree in physics (M.Sc.) from the University of Stuttgart in 1988, and the Ph.D. degree from the Technical University of Berlin in 1992. In 1988, he joined the Fraunhofer Institute for Telecommunications, Heinrich-Hertz-Institute. He has more than 20 years experience and expertise in modeling, design, technology, development and fabrication of a large variety of semiconductor FP- and DFB-lasers, tunable lasers, surface-emitting lasers, electroabsorption-modulated lasers, optical amplifiers, flip-chip compatible devices and monolithically integrated devices. At HHI he is head of the laser development group and manages projects with national and international partners. He holds several patents on laser devices and is author/co-author of more than 80 papers.

**Denis Molin** received the engineering diploma of the Ecole Supérieure d'Optique, now Institut d'Optique Graduate School, in 2000. He joined the System Design Team in Corvis-Algety the same year and the Fiber Optic R&D Unit in Alcatel in 2001 where he worked on modeling long-haul WDM transmissions. He's now with Prysmian Group, Marcoussis, France, working on single-mode & multi-mode fibers and systems modeling for communications and data applications. His activities particularly include the design of new multi-mode fibers for high-speed data applications with improved bending and bandwidth performances, and the support of new developments in International Standardization bodies. He also works on multi-gigabit Ethernet system modeling with a particular attention paid to the interaction between VCSEL sources and multi-mode fibers. He has authored and co-authored numbers of papers and holds more than 15 patents.

**Pascale Nouchi** received an engineering degree in Physics and Chemistry from Ecole Supérieure de Physique Chimie Industrielles (ESPCI-ParisTech) in Paris, France in 1988. She received her Ph.D. degree in Optical Sciences from the University of Southern California in Los Angeles, in 1992. Her work was devoted to photorefractive effects in BSO crystals. She then joined the Fiber Optics Department of Alcatel, where she was involved in the design and development of new optical fibers for communications, leading the corresponding group since 1996. In 2004, she joined Draka co-heading the Optical Fiber Product R&D group, in charge of the development of new fibers. She is now with Thales, responsible for the Waves

and Signal Processing Laboratory. She has authored and co-authored more than 70 papers and 30 patents.

**David Payne** joined British Telecom (BT) labs in 1978 working on single-mode fibre splicing and connectors, development of fused fibre couplers and FTTP. He wrote the first internal paper on shared access networks in 1983, which led to him co-inventing TAPON the first Passive Optical Network. David then moved to amplified PONs culminating in 1991 in an experimental 50-million way split, 500-km range PON carrying  $16 \times 2.5$  Gbit/s wavelengths. In the latter 1990s he moved into business and traffic modeling examining the drivers and economic justification for large-scale deployment of FTTP. From 1999 Dave led BT's optical research activities and was awarded the Martlesham Medal for his contribution to optical access networks in 2005. From 2007 he was "Principal Consultant on Optical Networks" working on extended reach PONs for very low-cost FTTP solutions. In September 2007 he took early retirement from BT and spent some time with the Institute of Advanced Telecommunications at Swansea University. He is now Professor of Optical Network Architectures in the CTVR center at Trinity College Dublin.

**Richard Penty** studied for his undergraduate degree from 1983 to 1986 at the University of Cambridge where he received a "Double First" in Engineering and Electrical Sciences. He carried out his doctoral research in the Cambridge University Engineering Department on optical fibre devices for signal processing applications, receiving his Ph.D. in 1989. He was then an SERC IT Research Fellow and also a Research Fellow at Pembroke College, Cambridge, from 1989–1990. He then became a lecturer in Physics at the University of Bath from 1990–1995, followed by a spell as lecturer in Optical Communications (subsequently being promoted to Reader and Professor) at the University of Bristol from 1996–2001. He returned to Cambridge in 2001, and became Professor of Photonics in 2002. He is a Fellow of Sidney Sussex College, where he was Vice Master in 2008. His research interests include high-speed optical communications systems, high brightness lasers, optical amplifiers, high-speed and high-power semiconductor lasers and radio over fibre and LAN systems. He has been an author of in excess of 700 refereed journal and conference papers and is Editor-in-Chief of IET Optoelectronics. He is a co-founder of Zinwave Ltd.

**Karsten Rottwitt** received the M.Sc. degree in electrical engineering in 1990 from the Technical University of Denmark and in 1993 he received the Ph.D. degree also from the Technical University of Denmark. His Ph.D. was on soliton propagation through distributed erbium-doped fiber amplifiers. After he finished his Ph.D. he continued in a Post Doc position until 1995, when he then moved to AT&T Bell Labs, NJ, USA. Here he worked within the Submarine Systems department. In 1998 Karsten Rottwitt joined the Fiber Research department within Lucent Technologies, Bell Labs, where he worked on Raman amplifiers. In 2000 Karsten Rottwitt moved back to Denmark, and from 2000 to 2002 he was at the University of Copenhagen. In 2002 he got a position as associated Professor at the Technical University of Den-

mark, where he is now heading activities in fiber optics, including fiber devices and nonlinear effects in fibers. He has been involved with organizing several international conferences including program chair for the OSA topical meeting on Nonlinear Photonics and general chair of the OSA Topical meeting on Sensors. He holds several patents, has authored and co-authored more than 140 journal and conference papers, and two book chapters.

**Matthias Seimetz** was born in Berlin, Germany, in 1974. He received the Dipl.-Ing. (FH) degree in electrical engineering from the Technical University of Applied Sciences, Berlin, in 2000. From 2002 to 2010, he was with Fraunhofer Institute for Telecommunications, Heinrich-Hertz-Institut, Berlin, Germany, where his research focused on the design of spectrally efficient WDM networks, optical access networks, coherent optical communication and optical modulation. On the basis of a thesis on higher order optical modulation formats, he received the Ph.D. degree from the Technical University of Berlin (TU Berlin) in 2008. He has published numerous papers in peer-review scientific journals, made a correspondingly high number of contributions to major international conferences, and authored the Springer monograph “High-Order Modulation for Optical Fiber Transmission” which appeared in 2009. In 2010, he became professor at the Beuth University of Applied Sciences, Berlin, where his main research interests include spectrally efficient optical networks and high-speed wireless communication.

**Yasuo Shibata** received the B.E. and M.E. degrees in electrical engineering, and Ph.D. degree in integrated design engineering from Keio University in 1985, 1987 and 2010, respectively. In 1987, he joined NTT Optoelectronics Laboratories, Nippon Telegraph and Telephone Corporation (NTT), Kanagawa, Japan, where he has been engaged in research on optical switches, optical filters and integrated devices. He is currently with NTT Photonics Laboratories, engaged in research on modulators, tunable lasers, SOAs, and functional devices. Dr. Shibata is a member of the Institute of Electronics, Information and Communication Engineers (IEICE), the Japan Society of Applied Physics (JSAP) and IEEE/Photonics.

**Pierre Sillard** received the engineering diploma of the École Nationale Supérieure des Télécommunications, Paris, in 1994 and the Ph.D. degree in physics from the University of Paris VI in 1998. His thesis work was pursued at the Laboratoire Central de Recherches of Thomson-CSF (now Thales Research & Technology) on the subject of non-linear interactions in laser resonators. Since 1999 he has been working in the field of optical fibers and he is now with Prysmian Group in Marcoussis, France. His activities include modeling and characterizing new optical fibers for telecommunications, data and specialty applications. In 2004 he received the TR35 innovator award from MIT's Technology Review. He has authored and co-authored more than 110 papers and holds more than 40 granted patents. He is a member of the OSA and IEEE communications societies.

**Thomas Vallaitis** was born in 1978 in Böblingen. He received the Dipl.-Phys. degree in physics from the Technische Universität München (TUM) in 2004, and the Dr.-Ing. (Ph.D.) degree in Electrical Engineering from the Karlsruhe Institute of Technology (KIT) in 2010. His research is focused on linear and nonlinear properties of highly nonlinear silicon-organic hybrid waveguides and quantum dot semiconductor optical amplifiers. In 2010, Dr. Vallaitis joined the photonics integrated circuits group of Infinera Corp., Sunnyvale, CA. Dr. Vallaitis is a member of the IEEE photonics society and of the Deutsche Physikalische Gesellschaft (DPG).

**Herbert Venghaus** studied physics and earned a Ph.D. degree at the University of Hamburg. Subsequently he joined the Max-Planck-Institute for Solid State Research in Stuttgart and focused on optic and magneto-optic properties of III–V- and II–VI-semiconductors. In 1980 he started working at the Corporate Research Laboratories of Siemens AG (München and Erlangen) and in 1986 he joined the Heinrich-Hertz-Institute (Berlin), which became a Fraunhofer Institute in 2003. His main responsibility as a department head at HHI has been the development of Indium Phosphide-based optoelectronic integrated circuits (OEICs) with particular emphasis on monolithic integration. More recently he has shifted his primary interest to the identification of new, non-telecom applications of devices and technologies initially developed for fibre optic communication, and these new topics included the development of THz systems based on telecom devices or biosensors based upon planar resonator structures. He has been actively involved in various European projects and has also been a member of the program committee of various international conferences. He holds several patents, has published more than 80 scientific papers, various book chapters and has been editor of two books as well.

**Hans-Georg Weber** received the degrees Dr. rer.nat. and Dr. habil. in Physics from the Universities Marburg and Heidelberg in Germany in 1971 and 1976, respectively. From 1977 to 1978, he served as a Max-Kade-Fellow at Stanford University (USA), and from 1979 to 1984, he was a Heisenberg-Fellow at the University of Heidelberg. In 1985, he became head of a research group at the Heinrich-Hertz-Institut (HHI) in Berlin, Germany, and in 1996 he became Professor of Physics at the Technical University of Berlin. He has been retired since 2006 and serves as a consultant for the HHI in Berlin. He is author and co-author of more than 400 journal articles in the field of optical communications. From 2001 to 2008, he was coeditor of the Journal of Optical and Fiber Communications Reports. He is co-editor of the book “Ultrahigh-Speed Optical Transmission Technology.” In 1999, he received the Philip Morris award and was nominated for the Innovation Award of the German Bundespraesident.

**Hiroshi Yasaka** received the B.Sc. and M.Sc. degrees in physics from Kyushu University in 1983 and 1985, and Ph.D. degree in Electronics Engineering from Hokkaido University in 1993. In 1985 he joined Atsugi Electrical Communication Laboratories, Nippon Telegraph and Telephone Corporation (NTT). Since then to 2008, he engaged in research and development on semiconductor photonic devices

for optical fiber communication systems. In 2008 he joined the Research Institute of Electrical Communication (RIEC) at Tohoku University as a professor and has been engaging in research on highly functional semiconductor photonic devices and their monolithically integrated devices. Professor Yasaka is a member of the Institute of Electronics, Information and Communication Engineers (IEICE), the Japan Society of Applied Physics (JSAP), the Physical Society of Japan (JPS), and IEEE/Photonics.

# Index

## Symbols

$V_{\pi}$ , 344  
 $\alpha$ -parameter for modulator, 160  
3 dB bandwidth, 178, 283  
90 %-to-10 % recovery time, 541, 548, 550  
90° optical hybrid, 350, 604

## A

absorption, 513  
acousto-optic tunable filter, 425  
active region, 519  
air-clad fibre, 483  
all-pass filter, 377  
alpha-factor, 146, 229, 528, 545, 550, 552  
amplified spontaneous emission, 480, 532, 585, 631  
amplitude shift keying, 589  
apodization, 402  
apodized fibre Bragg grating, 380  
arrayed waveguide grating, 392, 427  
attenuation of standard single-mode, 474  
Auger recombination, 522, 540, 629  
avalanche photodiode, 291

## B

backhaul network, 40  
backward-pumped Raman amplifier, 487  
balanced four-branch receiver, 356  
balanced receiver, 360  
band-edge filter, 411  
band-pass filter, 376, 411, 413  
bandfilling, 192  
bandgap shrinkage, 193  
bend-optimized fibre, 74, 79, 88  
blaze angle, 389

blaze wavelength, 389  
booster amplifier, 526  
broadband PON, 38  
bulk SOA, 520, 550  
buried heterostructure, 523  
butt-joint integration, 157

## C

carrier cooling, 543  
carrier density pulsation, 211  
carrier heating, 543  
cascaded microrings, 420  
cascaded MR filter, 421  
chirp, 146, 160, 228, 229, 232, 234  
chirp, facet-reflection induced, 161  
chirp, static, 162  
chirped grating, 403  
chromatic dispersion, 611  
clock recovery, 601  
co-pumped Raman amplifier, 487  
coherent detection, 336, 579  
coherent optical orthogonal frequency-division multiplexing, 331  
coherent OTDM receiver, 604  
colourless AWG, 396  
complex refractive index, 528  
confinement factor, 529  
constellation diagram, 328, 590  
contrast factor, 407  
coplanar strip, 309  
coplanar strip electrode, 251  
counter-pumped Raman amplifier, 487  
coupled mode theory, 383  
coupling length, 385  
critical coupling, 420  
cross-phase modulation, 11, 581

crosstalk, optical, 161

## D

dark current, 284  
 DBR laser, 195  
 DBR laser coarse tuning, 196  
 DBR laser fine tuning, 197  
 delay line interferometer, 337  
 detection limit, 285  
 dielectric multi-layer filter, 410  
 differential binary phase shift keying, 589  
 differential drive (push-pull) mode, 254  
 differential phase shift keying, 266  
 differential quadrature phase shift keying, 269, 328  
 diffraction grating, 387  
 diffraction order, 388  
 digital supermode DBR laser, 206  
 directional coupler, 383, 386, 457  
 dispersion, 480  
 dispersion compensation, 611  
 dispersion slope, 378  
 dispersion-tailored fibre, 73, 77

## E

echelle grating, 389, 427  
 edge filter, 414  
 effective alpha-factor, 545, 549  
 effective carrier lifetime, 540, 551  
 effective noise figure, 492  
 electro-optic (Pockels) effect, 241  
 electroabsorption (EA) modulator, 157, 159, 161, 164, 177, 179, 231  
 emitter-follower driving, 180  
 energy level diagram of  $\text{Er}^{3+}$ , 475  
 erbium-doped fibre amplifier, 474  
 etalon, 405  
 external cavity tunable laser, 216

## F

Fabry–Pérot interferometer, 405  
 ferrule, 444  
 fibre coupler, 383, 457  
 fibre coupler categories, 462  
 fibre dispersion, 6, 62, 72  
 fibre loss, 61, 77  
 filter dispersion, 378  
 finesse, 407  
 flame hydrolysis, 395  
 flat top AWG, 394  
 forward-pumped Raman amplifier, 487

four-branch 90° hybrid, 350  
 four-wave mixing, 11, 582  
 Franz–Keldysh effect, 231, 240  
 free carrier absorption, 191, 629  
 free spectral range, 196, 208, 210, 261, 388, 394, 407, 419  
 frequency-dependent gain, 292

## G

G-centre (in nanopatterned Si), 635  
 gain dynamics, 539  
 gain guiding, 523  
 gain-flattening filter, 381, 411, 414  
 GCSR laser, 205  
 gigabit PON, 38  
 Gires–Tourmois interferometer, 408, 424  
 Gray coding, 328  
 group delay, 378, 379  
 group delay ripple, 381  
 group velocity, 250

## H

heterodyne pump-probe technique, 547  
 heterostructure, 516  
 high power connectors, 454  
 high-pass filter, 376  
 higher order dispersion, 612  
 higher order filter, 420

## I

index guiding, 523  
 induced emission, 514  
 inline amplifier, 526  
 input power dynamic range, 550, 554  
 interband transitions, 540  
 interleaver, 422  
 intraband transitions, 542  
 IQ-modulator, 332, 343, 345, 591

## K

Kerr effect, 8, 10, 11, 242, 489

## L

large-signal analysis, 144  
 laser, 205  
 learning curve, 30  
 linewidth broadening function, 519  
 linewidth enhancement factor, 146  
 Littrow configuration, 388  
 long-period FBG, 403  
 low-pass filter, 376



lumped electrode structure, 246

## M

Mach-Zehnder delay interferometer, 266  
 Mach-Zehnder interferometer, 233, 428  
 Mach-Zehnder modulator, 233, 591  
 material dispersion, 7  
 material power gain, 518, 528  
 microring filter, 428  
 microring resonator, 417  
 minimum-phase filter, 378  
 mirror loss, 152  
 mode selection, 195  
 modulator, optical, 157  
 Moore's law, 626  
 MSM photodetector, 289  
 multimode fibre, 56, 62, 63  
 multiple-band filter, 413

## N

n-i-n isotype MZI modulator, 251  
 noise factor, 532  
 noise figure, 481, 502, 532, 550  
 noise figure of Raman amplifier, 492  
 nonlinear  $K$ -factor, 142  
 nonlinear gain compression factor, 545  
 nonlinear optical loop mirror, 596  
 notch filter, 376

## O

on-off Raman gain, 488  
 optical 90° hybrid, 349  
 optical circulator, 464  
 optical connector, 442  
 optical fibre cable, 83  
 optical gain, 152  
 optical gate, 595, 597, 600  
 optical isolator, 466  
 optical Kerr effect, 498  
 optical phase-shift keying, 266  
 optical pulse compression, 585  
 optical pulse generator, 583  
 OTDM demultiplexer, 607  
 OTDM transmission, 576

## P

p-i-n structure, 245  
 parametric amplifier, 502  
 passive optical network, 37  
 patch cord, 449

phase matching, 582  
 phase modulation formats, 328  
 phase shift keying, 589  
 phase velocity, 250  
 phase-diversity homodyne receiver, 604  
 phase-shift method, 379  
 photoreceiver, 312  
 plasma effect, 239  
 Pockels effect, 241  
 polarization dependence, 479  
 polarization mode dispersion, 7, 613  
 polarization-diversity, 606  
 polarization-independent optical isolator, 468  
 polarization-maintaining connectors, 451  
 population inversion, 515  
 power splitter, 386  
 power-equalization filters, 377  
 preamplifier, 526  
 propagation constant, 393  
 pulse cleaner, 583, 586  
 pulse compressor, 583  
 pump depletion, 493  
 push-pull operation, 235

## Q

Q-factor, 162, 176, 285, 428, 561, 564  
 quadrature amplitude modulation, 590  
 quadrature modulator, 342  
 quantum dot (QD) SOA, 522, 548, 550  
 quantum-confined Stark effect, 231, 240  
 quantum-confined stark effect, 157  
 Quantum-well (QW) SOA, 521, 550

## R

Raman amplifier, 485  
 Raman effective length, 487  
 Raman scattering, 636  
 rate equations, 141, 476  
 Rayleigh scattering, 5, 62, 495  
 receiver sensitivity, 285  
 reflective SOA, 564  
 refractive index variation, 194  
 relaxation oscillation frequency, 141  
 resolving power, 389  
 responsivity, 282, 288  
 return on capital expenditure, 30  
 ridge waveguide, 523  
 rod-type amplifier, 484

## S

sampled grating, 200

saturation input power, 538, 550, 551  
saturation power, 536  
scattering matrix, 458  
selective area growth, 157  
self-phase modulation, 10, 581  
short-cavity edge-emitting laser, 153  
shot noise, 284  
Si interstitial, 635  
silicon photonics, 426  
single-pass power gain, 531, 549, 550  
small signal modulation, 141  
small-signal frequency response, 141  
soliton, 581  
spectral efficiency, 326  
spectral hole burning, 542  
spontaneous emission, 513  
SSG-DBR laser, 204  
standardisation of fibres, 70, 73  
standardised ferrule, 444  
standards for optical connectors, 445  
star 16-QAM, 592  
star coupler, 463  
star QAM, 329  
stimulated Brillouin scattering, 9, 503  
stimulated Raman scattering, 10, 636  
super-structure grating, 204  
surface relief grating, 390

**T**

tandem-QPSK transmitter, 335  
tap coupler, 386  
thermal mismatch, 645

thermal noise, 284  
thin-film filter, 410  
timing jitter, 584  
transceiver package, 140  
transit time-limited bandwidth, 283  
transmission grating, 390  
travelling-wave electrode, 246  
TTG laser, 210  
tunable balanced receiver, 358  
tunable twin guide laser, 210  
tunable vertical cavity surface emitting laser,  
214

**U**

uncooled EA/DFB laser, 173

**V**

volume-phase holographic grating, 390

**W**

wafer bonding, 643  
waveguide dispersion, 7  
wavelength and power locker, 209  
wavelength conversion, 505  
WDM PON, 39

**Y**

Y-laser, 205